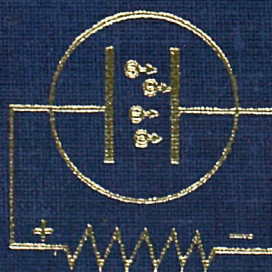
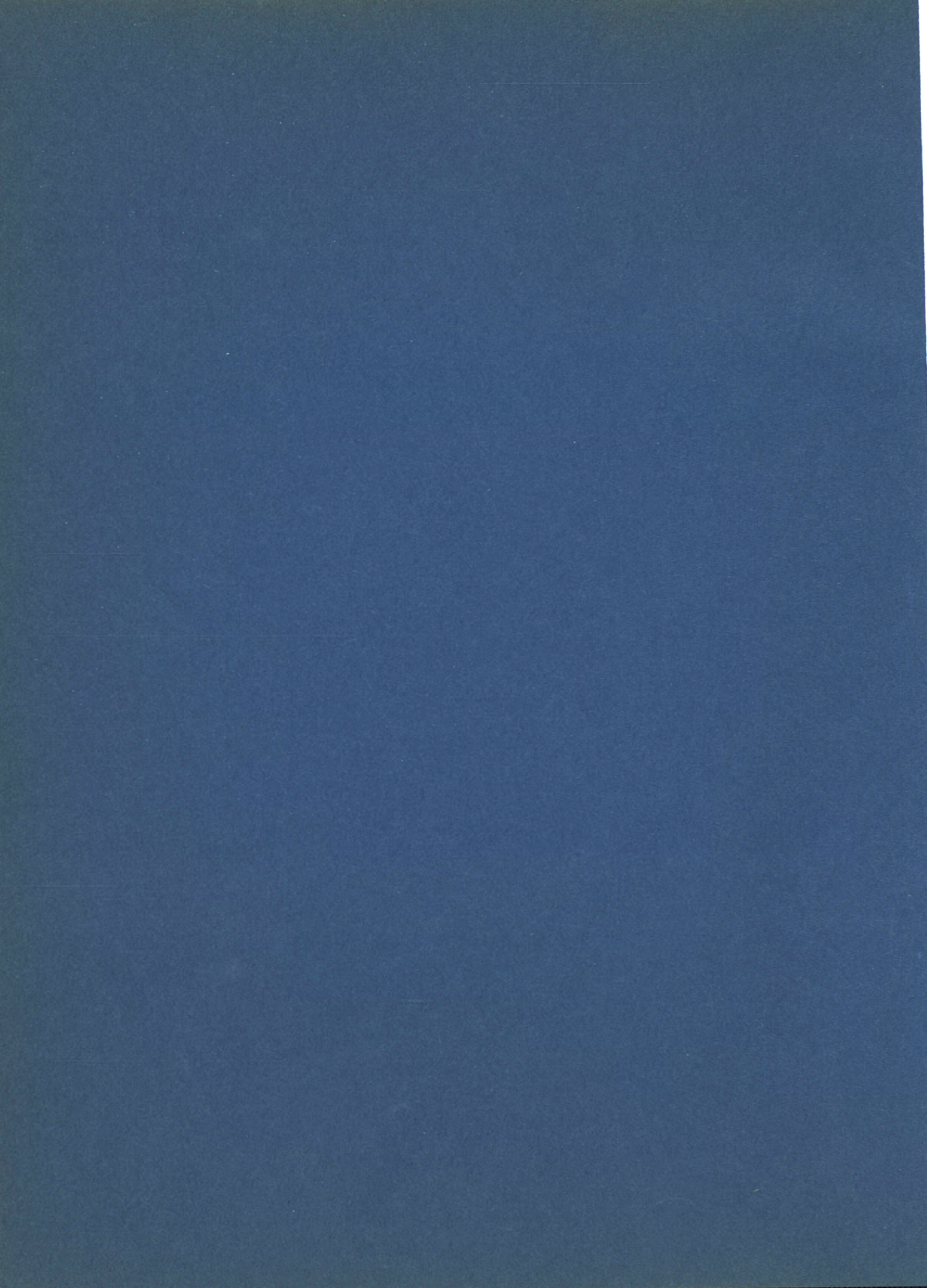


EUROPEAN ATOMIC ENERGY COMMUNITY
COMMUNAUTE EUROPEENNE DE L'ENERGIE ATOMIQUE
EURATOM

THERMIONIC
ELECTRICAL POWER GENERATION
PRODUCTION THERMO-IONIQUE
D'ENERGIE ELECTRIQUE



SYMPOSIUM
Sirena, Italy - May 27-31, 1963



EUROPEAN ATOMIC ENERGY COMMUNITY
COMMUNAUTE EUROPEENNE DE L'ENERGIE ATOMIQUE
EURATOM

SECOND INTERNATIONAL CONFERENCE ON
THERMIONIC ELECTRICAL POWER GENERATION

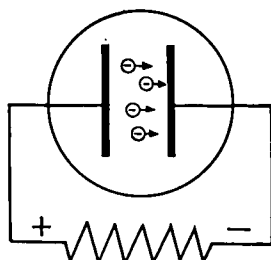
Stresa, Italy - May 27-31, 1968

DEUXIEME CONFERENCE INTERNATIONALE
SUR LA PRODUCTION
THERMO-IONIQUE D'ENERGIE ELECTRIQUE

Stresa, Italie - 27-31 mai 1968

under the auspices of the
European Nuclear Energy Agency - OECD
organized by Euratom - Joint Nuclear Research Centre, Ispra (Italy)

sous l'égide de
l'Agence Européenne pour l'Energie Nucléaire - O.C.D.E.
organisée par Euratom - Centre Commun de Recherche Nucléaire, Ispra (Italie)



Published by the Euratom Center for Information and Documentation

Publié par le Centre d'Information et de Documentation

EUR 4210 f,e

LEGAL NOTICE

The Commission of the European Communities and its departments are not responsible for the use which could be made of the following information.

Price : FB 1 000.— DM 80.— FF 100.— Lit. 12 500 Fl. 72.50 \$ 20.—

PROGRAM COMMITTEE

Dr. H. Neu (Chairman)	Ispra Joint Research Centre Establishment, Euratom, Ispra, Italy
Dr. L. Agnew	International Atomic Energy Agency, Vienna, Austria
Mr. B. Devin	Commissariat à l'Energie Atomique, Saclay, France
Dr. G. Hatsopoulos	Thermo Electron Corp., Waltham, Massachusetts, United States
Dr. R. Langpape	Brown, Boveri u. Cie., Mannheim, Germany
Dr. J. Myatt	Atomic Energy Research Establishment, Harwell, United Kingdom

F o r e w o r d

The first "International Conference on Thermionic Electrical Power Generation" was held in London, in October 1965. This second conference about two and a half years after the London conference gives evidence of the remarkable progress in thermionic energy conversion which has taken place since that time. The strong participation of scientists from the USSR has for the first time enabled an intensive exchange of information between East and West and has given the opportunity for further personal contacts between the Soviet scientists and their Western colleagues.

The proceedings include all papers which have been accepted or invited by the Program Committee and submitted to the conference Secretariat. Papers are reproduced in their original form as submitted by the authors. In addition, the proceedings include a contribution "Survey of Experimental Work in the USSR" by Dr. Y.A. DANILOV of the Moscow Aviation Institute, (Consultant of USSR State Committee for the Utilization of Atomic Energy) which was invited during the conference, and two introductions for the panel discussion by Dr. Gerald F. TAPE, Commissioner of the USAEC and Dr. Y.A. DANILOV.

The discussions which took place in the conference, are attached at the end of the respective papers, with the exception of Session D where the discussions are placed at the end of the Session.

I am grateful for the cooperation of the contributors who submitted their text early enough for publication in these proceedings. Unfortunately, no contributions or corrections of transcripts could be retained, which arrived later than August 8th. This deadline has been fixed in order to enable quick distribution of the proceedings, which is in the interest of all.

Further, I wish to thank Mrs. Dorpema of Ispra for providing the transcripts of the discussions, Dr. L.K. Hansen for his great help in editing these and Mrs. Stalpaert from the Euratom Information and Documentation Centre in Brussels for managing the publication of the proceedings.

Helmut NEU

Ispra, 8.8.1968

1. The first part of the document discusses the importance of maintaining accurate records of all transactions and activities. It emphasizes the need for transparency and accountability in financial reporting.

2. The second part of the document outlines the various methods and techniques used to collect and analyze data. It includes a detailed description of the experimental procedures and the statistical analysis performed.

C O N T E N T S

	<u>Page</u>
<u>OPENING SESSION</u>	
Welcome on behalf of the sponsoring organization, by Mr. L. BOXER, European Nuclear Energy Agency.	21
Welcome on behalf of the organizing institution, by Prof. H. KRAMERS, Euratom Research Establishment, Ispra.	22
Introduction to the Conference, by Dr. H. NEU, Euratom Research Establishment, Ispra.	24
<u>SESSION A "CONVERTER PERFORMANCE"</u>	
Chairman : Dr. R. W. PIDD	
Vice-Chairman : Dr. R. PRUSCHEK	
A-1 Summary of Applied Research Program in Thermionic Conversion during Recent Years F. RUFEB, D. LIEB and L. van SOMEREN, Thermo Electron Corporation, Waltham, Massachusetts, USA	29
A-2 Characteristics of a Thermionic Converter with a Chloride-Vapor-Deposited Tungsten Emitter and a Nickel Collector V. C. WILSON, General Electric Research and Development Center, Schenectady, New York, USA	45
A-3 Essais d'un convertisseur du type nucléaire muni d'un réservoir de césium à adsorption Ph. DEFRANOULD, Laboratoires de Recherches Générales, Compagnie Française Thomson Houston, France	51
A-4 Examen des couches réfractaires pyrolytiques au moyen du microscope électronique secondaire à balayage G. BLET et O. CAHEN, Laboratoires de Recherches Générales, Compagnie Française Thomson Houston, France	57
A-5 Thermionic Converter Technology P. ROUKLOVE, Jet Propulsion Laboratory, Pasadena, California, USA	61
A-7 High Pressure Cesium Thermionic Converter with a Cold Region B. STEFANOV, L. ZARCOVA, Bulgarian Academy of Sciences, Institute of Electronics, Sofia, Bulgaria	75
A-8 Convertisseur thermo-ionique chauffé par flamme	81

	<u>Page</u>
Mlle. LATOUCHE-HALLE, Laboratoires de Recherches Générales, Compagnie Française Thomson Houston, France	81
A-9 Arc-Mode Thermionic Converter Performance: Measurements and Interpretation	
A. E. CAMPBELL, Jr. and A. O. JENSEN, Electro-Optical Systems, Pasadena, California, USA	87
A-10 Technologie des convertisseurs thermo-ioniques plans et cylindriques	
A. M. SHROFF, Compagnie Générale de Télégraphie sans Fil, Centre de Physique Electronique et Corpusculaire, Corbeville, Orsay, France	103
A-11 Bilan des études de durée de vie des convertisseurs thermo-ioniques en laboratoire	
J. BLIAUX, M. CLEMOT, J. P. DURAND et B. GAYTE, Centre d'Etudes Nucléaires de Saclay, France	113
A-13 Investigation of a Ne-A Thermionic Generator	
M. BACAL, M. CRISTESCU and C. VOICI, Institute for Atomic Physics, Bucharest, Rumania	125
A-14 Module Thermo-ionique Nucléaire tout-métal	
B. DEVIN, J. P. DURAND, P. RAGOT, Centre d'Etudes Nucléaires de Saclay, France	133

SESSION B "INTEGRATED SYSTEMS"

Chairman : Mr. R. C. HOWARD
Vice-Chairman: Dr. S. V. RYABIKOV

B-1 The In-Core Thermionic Reactor as a Space Power Source	
H. ANDRAE, D. BUDNICK, F. GROSS, W. JAHNS, K. JAN- NER and A. JESTER, Brown, Boveri u. Cie AG., Mannheim; Interatom, Bensberg; Siemens AG., Erlangen, Germany	143
B-2 Results of Studies on Various Fast and Thermal Thermionic Reactor Systems	
R. PRUSCHEK, S. DAGBJARTSSON, D. EMENDÖRFER, M. GROLL, W. HAUG, B. RÖHRBORN, H. UNGER and E. WOLF, Institut für Kernenergetik, Universität Stuttgart, Germany	157
B-3 Multimegawatt Thermionic Reactor Systems for Space Appli- cations	171

	<u>Page</u>
C. D. SAWYER, P. R. HILL and D. R. WILKINS, Vallecitos Nuclear Center, General Electric Co., Pleasanton, California, USA	171
B-4 Thermionic Electric Propulsion System Characteristics and Capabilities	
W. A. RANKEN and E. W. SALMI, Los Alamos Scientific Laboratory, University of California, Los Alamos, New Mexico, USA	185
B-5 Thermionic Reactors for Electric Propulsion-Parametric Studies	
W. G. HOMEYER, C. A. HEATH and A. J. GIETZEN, Gulf General Atomic Inc., San Diego, California, USA	201
B-6 External-Fuel Thermionic Reactors	
M. J. ABBATE, C. L. EISEN, B. RAAB and A. SCHOCK, Republic Aviation Division of Fairchild Hiller Corporation, Farmingdale, New York, USA	221
B-7 Uninsulated In-Core Thermionic Diode Concept	
J. P. DAVIS, H. G. GRONROOS, Jet Propulsion Laboratory, Pasadena, California, USA	237
B-8 A Heat Pipe Thermionic Reactor Concept	
P. FIEBELMANN, H. NEU and C. RINALDINI, Euratom Joint Research Center, Ispra, Italy	243
B-9 Out-of-Core Thermionic Space Power	
W. E. LOEWE, Lawrence Radiation Laboratory, University of California, Livermore, California, USA	263
B-10 Stability and Control Considerations for Thermionic Reactors	
H. G. GRONROOS and J. P. DAVIS, Jet Propulsion Laboratory, Pasadena, California, USA	273
B-11 Development of a 100 Watt (e) Isotope Thermionic Electrical Power Module	
E. W. WILLIAMS, General Electric Missile and Space Division, Valley Forge, Penn., USA and R. C. HOWARD, Thermo Electron Corporation, Waltham, Massachusetts, USA	281
B-12 SNAP-13, Generator Development Program	
J. B. DUNLAY and R. C. HOWARD, Thermo Electron Corporation, Waltham, Massachusetts, USA	297
B-13 Design and Characteristics of an Actinium Fueled Thermionic Generator	
A. DE TROYER and E. NEVE de MEVERGNIES, Union Minière, Brussels, Belgium; M. J. BRABERS, P. DE JONGHE, Centre d'Etude de l'Energie Nucléaire, Mol-Donk, Belgium; G. GAMMEL, F. GROSS, M. F. KOSKINEN and R. LANGPAPE, Brown Boveri u. Cie AG., Heidelberg, Germany	305

	<u>Page</u>
B-15 A Miniature Atomic Battery Based on Thermionic Conversion N. S. RASOR, K. A. GASPER and J. G. DeSTEESE, McDonnell Douglas Corporation, Donald W. Douglas Laboratories, Richland, Washington, USA	337
B-16 Thermionic Electrical Power Generation from Re-Entry Plasmas K. J. TOURYAN and M. M. SLUYTER, Sandia Laboratory, Albuquerque, New Mexico, USA	345
 <u>SESSION C "IN-PILE TESTING"</u>	
Chairman : Mr. B. DEVIN	
Vice-Chairman : Dr. Yu. S. YURIEV	
C-1 In-Reactor Thermionic Converter Testing Experience at General Electric J. E. van HOOMISSEN and D. J. HOTSLAG, Vallecitos Nuclear Center, General Electric Co., Pleasanton, California, USA	353
C-2 Converter SD-4 Design and Summary of Test Results R. C. HOWARD and J. B. DUNLAY, Thermo Electron Corporation, Waltham, Massachusetts, USA	365
C-3 Long-Term Operations of In-Pile and Out-of-Pile Thermionic Converters J. W. HOLLAND, M. K. YATES, D. E. SCHWARZER and J. KAY, Gulf General Atomic Inc., San Diego, California, USA	385
C-4 Retention of Fission Gases in the UO_2 Phase of $MoUO_2$ - Cermets Irradiated at High Temperatures. W. A. RANKEN, M. C. CHANEY and A. J. PATRICK, Los Alamos Scientific Laboratory, University of California, Los Alamos, New Mexico, USA	411
C-5 Expériences de conversion thermo-ionique "SIRENE" en pile et examen après irradiation du convertisseur "SIRENE 302" J. BLIAUX, M. CLEMOT, B. DEVIN et P. DUMAS, Centre d'Etudes Nucléaires de Saclay, France	421
C-6 Laboratory Life-Test and In-Pile Irradiation Studies of Cylindrical Thermionic Converters A. JESTER, F. GROSS, H. HOLICK, R. KRAPF and R. ZÖLLER, Brown, Boveri u. Cie, AG., Mannheim, Central Research Laboratory, Heidelberg, Germany	437
C-7 Post-Irradiation Investigations of UO_2 -Fueled Thermionic Emitters F. GROSS and R. ZÖLLER, Brown, Boveri u. Cie. AG., Mannheim, Central Research Laboratory, Heidelberg, Germany	451

SESSION D "HEAT PIPE SYSTEMS"

Chairman : Dr. G. M. GROVER
Vice-Chairman : Dr. C. A. BUSSE

Invited Paper: Dr. C. A. BUSSE "Heat Pipe Research in Europe" 461

D-1 Advances in Heat Pipe Technology

G. M. GROVER, J. E. KEMME and E. S. KEDDY, Los Alamos Scientific Laboratory, University of California, Los Alamos, New Mexico, USA 477

D-2 High Temperature Lithium Heat Pipes

C. A. BUSSE, F. GEIGER and H. STRUB, Euratom Joint Research Center, Ispra, Italy; M. PÖTZSCHKE and G. KRAFT, Metallgesellschaft AG., Frankfurt/M., Germany 495

D-3 Pressure Balance and Maximum Power Density at the Evaporation Gained from Heat Pipe Experiments

F. REISS and K. SCHRETZMANN, Institut für Neutronenphysik und Reaktortechnik, Kernforschungszentrum Karlsruhe, Germany 507

D-4 Détermination théorique et expérimentale de la puissance thermique limite transférée par des caloducs à sodium

E. SCHMIDT et R. SEMERIA, Centre d'Etudes Nucléaires de Grenoble, Grenoble, France 515

D-5 Heat Pipe Design Theory

E. van ANDEL, Euratom Joint Research Center, Ispra, Italy 529

D-6 Liquid-Vapor Interaction and Evaporation in Heat Pipes

A. BÄHR, E. BURCK, W. HUFSCHMIDT, Euratom Joint Research Center, Ispra, Italy 543

D-7 Résultats préliminaires d'une étude sur les caloducs à haute température

M. ARMAND et A. M. SHROFF, Compagnie Générale de Télégraphie sans Fil, Groupement Scientifique et Technique, Domaine de Corbeville, Orsay, France 557

Discussions of Papers Session D

SESSION E "MATERIALS"

Chairman : Dr. A. M. SHROFF
Vice-Chairman: Dr. Yu. L. DANILOV

E-1 Chemical Vapor-Deposition of Tungsten Emitters of (110) Preferred Crystal Orientation

R. G. HUDSON, T. TAGAMI and L. YANG, Gulf General Atomic Inc., San Diego, California, USA 565

E-2 Fuel and Fission Product Transport Through Chemically Vapor-Deposited Fluoride Tungsten

L. YANG and R. G. HUDSON, Gulf General Atomic Inc., San 575

	<u>Page</u>
Diego, California, USA	
E-3 Dépôt par décomposition thermique en phase vapeur de tungstène, rhénium et niobium et d'alliage niobium tungstène A. M. SHROFF, Compagnie Générale de Télégraphie sans Fil, Groupement Scientifique et Technique, Domaine de Corbeville, Orsay, France	589
E-4 Deposition of Tungsten-Layers on Molybdenum and Interdiffusion M. PEEHS and H. STEHLE, Siemens AG., Zentrale Entwicklung und Forschung, Erlangen, Germany	603
E-5 Metal-To-Ceramic Seals for Thermionic Converters C. M. CAPPELLETTI and C. A. BUSSE, Euratom Joint Research Center, Ispra, Italy; E. A. DÖRRE, Feldmühle AG., Plochingen, Germany	613
E-6 Scellements céramique-métal A. M. SHROFF et S. ESNAUD, Compagnie Générale de Télégraphie sans Fil, Groupement Scientifique et Technique, Domaine de Corbeville, Orsay, France	633
E-7 Multi-Foil Thermal Insulation Using Oxide Particle Layer Separation J. B. DUNLAY, Thermo Electron Corporation, Waltham, Massachusetts, USA	639
E-8 A Special Technique for Manufacturing Insulating Collector Multilayer Tubes M. PEEHS, H. SCHÖRNER and H. STEHLE, Siemens AG., Zentrale Entwicklung und Forschung, Erlangen, Germany	647
E-9 Insulating Materials of Thermo-Emission Converters R. G. BELYANINA, V. L. BONDARENKO, A. A. BORISOVA, I. N. GORELOV, Yu. V. DVINAKIKH, I. P. ZASORIN, J. I. IEVLEVA, A. A. KOROLYOV, A. D. KUNKINA, N. P. MAXIMOV, B. A. MALYKH, V. P. SHAROV, I. M. SARATOV and D. D. YAKOVLEVA, Institute of Physics and Power Engineering, Obninsk, USSR	655
E-10 On the Effect of Barium on Converter Materials R. HENNE, Deutsche Versuchsanstalt für Luft- und Raumfahrt, e. V., Institut für Energiewandlung und Elektrische Antriebe, Stuttgart-Vaihingen, Germany	671
E-11 Thermal Contact Resistance in Cylindrical Elements in Thermionic Energy Converters Yu. I. DANILOV, V. K. KOSHKIN, T. V. MIKHAILOVA, Yu. S. MIKHEEV and S. A. ORLIN, USSR	683
E-12 Utilisation des alliages de titane en conversion thermo-ionique. M. CLEMOT, J. P. DURAND et L. SEGURENS, Centre d'Etudes	699

	<u>Page</u>
Nucléaires de Saclay, et E. R. JOSSO, Société Metallurgique d'Imphy, France	699
E-14 A Low Swelling, Oxide Fueled Thermionic Emitter H. HÜBNER, K. JANNER, M. PEEHS and H. STEHLE, Siemens AG., Zentrale Entwicklung und Forschung, Erlangen, Germany	711
E-15 Thermal Resistance of Multilayer Cylindrical Elements in the Thermionic Converters E. S. A. ARKIN, S. F. KUKUSHKIN, H. A. MURINSON, B. G. OGLOBIN, P. Z. CHEREPANOV, V. S. CHEKHOVICH, The Academy of Sciences, Moscow, USSR	721
E-16 High Temperature Compatibility of Refractory Metals in Contact with Refractory Materials J. J. HUET and J. VANGEEL, Centre d'Etude de L'Energie Nucléaire, Mol, Belgium	731
E-17 Etude de la soudure par diffusion du molybdène G. FUSTIE, B. JACQUIN, Société Bocuze, Les Echets, France, et J. P. DURAND, M. CLEMOT, Centre d'Etudes Nucléaires de Saclay, France	749
E-18 Investigation of Diffusion Interaction and Structural Stability of Cathode Material V. N. BYKOV, L. V. PAVLINOV, Yu. A. GORBAN, M. I. ZAKHAROVA, A. A. KOROLEV, V. A. MALYKH, I. P. MUKHIN, A. I. NAKONECHNIKOV, B. A. NEVZOROV, A. V. FROLOV, A. S. SHATALIN, USSR	761
E-19 Cermets as Material for Thermionic Emitters D. SCHMIDT, Deutsche Versuchsanstalt für Luft- und Raumfahrt e. V.; G. ONDRACEK, Kernforschungszentrum, Karlsruhe und E. GEBHARDT, Max-Planck-Institut für Metallforschung, Stuttgart, Germany	773
E-20 Cesium Sorption in Materials for Thermionic Converters M. K. YATES and G. O. FITZPATRICK, Gulf General Atomic Inc., San Diego, California, USA	783
E-21 Sur les applications aux études des émetteurs thermo-ioniques d'un nouveau réactif du molybdène R. HASSON, Centre d'Etudes Nucléaires de Saclay, France	795

SESSION F "CONVERTER AND SYSTEM DESIGN ANALYSIS"

Chairman : Dr. J. E. van HOOMISSEN
Vice-Chairman : Dr. G. M. GRAZIANOV

F-1 Theory of Thermionic Converter Operation with Applications to Thermionic Reactor Analysis D. R. WILKINS, C. D. SAWYER and P. R. HILL, General Electric Vallecitos, Pleasanton, California, USA	799
---	-----

	<u>Page</u>
F-3 Comparison of Methods for Calculating Radiative Heat Transfer A. SCHOCK and M. J. ABBATE, Republic Aviation Division of Fairchild Hiller Corporation, Farmingdale, New York, USA	813
F-4 Methods of Calculation and Optimization of Thermionic Electrogenerating Elements I. S. MOSEVITSKY, Kurchatov Institute of Atomic Energy, Moscow, USSR	821
F-5 Thermionic Converter Electrical Characteristics with Matrix Circuit Connections G. I. GUTSHIN, A. P. KOLMAKOV, E. B. PERESLAVTSEV, V. Ya. PUPKO, V. I. SUBBOTIN, G. M. CHERNUKHINA and Yu. S. YURIEV, Institute of Physics and Power Engineering, Obninsk, USSR	833
F-7 Theoretical Study of Transient Thermal Conditions During the Start-up of a Thermionic Converter E. S. A. ARKIN, A. N. LUPPOV, H. A. MURINSON, B. G. OGLOBLIN, P. Z. CHEREPANOV, The Academy of Sciences, Moscow, USSR	845
F-10 Failure Models and Reliability Analysis of Thermionic Converter Component Parts B. B. DIAKOV, Academy of Sciences of the USSR, A. F. Yoffe Physical Technical Institute, Leningrad, USSR	853
F-12 Analysis and Optimization of "Full-Length" Diodes A. SCHOCK, Republic Aviation Division of Fairchild Hiller Corporation, Farmingdale, New York, USA	865

SESSION G "THEORY OF CONVERTERS"

Chairman : Dr. J. BOHDANSKY

Vice-Chairman: Dr. Ch. WARNER

Invited Paper: Comments on Plasma Theories for Cesium Diodes by G. N. HATSOPOULOS	881
G-1 The Spacing Effect in the Ignited Mode Diode L. K. HANSEN, Institute for Theoretical Physics, Ruhr-University, Bochum, Germany	899
G-2 Theory of the Low-Voltage Arc in the Cesium Thermionic Converter E. B. SONIN, Institute of Semiconductors, Academy of Sciences Leningrad, USSR	911
G-4 The Voltage Drop of the Ignited Mode as a Function of Current Density B. SAGGAU and H. STRECKER, Institut für Gasentladungstechnik und Photoelektronik, Universität Stuttgart, Germany	923
G-5 Theoretical Considerations of the Ignited Mode C. WARNER, Atomics International, Canoga Park, California, USA	931

	<u>Page</u>
G-7 On Low-Voltage Arc in Cesium Vapor I. P. STAKHANOV and I. I. KASSIKOV, Institute of Physics and Power Engineering, Obninsk, USSR	945
G-8 A Coherent Elementary Description of Thermionic Converter Phenomenology (manuscript not received) N. S. RASOR, Donald W. Douglas Laboratories, McDonnell Douglas Corporation, Richland, Washington, USA	
G-9 Two Types of Potential Distribution in Collisionless Mode of Thermionic Converter Operation in the Presence of Trans- verse Magnetic Field A. ENDER, Academy of Sciences of the USSR, A. F. Yoffe Physical Technical Institute, Leningrad, USSR	957
G-11 Effect of Cesium Pressure on Thermionic Stability A. SCHOCK, Republic Aviation Division of Fairchild Hiller Corporation, Farmingdale, New York, USA	969
G-12 On the Theory of Electrode Layer of Plasma I. P. STAKHANOV and P. P. SCHERBININ, Institute of Physics and Power Engineering, Obninsk, USSR	979

SESSION H "CONVERTER PERFORMANCE ANALYSIS"

Chairman : Prof. P. D. DUNN
Vice-Chairman: Mr. P. ROUKLOVE

H-2 Calorimetric Measurements with a Heat Pipe Thermionic Con- verter J. BOHDANSKY and E. van ANDEL, Euratom Joint Research Center, Ispra, Italy	989
H-3 The Characteristics of Thermionic Converters Filled with Va- por Mixture V. D. BONDARENKO and Yu. K. GUSKOV, Institute of Physics and Power Engineering, Obninsk, USSR	999
H-4 Unignited Mode Converter Diagnostics with Regard to Emitter Work Function Patches E. WOLF, R. MAYER and M. SCHINDLER, Institut für Kern- energetik der Universität Stuttgart, Germany	1011
H-5 Some Peculiarities of I-V Curves of the Thermionic Converters in Cesium Vapor at the Pressure 10^{-2} - 5 Torr V. L. BORZENKO, S. V. DROBJAZKO, L. A. DROBJAZKO, V. N. KNIZHNIKOV, I. V. Kurchatov Atomic Energy Institute, Moscow, USSR	1019
H-6 Experimental Verification on the Razor Phenomenological The- ory of the Arc Mode Regime of a Cesium Thermionic Con- verter F. V. KONDRATIEV and G. V. SINYUTIN, I. V. Kurchatov Ato- mic Energy Institute, Moscow, USSR	1031

	<u>Page</u>
H-7 Ionization State of Cesium Thermionic Converter Plasma F.K. KOSYREV, N.P. KOSYREVA and E.I. LUNEV, I. V. Kurchatov Atomic Energy Institute, Moscow, USSR	1041
H-8 On the Development of a Low-Voltage Arc in a Thermionic Diode with Extended Electrodes V.I. DERBILOV, D.V. KARETNIKOV, N.P. KOSYREVA, A.F. NASTOJASHCHY, V.B. TURUNDAJEVSKY, I. V. Kurchatov Atomic Energy Institute, Moscow, USSR	1055
H-9 Kinetic Theory of Knudsen Arcs in the Mixture of Inert Gases with Cesium Vapour R. Ja. KUCHEROV, Physical Technical Institute, State Com- mittee of Atomic Energy, Sukhumi, USSR and A.E. NASTO- JASHCHY, Kurchatov Atomic Energy Institute, Moscow, USSR	1067
H-10 Current Oscillations and Electromagnetic Radiation in Low- Pressure Thermionic Converters I.G. GVERDTSITELI, V. Ya. KARAKHANOV, R. Ya. KUCHE- ROV, Z.A. OGANEZOV and V.K. TSKHAKAYA, Physical Technical Institute, Sukhumi, USSR	1079
H-11 Low-Voltage Arc in the Cesium-Barium Mixture I.G. GVERDTSITELI, R. Ya. KUCHEROV, G.I. TKESHE- LASHVILI and V.K. TSKHAKAYA, Physical Technical Institute, State Committee of Atomic Energy, Sukhumi, USSR	1091
H-12 Low-Voltage Knudsen Arc in the Cesium-Inert Gas Mixture I.G. GVERDTSITELI, V. Ya. KARAKHANOV, R. Ya. KUCHE- ROV, G.I. TKESHELASHVILI, V.P. TSIBEREV and V.K. TSKHAKAYA, Physical Technical Institute, State Committee of Atomic Energy, Sukhumi, USSR	1097
H-13 Investigations on Noble Gas Converters H. ALBRECHT, B. SAGGAU and H. STRECKER, Institut für Gasentladungstechnik und Photoelektronik, Universität Stutt- gart, Germany	1105
H-15 Low-Voltage Cesium Arc in Thermionic Converter with Exten- ded Cathode Surface M.B. BARABASH, E.P. BUSIGIN, V.G. GRIGORYJANTS and I.P. YAVOR, Yoffe Physical Technical Institute, Leningrad, USSR	1113
H-16 Electron Scattering in Thermionic Converters by Xenon, Kryp- ton and Argon F. RUFEB and D. LIEB, Thermo Electron Corporation, Walt- ham, Massachusetts, USA	1123
H-17 Pulse Investigation on Thermionic Converters V. ORLINOV, T. DONCEV and B. GORANCEV, Institute of Electronics, Bulgarian Academy of Sciences, Sofia, Bulgaria and G. MUSA, Institute of Physics, Academy of the Rumanian	1129

Socialist Republic, Bucharest, Rumania

- H-18 Pre-Ignition and Ignition Characteristics of Cesium Thermionic Diodes
K. SHIMADA, Jet Propulsion Laboratory, California Institute of Technology, Pasadena, California, USA 1139

SESSION J "PLASMA PROPERTIES"

Chairman : Dr. D.V. KARETNIKOV
Vice-Chairman : Dr. N.S. RASOR

- J-1 Theoretical and Experimental Investigation of Low-Voltage Arc in Thermionic Converter
F.G. BAKSHT, G.A. DJUZEV, V.B. KAPLAN, I.L. KOROBOVA, A.M. MARTZINOVSKIY, B.Ya. MOIZHES, G.A. SHAHNASAROVA and V.G. YURIEV, Institute of Semiconductors of the Academy of Sciences, Leningrad, USSR 1147
- J-2 The Electron Energy Distribution Function and the Rate of Non-Equilibrium Ionization in the Near-Cathode Layer of the Thermionic Converter
F.G. BAKSHT, B.Ya. MOISHES and Y.A. NEMCHINSKIY, Institute of Semiconductors of the Academy of Sciences, Leningrad, USSR 1161
- J-3 The Probe and Spectral Investigations of Dense Plasma Thermionic Converters
G.A. DJUZHEV, A.M. MARTSINOVSKIY, B.Ya. MOIZHES, G.E. PIKUS, V.B. KAPLAN, G.A. SHAHNASAROVA, V.G. YURIEV, Institute of Semiconductors of the Academy of Sciences, Leningrad, USSR 1173
- J-4 On the Plasma Sheath Theory
F.G. BAKSHT, B.Ya. MOIZHES and V.A. NEMCHINSKIY, Institute of Semiconductors of the Academy of Sciences, Leningrad, USSR 1185
- J-6 An Investigation of the Ionization Mechanisms in the Ignited Mode Cesium Thermionic Converter
E.L. BURGESS, Sandia Laboratory, Albuquerque, New Mexico, and D.O. AKHURST, University of Arkansas, Fayetteville, Arkansas, USA 1199
- J-7 Spectroscopic Investigations in a Thermionic Converter Plasma.
C.G. STOJANOFF, W. HOFFMANN and K. SEWING, Institut für Kernenergetik der Universität Stuttgart, Germany 1205
- J-8 Spectrum of the Low-Voltage Discharge in a Cesium-Filled Diode
D. GLAS, Eindhoven Technological University, Eindhoven, The Netherlands 1213
- J-9 Action du rayonnement sur le fonctionnement de convertisseurs 1219

thermioniques, conversion du rayonnement solaire

J. P. DAVID et F. FLORET, Faculté des Sciences de Marseille, Marseille, France

SESSION K "SURFACE PHENOMENA"

Chairman : Dr. E. A. NIEKISCH

Vice-Chairman : Dr. E. P. GYFTOPOULOS

Invited Paper: Comments on Work Function Theories
by E. P. GYFTOPOULOS

1225

K-1 Quantum-Thermodynamic Meaning of Electronegativity and Work Function

E. P. GYFTOPOULOS and G. N. HATSOPOULOS, Thermo Electron Corporation, Waltham, Massachusetts, USA

1249

K-2 A New Interpretation of the Thermionic Emission from Bare and Covered Metal Surfaces

J. BOHDANSKY, Euratom Joint Research Center, Ispra, Italy

1267

K-3 The Cathode Materials of the Thermo-Emission Converters Research

Yu. S. BELOMYTZEV, F. L. BABINA, I. B. DMITRIEVA, Yu. G. KOLOBKOV, V. A. MALYKH, Yu. I. MOSKALEVA, I. N. PRILEZHAEVA, M. M. PRIVALOVA, V. M. PUMPURS, E. M. SAVITZKII, L. N. SARATOVSKII, A. A. SMIRNOV, N. E. SOLOMONOV, G. V. SPYVAK, M. A. TILKINA, B. B. SHYAHKIN, Institute of Physics and Power Engineering, Obninsk, The Moscow State University, Moscow, USSR

1281

K-4 Work Function Measurements of Refractory Metals in a High Pressure Cesium Plasma for Low Probe Temperature Range

V. BUNDSCHUH, Institut für Technische Physik, Kernforschungsanlage Jülich, Germany

1295

K-5 Preparation and Investigation of Tungsten Surfaces with Preferred Orientations

P. BATZIES, J. DEMNY and H. E. SCHMID, Brown, Boveri u. Cie, AG, Central Research Laboratory, Heidelberg, Germany

1303

K-6 Recherche de surfaces de tungstène à travail de sortie élevé .

D. THIVELLIER, Centre d'Etudes Nucléaires de Saclay, France

1313

K-7 Evaluation of Semiconducting Collector Surfaces in Thermionic Converters

R. MALY, H. RAPP and W. KLUGE, Institut für Gasentladungstechnik und Photoelektronik, Universität Stuttgart, Germany

1321

K-8 Wetting of Some Refractory Metals by Cesium, Potassium and Sodium

H. F. WEBSTER, General Electric Research and Development

1329

	<u>Page</u>
Center, Schenectady, New York, USA	
K-9 Etude de l'adsorption du césium sur des monocristaux de tungstène T. ALLEAU et J. L. DESPLAT, Centre d'Etudes Nucléaires de Saclay, France	1337
K-10 Adsorption de gaz sur des monocristaux de tungstène F. P. DUMONT et J. MAURIES, Centre d'Etudes Nucléaires de Saclay, France	1347
K-11 The Influence of Oxygen on the Work Function of Tungsten P. BATZIES, Brown, Boveri u. Cie., AG., Central Research Laboratory, Heidelberg, Germany	1357
K-12 Work Functions of Polycrystalline W and Re in an Atmosphere of Cesium and Oxygen R. LANGPAPE and A. MINOR, Brown, Boveri u. Cie., AG., Central Research Laboratory, Heidelberg, Germany	1367
K-13 A Critical Experiment on the Nature of Adsorbed Cesium Films E. MUZ, Institut für Gasentladungstechnik und Photoelektronik, Universität Stuttgart, Germany	1381
K-14 Etude au microscope à émission de surfaces réfractaires en présence de vapeur de césium J. L. DESPLAT et Ph. DEFRANOULD, Laboratoires de Recherches Générales, Compagnie Française Thomson Houston, 92-Bagneux, France	1389
<u>SURVEY OF EXPERIMENTAL WORK IN THE USSR</u> by Yu. L. DANILOV, USSR	1399
<u>PANEL DISCUSSION: "Present and Future of Thermionic Energy Conversion"</u> Chairman: Prof. P. D. DUNN	
Invited Papers: 1) The United States' Thermionic Program Remarks by G. F. TAPE	1407
2) The Application of Thermionic Energy Conversion in the USSR Remarks by Yu. L. DANILOV,	1417
Discussion (Moderator: Prof. P. D. DUNN)	1421
AUTHOR INDEX	1436

OPENING SESSION

Welcome on Behalf of the Sponsoring Organization

by Mr. L. BOXER, Head of the Economical and Technical Division, European Nuclear Energy Agency, Paris.

Ladies and Gentlemen,

I am anxious to take up as little time as possible of this opening session, but on behalf of the Director General of the European Nuclear Energy Agency, I feel bound to record our pleasure in assisting in the opening of this Second International Conference on Thermionic Electrical Power Generation. Our pleasure is twofold, in the sense that as an organisation, we are proud to be associated with a function of such scientific importance, and secondly that we are always glad to have a further opportunity to undertake with Euratom a cooperative exercise, of which there are already plenty of examples. We all owe particular thanks to Dr. NEU, the Chairman of the Programme Committee of this Conference, and his colleagues at the Ispra Joint Research Centre, who have been responsible for all the material arrangements.

Those of you who have had a chance to glance through the little note on ENEA in the back of your preliminary programme, will have seen that scientific and technological cooperation between the twenty-one OECD countries on peaceful applications of nuclear energy is one of our principal activities. We firmly believe that there is a good deal of scope for more co-operative activity in those applications of nuclear energy which are still far from the stage of widespread commercial exploitation, and which thus require continuing governmental support. The technique of thermionic power generation from nuclear energy sources with its predominant application in space research, (an area which is already the subject of massive governmental investment), therefore falls very appropriately within our scope, especially in view of its connection with heat sources from radioisotopes, where we have a parallel interest, and indeed, an active cooperative Working Group on radioisotopic battery development.

As many of you know, at the end of 1966 ENEA took the initiative in setting

up a Liaison Group on Thermionic Electrical Power Generation, to provide a permanent mechanism for improving information exchange among specialists designated from OECD countries, and for advising on the planning of these conferences. So far the Group has been successful in bringing together experts from seven countries active in the field, also the international interests represented by Euratom and IAEA. It is planned to enlarge future participation in the Group with experts from Eastern countries.

Once again, as in the case of the First Conference, it has been possible to welcome fellow scientists and engineers from the USSR (and other Eastern countries) to our deliberations this week. Their presence here, and the scale of their contribution to this conference will be a significant element in the important new revelations which might well emerge during these five days.

We have a full, fascinating and very varied programme before us, from detailed theoretical considerations to design development, performance and experience with thermionic generators over a wide range of electrical output. I feel sure that the experts in this increasingly important area of science and technology will leave Stresa at the end of this week with the feeling that since the first conference in London three years ago, which ENEA had the privilege of organizing with the collaboration of the Institution of Electrical Engineers, a very considerable step forward has been achieved in the state of the art. If that is the result, then we shall feel that the little trouble we have taken to bring you here has been more than worthwhile.

Welcome on Behalf of the Organizing Institution

by Prof. H. KRAMERS, Director of the EURATOM Research Establishment,
Ispra.

Ladies and Gentlemen,

Whereas the European Nuclear Energy Agency has willingly given its sponsorship to this international and world-wide conference, the task - and the honour - of the scientific and material preparation was confided to the Ispra research

establishment of the Euratom organization.

As a representative of this research establishment I wish to thank you for your confidence in this preparatory work, which we could perform, amongst others, because of the presence at Ispra of a small, but highly proficient research group in the field of thermionic conversion.

We could have wished of course that our effort in this field would have been greater, but I have to recall, that the primary object of the countries which constitute the European Atomic Energy Community is the promotion of research, development and industrialization of nuclear power on a large scale and on an economic basis. We realize that the direct conversion of heat into electricity by application of the thermionic principle does not fall into this domain. On the other hand, we feel that among the various methods for direct conversion, the thermionic principle combined with nuclear heat, will sometime find its justified peaceful application, particularly in space-borne systems.

In the present competition between the various branches of "big science" such a statement is hardly convincing if it comes to getting the necessary government support in the form of funds. On the other hand, the development of thermionic power generation devices is just a field where the long term character, the high risk, the slow return on investment and the absence of direct national economic and industrial considerations can still greatly profit from free exchange of information and particularly from international collaboration. If we are able to understand this and to grasp the occasion of international collaboration, we - and I think now particularly of Western Europe - would be able to meet the challenge, not only of our powerful world neighbours, but also of the very advanced technology problems which are associated with this field of thermionic conversion - not to speak of "fall-out" or "spill-over", which always occurs but does not constitute in itself an argument for doing such work.

It is for reasons which I explained earlier, that we, as a host, consider this Second International Conference on Thermionic Electrical Power Generation to be of very great importance, not only to all participants, but also, and

particularly so, to ourselves.

I therefore express my sincere hope that the conference will be a complete success.

Introduction to the Conference

by Dr. H. NEU, Conference Chairman.

Ladies and Gentlemen,

I have the honour to welcome you in the name of the Programme Committee and to thank you for coming to Stresa. From the registration forms I learned that delegations of the following countries are present: Austria, Belgium, Bulgaria, Canada, Czecho-Slovakia, France, Germany, Italy, Rumania, Soviet Union, Switzerland, The Netherlands, United Kingdom and the United States of America. Furthermore, representatives of the following International Organizations are registered: European Space Research Organization, European Launching and Development Organization, the International Atomic Energy Agency and - who are the sponsors for this conference - the European Nuclear Energy Agency and EURATOM.

We are particularly glad that a strong delegation of the USSR has arrived and we are grateful for the support that the International Atomic Energy Agency in Vienna has given us to make this possible.

Research on Cesium filled thermionic diodes was started about 10 years ago in the laboratories of the USSR and independently in laboratories of the USA. We are happy to see here with us many of the pioneers of thermionic energy conversion.

It is not my intention to describe the events leading from the first experiments to the thermionic research of to-day. This will be demonstrated by the papers presented at this conference. I would like to stress only one significant feature. If you compare the programme of the London Conference with the Stresa Programme, you will find that many more of the present papers concern hard-ware performance of converters and results of longlife out-of-pile and

testing. The session on "Integrated Systems", that is to say conceptual engineering studies of reactors and isotope fueled power units (mostly for space power supply), has become the largest session. In this respect the Committee would like to thank the USAEC for making possible important contributions on subjects which are published for the first time.

Now let me tell you something about the scientific organization of this conference. Those who have attended the London conference may have already noted that we are not using the so-called "rapporteur system", that is the presentation of all the papers of one session by one or two speakers.

On the other hand, not all of the authors at this conference will be able to read their paper. I feel that it is very necessary to explain why this is and how it came about.

The Programme Committee felt strongly that we should try to give the Conference more the character of a working meeting than of a representative event. For this purpose, the "rapporteur system" has more inherent disadvantages:

1. Papers have to be submitted rather early to the organizers for distribution to the rapporteurs. Consequently the authors cannot always present the latest results and they may have to use material which has already been published before.
2. It seems to be difficult sometimes for the rapporteurs to find out from a written paper details of results which the author would regard as important.
3. The younger colleagues do not have an opportunity for personal presentation.

Thus it was thought that a system with presentation of papers by the authors is preferable and the Programme Committee decided to use this procedure. However, when we made the call for papers it happened that 142 abstracts arrived compared with about 100 in London. Although we were glad to see such a great interest in the conference, we feared that the reading of 142 papers in 4 days would not give sufficient time for discussion. We felt that

about a half of the session time is necessary for discussions.

What to do? Parallel sessions were not found to be a good solution because we expected that most of the participants will be interested in all subjects treated. This is quite understandable, as thermionic research is linked with different disciplines such as physics, metallurgy and engineering in such a way that each specialist in one field needs to know what happens in the other fields. Thus, the Programme Committee was forced to accept a solution in which only a selection of the papers are presented by the authors. The titles of the papers which are not presented orally will be read by the chairman and put to discussion.

The selection of papers for oral presentation was indeed a delicate task for the Programme Committee because it had to be done with only the preliminary abstracts available. We have tried to do our best to select those papers for oral presentation which we felt to contain the most of novelty or to be of a more general interest. This selection means absolutely no judgment of the scientific value of the content.

As a general rule, we suggest to the Session Chairman to give priority to questions and answers rather than general remarks, read and unread papers being treated equally. If time is available authors of unread papers may have a chance to make some remarks. It is quite possible that the Committee was not able to fully assess some of the papers from the abstracts alone, or additional time has become available because papers have been withdrawn. There will be a possibility to reexamine papers in this case together with the Chairman and the Vice-Chairman before each session.

In order to save time, we have recommended that some of the authors combine their papers if the contents are similar and we have also asked that two or more papers coming from the same laboratory should be presented by one speaker. In the session "Heat Pipe Systems" we have invited two speakers to summarize work in the USA and Europe. There is no oral presentation of papers foreseen at all on the subject of heat pipes since this does not - in our opinion - belong strictly to the research sphere.

Invited papers for introductory survey purposes have been limited to the session where it seems to us highly desirable, that is the "Theory of Con-

verters" and "Surface Phenomena".

As you will note, we have taken a full half day for a panel discussion about subjects which are not only of interest for the thermionic researchers but for those who attend this conference to get a more complete picture of the possible application of thermionic converters, the competition with other systems and the opinion of the specialists on present and future of thermionics. I have great pleasure in announcing that commissioner Gerald Tape of the USAEC will personally come to Stresa and give an introductory talk about "Space Applications of Thermionic Conversion and Comparison with other Systems". He also intends to participate on the discussion about this subject. You will agree with me, that this gives the panel discussion a special importance and weight.

With regard to the general organization, there is some information in the Programme literature you have received. If any problems arise, please do not hesitate to contact one of the persons with an orange coloured badge. I am most indebted to all who have contributed to bringing the conference to the point where it can now start. In particular, I would like to thank Dr. SMETS and Mr. BOXER of the European Nuclear Energy Agency in Paris and the members of the Programme Committee for the preparation of this conference. Many thanks also go to Prof. KRAMERS, director of Ispra for his great interest and support, the authors of papers for their collaboration in submitting their preprints in time, the members of the conference secretariat for their very efficient work and, last but not least, the staff of the Public Relations Office at Ispra for making all arrangements for the successful running of this conference.

Ladies and Gentlemen, I have the great honour to declare the "Second International Conference on Thermionic Electrical Power Generation" open.

SUMMARY OF APPLIED RESEARCH PROGRAM
IN THERMIONIC CONVERSION DURING RECENT YEARS*

F. Rufeh, D. Lieb and L. van Someren

Thermo Electron Corporation
85 First Avenue, Waltham, Massachusetts

I. ABSTRACT

This paper summarizes the results of an applied research program which has been in progress for several years. Two new techniques have been developed for treating emitter surfaces. These techniques, which have resulted in substantial improvement in performance, are combinations of heat treatment with electropolishing and with electroetching. Emitters prepared by these methods were incorporated in variable-spacing converters, and parametric data was obtained. These data are useful both for calculations of converter designs and for theoretical analysis. Another technique investigated for improving converter performance was the use of oxygen. Cesium oxide was found to be a good source of oxygen and cesium.

II. TEST CONVERTER

A versatile variable-spacing converter was developed to obtain parametric data for the various emitter surfaces. A schematic diagram of this converter is shown in Figure 1. The molybdenum collector is surrounded by an active molybdenum guard ring which is maintained at the same temperature and electrical potential as the collector. Flexible bellows allow the interelectrode spacing to be varied from 0.5 to 100 mils.

* This work was performed for the Jet Propulsion Laboratory, California Institute of Technology, sponsored by the National Aeronautics and Space Administration under contracts NAS 7-100 and NAS 7-508.

III. CONVERTERS WITH ELECTROPOLISHED RHENIUM EMITTERS

A. Emitter Preparation¹

The emitters used in this work were discs of polycrystalline rhenium made by rolling sintered-powder ingots. The material was at least 99.99% rhenium, and had a well developed preferred orientation with basal (001) planes parallel to the emitter surface.

The disc surfaces were ground flat, and hohlraums with the $\frac{L}{D}$ ratio of 5 were made by spark-machining. An anneal for 30 minutes at 1700°C at a pressure of less than 10^{-6} torr followed grinding because this was found to facilitate electropolishing.

The specimen was then electropolished, heat-treated and incorporated into a variable-spacing converter with a molybdenum collector.

B. Parametric Data

The electrode work functions were measured, and the performance of the converter was recorded in terms of variable-cesium-temperature families. A typical family is shown in Figure 2. It defines an envelope which is tangent to each I-V curve and represents the cesium optimized performance. Such families were obtained at optimum collector temperature for a wide range of emitter temperatures and interelectrode spacings. The envelopes of these families are summarized in Figures 3 to 5. Each of these figures shows the fully optimized performance with respect to cesium temperature, interelectrode spacing and collector temperature. The output is corrected for emitter lead voltage loss which is 3 mV/amp. The fully optimized performance for interelectrode spacing ≥ 5 mils and the emitter temperature range of 1680 to 2040°K is summarized in Figure 6. The set of data shown in Figures 3 to 6 is useful for converter design calculations.

IV. CONVERTERS WITH ELECTROETCHED RHENIUM EMITTERS

A. Emitter Preparation

The emitter preparation for these emitters is similar to the electropolished emitter with the following difference: After being electropolished, the emitters were subjected to electroetching. This process removes material selectively from different crystal faces, so that some grains are etched faster than others. A rough jagged surface is developed, which has a larger fraction of the slow-etching basal planes than did the original surface. Since these basal planes are favorable for cesiated thermionic emission, the etching technique is expected to produce an emitter with a thermionic performance superior to that of the electropolished surface from which it was derived.

These surfaces also were heat-treated for 3 hours at 2380°C to ensure stability during converter operation.

B. Performance Data

Families of volt-ampere characteristics were generated by varying the cesium reservoir temperature. The performance of the device has been summarized in Figures 7 to 10, using envelopes of the variable-cesium-temperature families. The collector temperatures were selected near the optimum value corresponding to the emitter temperature used. The dashed line in these figures represents the envelope of the spacing envelopes corrected for emitter lead voltage loss. It corresponds to the output at the electrodes under fully optimized conditions for the emitter temperature indicated. The optimized performances of electroetched

and electropolished emitters are compared in Figure 11. The interelectrode spacings in this set are equal to or larger than 5 mils and the output is corrected for emitter lead voltage loss. Etched rhenium shows a substantial improvement over polished rhenium.

C. Emitter Work Function

Emitter work function was determined from the measured saturation current under ion-rich conditions. The data is presented in Figure 12 as a function of $kT_E \ln P$, where k is the Boltzmann constant, T_E is emitter temperature, and P is cesium pressure. This data was also plotted as a function of T_E/T_R , where T_R is cesium reservoir temperature. It showed a maximum scatter of about 0.1 volt, indicating that work function does not depend only on T_E/T_R , but still has a small dependence on T_E .

A new correlation was tried by plotting ϕ_E versus $kT_E \ln (P/C)$, where $C = 3.6 \times 10^7$. The constant C is chosen in an attempt to obtain a universal relation between ϕ_E and T_E and P . The scatter in the data for this correlation is reduced to 0.05 V.

D. Variable-Spacing Data

Families of volt-ampere characteristics were generated by varying the interelectrode spacing while all the other parameters were held constant. The cesium pressure, emitter temperatures and interelectrode spacings in these families were selected in such a way as to yield the volt-ampere characteristics at various combinations of Pd and ion richness values. The data is useful for plasma analysis and is shown in Figures 13 to 19.

V. ELECTRONEGATIVE ADDITIVES

A. Effect of Cesium Fluoride

In previous investigations^{3, 4, 5} fluorine appeared to produce a substantial change in the emission characteristics of metal surfaces. Experimental studies in the presence of cesium showed a definite improvement

in performance, but the effect was not reproducible and disappeared after a short time. A mass-spectrometric examination of the outgassing of cesium fluoride showed that, in the previous measurements, the vapor pressure of water was high enough to affect the emission characteristics and overshadow the effect of fluorine. An elaborate test vehicle was used to study the effect of specially purified CsF pellets. These and other⁶ results showed that even where there is significant fluoride coverage, the emitter work function is not increased as much as in the presence of oxygen. The increase in work function produced by fluoride is 0.3 eV, while that produced by oxygen is 0.7 eV. The conclusion is that, in the previous studies, water vapor contamination had been responsible for the initial improvement and the later deterioration of performance.

B. Converter Performance with Cesium plus Cesium Oxides⁷

Cesium oxides were formed on the collector and guard surfaces of a variable-spacing converter. The additive pressure was controlled by the temperature of the collector and guard, and cesium pressure was controlled by the cesium reservoir temperature. A definite oxygen effect was observed when the collector and guard temperatures were raised in the range of 600 to 900°K. Oxygen produced a decrease of 0.3 volt in the cesiated work function of the emitter.

The performance improvement was equivalent to an increase in spacing by a factor of four at the same output. A 300-hour life test showed stable performance within $\pm 10\%$.

C. Converter Performance with Cesium Oxide Only⁸

Preliminary data was obtained to study the possibility of using cesium oxides as a source of both cesium and oxygen. A fixed-spacing converter with only one reservoir containing cesium oxides was used. The data from this converter was compared with data from the same emitter and collector in a cesium-only converter. In the cesium-only data, the

temperature range of cesium was from 560 to 640°K. In cesium-oxide-only data, the temperature range of cesium oxide was 670 to 700°K. Therefore, the coldest component of the cesium-oxide-only converter is about 100°K hotter than the coldest component of the cesium converter. There is a possibility that the operating temperature of the cesium-oxide reservoir can be further increased. A higher temperature range would make cesium-oxide-only converters more attractive for most applications. Figure 20 shows a comparison of the envelopes of the cesium-only and the cesium-oxide-only families. The cesium-oxide envelope has a steeper slope than the cesium envelope because the cesium pressures are lower and electron scattering is less.

A 400-hour life test showed stable performance within $\pm 10\%$.

ACKNOWLEDGMENT

The authors acknowledge the technical assistance of Dr. C. Wang of Thermo Electron Corporation.

REFERENCES

- (1) VAN SOMEREN, L. ; LIEB, D. ; KITRILAKIS, S. S. , "Evaluation of Thermionic Emitter Surfaces," Proceedings of Thermionic Conversion Specialist Conference, San Diego, 1965.
- (2) RUFEB, F. ; KITRILAKIS, S. S. , "Thermionic Converter Performance in Presence of Inert Gases," Proceedings of Thermionic Conversion Specialist Conference, Houston, 1966.
- (3) JESTER, A. A. , "The Influence of a Cesium Fluoride Additive on the Power Output of Cesium Diodes with Molybdenum and Rhenium Emitters," Thermionic Conversion Specialist Conference, Cleveland, 1964.
- (4) LANGPAPE, R. ; MINOR, A. , "Influence of CsF and Cs + CsF on the Work Function of Refractory Metals," Thermionic Conversion Specialist Conference, Cleveland, 1964.
- (5) LIEB, D. , "Performance of Tungsten-Emitter Thermionic Converter in the Presence of Cesium Fluoride Additive," Proceedings of Thermionic Conversion Specialist Conference, San Diego, 1965.
- (6) RASOR, N. S. ; GAMMEL, G. , "Correlation of Emission Processes for Cesium-Additive Emitters," Thermionic Conversion Specialist Conference, Houston, 1966.
- (7) LIEB, D. ; KITRILAKIS, S. S. , "The Influence of CsF on the Work Function of a Tungsten Surface," Proceedings of Thermionic Conversion Specialist Conference, Houston, 1966.
- (8) RUFEB, F. ; LIEB, D. ; FRAIM, F. , "Recent Experimental Results on Electronegative Additives," Proceedings of Thermionic Conversion Specialist Conference, Palo Alto, 1967.

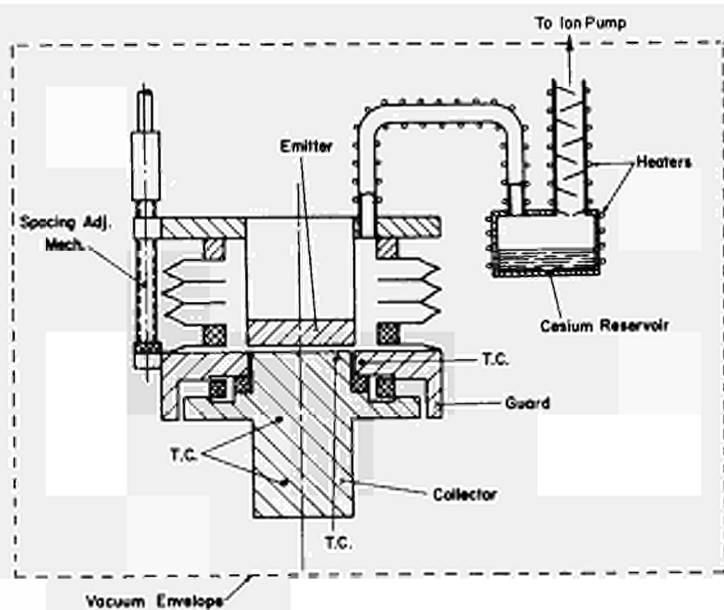


Fig. 1. Converter Schematic.

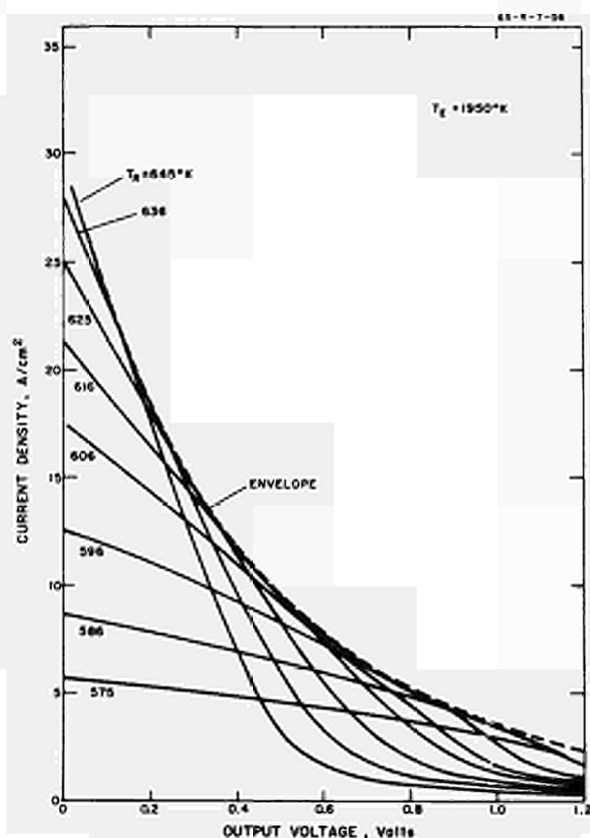


Fig. 2. A Typical Family of Current-Voltage Curves.

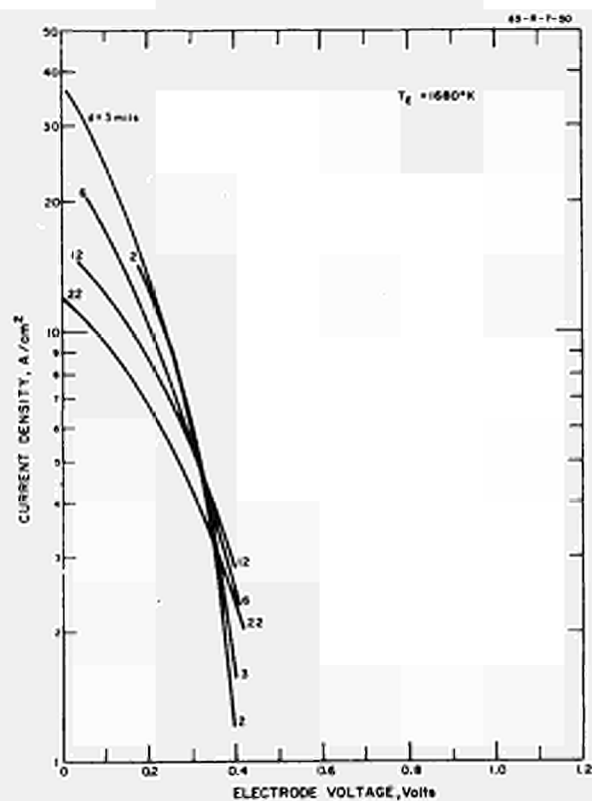


Fig. 3. Cesium Envelopes at $T_e = 1680^\circ\text{K}$ and Several Spacings.

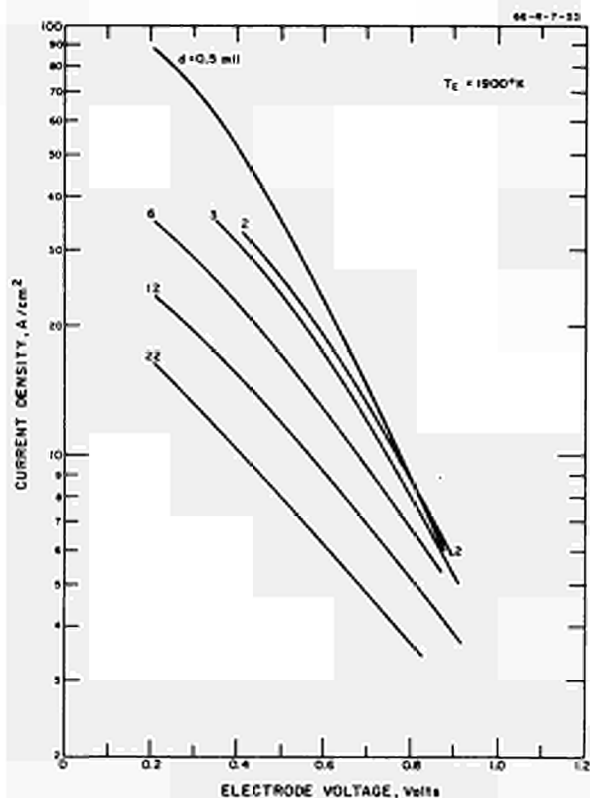


Fig. 4. Cesium Envelopes at $T_e = 1900^\circ\text{K}$ and Several Spacings.

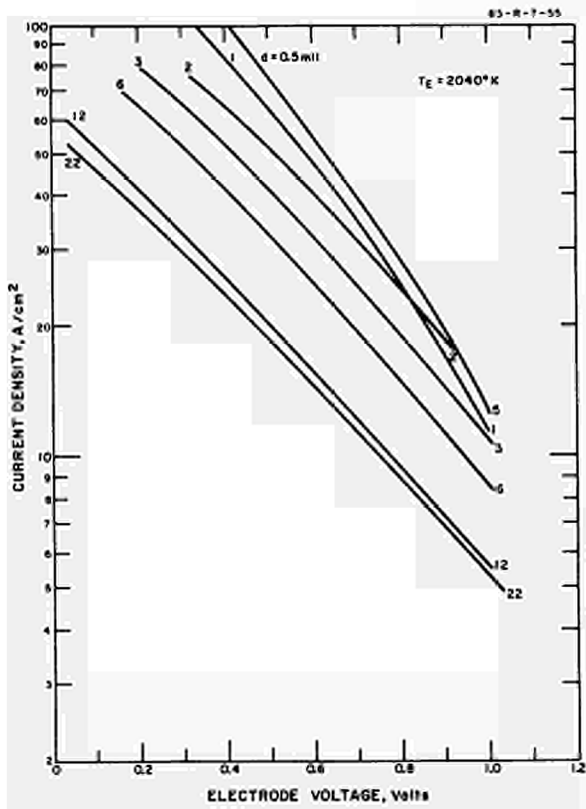


Fig. 5. Cesium Envelopes at $T_e = 2040^\circ\text{K}$ and Several Spacings.

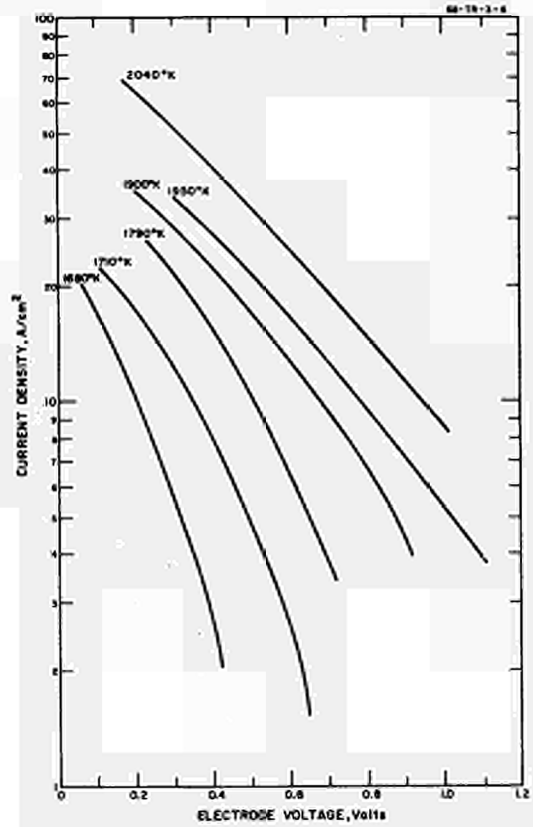


Fig. 6. Optimized Envelopes at Various Emitter Temperatures, $d \geq 5$ mils.

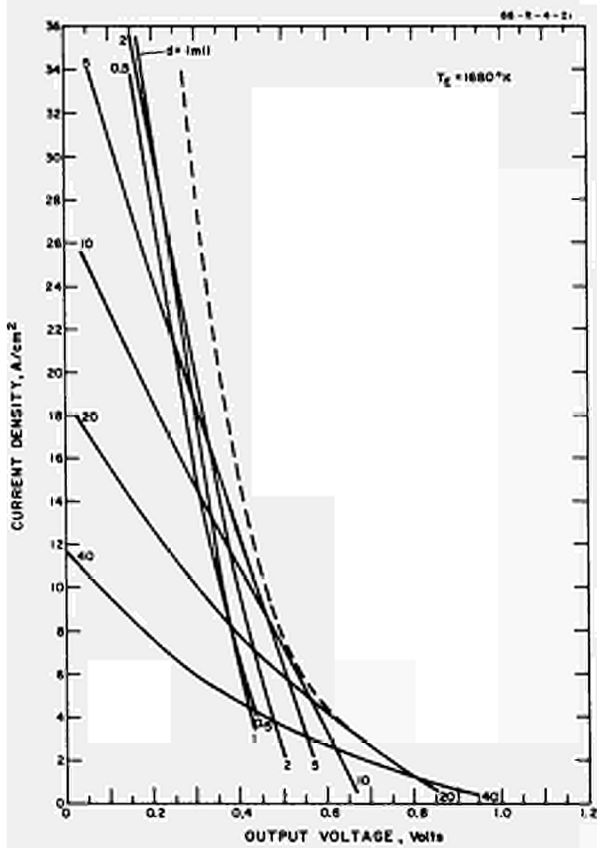


Fig. 7. Cesium Envelopes at $T_e = 1680^\circ\text{K}$ and Several Spacings.

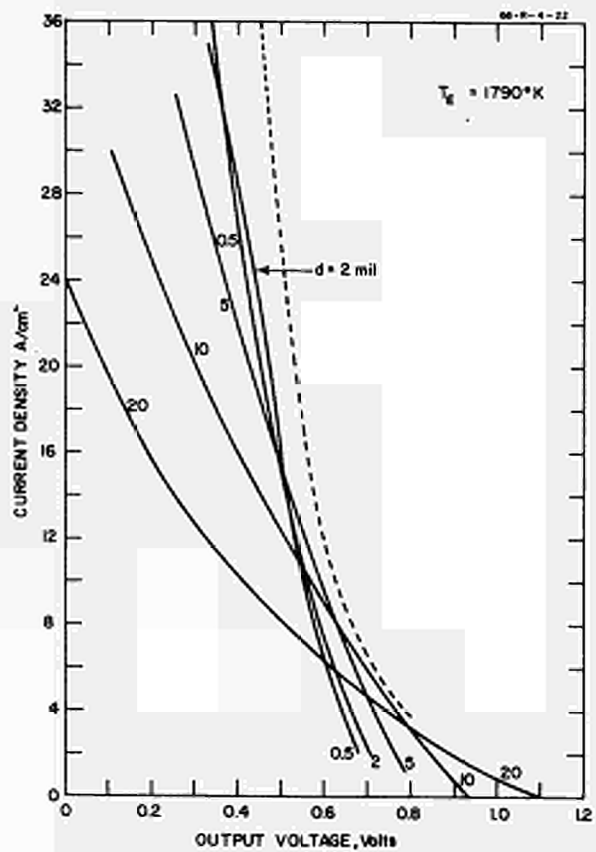


Fig. 8. Cesium Envelopes at $T_e = 1790^\circ\text{K}$ and Several Spacings.

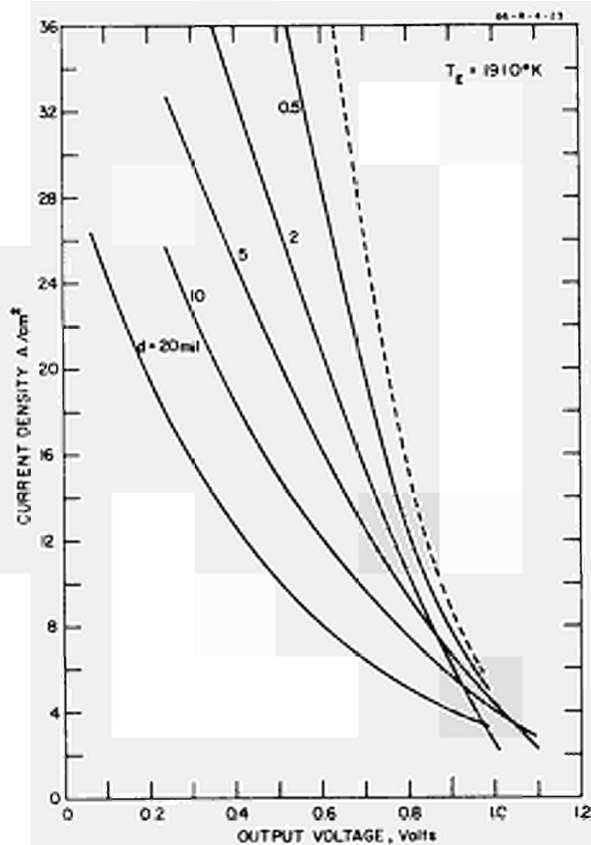


Fig. 9. Geosium Envelopes at $T_e = 1910^{\circ}\text{K}$ and Several Spacings.

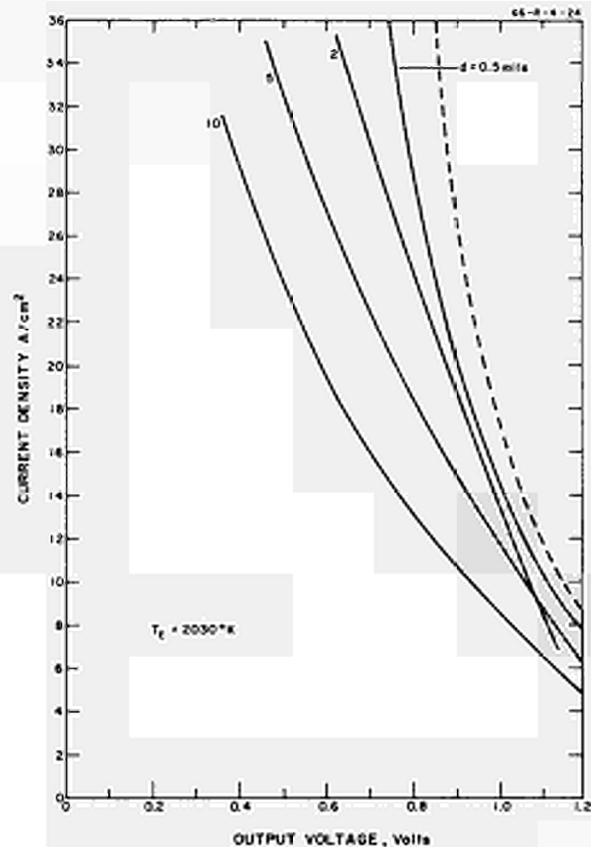


Fig. 10. Geosium Envelopes at $T_e = 2030^{\circ}\text{K}$ and Several Spacings.

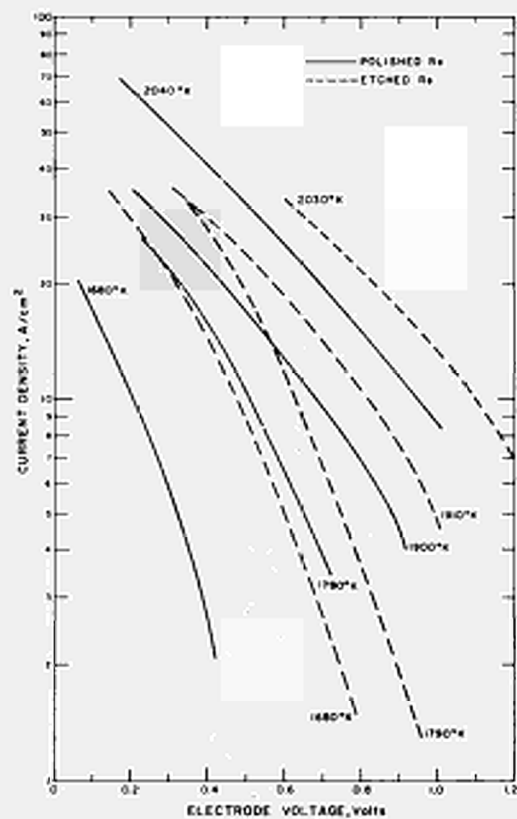


Fig. 11. Comparison of Optimized Performance for Electro-polished and Electroetched Rhenium Emitters. $d \geq 5 \text{ mil}$.

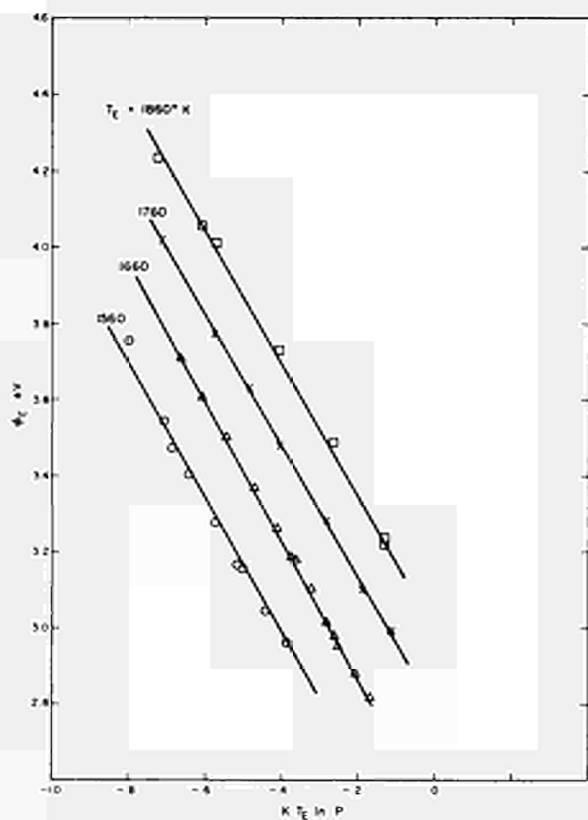


Fig. 12. Work Function Data at Several Emitter Temperatures.

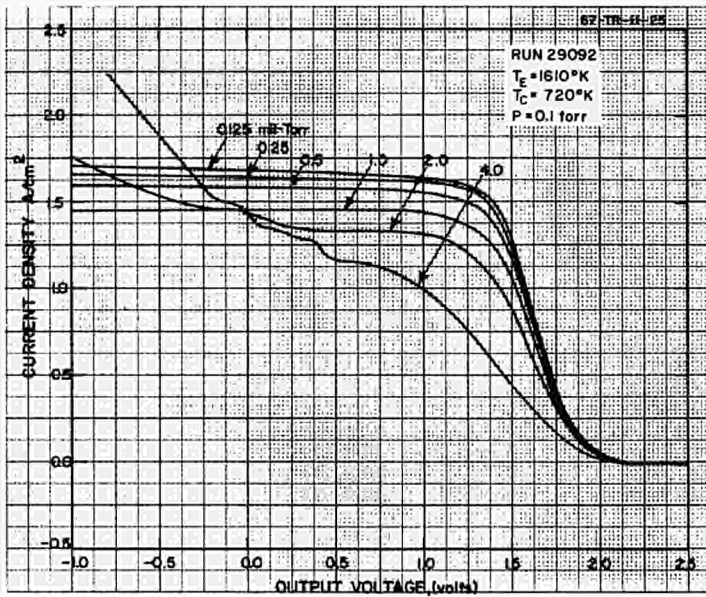


Fig. 13. Variable-Spacing Family at $T_e = 1610^{\circ}\text{K}$ and $P = 0.1 \text{ torr}$.

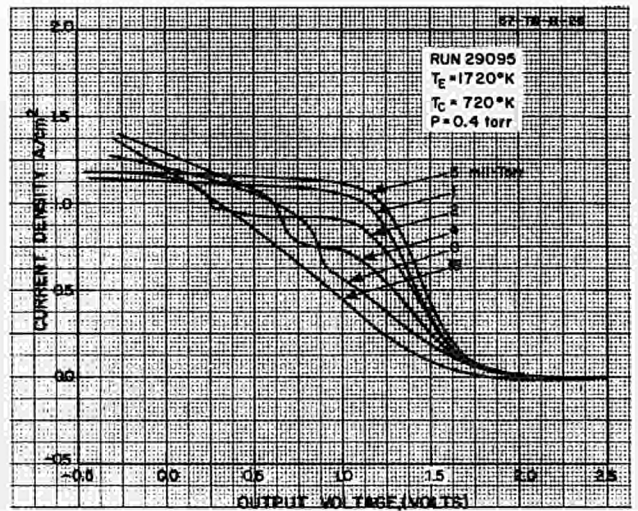


Fig. 14. Variable-Spacing Family at $T_e = 1720^{\circ}\text{K}$ and $P = 0.4 \text{ torr}$.

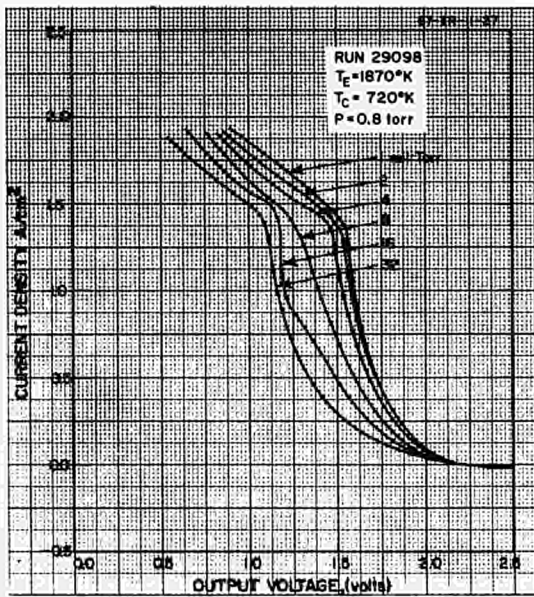


Fig. 15. Variable-Spacing Family at $T_e = 1870^{\circ}\text{K}$ and $P = 0.8 \text{ torr}$.

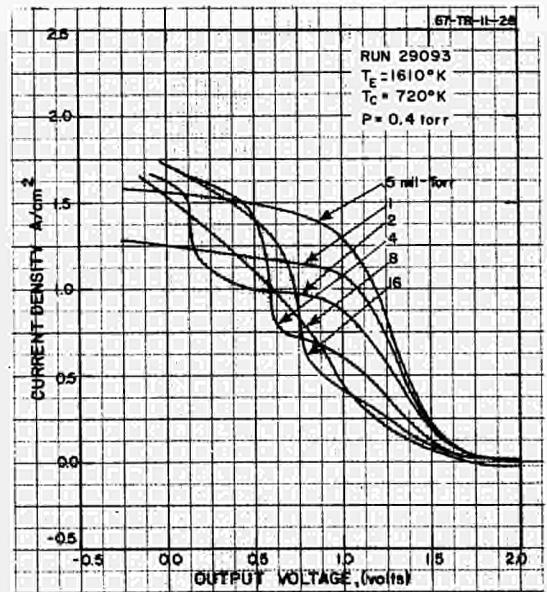


Fig. 16. Variable-Spacing Family at $T_e = 1610^{\circ}\text{K}$ and $P = 0.4 \text{ torr}$.

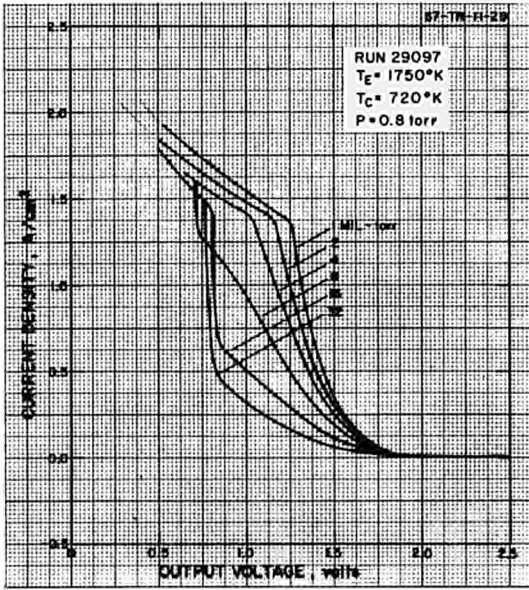


Fig. 17. Variable-Spacing Family at $T_g = 1750^{\circ}\text{K}$ and $P = 0.8$ torr.

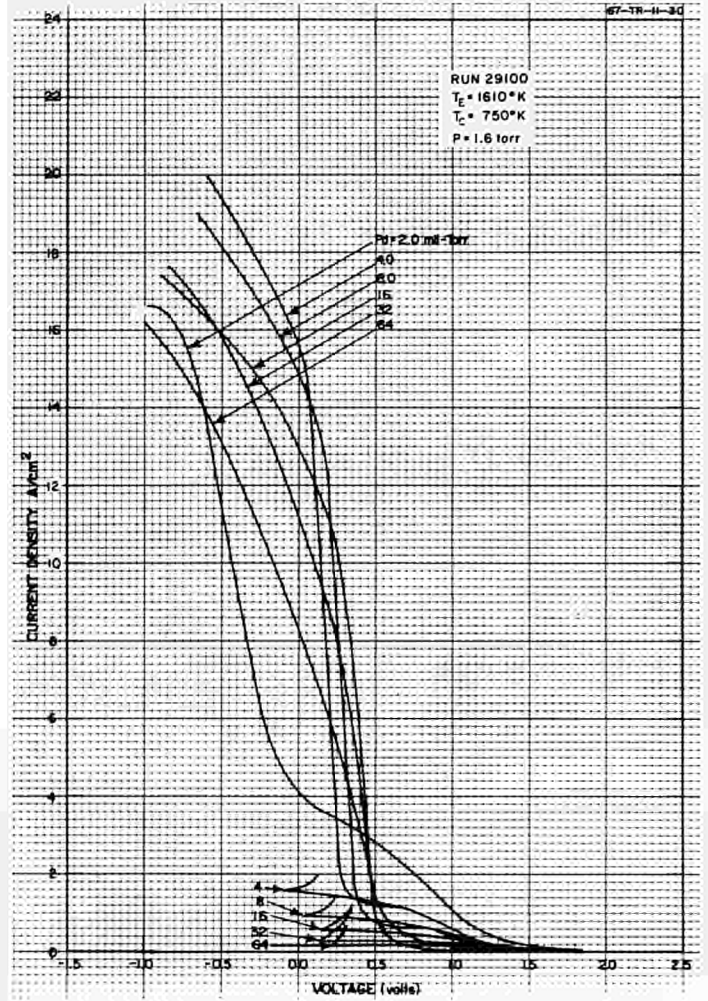


Fig. 18. Variable-Spacing Family at $T_g = 1610^{\circ}\text{K}$ and $P = 1.6$ torr.

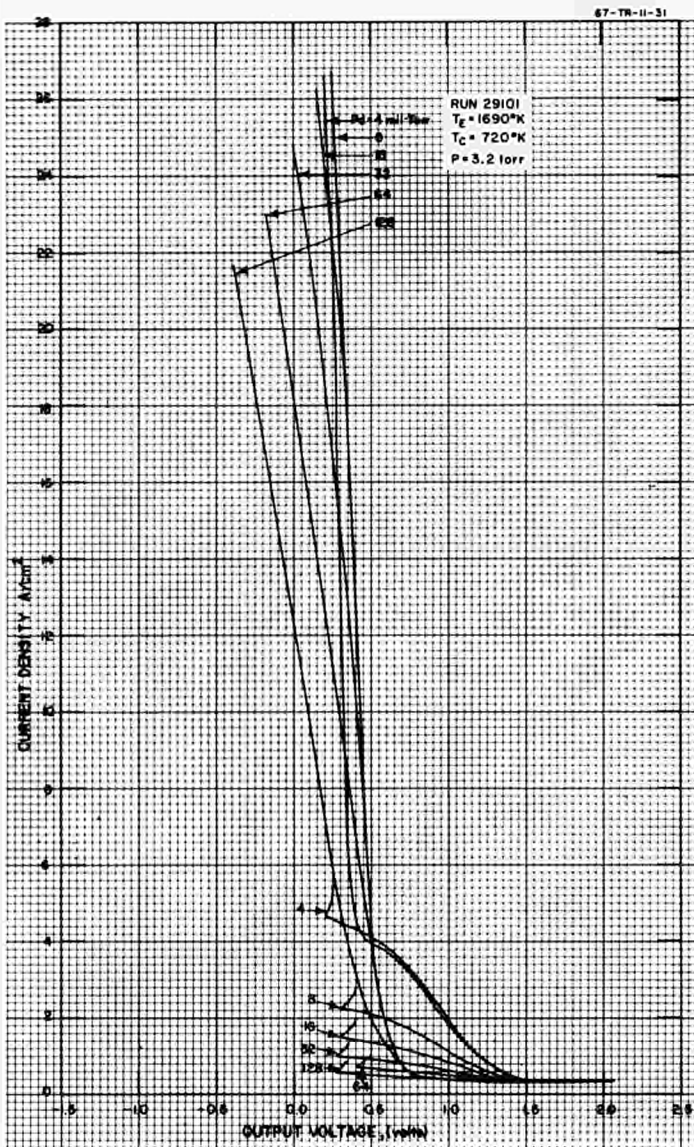


Fig. 19. Variable-Spacing Family at $T_g = 1690^{\circ}\text{K}$ and $P = 3.2$ torr.

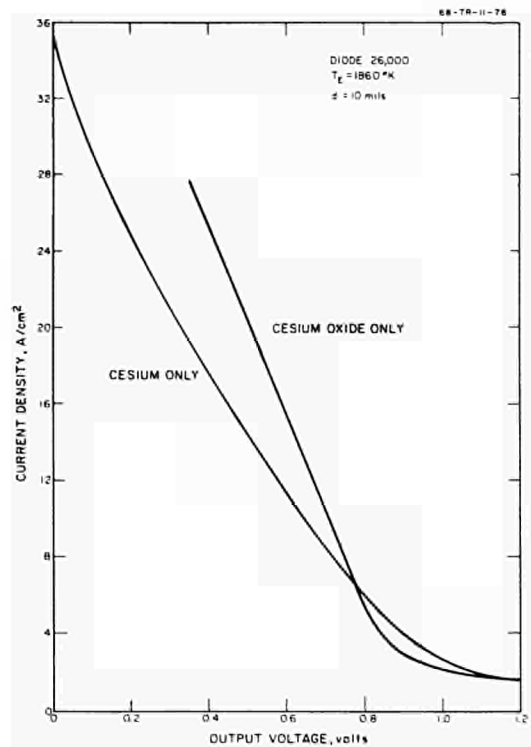


Fig. 20. Performance Comparison of the Cesium-Oxide Connector with a Cesium Converter at $T_g = 1900^{\circ}\text{K}$.

DISCUSSIONS

Speaker of paper A-1: G. N. HATSOPOULOS

KNOERNSCHILD (Germany):

How do you measure the degree of ion richness? You mention that spectacular improvements were obtained with additives like Cs-chloride. How large was this improvement?

HATSOPOULOS (USA):

We did not measure the ion-richness unfortunately. We have not found any good techniques of doing so. We calculated it from the emitter work-function that we measured at that point and the Saha-Langmuir equation. This is the ion-richness based on that calculation. As far as some of the spectacular results that I mentioned are concerned, the best results that were obtained were inadvertently with wet Cesium-Fluoride. The water present in the Cesium-Fluoride produced the effect.

Compared, for instance, to the data that I showed here, the power density at the same voltage and at the same temperature would be about twice. Next best data that we obtained were with oxygen on the collector, where we could adjust the oxygen pressure by adjusting the collector temperature. The results in that case, were about 50% better than the results I presented here.

PRUSCHECK (Germany):

Fig. 12 shows a linear dependence of ϕ_E versus $kT_E \ln p$. The last term is the expression for isothermal change of state (compression or expansion work) if p could be replaced by a pressure ratio (which is also required from dimensional reasons). Can the linear dependence be explained by thermodynamics?

HATSOPOULOS:

In this way of plotting the work function, which shows here a much better correlation of the data, has been suggested thermodynamically because the chemical potential of the vapor, which really is the measure of what forces absorption on the surface, is proportional to $kT_E \log p$. Now, as an approximation you know, $kT_E \log p$ varies as the ratio of T_E/T because of approximately exponential nature of the Cesium pressure line.

That is why you end up with the T_E/T_R plot of RASOR. The T_E/T_R plot does have some error in it and once you have good data it is better to plot it in $kT_E \log p$; then you get a much better correlation. There is a thermo-

dynamic basis of that.

Yes, it should be a pressure ratio; it should be p over some standard pressure p_0 , but that would require some calculations. From here you can find what is an appropriate standard pressure to use which could collapse all the data into one line. In fact in some curves that I have not shown, by taking appropriate pressure p_0 you can get all these lines, all of which are parallel, to collapse into one.

PIDD (USA):

Is there any limitation to the life time at elevated temperature of the etched surfaces you described?

HATSOPOULOS:

I do not believe that there is a limitation on life time on this surface. We have not observed over several hundred hours any change of these data that I report here for the etched surfaces. Another etched converter, incidentally not as good but almost as good as this one, is the one which we are reporting tomorrow on an in-pile test and that was for several thousands of hours perfectly stable. So we feel that etching, a proper etching with heat-treatment, stabilizes the surface, and, from there on, it is a stable surface.

PIDD:

You get an enhanced performance by treating the surface, but you also can get an enhanced performance by electronegative additives. Do those two improvements combine?

HATSOPOULOS:

That is a good question. Our problem with electronegative additives is that we still don't know how to control them reproducibly, so as to make a critical experiment with an etched surface with an electronegative additive. We are planning to do this in fact and we hope we will do it soon. Now as to the speculation whether they add or not, both effects were tending to increase the bare work function of the surface. Now, there is a question of how much you can increase the bare work function of the surface before that becomes a disadvantage, because after a while any theory predicts that if you go to a bare work function of 7 Volts then things will not be so good. So I don't know the answer to that question.

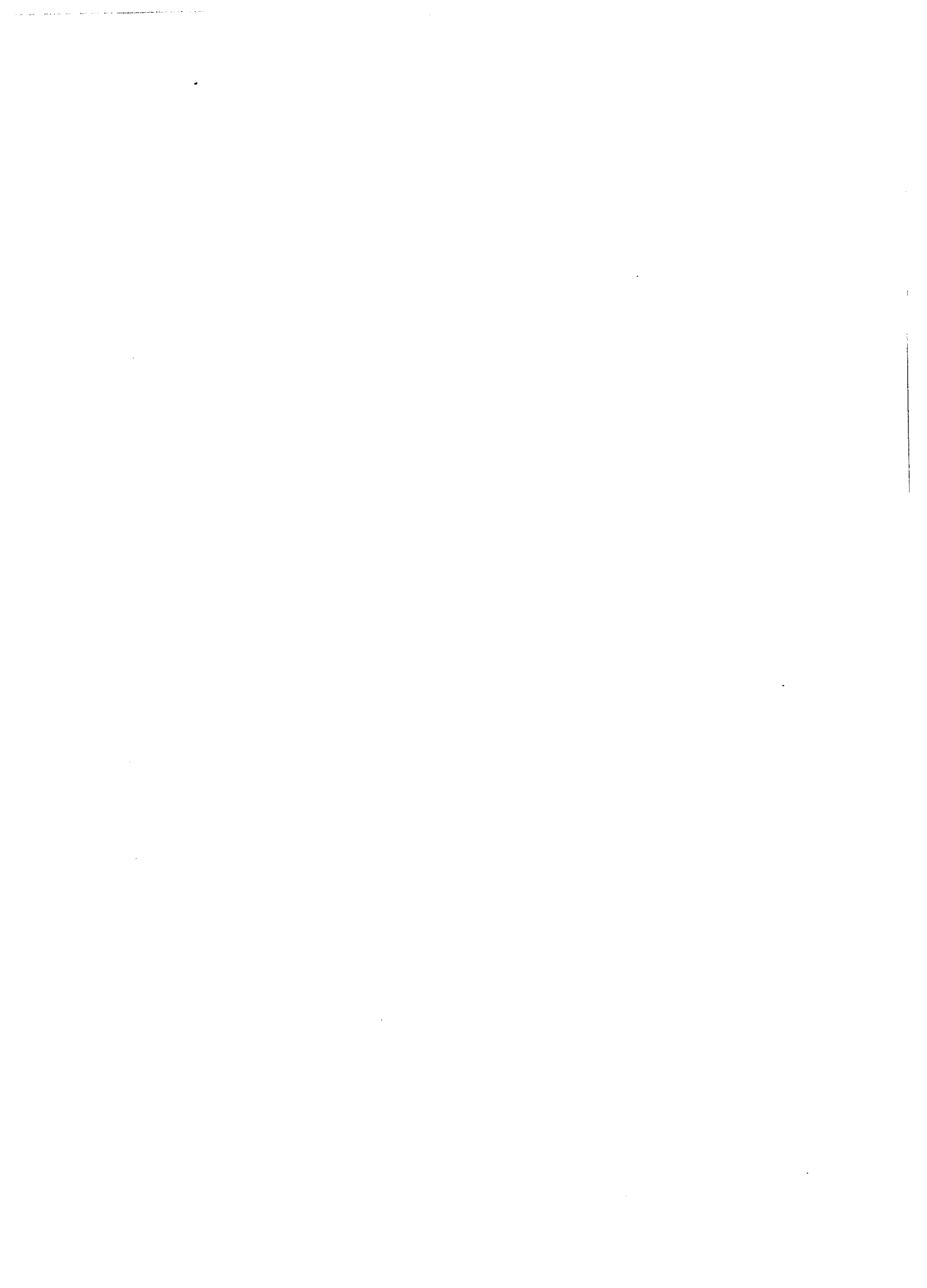
GROSS (Germany):

Concerning the question of Dr. PIDD, whether the work function can be in-

creased by additives: The answer is yes. We will present measurement in this conference, showing that the bare work function of (110) tungsten will be increased by oxygen up to 6 eV.

HATSOPOULOS:

We have as much concern about bare work function measurement as you have had and I understand that you have developed a criterion of being able to pin down bare work function measurements. The trouble with bare work function measurements is, as you know, the presence of oxygen in your vacuum. So I do not trust very much our bare work function measurements, but for whatever they were the etching produced about a 0.3 eV rise in the work function. But that may not be the proper number because bare work function measurements are not very reliable until we develop good control of vacuum, - and I think you have done a very nice job recently in this direction.



CHARACTERISTICS OF A THERMIONIC CONVERTER WITH A CHLORIDE-VAPOR-DEPOSITED TUNGSTEN EMITTER AND A NICKEL COLLECTOR*

V.C. Wilson
General Electric Research and Development Center
Schenectady, New York

ABSTRACT

A chloride-vapor-deposited (110) tungsten emitter with a vacuum work function of 4.96 e.v. was built into a 0.005-inch-spaced converter with a nickel collector. This converter yielded almost the same output power as did a converter with a single-crystal (110) tungsten emitter, 0.002 inch spacing and a molybdenum collector.⁶ It is also compared with two other similar converters. The vapor-deposited (110) tungsten surface is extremely stable. The collector work function decreased when the device was left at room temperature for one month.

At intermediate Cs coverages, the (110) plane of tungsten yields a higher electron emission than any other plane of tungsten.¹ This plane is also the most densely packed and the most stable thermally. The San Fernando Laboratories have developed a chloride process for vapor-depositing tungsten with the (110) planes parallel to the bulk surface. Several samples

*This work was supported by the NASA, Lewis Research Laboratory under Contract No. NASA 3-8511.

of these deposits were mechanically polished, electropolished, electro-etched to expose the (110) planes,² and had the orientation checked by x-ray diffraction. Measurement of the surface work function by electron thermionic emission in vacuum appeared to be the best criterion for selecting a well oriented and uniform sample. Heating to 2700°K for 1/2 hour produced large (110)-oriented crystals 1 to 2 mm in diameter. These grew at the expense of crystallites with other orientations. As the percentage of (110)-oriented surface increased, the vacuum work function increased and approached 5.0 e.v. Additional heating did not change the work functions and the surfaces appeared to be very stable. L. Yang and R.G. Hudson³ have made similar observations.

A sample with $\phi = 4.96$ e.v. was used as an emitter in a 5-mil-spaced thermionic converter with a nickel collector. Figure 1 shows a typical family of load lines. Figure 2 shows the envelope of such families at 6 different emitter temperatures. The 3 solid lines of Fig. 3 compare this converter with two other converters also having 5-mil spacing and nickel collectors⁴ at 20 amp/cm². In this design the heat from the collector is removed by radiation. As may be seen from Fig. 1, at $T_E = 2153^\circ\text{K}$ the collector ran at 1061°K for the curve that gave the optimum output at 20 amps/cm². It is believed that for maximum output this is too high a collector temperature

for this emitter temperature. The dashed extension of the curve for this converter in Fig. 3 is a probable output that one would obtain if the collector could be kept cooler.

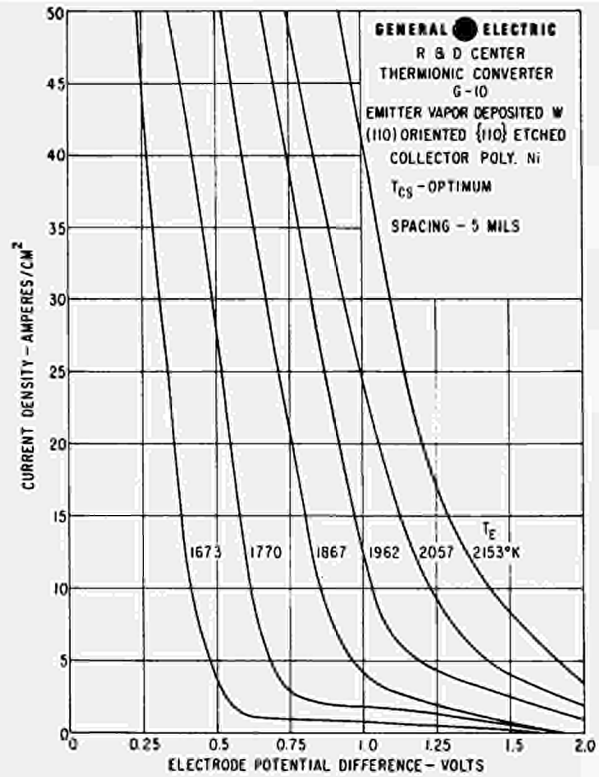
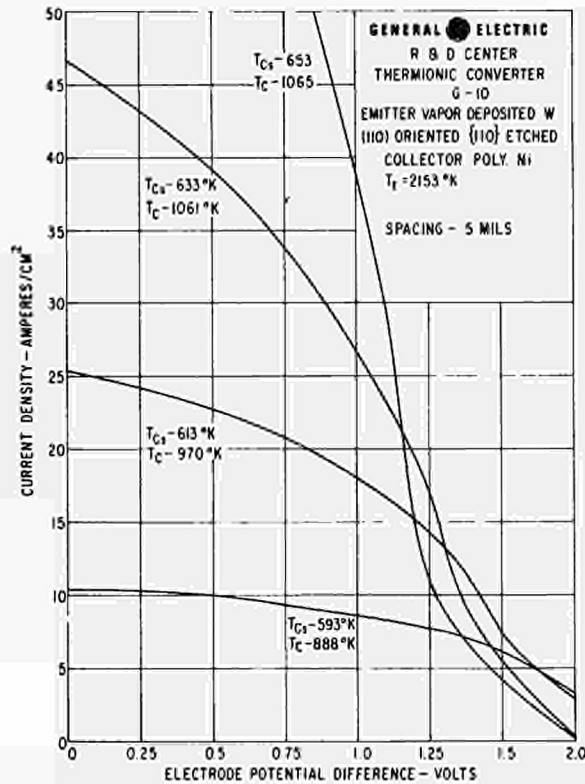


Fig. 1 A family of load lines. Fig. 2 Envelopes of load lines.

Originally the collector exhibited a minimum work function of 1.61 e.v. in Cs vapor. After a month at room temperature, ϕ_c was measured to be 1.43 e.v. Data presented here are with this low ϕ_c . In another experiment⁵ a similar result was observed; i.e. the work function of a tungsten surface in cesium vapor changed from 1.72 to 1.47 e.v. in three weeks at room temperature. In both cases during the initial operation period of several hours there was no apparent change in

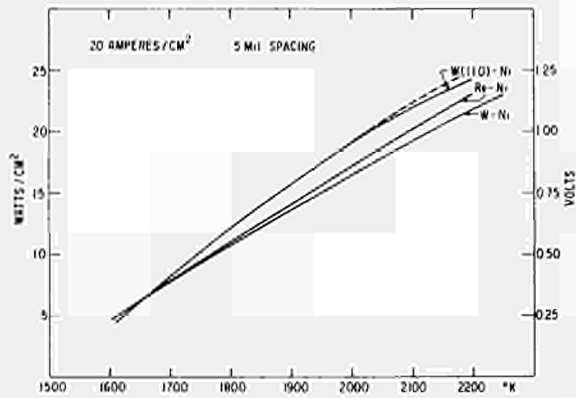


Fig. 3 Output performance for three converters.

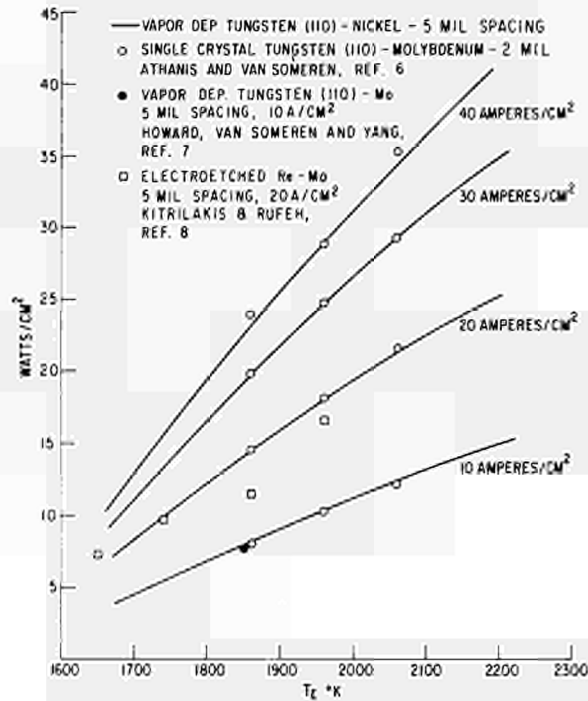


Fig. 4 Comparison of four similar converters.

converter performance. The changes appeared to occur while the converters were left for a few weeks at room temperature. One possible hypothesis is that in converters that have been carefully cleaned and contain cesium, which acts as a getter, the oxygen pressure is so low that it takes a few days for a monolayer of oxygen to accumulate on the collector surface. The low work function surface may be a Ni-O-Cs or a W-O-Cs compound formed at room temperature or possibly formed the next time the collector is warmed.

Figure 4 compares the output power of four converters. The solid lines represent this converter. The open circles give data presented by Athanis and vanSomeren⁶ for a thermionic

converter with a single-crystal (110)-surface tungsten emitter and a molybdenum collector. The data from Athanis and vanSomeren has been corrected for the ohmic voltage drop in the emitter lead and for a 40°K temperature drop through the emitter. It is surprising that the two converters had almost identical output powers because the Athanis and vanSomeren converter had a 2 mil spacing, whereas the converter of this report had a 5 mil spacing and, of course, the collectors are different. Possibly nickel is a slightly better collector than molybdenum and is sufficiently better to compensate for the difference in the spacing. One can conclude that the vapor-deposited polycrystalline tungsten emitter oriented with the (110) crystallites exposed is as good as a single-crystal tungsten emitter. This fact is significant. Also Fig. 4 shows, for comparison, data from two other similar converters.^{7,8}

CONCLUSIONS

Although this converter was not operated for a long period of time to demonstrate stable operation with a long life, there were no indications of a reduction in output power with operation. Extensive heat treatments of the emitter monitored by microscopic observation and work function measurements, indicated that the (110) surface was extremely stable.

The converter with the (110) oriented polycrystal tungsten emitter gave almost identical output to one with a single-

crystal (110) tungsten emitter.

The collector work function decreased while standing at room temperature for one month.

REFERENCES

- (1) MARTIN, S.T., "On the Thermionic and Adsorptive Properties of the Surfaces of a Tungsten Single Crystal", Phys. Rev. 56, 947 (1939); WEBSTER, H.F. and READ, P.L., "Results Obtained with the Sphere-to-Plane Thermionic Emission Microscope", Surf. Sci. 2, 200 (1964).
- (2) WILSON, V.C. and LAWRENCE, J., "Characteristics of a Thermionic Converter with a Fluoride Vapor Deposited Tungsten Emitter Etched to Preferentially Expose the (110) Crystal Planes", Therm. Conv. Spec. Conf., 1 (1967).
- (3) YANG, L. and HUDSON, R.G., "Effects of Preferred Crystal Orientation and Surface Treatment on the Work Function of Vapor-Deposited Tungsten", Therm. Conv. Spec. Conf., 395 (1966).
- (4) WILSON, V.C. and LAWRENCE, J., "Operating Characteristics of Two Thermionic Converters Having Rhenium-Nickel and Tungsten-Nickel Electrodes", Adv. Energy Conv. 4, 195 (1964).
- (5) LAWRENCE, J. and PERDEW, J.P. "Effect on Thermionic Converter Performance of Emitter Material Evaporated on a Low Work Function Collector", Therm. Conv. Spec. Conf., 289 (1965).
- (6) ATHANIS, T. and vanSOMEREN, L., "Planar Converters for Radioisotope Generators", TEECO Tech. Rpt. AFAPL-TR-67-99 (1967).
- (7) HOWARD, R.C., vanSOMEREN, L., and YANG, L., "Preliminary Results on the Thermionic Performance of a Vapor-Deposited Tungsten Emitter Having (110) Preferred Orientation", Therm. Conv. Spec. Conf., 10 (1967).
- (8) KITRILAKIS, S.S. and RUFEN, F., "The Output Characteristics of an Electroetched Rhenium Surface", Therm. Conv. Spec. Conf., 19 (1966).

ESSAIS D'UN CONVERTISSEUR DU TYPE NUCLEAIRE
MUNI D'UN RESERVOIR DE CESIUM A ADSORPTION.

par Ph. DEFRANOULD

Laboratoires de Recherches Générales
Compagnie Française THOMSON HOUSTON - HOTCHKISS BRANDT
92 - BAGNEUX

Résumé -

Nous avons réalisé un type de convertisseur cylindrique muni d'une structure adsorbante poreuse et d'un réservoir à césium liquide séparés par une vanne actionnable lorsque le convertisseur est en fonctionnement. Cette disposition permet d'effectuer sur le même convertisseur de nombreux essais de conversion avec ou sans phase liquide de césium. Les premiers essais (quelques dizaines d'heures) ont montré un fonctionnement satisfaisant du convertisseur lorsqu'il travaillé uniquement avec une structure à césium adsorbé..

1 - Introduction

La structure la plus simple que l'on puisse envisager pour un réacteur thermoionique est celle du réacteur formé par un assemblage de diodes individuelles travaillant en vapeur sèche, c'est-à-dire exempte de réservoir à césium liquide, c'est-à-dire de point froid. Un moyen de faire fonctionner une cellule de cette manière est d'incorporer dans l'enceinte une structure métallique poreuse pouvant adsorber une quantité de césium suffisante pour assurer le bon fonctionnement du convertisseur.

Le principe de la présente étude est le suivant : le convertisseur est muni d'une structure adsorbante et d'un réservoir à césium liquide séparé par une vanne d'isolement. Le convertisseur peut donc fonctionner avec et sans phase liquide par simple action sur la vanne ; nous avons ainsi pu comparer et suivre l'évolution des performances dans les deux cas de fonctionnement.

2 - Description du système d'essais

La cellule convertisseuse (figure 1) proprement dite comporte un émetteur à paroi épaisse (4 mm) de façon à avoir une température homogène. La surface émettrice est de 20 cm². 4 thermocouples W-Re 5 %, W-Re 26 %

sont disposés à différentes hauteurs dans l'épaisseur de la paroi d'émetteur. Deux natures d'émetteur ont été essayées : molybdène et tungstène. L'émetteur tungstène est obtenu par dépôt pyrolytique (réduction de WCl_6) sur une ébauche en molybdène massif ; l'épaisseur du dépôt est de 50 à 100 μ . Le collecteur est en molybdène, l'espace interélectrode est de 250 μ à froid, soit environ 150 μ à chaud. La diode est munie d'un queusot de pompage sur lequel sont disposés, en partant de la cellule : la structure adsorbante, puis la vanne métallique et enfin le réservoir à césium liquide. Après pompage et dégazage, l'extrémité du queusot est obturée.

Les structures adsorbantes choisies sont des éponges métalliques obtenues par frittage de poudres fines (grains de 1 à 5 μ) de tungstène ou de molybdène. Le frittage est effectué à 1 600 °C, il est poursuivi jusqu'à ce que la porosité de la structure tombe à environ 25 % ; le diamètre des pores est d'environ 5 μ . Quelques centimètres cubes de cette éponge sont placés dans le convertisseur, la surface totale d'adsorption présentée est d'environ 1 m². La vanne d'isolement, entièrement métallique, a été conçue de façon à pouvoir fonctionner à 500 °C.

Le convertisseur, muni d'un système de chauffage d'émetteur et d'un système de refroidissement de collecteur est placé sur un montage d'essais entièrement sous vide (figure 2). Ce montage d'essais permet d'amener, puis de stabiliser le convertisseur à un point de fonctionnement quelconque ; les paramètres suivants peuvent être réglés indépendamment : puissance d'entrée, température du collecteur, température de l'adsorbant, température du réservoir de césium, résistance de charge. En outre, douze paramètres sont enregistrés en permanence : puissance d'entrée, pression dans l'enceinte, températures en quatre points de l'émetteur, températures en deux points du collecteur, température de l'adsorbant, température du réservoir à césium liquide, courant de sortie, tension de sortie.

Un système de transmission, électriquement isolé et étanche, permet de manoeuvrer la vanne de l'extérieur lorsque le convertisseur est en fonctionnement.

3 - Résultats

3.1. Fonctionnement vanne ouverte

La première partie des essais est effectuée vanne ouverte, c'est-à-dire avec réservoir à césium liquide. Cette première phase a pour but, d'abord de vérifier les performances de la cellule en fonctionnement normal (avec phase liquide) et simultanément de permettre au césium de s'adsorber progressivement sur la structure poreuse : la température de cette dernière est maintenue à une valeur légèrement inférieure à la température du collecteur, elle détermine le nombre de particules adsorbées à l'équilibre (fonctionnement à pression de césium constante). Les figures 3 et 4 donnent les principaux résultats, puissance de sortie et rendement en fonction de la puissance d'entrée et de la température d'émetteur pour les deux types

d'émetteur essayés : molybdène et tungstène. Une puissance de sortie de 5 W/cm^2 et un rendement de 11 % sont atteints à $1\ 650\ ^\circ\text{C}$ pour le tungstène et à $1\ 750\ ^\circ\text{C}$ pour le molybdène. Les figures 5 et 6 représentent les profils de température d'émetteur relevés pendant le fonctionnement du convertisseur. Nous voyons que la répartition de température sur l'émetteur est assez plate (sauf du côté de la connexion), lorsque la puissance de sortie est maximale. Par contre, lorsque la puissance de sortie n'est pas maximale l'écart de température entre les deux extrémités de l'émetteur peut devenir très important ; par exemple (figure 6) pour $P_s/P_s \text{ MAX} = 75\ \%$, on a : $\Delta T \approx 300\ ^\circ\text{C}$.

3.2. Fonctionnement vanne fermée

Après cette première phase d'essais (environ une centaine d'heures), le convertisseur a été stabilisé à un point de fonctionnement donné, la communication avec le réservoir à césium liquide étant maintenue. Pendant ce temps, l'équilibre s'établit dans l'enceinte de la cellule : les taux de recouvrement s'établissent, sur les surfaces à différentes températures (émetteur, collecteur, adsorbant, queusot, etc...), de façon à ce que en tous points de la cellule, il y ait équilibre entre la pression de césium (imposée par la phase liquide), la température et le taux de recouvrement du point considéré. L'équilibre est atteint lorsque le flux total d'atomes de césium, traversant une section quelconque située entre le convertisseur et le césium liquide, est nul. A ce moment, l'isolement du réservoir de césium liquide par simple fermeture de la vanne, peut être réalisé sans perturber l'équilibre. La quantité de césium emmagasinée dans la cellule est alors juste celle nécessaire au maintien de la pression optimale (pour le point de fonctionnement initial). Plusieurs essais d'une vingtaine d'heures ont été effectués ; la figure 7 représente l'évolution de puissance de sortie en fonction du temps (temps compté après la fermeture de la vanne) : la baisse de performances enregistrée est de l'ordre de 10 à 20 %. Cette baisse est due à une baisse de la pression de césium, puisqu'en effet, la remise en communication (par réouverture de la vanne) du réservoir liquide (à température optimale) et de l'enceinte interélectrode provoque la remontée immédiate de la puissance de sortie à sa valeur initiale. La quantité de césium provoquant cette baisse de pression peut être estimée à l'aide des courbes donnant, d'une part la puissance de sortie en fonction de la pression de césium (relevée expérimentalement, figure 8), d'autre part la pression de césium en fonction du nombre total d'atomes présents dans l'enceinte (calculée à partir des équations de l'adsorption, figure 9). Ainsi, aux baisses de performances considérées (figure 7) correspond une consommation moyenne de césium d'environ $1\ \mu\text{g/heure}$.

Pendant le fonctionnement en vapeur sèche, deux sortes d'opérations ont été faites (figure 7) :

- Arrêt, puis redémarrage du convertisseur, après rétablissement des températures aux valeurs initiales, nous retrouvons sensiblement les mêmes performances (le temps d'arrêt et de remise en route a été décompté, il n'apparaît pas sur la figure 7).

- Augmentation de la température de l'adsorbant après un certain temps de fonctionnement : on enregistre alors une remontée de la puissance de sortie à une valeur proche de sa valeur initiale. Cette remontée est due à la remontée de pression de césium à sa valeur optimale.

4 - Conclusion

Les premiers essais (quelques dizaines d'heures) de convertisseurs sans phase liquide de césium (vapeur sèche) ont mis en évidence un fonctionnement satisfaisant. Toutefois, nous avons enregistré dans le temps une baisse de performances consécutive à une baisse de pression de césium : ceci montre que le flux d'atomes incidents était supérieur au flux d'atomes réfléchis au moment de la fermeture de la vanne. Deux hypothèses peuvent être avancées :

- l'équilibre n'est pas atteint au moment de l'isolement et la structure poreuse continue d'adsorber du césium,

- il y a une consommation réelle de césium due à des réactions chimiques internes.

Les essais de plus longue durée en cours doivent permettre d'élucider le phénomène et de réduire cette baisse de pression : en effet, pour que le système soit stable, il faut que la consommation de césium (réelle ou apparente) soit de l'ordre de 10^{-3} $\mu\text{g}/\text{heure}$, c'est-à-dire mille fois moins que le taux actuellement mis en évidence.

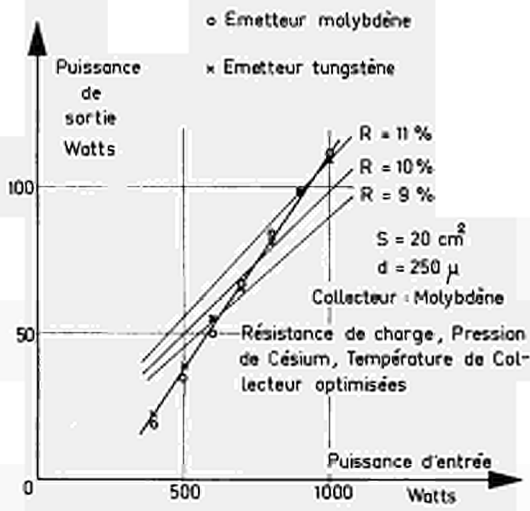
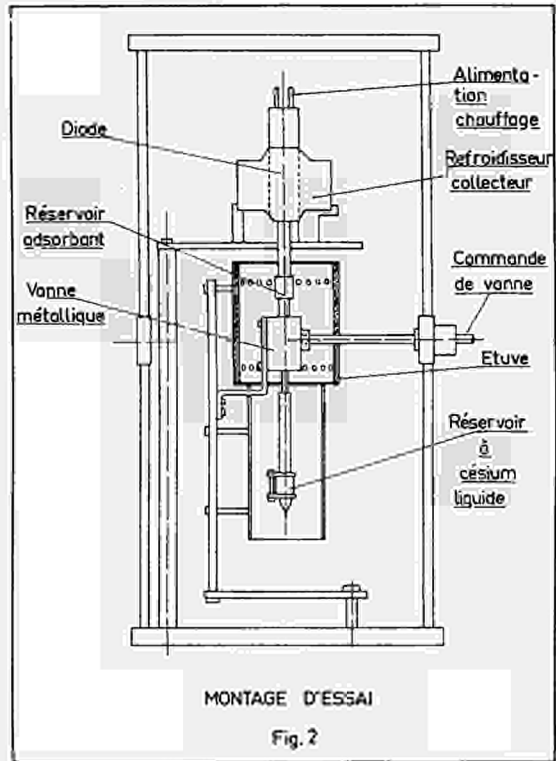
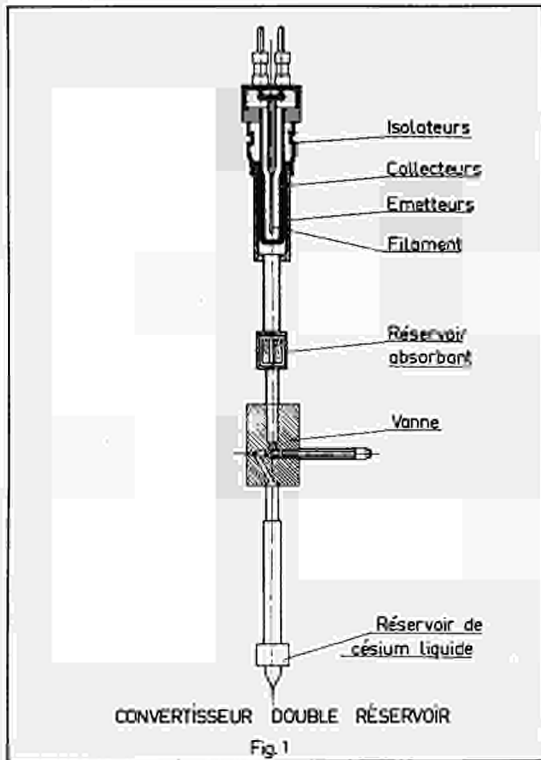


Fig. 3

Emetteur tungstène {
▲ Rendement optimal
○ Puissance de sortie optimale
● Emetteur molybdène }

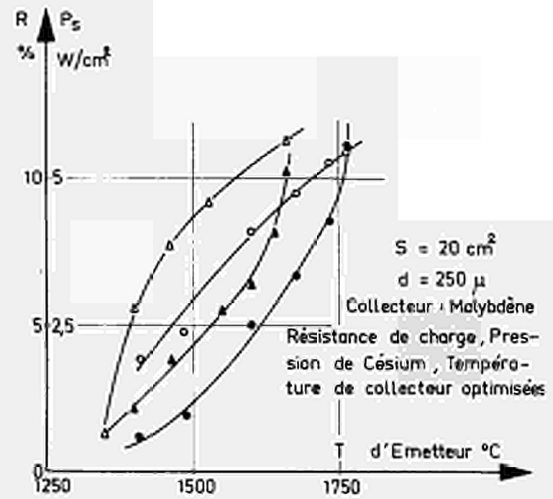
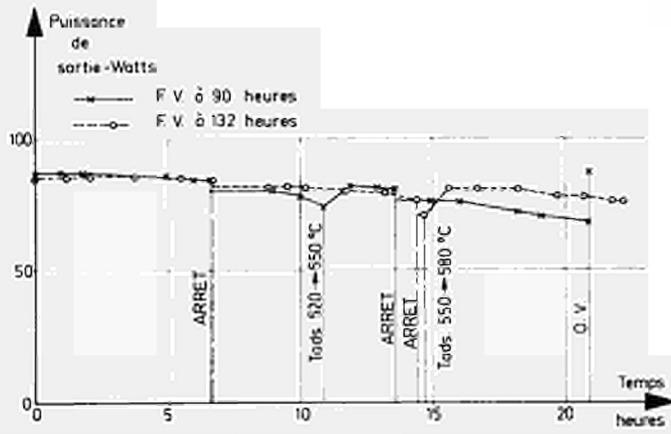
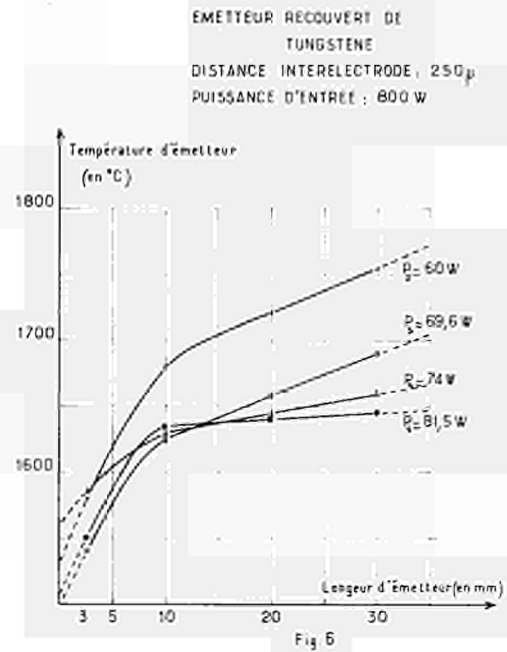
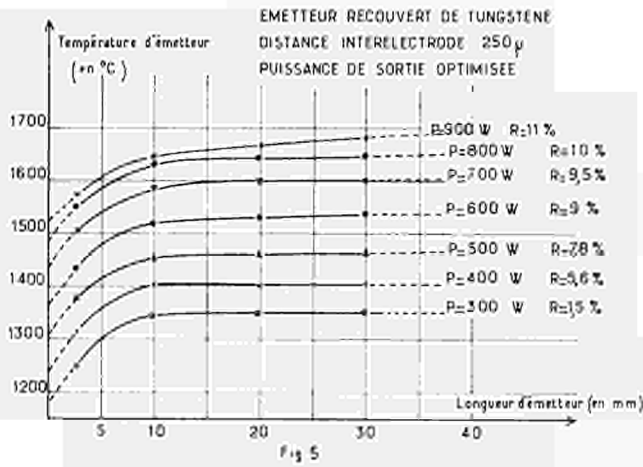
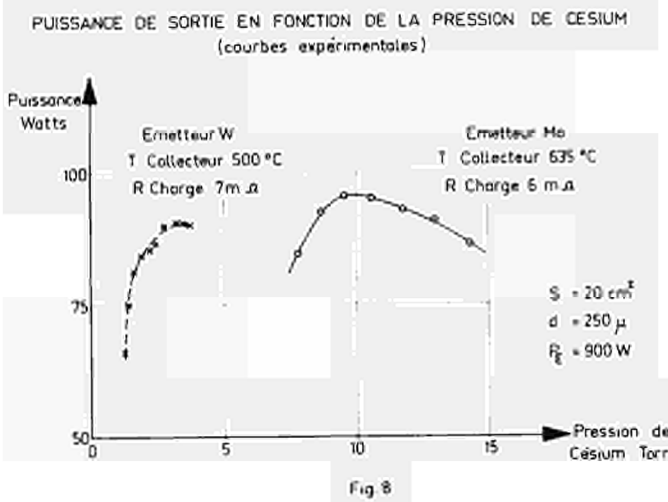
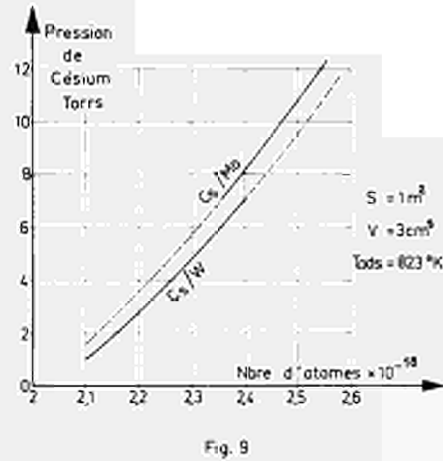


Fig. 4



COURBES THEORIQUES DONNANT LA PRESSION DE CESIUM DANS UNE ENCEINTE ISOTHERME CONTENANT UNE STRUCTURE ADSORBANTE



EXAMEN DES COUCHES REFRACTAIRES PYROLYTIQUES
AU MOYEN DU MICROSCOPE ELECTRONIQUE SECONDAIRE A BALAYAGE

par G. BLET et O. CAHEN

Laboratoires de Recherches Générales
Compagnie Française THOMSON HOUSTON - HOTCHKISS BRANDT
92 - BAGNEUX -

L'examen des dépôts pyrolytiques se fait habituellement au microscope optique : on obtient ainsi une idée approximative de la structure de la couche et on en déduit les directions préférentielles de croissance. En fait, on ne peut observer les dépôts qu'après une préparation soignée de l'échantillon : enrobage dans une résine thermodurcissable, coupe, polissage mécanique, attaque chimique. Cette préparation peut parfois altérer l'état de l'échantillon, par exemple en introduisant des poussières métalliques dans les interstices des cristaux. De plus, la surface examinée est plane, et on ne peut observer la direction des lignes caractéristiques qui coupent le plan de la préparation. Ces lignes sont très importantes quand il s'agit d'une croissance cristalline de type basaltique comme c'est le cas dans la décomposition des halogénures en phase vapeur.

Le microscope électronique secondaire à balayage "Stéréoscan" est un appareil, récemment mis au point, qui permet d'observer des échantillons de forme quelconque, avec un grossissement supérieur à celui du microscope optique et une profondeur de champ considérable. Dans cet appareil, un pinceau électronique très fin explore la surface apparente de l'échantillon par un balayage linéaire de type télévision. Un détecteur recueille les électrons secondaires, quel que soit leur point de départ à la surface de l'échantillon. Le même balayage linéaire est appliqué aux bobines de déflexion d'un oscillographe cathodique, dont la luminosité est modulée par le courant d'électrons secondaires issu de l'échantillon et convenablement amplifié. Sur chaque photographie réalisée à l'aide du Stéréoscan, la brillance d'un point correspond au nombre d'électrons secondaires émis par le point représenté sur l'échantillon. Cette quantité dépend du matériau et de l'incidence des électrons sur la surface.

Les photographies ci-dessous montrent des échantillons de dépôts de tungstène, sur substrat molybdène et de carbure du tungstène obtenu par cracking sur un fil de tungstène.

La photographie n° 1 au grossissement 10.000, montre la finesse de résolution de l'appareil, qui met clairement en évidence une faille de largeur 0,2 μ .

...../

Sur la photo N° 2 (grossissement 2.000), on distingue les cristallites de molybdène, de dimensions 5 à 10 μ , les colonnes prismatiques de tungstène de diamètre 1 à 2 μ , des bulles aux points de grains entre les colonnes, dont le diamètre est inférieur à 1 μ , et une couche superficielle qui recouvre une grande partie de l'extrémité des colonnes. Certaines colonnes émergent à travers cette couche. On constate que le tungstène déposé à partir de hexaschlorure présente des bulles, comme celui qui est déposé à partir d'hexafluorure, mais de beaucoup plus petites dimensions, ce qui les rendait inaccessibles à l'observation au microscope optique.

Sur la photo N° 3, on remarque que la surface est constituée de grosses cristallites sphériques (10 à 30 μ), elles-mêmes formées de grains approximativement sphériques de moins de 500 Å. Les plus grosses cristallites ont peu de cohésion, certaines se sont déchaussées spontanément.

La photo n° 4 montre une surface de tungstène que le cracking n'a pas carburée, mais où il a fait apparaître des cristaux hexagonaux spiralisés de tungstène de 5 μ environ.



Photo N° 1

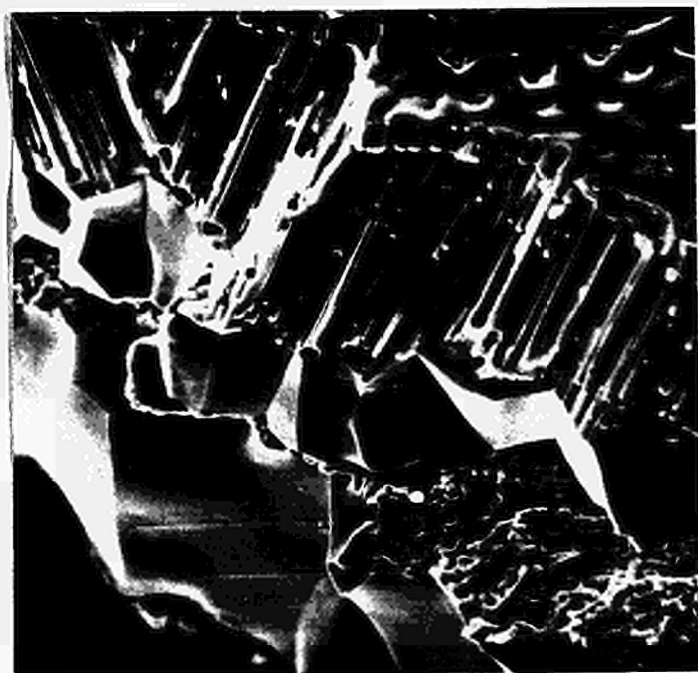


Photo N° 2



Photo N° 3



Photo N° 4

THERMIONIC
CONVERTER TECHNOLOGY *

by

Peter Rouklove

Jet Propulsion Laboratory
California Institute of Technology
Pasadena, California

ABSTRACT - This paper covers the methods used at JPL to improve the reliability and efficiency of thermionic converters. Test of more than 135 thermionic converters demonstrated that converters, assembled from carefully processed parts and properly evacuated, were capable of long-term operation with high output power densities at high emitter temperatures. Analysis of the most common causes of converter failures is also included.

INTRODUCTION - The effort at the Jet Propulsion Laboratory to improve thermionic converters was carried out in the following ways:

- a) Systematic parametric and diagnostic testing of the converters.
- b) Long term life testing.
- c) Ancillary experiments involving cesium compatibility, reactions between insulators and refractory metals, etc.
- d) Detailed metallographic examination of converters with abnormal behavior.
- e) Incorporation of improvements resulting from the above examinations in subsequent converters.

Since initiation of the program in 1960, more than 135 converters have been tested. The progress reflected by Table 1 can be attributed mainly to a better understanding of the materials used in a converter and improvements in their preparation and in the care of processing the converter itself.

LIFE TESTING - A program of testing converters to obtain reliable data on their life and failure modes for statistical purposes has been actively pursued at JPL. Part of the life testing facilities are shown in Figure 1.

The majority of the converters examined were those with a planar electrode configuration with an emitter area of 2 to 2.55 cm² and an interelectrode

*This paper presents the results of one phase of research carried out at the Jet Propulsion Laboratory, California Institute of Technology, under Contract No. NAS 7-100, sponsored by the National Aeronautics and Space Administration.

spacing of approximately 50 microns. Some converters tested, however, were built with wider interelectrode spacing to corroborate the performance observed in research-type, variable-spacing vehicles, while other converters had a cylindrical configuration designed to operate with emitter heat pipes. Figure 2 illustrates typical configurations of the latest converters.

Output power densities of 17 to 20 w/cm² at emitter temperatures between 1900°K and 2000°K have been observed in the laboratory during successful life tests uninterrupted throughout 8,000 to 15,000 hours. Current state of the art performance based on these results and independent tests (Ref. 1) for carefully processed converters, operating under the above mentioned conditions, appears to be a lifetime of approximately 8,000 hours. Converters operating at lower emitter temperatures, therefore being subjected to less stress, are expected to achieve even longer life. Our tests indicate that the rule of "a factor of two for each 50°" may apply to thermionic converters but additional data is needed to substantiate this point of view.

Figure 3 presents the current-voltage characteristics of five converters which are representative of a lot of 40 built at the same time on a semi-production basis. The electrodes consisted of a rhenium emitter and a molybdenum collector, with 50 microns interelectrode spacing.

From examination of the latest hardware-type converters capable of long term operation at an emitter temperature around 2000°F, it appears that a plateau or level has been reached in regard to their performance characteristics. These levels are output power densities of 17 to 20 w/cm² at 0.6-0.7 v, device efficiencies of 10 to 12%, and a weight-to-power ratio of 1.8 gm/watt. Recent improvements have allowed reduction of the emitter temperature by 200°C for a given power output density; and outputs of 4 w/cm² at 0.7 v have been observed in cylindrical converters operating at 1700°K. Further technical advancements are required if these performances are to be surpassed. For example preliminary results have indicated that the injection of a controlled amount of O₂ as an "additive" in the interelectrode spacing changes the emitter work function. The corresponding performance could permit an increase of the interelectrode spacing by a factor of 4 for the same operating conditions (Figure 4). Several methods (Ref. 2) for the introduction of limited amounts of oxygen have been tried including the decomposition of Cu₂O, MoO₃, Cs₂O₂ etc. However, long term compatibility and insensitivity of the converter materials to reactions have not been demonstrated.

FAILURE ANALYSIS - The examination of converters at JPL, revealed the following abnormal behaviors according to their order of importance.

- a) Output power degradation (an unstable condition generally leading to open circuit) characterized by a gradual decrease in output power or by a dramatic reduction over a very short time.
- b) Open circuit (with loss of power output and increase in output voltage).
- c) Short circuit

Determination of the causes of defective operation can be complicated by such phenomena as self healing of pin holes or change in material conditions resulting from manipulations during metallographic examinations. However, it was observed that in each type of failure the defects were generally localized in certain portions of the converter. Table 2 gives the most common causes and effects of converter failure arranged by location rather than by nature.

Output power degradation was generally traced to a change in the state of the electrode surface, which altered its thermal or thermionic properties. Metallic interdiffusion or injection of gaseous products such as fission products or desorbed gases altered the thermal state of the electrodes; the deposition of reaction products or the migration of foreign products onto the electrode surfaces affected their work functions. Gradual degradation in power was also traced to slow leakage of cesium vapor. Degradation in performance also was observed as a result of changes in contact potential resistance at the junction between the converter and the power output leads.

The open circuit condition, except when related to mechanical failures in the electrical circuit or poor connections, was always the result of loss of cesium vapor, either by slow leakage or by catastrophic failure. In case of slow leakage, open circuit failure was preceded by gradual degradation of performance.

THE ELECTRODES - The short circuit condition in a converter was generally traced to mechanical perturbations of the electrodes and occasionally to excessive deposition of emitter material on the collector surface by mass transport action. Mechanical deformations resulted from following:

- a) Electrode swelling or bowing due to thermal stresses
- b) Creep of the envelope
- c) Separation of portions of the electrode from the substrate by Kirkendall diffusion or crystal growth
- d) Failure of weldments

Emitter - Major improvements in the converter resulted from the use of rhenium as electrode material and the utilization of emitter surfaces with preferred orientation obtained either by chemical vapor deposition (CVD) and/or by surface treatment. Converters with higher performance and with greater reliability are possible with rhenium because it is more stable than tantalum or molybdenum or tungsten and has a very high "bare" work function. Machining of rhenium requires periodic re-annealing and is best carried out with the spark discharge method and electron beam (EB) welding. Deposition of thin rhenium layers by pyrolytic vapor deposition (CVD) or their bonding by isostatic pressure on another metallic substrate (especially tantalum) resulted in intermetallic diffusion which, in turn, caused converter power degradation and eventual failure by Kirkendall diffusion (Figures 5 and 6). Rhenium surfaces are rather insensitive to chemical reactions and carburization and tend to remain stable if thermally treated (2200°C, 10 hr). The bare work function of polycrystalline rhenium was observed to be 4.9 ± 0.1 eV depending on its surface preparation.

Rhenium surfaces (Ref. 3) obtained by CVD from chloride vapor with 80% of the surface composed of (0001) planes oriented within 10° normal to the surface have values of the bare work function between 5.09 ev (as measured by the emission method) and 5.28 ev (electron microscope method). Such surfaces have resulted in measured cesiated work functions as low as 1.4 ev. The "apparent" work function of cesiated rhenium observed at JPL in hardware converters was ≈ 3 ev. Tungsten surfaces obtained by the decomposition of tungsten fluoride (WF_6) had a tendency to expose (100) planes as a preferred orientation, with a measured "bare" work function of 4.5 to 4.7 ev. The surfaces obtained by decomposition of tungsten chloride (WCl_6) however, showed preferred orientation of the (110) planes with a measured work function of 4.7 to 5.05 ev (Ref. 4). In the case of tungsten, like that of rhenium, the surface properties with the higher work functions did not seem to be improved by electroetching or thermal treatment. However, the polycrystalline surfaces of both metals have been improved after proper surface treatment, and in the case of rhenium a 40% improvement in converter performance has been observed.

It was our observation confirmed by other experiments (Ref. 5), that surface layers less than 10 mils thick (obtained from vacuum evaporation, CVD, or bonding by isostatic pressure) result eventually in heterogeneous surfaces. These surfaces result from volume diffusion of the surface deposit with the substrate with corresponding change in the work function. A newly observed phenomenon was the appearance of Kirkendall porosities on the emitter side facing the electron bombardment filament. The effect was traced to the diffusion of emitter material into a tungsten layer deposited from the filament. This effect, and abnormal crystal growth after long-term operation, tended to change the heat transfer characteristics between the heat source and the emitter surface. Deformation and sagging of the electron-bombardment filament during the life test also led to abnormal heat distribution on the emitter surface.

Collector - Collectors examined at JPL were of molybdenum, rhenium, palladium and niobium. Experimental studies of hardware converters indicated that rhenium (when used with a rhenium emitter) was the best collector surface material. Its measured "apparent" work function was 1.47 ev. Molybdenum was the second best collector surface material with a work function of 1.55 ev, followed by palladium with a work function of 1.51 ev; and finally niobium with a work function of 1.55 ev. The last three values are uncertain due to possible "additive" contamination.

Converters examined after long-term operation had a deposit of emitter material on the collector (500Å thick after 5000 hr operation). This accumulation makes it desirable to build the converters using identical materials for the electrodes. However, converters exhibiting degradation in power output as a result of a change as great as 0.3 ev in the collector work function possessed a heavy deposit (Fig.7). These deposits were of a semiconductor nature, their resistance varying from 0 to 20 milliohms as a function of the collector temperature. Generally, these deposits were found to contain not only the emitter material but also contaminants generally present in the cesium and others believed to be products of reactions (Ref.6). The rapid decrease of converter output and the presence of large amounts of emitter materials indicated a fast mass transport reaction. Based on the electrical behavior of the converters it is believed that

these reactions were produced by uncontrolled amounts of gases (O_2 or H_2) which had diffused from the converter components or had leaked through the converter envelope. Also, the deposits were related to impurities such as silicon, carbon, and aluminum introduced by chemical reactions between converter components or by impure cesium (Fig. 8).

In an attempt to mold the configuration of the converter to a specific multi-converter solar-generator design, the converter configuration was encompassed in a 30° angle. Difficulties were encountered in adjusting the collector surface temperature to that for optimum operation at high output power densities. To correct this problem, a heat pipe covered with a chromium oxide coating was used as a heat transfer and rejection system for the collector. The heat pipe (Ref. 7) was constructed from niobium tubing, with two layers of stainless steel #400 mesh as a wick and with sodium as the operating fluid. Unfortunately, nucleate boiling of the liquid at the collector interface led to overheating of the pipe when the collector was operating at power densities of 160 w/cm^2 . The overheating caused the mesh and the pipe walls to alloy and the pipe to fail. Improved vapor transfer methods and the use of niobium mesh should overcome this difficulty. Figure 9 represents the converter with its heat pipe and Fig. 10 illustrates the improvement in collector surface temperature due to use of the heat pipe which also reduced the converter weight by a factor of 4 (from 378 gm to 90.5 gm).

ENVELOPE - Emitter Sleeve - Of the two main components of the envelope, the supporting emitter member and the metal-to-ceramic seal structure, the former was found to be the predominant reason of converter failure. This thin member is subjected to heavy mechanical and thermal stresses and is exposed to chemical reactions from both inside and outside the converter. Leakage of cesium vapor through the emitter sleeve results in catastrophic failures not only by open circuit but also by deformation of the emitter as result of overheating due to the absence of electron cooling. Examples of recrystallization and impurity segregation at the crystal boundaries are presented in Fig. 11 and in Ref. 8. The reactions appear to be more pronounced in tantalum and tungsten than in more stable materials such as rhenium and it is suggested that whenever possible tantalum should be replaced by other materials more resistant to chemical reactions. A design of a re-entrant, convolute, emitter-support sleeve (Fig. 12) using heavier gauge material was tried and was apparently successful.

Preferably EB welding should be used for attachment of the thin emitter sleeve, as inert gas welding appears to accelerate the recrystallization (probably as a result of contaminants in the welding atmosphere). It appears that further technological improvements are required in the area of emitter-support structure, especially in devices with high current outputs.

Ceramic Seal Structure - Metal-to-ceramic seals using metallized high purity alumina and niobium as the metal member appear to be limited to an operating temperature of 800°C for long term operations. Less pure alumina or material with large grain concentrations of impurities is even more prone to deficiencies (Ref.9). The metal-to-ceramic interface and the ceramic itself appear to be the limiting components of the structure. Recent experiments have shown that

pure alumina loses some of its tensile strength and resistivity when subjected to high temperatures in a cesium atmosphere, especially when this state is compounded by high radiation doses. Slow reactions (with adsorption of cesium and eventual collapse of the seal structure) were observed at the metal-to-ceramic interface after exposure at high temperature for long periods of time. These reactions appear to be due to slow diffusion of the braze material and attack by cesium of the metallized layers (Ref. 10). Steps have been taken to reduce the metal-ceramic transition by cermets or graded seals and by the use of high temperature eutectic braze (Refs. 1, 12, and 13) materials. Cermet and graded seals appear to have distinct advantages over the standard metallized ceramic-to-metal seal, including mechanical work possibilities. Further work is required to develop long term metal-ceramic seals capable of operation at high temperature (1100°C and above). Such seals, moreover, could partially assist in the solution of the emitter support problem by allowing the use of heavier material.

GASEOUS CONTAMINANTS - The cesiated interelectrode spacing may be contaminated through the following process:

- a) Slow outgassing of the components of the converter.
- b) Introduction of cesium impurities.
- c) Reactions between cesium and other materials.
- d) Slow leakage or gaseous permeation from within (fission products) or from outside the converter envelope.

This accumulation of gaseous impurities is one of the major reasons for decay of converter performance. The most prevalent residual gases observed in well-exhausted converters are as follows: Ar, N₂, CO, CO₂, CH₄, H₂O and H₂. Hydrogen forms 90% of the gaseous bulk. The hydrogen not only promotes mass transfer reactions and/or metal embrittlement but is also responsible for a reduction in the converter performance (Ref. 14). With oxygen, hydrogen is responsible for water cycle type reactions and also reacts with cesium (and oxygen) to form cesium hydroxide which may attack materials, especially tantalum (Ref. 15).

It was found that large amounts of H₂ could be evolved from the O.F.H.C. copper (up to 16 volumes of H₂) used in the construction of the converter, especially if it had been fired with H₂ prior to its use. Another source of hydrogen is in the cesium in solute or hydride form. Argon and the fission products krypton, xenon and iodine not only are detrimental to the converter performance (Refs. 16 and 17) but also unfavorably affect the heat transfer balance in the converter. Oxygen in small amounts appears to improve the performance and cesiated electrode "apparent" work function changes from 1.5 - 1.6 ev (prior to oxidation) to 1.32 - 1.35 ev (after oxidation) have been observed.

CESIUM - The most common contaminants found in cesium are as follows: Ca, Fe, Mn, Si, Na, K, Rb, O, and H (some in the form of oxides or hydroxides).

Table 3 presents several cesium analyses of as received and after-use material. The observed increase of Mg in one case can be attributed to a reaction with "Lucalox" (containing 5000 ppm of Mg) while the copper probably comes from reactions with the ceramic metallizing layer (Ref. 18). Although most of the materials used in modern converters are not attacked by cesium, reactions have been observed with some types of ceramics and brazes. Also reactions were observed to be originated by cesium hydroxide or by the products of reactions of matter (SiO and Ta) transported by the cesium. Cesium considered for converter use should be purified by multiple distillation (Ref. 6) using a heat pipe or by cryogenic entrapment.

SUMMARY - The current state-of-the-art of thermionic converters properly processed and assembled from high-priority materials and operating at emitter temperatures of 1900 - 2000°K consist of power output densities of 17 - 20 w/cm² and quite respectable average life times of about 8000 hours. Progress in the development of thermionic converters has leveled off and a substantial breakthrough in technology is required before the present performance can be surpassed. Future activity for converter improvement should involve the following fields:

- 1) Reinforcement of the delicate emitter support structure.
- 2) Improvement of metal-to-ceramic seals for operation at higher temperature for longer periods of time.
- 3) Introduction of "additives" to improve converter performance.
- 4) Control and preparation of electrode surfaces to increase the power output.

ACKNOWLEDGEMENTS - Appreciation is expressed to the National Aeronautics and Space Administration and the Jet Propulsion Laboratory for the opportunity to present the results of this investigation. The author is also grateful to the following individuals for their assistance on this project: R.F. Gruber, K.W. Koerner, Dr. R. Marshall, Dr. K. Shimada, G. Stapfer and T.R. Wilson.

REFERENCES

- Ref. 1 Thermo Electron Co., Thermionic Converter Life and Repeatability Investigation - Contract AF 33 (615) - 1348 - Task 817305-30 Final Report. AF Aero Propulsion Lab., Wright Patterson A.F.B., Ohio.
- Ref. 2 Rufe, F., Lieb, D., and Fraim, F., Recent experimental results on electronegative additive - Proceedings of Thermionic Conversion Specialist Conference, Palo Alto, Calif., October, 1964. pp.25-28
- Ref. 3 Campbell, A.E. and Jacobsen, D.L., Thermionic Research and Development Progress. Final Report EOS-7118-NASA Contract NAS7-514.
- Ref. 4 Yang, L., and Hudson, R.G., Evaluation of C.V.D tungsten as electron emitters, Proceedings of the C.V.D of Refractory Metals Conference, Gattlingburg, Tenn., Sept., 1964. pp. 329-347 Interstate Printers.
- Ref. 5 Alleau, T., Clemot, M., Hasson, R., Post Mortem Examinations of Thermionic Emitters, Proceedings, Ref. 2, pp.312-320.

REFERENCES (Contd)

- Ref. 6 Rouklove, P., Thermionic Converters and Generators for Space Application - Part I Thermionic Converter Performance and Material Problems - Proceedings of the First International Conference on Thermionic Electrical Power Generation, London, Sept., 1965.
- Ref. 7 Brosens, P., Heat Pipe Converter Development - JPL Contract 951465, - Final report TE-4067-61-68, December, 1964.
- Ref. 8 Van Landruyt, J., and Wayman, C.M., On the habit planes of the sub-oxide phases TaO and TaO_2 . Journal of the Less Common Metals - Vol. 14, No.2, Feb., 1968 - pp. 248-249.
- Ref. 9 Higgins, J.K., Reaction of Alumina with Cesium Vapor. Transactions of the British Ceramic Society, Vol. 65, No. 12, pp. 643-659.
- Ref. 10 Hudson, R.G., Buzzelli, G., and Yang, L. - Post Operational Determination of Cesium Contents in Life-Test Converter Components. Proceedings, Ref. 2 - pp. 271-276.
- Ref. 11 Kaufman, W.B., Breitwieser, R., and Tishler, F. - High Temperature, Electrically Insulated Cermet Seal. Proceedings, Ref. 2 - pp. 260-270.
- Ref. 12 Gibson, H. - Fabrication and Evaluation of Graded Type Ceramic to Metal Seals. Proceedings, Ref. 2 - pp. 271-276.
- Ref. 13 Milch, A. et al. - Refractory Ceramic to Metal Seal. Electrochemical Technology, Vol. 5, No. 3-4, March-April, 1967. pp. 83-86.
- Ref. 14 Hall, W.B., and Shoemaker, R.E. - Control of Gas Temperatures in Thermionic Converter - Proceedings of Specialist Conference, Cleveland, Ohio, Oct., 1964, pp. 110-114.
- Ref. 15 Subbotin, V.I., et al. - State of Impurities in Cesium Used in a Thermionic Converter, Teplofizika Vysokih Temperatur - Vol. 5, No. 2, March-April, 1967, pp. 377-379.
- Ref. 16 Davis, M.V., and Backus, C.E., Effect of iodine and the inert gases as additives in a cesium arc diode. Proceedings of Thermionic Specialist Conference, Houston, Texas, Nov., 1966, pp. 376-381.
- Ref. 17 Rufeh, F., and Kitrilakis, S.S., Thermionic converter performance in presence of inert gases. Proceedings, Ref. 16, pp. 91-98.
- Ref. 18 Scott, J.M., Denko, J.C., and Case, J.M. - Post Test Examination and Analysis of a Cylindrical Thermionic Converter. Proceedings, Ref. 2, pp. 304-311.

Table 1. Thermionic Converter Progress

Parameters	1962	1963	1964	1965	1966	1967	Improvement Factor
Power Output (w)	12	25	36	44	50	50	4.2
Power Density (w/cm ²)	6	12	18	22	20	20	3.8
Efficiency (%)	3	5	8	12.5	10	11	4.2
Maximum Life (hr)	119	1500	3200	13,150	15,210	†	128
Vibration (20 g at 0 to 2000 cps)	*	*	*	OK	OK	†	100%
Shock (100 g for 0.5 msec)	*	*	*	OK	OK	†	100%
Power to Weight Ratio (w/lb)	16	33.6	54.0	72.0	57.0	280	17.5
Weight to Electrical Power (lb/kw)	63.5	30.5	18.5	14	17.6	3.6	17.5

*Test failed
†No data available or test not performed.

Table 2. Cause and Effects of Converter Failure

	Open Circuit	Degradation	Short Circuit
Emitter			
Recrystallization	X	X	X
Mechanical Deformation		X	X
Fuel Swelling		X	X
Increase in Thermal Resistance		X	X
Intermetallic Diffusion		X	X
Change in Surface Properties		X	X
Material Peeling			X
Collector			
Cracking	X		
Deficient Brazing		X	
Change in Surface Properties		X	X
Mass Transport Deposition		X	X
Leads			
Poor Connection	X	X	
Short Circuit of Leads			X
Brazes			
Porosity	X	X	
Material Contamination		X	
Intermetallic Diffusion	X		
Sleeve			
Pinholes	X		
Recrystallization	X		
Contamination	X		
Processing Deficiencies	X		
Creep			X
Metal Ceramic Seal			
Diffusion of Brazing	X		
Deposition on Insulator		X	X
Stress Cracking of Ceramic	X		
Tubulation			
Stress Cracking	X		
Collapse of Brazing	X	X	
Cesium Reservoir			
Poor Brazing	X		
Defective Pinch-Off	X		
Processing			
Insufficient Outgassing		X	X
Cesium Contamination		X	X
Inefficient Supervision		X	X
Material Incompatibility		X	X
Estimated Overall Percentages of Failure	70	20	10

Table 3. Analyses of Cesium Impurities

Elements	As Received* (ppm)			After Use in Converter (†) (ppm)	
Al	3	5	18	5	5
Ba	8	8	8	-	-
B	20	16	16	-	-
Ca	37	24	226	-	15
Cu	2	5	37	500	153
Cr	3	2	5	10	-
Fe	27	26	81	10	27
Mg	5	8	18	150	50
Mn	8	3	129	-	-
Ni	2	2	10	-	22
Pb	2	2	2	-	-
Si	18	24	29	5	60
Sr	8	2	16	-	-
Li	2	16	3	-	-
Ti	16	2	2	-	20
Tl	2	2	-	-	-
Na	19	29	66	20	30
K	13	13	36	-	25
Rb	19	115	1420	-	120
O	23	-	-	-	-

*Data from Dow, GE, and JPL
(†) Limited analysis due to small amounts

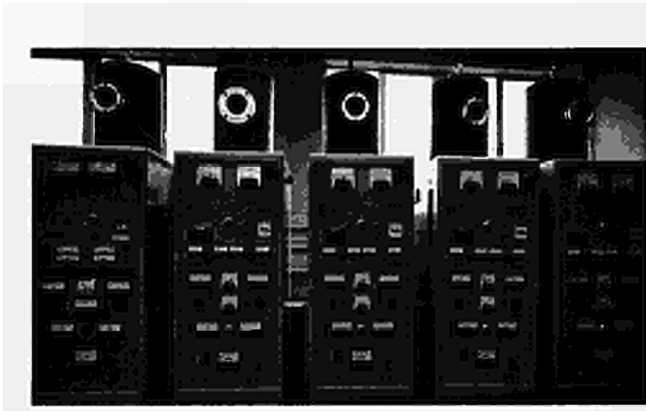


Figure 1. Partial View of Life Testing Converters

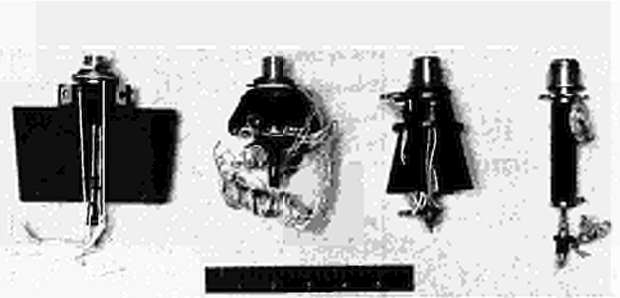


Figure 2. Configuration of Typical Converters

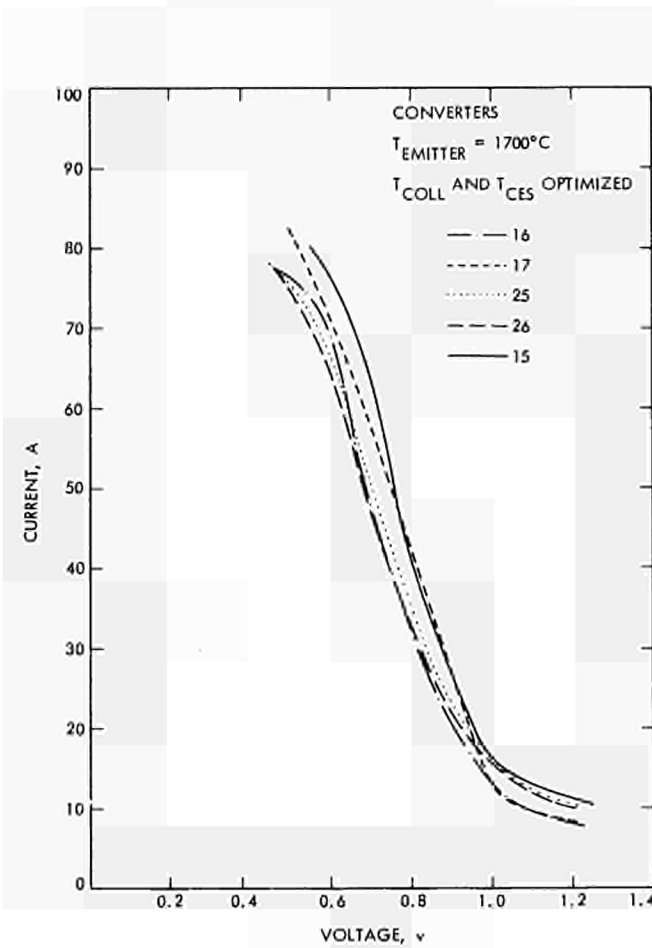


Figure 3. Current-Voltage Characteristics (emitter area 2 cm^2)

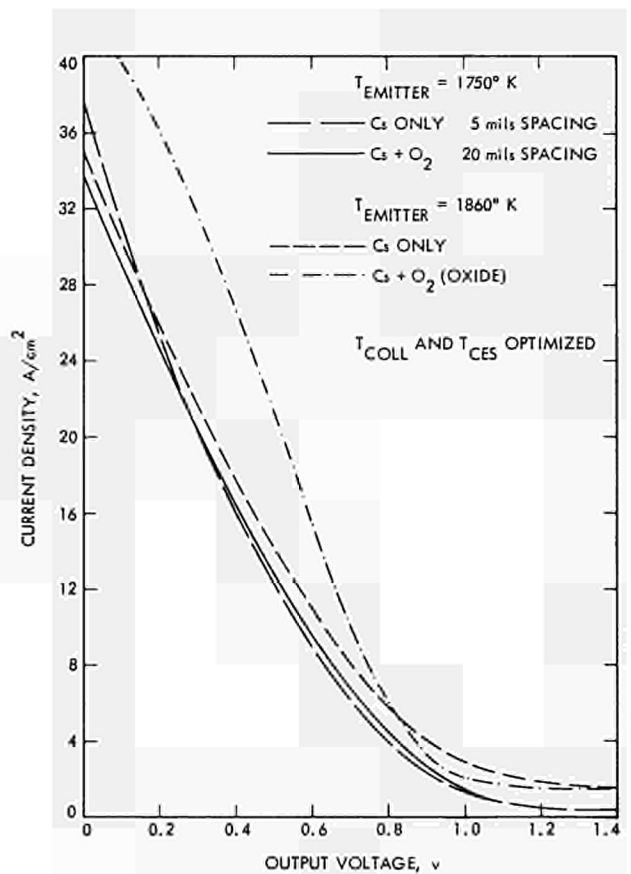


Figure 4. Effects of Oxygen as an "Additive"

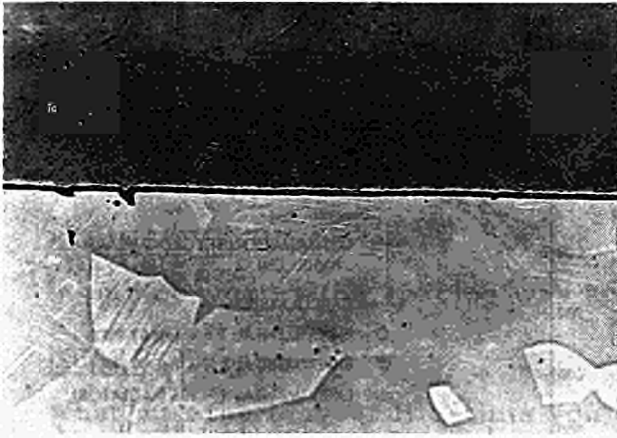


Figure 5. Tantalum - Rhenium Pressure - Bonded Interface (central stage)

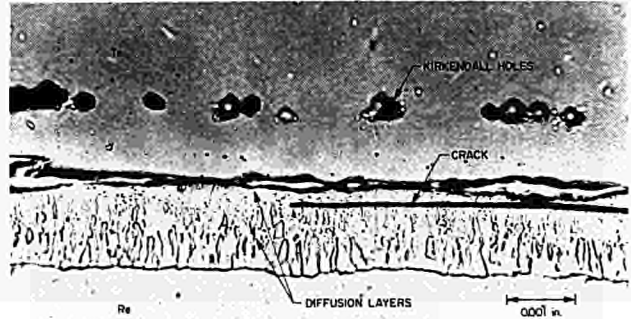


Figure 6. Tantalum - Rhenium Pressure - Bonded Interface (after 1500 hr operations)

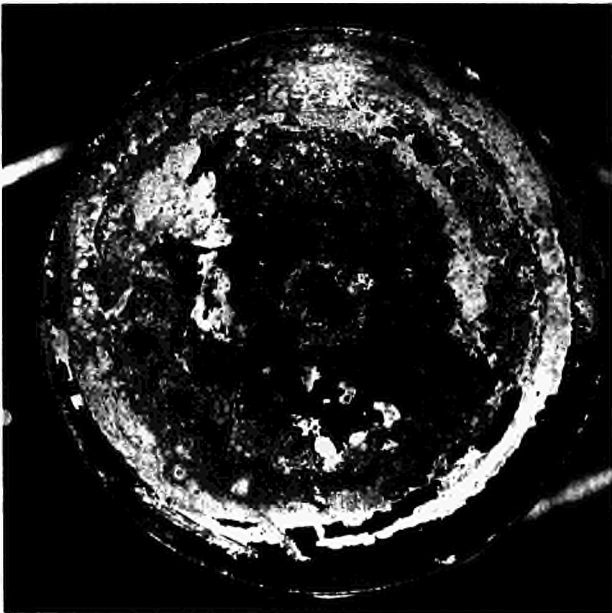


Figure 7. Collector Deposit

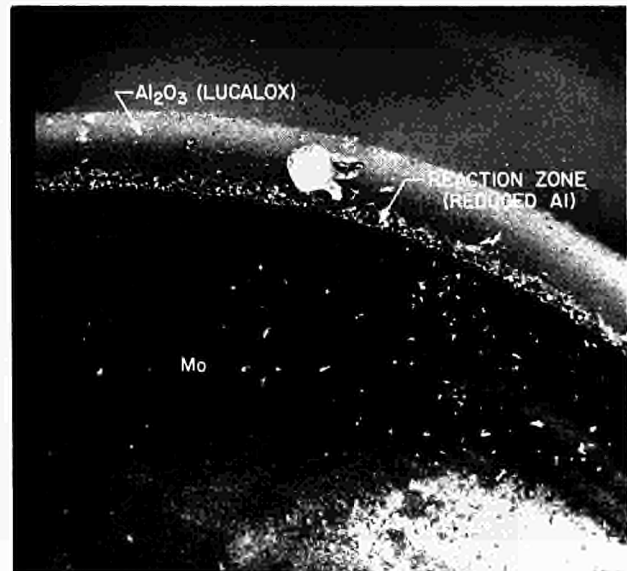


Figure 8. Reaction of Al₂O₃ and Mo - in Presence of Cesium



Figure 9. Converter with Collector Heat Pipe

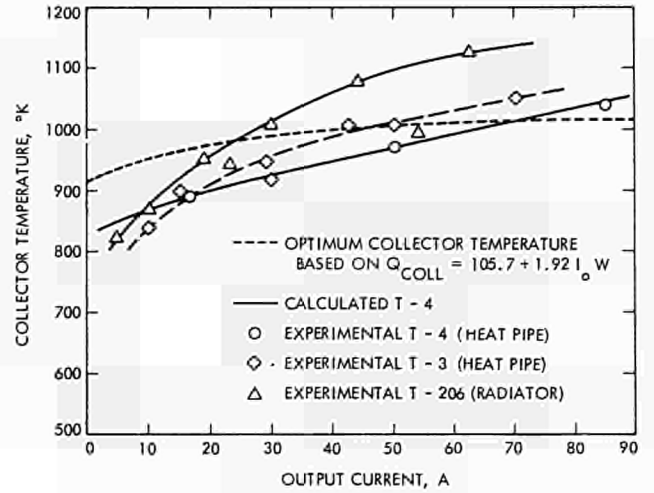


Figure 10. Collector Surface Temperature Performance with and without Heat Pipe

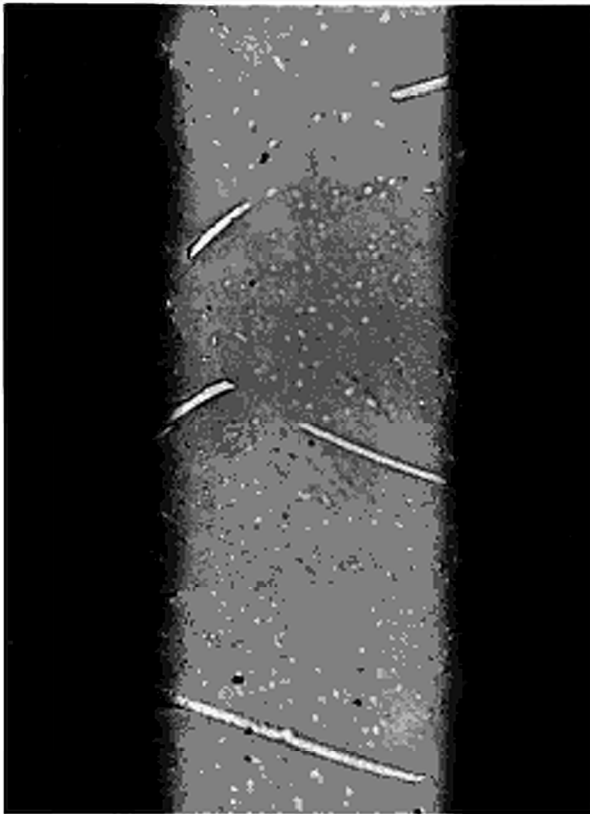


Figure 11. Recrystallized Tantalum-Emitter Support Sleeve (4 mils thick, tantalum sub-oxide platelets in the [320] planes)

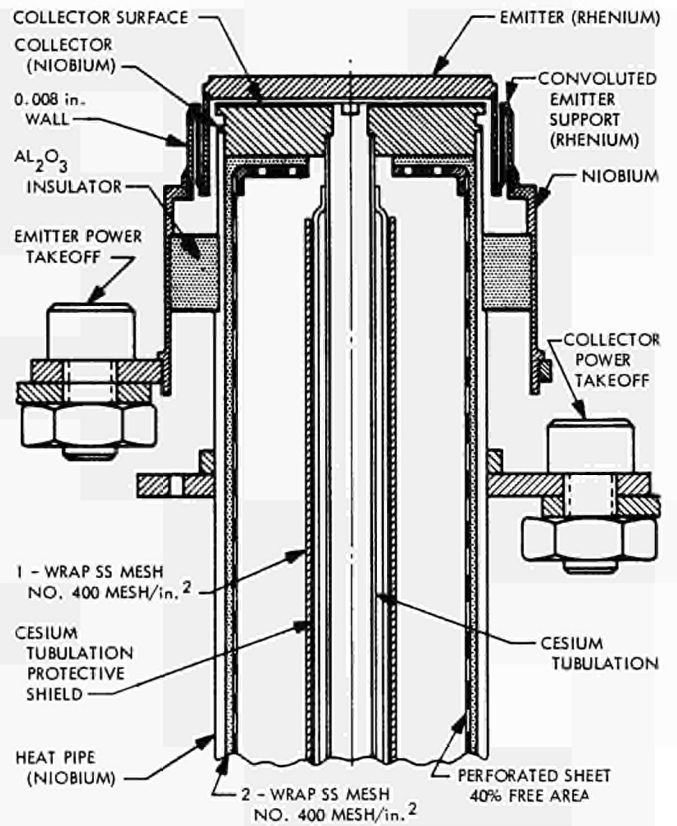


Figure 12. Convolute Emitter Support Structure and Heat Pipe Collector Assembly

DISCUSSION

Speaker of paper A-5: P. ROUKLOVE

KNOERNSCHILD (Germany):

What spacing did you use?

ROUKLOVE (USA):

In our converter the spacing was approximately 50 microns.

BUSSE (Euratom):

What was the longest life-time you observed with a heat pipe converter?

What was the working fluid and the operating temperature of the heat pipe?

ROUKLOVE:

We have had a life-time of about 6,000 hours and the converter is still running. The collector temperature was 875°K. The working fluid of the heat pipe was sodium.

HIGH PRESSURE CAESIUM THERMIONIC CONVERTER

WITH A COLD REGION

B. Stefanov and L. Zarcova

Bulgarian Academy of Sciences, Institute of Electronics,
Sofia, Bulgaria.

ABSTRACT. The possibility to have a room temperature region in a caesium thermionic converter is investigated. For this purpose the distribution of partial caesium pressure in a heated argon-filled vertically placed tube with a cold region at the top is evaluated by two simple methods. Measurements are made in the interval of $p_{Cs} = 10^{-5}$ to 10 Torr and $p_{Ar} = 2$ to 20 Torr. The results show that in the beginning of the operation the distribution of p_{Cs} is linear along the axis of the tube. This linear distribution is determined by the furnace temperature at the bottom and by the room temperature near the furnace end. After some period of time (usually several hours) of work, depending on the ratio p_{Cs}/p_{Ar} , in the whole heated region p_{Cs} becomes constant sharply diminishing near the furnace end. This makes possible the development of thermionic converters in which the insulators and vacuum sealing can be fitted at room temperature.

1. INTRODUCTION. It is convenient to have a room temperature region in a thermionic converter for various applications. This cold region makes possible to solve easily the problems connected with the electrical insulation of the leads and with vacuum sealed assembling. The difficulty arising in the case of high pressure caesium thermionic converter is that p_{Cs} is determined by the temperature of this cold region. To avoid it a new type of argon-filled converter operating in conditions of caesium-in-argon diffusion is proposed here. A similar device was reported several years ago by Bohdansky and Schins (1) for measurement of saturated caesium pressure. Although

this device operated for equal p_{Ar} and p_{Cs} , this later was determined only by p_{Ar} provided the heat power of the furnace is sufficient. It will be shown below that also in the case when $p_{Cs} < p_{Ar}$ it is possible to have a region with p_{Cs} constant. The main difference between the case of Bohdanský ($p_{Cs} = p_{Ar}$) and ours ($p_{Cs} < p_{Ar}$) is a full stratification of the mixture Cs-Ar when $p_{Cs} = p_{Ar}$ and diffusion condition with presence of Ar in the Cs layer when $p_{Cs} < p_{Ar}$. Thus our purpose was to evaluate Cs concentration along the axis of a vertically placed tube in the presence of argon.

2. EXPERIMENTAL DEVICE. The experimental tube was a glass one (inner diameter 2 cm and useful length 15 cm) with axially stretched tungstene filament (diameter 0,01 cm and length 7 cm) and one or two anode rings (diameter 0,8 cm). Some quantity of metallic caesium (of the order of 1 g) was introduced into the bottom of the tube. The distance between the bottom and the anodes in various investigated tubes was 10 to 14 cm. The lower part of the tube was placed in a movable furnace so that the length of the heated part could be regulated by a displacement of the furnace. The temperature distribution in the furnace was constant within $\pm 2^{\circ}K$ except near the upper end where a transition from T_f (temperature of furnace) to T_o (room temperature) takes place along 1 to 2 cm.

3. EXPERIMENTAL METHOD. As mentioned above, two methods were used. The first one was elementary enough and consisted in the measurement of anode current when the filament was directly heated to $\sim 1300^{\circ}K$. The necessary anode-cathode voltage was supplied by the voltage drop along the cathode (the tungsten filament). In this way it is possible to make only relative measurements, i. e. to establish two position of the anode in the heated part of the tube where two values of p_{Cs} are equal (since T_c is constant, the emission current is determined only by p_{Cs}). The second method consists in the measurement of anode currents I_a in converter conditions with a half

period rectifier technique using a calibrated oscilloscope. The dependence of I_a on the cathode temperature T_c was measured near the low-temperature maximum of I_a and the exact position of this maximum as well as its value was a basis to evaluate the relative variation or absolute value of p_{Cs} .

4. RESULTS AND DISCUSSION. The first several hours (this time depends on p_{Cs} and p_{Ar}) the top of the tube was clean without traces of caesium. For this initial period the measurements showed that p_{Cs} has its maximum value at the bottom of the tube and decreases to zero at the cold top. After this initial period visible amounts of caesium are deposited on the cold end of glass near the end of the furnace. For this final period p_{Cs} is constant in the whole heated volume of the tube and corresponds to the maximum initial value of p_{Cs} at the bottom. In the vicinity of the furnace end p_{Cs} sharply diminishes. The initial and the final distribution of p_{Cs} as well as the temperature distribution along the vertical axis are schematically shown in fig. 1.

A sample of the measurements made by the first method (anode current with applied voltage) for the initial time is shown in fig. 2. The two curves represent the dependence of the anode current I_a on the furnace temperature T_f . Curve 1 corresponds to a distance between the anode and the furnace end $h = 4,7$ cm and curve 2 - to $h = 2$ cm. The difference in the two curves is obtained only by 2,7 cm displacement of the furnace. The distance bottom - anode is 13,3 cm. Obviously two points on the two curves with the same I_a have the same p_{Cs} . If we assume linear distribution of p_{Cs} we shall be able to calculate the ratio of p_{Cs} at the bottom for these two conditions: $p_{Cs1}/p_{Cs2} = \frac{2}{15,3} / \frac{4,7}{18} = 0,5$. Experimental results obtained by comparing pressures corresponding to T_1 and T_2 give this ratio equal to 0,4 for 350°C, 0,5 for 310°C and 0,6 for 240°C. These small discrepancies can be explained by the displacement of the condensation zone into the furnace for higher temperature because of the temperature non - uniformity.

After a period of time curve 2 begins to move towards

curve 1 until coinciding with it. Then the final conditions are obtained, p_{Cs} being constant in the heated volume. Some simple analytic considerations can be given here. If the length of the tube is much greater than the diameter, one dimensional diffusion equation may be considered for the initial time. In our case there are no sources and the diffusion equation is $d^2c/dz^2 = 0$ with boundary conditions $c = c_0$ when $z = 0$ (at the bottom) and practically $c = 0$ when $z = L$. Here L is the length of the heated part and c is the Cs concentration proportional to p_{Cs} . Obviously the solution has the form $c = c_0(1 - z/L)$. The diffusional flow of Cs through Ar is given by the expression $q = -Ddc/dz = Dc_0/L$, where D is the diffusion coefficient of Cs through Ar. In our previous paper (2) we obtained the Lennard - Jones potential parameters for Cs - Cs interaction $\sigma = 5,66 \text{ \AA}$ and $\epsilon = 500^\circ\text{K}$. Combining these values with values for argon recommended in (3) according to the formulae $\sigma_{12} = (\sigma_1 + \sigma_2)/2$ and $\epsilon_{12} = \sqrt{\epsilon_1 \epsilon_2}$ we obtained for Cs - Ar interaction $\sigma = 4,56 \text{ \AA}$ and $\epsilon = 241^\circ\text{K}$ so that $D = 85/p_{Ar} \text{ cm}^2/\text{sec}$ if $T = 400^\circ\text{K}$, $p_{Cs} \ll p_{Ar}$ and p_{Ar} is taken in Torr. Taking into account that c_0 is proportional to $p_{Cs}(T_f)$ it is clear that q is proportional to the ratio $p_{Cs}(T_f)/p_{Ar}$. The calculation show that for $p_{Cs}/p_{Ar} = 0,1$ the rate of Cs deposition on the cold wall is $4 \cdot 10^{-6} \text{ g/cm}^2\text{sec}$. To have some quantity of liquid Cs which can flow down (of the order of 1 g) a period of 2 hours is necessary.

Qualitatively the same results were obtained by the second method. In fig. 3a and 3b the anode current of a converter is plotted against the cathode temperature T_c for $T_f = 140^\circ\text{C}$. There were in this case two identical anodes in the tube situated one above another at a distance of 2,5 cm. The heated part of the tube was 14 cm long. The upper curves in fig. 3a and 3b correspond to the lower anode, placed 4 cm below the furnace end. The lower curves correspond to the upper anode, placed 1,5 cm below the furnace end. Fig. 3a is drawn for the initial period of work and fig. 3b is for the final one. It is seen that in the first case 3a the maxima of the curves are dislocated and correspond to $T_c = 1190^\circ\text{K}$ and 1225°K .

The case of uniform p_{Cs} distribution is given in fig. 3b, where the two maxima coincide at $T_c = 1310^\circ K$.

To correlate the position of the maxima with the value of p_{Cs} we assumed that $\lg p_{Cs}$ is a linear function of $1/T_c$ (p_{Cs} and T_c taken for the maximum). This linear function is identical with the curve which corresponds to the condition of full compensation of the space charge (see for example (4)). We proved that our assumption is true by plotting $\lg p_{Cs}$ vs $1/T_c$ at low - temperature maximum for a converter with similar geometry (5). The coincidence between the experimental points and this linear function was very good. Taking the values of $T_c = 1190; 1225; 1330^\circ K$ it is possible to find corresponding values of $p_{Cs} = 0,55 \cdot 10^{-3}; 1,1 \cdot 10^{-3}; 4,8 \cdot 10^{-3}$ Torr. We considered these values as experimentally determined. The calculation of the same values gives $0,5 \cdot 10^{-3}; 1,4 \cdot 10^{-3}; 5 \cdot 10^{-3}$ Torr (the first two are calculated according to a linear distribution and the last corresponds to T_p).

5. CONCLUSION. A thermionic converter based on caesium-in-argon diffusion would be very convenient for operation. The two observed modes of work can be used in different ways. The initial mode has a linear distribution of caesium pressure. It is useful in experiments where simultaneous measurements for a whole pressure interval are needed. The final mode has constant caesium pressure in the volume and this fact can also be used. The presence of moderate quantity of argon (up to $p_{Ar}/p_{Cs} = 100$) in a device of such a type is of no importance for electronic experiments since the electron-atom effective cross - section of Cs is 1000 times greater than that of argon.

REFERENCES

1. J. Bohdanský and H. E. J. Schins, "New Method for Vapour Pressure Measurements at High Temperature and Pressure", J. Appl. Phys. 36, (1965), 3683.
2. B. Stefanov and L. Zarcova, "Experimental Study of Thermal Conductivity Coefficient of Caesium Plasma", Proceedings of the VII International Conference on Phenomena in Ionized Gases, Beograd 1965.
3. J. O. Hirschfelder, Ch. F. Curtiss, R. B. Bird, "Molecular Theory of Gases and Liquids" John Wiley and Sons, New York, Chapman and Hall, London, 1954.
4. B. Ya. Moizhes and G. E. Pikus, "On the theory of the plasma thermoelement", Solid State Physics USSR, 2, (1960), 756.
5. V. Orlinov and L. Zarcova, private communication.

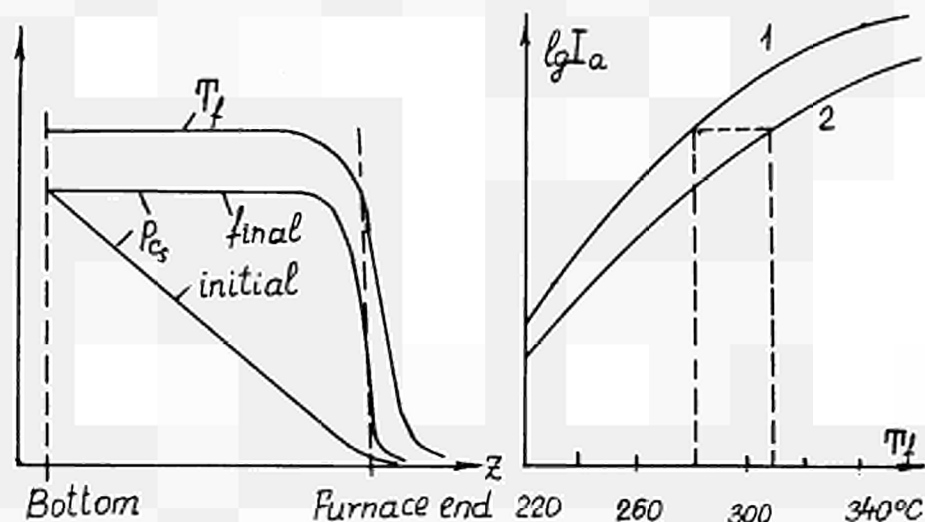


Fig. 1

Fig. 2

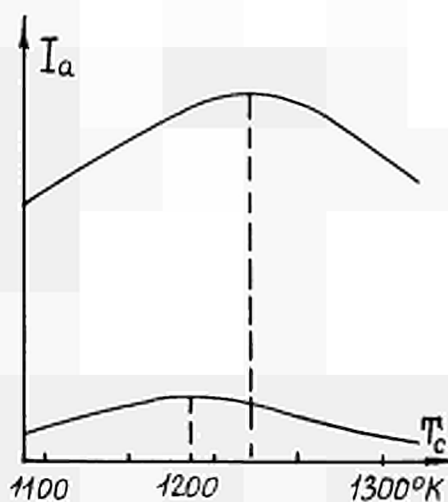


Fig. 3a

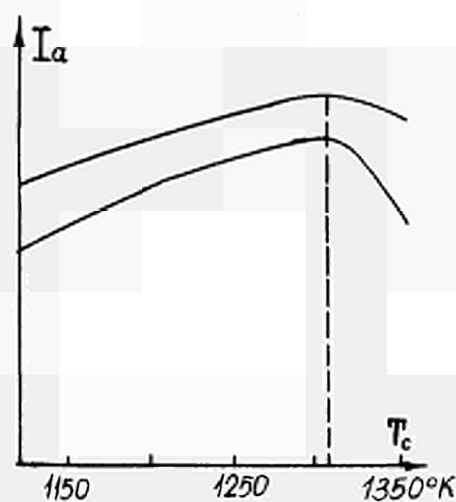


Fig. 3b

CONVERTISSEUR THERMOIONIQUE CHAUFFE PAR FLAMME

par Melle M. LATOUCHE-HALLE

Laboratoires de Recherches Générales
Compagnie Française THOMSON HOUSTON - HOTCHKISS BRANDT
92 - BAGNEUX -Résumé -

Une part importante du travail effectué sur le convertisseur thermoionique à flamme revient à la protection de la paroi de l'émetteur qui est portée à une température supérieure à 1 400 °C dans l'air. La mise au point d'un revêtement de mullite et de silice sur molybdène a permis d'obtenir des performances intéressantes sur des convertisseurs chauffés par une flamme.

En vue de réaliser un générateur d'électricité de quelques centaines de watts, portable, nous avons étudié expérimentalement une cellule chauffée par une flamme, pouvant fournir une puissance électrique de 10 watts à 1 450 °C de température d'émetteur.

Ce convertisseur thermoionique à flamme est identique dans son principe au convertisseur thermoionique nucléaire, mais il a ses problèmes propres, essentiellement d'ordre technologique, résultant de l'atmosphère oxydante et corrosive dans laquelle il travaille. En fait, le problème du fonctionnement des convertisseurs à flamme a été résolu avec celui de la protection des parois portées à haute température.

La cellule thermoionique à flamme se compose essentiellement d'un émetteur protégé, d'un collecteur et d'un réservoir de césium.

L'émetteur est le fond d'une capsule cylindrique en molybdène de 50 mm de long, 20 mm de diamètre et 5/10 mm d'épaisseur de paroi. Les capsules ont été faites soit à partir de molybdène embouti, soit par usinage de molybdène coulé sous vide. Nous n'avons pas observé de différences entre les deux procédés quant aux performances des convertisseurs.

Le collecteur est un cylindre de molybdène (molybdène coulé sous vide) d'environ 18 mm de diamètre.

La distance interélectrode est 1/10 mm. Ces deux électrodes sont isolées par une alumine de qualité AL 300 Wesgo, métallisée au titane manganèse et brasée au cuivre. Le centrage des électrodes est assuré par un emboîtement de la base du collecteur.

Avant d'être brasée à l'ensemble du tube, la capsule de molybdène est protégée contre l'oxydation et la corrosion de la flamme par un revêtement réfractaire étanche. L'étude de cette protection constitue une part importante du travail fait sur la conversion à flamme.

Les premiers revêtements ont été faits sur capsules de niobium. Ils étaient constitués d'alumine et d'un émail bien accordé en dilatation avec le niobium, à base d'alumine, de silice et de magnésie. Mais les résultats n'ont pas été très satisfaisants et il a fallu chercher un nouveau revêtement. Comme le niobium présentait par ailleurs des inconvénients (traitements thermiques sous vide exclusivement, propriétés électroniques inférieures), la recherche du nouveau revêtement s'est orientée vers un support molybdène.

De nombreux essais ont alors été faits, et le revêtement finalement adopté est à base de mullite et de silice. Une couche de mullite (eutectique $3\text{Al}_2\text{O}_3, 2\text{SiO}_2$) est déposée par projection au pistolet à flamme sur la capsule de molybdène. Cette couche assez inégale après dépôt est rectifiée afin que son épaisseur soit constante, et connue et que l'état de surface soit convenable. Elle est alors recouverte de silice qui, fondue sur la mullite, donne un émail de porosité nulle (au test électrolytique). La silice est mise en suspension dans un liant et déposée au pistolet à peinture sur la capsule, puis portée à 1 800 °C dans un four haute fréquence, sous hydrogène, pour fusion de la silice avec la mullite. En fait, la silice est déposée et fondue en plusieurs couches minces successives, pour ne pas entraîner toute la mullite dans la fusion et dégarnir complètement la capsule.

Le revêtement ainsi obtenu est gris clair et brillant, très homogène en épaisseur, et présente peu de pores (figure 1). Si l'élaboration de ce revêtement est assez compliquée, du fait de nombreuses opérations successives mécaniques et thermiques, il est du moins possible de juger à l'oeil nu, immédiatement après la dernière opération de fusion, si le revêtement est valable. S'il ne présente aucun éclat, en particulier sur l'angle vif du fond de la capsule, aucune fêlure ou microcraquelure, ni aucune sur-épaisseur locale qui deviendrait un point chaud dans la flamme, il constitue une protection efficace dont la durée de vie est supérieure à 100 heures, mais n'a pas été éprouvée au-delà.

Dans la version actuelle des convertisseurs à flamme (figure 2), la capsule protégée est, après son élaboration, brasée au reste de la cellule thermoionique, mais c'est une solution provisoire parce que la brasure, se trouvant dans une zone encore assez chaude, se corrode très vite et limite ainsi la durée de vie de la cellule. Cette brasure sera ultérieurement remplacée par une soudure par bombardement électronique qui pourra être protégée efficacement en même temps que la capsule.

En ce qui concerne les essais des convertisseurs, nous avons remarqué un temps de formation (temps nécessaire pour que le courant optimal s'établisse) plus ou moins long, allant d'une petite fraction d'heure à plusieurs heures. Ce phénomène est difficile à expliquer. Il ne semble pas dépendre de la différence d'origine des émetteurs (capsules embouties ou usinées dans de la barre) ni du temps de pompage. Il est possible que de légères différences dans les traitements mécaniques ou thermiques modifient l'état de surface de l'émetteur et entraînent une différence sur le mouillage du césium.

La figure 3 montre la variation de la puissance en fonction de la température de l'émetteur, lue au pyromètre optique sur le fond de la capsule chauffée, et la figure 4, la variation de la puissance en fonction du temps pour l'un des convertisseurs. On peut remarquer que la puissance maximale a été atteinte au bout d'un temps relativement long par rapport à la durée de vie totale du convertisseur.

Au cours d'un essai, la puissance de 10 watts a été obtenue sur une cellule, mais la moyenne se situait aux environs de 5 watts, soit $1,6 \text{ W/cm}^2$ d'émetteur, à 1400°C .

Cinq convertisseurs ont été montés en série. Le dispositif expérimental était très simple. Les cinq convertisseurs ont été placés côte à côte, assez près l'un de l'autre pour réduire les longueurs de connexion, et ils étaient chauffés chacun par un chalumeau gaz-oxygène.

Il est intéressant de noter que le fonctionnement en série de plusieurs convertisseurs ne présente aucune difficulté, en ce qui concerne l'amorçage des convertisseurs, en particulier. Le montage était conçu de telle sorte qu'il était possible de mettre en court-circuit chacun des convertisseurs sans les déconnecter du montage en série. Le premier convertisseur étant amorcé, il suffisait d'ouvrir le court-circuit du suivant pour qu'il s'amorce, et ainsi de suite. Avec cinq convertisseurs en série, nous avons obtenu plus de 20 W pendant 10 heures (tension 1,3 volts, courant 18,8 A).

En conclusion, s'il reste quelques petits problèmes technologiques à résoudre, la mise au point d'une paroi étanche, ne se dégradant pas, a permis de faire fonctionner très correctement les convertisseurs en les chauffant par une flamme.



Figure 1 - Coupe micrographique du revêtement mullite-silice

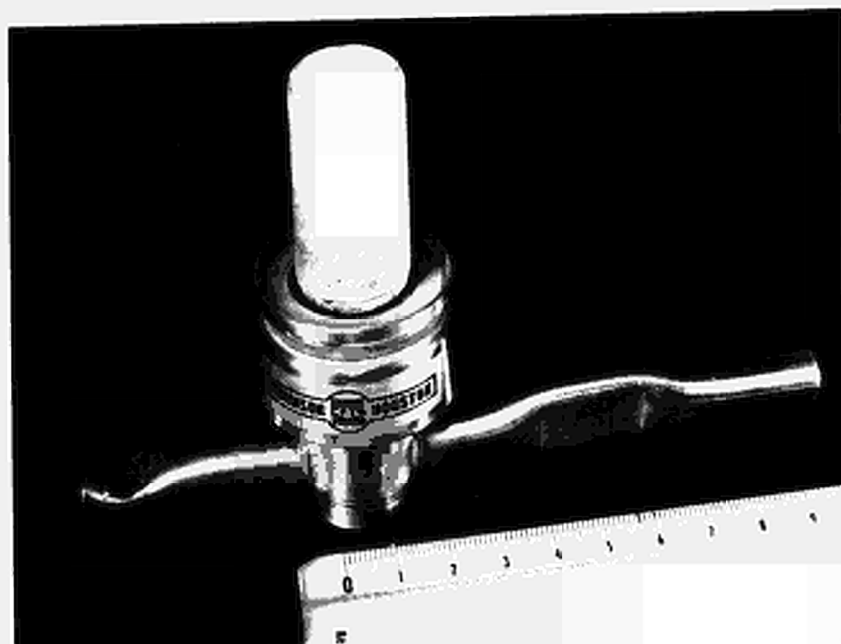


Figure 2 - Convertisseur thermoionique à flamme.

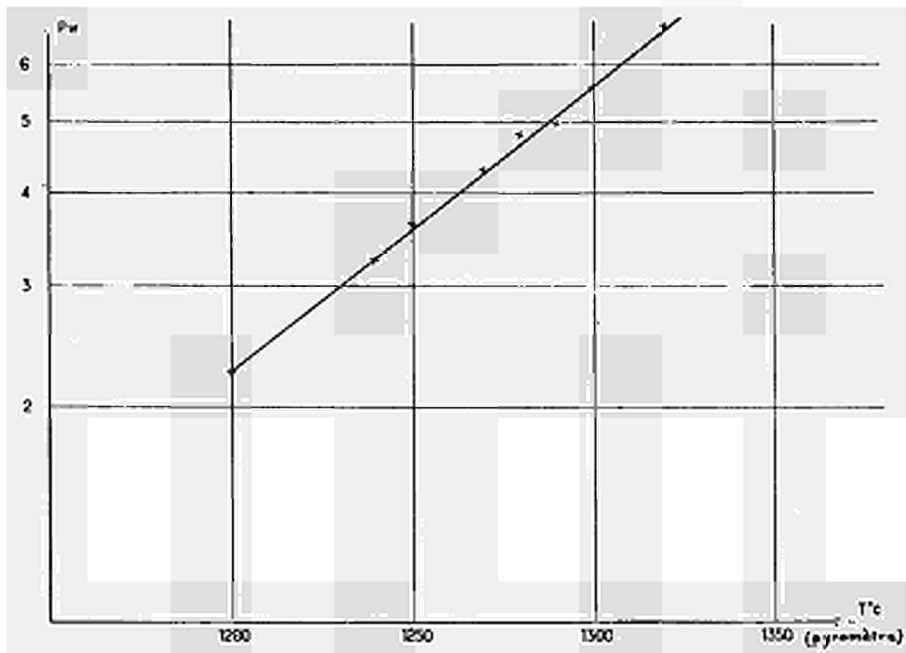


Figure 3 - Variation de la puissance en fonction de la température

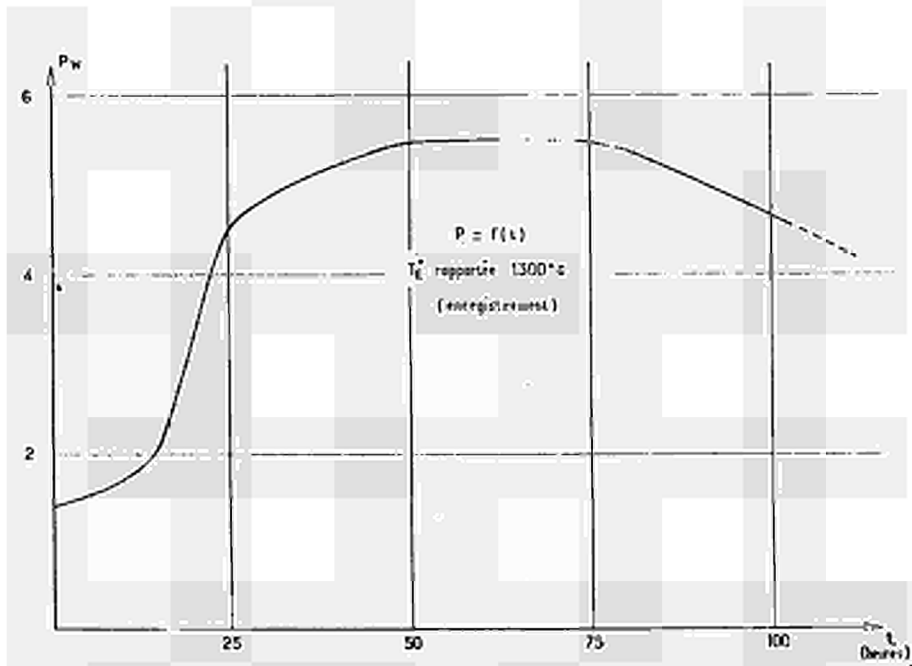


Figure 4 - Variation de la puissance en fonction du temps.



ARC-MODE THERMIONIC CONVERTER PERFORMANCE:
MEASUREMENTS AND INTERPRETATION

by

A. E. Campbell, Jr. and A. O. Jensen
Electro-Optical Systems, Inc., A Xerox Company
Pasadena, California

ABSTRACT

The performance of thermionic converters has been analyzed by means of precision measurements from specially constructed test vehicles with guard-ringed collectors and variable emitter-collector spacing. Data accumulated for 2500 hours testing time established that:

- Maximum power output of a converter occurs at a pressure-distance or pd product of 16 ± 0.8 torr-mils, independent of the emitter temperature, current level, or collector material.
- The results of the measurements from the variable-spacing test vehicle can be used to predict converter performance accurately and are directly applicable to practical converter designs.

The test vehicles were completely instrumented for measurement and control of spacing and of emitter, cesium, and collector temperatures as well as output voltage and current. Steady state measurements were made of the test vehicle voltage versus spacing at constant current, constant emitter temperature, constant cesium vapor pressure, and constant collector temperature. Three distinct regions of interelectrode spacing were found in which a particular mode of operation prevailed.

In order to establish correlation between research test vehicle data and hardware converter performance, several fixed-spacing planar thermionic converters were built to reproduce the performance characterized by operation within these three regions. Under identical conditions of operation and test, converter performance agreed within 1% to 2% with the data obtained in the test vehicle.

INTRODUCTION

The significance of an optimum pressure-distance or pd product for optimum arc-mode cesium vapor thermionic converter operation has been realized for some time. However, the lack of precision test vehicle measurements which correlated with converter hardware performance has obscured the practical application of the optimum pd product. This paper provides precision data from variable-parameter test vehicles which correlate precisely with data obtained from operating converter hardware. In addition, the basic character of cesium vapor thermionic converter performance is experimentally examined in the various modes of operation: (1) close-spaced or electron space-charge limited, (2) plasma arc, and (3) fully developed positive column.

The converter performance presented in this paper was obtained from practical devices of high efficiency (12% to 18%), measured performance (23 to 25 W/cm²), and demonstrated lifetime (>8000 hours). These converters were fabricated utilizing electron-beam welding and prefabricated subassembly techniques, which improved fabrication reliability and led to increased lifetime. The thermionic test vehicle data was obtained with high-precision (0.1%) measuring equipment and was reproducible within experimental error over a period of 2000 to 3000 hours of continuous operation. A key element in the correlation of data from these two different devices was the use of standardized test procedures, test setups, and test equipment.

DISCUSSION

The thermionic test vehicle shown in Fig. 1 is a guard-ringed structure with plane-parallel electrodes. The emitter, approximately 3/4 inch in diameter, is indirectly heated by electron bombardment from a counterwound, pancake

filament heater. Emitter temperatures are measured with a micro-optical pyrometer which is directly sighted into a 10:1 depth-to-diameter hohlraum. The emitter hohlraum is positioned so that extraneous radiation from the filament heater does not interfere with the hohlraum temperature measurement. Variable spacing is provided by a single-convolute bellows of niobium which allows expansion from a condition of shorted electrodes to spacings of 0.030 inch. An external drive mechanism utilizing a differential thread technique allows discrete spacing changes of 0.0001 inch as determined by means of dial indicators which can be read to within 0.00005 inch. Return movement is provided by spring-loaded ceramic rods so that the spacing variation is always a positive movement. In practice this system can operate for 400 to 600 hours before the indicators require replacement.

The test vehicle collector is 2.00 cm^2 in area and is connected thermally to a heat sink which is provided with forced cooling and resistance wire heaters to permit operation of thermionic current levels (dc) varying from 10 to 100 A/cm^2 while maintaining control of the collector temperature. The cesium reservoir is thermally isolated from the test vehicle body so that a unique cesium reservoir temperature (and vapor pressure) can be established and maintained independently of the temperature of the remainder of the test vehicle. The electrode materials selected for investigation were rhenium emitter, rhenium collector; and rhenium emitter, molybdenum collector.

The test vehicle was instrumented to measure the voltage output as the inter-electrode spacing was varied. The drift current, all element temperatures, and the cesium vapor pressure were maintained constant throughout each run. In this manner the critical properties of the plasma, such as electron temperature, electron number density, the sheath voltage values, the electrode

work functions, and device thermal expansions, remained fixed, permitting precision measurement of the test vehicle voltage profile.

Figure 2 shows a typical curve of output voltage versus interelectrode spacing with the other parameters fixed. The curve is divided into three regions, since the operation of the test vehicle is characterized by distinctly different phenomena within each region. Region I is designated the electron space charge region and extends from zero interelectrode spacing to a minimum identified as the plasma onset point. Within this region the output voltage is governed by the space charge created from electrons emitted by both emitter and collector in the absence of an adequate number of cesium ions to neutralize the space charge.

Region II is a region of plasma formation extending from the onset point to the point of maximum voltage output. The increase in voltage output in region II is due to the presence of cesium ions in the interelectrode space and the subsequent reduction of electron space-charge. The generation rate of ions in this region increases to a point of voltage output where the volume processes of ionization are maximized. Any further increase in spacing results in electron-atom scattering losses which increase linearly with spacing.

This region of wide spacing is region III, which is characterized by the linear decrease in voltage output as a function of increased spacing.

Region III is referred to generically as the positive column region.

Figure 3 is a specific curve of output voltage versus interelectrode spacing for a rhenium electrode system under conditions of constant emitter temperature, collector temperature, cesium vapor pressure, and drift current. In

Fig. 3, region I extends from 0 to 0.5 mil, region II encompasses the spacing from 0.5 to 4 mils, and region III is the linear portion of the curve beyond 4 mils.

Figure 4 is a volt-ampere characteristic obtained in region I of Fig. 3 at an interelectrode spacing of 0.2 mil for the conditions of 2008° K emitter temperature, 990° K collector temperature, and cesium vapor pressure of 4.1 torr. The volt-ampere curve is an oscilloscope trace of a 60-Hz ac voltage impressed about the dc current level of 38A. The ignition or breakdown point is observed at the top of the figure near 64A, providing certain evidence that operation at lower current levels (e.g., 38A) is in the electron space-charge mode.

A rhenium-emitter, rhenium-collector, close-spaced thermionic converter was built and operated in the electron space-charge mode. The voltage output from this converter is plotted in Fig. 5, which is a replot of region I in Fig. 3 and indicates the agreement of performance between a variable-parameter test vehicle and a converter. While converter output in region I can exceed 25 W/cm^2 at voltages in excess of 0.8V, the difficulty of building a number of converters with controlled and predictable spacing of a few tenths of a mil dictates against this approach.

The most useful region from thermionic converter design considerations is region II, which encompasses the arc-mode operation and, for certain electrode material combinations and emitter temperatures, includes interelectrode spacings of practical significance. Figures 6 through 10 are an assortment of voltage output versus spacing curves obtained over a wide range of emitter temperatures, cesium vapor pressures, and drift current levels. In each curve the maximum voltage output in region II is designated with a cross (x)

which signifies that this is the point of maximum power output for the selected voltage level and that an arc-mode thermionic converter has been fabricated and operated at that voltage and power output for identical conditions of operation which occurred in the test vehicle. The difference in performance obtained in the test vehicle and the converters was within the experimental error of 1% to 2%. Perhaps the most significant aspect of these curves (and all others which were examined) is that the point of maximum voltage output always occurs at a value of 16.0 ± 0.8 mil-torr as indicated in a summary listing of pd values (see Table I). This is true for different collector materials as shown in Fig. 11, wherein rhenium and molybdenum collectors are compared. Note that the optima occur at the same pd value, but at different voltage output levels, owing to their difference in minimum collector work function values (Ref. 1). Further, it is hypothesized that the 16 mil-torr value should apply for different emitter materials, since Figs. 6 through 10 cover a wide range of effective work function values which could also be achieved by an emitter material other than rhenium operating at a different temperature.

In region III, voltage output versus interelectrode spacing curves have been examined over a pressure range from 1 to 100 torr and from current levels of 6.85 to 50 A/cm^2 . These data are being analyzed and indicate the formation of a positive column wherein the computed values of electric field are constant with increased spacing. Figures 12 and 13 are plots of electric field versus interelectrode spacing for drift current densities of 6.85 and 25 A/cm^2 . Similar values for electric fields have been reported (Ref. 2) from spectroscopic data obtained in wide-spaced converters (Ref. 3) and demonstrate good agreement, considering that the methods of obtaining the data are totally different. Two thermionic converters were fabricated with

interelectrode spacings for operation in region III. The converter performance is plotted in Fig. 14 (which is Fig. 3 redrawn) with a cross indicating the individual converter output.

In summary, a direct agreement of research test vehicle data and converter hardware performance has been established within 2% over a wide range of emitter temperatures and interelectrode spacings.

Also, the fundamental nature of the pressure-distance or pd product has been examined, and the value of 16 mil-torr ± 0.8 mil-torr is found to optimize the converter plasma for maximum power output as established by the fabrication and test of nine thermionic converters.

TABLE I
SUMMARY OF PRESSURE-DISTANCE DATA TAKEN FROM
INTERELECTRODE SPACING VERSUS VOLTAGE OUTPUT CURVES

<u>T_{emitter} (°C)</u>	<u>T_{Cs res} (°C)</u>	<u>P_{Cs} (torr)</u>	<u>pd (mil-torr)</u>
1327	289	1.33	16.7
1427	291	1.43	15.7
1427	303	1.96	15.6
1527	310	2.35	16.8
1527	320	3.01	15.9
1527	331	4.02	15.7
1627	331	4.02	15.7
1735	331	4.02	15.7
1735	344	5.30	15.9
1735	350	6.06	16.3

REFERENCES

- (1) CAMPBELL, A. E.; JENSEN, A. O., "Performance of Prototype Thermionic Converters," Proc. of the 1966 IEEE Thermionic Conference (Houston).
- (2) NIGHAN, W. L., "Electron Transport Phenomena in Thermionic Converter Plasmas," Proc. of the 1966 IEEE Thermionic Conference (Houston).
- (3) REICHELT, W. H.; KRUER, W. L., "Spacing and Cesium Pressure Dependence of Electron Temperatures and Ion Densities in Thermionic Converter," Proc. of the 1965 IEEE Thermionic Conference (San Diego).

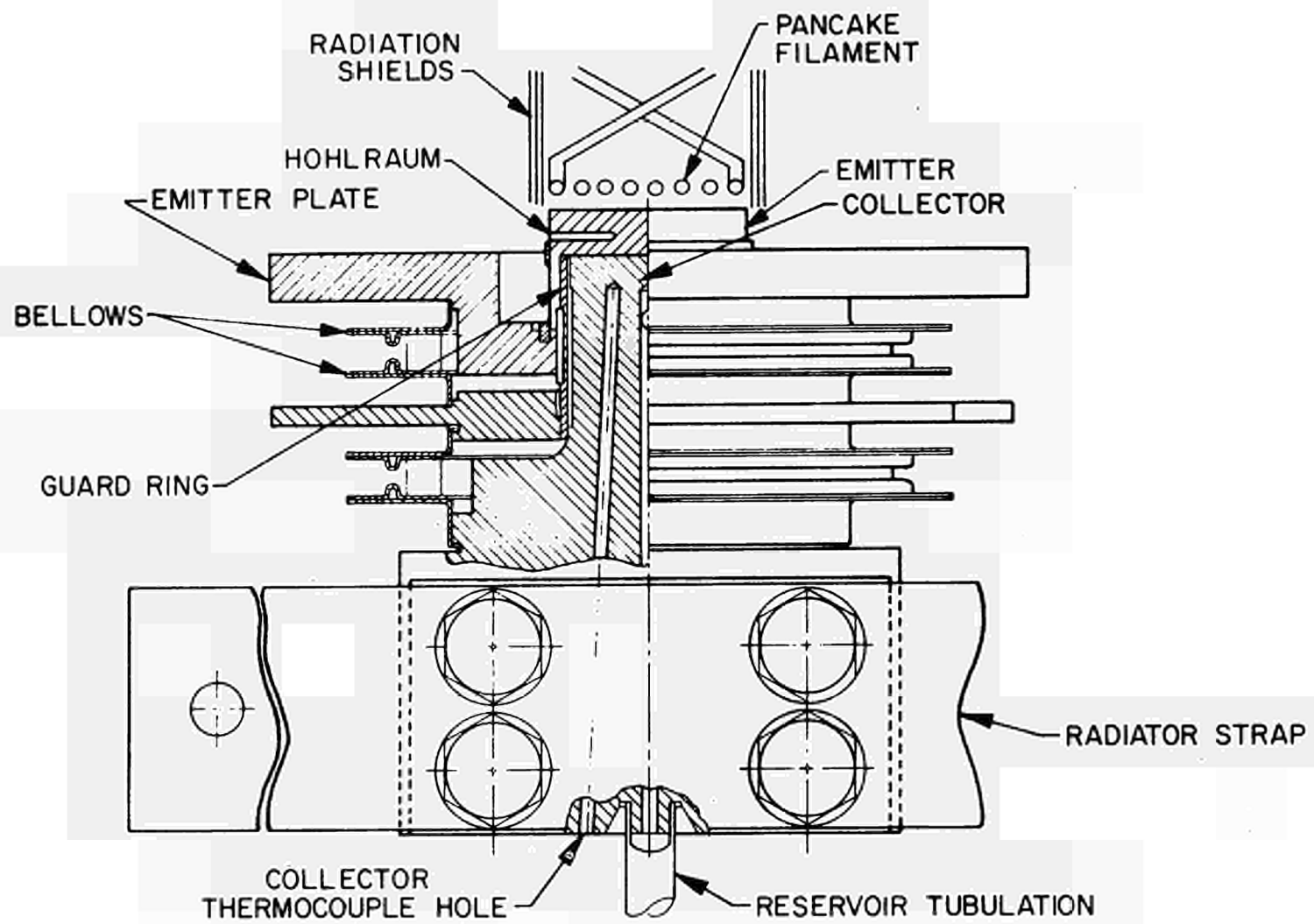


Figure 1. Thermionic Test Vehicle

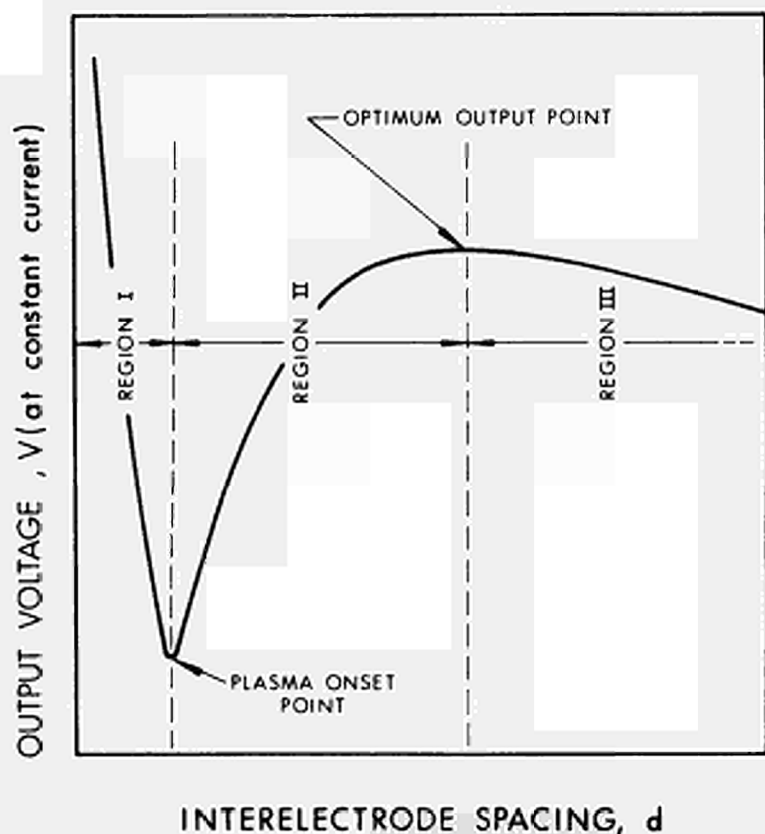


Figure 2. Typical Voltage Output versus Interelectrode Spacing Curve, Identifying the Three Characteristic Regions of Converter and Test Vehicle Operation

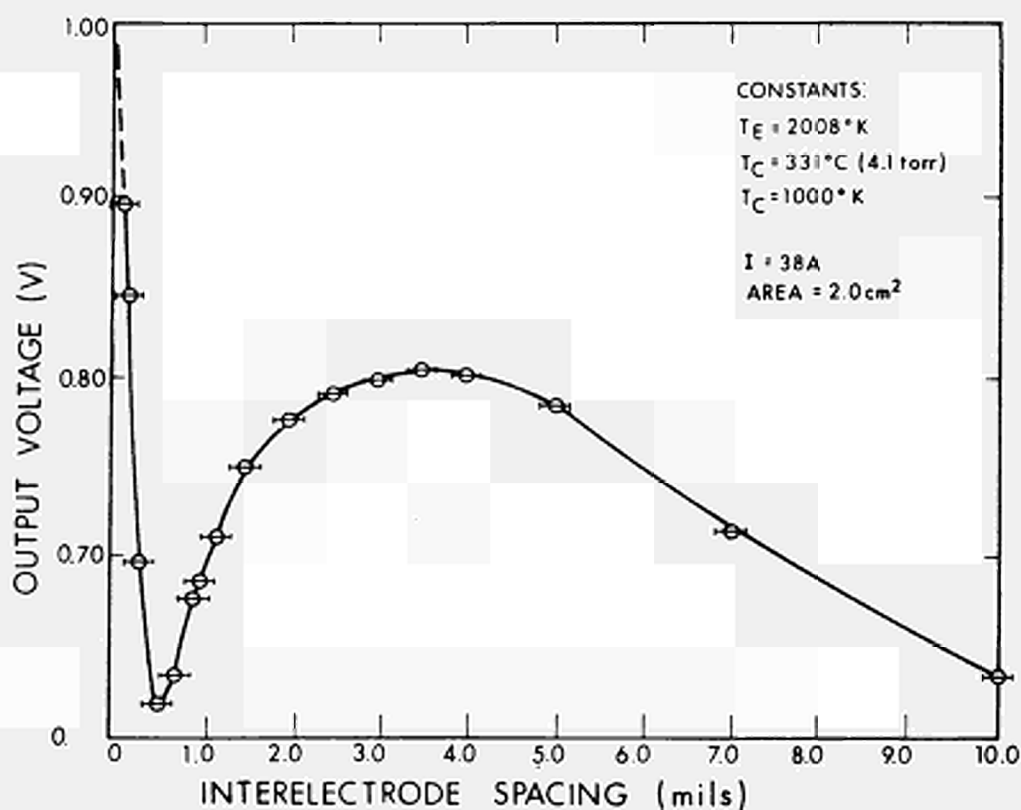


Figure 3. Interelectrode Spacing versus Voltage Output for Constant Emitter, Collector, and Cesium Reservoir Temperature (all data points are dc, steady state)

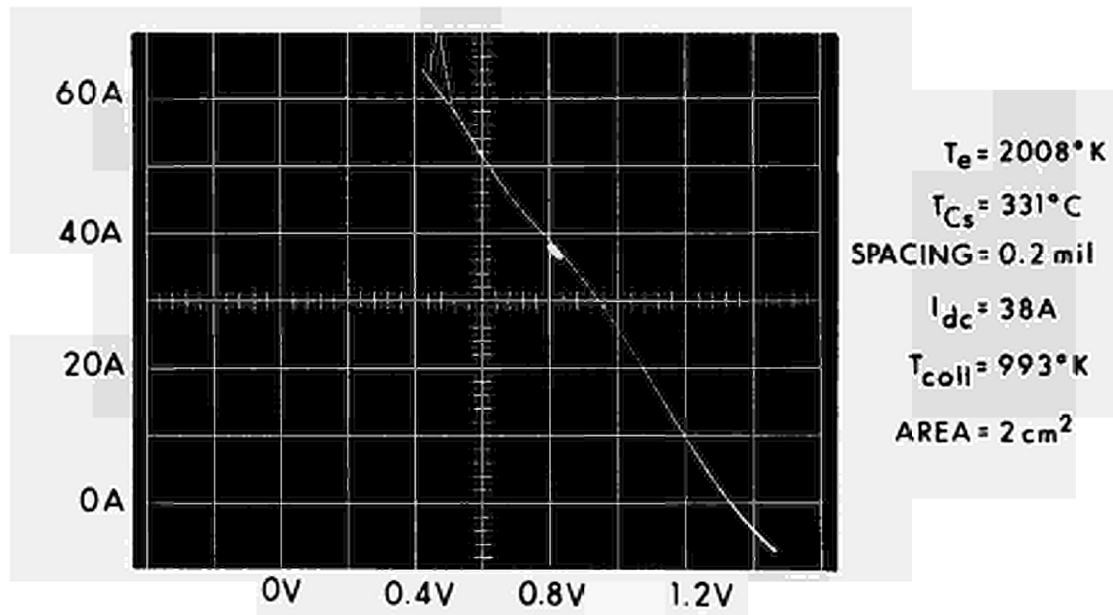


Figure 4. Volt-Ampere Characteristic Obtained in Region I
(refer to Fig. 3)

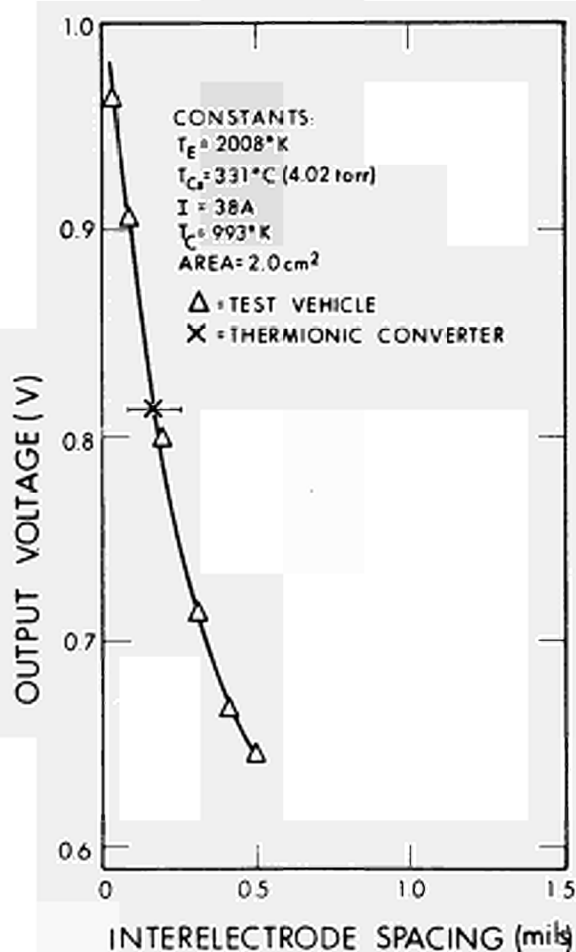


Figure 5. Region I (refer to Fig. 3) Performance Comparison of Test Vehicle to Close-Spaced Thermionic Converter

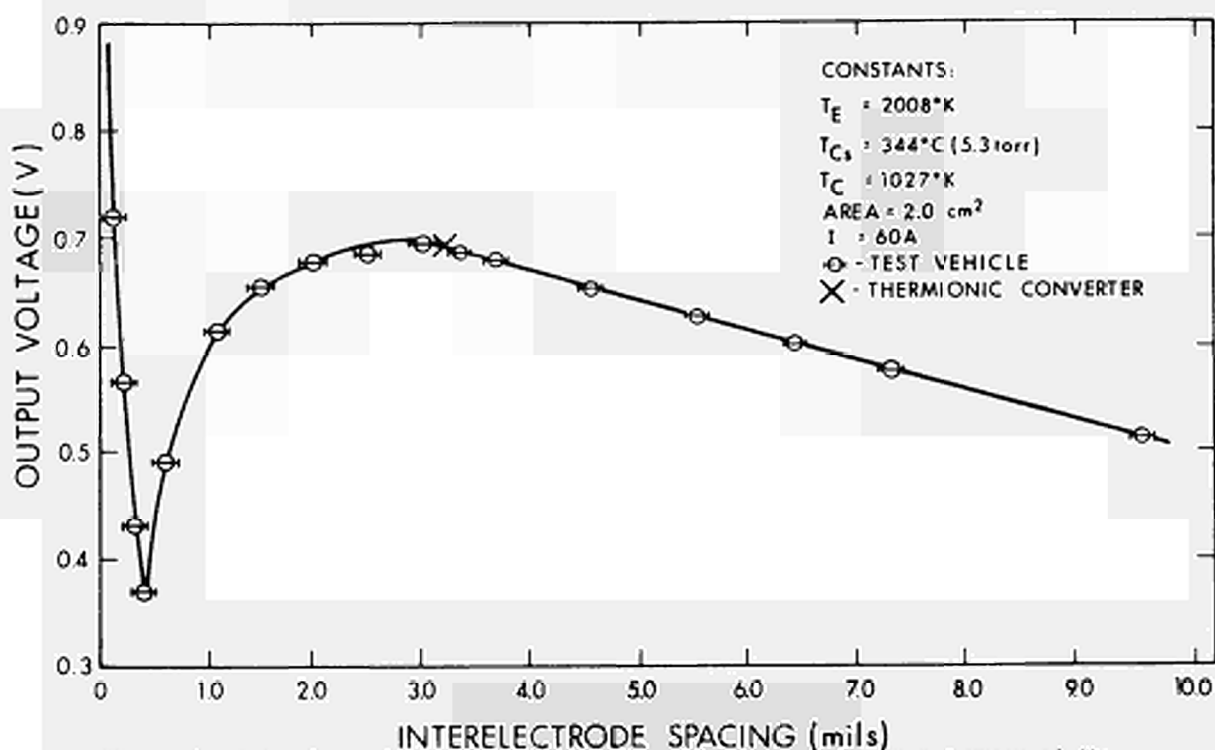


Figure 6. Interelectrode Spacing versus Voltage Output at a Constant Current of 60A (all data points are for dc data)

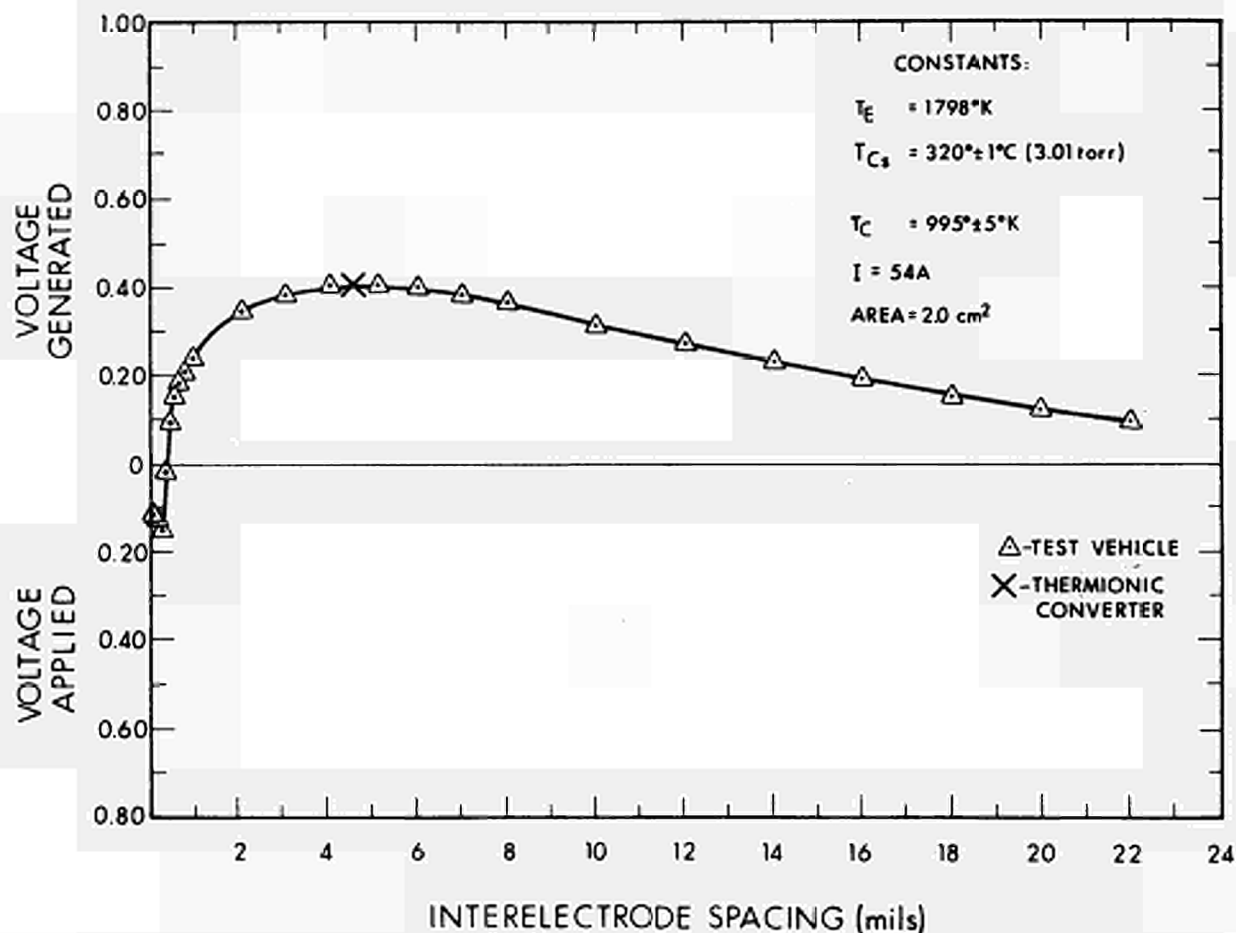


Figure 7. Voltage versus Interelectrode Spacing Relationship for $T_E = 1798^{\circ}\text{K}$, Optimized for 0.40V Output (all points are for dc data)

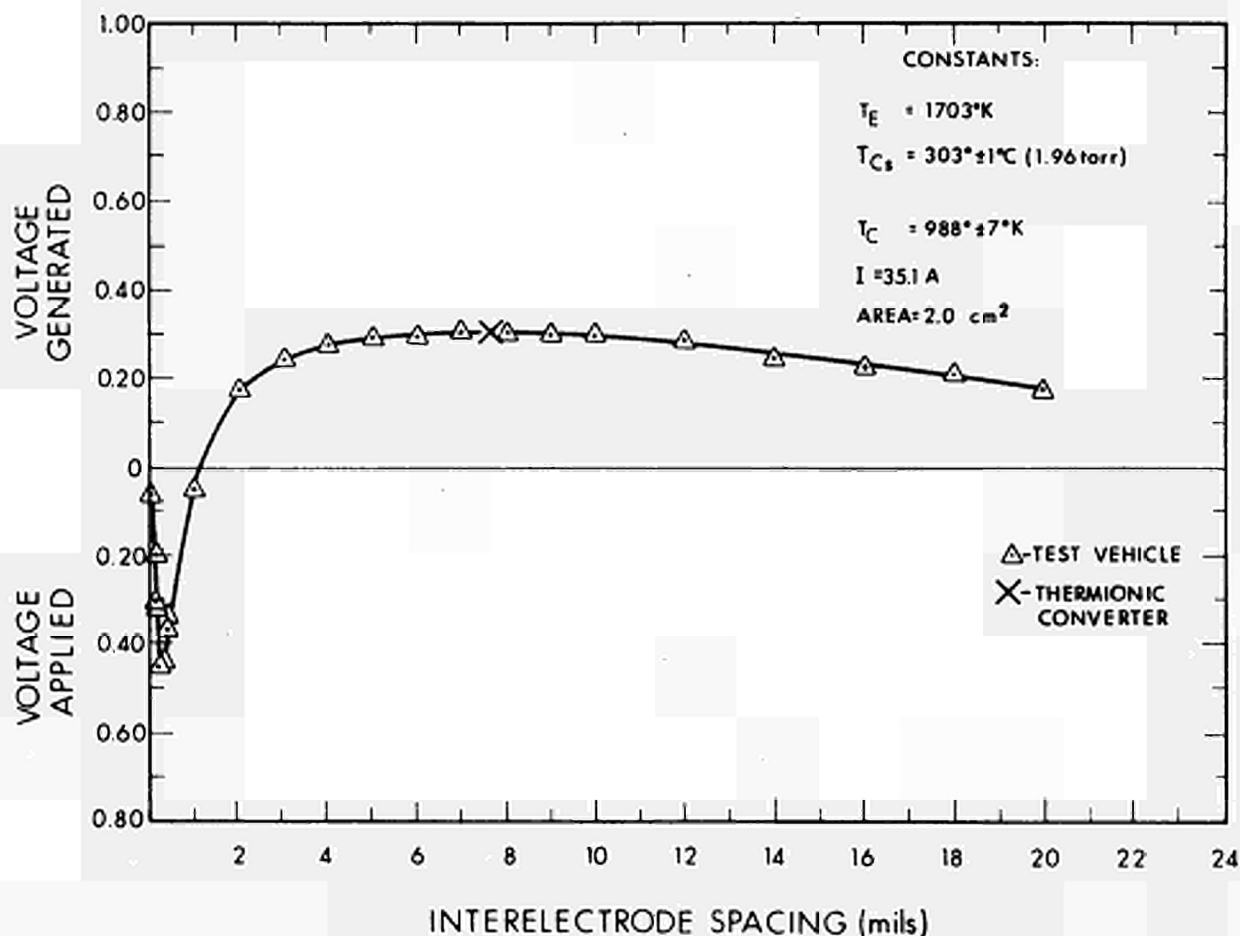


Figure 8. Voltage versus Interelectrode Spacing Relationship for $T_E = 1703^{\circ}\text{K}$, Optimized for 0.3V Output (all points are for dc data)

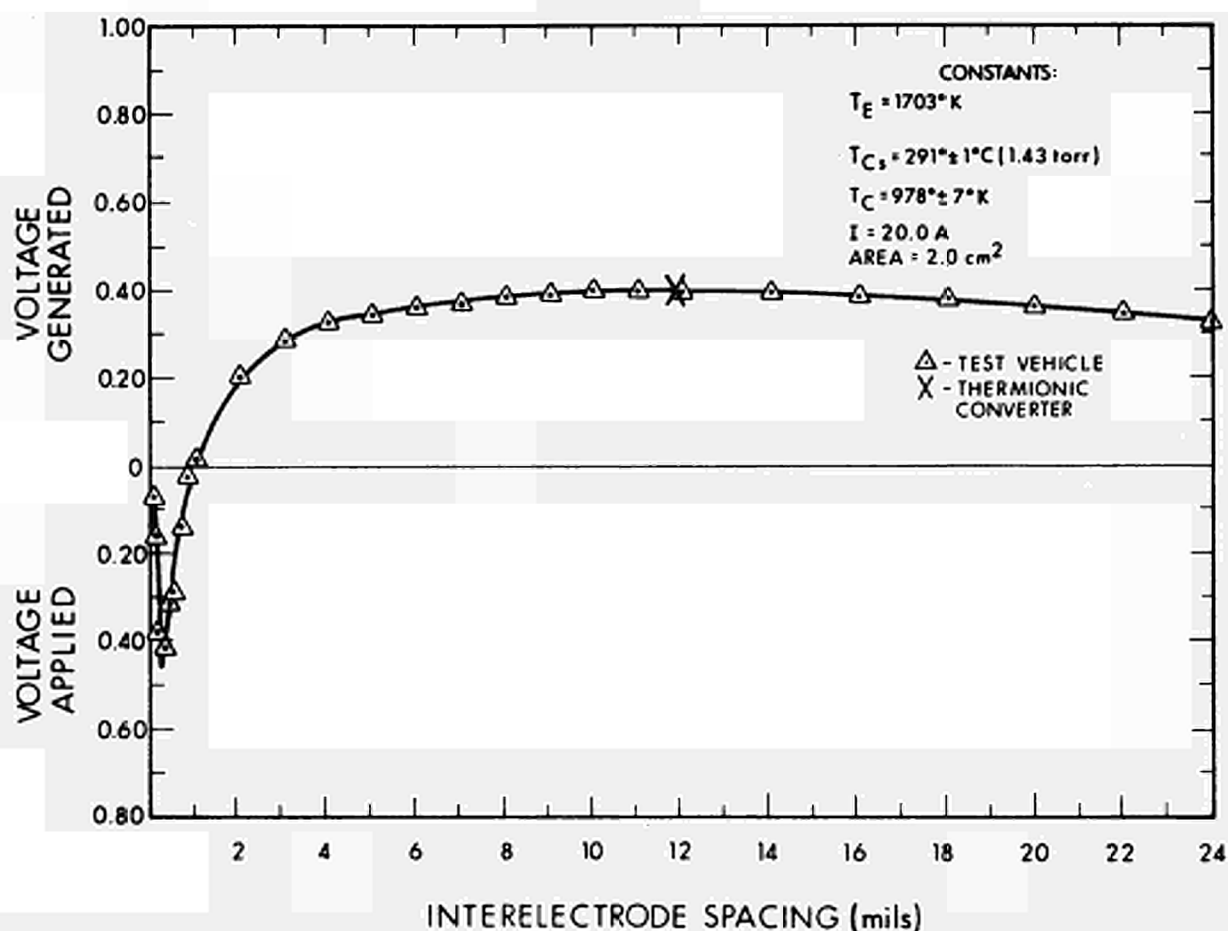


Figure 9. Voltage versus Interelectrode Spacing Relationship for $T_g = 1430^\circ\text{C}$, Optimized for 0.40V Output (all points are for dc data)

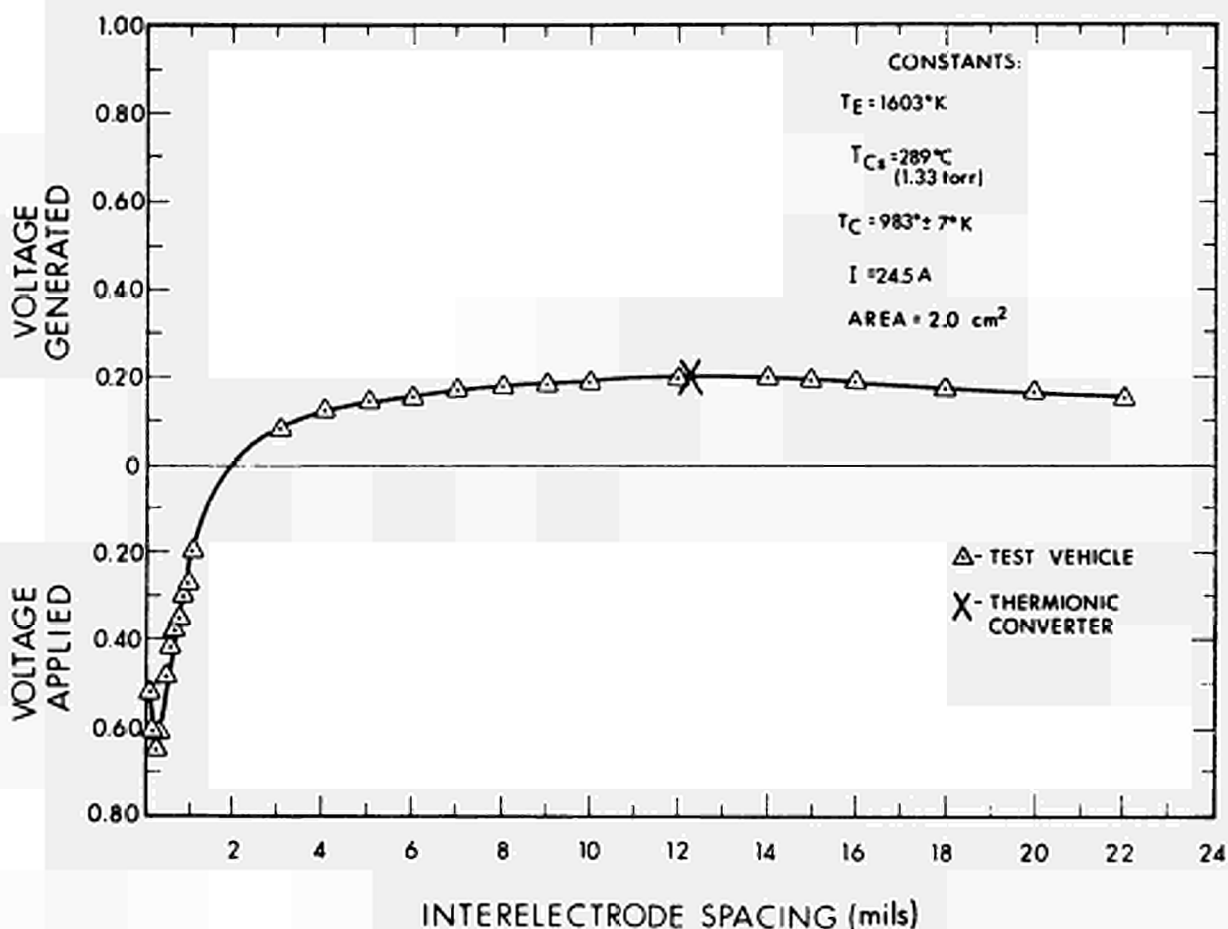


Figure 10. Voltage versus Interelectrode Spacing Relationship for $T_g = 1603^\circ\text{K}$, Optimized for 0.20V Output (all points are for dc data)

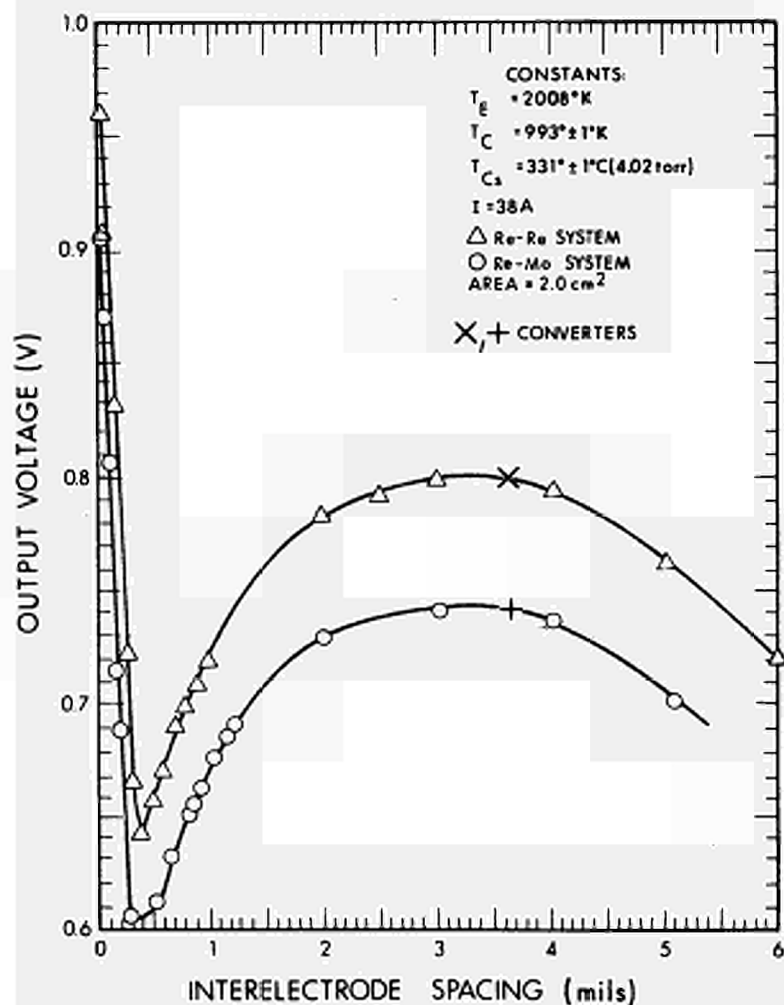


Figure 11. Comparison Plot of Re-Re System to Re-Mo System Showing Voltage Output Difference of 0.060V to 0.080V Over Entire Spacing Range. Note Agreement of Two Converters (Re-Re, Re-Mo) With Test Vehicle

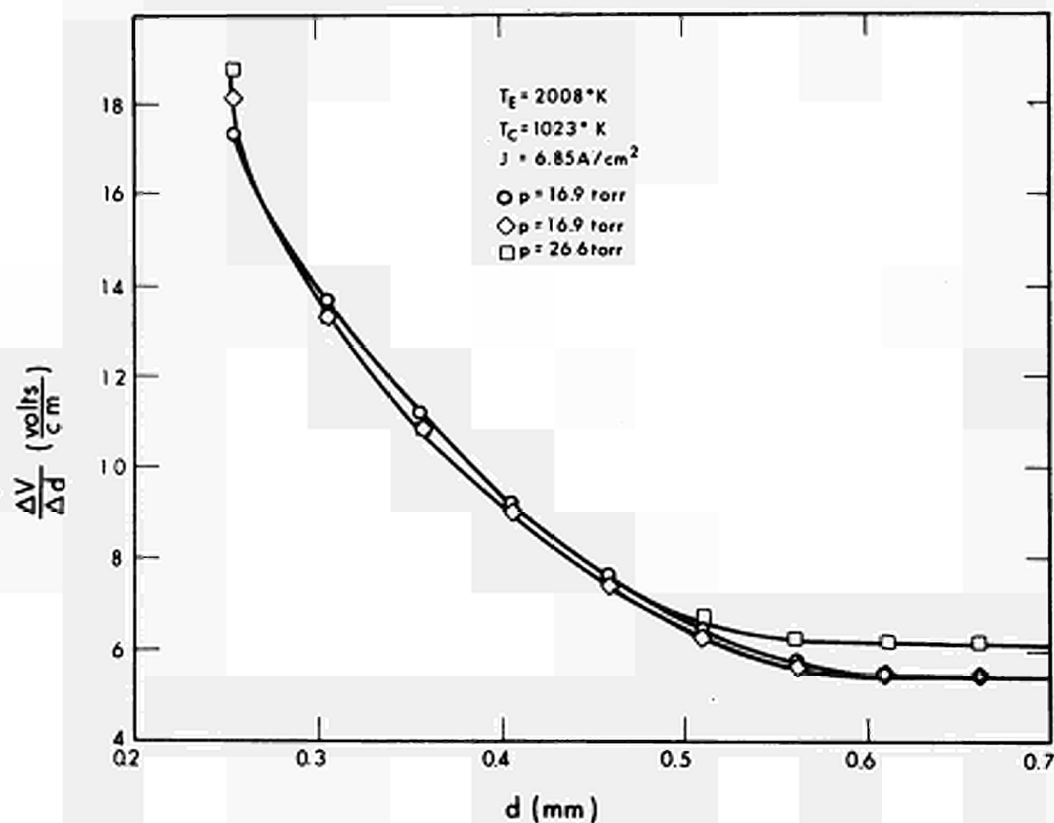


Figure 12. Electric Field as a Function of Interelectrode Spacing for Constant-Drift Current

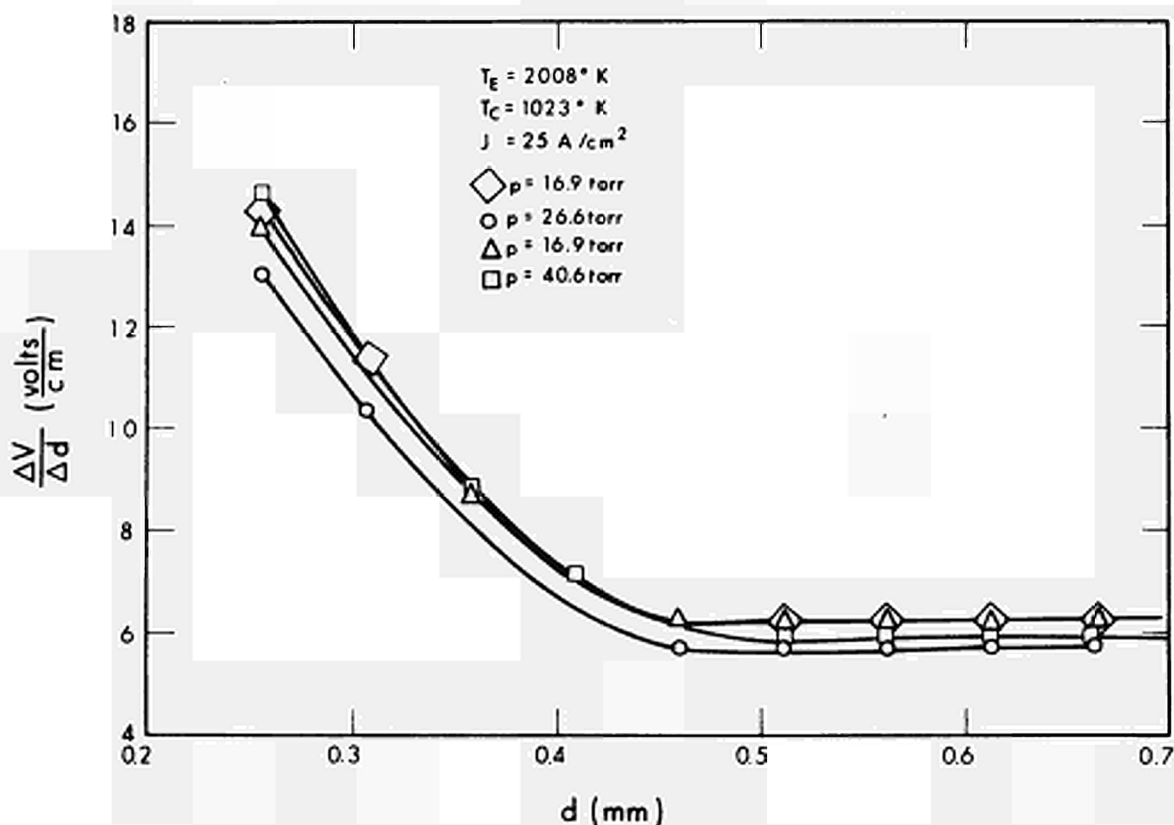


Figure 13. Electric Field Intensity versus Interelectrode Spacing for Constant-Drift Current

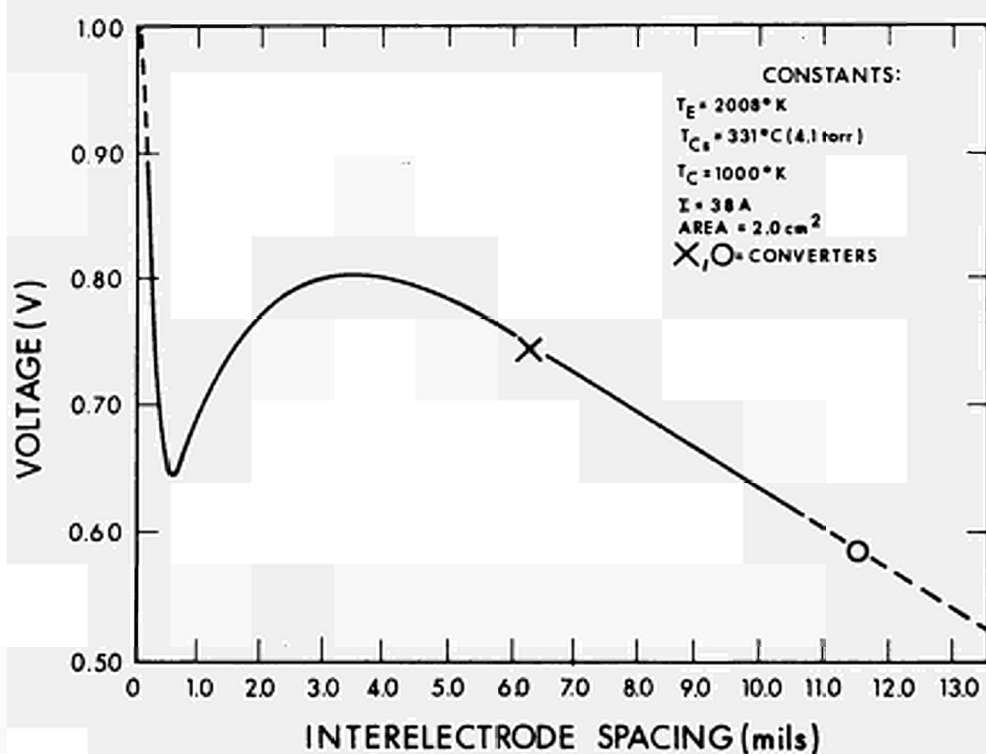


Figure 14. Replot of Test Vehicle Output (refer to Fig. 3) for Comparison With Converter Performance in Region III

TECHNOLOGIE DES CONVERTISSEURS THERMOIONIQUES
PLANS ET CYLINDRIQUES

A.M. Shroff

Compagnie Générale de Télégraphie sans Fil,
Centre de Physique Electronique et Corpusculaire
Corbeville, Orsay, France

I. Introduction

On a étudié des convertisseurs thermoioniques plans et cylindriques en vue de réaliser des générateurs d'électricité chauffés par une flamme, oxygène-propane par exemple, par la concentration du flux de chaleur solaire, ou par flux nucléaire.

On décrira les différentes technologies utilisées ainsi que les résultats obtenus sur les convertisseurs cylindriques.

II. Convertisseurs thermoioniques plans⁽¹⁾⁽²⁾

Plusieurs convertisseurs thermoioniques plans à distance émetteur collecteur fixe ou variable et matériaux d'émetteurs différents ont été réalisés en vue d'étudier l'influence de l'espacement interélectrodes et du travail de sortie de l'émetteur sur la densité de puissance électrique délivrée.

II.1. Structure de la diode

La figure 1 montre le schéma de deux convertisseurs l'un à distance émetteur-collecteur fixe et l'autre variable.

L'émetteur et le collecteur sont constitués par des surfaces planes de π cm².

L'émetteur est réalisé soit par usinage dans la masse, soit par fluotournage. La paroi latérale a une épaisseur de 5 à 6/10 mm. La partie émissive a une épaisseur de 5 mm afin d'assurer une bonne homogénéité de la température. La longueur de la jupe est de 5 cm; cette dernière est soit brasée, soit soudée par bombardement à une bride en acier inoxydable.

Les matériaux les plus fréquemment utilisés, sont le molybdène fondu sous vide ou le tantale. Les émetteurs ont été utilisés soit nus, soit recouverts de tungstène

(monocristallin ou polycristallin) ou de rhénium.

Le monocristal de tungstène est brasé à 2 500° C au tantale à l'aide d'une feuille de niobium, le tungstène orienté polycristallin est déposé, par décomposition chimique en phase vapeur, à la surface d'un émetteur en molybdène.

Le rhénium est brasé au tantale avec du ruthénium; cependant étant donné la grande vitesse de diffusion entre le ruthénium et le tantale on dépose par évaporation sur ce dernier, avant brasage, une couche de rhénium servant de barrière de diffusion. La distance émetteur collecteur peut être fixe ou variable à l'aide de trois vis déformant une membrane mince solidaire du collecteur.

L'émetteur est entouré d'écrans thermiques et d'un anneau de garde afin de bien définir la surface d'émission. Pour mesurer la température, un trou est ménagé dans la partie latérale de la surface émettrice.

L'isolant qui sépare la région de l'émetteur et du collecteur est constitué par une alumine du type Lucalox brasée sur les parties métalliques en niobium.

Deux fenêtres en saphir sont brasées directement sur l'alumine ou sur des tubes de niobium, afin de permettre la mesure de la distance émetteur collecteur et la température à l'aide d'un pyromètre optique. Le trou de pyrométrage dans l'émetteur est dans l'axe d'une des fenêtres.

Le réservoir de césium est constitué par le guesot de pompage. Un bloc de cuivre entouré d'une résistance de chauffage permet de réguler et d'uniformiser la température.

Le collecteur est refroidi par une circulation d'eau.

Les températures du collecteur, du réservoir de césium, de la paroi de la diode sont mesurées à l'aide de thermocouples.

Le pompage et le dégazage sont effectués dans une cloche à vide.

Le chauffage de l'émetteur est effectué par bombardement électronique. L'intérieur de la diode est pompé simultanément par un autre système de pompage. (Fig. 2 - Fig. 3)

A partir de ces études on a réalisé des convertisseurs plans chauffés par le soleil et des convertisseurs plans chauffés à la flamme. Dans les deux cas, l'émetteur était en molybdène protégé par une couche de disiliciure de molybdène; cependant la stabilité dans le temps à 1 900° K de cette couche a été une limitation à des durées de vie pouvant intéresser des dispositifs techniques.

III. Convvertisseurs cylindriques⁽³⁾⁽⁴⁾

III.1. Structure de la diode

La figure 4a représente le schéma de la diode construite pour les essais en pile et hors pile. La figure 4b représente le schéma de la diode compacte

Elle comprend dans les deux cas, un émetteur cylindrique en molybdène fondu sous vide recouvert sur 20 cm^2 d'une couche de tungstène déposé en phase vapeur de 200μ d'épaisseur^(5, 6, 7).

L'émetteur est brasé au sommet sur une bague en niobium.

Le collecteur dans les premières diodes étaient en niobium pur, mais comme à 1000°K il tend à perdre la plus grande partie de ces propriétés mécaniques - il passe de $11\,200 \text{ kg mm}^{-2}$ à $9\,800 \text{ kg mm}^{-2}$ - il a été remplacé par du niobium à 1 % de zirconium pour lequel jusqu'à 980°C il n'y a pas grande variation. La distance entre émetteur et collecteur est 200μ à froid et se réduit à 160μ lorsque l'émetteur est à 2000°K et le collecteur à 1000°K .

Un dispositif de centrage a été utilisé de manière à éviter les courts-circuits émetteur-collecteur en cours de fonctionnement en durée, courts-circuits qui peuvent avoir pour cause la déformation du collecteur ou de l'émetteur par fluage des matériaux.

Ce dispositif de centrage ne doit pas se détériorer dans le temps, et ne doit pas amener de perturbation thermique sur l'émetteur.

L'isolement entre émetteur et collecteur est obtenu à l'aide d'une céramique du type Lucalox brasée directement au niobium à l'aide d'un alliage titane nickel⁽⁸⁾. Le scellonement peut travailler à une température de 900°K sans inconvénient en atmosphère de césium. Les durées actuellement atteintes dépassent 6 000 heures.

Le haut du collecteur est raccordé à l'embase émetteur par une soudure par bombardement électronique.

Le réservoir de césium est en niobium à 1 % de zirconium et le césium est adsorbé sur du graphite. Ce type de réservoir permet de travailler sans inconvénient à la température de fonctionnement du collecteur, c'est-à-dire 1000°K .

La diode est placée dans une cloche à vide dans laquelle règne une pression inférieure à 10^{-6} Torr, de manière à éviter toute oxydation des parties en niobium

et en molybdène. La diode elle-même est pompée séparément.

On introduit après dégazage le césium, puis on effectue le scellement en deux temps. Premièrement du queusot de verre et ensuite par pincement du queusot en niobium. Ce dernier est ensuite soudé par bombardement électronique. La figure 5 montre une diode cylindrique en cours de pompage.

III.2. Montage dans la capsule d'irradiation

La figure 6 schématise la conception de la capsule d'irradiation. Elle comprend trois parties :

- la partie active (diode, shunt thermique)
- la partie de câblage
- l'enveloppe extérieure et le pied.

La figure 7 montre la diode montée avec le shunt thermique de collecteur, le shunt thermique de l'embase émetteur ainsi que le shunt thermique du réservoir de césium.

L'isolement entre le collecteur et le shunt thermique est réalisé par schoopage d'alumine au pistolet à plasma d'argon. L'isolement entre le côté réservoir et le côté embase émetteur est réalisé à l'aide d'une céramique, brasée au kovar à l'aide de l'eutectic argent cuivre.

Le queusot de pompage est situé du côté réservoir de césium.

De la diode partent sept thermocouples de mesure, les connexions de chauffage de la chaufferette césium ainsi que la chaufferette du shunt thermique, et aboutissent à un anneau d'où ils sont repris par les fils de câblage.

Dans la zone du câblage, tous les fils de thermocouples sont fixes, guidés à travers quatre tubes et isolés les uns des autres; en bout de cette zone ces fils aboutissent sur un autre anneau qui sert de point froid de référence arbitrairement choisi. De là ils sont soudés sur le pied à vingt quatre passages (Fig. 8).

L'ensemble ainsi préparé est monté dans des manchons en acier inoxydable qui sont alignés sur un banc d'optique et positionnés par des points de soudure à l'argon arc, puis définitivement soudés sous vide par bombardement électronique. On compte huit soudures.

La longueur hors tout de l'ensemble est de 1,35 m pour un diamètre 70 mm.

La capsule ainsi préparée est pompée et dégazée à environ 200° C. Le dégazage de chacun des éléments de chauffage est effectué dans un vide ne dépassant pas 10^{-5} Torr. Le temps d'opération est de 12 heures. On laisse refroidir, puis on scelle le queusot verre, on pince à la presse le queusot en acier inoxydable que l'on soude ensuite par bombardement électronique.

III.3. Résultats

Des durées effectuées sur des diodes en laboratoire montrent que certaines ont dépassé 5 000 heures. En pile le contractant nous a communiqué les durées suivantes : première diode dans la capsule 1 600 heures à 85 watts, deuxième diode dans la capsule 1 800 heures et la durée se poursuit. Dans les deux cas le fonctionnement des différents éléments (thermocouples, éléments de chauffage, connexions intermédiaires) a montré une grande fiabilité. Le scellement kovar-céramique brasé à l'eutectique et le scellement niobium-alumine brasé au titane nickel n'ont pas montré de défaillance sous le flux de neutrons.

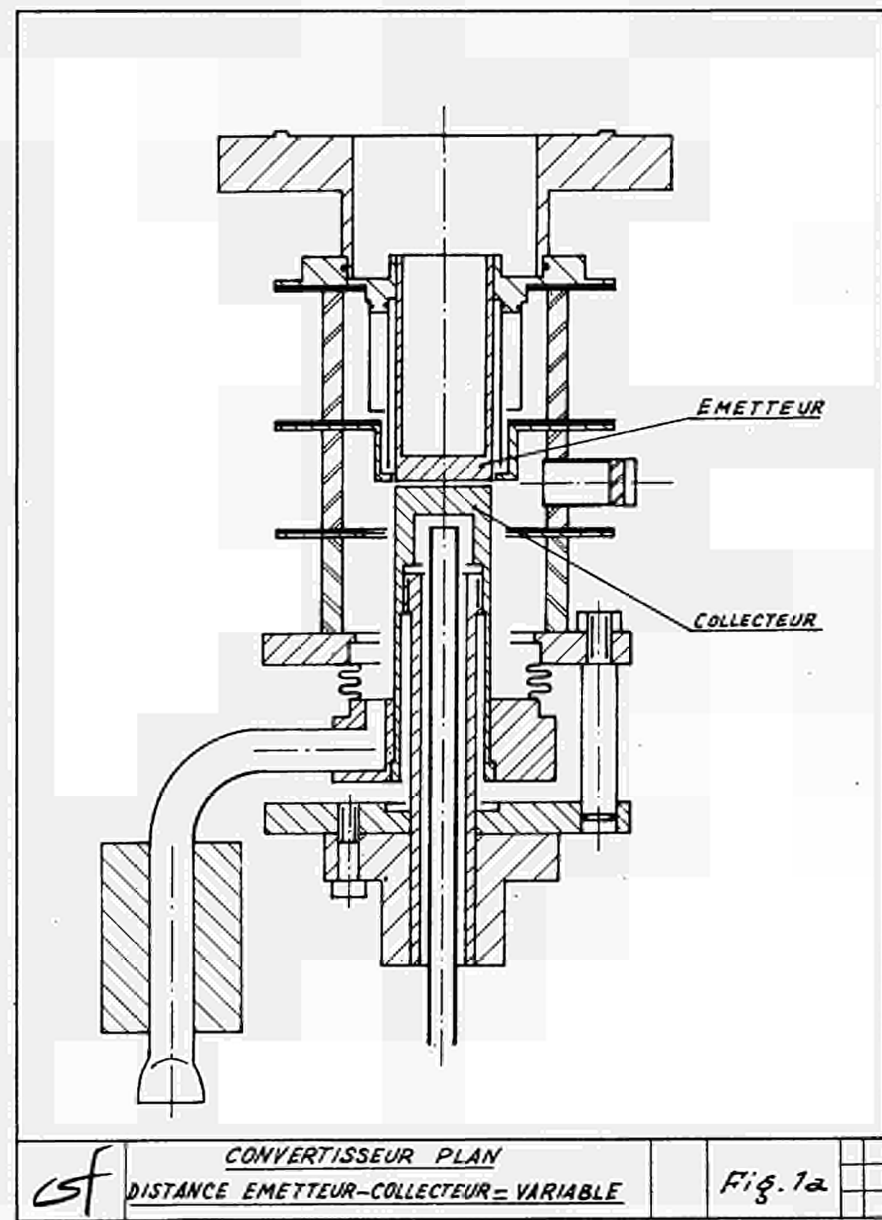
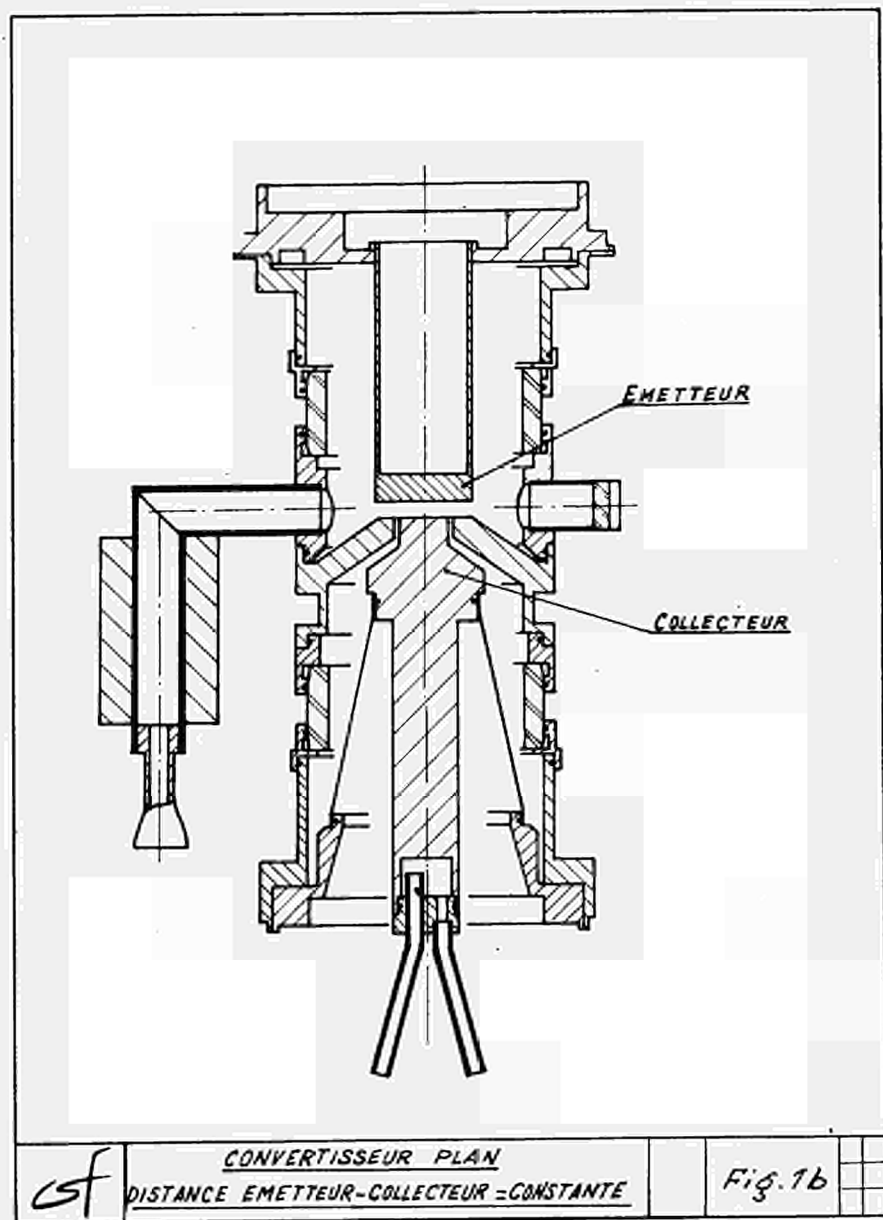
IV. C o n c l u s i o n

En résumé les conclusions suivantes peuvent être tirées :

- la technologie utilisée pour la réalisation des diodes planes ou cylindriques et les capsules d'irradiation est au point. En particulier en ce qui concerne les scellements céramique métal.
- Les dépôts en phase vapeur ont montré quelques défauts à long terme.
- La fiabilité de fonctionnement des différents éléments a été excellente.
- L'utilisation du bombardement électronique a permis d'apporter une solution simple aux différents problèmes d'assemblage et de scellements.
- Des performances répétées de plus de 1 000 heures en pile ont été obtenues.

B i b l i o g r a p h i e

- (1) J.P. Freytag et al. : "Etude expérimentale de convertisseurs thermoioniques à plasma de césium", Thermionic Power Generation, London 1965.
- (2) J.P. Freytag et al. : "Application possible des convertisseurs thermoioniques à plasma de césium à l'énergie solaire", Thermionic Power Generation, London 1965.
- (3) CEA : contrat 8538/h.
- (4) A.M. Shroff : "Thermionic Converter for In-pile Tests", Thermionic Specialist Conference, Palo Alto, Oct.-Nov. 1967.
- (5) A.M. Shroff : "Dépôt en phase vapeur de matériaux réfractaires", Stresa, Mai 1968.
- (6) A.M. Shroff, J. Guyonnet : "Propriétés des dépôts en phase vapeur de tungstène" En cours de parution.
- (7) EURATOM : contrat 017 65 5 CODE.
- (8) A.M. Shroff : "Scellement céramique métal", Stresa, Mai 1968.



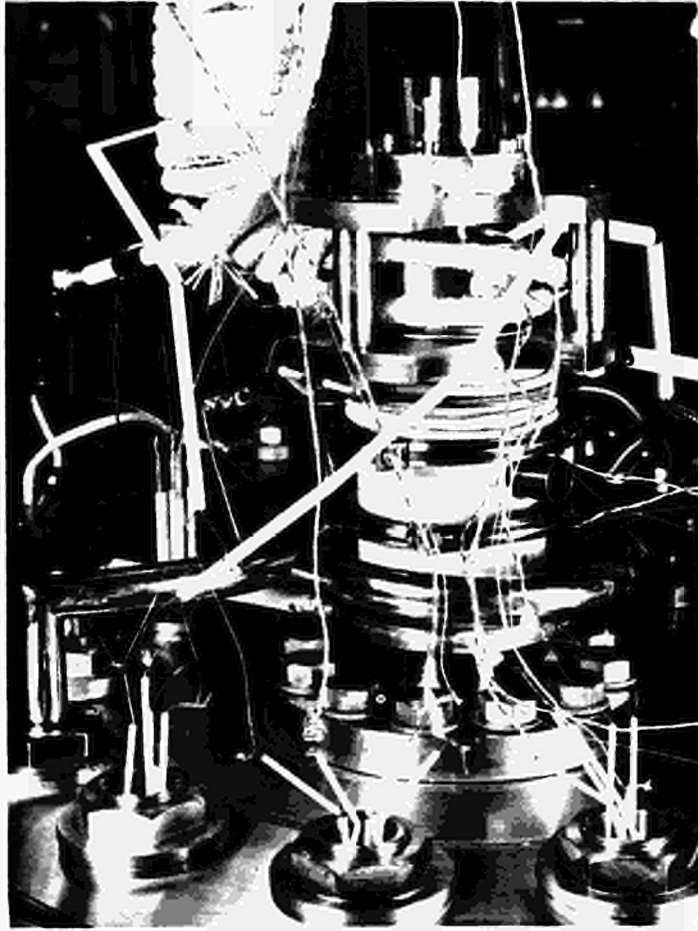


Fig. 2

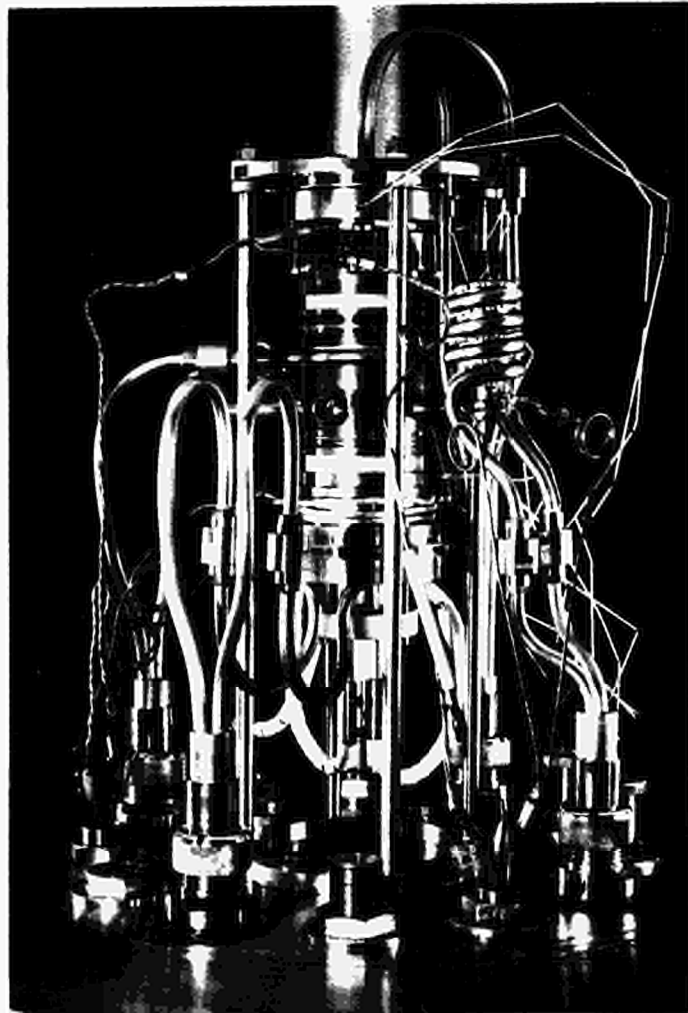


Fig. 3

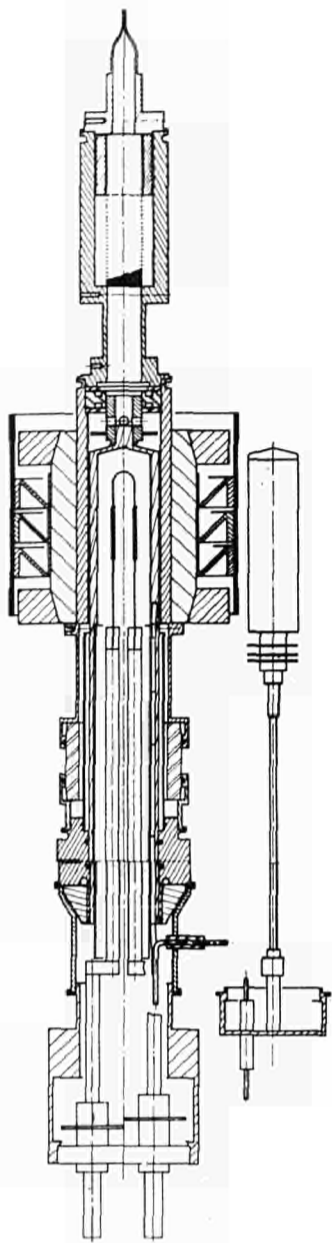


Fig. 4 a

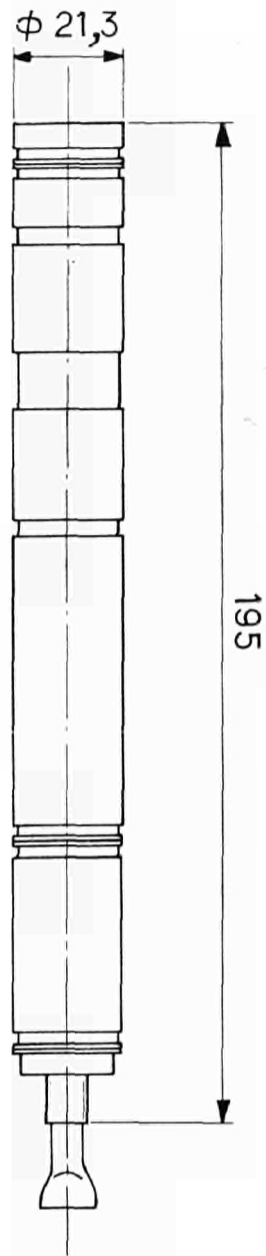


Fig. 4 b

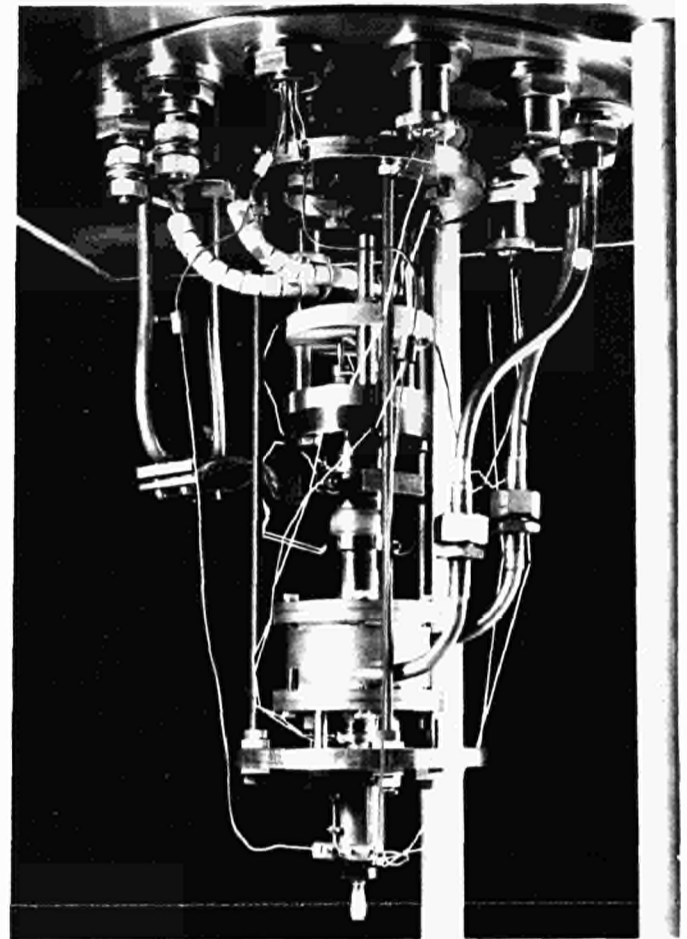


Fig. 5

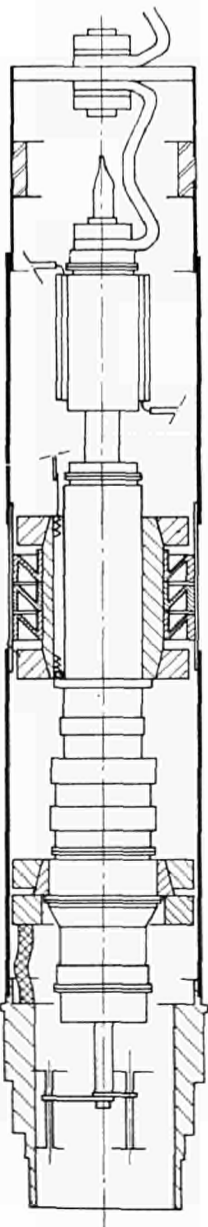


Fig. 6

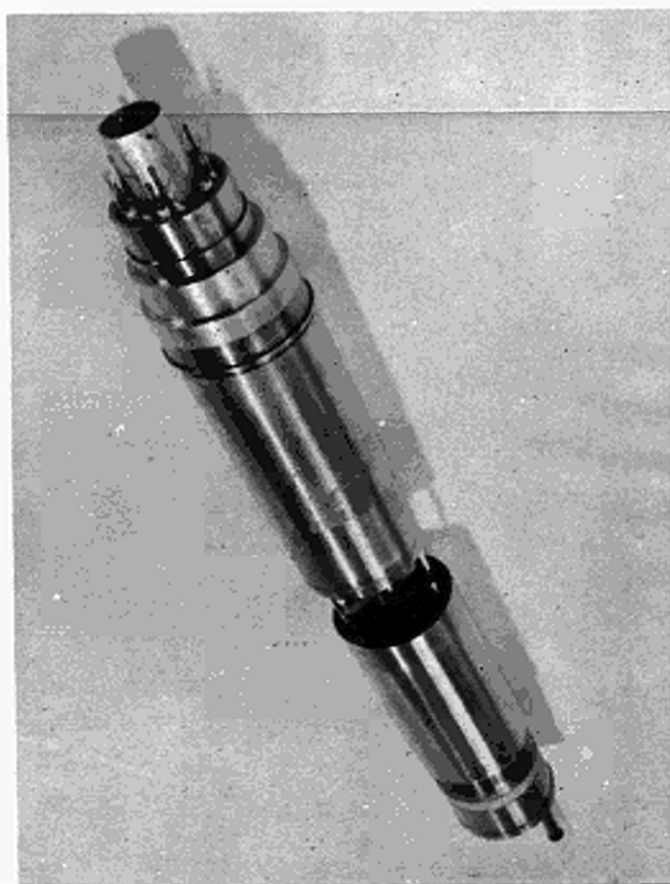


Fig. 7

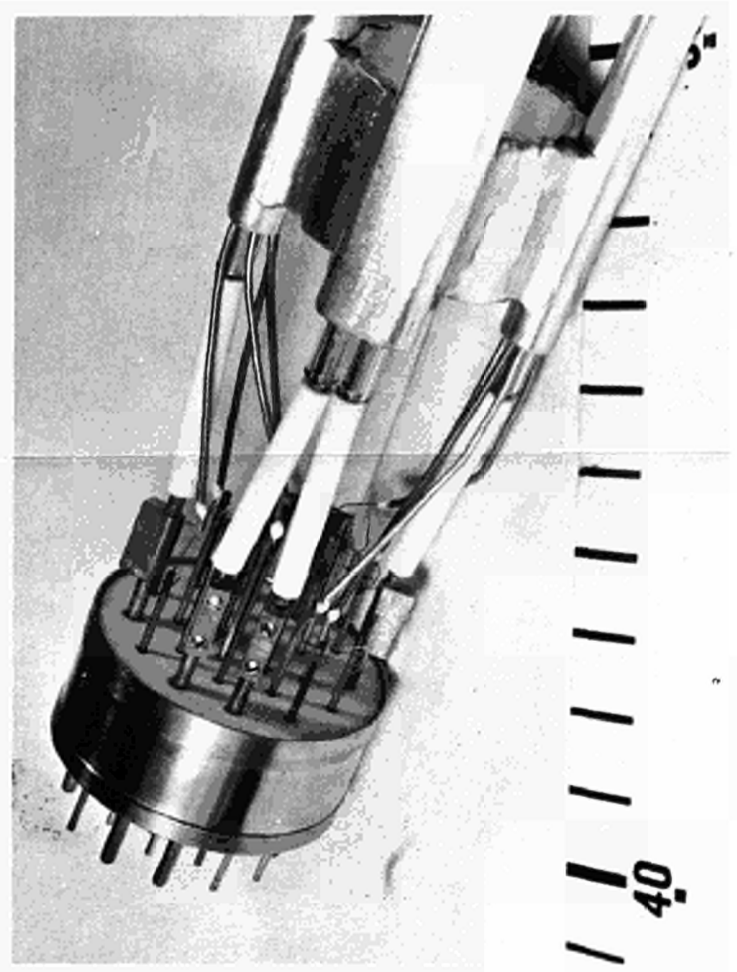


Fig. 8

BILAN DES ETUDES DE DUREE DE VIE DES CONVERTISSEURS THERMO-IONIQUES
EN LABORATOIRE.

J. BLIAUX, M. CLEMOT, J.P. DURAND, B. GAYTE

Service d'Electronique Physique, Centre d'Etudes Nucléaires de Saclay,
91 - Gif-sur-Yvette (France)

Introduction.

Afin d'éprouver la fiabilité des convertisseurs thermo-ioniques, le S.E.P. du C.E.N. Saclay a mis en service 8 postes d'essais de durée de vie. Au cours des années 1966 et 1967, seize convertisseurs de différentes origines ¹⁾ ont été testés. Les expérimentations ont porté sur l'essai des convertisseurs avant leur mise en pile, sur des études fondamentales de fonctionnement et sur les études de durée de vie. Après arrêt, les convertisseurs ont été examinés afin de déterminer les causes de défaillance et d'y apporter les améliorations technologiques nécessaires. La présente communication rend compte essentiellement des performances de durée de vie des convertisseurs et des examens "post-mortem" effectués.

1. Bancs d'essais - Système de mesures.

Les postes d'essais (fig. 1) ont été prévus pour recevoir des convertisseurs de 100 à 200 watts de puissance électrique. Les éléments constitutifs principaux sont :

- Alimentation de bombardement 1 500 V - 1 A pour chauffage des émetteurs.
- Dispositifs de pompage de l'enceinte d'essai (prévidage, pompage ionique).
- Alimentation diverses simples et régulées (chauffage du collecteur, du réservoir de césium).
- Appareils de mesures et enregistreurs.

L'ensemble est entièrement automatisé et permet le fonctionnement sans interruption, il comporte également une platine de sécurité assurant les fonctions alarme (qualité du vide, température d'émetteur).

Le circuit de charge utilisé est représenté par la figure 2. Il comprend :

- a) Un circuit à résistance de charge fixe (mise en durée des convertisseurs).
- b) Un circuit à résistance de charge variable constitué d'une génératrice à courant continu (étude du convertisseur avant mise en durée). L'excitation variable de la génératrice permet l'exploration complète des caractéristiques I (V), du circuit ouvert au court-circuit. Un système à horloges électriques définit les points de mesures et les temps de stabilisation thermique.

Le relevé systématique des paramètres des convertisseurs est effectué soit

1) Convertisseurs fabriqués au titre des contrats C.E.A./C.S.F., C.E.A./C.F.T.H.H.B.

sur machine imprimante, soit mis en mémoire sur bande perforée (figure 3). La description complète du système de traitement de l'information utilisé et de son application aux convertisseurs thermo-ioniques a fait l'objet d'une communication précédente [1].

2. Convertisseurs.

Les convertisseurs étudiés sont de structure cylindrique, prévus pour un fonctionnement à une puissance nominale de 100 watts électriques, ils sont identiques aux modèles essayés en pile [2]. Leur surface émettrice est de 20 cm², la figure 4 présente un des modèles utilisés.

Le convertisseurs est placé sous une cloche métallique dans un vide inférieur à 10⁻⁵ torr. Il est maintenu dans un ensemble pont thermique, refroidi par eau, et muni d'une chaufferette pour réguler la température du collecteur. Les températures des points suivants sont contrôlées en permanence :

haut émetteur	bas collecteur
milieu émetteur	réservoir césium
embase émetteur	pont thermique collecteur
haut collecteur	eau de refroidissement.

Les caractéristiques technologiques des 16 convertisseurs testés sont consignées dans le tableau 1. On distingue 2 séries se différenciant par la nature du collecteur, de l'émetteur et du scellement métal-céramique.

Série 1 : convertisseurs n° 6 - 7 - 8 - 10 - 15 - 20 - 21 - 29 - 30

Série 2 : convertisseurs n° 201 - 204 - 205 - 206 - 207 - 208 - 307.

Convertisseur n°	Année de fabric.	Nature collecteur	Nature émetteur	d.inter-électrodes [μ]	Scellement métal-céramique brasure	Centrage émetteur	Nature du réservoir Cs
<u>Série 1</u>							
6	1966	Mo	Mo	300	Al ₂ O ₃ Wesgo/Kovar brasure Cu	oui	Cs liquide
7	"	Mo	Mo	300	"	oui	"
8	"	Mo	Mo	300	"	non	"
10	"	Mo	Mo	250	"	oui	"
15	"	Mo	Mo	250	"	oui	"
20	"	Mo	Mo	250	"	oui	"
21	"	Mo	Mo	250	"	oui	"
29	1967	Mo	Mo/W (e=50μ)	200	Al ₂ O ₃ Wesgo/W/Nb brasure Cu-Ni	oui	"
30	"	Mo	Mo/W (e=50μ)	200	"	oui	"
<u>Série 2</u>							
201	1966	Nb	Mo/W (e=200μ)	200	Al ₂ O ₃ Lucalox/Nb brasure Ni-Ti	non	"
204	"	Nb	Mo/W (e=200μ)	200	"	non	"
205	"	Nb	Mo/W (e=200μ)	200	"	non	"
206	"	Nb	Mo/Re (e=50μ)	200	"	non	"
207	"	Nb	Mo/Re (e=50μ)	200	"	non	"
208	"	Nb	Mo/Re (e=50μ)	200	"	non	"
307	1968	Nb 1% Zr	Mo/W (e=200μ)	200	"	oui	Cs graphi- te C ₁₀ Cs ↔ C ₂₄ Cs [3]

TABLEAU 1.

1) Les dépôts de W constituant les couches émettrices sont effectués par décomposition en phase vapeur de WF₆ sur substrat en Mo (e = 2 mm) ; les dépôts de Re sont obtenus par dissociation de ReCl₃.

3. Performances.

On ne rend pas compte ici, des mesures effectués sur les convertisseurs. Leur étude a cependant fait l'objet de travaux précédents [4]. Des réseaux complets de caractéristiques ont été relevés et sont illustrés par les figures 5 et 6.

3.1. Optimalisation du convertisseur pour mise en durée.

Le point nominal de fonctionnement est choisi pour une puissance d'entrée donnée ($P_E = P_F + P_B$, avec P_F = puissance chauffage filament, P_B = puissance de bombardement), de telle sorte que :

- a) la résistance de charge soit optimum,
- b) la température du réservoir de césium soit optimum,
- c) la température du collecteur soit optimum.

On obtient ainsi le fonctionnement du convertisseur au point de rendement maximum $\eta = \frac{P_S}{P_E}$ (P_S : puissance délivrée) pour une puissance d'entrée P_E fixée. Cette détermination est effectuée par des relevés statiques des courbes $I(V)$.

Compte tenu d'une valeur limite choisie de la température d'émetteur : $T_E \leq 1\,900$ °K, le point nominal correspond à un fonctionnement à $P_S \approx 100$ W (5 W/cm²). Les rendements $\eta = \frac{P_S}{P_F + P_B}$ mesurés pour les convertisseurs étudiés sont compris entre 9 et 12 % (9 à 10 % pour émetteurs en Mo, 10 à 12 % pour les émetteurs en W et Re).

3.2. Point de fonctionnement.

A titre d'exemple, on indique les caractéristiques de point de fonctionnement du convertisseur n° 30, actuellement en essai de durée :

Valeurs mesurées à $t = 3\,260$ heures (2 mai 1968) :

$P_E = 1\,300$ W	$\eta = 10,7$ %
$I_S = 162$ A	$T_E = 1\,570$ °C
$V_S = 0,87$ V	$T_C = 605$ °C
$P_S = 140$ W	$T_{Cs} = 320$ °C.

3.3. Durée de vie.

Le tableau 2 indique les durées de vie de chaque convertisseur, leur cause d'arrêt, ainsi que l'énergie totale convertie. Le fonctionnement des convertisseurs pendant le test a été fréquemment interrompu par des arrêts dus à l'appareillage annexe : alimentations changement de filament, métallisation des passages haute tension.

Les diagrammes de durée de vie sont représentés par les figures n° 7 pour les meilleurs éléments.

Convertisseur n°	Durée de vie [heures]	Energie totale convertie [KWh]	Causes d'arrêt		Remarques.
			court-circuit	fuite de Cs	
<u>Série 1</u>					
6	10	0,5		x →	Scellement métal-céramique
7	58	5		x →	"
8	93	5		xx →	Scellement métal-céramique + émetteur percé
10	250	24	x		
15	262	21	x	x →	Scellement métal-céramique
20	450	25	x		
21	1 203	80	x	x →	Scellement métal-céramique
29	300	15			50 h. fonctionnement en pile [2]
30	3 260	250			Actuellement en fonctionnement
<u>Série 2</u>					
201	1 120	65	x		
204	250	15		x →	Scellement métal-céramique (incident mécanique de montage)
205	172	10	x		
206	5 600	450	x		
207	745	25,5		x →	Emetteur percé (base Mo)
208	230	9,5	x		
307					Actuellement en fonctionnement

TABLEAU 2.

Pour les convertisseurs de la série 1, les causes d'arrêt prématuré ont été principalement dues à des fuites de césium au scellement métal-céramique. L'amélioration de ce dernier (convertisseurs n° 29 et n° 30) a permis de passer de durées de vie de quelques centaines d'heures à plus de 3 000 heures de fonctionnement.

Pour la série 2, les courts-circuits d'abord intermittents puis permanents ont constitué les causes d'arrêt. Le convertisseur n° 206, a cependant fonctionné pendant 5 600 heures.

Les différents examens effectués après durée de vie, ont pu expliquer ces défaillances.

4. Examens post-mortem.

4.1. Convertisseurs série 1 (n° 6, 7, 8, 10, 15, 20, 21).

Les examens ont mis en évidence :

a) Une évaporation importante de l'émetteur en Mo nu (jusqu'à 150 μ). La figure 8 donne le profil d'un émetteur, l'hétérogénéité de température au centre explique l'importance de l'évaporation.

b) Une recristallisation importante de la surface émettrice (figure n° 9).

c) Une fragilité excessive de la jonction métal-céramique $Al_2O_3/Cu/Kovar$, due à l'inadaptation en dilation, à haute température de l' Al_2O_3 et du Kovar.

4.2. Convertisseurs série 2 (n° 201, 204, 205, 206, 207, 208).

Les examens ont montré que les matériaux constituants présentaient un bon comportement aux vapeurs de césium. Seuls les émetteurs (Mo/Re, Mo/W) présentaient après fonctionnement, une altération importante. Leur étude complète, qui a fait l'objet d'une communication [5], comportait :

a) des examens micrographiques (fig. 10, 11).

b) l'étude de la diffusion des couches émettrices Mo/Re, Mo/W par microdureté et mesures à la microsonde de Castaing (fig. 12).

c) la mesure de variation du travail de sortie au microscope à émission thermo-ionique (fig. 13).

En résumé, les courts-circuits intermittents observés avant arrêt complet des convertisseurs ont été vraisemblablement causés par des arrachements et décollements des couches de W et Re.

Ces altérations sont dues à la formation de phases intermétalliques Mo-Re fragiles dans le cas du Re (fig. 10).

Dans le cas des émetteurs de W, le phénomène d'interdiffusion Mo-W associé aux défauts du dépôt (pores, gaz occlus) ont provoqué les soufflures et arrachements de la couche émettrice (fig. 11).

Depuis, ces résultats ont été confirmés par l'examen en cellule chaude du convertisseur nucléaire SIRENE 302 [2].

Conclusions.

Les renseignements statistiques obtenus sur les convertisseurs soumis aux essais de durée de vie permettent d'éprouver et d'améliorer leur fiabilité. Ceci est illustré par les résultats obtenus pour la série 1 : plus de 3 000 heures de fonctionnement après modification du scellement métal-céramique.

La technologie des éléments de la série 2 est satisfaisante, un fonctionnement de 5 600 heures a ainsi pu être enregistré. La seule difficulté réside dans la stabilité des couches émettrices Mo/W. Les études entreprises dans le domaine de l'interdiffusion et dans celui du dépôt de W, conduiront vraisemblablement à une nouvelle amélioration des durées de vie et à une plus grande stabilité des performances.

Références.

- [1] BLIAUX J., GAMBIER G., "Automatic measurements and data processing on nuclear thermionic converters"
Thermionic Conversion Specialist Conference, Palo Alto, California, October 30, 1967.
- [2] BLIAUX J., CLEMOT M., DEVIN B., DUMAS P., "Expériences de conversion thermo-ionique 'SIRENE' en pile et examens après irradiation du convertisseur 'SIRENE 302'", Stresa, Italie, 27-31 Mai 1968.
- [3] DEVIN B., LESUEUR R., SETTON R., "Vapor pressure of cesium above graphite lamellar compounds"
Thermionic Conversion Specialist Conference, Palo Alto, California, October 30, 1967.
- [4] LANDROT J.P., "Etude des régimes transitoires des convertisseurs thermo-ioniques", Thèse, Paris, 1967.
- [5] ALLEAU T., CLEMOT M., HASSON R., "Post mortem examinations of thermionic emitters",
Thermionic Conversion Specialist Conference, Palo Alto, California, October 30, 1967.

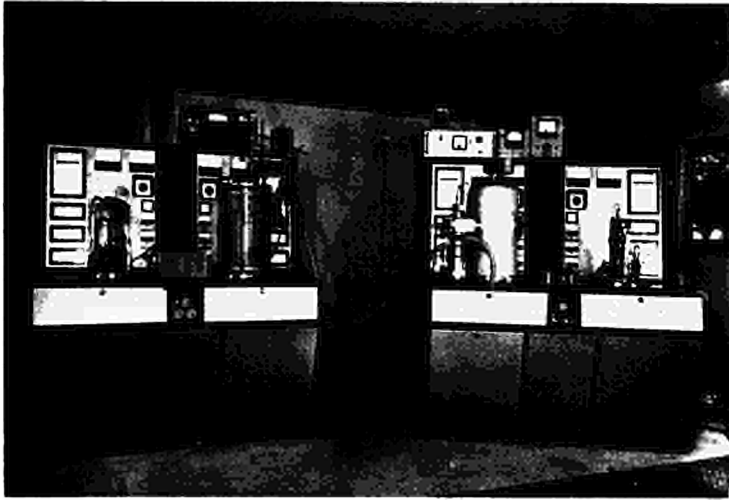


Fig.1 - Bancs d'essais de durée

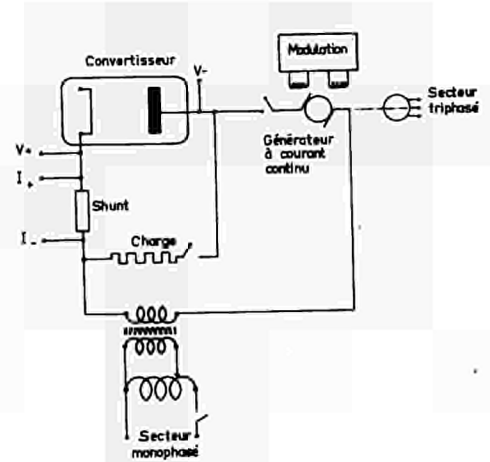


Fig.2 - Schéma circuits de mesures

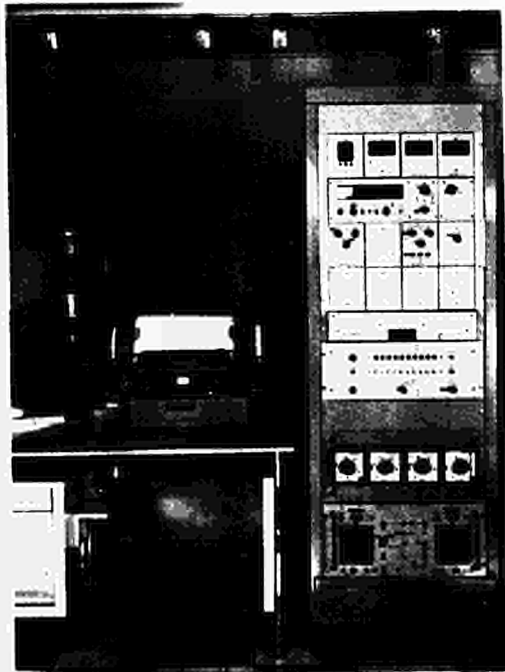


Fig.3- Ensemble de centralisations de mesures

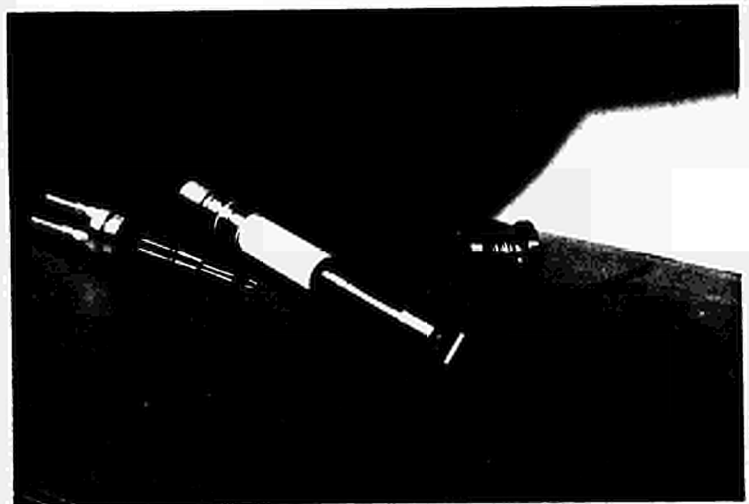


Fig.4 - Modèle de convertisseur testé, filament de chauffage, chaufferette de césium.

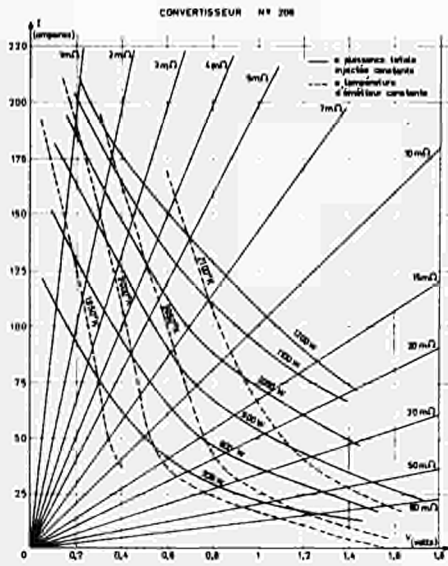


Fig. 5- Caractéristiques I(V)

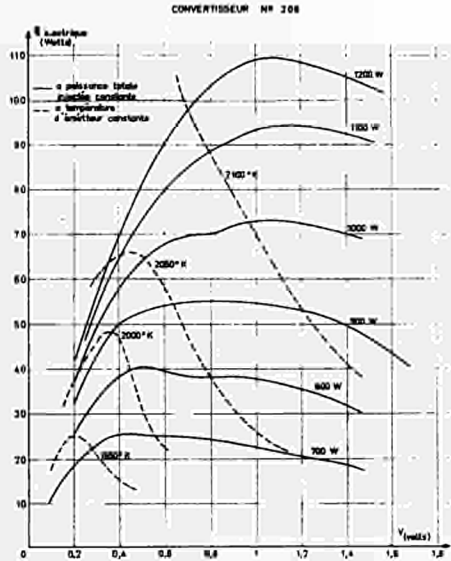


Fig. 6 - $P_g = f (V_g)$

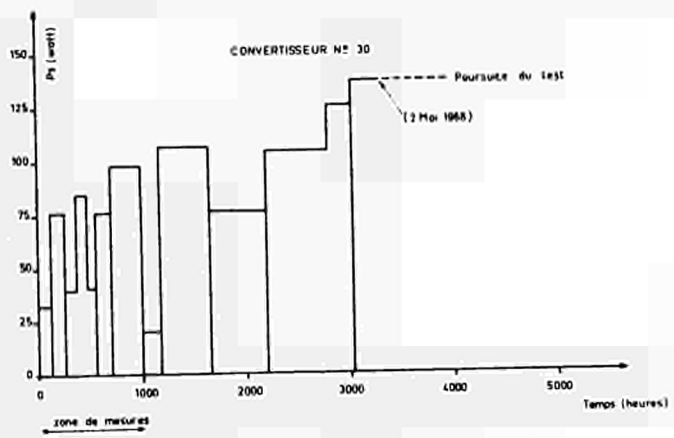
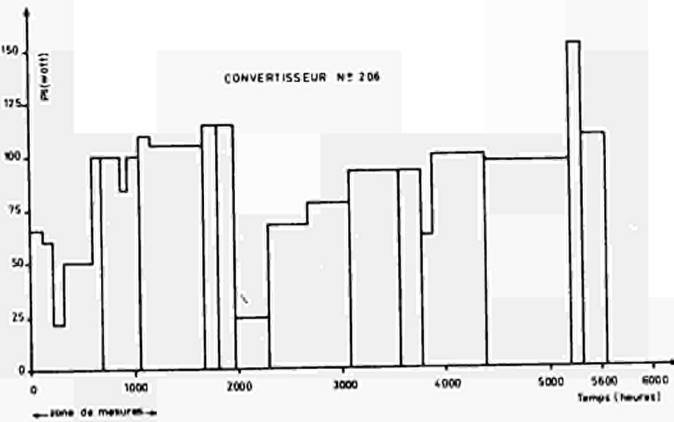


Fig. 7 - Diagrammes de durée de vie

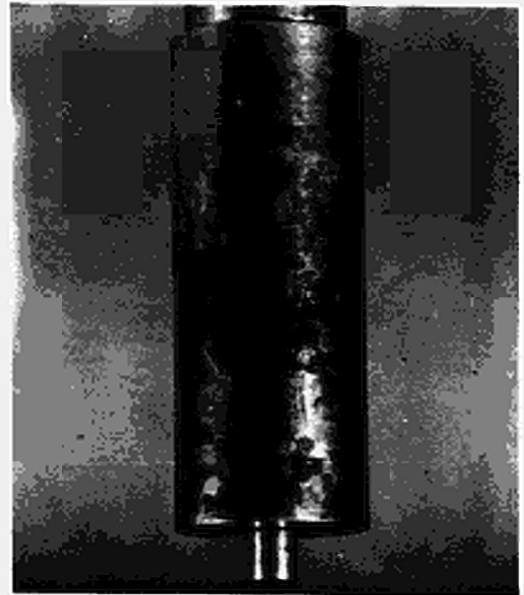


Fig. 8- Emetteur n°20 (Mo, 450 heures)

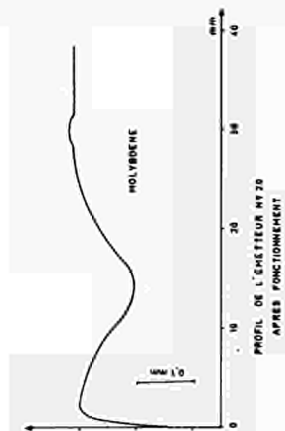
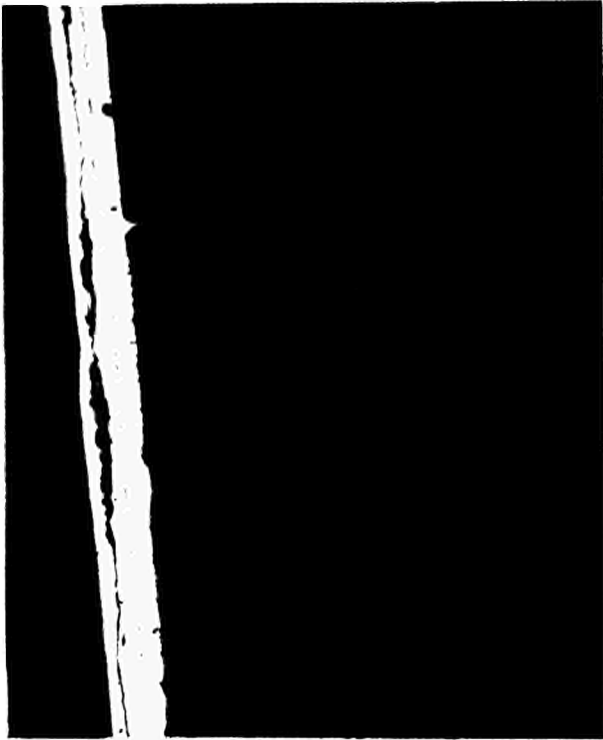
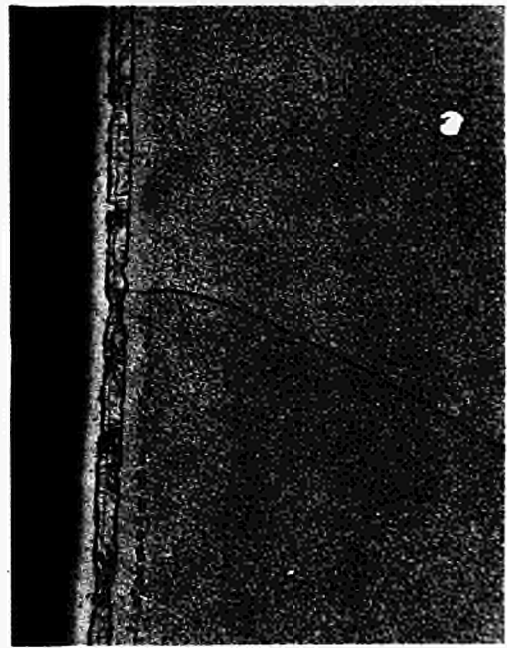


Fig. 9

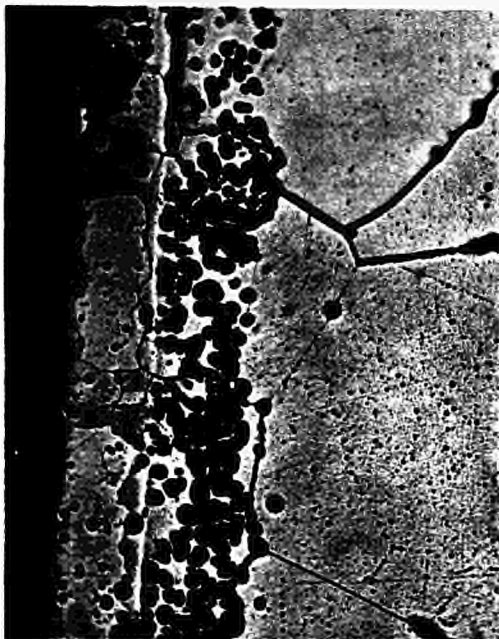


Phases intermétalliques Mo/Re (x 110)

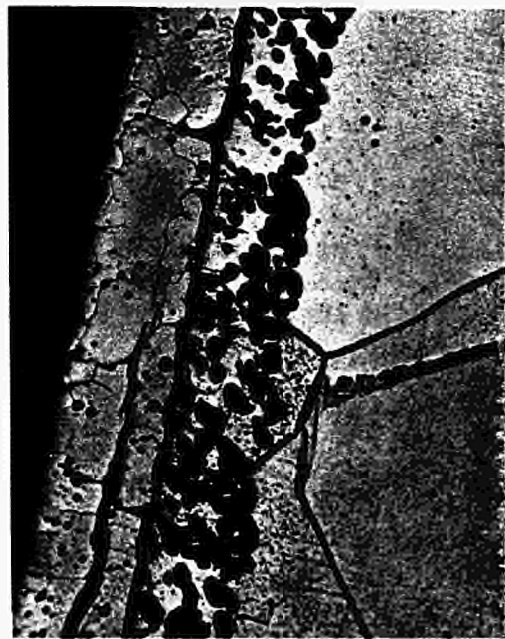


Porosités à l'interface Mo-Re (x 190)

Fig.10 - Emetteur 208 Mo/Re ,230 heures



Porosités à l'interface Mo-W
et dans le W (x 74)



Fissures et arrachements
du W (x92)

Fig.11 - Emetteur 201 Mo/W, 1120 heures

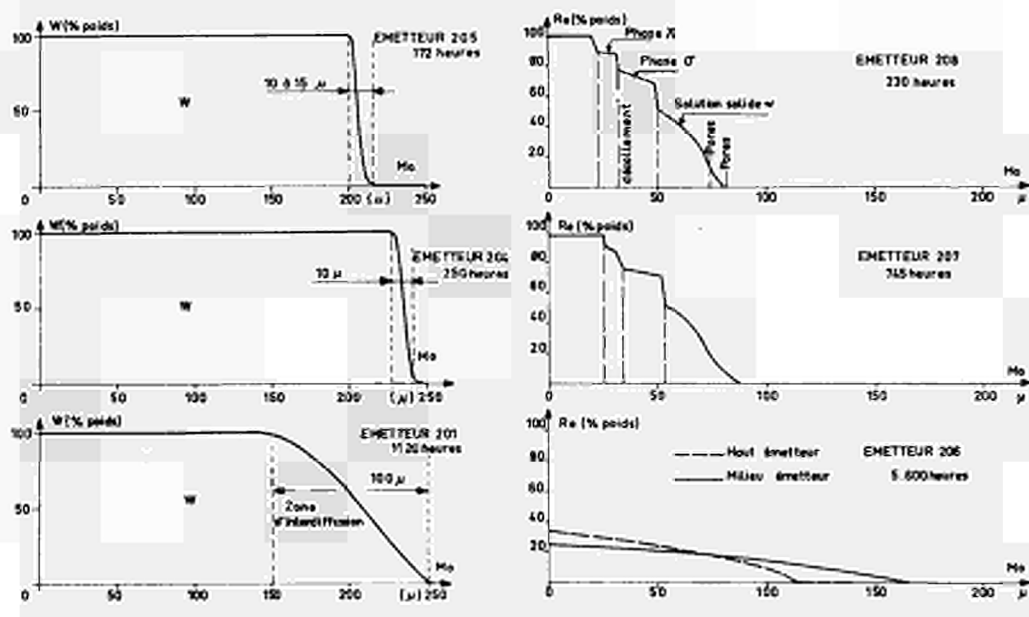


Fig.12 - Etude de la diffusion (mesures microsonde de Castaing)
des émetteurs Mo/W, Mo/Re après fonctionnement

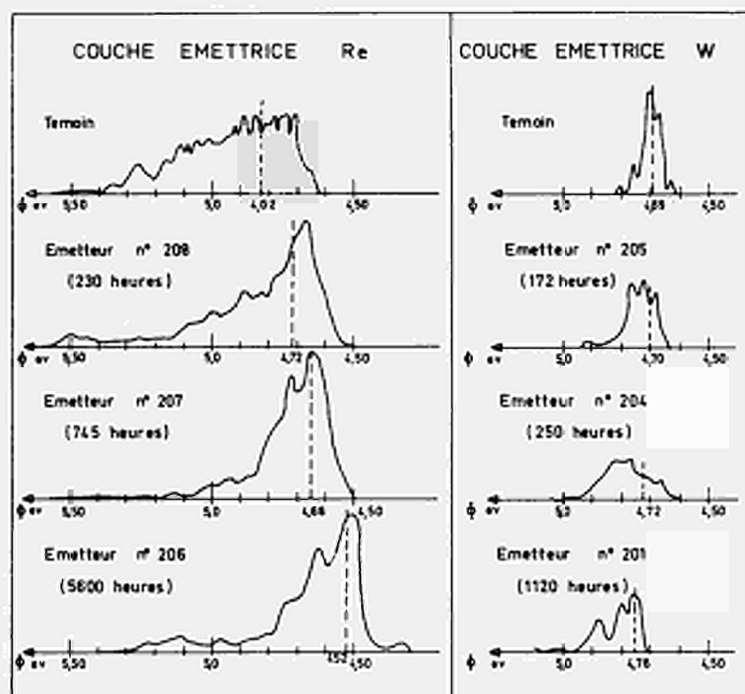


Fig.13 - Variation du travail de sortie des couches émettrices
Mo/W, Mo/Re

INVESTIGATION OF A Ne-A THERMIONIC GENERATOR

Martha Bacal, Maria Cristescu and C. Voci

Institute for Atomic Physics, Bucharest, Rumania

ABSTRACT. The results are presented of an experimental investigation of an auxiliary discharge thermionic converter filled with a Penning mixture (Ne 99.5% - A 0.5%). The measurements effected in the pressure range 1.25 - 4.8 Torr have shown that the pressure increase in this range led to an improvement of the converter performance and also to a reduction of the minimum auxiliary discharge voltage at which the converter operation became possible. It was found that the effect of Penning ionization in a mixture at an auxiliary discharge voltage near the excitation potential of the lighter constituent gas is comparable to the effect of the ionization processes acting in the pure heavier constituent gas at an auxiliary discharge voltage near to its ionization potential. Two discontinuities of the collector current were noticed at positive collector voltages. The fact that the current increase in the Ne-A mixture at the first discontinuity is much lower than that observed in Argon, corroborates the view that this discontinuity is due to the ionization of metastables by electrons.

Our recent investigation of an Argon gas filled auxiliary discharge thermionic converter (1,2) has pointed out that a considerable stepwise increase of the collector

current took place for two values of the positive collector voltage (denoted as V_1^A and V_2^A). This effect was explained in terms of ionization of Argon metastable atoms by electrons and suggested the idea of using the metastables for ion generation by way of Penning ionization in a noble gas mixture. It was expected that in a mixture the metastables would be used to a higher extent for ionization in the range of the emitter-collector voltage, which is of interest for thermionic conversion. Greaves and Kerry (4) have shown recently that the Penning effect does not significantly improve the efficiency of positive ion generation in the noble gas thermionic converter. However no explanation of this result was suggested. The present work was performed in order to investigate the effect of replacing the pure Argon gas with a Penning mixture Ne-A (99.5% Ne - 0.5% A) upon the characteristics of the auxiliary discharge thermionic converter and especially upon the discontinuities of the I-V characteristic in the positive voltage range. The same experimental device and measurement set-up as described in the previous works (1,2) has been used. Measurements were made at five pressures of the Ne-A mixture in the range 1.25 Torr - 4.8 Torr.

In Fig. 1 the maximum load current I_C^{\max} (i.e. the value I_C at $V_C = 2.7$ V), measured at an auxiliary discharge voltage (V_{aux}) slightly exceeding the ionization potential of Neon, is plotted against the auxiliary discharge current. The increase of the pressure in the mentioned range leads to an improvement of the converter performances. The comparison of these data with those obtained for pure A gas, for V_{aux} slightly excee-

ding the ionization potential of Argon ($V_{\text{aux}} = 16 \text{ V}$ - ref. 1, Fig. 3) points out that similar I_C^{max} values are obtained for the same auxiliary discharge currents and near pressures.

The auxiliary discharge could be operated also at V_{aux} values lower than the ionization potential of Ne. In order to investigate this effect, the minimum auxiliary discharge voltage $V_{\text{aux}}^{\text{min}}$ at which the load current suddenly appears (for $V_C = 0$) was measured (Fig. 2). The data obtained in similar conditions in pure Argon gas, are also shown. The pressure increase leads to a reduction of $V_{\text{aux}}^{\text{min}}$ from a value near to the ionization potential (of Ne - in the case of the Ne-A mixture, and of A - in the case of pure A gas), to values which are near to the excitation potential of the metastable states of Ne - in the case of the Ne-A mixture, and of A - in the case of pure A gas. Therefore, as was also observed by Greaves and Kerry (3), the values $V_{\text{aux}}^{\text{min}}$ in the Penning mixture are higher than those in the heavier constituent gas alone, i.e. in A gas.

For some values of the auxiliary discharge current, two discontinuities of the collector current may be noticed, at collector voltages which will be denoted as $V_1^{\text{Ne-A}}$ and $V_2^{\text{Ne-A}}$. A greater current increase takes place at $V_2^{\text{Ne-A}}$; its occurrence is accompanied by a bright red glow at the boarder of the cathode-collector space. The mentioned discontinuities of the collector current can be observed only in a limited range of the auxiliary discharge parameters (Fig. 3). The discontinuities always appear for auxiliary discharge voltages near to

the excitation potential of the metastable states of Ne (in the Ne-A mixture) and of A (in the pure A gas).

In Fig. 4 the I-V characteristic obtained in a Ne-A mixture at a value $V_{aux} = 17$ V, slightly exceeding the excitation potential of Ne metastable states ($V_{ex} = 16.61$ V and 16.72 V for the Neon 3P_2 and 3P_0 levels respectively) is compared with a characteristic obtained in pure A gas at a value $V_{aux} = 16$ V which is slightly higher than the ionization potential of Argon ($V_1 = 15.75$ V). The emitter temperature and the auxiliary discharge current were the same in the two cases. The fact that nearly equal currents were obtained for $V_c < 3.6$ V supports the view that the effect of the Penning ionization process in a mixture at an auxiliary discharge voltage near to the excitation potential of the lighter constituent gas, is comparable to the effect of the ionization processes acting in the pure heavier constituent gas at an auxiliary discharge voltage near to its ionization potential. Concerning the discontinuities of the collector current which are present in Fig. 4 (V_2^A and V_1^{Ne-A}), it can be observed that:

- 1) The current increase in the pure A gas at V_2^A is significantly greater than that occurring in the Ne-A mixture at V_1^{Ne-A} .
- 2) V_1^{Ne-A} is somewhat higher than V_2^A , namely $V_1^{Ne-A} - V_2^A \approx 0.8$ V. These facts corroborate the view that the same process - namely the ionization of metastable atoms by electrons - may be responsible for the discontinuities at V_1^{Ne-A} (in the Ne-A mixture) and at V_2^A (in pure A gas). Indeed, it was shown that for the case of pure A gas (1,2) a correlation existed between V_2^A and the difference $V_1^A - V_{ex}^A$, namely: $V_2^A \approx V_1^A - V_{ex}^A - V_{cp}$;

where V_{cp}' is the contact potential difference between the main emitter and the collector. Of course, for some converter conditions the electrons emitted by the main emitter are accelerated by the potential difference across the emitter sheath, which may be equal or higher than the applied cathode-collector voltage. Therefore, when $V_C = V_2^A$, a large number of electrons with an energy sufficient for ionization of the A metastable atoms may be available. As $V_1^{Ne} - V_{ex}^{Ne} = 4.95$ V, while $V_1^A - V_{ex}^A = 4.26$ V, it is to be expected that the current increase due to the ionization of the Ne metastables by electrons should take place at a cathode-collector voltage higher with about 0.7 V than in pure A gas. As V_1^{Ne-A} fulfills this requirement (Fig. 3 and 4), it seems possible that the current increase at V_1^{Ne-A} might be caused by the ionization of Ne metastables by electrons. The fact that the current increase due to this effect in the Ne-A mixture is not as important as that observed in pure A gas, may be explained by a depopulation of the Ne metastable levels in the Ne-A discharge, due to the Penning effect (4).

The efficiency of the Penning ionization process might be reduced in the thermionic converters owing to:

- 1) the high electron densities present in these devices; the interaction thermal electron - excited atom may reduce the concentration of the excited atoms available for Penning ionization (5);

- 2) the separation of the Penning mixture components due to thermo-diffusion, leading to a reduction of the concentration of the heavier atoms near the hot surfaces (6).

REFERENCES

- (1) BACAL, M.; GRABARI, V.; "Investigation on noble gas-filled thermionic converters", International Conference on Thermionic Power Generation, London, September 1965.
- (2) BACAL, M.; GRABARI, V.; TEODORESCU, M., "Investigation on a noble gas-filled auxiliary discharge thermionic energy converter", Rev. Roumaine Phys., 11, (1965) 135.
- (3) GREAVES, C.; KERRY, D.C., "Investigation into the use of auxiliary discharges in thermionic generation", Brit.J.Appl.Phys., 15, (1964) 177.
- (4) SINDA, Th.; WATEL, G., "Etude de la production d'un faisceau d'atomes métastables d'énergie thermique", Compt. rend. Sér. B 266 (1968) 768.
- (5) DIXON, J.R.; GRANT, F.A., "Decay of the triplet P levels of Neon", Phys. Rev., 107 (1957) 118.
- (6) BEKMUHAMBETOV, E. S.; GUSKOV, J.K.; KASIKOV, I.I.; LEBEDEV, S.J.; STAHANOV, I.P.; RODIN, A.V., J.Tech. Phys. (USSR), 36 (1966) 1481.

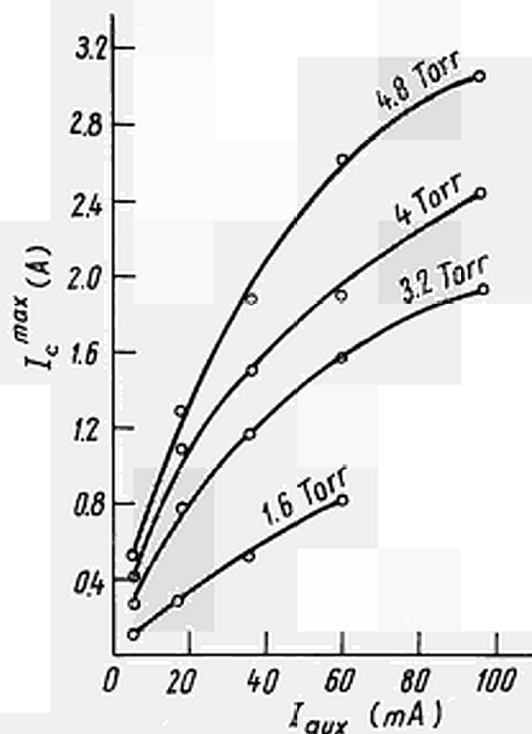


Fig. 1. I_C^{max} vs I_{aux} , with Ne-A mixture pressure as parameter, for $V_{aux} = 23$ V, $T_{em} = 1170^\circ\text{C}$.

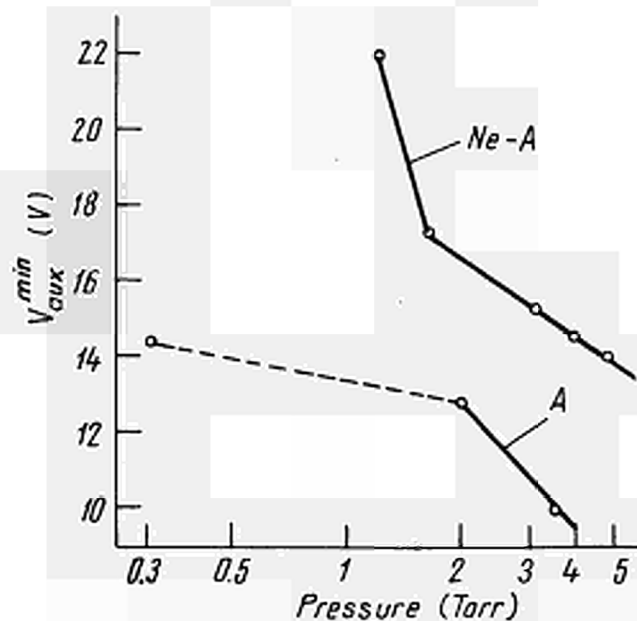


Fig. 2. Dependence of V_{aux}^{min} vs pressure for Ne-A mixture and A gas ($T_{em} = 1100^\circ\text{C}$, $I_{aux} = 10$ mA).

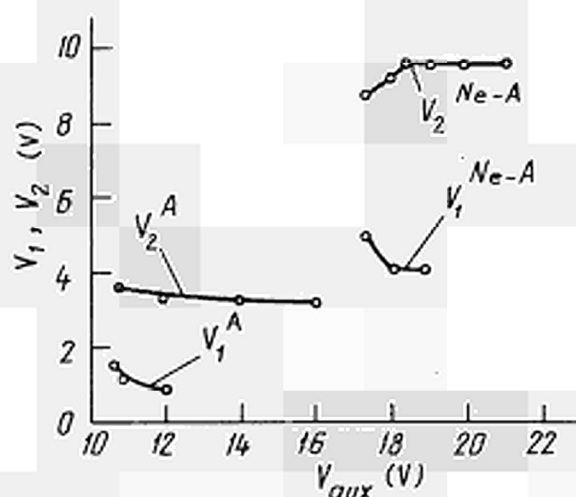


Fig. 3. V_1 and V_2 vs V_{aux} for Ne-A mixture at 4.8 Torr, and for pure A gas at 3.5 Torr ($T_{em} = 1100^\circ\text{C}$ and mean auxiliary emitter heating current $i_{f(aux)} = 0.7\text{A}$).

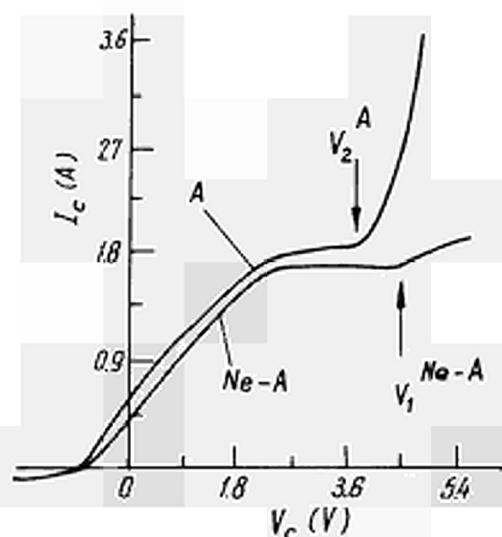


Fig. 4. I - V characteristics measured in Ne-A mixture (4.8 Torr, $V_{aux} = 17\text{ V}$) and in A gas (3.5 Torr, $V_{aux} = 16\text{ V}$). $T_{em} = 1100^\circ\text{C}$, $I_{aux} = 64\text{ mA}$.

MODULE THERMOIONIQUE NUCLEAIRE TOUT-METAL

B.DEVIN, J.P. DURAND, P.RAGOT

Service d'Electronique Physique
 Centre d'Etudes Nucléaires de Saclay
 91 - Gif-sur-Yvette (France)

INTRODUCTION.-

On a cherché à réaliser un module thermoionique, de construction simple, industrialisable, et ne faisant pas appel à la technique métal-céramique dont la mise en oeuvre est délicate et qui s'est révélée être une cause non négligeable de pannes au cours des essais de durée de vie. Notons d'ailleurs que les défauts du scellement ont été aussi bien des problèmes de corrosion (évolution à long terme du scellement) que des défauts mécaniques apparus à la suite de manipulations répétées.

La conception d'un convertisseur "modulaire", placé entièrement à l'intérieur du flux neutronique, exige également l'élimination des matériaux susceptibles de subir une altération grave sous irradiation (gonflement de l'alumine). Enfin, la diode "modulaire", placée en "série" à l'intérieur des canaux d'un réacteur doit présenter une surface externe lisse, sans aspérités, pour le passage du fluide caloporteur, et se prêter aux connexions électriques "en bout", ce qui fait rejeter la fermeture par queusot.

Le module "tout métal" remplit toutes ces conditions. L'idée n'en est d'ailleurs pas nouvelle puisque le premier convertisseur essayé en pile en Europe ne comportait aucun isolateur étanche⁽¹⁾.

I - STRUCTURE ET REALISATION DU MODULE NUCLEAIRE .-Disposition mécanique -

La figure 1 montre la structure du module métallique ainsi que les 4 éléments indépendants qui le composent.

Il se distingue d'une diode cylindrique normale par l'ensemble "collecteur". Le collecteur de molybdène est recouvert par projection d'une couche d'alumine. Il est ensuite placé à l'intérieur d'un tube d'alliage de titane et d'aluminium mince^{(2),(3)}, qui est fretté sur la couche d'alumine par pressage isostatique à chaud. De cette manière on assure par le jeu de la dilatation différentielle une conductance thermique radiale élevée ($3^\circ \times \text{cm}^2/\text{W}$) entre le collecteur proprement dit et la face externe du convertisseur.

La base de la structure du collecteur comporte un logement pour le réservoir de césium intégré (dans la version finale). Celui-ci travaille à la température du collecteur. Le réservoir est chargé séparément en graphite césié.

Le tube de titane-aluminium servant d'isolateur est soudé d'une part à la base du collecteur, et d'autre part à une embase de molybdène, séparée du collecteur par une cale d'alumine. Cette embase reçoit l'émetteur qui y est soudé par bombardement électronique pendant la phase finale de montage. L'opération d'assemblage-pompage s'effectue dans une enceinte à vide comportant la spire HF de dégazage et le canon électronique de soudure (fig.2); le réservoir de césium est ensuite percuté : il n'y a aucune opération ultérieure de

pompage, ni de queusotage.

Le modèle prototype présenté figure 3 comporte un réservoir non intégré externe pour l'étude des performances en fonction des températures relatives de l'anode et du réservoir ; le queusot auxiliaire a servi à la séparation de l'ampoule de verre contenant la charge de césium.

Dimension optimale du module -

On conçoit aisément que la présence d'une dérivation parasite sur le circuit de charge affecte le rendement global du convertisseur. Etant donné que le courant engendré par le convertisseur augmente avec la longueur de l'émetteur, tandis que le courant dérivé par le tube externe diminue, on aurait intérêt à construire le convertisseur aussi long que possible. Mais la perte Joule dans la paroi de l'émetteur et dans celle du collecteur croît rapidement avec leur longueur : il y a donc une dimension optimale de la diode qui fait le meilleur compromis possible entre les pertes internes ohmiques et les pertes externes dans la structure métallique.

Un calcul très simplifié peut être fait en considérant le point nominal de fonctionnement de la diode unitaire, choisie comme référence, et dont la caractéristique I (V) à puissance d'entrée constante a l'allure représentée figure 4.

La figure 5 donne le schéma équivalent : A de la diode unitaire, B de la diode cylindrique à isolateur céramique, C de la diode tout-métal. S, R_e et R_f désignent respectivement la surface de l'émetteur, la résistance de l'émetteur et la résistance du tube externe.

L'application du théorème de Thévenin à la diode tout-métal conduit au circuit équivalent D (figure 4) avec :

$$V = V_0 \frac{R_f}{R_i/S + R_e + R_f} \quad R = \frac{R_f (R_i/S + R_e)}{R_f/S + R_f + R_e}$$

d'où les caractéristiques du point optimal de fonctionnement de la diode tout-métal

$$V_S = V_0 \frac{R_f}{R_i/S + R_e + R_f} \quad J_S = J_0 \frac{R_i}{R_i/S + R_e}$$

Le rendement relatif de la diode tout-métal par rapport à la diode unitaire est appelé rendement de structure de la diode métallique (η_{Sm}). Il s'écrit :

$$\eta_{Sm} = \frac{V_S I_S}{V_0 J_0 S} = \frac{R_f R_i/S}{(R_e + R_i/S)(R_e + R_i/S + R_f)} \quad (1)$$

Alors que le rendement de structure de la diode de même dimension mais avec isolateur céramique serait (η_{SC})

$$\eta_{SC} = \frac{R_i/S}{R_i/S + R_e}$$

En exprimant l'équation (1) en fonction des dimensions géométriques du convertisseur, de la nature des matériaux et en imposant, de plus, une chute de tension égale dans la paroi de l'émetteur et dans celle du collecteur, la longueur optimale du convertisseur L, à rayon d'émetteur r_e constant est donnée par

$$L^4 = \frac{a^2}{bc (1 + \frac{b}{c})} \quad (2)$$

$$\text{où : } a = \frac{V_0}{2 \pi r_e J_0} \quad b = \frac{\rho_{ém}}{2 \pi r_e^2} \quad c = \frac{\alpha \rho_{tube}}{e \cdot 2 \pi r_c}$$

avec r_c : rayon du tube, α : excès de longueur du tube sur l'émetteur et e : épaisseur du tube. $\rho_{ém}$ est la résistivité de l'émetteur à la température de fonctionnement. Cette valeur est remplacée par la "résistivité équivalente" lorsque l'émetteur est creux et destiné à être chargé par un combustible non conducteur (UO_2 par exemple) (soit $\rho_{ém}^* = \frac{\rho_{ém}}{1 - (\frac{r_{int}}{r_{ext}})^2}$) C'est le cas pour le modèle présenté.

La longueur optimale est donc fonction du diamètre de la surface émettrice, de la densité de courant émise dans les conditions nominales et des caractéristiques électriques et mécaniques du tube externe.

Le filage à chaud des lingots d'alliage Ti-Al conduit à des ébauches de tube qui, par rectification finale, peuvent être amenés à une épaisseur de 0,3 mm ; la variété d'alliage retenue pour les essais présente une résistivité ρ_t de 195 micro-ohm.cm.

La figure 6 donne, en fonction du rayon de l'émetteur, la longueur optimale d'une diode tout-métal à émetteur creux conforme au schéma de la figure 1. On a porté également sur cette figure la puissance nominale de sortie ainsi que le rendement de structure η_{S_m} . La valeur portée en paramètre est la quantité sans dimension caractéristique de la structure métallique

$$\mu = \frac{\alpha \rho_t}{e_t} \times \frac{r_{em}}{r_t}$$

A titre de comparaison, on a représenté sur la figure 6 le rendement de structure de la diode céramique et de la diode tout-métal en fonction de la longueur de l'émetteur. La présence d'une longueur optimale est claire et la perte par rapport à la diode céramique devient très faible aux puissances de sortie élevées.

Les convertisseurs à émetteur plein, conducteur (Cermet UO_2 Mo), sont avantagés par cette structure. La courbe en pointillé sur la figure 6 en témoigne.

II - RESULTATS EXPERIMENTAUX.-

La diode de la figure 2 a été construite aux dimensions suivantes :

ϕ_{em}	L_{em}	épaisseur	ϕ_{tube}	L_{tube}	épaisseur	résistivité	μ
16mm	55 mm	2mm(Mo)	19,4 mm	70 mm	0,35 mm	0,000195	0,0056

Dans le réseau de la figure 7, son point figuratif est représenté par le triangle. La diode n'a pas été construite optimale. Les dimensions ont été choisies afin qu'elle s'adapte aux appareils d'essais existants. Il s'agit là uniquement d'un prototype destiné à mettre au point la méthode de fabrication.

Les performances prédites par le calcul et mesurées sont comparées dans le tableau ci-dessous.

	VS	J_S	T_{em}	T_{coll}	T_{CS}	η_m	R_f
calculé	0,474	187	1600°C	600	682	6,3	6,2 mΩ
mesuré	0,453	182	1630°C	621	678	6,2	5,6 mΩ

V_o	J_o	T_{em}	T_{coll}	T_{CS}	η_m
0,8	7A/cm ²	1600	600	682	11 %

Caractéristique courant-tension :

Elle est tout à fait conventionnelle ; elle permet de restituer la caractéristique I (V) du convertisseur sans tube externe, par addition du courant dérivé dans la résistance R_f (figure 8).

CONCLUSION. -

Il n'est pas désirable d'entrer ici dans le détail technologique des divers assemblages qui conduisent à la réalisation du convertisseur. Leur caractéristique commune est d'être "industriels" , c'est à dire que chaque étape de préparation des éléments peut s'effectuer simultanément sur un grand nombre de pièces. Le temps d'assemblage final conduisant depuis les 4 éléments séparés jusqu'à la diode opérationnelle est d'environ quatre heures. Beaucoup d'espoirs sont fondés sur ce type de convertisseurs dont on attend que le sacrifice consenti sur le rendement de structure soit largement compensé par la simplicité de fabrication, la robustesse et le prix de revient.

REFERENCES. -

- 1 P.D.DUNN, Nature 195, p.65, 7 Juillet 1962
- 2 M.CLEMOT, C.BORDE, 1ère Conférence Internationale sur la Production Thermo-ionique de Puissance Electrique, Londres, 1965, Session 7b.
- 3 M.CLEMOT, J.P.DURAND, P.SEGURENS , 2ème Conférence Internationale sur la Production Thermoionique de Puissance Electrique, Stresa, 1968, Session E : Matériaux.

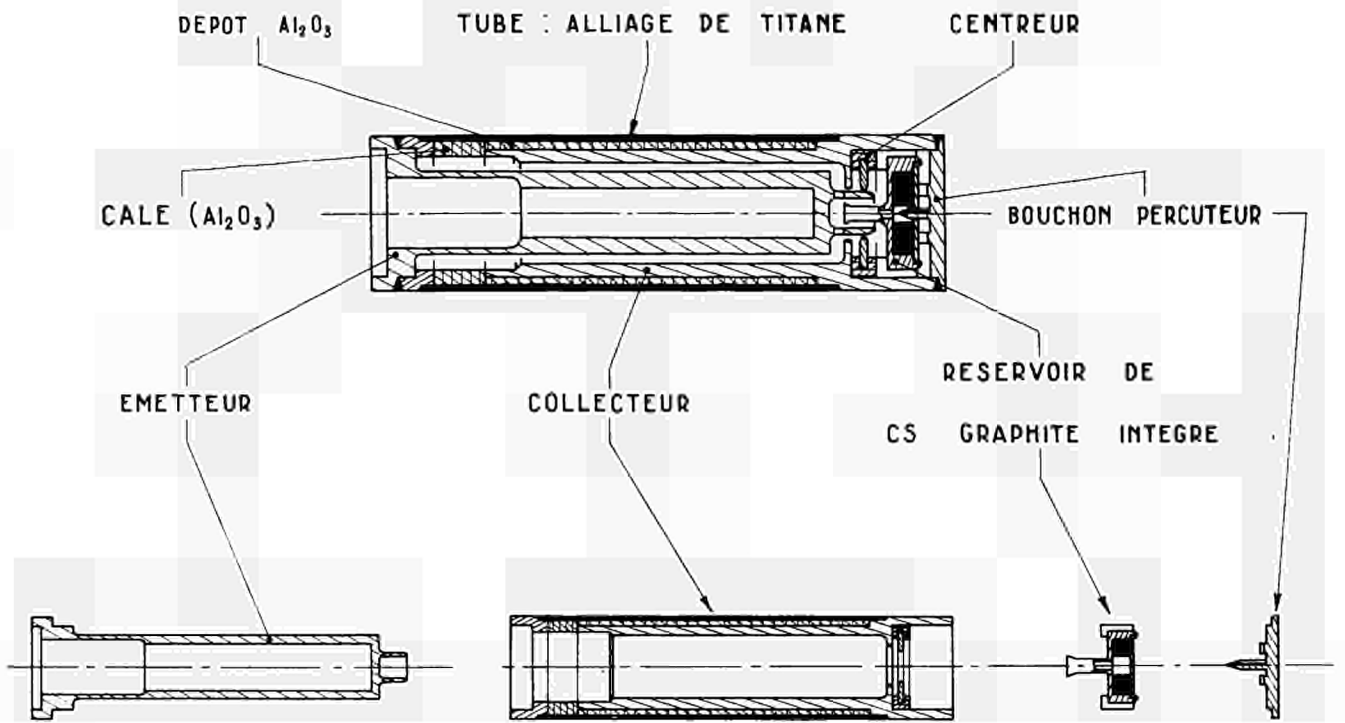


FIG. 1 MODULE THERMOIONIQUE TOUT METAL

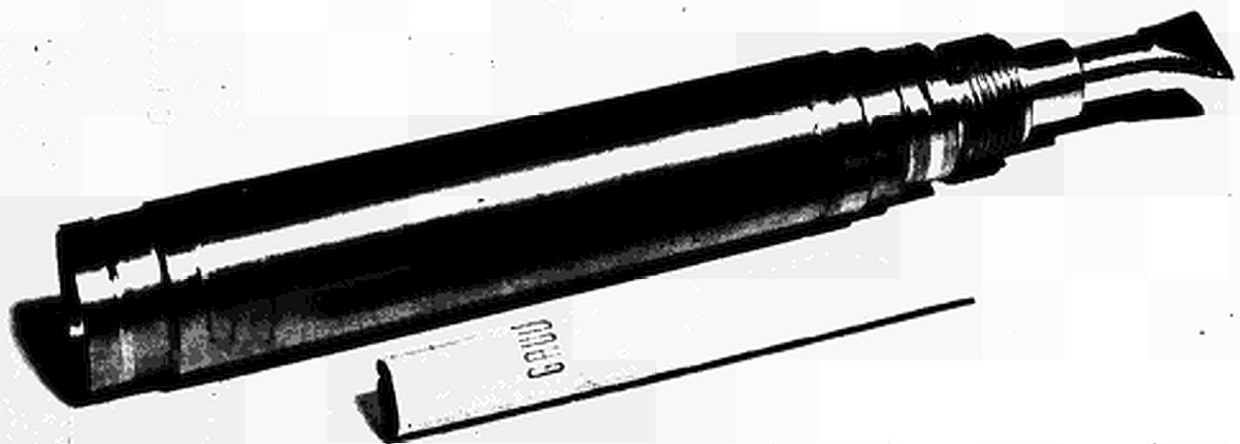


FIG. 3

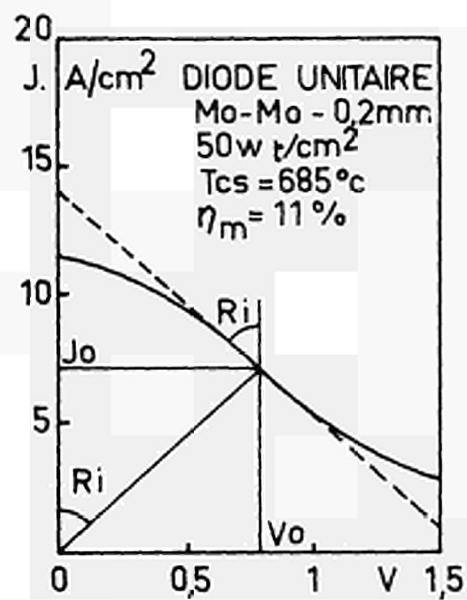


Fig.4 CARACTERISTIQUE DE REFERENCE

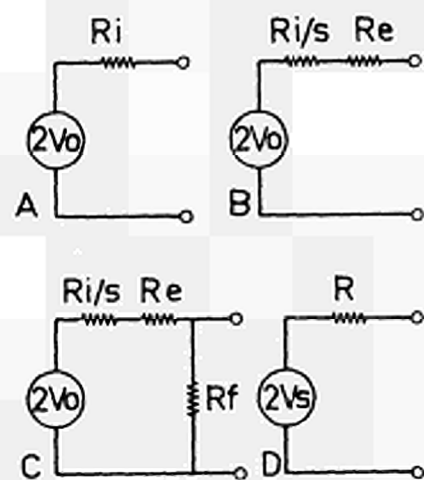


Fig.5 SCHEMA EQUIVALENT

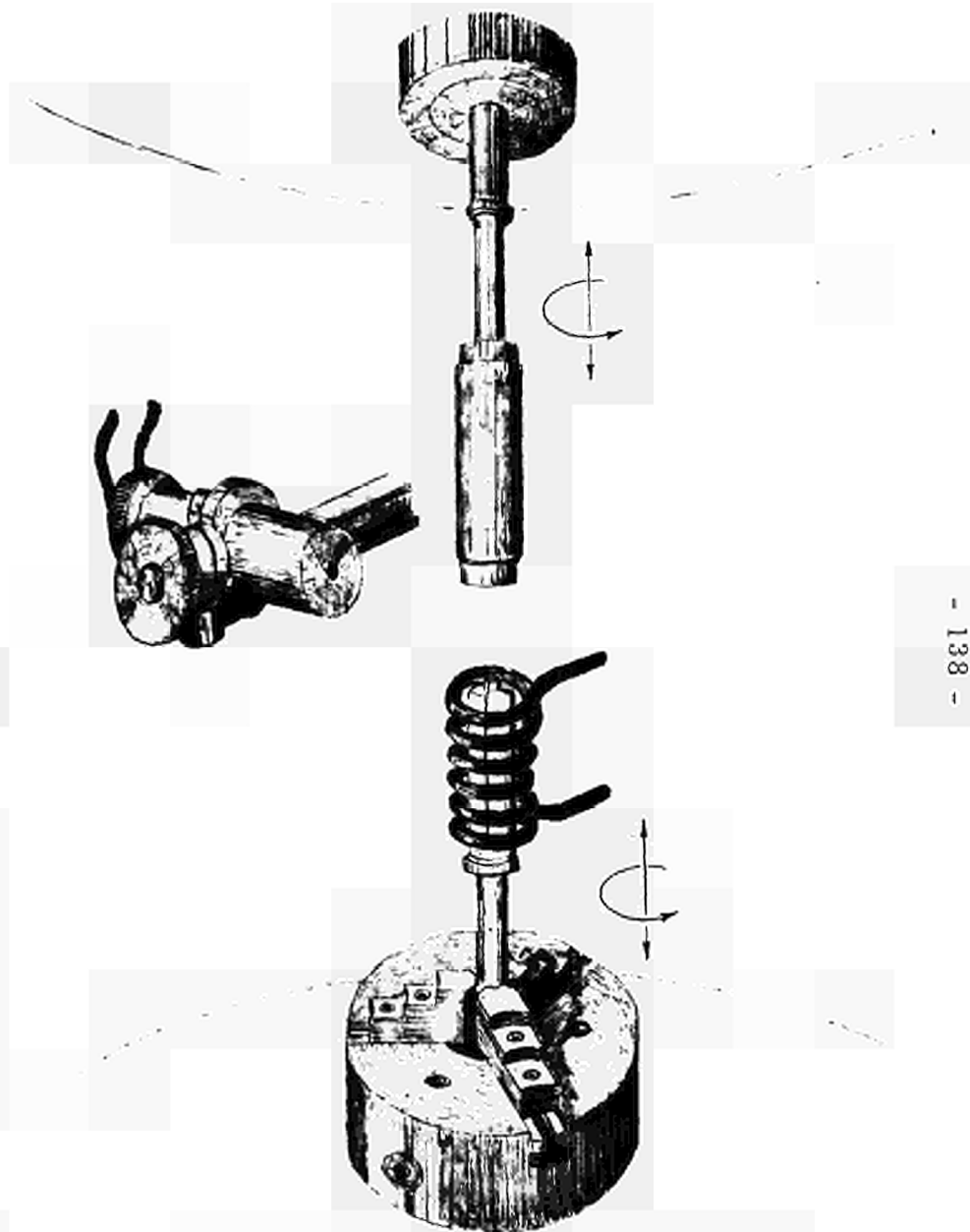


FIG.2 ASSEMBLAGE POMPAGE

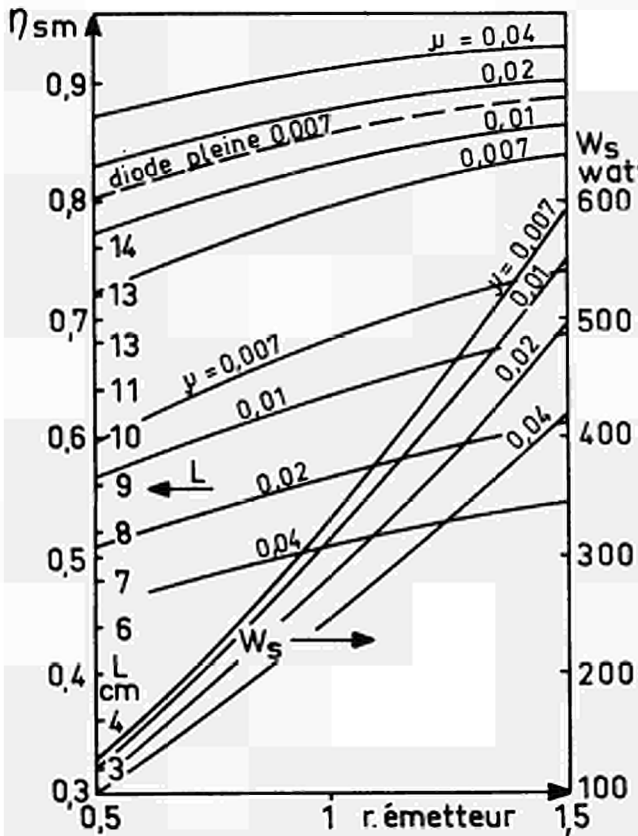


Fig. 6 CARACTERISTIQUE DES DIODES "TOUT METAL" OPTIMALES

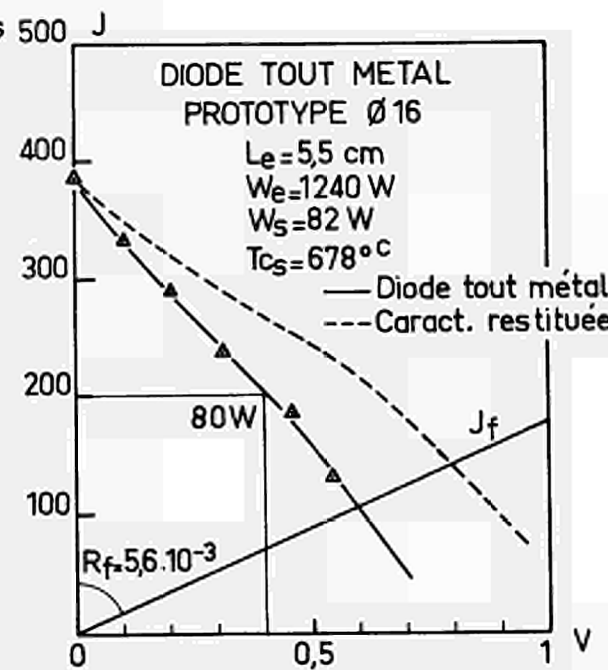


Fig. 8 : CARACTERISTIQUE I (V)

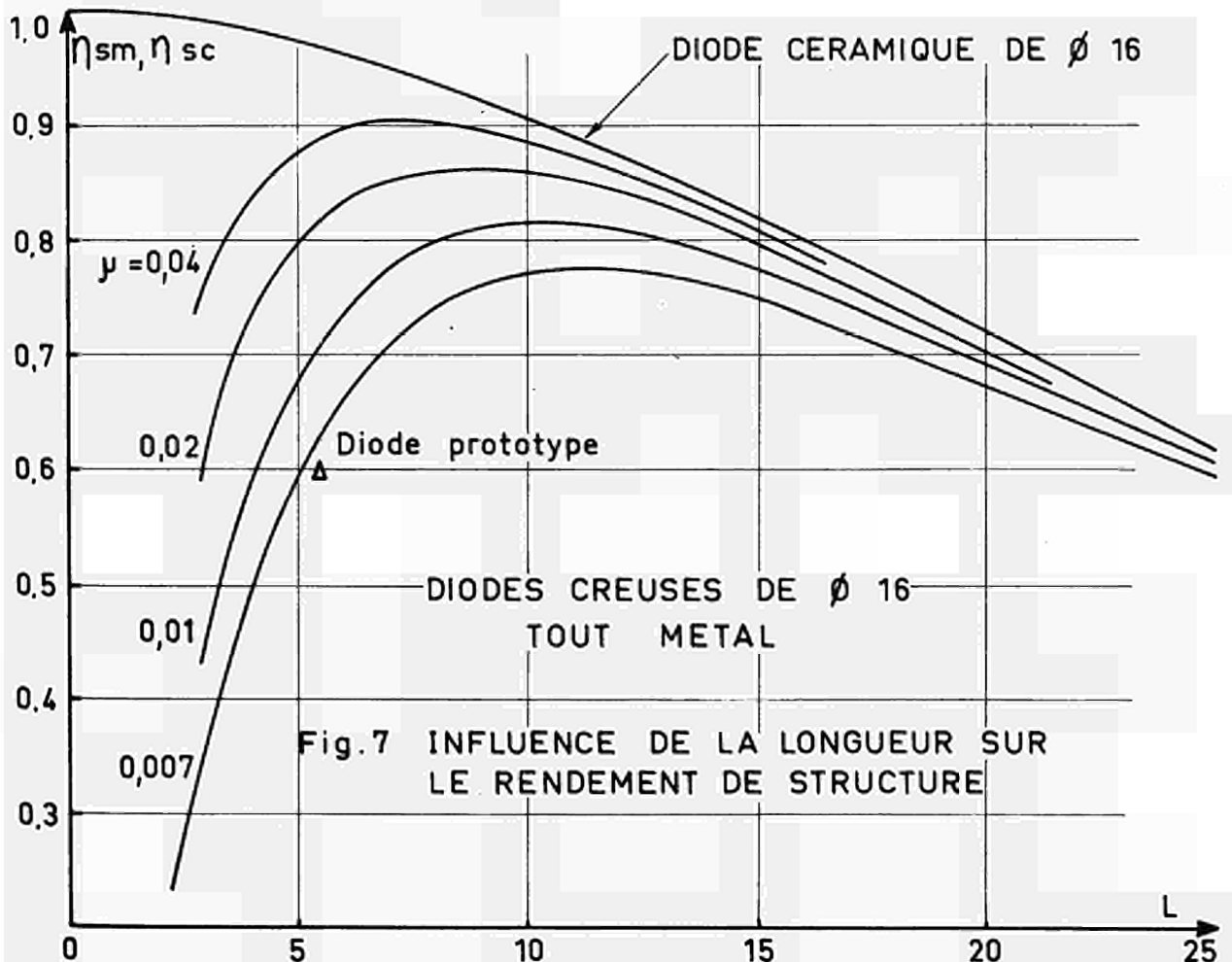


Fig. 7 INFLUENCE DE LA LONGUEUR SUR LE RENDEMENT DE STRUCTURE

DISCUSSION

Speaker of paper A-14: B. DEVIN

HOLLAND (USA):

What would the electrical resistivity and melting point of the titanium-aluminium alloy be?

DEVIN (France):

L'alliage de titane-aluminium utilisé a une résistivité de $195 \mu\text{Ohm-cm}$. Son point de fusion est légèrement inférieur à celui de titane; il n'a pas été mesuré je pense qu'il serait de 1600° à peu près. Il est possible d'utiliser d'alliages d'une résistivité plus élevée, $250-280 \mu\text{Ohm-cm}$, mais ces alliages sont extrêmement durs et cassant et il est pratiquement impossible pour le moment de les transformer en tubes minces. Les alliages que nous avons utilisé ont été transformés par filage à chaud sous gaine comme on fait les macaroni. C'est une opération assez délicate pour obtenir du premier coup une épaisseur voisine de l'épaisseur finale. Pour le moment les ébauches de tubes font une épaisseur comprise entre 1 mm et 1.5 mm; ils sont réduits à l'épaisseur de 0.3 mm par rectification. Toutes les opérations de soudure se font de bombardement électronique et il n'y a aucune brasure dans le convertisseur.

BUSSE (Euratom):

What was the thickness of the wall which you assumed in the calculations of the resistances?

DEVIN:

Nous avons pris pour les calculs de la courbe inférieure l'épaisseur que nous avons réalisé actuellement qui est de 0.3 mm. La courbe supérieure, la plus élevée, qui est dans la figure, suppose une épaisseur de 0.1 mm; et une résistivité de l'ordre de $200 \mu\text{Ohm-cm}$. Ça ne paraît pas hors d'atteinte.

BUSSE:

Do you think you can solve the problem of brittleness of the alloy?

DEVIN:

Il n'y a pas de problèmes de fragilité avec l'alliage qui donne la résistivité de $195 \mu\text{Ohm-cm}$. C'est un alliage commercial et utilisé dans la technique d'aviation.

BOHDANSKY (Euratom):

Do you know whether the alloy changes its resistivity due to radiation in the

reactor?

DEVIN:

Aucune expérience pour le moment. Je ne pense pas qu'il y ait beaucoup à craindre de ce côté là parce que il est dans un état de pureté extrêmement pauvre et la cristallisation de grains est tout-à-fait quelconque, c'est vraiment de tout venant. Et je ne pense pas que les radiations puissent beaucoup altérer la structure. Maintenant, d'autre part, le titane et l'aluminium même ont des sections de capture neutronique assez faibles et je ne vois pas de danger de ce côté là. Enfin, la couche d'allumine qui sépare le collecteur de molybdène de la paroi extérieure de titane, elle-même est sous forme quasipulvérulente puisqu'elle est déposée au chalumeau il n'y a pas de problèmes là non plus.

HOLLAND (USA):

How does the capital cost of an all metal converter compare with the cost of a converter made with an ordinary ceramic seal?

DEVIN:

Nous n'avons pas comparé le coût du convertisseur avec le convertisseur normal. La réduction de coût entendu pour ce type de convertisseur ne tient pas au fait qu'il soit entièrement métallique. La réduction de coût est liée au fait qu'il est assemblé entièrement sous vide, sans pompage par un queusot par exemple, et cette réduction de coût s'applique à mon avis aussi bien aux convertisseurs avec isolateurs de céramique assemblés par la même procédure.

PRUSCHECK (Germany):

By what means can titanium-aluminium be connected to other materials (by electron beam welding, arc welding, soldering)?

DEVIN:

Oui, par toutes les méthodes classiques pour relier ensemble deux métaux dont les points de fusion sont différents, mais je peux dire qu'en ce qui concerne des alliages titane-aluminium et de molybdène il est possible de procéder directement par électron-beam-welding avec certaines précautions sur les épaisseurs de paroi.

The Incore Thermionic Reactor as a Space Power Source

by

H. Andrae, D. Budnick, F. Groß, W. Jahns, K. Janner, A. Jester.
BROWN, BOVERI & CIE AG, Mannheim; INTERATOM, Bensberg;
SIEMENS AG, Erlangen.

1. Summary

The Incore Thermionic Reactor ITR is a UO_2 -fueled, sodium-cooled reactor incorporating 7, 19, 37 or more thermionic fuel elements arranged in a solid-hydride moderator, surrounded by homogeneous, fully enriched uranium-metallic-hydrided booster elements and a beryllium reflector. The electrical power output can easily be matched to the requirements within wide limits by varying the thermal reactor power and the number of thermionic fuel elements.

As a first step towards space application an earth bound prototype reactor has been designed which has 19 thermionic fuel elements. The electrical power output of each fuel element amounts to 1 - 2 kW and is generated by seven series-connected cylindrical high-pressure cesium-cells of 20 mm diameter and 54 mm length of the emitter. The electrical power density for a 20 kW unit is about 5 W/cm^2 . The present state of development is outlined.

2. Reactor and fuel rod design

During the last six years extensive studies and experiments in the field of thermionic energy conversion and advanced reactor development have been carried out in the Federal Republic of Germany, supported by the "Bundesministerium für wissenschaftliche Forschung". The aim of these efforts was the development of an Incore Thermionic Reactor suitable for installation in spacecraft. Recent work at BBC, INTERATOM and SIEMENS has been concentrated on a small metal-hydride-moderated power reactor using highly enriched uranium as fuel and liquid sodium as the coolant [1]. Fig. 1 shows a model of the reactor.

The core is 45 cm high and its diameter is about 35 cm. The interior is a metal-hydride moderator matrix containing 19 thermionic fuel rods arranged in a hexagonal lattice. This subcritical assembly is surrounded by a booster zone, which consists of closely packed fuel rods containing a homogeneous fuel-moderator mixture. They provide criticality of the reactor and contain very little structural material in order to keep the reactor as small as possible. The outside of the whole core is surrounded by a beryllium reflector fitted with adjustable segments to allow reactor control by variation of neutron leakage. The electrical power output level is 20 kW and is generated in the thermionic fuel rods, each of them containing seven series-connected cylindrical converter cells. The waste heat is conducted to the outside of each rod, transferred to the liquid sodium coolant flowing in a separate channel and then removed from the reactor. In the booster zone, the fuel rods are also cooled by sodium flowing through the gaps between the elements.

The following considerations have contributed to the selection of this type of reactor:

Extensive system studies have shown thermal and intermediate reactors to be highly suitable for electrical space power supply systems in the range up to several hundred kW [2]. Some reactors are already in the final development stage and have attained a high degree of reliability, as proven in the United States by the reactors of the SNAP-Series, one of which,

SNAP 10 A, has already been operating in space [3]. The use of metal-hydride as a moderator permits the construction of small reactors with a few kg of inserted fissionable material and is suitable for relatively high temperatures [4]. Sodium coolant allows high power densities at relatively low flow velocities and vapor pressures and thus limits mass for pumps and structural material [5]. Sodium has already been successfully used as a reactor coolant.

The arrangement here differs from conventional systems in that thermionic fuel rods are introduced [6], which are shown in Fig. 2. The emitter is a cylindrical body of molybdenum with a length of 54 mm and a diameter of 20 mm, containing 46 g UO_2 -fuel (93 % enriched) in 10 holes drilled into the wall.

In order to improve converter performance and to extend the lifetime, tungsten is deposited on the emitter surface [7]. The electrode spacing is 0.17 mm. The collector system (sandwich) consists of layers of 2.3 mm niobium, 0.2 mm ceramic insulation and 1 mm external Nb1Zr-cladding tube. The coolant gap is about 3.6 mm.

The cells of a fuel rod are electrically series connected. The support pin has separate passages for cesium-vapor (dotted line) and gaseous fission products, which are removed from the rod by holes in the collectors (dashed line). A metal ceramic seal between adjacent cells keeps the cesium and fission gas separated. The emitter is centered in the collector by the support pin at one end and a ceramic ring at the other end, in which a centering Mo-membrane can slide freely. This design leads to relatively large distances of about 16 mm between the fuel-pins of adjacent cells; while this is a disadvantage from the reactivity point of view, it provides a very rigid construction. A central hole of 5 mm diameter permits electrical heating of the emitter for the testing of each cell before assembly. Further development in fuel and technology may lead to less complicate designs when more information about long-

time behaviour is available from inpile reactor tests.

The preliminary operating data are:

- 1800°K emitter temperature
- 5 Watts/cm² electrical power density and
- 10 % conversion efficiency [8]

In laboratory and inpile tests much higher power densities have been obtained. Fig. 3 shows an experimental arrangement that is suitable for both nuclear and electrical heating. Detailed information is given in a paper to be presented at this conference [9].

Several inpile tests [9,10,11], which were performed from 1966 to 1968, yielded electrical power outputs between 7,5 and 9 Watts/cm² at emitter temperatures of 1900° and 2000°K respectively. These data are intended only for orientation; short duration tests gave much higher values. Altogether, several generations of converter cells have been built and tested and a wealth of experience is available on converter technology.

3. Optimization studies

The relationship between thermal and electrical power for the case of the reactor with 19 thermionic fuel rods, taking into account electrical and thermal losses in the series-connection-bridges, is shown in Fig. 4. These data are calculated from current-voltage characteristics measured by Lawrence and Wilson [12] on tungsten niobium converters with 0.17 mm spacing between the electrodes. The cesium-pressure was optimized with respect to maximum power density. With increasing current density at constant temperature the electrical power output reaches a maximum value at the chain-dotted line.

While 12 kW of electrical power is available at 1673°K it is possible to obtain 60 kWatts with the same arrangement at 2150°K. Maximum efficiency gives lower values. The designed power of 20 kW is well down in the low power region and can be enhanced considerably.

In Fig. 5 the specific mass of a space power system of this kind is plotted versus the electrical power. For low emitter temperatures the region of small specific mass is very narrow, whereas for high temperatures there is a broad minimum. It can be seen that operation at maximum power (chain-dotted line) is not favourable; the specific mass is about 5 kg/kW higher due to higher electrical losses in bridges and electrodes. For the reactor and shadow-shield, a total mass of 680 kg was assumed. The thermal power in the booster zone, which is four times higher than in the thermionic zone, has been regarded as waste heat which is radiated into space with an effort of half a kg per thermal kW power. At a power level of 20 kW_{e1} a specific mass of 60 kg/kW_{e1} can be expected.

These data are estimated values, since not much is known at present about the components of the flight-system. However, the data show the tendency and characterize the range of the development program.

Another method of increasing the power level is to introduce a larger number of fuel rods which can operate at lower temperatures, thus avoiding the material problems. Fig. 6 shows the specific mass of space power systems over the electrical power when reactors with 19, 37, or 61 thermionic fuel rods are used. The specific mass decreases from 100 kg/kW at 10 kW through 60 kg/kW at 20 kW to less than 40 kg/kW at 40 kW. At this power level the 19 TI-rod reactor operates with an emitter temperature of 2000°K, whereas a 37 TI-rod reactor only needs the original design temperatures of 1800°K.

The specific masses of the two systems are not very different at this point, because the ratio of thermal power in the booster zone to thermal power in the thermionic core decreases with an increasing number of thermionic fuel elements. Hence a larger reactor and shield mass is partially compensated by a smaller radiator mass. This is quite advantageous, since it offers two ways of attaining a desired power level, at the same time allowing account to be taken of the latest state of development in the design of thermionic cells.

In all cases thermionic fuel rods consist of identical cells with constant fuel concentration, which are interchangeable and can be inserted into any position of the inner core. To obtain nearly optimum operating conditions for all cells, the power density can be flattened by variation of the moderator density and adjustment of the axial reflector. In the radial direction suitable coupling to the booster zone is used to reach a macroscopic maximum-to-minimum power ratio of about 1.1.

4. Development Program

In the design of the reactor emphasis was laid on practicability and functional reliability. An optimum specific mass must not be achieved at the expense of introducing difficult material problems. Under consideration at present are zirconium or yttrium hydride as a moderator, designs with one common or two separate coolant loops and two versions of the reflector control system. A decision will be made within the next few months.

The first two steps in the ITR-Project are the development and assembly of a terrestrial prototype reactor. The reactor will be installed into a spherical pressure vessel of approx. 3 m diameter which can be evacuated. Its thermal power will be approximately 1 MW, the coolant inlet temperature is 500° C, and the outlet temperature 650° C. The location has not yet been fixed, but the test plant will be built in the grounds of a nuclear research centre in Germany and has to be suitable for several years' continuous operation. Approximately five years will be necessary for development and construction of this plant.

Besides the development groups of BBC, INTERATOM and SIEMENS in the recent years several German research groups at universities and nuclear research centres have worked in this field, chiefly on fundamental problems. The thermionic group of EURATOM at Ispra has also contributed to thermionics and related areas. Now the size of the outlined project presents an opportunity to set a common goal to all laboratories.

References:

- [1] BBC, INTERATOM, SIEMENS.
"ITR, Incore-Thermionik-Reaktor zur Energieversorgung von Raumflugkörpern".
Kolloquium über Thermionische Energiewandlung im
BMwF, Bad Godesberg 23.6.1967.
- [2] Pruschek, R., Dagbjartson, S., Emendörfer, D.,
Groll, M., Haug, W., Röhrborn, B., Unger, H., Wolf, E.
"Ergebnisse von Studien über Thermionikreaktor-Systeme"
DGLR-Symposium "Energieversorgung im Weltraum" München,
14.3.1968, Paper No. 68-007
- [3] Wilson, R.F., Dieckamp, H.M.
"What happened to SNAP 10 A?"
Astronautics and Aeronautics 3 (1965), No.10, pp. 60 to 65
- [4] Einfeld, H.
"Über den Projektvorschlag für ein nukleares Energie-
versorgungssystem für Raumfahrtanwendungen".
DGRR/WGLR-Jahrestagung, Bad Godesberg, Okt. 1966,
Vortrag Nr. 66-095
- [5] INTERATOM
"Fortsetzung der Studie über die Entwicklung optimaler
Reaktorsysteme zur Energieversorgung von Raumflugkörpern".
Jahresbericht 1964/1965, INTERATOM, INTAT-34.
- [6] Budnick, D., Janner, K., Jung, W., Oldekop, W., Peehs, M.
"Thermionische Kernreaktor-Energieversorgungsanlagen für
einen Leistungsbereich von 5 - 50 kWe".
DGRR-Fachbuchreihe, Bd. "Fortschritte in der Raumfahrt-
forschung" (1966) pp. 235 to 248
- [7] Gregorius, K., Janner, K., Peehs, M.
"Physikalische Untersuchungen an speziellen Thermionik-
Anordnungen"
Jahresbericht 1967 SIEMENS AG, BMwF-RV 1 - 624/13/66
- [8] Budnick, D., Janner, K.
"Projektierung des Thermionikeinsatzes, Optimierung
und Integration in das Gesamtsystem".
Jahresbericht 1966/67 SIEMENS AG, BMwF-RV 1-624/12/66.

- [9] Jester, A., Gross, F., Holick, H., Krapf, R.
"Inpile and out-of-pile tests of cylindrical thermionic converters".
2nd. Int.Conf. on Thermionic Electr.Power Generation,
Stresa, May 1968
- [10] Batzies, P., Demny, J., Gammel, G., Gross, F.,
Heidtmann, U., Holick, H., Jester, A., Krapf, R.,
Langpape, R., Minor, A., Schmid, H.E., Winkenbach, H.,
Zöller, R.
"Entwicklung eines neuartigen Reaktor-brennstoffelements"
Schlußbericht 1967, BROWN, BOVERI u. CIE., BMwF-At T 88.
- [11] Jester, A., Gross, F., Holick, H., Krapf, R., Busse, C.A.
"Bestrahlungsversuch an einem nuklear beheizten
thermionischen Energiewandler".
BBC-Nachrichten 49 (1967), pp. 492 to 497
- [12] Lawrence, J., Wilson, V.C.
"A comparison of niobium and nickel as thermionic
converter collector materials".
Thermionic Conversion Specialist Conference, Houston,
Texas 3.11.1966. IEEE-Conf. 15 C 41, pp. 6 to 11

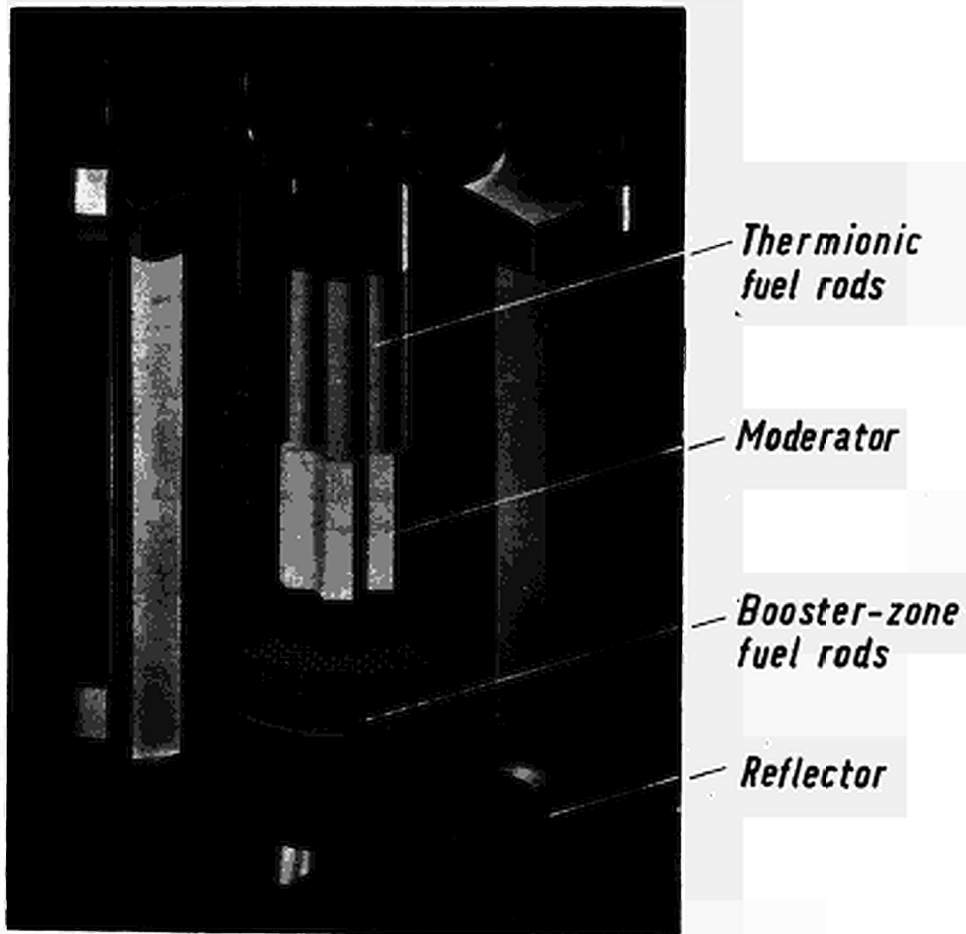


Fig.1 Incore Thermionic Reactor ITR

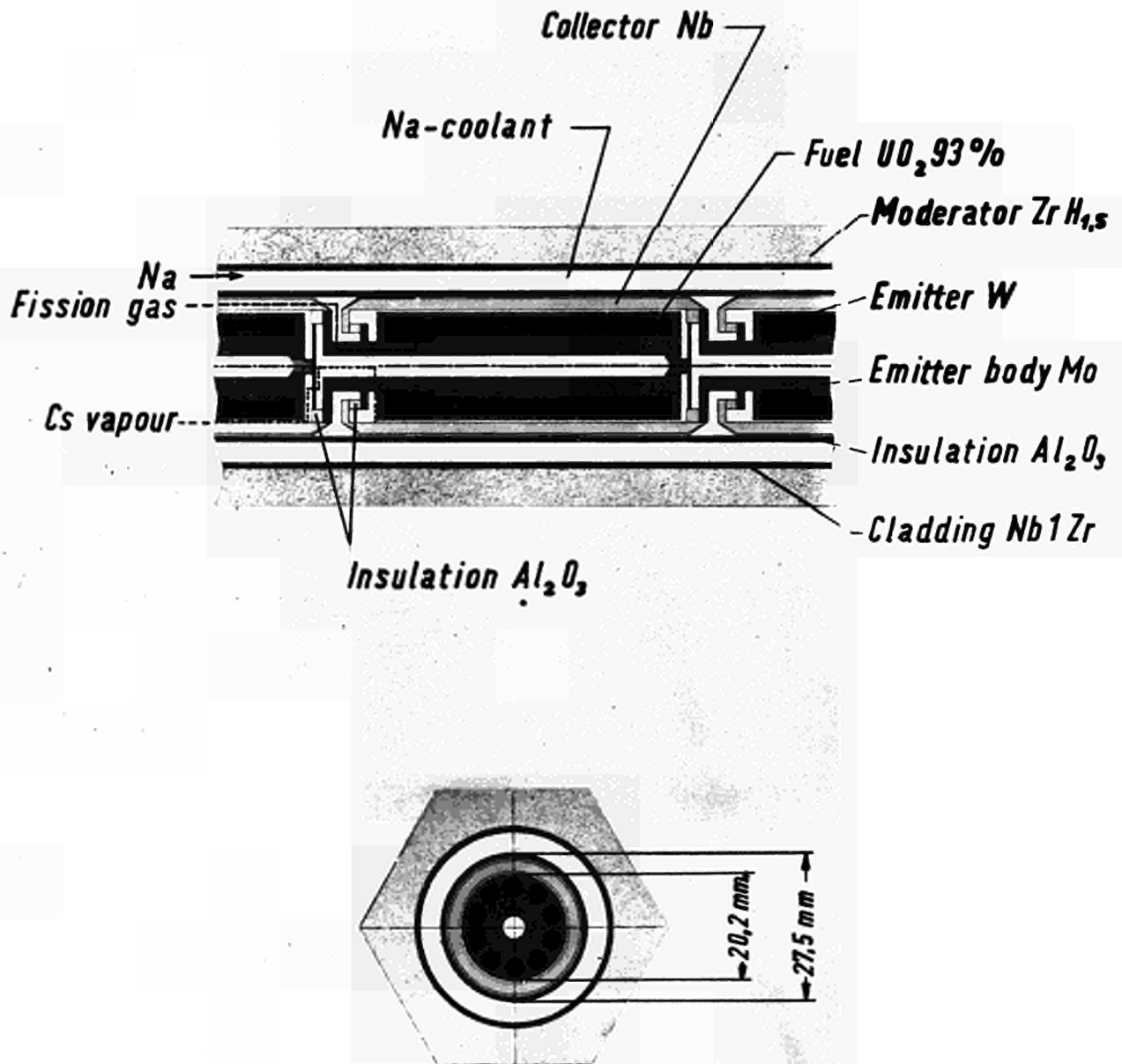


Fig. 2 Series-connected thermionic in-pile converter (schematic)

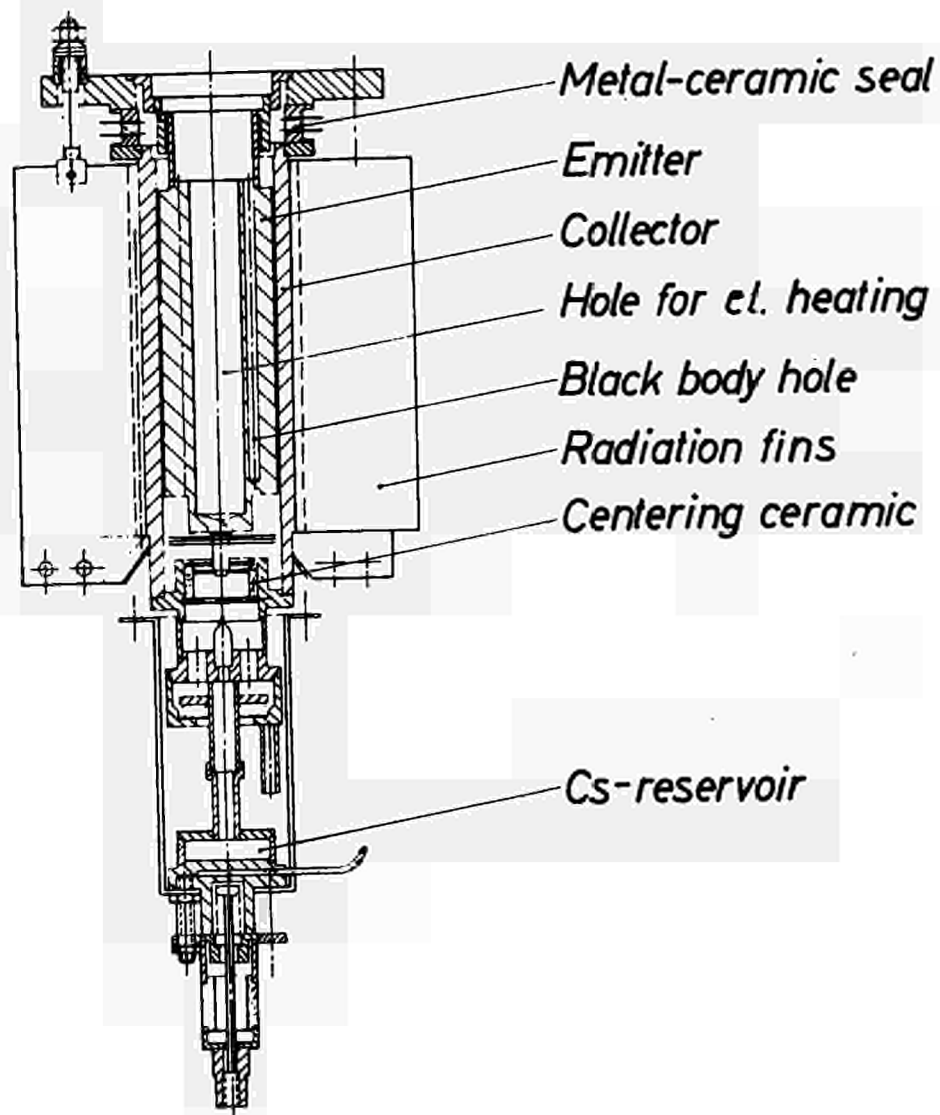


Fig.3 Experimental thermionic converter

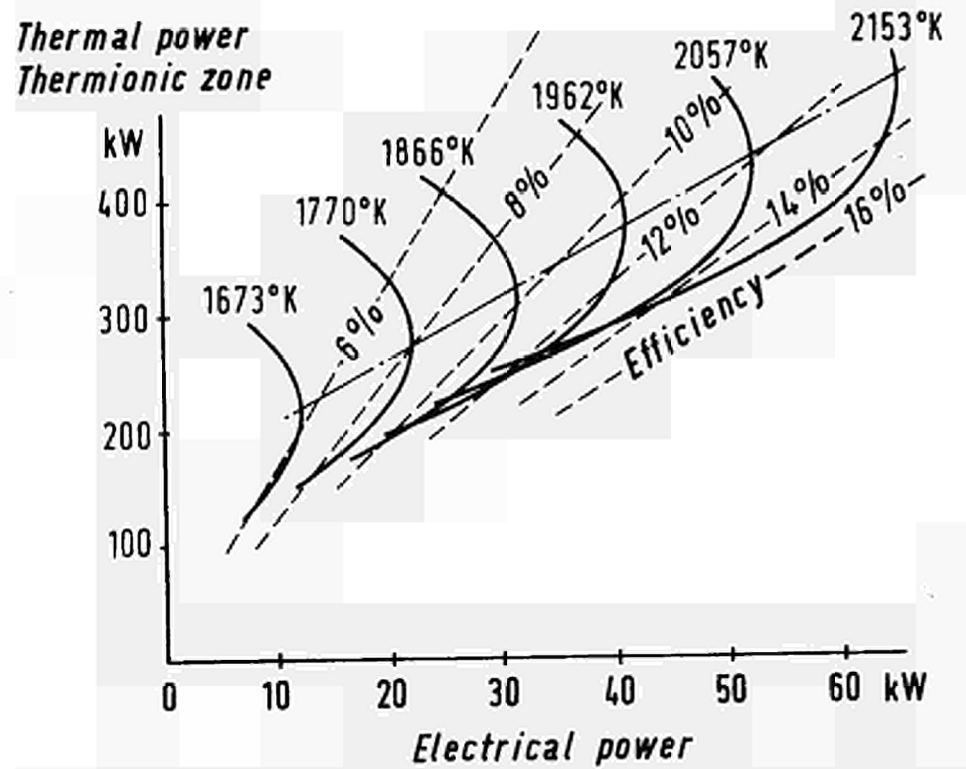


Fig. 4 19 Thermionic fuel rods, thermal and electrical power

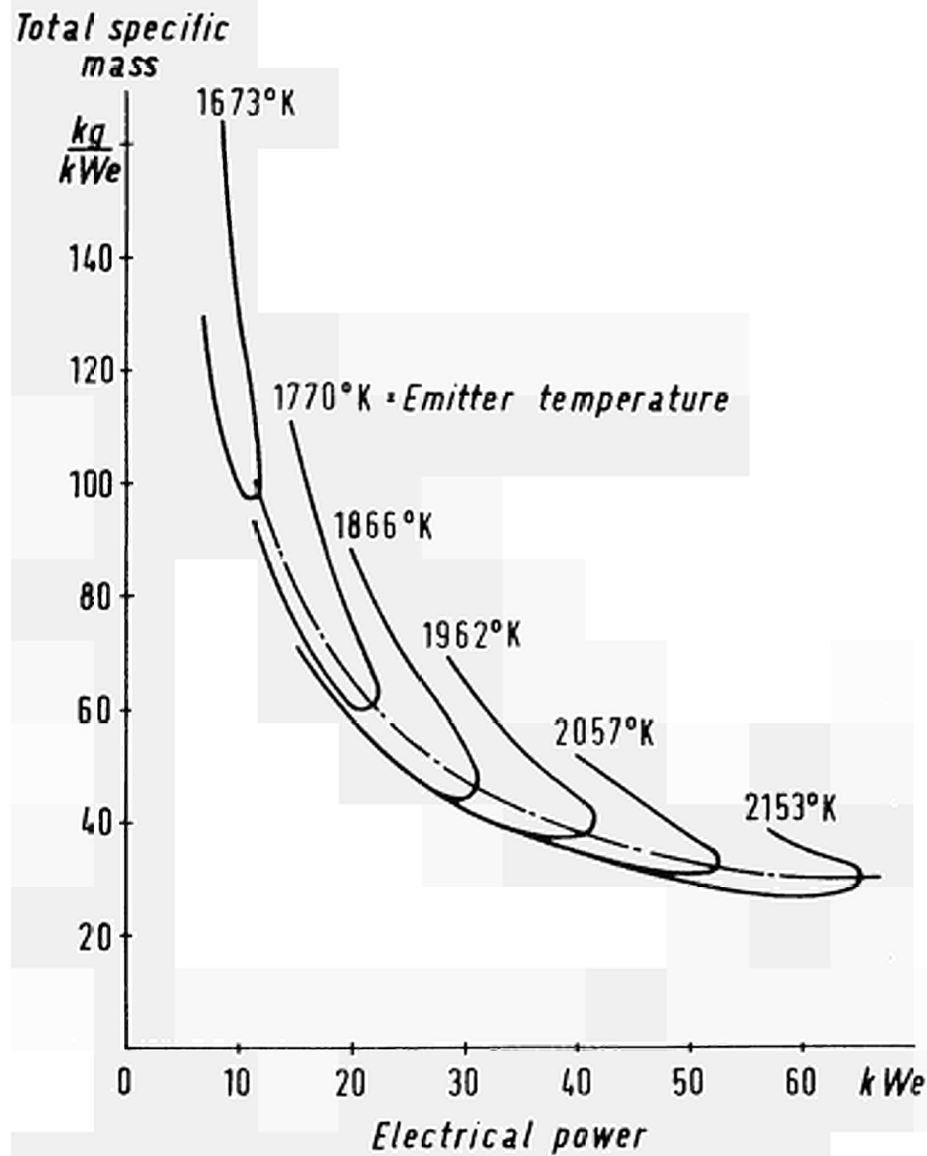


Fig. 5 Specific mass of the space power system
 Reactor: Zirconium-hydride moderated + 19 TI rods
 Shield: Lithium-hydride
 Radiator: Beryllium

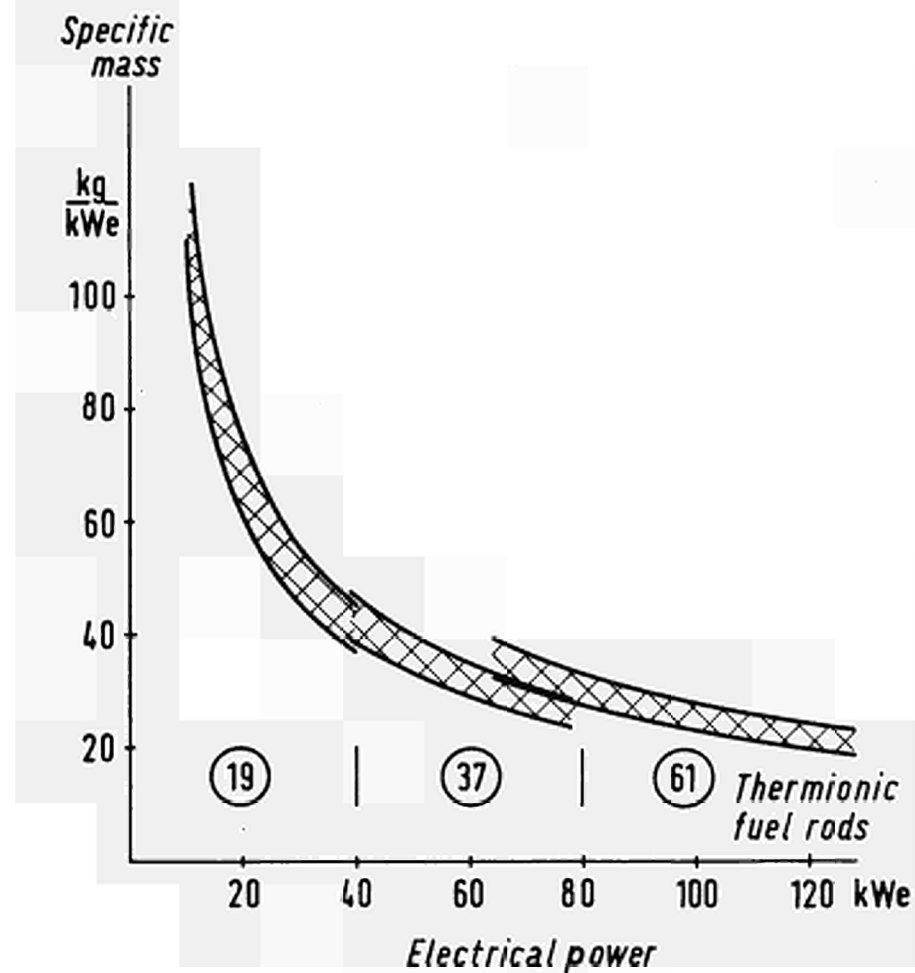


Fig. 6 Specific mass of space power systems,
 ITR with 19, 37 and 61 thermionic fuel rods

DISCUSSION

Speaker of paper B-1: D. BUDNICK

SCHOCK (USA):

I am interested in the seals which you have between each consecutive diode. What are the dimensions of the seals, how are they fabricated and how much experience have you had with them?

BUDNICK (Germany):

Mr. JESTER will be so kind to answer your question concerning the seals of the converter cells.

JESTER (Germany):

Until now we have used alumina seals brazed to niobium sheets. In the design we first looked for thermal shock resistance. The sheets which are brazed to the alumina are made very thin so they can match the differences in the thermal expansion. On the other hand we are looking for a design in which the seals between the cesium vapor space and fission gas room must not be vacuum tight. This is possible when sufficient gas products are vented from the fuel of the emitter through a separate channel.

RESULTS OF STUDIES ON VARIOUS FAST AND THERMAL THERMIONIC REACTOR SYSTEMS

R. Pruschek, S. Dagbjartsson, D. Emendörfer, M. Groll, W. Haug,
B. Röhrborn, H. Unger, E. Wolf

Institut für Kernenergetik, Universität Stuttgart (Germany)

Abstract

The results of various studies on five different thermionic reactor systems are reported. Information is given on characteristic data of these devices as the amount of fissile material, power output, specific power, mass of components, total mass etc. Problems of power flattening, long time behaviour, integration of converters to the nuclear heat source as well as specific design features of the following types of thermionic reactors are discussed:

1) moderated incore thermionic reactor (TRIKT), 2) moderated double diode thermionic reactor (DD-TR), 3) fast incore thermionic reactor (SRIKT), 4) fast out-of-core thermionic reactor, emitter heated by heat pipes (WR-TR), 5) fast out-of-core thermionic reactor, emitter heated by thermal radiation (SRAKT-WR). Among the concepts considered the moderated incore thermionic reactor system (TRIKT) is the most attractive within a few ten to a few hundreds of kW_{el} . In the lower power range the "Teilthermionikreaktor" (ITR) seems reasonable.

1. INTRODUCTION

Studies on five thermionic reactor systems as power supply for space crafts are carried out to get information on the preferable reactor design, the components, shadow shield, and radiator layout as well as on the required material properties and converter performance. The problems are discussed best on the basis of design studies where physical and technical aspects are comprised. Moreover, clues on the specific power of such systems are obtained this way. Two of the thermionic reactor systems taken into consideration are based on moderated reactors while the other three are fast reactors. The five systems can also be subdivided into three incore types (TRIKT, DD-TR, SRIKT) and two out-of-core types (WR-TR, SRAKT-WR). Data on converter performance are employed according to experimental results from out-of-pile converter tests and according to some reports on in-pile experiments. The prediction of the performance of converters connected in a series-parallel-network is based upon converter models as described in literature. Specific design data of the five systems based on 93 % enriched uranium are presented in tables 1 to 5.

2. MODERATED INCORE THERMIONIC REACTOR (TRIKT)

The emitters are in contact with the nuclear fuel. The waste heat from the collectors is removed by means of a liquid metal coolant which is recirculated via a finned tube radiator by an EM-conduction pump. The reactor is suitable for the power range from about 50 kW_{el} to a few hundred kW_{el} [1,2,3]. As for the application in the lower power range down to about 20 kW_{el} the design has to be modified. Some of the outer thermionic fuel elements are replaced by ordinary fuel rods. The thermionic fuel element zone in the center of the core is subcritical for itself and is driven like an exponential pile by neutrons from the surrounding zone. The heat generated in the surrounding zone is removed without use for electrical

This work was supported by the Bundesministerium für wissenschaftliche Forschung of the Federal Republic of Germany.

power generation (Teilthermionikreaktor ITR [4]). The execution of such a system was recently approved by the government.

Reactor

Two different types of fuel are considered. One type consists of a molybdenum- UO_2 matrix. The uranium oxide is filled into several holes of the cylindrical molybdenum emitter body which is surrounded by vapor plated tungsten. From inpile tests with UO_2 -Mo-fueled emitters it can be concluded that the required life time of TRIKT-converters will be obtained [5]. The other type is based on zirconium stabilized uranium carbide fuel which is surrounded by tungsten plated molybdenum. The data given in tables 1 to 5 refer to this type of fuel. The moderator is assembled of zirconium hydride prisms of hexagonal cross section. The thermionic fuel rod is arranged within the central hole of the moderator prism. The hydrogen diffusion and the associated leakage during operation has to be reduced by diffusion barriers (e.g. Al_2O_3). The core is surrounded by a beryllium reflector (Fig.1). The radial reflector consists of a rigid part and six angular rotatable semi-cylindrical beryllium drums operated by stepper motors. Power density flattening within the core [6] is achieved by variation of lattice pitch ratio in the radial direction and variation of the hydrogen concentration in the axial direction. Reflector thickness and cell dimensions are optimized with respect to maximum specific power.

Thermal group cell calculations are accomplished by means of multiple collision theory within the fuel region and diffusion theory in the converter and moderator zone according to Amouyal-Benoist [7]. In some cases multigroup first collision theory with 27 energy groups is applied. Spectra are calculated using one-dimensional diffusion theory with 49 energy groups [8]. Critical reactor dimensions are obtained from two-dimensional two-group diffusion theory.

Thermionics and Energy Transport

There are eight cylindrical converter cells per fuel rod connected in series. These may be connected to a series-parallel-network out of the core. The feasibility of such a network with cross connection resistors within the core is investigated in detail at present. The calculated net power output of the system amounts to 50 kW_{e1} .

Measured I-V-characteristics of converters with W/Ni-electrodes as reported by Lawrence and Wilson [9] are extrapolated to our converter dimensions by means of a converter model from Rasor [10]. The operation point given in table 2 corresponds to maximum efficiency of the thermionic fuel rods at optimum reservoir temperature (615 K) and optimized connection leads.

Advantages of the System

- Low fuel inventory (approx. 10 kg U 235) is required for criticality or the excess reactivity, respectively. Specific costs per kW installed in the orbit are therefore low compared to fast reactor systems for power units below approx. 100 kW_{e1} .
- The damage flux is not a limiting design factor.
- The emitters are attached to the heat source directly which is favourable from thermodynamic reasons.

Disadvantages of the System

- The converters may fail by diffusion of fuel and fission products through the emitters, due to swelling of fuel resulting in short circuiting (however, inpile experiments with UO_2 -Mo-fueled emitters of the BBC-design have shown that these problems may be solved satisfactorily).
- The burnup related to the total number of metal atoms within the fuel after 400 d is approx. 1 %. Nevertheless, the reactivity loss of a TRIKT-system is rather high (5 % caused by burnup and fission product poisoning plus some additional percentage caused by hydrogen loss. Therefore, burnable poison or high control reactivity is required at the time of startup.

Comparison of Phoenix Fuel and U 235 with Respect to the Longtime Behaviour

To get a smaller reactivity loss during burnup the use of phoenix fuel (PuO_2) was taken into consideration. The calculations are based on a converter geometry similar to the BBC cell design [5]. Three different compositions of Pu-isotope-mixtures obtained by reprocessing of fuel elements of boiling water reactors were considered for the computations. For the burnup calculation the assumed reactor operation time of 400 d at full power was divided into four time intervalls. The time dependent neutron flux was calculated at each time intervall by transport theoretical methods.

The phoenix effect (formation of Pu^{241}) depends on the concentration of the neutron absorber Pu^{240} within the isotope mixture. The greater the initial portion of the isotope Pu^{240} the greater the formation of Pu^{241} can be expected. However, the effective absorption cross section of Pu^{240} decreases with increasing Pu^{240} concentration due to the self shielding effect.

For discussion of the burnup behaviour of phoenix fuel two further facts are of importance which diminish the expected benefit:

- a) It is rather difficult to maintain the reactivity constant during operation by means of the Pu^{240} -concentration. Because of the high initial Pu^{239} concentration in the fuel additional Pu^{240} is built up which impairs the time dependent reactivity characteristics.
- b) The effective absorption cross section of the fission products from Pu -fissions is greater than the absorption cross section of the U^{235} fission products. The calculations carried out so far have shown the existence of the phoenix effect. However, it is too small to be attractive for use in moderated thermionic reactors. At the same total number of fissile atoms and at the same concentration even greater reactivity loss is caused by burnup and fission product poisoning if U^{235} is replaced by phoenix fuel. This is true for $N_H/N_U = 20$ and $N_H/N_{Pu} = 20$, respectively. For higher hydrogen concentrations two of the three phoenix fuels in consideration yield smaller reactivity losses than U^{235} . Calculations for $N_H/N_U > 60$ have not been carried out. If there should be an advantage in the reactivity behaviour compared to U^{235} , the weight increase might overcome the gain in reactivity performance.

Table: Reactivity loss $\Delta k/k$ of the reactor cell by burnup and fission product poisoning. Time of operation at full power 400 d; no fission product release; heat flux density 60 W/cm^2 at the emitter; $N_H/N_U = N_H/N_{Pu} = \alpha$ (N = number of atoms in the core).

Isotope-mixture (%)	U 235 (100)	Pu 239 (95) Pu 240 (4,7) Pu 241 (0,3) Pu 242 (0)	Pu 239 (74) Pu 240 (19) Pu 241 (6,2) Pu 242 (0,8)	Pu 239 (50) Pu 240 (32) Pu 241 (13,5) Pu 242 (4,5)
fuel 95 % theor. density	UO ₂	PuO ₂	PuO ₂	PuO ₂
$\Delta k/k$ % for $\alpha = 20$	-1,94	-1,99	-2,07	-2,46
$\Delta k/k$ % for $\alpha = 60$	-2,35	-1,80	-2,01	-2,46

3. MODERATED DOUBLE DIODE THERMIONIC REACTOR (DD-TR)

The double diode reactor concept was proposed by the Brown Boveri Cie. Its power range amounts from 5 to 50 kW_{e1}. This thermal incore thermionic reactor is composed of fuel rods which are assembled of two diodes each (Fig.2). The fuel is used to contribute to the electric conduction, whereas the coolant cannot be utilized to enlarge collector conductivity; otherwise a current leakage would occur between converter electrodes and EM-conduction pump. The data given in tables 1 to 5 refer to a criticality limited reactor. By increasing the moderator-to-uranium ratio the emitter area of the critical reactor can be reduced.

Reactor

The core is assembled of 84 cylindrical hollow thermionic fuel rods (double diodes). Mo-UO₂-cermet is used as fuel. The hydrogen concentration is only 85 % of the values of ZrH_{1,7}. If power density flattening should be necessary, the H-concentration could be raised to its maximum value in the outer region of the core. The core is surrounded by a beryllium reflector. Both top reflectors, however, are of little effectiveness due to the multiple feed through required for tubes and leads. The reflector shell consists of a rigid part and six angular rotatable semicylindrical beryllium drums for control purpose. The reflector thickness is optimized with respect to maximum specific power. Core cell dimensions and maximum obtainable concentration of fissile material are considered as given quantities. The N_H/N_U-ratio is adjusted to criticality requirements for a power output of 20 kW_{e1}.

Thermionics and Energy Transport

Molybdenum is used as emitter material and Nb-1Zr as collector. The two diodes of each fuel rod are connected parallel electrically. The long diodes give rise to high currents. The converters are therefore operated in the unignited mode. The thermal and electrical data are based on a mean converter power density of 1,2 W/cm² and a total efficiency of 5 %. A series-parallel-network is feasible out of core. The 84 fuel rods are divided into four groups of 10 rods each and four groups of 11 rods each. The coolant of each subassembly is circulated by one thermoelectric pump [11]. The redundancy could be increased by using collector heat pipes for each double diode. The power output of this system can only be increased by multiplying the number of double diodes. Therefore, the shape of the reactor would become a flat disc at high power which is unfavourable from neutron economy as well as from shielding requirements. However, the system power could be

increased by using two reactors of this type joined together at that top side which is free from coolant headers, taking criticality considerations into account. For that reason the coolant of each double diode is conducted in counterflow through two coaxial coolant channels (Figs.2 and 3) which results in an additional pressure loss caused by the reversal of the flow around 180 degrees (Fig.3). Furthermore, the core structure is loosened up. It was necessary to insulate the two flow channels by a gap. Thus heat is exchanged by radiation only. By that means the temperature at the reversal point is raised only by 1 K above the outlet temperature.

Advantages of the System

- Each converter is a vacuum tight self-contained system. A leak in one converter does not effect the operation of the remainder.
- Each converter fuel element is vented for fission product release. The cavity can be used for testing each converter before reactor startup (Fig.3). For this purpose an electron bombardment heater can be inserted into the cavity.

Disadvantages of the System

- There are similar material problems as involved with the TRIKT-system.
- At higher power (level from about 20 kW_{e1}) the application of thermoelectric pumps is no longer favourable since they need large volume. Furthermore, the height-to-diameter ratio decreases with increasing power which results in flat and, therefore, heavy thermionic reactors.
- Moderate converter performance due to the large emitter area required by the reactor design.

4. FAST INCORE THERMIONIC REACTOR (SRIKT)

In comparison to the moderated TRIKT-system the fast reactor has - at the same power level - only 2/3 of the TRIKT mass although the quantity of fissile material is several times that of TRIKT.

Reactor

The core consists of 37 thermionic fuel elements with UC as fuel [12]. It is surrounded by a beryllium reflector. The reflector is divided into an inner fixed and an outer movable part which consists of two shells sliding in axial direction (Fig.4). These reflector shells of 10 mm thickness have a reactivity worth of approx. 4 %. Each of them is infinitely variable driven by a servomotor. Power flattening in the core can be achieved to a good degree by adjustment of the reflector thickness.

The dimensions of SRIKT given in tables 1 to 5 are based on parametric studies with variation of the reflector thickness, fuel element thickness and height-to-diameter ratio. Criticality, axial and radial flux distribution have been calculated by means of multigroup diffusion theory [8] using the 26-group cross section set of Bondarenko et al. [13].

Thermionics and Energy Transport

The described design study is based on the performance characteristic of a Cs-Ba-converter although there is no experience on longtime-behaviour. Each of the converter cells is operated at the point of maximum power of the I-V-curve at optimum Cs-pressure. By choice of different emitter lengths the condition of constant current can be satisfied although the heat input to the converters connected in series varies. For calculation of the

electrical output data the results of experiments with a Cs-Ba-converter carried out by Psarouthakis have been used [14]. The emitter temperature of the converter cell operated at maximum heat input is limited to 2070 K by design. At this temperature, the heat flux to the emitter amounts to 69 Watts/cm². With the fuel element arrangement chosen in this design, an efficiency of 14 % is achieved. Because of non-uniform heat generation in the fuel elements the gross efficiency of the plant is lowered to 12 %. This corresponds to a mean electric power density of 6,5 Watts/cm² and to a net power of 50 kW_{e1}. The collector temperature of 1140 K is somewhat higher than the barium reservoir temperature (1100 K).

Advantages of the System

- High specific power, therefore applicable for electric propulsion [1].
- SRIKT-systems are suitable for long-time missions because of their low reactivity loss during burnup.

Disadvantages of the System

- High fuel inventory which causes higher costs than a thermal system in the low power range (100 kW) [1].
- Compatibility problems between nuclear fuel and emitter arise in the SRIKT-system likewise. The selection of the emitter and fuel materials however is not restricted severely by neutron capture considerations.
- The damage flux in the Al₂O₃-ceramic insulation within the core has here its highest value (about $1,6 \cdot 10^{13}$ MeV/cm²s) of all systems discussed in this paper.

5. FAST OUT-OF-CORE THERMIONIC REACTOR, EMITTER HEATED BY HEAT PIPES (WR-TR)

The fission heat is transferred by means of heat pipes [16,17] from the core through the reflector to the emitter. The converters are located outside of the top reflectors (Fig.10). The collectors are also cooled by heat pipes. Therefore, no pumps are required. According to the calculations carried out so far, a heat pipe thermionic reactor of this type seems to be suitable for approx. 100 kW_{e1}.

Reactor

The cylindrical core is an assembly of 367 fuel elements which consist of two symmetric parts [18]. The UO₂-fuel is filled in holes of molybdenum matrix elements of hexagonal cross section. The emitter heat pipe is fitted in the central hole of each matrix element. These have no mutual contact within the core. Therefore, a series-parallel-connection of the converters of different fuel elements is feasible. The core is reflected by graphite. Power density flattening in axial direction is not absolutely necessary, since emitter heat pipes are used for heat transfer.

Thermionics and Energy Transfer

The two converters of each fuel element are connected in parallel (Fig.6). In order to exploit the thermal power of a fuel rod, the converters must have large electrode areas and generate therefore high currents. The emitter and the collector temperatures are constant within each converter due to the application of heat pipes. The emitter heat pipe consists of a Ta-10 W-tube whose inner face is plated with tungsten. Lead is used as heat carrier. For the collector heat pipe, Nb-1Zr is chosen as structure material and sodium

as heat carrier. The waste heat is rejected by radiator heat pipes (Nb-1Zr/Na). They are fitted to the collector heat pipes and soldered together. Therefore, no temperature drop at this interface occurs. The radiator heat pipes are combined to a truncated cone shaped radiator (Fig.5).

Advantages of the System

- Converters are outside of the core. The insulation is not exposed to the high neutron flux of the core.
- Problems associated with the direct contact of fuel and emitter occurring in incore reactors are evaded.
- A high redundancy of the system can be obtained because each of the numerous converters is a self-contained system.

Disadvantages of the System

- Fuel inventory and total weight are high.
- One part of the radiator is located between reactor and shield (Fig.5, the shield is not indicated there). From this, a heavy shield results. The development potential of this design to higher power output is therefore limited.
- The long-time operation of emitter heat pipes has not been demonstrated satisfactorily so far.

6. FAST OUT-OF-CORE THERMIONIC REACTOR, EMITTER HEATED BY THERMAL RADIATION (SRAKT-WR)

The cooling of the power plant is done exclusively by heat pipes (heat carrier sodium), therefore, no circulation pumps are necessary. In the power range from 5 to 25 kW_{e1}, 70-80 kg U 235 are needed to obtain criticality.

Reactor

The cylindrical core of UC (93 % U 235) is surrounded by a tungsten canning. The radial reflector of beryllium consists of a 20 mm thick rigid inner shell; the outer shell consists of two 80 mm thick rigid rings at each of the core edges and a central part of 50 mm thickness (Fig.8). The central part is divided into six larger and six smaller segments for trimming and fine reactor control. Each segment can be moved radially by a magnetic jack. For power density flattening in axial direction, the thickness of the radial reflector has been increased towards the core edges.

Thermionics and Energy Transport

The core is surrounded by 12 x 12 planar Cs-converters which are heated by radiation from the surface of the core [19,20]. The heated emitter shoe area of 13 cm² is of rectangular cross section, whereas the emitter area of 8 cm² is of circular shape. The planar converter is assembled of a molybdenum emitter and a Nb-1Zr-collector. Because of the series-connection of 12 converters at the surface, each half of the reactor has six converter rings which are connected to a 12 x 6-matrix. For a given maximum temperature in the fuel the thermal power was calculated taking into consideration the two-dimensional distribution of heat sources and the boundary conditions which are effected by the converter performance at the surface of the core. The converter performance data were predicted by using a theoretical converter model [10].

The heat is removed from the collectors by short cylindrical Nb-1Zr-heat pipes. The collector heat pipes of 12 axially arranged converters are mounted to one transport heat pipe which transfers the waste heat to the heat pipe radiator (Fig.7). The transport heat pipes are insulated from the collector heat pipes by an Al_2O_3 -layer. A portion of the waste heat transferred by the 12 transport heat pipes is conducted to the reflector which radiates approx. 15 % of the waste heat into space. The radiator is formed by 12 rectangular radiator heat pipes.

Advantages of the System

- Simple design based on demonstrated components (e.g. converters [12], heat pipes [22], core [23]).
- The converters are separated from the core. The Al_2O_3 -insulators are only exposed to a low neutron flux.
- The converter network and the radiator can be designed for high redundancy.
- Converters with collector-heat pipes can be tested individually and when connected to a converter network. Simulation of the core by an electric heater is possible [24].

Disadvantages of the System

- High amount of fuel is required (approx. 70-80 kg for power plants of 5-25 kW_{e1}).
- The specific power is relatively low.
- The radiator heat pipes used for this design are of complicated structure.

7. CONCLUSION

The results of design studies on five different thermionic reactor systems carried out at the Institut für Kernenergetik are discussed. The design studies are based on nuclear engineering and thermionic conversion aspects. A classification of the types taken under consideration with respect to the power range could be quoted as follows: SRAKT-WR is applicable in the power range from 5 to 25 kW_{e1} ; while the TRIKT-system is suitable from some ten to a few hundred kilowatts. The "Teilthermionikreaktor" covers the lower power range. TRIKT-Systems are characterized by low fuel inventory. The fast incore thermionic reactor SRIKT is preferable to TRIKT from about hundred kilowatts to megawatts. It is characterized by high specific power. The thermal and the fast incore types cover a large power range with reasonably high specific power, whereas the application of the considered out-of-core type with emitter-heat pipes is restricted to power outputs in the order of 100 kW_{e1} .

References

- (1) PRUSCHEK, R., Atomkernenergie 10 (1965), 327.
- (2) WOLF, E.; HAUG, W., Atomkernenergie 10 (1965), 333.
- (3) HAUG, W.; FRITZ, R.; PRUSCHEK, R.; WOLF, E., Atomkernenergie 10 (1965), 363.
- (4) BUDNIK, D., Energieversorgung im Weltraum II, DGLR-Symposion München (1968).
- (5) BBC-Nachrichten, Sonderheft: Direktumwandlung in elektrische Energie (1967).
- (6) HINZE, Ch., Dissertation, Universität Stuttgart (1967).
- (7) Reactor Physics Constants, ANL 5800, (1963), 256.
- (8) SIEGERT, H.J.; KUNERT, K., Forschungsbericht K 67-06 des Bundesministeriums für wissenschaftliche Forschung (1967).
- (9) WILSON, V.C.; LAWRENCE, J., Adv. Energy Conversion 4 (1964), 210.
- (10) RASOR, N.S., Int. Conf. on Therm. Electr. Power Gen., London (1965).
- (11) SCHLITT, R., Internal Report, IKE 5-49d (1967).
- (12) SCHRÖDER, J., Internal Report, IKE 5-26d (1966).
- (13) BONDARENKO, I.I., Group Constants for Nuclear Reactor Calculations, Consultants Bureau New York (1964).
- (14) PSAROUTHAKIS, J., Therm. Conv. Spec. Conf., Cleveland (1964).
- (15) LUTZ, D.; STEINER, D.; UNGER, H.; WÖSSNER, G., Atomkernenergie 10 (1965), 368.
- (16) GROVER, G.M.; COTTER, T.P.; ERICKSON, G.F., J. Appl. Phys. 35 (1964), 1990.
- (17) BUSSE, C.A.; CARON, R.; CAPPELLETTI, C., Int. Conf. on Therm. Electr. Power Gen., London (1965).
- (18) HANKE, H., Internal Report, IKE 5-46d (1968).
- (19) ZIMMERMANN, P., Internal Report, IKE 5-43e (1967).
- (20) DAGBJARTSSON, S.; GROLL, M.; ZIMMERMANN, P., Internal Report, IKE 5-51 (1968).
- (21) Solar Heated Thermionic Diode-Model A 103. Thermo Electron Engineering Corporation, Waltham/Mass. (1966).
- (22) BUSSE, C.A.; CARON, R.; GEIGER, F.; PÖTZSCHKE, M., Int. Conf. on Therm. Electric. Power Gen., London (1965).
- (23) MILLIONSHCHIKOV et al., 3. UN Intern. Conf. on the Peaceful Uses of Atomic Energy, Geneva (1964), P 873.
- (24) KOEPPE, A.; PRUSCHEK, R., Atomkernenergie 10 (1965), 392.
- (25) Wissenschaftlicher Bericht 1966 des IKE, Forschungsbericht K 67-46 des Bundesministeriums für wissenschaftliche Forschung (1967).

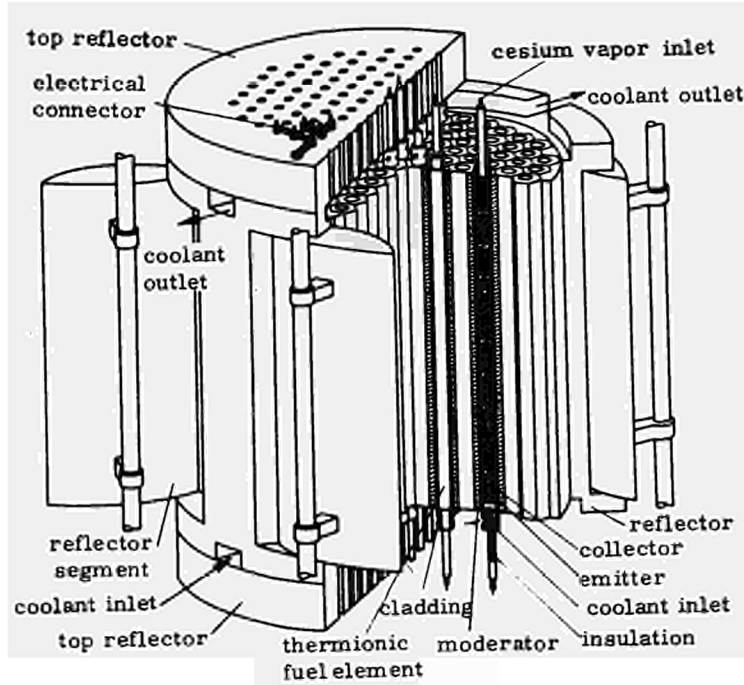


Fig. 1: Zirconium Hydride Moderated Incore Thermionic-Reactor, TRIKT.

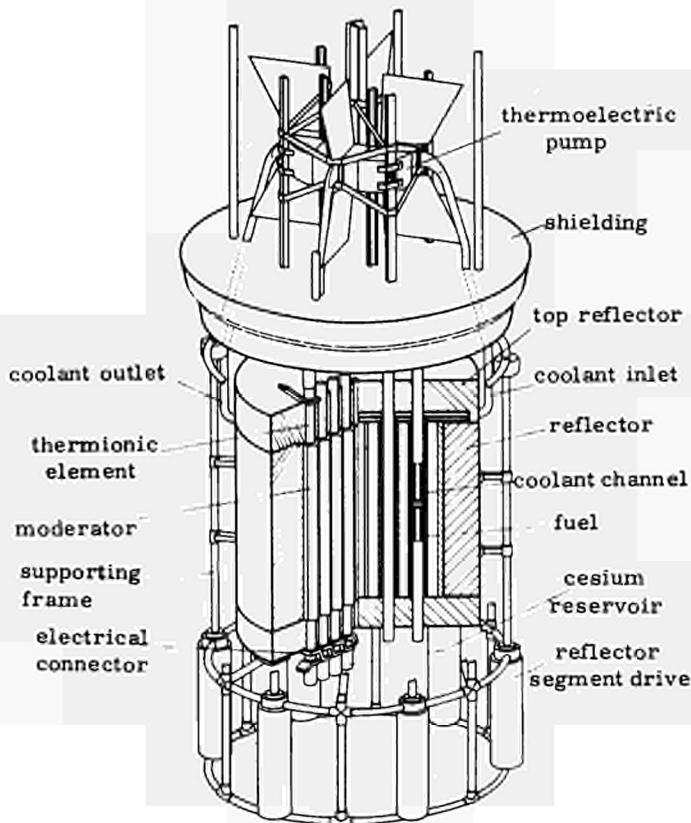


Fig. 2: Double Diode Thermionic-Reactor, DD-TR. (proposed by BBC).

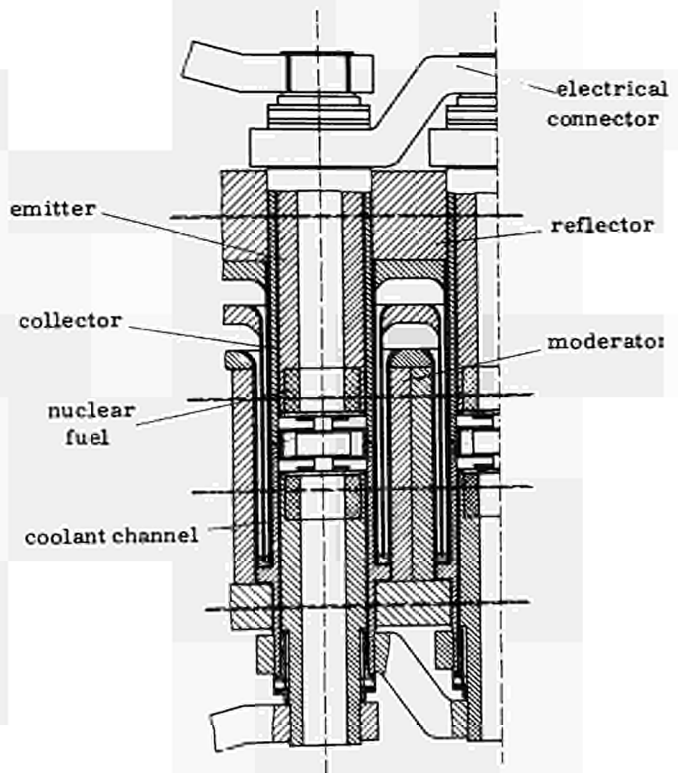


Fig. 3: Cross Section of a Double Diode.

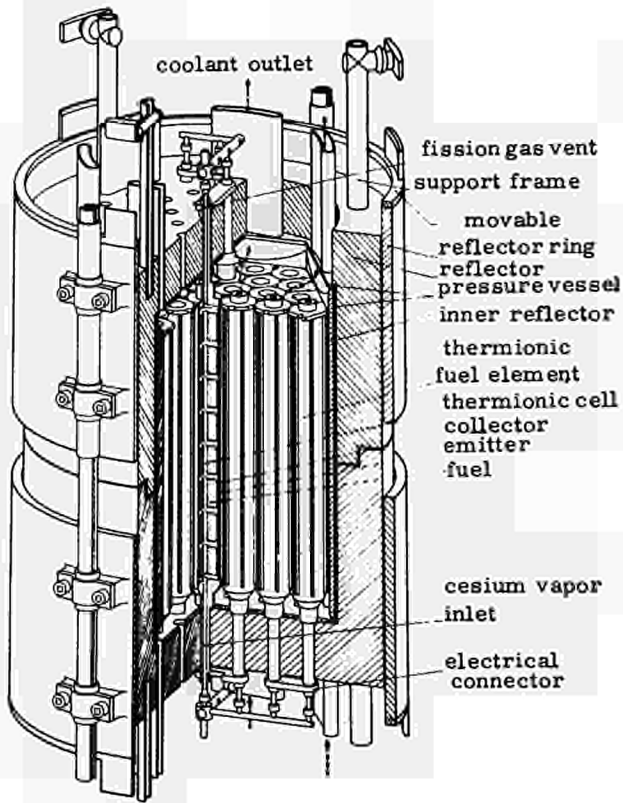


Fig. 4: Fast Incore Thermionic-Reactor, SRIKT.

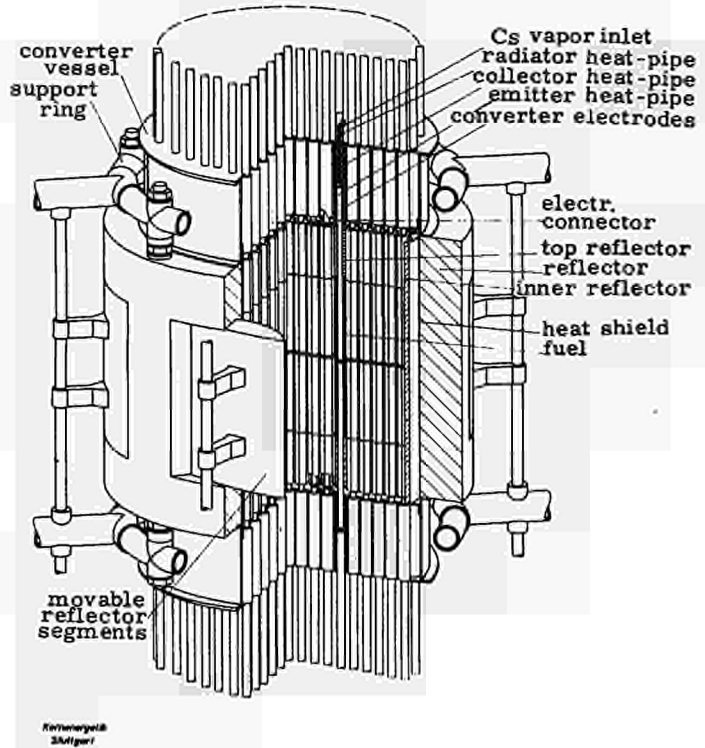


Fig. 6: Fast Heat-pipe Thermionic-Reactor WR-TR

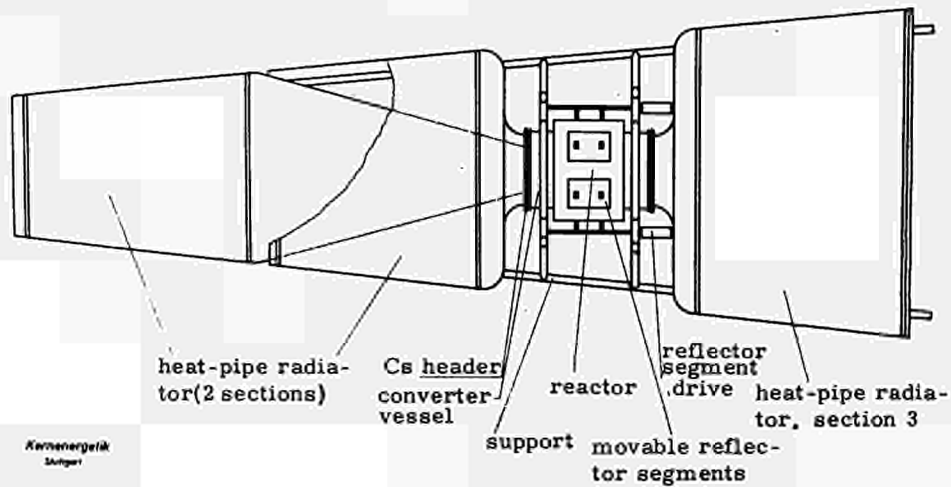


Fig. 5: Powerplant including a Fast Out-of-Core Heat pipe Thermionic-Reactor, WR-TR.

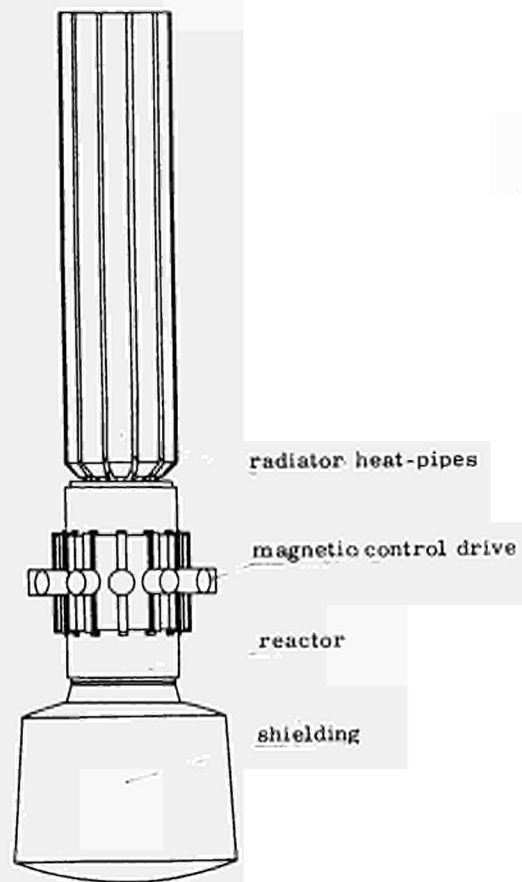


Fig. 7: Power Plant including a Fast Out-of-Core Thermionic-Reactor, SRAKT-WR

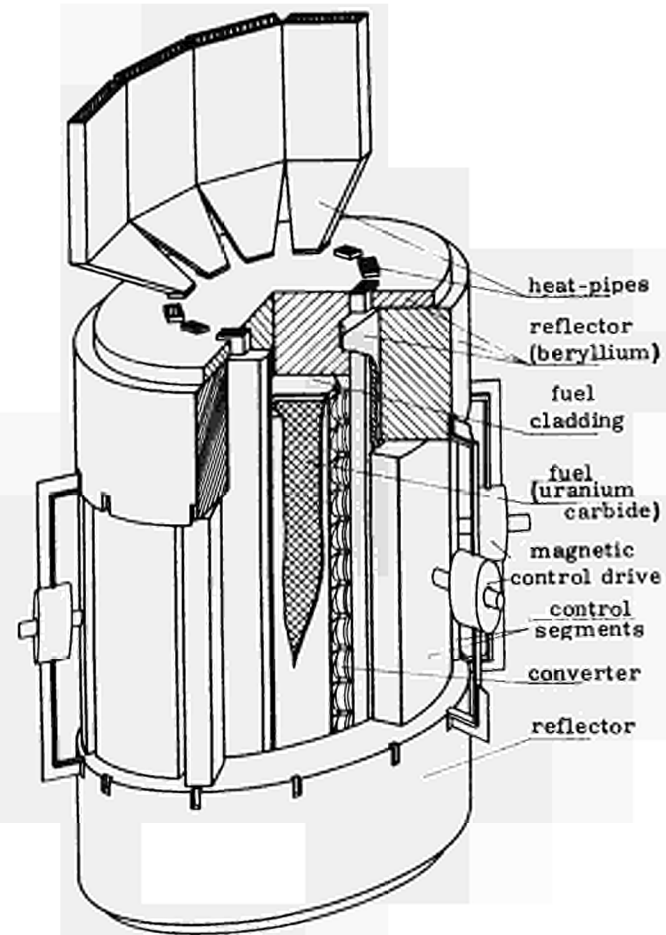


Fig. 8: SRAKT-WR. Emitter Heating by Thermal Radiation from Reactor Core Surface, Collector Cooling by Heat-pipes.

Tab. 1 : Nuclear Data

	Dim.	TRIKT	DD-TR	SRIKT	WR-TR	SRAKT-WR
fuel (93% enrichment)	-	(UC) _{0,3} (ZrC) _{0,7}	UO ₂ -Mo-Cerm	UC	UO ₂	UC
fissionable atoms/total atoms of the fuel	-	0,14	0,094	0,47	0,31	0,47
mass of U ²³⁵	kg	10	25	61	104	72
number of fuel rods	-	120	84	37	367	-
moderator	-	ZrH _{1,7}	ZrH _{1,7}	-	-	-
reflector	-	Be	Be	Be	C	Be
reflector thickness	mm	90	76	60	100	100
peak-to-average ratio of heat flux density	-	1,24	1,25	1,28	1,42	1,09
core diameter	mm	362	374	238	488	132
core height	mm	382	373	294	300	460
neutron spectrum	-	thermal	thermal	fast	fast	fast
displacement of control reflectors by	-	rotation	rotation	axial shift	rotation	radial shift
reactivity loss after 400 d operation	%	5,25	-	0,2	-	0,05

Tab. 2 : Converter Data

	Dim.	TRIKT	DD-TR	SRIKT	WR-TR	SRAKT-WR
electrode geometry	-	cylindrical	cyllindr.	cyllindr.	cyllindr.	planar
emitter length	mm	40	188	30	60	-
emitter diameter	mm	10	19	30	12	32
emitter area	cm ²	12,6	112	28,3	22,6	8,05
spacing	mm	0,25	0,2	1	0,3	0,075
emitter thickness	mm	0,6	1,0	0,8	1,25	4
collector thickness	mm	0,5	1,5	0,7	2,1	3
insulation thickness (anode tri-layer)	mm	0,3	0,3	0,3	-	-
wall thickness of outer casing	mm	0,5	0,3	0,6	-	-
emitter	-	W on Mo	Mo	W	Re on Mo	Re on Mo
collector	-	Nb-1 Zr	Nb-1 Zr	Nb-1 Zr	Nb-1 Zr	Nb-1 Zr
insulations	-	Al ₂ O ₃	Al ₂ O ₃	Al ₂ O ₃	Al ₂ O ₃	Al ₂ O ₃
outer casing	-	Nb-1 Zr	Nb-1 Zr	Nb-1 Zr	-	-
emitter-collector lead	-	Mo	Mo	Mo	Mo	Nb-1 Zr
mode of converter operation	-	ignited	unignited	unignited	ignited	ignited
average emitter heat flux density	W/cm ²	49	24	54	75	54
average current density	W/cm ²	7	0,8	7,6	10	11,7
average cell voltage	V	0,7	1,5	0,85	0,75	0,46
efficiency	%	10	5	12	10	10
number of converters per fuel rod	-	8	2	8	2	-
total numbers of converters	-	960	168	296	734	144

Tab. 3 : Temperatures

	Dim.	TRIKT	DD-TR	SRIKT	WR-TR	SRAKT-WR
max. fuel temperature	K	2050	2015	2220	2160	2300
max. emitter temperature	K	2000	2000	2070	2000	1780
average collector temperature	K	1000	1000	1140	1050	800
reactor coolant inlet temperature	K	883	873	1073	-	-
reactor coolant outlet temperature	K	923	947	1113	-	-
surface temperature of emitter heat pipe	K	-	-	-	2000	-
surface temperature of collector heat pipe	K	-	-	-	1050	800

Tab. 4 : Heat Rejection System

	Dim.	TRIKT	DD-TR	SRIKT	WR-TR	SRAKT-WR
radiator design	-	finned tubes	finned tubes	finned tubes	heat pipe rad.	heat pipe rad.
coolant	-	Na	NaK 78	Na	-	-
working fluid of emitter heat pipe	-	-	-	-	Pb	-
working fluid of collector/radiator heat pipe	-	-	-	-	Na	Na
total length of radiator	mm	5900	-	-	6450	1200
radiator width min	mm	800	-	-	885	420
radiator width max	mm	1960	-	-	2285	420
outer diameter of radiator tube	mm	16	-	-	15,6	98 x 25
tube or heat pipe material	-	Be	-	-	Nb-1 Zr	Be
tube wall thickness	mm	2,2	-	-	0,8	2,5
liner material	-	stainless steel	-	-	-	-
radiator surface emissivity	-	0,9	-	-	0,9	0,9
radiating area	m ²	16,2	-	-	24	1,58
radiated waste heat	kW	450	450	400	1300	48
pump design	-	d. c. conduction	thermo-electric	d. c. conduction	-	-
number of pumps	-	1	8	1	-	-
electrical input power of the pumps	kW _{el}	4	-	3	-	-

Tab. 5 : Mass of Components and Power Output

	Dim.	TRIKT	DD-TR	SRIKT	WR-TR	SRAKT-WR
reactor :						
fuel	kg	20	43	68	249	82
moderator	kg	142	121	-	-	-
reflector	kg	150	123	81	228	115
converters	kg	55	55	49	147	17
structure	kg	27	30	10	224	9
supporting frame	kg	31	28	11	-	-
heat and meteoroid shields	kg	10	-	4	140	-
control reflector drives	kg	30	29	26	-	4
coolant within reactor	kg	20	33	35	8	-
miscellaneous	kg	10	7	6	-	2
total reactor mass	kg	495	479	290	998	229
radiator :						
radiating part	kg	41	-	-	450	17
piping	kg	25	-	-	230	11
coolant within radiator	kg	32	-	-	22	-
total radiator mass	kg	98	100	-	702	28
additional components :			(estimated)			
pumps	kg	65	48	-	-	-
bus-bars of pumps	kg	30	4	-	-	-
miscellaneous	kg	43	24	-	-	2
total mass of additional components	kg	138	76	-	-	-
power plant, shadow shield not included	kg	731	655	-	1898	259
power plant incl. shadow shield	kg	1000	-	-	-	412
net electrical power	kW	50	20	50	102	6,2
specific power shadow shield not included	kW/kg	0,07	0,03	-	0,06	0,024

DISCUSSION

No speaker of paper B-2

HEFFELS (ESRO):

In specific power calculations, did the authors include power conditioning and what kind of radiation shielding?

BUDNICK (Germany):

In these power calculations power conditioning is not included, but the power conditioning will need about 1 to 2 kg per kW electrical power. Radiation shields of lithium hydride are used for the shielding calculations. Calculations were made only for unmanned missions.

MULTIMEGAWATT THERMIONIC REACTOR SYSTEMS FOR SPACE APPLICATIONS*

C. D. Sawyer, P. R. Hill, D. R. Wilkins
General Electric Company
Nuclear Thermionic Power Operation
Pleasanton, California
United States of America

ABSTRACT

A review of selected portions of the General Electric Company thermionic reactor development program is presented. Typical design features and performance characteristics of thermionic reactors with electrical ratings in the multimegawatt class are presented by reference to the results of a reactor design study carried out for a hybrid nuclear rocket/nuclear electric Mars mission. Important elements of related technology from other elements of the General Electric program are also presented. In particular, a summary of the results of a thermionic reactor critical experiment and the results of preliminary reactor stability studies is discussed.

REACTOR DESIGN STUDIES

In the development of the technology of the nuclear thermionic reactor concept, primary attention has been given to the technology of the thermionic converter, high temperature materials, and the fabrication and test of thermionic devices using nuclear heating. Since there are several concepts of thermionic reactors, and each differs in content and priorities in its respective development programs, it is important to examine the potential applications of each to identify more clearly the major problems to ensure that the programs are being directed effectively toward the desired goal. It is essential to define the intended application of the power system and to interpret the various interactions and constraints which connect the application and the power system into an effective power plant design. The use of the thermionic reactor to provide large quantities of electrical power to an electrical propulsion system for high energy, long time space missions is a particularly attractive example of the potential application of nuclear thermionic power systems.

POWER PLANT CONCEPT

A conceptual arrangement of the thermionic reactor and the other major power plant components is shown in Fig. 1. The thermionic reactor with its shadow shield is located at the apex of a conical radiator. The shield is split to accommodate an intermediate heat exchanger and the pumps which circulate liquid metal through the reactor cooling loop. Actuating motors for the reactor control elements could be located at this place or with the balance of the power plant auxiliaries on the far side of the equipment shield. Auxiliaries include the liquid metal circulating pumps for the radiator loop and the instrumentation and control package which provide for over-all control of the reactor and power plant. Also included is the power conditioning equipment with its cooling system. This equipment provides for conversion of the low voltage direct current output from the thermionic fuel elements (TFEs) to power plant distribution voltage. A number of variations upon this arrangement (Fig. 1) may be considered. The optimum arrangement will almost certainly depend upon the specific application and the particular characteristics and limitations of the boost vehicle used.

*This work was supported by the National Aeronautics and Space Administration and the United States Atomic Energy Commission.

REACTOR CONCEPT

A section of the reactor in a plane containing the reactor central axis is shown in Fig. 2. At the shield end of the reactor the coolant plenum, which collects the core exit flow, is penetrated by the TFE sheath extensions containing the electrical leads and cesium vapor supply passages. These extensions penetrate the reactor vessel head through welded closures. The metal-to-ceramic seals located external to the face of the reactor vessel head permit access to the electrical lead and form a closure to the cesium vapor envelope. In addition, this region also contains the electrical connectors and Cs vapor supply system. Reactor control is achieved by motion of segments of the radial reflector which consists of 4 in. of Be immediately adjacent to the external lateral surface of the reactor vessel.

The reactor core consists of bundles of TFEs in a hexagonal configuration (Fig. 3). The bundle consists of a 40-mil hexagonal stainless steel can holding two or more rings of fuel elements. Spacer and filler elements serve the dual function of spacing and restraining the fuel elements while also diverting coolant flow to provide uniform cooling around the sheath circumference. Coolant flow is controlled by triangular spacers in the cusp-shaped region around the periphery of the fuel bundles and by small circular spacers in the internal cusp-shaped region between each fuel element. Contact between the spacers, and the fuel elements is limited to small local regions of projections and ridges in the spacers and the fuel element sheath. The dual function of these spacers is important in restraining thermally or mechanically induced motion of the fuel elements which could introduce serious reactivity fluctuations and result in reactor instability. The improvement in flow distribution helps suppress instability by reducing the thermal gradients in the sheath which cause motion and also reduces stress levels in the sheath and insulator assembly caused by the nonuniform sheath temperature.

The fuel element bundles are arranged into an approximately circular cross section in a cylindrical reactor vessel. Coolant flows in two passes through the vessel with the flow proceeding down through the annulus between the core and reactor vessel wall and returning up through the core. The coolant inlet and outlet pipes are located at the shield end of the reactor.

The essential features of the TFE are shown in Fig. 4; the materials and dimensions (inches) of the TFE are:

<u>Item</u>	<u>Material</u>	<u>Thickness</u>	<u>Outside Diameter</u>	<u>Item</u>	<u>Material</u>	<u>Thickness</u>	<u>Outside Diameter</u>
Sheath	Kovar	0.020	0.60	Gap	Cs Vapor	0.007	-
Insulator	Al ₂ O ₃	0.020	-	Emitter	W	0.030	-
Collector	Nb	0.020	-	Fuel	UO ₂	-	0.406

These dimensions were selected on the basis of the results of previous optimization studies. The most important variable here is the sheath diameter of the TFE which is selected to maximize the emitter area density in the core. The 0.6-inch value represents the practical optimum, the mathematical optimum yielded values of sheath diameter below that considered favorable in the fabrication sense. The values of material thicknesses are selected at the minimum practical value except for emitter and collector. Optimization of the emitter and collector thickness involve cell length, emitter area density, fuel volume fraction, and electrode voltage loss. The thicknesses shown here reflect fabrication and reliability considerations, but are near optimum values. Emitter length is then established by selecting an arbitrary 5% loss of voltage in the electrodes for the thermionic design point selected. The precise optimum is believed to be in the range of 3 to 10% and causes relatively small variations in over-all system characteristics in this range.

ELECTRICAL DESIGN CONSIDERATIONS

The thermionic reactor consists of numerous converter cells each operating at a relatively low output voltage. Since this voltage for each cell is usually less than 1V, the need for series connections to limit the reactor output current becomes quite apparent. The TFE concept already provides series-connected groups of 12 or more cells. Further advantages might be obtained if more series connections of TFEs were provided (e. g. , lower weight of power cables between the reactor and power conditioning equipment, and more efficient, lightweight power conditioning equipment).

On the other hand, the series connection of TFEs for voltage buildup could adversely affect reliability. Some upper limit on voltage across the TFE sheath insulator exists and should not be exceeded to prevent insulator breakdown and arcing to ground. The mechanical design of the reactor is made more complex by requiring internal electrical connections, or penetrations of the reactor vessel at both ends for TFE electrical series connections. In addition, the consequences of an open circuit failure become increased in proportion to the number of TFEs which are series connected.

For the reactor designs being investigated, the design choice involves grounding the end of the TFEs internal to the reactor while alternating the output voltage of pairs of TFEs positive and negative about ground (Fig. 5). The circuit diagram shown here implies that pairs of positive and negative TFEs have individual power cables and power conditioning modules. While this approach can potentially provide a degree of redundancy in the power conditioning system and result in improved over-all reliability, it may be desirable to consider parallel-connected groups of TFEs connected to a single power conditioning module in terms of weight, efficiency, or complexity. Further study is required to make this choice.

This method of connecting pairs of TFEs results in effectively series-connecting two TFEs without requiring internal electrical connections or additional vessel penetration. The maximum voltage across the sheath insulator is one-half the effective output voltage of the core. The consequences of an open circuit failure in a TFE can be designed to cause a loss in output from only that TFE if provision is made in the power conditioning and switching circuitry.

BACKGROUND TECHNOLOGY

The background technology of this study in the area of thermionics will be covered in part in other papers presented at this conference. In particular, the information presented by Wilson,⁽¹⁾ VanHoomissen,⁽²⁾ and Wilkins⁽³⁾ represent development knowledge and techniques which have contributed directly to the evaluation of the reactor system presented in this paper.

The results of a thermionic reactor critical experiment and studies devoted to thermionic reactor stability characteristics not previously been reported are presented next. The Thermionic Reactor Critical Experiment (TRCE)⁽⁶⁾ was directed toward an evaluation of thermionic reactor cores in the lower power range of a few hundred kilowatt electrical. The results of the experiment are useful in developing a better understanding of the physics of thermionic cores over a broad range of power levels.

CRITICAL EXPERIMENT

The TRCE was a small, compact, uniformly reflected, fast spectrum reactor. Two experimental configurations were examined. The first, a Be-reflected system, was used principally to examine experiment-to-analysis correlations. The second, performed on Be- and stainless-steel-reflected systems was directed more toward investigating the influence of reflector variations.

Physically, the TRCE was positioned in the hexagonally shaped cells of the Al matrix of a horizontally oriented split table assembly; one table was fixed and the other movable (Fig. 6). The basic cell structure consisted of stacked hexagonal Al tubes with a nominal spacing of 1.785 inches across the flats. The Al walls of the tubes were 0.031 inch thick. Six inches of the 14.76-inch-long core was in the fixed table. An axial layout of the initial configuration, Configuration A, is shown in Fig. 7. The loading of each hexagonal cell within the core and transition region was done with small diameter (~0.18 inch) rods, and the loading of the reflector region was done with full and half-hex size pieces.

There were five variations of the basic configurations studied. Configuration A consisted of a 0.875-inch-thick transition region surrounding the core and a nominal 6-inch Be radial and axial reflector and made as symmetric a system as was practical. In Configuration B1 the axial transition region was removed and the axial reflector modified to include a significant amount of stainless steel to make the axial direction conform to a situation thought to be more typical of the end reflectors of a thermionic reactor design. In the remaining configurations (Table 1) the influence of the composition and dimension of the radial reflector was investigated.

A summary of loading data for the five configurations is presented in Table 1. Modifications of published cross section data⁽⁴⁾ were used with S_4 quadrature.

Typical power profiles in the radial and axial directions and the calculated results are shown in Fig. 8 and 9. The discrepancy in the axial profile is attributed to a marked streaming effect by reflected low energy neutrons in this direction. The stainless-steel-reflected cores exhibited power profiles with a much smaller minimum-to-centerline power ratio and no peaking at the core edge. Gross spectral determinations were made by fission ratios:

Element	Configuration A		Configuration B4		Element	Configuration A		Configuration B4	
	Calculated	Measured	Calculated	Calculated		Calculated	Measured	Calculated	Calculated
U-235	1.	1.	1.	1.	Np-237	0.47	0.50	0.50	0.50
Th-232	0.019	0.020	0.021	0.021	Pu-239	0.99	1.10 ± 0.07	1.00	1.00
U-233	1.60	1.47	1.61	1.61	Pu-240	0.52	0.50	0.56	0.56
U-238	0.080	0.082	0.087	0.087					

There is general agreement between measurement and calculation for the threshold detections which indicates a reasonable spectral determination in the calculations. The discrepancies in the U-233 and Pu-239 ratios are indicative of the present precision of high energy fission cross section data for these isotopes.

Neutron lifetime measurements were made by both the Rossi-alpha technique and by the 1 V poisoning technique. For TRCE-A, the neutron lifetime was $9.4 \pm 0.9 \mu\text{sec}$ and for TRCE-B4 it was $0.6 \pm 0.1 \mu\text{sec}$.

Material worth measurements were performed on various materials both at core centerline and for core average (core length samples). A selection of experimental results obtained on Configuration A are:

Material	Worth (% $\Delta k/\text{gm}$)	Material	Worth (% $\Delta k/\text{gm}$)
Ni	+ 1.3×10^{-5}	W	- 1.3×10^{-5}
Stainless Steel	+ 3.8×10^{-5}	Re	- 2.3×10^{-4}
Nb	< 10^{-6}	Ta	- 1.2×10^{-4}
Mo	+ 1.6×10^{-5}	-	-

TABLE 1. Summary of Loading Data for TRCE

	Length (in.)	Volume Fraction (V)				
		Oy*	Al ₂ O ₃	Stainless Steel	Be	Al
Core**						
A	14.76	0.171	0.046	0.108	-----	0.069
B1	14.76	0.174	0.043	0.108	-----	0.069
B2	14.76	0.195	0.019	0.108	-----	0.069
B3	14.76	0.225	-----	0.092	-----	0.069
B4	14.76	0.217	-----	0.102	-----	0.069
Reflector						
Radial						
A†	28	-----	-----	-----	0.881	0.069
B1†	28	-----	-----	-----	0.881	0.069
B2††	28	-----	-----	-----	0.873	0.069
B3‡	28	-----	-----	0.830	-----	0.069
B4†	28	-----	-----	0.828	-----	0.069
Axial						
A	6	-----	-----	-----	0.89	0.069
B1	6	-----	-----	0.108	0.636	0.069
B2	6	-----	-----	0.108	0.636	0.069
B3	6	-----	-----	0.108	0.636	0.069
B4	6	-----	-----	0.108	0.636	0.069
Transition Region† ‡						
Radial						
A	16.51	-----	-----	0.553	-----	0.094
B1	28	-----	-----	0.553	-----	0.094
B2	28	-----	-----	0.553	-----	0.094
B3	28	-----	-----	0.553	-----	0.094
B4	28	-----	-----	0.553	-----	0.094
Axial						
A	0.875	-----	-----	0.553	-----	0.094
B1	-----	-----	-----	-----	-----	-----
B2	-----	-----	-----	-----	-----	-----
B3	-----	-----	-----	-----	-----	-----
B4	-----	-----	-----	-----	-----	-----

	k_{eff}	
	Experimental	Calculated
A	1.0021	1.0060
B1	1.0010	1.0200
B2	1.0013	1.0070
B3	0.9981	1.0120
B4	1.0018	1.0200

V Volume fractions of theoretically dense materials
 *Oralloy, density 18.8 gm/cm³ at 93.2 at. % U-235
 **All cores contain V(WO₃) = 0.311 V(Ni) = 0.070
 †6.15 in. thick
 ††3.52 in. thick
 ‡4.4 in. thick
 ‡‡0.875 in. thick

Reflector replacement studies also included a 60° sector of radial reflector replaced by BeO in Configuration A. This indicated a lower power peaking at the core edge and an extrapolated gain of 2.4% Δk for a radial BeO reflector. Preliminary control element studies were also made and the effect of a 4.4-cm displacement of a 60° radial sector of reflector was measured. This displacement produced 2.1% Δk and 1.5% Δk reductions in reactivity for TRCE-A and TRCE-B4, respectively.

REACTOR STABILITY

A detailed analysis of the stability characteristics of the thermionic reactor was performed. The nonlinear differential equations which describe time-dependent phenomena in the reactor components were linearized about an appropriate operating point, and written in matrix form. The eigenvalues of the system matrix were evaluated numerically to determine the stability properties of the system, and key stability parameters were identified through a series of parametric studies. In this manner, it was determined that two key stability parameters in a thermionic reactor are the fuel and emitter temperature coefficients of reactivity, α_F and α_E , respectively. Approximate stability criteria for these parameters were derived from a two-region reactor model, and were in excellent agreement with the numerical results. These criteria are:

$$\alpha_E \leq - (1 + H_E/H_{FE}) \alpha_F; \alpha_E \geq (C_E/C_F) \alpha_F - \gamma; \gamma = (\tau H_E/P_T) [H_{FE}/C_F + (H_{FE} + H_E)/C_E] \quad (1)$$

where C_F and C_E are the fuel and emitter heat capacities, respectively; H_{FE} and H_E are the fuel-emitter and emitter-collector heat conductances, respectively; τ is an "effective neutron lifetime;" and P_T is the steady-state thermal power of the reactor. An approximate requirement for the reactor to be stable is that the sum of the fuel and emitter temperature coefficients of reactivity be negative. Computations of the Doppler coefficients for the small reactor design yield $\alpha_F = + 1.0 \times 10^{-7}/^\circ\text{K}$ and $\alpha_E = - 6.0 \times 10^{-7}/^\circ\text{K}$. On this basis, it is concluded that such reactor designs are stable.

PARAMETRIC STUDIES

Parametric studies were made for the reactor concept described in this paper. Reactor electrical output was varied over the range of a few thousand to twenty thousand kilowatts electrical output, for the two levels of converter electrical performance shown on the following page. At each reactor power level, the effects of core length-to-diameter ratio, the TFE bundle size, the reactor coolant pressure drop and temperature rise, and the effects of Na in place of NaK were investigated for all appropriate combinations and permutations. Reactor criticality was not considered in this study since for all reactor sizes above a few thousand kilowatts electrical output criticality is not limiting. The study also assumed that the fission power distribution had been flattened so that each converter cell throughout the core produced the same thermal power. The primary range of interest in this study involves core sizes for which power flattening can be achieved to a very high degree; therefore, reactor physics evaluations may be deferred until electrical, thermal, and mechanical design considerations are resolved. The studies were primarily directed toward reactor geometry and weight and performed so that core designs involving integral numbers of fuel bundles having a favorable core pattern and integral numbers of converter cells in each TFE were specified. This constraint along with the fixing of electrical performance results in reactors which do not always have the exact electrical output desired. The studies also incorporate a variety of thermal and hydraulic design criteria developed in related programs so that this aspect of the design is also adequate.

Parameter	Converter		Parameter	Converter	
	Standard	Advanced		Standard	Advanced
Temperature, °K					
Emitter	1828	2130	Current, A/cm ²	9.0	18.1
Collector	975	1080	Net Voltage, V	0.63	0.86
Cesium	593	633	Net Output, W/cm ²	5.64	15.5
Emitter Length, in.	1.114	0.835	Cell Efficiency, %	14.8	18.3

The thermionic performance data used in the reactor parametric studies were taken from the work of Wilson. (5) For the "standard" converter, a low emitter temperature of 1828°K was selected while an emitter temperature of 2130°K was selected to represent a more "advanced" level of converter performance. In both cases, the individual converter cell has been optimized for voltage and thermal losses and output current density to yield maximum over-all cell efficiency. The selection of maximum cell efficiency minimized the size and weight of the heat rejection system. Selection of current densities which maximize thermionic electric power density would result in reductions in reactor and shield size, but at the expense of conversion efficiency. The true optimum is somewhere between these limiting cases, and experience indicates selection of the maximum efficiency condition is more nearly the optimum condition for large power plants.

Figure 10 represents a summary of the results of the reactor design calculations. Clearly, the most important parameter is emitter temperature level with reactor power level being second in importance. The variation with power level presented here is an underestimate since the calculated reactor weight assumes a full fuel loading in the available fuel volume. For the lowest power levels, this is appropriate, but at higher power levels less fuel would be loaded so that the actual specific weight is slightly less than that shown. The influence of all other parametric variations is small in terms of specific weight covering a range of about ± 5% about the mean line for the total range of parametric variations considered. The implication of these results is a strong incentive to select the best possible level of thermionic performance. Other reactor parameters may be selected on the basis of considerations other than reactor specific weight.

The results presented in Fig. 10 provide no information relative to the selection of the reactor coolant outlet temperature. This temperature essentially determines the converter collector temperature and the radiator temperature. Maximum thermionic electrical power density and conversion efficiency for a fixed emitter temperature was found as collector temperature is varied. As before, high-power density lowers reactor and shield weight while high conversion efficiency and increased collector temperature lower heat rejection system weight. Evaluation of the optimum coolant temperature requires consideration of the total system. To accomplish this optimization, a simple version of the configuration shown in Fig. 1 was assumed. Trade-offs in reactor, shield, and radiator weights were examined for this configuration as reactor coolant temperature was varied.

Figure 11 presents the weight variation of the major groups of system components and total system specific weight variation for two levels of radiator technology. Light-weight radiators yield a minimum at a collector temperature of about 1000°K while heavier radiators result in a minimum at collector temperatures of about 1075°K. The influence of the decrease in conversion efficiency is seen in the radiator curve which shows an increase above 1150°K. The implications of this result are quite profound in evaluating long-term reactor development program requirements. It is seen that very little is gained by increasing reactor outlet temperature above 1000°K. At this level, ferrous alloy technology can be used as the basis for reactor design. It does not

appear that increases in this temperature could result in significant performance improvements. While it must be recognized that future developments in thermionic technology may alleviate the fall off in conversion efficiency with increasing collector temperatures, extension of heat transfer system technology into the range beyond 1000°K does not appear to be required for the thermionic reactor concept.

REFERENCE DESIGN

The information developed in the reactor parametric studies and in the coolant temperature optimization studies were used to identify a reference reactor design of 3880 kWe capacity. The configurational features of this reactor are:

Number of Fuel Bundles	73	Reactor Vessel Outside Diameter at Active Core, inches	31.3
Number TFEs	1387	Over-All Length to End of Leads, inches	61.4
Design UO ₂ Loading, kg	700	Active Core Length, inches	37
Over-all Diameter at Active Core, inches	40.0	Axial Reflector Length (Lower), inches	4.5
Hexagonal Bundle Pitch, inches	3.04	Axial Reflector Length (Upper), inches	6
Radial Reflector Thickness, inches	4		

Each fuel element has 37 converter cells stacked up in series for a total of 51,319 converters in the entire core. At the upper end of the reactor, space is required for the coolant pipes, structural members, electrical connections and power cables, and the Cs vapor supply system.

The performance parameters of great interest for the reference reactor are:

Emitter Temperature, °K	2,000	Average Cell Efficiency, %	13.8
Collector Temperature, °K	1,075	Electrical Output, Reactor Terminals, MW(e)	3.88
Average Thermionic Output, W/cm ²	9.2	Reactor Outlet Temperature, °K	1,000
Voltage, V	51.4	Reactor Pressure Drop, psi	10
Current, A	75,500		

For this reactor, a converter performance level of 2000°K has been selected in recognition of the important benefits provided in comparison with the minimum emitter temperature of 1828°K considered in the parametric study. The reactor electrical output is 3880 kW at 51.4 V and 75,500 A at the reactor output terminals. The heat production rate in the reactor core is approximately 28,000 kWt.

The weights of various reactor components and the total reactor weight are shown in the adjacent tabulation. The TFEs are the dominant contribution to the reactor weight. This is characteristic of an efficient design since the objective is generally to maximize fuel fraction or maximize emitter area density or some compromise between the two. The reflectors are relatively light primarily because of the very low density of Be.	TFE	5,550
	Core Structure, lb	850
	Reactor Vessel, lb	650
	NaK Coolant Inventory, lb	630
	Control Units, lb	350
	Radial Reflector, lb	1,240
	Axial Reflector, lb	150
	Total Pounds	9,420

CONCLUSIONS

Comprehensive reactor optimization studies were made and included the interactions of geometry, thermal design, hydraulic design, and thermionic performance. The results indicated that the reactor size and weight were established primarily by the electrical power output required and the thermionic performance. The geometric parameters of the reactor, e. g., core length-to-

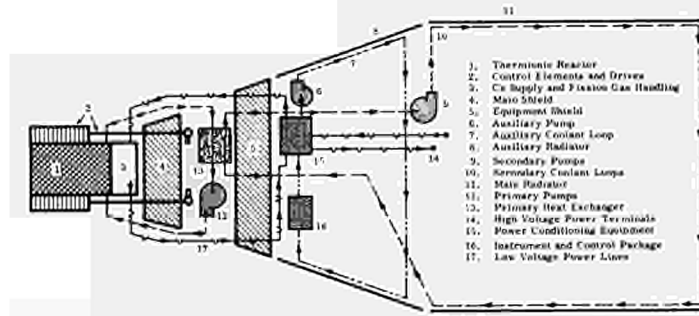
diameter ratio and fuel element bundle size, may be selected on the basis of influences other than those of reactor size and weight. In addition, coolant temperature optimization studies indicate that the benefits of increasing reactor coolant outlet temperature beyond 1000°K are minimal within the limits of present knowledge. This important result permits the consideration of a reactor development program which avoids the problems inherent in high-temperature refractory metal heat-transfer systems.

The temperatures and material of the thermionic converter have been chosen as a result of extensive thermionic development programs for both electrically and nuclearly heated test devices. Liquid metal system conditions and materials have been chosen to remain within the bounds of existing technology. The reactor core design incorporates the structural features required to provide the required mechanical, hydraulic, and nuclear characteristics.

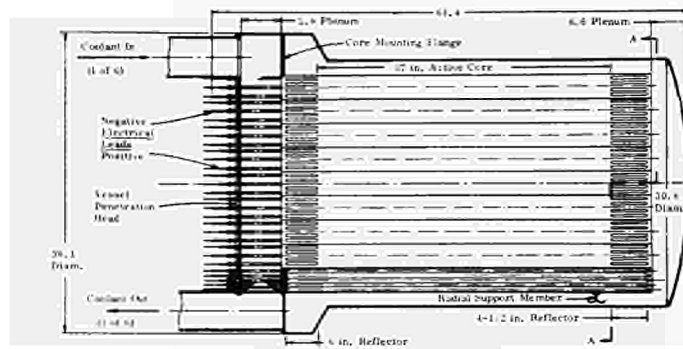
Finally, the weight, size, and efficiency of this reactor represent attractive performance levels. The values presented are believed to be realistic and represent a design which provides for all the reactor requirements that can be recognized at this time. The ability to achieve the level of thermionic performance required has been and can be demonstrated in test devices with confidence. The achievement of this same level of performance in large scale thermionic fuel elements appears to be completely feasible. Accomplishing the degree of power flattening required in the core will present reactor development problems, but no technological barrier to accomplishing the required goal can be identified. The thermionic reactor core with its very high redundancy which results from its incorporation of numerous inherently long-lived thermionic converters should provide a power system of great reliability.

REFERENCES

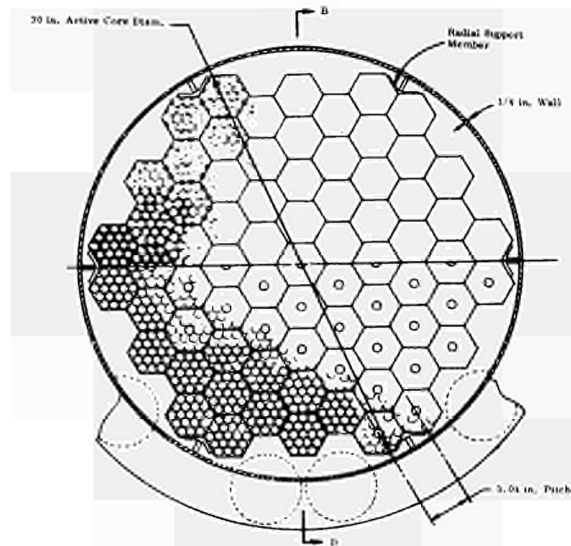
1. Wilson, V. C. , "Second International Conference on Thermionic Electrical Power Generation," Stresa, Italy, May 1968.
2. VanHoomissen, J. E. and Holslag, D. J. , Ibid..
3. Wilkins, D. R. , Sawyer, C. D. , and Hill, P. R. , Ibid.
4. Bondarenko, I. I. , et al. , "Group Constants for Nuclear Reactor Calculations," Consultants Bureau, N. Y. , 1964.
5. Wilson, V. C. and Lawrence, J. , "Operating Characteristics of Two Thermionic Converters Having Rhenium-Nickel and Tungsten-Nickel Electrodes," September 1964.
6. Kunze, J. F. , et al. , Unpublished Data, August 1966, "Thermionic Reactor Critical Experiment Data Report."
7. Wilkins, D. R. , "SIMCON A Digital Computer Program for Computing Thermionic Converter Performance Characteristics," January 1968, Report No. GESR-2109.



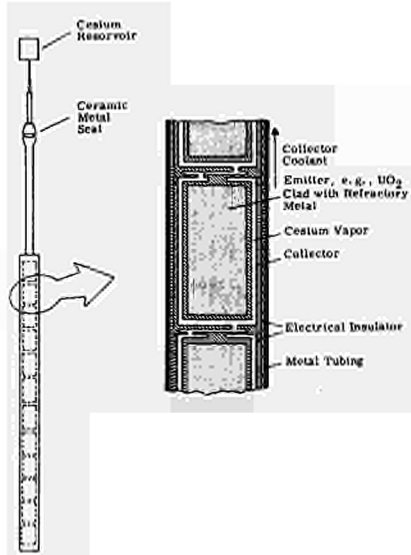
1 Conceptual Component Arrangement For A Thermionic Reactor Power Plant



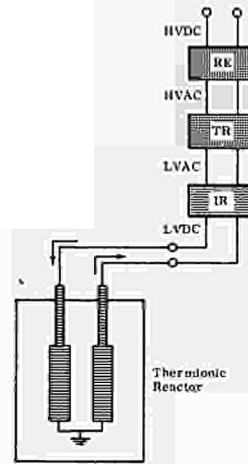
2 Reactor Configuration



3 Bundle Drawing

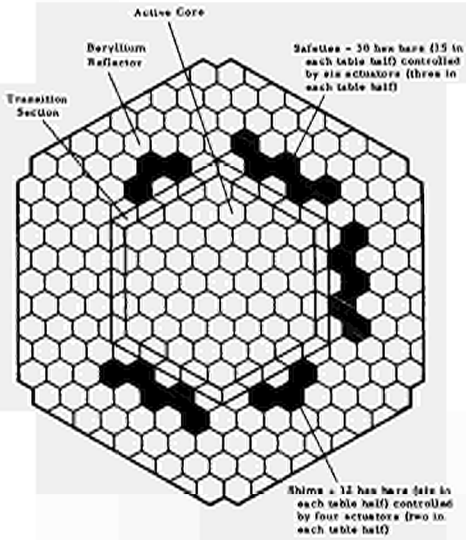


4 Thermionic Fuel Element

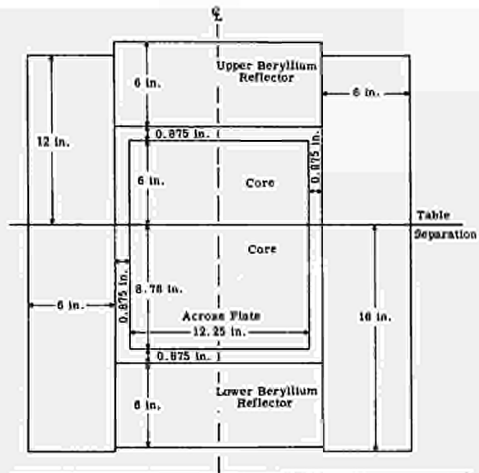


LVDC Low Voltage Direct Current
 LVAC Low Voltage Alternating Current
 HVAC High Voltage Alternating Current
 HVDC High Voltage Direct Current
 IR Inverter Regulator
 TR Transformer
 RE Rectifier

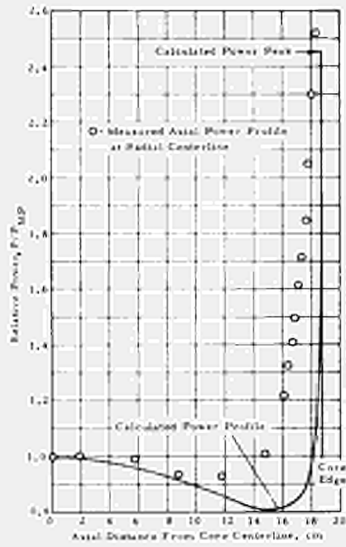
5 Basic Electrical Module



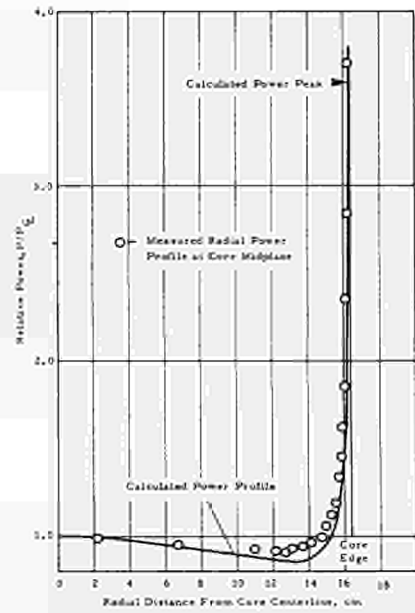
6 TRCE Radial Layout



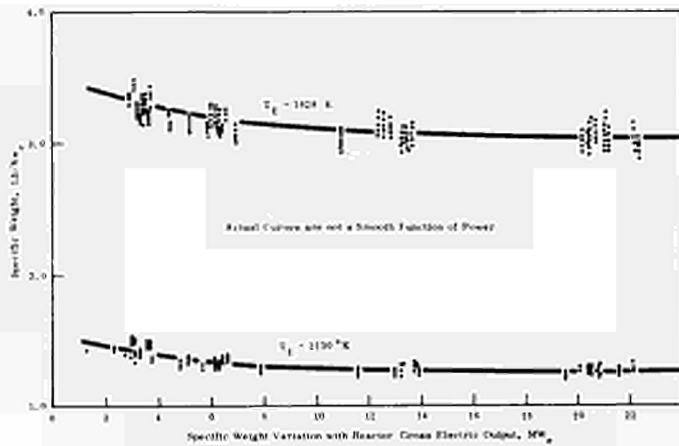
7 Axial Layout of Configuration A



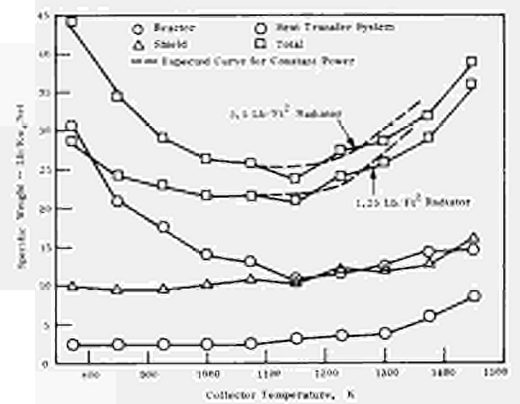
8 Relative Axial Power Profile Configuration A



9 Relative Radial Power Profile Configuration A



10 Specific Weight Variation With Reactor Power



11 Specific Weight Versus Coolant Temperature

DISCUSSION

Speaker of paper B-3: P. R. HILL

PRUSCHECK (Germany):

Did you take a non-uniform heat source distribution into account in your parameter studies?

HILL (USA):

In performing the calculations on this reactor we found that this system had a significant criticality margin and so in order to minimize the cost of this study we assumed that we could in fact distribute UO_2 and flatten the thermal power throughout the core. We did not demonstrate the ability to do that however.

KNOERNSCHILD (Germany):

What is the weight of the power conditioning? At what temperature is the heat of the power conditioner released to the ambient surroundings? What is the voltage entering the power conditioner?

HILL:

We have assumed solid state equipment of the germanium transistor or silicon transistor type and this is typically limited to temperature levels in the range of $100^{\circ}C$, so this is characteristic for that temperature. The voltage of the reactor was approximately 50 Volts.

JANNER (Germany):

What is done in this construction or design to prevent a swelling of the emitter by fuel gas?

HILL:

A number of methods for dealing with this problem have been investigated. I would suggest that we delay the discussion of that subject until Dr. VAN HOOMISSEN's paper in a later session which discusses our in-pile results.

EINFELD (Germany):

What is the reason for locating the power conversion system at the shield plane? Semi-conductors are used and the radiation dose at the shield is higher than at the location of the pay-load. On the other hand the cable weight increases. Has the system been optimized in this respect?

HILL:

Perhaps I was not clear in my explanation of the first slide. The power con-

conditioning equipment was located on the far side of the shield from the reactor, and therefore protected. The length of the leads is an important design parameter, in terms of weight and the electrical losses associated with them. These have been studied on a number of occasions. There is a strong incentive to keep the low voltage cables short.

THERMIONIC ELECTRIC PROPULSION SYSTEM CHARACTERISTICS AND CAPABILITIES*

W. A. Ranken and E. W. Salmi
Los Alamos Scientific Laboratory
University of California
Los Alamos, New Mexico

ABSTRACT

Some of the important parameters influencing the design of a thermionic reactor for use in an electrical propulsion system are available energy content of the reactor fuel form, fast neutron flux level and specific reactor power. The relative importance and interrelationship of these parameters are discussed and conclusions relating to thermionic reactor design criteria are presented. A proposed electric propulsion system utilizing a heat pipe cooled, moderated thermionic reactor in conjunction with an arc jet thruster and a highly redundant heat pipe radiator is described. The performance of this system is compared with that of NERVA for a 456 day manned Mars mission.

I. INTRODUCTION

As progress continues to be made in the exploration of the solar system the missions attempted will become increasingly more difficult. As the difficulty increases the fraction of the starting package which can be delivered to the objective by chemical propulsion vehicles will shrink to such low values as to make the missions prohibitively costly. Solid core nuclear reactors such as NERVA will alleviate this situation to a degree by increasing the available propellant I_{sp} from 400 to 800 sec, but in the long run this increase will not be sufficient and I_{sp} values of 5000 and up will be required. At present, the only feasible means of attaining such high propellant exhaust velocities is by nuclear-electric propulsion. It is the intention of this discussion to show how a beryllium moderated thermionic reactor can form the foundation for a very attractive electric propulsion system. In particular, it will be shown how an array of such reactors, coupled with arc jet thrusters and heat pipe space radiators, can be used to perform a manned Mars landing mission in the same time as can be done for the same mission with "conventional" nuclear propulsion and with considerable savings of initial weight in low earth orbit.

*Work performed under the auspices of the U. S. Atomic Energy Commission.

II. SOME FACTORS INFLUENCING THERMIONIC PROPULSION REACTOR DESIGN

Some of the more important factors influencing thermionic propulsion reactor design are the available energy content of the reactor fuel form, the fast neutron flux level, specific reactor power and the total ^{235}U inventory. Space limitations prevent a detailed treatment of these factors and their inter-relationship, but some often overlooked considerations will be discussed.

The available energy content of the reactor fuel form might be thought to refer to the loss of reactivity caused by ^{235}U burnup. While this effect cannot be neglected it is not likely to be the factor limiting the amount of energy available from the fuel. What will be the limiting factor is the amount of fuel swelling caused by the accumulation of fission gases in the fuel body. While it is true that fuel configurations can be devised which will vent large fractions of the fission gases from the fuel form, it should be recognized that except in the unlikely case that 100% gas release is attained, the problem of high temperature creep of fuel form materials will be alleviated but not removed by venting.

Not nearly enough is known about the behaviour of various fuels and fuel configurations under irradiation to be able to predict what the energy limit for a given fuel is, but certainly it is dependent of fuel temperature, fission power density, desired fuel lifetime, fission gas retention fraction, thermionic emitter diameter, clad thickness, etc. A rough idea of the sort of behaviour to expect can be obtained from Foreman's calculation of the swelling of reactor fuel during irradiation, due to the formation of a uniform distribution of fission gas bubbles.¹ In terms of the tolerable increase in diameter, Δd , of a fueled thermionic emitter (an increase which will give a small probability of shorting out a given thermionic diode) Foreman's result for a given emitter temperature suggests:

$$\Delta d \propto d_0 p^{1.4} t^{1.8}$$

d_0 = initial emitter diameter

p = fission power density in the fuel

t = time

Here Foreman's I_n integral has been approximated in the range of tolerable swelling (a few volume percent) by the relation $I_n \propto (\Delta d/d)^{2.8}$ and n , the power dependence of creep rate on applied stress, has been taken to be 4. This result may be assumed to apply when all the fission gases remain in the fuel and probably applies also when a constant fraction of the fission gases is retained.

The main point to be derived from the above expression is that the energy density which can be derived from a given fuel form is not constant, even for a fixed emitter temperature. The assumption of the constancy of available energy density is frequently made and results in extrapolations such as: if a dimensional increase limited lifetime of 2000 hr is attained for a fueled emitter 1 cm in diameter, then increasing the diameter to 2 cm (and thus halving the fission power density) will double the lifetime. The formula above would predict a relatively inconsequential gain in lifetime and a loss of almost half the energy density available from the fuel. Such a loss would be intolerable because available energy density is the most important parameter in determining how difficult a mission a nuclear-electric propulsion system can accomplish.

Energy density available from the fuel is not the only basic limiting factor in thermionic propulsion reactor design. Of almost equal importance is the question of fast neutron damage. Keilholtz et al.² have shown that Lucalox begins to develop internal microcracks for fast neutron (neutron energy > 1 MeV) doses above 2.3×10^{21} nvt. It is likely that microcrack formation may be accelerated in a cesium atmosphere.³ To be sure, small grain size, high strength alumina such as Coors AD 999 should show better fast neutron irradiation resistance, but a limit will nevertheless exist. Since, for a given neutron spectrum and a given fuel density, the amount of neutron damage will be proportional to the energy density removed from the fuel, the damage limit can be considered as a limitation on the available energy density in the fuel. In this case doubling the emitter diameter will increase the neutron damage limited lifetime by a factor of two. However, it will also increase the specific weight of the system (kg/kWe) - by an amount approaching two for a fast reactor - and will necessarily double the ^{235}U inventory required for a given reactor power output. An alternate way of dealing with the damage limit problem is to introduce moderator into the reactor system to increase the fraction of fissions produced by thermal neutrons and thereby decrease the fast flux in the reactor. Figure 1 consists of some curves developed by Anderson⁴ which show how the introduction of beryllium into a reactor fueled with 100% UO_2 , Mo 60 v/o UO_2 and Mo 40 v/o UO_2 reduces the damage flux when the fission power density in the fuel is held constant. In calculating the damage flux it is assumed that the damage done by a neutron is proportional to its energy. In general the damage flux given in Figs. 1 and 2 is approximately proportional to the flux of fast neutrons with energy greater than 1 MeV, with a proportionality factor that varies from 5.1 to 3.9, as the $\text{Be}/^{235}\text{U}$ atomic ratio

varies from 0 to 150. Although the variation of the proportionality factor is relatively minor, it should not be entirely overlooked. It is in such a direction that the incipient microcracking Keilholtz saw in Lucalox for a fast neutron ($E_n > 1$ MeV) fluence of 2.3×10^{21} nvt (in a water moderated reactor) will occur at a value of 1.7×10^{21} nvt in an unmoderated thermionic reactor.

Anderson⁴ has also calculated the variation of specific mass of a reactor versus damage flux as the latter is reduced by the addition of moderator. This result is shown in Fig. 2. The important consideration here is that increasing the reactor specific weight by a factor of two can, in this case, reduce the damage flux to one-fourth the unmoderated value, with no loss of available energy density from the fuel.

III. PROPOSED THERMIONIC PROPULSION REACTOR CONFIGURATION

The thermionic reactor proposed for the manned Mars landing mission described in Section V is a heat pipe cooled, beryllium moderated array of U-shaped, series-stacked, thermionic fuel rods. Typical construction of the fuel rods is shown in Fig. 3 and the general reactor configuration appears in Fig. 4 with the radiator not drawn to scale. Beryllium was chosen as the moderator because of its high temperature compatibility with liquid sodium and because of the possibility of using it for limited structural support.

The emitters are fueled with a Mo UO₂ cermet. The fuel was selected on the basis of preliminary irradiation tests which indicated that Mo 40 v/o UO₂ would be useful at a thermal power density of 300 W/cc for 5000 hr in an emitter 1.27 cm in diameter. At this power density, the electrical power flux from the emitter is 12 W/cm² (assuming 13% efficiency).

The amount of beryllium required to moderate the reactor was determined on the basis of fast neutron damage considerations. It was assumed that the cell insulators, sheath insulators and ceramic-metal seals could withstand fast neutron exposures of 9×10^{20} nvt at 750°C, and the ratio of Be to ²³⁵U was adjusted until this requirement was fulfilled in a 5000 hr lifetime. The resulting ratio was 100 Be atoms per atom of ²³⁵U. Actually, the results of Keilholtz² indicate the tolerable fast neutron flux limit selection was conservative. However, the most promising available ceramic-metal seal irradiation test results⁵ have been exceeded by a factor of four.

Control of the reactor is achieved by a number of rotating drums placed in the radial reflector. Thermal neutron poison is placed on one side of each drum.

Reactor criticality calculations were made with the DTK program^{6,7} which solves multigroup, angle- and space-dependent neutron transport equations by means of the angular segmentation (S_n) method. The calculations were done with 18 neutron energy groups and the S_4 approximation. Los Alamos group-averaged cross sections⁸ were used. The reflector used in all criticality calculations was 10 cm of beryllium.

Heat pipe cooling of the reactor is very desirable from the standpoint of eliminating the necessity for traditional liquid metal pumps. There are many possible heat pipe configurations which might be used. One of these is sketched in Fig. 4. In calculating reactor criticality the effect of the heat pipes was taken into account by placing a 15% void in the moderator. This is barely sufficient for sodium heat pipes, operating at their ultimate limit at 750°C, to provide the necessary heat removal capability and leaves only a factor of two margin for potassium heat pipes operating at the same temperature.

Power flattening was achieved by two methods. The first of these consisted of varying the volume percentage of UO_2 in the cermet over a range of 26 to 49. This did not prove to be sufficient. A wider variation of UO_2 volume percentage was not utilized because of a ground rule that the fuel composition not vary too much from the tested composition. The method used to flatten the power distribution further was to vary the enrichment of the uranium in the cermet over a range of 51 to 93%. This method has the disadvantage of adding negative reactivity to the system because of the absorption cross section of ^{238}U . The other obvious method of power flattening - that of removing fuel from the center of the fueled emitters - was not attempted because it leads to marked increases of power density in the cermet which could possibly result in an increased fuel swelling rate.

The final power flattened reactor configuration has a power output of 2.6 MWe, a core height of 97.5 cm and core diameter of 98.1 cm. Because ^{235}U was removed to flatten the power distribution, the $Be/^{235}U$ ratio increased from the nominal value of 100 to an average value of 140. The total variation of ^{235}U density required to flatten the initial power distribution was 2.5 to 1. This results in the occurrence of differential fractional burnup. In a 5000 hr lifetime this effect causes the power density ratio to increase from unity to 1.05 as is shown by the dashed line in Fig. 5 where relative power density is plotted as a function of reactor radius. The effect is compounded by the fact that at the start of life the control drums are positioned with

the poison towards the core whereas at the end of 5000 hr the poison will be substantially oriented away from the core. This produces a change in the thermal neutron power density peak in the outer ring of fuel rods so the power density ratio is increased by an additional 13% as is also shown in Fig. 5. While the total end-of-life power density variation of 1.18 is not intolerable it can readily be reduced to 1.09 by designing a 1.09 to 1 imbalance in the start-of-life power distribution which will partially compensate for the effects of burnup and control.

The total weight of the power flattened reactor is 2930 kg of which the core constitutes 1917 kg and the reflector 1013 kg. The mass of ^{235}U is 147 kg. No allowance has been made for weights of cesium reservoirs, electrical and plumbing connections and control rod drives. The weight per unit power of the reactor is 1.11 kg/kWe which is broken down as follows:

Fuel emitters	0.240 kg/kWe
Diode hardware	0.192
Moderator	0.295
Reflector	<u>0.384</u>
Total	1.111 kg/kWe

The moderator represents slightly more than 1/4 of the total reactor weight. It should be recognized that its presence results in a larger reactor core diameter for a given power output vis-a-vis a fast reactor and hence in a larger relative weight per unit power for the reflector.

IV. PROPOSED THERMIONIC PROPULSION SYSTEM

The discussion in the previous section demonstrates that the in-core thermionic reactor concept results in a very lightweight electrical power supply even if considerable leeway is taken in its design. It is important in selecting the other components needed in a propulsion system that this lightweight capability not be compromised. This is the compelling reason for choosing an arc jet with lithium propellant to provide the propulsive power. The arc jet thruster is a low impedance device which gives promise of permitting direct coupling to the thermionic reactor, thereby eliminating the need for power conditioning equipment.

In this study the thruster is assumed to have the capability of accelerating lithium to an I_{sp} of 5000 sec with an efficiency of 75% for an applied

voltage of 120 V. The I_{sp} value appears to be within the capability of present day arc jets but considerable development lies ahead before the values of efficiency and lifetime assumed here are demonstrated.

The radiator envisioned in this study makes use of the heat pipe as the heat transfer mechanism. It can be coupled to the reactor heat pipe system in a header configuration at one end of the reactor and thus eliminate the need for conventional liquid metal pumps. The main advantage of the heat pipe for this application is that each individual unit is in itself a lightweight and inexpensive pumping system. Thus it is possible to use a large number of these units in a highly redundant arrangement which will greatly reduce the armor thickness (and weight) needed to give the required probability of survival against destruction by meteorites. One such redundant arrangement is shown in Fig. 6 where it is demonstrated how a series-parallel configuration of many small heat pipes can be used to by-pass meteorite punctures. This configuration leads to a gradual, and continuously predictable, degradation of the radiator rather than the go-no-go performance of more conventional radiator designs for which an entire pumping circuit can be destroyed by one meteorite puncture.

Figure 7 shows how the reactor, radiator and arc jet thruster can be combined to form a propulsion module. This modular concept has the advantage of allowing considerable flexibility in mission planning and also of eliminating the need for developing different propulsion units for different missions.

V. MANNED MARS MISSION

The manned Mars mission requires several of the reactor-thruster-radiator modules described above. One possible arrangement of the modules is to mount them in a circular array on the order of 75 m in diameter and 50 m to the rear of the command module. In this configuration the neutron and gamma ray shielding associated with the individual reactors is just sufficient to protect the radiation-resistant control rod actuators. The bulk of the shielding for the command module is provided by the 117,000 kg of lithium propellant required for the Mars mission. This arrangement has the obvious drawback that the shielding is used up as the mission progresses. For this reason a separate shield consisting of 18,700 kg of water is placed between the actual control module and the crew living quarters. It is anticipated that during the last 40 days of the mission the crew will have to exist in the rather cramped quarters of the control module.

The weights associated with the various components of the propulsion modules have either been calculated - as in the case of the reactor, radiator, busbars, control rod actuator shield - or estimated. For each module these weights are:

Reactor core	1920 kg
Reactor reflector	1010
Equipment shield	100
Radiator	1740
Controls	80
Busbar	300
Arc jet	90
Lithium tankage and support structure	<u>490</u>
	5730 kg

Since the electric power output per reactor is 2.6 MW and the arc jet efficiency has been assumed to be 75%, the jet power per module is 1.9 MW. This gives a value for the weight per unit power of

$$\alpha = 3.0 \text{ kg/kWe}$$

There is little question but that this value is optimistic. However, the mission analysis results show that a value twice this great is still very favorable.

In order to determine the usefulness of propulsion systems with α values in the range of 3 to 7 kg/kW a series of propulsion requirement calculations was made for a manned Mars landing mission. The mission profile chosen was that described by Chovit et al.⁹ in their determination of propulsion requirements to do the manned Mars mission with nuclear rocket propulsion. The various payload masses used were either the same or larger than those used in the above reference and included the following: crew capsule and earth reentry vehicle, 31,400 kg; capsule shielding, 18,600 kg; and Mars lander, 36,400 kg. The mission time used for comparison purposes was a round trip manned time of 456 days with 20 days on the Mars surface. The nuclear-electric propulsion system was used to go from a 480 km Earth orbit to a 300 km Mars orbit and back to a high Earth orbit. The I_{sp} was taken to be constant at 5000 sec and the interplanetary transfer parts of the mission were accomplished by a propulsion-coast-propulsion cycle.

One point of difference between the NERVA and the electric propulsion mission involved the transfer from a 480 km Earth orbit to a high level Earth

orbit. This requires 40 to 60 days to accomplish with the electric propulsion system and must be unmanned because of the long time spent in the Van Allen belts. It is assumed that the crew will be delivered to the electric propulsion vehicle by a chemical rocket with Saturn V capability when the former has reached the high level orbit. In making the comparison with the NERVA mission the initial masses required in low Earth orbit for the electric propulsion system were increased by 109,000 kg to account for the capability of the extra Saturn V. Trip times were equated on a basis of total manned time.

Mission calculations were made using the formulation of Handlesman et al.¹⁰ for Earth-Mars transfers calculated for co-planar circular orbits. Figure 8 shows the minimum mass in a 480 km Earth orbit required to accomplish the mission plotted as a function of the α value of the power supply. For an α of 6 kg/kW the mission requires four Saturn V launch vehicles, three of which are used to place the electric propulsion system into low Earth orbit with the fourth delivering the crew when the system has reached a high level Earth orbit. For an α value of about 10.5 kg/kW the electric propulsion system requires the same equivalent mass in Earth orbit as is required for the comparable NERVA mission.

Because power supply lifetime is a likely limiting factor in determining mission capability, it is instructive to see how it is affected by α . This is shown in Fig. 9 for the mission profile requiring four Saturn V payloads. The curve shows that reducing α from 6 to 5 kg/kW reduces the required propulsion time from 7500 to 4500 hr.

The effect shown in Fig. 9 is true of electric propulsion missions in general. If mission calculations are made with a view toward reducing propulsion time, the decrease in α required need not be large. Currently there is an overemphasis on developing nuclear-electric power supplies with very long lifetimes. It would appear that a better place to put the emphasis would be on the development of truly lightweight propulsion systems.

REFERENCES

1. FOREMAN, A.J.E., "Calculations of the rate of swelling of gas bubbles in uranium," AERE T/M 134, (1958).
2. KEILHOLTZ, G.W.; MOORE, R. E., "Irradiation damage to aluminum oxide exposed to 5×10^{21} fast neutrons/cm²," Nuc. Appl. 3, (1967) 686.
3. HIGGINS, J.K., "Reaction of alumina with cesium vapour," AERE-R 4781, (1964).
4. ANDERSON, R. C., "Damage flux in critical assemblies," 1967 IEEE Conference Record of the Thermionic Conversion Specialist Conference, (1967) 332.
5. PATRICK, A.J., "Irradiation damage to ceramics, metallic-ceramic bonds, and brazing alloys," LA-3285-MS, (1965).
6. CARLSON, Bengt, "Numerical solution of transient and steady state neutron transport problems," LA-2260 (1959).
7. LEE, C.E., "The discrete S_n approximation to transport theory," LA-2595 (1962).
8. CONNOLLY, L. D., "Los Alamos group-averaged cross sections," LA-2941-MS (1963).
9. CHOVIK, A.R.; KLYSTRA, C.D.; PLEBUCH, R.K., "Defining nuclear rocket performance," Astronaut. Aeron. 3, No. 6 (1965) 36.
10. HANDELSMAN, M.; WALLACK, P.J., "Calculus of variations of two dimensional heliocentric circular orbit transfers," Aeronautical Engineering Report No. 717c 1 & 2, Princeton University, (1965).

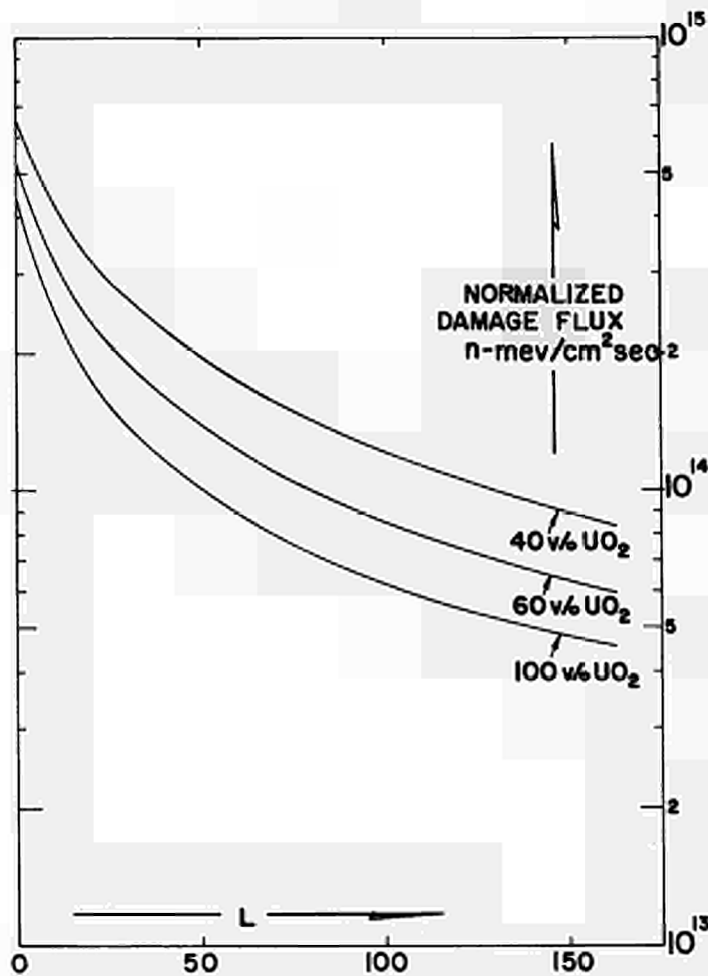


Fig. 1. Fast neutron damage flux versus moderating ratio, $L = (N_{\text{Be}}/N_{235\text{U}})$, for critical assemblies containing 1.27 cm diameter emitter configurations operating at a power density of 300 W/cc and fueled with UO_2 , Mo 60 v/o UO_2 and Mo 40 v/o UO_2 . (Damage flux = 3 to 4 times neutron flux of energy >1 MeV.)

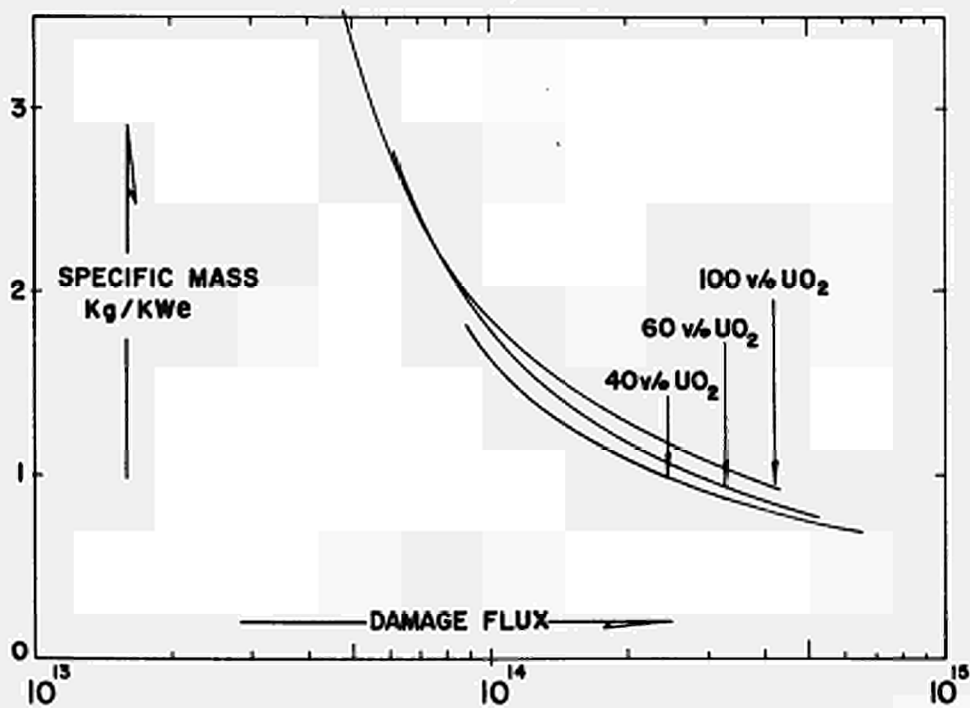


Fig. 2. Specific weight versus fast neutron damage flux for critical assemblies described in Fig. 1.

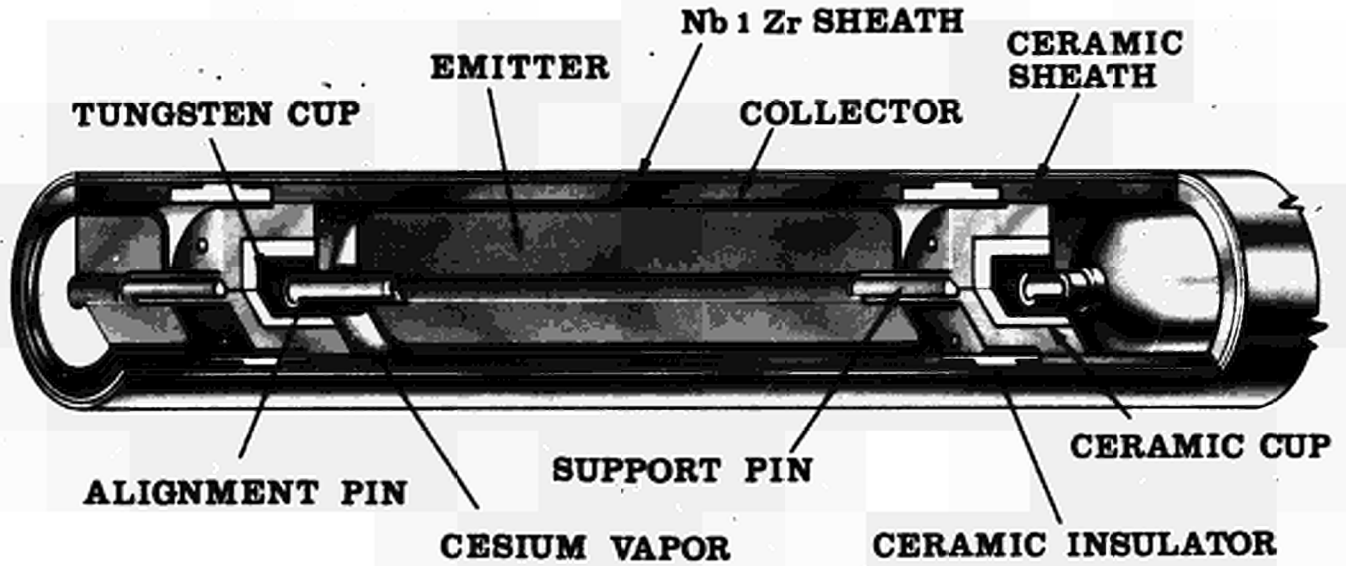


Fig. 3. Cutaway drawing showing section of thermionic fuel rod.

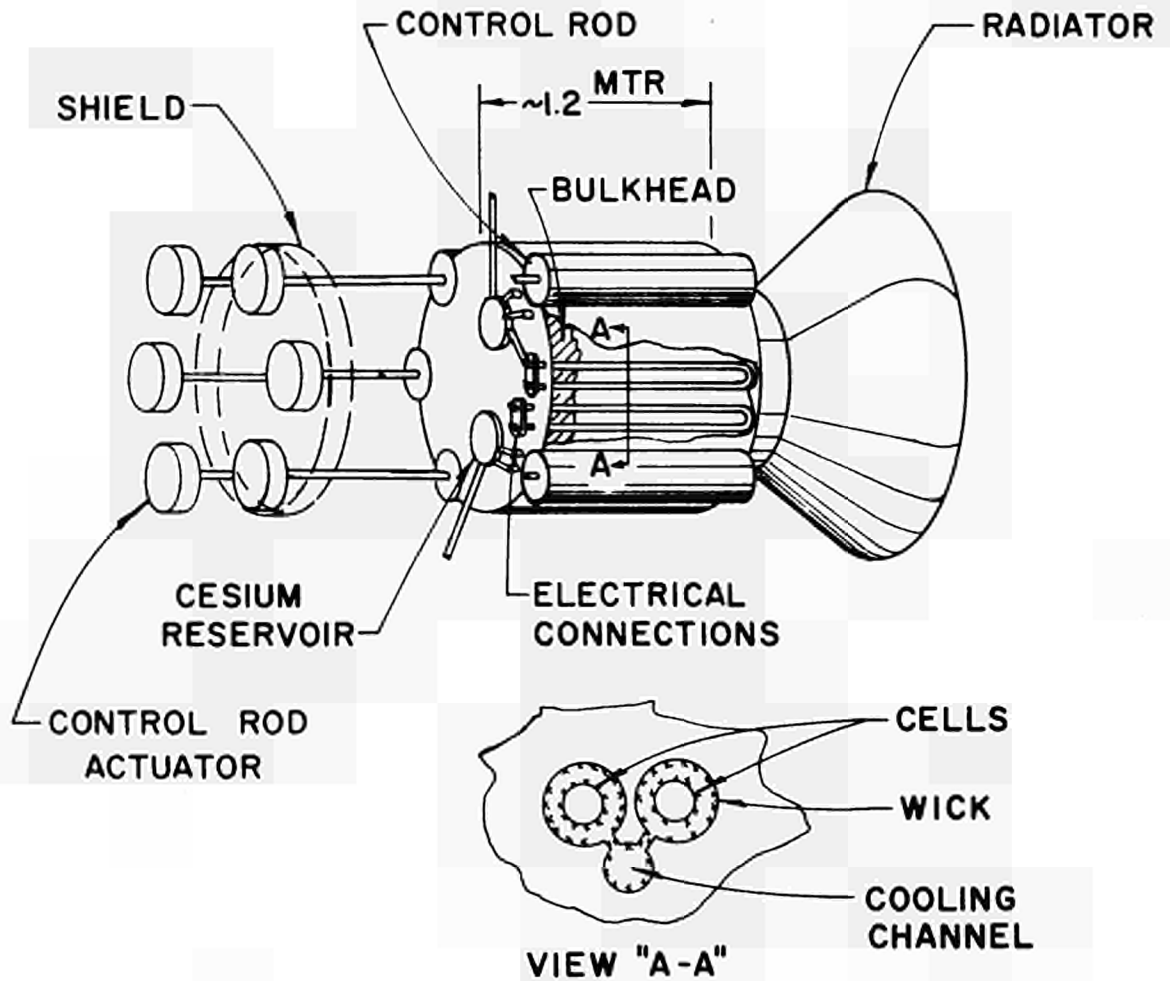


Fig. 4. Sketch of beryllium-moderated thermionic reactor configuration showing possible arrangement of heat pipe cooling channels.

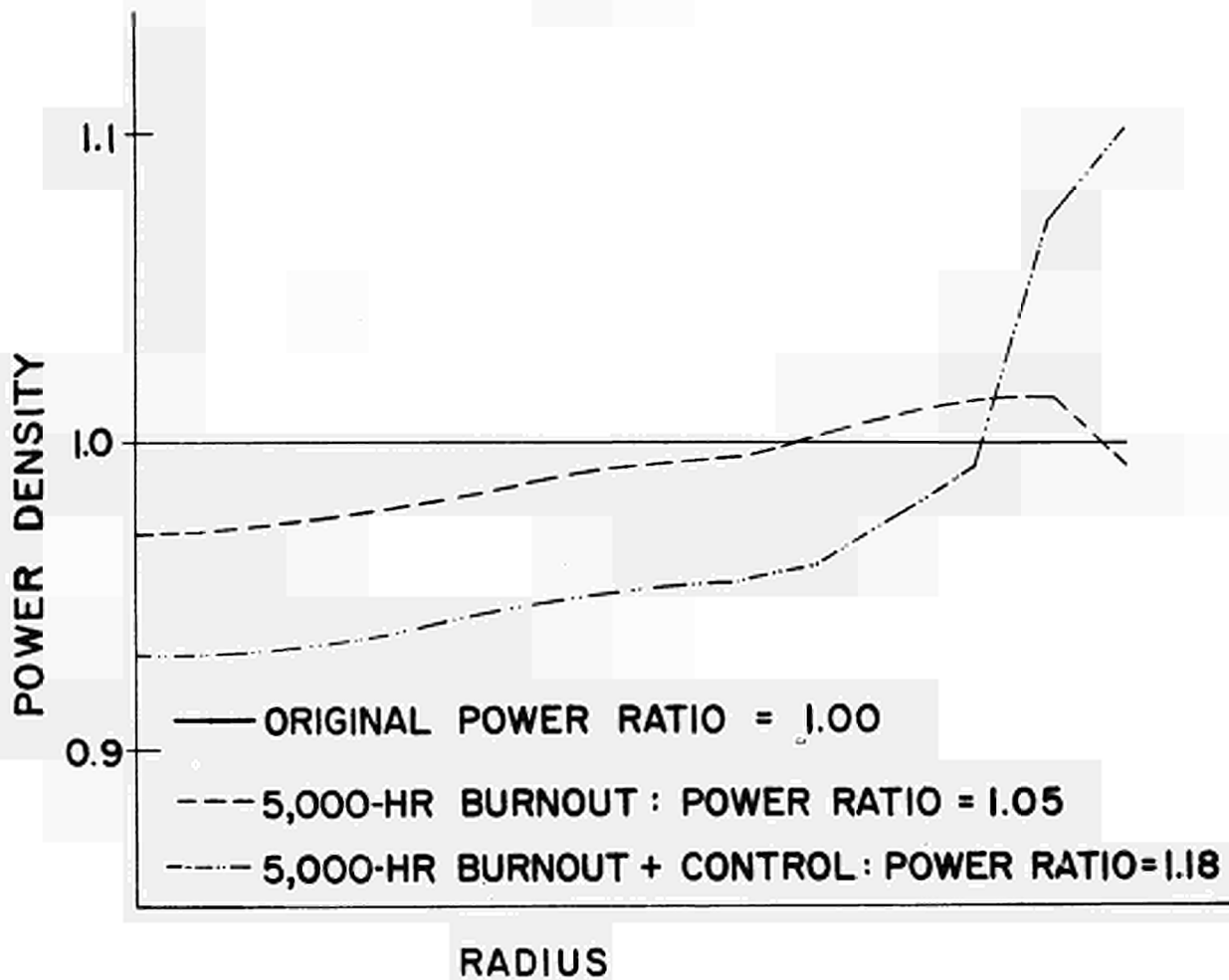


Fig. 5. Curves showing relative fission power density versus reactor radius.

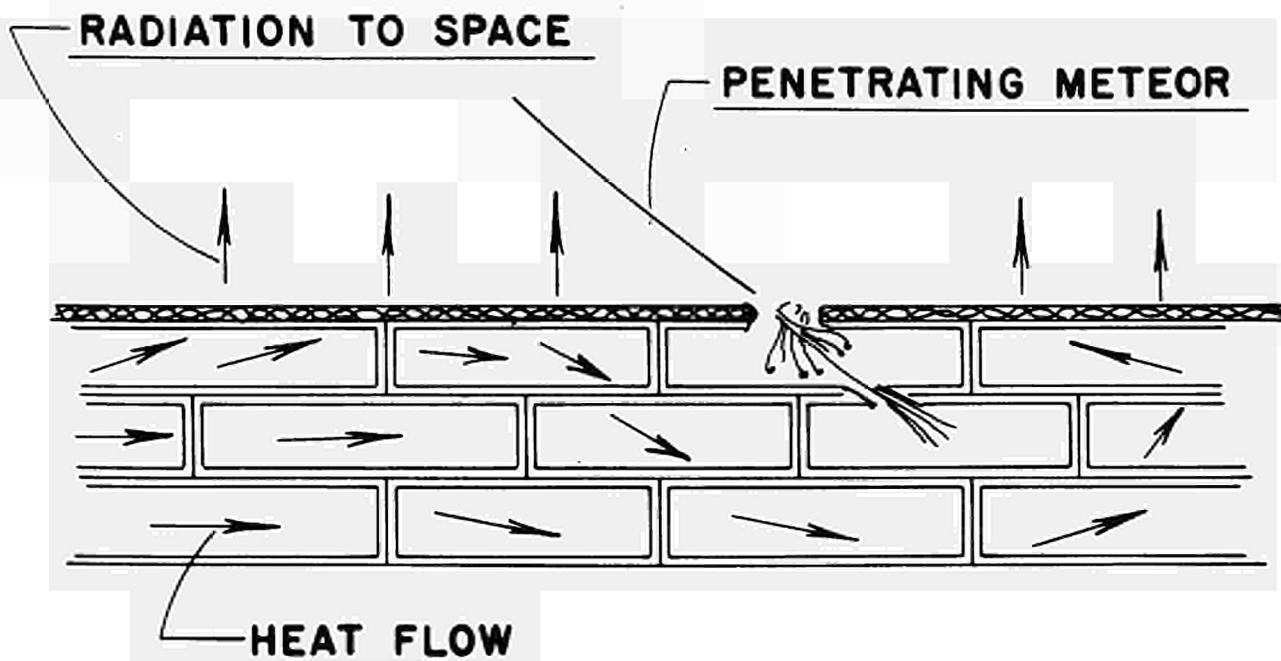


Fig. 6. Section of multi-cellular heat pipe radiator showing by-pass capability of series-parallel arrangement. Required armor thickness for Mars mission is approximately 0.01 cm.

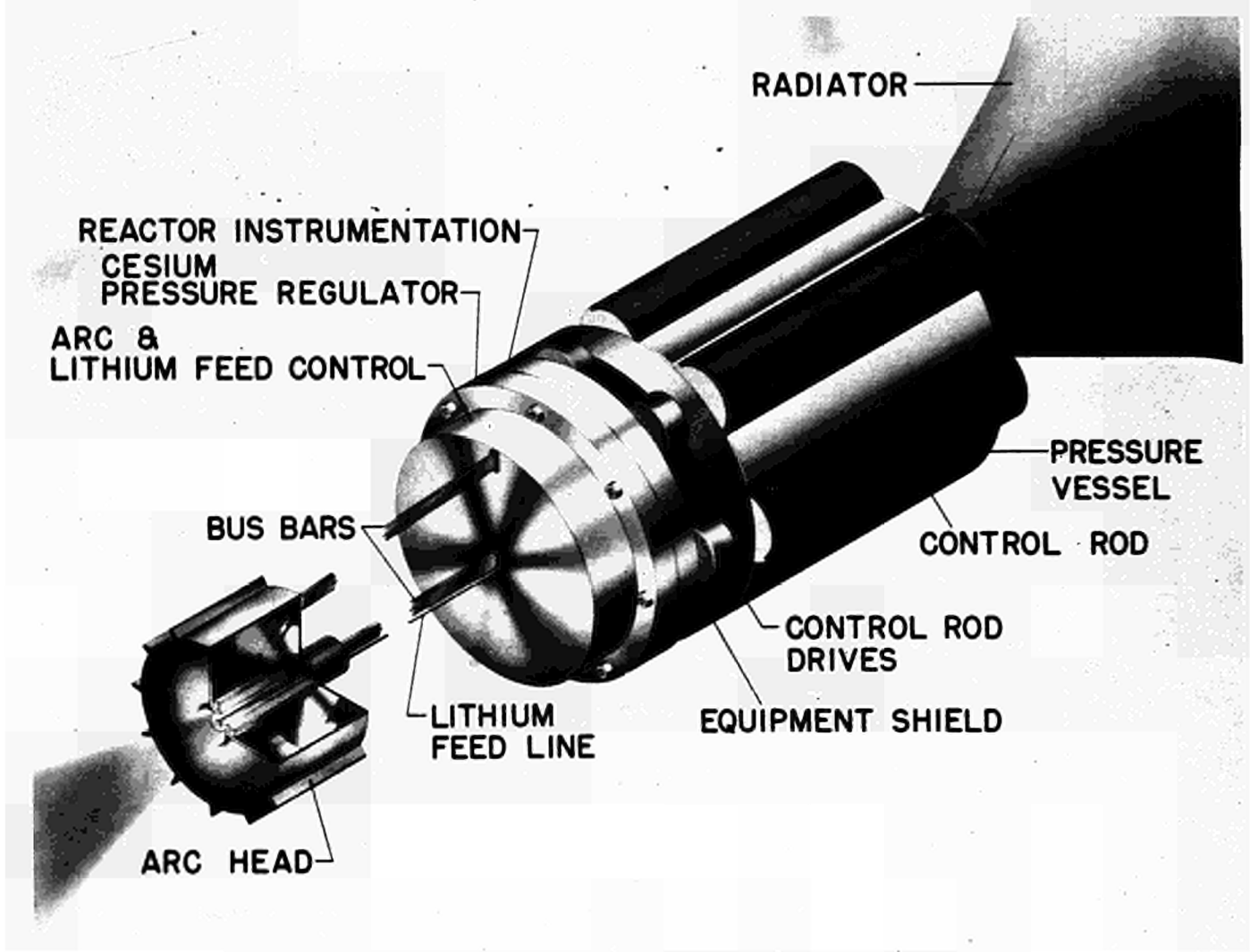


Fig. 7. Illustration of how reactor, radiator and arc jet thruster can be combined to form propulsion module.

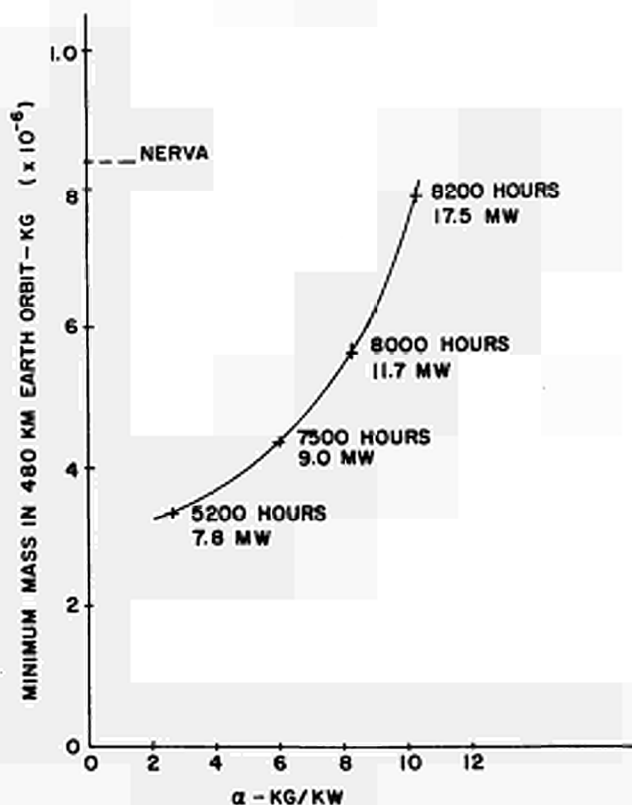


Fig. 8. Minimum mass in 480 km Earth orbit vs α of nuclear-electric propulsion system. Manned mission time = 456 days; payload delivered back to high earth orbit = 50,000 kg; Mars lander mass = 36,400 kg. Saturn V low earth orbit payload of 109,000 kg has been added to electric propulsion system values to account for Saturn V used to deliver crew. Numbers by each calculated point are the total electric power required and the total propulsion time.

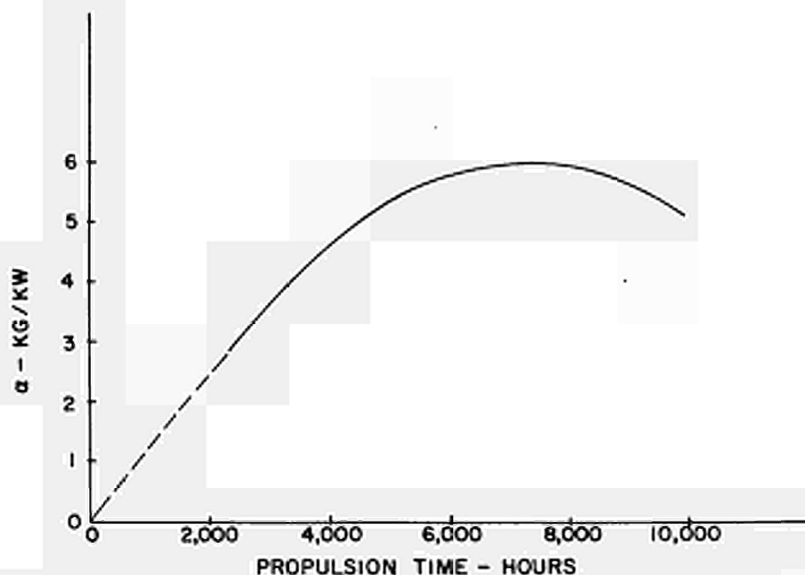


Fig. 9. Required propulsion time versus α for 456 day mission with electric propulsion system requiring four Saturn payloads (327,000 kg in low earth orbit plus 1 crew delivery vehicle).

DISCUSSION

Speaker of paper B-4: W. A. RANKEN

KNOERNSCHILD (Germany):

What is the permissible damage flux that you have taken into consideration for your calculations?

RANKEN (USA):

Based on presently existing experimental data, the permissible damage flux is about 1.7×10^{21} nvt of neutrons with energy greater than 1 MeV. In the reactor design presented here the damage flux predicted for a 5000 h lifetime is approximately 0.7×10^{21} nvt so that damage to the ceramic should not be a problem. However, ceramic-metal seals have not been tested to quite such large fluences. The damage flux numbers in the paper are obtained by integrating neutron flux times energy over the entire neutron spectrum and normalizing by taking the damage done by a 1 MeV neutron to be unity. The damage flux numbers are approximately three times larger than the values for neutron flux above 1 MeV, but the exact ratio depends on the shape of the neutron spectrum.

KNOERNSCHILD:

Did you take into account the difference between the damage flux within the fuel element and the location of the insulators?

RANKEN:

Yes, we did.

THERMIONIC REACTORS FOR ELECTRIC PROPULSION - PARAMETRIC STUDIES*

W. G. Homeyer, C. A. Heath, and A. J. Gietzen
Gulf General Atomic Incorporated
San Diego, California

ABSTRACT

In-core nuclear thermionic power plants consist of a reactor containing thermionic cells, a nuclear radiation shield, a heat rejection system, and electrical transmission lines and power conditioning equipment. The influence of design parameters on size, mass, and reliability is evaluated over a range in power output from tens of kilowatts to several megawatts. Methods of achieving high reliability with a minimum sacrifice in size and mass are described. The importance of the multiplicity of components and their manner of connection is evaluated.

Major parameters of the reactor include the emitter and collector temperatures and electrical power density, the emitter size, the nuclear fuel fraction, and the fissile nuclide. The parameters affecting the shadow-shield mass include the cone angle, the dose rate allowable, and the distance between the reactor and the region to be shielded. For the heat rejection system, the coolant composition, the temperature, and the multiplicity of components (pumped loops and heat pipes) are important factors. Transmission lines are characterized by their composition, temperature and length, and by the voltage output of the reactor. Power conditioning design is based on voltage input and component ratings.

*This work was sponsored by the U.S. Atomic Energy Commission under Contract AT(04-3)-167, Project Agreement 14, and the National Aeronautics and Space Administration under Contract NAS3-6471.

INTRODUCTION

In-core nuclear thermionic power plants consist of a nuclear reactor containing fueled thermionic converters, a nuclear radiation shield, a heat rejection system, and electrical transmission lines and power conditioning equipment. The arrangement of three of these components, the reactor, shield, and heat rejection system is shown in Fig. 1. The radiation shield is a "shadow" shield which protects only the region occupied by the crew from radiation. Located within the shield is a heat exchanger within which heat is transferred from the activated reactor coolant to a secondary coolant which carries heat to the radiator panels. The radiator panels are made up of many heat pipes (Ref. 1) which serve as fins for radiation of heat from the secondary coolant loops. The radiator is located within the shadow of the shield where it cannot scatter nuclear radiation toward the crew. The power conditioning equipment may be either a compact unit located within the radiator and cooled by separate low temperature cooling loops connected to a radiator or may be distributed so as to radiate waste heat directly to space. In the latter case, it would be located to the right of the radiator shown in Fig. 1.

REACTOR

The arrangement assumed for the reactor is shown in Fig. 2, and the dimensions assumed are given in Table 1. The core contains cylindrical thermionic fuel elements and is surrounded by a 10 cm thick BeO neutron reflector. In the radial direction, the fuel elements are characterized by an emitter diameter, by an emitter clad thickness, and by a center-to-center (pitch) spacing. The pitch spacing has been assumed to be 0.5 cm greater than the emitter diameter to allow space for the plasma gap, collector, insulator, sheath, and coolant. In the axial direction the diodes consist of a fueled emitter region and an unfueled region in which no power is generated and where electrical connections between diodes are made. The average density of UO_2 fuel within the emitter cavity was assumed to be no more than 80% of theoretical to allow for fuel zoning to flatten the fission power distribution in the reactor. The electrical power density of 5 W/cm^2 assumed is the average over the core and includes allowances for electrical losses in electrodes and inter-diode connectors.

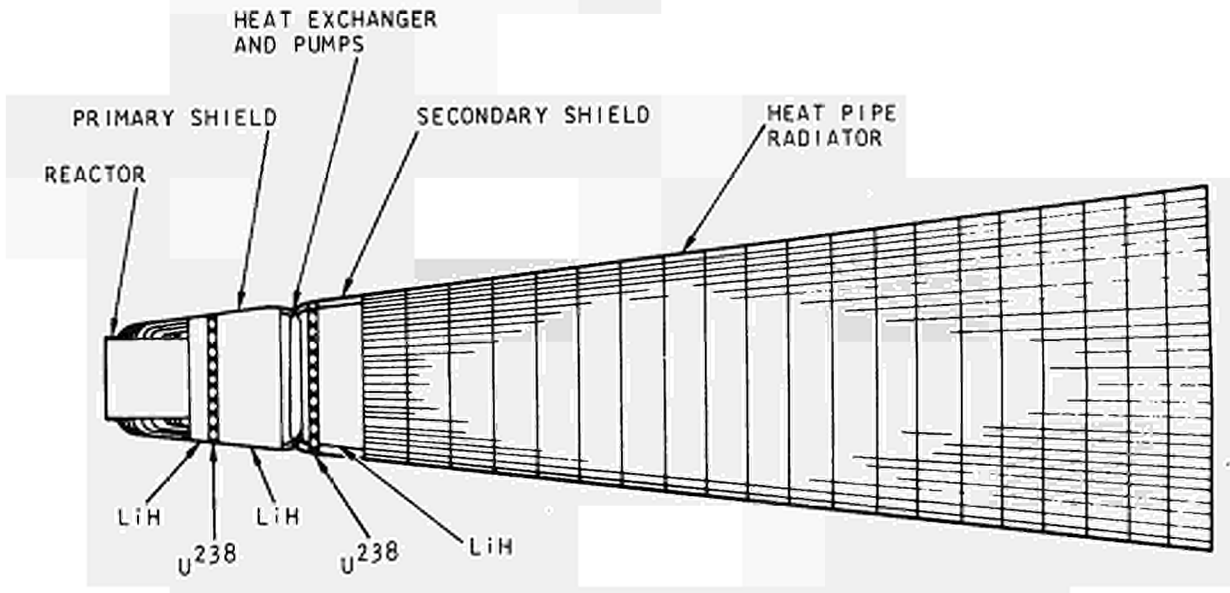


Fig. 1. Schematic of reactor, shield, and radiator

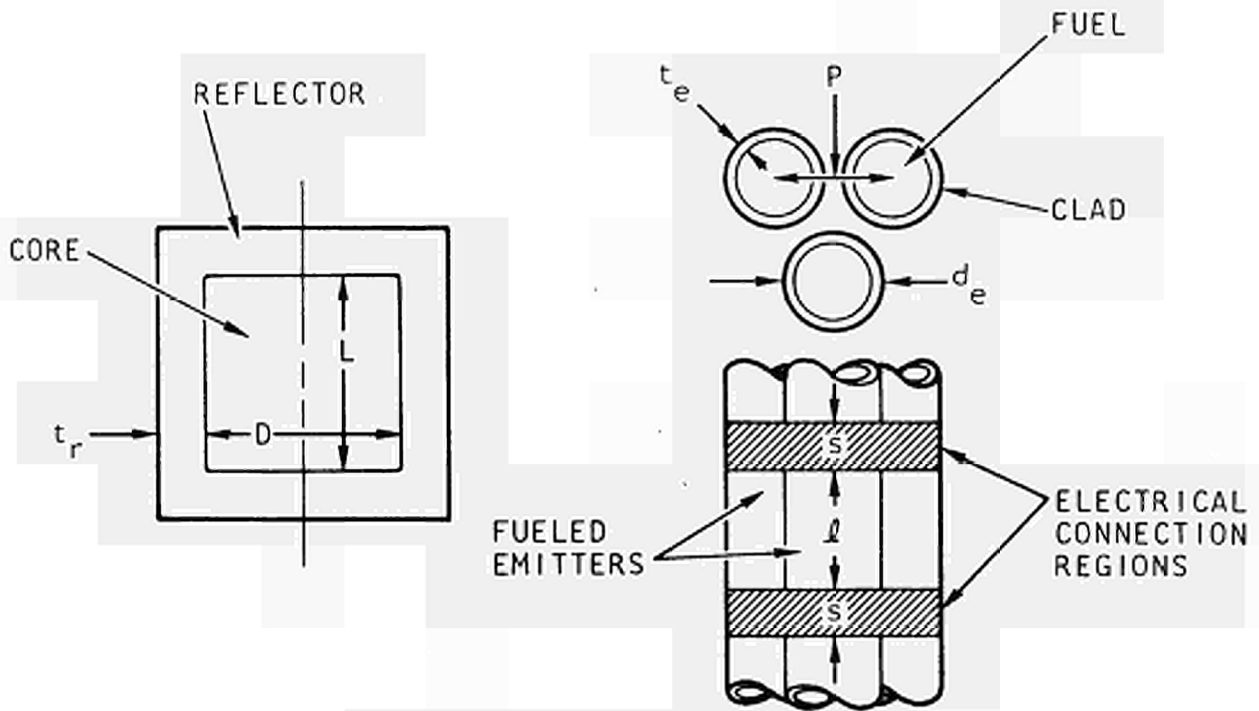


Fig. 2. Reactor and cell schematics

TABLE 1
REACTOR AND CELL DIMENSIONS

Reflector thickness	t_r	10 cm
Core length-to-diameter ratio	L/D	1
Emitter diameter	d_e	1, 2, 3 cm
Pitch spacing of cells	P	1.5, 2.5, 3.5 cm
Emitter clad thickness	t_e	0.1 cm
Length of fueled emitter	l	5 cm
Length of connection region between fueled emitters	s	2 cm
Density of UO_2 fuel		$\leq 80\%$
Average thermionic electrical power density (net)		5 W/cm^2

The variation in the diameter of the thermionic reactor with reactor output power and with emitter diameter is shown in Fig. 3. The UO_2 is assumed to be 93% enriched in U-235. As shown in the figure, the diameter of the reactor can be reduced if lower power output is required, but only to a point at which the criticality limit is reached. At this point, which is indicated by the sharp knee in the curves in Fig. 3, the reactor diameter can no longer be reduced. Lower power levels are reached by lowering the electrical output of the diodes. It is apparent from Fig. 3 that emitters of smaller diameter are advantageous at higher power levels where the size of the reactor is fixed by requirements for electrical output. For lower reactor power levels, where nuclear criticality is a limitation, emitters of larger diameter which have more space for fuel produce a smaller reactor.

The specific mass of the reactor in kg/kWe (kilograms per kilowatt of electrical output) is shown in Fig. 4 as a function of the reactor output power and the emitter diameter. Smaller emitters are shown to produce a lighter reactor at high power levels, but at low power levels, where criticality limits are reached, they result in a much heavier reactor. As in

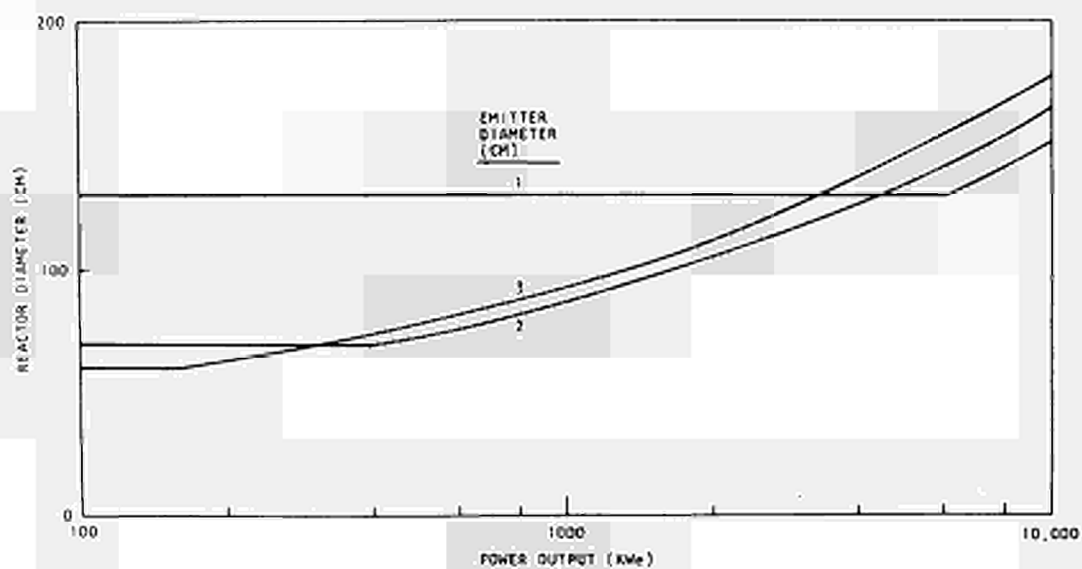


Fig. 3. Reactor diameter and emitter diameter

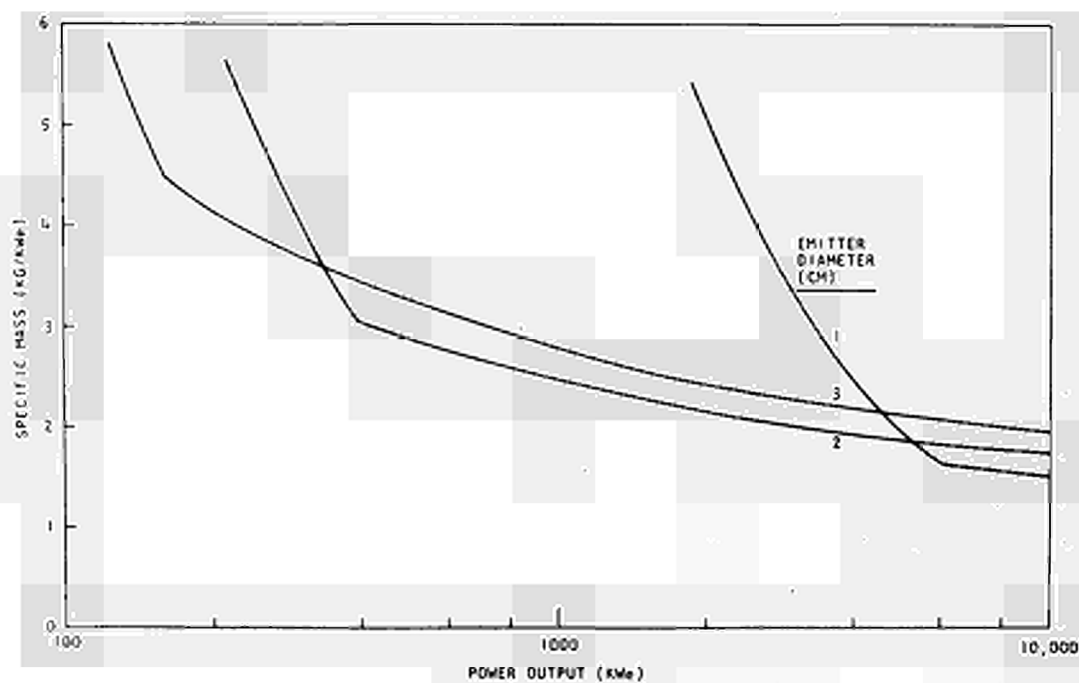


Fig. 4. Specific mass and emitter diameter

the previous figure, the portions of the curves to the left of the knee are criticality limited reactors with electrical output from the diodes reduced below 5 W/cm^2 . Also shown in Fig. 4 is the tendency for large reactors with high power output to have a lower specific mass than low power reactors. This trend results from the mass of the reflector becoming a smaller fraction of the total mass as the size of the reactor is increased.

The specific mass of the reactor is shown in Fig. 5 as a function of the power level of the reactor, and the thermionic electrical power density. The emitter diameter is 2 cm.

Two families of curves are shown, one for U^{233}O_2 fuel, and one for U^{235}O_2 fuel. At the left of each family of curves is the criticality limit for an average fuel density of 80%. As shown here, U^{233}O_2 permits much lighter reactors to be produced for low power levels than does U^{235}O_2 . For higher power levels, above the criticality limit for U^{235}O_2 , the difference in reactor mass between the two fuels at any given thermionic power density is much smaller. This small difference results from the difference in fuel density required for criticality, and does not reflect a difference in size of the reactor. Figure 5 also illustrates the point that very low thermionic electrical power densities may be adequate with certain combinations of emitter diameter, nuclear fuel, and power output requirement from the reactor. If lower thermionic power densities are required, lower emitter temperatures may be employed and conversion efficiencies will be reduced as shown in Table 2.

The number of thermionic cells in the reactor is given in Table 3 for several power levels and emitter diameters. The number of cells in the reactor has an important influence on the reliability of the reactor and on the mass of the electrical transmission lines.

RELIABILITY

The connection of thermionic cells in series-parallel networks to enhance the reliability of electrical power generation has been the subject of considerable study. The effects of open and short circuit failures of cells in an electrical network on the output of the network were

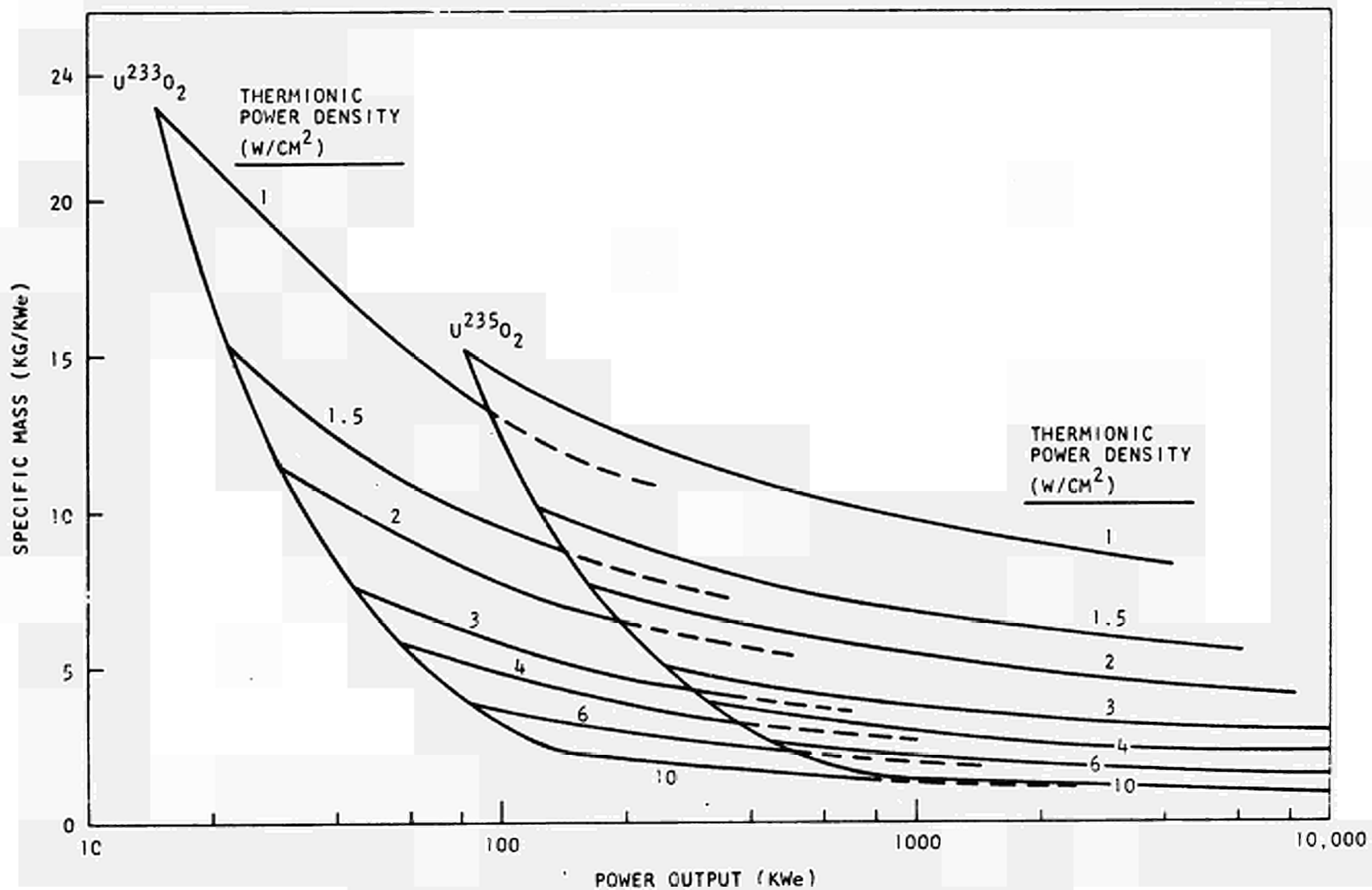


Fig. 5. Specific mass and thermionic power density

TABLE 2

EMITTER TEMPERATURE, POWER DENSITY, AND EFFICIENCY

Thermionic Power Density (W/cm ²)	Emitter Temperature (°K)	Conversion Efficiency (%)
1.0	1550	5.4
1.5	1610	6.4
2.0	1650	7.4
3.0	1720	8.9
4.0	1790	10.0
6.0	1930	11.7
10.0	2180	13.9

TABLE 3

NUMBER OF CELLS IN THE REACTOR

Power Level (kWe)	Number of Cells for Emitter Diameter of		
	1 cm	2 cm	3 cm
100	76,657	2,542	684
200	76,657	2,542	849
500	76,657	3,184	2,123
1,000	76,657	6,367	4,245
2,000	76,657	12,733	8,489
5,000	76,675	31,833	21,222
10,000	127,329	63,665	42,443

studied by Holland (Ref. 2) who concluded that the fraction of power lost was independent of the size and shape of the network and was approximately twice the fraction of cells which failed. This work was extended by Yates (Ref. 3) to the case of short circuits through the coolant system. Here we will discuss only one aspect of this question, the influence of the number of cells on the reliability of an electrical network.

If several cells in an electrical network suffer open circuit failure, the possibility arises that the failures will be so located as to cause an open circuit of the entire network. The reliability of a network to escape this type of failure is shown in Fig. 6 as a function of the number of diodes in series and the number in parallel. In this case the probability of open circuit failure of a cell was assumed to be 0.05. As shown here, the open circuit reliability is extremely sensitive to the number of cells in parallel but relatively insensitive to the number in series. Increasing the number of cells in parallel from 3 to 4, for example, reduces the probability of an open circuit failure of the network by more than a factor of 10.

A second type of network failure which may occur results from failure of a sufficient number of cells to cause the power output of the network to drop below the minimum allowable level. This type of failure can be prevented by designing the network with an initial power capacity which includes excess or redundant power to offset losses resulting from cell failures. The addition of a large quantity of redundant power, however, increases the size and weight of the power plant. The quantity of excess power required depends upon the reliability of the individual diodes, upon the number of diodes, and upon the reliability required for the network. The relationship between power redundancy, network reliability, and the number of diodes is shown in Fig. 7 for the case where the diode reliability is 0.9. This reliability, which was selected arbitrarily, might correspond, for example, to an open circuit probability of 0.05 and a short circuit probability of 0.05. As shown in the figure, the reliability of the network to maintain minimum power can always be increased by increasing the quantity of redundant power, regardless of the number of cells. The additional power required to produce a given increment in reliability is

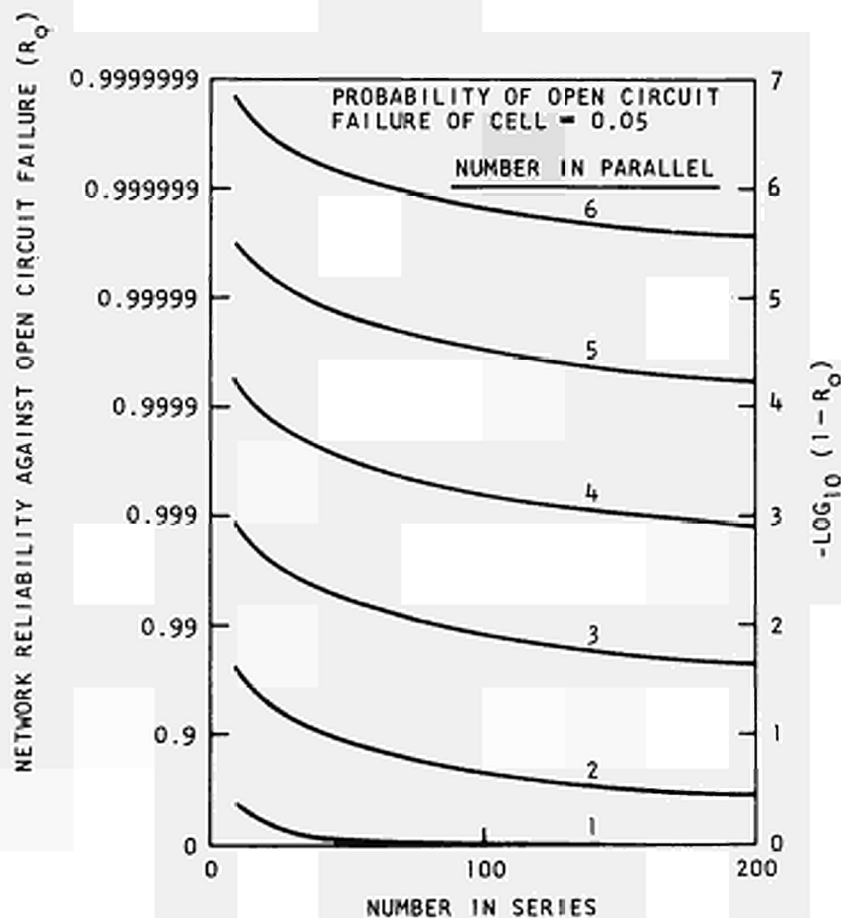


Fig. 6. Reliability against open circuit for various network sizes and shapes

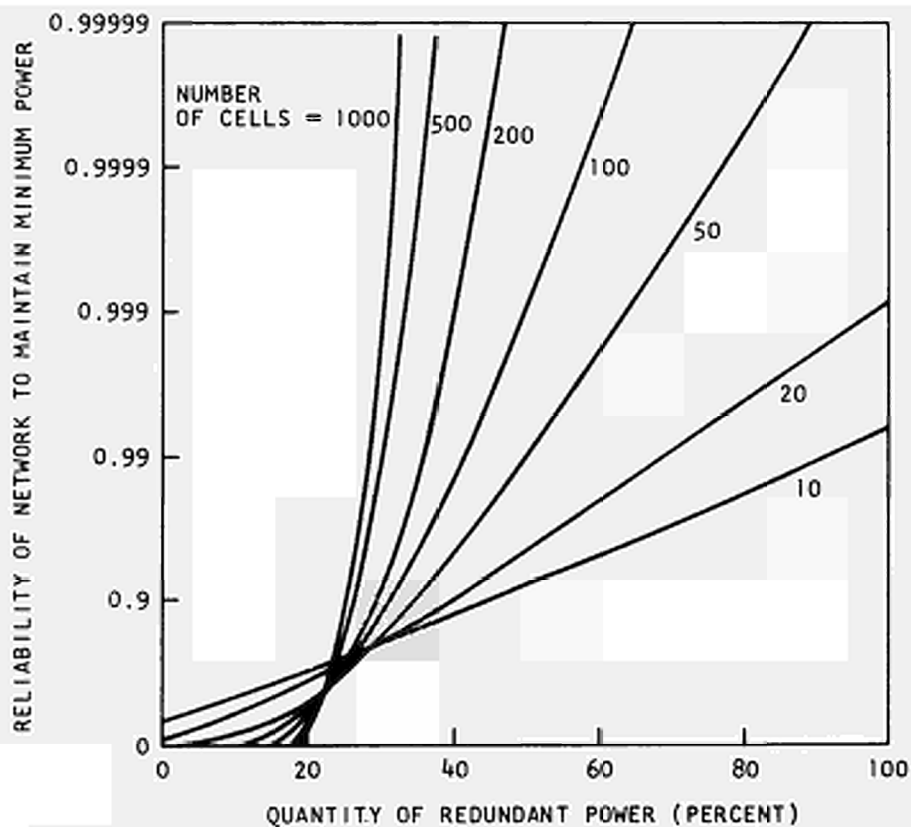


Fig. 7. Network reliability as a function of number of cells and quantity of redundant power

much greater, however, for networks with fewer cells. A network reliability of 0.99, for example, can be obtained with less than 30% redundant power if there are 1000 cells, but requires nearly 100% redundant power if there are only 10 cells. This difference results from the increased statistical predictability of larger numbers. All of the curves are observed to cross between 20 and 25% redundant power. This is near the most probable power loss for 90% reliable cells in a network where fractional power losses are about twice the fraction of cells which fail. Figure 7 shows that very high network reliabilities can be achieved with a small quantity of redundant power if the networks are large. Comparison of Table 3 with Fig. 7 indicates that the number of cells is sufficiently large, even at 100 kWe, for the redundancy requirement to be small.

RADIATION SHIELDING

The radiation shields consist of layers of lithium hydride to attenuate neutrons and depleted uranium to attenuate gamma rays as shown in Fig. 1. The primary shield attenuates radiation from the reactor and protects the secondary coolant from activation. The secondary shield attenuates gamma radiation from the activated primary coolant in the heat exchanger and further attenuates radiation emitted from the reactor.

The mass of the radiation shield is influenced by the size of the reactor, the angle of the cone protected by the shield, and the dose rate to which radiation levels are to be reduced at a given distance from the reactor. Figure 8 shows the variation in specific mass of the shield with the electrical power output of the reactor and the central angle or half angle of the shielded cone. Also shown here in tabular form are the influences of the distance from the reactor and the dose rate to which radiation levels at this distance are to be reduced. The curves show a rapid decrease in the specific mass of the reactor as the electrical power level is increased. The sensitivity of the shield mass to cone angle is also shown. Increasing the half angle of the shadow cone from 5 to 15 degrees more than doubles the mass of the shield. The dose rate and separation distance have much less influence on the mass of the radiation shield.

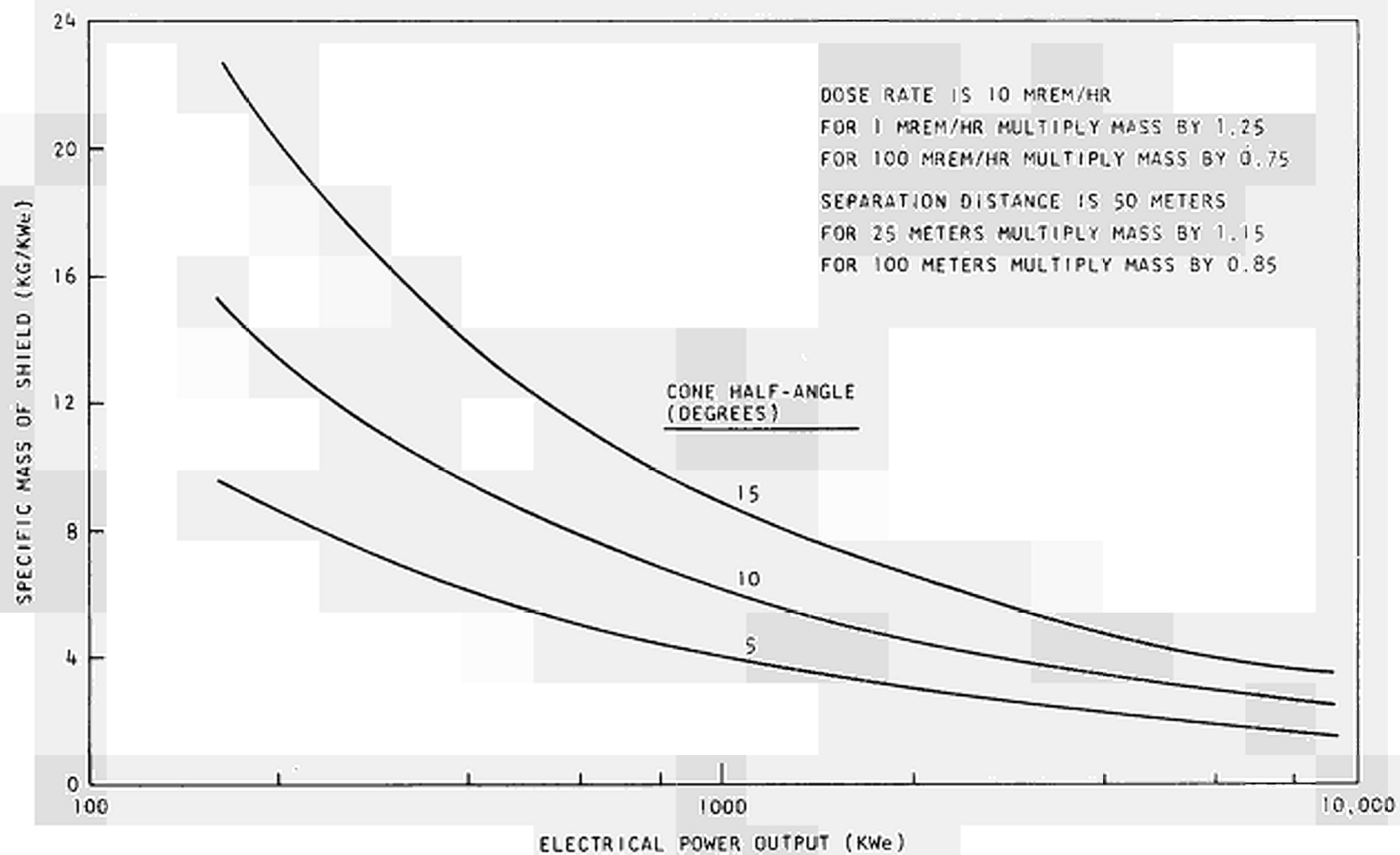


Fig. 8. Shield mass

HEAT REJECTION

The arrangement of the heat rejection system is illustrated in Fig. 1. A compact heat exchanger is used to transfer heat from the primary coolant to the secondary coolant. The secondary loops distribute the heat to the radiator panels which make up the surface of the radiator. These panels are composed of many heat pipes which serve as highly efficient fins to increase the effective radiating surface area.

One question of particular interest is the influence of the collector or coolant temperature on the mass of the heat rejection system. Higher temperatures increase the radiant heat flux and reduce the radiator area, but increase the wall thicknesses required due to the loss in strength of structural materials and the increase in fluid pressure within the heat pipes. In addition, the efficiency of thermionic energy conversion varies with collector temperature, passing through a maximum in the vicinity of 1000°K . The net effect of these factors is shown in Fig. 9. The specific mass of the heat rejection system is shown to pass through a broad minimum at a collector temperature of about 1080°K . The mass of the reactor, shield, and heat rejection system combined is minimum at a lower collector temperature, 1050°K , and remains within 10% of the minimum over the interval between 950 and 1150°K . Results shown in Fig. 9 are for a 300 kWe power plant, but the location of the minimum is relatively insensitive to the power level.

The heat pipe fins in the radiator make up more than half of the mass of the heat rejection system. The multiplicity of these heat pipes was varied to determine if there was an optimum. As shown in Fig. 10, the mass of the heat rejection system decreases continuously as the multiplicity of heat pipes increases. This advantage of smaller, more multiple heat pipes results from structural factors and meteoroid survival requirements. The lengths of the walls of smaller heat pipes are shorter, and the area they expose to meteoroids in space is less. Both factors allow the walls of small heat pipes to be made thinner with equivalent material stresses and meteoroid survival probabilities.

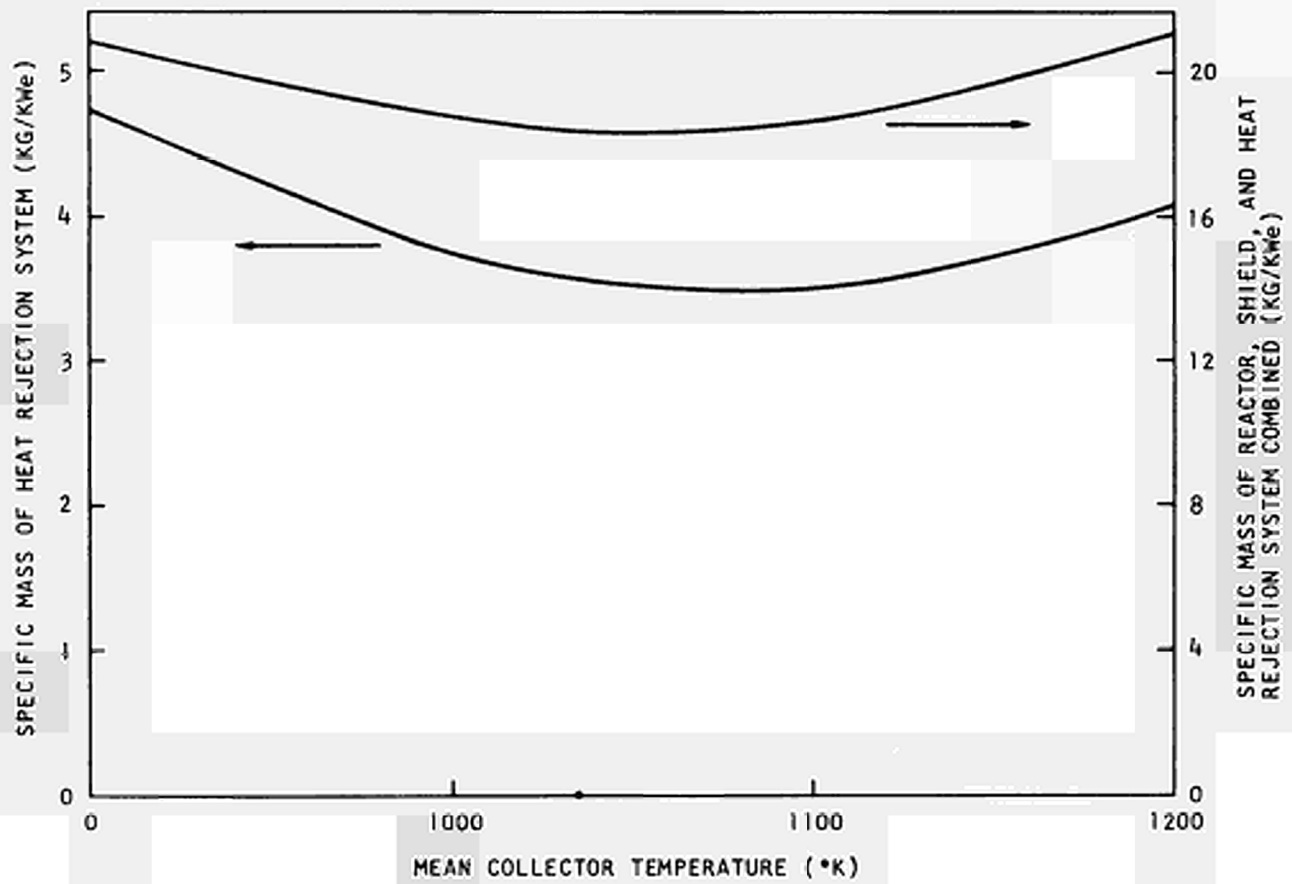


Fig. 9. Heat rejection system mass and collector temperature

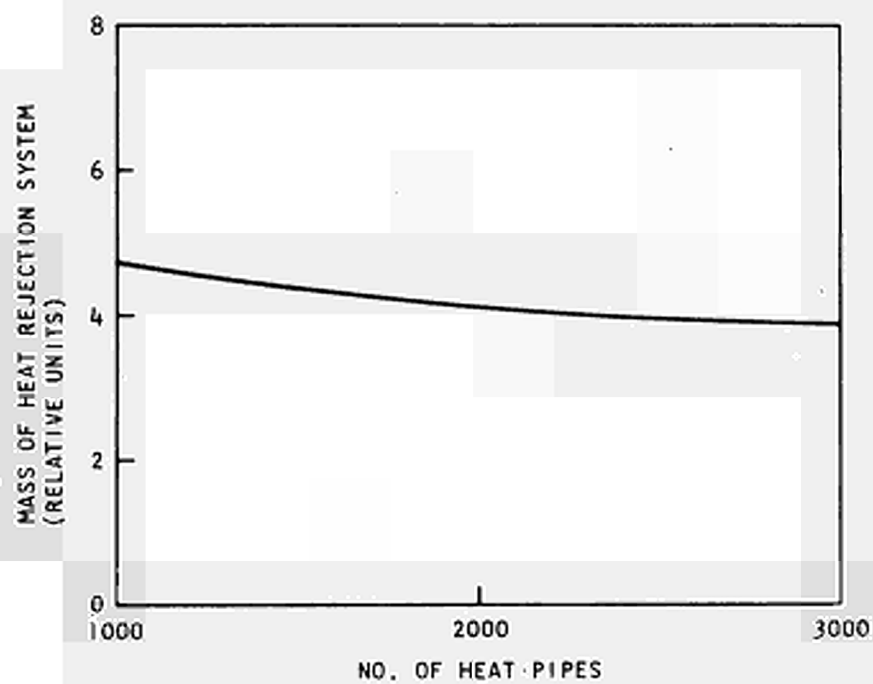


Fig. 10. Variation of mass of heat rejection system with heat pipe multiplicity

TRANSMISSION LINES

Transmission lines are required to carry the current output from the reactor to the power conditioning equipment and back to the reactor. The mass of these lines is proportional to their length, cross sectional area, and density, while the electrical losses in the lines are proportional to their length and resistivity and depend also on their cross sectional area and current. If the additional mass of reactor, shield, and heat rejection system necessary to produce an increment of power is known, the cross sectional area of the transmission lines can be optimized for minimum total mass of the power plant. Characteristics of such optimized transmission lines are given in Table 4 for an incremental mass-to-power ratio of 10 kg/kWe. The specific mass of the lines is given as a function of the output voltage of the reactor and the total length (to and from the reactor) of the lines. Also shown here is the variation in the mass of an optimized transmission line with operating temperature (due to differences in resistivity) and the variation with material at the same operating temperature (due to differences in density and resistivity). As indicated in the table, the specific mass of the transmission lines varies directly with their length and inversely with the voltage output of the reactor. Low transmission line temperatures are advantageous if the lines can be readily cooled below the reactor and radiator temperatures. Lithium, aluminum, and beryllium can provide lighter transmission lines than copper because their high resistivity is more than offset by their low density. Only the specific mass of the lines is given in Table 4, but other quantities of interest can be derived from these numbers easily. The percentage of the reactor output power lost in the lines is ten times the numbers in Table 4; e.g., 4% of the power output of a reactor with a 50 volt output is lost in optimized transmission lines 10 meters long. The additional mass of power plant required to produce the power dissipated in the lines is equal to the mass of the lines, so the total mass penalty for power transmission is approximately twice the numbers given in Table 4.

TABLE 4

TRANSMISSION LINE PENALTIES

Length (meters)	Specific Mass of Transmission Lines* (kg/kWe)		
	50 Volts	100 Volts	200 Volts
10	0.4	0.2	0.1
20	0.9	0.4	0.2
50	2.1	1.1	0.5
100	4.3	2.1	1.0

* Copper at 873°K

Variation with Temperature

<u>T (°K)</u>	<u>Relative Mass</u>
673	0.88
873	1
1073	1.13

Variation with Material at 873°K

<u>Material</u>	<u>Relative Mass</u>
Lithium	0.63
Aluminum (673°K)	0.66
Beryllium	0.88
Copper	1

POWER CONDITIONING EQUIPMENT

Power conditioning equipment for electric propulsion by ion engines transforms most of the reactor output power from low voltage dc to high voltage (3 to 4 kilovolts) dc. Design studies of power conditioning equipment employing present day solid state components have indicated that modules with 90% efficiency radiating their waste heat directly to space from their chassis can be constructed with a specific mass of 2 kg/kWe. These modules employ highly multiple components and include redundant components to provide high reliability.

SUMMARY

As shown in the previous sections, the masses of the power plant components depend on a number of parameters. An arbitrary but consistent set of assumptions was made to permit an overall comparison to be made. This is given in Table 5. The specific mass of the power plant is shown to vary from 35.1 kg/kWe at 100 kWe to 10.7 kg/kWe at 10,000 kWe. This variation in specific mass is due primarily to the radiation shield and reactor. The specific masses of the other components are relatively constant over this power range, with the specific mass of the heat rejection system actually increasing with power level. At 100 kWe the shield is 64% of the total mass of the power plant and the reactor 21%, while at 10,000 kWe the heat rejection system has become the dominant factor, contributing 35% to the total mass.

Comparison of Table 3 with Fig. 7 shows that a network reliability of 0.999 or higher can be achieved with a small quantity of redundant power (~ 30% for 0.9 reliable cells). Comparison of Table 3 with Fig. 6 indicates that a voltage output of 100 volts or more can be obtained from the reactor even at 100 kWe without compromising the reliability of the network.* Figure 10 indicates that a large number of heat pipes can be used in the radiator to increase reliability with no sacrifice in mass of the heat rejection system.

*There are more than 680 cells in the 100 kWe reactor (Table 3) and 4 cells in parallel are adequate for an open circuit reliability of 0.999 (Fig. 6). Thus the number of cells in series is 170, which results in an output of 102 volts at 0.6 volts per cell.

TABLE 5

SUMMARY

Component	Specific Mass (kg/kWe) at a Power Level of						
	100 kWe	200 kWe	500 kWe	1000 kWe	2000 kWe	5000 kWe	10,000 kWe
Reactor	7.3	4.2	2.9	2.5	2.2	1.9	1.6
Shield	22.5	15.0	9.5	6.5	4.5	3.5	2.5
Heat rejection system	3.1	3.2	3.3	3.4	3.5	3.6	3.8
Transmission lines	0.2	0.2	0.2	0.2	0.3	0.6	0.8
Power conditioning	2.0	2.0	2.0	2.0	2.0	2.0	2.0
Total power plant	35.1	24.6	17.9	14.6	12.5	11.6	10.7

Assumptions

Emitter diameter of 1, 2, or 3 cm chosen to produce smallest reactor with U-235 and a power density of 5 W/cm^2 .

Shield cone half angle of 10° , dose rate of 10 mrem/hr, separation distance of 50 meters.

Collector temperature optimized.

Voltage output as large as possible but ≤ 400 volts.

Power conditioning located on far side of radiator from reactor.

REFERENCES

- (1) GROVER, G.M.; COTTER, T. P.; ERICKSON, G. F., "Structures of Very High Thermal Conductance", J. Appl. Phys. 35, 1990 (1964).
- (2) HOLLAND, J. W., "Thermionic Reactor Reliability", International Conference on Thermionic Electrical Power Generation Proceedings, London, England, September 20-24, 1965.
- (3) YATES, M. K., "Influence of the Relative Probability of Converter Failure Modes on Thermionic Reactor Design", Thermionic Conversion Specialist Conference Proceedings, Houston, Texas, November 3-4, 1966, p. 430.

DISCUSSION

Speaker of paper B-5: W. G. HOMEYER

SCHOCK (USA):

What were the dimensions of the radiator heat pipes?

HOMEYER (USA):

The heat pipe diameter is variable and on the order of 0.5 to 1.0 cm.

The length is about 10 cm. Heat is carried from the heat exchanger within the shield to the array of heat pipes in the radiator by forced convection loops.

KNOERNSCHILD (Germany):

Why do you show the conservative values of 5 to 10 Watts/cm². This morning's session indicated that future projects may use 20-30 Watts/cm², and your work is directed to future applications?

HOMEYER:

Such power densities as 30 Watts/cm² are generally obtained at high current densities, and may be difficult to achieve when electrode and lead losses are considered.

HCWARD (USA):

I think the papers this morning had lead losses associated with them, but I think the spacing of many of those converters was much smaller than the spacing that you are talking about. Most of those results were with 2 mil spacing, but they were not electrode power densities, they were terminal power densities.

EXTERNAL-FUEL THERMIONIC REACTORS*

By

M. J. Abbate, C. L. Eisen, B. Raab, A. Schock
Republic Aviation Division of Fairchild Hiller Corporation
Farmingdale, New York

Abstract

The concept of the external-fuel thermionic converter, in which the fuel surrounds an inner emitter annulus, is introduced and the major advantages of its use in a thermionic reactor are discussed. In-core reactors, ranging from 15-ekW to megawatts, can be designed based on external-fuel converter modules of fixed emitter and collector dimensions. Sizes and weights of typical reactors in this power range are shown.

Introduction

Most in-core thermionic reactor designs are based on internally fueled cells, i. e., the nuclear fuel is contained within a surrounding cylindrical emitter. At Republic Aviation, we have been experimenting with converters and analyzing reactor designs based on externally fueled cells, with the fuel surrounding an inner emitter annulus. The collector-coolant tube is positioned within the emitter. Figure 1 illustrates the cell configuration in cross section. The emitter and collector dimensions can remain fixed for a wide range of reactor power levels; only the fuel thickness and number of cells are changed to satisfy the nuclear and electric constraints for reactors of widely varying electric output.

Among the advantages arising from the external fuel configuration are fuel ventability, low fuel temperature drop, easy power and temperature flattening, low open-circuit temperature rise, simple coolant channel geometry, and high fuel volume fraction.

The inherently high fuel volume fraction capability of the configuration makes it practical to design external-fuel reactors bridging the spectrum from approximately 15-ekW to megawatts.

The externally fueled configuration also permits the design of very long diodes without excessive ohmic loss in the electrodes, a fact which permits a single (double-ended) converter to extend the full length of the reactor core. As

* Research supported by the U. S. Atomic Energy Commission

will be seen, this concept permits elimination of the high voltage insulator from the reactor core, where fast neutron damage might seriously degrade its physical properties with time. *

The internal cooling feature also lends itself readily to the use of a heat pipe for collector cooling, as well as to flow-through liquid metal or even water cooling, if this should be desirable, e. g. , in laboratory testing.

These advantages will be discussed in greater detail in the following section. This will be followed by a description of the size and weight characteristics of a family of reactors based on the full-length external-fuel concept, with heat pipe cooling. Sample radiator and shield weights are also calculated based on nominal input values of radiator specific weight and shield thicknesses and locations.

Summary of Advantages of External Fuel Design

1. Venting of Fission Products

At thermionic fuel temperatures venting of fission products may be necessary to prevent fuel swelling. The external-fuel configuration permits venting directly into the inter-diode space and thence to space or to a storage condenser.

2. Testing of Fueled Diodes

To maximize the reliability of a thermionic reactor, each converter module will have to be thoroughly tested prior to assembly of the reactor core. It is clearly desirable to conduct these performance tests out-of-pile, by electrical heating, since in-pile testing does not readily lend itself to a routine checkout procedure for large numbers of converters, and also requires subsequent assembly of radioactive modules.

* Based on a conception of J. P. Davis of Jet Propulsion Laboratory, Propulsion Research & Advanced Concepts Section.

With the external-fuel configuration, electrically-heated testing of the complete, fueled converters can be readily accomplished by radiofrequency induction. Figure 2 shows a full-length converter under test by rf-heating. *

3. Power and Temperature Flattening

Since thermionic performance is a very sensitive function of emitter temperature, thermionic reactors require a much higher degree of temperature flattening than conventional reactors. To achieve this, internally-fueled designs usually postulate power flattening by compositional variation. In the external-fuel design, flattening can be readily achieved geometrically by varying the fuel volume associated with each diode, since this can be done without changing diode dimensions or performance. As a result, power flattening can be attained with a uniform fuel composition. In addition, the use of full-length converters makes it possible to shape the axial heat generation profile to compensate for heat loss to the emitter leads.

4. Fuel Temperature Drop

Fuel temperature drop is the difference between emitter temperature and maximum fuel temperature. Under certain design conditions for internally fueled cells (large cell diameter or ceramic oxide fuel) this can be excessively high, leading to a design compromise between maximum fuel centerline temperature and emitter temperature. In any practical design, particularly where the fuel is to be vented, the maximum fuel temperature must be limited in order to reduce its volatility and enhance its chemical and mechanical stability.

For given values of fuel thermal conductivity, emitter heat flux, and fuel volume fraction, the fuel temperature drop in the externally fueled design is only

* Experimental development supported by U. S. National Aeronautics and Space Administration.

40-50% of that in the internally fueled design. This advantage, which can be demonstrated mathematically, arises simply due to the geometric re-arrangement of heat flow path, since the heat flows radially inward rather than outward.

5. Open-Circuit Temperature Rise

In efficient thermionic converters, electron cooling accounts for a major fraction ($> 50\%$) of the emitter heat flux. Under these conditions, open-circuit failure (e.g., loss of cesium) of an internally fueled diode can lead to an emitter temperature rise of several hundred degrees. Such temperature excursions of a given fuel-emitter subassembly may result in fuel melting and eventual failure propagation.

In the external-fuel diode, the open-circuit temperature rise is substantially reduced by an additional cooling mechanism not available in the internal-fuel designs, i. e., heat transfer to adjacent fuel elements. Radiative heat transfer between the fuel elements is sufficient to limit the open-circuit temperature rise to about $\frac{1}{3}$ of the corresponding value of the internally fueled design. Moreover, an additional reduction of the open-circuit temperature rise can be achieved by providing thermal contact or noble gas atmosphere between adjacent fuel elements.

6. Cell Length

In general, a maximum possible cell length is desired in order to minimize the number of cells which must be series-connected over the height of the reactor core. This is desirable in order to keep unfueled volume to a minimum, to reduce complexity in design and assembly, and to minimize the effect of emitter temperature non-uniformity due to heat conduction in the emitter lead.

The limitation on cell length arises from the build-up of ohmic losses in the electrodes of the diode itself as its length is increased. This not only consumes useful power, but causes different parts of the diode to operate at different voltage points on the I-V characteristic, thereby further degrading power output.

Ohmic losses can be minimized by increasing the thickness (cross-sectional area) of the electrodes, particularly the emitter electrode. In internal-fuel designs, the cross-sectional area of the emitter can be raised either by decreasing its inner diameter, which leads to an undesirable reduction in fuel volume fraction, or by increasing its outer diameter and hence its circumference, which raises the diode current per unit length and diminishes the resultant reduction in ohmic loss. In the external-fuel configuration, by contrast, increasing the emitter and/or fuel thickness does not affect the emitter surface area. Therefore, the electrical conductance can be increased without simultaneously raising the diode current, thus obtaining the full benefit in ohmic loss reduction. As a result, for a given fuel volume fraction and power density, the optimum length for external-fuel diodes is greater than that for internal-fuel diodes, which makes it practical to design and operate a single (double-ended) converter which extends over the full length of the reactor core. The full-length module introduces several advantages of its own:

- a) Ceramic seals and leads are located beyond the ends of the reactor core.
- b) Fuel-emitter thermal expansion contributes to reactor stability.
- c) A high voltage insulator is not needed within the reactor core.

This last advantage can be realized either if a non-conductive coolant is used, if a separate liquid metal loop is used to cool each parallel group of modules, or if heat pipes are used for cooling. The parametric study results presented in the

next section are based on heat pipe cooling, although use of the other cooling options yield similar results.

7. Fuel Volume Fraction

Because the fuel is the outermost element, with the largest cross-sectional area, the external-fuel cell will tend to have the largest fuel volume per cell when compared with the internal-fuel cells of similar volumetric power density.

A high fuel volume fraction is especially important in low power systems since these are usually criticality limited. Our studies have shown that the external-fuel configuration permits practical designs with fuel volume fractions of over 80% by the use of full-length diodes, and volume fractions of more than 65% with stacked diodes. Thus, criticality can be achieved in extremely small reflected core volumes since such cores are virtually homogeneous blocks of fuel pierced by a number of small holes containing converters. This makes it possible to design an in-core thermionic reactor with fewer than 20 converter modules, which would produce 10-to-15-ekW.

Higher power reactors are not so clearly limited by criticality requirements. However, the high fuel-volume fraction possible with the external-fuel design results in an enhanced capability for power flattening by fuel distribution, and also permits a wide latitude in choice of fuel itself, either as to isotope (U-233, U-235), composition, enrichment, diluent fraction (e. g. , high metal-fraction cermets), or the possible addition of resonance absorbers to enhance stability by increasing the fuel Doppler coefficient.

Heat-Pipe Cooled System

The simple cylindrical coolant channel realized in the external-fuel design makes it practical to consider the use of heat pipes for collector cooling (Figure 3). In order to keep the heat pipe diameter small and thereby limit the core volume devoted to the coolant space, the effective length of each pipe is minimized by introducing a liquid metal heat exchanger at each end of the reactor. The condenser ends of the pipe extend into the heat exchanger tubes and are cooled by a cross-flowing liquid metal (e. g. , NaK). In this design option, the high voltage insulator is in the heat exchanger section where fast neutron flux is considerably reduced.

The designs were based on an axial heat transfer limit imposed by the vapor flow speed. Although vapor speeds approaching Mach 1 have been achieved in high-performance heat pipes, ⁽¹⁾ the designs were conservatively based on a limiting vapor speed of Mach 0.3.

In order to permit a broad survey of large numbers of design variables to see how these effect reactor size and weight, a computer program (PASER) was constructed which optimizes converter electrode dimensions to minimize overall system weight. In any one calculation diode length is specified so that the optimization in effect produces the minimum core diameter consistent with the specified output electric power and number of converters. Diode length and number of converters are then varied in discrete steps for given output electric power, thereby covering the complete range of system variables at the disposal of the designer.

In order to permit the analysis of a large number of cases a number of simplifying assumptions were made in the PASER program:

1. Critical size was assumed to be a function only of fuel volume fraction; the variations in volume fractions of the non-fuel materials were assumed to be of secondary importance.
2. A large number of one-dimensional 26-group neutron transport calculations were run to determine radial and axial reflector savings and geometrical buckling for the necessary range of fuel volume fractions, with other materials being represented in typical volume fractions. These calculations were then correlated and used to determine critical core size in the parametric survey calculations.
3. Emitter temperature was taken to be constant over the length of the diode and emitter lead was optimized for maximum efficiency.
4. The diode current-voltage characteristic was taken to be a straight line tangent to the point of maximum power.

With these assumptions, converter internal losses are accurately taken into account both as to ohmic dissipation and as to variations in local voltage along the length of the converter. The program then proceeds to optimize emitter diameter, emitter thickness and collector thickness for minimum system weight. Both radiator weight and shield weight are calculated based on the following assumptions:

$$\text{Radiator specific weight} = 1.15 \text{ kg/m}^2 \text{ (2 lb/ft}^2\text{)}$$

$$\text{Radiator emissivity} = 0.84$$

Shields: 5.08 cm tungsten

96.4 cm LiH

Shielded angle = 15 degrees

Among the more significant results of the survey is the finding that, at least for systems in the submegawatt power range, optimum converter length is in the range of 20-to-25 cm. It was also seen that decreasing the emitter diameter of the converter (and hence the power per converter) and increasing the number of converters invariably resulted in a decrease in overall system size and weight.

These findings are illustrated in Figure 4 for the 360-ekW system. It can be seen that for emitter diameters greater than 1.15 cm , a converter approximately 23 cm in active length is optimum. This optimum is a broad one; the weight penalty paid for a 20cm converter length for a fixed total number of converters is less than 1 percent.

Converters of approximately 1.25 cm in emitter diameter and 20 cm in length have been built and successfully tested in the laboratory; however, for conservativeness in mechanical design the reference designs selected at the various power levels are based on converters with emitter diameters in the range of 1.5 to 1.75 cm. The results for systems ranging from 15 to 3600 ekW are shown in Table 1.

It should be noted that all of the systems could be designed with modules of identical size; this would merely result in slightly off-nominal output power at each power level.

More exact design calculations done at the 360-ekW power level, which take into account the actual emitter temperature distribution and true converter current-voltage characteristic as well as more precise nuclear calculations indicate that the PASER calculations result in an underestimate of system size and weight by some 3-to-6 %. From Figure 4 it can be seen that this can be compensated by a decrease in emitter diameter to the range of 1.2 to 1.3 cm , if desired.

Conclusions

External-fuel thermionic reactors are seen to offer a number of design advantages over the more common internal-fuel designs. Static design calculations

illustrate the extreme flexibility of the concept in satisfying a wide range of power requirements without variation in converter design. This makes it practical to build and prove the feasibility of an in-core thermionic reactor at a modest power level and to confidently extrapolate the experience so gained to larger, more costly, systems.

References

- (1) KEMME, J. , "High Performance Heat Pipes," Thermionic Conversion Specialist Conference, Palo Alto, California, 1967.

Table 1. PASER-Calculated Reference Designs -- Heat Pipe Cooled Systems

Output Power (ekW)	15	30	60	360	1200	1800	3600
No. of Diodes	18	36	90	468	1386	2106	4920
Active Diode Length (cm)	20.3	20.3	20.3	22.9	22.9	22.9	22.9
Emitter Diameter(cm)	1.74	1.74	1.50	1.62	1.75	1.74	1.57
Heat Pipe ID (cm)	0.980	0.980	0.890	0.955	1.00	1.07	0.935
Power Per Diode (watts)	833	832	666	769	865	854	731
Net Efficiency(%)	11.1	11.1	11.0	10.9	11.0	11.0	10.9
Fuel Volume Fraction	0.813	0.720	0.629	0.397	0.33	0.319	0.307
Core Diameter (cm)	22.1	25.1	29.7	57.1	100	122	167
Core Volume (cu. M)	0.0079	0.010	0.014	0.059	0.18	0.27	0.50
Uranium Inventory(kg)	50	58	71	190	483	6884	1231
Core Mass (kg)	74	97	132	524	1721	2512	4615
Reactor Mass (kg)	322	383	477	1376	3677	5196	9194
Shield Mass (kg)	569	624	708	1378	2720	3571	5755
Radiator Mass (kg)	24	49	99	593	1994	2996	6059
Total Mass (kg)	915	1056	1284	3347	8393	11764	21008
Burn-up(a/o per yr.)	0.105	0.185	0.308	0.710	0.862	0.914	1.08
Volts	3.6	7.2	18.0	47.0	70	108	123

Emitter Temperature = 2000°K
 Collector Temperature = 1000°K
 Cesium Reservoir Temperature = 620°K

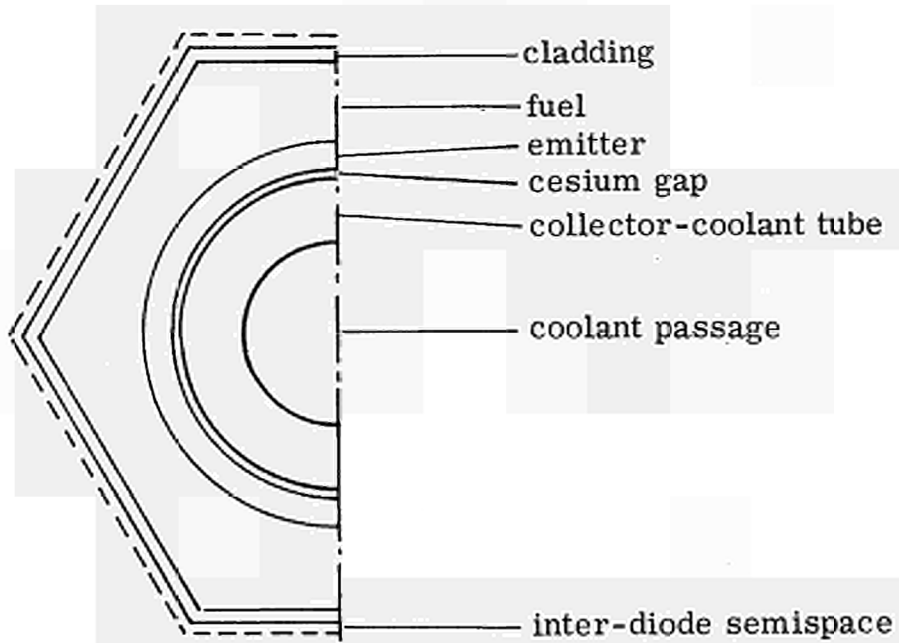


Figure 1. Externally fueled cell in Cross Section



Figure 2. External-Fuel Diode Under Test by RF-Heating

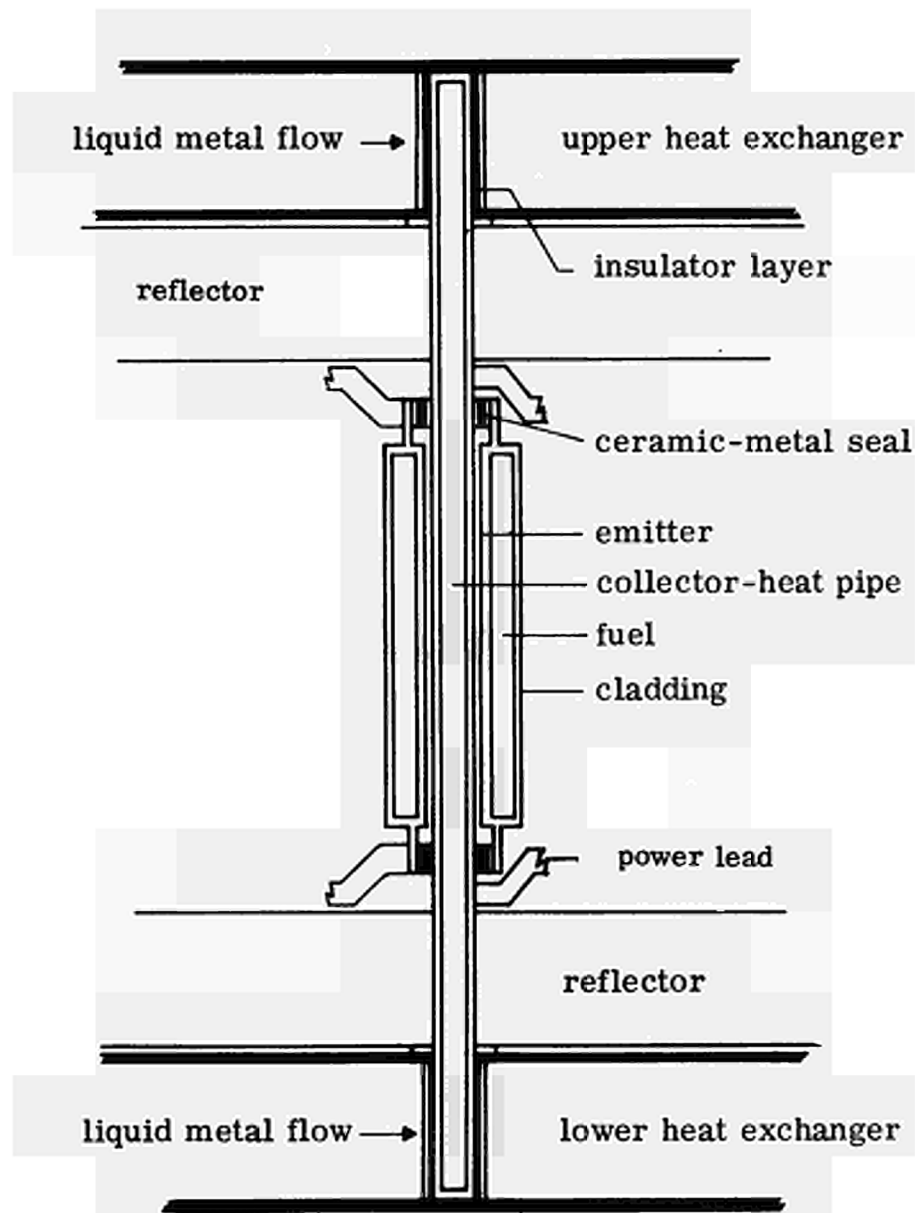


Figure 3. Schematic Drawing of Heat-Pipe Cooled Full Length Module

DISCUSSION

Speaker of paper B-6: A. SCHOCK

BUSSE (Euratom):

Mr. SCHOCK presented the interesting external fuel-concept with a quite impressive list of advantages. I would like to ask him if he could comment also on the disadvantages of this concept. In what way would this concept be inferior to the normal concept with interior fuel?

SCHOCK (USA):

First, the fuel element geometry is more complicated and therefore is more difficult to make. Hexagon fuel elements with a hole have been made of course but it is not quite as easy as making a simple cylindrical element that expands outward. Another problem occurs with the full-length diode. If one gets into megawatts power, or above, one must stack the core. The advantages of the external fuel concept are not so clear in this case.

DAVIS (USA):

I would like to add a few comments. I think that one of the major uncertainties in this design concept is the long term maintenance of the inter-electrode gap and spacing between modules for these relatively long 8 to 10 inch diodes. Also at least as far as our analysis is concerned, these diodes are not exactly "Ferraris" in performance; there are some losses due to the increase in I^2R performance degradation of both the emitter and the collector. In general I think their performance is somewhat below what could be achieved by much smaller internally fuelled diodes. But the penalty is not profound.

GROSS (Germany):

Mr. SCHOCK said that the fuel is not overheated because you concentrate the heat, but can you give some data on the radial heat fluxes along the fuel which you expect. Secondly, you said that the ceramic-metal seal is not inside the neutron flux. Looking at your figure 3, I would expect that high fluxes of fast neutrons would be just there, where your metal-ceramic seals are.

SCHOCK:

Let me answer the second question first. I said that the high voltage insulator, that is the insulator that sees the reactor voltage rather than the individual diode voltage, is outside of the core. With regard to the first question, our emitter heat flux is the same as everybody else's emitter heat

flux; of course the heat flux becomes smaller as you get further away from the emitter. It is not obvious, but if you go through the mathematics, you find that for a given fuel volume fraction and a given fuel conductivity and a given emitter heat flux, the ΔT in the fuel is about half as much when you go from the outside to the inside as the other way round.

UNINSULATED IN-CORE THERMIONIC DIODE CONCEPT*Jerry P. Davis⁺Henrik G. Gronroos[#]

Jet Propulsion Laboratory
California Institute of Technology
Pasadena, California, U.S.A.

ABSTRACT

A major area of uncertainty concerning the feasibility of in-core thermionic diodes is the performance of insulator material. Of particular concern is the performance of the sheath insulator required to prevent shorting to the liquid metal cooling system.

It is possible to conceive of an in-core thermionic reactor design which eliminates all insulator materials from the core itself and still permits series connection of diodes to build output voltage to a reasonable magnitude. The emitter-collector seals in the full core-length externally fueled diode are already outside the core. The collector-insulator-sheath trilayer construction could be eliminated by utilizing the liquid metal-filled coolant tube itself to carry the current out of the core. Just outside the reflector, the desired series-parallel connections could be made by substantial busbars. These busbars would also serve as the structural members maintaining the tube-to-tube spacings.

* This work presents the results of one phase of research carried out in the Propulsion Research and Advanced Concepts Section of the Jet Propulsion Laboratory, California Institute of Technology, under Contract NAS7-100 sponsored by the National Aeronautics and Space Administration.

+ Group Supervisor

Senior Scientist

Independent circuits would be established to form the radiator. One tube would make several loops in the radiator with appropriate finning. Finning would be electrically interrupted where one coolant loop was adjacent to another loop at a different potential. Inches of separation could be employed and insulated supports could be utilized for structural integrity. No current flows through these coolant tubes beyond the point of busbar coupling; they are simply isopotential surfaces.

Two major areas of uncertainty concerning feasibility of in-core thermionic diodes are the nuclear fuels and insulator materials. For systems of 10,000-h life yielding 50 kWe net power delivered to an ion engine for propulsion application, fuel burnups are fairly low, ~ 0.3 at. %, for which fuel swelling for vented carbides, vented UO_2 , or unvented UO_2 -W is hoped to be tolerably small. Insulator performance, however, remains a distinct area of uncertainty for present thermionic reactor concepts.

Insulators are required for seals to contain the cesium inter-electrode gas, and to insulate collector structure from the liquid metal coolant, thereby permitting voltage output to be increased by series connection of diodes from the base 0.7 V available for an individual diode. For the externally fueled and pancake reactor designs, this collector or sheath insulator is not exposed to cesium gas. In the flash-light design, the sheath insulator is exposed to cesium. Radiation damage to insulators in the expected range of integrated fast neutron fluxes has indicated that potential cracking problems may exist. The dielectric

strength of cracked insulator, both exposed and unexposed to cesium gas, is presently not known. Several experimental programs, including one being funded by JPL, are presently under way at various facilities. Seal insulators can be located outside the core itself for both the externally fueled and flashlight designs where integrated fast neutron flux is somewhat lower than within the core. In the pancake design, seal insulators are necessarily located within the core. At the present time, therefore, the question of insulator integrity is a significant and uncertain area of concern affecting, in various degrees, all the presently contemplated thermionic reactor designs.

It is possible to conceive of an in-core thermionic reactor design which eliminates all insulator materials from the core itself and still permits series connection of diodes to build output voltage to a reasonable magnitude. The cesium seals in the full core-length double-ended externally fueled diode, as proposed by Republic Aviation, are already outside the core. The collector-insulator-sheath trilayer construction could be eliminated by utilizing the liquid metal-filled coolant tube itself to carry the current out of the core. Just outside the reflector, the desired series-parallel connections could be made by substantial busbars. These busbars would also serve as the structural members maintaining the tube-to-tube spacings. The emitter and fuel structure is basically hung from its respective coolant tube. Additional support, if required, could be obtained from pins at the top and bottom of the fuel element cladding, which are electrically insulated from grid plates above and below the core. Since temperatures are relatively low and space is not a problem, substantial insulator sections could be employed.

In a 50-kWe design, roughly 130 diodes are required. These could be connected, for example, 7 in parallel and 19 in series for about 12-V output. The paralleled diodes could have their coolant tubes manifolded to a single tube which then proceeds to the radiator. Thus 19 independent circuits would be established to form the radiator. One tube would make several loops in the radiator with appropriate finning. Finning would be electrically interrupted where one coolant loop was adjacent to another loop at a different potential. Again, inches of separation could be employed and insulated supports could be utilized for structural integrity. No current flows through these coolant tubes beyond the point of series-parallel busbar coupling; they are simply isopotential surfaces.

A significant advantage of this concept is inherent protection against potential shorts to ground. Where the coolant loop is isolated from the electrical system as in all other in-core diode concepts, insulator breakdown from collector to sheath represents a short to ground. This type of failure is intolerable and must be protected against by fusing or some other positive means. In this concept, no such grounding possibility exists within the core itself. Outside the core, massive insulation can be provided to protect against this type of failure.

Since it is generally desirable to arrange diodes in a series-parallel matrix to minimize power loss from open and short circuit failures, it is further possible to arrange the paralleled diodes in a single fuel

element having a continuous fuel region. Several additional advantages result from such an arrangement: (1) It is possible to parallel the diodes within the core itself by means of tungsten webs which also serve to couple the outer fuel clad electrically to the emitter reducing the axial resistance to current flow. Only series coupling need be accomplished above and below the core. (2) Open circuit failure of a single diode in the module results in very much lower temperature rise, on the order of only 100 to 200°C, than internally fueled diodes. This is brought about by the direct thermal conduction coupling of the fuel and web region to the other diodes in the module. (3) Volume required for spacing between modules is reduced over that required for single diode externally fueled designs. Spacing may be increased to 1/8" or greater still maintaining high fuel volume fractions within the core. A typical seven-diode module and overall conceptual arrangement is shown in Fig. (1).

The major uncertainty in this design concept is the long-term maintenance of the inter-electrode gap and spacing between modules for these ~10-in long diodes. Relative to the inter-electrode gap stability, thermal cycling tests and diode operations by Republic Aviation Division on their externally fueled diode designs have not resulted in inter-electrode shorts to date.

A toroidal pump design has been evolved which permits a single pump structure to provide flow requirements, maintain electrical isolation between independent coolant loops, and operate directly from unconditioned reactor output current. Pumping power requirement is of the order of 5% of reactor output.

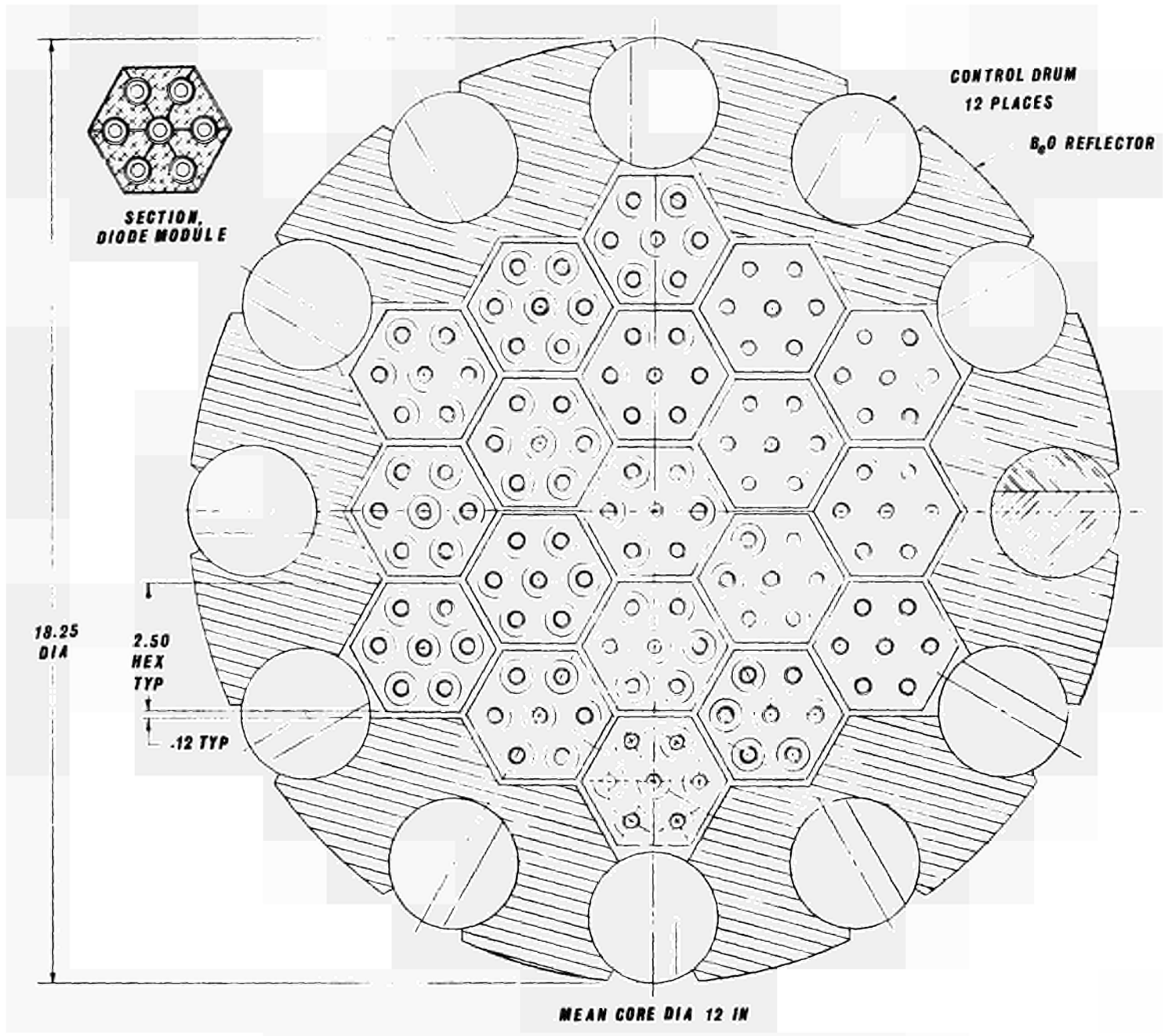


Figure 1: THERMIONIC REACTOR ARRANGEMENT

A HEAT PIPE THERMIONIC REACTOR CONCEPT

P. FIEBELMANN, H. NEU, C. RINALDINI
Euratom CCR, Ispra (Varese), Italy

Abstract

An out-of-core thermionic reactor concept is presented for space power supply in the range of 30 to 100 kWe using Lithium heat pipes in crossed layers, each heat pipe bearing one converter. The concept is based on the assumption of a successful development of high temperature heat pipes (1500 to 1600°C) and related converter systems for long period operation, since considerable progress has been achieved in this field at Ispra.

The converters are located outside the Beryllium reflector on four sides of a nearly cube shaped fast reactor core. Heat is transported from the (UZr) carbide fuel to the heat pipes by thermal heat radiation hence eliminating high temperature compatibility- and electrical insulation problems. The crossed layer arrangement combined with radiative heat transfer allows a simple core structure with a highly reliable cooling system using the redundancy principle. Four movable reflector segments on the top side serve for reactor start-up and power control.

Critical mass and reactivity control calculations have been made for two core designs "A" and "B" varying the core size and the number of converters. Engineering studies of the reactor and its integration into a space power plant of 50 kWe resulted in specific masses of about 12 to 17 kg/kW without and 21 to 27 kg/kW with a shadow shield. The concept seems to be particularly attractive with respect to engineering, simplicity of the reactor core and reliability.

1. THE CONCEPT

Heat pipes are useful for extracting heat from compact reactor cores and transferring it to thermionic converters outside the reflector [1] .

Several proposals for "heat pipe thermionic reactors" have been discussed in the literature, having an output electrical power of 50 kW [2] , 1 MW [3] and 10 MW [4] .

In this paper an engineering concept is presented for the power range of about 30 to 100 kWe. The concept is based on the assumption of a successful development of high temperature heat pipes operating at 1600°C (or at least 1500°C) for time periods of over one year. There is actually no indication that heat pipe corrosion would be an obstacle to reach this aim. Early tests with W/Li heat pipes after 1000 h operation at 1600°C showed extremely low corrosion [5] and demonstrated that (in principle) a solution is possible, although tungsten is not a suitable structural material.

RCA reported on the operation of a titanium-zirconium-molybdenum alloy tube with lithium for 9000 hrs at 1475-1500°C [7] . Recent progress in the understanding of the corrosion mechanism has resulted in large improvements in the life of Li heat pipes making use of ductile wall materials (Nb-1 Zr and Ta). The SGS-Ta/Li system seems to hold particular promise for long life operation at 1600°C (this will be reported in another paper of this conference [6]).

Lithium has been found to be the best working fluid for an operation temperature of 1500 to 1600°C, having a large heat transport capacity. A maximum heat flow of about 7 kW has been measured with a pipe about 50 cm long and a vapor channel diameter of 0.76 cm [6] , a result which is in good agreement with calculations [8] .

The concept further profits from the fact that the technology of the out-of-core thermionic converter is in a rather advanced state and that out-of-core converters of high reliability and lifetime have already been developed [9] .

The first prototype of a "heat pipe thermionic converter", which combines a normal thermionic converter with a high temperature heat pipe (1500°C - 1600°C) for the emitter heat supply (emitter heat pipe) and a low temperature heat pipe (700°C-800°C) for heat rejection from the collector into space (collector heat pipe), has been presented at the London Conference in 1965 [10] . Several other converters of the same type have been built and tested since that time in Ispra. Life tests are in preparation. If the corrosion problem of the emitter heat pipes could be solved, there does not seem to be a major technical obstacle which could prevent the development of such converters with the same reliability as other types of out-of-core converters.

Except for the heat pipe thermionic converter itself, all other reactor components needed in this concept can either be made by applying existing techniques or could actually be developed without foreseeable major difficulties.

Fig. 1 shows the principal arrangement of the reactor, the reflector and the conversion system. It is characterized by the following features:

- fast, parallelepiped shaped core with a (UZr, C) mixed fuel and a Be reflector of the same shape,
- thermionic converter located outside the reflector on four sides of the

- parallelepiped in such a manner that the emitter heat pipes are arranged in crossed layers, each emitter heat pipe bearing one converter,
- heat transport from the nuclear fuel to the heat pipes by thermal radiation, hence eliminating high temperature compatibility and electrical insulation problems,
 - reactor control by four movable reflector segments on the top side of the core.

The crossed heat pipe layer arrangement provides sufficient space for locating the converters. It represents furthermore a highly reliable core cooling system by using the redundancy principle: If a heat pipe fails (e. g. through a leak or destruction of the capillary system) its equivalent thermal conductivity drops, its temperature rises rapidly, hence blocking the normal heat flux from the fuel to the defective heat pipe. In this case each heat pipe of the neighbouring layers, which cross the defective heat pipe take over part of the heat flux.

If n is the number of heat pipes in one layer, this part can be estimated to be about $1/2 n$ if a heat pipe fails in one of the internal layers and $1/n$ if a heat pipe fails in the two outer layers. The resulting increase in heat flux of all participating heat pipes remains therefore small enough to avoid intolerable overheating.

This cooling system is also applicable to a thermal reactor core, where the moderator is located between sets of at least two heat pipe layers. Critical mass calculations of a zirconium hydride moderated core, however, have shown that a thermal core of this type offers no advantage with respect to the total reactor mass (except that the U_{235} content is much smaller) against a fast core. It has been found that the engineering of such a thermal core is more complicated than that of a fast core.

2. DESIGN PARAMETERS OF THE REACTOR AND THE CONVERSION SYSTEM

Four different design types of the heat pipe thermionic reactor (HPTR) concept described above have been chosen, the variations being in core size, converter central spacing (see Fig. 2), and the cooling of the collectors.

The meanings of the following symbols are:

- "A" - a design with 192 heat pipes and converters (8 lines of 6 converters on each of the four sides), a central spacing of 6 cm and a core size of 36 x 36 x 41.6 cm (without reflector).
- "B" - a design with 120 heat pipes (6 lines of 5 converters), central spacing of 5 cm and a core size of 25 x 25 x 26 cm.

"L" - cooling of the collectors with a liquid metal loop.

"H" - cooling of the collectors with heat pipes.

One of the characteristic data of the HPTR concept is the average heat flux Q_r per cm^2 of the heat pipe surface which depends on the produced thermal power and is different for the core designs "A" and "B". The temperature of the fuel surface, which is limited by the material properties, depends on the heat flux \dot{Q}_r , the surface temperature T_H of the heat pipes, the emissivities ϵ of the fuel and heat pipe surfaces and the geometry of fuel and heat pipes (which is different for the design "A" and "B").

This is demonstrated in Fig. 3 for a fixed emitter temperature of 1600°C assuming an overall conversion efficiency of 10%. For simplicity the emissivity of the fuel surface is taken equal to that of the heat pipe. Assuming that ϵ -values over 0.8 could hardly be achieved, from Fig. 3 it can be deduced that in order to avoid intolerably high fuel temperatures (fuel surface should be below 2000°C) design "A" has a limit at about 130 kWe and design "B" at about 50 kWe.

Tables 1 to 4 give design data for three reactors:

1. "A"-reactor for 50 kWe output (50-A), using either liquid metal or heat pipe collector cooling. An ϵ -value below 0.5 is necessary for a fuel surface temperature of 1900°C . This reactor may therefore be considered on the safe side of performance and engineering.
2. "B"-reactor for the same power output (50-B), representing a compact and advanced core design.
3. "A"-reactor for 100 kWe (100-A) with a similar heat transfer characteristic as the 50-B reactor, but requiring rather large converters of 520 Watt power each.

For the converters, normal performance data are taken (see Table 1 and Fig. 2). With constant emitter temperature and constant electrical power density of the converters, the various power outputs are achieved by different emitter areas.

3. NUCLEAR CHARACTERISTICS

3.1 Critical mass and reflector thickness

For a parametric study of the critical mass the following material compo-

sition was assumed:

- a fuel of Uranium carbide stabilized with 30 percent by volume of Zirconium (UC + 30 v/o ZrC), 93% enriched, density 11 g/cm^3 at 20°C , operation temperature 1900°C ,
- reflector of beryllium, density 1.85 g/cm^2 at 20°C , operation temperature 700°C ,
- heat pipes of tungsten with 8 mm inner diameter and 10 mm outer diameter, density 19.3 g/cm^3 at 20°C , operation temperature 1600°C .

Two different calculation methods (diffusion and "Monte Carlo") were employed.

In performing the parametric analysis a multigroup (19 groups) one dimensional (spherical geometry) diffusion calculation was adopted. The Gaze [11] computer program was employed and the neutron cross-section library was obtained by condensation of the 200 group GGC-II [12] library. Two dimensional diffusion calculations in cylindrical geometry were also done with the same library for some particular cases. The computer program SQUID [13] was employed for this purpose.

For the final assessment of the critical mass of the chosen reactor, three dimensional Monte Carlo calculations were performed with the aid of the TIMOC [14] computer program, using a multigroup (26 groups) cross-section library especially adapted to fast reactors [15] .

A discrepancy of about 1.5% in reactivity resulted between the Monte Carlo calculations and the diffusion calculations. This incorporates both the differences between the transport and diffusion approach and the differences in the neutron cross-section libraries. A correction of 1.5% in k_{eff} was therefore introduced in all diffusion calculations.

As the dimensions of the reactor core were fixed for the "A" and "B" designs, the fuel volume fraction and reflector thickness were varied to get $k_{\text{eff}} = 1.03$ in the diffusion calculations for the hot core. For the "A" design, calculations were made with a spherical core of 24 cm radius corresponding to the 36 x 36 x 41.6 cm parallelepiped; for the "B" design with a 25 x 25 x 26 cm core, the corresponding radius is 16.1 cm. Some results of the calculations modified for parallelepiped shapes and adapted to the results of additional Monte Carlo calculations are presented in Figs. 4 and 5.

It can be seen from Fig. 4 that the reactor mass has a minimum for a

reflector thickness of about $d = 7$ cm. However, with increasing reflector thickness the U_{235} content decreases (Fig. 4) and the power distribution becomes more flattened (Fig. 5). A reflector thickness of 11 cm was chosen for both designs "A" and "B". The corresponding core data are given in Table 2. It may be noted that results of a two dimensional calculation of the power distribution in a cylindrical geometry show no dangerous peak power at the reflector boundaries. We expect that this is also valid for parallelepiped shaped cores.

3.2 Temperature coefficient

Preliminary temperature coefficient calculations of the reactivity were carried out because of the influence of the thermal expansion. Using the following linear thermal expansion data: $13 \cdot 10^{-6} (\text{°C})^{-1}$ for the fuel, $4.32 \cdot 10^{-6} (\text{°C})^{-1}$ for W and $17.2 \cdot 10^{-6} (\text{°C})^{-1}$ for Be it follows that $\Delta k/k = -3 \cdot 10^{-6} (\text{°C})^{-1}$ for the "A" design. No attempt is made to evaluate the actual temperature coefficient by including the Doppler effect.

3.3 Reactor control

Monte Carlo three dimensional calculations for the "A" core result in a reactivity decrease of 7.8% when taking off the whole top reflector. This offers the possibility of subdividing the top reflector into 4 segments (Fig. 6) and a support frame which remains fixed during normal operation, but which may be removed explosively in accident conditions and the reactor thereby shut down.

It is estimated that normal operation of 50-A reactors will not actually require a reactivity control higher than 2%. This includes both the passage from cold to hot conditions after start-up and the reactivity loss due to burn-up for the reactor running at 500 kWth for two years.

From Monte Carlo calculations, using the shape approximation of Fig. 6, it follows that the four segments control 0.9% reactivity each when the supporting arm opens them by 40° , resulting in a total of 3.6%. To start the reactor, two of the segments are moved in by a spring load to give cold criticality [16], while the others are moved by stepper motors or an adequate hydraulic system for fine regulation purposes.

4. CONCEPTUAL ENGINEERING

The engineering studies have been performed mostly with the aim of finding whether serious design problems exist and making realistic mass estimations. The following is related, particularly with regard to dimensions and data, to the large core design "A" for 50 kWe. The structure of the "B" design is in principle quite similar, however.

4.1 Core structure

Fig. 7 and 8 show the reactor and converter assembly partially sectioned and in view.

The almost cubic active zone consists of crossed layers of 208 equidistant (UZr, C) fuel bars. In this way rectangular channels 1.92 x 2.6 cm running through the whole core are achieved, providing a minimum distance between fuel and heat pipes (outer diameter 1 cm) of 0.46 cm at operation temperature.

There are two possible design solutions of interest for the fuel set up:

- 1) The different fuel layers are mechanically interlocked and partially sintered together in order to form a strong selfsustaining unit (see fig. 8). The fuel assembly is fixed in the center of the bottom reflector. During heating up the core from room temperature to operation temperature, the heat pipes change their cold geometric position inside the heat pipe channels. This imposes no problems as the horizontal distance between fuel and outer heat pipe in the top layer changes by 0.228 cm for an average core temperature of 1900°C and an average Be-reflector temperature of 700°C.
- 2) In an alternative solution the fuel bars are made up of a reflector piece at one end, thermal insulation sections and a centering piece at the other end (see Fig. 7). In this case single fuel bars are introduced through holes inside the reflector and fixed from the outside. A minimum clearance of 0.033 cm between the fuel layers is required to meet the expansion difference existing between the reflector and the fuel. Such an arrangement provides the most exact heat pipe positioning, but may give rise to serious problems for the fuel (touching and sintering). As the thermal core expansion perpendicular to the fuel layer planes is determined by the reflector, the negative reactivity temperature coefficient is smaller.

The high fuel surface temperatures require an effective coating against vaporisation. W or W/Re alloys are potential candidates for this [17] . This protection layer must however follow the expansion of the fuel. The thermal insulation of the core to the reflector is made up of W and Ta foils reducing the heat losses to the reflector to about 1%.

4.2 Reflector

All emitter heat pipes are fixed inside the reflector and electrically insulated from it. Each side part of the reflector contains 48 holes provided with electrical ceramical insulators (see e.g. Fig. 1). Coolant passages inside the reflector keep the temperature in the 650°C to 700°C range.

The heat generated inside the reflector and the heat losses from the core,

(about 3.2 kW_{th} for each face) are extracted either by liquid metal in a bypass or by heat pipes.

The top reflector and the movable control segments radiate their waste heat directly to the protection housing (see Fig. 9 and 10), the surface of which is sufficiently large to radiate it into the space.

4.3 Converters and their cooling

The converter collectors are cooled either by Na or NaK loops ("L" design) or by collector heat pipes ("H").

Fig. 7a shows the general "L" converter arrangement and Fig. 7b a simplified cross-section of a converter. Each converter has a collector sandwich. The 48 converters of each face are welded into a stainless steel box forming a compact heat exchanger cooled by 2360 cm³/sec of Na at an inlet temperature of 620°C and an outlet temperature of 665°C.

The corresponding collector temperatures are 705°C at the inlet and 750°C at the outlet.

The "H" arrangement is shown in Fig. 8. Each of the two collectors are cooled by one Na heat pipe (channel cross-section about 4 cm²), which carries away about 4.7 kW waste heat. A standard electrical insulation is required between neighbouring collector heat pipes operating at 800°C.

In order to avoid too large a reactor diameter (larger shadow shield mass) the actual converters are not optimized to minimum mass (having larger diameters and being shorter). The converters are arranged in parallel series connection with cross connector resistances [18] and current leads with optimized cross-sections [19]. The "L" design has network units of 3 x 8 converters, the "H" design units of 4 x 6 converters.

4.4 Radiator systems

In the HPTR-50-BL space power plant (Fig. 9) the waste heat from the four converter modules is transported by Na to two annular ducts (heat exchangers) where the heat is transferred to the heat pipe ends. The liquid metal is then fed back by an EM-pump (620°C) to the converters. The conically shaped radiator consists of 302 independent Na-SS-heat pipes arranged in four single rows, mechanically held together by stiffener rings, of which two serve as heat exchangers. This structure is covered on the outside by a copper radiating skin (radiator surface). For 475 kW thermal power the radiating area is 18.9 m². Assuming $\epsilon = 0.9$ [16] the average radiation temperature is 640°C.

In the HPTR-50-BH plant (Fig. 10) 96 approx. 2.20 m long collector heat pipes distributed around the shadow shield form a conically shaped radiator working at 800°C with a surface area of 7 m² ($\epsilon = 0.9$). Although this radiator system looks more simple than the "L" radiator, there are some technological uncertainties involved.

4.5 Shadow shield and reactor support

The lithium hydride shadow shield is 76 cm thick and housed in a SS-vessel. In this set up the integrated flux at a distance of 10 m will be 10¹² nvt after 2 years. Gamma radiation was found to be negligible [20] [21]. The shield top section, where most of the heat is generated, is cooled by a heat pipe radiator system to 550°C. The heat removal is more difficult for the "H" design because of the closely spaced radiator heat pipes surrounding the shadow shield, and neutron scattering requires special attention.

For launching conditions the reactor is supported by the radiator system and a centrally positioned telescope boom, providing the required distance from the payload in space and serving as the electrical power lead.

4.6 Meteorite protection

The meteorite protection is designed for a survival probability of 99% over a period of two years for the "L" radiator system and 99.9% for the more sensitive parts, which are the control systems, the converters, the liquid metal tubing and the "H" radiator heat pipes [22]. The "L" radiator system is less sensitive to meteorite damage than the "H" radiator because failure of heat pipes in the "L" radiator does not interrupt converter cooling. Therefore, the heat pipes of the "L" radiator are protected by a 0.8 mm SS wall on the outer side, those of the "H" radiator by a 2 mm SS wall.

5. RESULTS

Considering specific masses and technical performance there is a strong competition between in-core (fast or thermal) and out-of-core space reactor concepts in the power range up to 100 kW electrical output. Results of this study have to be evaluated in this light.

5.1 Mass analysis

One of the interesting results is that the HPTR concept with radiative heat transfer to the heat pipes shows specific mass data which are quite comparable or inferior to in-core data (as far as available e. g. [23] [24]) in the power range 30 to 100 kWe.

The reactor mass of the HPTR concept depends strongly on the heat transfer conditions (ϵ -values and fuel temperature). In Fig. 11 mass data of table 4 are presented. Two shaded bands give an estimation for mass regions without and with shadow shield, taking the 50-A design as the most pessimistic and the 50-B design as the most optimistic solution. It should be noted that the "H" designs (collector cooled with heat pipe) show smaller masses than the "L" designs (loop cooling).

These results are at first sight somewhat surprising because the HPTR cores are rather large in size (Table 2), having an average thermal power density which is rather small (Table 3) and a quite high fuel mass (Table 4). There is, however, an explanation why in-core reactors also have no smaller specific masses: the total emitter area is determined for a certain electrical power output through the necessity of a high heat flux from the fuel to the emitter in order to obtain a high conversion efficiency. This seems to be difficult to bring into agreement with the criticality condition in the small power range. For internal fuel systems (fuel inside the emitter) emitter diameters become unfavorably large [25]. Another possible solution is a two-zone core with an active conversion zone and a booster zone. As no electrical

power is generated in the booster zone the overall efficiency can be rather small (below 50 kWe only a few percent), hence increasing the specific radiator mass. For thermal cores calculations have shown [24] that the booster zone solution is the preferable one. It is well understood that these incompatibility problems do not exist for heat pipe cooled cores, because heat pipes can be used as flux transformers, allowing a high heat flux on the emitter and a smaller heat flux at the fuel surfaces.

5.2 Engineering and critical technological areas

The main characteristic features of the HPTR engineering are:

- i — very simple core structure,
- ii — no electrical insulation and compatibility problems between fuel and heat pipes at high temperatures,
- iii — highly reliable core cooling system (under the assumption that the heat pipe corrosion problem is solved),
- iv — small fuel burn-up (0.15 to 0.3 atomic % per year); therefore probably no fuel swelling problem,
- v — vacuum tight metal ceramic joints are not exposed to the main neutron flux,
- vi — all ceramic parts are operating at temperatures below 800°C,
- vii — no inherent engineering problems for incorporation of the reactor into a space power system,
- viii — heat pipe converters can be life-tested out-of-pile under the same working conditions as later on in the space plant; only the emitter heat pipes have to be tested in-pile,
- ix — the whole conversion system can be assembled and tested out-of-pile before mounting into the space plant.

Among the main critical technological fields are the following:

- i — development of high temperature heat-pipes for long life-times (see Chapter 1),
- ii — high operation temperature of the fuel (1900°C to 2000°C),
- iii — development of high emissivity surfaces of fuel and heat pipes; reported ϵ -values for refractory metal surfaces are in the range 0.5 to 0.6 and not sufficiently high; there are however, good hopes that by special preparation (e. g. blackening by sintering powders on the radiative surfaces, slotting of surfaces) stable ϵ -values up to 0.75 may be obtained,
- iv — checking experimentally whether the reactor has a sufficiently large negative temperature coefficient of the reactivity.

If a technical solution for a high temperature metal-ceramic-metal sandwich (direct thermal contact between fuel and heat pipe at 1600°C) could be found (as seems to be assumed in [2] [3] [4]), this would enable an increase in the power output of the HPTR concept considerably above 100 kWe and decrease the specific masses compared to those reported here for the radiative heating system.

5.3 Conclusion

The HPTR out-of-core concept is competitive with in-core concepts with respect to specific mass and seems to be particularly attractive with respect to engineering, simplicity of the core and reliability.

ACKNOWLEDGEMENT

The authors are indebted to thank C.A. Busse and H. Hausner for valuable contributions; R. Narzul and U. Buzzi for design work; J. Devos for neutron calculations; and the heads of the Engineering Department, S. Finzi, and Reactor Physics Department, V. Raievski, for their support.

REFERENCES

- [1] GROVER, G.M., BOHDANSKY, J. and BUSSE, C.A., "The use of a new heat removal system in space thermionic power supplies", EUR-Report 2229-e
- [2] RÜHLE, R, et al., "Verwendung von Wärmetübertragungsrohren für Thermionik-Reaktoren", Atomkernenergie 10, H. 9/10, (1965) 399
- [3] PEDERSEN, E.S., "Heat Pipe thermionic reactor concept", Nucl. Engineering, 2 (1967) 112
- [4] BARNETT, C.S., Trans. Am. Nuc. Soc. 9 (1966) 338
- [5] BUSSE, C.A., GEIGER, F., QUATAERT, D., PÖTZSCHKE, H., "Heat pipe lifetests at 1600°C and 1000°C", Proc. Thermionic Conversion Specialist Conference, Houston, 1966, 149
- [6] BUSSE, C.A. et al., "High temperature lithium heat pipes", this conference, paper D-2
- [7] C & EN, Aug. 21, p. 16 (1967)
- [8] VAN ANDEL, E., "Heat pipe design theory", this conference, paper D-5
- [9] see e.g. different papers "Thermionic Specialist Conferences" in Houston 1966 and Palo Alto 1967
- [10] BUSSE, C.A., CARON, R., CAPPELLETTI, C., "Prototypes of heat pipe thermionic converters for space reactors", Proc. Int. Conference on Thermionic Electrical Power Generation, London, 1965
- [11] LENIHAN, S.R., "Gaze-2, a one-dimensional, multigroup, neutron diffusion theory code for the IBM-7090", GA-3152 (1962)

- [12] GA-4265, GA-4132 (1963)
- [13] DANERI, A., GABUTTI, B., SALINA, E., "SQUID-360. A multi-group diffusion programme with criticality searches for the IBM-360", Fiat Report FN-E-86 (1967)
- [14] RIEF, H., KSCHWENDT, H., "Reactor analysis by Monte Carlo", Nucl. Science and Eng. 13 (1967) 395
- [15] ABAGJAN, L. P. et al., "Gruppen Konstanten schneller und intermediärer Neutronen für die Berechnung von Kernreaktoren", Karlsruhe-Report KFK-tr-144 (1963)
- [16] DIECKAMP, H. M., Nuclear Space Power Systems, Atomic International, Canoga Park, California (1967)
- [17] LINYANG, HUDSON, R. G., CARPENTER, F. C., "Some high temperature diffusion studies on materials of thermionic interest", Proc. Int. Conf. Thermionic Electrical Power Generation, London 1965
- [18] HOLLAND, J. W., "Thermionic reactor network reliability", Proc. Int. Conf. Thermionic Electrical Power Generation, London, 1965
- [19] BUSSE, C. A., "Optimization of heat pipe thermionic converters for space power supplies", EUR-Report 2534-e (1965)
- [20] CANALI, U., Euratom CCR Ispra, Reactor Calculation Division: private communication
- [21] KESHISHIAN, V., "Shield design for SNAP reactors", Space Power Systems Conf., Santa Monica, California, Sept. 27-30, 1960
- [22] SUMMERS, J. L., CHARTERS, A. C., "High-speed impact of metal projectiles in targets of various materials", Proc. 3rd Symp. on Hypervelocity Impact, Armour Research Foundation, Chicago (1959)
- [23] HAUG, W. et al., "Entwurfsstudie einer Energieversorgungsanlage für Raumfluggeräte mit einem thermischen Kernreaktor (TRIKT-50)", Atomkernenergie 10, H. 9/10 (1965) 363
- [24] BUDNICK, D., "In-core-Thermionik-Reaktor zur Energieversorgung von Raumflugkörpern", Kolloquium Bad Godesberg (1967)
- [25] PERRY, L. W., HOMEYER, W. G., "Synthesis of thermionic power conversion to nuclear reactors for space power applications", Proc. Int. Conf. on Thermionic Electrical Power Generation, London, 1965

Table 1 Conversion system data for "L" and "H" cooling *				
HPTR design		50-A	50-B	100-A
Total electrical power output P_e	kW	50	50	100
Electric power density w	W/cm ²	6	6	6
Emitter temperature T_E	°C	1600	1600	1600
Collector temperature T_C	°C	730/800 *	730/800 *	730/800 *
Electrical output of one converter	Watt	260	417	520
Overall efficiency	%	10	10	10
Number of converters equal number of heat pipes N		192	120	192
Cell center spacing U (fig.2)	cm	6	5	6
Emitter diameter D_e (fig.2)	cm	4.5	3.5	4.7
Emitter length L_E	cm	3.2	6.3	5.9
Overall converter outer diameter D_c (Fig.2)	cm	5/5.8	4/4.8	5.2/5.8

Table 2 Core and reflector data				
HPTR design		50-A	50-B	100-A
Core size (parallelepiped)	cm	36x36x41.6	25x25x25.95	36x36x41.6
Fuel (93% enrichment)		UC+30 %ZrC	UC+30 %ZrC	UC+30 %ZrC
Mass of U 235	kg	151.3	73.3	151.3
Fuel volume fraction	%	35	56	35
Atomic burn-up per year	%	0.15	0.31	0.3
Average thermal fuel power density	W/cm ³	26.6	55	53.2
Reflector material		Be	Be	Be
Reflector thickness d	cm	11	11	11
Reactivity control	%	3.6	--	3.6

Table 3 Data for heat transfer inside the core				
HPTR design		50-A	50-B	100-A
Average thermal core power density q	W/cm ³	9.3	30.8	18.6
Average radially radiated heat flux on the heat pipes q_r	W/cm ²	23	59	46
Surface temperature of heat pipes T_H	°C	1600	1600	1600
Surface temperature of nuclear fuel T_F		see Fig.3	see Fig.3	see Fig.3
Working fluid of heat pipes		Li	Li	Li
Heat pipe channel	cm	1.92x2.6	1.6 \emptyset	1.92x2.6
Heat pipe outer diameter D_u (Fig.2)	cm	1	1	1
Heat pipe vapor channel diameter D_v	cm	0.76	0.76	0.8

Table 4 Mass data for "L" and "H" cooling *				
HPTR design		50-A	50-B	100-A
Fuel mass	kg	222	107	222
Reflector and control system	kg	281	160	281
Emitter heat pipes (SGS - T_a)	kg	43	27	43
Converters	kg	74/85 *	54/61 *	119/130 *
Heat removal system	kg	215/ 119	208/ 142	344/ 224
Structure and local meteoroid protection	kg	103/ 118	94/ 114	207/ 277
Total mass without shield	kg	938/ 868	650/ 611	1216/1177
Shield mass	kg	462/ 490	383/ 419	564/ 602
Total mass with shield	kg	1400/1358	1033/1030	1780/1779
EM-pump power consumption	kW	3/ --	3/ --	4/ --
Power output	kW	47/ 50	47/ 50	96/ 100
Specific mass without shield	kg/kW	20/17.4	13.8/12.2	12.7/11.8
Specific mass with shield	kg/kW	29.8/27.2	22.0/20.6	18.6/17.8

* "L" "H" Converter collectors cooled by liquid metal/Converter collectors cooled by heat pipes

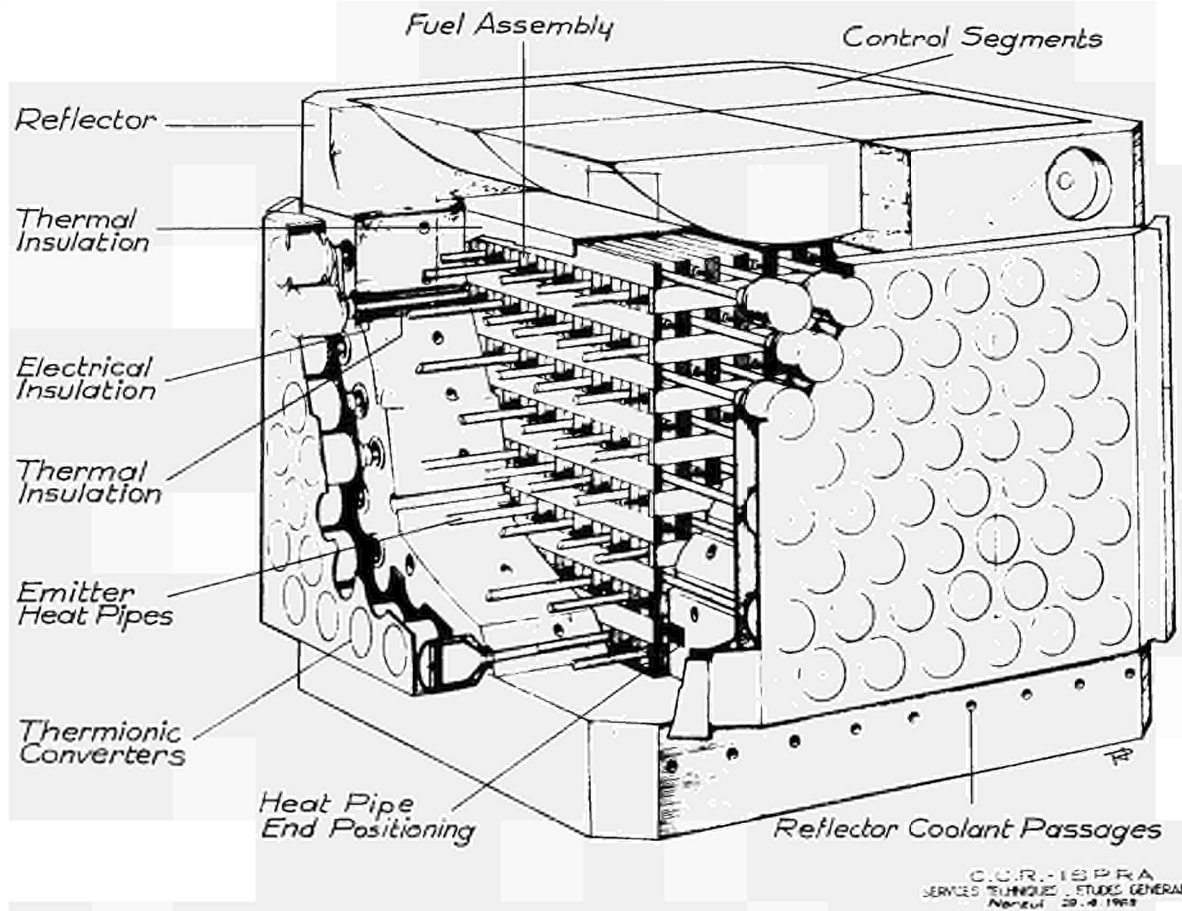


Fig. 1 Heat Pipe Thermionic Reactor (HPTR) concept - principle arrangement -

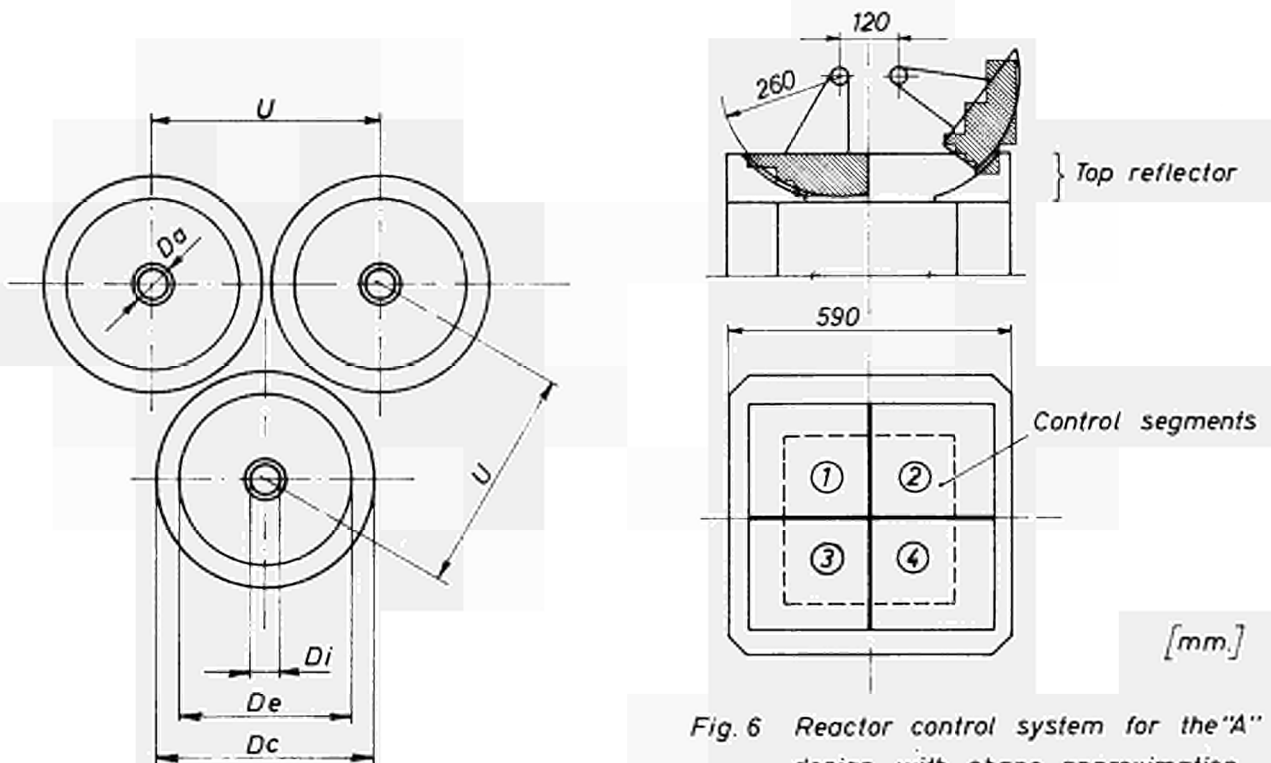


Fig. 2 Converter arrangement on the reflector surface.

Fig. 6 Reactor control system for the "A" design with shape approximation of the segments for calculation purposes.

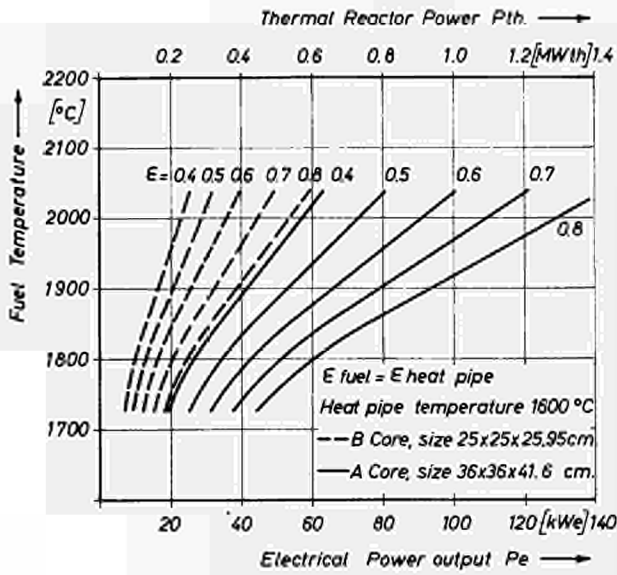


Fig. 3 Fuel surface temperature for different thermal emissivity and different design "A" and "B"

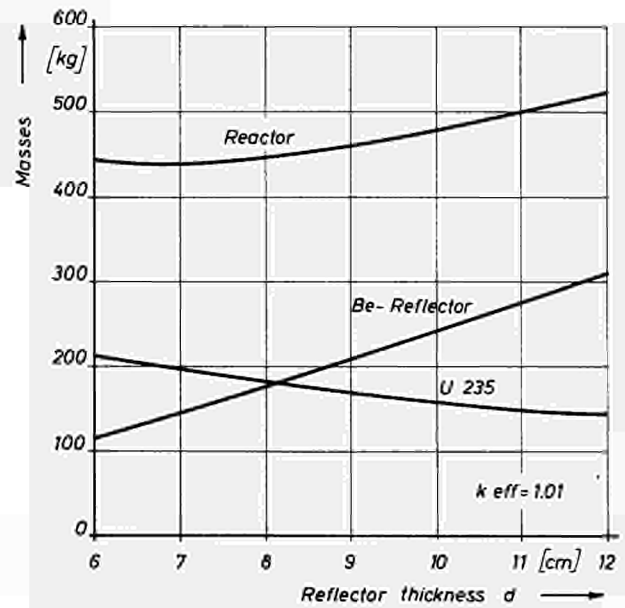


Fig. 4 Masses of U 235, Be reflector and of fuel and reflector vs the reflector thickness for a parallelepiped shaped core 36x36x41.6 cm.

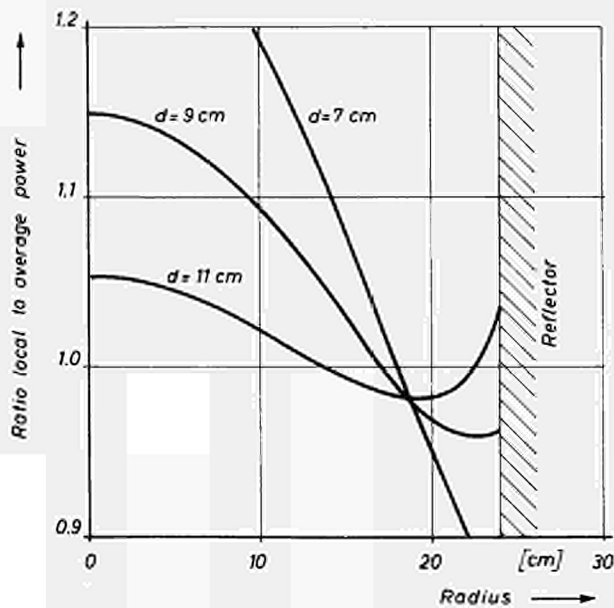


Fig. 5 Power distribution of a spherical core [equivalent to a parallelepiped shaped core 36x36x41.6 cm] for different reflector thicknesses d.

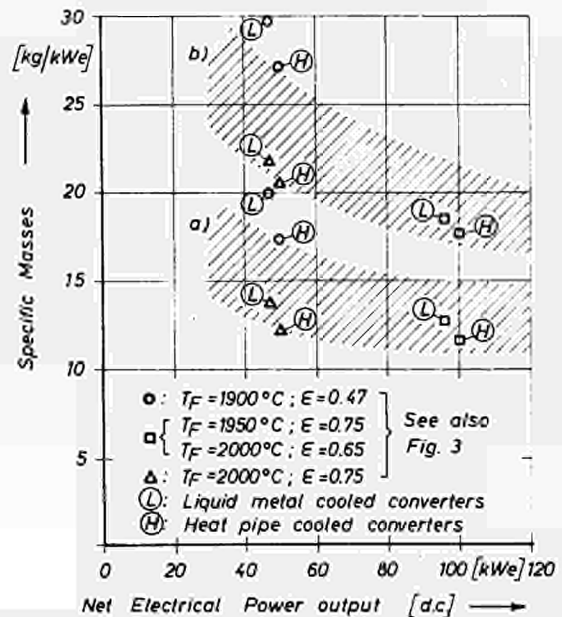


Fig. 11 Specific masses of HPTR space power plants a) without, b) with shadow shield according to data table 4;
 // // // // estimated region for "H" design
 T_F = fuel surface temperature,
 E = thermal emissivity.

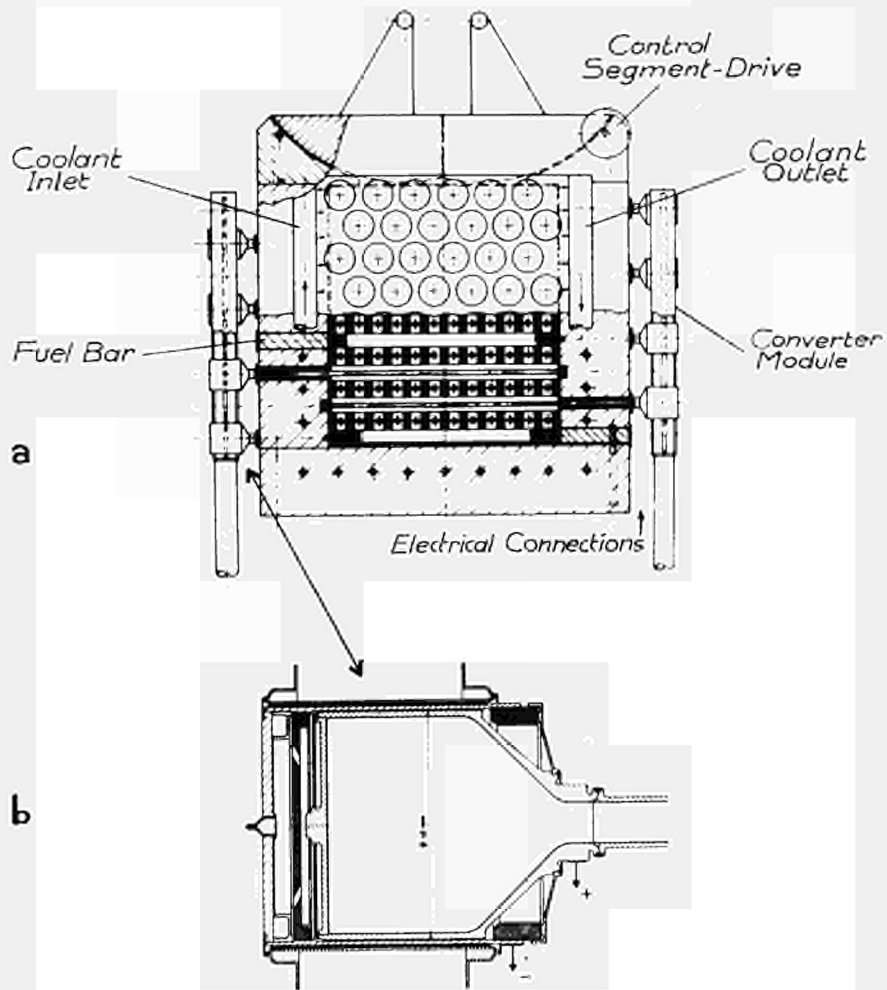


Fig.7 Core with liquid metal cooled converters
 - HPTR-50-AL -

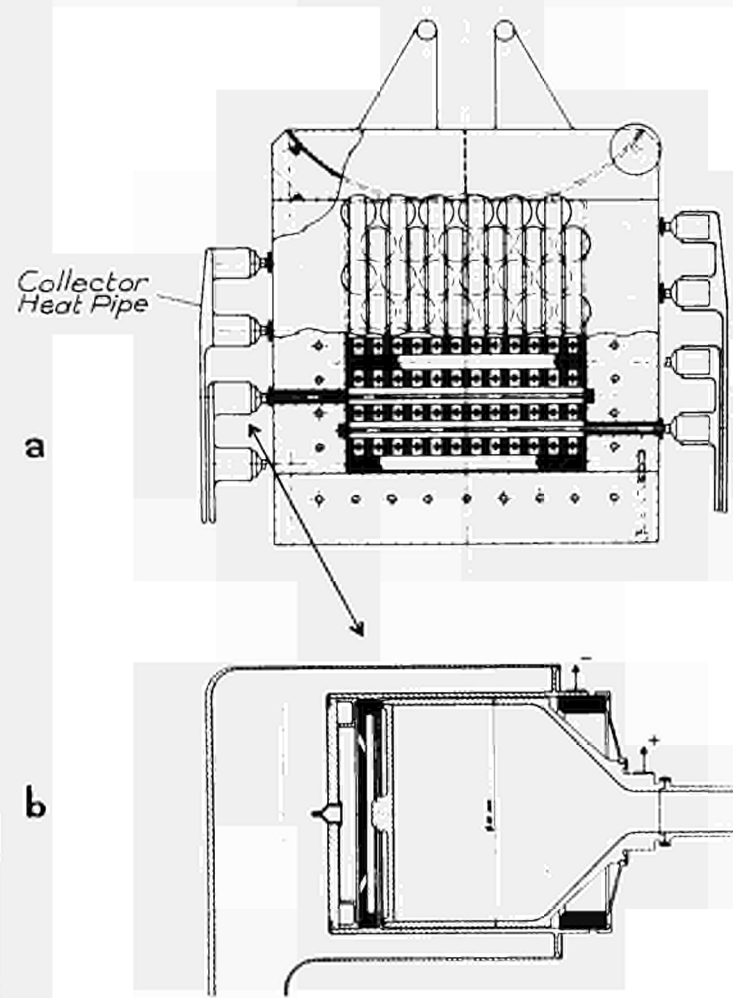


Fig.8 Core with heat pipe cooled converters
 - HPTR-50-AH -

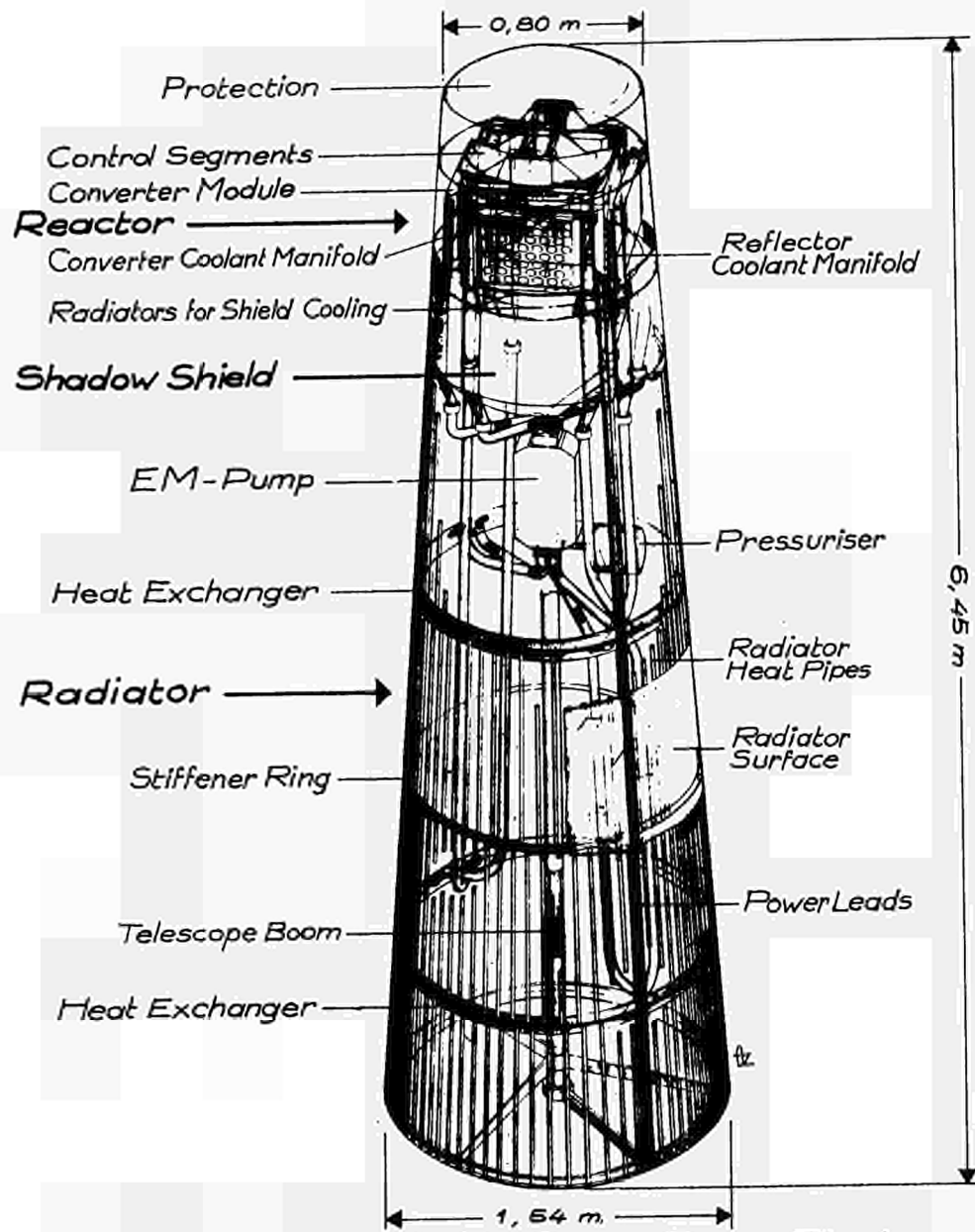


Fig.9 HPTR-50-AL Space Power Plant
— General View —

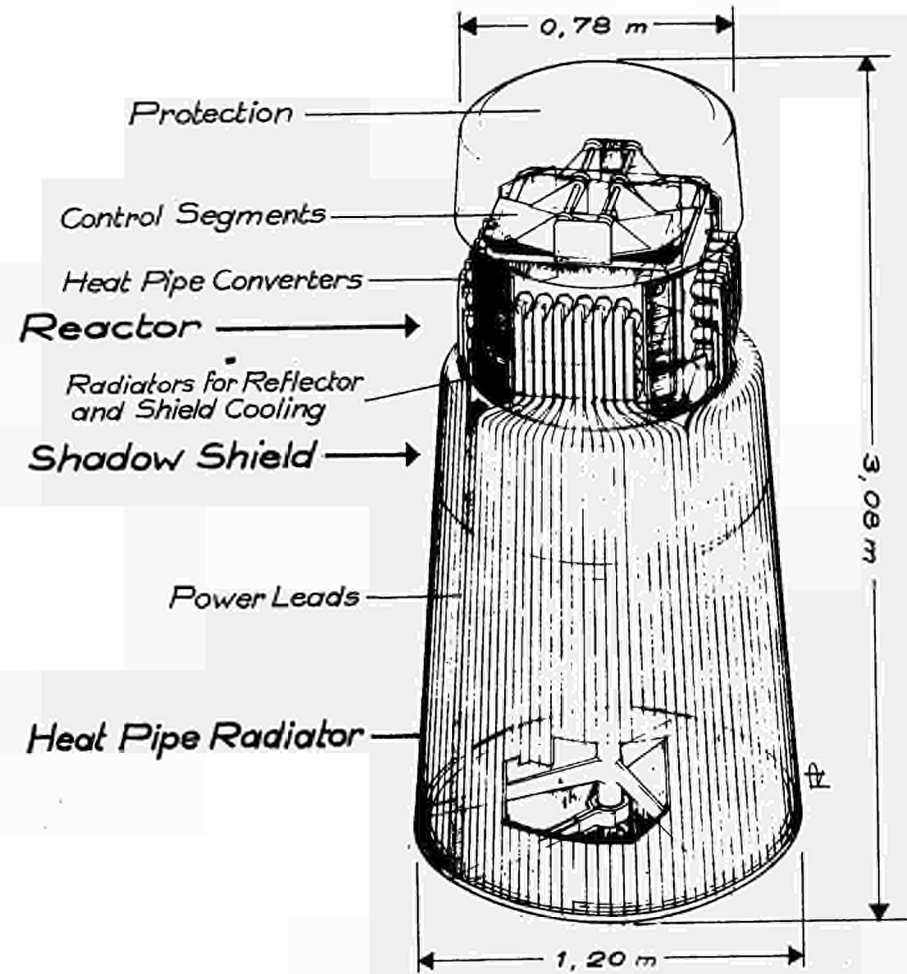


Fig.10 HPTR-50-AH Space Power Plant
— General View —

DISCUSSION

Speaker of paper B-8: H. NEU

RASOR (USA):

You have quoted specific weights for 2000°C and, I believe, 1900°C fuel temperatures? What is the temperature of the emitter heat pipe?

NEU (Euratom):

The temperature of the emitter heat pipes is assumed to be 1600°C in both cases (fuel surface temperature 1900°C and 2000°C).

RASOR:

Did the specific masses not include the weight of the shield?

NEU:

There are two regions of specific mass shown in Fig. 11: One including the shadow shield mass and the other excluding the shadow shield mass. The shadow shield masses were calculated under the assumption, that in a distance of 10 meter from the reactor core the integrated flux is 10^{12} nvt after 2 years. As this indicates shielding is not provided for manned missions.

GRIAZNOV (USSR):

Which components were taken into account in the weight evaluation of the power station? In particular, were the weights of the components for radiation protection and the semi-conductor power conditioner taken into account? What was the output voltage?

NEU:

In the weight estimation we included the reactor, the converters, the radiator, the radiation and meteoroid protection and other components, which belong to a space power plant. The power transmission line from the end of the radiator to the payload and the power conditioning equipment were not included. The output voltage is about 20 Volts.

GRIAZNOV:

Which thermionic elements did you consider, elements of several converters in series or single converter elements?

NEU:

Each emitter heat pipe is transporting the heat from the core to the emitter of one single converter. The upper part of the emitter heat pipe serves directly as the electron emitter. The collector can be cooled by another heat

pipe.

PRUSCHECK (Germany):

A cladding of the fuel elements will be required. What materials do you consider for this purpose and are they compatible with the fuel? Did you check the thermal emissive properties of such claddings at the temperature necessary during operation?

NEU:

We suggest that a tungsten-rhenium alloy is a suitable cladding material. There is one problem involved, which I have not mentioned: In order to allow fuel expansion and therefore to produce a negative temperature coefficient of the reactivity, this cladding has to follow the fuel expansion. Therefore it must be a ductile material. We have just begun to study this problem.

Concerning the compatibility of the fuel with a refractory metals cladding, there are results published in London by General Atomics which show, that (U,Zr)C is compatible with tungsten at 1800°C. It may be that a W-Re alloy with a small amount of Re is compatible also.

We did not yet check the stability of the thermal emissivity values during long time operation. We suggest, that a stable value of 0.5 may be obtained with no major difficulties; a higher value (e. g. 0.75) may be possible with grooved surfaces or by other blackening methods.

UNGER (Germany):

Why does this reactor have a cubic and not a cylindrical form? A cubic form makes power flattening more difficult.

NEU:

The approximately cubic core shape results from a cooling system with crossed heat pipe layers. This system provides more space for locating the converters and is more reliable than a system where all heat pipes are parallel. If one of the heat pipes fails, than the neighbouring heat pipes have to transport additional heat, the temperature of the heat pipe rises and the converters have to operate with a larger heat input. In our system, if, for instance, 20 other heat pipes cross this defective heat pipe, the heat flow of the other heat pipes is increased only to 5%.

UNGER:

This is true. In the cylindrical form, if one heat pipe fails, the heat goes, in a hexagonal system, to 6 other heat pipes which then accommodate the heat.

OUT-OF-CORE THERMIONIC SPACE POWER⁽¹⁾

William E. Loewe

Lawrence Radiation Laboratory, University of California

Livermore, California

Abstract

A survey of conceptual out-of-core thermionic systems using heat pipes has been made to identify critical technology areas, investigate feasibility for space application, locate parameter regimes of interest, and estimate specific mass values. The survey included preliminary comparisons of required, current, and projected state-of-the-art in these critical areas of technology. Temperatures and powers were surveyed in the ranges from 1400°K to 2200°K and from 10 kWe to 10MWe, respectively. A cylindrically symmetric geometry with a linear display of system components was studied.

In general, out-of-core thermionic systems with heat pipes appear to be attractive candidates for use in space over a broad range of electric power levels, meeting the requirements of both advanced auxiliary power and nuclear (electric) propulsion.

I. Introduction

The advantages of thermionic conversion for space power generation have been discussed frequently, and need little discussion at this conference. A convenient reference is an article by B. G. Voorhees.⁽²⁾ A heat source that can be easily matched with thermionic conversion over a range of powers from a few tens of kWe to many MWe, is the nuclear reactor. A sizable body of literature has grown that discusses such a union, with convenient references being again Voorhees⁽²⁾ and also Schreiber and Salmi.⁽³⁾ The major activity has been centered on in-pile concepts. Intrinsic difficulties with this concept, however, result from the fact that use in space implies relatively high temperatures, long lifetimes, and high power densities to provide low specific mass. This combination (1) causes swelling of fuel that distorts the sensitive diode gap, (2) causes release of fission products into the similarly sensitive diode plasma, and (3) causes radiation degradation of in-core electrical insulation. Furthermore, the investigation of these problems is extremely costly, requiring long-time irradiation in fast spectrum reactors at very high neutron fluxes and temperatures.

The disadvantages of in-pile systems can be circumvented by the use of nearly isothermal heat pipes to transport the reactor power with a low temperature loss to an externally located thermionic convertor.⁽⁴⁾ Furthermore, the heat flux transformer properties of heat pipes refine the match between source and convertor, and retain conversion efficiency lost in the in-pile system by axial power flattening problems.

The Lawrence Radiation Laboratory reviewed out-of-core thermionic space power in 1966, and reported an interesting conceptual design for a 2000°K emitter, 10 MWe system intended for use with electric propulsion, with a calculated 6-9 kg/kWe.⁽⁵⁾ This system showed the compatibility of heat pipes, nuclear reactors, and thermionic conversion in the context of space power generation. Subsequently, Heath and Lantz studied the conceptual feasibility of an 1800°K emitter, 36 kWe system having a specific mass of 8.3 kg/kWe using U²³³ and based on technology available relatively early.⁽⁶⁾ E. S. Pedersen has also studied this general concept, apparently independently. Pedersen studied a 2100°K emitter, 1 MWe system and obtained 5.3 kg/kWe.⁽⁷⁾

During this same period, the performance of heat pipes in a zero-gravity (space) environment has been demonstrated,⁽⁸⁾ and many laboratories have successfully tested a variety of heat pipe sizes, materials, temperatures, and internal and external configurations.⁽⁹⁾ Limitations on heat pipe performance appear, within the approximate bounds set forth originally by Cotter,⁽¹⁰⁾ to be previously caused by incautious preparation (undue contamination), and presently to the availability of laboratory environmental equipment that can function at the desired temperatures and heat fluxes. Also, anticipated problems with start-up and catastrophic burnout seem to have been conquered, and even higher axial fluxes than predicted originally by Cotter may be possible if special precautions are taken.⁽¹¹⁾

Continuing effort at Lawrence Radiation Laboratory on out-of-core thermionic space power has been to elucidate more realistic conceptual system designs and to develop a consistent and explicit basis for evaluating these systems as space power sources for all reasonable power levels and with reasonable temperatures, for both manned and unmanned applications. A secondary objective is to show the growth potential in both power and power per unit mass, as needs increase and as available materials improve in temperature capability, respectively. This will ensure that investment in the required development will provide worthwhile long-term returns.

This paper is a progress report on a survey of out-of-core systems in which the primary variables are reactor temperatures between 1400°K and 2200°K and electric power levels between 10 kWe and 10 MWe, and in which a variety of property specifications or component models are available for individual investigation in terms of their effect on system performance. The results of this survey will permit, with increasing confidence as models are improved, 1) assessing the feasibility and competitive performance of these systems, 2) selection of power and temperature ranges, 3) identification of vital technologies for emphasized activity, and 4) credibility that comes from spanning a set of conditions that is wide enough to identify trends, in a manner detailed enough to permit comparisons with component specifications from other systems without undue extrapolation.

This survey is accomplished by a computerized optimization of four independent variables that describe the system. A trade-off among these variables minimizes specific mass within specified constraints for each system. The system is characterized by reactor temperature, electric power output, and, at present, by an imposed geometry that is cylindrically axisymmetric and requires a linear ordering of reactor, heat exchanger, shield, electrical insulator/heat exchanger, thermionic diode array, radiator, and (at a distance in space) payload. Each of these components is described by a model intended to be the simplest that is still adequate to retain the essential features of the component.

II. Discussion of Models and Property Values

A plan view of the system is shown in Figure 1. The three lengths, R_1 , R_2 , and R_3 , have been arbitrarily held fixed at values of 15 cm, 5 cm, and 5 cm, respectively (future model improvements will link these to heat fluxes and control requirements that vary from system to system). The flare half-angle, θ , is one of the four independent variables by which a partially optimized system is obtained. The remaining three independent variables susceptible to variation for minimum specific mass, within the constrained volume of phase space searched, are the volume fraction of fuel in the reactor core, the temperature drop across the electrical insulation in the insulator/heat exchanger, and the temperature of the diode collector.

A. Geometry

The geometric description of the system model shown in Fig. 1, although greatly simplified, permits a realistic treatment of all important interactions characteristic of a shadow-shielded system. Enveloping (4π) shields, obviously much more massive, are excluded from the present study although their feasibility is not questioned.

A fixed payload distance of 50 m is assumed, and systems having a shield flare angle adequate to cover any desired shadow diameter at this distance can be selected.

B. Heat Pipes

Heat pipes throughout the system are 1-cm (ID) cylindrical tubes made of tungsten alloy that contain the customary grooves plus screen capillary structures. The wall thickness is determined by vapor pressure of the heat pipe fluid and tungsten alloy creep strength, except that a fabricability minimum of 0.5 mm is set. The creep strength used throughout is for pure tungsten, shown in Figure 2, but a tungsten alloy is supposed to be the material actually used. For several reasons lithium is the heat pipe fluid except in the radiator, where lower temperatures may make sodium desirable for its higher vapor pressure. First, lithium is compatible with the tungsten and UN materials technology being developed for reactors, within this survey's temperature range, under a current LRL program. Second, above perhaps 1200°K, it is a superior heat pipe fluid to any other until its vapor pressure becomes so high, at very high temperatures, that the weight penalty for tungsten creep resistance (also a function of temperature—see Figure 2) is prohibitive. Third, the only other apparent candidate, silver, is inferior in this application for all temperatures of interest, because its improved heat pipe capabilities compared to lithium appear only at temperatures too high to be of practical interest (at the end of the survey range, around 2000°K).

Axial heat fluxes for these heat pipes are first computed according to optimized internal dimensions derived at LRL and elsewhere using Cotter's equations⁽¹⁰⁾ for the case where screen and channel characteristic dimensions are equal. These are shown in Figure 3 for a 100-cm-long pipe. In the radiator, a pressure drop appropriate to an adiabatic transport section is introduced. As remarked in the introductory section to this paper, J. Kemme⁽¹¹⁾ is decoupling groove and mesh dimensions to obtain still higher axial fluxes. Deserving emphasis is the fact that the axial heat fluxes actually used in this survey are constrained to be no more than 50% of the values shown in Figure 3 (cf. Table 1). Since Cotter's equations⁽¹⁰⁾ have shown reasonable agreement with experiment for sodium except at very low temperatures⁽¹²⁾ (i.e., low vapor pressure), the axial heat fluxes used seem comfortably realizable. (As also remarked earlier, limitation on experimental demonstration of lithium heat pipes presently stems from equipment, not heat pipe

capability or fabrication.) Implied groove and screen dimensions are within present fabrication capability.

Radial heat fluxes into the heat pipes are constrained to be less than 400 W/cm^2 . Such a value is reasonable, when compared with customarily observed values in excess of several hundred W/cm^2 into sodium-filled heat pipes. The reasonableness of comparing sodium to lithium in the absence of experimental data follows if it is assumed that heat pipe limits are set by phenomena (probably incipient boiling) similar in gross mechanism to the phenomena operating to produce burnout heat fluxes at solid-liquid interfaces. The latter fluxes are in fact very similar to those achieved in heat pipes, regardless of mechanism identification, and correlations of burnout data show that lithium should permit almost 10^3 W/cm^2 . Deverall and Kemme⁽¹³⁾ have already run $\sim 200 \text{ W/cm}^2$ Li heat pipes. Actually the point is nearly academic, since in the reactor, radial heat fluxes are rarely or never as high as 400, because other limitations are more stringent than heat pipe capability. This is particularly true of lower power systems of earliest interest, where very modest ($< 10^2 \text{ W/cm}^2$) radial fluxes appear in the reactor.

C. Reactor

The reactor consists of a core plus a weightless, unspecified region surrounding it that is described by the dimensions R_1 , R_2 , and R_3 , mentioned earlier. This surrounding region will contain, as necessary, a reflector and/or control system. The bare core itself is required to have a multiplication factor, k_{eff} , of 0.9, thus permitting adequate shutdown margin when unreflected. The fuel is uranium nitride, of the necessary enrichment, and all structural material is assumed to be the same tungsten alloy used in heat pipes. The core is composed of UN, W, Li (heat pipe fluid), and a reserve volume, proportional to the fuel volume, which is assumed in the calculations to date to have the properties of Li but which can represent (1) any other thermal bonding fluid, (2) a space to accommodate fuel swelling, (3) a means for creating an effective fuel density less than theoretical, or a combination of these, possibly time dependent. Although this bond-swelling-density volume can be varied parametrically, it has not proven to be a strongly influential parameter in the range of zero to 25% of the fuel volume fraction for the systems studied most carefully to date. Therefore, in the data reported here, this volume is set at a representative value of 15% of the fuel volume.

A constraint is placed on the stress in the fuel that results from the thermal gradient between the fuel centerline in a regular array and the associated heat pipe wall. Although systems limited by three different values of maximum stress have been investigated in detail, the results to be presented here will be based on a limit of 10,000 psi. This stress limit, and the associated temperature drop itself, are interpreted as a limit on radial heat flux into the heat pipe. An acceptable radial heat flux into a reactor heat pipe, therefore, is always less than or equal to the smallest of three values: 1) 400 W/cm^2 set by heat pipe considerations, 2) the flux derived from a maximum allowable thermal fuel stress, 3) the flux derived from a maximum allowable temperature drop across the fuel.

A basic variable for a particular system is the reactor temperature, from which all other temperatures are derived. This is a spatially independent, average temperature. A local maximum (i.e. centerline) fuel temperature is immediately available by adding the fuel ΔT just described. Axial temperature variations are reduced greatly by the properties of heat pipes. Gross radial variations have been ignored, in the belief that radial power flattening can be readily achieved in non-criticality-limited reactors, and that a nonuniform distribution of heat pipes in the core can alleviate the problem in criticality-limited cores. (Nonuniform distribution of heat pipes in the reactor heat exchanger is an additional possibility for obtaining radially uniform thermionic diode array temperatures.) Since all data generated have been based on U^{235} fuel, radial power flattening by the use of U^{233} is an available method to achieve uniform radial core temperature profiles.

The reactor core length is established as the largest required by the following three criteria: 1) the total volume of fuel must be enough so that the burnup does not exceed a preset maximum; 2) the heat pipe flux limit in the core must not be exceeded; 3) the (bare) core must have a multiplication factor, $k_{\text{eff}} = 0.9$. To date, a 20,000-hour lifetime and a 3% burnup limit have been set for all systems surveyed.

D. Shield

The shield is assumed to be BeO , to tolerate the high temperature heat pipes piercing it in transit from reactor to convertor. The effect of neutron streaming through these heat pipes is not explicitly included in the calculations, which are otherwise based on simple one-group removal theory. The adequacy of this approximation was tested in one instance by comparison against a multiregion, one-group neutron and 6-group gamma shielding calculation for the entire system, and was found to agree within 10% in shield mass. If the neutron streaming issue should prove serious, even though the length-to-diameter ratio of these holes is quite small, curved or bent

heat pipes are believed possible. Furthermore, although the highest power systems have quite high heat-pipe (i.e. streaming path) volume fractions, these systems lie well in the future in terms of need, and the low power systems of early interest have streaming path volume fractions that are 5% to 10% or less. That is, neutron streaming, which is ignored in these calculations, may present no problems of significance, and, if it does, solutions appear to be either at hand or realizable by the time a solution becomes necessary for distant future needs.

Shield attenuation is fixed by the following requirements. For manned payloads a 20,000-hour dose of about 17 rem is allowed, leaving a margin for additional natural dose (e.g. solar flares). This implies a shield dose attenuation requirement, which then determines the shield thickness. Unmanned shields are set to provide only a shield dose attenuation 10^{-3} less than man rated shields.

E. Insulator Heat Exchanger

Both this heat exchanger and the reactor heat exchanger (see Figure 1) are regions where heat flows from one set of heat pipes to another. In both cases, the heat flux is 400 W/cm^2 , and the flow path is as implied by the left-most portion of Figure 4a. The difference between the two cases is that no BeO spacer-insulator intervenes in the case of the reactor heat exchanger. This re-entrant heat pipe joint is also a characteristic of the thermionic diode (see below), as Figure 4a shows. The mass of both heat exchanger regions is invariably a small proportion of the system mass. It is calculated according to the heat-pipe wall thickness, times the density of W, times the area implied by the thermal power transported divided by the preset heat flux, 400 W/cm^2 . (The weight of the very thin layer of BeO is ignored.)

No temperature drop is accounted for in the reactor heat exchanger. In the insulator heat exchanger, the temperature drop across the BeO is one of the four independent variables. This insulator provides high temperature electrical insulation along with acceptable thermal conductivity, and is shielded from the nuclear radiations in the core. This insulator makes possible series connection of many diodes to obtain the desired output voltage (see below). A corresponding insulator is required in the in-pile thermionic concepts (which have the electrical insulation within the reactor core).

A power loss in the insulator is calculated from the thermal and electrical conductivities of BeO and the maximum (series string) voltage sustained across the insulation. This voltage has been arbitrarily fixed at 400 volts. The BeO electrical resistivity used is LRL data on ultra-pure material,⁽¹⁴⁾ and is shown in Figure 5. The BeO thermal conductivity is assumed to be $0.15 \text{ W/cm}^2\text{-}^\circ\text{C}$ at all temperatures, and is obtained from work reported by M. T. Simnad, et al.⁽¹⁵⁾ Earlier system survey calculations have shown that if the BeO is removed and heat transport is accomplished by blackbody radiation, the result is a heavier system at all temperatures of interest. On the other hand, the increase in specific mass can be regarded as an upper limit on any penalty caused by difficulties that might not be resolved in connection with thermal contact between W and BeO. For example, this upper limit is less than 25%, at 1800°K for powers of 100 kWe and less.

F. Thermionic Converter

The converter is assumed to be an array of diodes formed by concentric cylindrical surfaces in a manner illustrated in Figure 4. Concentric cylindrical heat pipe/diode configurations have been suggested by Busse.⁽¹⁶⁾ The properties of the converter are assumed to be determined by emitter and collector temperatures, and are characterized by a conversion efficiency, an emitter power density, and an effective end-on array electrical power density. The conversion efficiency is assumed for simplicity to be a separable product of a function $\eta_1(T_E)$ of the emitter temperature and a function $\eta_2(T_C/T_E)$ of the ratio of the collector temperature to the emitter temperature, with two alternatives each [thus, yielding four possible ways to obtain a value for the array efficiency, $\eta(T_E, T_C)$]. This assumption is suggested by Leonard's work (see below), and is not inconsistent with experimental data. In all cases, it is assumed that electrode spacing, plasma pressure, surface properties, and materials have been held at values yielding maximum efficiency. (Masses of diodes specifically, and properties generally, have been thought of as corresponding to tungsten emitter, molybdenum collector, and cesium plasma.)

The diode efficiency used, as a function of emitter temperature for the case of no back emission (negligible T_C/T_E), is either the value quoted by Leonard,⁽¹⁷⁾ or that value less a fixed decrement of 0.05. The justification for the use of Leonard's data (shown in Figure 6) is that controlled introduction of electronegative or electropositive additives might result once again in the better values obtained before 1965, when trace quantities of impurities spoiled reproducibility, but occasionally produced the efficiencies quoted by Leonard from the literature available at that time. The justification for the much more pessimistic but reproducible efficiencies, obtained by subtracting 0.05 (5%) from Leonard's data, is that they compare satisfactorily with data obtained by Lieb and Rufe,⁽¹⁸⁾ by Wilson and Lawrence,⁽¹⁹⁾ and computed by Wilkins using the SIMCON semi-empirical computer code.⁽²⁰⁾ Leonard's data include losses caused by thermal

conduction along interconnections in arrays, but not resulting from I^2R losses. Since the diode weight is a relatively small proportion of the system weight in most cases of interest, a simplifying but not significant assumption can be made. This is, that when the diode array is optimized as constrained by its inclusion in an entire system, so that efficiency is more important than specific mass, small losses in efficiency will result in going from diode to diode array. This assumption has been implied as a first approximation by Busse.⁽¹⁶⁾

Information on the influence of collector temperature on maximum diode efficiency is not well-established. A priori, it may be supposed that a factor, depending on T_C relative to T_E and multiplying $\eta(T_E)$ as discussed above, would be unity (at temperatures above the Cs reservoir temperature) until back emission becomes significant, and then fall monotonically until $T_E = T_C$, where a zero efficiency might be expected to occur. Such an over-simplified model has been used in the survey to date, with the efficiency falling linearly to zero at $T_C/T_E = 1$ from either $T_C/T_E = 0.55$ or $T_C/T_E = 0.67$. The former value is consistent with experimental data of Blue and Ingold⁽²¹⁾ and Wilson and Lawrence,⁽²²⁾ as approximated by straight lines, and the latter value is similarly implied by Leonard's data.⁽¹⁷⁾ As these data mature, they can be readily introduced into the survey results.

The power density of the emitter surface influences only the converter specific mass, itself a relatively small proportion of the system specific mass. It does so by determining the total emitter area required to produce the demanded system electric power. (The emitter and collector thicknesses are set at 2 mm and 1 mm, respectively.) The emitter surface power density used was obtained by adjusting the data of Lieb and Rufe⁽¹⁸⁾ to the conditions where maximum efficiency is expected to occur, namely around 0.8 volt and a gap of about six mils. The result of a fit to this adjusted data is shown in Figure 7. The specific mass of the diode array actually has an additive term independent of area, intended to account for array structure, amounting to 0.8 kg/kWe.

The overall array power density, defined as the system total electric power output divided by the frontal area presented by the array perpendicular to the system axis, is constrained to be less than 250 W/cm². This is a reasonable although somewhat optimistic value presently undergoing further investigation at LRL. This parameter is important at very high system powers but has no influence at low and intermediate powers.

G. Radiator

The radiator is composed of heat pipes, probably with sodium as working fluid, and arranged to have a high redundancy. A possible configuration is the truncated cone suggested by Salmi,⁽²³⁾ although the achievement of sufficiently low temperature drops between heat pipes may be problematical. Flat heat pipe radiators that are redundant except for an armored central feed and return line are being designed at LRL, and appear attractive. A radiator configuration is not specified in this survey, except that the radiator must fit in the shadow cone of the shield and not have an unreasonable ratio of length to width (or diameter). The weight is computed first as proportional to the required radiating area for blackbody radiation, assuming an emissivity of 0.8. The proportionality constant is 1.8 g/cm². In order that unreasonably long radiators not be produced by the optimization process, this proportionality is arbitrarily modified to increase the radiator weight by a factor $[1 + 0.2 (L/D - 1)]$, where L/D is a figure of geometrical merit computed conveniently as the ratio of a flat radiator length to twice the value of S_2 shown in Figure 1. Very long radiators are undesirable because of temperature drops incurred from heat pipe to heat pipe, and to the mechanical rigidity required to resist flexing. Although this modifying expression produces reasonable system configurations, it is expected that future careful design of actual radiators will yield a realistic modifier that reflects the undesirability of extremely long radiators, and that the modifier used here will be interpretable as a first-order approximation. This procedure is believed to produce a reasonable system mass, inasmuch as the radiator proportionality factor typically turns out to be 2.5 g/cm² or more for the systems investigated, compared to the geometry-independent value of 1.8 g/cm². When the total system is recomputed without the inclusion of this modifier, but having preset flare angles as determined by earlier calculations using this modifier, total specific masses are indeed reduced somewhat (at 1800°K, for example, by roughly 1 kg/kWe).

III. Results

Figure 8 shows the total system specific mass for a system with a man-rated shield and Figure 9 shows corresponding data resulting from shielding requirements for unmanned payloads. There is a heavy incentive for exceeding temperatures in the reactor core of 1400°K, while 1800°K is both attractive and reasonable. 2000°K yields a small improvement, and 2200°K, omitted for purposes of clarity, is actually harmful to specific mass (due to the need for thicker-walled heat pipes).

Figure 10 shows the incentive to obtain the more optimistic conversion efficiencies (see discussion of models). The ordinate in Figure 10 is the ratio of data obtained with the pessimistic conversion efficiencies (Figure 6 less 5% and an efficiency break point at $T_C/T_E = 0.55$) to the data shown in Figure 6 with an efficiency break point at $T_C/T_E = 2/3$. In the power range of early interest, penalties of the order of 1.5 are seen to be assessed in system specific mass (at 1800°K).

Figure 11 is a cross plot at 100 kWe of the data shown in Figure 9. It shows explicitly the typical rapid rise in specific mass below 1800-1900°K, the temperature-independent region around 2000-2200° K, and the upswing beginning at 2200° K.

Characteristic parameters typical of the systems described by this study are illustrated in Table 1. The system described there would supply 100 kilowatts of auxiliary power for a manned mission. Its 10° shield flare angle would shadow a circle more than 17 m in diameter at the crew vehicle distance assumed (50 m), providing substantial room for extravehicular activity.

The data obtained here will doubtless change, as refinements are made in the component models used, and the specific mass will in general increase as realism is improved. For example, some additional tens of degrees in temperature will be lost at various heat pipe/heat pipe interfaces, and small additional weight will be necessary to realize the reflector control system for the reactor. However, relatively little change in the system specific mass is expected after re-optimization. Therefore, it is believed justifiable to draw certain general conclusions from the foregoing results.

IV. Conclusions

Thermionic converters can be linked with nuclear reactor power sources and heat pipe thermal transport, to produce conceptually sound and reasonable electric power generators for space applications. Such generators are competitive in specific mass at reasonable temperatures, have a high degree of performance improvement potential, and great power up-rating potential from low levels. The advantages of such a generator that were anticipated in the Introduction section appear realizable. Conservatism in expected heat pipe performance is not a heavy penalty. It needs to be shown that thermionic converters, when freed from the rigors of a nuclear core, can yield reliably the high efficiencies obtainable in the laboratory, over lifetimes of 20,000 hours and more. For this purpose, an emitter temperature of 1800°K seems to be satisfactory, and significantly lower temperatures are acceptable initially if necessary to achieve the required lifetimes.

A place in the space program awaits reliable, long-life thermionic conversion systems. The course of their development and their application no longer appears to require diode placement in the extremely high intensity nuclear radiation fields found in compact power reactors.

V. Acknowledgments

This paper would not exist without substantial contributions from many staff members who have been part of the Laboratory's Reactor Project. Although many of these contributions were, in this context, vital and therefore deserving of personal recognition, the number of staff members involved prohibits mention of any except M. Janssen, who structured much of the earlier thinking and participated in the original conception of an out-of-core thermionic space power generator using heat pipes, and M. Jester, who gave his advice and time unstintingly at critical times.

REFERENCES

- (1) Work performed under the auspices of the U. S. Atomic Energy Commission.
- (2) VOORHEES, B. G., "Thermionic Conversion for Space Auxiliary Power Generation," Chemical Engineering Progress Symposium Series No. 75, 63, pp. 110 et seq.
- (3) SCHREIBER, R. E., and SALMI, E. W., A Look at Nuclear Thermionic Systems, *Astronautics and Aeronautics*, (1968) pp. 50 et seq.
- (4) GROVER, G. M., et al., EUR 2229, e
- (5) BARNETT, C. S., *Trans. Am. Nuc. Soc.* (1966) No. 9, 2, pp. 338, 339.
- (6) HEATH, C. A., and LANTZ, E., "A Reactor Concept for Space Power Employing Thermionic Diodes and Heat Pipes," National Aeronautics and Space Administration Report NASA TM X-52370, 1967.
- (7) PEDERSEN, E. S., "Heat Pipe Thermionic Reactor Concept," RISO-M-514, Atomenergi-kommissionens, 1967.
- (8) DEVERALL, J., and SALMI, E., "Heat Pipe Performance in a Space Environment," Thermionic Conversion Specialist Conference (Palo Alto, California) pp. 359 et seq., 1967.
- (9) WALL, R. B., "Heat Pipe Experiments," Thermionics Specialists Conference (AIAA), 1965. BUSSE, C. A., GEIGER, E., PATZSCHKE, M., and QUATAERT, D., "Heat Pipe Life Tests at 1000°C and 1600°C," Thermionic Conversion Specialist Conference, 1966. KEMME, J. K., "Heat Pipe Capability Experiments," Thermionic Conversion Specialist Conference, 1966.
- (10) COTTER, T. P., Theory of Heat Pipes, Los Alamos Scientific Laboratory Report LA-3246-MS, 1965.
- (11) KEMME, J., "High Performance Heat Pipes," Thermionic Conversion Specialist Conference (Palo Alto, California) pp. 355 et seq., 1967.
- (12) KEMME, J. E., Heat Pipe Capability Experiments, Los Alamos Scientific Laboratory Report LA-3585-MS, 1966.
- (13) DEVERALL, J. E., and KEMME, J. E., "High Thermal Conductance Devices Utilizing Boiling of Lithium and Silver," Los Alamos Scientific Laboratory Report LA-3211, 1964.
- (14) NEWKIRK, H. W., and CLINE, C., "Electronic and Ionic Conductivity in Polycrystalline BeO," Lawrence Radiation Laboratory Report UCRL-6513-T, 1961.
- (15) SIMNAD, M. T., et al., "BeO; Review of Properties for Nuclear Reactor Applications," Proceedings of the Conference on Nuclear Applications of Non-Fissionable Ceramics, Washington, D.C., pp. 169-228, 1966.
- (16) BUSSE, C. A., "Optimization of Heat Pipe Thermionic Converters for Space Power Supplies," Joint Nuclear Research Center Ispra Establishment, Italy, EUR 2534.e, 1965.
- (17) LEONARD, A., "Out of Pile Thermionic Space Power Systems Using a Gaseous Heat Transfer Fluid," Rand Corporation, Santa Monica, RM 4469-PR, 1965.
- (18) LIEB and RUFEB, "Performance and Potential Capabilities of Thermionic Conversion Devices," presented at Electron Devices Meeting, Washington, D.C., 1966.
- (19) WILSON and LAWRENCE, *Advanced Energy Conversion*, 4, pp. 195, 1964.
- (20) WILKINS, D. R., "Theoretical Description of Thermionic Converter Output Performance Characteristics," Thermionic Conversion Specialists Conference, Houston, 1966.
- (21) SUTTON, G. W., *Direct Energy Conversion*, McGraw-Hill Book Company, 1966.
- (22) WILSON and LAWRENCE, *Advanced Energy Conversion*, 4, pp. 195 et seq., 1964.
- (23) SALMI, E. W., A Study of a Nuclear Thermionic Propulsion System, AIAA Paper No. 67-229, New York, 1967.

Table 1. 100 kWe Electric Power Generated at 1800°K Reactor Temperature System Configuration, Manned Payload.

Values of Geometrical Parameters in Figure 1:		Core Data:	
$R_1 = 15 \text{ cm}$	$\theta = 10.0^\circ$	Volume fractions	
$R_2 = 5 \text{ cm}$	$S_1 = 26.8 \text{ cm}$	Heat Pipes (ID)	0.18
$R_3 = 5 \text{ cm}$	$S_2 = 41.1 \text{ cm}$	Heat Pipe Wall (W)	0.04
$R_C = 10.1 \text{ cm}$	$L_S = 81.3 \text{ cm}$	Fuel	0.679
$L_C = 46.1 \text{ cm}$	Payload diameter = 17.6 meters	Bond/Swell	0.101
			1.000
		Number of Heat Pipes - 75	
		Axial Heat Pipe Flux - 14.4 kW/cm ²	
		Radial Heat Pipe Flux - 78 W/cm ²	
		Thermal Stress in Fuel - 10,000 psi	
		Fuel Centerline Temp - ~1850°K	
		Burnup in 20,000 hrs - 0.63%	
		U ²³⁵ Fuel	
Shield Data:		System Data:	
Heat Pipe Axial Flux - 8.6 kW/cm ²		Electric Power - 100 kWe	
Heat Pipe Volume Fraction - 5.3%		Electric Voltage - 400 volts	
Converter Data:		Thermal Power - 850 kW _{th}	
Emitter Temperature - 1790°K		Specific Masses, kg/kWe	
Collector Temperature - 1330°K		Reactor	- 1.48
Diode Efficiency - 12.5%		Reactor Heat Exchanger	- 0.02
Array Efficiency - 11.8%		Shield	- 9.00
Array end-on Power Density - 18.8 W/cm ²		Insulator Heat Exchanger	- 0.04
		Converter	- 1.67
		Radiator	- 1.27
		TOTAL	13.48
Radiator Data:			
Radiating Area - 5.3 m ²			
Length of Flat Radiator, L _F - 2.2 m			
Figure of Merit, L _F /2S ₂ - 2.7			

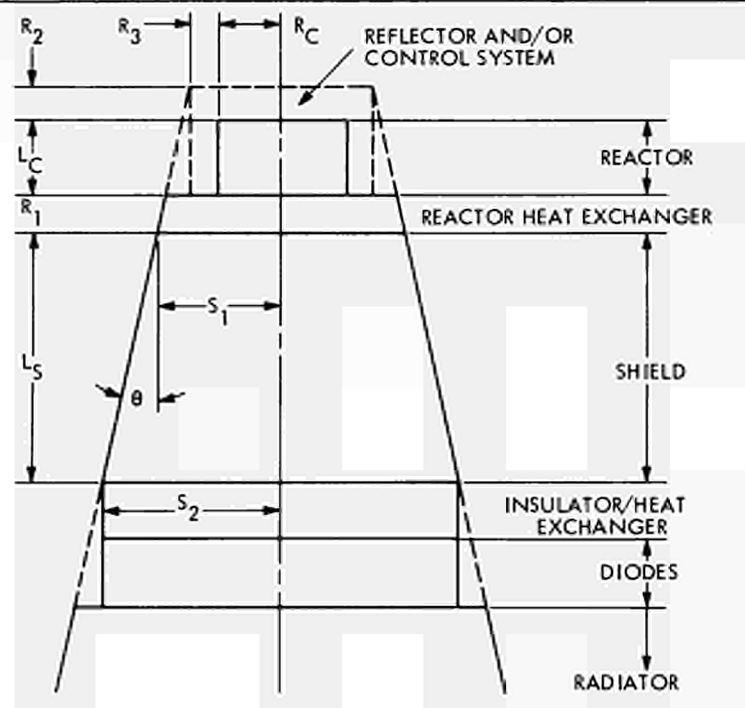


Figure 1. System Geometry.

STRENGTH DATA FOR TUNGSTEN

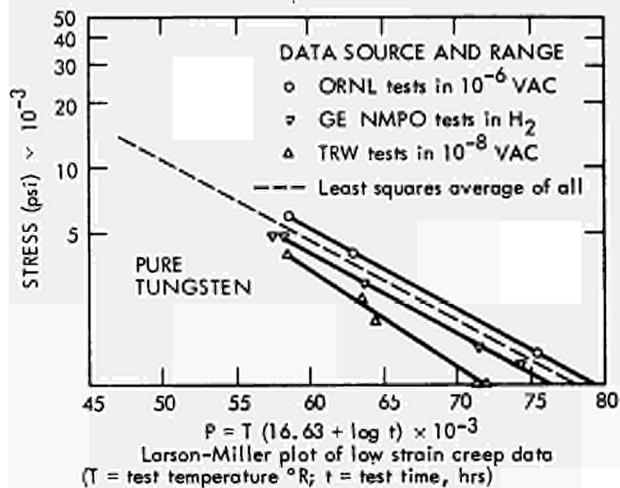


Figure 2. Strength Data for Tungsten.

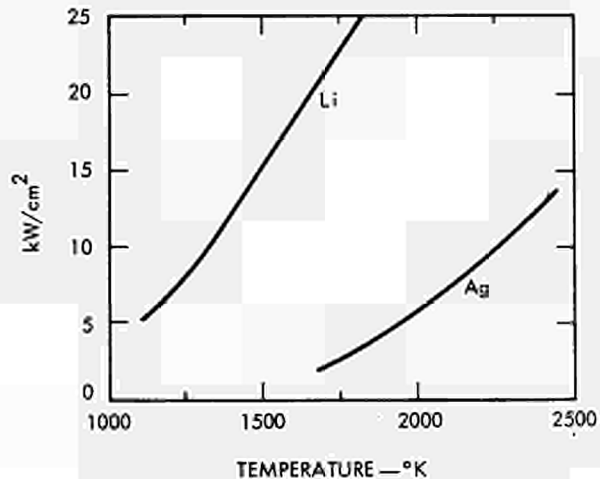


Figure 3. Axial Fluxes for 100-cm Heat Pipes.

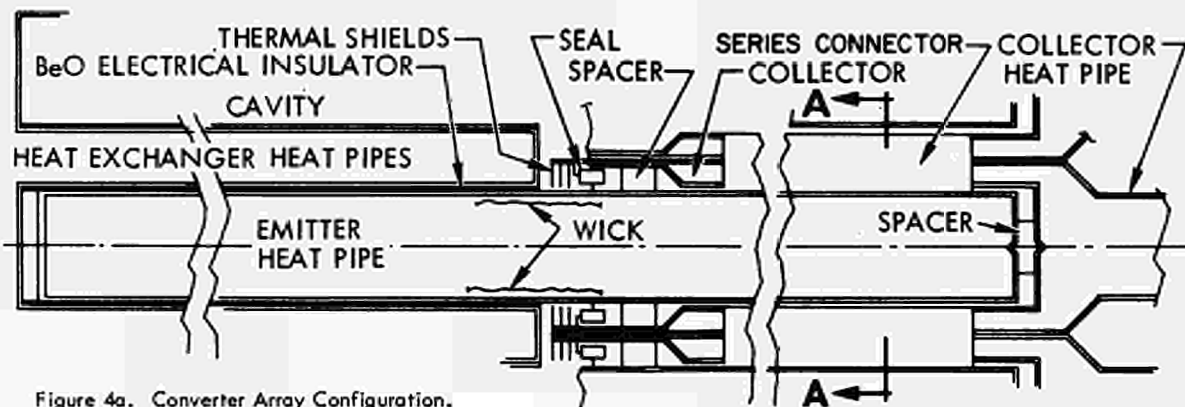


Figure 4a. Converter Array Configuration.

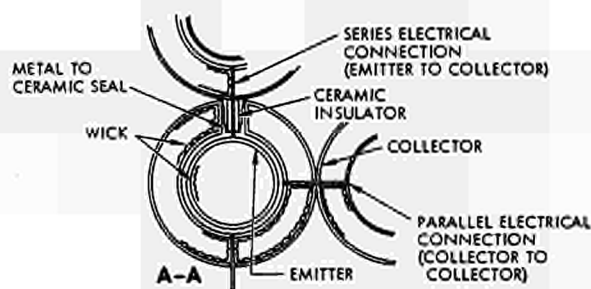


Figure 4b. Details of Converter Array.

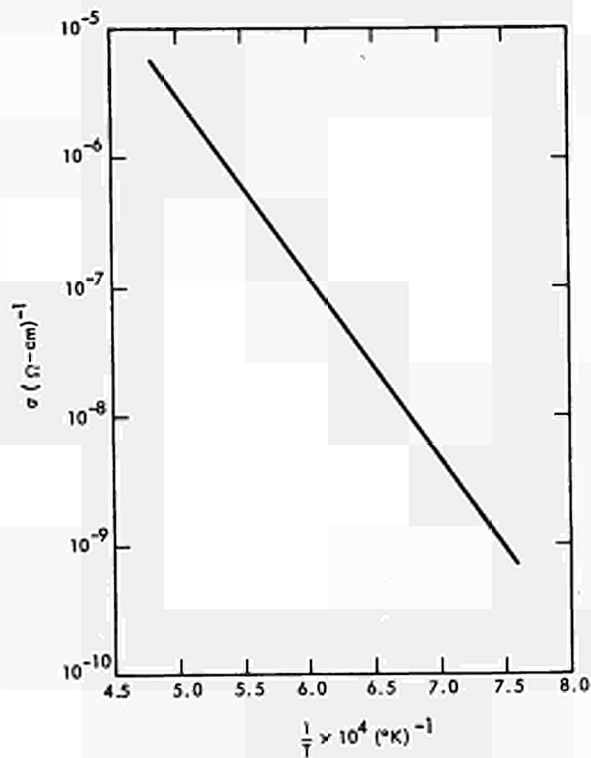


Figure 5. Electrical Conductivity of BeO.

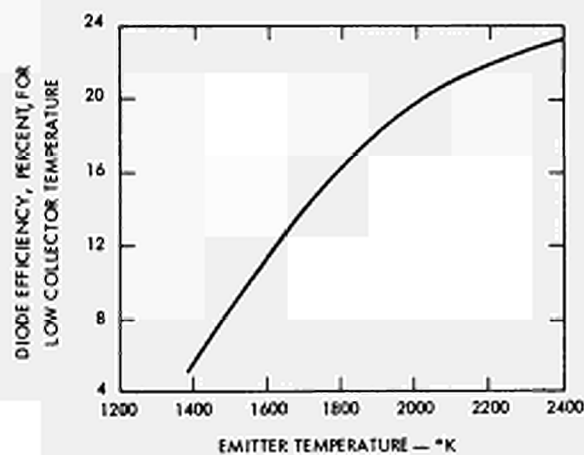


Figure 6. Diode Efficiency vs. Emitter Temperature.

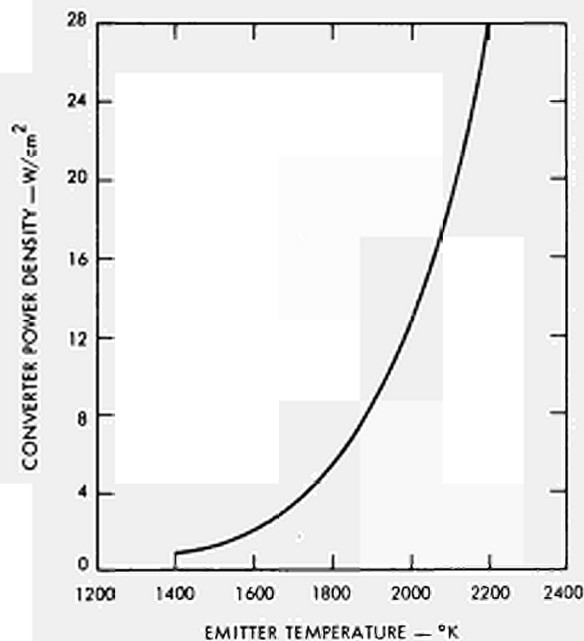


Figure 7. Converter Power Density vs. Emitter Temperature.

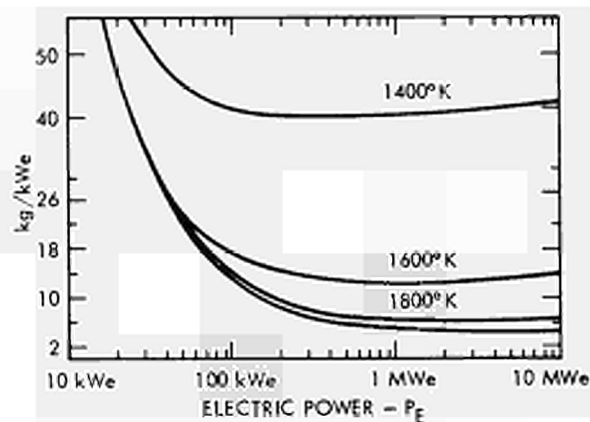


Figure 8. System Specific Mass vs. Electric Power — Man-Rated Shields.

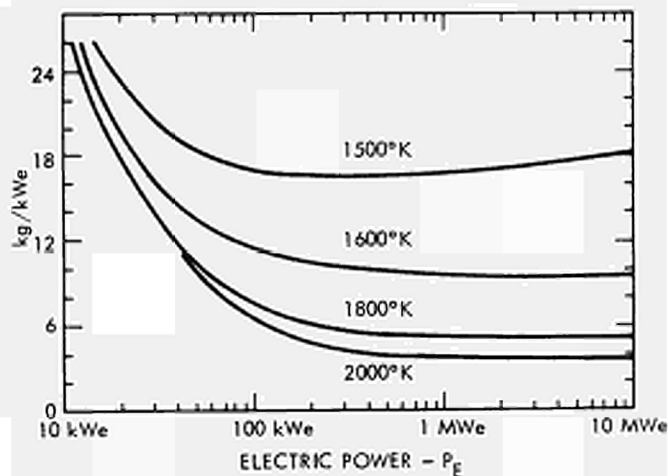


Figure 9. System Specific Mass vs. Electric Power — Unmanned Payloads.

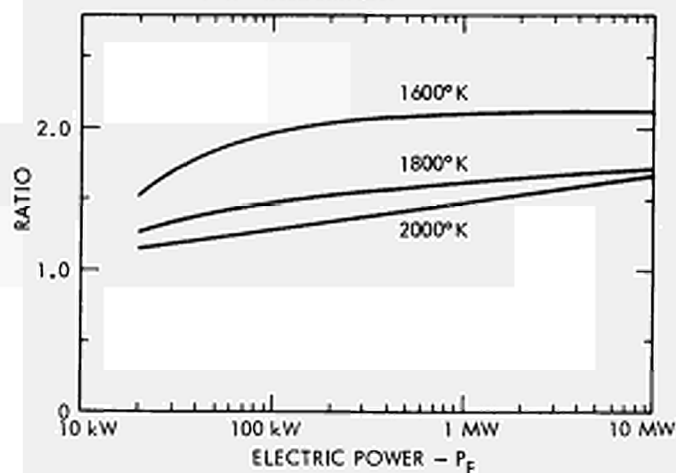


Figure 10. Ratio of System Specific Mass, Pessimistic to Optimistic Converter Performance, vs. Electric Power.

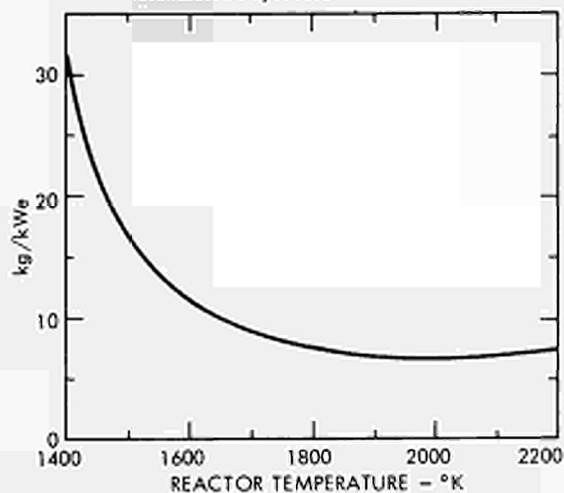


Figure 11. System Specific Mass vs. Temperature for 100-kWe Generator — Unmanned Payload.

STABILITY AND CONTROL CONSIDERATIONS FOR
THERMIONIC REACTORS*

Henrik G. Gronroos⁺ and Jerry P. Davis[#]

Jet Propulsion Laboratory
California Institute of Technology
Pasadena, California, U.S.A.

ABSTRACT

Results of stability and control studies of in-core thermionic reactor space powerplants are discussed. Stability criteria obtained from linear models are found to apply satisfactorily to non-linear models, provided the thermionic diode operates in a region where the current-voltage value is determined by a unique emitter temperature. The implications of cross-over of the characteristic curves are discussed. Analog simulation is used to obtain the dynamic behavior of non-linear plant models.

Control concepts are discussed, and it is concluded that a controller maintaining constant output voltage for expected load conditions appears feasible. Although the system is non-linear, a controller design based on linear theory should perform satisfactorily. It appears that the effects of non-linearities and disturbances can be made small without recourse to sophisticated control systems.

1. Introduction

This paper presents a summary of some results of dynamics studies of small, fast in-core thermionic reactor space powerplants. The main objective of these studies has been to delineate the problems of stability and control. The investigations are motivated by the novel character of the thermionic reactor concepts, and therefore a relative lack of knowledge of their dynamic behavior.

In a thermionic reactor, electric load variations are directly and instantaneously reflected into the reactor core and affect its thermal balance. In addition the cesium space charge gas pressure significantly affects

* This work presents the results of one phase of research carried out in the Propulsion Research and Advanced Concepts Section of the Jet Propulsion Laboratory, California Institute of Technology, under Contract NAS7-100 sponsored by the National Aeronautics and Space Administration.

+ Senior Scientist

Group Supervisor

the thermionic conversion performance, and the possibility of "emitter temperature runaway", and its consequences, are discussed subsequently.

A series stacked internally fueled diode assembly constitutes the basic module selected for detailed numerical evaluations. The chosen design values represent values close to those expected for a 50 to 100 kwe system.

The control system studies have been based on the chosen reference design, and have applied state variable feedback design techniques.¹ This is a linear design method, but application of results to the non-linear system indicate that the method is satisfactory. Earlier reported control system studies² have been expanded, and some of these developments are commented upon.

2. Analytical Model

The analytic model of the thermal-hydraulic system in a thermionic reactor powerplant is relatively straightforward for all components, except for the thermionic diodes, and can draw from a large experience. The neutron kinetic equations are also well known; however, the determination of the temperature coefficients of reactivity requires extensive calculations. The coefficients generally have large error margins, and therefore have been treated as variables in order to define stability regions. For the class of small fast reactors considered, a point kinetics model for the neutron density has been found to be applicable. The representation utilized in the investigations at the Jet Propulsion Laboratory is illustrated

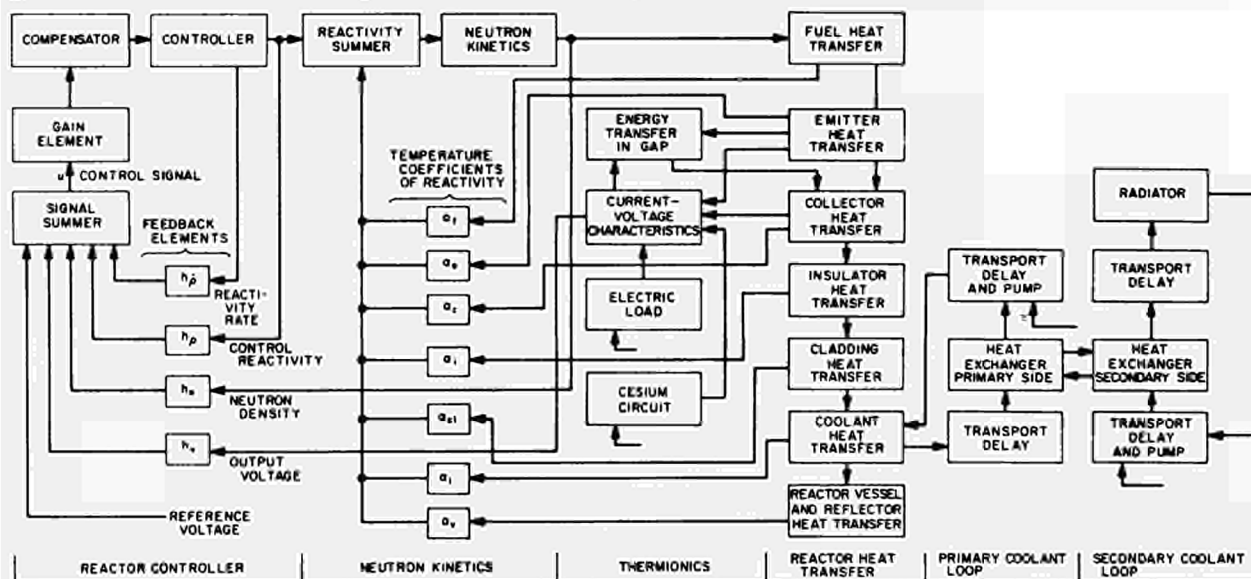


Figure 1: Diagram for Analysis of a Thermionic Reactor Space Powerplant.

by the block diagram in Figure 1. Significant non-linear elements are introduced by the neutron kinetics, the diode current-voltage characteristics, and the energy transfer in the interelectrode gap. Non-linear system models up to twentyfourth order have been investigated by analog simulation methods, including digital computers in a hybrid arrangement for time delay simulation.

The current-voltage characteristics were represented as shown by Figure 2.a. and neglected cesium reservoir temperature variations. This representation may be applied in a limited range to a thermionic converter operating at higher than optimum cesium pressure. If the cesium pressure is optimized with respect to a given operating point, the characteristic curves will cross over as illustrated by Figure 2.b. This situation may for some operating conditions lead to emitter temperature runaway, which in turn may cause the reactor system to oscillate. To illustrate this possibility consider Figure 2.c. where the current density is plotted against the emitter heat input for a given load. If the heat input is increased over the maximum allowed, the operating point is driven to a high emitter temperature and small electrical power output. When the thermal power is lowered a critical value is again reached and the converter is driven to a low emitter temperature. Depending on the magnitude of the feedback coefficients of reactivity and thermal lags, conditions for sustained oscillations can exist at least for the open loop uncontrolled system.³ A lowering of the cesium pressure may also bring an originally stable system into the unstable mode.

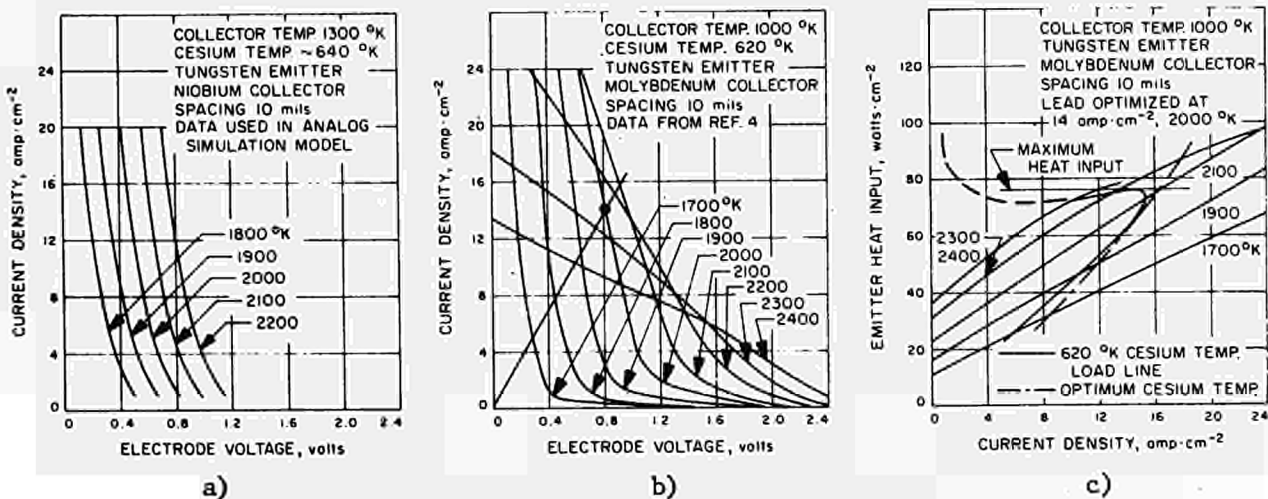


Figure 2: Performance Characteristics for Thermionic Diodes

Emitter temperature runaway, which has been observed experimentally, requires a non-linear analytical description if it is to be accounted for in a stability analysis. If characteristics as shown in Figure 2.a. apply, a linearized description is usually sufficient.

3. Open Loop Stability

Although linear analytical models only approximately describe transients, they are useful for evaluating stability criteria. For simplified analytical models it is observed that for the magnitudes of temperature coefficients of reactivity conceivable for the reference design, the zero-frequency instability is the only type observed.⁵ Only by increasing the expected values of the coefficients by factors of ten or more can oscillatory instabilities occur.

In general the temperature coefficients of reactivity are negative. Only for particular combinations of reactor size and composition and liquid metal coolant volume fractions does the coolant (Li-7, NaK) contribute a positive temperature coefficient of reactivity. However, in a low power core requiring fully enriched unalloyed nuclear fuel the Doppler coefficient of reactivity may be positive for the fuel region. There is considerable uncertainty both with respect to sign and magnitude of this coefficient. Furthermore the fuel-emitter complex expands into a void, i.e. into the inter-electrode gap and the axial separation, which greatly reduces prompt fuel expansion effects on reactivity. The combination of Doppler coefficient and fuel expansion may therefore yield a net positive, but small, temperature coefficient of reactivity; a destabilizing effect. The emitter provides a negative contribution, as do other structural regions. The latter are delayed. The magnitudes of the temperature coefficients obviously depend strongly on the design of the reactor.

A plot of the necessary ratio of $\alpha_{\text{fuel}}/\alpha_{\text{emitter}}$ for stability for the complete model is shown in Figure 3.a. Other temperature coefficients of reactivity have been set to zero. The general shape of the curves in Figure 3.a. has been confirmed with the analog computers both for linear and non-linear models. Such a simple characterization of stability is not generally applicable. An illustration of this is shown in Figure 3.b., which gives the computer-measured stability regions for $\alpha_{\text{collector}}$ versus $(\alpha_{\text{fuel}} + \alpha_{\text{emitter}})$. The curves show a knee at $\alpha_{\text{collector}} = -4 \cdot 10^{-6} \delta k/k \cdot \text{°K}^{-1}$. The large radiator mass introduces a thermal time constant leading to resonance peak at about 0.007 Hz.

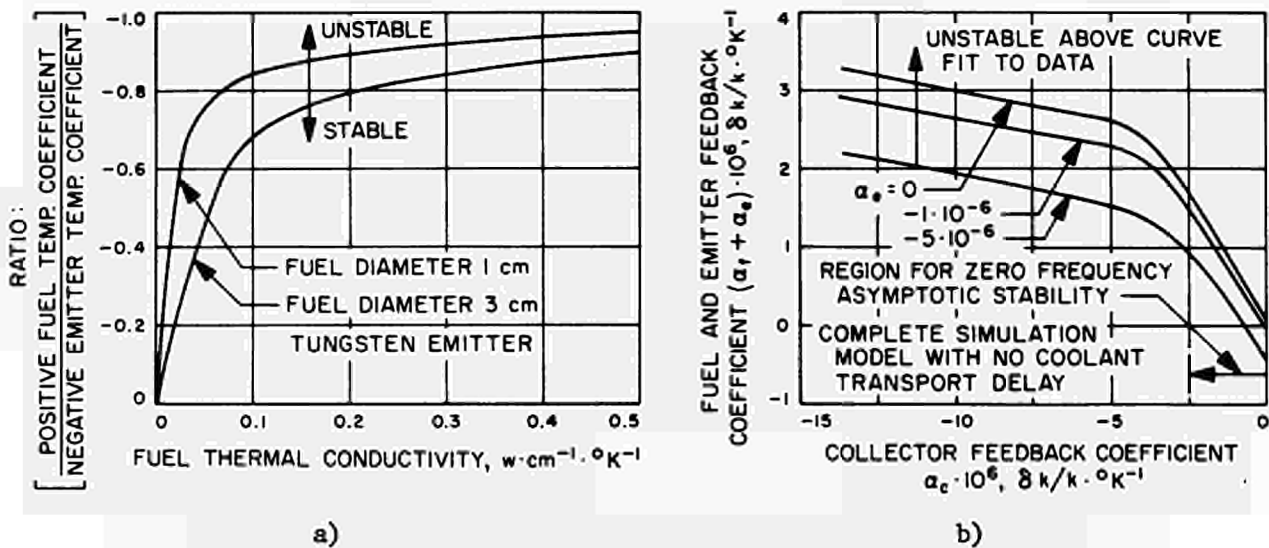


Figure 3: Stability in a Thermionic Reactor Powerplant as a Function of Temperature Coefficients of Reactivity.

The overall conclusions from the stability and transient studies are that the system is inherently stable excluding the previously discussed possible consequences of emitter temperature runaway. However, the generally small inherent feedback leads to a relative large change in operating point even for minor perturbations. The self regulation is inadequate, necessitating active control. However, the thermal transients following various perturbations can be controlled with a conventional control system.

4. Controls

The design of a controller and the control philosophy depends on the application of the thermionic reactor powerplant. As was indicated above, the inherent response to a load perturbation is not consistent with maintaining satisfactory operation over a range of electric loads. Through reactivity control, and thus thermal power control, the desired response must be programmed into the controller function.

An important question is whether the reactor should provide the controlled output, thus simplifying the power conditioning; or all controlled electrical power is supplied by a power conditioner accepting any output from the reactor. In the latter case a programmed reactor response along the maximum power or maximum efficiency locus, or constant emitter temperature control for minimizing thermal stress, are possible control modes. In the former case constant output voltage at the reactor terminals appears to be the best control mode. Our studies have concentrated on this

control mode. A separate study has indicated that only minor efficiency penalties are incurred by constant voltage control over optimum voltage control down to as low as 10% of rated full power.

If a load perturbation is relatively small or of short duration there is no need for adjustment of the reactor power level during the transients. The thermal lag of the reactor system will generally give small temperature perturbations even for relatively large, but short time, load variations. Dead band and dead time for reactor control element activation are essentially determined by the specifications on the output and the time it takes for the emitter to change temperature by a set amount, say 50°K . For the worst case, open circuit at the reactor terminals, this time is about 3 seconds for the reference design under study.

Reactivity rate and total reactivity insertion limits, can be implemented by limiting the control signal (u in Figure 1). Placing a limit on this signal will not cause stability problems. This is not necessarily true if a limit is placed on other state variables. A second order controller, with a compensator, has been evolved by linear design techniques, and applied to the non-linear simulated system with good results.

The studies so far have not considered cesium reservoir temperature perturbations. Since the optimum reservoir temperature increases with increasing emitter temperature and with increasing electric current there is incentive to couple the reservoir temperature control to power demand. Also, the prevention of emitter temperature runaway would imply the desirability of this. The internal reservoir design concepts would have some inherent temperature compensation if properly coupled to the emitter temperature or power level.

5. Conclusions

This paper has discussed some of the main points in thermionic reactor stability and control. It may be stated that the investigations have built up a theoretical understanding of the kinetic behavior of a thermionic reactor. Stability of the system appears to be attainable under foreseeable circumstances. The control start-up and variable power operation appear feasible with conventional controller systems. Several problem areas were pointed out, and some of their consequences were indicated.

REFERENCES

1. Weaver, L. E., and Vanesse, R. E., "State variable feedback control of multiregion reactors," Nuclear Science and Engineering 29 (1967) 264.
2. Gronroos, H., Davis, J. P., Weaver, L. E., and Guppy, J. G., "A control system study for an in-core thermionic reactor," 1967 IEEE Thermionic Conversion Specialist Conference, Oct. 30-Nov. 1, 1967, Palo Alto, California, U.S.A.
3. Schock, A., "Effect of Cesium Pressure on Thermionic Stability," Second International Conference on Thermionic Electrical Power Generation, May 27-31, 1968, Stresa, Italy.
4. Wilkins, D. R., "General Electric, Vallecitos, California, U.S.A. Private Communication of SIMCON code calculated thermionic diode performance.
5. McCarthy, Jr., W. J., and Okrent, D., "Fast reactor kinetics," The Technology of Nuclear Reactor Safety, Vol. 1, The M.I.T. Press, Cambridge, Massachusetts, U.S.A., 1964.

DEVELOPMENT OF A 100 WATT(e)
ISOTOPE THERMIONIC ELECTRICAL POWER MODULE

E. W. WILLIAMS
GENERAL ELECTRIC MISSILE AND SPACE DIVISION
VALLEY FORGE, PENNA. (USA)

R. C. HOWARD
THERMO-ELECTRON CORPORATION
WALTHAM, MASS. (USA)

INTRODUCTION

On June 30, 1966 the United States Atomic Energy Commission initiated a four-phase program leading to the development of 100 watt(e) isotope thermionic modules employing curium 244 and polonium 210 as isotopic fuels. These modules are to be used as basic power units, which in multiples, can supply spacecraft electrical power requirements in the 0.5 - 2 kw range.

This program was an outgrowth of the SNAP-13 Program which represented the initial United States effort toward development of the basic technology needed to realize an isotope thermionic generator. The principal difference between SNAP-13 and the current program involves the degree to which space flight requirements are considered. The basic objective of the SNAP-13 Program was to demonstrate the isotope thermionic principle by means of building and testing an electrically-heated laboratory device on which no flight requirements were imposed. The current program is directed toward the development of an isotope fueled thermionic module which is capable of satisfying the flight qualification and nuclear safety requirements associated with space flight.

The Isotope Thermionic Module Development Program is being conducted for the Atomic Energy Commission by the General Electric Missile and Space Division. General Electric is being supported in this effort by Thermo-Electron Corporation who is performing the thermionic diode work and contributing to the overall module design.

This paper deals with the results of the Phase I effort which was completed in February, 1967. Phase I was concerned primarily with developing preliminary module designs and Phases II - IV involve hardware development and testing of these designs.

DESIGN REQUIREMENTS AND GUIDELINES

The module designs are to satisfy the following requirements:

- 1) Module Power Output at End-of-Mission (EOM): 100 watts(e)
- 2) Mission Duration:
 - Cm-244 module - 1 year*
 - Po-210 module - 90 days*
- 3) Total System Power (EOM): 0.5 to 2 kw(e).
- 4) Spacecraft Bus Voltage: 28 v \pm 10% continuously for mission duration.
- 5) Dynamic environment generally in accordance with MIL-STD-810A.
- 6) The system nuclear safety philosophy is based on containment of the fuel during all operating conditions and accident environments. Those cases involving long-term deleterious environments which may ultimately result in fuel release are to be limited by the design to situations in which such release will not represent significant radiological hazards.

*Both designs allow for an additional 35 days between assembly and launch, since the modules are in an operating condition as soon as they are assembled.

DESIGN ENVIRONMENTS

The module design environments are divided into the following five categories:

- 1) Normal operating environment
- 2) Dynamic qualification environment
- 3) Re-entry environment
- 4) Impact environment
- 5) Post impact environment

The modules are required to be operating and to deliver the specified performance under environments (1) and (2). It is not necessary for the modules to remain operational under the remaining three environment groups.

The selected design environments are summarized in Table 1. In the absence of a specific application these environments were chosen as being representative of a variety of typical space missions.

DESIGN DESCRIPTIONS

The module design concept is shown in Figure 1. The curium and polonium designs are identical except for a slightly larger fuel capsule and emitter in the polonium design. Consequently, Figure 1 is illustrative of both designs and these are described simultaneously below.

The modules consist of the following major subassemblies:

- 1) Heat Source
- 2) Thermionic Diode
- 3) Thermal Insulation
- 4) Electrical Leads and Lead-Throughs
- 5) Module Housing and Helium Filter

Each of these subassemblies is described below:

Heat Source

The heat source is composed of the isotope fuel compound and its associated metal matrix, the fuel liner, and the fuel capsule.

The curium 244 and polonium 210 isotope compounds are combined with a refractory metal to increase the thermal conductivity of the resulting fuel form and in the case of polonium 210 to reduce the power density to a useable level.

The fuel matrix is enclosed in a liner to provide containment and allow decontamination prior to introducing the fuel into the hot cell where the module fueling operation will be performed.

Curium 244 and polonium 210 are both alpha-emitters and as such generate helium gas as they decay. This gas must be restricted, during the mission life, from the module housing volume surrounding the fuel capsule because it would thermally short the insulation. Several potential approaches for handling the helium are outlined below:

- Contain the helium within a cermet fuel form for the mission life.
- Provide sufficient void volume within the fuel capsule to allow containment of the helium for the mission life.
- Vent the helium to the aft compartment of the module housing.
- Vent the helium to the surrounding environment.

Further development work is required before a final selection of the method of handling the helium can be made.

TABLE 1. DESIGN ENVIRONMENTS

ENVIRONMENT	NORMAL OPERATING ENVIRONMENT	DYNAMIC QUALIFICATION ENVIRONMENT	RE-ENTRY ENVIRONMENT	IMPACT ENVIRONMENT	POST-IMPACT ENVIRONMENT
Ambient Temperature	Ground 0°F to 140°F Space 400°F	10°F to 202	Negligible	-40°F to 120°F	30°F to 80°F (Water) -40°F to 120°F (Load)
Ambient Pressure	1 Atm 10^{-3} Torr or less	1 Atm	Negligible	1 Atm	300 ft Sea Water 1 Atm (Land)
Vibration (Sinusoidal)		Freq (cps) 5-15 15-500 one octave/min/axis Amplitude 0.2 in. D. A. ± 5g			
Vibration (Random)		Freq (cps) Below 70 70-400 400-600 600-1000 1000-2000 PSD (g ² /cps) 0.25/Oct. 0.3 0.25/Oct. 0.14 0.25/Oct.			
Shock		35g ± 10% 11 ms ± 10% Peak Terminal Sawtooth			
Acceleration		12g 3 - 4 Minutes	See Notes 1 & 3		
Stagnation Point Heat Flux			See Notes 2 & 3	See Note 4	
Dynamic Pressure			See Notes 1 & 3		
Terminal Velocity				250 ft/sec	
Surface Hardness				Smooth Granite	
Module Orientation				See Note 4	

Notes: 1 - Acceleration and dynamic pressure environments to be based on re-entry into the earth's atmosphere under the following conditions:
 $V_a = 30,000$ ft/sec
 $\gamma_a = 30^\circ$ (measured down from the local horizontal)
 $h_a = 300,000$ ft.
 2 - Stagnation point heat flux environment to be based on worst design conditions resulting from reentry into the earth's atmosphere under the following conditions:
 case 1 - $V_a = 35,359$ ft/sec
 $\gamma_a = 0.1^\circ$ (measured down from the local horizontal)
 $h_a = 430,000$ ft.
 case 2 - $V_a = 30,900$ ft/sec
 $\gamma_a = 0^\circ$ (measured down from the local horizontal)
 $h_a = 430,000$ ft.
 3 - Preliminary definition, more detailed re-entry studies required
 4 - Definition requires more detailed re-entry studies.

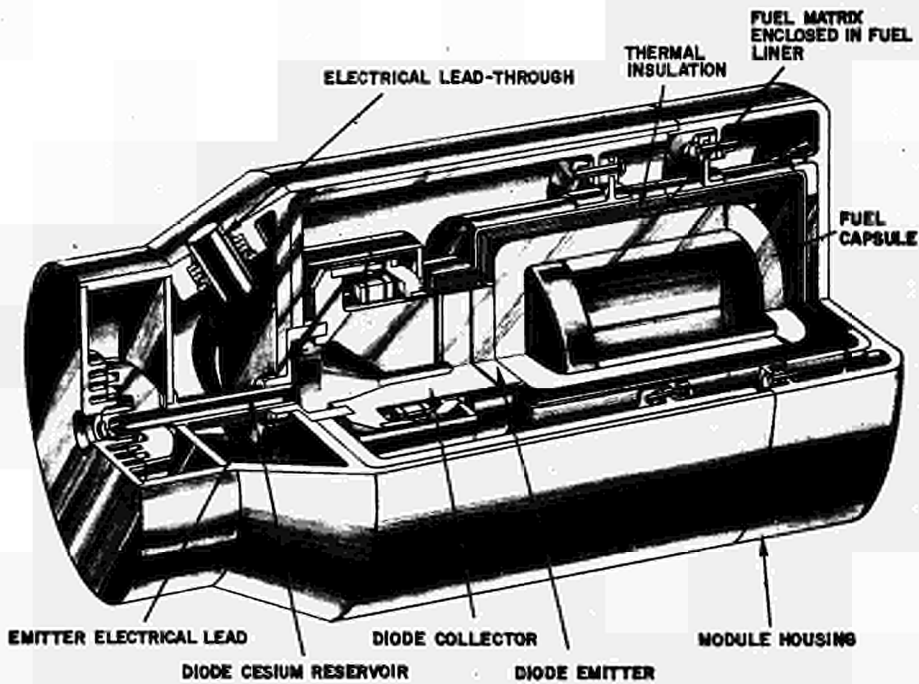


Figure 1. Isotope Thermionic Module Configuration

Thermionic Diode

A planar thermionic diode is used as the energy conversion device. The emitter and collector materials are etched-rhenium and nickel respectively. The emitter surface is diffusion bonded to the fuel capsule allowing conduction heat transfer between the fuel capsule and the emitter. The interelectrode spacing is nominally five mils and is established by thermal expansion of the rhenium diode sleeve. The heat source and emitter are cantilevered from the diode sleeve and the diode is brazed at the base of the collector to the module housing center bulkhead. Copper inserts are used in the collector structure to reduce the thermal impedance and consequently, the temperature drop through the collector.

The cesium reservoir is located on the aft end of the module housing and is connected to the diode collector by a Kovar tube. A passage is provided in the collector to allow cesium vapor to pass from the reservoir to the interelectrode gap between the emitter and the collector. The cesium reservoir location must be remote from the other diode components because it operates at significantly lower temperatures.

Thermal Insulation

In order to minimize thermal losses the fuel capsule and diode sleeve are thermally insulated. Multi-layered radiation shields are used to perform this function. The module reference designs use 120 shields packaged in three 40 - layer groups. The shield packages adjacent to the high temperature surfaces are made from layers of one mil tungsten foil separated by thorium oxide (ThO_2) powder.

The 40 layers are packaged between two concentric tungsten cylinders each with a wall thickness of three mils. The outer two shield packages are constructed in a similar manner except the foil material is 0.3 mil tantalum packaged between three mil tantalum cylinders. The mean spacing between all foil layers is 0.0014 inch. The shield assembly is made in two parts with a slip joint to facilitate the module fueling and final assembly operation. One part of the shield assembly is supported from the thermionic diode, and the remaining portion is supported and electrically insulated from the module housing.

Electrical Leads and Lead-Throughs

The module housing is used as the diode collector electrical lead in order to minimize the number of module housing penetrations. The electrical connection from the collector to the module housing is made at the base of the collector where it is brazed to the housing center bulkhead. A copper bus serves as the emitter lead and is connected electrically to the emitter through the insulation support ring, the emitter ring, and finally the emitter sleeve. The copper lead is clad with nickel to prevent vaporized copper from plating out on other module components and causing electrical shorts.

The emitter lead passes through the module housing center and aft bulkheads, and is electrically insulated from the housing at both these points. A conventional ceramic to metal lead-through is used to support and electrically insulate the emitter lead from the module housing at the center bulkhead. An all-metal lead-through performs this function at the aft bulkhead because it can withstand earth impact and thermal shock better than a ceramic to metal seal. The all-metal lead-through provides a high impedance path between the emitter lead and the module housing by connecting these two components by a long, thin metal path. The metal path consists of a series of concentric Haynes-25 cylinders where each cylinder is welded at one end to the cylinder enclosing it and at the other end to the cylinder it encloses. The resulting high impedance between the lead and the housing allows the power loss through the all-metal lead-through to be held to less than 2.5 percent of the diode power output.

Module Housing

The module housing serves numerous functions. Its primary purpose is to provide containment for the isotope fuel under accident and abort induced environments such as earth re-entry, earth impact, and water submergence. In addition, it serves as the module mounting surface, the collector electrical lead, the radiator from which the waste heat is dissipated, and maintains a protective environment for the oxidation sensitive internal components.

To accomplish these functions the module housing is a composite structure. The basic impact shell is made of Haynes-25. A copper sleeve is diffusion bonded to the Haynes-25 shell over a portion of its inner surface area to improve the thermal conduction path from the diode mounting point on the module housing center bulkhead to the cylindrical surface area which is used as a radiator. The copper is clad with nickel to prevent vaporized copper from plating out on other module components and causing electrical shorts. The nickel clad is diffusion bonded to the copper.

A foamed Haynes-25 insert is brazed to the forward end of the module housing to partially absorb and distribute impact loads.

In those power system applications where the waste heat is dissipated directly from the module housing to space by thermal radiation a high emissivity coating will be applied to the external housing surface.

PERFORMANCE

The principal performance parameters for the curium 244 and polonium 210 reference designs are summarized in Tables 2 and 3 respectively. Module power output (P_M) and efficiency (η_M) as a function of time into the mission are shown in Figures 2 and 3.

In order to minimize fuel loading requirements the modules are designed to operate at peak diode efficiency at the end-of-mission (EOM). In addition, to avoid wide and repeated variations in diode emitter and isotope fuel operating temperatures, resulting from changes in spacecraft power demand, the modules are operated at a constant output voltage. The output voltage selected is that value corresponding to the diode peak efficiency point at EOM. The control necessary to operate the modules at constant voltage is provided by the power conditioning equipment.

Curium 244 with a half-life of 18.4 years requires essentially no power flattening over the one year mission duration. Polonium 210 with its relatively short half-life of 90 days, requires considerable power flattening. A completely passive technique which is controlled by the natural decay of the isotope fuel is used to accomplish the power flattening. Consider the polonium module design (Figure 3). At the beginning-of-mission (BOM) the excess thermal energy available from the isotope fuel naturally causes the cesium reservoir to operate at a higher temperature than it does at EOM. This higher than optimum cesium reservoir temperature causes a high diode current flow and consequently large quantities of energy are removed from the heat source by electron cooling. The removal of energy by this technique accomplishes the power flattening and holds the emitter and fuel operating temperatures down to acceptable levels. As the mission proceeds the isotope energy output decays and the cesium reservoir temperature naturally decreases, resulting in a decrease in the energy transferred from the heat source by electron cooling. This trend continues until at EOM the cesium reservoir temperature is optimum and the module is operating at the peak efficiency design point. The effectiveness of this power flattening approach is illustrated in Figure 3 which indicates that the polonium module operates at essentially constant efficiency.

CONCEPTUAL POWER SYSTEM DESIGNS

The isotope thermionic modules described above are employed in multiples and combined with other components to form a space power system. The basic isotope thermionic power system concept and designs for two specific missions are presented in the following paragraphs.

Power System Concept

A block diagram of a typical curium 244 isotope thermionic power system is shown in Figure 4. The power system consists of the following major components:

- 1) Isotope Thermionic Modules
- 2) Low Voltage Electrical Leads
- 3) Power Conditioning Equipment
- 4) High Voltage Leads

The power system is made up of a number of thermionic modules arranged in a series-parallel circuit and connected to the power conditioning equipment by the low voltage leads. The number of modules required is defined by the spacecraft power requirements and the efficiency of the components connecting the modules to the spacecraft load. The power conditioner consists of a DC/DC converter and a shunt regulator. The DC/DC converter steps the voltage output of the modules up to the nominal 28 volts supplied to the spacecraft bus. The shunt regulator provides the control necessary to operate the modules at a constant output voltage and regulates the voltage supplied to the bus. The module voltage operating point selected is that value associated with the diode peak efficiency point at the end-of-mission. The shunt regulator accomplishes this function by sensing the output voltage of the DC/DC converter. When the spacecraft power requirements decrease from their maximum value the voltage output at the DC/DC

TABLE 2. CURIUM MODULE PERFORMANCE PARAMETERS

MODULE PERFORMANCE	BOM	MOM	EOM
Diode Interelectrode Spacing, d - inches	0.005	0.005	0.005
Diode Sleeve Size Parameter, $A_E/L_E A_E$ - 1/cm	0.00870	0.00870	0.00870
Diode Emitter Temperature, T_E - °K	1879	1871	1863
Diode Efficiency, η_D - percent	14.22	14.40	14.60
Diode Output Voltage, V_D - volts	0.717	0.717	0.717
Diode Output Current Density, J - amps/cm ²	10.70	10.60	10.50
Diode Output Power, P_D - watts	111.2	110.6	110.0
Diode Cesium Reservoir Temperature, T_R - °C	310	307	305
Diode Emitter Area, A_E - cm ²	14.52	14.52	14.52
Diode Output Current, I_D - amps	155.5	154.3	153.0
Diode Emitter Diameter, D_E - inches	1.698	1.698	1.698
Diode Lead Resistance, R_L - ohms	0.000108	0.000108	0.000108
Diode Lead Voltage Drop, ΔV_D - volts	0.0168	0.0167	0.0165
Diode Lead Electrical Power Loss - watts	2.61	2.57	2.53
Module Output Voltage, V_M - volts	0.701	0.701	0.701
Module Lead-Through Resistance, R_{LT} - ohms	0.234	0.234	0.234
Module Lead-Through Current, I_{LT} - amps	3.06	3.06	3.06
Module Lead-Through Electrical Power Loss - watts	2.19	2.19	2.19
Module Output Current, I_M - amps	152.44	151.24	149.94
Module Electrical Power Output, P_M - watts	107.0	106.0	105.3
Diode Thermal Input, Q_D - watts	782	768	754
Shield Insulation Loss, Q_S - watts	28.60	28.00	27.50
Joint Insulation Loss, Q_J - watts	19.74	19.36	18.97
Diode Sleeve/Insulation Edge Loss, Q_{SE} - watts	42.70	41.70	41.20
Helium Vent Tube Loss, Q_H - watts	2.68	2.67	2.66
Total Thermal Insulation Loss, Q_T - watts	93.72	91.73	90.33
Module Overall Thermal Power Req'd, Q_T - watts	876	860	844.33
Percent Thermal Insulation Loss, percent	10.70	10.69	10.68
Module Overall Efficiency, η_M - percent	12.20	12.32	12.49
Module Overall Dimensions - inches	4 Dia x 10		
Module Weight - pounds	13.35		
Module Specific Power-watts/lb	7.88		

TABLE 3. POLONIUM MODULE PERFORMANCE PARAMETERS

MODULE PERFORMANCE	BOM	MOM	EOM
Diode Interelectrode Spacing, d - inches	0.005	0.005	0.005
Diode Sleeve Size Parameter, $A_S/L_S A_E$ - 1/cm	0.00870	0.00870	0.00870
Diode Emitter Temperature, T_E - °K	1870	1802	1740
Diode Efficiency, η_D - percent	12.68	12.80	12.90
Diode Output Voltage, V_D - volts	0.574	0.574	0.574
Diode Output Current Density, J - amps/cm ²	14.16	11.40	9.00
Diode Output Power, P_D - watts	173.2	139.5	110.0
Diode Cesium Reservoir Temperature, T_R - °C	326	305	280
Diode Emitter Area, A_E - cm ²	21.30	21.30	21.30
Diode Output Current, I_D - amps	302.0	243.0	191.8
Diode Emitter Diameter, D_E - inches	2.050	2.050	2.050
Diode Lead Resistance, R_L - ohms	0.000108	0.000108	0.000108
Diode Lead Voltage Drop, ΔV_D - volts	0.0326	0.0259	0.0205
Diode Lead Electrical Power Loss - watts	9.85	6.21	3.88
Module Output Voltage, V_M - volts	0.542	0.549	0.554
Module Lead-Through Resistance, R_{LT} - ohms	0.234	0.234	0.234
Module Lead-Through Current, I_{LT} - amps	2.45	2.45	2.45
Module Lead-Through Electrical Power Loss - watts	1.405	1.405	1.405
Module Output Current, I_M - amps	299.55	240.55	189.35
Module Electrical Power Output, P_M - watts	162.2	132.0	104.8
Diode Thermal Input, Q_D - watts	1362	1090	852
Shield Insulation Loss, Q_S - watts	32.20	27.30	24.80
Joint Insulation Loss, Q_J - watts	19.53	16.49	14.99
Diode Sleeve/Insulation Edge Loss, Q_{SE} - watts	49.15	43.17	37.52
Helium Vent Tube Loss, Q_H - watts	2.66	2.64	2.62
Total Thermal Insulation Loss, Q_I - watts	103.54	89.60	79.93
Module Overall Thermal Power Req'd, Q_T - watts	1465.0	1180.0	931.9
Percent Thermal Insulation Loss - percent	7.07	7.60	8.59
Module Overall Efficiency, η_M - percent	11.08	11.18	11.26
Module Overall Dimensions - inches	4 Dia x 10.5		
Module Weight - pounds	14.70		
Module Specific Power - watts/lb	7.13		

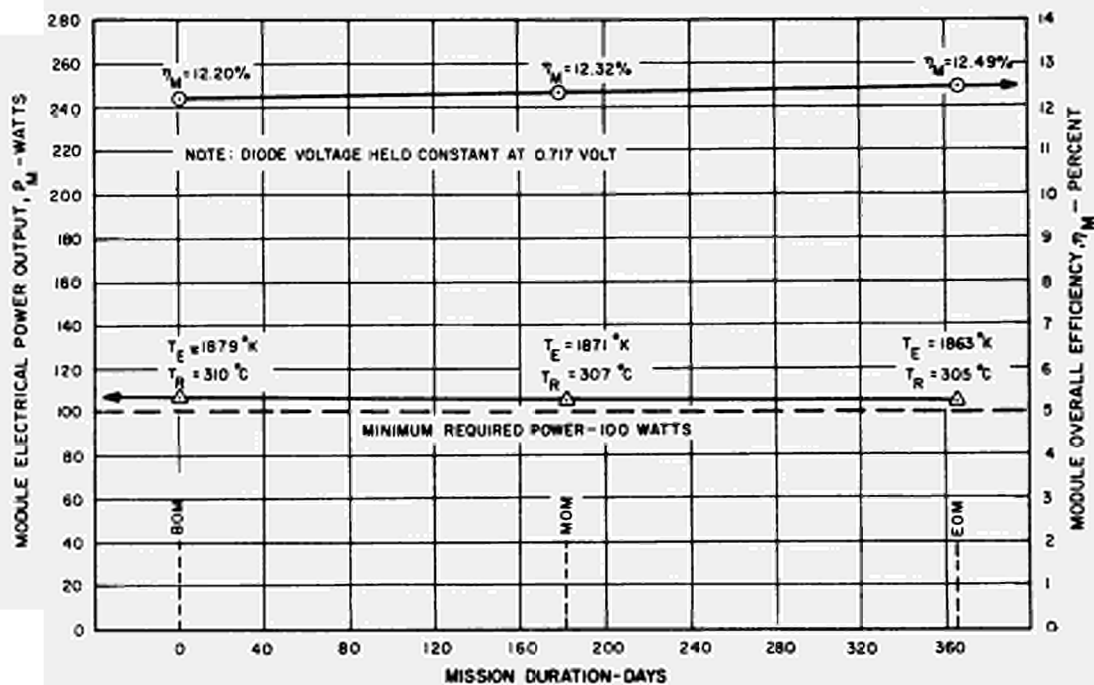


Figure 2. Curium Module Performance

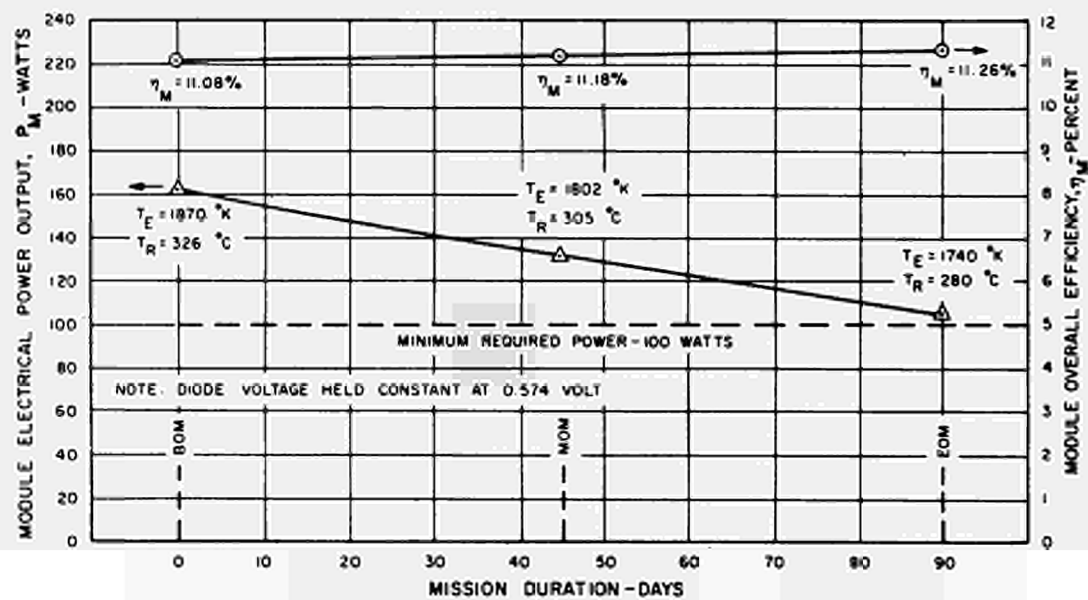


Figure 3. Polonium Module Performance

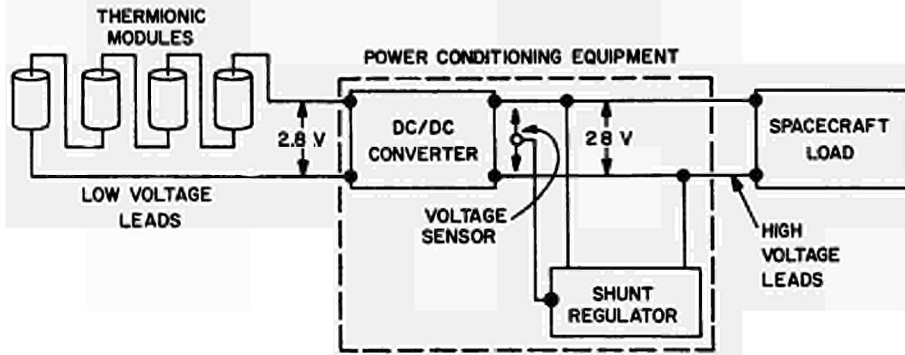


Figure 4. Block Diagram of a Typical Curium 244 Fueled Isotope Thermionic Power System

converter terminals attempts to increase. The shunt regulator senses this changing voltage and compensates for the change in spacecraft load by varying a load resistance which is in parallel with the spacecraft load. This technique allows the DC/DC converter, and consequently the thermionic modules output voltage to be held constant regardless of variations in the spacecraft power demands. Finally, the power conditioning equipment is connected to the spacecraft bus by the high voltage electrical leads.

The polonium 210 fueled power system operates in essentially the same manner as the curium 244 fueled power system except the shunt regulator also performs a power flattening function. The power output generated by each module above the required 100 watts is dissipated in the shunt regulator variable load resistors in the same manner that changes in spacecraft power demands are handled. For this reason the shunt regulator precedes the DC/DC converter in the polonium 210 power system to eliminate the necessity of handling relatively large quantities of power in the DC/DC converter which is not going to be used by the spacecraft load.

In order to satisfy the nuclear safety intact re-entry philosophy, the clustered modules require re-entry protection. One approach for providing this protection is shown in Figure 5. In this concept the modules are grouped within a common re-entry vehicle and the vehicle side panels are used as the space radiator. There are numerous approaches for providing the required re-entry protection and each application must be considered on the basis of its specific requirements.

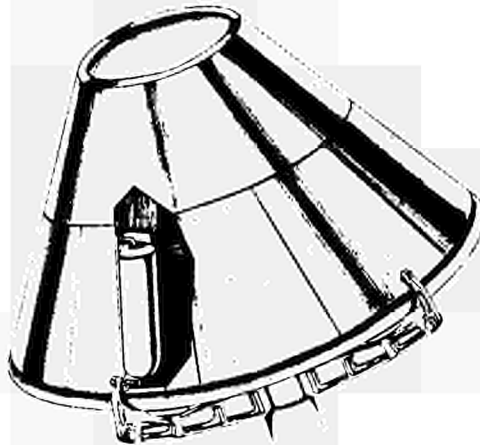


Figure 5. Clustered Module Power System Concept-Apollo Re-entry Vehicle Configuration

Power System Designs

During the Phase I Program conceptual power system designs were developed for a Mars orbiter (Voyager) and a lunar roving vehicle (Lunar Scientific Survey Module). Conceptual drawings of these spacecraft, equipped with isotope thermionic power systems, are shown in Figures 6 and 7.

Table 4 summarizes the principal performance parameters associated with the Voyager and Lunar Scientific Survey Module power system designs. Table 5 presents a percentage weight breakdown for the major components making up the power system.

Table 6 compares the weight of an isotope thermionic power system with the weights of the other types of power systems designed for the Voyager and Lunar Scientific Survey Module spacecraft.

SUMMARY AND CONCLUSIONS

To the extent that experience exists, the preliminary designs presented have been based on current state-of-the-art in the areas of diode performance, isotope characteristics, thermal insulation effectiveness, material combinations, and fabrication techniques. A reasonable development effort is expected to lead to prototype units capable of satisfying all the design and nuclear safety requirements.

During the Phase I study the module designs presented here were shown to be compatible with a variety of space missions and to offer attractive performance when compared with other competing types of power systems. The principal features of the isotope thermionic modules are:

1) High Efficiency (~12%) - The high thermal to electrical efficiency results in reduced fuel cost, improved fuel availability, and simplifies the nuclear safety problem. Compared to state-of-the-art isotope thermoelectric generators the isotope thermionic modules require approximately one-third the fuel loading for the same power output.

2) High Heat Rejection Temperature (~500°C) - The high heat rejection temperatures result in small radiators and make the system insensitive to its surrounding environment. This latter condition makes isotope thermionic systems particularly well suited to applications where the environmental sink temperature is high and/or continually varying over a wide range (lunar surface, solar probes, etc.).

3) High Specific Power - The isotope thermionic modules offer a specific power of 7 to 8 watts/lb. compared with isotope thermoelectric generator values which are typically around 1.5 watts/lb.

4) Small Size - The isotope thermionic modules deliver 100 watts (e) at EOM from a cylinder 4.0 inches in diameter and 10.0 inches long. This compares with the SNAP-27 isotope thermoelectric generator which develops 56 watts (e) and is 15.7 inches in diameter by 18.1 inches long.

These characteristics make isotope thermionic power systems particularly attractive for planetary exploration since the system is suitable, without significant modifications for missions toward and away from the sun.

The above conclusions are based on current state-of-the-art thermionic diode performance. There is every reason to expect that diode performance will continue to improve with a corresponding improvement in the performance estimates made in this study.



Figure 6. Voyager Spacecraft Concept with Isotope Thermionic Power System

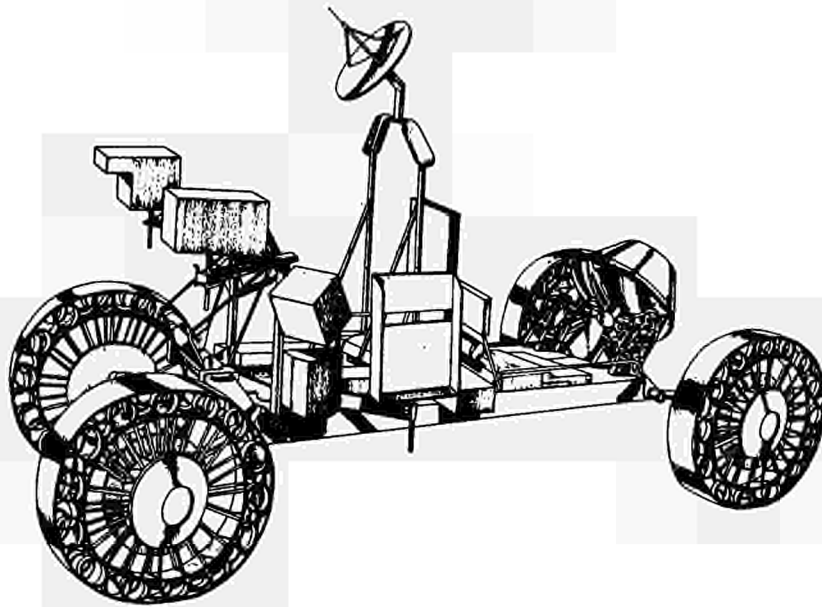


Figure 7. Lunar Scientific Survey Module Concept with Isotope Thermionic Power System

TABLE 4. SUMMARY OF POWER SYSTEM PERFORMANCE

MISSION	LIFE	FUEL	POWER OUTPUT (WATTS)	OVERALL SYSTEM EFFICIENCY (PERCENT)	POWER-TO-WEIGHT RATIO (WATTS/POUND)
Voyager LSSM	1 year	Cm-244	640	9.6	1.83
	90 days	Po-210	411	8.8	2.16

TABLE 5. PERCENTAGE BREAKDOWN OF POWER SYSTEM WEIGHTS

POWER SUPPLY COMPONENT	WEIGHT-PERCENT OF SYSTEM	
	VOYAGER	LSSM
Thermionic Modules	30	37
Re-entry Protection	19	31
Low Voltage Leads	9	6
DC/DC Converter-Regulator	15	11
Shunt Resistors	2	4
Mountings, Booms, and Separation Devices	25	11

TABLE 6. COMPARISON OF POWER SYSTEM WEIGHTS-POUNDS

MISSION	ISOTOPE THERMIONIC	SOLAR ARRAY	FUEL CELL	ISOTOPE THERMOELECTRIC
Voyager LSSM	355	425	NA	735
	190	NA	NA	287

NA - not applicable

DISCUSSION

Speaker of paper B-11: E. W. WILLIAMS

RASOR (USA):

The safety design philosophy was described as total containment of the isotope. Can the system survive earth-burial on re-entry?

WILLIAMS (USA):

We have looked at a large number of these abort environments in the safety analysis. Earth burial (in some soils) is one of the abort environments that we can not survive and a question of the fuel solubility and reaction in the earth must be answered before we can determine what the magnitude of that hazard might be. You have trouble with two environments out of about 10 or 12 that are fairly significant. One of those is earth burial, the other is the launch-pad fireball, which can be gotten around but requires additions to the system. Whatever the concept is, when you put the total system together we have to consider this problem. I should add that I know of no isotope thermoelectric flight system in which the fuel containment does not melt on earth burial in certain types of soil.

KNOERNSCHILD (Germany):

You showed in the first slide of the entire assembly the thermal insulation and you said that you had an oxide coating on those sheets of metal in order to reduce the heat loss, but do these sheets now have contact to each other, then it is not radiation shielding but it is...

WILLIAMS:

The way this shielding body is made up, it is a very thin refractory metal foil usually about 0.3 mil in thickness and you actually wrap this on itself, but before you make each wrap you spray or paint this oxide-powder to provide a separation between the metal shields. The oxide of course has a very poor thermal conductivity so that there is a conduction component but this is very small; the radiation is the predominant component. I think there will be a paper presented on this to-morrow I believe by Mr. DUNLAY, and it is probably not worth going in to greater detail at this time.

KNOERNSCHILD:

If the sheets are pressed together so there is no air space, then there would be only conduction. But I presume your dioxide powder sprayed on the foil has a porous structure, so that at high vacuum heat is mainly transferred

by radiation.

WILLIAMS:

Well, the metal pieces do not come together of course. The oxide provides the separation between the adjacent metal wrappings, but I think you probably can see it tomorrow. They will probably show you some samples.

EINFELD (Germany):

What is the reason for the higher safety of the thermionic system in comparison to the thermoelectric system? Due to the higher operating temperatures of the fuel of the thermionic generator, the fuel capsule strength is less than in the case of thermoelectrics.

WILLIAMS:

First of all I did not mean to say that the safety problems were less in a thermionic device than they were in a thermoelectric device. I do not believe that I said this, at least I did not mean to. I said that fuel required was substantially less which reduced the cost, and... Oh, I probably know where you got it, I said it reduced the nuclear safety problems. The reason it does reduce the problems is because for the same power output of course you have less fuel, that is the point I meant to make there. For the same power output, you would have 1/3 of the fuel involved in the case of a thermionic device, versus a comparable power output for a thermoelectric generator. That was the only point I meant to make.

To answer your other question. The thermionic design is quite different from the thermoelectric generator. In most thermoelectric generators, the fuel capsule actually serves as the containment vessel for the fuel from the nuclear safety standpoint. This means it takes the impact loads, earth burial, etc., so that the capsule is the device which provides the containment for the fuel. At the high temperatures involved in thermionic generators, we can not use that approach because first of all we have to use refractory metals which oxidize quite easily, so we divide the responsibility of this nuclear safety containment of the fuel between this inner refractory metal capsule which simply contains the fuel under all known operating conditions and this outside module housing which actually is, from the nuclear safety standpoint, the containment housing. That is the container that we do not want the fuel to get out of.

Now, some of the problems are simplified, we believe, in comparison to thermoelectrics. This outside cylinder for instance operates in our case at

a temperature of about 500°C. In the case of a thermoelectric generator the comparable temperature is about 850°C for the body which is containing the fuel. Also because of our small size we have at General Electric some impact experience on capsules of this size and in this temperature range, and this leads us to believe that the impact capability of the module housing will be pretty good. However, we have not conducted tests on this particular device to answer that question as yet.

DANILOV (USSR):

What was the specific power at the emitter?

WILLIAMS:

The diode current density was 10.7 Amps per cm².

DANILOV:

Please indicate the full charge of the isotopes.

WILLIAMS:

In a curium design we had about 880 Watts in the initial fuel loading. In the case of the Polonium 210 design the fuel loading is about 1700 Watts because you have a big power flattening problem of course with the Polonium, which has a very short half-life.

DANILOV:

How did the characteristics of the converter change in the time with the use of Po210; does this isotope present any interest?

WILLIAMS:

I did not include the Polonium - module performance simply because of time limitations. Slide 11 (Fig. 3) shows the predicted performance with the Polonium - module. An approach which is totally passive is used to accomplish the power flattening, it works like this: At the beginning of mission when you have a great deal of excess energy available from the isotope the cesium reservoir tends to run at a much higher temperature than the optimum value. This higher cesium reservoir temperature results in higher current flow and consequently a greater electron cooling term. This higher electron cooling term thereby takes away a great deal of the excess energy from the fuel. This holds the fuel and diode emitter temperatures down to acceptable levels. Now as time passes and the isotope power decays the cesium reservoir temperature naturally decreases, and it tends to move towards the optimum value that we desire at the end of mission. With an

initial trim of the system at the beginning we are able to use this completely passive technique to provide the power flattening.

GRIAZNOV (USSR):

What is the comparison of the specific weight characteristics (kg/kwe) of the generator devices with thermoelectric and the thermionic converters?

WILLIAMS:

A comparison has been made. We had also conducted studies separate from this program for isotope thermoelectric generators, to carry out those missions. The figures that you see in the far righthand column of slide 17 (Table 6) represent the weights of those isotope thermoelectric systems compared with the weight shown here for the isotope thermionic system. These weights include all the comparable components that I listed before for the thermionic devices. I do not know the exact efficiencies of those systems but I'm sure they are in the range of 4-5%.

GRIAZNOV:

What is the value of the electric power, where reactor systems begin to be competitive with isotope systems, considering the weight, economy and radiation (in the sense of safety)?

WILLIAMS:

I have not looked at that area myself in a very long time and I do not feel that I am in a good position to answer that question. We looked in this program at thermionic systems up to 2 kW. The only reason we limited ourselves to 2 kW was the particular module size that we had picked - the 100 Watt module size. We looked at one system which was a manned earth orbiting vehicle, which was 2 kW and at that size this 100 Watt module size was getting a little small. We could have acquired a lighter system if we had gone to a larger module size, maybe to 200-250 Watts. I'm sure that the isotope thermionics will look attractive - well above the 2 kW number.

SNAP-13 GENERATOR DEVELOPMENT PROGRAM

by

J. B. Dunlay and R. C. Howard
Thermo Electron Corporation
Waltham, Massachusetts, USA

ABSTRACT

In 1961, the United States Atomic Energy Commission undertook a program to develop the technology required for the construction of isotope-heated thermionic converters. Under a sub-contract to the Martin Company, Thermo Electron Corporation conducted the thermionic generator development and testing. The reference design used throughout the program incorporated a 12.5 watt diode enclosed in a vacuum-tight envelope. The isotope fuel was assumed to be an alpha-emitter.

An extensive program of design, development, and testing was carried out on the generator to determine its lifetime, performance, and resistance to dynamic loads. More than twenty generators were fabricated and tested with electrical heaters simulating the isotope heat source. All the generators were performance tested, some were life-tested, and three were environmentally tested. By the conclusion of the program, a generator had successfully survived shock and vibration testing and the life and performance goals had been substantially exceeded.

The purpose of this paper is to describe the generator design and to summarize the major results achieved during the electrically heated tests. The efficiencies, power outputs, and lifetimes will be presented. The design iterations leading to the successful environmental tests will be described.

DESCRIPTION OF GENERATOR DESIGN

The configuration of the SNAP-13 isotope thermionic generator is shown in Figure 1. The generator is fabricated in three components: the fuel capsule, the upper casing assembly and the lower casing assembly. The thermal shields are attached to the upper casing assembly. The lower casing assembly contains the remaining parts of the generator including the cesium diode, the cesium reservoir, and the auxiliary heaters and thermocouples.

Final assembly of a fueled generator would be accomplished in a remotely operated fueling fixture. First the fuel capsule would be brazed to the back of the emitter structure using an electron bombardment heater. Then the upper and lower casing assemblies would be joined and brazed together using a second electron bombardment heater. After casing outgassing, the pump-out tube extending from the bottom of the generator would be remotely pinched off to complete the generator assembly.

A cross section of the generator is shown in Figure 2. The generator case is 4.2 inches long and has a diameter of 2.64 inches. The case is a thin walled stainless steel vessel lined with copper to provide good thermal conductance. The case serves both as the vacuum containment for the diode and the heat rejection radiator. The diode and isotope capsule are cantilevered from the bottom of the case and are free to expand within the casing. The fuel capsule is not constrained by the thermal shield assembly which is supported from the top of the casing. Projecting through the bottom of the case are the emitter lead, the cesium reservoir tubulation and the casing pump-out tube. When a generator is fabricated with an electrical heater simulating an isotope fuel, the heater leads penetrate the sealed casing through the lead-throughs located at the top of the casing.

The converter is a planar cesium diode employing a rhenium emitter and a molybdenum collector with an area of 4.8 cm^2 . The emitter-collector spacing is 0.009 inch. The emitter is supported from the bottom of the collector through the diode lead-through structure and the emitter spacer. The cylindrical spacer has a 0.005 inch wall thickness. With this wall thickness and using a high strength tantalum alloy (Ta-8 W-2 Hf), the spacer provides adequate structural support for the fuel capsule during dynamic load testing. The fuel capsule is 1 inch in diameter, 1.7 inches long, and weighs approximately 0.5 pound.

The efficiency of the SNAP-13 generator is directly influenced by the effectiveness of the thermal shields surrounding the isotope fuel capsule. The purpose of the shields is to minimize the loss of heat from the top and sides of the fuel capsule. This in turn forces the major portion of the heat generated by the isotope fuel to flow into the emitter. With the thermal shield configurations available during the SNAP-13 program, the heat loss was somewhat less than 0.5 watt cm^2 of capsule surface area at a generator output power level of 12.5 watts. This results in a shield effectiveness greater than 85%. As discussed in another paper, thermal insulation with much greater effectiveness is now available.

The combination of high dynamic loads and the required high-temperature and long-life operation imposes severe restrictions on the design of the diode heater used to test the generators. The life test generators used a resistance heated tungsten filament which radiated from the filament to the walls of the surrounding heater capsule. While suitable for life testing this type of heater does not exhibit sufficient structural strength for dynamic testing of the generators.

A conduction diode heater was used in generator No. 11A and fulfilled the high structural strength requirements. The design of this heater is shown in Figure 4. The heater used a sheath heater element consisting of a tantalum center conductor, BeO insulation, and tantalum sheath. The coiled heater element was mounted and brazed to a grooved tantalum core to provide a good thermal conduction path between the heater element and the capsule base.

TEST RESULTS (LIFE AND PERFORMANCE)

The design goals for the generators were long life, high efficiency, high structural strength to withstand dynamic loading, and remote component assembly. A summary of the design specifications and the generator test results are shown in Table 1. Generators No. 8A-1 and No. 8B-1 were constructed to establish the long-term operating life. Efficiency and dynamic load characteristics were investigated with generator No. 11A. Remote assembly was accomplished on Generator No. 13.

Generators No. 8A-1 and No. 8B-1 were completed in September 1962 and placed on life test. Due to uncertainties in the long-term operating life of the diode heaters, the gross input power to each generator was limited to 170 watts. With this input power, the generators produced an output of approximately 6 watts. The life test of both generators continued into August, 1963, without significant change in output. A resistance change then occurred in the diode heater of generator No. 8B-1. The decision was made to terminate the life test of generator No. 8A-1 before diode heater damage occurred and use this generator in the dynamic test program. Accordingly, the life test of generator No. 8A-1 ended on August 27, 1963, after a total of 5470 hours of operation. The life test of generator No. 8B-1

continued until its diode heater failed on September 26, 1963, accumulating a total of 6404 hours of generator operation.

The casing was removed from generator No. 8B-1 and diode operation checked with an electron bombardment heater. The diode output was identical with the design output observed after fabrication. The diode was then stored for 11 months until a vacuum station became available for additional life testing. Generator No. 8B-1 was placed back on life test in August 1964 at a power level of 12.5 watts. Operation at the 12.5 watt level continued to December 1964 when a full year of life testing was achieved. The power level was then increased to 20 watts. A total of over 13,000 hours of operation was accumulated. No degradation was observed throughout the life-testing.

Generator No. 11A was fabricated with a conduction diode heater to obtain measurements of the generator efficiency and to permit dynamic testing of the generator at operating temperatures. The output characteristics of the generator are given in Figure 4. The net efficiency of the generator for a 1500°C capsule temperature was 8.7%. At this operating condition, the temperature difference between the heater capsule and the emitter face was approximately 35°C and resulted in an emitter temperature of about 1465°C. The net efficiency of the generator at the 12.5 watt operating condition was approximately 7% with a corresponding emitter temperature of about 1375°C.

DYNAMIC TESTING

Dynamic load tests simulating an Atlas Centaur launch were carried out on three generators; No. 8A-2, No. 8A-1, and No. 11A. Generators No. 8A-2 and No. 8A-1 were not specifically designed to withstand dynamic loading but the tests yielded preliminary experimental data on the structural aspects of the basic generator design.

Generator No 8A-2 was dynamically tested at room temperature. With the exception of inadequate strength in the design of the cesium reservoir tubulation, the generator successfully passed the acceleration, vibration and shock tests without detrimental effect. Diode operation was checked at the completion of the dynamic tests and no change was detected.

The life-test generator No. 8A-1 was dynamically tested at operating temperature after 5470 hours of operation. Again the cesium reservoir was physically restrained. No damage occurred to the generator under full acceleration and shock loads and under vibration testing at 25% and 50% of full load. At full vibration loading, de-ignition occurred immediately and normal operation could not be restored. The post-test examination showed that the thin-walled emitter spacer has been damaged.

The design of generator No. 11A included higher strength components for the spacer and the cesium reservoir tubulation. The spacer was strengthened by using the tantalum alloy (Ta-8 W-2 Hf) to replace the pure tantalum spacer used in earlier generators. The strength of the reservoir tubulation was increased by adding a stainless steel outer tube. The adequacy of the improvements in the generator structural design were confirmed by the dynamic testing of generator No. 11A. Full level vibration loading was applied at operating temperature without failure.

Remote component assembly of the SNAP-13 generator was successfully performed on generator No. 13 (electrically heated) in November 1964. Before final assembly, the generator was tested for 24 hours at power levels from 12.5 watts to 35 watts to insure satisfactory operation. The generator components were then installed in the fueling fixture and the capsule and casing brazes

completed. Tests during and after the final assembly confirmed that the operation of the completed generator was not affected by the remote assembly procedure.

ACKNOWLEDGMENTS

Many people at Thermo Electron contributed to the success of the SNAP-13 Generator Program. The authors would like to acknowledge the efforts of T. Robinson and R. Harvey in evolving the basic design of the generator and insulation during the early stages of the program. Significant contributions were also made to the fabrication technology by F. Campagna, L. Lanzarotto, and H. Hardister.

TABLE 1
SNAP-13 GENERATOR SUMMARY

DESIGN SPECIFICATIONS	
End-of-Life Power Level	12.5 watts
Operating Life	130 days
Isotope	Alpha Emitter
Generator Weight	4 pounds
Dynamic Loading	10 g acceleration, 18 g vibration, 25 g shock

TEST RESULTS (electrically heated)		
Type	Test Generator	Results
Power	11B, 13, 14, 15	up to 35 watts
Life	8B-1	over 13,000 hours
Efficiency	11A	7% at $T_E = 1375^\circ\text{C}$, $P = 12.5$ watts
		8.7% at $T_E = 1465^\circ\text{C}$, $P = 20$ watts
Dynamic Loading	8A-2	passed acceleration, vibration shock (room temperature, reservoir restrained)
	8A-1	passed acceleration, shock (operating temperature, reservoir restrained)
	11A	passed vibration (operating temperature)



Figure 2. Cross Section of Generator #14

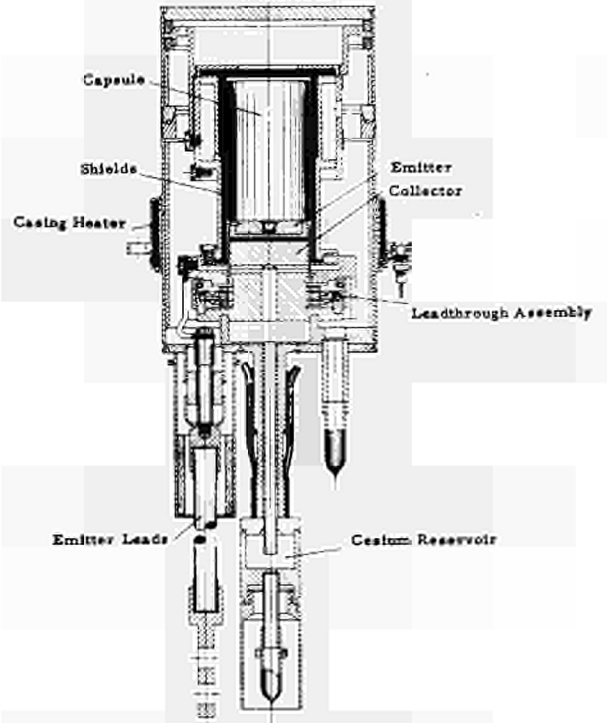


Figure 1. Generator #14 Components

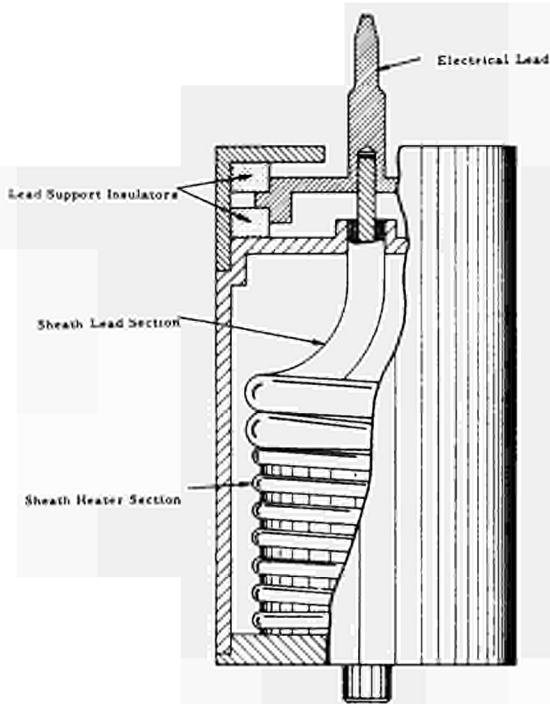


Figure 3. Cross Section of Conduction Heater

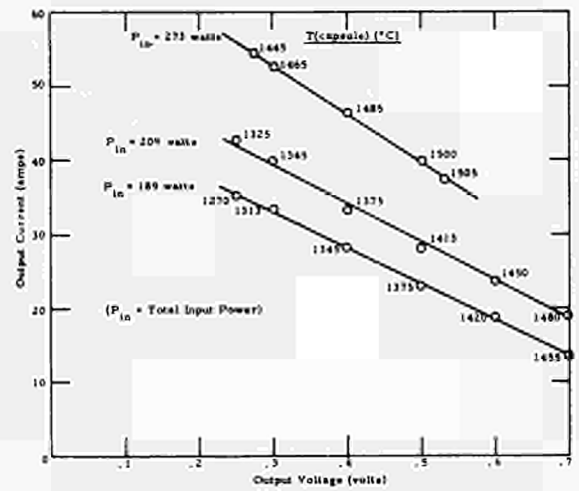


Figure 4. Generator #11A Output Characteristics

DESIGN AND CHARACTERISTICS OF AN ACTINIUM FUELED
THERMIONIC GENERATOR

A. De Troyer and E. Nève de Mévergnies
(Union Minière, Brussels, Belgium)

M.J. Brabers and P. Dejonghe
(Centre d'Etude de l'Energie Nucléaire,
Mol-Donk, Belgium)

G. Gammel, F. Gross, M.F. Koskinen and
R. Langpape
(Brown, Boveri & Cie A.G., Heidelberg,
West Germany)

Abstract :

The thermionic generator to be built in cooperation between U.M. and B.B.C. is presented. A detailed description of the design and the optimization of the generator as it stands now is given. Experimental results of measurements with a plane parallel diode using a polycrystalline tungsten emitter and a molybdenum collector at emitter temperatures between 1800°K and 1900°K will be discussed.

The compatibility of systems containing the following elements or compounds have been considered : La_2O_3 , PbO , Pb , ThO_2 , Th , W , O_2 , He . The experiments are carried out at temperatures up to 2500°K. Tests up to 2.000 hours are conducted at 2100°K. The permeability of ThO_2 -coatings for helium has been tested on boron-containing spheres. Helium release is measured by heating the particles and collecting the gas. The metal ceramic seal has been developed, tested for about 5.000 hours at 1000°K and 20 torr cesium pressure; it is still leak tight. A Nb 1 % Zr collector heat pipe filled with sodium is running for about 12.000 h at 1100°K without degradation. The emitter lead has been proven to withstand temperature cycles between 750°K and 2200°K.

INTRODUCTION

Brown, Boveri & Cie A.G., Mannheim (BBC) and the Union Minière (UM) have undertaken the development of an actinium fueled thermionic generator. The purpose of this undertaking is to demonstrate the feasibility of such systems and to accumulate experience for the future production of operational units. A project goal is to have the generator operating and under test in 1969-1970.

1. GENERAL DESCRIPTION AND OPTIMIZED CONCEPTION

The generator general design is shown in figure 1. The cylindrical heat source is surrounded by a removable thermal shield and its lower base is joined to the emitter of the plane parallel thermionic converter.

The fuel will be actinium oxide in the form of spherical particles having a diameter of 500μ , coated with a 25μ thick layer of thorium oxide and embedded in a porous sintered tungsten matrix. The power density of this matrix will be 45 W/cm^3 , pure actinium oxide having a power density of 119 W/cm^3 .

The actinium oxide itself is limited to a density of about 90 % to allow the swelling due to the production mainly of lead and due to the oxidation of the oxygen gettering material. A ThO_2 coating of the order of 25μ thickness will confine the fuel inside the spherical particles. It will

allow helium to escape at the operation temperature. A supplementary 5μ thick layer of tungsten is required to insure good bonding with the matrix.

The matrix is made by filling the void between the fuel particles with tungsten powder and by sintering at high temperature. An adequate porosity for helium venting is so ensured.

The overall conductivity has not yet been measured, but the equations given by A.E. Powers (1) yield for the overall conductivity of the fuel matrix combination a value of approximately 22 % of the thermal conductivity of pure tungsten. These results were found relatively insensitive to the thermal conductivity assumed for Ac_2O_3 , which was taken equal to a preliminary value measured for La_2O_3 at $2000^\circ K$ ($10^{-2} W/cm^\circ C$).

The filling percentage of tungsten was chosen to maximize the product of thermal power density and thermal conductivity, to assure the minimum temperature rise in the fuel.

The matrix is enclosed in a W-25 % Re cylindrical capsule joined to the emitter block; the other faces of the capsule are surrounded by a thorium oxide spaced thin metallic foils heat shield.

The plane parallel converter (fig. 1) has a high barework function-emitter, such as e.g. W (110), Re or W-Re, with an area of 4 cm². The inter electrode spacing will be optimized to obtain a maximum overall efficiency. The waste heat is

removed from the Mo-collector plate by a Nb- 1 % Zr heat pipe filled with Na and provided with fins.

The pumping lead, which passes through the radiatively cooled cesium bath, is introduced through the center of the heat pipe. The emitterlead is W-25 % Re, 27 mm in diameter, 40 mm long and has a 0.2 mm wall thickness. The metal-ceramic seal is of high purity alumina brazed between 0.1 mm molybdenum diaphragms which are in turn brazed into Nb-1 % Zr rings. The mechanical spacing of the electrodes is rigidized through a segmented ceramic brazed between the two rings.

From the best data available on plane parallel diodes, a practical optimum operating point for the emitter was chosen at 1800°K and an heat flux through the emitter surface of about 40 W/cm². With a total heat production of 250 W, heat fluxes and temperature distributions calculations yielded the present generator configuration. In these calculations, the best data available for heat conductivities, materials strength at high temperature and chemical compatibilities were used.

The present state of the generator configuration and performance is as follows :

capsule diameter 27 mm

wall thickness 4 mm

total length of the capsule 31 mm

gap between the top of the matrix and
the upper wall 1 mm.

Heat losses through the thermal shield	13 W
Heat losses from the inactive part of the emitter	17 W
Heat losses through the emitter leads	<u>65 W</u>
Total losses	95 W
maximum temperature of the fuel	1980°K
emitter temperature	1800°K
temperature difference between center and outerpart of the emitter	\pm 5°K
collector temperature	970°K
output voltage	0.55 V
available electrical power output	23 W
overall efficiency	9 %

This present optimum configuration will be continuously redesigned as new results become available from the converter or the heat source.

2. FUEL BEHAVIOUR

It is envisaged to put the fuel in the form of spheres containing an oxygen getter and coated with ThO_2 . The spheres are prepared by the agglomeration process.

The spheres together with tungsten powder are vibro-compacted into a tungsten-rhenium capsule.

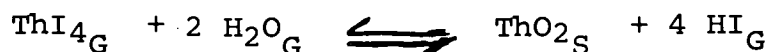
2.1 Preparation process

The preparation process of the spheres of a diameter

of 400-500 μm has been studied by agglomeration of La_2O_3 -powder as a simulator for Ac_2O_3 . Sintering is carried out at temperatures up to 1800°C under an atmosphere of dried argon. The density varies between 80 and 92 % T.D. depending on the sintering temperature. The yield of the preparation process is 98 % when carried out on batches of more than 20 g powder.

For the preparation of the coating of ThO_2 two processes have been studied : agglomeration of ThO_2 -powder onto the spheres and fluidized bed technique.

The agglomeration process has many advantages over the fluidized bed technique because the equipment is simple to use and is the same as needed for the spheroidization. So, it is a suitable process for application in hot cells. It has been possible to prepare coating in this way as thin as 20 μm . Sintering occurs at about 1600 - 1800°C under argon. The fluidized bed process is based on the reaction :



ThI_4 is prepared separately from the fluidized bed system. The vapour is carried to the fluidized bed by argon as carrier gas. Reaction takes place at 1000°C in hydrogen with an excess of water vapour (five times the calculated necessary amount). The

hydrogen concentration is 30 v/o of the total gasflow. The partial pressure of ThI_4 is 0.1 - 0.3 mm Hg. Fluidization occurs in an inconel tube of diameter 20 or 25 mm in a gasflow of 3 or 5 l/min. The deposition rate at 1000°C is 1 to 1.5 $\mu\text{m}/\text{hour}$.

The coatings prepared in both ways are very adherent. However, the fluidized bed coatings are not exactly spherical, which may cause difficulties in vibro-compaction (fig. 2 and 3).

The free energy of formation of La_2O_3 H_f^{298} is $-428.57 \text{ kc}^\circ\text{l}/\text{mole}$. The oxide may dissociate according to $\text{La}_2\text{O}_3\text{S} \rightleftharpoons 2\text{LaO}_\text{G} + \text{O}_\text{G}$. This dissociation, though small, is not negligible. Therefore, high vacuum and hydrogen atmosphere must be avoided in all high temperature processes. La_2O_3 is also very sensitive to humidity. In normal (humid) air complete desintegration of spheres occurs in a short time.

2.2 High temperature reactions

Very complicated systems arise during decay of the fuel. Besides the starting materials, Ac_2O_3 , ThO_2 and W, shortlived daughter products, lead helium and oxygen are formed, while the oxygen may give rise to formation of PbO and of W_xO_y . The helium formed in the decay process and the lead or leadoxide vapour and the oxygen might give very high gas pressures at

2000°K if retained in the spheres. In the study of the high temperature reactions it has been assumed that each product may come into contact with any other possible product. So, combinations of the system $\text{La}_2\text{O}_3 - \text{PbO} - \text{Pb} - \text{O} - \text{ThO}_2 - \text{W} - \text{W}_x\text{O}_y$ have been examined at temperatures up to 2500°K.

Pb + O. The vapour pressure of lead is given by :
 $\log p$ (in mm Hg) = $-10,130 T^{-1} - 0.958 \log T + 11.16$
and that of PbO by the formula : $\log p(\text{atm}) = 8.7002 - 13,858/T$.

The dissociation of PbO is rather high. The vapour pressures of lead and lead oxide give considerable contributions to the total pressure at 2000°K. Besides the oxygen from the dissociation of PbO free oxygen is left from the decay of Ac_2O_3 .

$\text{La}_2\text{O}_3 + \text{Pb}$. Lead does not react with lanthanumoxide. On heating a mixture of lanthanum oxide and lead the latter gradually escapes by diffusion. After cooling down to room temperature lead may be found as small spheres on the outer surface of the La_2O_3 -spheres.

$\text{La}_2\text{O}_3 + \text{PbO}$. Lead oxide does not react with lanthanum oxide, however it lowers the melting point (2). The melting point of lanthanum oxide containing 10 mole % PbO is estimated to be 2200°C. In practice lead oxide escapes from the spheres probably after disso-

ciation into lead and oxygen. Lead may be temporarily found in lanthanum oxide after heat treatment of a mixture of lanthanum oxide and lead oxide at high temperature. The oxygen may cause reactions with tungsten or other oxygen getters.

La₂O₃ + PbO + W. The tungsten present in the neighbourhood of the spheres is oxidized by the oxygen from PbO. Lead vapour escapes by diffusion preferentially by grainboundary diffusion. When a barrier is present this may temporarily stop the migration of lead (fig.4). Tungsten acts as an excellent oxygen getter being oxidized to W_xO_y of variable composition (fig.5). In a mixture of lanthanum oxide and tungsten, this W_xO_y reacts with lanthanum oxide to give 3La₂O₃. WO₃ (melting point 2050°C), which is retained in lanthanum oxide (fig.6).

La₂O₃ + W. No reaction between lanthanum oxide and tungsten has been observed. It has been reported that some LaO may dissolve into tungsten (3). This has not yet been confirmed.

ThO₂ + W. The sphere coating material, ThO₂ has been found compatible with tungsten up to the maximum testing temperature, 2500°C.

ThO₂ + Pb. Also no reaction has been found between thorium oxide and lead. The lead easily diffuses

through thorium oxide.

W + Pb. Tungsten and lead are compatible as long as no oxygen impurities are present.

ThO₂ + PbO + W. The PbO formed in La₂O₃ readily diffuses outwards through the ThO₂ coating towards tungsten which is oxidized to W_xO_y of variable composition (fig.7). In a closed system this tungsten oxide may diffuse into thorium oxide. After cooling down to room temperature PbWO₄ has been found preferentially on the grain boundaries (fig.8). On micrographs different tungsten oxides are clearly visible. The lead from the dissociation of lead oxide evaporates from thorium oxide.

La₂O₃ + ThO₂. Lanthanum oxide and thorium oxide do not react. However, lanthanum oxide diffuses into thorium oxide giving a zone of composition (Th,La)₂O₃ (fig.9). The reactivity of (Th,La)₂O₃ is similar to that of pure ThO₂. Even at 2500°K no reaction has been observed of (Th,La)₂O₃ with either W_xO_y or tungsten. The interdiffusion zone seems to be very stable.

Gaspressure

For each disappearing Ac-atom five He-atoms are formed. This helium if retained in the fuel would exert at 2000°K a very high pressure after a decay time of half a year. All the fuel materials have therefore to

be permeable for helium. This has been investigated in a simulation test. In spheres of La_2O_3 containing a boron compound and coated with thorium oxide helium has been produced by $^{10}\text{B}(n,\alpha)$ reaction in the high flux testing reactor BR2. Most of the boron compounds lower the melting point of La_2O_3 to low values (e.g. 1200°C). Two types of coatings have been examined : fluidized bed coatings of 8 and 18 μm and agglomeration coatings of 20 and 40-50 μm thickness (fig.10). After irradiation the spheres have been heat treated at rising temperature up to 1650°C . Helium release was measured by means of a helium leak detector. In the case of the fluidized bed coatings helium release already started at room temperature and was completed at about 1000°C . The ThO_2 coatings prepared by agglomeration process showed a helium release starting at about 400°C . The release rate is rapid at 550°C and still increases with increasing temperature. The rate at constant temperature is initially very rapid but gradually slows down. The release is complete at about 1600°C after a few hours. The higher He release rate, which fluidized bed coatings show, is ascribed to impurities of iodine. Iodine could be detected during the heat treatment.

From these experiments it has been concluded that the helium pressure will be very low, because helium will

readily diffuse out.

The oxygen pressure will be kept at very low values when an oxygen getter, like tungsten is present. As has been mentioned, oxidized tungsten reacts with Lanthanum oxide and is retained in the fuel. When no getter is present, oxygen disappears from the fuel and then reacts with the filler material. It is therefore concluded that also the oxygen pressure in the fuel can be maintained at a low value.

Lead oxide, or lead and oxygen diffuse through thorium oxide (fig.11). In short term tests at 2000°C some lead has been found after heat treatment of a mixture of lanthanum oxide and lead oxide. This lead apparently did not give any cracks. After cooling it was retained in lanthanum oxide as small grains at the outer surface.

It may be concluded that the total gas pressure in the spheres might be kept at a very low value, certainly so when one considers that in a real actinium oxide case the conditions are much less severe than in these experiments.

3. CONVERTER DEVELOPMENT.

The thermionic converters built until now differ from the converter to be joined to the capsule only in the use of a

polycrystalline tungsten emitter and a tantalum emitter lead. The material for the collector is molybdenum. The interelectrode gap in this converter is 0.14 mm being nearly independent of the emitter temperatures in the range of 1800 to 1900°K.

Figure 12 shows one of the thermionic converters completed

3.1 Measurements

Current-voltage curves were measured with the converter shown in figure 12. The polycrystalline tungsten emitter was heated by electron bombardement. The emitter temperatures were measured pyrometrically.

The converter was outgassed at temperatures of about 150°K higher than the highest working temperatures before filling it with cesium by distillation, while being pumped by a Vac Ion-pump. Outgassing was checked by measuring the bare work function of the emitter. After about 50 hours pumping, the work function stabilized at a value of 4,65eV.

The vacuum read on the Vac Ion-pump was better than 10^{-8} torrs.

In order to measure families of current-voltage curves, the collector temperature and the cesium bath temperature were varied, by additional heaters at the collector and the cesium bath.

At constant emitter and collector temperature, a family

of I-V curves was measured at different cesium temperatures. In the same way, families for three collector temperatures in the range of 930 and 1010°K were taken at emitter temperatures of 1800°K, 1850°K and 1900°K respectively. The results are given in fig. 13. These curves show the maximum output power versus the output voltage.

For clearness sake, only the envelopes of the families of curves taken at the fixed emitter temperatures with different collector temperatures, are given. Thus, these curves are optimized with respect to cesium pressure and collector temperature. The voltage was measured between the collector and the cold end of the emitter lead, so these curves show the available power output.

In the same figure, the lower curves give the electrode efficiency versus the output voltage; they are again optimized with respect to collector temperature and cesium temperature.

The electrode efficiency was calculated according to a proposal of Block et al (4).

$$\eta_e = \frac{j \cdot V_E}{j \phi^* + q_k + q_w}$$

j = net current density

V_E = voltage measured at the electrodes

$\phi^* = \phi - 0,17$, where ϕ is the Richardson-work-function corresponding to the net current as given by Kitrilakis et al (5).

q_r Heat loss by inter electrode radiation, given by

$$\bar{\epsilon} \sigma (T_E^4 - T_C^4) \quad \text{with} \quad \bar{\epsilon} = 0.18$$

q_u Heat loss by cesium gas conduction calculated according to Kitrikalis et al (6).

For the discussion of these curves, it must be considered that the data are not fully optimized because the electrode spacing was always constant. At 1800°K the spacing was about twice the optimum spacing, at 1900°K, it was about six times larger than the optimum value. Therefore, these data are somewhat lower than those which are to be expected under fully optimized conditions. From the measured data at 1800°K, one calculates an electrode efficiency of 15 %, at an output voltage of 0.55 volt, the output power being about 20 watts. At 1900°K, the converter delivers 32 watts electrically at 0.65 volt output voltage with an electrode efficiency of 18 %.

3.2 Component Tests

The most critical parts of the thermionic converter are the metal ceramic seal, the emitter lead and the heat pipe collector. Special attention is therefore paid to development and testing of these components.

3.2.1 Metal Ceramic Seal

The metal ceramic seal has to work at about 1000°K. It must be leak tight at this temperature and stable with regard to cesium attack and thermal shocks. Some of these metal ceramic seals are already constructed and are being tested. A cross section is given figure 14.

For testing, the metal ceramic seal is closed by plates on both sides, one plate being connected with the cesium bath. The device is continuously evacuated by a Vac Ion-pump. Radiant heaters are facing the end plates. The cesium bath is also heated by a radiant heater. The entire assembly is thermally shielded, both on the ends and sides, with several layers of tantalum foil. Furthermore, different collector materials can be tested in this device. In this first seal, a nickel- and a molybdenum electrode have been integrated. The first metal ceramic seal is running now for 5.000 hours in a cesium atmosphere of about 20 torrs at 1000°K. During this time, it has been thermally shocked 30 times between 300 and 1000°K. The metal ceramic seal is still leak tight.

3.2.2 Collector material tests

In the thermionic Conversion Specialist Confe-

rence 1967, Palo Alto(7), preliminary measurements of the effective work functions of nickel and molybdenum have been reported. In the meantime, these measurements have been repeated several times. The results are given in fig.15 which shows the difference in the effective work function between nickel and molybdenum as a function of the ratio T_V/T_{Cs} (=collector temperature/cesium bath temperature). The work function was computed by the Richardson equation. The saturation current was determined by the measured I-V curves. The collector temperature was 723°K, the cesium bath temperature was varied between 373°K and 500°K. Curve 1 of fig.15 was measured during a period of 170 hours. The work function of the nickel electrode is 0.025 eV to 0.12 eV higher than that of the molybdenum electrode, depending on the value of T_C/T_{Cs} .

To test reliability of these results, the measuring cell was operated at 1000°K with a cesium bath temperature of 660°K for 80 hours. After that time, measurements were repeated at 723°K, resulting in a larger difference between the work functions, as shown in curve 2.

The work function of the molybdenum electrode is 0.05 to 0.14 eV lower than that of the nickel electrode. This indicates that for collector material

molybdenum is superior to nickel. The data taken after 4500 hours, marked by crosses in fig.15 agree with those of curve 2, indicating that the values reached after about 250 hours operation remained stable. The work function data of the molybdenum collector are shown in fig.16. The work function rose slightly between curves 1 and 2 approaching a stable value after 250 hours (curve 2).

3.2.3 Emitter lead

According to optimization calculations, the emitter lead should be thin and long. Therefore, the emitter lead is one of the most critical parts of the converter. For the first series of converters, a tantalum emitter lead of optimum geometry has been chosen. It has a length of 27 mm, a diameter of 27 mm and a wall thickness of 0.15 mm. In order to reduce the heat losses by radiation, the lead was polished inside and outside. The tungsten emitter block was joined to a tantalum transition piece by brazing with niobium at 2500°C. The emitter lead was then electron beam welded to the transition piece. The tantalum emitter was brazed to the Nb 1 % Zr support ring with Nb 78 % Zr. Such an emitter subassembly, shown in fig.17, has been submitted to 35 thermal shocks (27°K/sec) between 700 and 2300°K.

Thereby, the dimensions of the emitter lead did not change and the joints remained leaktight.

3.2.4 Collector - Heat Pipe

The lifetime of a heat pipe is mainly determined by the corrosion of the wall material by the working fluid. The heat pipe of the thermionic converter consists of Nb 1 % Zr and is filled with sodium. Such a heat pipe is presently life tested in a horizontal position in order to approach space conditions. It has been running until yet for 13.000 hours at a temperature of about 1100°K, transferring a power of 500 watts. Until now, it shows no signs of deterioration.

4. DISCUSSION

In a general way, the results obtained up to now have proven the feasibility of the concept of the generator as outlined in Chapter 1.

Further experiments and developments are mainly oriented to determine the final specification of the system and to improve its reliability and lifetime.

4.1 Fuel

The compatibility tests on the fuel materials have shown that no difficulties are to be expected when it is assumed that the behaviour of actinium oxide is similar

to that of lanthanum oxide. The starting materials are compatible with one another. Reactions between different components are due to oxygen donors. In presence of tungsten, either added to the fuel as a getter or outside the spheres as filler material, oxygen is immediately bonded to products which are not harmful. Helium easily escapes from the spheres together with lead or lead oxide. The gas and vapour pressures are therefore kept at a very low value. The reactions and the diffusion processes already take place at rather low temperatures, and the rate of reaction and diffusion at 1600°C is rapid. Therefore, a temporary increase in temperature would only have as result a higher diffusion rate and a more rapid escape of the gases.

The picture of the fuel behaviour at high temperature is not essentially altered by a change in temperature between 1600 and 2000°C. This has been confirmed by short term tests.

A first long term test has been performed at 1700°C for about 1000 h. The results show that the particles after this treatment were unchanged, the coating too was still perfect. The La_2O_3 itself showed some porosity, the lead and lead oxide had diffused out. Further long term tests are being carried out at this moment, with fuel containing different getters and with different

compositions.

4.2 Converter development

As a first step to optimize the converter, an evaluation of the performance characteristics based on the measured values given in fig.13 and using a procedure developed by Rasor (8) and Kitrikalis (9), has been made.

Using this analysis, the performance for optimum conditions including optimum spacing were calculated. The results of the calculation at an emitter temperature of 1800°K are shown in fig.18.

With a heat flux of 40 W/cm² which was obtained and used in the optimization calculation of the heat source, the electrode efficiency is 15 % with an electrical output at the electrodes of 6 W/cm² and a voltage of 0.6 V at the electrode (fig.18). Taking into account the losses in the optimized emitter lead, the data given in Chapter 1 are obtained. These data were already nearly realized in the measurements performed with a converter using a polycrystalline W emitter (fig.13). For polycrystalline W the optimum spacing at this point would be 0.08 mm, but emitters with a higher bare work function will yield a larger optimum spacing, thus improving the reliability of the converter. Therefore, further measurements with converters having W(110) and W-Re emitters will be carried out in a near future. The data

obtained by this measurement will be used to recalculate the optimization of the converter. This improved characteristic of the converter will be used for the final optimization of the whole generator.

To test lifetimes of the most critical parts of the converter, several life test units are under construction.

Although the resistance of the emitter structure, including welds and brazes, have been proved sufficiently stable against thermal shocks, no emitter structures including the emitter leads have been life-tested so far. It is planned to test converters with Ta-emitter leads and with W-Re emitter leads.

The metal ceramic seal and the heat pipe are nearly completely developed and further life-tests are underway, although no serious problems are to be expected with these components.

REFERENCES

- (1) POWERS, A.E., "Conductivity in Aggregates".
KAPL 2145, 1961.
- (2) WARZEE, M.H.; MAURICE, M.; FALLA, F.; RUSTON, W.R.,
"Phases in the binary systems PbO-La₂O₃, Gd₂O₃, and
Sm₂O₃". J. Am. Cer. Soc. 48 (1965) 15.
- (3) KONDRATOV, I.J.; PODTSCHERNJAEVA, I.A.; SAMSONOV, G.V.;
FOMENKO, V.S., "Über die Thermoemissionseigenschaften
von Legierungen des Systems W-La₂O₃." Planseeberichte
für Pulvermetallurgie Bd.15 (1967) 127.
- (4) BLOCK, F.G.; HATSOPOULOS, G.N.; WILSON, V.C.,
"The Definition of Conversion Efficiency of Thermionic
Energy Converters". Thermionic Conversion Specialist
Conference, San Diego, Calif., Oct. 25th 1965.
- (5) KITRILAKIS, S.S.; BROSENS, P., "Experimental Corre-
lation of Electron Emission Cooling and Optimum
Collector Temperature". Thermionic Conversion Specia-
list Conference, San Diego, Calif., Oct. 25-27th 1965.
- (6) KITRILAKIS, S.S.; MEEKER, M., "Experimental Determi-
nation of the Heat Conduction of Cesium Gas".
Advanced Energy Conversion, Vol.3, pp. 59-68,
Pergamon Press (1963).
- (7) KOSKINEN, M.F.; GAMMEL, G., "A Direct Comparison of
Molybdenum and Nickel as Collector Materials".
Thermionic Conversion Specialist Conference, Palo Alto,
Calif., Oct. 30th 1967.
- (8) RASOR, N.S., "Analytical Description of Cesium Diode
Phenomenology". 1st. International Conference on
Thermionic Electrical Power Generation, London,
Sept. 20-24th 1965.
- (9) KITRILAKIS, S.S.; RUFEB, F., "Experimental Correlation
of Converter variables in the Ignited Mode".
1st. International Conference on Thermionic Electrical
Power Generation, London, Sept. 20-24th 1965.

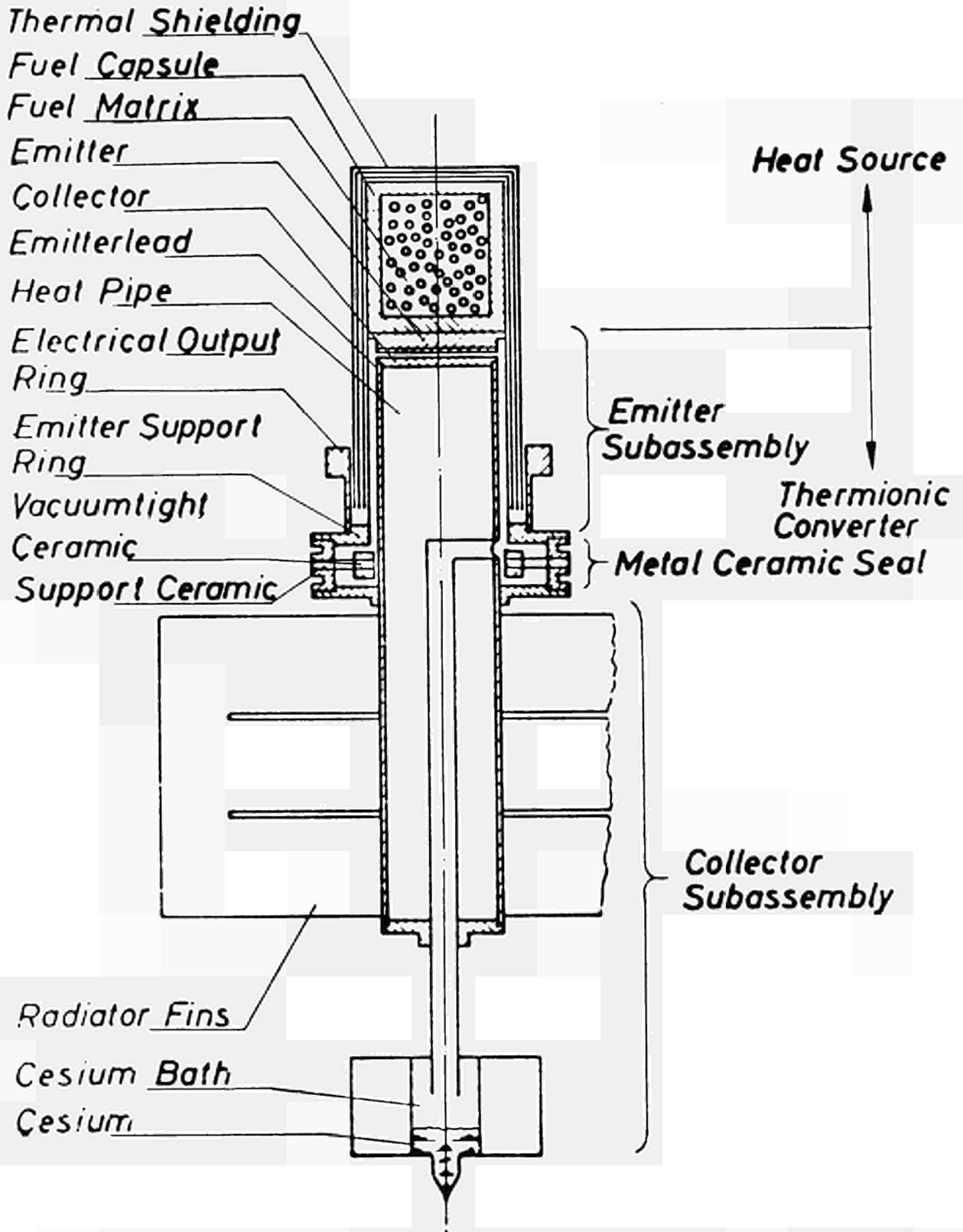


Fig. 1 *Isotope Fueled Thermionic Generator*

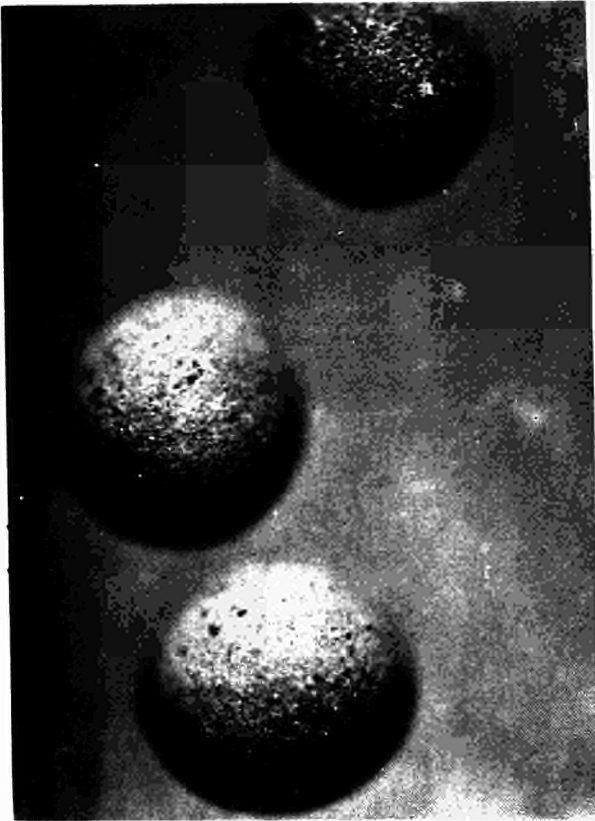


Fig. 2

Spheres of $\text{La}_2\text{O}_3 + \text{PbO}$ coated with ThO_2 ($\times 50$)



Fig. 3

ThO_2 coating on La_2O_3 spheres ($\times 150$)



Fig. 5

Lead retained in spheres of $\text{La}_2\text{O}_3 + \text{PbO}$ after heat treatment at 1700°C ($\times 1000$)



Fig. 4

W-oxygen getter in La_2O_3 . W-particles are surrounded by lead ($\times 1000$)

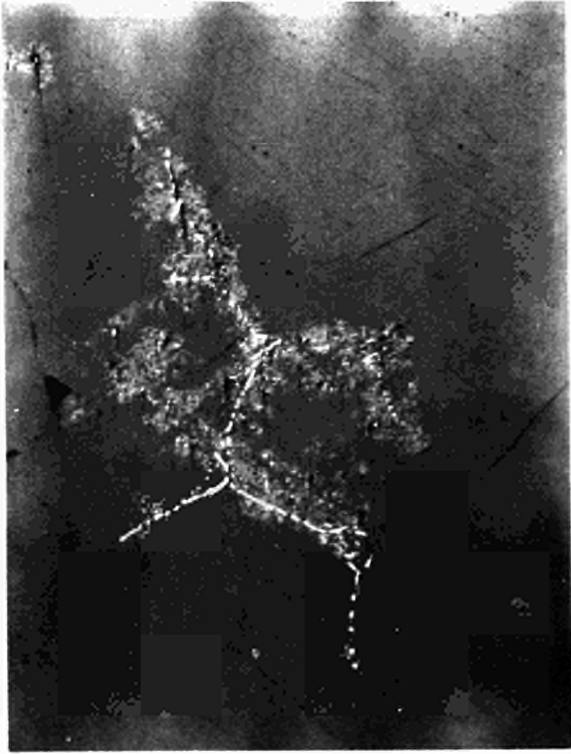


Fig. 6

Heat-treated sphere of ($\text{La}_2\text{O}_3 + \text{PbO} + \text{W}$).
Formation of $3 \text{La}_2\text{O}_3 - \text{WO}_3$ and some lead ($\times 500$)



Fig. 7

Oxidized tungsten. Different tungsten-oxides
are visible ($\times 500$)



Fig. 8

Formation of PbWO_4 in ThO_2 ($\times 1000$)

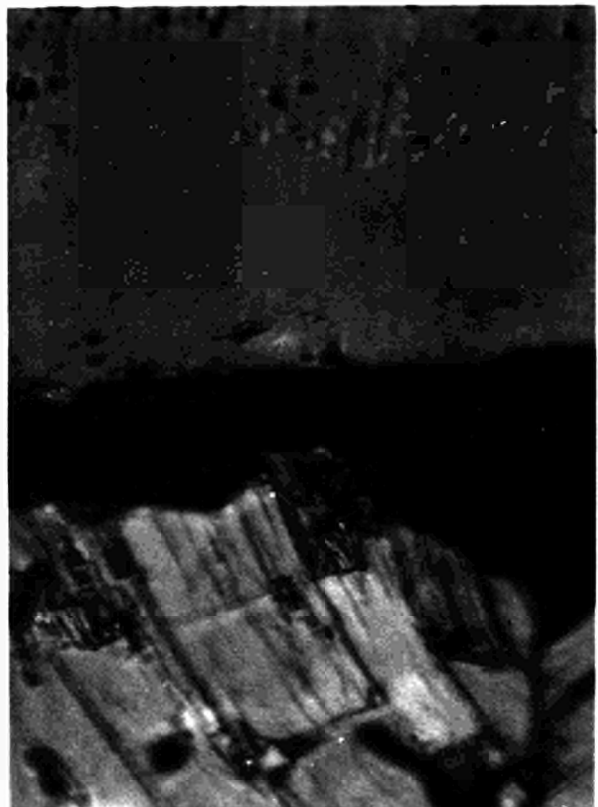


Fig. 9

Diffusion zone between La_2O_3 and ThO_2 ($\times 1000$)

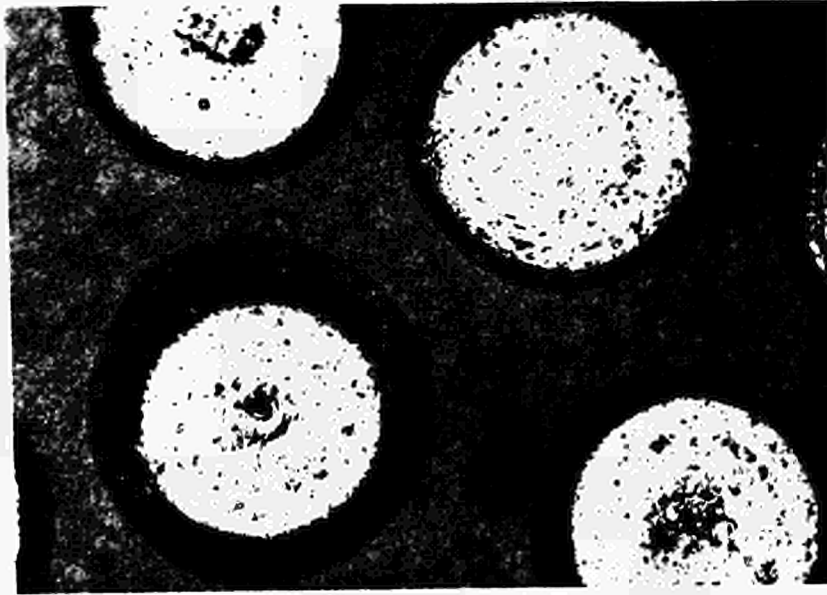


Fig. 10

La_2O_3 spheres containing titanium boride coated with $20\ \mu\text{m}$ ThO_2 by agglomeration ($\times 100$)

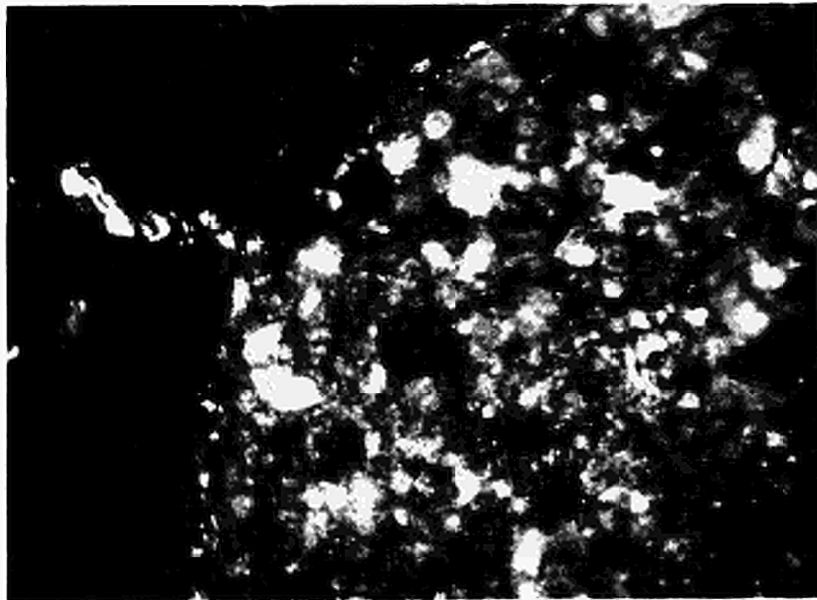


Fig. 11

Diffusion of lead from sphere of $\text{La}_2\text{O}_3 + \text{PbO}$ through ThO_2 coating ($\times 500$)

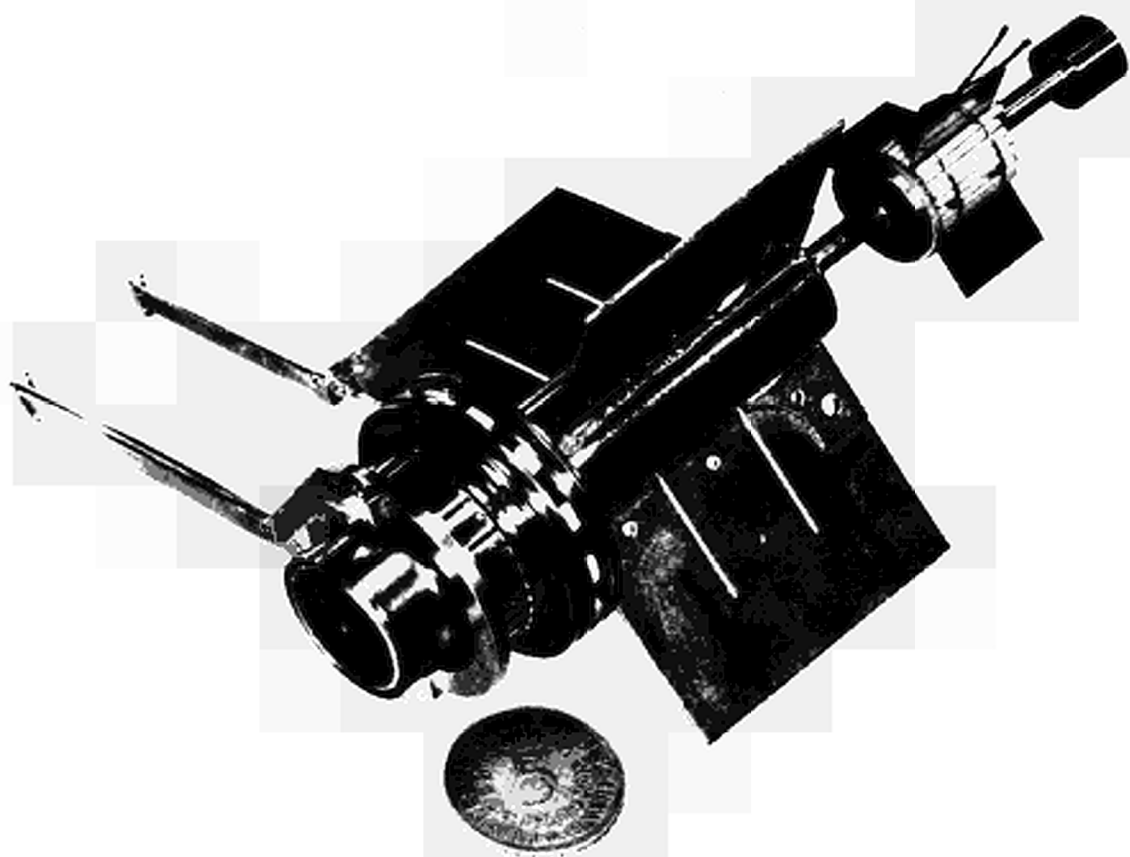


Fig. 12 : Thermionic Converter

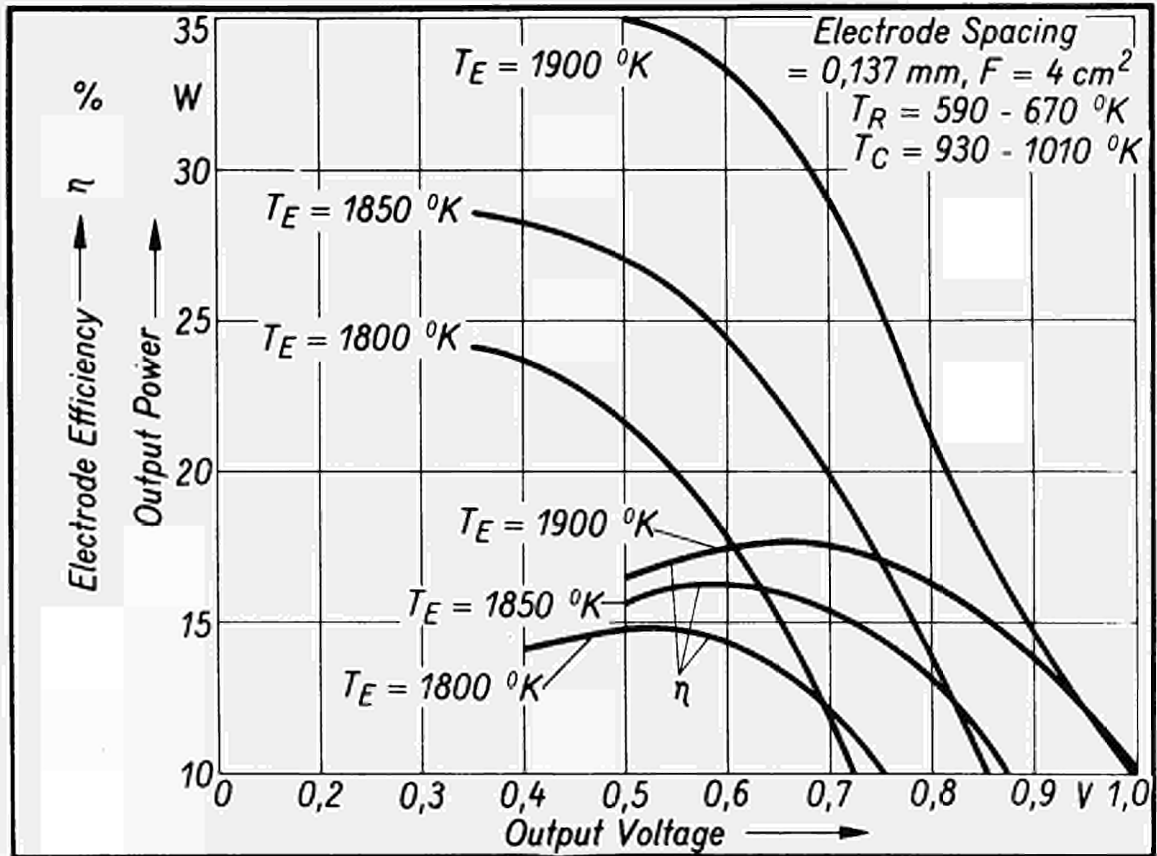


Fig. 13 Maximum Power and Computed Electrode Efficiency versus Output Voltage

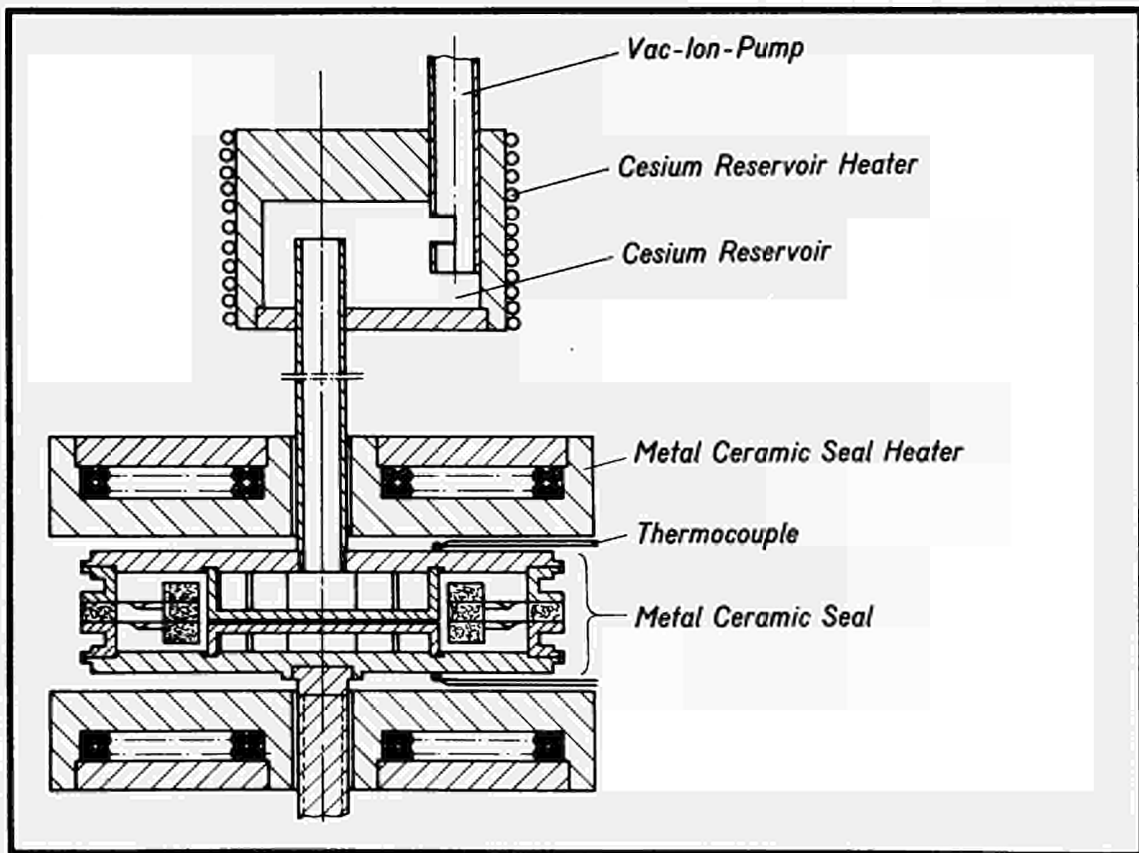


Fig. 14 Metal-Ceramic-Seal with Cesium Reservoir

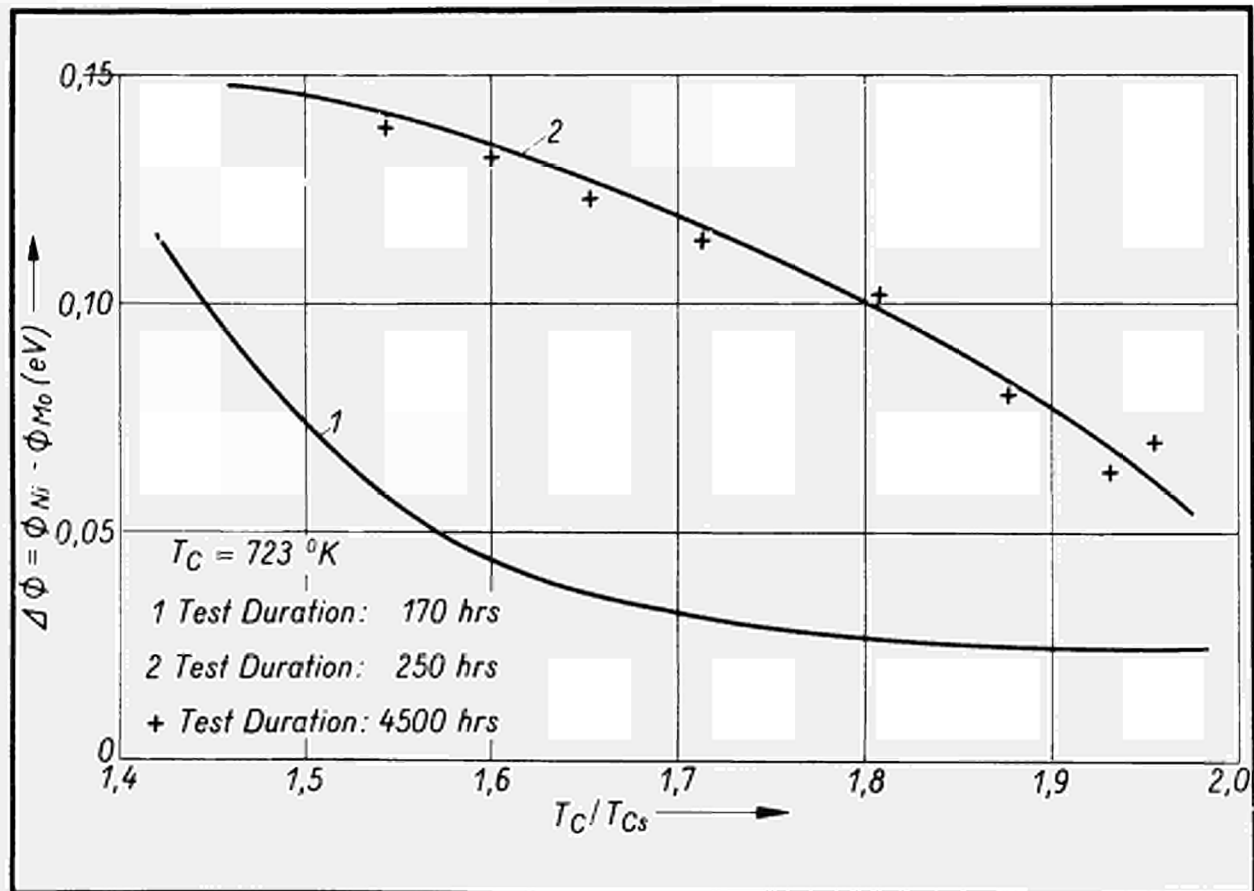


Fig. 15

Difference in Work Function between a Nickel and a Molybdenum Collector

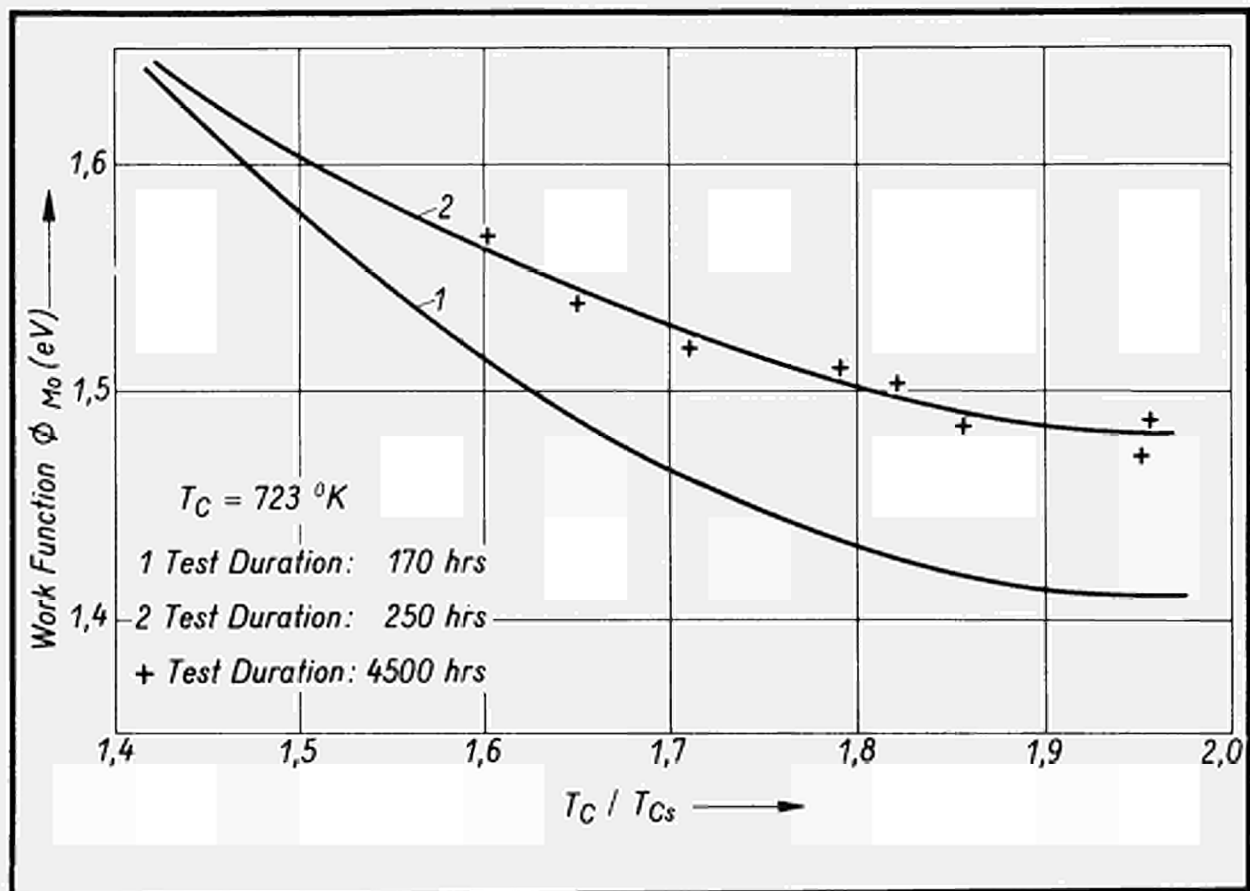


Fig. 16

Work function of Molybdenum Collector

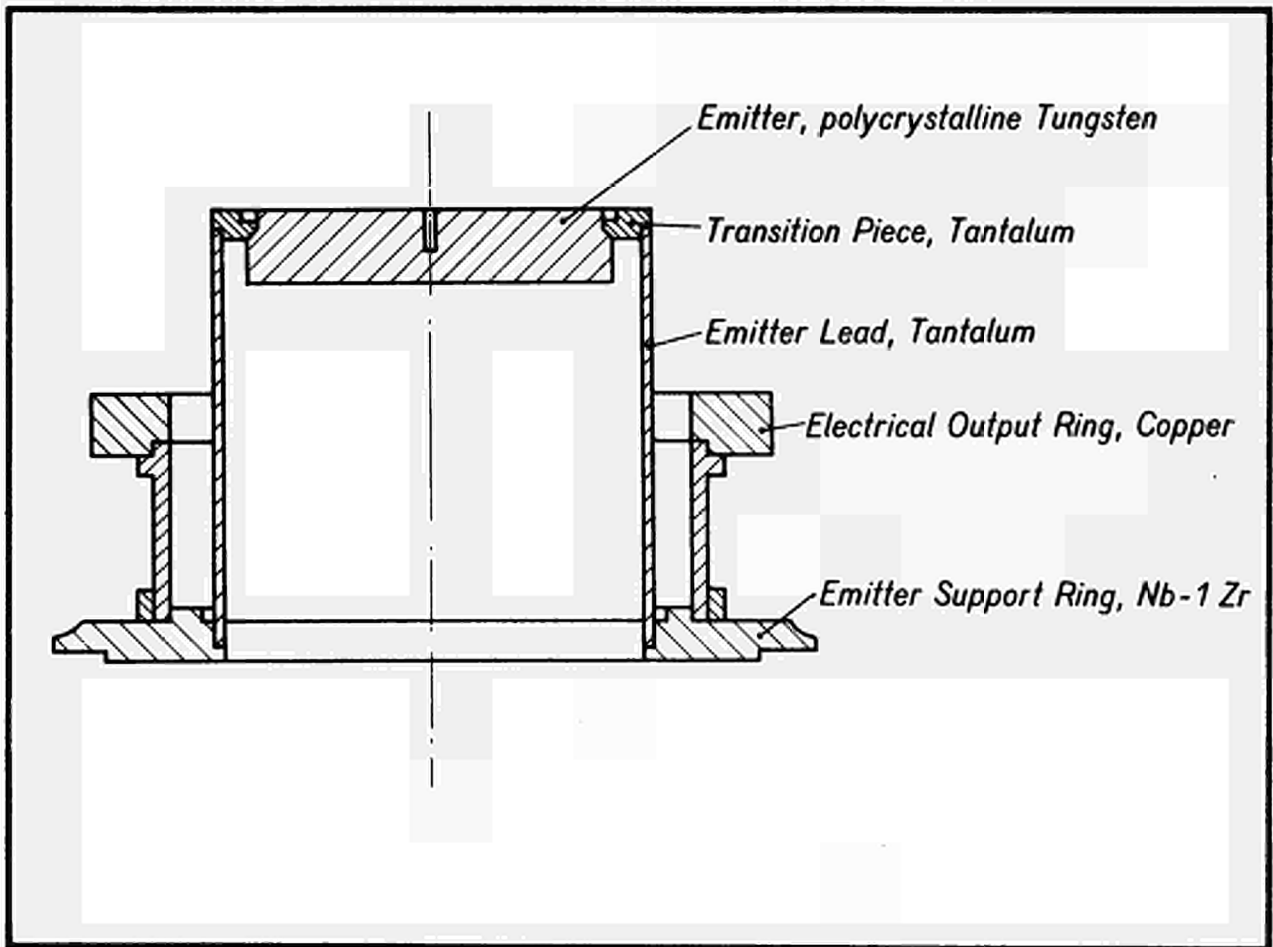


Fig. 17 *Emitter Subassembly*

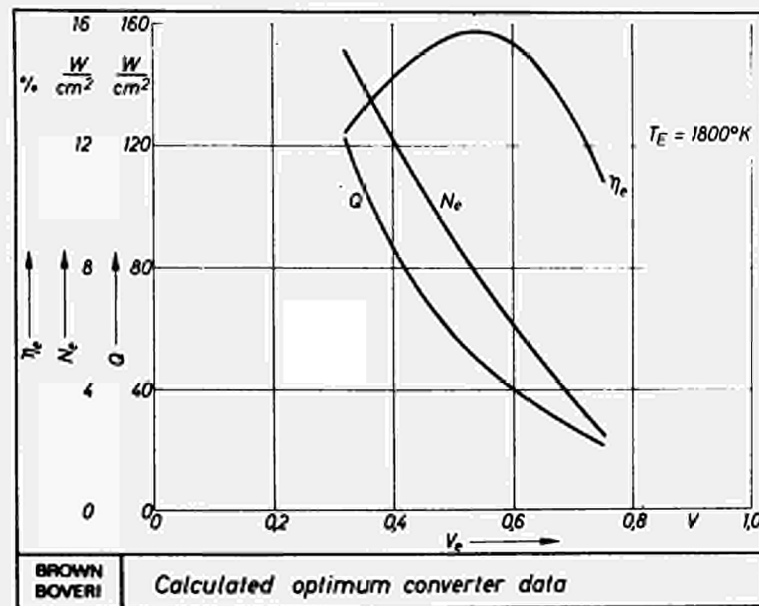


Fig. 18 : Electrode efficiency η_e , electrical power output N_e at the electrodes, and heat flux Q from the emitter surface to the collector surface as functions of the output voltage V_e at the electrodes (calculated for optimum conditions).

DISCUSSION

Speakers of paper B-13: M. J. BRABERS and F. GROSS

ROUKLOVE (USA):

Why was a finned radiator used instead of the direct radiation by the heat pipe?

GROSS (Germany):

We have made some calculations regarding heat radiation. The result was that finned radiators have a lower weight-power ratio, than a system using a directly radiating heat pipe.

A MINIATURE ATOMIC BATTERY BASED
ON THERMIONIC CONVERSION

N. S. Rasor*, K. A. Gasper, J. G. DeSteeese

McDonnell Douglas Corporation
Donald W. Douglas Laboratories
Richland, Washington

ABSTRACT

A general optimization of the radioisotope-fueled thermionic converter reveals an attractive and previously unrecognized region of practical importance at the fractional-watt level. Optimum interaction of variables is defined analytically. Illustrative examples are given of what can be achieved with present and projected technology. A demonstrated 1 mw converter fueled with Pm-147 is described and device applications are outlined.

INTRODUCTION

Recent developments in the technology and application of microcircuits have stimulated increased interest in fractional-watt radioisotope-fueled electric power supplies, generally known as "atomic batteries". It will be shown herein that thermionic energy conversion possesses attractive features at power levels in the range of 10 μ w to 1 w. This previously unrecognized region of practical importance for thermionic conversion appears as a consequence of the employment of much lower current densities than previously considered. Lower current densities permit the use of much larger electrode spacings, much lower electrode temperatures and a greatly simplified configuration. These considerations in turn permit the use of electronic and thermal design factors which are impractical at high current densities, but which are readily available to obtain attractive device sizes and efficiencies for the fractional-watt applications. The optimum interaction of variables for this new region of thermionic converter application will now be defined.

OPTIMIZATION

Basic Constraints - The reference configuration chosen is shown in Figure 1. The fuel pellet is a right circular cylinder of height h and diameter D , which includes the emitters of thermionic diodes on its surfaces. Five variations considered are: (a) emission from one planar surface only; (b) emission from both planar surfaces only; (c) emission from all surfaces; (d) emission from the cylindrical surface only; and (e) emission from the cylindrical and one planar surface only. Figure 2 shows the relationship among the variables imposed by thermal and electron emission constraints, as derived in Appendix A, for the optimum height-to-diameter ratio r . The fuel pellet diameter D and emitter temperature T_e are related to the effective collector work function ϕ'_c , the output voltage V , the total output current I , the configurational parameter a (Figure 1), the net thermal emissivity of the cylindrical region ϵ_c , and the net thermal volume power density of the fuel pellet ρ' . The net power density ρ' is computed from the difference between the heat generated in the fuel pellet (of average power density ρ) and that removed from it by electron cooling and conduction through the emitter supports.

*Consultant to Donald W. Douglas Laboratories

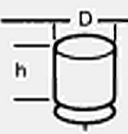
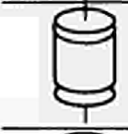



VARIATION	CONFIG. PARAMETERS (m,n,p,q)	$r = \frac{h}{D} \text{ opt}$	α
 (a)	(1101)	$\frac{\epsilon_d + \epsilon_o}{2\epsilon_o}$	1
 (b)	(2001)	$\frac{\epsilon_o}{\epsilon_d}$	2
 (c)	(2010)	1	6
 (d)	(0210)	$\frac{\epsilon_o}{\epsilon_d}$	$4 \frac{\epsilon_o}{\epsilon_d}$
 (e)	(1110)	$\frac{\epsilon_d + \epsilon_o}{2\epsilon_d}$	$3 + 2 \frac{\epsilon_o}{\epsilon_d}$

FIGURE 1. CONFIGURATIONAL VARIATIONS

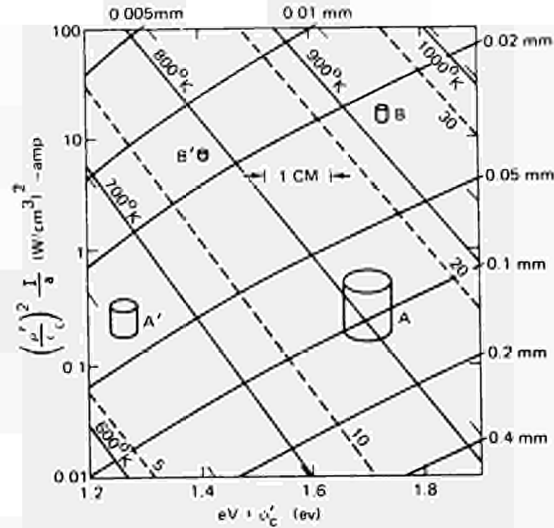


FIGURE 2. INTERRELATION OF VARIABLES. SOLID LINES ARE LOCI OF T_e (IN °K) AND x_o (IN MM). BROKEN LINES ARE LOCI OF $\mu'D/\epsilon_c$ (IN WATTS/cm²). DRAWINGS REPRESENT FUELED EMITTERS FOR 1 MW OUTPUT (SEE TABLE III).

Optimum Battery for Given I and ϕ'_c - Figure 3 shows values of output voltage V'_{max} which yield the smallest battery for given values of I and ϕ'_c with negligible electron cooling. The values V'_{max} for significant electron cooling are somewhat higher than $V'_{max'}$, as shown in Equation B-2 of Appendix B.

Vacuum Mode - For a vacuum thermionic diode with electrode spacing d, true collector work function ϕ_c , and emitter work function $\phi_e < eV + \phi_c + 2kT_e$, a sufficiently good approximation for present purposes is

$$\begin{aligned} \phi'_c &= \phi_c + kT_e \left(\frac{d}{x_o} - 1 \right)^2 && \text{for } d > x_o \\ \phi'_c &= \phi_c && \text{for } d < x_o \end{aligned} \tag{1}$$

where

$$x_o = b (\pi a / I)^{1/2} T_e^{3/4} D \tag{2}$$

and $b = 1.4 \times 10^{-6} (\text{amp})^{1/2} / \text{°K}^{3/4}$. Values of x_o are included in Figure 2. The performance of the battery in the vacuum mode therefore is independent of spacing for $d < x_o$. However, as can be seen from Equation 1 and Figure 2, the battery diameter D required for a given I increases rapidly for spacing d appreciably greater than $2x_o$.

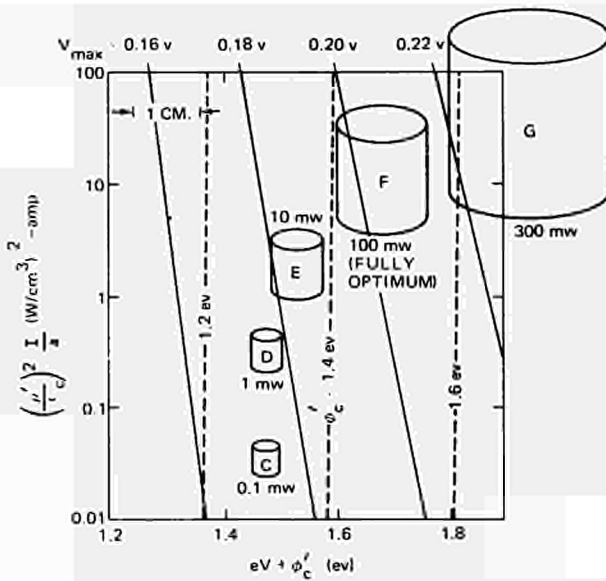


FIGURE 3. LOCI OF OPTIMUM OUTPUT VOLTAGE V_{max} AND ASSOCIATED ϕ_c' . DRAWINGS REPRESENT FUELED EMITTERS FOR INDICATED OUTPUT POWERS WITH $D/d \neq 300$ AND $\rho_0 = 1 \text{ WATT/cm}^2$ (SEE TABLE III).

In practice, the diameter-to-spacing ratio D/d often is more closely related to what is practically achievable than is the spacing d alone. It can be shown that for constant I and D/d , minimum battery size occurs near $V = V_{max}$ for $\eta < 0.05$. Maximization of efficiency η with respect to I (using $V = V_{max}$ in Equation B-1), shows that with a given achievable value of D/d maximum efficiency occurs for $\phi_c' = 1.09 \phi_c$ over the range of Figures 2 and 3. This in turn leads, via the previous equations, to the rather remarkable conclusion that for given values of ρ , ϵ_c , ϕ_c , and D/d , there exists an optimum total output power for which the efficiency is a maximum. For this fully optimized case, $d_{opt} = 2.2x_0$, and the optimum total current is

$$I_{opt} = (3 \times 10^{-11}) a T_e^{3/2} \left(\frac{D}{d}\right)^2 \text{ amp} \quad (3)$$

Because T_e and V_{max} are insensitive to all variables, the optimum total output power is relatively insensitive to all properties of the device except the diameter-to-spacing ratio D/d .

Discharge Modes - The preceding formalism is readily applied to both the ignited and unignited discharge modes of the cesium diode, but sufficient space is not available for its description here. However, it can be shown that for a given D/d , the efficiency in the vacuum mode is greater than that in either the ignited or extinguished modes for emitter temperatures below about 1400°K. This in turn establishes, through Equation 3, the maximum total power for which the vacuum mode is superior for a single cell (≤ 1 watt).

Effect of Collector Temperature in the Vacuum Mode - It can be shown that a collector-to-emitter temperature ratio up to $T_c/T_e \approx 0.78$ will not appreciably affect the electrical output of the optimized battery. However, radiant heat transfer is reduced by a factor of about 0.6 for this condition, which is equivalent to a similar reduction in the value of ϵ_c in the foregoing results.

COMPONENT TECHNOLOGY

Relative Importance of Properties - Table I summarizes the preceding results through the use of approximations appropriate in the region of variables of Figures 2 and 3. Although the relations in Table I are not precise, they are useful for recognizing the relative importance of the diode properties. Values of these properties which already have been achieved in experimental devices, and those which should be obtainable with existing technology, are summarized in Table II and are then discussed.

Table I - Approximations for Vacuum Mode Operation

Case	I (amp)	$V'_{max}(v)$	Efficiency, η (for $\eta < 0.06$)
$d \leq x_0 = 10^{-3} \left(\frac{a}{I}\right) \frac{1}{2} \frac{\epsilon_c}{\rho} \phi_c^5$ cm	Given	$0.14 \phi_c$	$\left[10^8 \frac{\epsilon_c \phi_c}{a} x_0^2 + 9\right]^{-1}$
$\frac{D}{d}$ given	$(5 \times 10^{-7}) a \phi_c^2 \left(\frac{D}{d}\right)^2$ (optimum)	$0.15 \phi_c$	$\left[(2 \times 10^8) \frac{\epsilon_c^3 \phi_c^{10}}{a \rho_0^2} \left(\frac{d}{D}\right)^2 + 9\right]^{-1}$

$(\rho_0$ in watts/cm³, ϕ_c in ev)

Table II - Properties Obtainable with Known Technology
(demonstrated - projected)

d	D/d	a	ϕ_e	ϕ_c	ϵ_c	ρ
0.2 - 0.02 mm	100 - 1000	6	1.5 - 1.3 ev	1.5 - 1.0 ev	0.05 - 0.02	0.3 - 100 w/cm ³

Electrode Configuration - The spacings ($0.02 \leq d \leq 0.2$ mm) and diameter-to-spacing ratios ($100 \leq D/d \leq 1000$) presently employed in high power thermionic converters are quite conservative for the low power devices described here, because of the much lower temperature and heat flux requirements. In addition, the fuel can be fully enclosed within a cylindrical emitter (Figures 1c-e), so that $4 < a < 6$ is quite feasible without the use of complex thermal shielding.

Surface Properties - At the low emitter operating temperatures and current densities, the required emitter work function ϕ_e can be obtained with conventional refractory metals immersed in cesium vapor at pressures so low that no significant electron scattering occurs. The emitter operates near the work function minimum where the collectors of conventional converters usually operate. Furthermore, it is now feasible to use very low work function photocell surfaces as the collector. Similarly, a lower value of radiant emissivity ϵ_c can be maintained at the lower temperatures employed here.

Net Fuel Power Density - The power density ρ obtainable with available radioisotopes and the general technology of their use as heat sources are discussed adequately elsewhere. However, the relatively low temperature and small size of the fuel capsule in the present application greatly suppress problems of materials compatibility and helium containment which have arisen in previous radioisotope-thermionic devices.

Part of the total fuel heat is lost through the emitter supports and by electron cooling. This reduces the effective power density of the fuel capsule. The effective power density ρ_0 (defined in Equation B-1) takes into account the reduction in ρ caused by electron cooling in the absence of lead and support losses. Again because of the relatively low temperature involved, and due to the absence of thermal insulation or radiation shields, a wide variety of materials and methods can be used, including ceramic spacer grains in multifoil insulation.

Illustrative Examples - Scale drawings of the fuel capsule for a 1 milliwatt battery are included in Figure 2 with the operating point at the center of the drawing for each case. Each case also is summarized in Table III. Case A represents diode property values which already have been demonstrated, combined with a fuel power density $\rho_0 = 1$ watt/cm³, which can be achieved with many radioisotopes. This includes Pm-147

TABLE III
SUMMARY OF EXAMPLES SHOWN IN FIGURES 2 AND 3
($\epsilon_c = 0.05, a = 5$)

CASE	OUT-PUT PWR. (MW)	ϕ_c (ev)	ρ_o $\frac{w}{cm^3}$	* V (volt)	T_e ($^{\circ}K$)	** η (%)	*** d (mm)	D (cm)
A	1	1.5	1	0.20	810	0.3	0.09	0.74
B			10	0.23	920	1.8	0.02	0.20
A'		1.1	1	0.17	650	2.2	0.04	0.40
B'			10	0.35	780	9.6	0.02	0.11
A	3	1.1	1	0.60	810	1.0	0.09	0.74
B	2.7		10	0.63	920	5.0	0.02	0.20
C	0.1	1.3	1	0.17	690	0.2	0.20	0.40
D	1			0.18	730	0.9	0.06	0.52
E	10			0.23	780	2.4	0.03	0.81
F	100			0.27	900	4.2	0.05	1.44
G	300			0.30	1030	3.0	0.08	2.35

* OPTIMUM; EXCEPT FOR 0.60 AND 0.63 v IN CASES A AND B

** DOES NOT INCLUDE LEAD AND SUPPORT LOSSES

*** MAXIMUM; CASES C-G ARE FOR $D/d \leq 300$

$D/d \leq 300$ and $\rho_o = 1 \text{ watt/cm}^3$. As can be seen in Table III, the 100 milliwatt case is approximately fully optimum (maximum efficiency) in accord with the expressions in Table I for this D/d .

(half-life 2.6 years) and Pu-238 (86 years), which would require no shielding for most applications. Case B represents the same diode property values as Case A, but with $\rho_o = 10 \text{ watt/cm}^3$, such as could be obtained using Po-210 (0.4 years), or Cm-244 (18 years), requiring minor and moderate shielding respectively for biological applications. Cases A' and B' show the reduction in the size obtained for Cases A and B when a technically feasible lower collector work function is employed. Alternatively, Cases A and B show the change in Cases A' and B' which would occur if the output voltage were increased from the optimum $V_{max} \approx 0.2 \text{ volt}$ to $V \approx 0.6 \text{ volt}$.

Doubling the indicated spacing would increase the diameter by less than 10% for all cases. Optimizing the collector temperature would decrease the diameter by as much as 30% and increase the efficiency by as much as a factor of 2.

The drawings in Figure 3 represent fuel capsules for various power levels with

EXPERIMENTAL MODELS

Several miniature thermionic batteries have been constructed and operated using Pm-147 or electrical heat sources. Cylindrical tantalum electrodes, spaced 0.25 mm apart with sapphire balls, have been used as a readily available and reproducible means of verifying the primary principles of the concept, and for developing fabrication, assembly, diagnostics and integral reservoir technology. A device with a 2 cm diameter emitter containing triply encapsulated Pm_2O_3 powder as fuel, delivers about 1.5 milliwatts with an effective fuel capsule power density of 0.3 watts/cm^3 . This device, shown in Figure 4 has operated in excess of 2500 hours in a continuing test with no observed degradation beyond that expected due to radioisotope decay. The experimental results generally give confidence that Cases A and B in Figure 2 can be achieved with demonstrated materials and techniques. Future diode technology development will be directed primarily toward utilizing lower collector work functions, and improving the emitter support and assembly design.

APPLICATIONS

A lengthy discussion of the areas of practical use for miniature thermionic batteries is neither possible nor appropriate here. However, several existing general areas of potential use for such devices can be cited: electric watches (10 μw); biomedical

sensors and stimulators, including cardiac pacemakers (0.1 to 1 mw); and various ecological, geophysical and military telemetry units (1-1000 mw). In addition, multiple cell miniature thermionic batteries (0.1-1 watt/cell) can compete favorably in size and weight with more conventional isotope-powered generators up to tens of watts. Furthermore, such arrays possess a much higher degree of redundant reliability than previous thermionic generators. Modular encapsulation and the much lower temperatures of the miniature diode system should also greatly reduce crucial fuel handling and containment problems.

APPENDICES

A - Basic Thermal, Emission and Configuration Constraints - At steady state, the rate of heat generation P_g in a fuel pellet of average volume power density ρ is equal to the rate at which heat is lost by thermal radiation P_r , by electron cooling P_e , and by conduction P_c through the emitter lead and supporting structure with thermal conductance G , i. e.,

$$P_g = P_r + P_e + P_c = \pi D^2 h \rho / 4 \tag{A-1}$$

where $P_e = I(eV + \phi'_c + 2kT_e)$, $P_c = G(T_e - T_c)$,

$$P_r = \sigma(T_e^4 - T_c^4)(m\epsilon_d \frac{\pi D^2}{4} + n\epsilon_o \frac{\pi D^2}{4} + p\epsilon_d \pi Dh + q\epsilon_o \pi Dh) \tag{A-2}$$

and T_e and T_c are the respective emitter and collector temperatures, σ and k are the Stefan-Boltzmann and Boltzmann constants respectively, e is the electronic charge, and ϵ_d and ϵ_o are the net thermal emissivities of the diode and non-diode regions respectively. The configurational variations are represented by the set of parameters (m, n, p, q) given for each in Figures 1a-1e.

For a given current I , the heat removed by conduction and electron cooling is relatively insensitive to all variables. It is convenient, therefore, to define a net heat generation rate $P'_g = P_g - (P_e + P_c)$, with an associated net volume power density

$$\rho' = \rho - \frac{4}{\pi} \frac{P_e + P_c}{rD^3} \tag{A-3}$$

Accordingly, to a good approximation, the minimum fuel pellet volume is obtained when $dP'_g/dh = 0$, which from Equations 1 and 2, occurs for the optimum height-to-diameter ratio

$$r = \left(\frac{h}{D}\right)_{opt} = \frac{1}{2} \frac{m\epsilon_d + n\epsilon_o}{p\epsilon_d + q\epsilon_o} \tag{A-4}$$

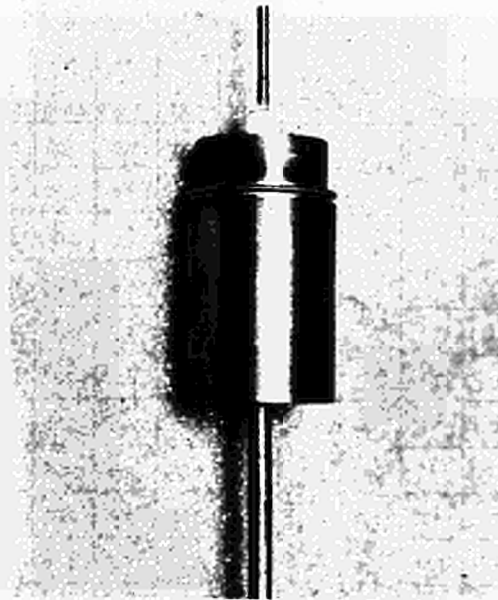


FIGURE 4. Pm-147 FUELED 1 MILLIWATT THERMIONIC BATTERY (ACTUAL SIZE)

The value of the optimum ratio r for each configurational variation is given in Figures 1a-1e. Note that a square cylinder is optimum for all variations if $\epsilon_d = \epsilon_o$. Furthermore, Equations A-2 and A-4 require that

$$D = 6 \sigma \epsilon_c (T_e^4 - T_c^4) / \rho' \quad (A-5)$$

where $\epsilon_c = p\epsilon_d + q\epsilon_o$ is the net thermal emissivity of the cylindrical region. For negligible collector emission, Equations A-4 and A-5, and the Richardson equation combine to give

$$T_e = (eV + \phi'_c) / k \ln \left[\left(\frac{3 \sigma \epsilon_c}{\rho'} \right)^2 \frac{A \pi a T_e^2}{I} (T_e^4 - T_c^4)^2 \right] \quad (A-6)$$

where A is the Richardson constant.

The values of $a = m + 4pr$ for each configurational variation are included in Figure 1. The unique relationship of T_e and $\rho'D/\epsilon_c$ to the quantities $eV + \phi'_c$ and $(\rho'/\epsilon_c)^2 I/a$, for $T_e \gg T_c$, is shown in Figure 2. The appropriate value of ρ' can be found by iteration, using values of T_e , D and $eV + \phi'_c$ attained from Figure 2 in Equations A-2 and A-3.

B - Optimum Battery for Given I and ϕ'_c - The efficiency of conversion of heat into electrical power, neglecting conduction and lead losses but including electron cooling, is

$$\eta = \frac{IV}{P_g} = \alpha \eta' \quad (B-1)$$

$$\text{where } \eta' = \frac{4IV}{\pi \rho_o D^3 r} ; \quad \alpha = \left(1 + \frac{eV + \phi'_c + 2kT_e}{eV} \eta' \right)^{-1} \quad \text{and } \rho_o = \rho - \frac{4}{\pi} \frac{P_e}{rD^3}$$

The smallest battery is obtained when the efficiency η is maximized. Differentiation of Equation B-1 with respect to V , with $T_e \gg T_c$, shows that maximum efficiency is obtained for a given current I and effective collector work function ϕ'_c when the output voltage is

$$V_{\max} \approx V'_{\max} (1 + 7\eta') \quad \text{for } \eta' < 0.1 \quad (B-2)$$

$$\text{where } V'_{\max} = (\phi'_c + 10kT_e) / 11e$$

Values of V'_{\max} and corresponding values of ϕ'_c are included in Figure 3.

DISCUSSION

Speaker of paper B-15: J. DESTEESE.

PRUSCHECK (Germany):

What are the electrode materials. Especially, what is the material of the collector?

DESTEESE (USA):

The collector material was tantalum with controlled surface impurities. These surfaces show work functions in the range 1.4 to 1.5 eV.

KARETNIKOV (USSR):

Could you give the volt-ampere characteristic of such a diode in the range of parameters which you cited at the beginning of your paper?

DESTEESE:

Figures 2 and 3 are a better indication of performance than specific current-voltage characteristics. These devices can be built to have practically any current-voltage characteristic within the domain shown in Fig. 2 and in fact you may consider Fig. 2 as a modified current-voltage plot.

THERMIONIC ELECTRICAL POWER GENERATION
FROM REENTRY PLASMAS*

- I. PERFORMANCE
- II. INTEGRATED SYSTEM

K.J. Touryan and M.M. Sluyter
Sandia Laboratory, P.O. Box 5800
Albuquerque, New Mexico 87115

ABSTRACT

The paper describes the theory of a plasma power generator from a re-entry vehicle. The nose cone serves as a thermionic emitter and the vehicle afterbody as collector. Performance parameters are identified. Experiments indicate satisfactory correlation with the theory. Moreover, to increase the conductivity of the plasma, the nose cone was impregnated with cesium. Various size pore emitters were used. Experiments show significant increase in the electron density. Finally, an integrated system is described. The system uses the electrical power derived thermionically to produce magnetic fields which interact with the conducting flow field. It is suggested that a possible application of such a device would be for trajectory control of re-entry vehicles.

*This work was supported by the U. S. Atomic Energy Commission.

SECTION I: CONVERTER PERFORMANCE

INTRODUCTION

During atmospheric entry the surface of a vehicle is heated by the hot ionized air surrounding it, to temperatures where thermionic emission could become significant. Temperatures near the stagnation point of the nose cone may be in excess of 10,000°K, while those on the vehicle afterbody may be about 3000-5000°K.

Extensive studies at the Sandia Laboratory¹⁻³ have shown that such energy levels could be used readily to generate DC-power if the vehicle could be allowed to operate as an "external" thermionic converter.

This paper describes the theory of such a converter and a potential application in which the power obtained is used for the control of a re-entry vehicle.

THEORY

The schematic of a re-entry body is shown in Figure 1. The nose cone serves as the emitter. The electrons are conducted through the ionized air plasma and collected over the afterbody which serves as an anode. An internal load between the cathode and the anode completes the circuit. The plasma mode of the generator operates in the region where the Debye sheath is essentially collisionless and is smaller than the electron or ion Larmor radii.

Neglecting capillary ion emission and assuming a space-charge neutralized emission, the current-voltage (C-V) characteristic of the device is:

$$V = \frac{kT_1^-}{e} \ln \frac{\left\{ \left[n_2^- e A_c / (I + I_c^+) \right] (kT_2^- / 2\pi m_e)^{1/2} \right\}^{T_2^- / T_1^-}}{\left\{ \left[n_1^- e A_{em} / (I_t + I_{em}^+ - I) \right] (kT_1^- / 2\pi m_e)^{1/2} \right\}} + (\phi_{em} - \phi_c) \quad (1)$$

$$- I \sum_j \left(\frac{\sigma_j}{1 + \omega_e^2 \tau_e^2} \right)^{-1} - I r \text{ (internal)}$$

For the space-charge controlled sheath at the cathode, the first term in Eq 1 is modified to include the effect of a double sheath. This implies the possibility of trapped electrons near the wall and, consequently, the current density is determined using a more detailed number density balance near the cathode,⁴ including a simple first-collision model.⁵

Unlike a plasma diode, the device acts more like a plasma generator. The primary contribution to the voltage comes from the first term of Eq 1. It can be seen that the following performance parameters are critical:

1. Large emitter area for increased short-circuit current.
2. Large collector-to-emitter area ratio for increased short-circuit current.
3. $T \text{ (emitter)} \gg T \text{ (collector)}$.
4. High plasma electron temperature T^- for high-voltage operation.
5. High plasma conductivity and short emitter-collector separation.
6. Emitter and collector materials.
7. Capillary ion emission from a porous emitter.

EXPERIMENTS

To verify the analytical prediction, an extensive set of experiments were performed in the Sandia Laboratory plasma arc jets. Satisfactory correlations were obtained between the simplified theory (see Eq 1) and experiments.

To further neutralize the space charge and increase the plasma conductivity, a series of seeding tests were conducted using capillary Cs-ion emission from porous tungsten, and tungsten-rhenium emitters (nose-cone).

The porous emitters were tested at surface temperatures in the range $2800^{\circ}\text{C} < T_s < 3200^{\circ}\text{C}$. Figure 2 shows the short-circuit current output from fine pore size, coarse pore size, and solid emitters. The relatively poor performance of the fine-pore-size emitters could be traced to the sintering of tungsten prior to depletion of cesium.

Both argon and nitrogen were used in the arc-jet tests and electron density profiles in the emitter vicinity were obtained from H_{γ} -line broadening measurements (by adding traces of hydrogen). They indicate a factor of 3 to 5 increase in electron density over the no-seeding, solid-tungsten emitter case.

Calculations similar to those given by Taylor and Langmuir,⁶ or more recently by LeBihan and Maugis,⁷ show that zero-field cesium-ion current densities average 10 ma/cm^2 for the coarse-pore-size emitters. This is in good agreement with experimentally measured current values.

SECTION II: AN INTEGRATED SYSTEM

An average re-entry trajectory is characterized by large velocity and density changes with gradients which are directly proportional to the re-entry angle. For a realistic estimate of thermionic power generation,

several sets of flow-field calculations were made, for both ballistic trajectory and orbital re-entry path.

The dissociated-ionized air model consisted of 12 air species, as well as Cs and Cs⁺. The resulting electron temperatures and number density curves were used with estimates of emitter-collector surface temperatures to calculate the thermionic performance characteristics of the re-entry vehicles. Figures 3 and 4 show the expected power output from these generators. Clearly, an orbital entry yields a higher power level and maintains a more uniform output than a ballistic entry.

A potential application of these properties is an integrated system in which the converter-derived power is utilized for orbital re-entry flight control. In concept this envisions the use of electrical power to generate magnetic fields which, by interacting with the conducting flow field around the body, will produce forces and torques. A theory for the magnetic and fluid dynamic interaction has been worked by the authors for spinning bodies of revolution.⁸ The system consists of a conventional structure of copper coils capable of generating a peak field of 1000 gauss. The coils would weigh 0.9 kg and occupy a space of $0.012 \times 10^{-4} \text{ m}^3$. The power consumption is calculated at 2.8 kw. The effect of the magnetic field is to decrease the velocity and the axial drag. Moreover, the original torque exerted by the viscous fluid and opposing the spin is reduced as a result of the magnetic interaction.

Scalar electrical conductivity was assumed throughout since reduction in conductivity, due to its tensor nature, is shown to be of small magnitude.

REFERENCES

- (1) LEBLANC, A. R., Hypersonic plasma thermionic generator, Parts I and II, Sandia Corporation Report, SC-DC-2848 (August 1962).
- (2) TOURYAN, K. J., "A hypersonic plasma power generator," AIAA Journal, 3, No. 4 (April 1965), 652-659.
- (3) TOURYAN, K. J.; SLUYTER, M. M., "Thermionic power generation from reentry vehicles," IEEE Transactions on Aerospace and Electronic Systems, AES-2, No. 4 (July 1966).
- (4) HU, P. N.; ZIERING, S., "Collisionless theory of a plasma sheath near an electrode," Physics of Fluids, 9, No. 11 (November 1966).
- (5) KUCHEROV, R. YA; RIKENGLAZ, L. E., "Kinetic theory of the low density plasma diode," Soviet Physics - Technical Physics, 7, No. 10 (April 1963).
- (6) TAYLOR, J. B.; LANGMUIR, I., "The evaporation of atoms, ions, and electrons from cesium films on tungsten," Physics Review, 44 (1933), 423-548.
- (7) LEBIHAN, R.; MAUGIS, D., "Etude theorique et experimentale de structures creuses a plasma de cesium, sources d'ions or d'electrons," Ann. de Radioelectricite, 20 (1965), 124.
- (8) SLUYTER, M. M.; TOURYAN, K. J., The effect of a magnetic field on a rotating cone in compressible flow, Sandia Corporation Report, SC-RR-67-2965.

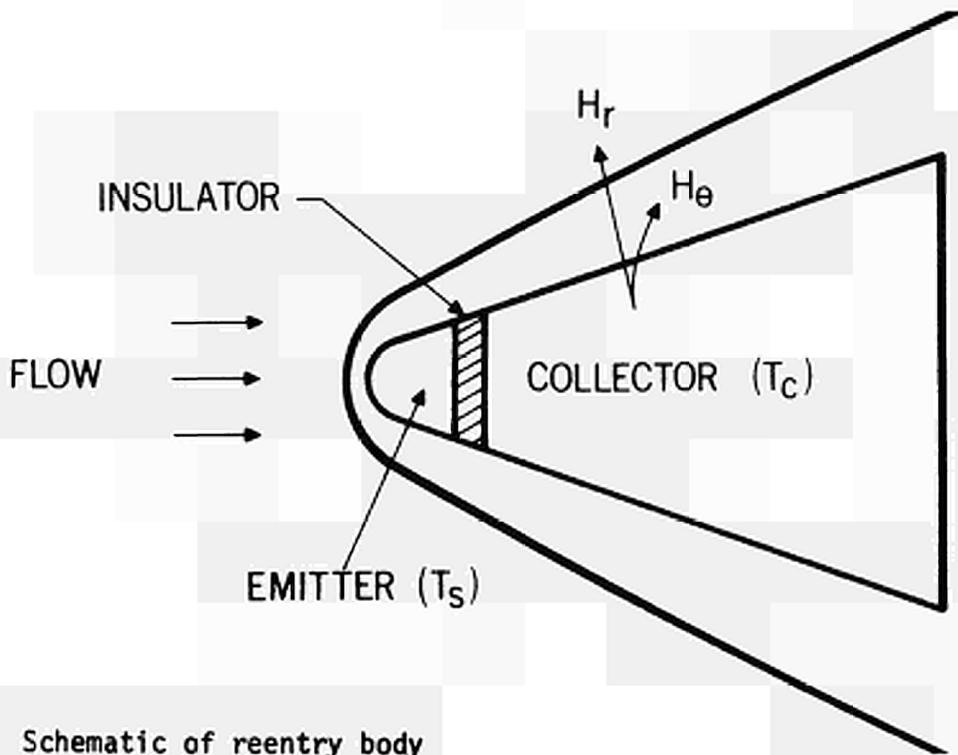


Fig. 1. Schematic of reentry body

T_c = average collector temperature, T_s = average emitter surface temperature

H_r = radial magnetic field, H_θ = azimuthal magnetic field

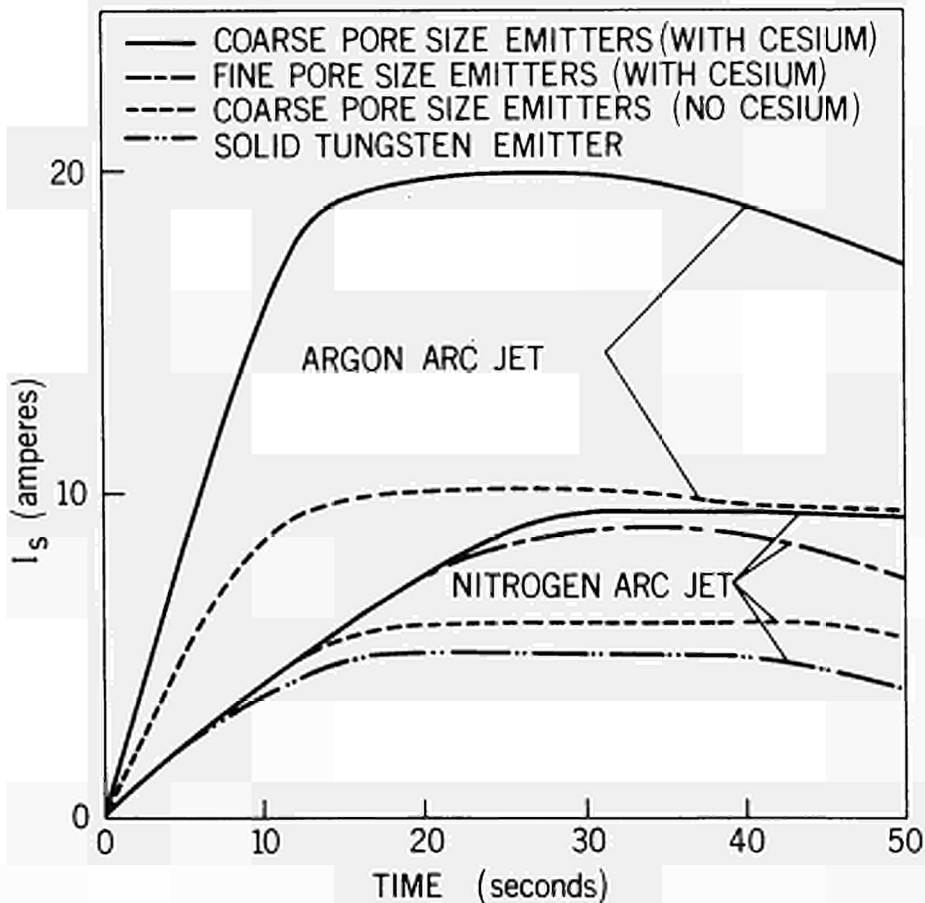


Fig. 2. Short-circuit current output with and without seeding (0.1 gm/sec) from tungsten emitters, 3/4 inch diameter

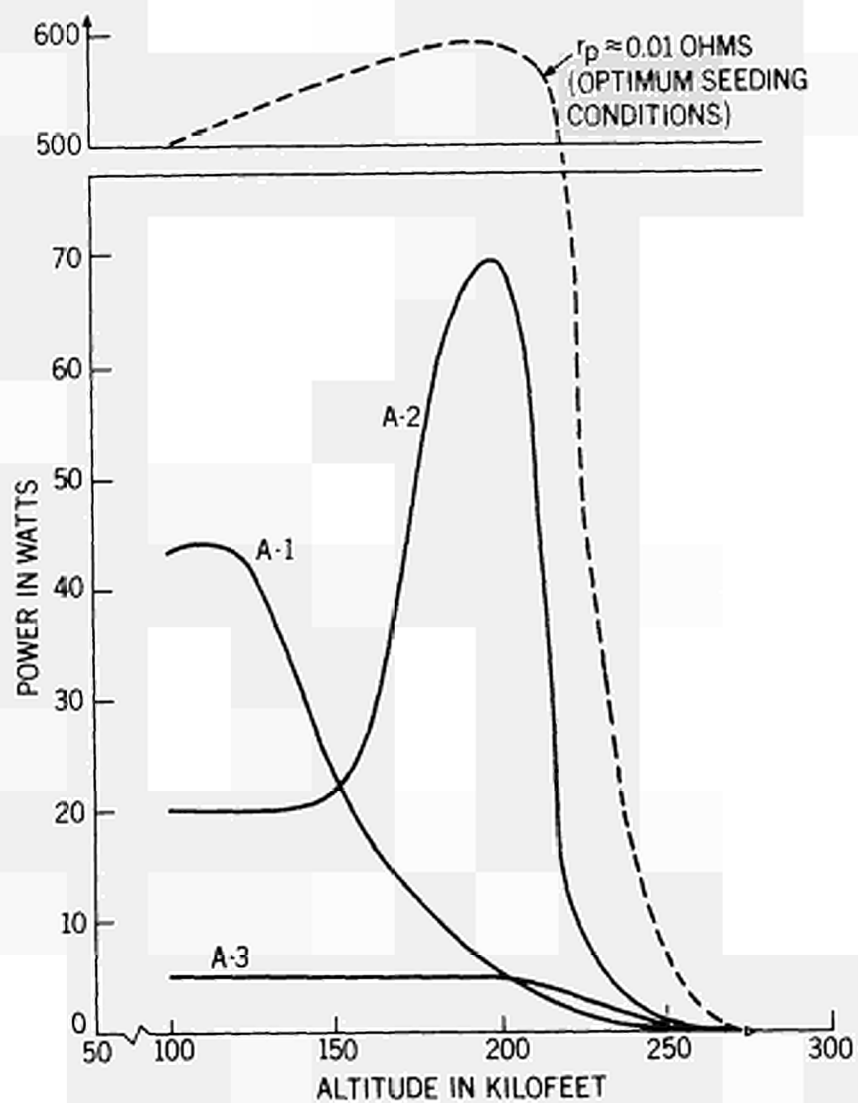


Fig. 3. Power output versus altitude for Models A-1, 2, 3 at 200 kilofeet altitude, suborbital trajectories
 A-1, hemisphere-cylinder shape; A-2, hemisphere-cone shape;
 A-3, simple cone

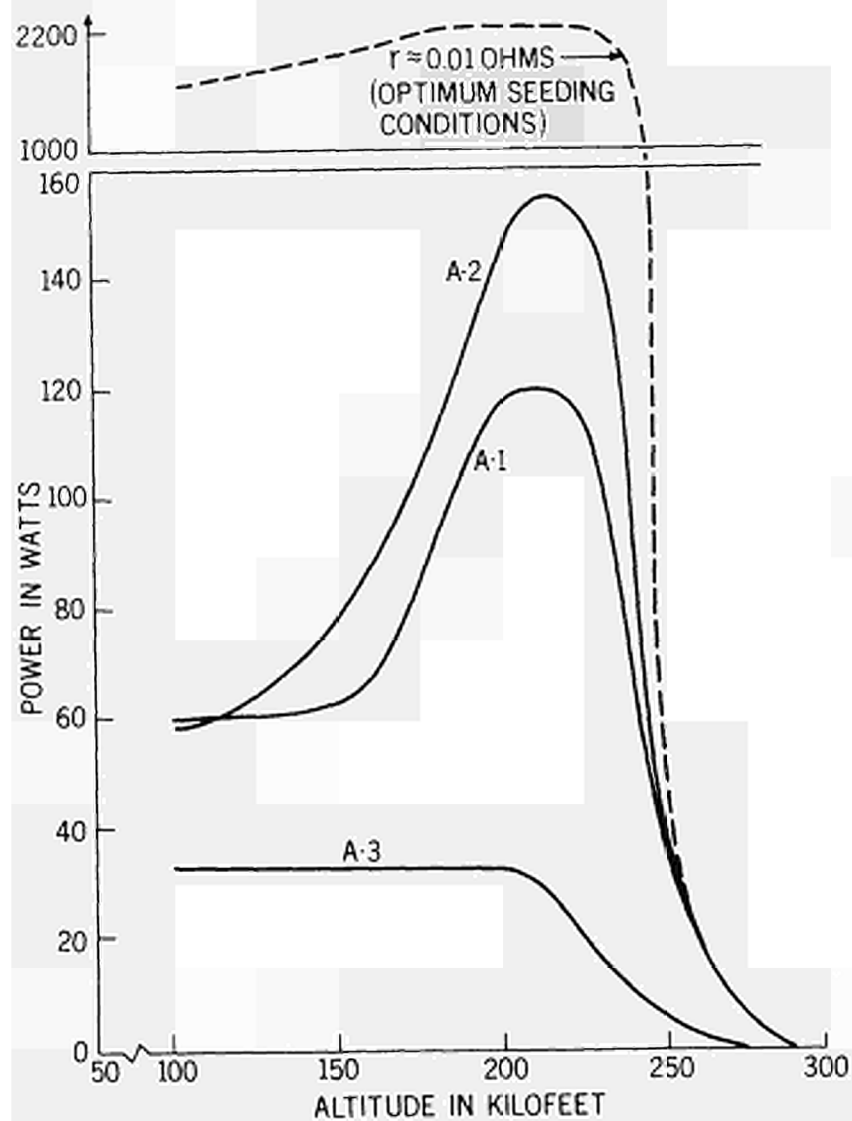


Fig. 4. Power output versus altitude for Models A-1, 2, 3 at 200 kilofeet altitude, superorbital trajectories

IN-REACTOR THERMIONIC CONVERTER TESTING
EXPERIENCE AT GENERAL ELECTRIC*

J. E. VanHoomissen and D. J. Holtslag

General Electric Company, Pleasanton, California
United States of America

ABSTRACT

The design and testing of two single-cell fission powered thermionic converters is presented. Single-Cell In-Pile Test 509 (SCIP-509) contained a vent in the emitter clad which allowed fission gases to pass into the interelectrode space. Single-Cell In-Pile Test 510 (SCIP-510) had a sealed emitter clad structure which contained fission gases within the clad. Layouts and photographs of the hardware, operational current-voltage characteristics, and post-operational results are presented.

INTRODUCTION

A significant decision in the design of a fission powered thermionic converter is the choice of method for accommodation of the fission product gases generated in the fueled emitter structure. It is the purpose of this paper to present the design and testing of two single-cell converter tests alike in all significant design features, except in the handling of the fission product gases. Single-Cell In-Pile Test 509 (SCIP-509) contained a vent in the emitter clad which allowed the fission gases to pass into the interelectrode space; Single-Cell In-Pile Test 510 (SCIP-510) had a sealed emitter clad structure which contained the fission gases within the clad. The extended operation of these two converters allows at least a qualitative comparison between the operation of vented and non-vented converter configuration.

A discussion of the design of the SCIP converters, the testing environment and method of testing, the operational results, and finally post-operational examination allow a framework from which the qualitative comparison can be made. To aid in the clarity of presentation, the SCIP-510 test is reviewed first.

*This work was performed for the Atomic Energy Commission under Contract No. AT(04-3)-189, P. A. 32.

SCIP-510 Design

Construction details of SCIP-510 are shown in Figure 1. At the left is a cut-away drawing of the complete converter. At the center is an enlarged view of the active diode region, while at the far right is a photograph of the emitter.

The emitter was fueled with uranium dioxide in the form of a cored pellet. This pellet was enclosed in a tungsten emitter clad. The vapor-deposited tungsten cylinder was sealed at both ends by electron beam welding vacuum arc cast tungsten caps in place. To one of these end caps, a tungsten pin was attached to stranded copper wire which led to the support post in a metal-to-ceramic seal assembly. The spacing of the emitter from the nickel collector was accomplished by the use of small tungsten pins imbedded in a molybdenum ring, which in turn was supported by a pair of alumina insulators placed in a machined groove in the collector. Identical assemblies were located at each end of the emitter. The cesium reservoir assembly contained one gram of liquid cesium. The nickel collector assembly was welded to the ceramic-to-metal seal assembly by a nickel to Inconel weld. Electric output of the thermionic converter appeared across the metal-to-ceramic seal.

Encapsulation of the converter and installation in the test reactor are shown in Figure 2. At the left is a photograph of the encapsulated converter without its outer capsule can, which is shown in the photograph at the center. At the far right is a schematic drawing of the capsule installation in the reactor.

The collector heat distributor, electric trim heater, and the variation of helium-argon gas mixture in the capsule permitted temperature control of the collector during operation. A similar arrangement of heat distributor, heater, and gas gap controlled the cesium reservoir temperature. The irradiation capsule was located in a positioning device next to the active core and just outside the pressure vessel of the irradiation reactor. This arrangement allowed variation of converter power input by movement of the converter toward and away from the reactor core. A flexible metal hose, containing instrumental and power leads, connected the capsule to a control console.

SCIP-510 was originally installed in the test reactor during March, 1966. During insertion, a slow rise to power was made to permit acquisition of current-voltage

characteristics over a wide range of test conditions. After reaching the life test output of six watts per square centimeter, current-voltage characteristics were again taken. Throughout the test period of 3,596 hours, current-voltage characteristics were obtained approximately every 200 hours. Input power was somewhat variable due to reactor operation and method of test control. Emitter temperature was inferred by the examination of the I-V characteristics and their comparison with out-of-reactor tests of similar converters. Figure 3 presents I-V characteristics measured very soon after the start of test and shortly before the test ended. It is seen that for essentially the same emitter and cesium reservoir temperatures, the characteristics of the diode remained unchanged throughout the course of the testing.

After 3,596 hours of testing, a short circuit appeared between the emitter and collector. The site of the short circuit was examined in a hot cell, and the emitter was found to be bulged by about 0.007-inch at the maximum. No detectable fission products were found external to the tungsten emitter, thus documenting the leak tightness of the tungsten clad throughout the operation. The results of the measurements in the hot cell are consistent with the hypothesis that the fission gas pressure internal to the tungsten clad had caused creep in the tungsten wall, such that the tungsten eventually shorted to the nickel collector. Analytical calculations based on approximately 100% release of fission gases and using available creep data for tungsten corroborate the hypothesis.

SCIP-509

SCIP-509 was essentially identical to the SCIP-510 described in the preceding except for the design of the emitter structure itself. A vent in one end of the emitter allowed the fission gases to escape into the interelectrode spaces while containing the UO₂ fuel in the tungsten emitter. The diameter of the vent (Figure 4) was 0.020-inch.

The operation of SCIP-509 was similar in all important aspects to that of SCIP-510. The device operated in the reactor for 2,812 hours, at which time a leak in the envelope developed allowing gases from the capsule into the converter, and the converter was withdrawn from the reactor. The behavior of the converter was consistent with the hypothesis that the buildup of fission gases in the interelectrode space caused an increase in the thermal losses from the emitter, thereby reducing the efficiency of

conversion. For constant load current and emitter temperature, an increase in input power of approximately 10% was required to overcome the increased thermal cooling effect of the fission gases. This effect increased asymptotically during the first 1,000 hours of operation and thereafter remained essentially constant. Thermionically, the major effect noted was a lowering of the optimum cesium reservoir temperature. Figure 5 shows comparative output characteristics from SCIP-510 and SCIP-509 at around the 2,700-hour operating time. It can be seen that SCIP-509 continued to produce comparable output but at lower cesium reservoir temperatures. From these characteristics it is seen that although the effect of the fission gases is certainly measurable, the overall effect is not large.

Upon disassembly of the converter in the hot cell, the emitter was measured to show no detectable change in dimensions and generally was in excellent condition. Figure 6 is a photograph of the SCIP-509 emitter as it appeared after operation. The vent hole can be seen in the end cap. No detectable amounts of uranium were found external to the emitter, and fission products other than the inert fission gases were present only in tract amounts. A total of 1.63 standard cubic centimeters of xenon plus krypton were found in the diode space. This corresponds to a pressure of 178 torr of pressure at operating temperature. Significantly, this is some 10^6 times the cesium pressure associated with the 290°C optimum cesium reservoir temperature.

SUMMARY

In conclusion, two in-pile thermionic tests have been operated for times of approximately 3,000 hours, one with a sealed emitter and one with a vented emitter. The sealed emitter test was terminated by the shorting of the emitter to the collector, probably due to creep of the tungsten clad caused by internal fission product gas pressure. The vented test was terminated due to a failure of the envelope, an independent event. The fission product gases were released from the emitter as intended. The UO_2 fuel was contained in the emitter as intended, and the overall effect on the operation of the converter was hypothetically explained by the increased thermal losses from the emitter to the collector.

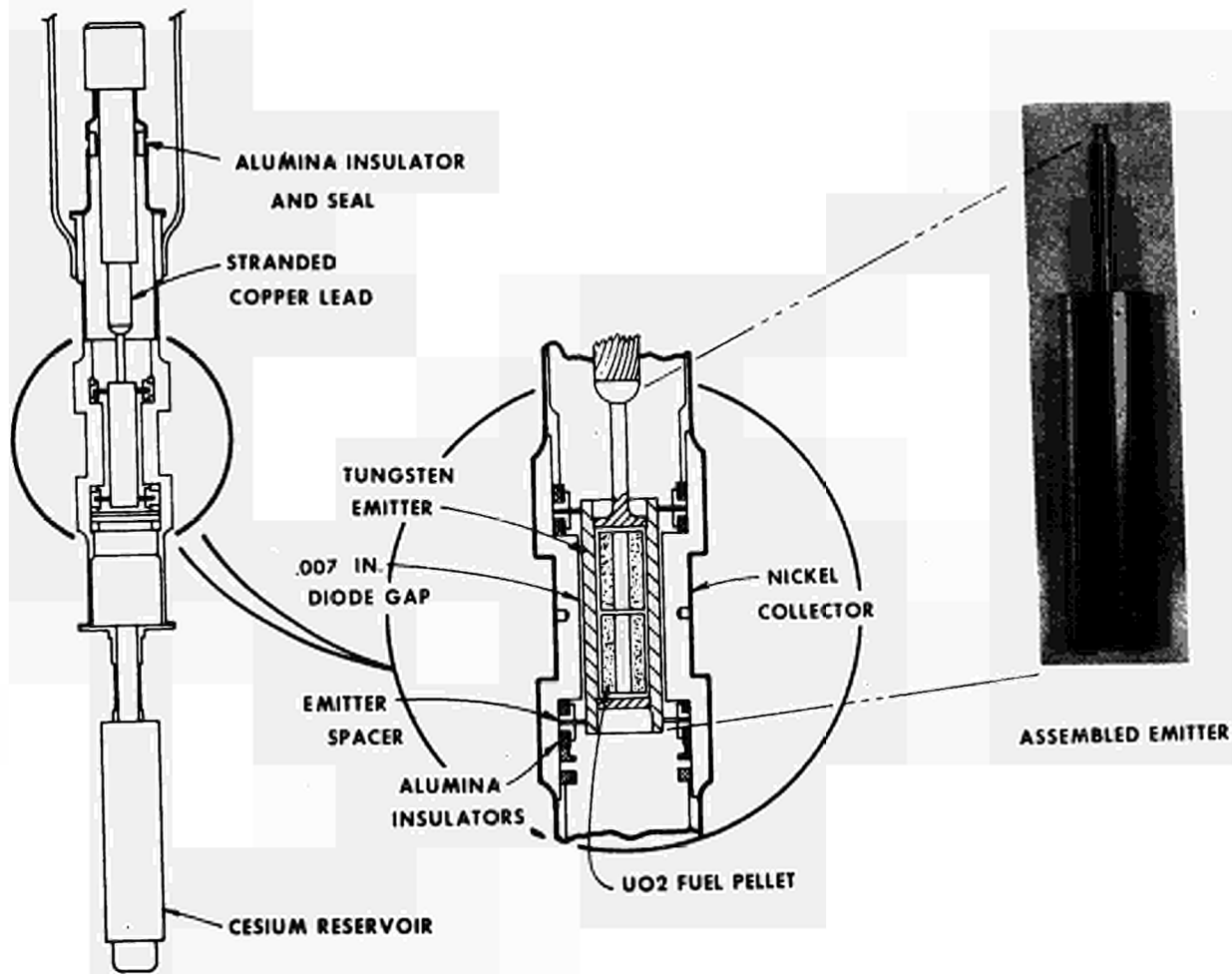
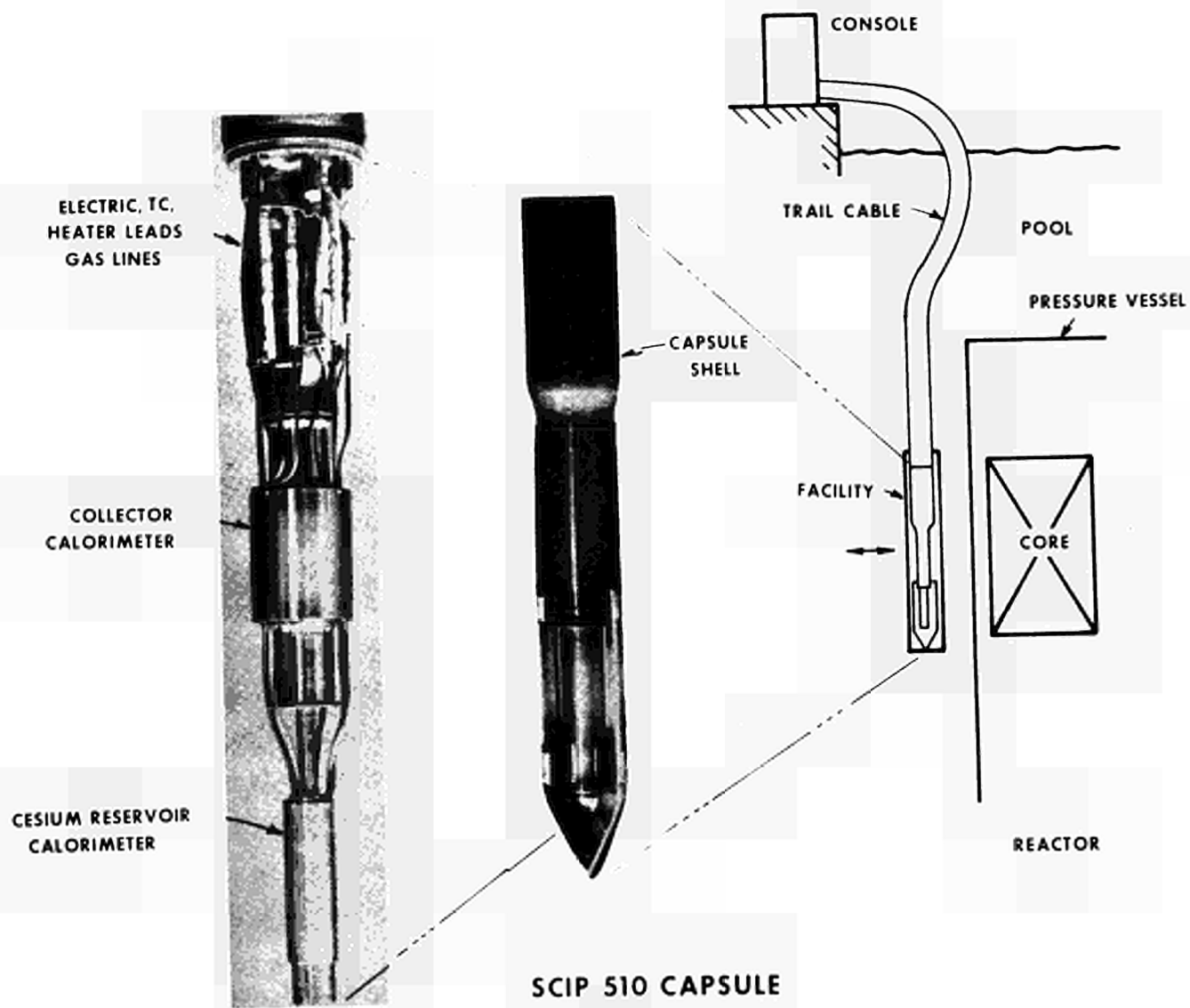
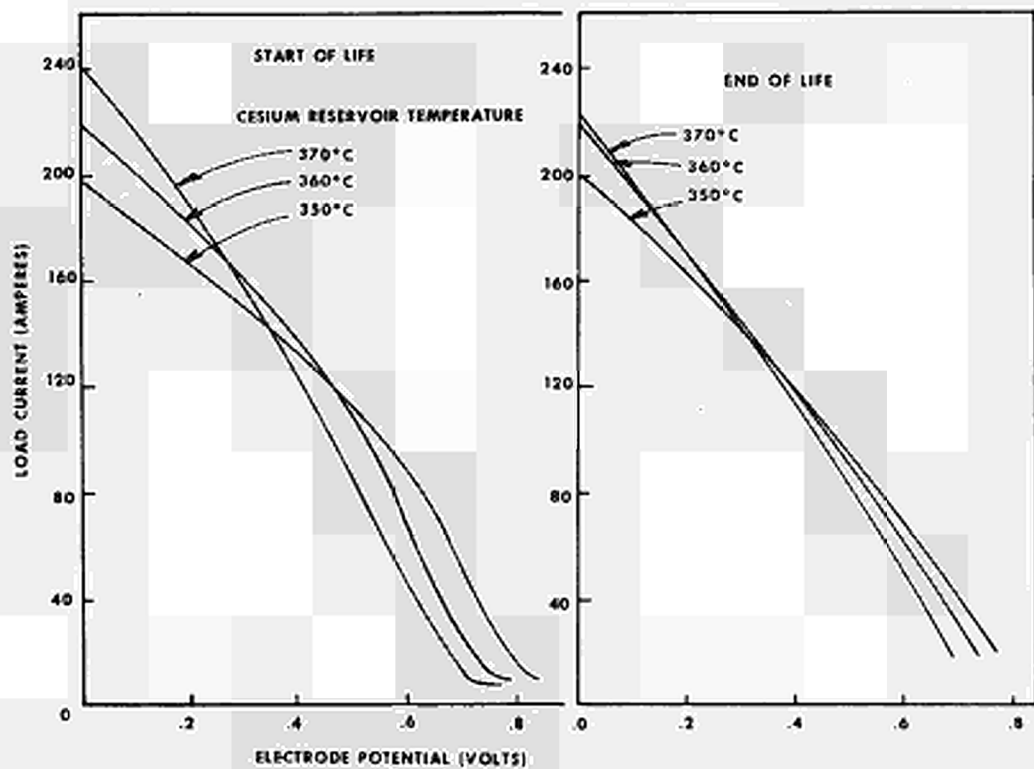


FIGURE 1 CONVERTER SCIP 510



SCIP 510 CAPSULE

FIGURE 2



SCIP 510 OUTPUT CHARACTERISTICS

(FOR 1600°C EMITTER TEMPERATURE)

FIGURE 3

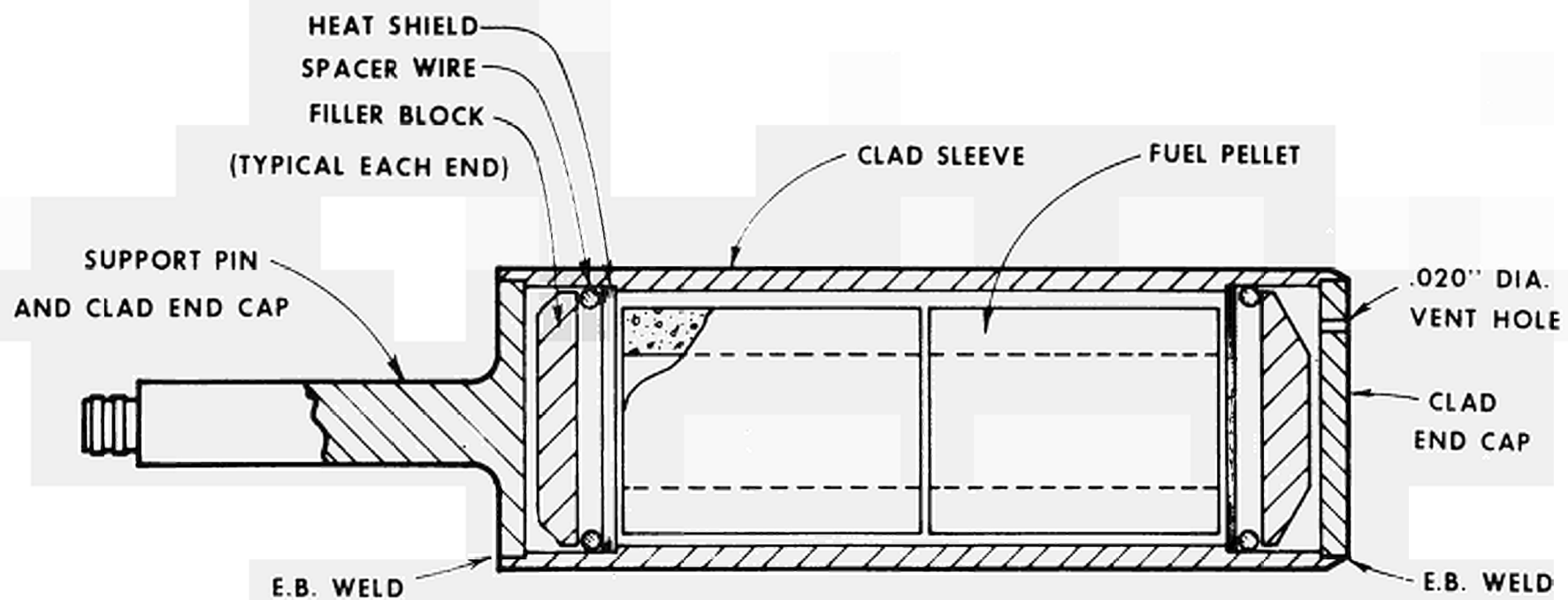
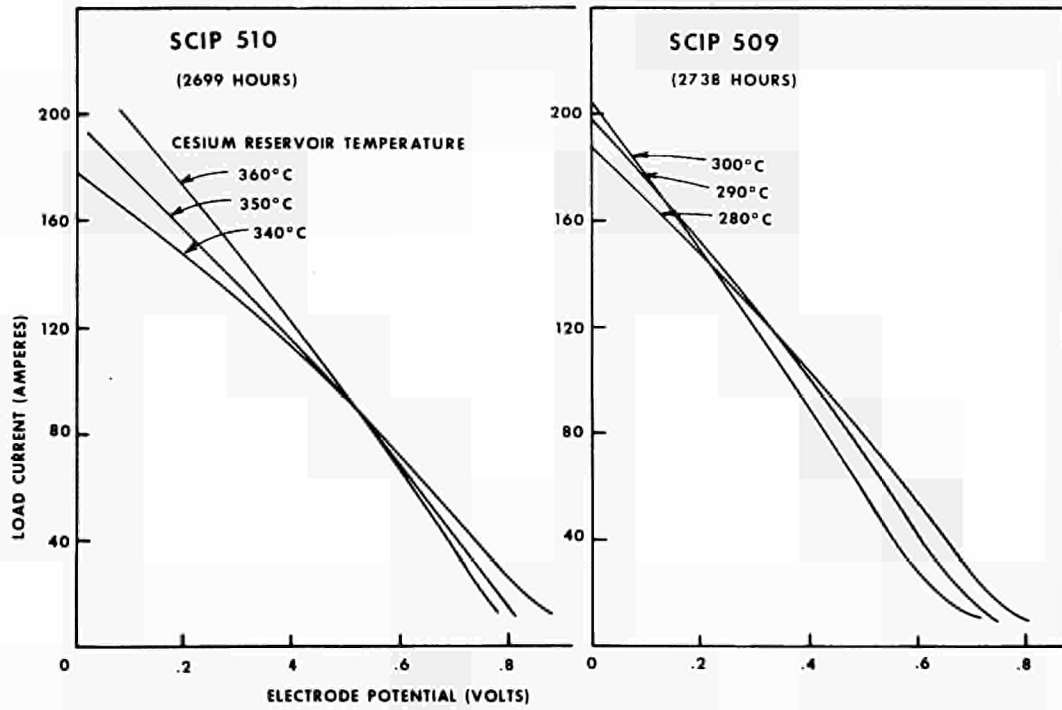


FIGURE 4

SCIP 509 EMITTER DETAIL



COMPARISON OF SCIP 510 & 509 OUTPUT CHARACTERISTICS
(FOR 1600°C EMITTER TEMPERATURE)

FIGURE 5

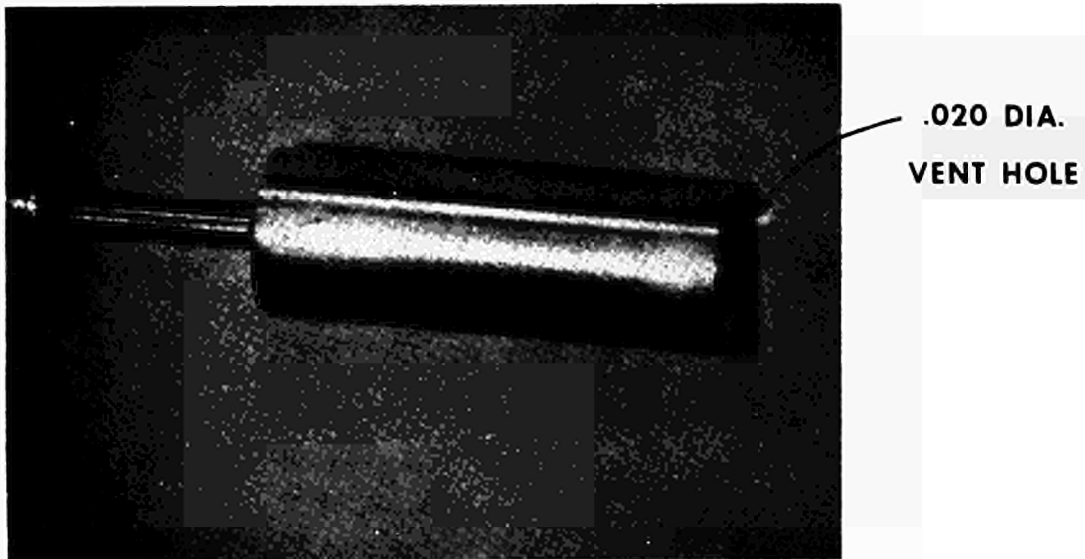


FIGURE 6 SCIP 509 EMITTER AFTER OPERATION

2812 HOURS
CALCULATED BURNUP 2.2×10^{20} F/CC

DISCUSSION

Speaker of paper C-1: J. E. VAN HOOMISSEN.

BUGL (Euratom):

What was the wall thickness of the tungsten emitter? How high was the pressure due to fission gas release in your closed system? What was the fast flux you accumulated during the test on the tungsten emitter?

VAN HOOMISSEN (USA):

The wall thickness of the emitter was 40 mils, the fission gas pressure in the converter was roughly 200 Torr and we would multiply it by about 20 to take it back into the confines of the emitter so that there might be a pressure of 4000 Torr. I do not have a number at the moment for the fast flux above 1 MeV.

SCHOCK (USA):

How was the emitter temperature measured?

VAN HOOMISSEN:

The emitter temperature was inferred by looking at the I-V characteristics which were compared with out-of-pile results. There was no thermo-couple on the emitters themselves. We also at the same time had relatively good calorimetric measurements. One can calculate back to the emitter temperature with this information. There were no direct measurements.

SCHOCK:

Have you any explanation why the optimum cesium pressure was so different in the vented and unvented tests?

VAN HOOMISSEN:

I don't. I think that the theoreticians could have some opinions but we do not have a definite explanation.

PEEHS (Germany):

Have you sectioned the emitter after irradiation? Have you found some UO_2 behind the heat shield?

VAN HOOMISSEN:

We have not completed the longitudinal sectioning of the vented case, so we cannot state whether or not there is any UO_2 behind the tungsten disc.

PEEHS:

Have you some information about the temperature distribution during irra-

diation?

VAN HOOMISSEN:

No direct measurements of course, however, one can make analytical estimates.

PEEHS:

How do you explain the mechanism that no UO_2 -loss occurs?

VAN HOOMISSEN:

As one can see from the structure of the vent, one passes through a relatively cooler area as one moves out of the emitter. We have looked at this experimentally out of the reactor and have set the vent size at an optimum so that the fuel will stay in and the gas come out.

DEVIN (France):

What was the spacing of the converter?

VAN HOOMISSEN:

7 mils.

DEVIN:

Were your I-V curves taken with DC or an AC sweep?

VAN HOOMISSEN:

AC.

DEVIN:

And what were the steady conditions?

VAN HOOMISSEN:

They were not always exactly the same, but for the ones presented we used approximately 10 Amps/cm^2 DC.

SCHOCK:

If the vent hole was appreciably cooler than other parts of the fueled emitter, how can you be certain that the vent was not plugged with UO_2 after a while?

VAN HOOMISSEN:

Just by examining it afterward. It does not appear to be plugged at all.

CONVERTER SD-4 DESIGN AND SUMMARY OF TEST RESULTS

by

R. C. Howard and J. B. Dunlay
Thermo Electron Corporation
Waltham, Massachusetts, USA

ABSTRACT

Under United States Atomic Energy Commission sponsorship, Thermo Electron Corporation is conducting an Advanced Technology Program aimed at improving the life and performance of in-pile converters. This program involves the in-pile and out-of-pile testing of thermionic converters incorporating improved electrode surfaces. Several different tungsten and rhenium emitter surfaces are being investigated over a five-year period.

As an initial phase of this effort, Thermo Electron Corporation has conducted a long-term in-pile test of Converter SD-4 in the Battelle Memorial Institute Reactor. The cylindrical converter had an etched-rhenium emitter, a molybdenum-coated niobium collector, and a uranium-dioxide vs tungsten cermet fuel. Both in-pile and out-of-pile tests were performed on SD-4.

This paper describes the design of SD-4 and the test results obtained in-pile and out-of-pile. A comparison is presented for the diode performance at various times throughout its test history. The collector temperature, cesium reservoir temperature, power output, power input, and efficiency are reported. Based on emitter temperatures measured during out-of-pile tests, estimates are presented of the emitter temperatures during in-pile tests. The in-pile calorimetry techniques used to measure power input are described with supporting test data.

INTRODUCTION

In September of 1965, Thermo Electron started an in-pile test at the BMI reactor under USAEC sponsorship. The test consisted of a cylindrical thermionic converter with a rhenium emitter fueled with a cermet of UO_2 -W. The external environment of the converter was a static vacuum formed by an initial pump-out and seal-off of a stainless steel housing. The test operated in-pile for 8125 hours over a period of about two years. More than 80 cycles between shutdown and full power occurred during this period. The average electrode power density throughout the test lifetime was 7.8 watts/cm^2 . For fixed reference levels of reactor power, cesium pressure, and collector temperature, the diode performance was stable throughout the life of the test. The test was terminated when difficulties occurred in auxiliary heaters and coolant systems which caused a loss in control of the cesium reservoir temperature.

In the following sections, the design of the converter and the test capsule is described. In the subsequent section, the test history and a summary of the test data are presented

DESIGN

The converter design used in the in-pile program (Figure 1) permits either out-of-pile testing with electrical heating or in-pile testing with fission heating. The basic design philosophy is to allow complete testing of the diode out-of-pile with only minor modifications necessary for testing in-pile. The design includes provisions for independent control of emitter, collector, and cesium reservoir temperatures. In addition, the collector cooling arrangement permits an accurate calorimetric measurement to be made of total heat rejected. Thus a reliable estimate of converter efficiency can be

obtained during both out-of-pile and in-pile testing. In Table 1, a summary of the converter design parameters is presented.

The cermet fuel is in a hollow, cylindrical shape and is clad internally with tungsten and externally with rhenium. The purpose of the internal clad is to suppress evaporation of the uranium contained in the cermet. By preventing this evaporation, loss of fuel is minimized and the stability of electron bombardment heating is greatly improved. Thermocouple holes at three axial locations in the fuel annulus are provided to obtain an axial temperature profile of the fueled-emitter during out-of-pile testing. The rhenium external clad on the fuel also acts as the emitter. This clad has an extension approximately 0.4 inch longer than the fueled length, which serves as the "optimized lead." The extension is joined to a molybdenum support ring which, in turn, joins to one of the niobium seal flanges. The other end of the rhenium emitter has a small diameter pin which fits into an insulated hole in the collector bottom. This pin provides additional support and alignment for operation and for any shock and vibration which might occur during shipping and handling.

Inside the inner tungsten liner of the fuel is a cavity to permit electron bombardment heating of the fueled-emitter. The electron bombardment gun which occupies this cavity during out-of-pile testing, consists of a helical filament attached to a massive central rod for alignment. The gun includes electrical insulators and its own radiator to dissipate heat conducted out of the cavity. After electrical testing is completed, the gun is removed and the "closure plug" is welded as shown in Figure 1. In making this weld, no other part of the diode structure is heated, thus eliminating any temperature effect on the rest of the structure. This is a key aspect of the design because it insures that a valid comparison can be made of in-pile to out-of-pile diode behavior. If the converter were thermally cycled or otherwise

affected during this operation, the cause of any change in behavior could not be reliably determined.

At a radial gap of about 0.010" from the emitter, there is a cylindrical collector made of massive niobium. At one end, the collector is joined to one of the niobium seal flanges and, at the other end, to the bottom collector plug. Sheathed heaters are imbedded in the outside surface of the collector. A niobium tube covers these heater wires and provides a smooth surface for the "heat choke" fins which maintain the difference between the collector temperature and the water coolant temperature. These fins are made of niobium and are joined on their outside surface to a water cooling jacket also made of niobium. The combination of the heater wires with the heat choke fins constitutes the collector temperature control scheme. Since this entire structure is brazed together, accurate prediction and control of collector temperature is possible. The thickness of the collector was selected as a compromise between the space available in the in-pile test hole (2.75") and the temperature uniformity of the collector. Three holes are provided in the collector walls for sheathed thermocouples to obtain a measurement of the axial temperature variation.

The cesium reservoir tubulation is joined to the bottom collector plug and communicates with the diode through slanted holes in the bottom plug. At the other end of the tubulation, there is a cesium reservoir chamber. The design of this chamber prevents liquid cesium from spilling into the diode regardless of its inclination. Thus, during disassembly in the hot cell, all cesium can be removed from the converter by cutting-off the cesium reservoir and, therefore, no contamination of the diode interior with cesium oxide need occur. Sheathed heater wire is brazed to the reservoir and copper straps are connected from the reservoir to the water cooling jacket surrounding the collector. This combination of heater wire and cooling straps permits control of the

cesium reservoir temperature despite the uncertainties in gamma heating rates

The main diode insulator-seal is of the "SET" type of construction and consists of niobium flanges brazed to alumina rings. The emitter current leads are connected to the emitter support ring with threaded screws. The collector current leads are connected to a flange on the outside coolant jacket with threaded rods held by nuts. Inlet and outlet water tubes are brazed at the top end of the coolant jacket which contains a double thread for water flow.

The converter is supported within a 2.75" tube which occupies a fuel element position in the BMI reactor. This tube is evacuated after outgassing and then sealed off with a valve. Except for a zirconium getter heated by gamma radiation, the vacuum within the tube is static. In Figure 2, a photograph of the completed in-pile assembly is shown prior to insertion into the in-pile tube. This assembly consists of the converter, two water cooling lines, six sheathed heater leads, twenty thermocouple leads, six voltage leads, and the emitter and collector bus bars.

TEST HISTORY

Converter SD-4 has been operated for 100 hours out-of-pile and about 8125 hours in-pile. The results obtained during most of the test period are summarized in Figure 3 which displays power input, power output, efficiency, cesium reservoir temperature, and collector temperature. The points shown represent the data recorded at periodic intervals by the reactor operating technicians. In general, the cesium reservoir and collector temperatures were maintained near optimum levels. However, day-to-day drifts in cesium reservoir temperature and in collector temperature occurred throughout the test duration.

The total testing time can be divided into eight periods. The first period was the 100 hour out-of-pile test, shown in Figure 3 to the left

of zero-hours of in-pile operation. The second period was the initial 25 hours of in-pile testing. The third period consisted of a transient in emitter temperature caused by a reduction in power input to the emitter. This transient lasted until the 600 hour point, although it was virtually over by the 300 hour point. The fourth period was a steady run of about 300 hours at a slightly reduced reactor power level necessitated by another experiment on the reactor. The fifth period was a steady run from about the 1400-hour point to about the 2600-hour point at full reactor power levels. The reactor was shut down for modifications at about the 2600-hour point. The sixth period was a fairly steady run after the reactor was re-started until the 6100-hour point, when a malfunction in the cesium reservoir heater occurred. The seventh period consisted of operation without the cesium reservoir heater and extended from the 6100-hour point to the 7327-hour point. During the initial part of this period, Dowtherm instead of water was used as a coolant to achieve the desired cesium reservoir temperature. This period ended when the cooling lines became clogged with a carbon-type substance caused by dissociation of the Dowtherm. The eighth test period was started after the carbon scale was flushed out of the coolant lines. However, the scale built up again during this period and finally led to termination of the test after 8125 hours. In the following paragraphs, each of these test periods is summarized.

Throughout all eight test periods no performance degradation of the converter was observed. At periodic intervals the cesium temperature, collector temperature and power input were re-set at reference levels corresponding to a data point taken during the first 25 hours. These points are shown in Figure 4 at the 25-hour, 1711-hour, 2615-hour, 3110-hour, 4300-hour, 7000-hour, and 7890-hour points. These points are shown in relation to a sweep curve taken during the initial out-of-pile tests. During the first 2615 hours the reference

points were taken at very closely set cesium reservoir and collector temperatures. As mentioned in the following discussion, a shift in the cesium reservoir thermocouples occurred during the shutdown after the 2615-hour point. Therefore the indicated cesium reservoir temperatures shown for subsequent points are somewhat higher. However, no significant difference is believed to exist in the actual cesium reservoir temperature for any of the points shown in Figure 3 at less than 5000 hours. At about the 6150-hour point, one of the cesium reservoir thermocouples failed completely. For the last two points (7000 and 7890) it was impossible to get the cesium reservoir temperature lower than those values shown in Figure 3. Despite these difficulties, remarkably close agreement was observed over a wide range of the I-V curve throughout the 8125 hours of testing. A summary of the operating characteristics of the converter over its test history is shown in Table 2.

A Out-of-Pile Test Period. The converter was operating out-of-pile for approximately 100 hours at a variety of test conditions. Over 90 percent of the operating time was at output power levels above 8 w/cm^2 (electrode power density). In Table 3, a typical operating point during these tests is described. No evidence of performance degradation was observed between the beginning and end of the test period. In addition to steady-state operating data, parametric sweep data were obtained as shown in Figure 4.

Heat transfer measurements were made on the cesium reservoir straps and the heat choke fins. The thermal resistance of the straps was determined by measuring the cesium reservoir temperature as a function of power input to the cesium reservoir heater. Since gamma heating of the reservoir and the straps occurs during in-pile operation, this resistance was critical to the achievement of reservoir temperature control in-pile. Since the heat choke fins represent a fixed thermal

resistance through which the heat rejected from the collector must flow, the temperature drop across the fins can be used as a thermal power indicator. Therefore, the relationship between power input and this temperature difference was determined for SD-4 during the out-of-pile tests. These data provided input and efficiency measurements during in-pile operation.

B. Initial In-Pile Test Period. During the first 25 hours of operation, the performance of the diode was steady and closely duplicated the performance observed in the 100 hour out-of-pile test. At periodic intervals during the in-pile test, diode current-voltage characteristics were determined by sweeping around the static operating point. In Figure 4 an in-pile I-V characteristic taken during this period is compared to one of the out-of-pile characteristics. The out-of-pile I-V curve corresponds to a measured cesium reservoir temperature of 290°C , a measured collector temperature of 670°C , and an estimated emitter temperature of 1575°C . The in-pile points (circles) correspond to a measured cesium reservoir temperature of $290^{\circ}\text{C} - 305^{\circ}\text{C}$, a measured collector temperature of 682°C , and an estimated emitter temperature of 1575°C . The two measured cesium reservoir temperatures correspond to two different thermocouples attached to the cesium reservoir. The difference between the readings is attributed to the method of thermocouple attachment. In Table 4, the performance is described in more detail and compared to two subsequent operating periods. The excellent agreement between the in-pile and out-of-pile I-V characteristics strongly reinforces the validity of the emitter temperature estimates. The agreement also indicates that the in-pile performance of diode SD-4 was virtually identical to its out-of-pile performance.

C. Third Period. After the first 25 hours of steady operation, a drop-off in power output was observed at a fixed reactor power level. The reduction in power output was accompanied by a corresponding reduction in

optimum cesium reservoir and collector temperatures and by a shift of the diode ignition voltage to lower levels. The emitter temperature was obviously going down. The reduction in emitter temperature continued for about 75 hours and then started to recover. After 300 hours of in-pile operation the diode output had recovered to within about 85% of its initial level. After 600 hours, the recovery in emitter temperature and output was essentially complete.

It is apparent that some heat loss mechanism existed during this period which prevented the emitter from receiving its "normal" fraction of the heat generated in the fuel. The "normal" fraction is defined here as that fraction which it received prior to and after the reduced emitter temperature test period. This normal fraction is about 98%, the 2% loss being caused by thermal radiation out of the cavity. Of course, of the heat reaching the emitter, a significant fraction is conducted and radiated from the emitter support sleeve. One possible mechanism for the additional heat loss could have been conduction from the fueled-emitter and its support sleeve through gases present in the cavity. Although accurate analytical predictions of such heat losses in the cavity would be extremely complicated, approximate calculations indicate that heat losses of a few hundred watts might occur if air or nitrogen were present at tens of millimeters of pressure.

A likely source of gas could have been outgassing of the nickel plug which was used to close the gun cavity after out-of-pile operation was completed. Since the nickel closure plug was not exposed to the diode interior, it was not thoroughly outgassed at a temperature above its expected operating level. When the diode began operation in-pile, gamma heating plus conduction from the emitter sleeve raised the temperature of the nickel to an estimated 800°C. Extensive outgassing undoubtedly occurred, causing the pressure in the sealed cavity to rise substantially. This gas could have been eventually removed from the cavity by the

"gettering" action of the emitter support ring which is made of well-outgassed molybdenum. Removal of the gas could have corresponded to the recovery in emitter temperature.

The gas might have been due to another source, communication between the cavity and the environment surrounding the diode. If a leak developed in the closure plug weld or in one of its brazes, gas could have entered the cavity from the capsule tube region. This possibility is enhanced by the fact that the pressure in the tube increased rapidly at the beginning of the in-pile operation and recovered rapidly after about 300 hours of operation. The initial surge in pressure was due to outgassing of the sheathed heater leads and other components in the tube and the recovery in pressure resulted from the pumping action of the zirconium getter located at the bottom of the tube. The pressure gauge in the tube had a full scale reading of 25 microns. Within 25 hours, the needle on the pressure gauge went off-scale and did not come back on-scale until the 300 hour point. The close correspondence of this pressure transient with the emitter temperature transient suggests that they may have been related.

Regardless of the cause there is no doubt that the temporary reduction in output power was due to a reduction in emitter temperature. If the diode had undergone degradation of emitter surface properties, the optimum cesium temperature would have increased rather than decreased. Furthermore, the complete recovery of the output and all other diode temperature parameters essentially eliminates any effect other than a transient emitter heat loss. As additional confirmation, a test was performed during this period to show that the full output could be recovered by increasing the emitter temperature. This was accomplished by operating at a static point corresponding to terminal output voltage of 0.8 volt instead of 0.7 volt. The I-V sweep curves obtained at each condition are shown in Figure 5. The difference in the

average current between the sweep curves is 18 amps which corresponds to a difference in electron cooling of about 50 watts. Based on out-of-pile parametric results, this 50 watt difference corresponds to a difference in emitter temperature of about 35°C. The electrode power density for curve "A" at a terminal output voltage of 0.7 is 7.9 w/cm² instead of 7.0 w/cm² for curve "B". The 7.9 w/cm² is equal to the power density obtained under static conditions prior to and after the emitter temperature transient. Thus, by increasing the emitter temperature by 35°C, full output power density was recovered.

D. Fourth Period. As mentioned previously, the diode output had completely recovered by about the 600-hour point. The power input and power output remained essentially constant for about the next 200 hours. At the 760-hour point, the reactor power level was reduced to accommodate another experiment in the reactor. This reduced reactor power level was maintained until the 1400-hour point when the other experiment was withdrawn from the reactor. The reduced reactor power resulted in a reduction in diode input power of about 30 watts and a corresponding reduction in diode output power of about 9 watts. The diode output power density at the electrodes averaged about 7.3 w/cm² during this period.

E. Fifth Period. After the reactor power was restored to its normal level, a constant power test period of over 1200 hours was accomplished. The average electrode power density during this time was about 8 w/cm² and the overall efficiency varied from about 13.5% to 14%. The diode characteristics remained very constant except for a slight improvement in overall efficiency with increasing time. At the 2615 hour test point the diode was removed from the reactor to permit modifications to be made to the reactor.

At about the 1700 and the 2600 hour points, experiments were performed to examine the diode characteristics very carefully for traces of degradation. At each point, the cesium reservoir temperature, the collector temperature, and the power input were set at the same levels

as existed at the 25-hour point. Both static and sweep data were taken at each point. The results of the static experiments are summarized in Table 4. The reproducibility of the three points is quite remarkable, the only noticeable change being a slight improvement in overall efficiency. Since there is some uncertainty in the determination of input power, this improvement is probably not significant.

F. Sixth Period. When the reactor was re-started at the 2615-hour point after the three month shutdown, the diode returned to its former performance level. Since the reactor fuel elements had been re-shuffled, some uncertainties existed in neutron and gamma flux levels and distributions. A period of several days was required to re-establish equilibrium. After stable operation was restored, at about the 2800-hour point the diode output and input were slightly higher. The only significant change in conditions was a 12°C increase in the optimum indicated cesium reservoir temperature. Since the cesium reservoir thermocouples are only mechanically attached, their position could have been shifted by handling of the capsule during the reactor modifications. Consequently, it is not certain that a 12°C change in actual cesium reservoir temperature did occur. As is evident in Figure 3, the collector temperature also increased by about 20°C . In Figure 4, the data points taken from sweep measurements at 3110 hours and 4300 hours are shown with previous results. The striking reproducibility of all the data points strongly suggests that no significant changes in diode operating conditions or performance have occurred. This stable operation continued until the cesium reservoir heater failed at the 6100-hour point.

G. Seventh Period. After remote attempts to repair the cesium reservoir heater were unsuccessful, the water coolant surrounding the collector was replaced with Dowtherm "A," an organic liquid capable of higher operating temperatures. Since the cesium reservoir is connected to the cooling jacket through two copper straps, the increased temperature of

the cooling jacket resulted in higher cesium reservoir temperatures. Control of the cesium reservoir temperature was achieved by varying the flow rate and inlet temperature of the Dowtherm. Operation of the diode for the seventh test period was resumed using this control technique, which proved quite adequate. However, during startup and early operation of the seventh period, the collector thermocouples indicated absurdly low temperatures. After about twenty hours, the indicated temperatures increased but still were about 60°C lower than the previous data. Since the reactor power level and core position were unchanged, it is assumed that the difference was caused by movement of the thermocouples within the test capsule. This movement could have been caused by the higher pressures within the coolant tubes, resulting from the higher pressure drops necessary with Dowtherm as compared with water. Since the input power measurements are based upon the measured temperature differences between the collector and the coolant jacket, no input power or efficiency estimates were made beyond the 6103-hour point.

During the first few hundred hours of the seventh test period, an increase was noted in the thermal impedance between the coolant and the cesium reservoir. To offset this increase the Dowtherm flow rate was increased, thus lowering the coolant jacket temperature, and thereby the cesium reservoir temperature. At about the 6360-hour point, the impedance had increased enough to permit water to be used instead of Dowtherm as the coolant. Accordingly, the Dowtherm was flushed out of the lines and replaced by water, and operation was continued until the 7327-hour point. During the last few hundred hours, the pressure drop in the water coolant system increased appreciably. Eventually, the pressure drop caused too great a reduction in flow rate to permit safe operation. Therefore, testing was stopped to examine the condition of the coolant lines and system. A carbon-type scale was found in the

water coolant, which was causing clogging of the flow passages. Apparently, this scale was created by radiation damage to the residual Dowtherm left in the system after it was flushed with water. Several attempts were made to remove this scale. Reverse flushing with water and soaking and flushing with acetone were performed alternately for several weeks. Finally enough scale was removed to allow the original flow rate to be restored, and operation of the converter was resumed. Except for the problems with the flow rate and the collector thermocouples, the performance of the diode was quite stable throughout the seventh test period. The electrode power density averaged about 8 watts/cm^2 , with fluctuations of $\pm 1 \text{ watt/cm}^2$. These fluctuations were caused by day-to-day changes in reactor power level and in cesium reservoir temperature.

H. Eighth Test Period. The eighth and final test period ran from the 7327-hour point to the 8125-hour point. Dowtherm was used initially as the coolant, and control of cesium pressure was achieved by varying the Dowtherm flow rate. As before, fouling of the coolant jacket surface gradually occurred due to decomposition of the Dowtherm. Eventually this fouling caused a very high pressure drop and consequent reduction in flow rate. At about the 7890-hour point the Dowtherm was replaced by water to reduce the coolant jacket temperature, and thereby the cesium reservoir temperature. This permitted an additional 235 hours of testing before the clogging became too great to keep the cesium reservoir temperature down to acceptable levels. After further attempts to unclog the coolant passages were unsuccessful, the diode was removed from the reactor for hot cell examination. As can be seen in Figure 3, the performance of the diode was normal throughout this test period. During the last 65 hours the clogging caused the cesium temperature to be well above its normal level and therefore caused a slight reduction ($\sim 15\%$) in the converter output. However, the reduction was about that expected for such off-optimum cesium reservoir conditions.

ACKNOWLEDGMENTS

Many people from Thermo Electron and BMI contributed to this experiment. The authors would like to acknowledge in particular the efforts of Jack Kalajian, Victor Poirier, Frank Campagna, and Harold Hardister of Thermo Electron, who performed the detailed design and fabrication of the diode and the in-pile capsule. The major contributors from BMI include E. Speidel, W. Carbienier, and J. Allgeier.

TABLE 1
SUMMARY OF SD-4 DESIGN PARAMETERS

Fuel Form:	
Type	Cermet
Fuel	UO ₂
Diluent	W
Loading, vol. % UO ₂	80
Density, %	95
Geometry	Annular
Thickness, inches	0.080
Inner Clad	W
Emitter:	
Material	Rhenium
Thickness, inches	0.018
Surface Condition	Treated
Diameter, inches	0.500
Length, inches	1.500
Area, cm ²	15
Diode Structure:	
Insulator	Al ₂ O ₃
Flanges	Nb
Collector	Nb (Mo coated)
Cesium Reservoir	Ni
Emitter support	Mo
Exterior Environment	Vacuum (~10 microns)

TABLE 2
SUMMARY OF SD-4 OPERATING CHARACTERISTICS

Out-of-Pile:	
Test Time, hours	100
Average Electrode Power Density W/cm ²	8.0
Average Overall Efficiency, * %	13.1
Average Estimated Emitter Temperature, °C	1600
Diode Characteristics	Stable
In-Pile:	
Test Time, hours	8125
Average Electrode Power Density, W/cm ²	7.8
Average Overall Efficiency, † %	13.7
Average Estimated Emitter Temperature, °C	1575
Diode Characteristics	Stable
Fuel Characteristics	
Power Density, W/cm ³	324
Equivalent Lifetime of Solid 0.9" Fuel Rod, hours	26,700
Average Burnup, fission/cm ³	3.1 × 10 ²⁰
Maximum Burnup, fission/cm ³	7.3 × 10 ²⁰
Average Burnup, U ²³⁵ atom %	1.7
Maximum Burnup, U ²³⁵ atom %	4.0
Total Number of Cycles	~80

* Power output at the terminals divided by total electrical power input (bombardment plus filament power).

† Power output at the electrodes divided by the total nuclear power input to the emitter as estimated by calorimetry.

TABLE 3
TYPICAL OPERATING CONDITIONS FOR SD-4
DURING OUT-OF-PILE TESTS

Total Operating Time (hours)	100
Filament Power, watts	141
Bombardment Power, watts	705
Total Power Input, watts	846
Estimated Average Emitter Temperature, °C	1600
Average Collector Temperature, °C	650
Cesium Reservoir Temperature, °C	298
Output Current, amps	168
Voltage Drop in Emitter Lead, volts	0.101
Output Voltage (At Diode Output Terminals), volts	0.680
Output Power (At Diode Output Terminals), watts	114
Output Power Density (At Diode Output Terminals), watts/cm ²	7.60
Output Power Density (At Diode Electrodes), watts/cm ²	8.75
Overall Efficiency (Electrical Power at Terminals with no Heater Cavity Correction), %	13.5
Net Efficiency (Electrical Power at Terminals with a 60-watt Heater Cavity Correction), %	14.5
Net Design Efficiency (Electrical Power at Electrodes with a 70-watt Heater Cavity Correction), %	16.7

TABLE 4
SUMMARY OF SD-4 REPRODUCIBILITY TESTS

Accumulated In-Pile Test Time, hours	25	1711	2614
Reactor Power Level, megawatts	2.0	2.0	2.0
Estimated Average Emitter Temperature, °C	1575	1575	1575
Average Collector Temperature, °C	680	685	682
Average Cesium Reservoir Temperature, °C*	298	299	298
Output Current, amps	150	148	149
Voltage Drop in Emitter Lead, volts	0.09	0.09	0.09
Output Voltage (At Diode Output Terminals), volts	0.70	0.70	0.70
Output Power Density (At Diode Output Terminals), w/cm ²	7.00	6.92	6.96
Output Power Density (At Diode Electrodes), w/cm ²	7.90	7.80	7.85
Estimated Input Power, watts	780	770	760
Overall Efficiency, †, %	13.4	13.4	13.7

* This temperature is the average of the two thermocouples on the cesium reservoir.

† Power output at the terminals divided by the total nuclear heat generated in the fuel.

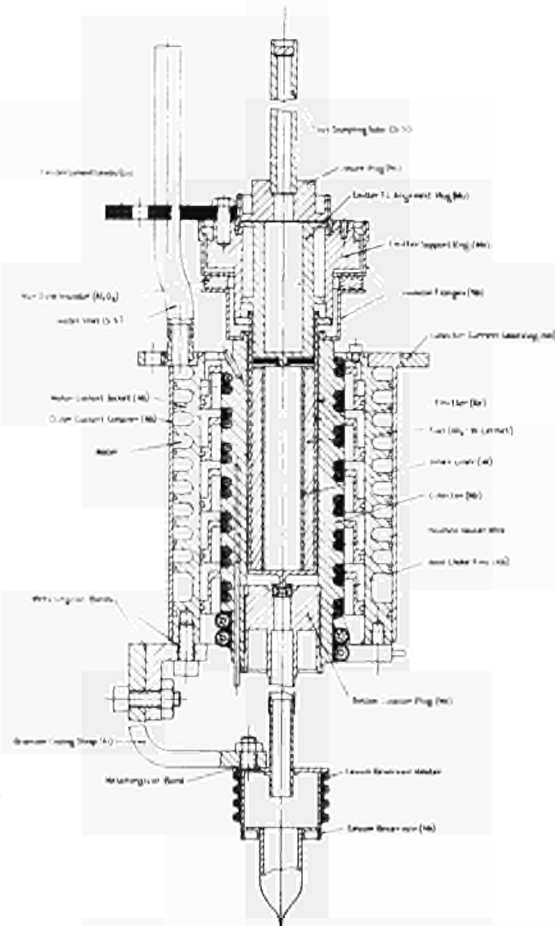


Figure 1. Design of Converter SD-4

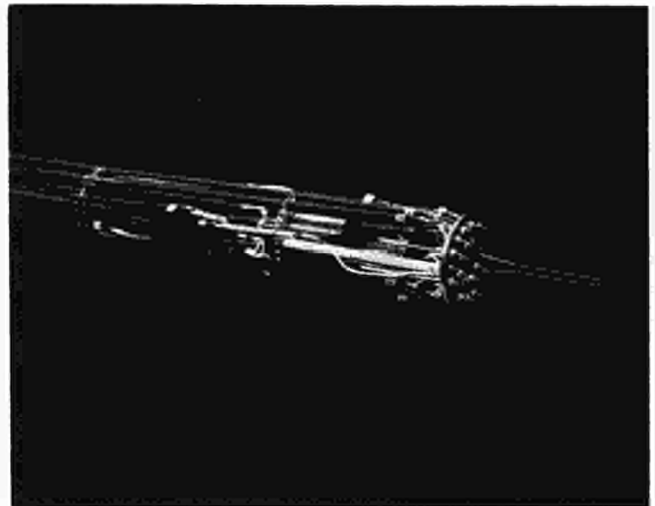


Figure 2. In-Pile Assembly

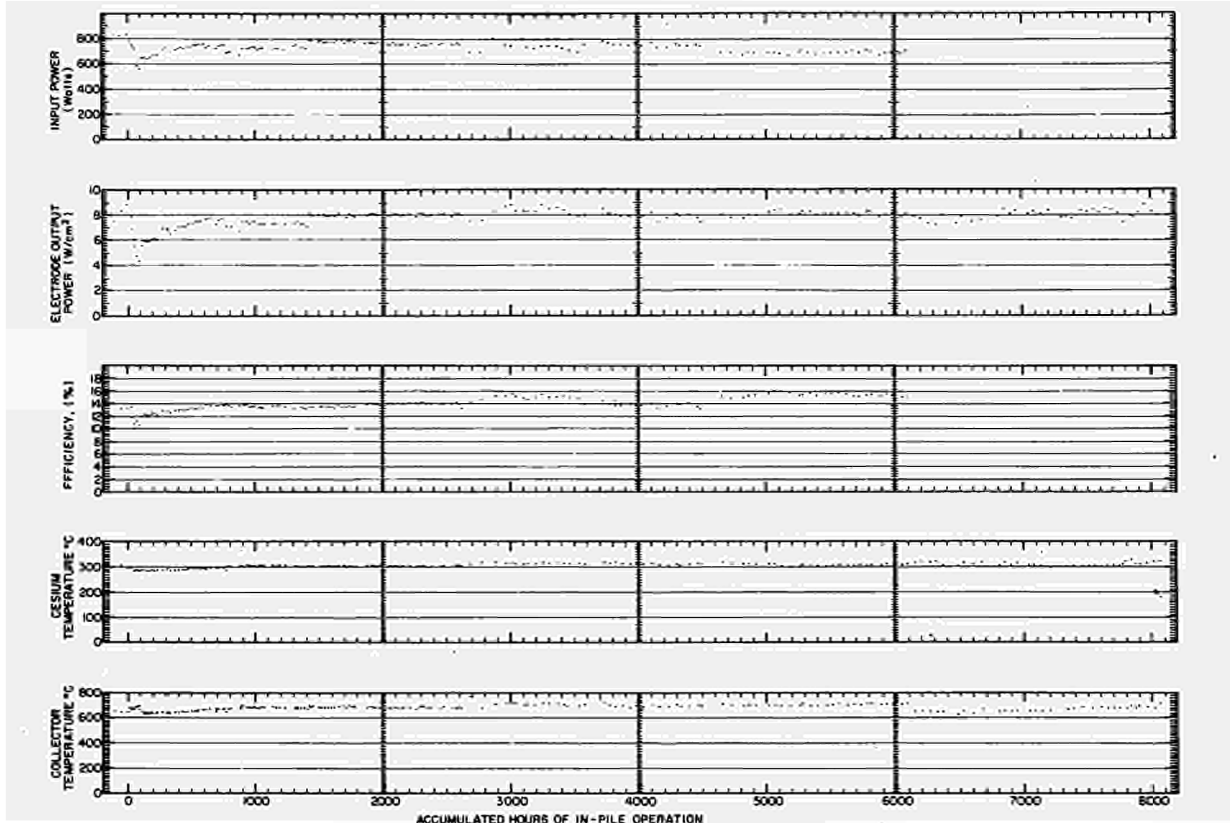


Figure 3. Performance Summary

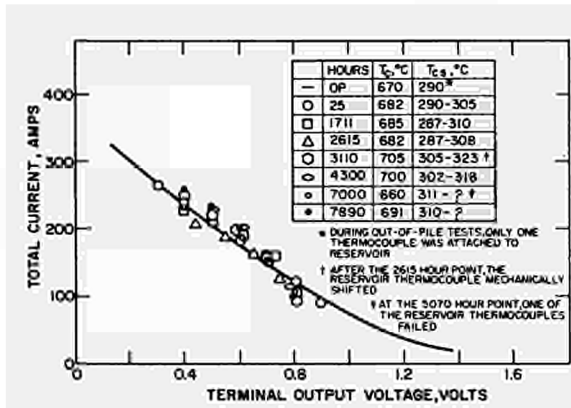


Figure 4. Comparison of I-V Sweep Data at Controlled Reference Points during Out-of-Pile and In-Pile Operation

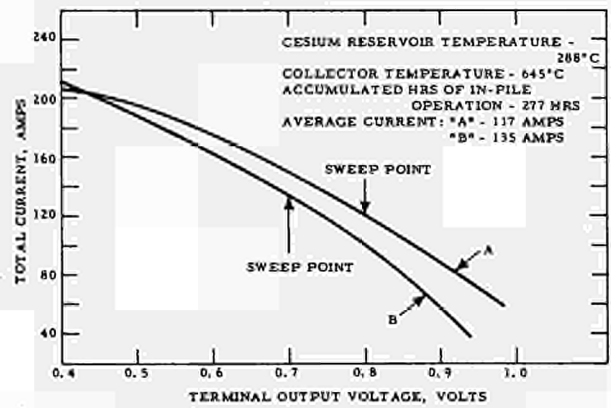
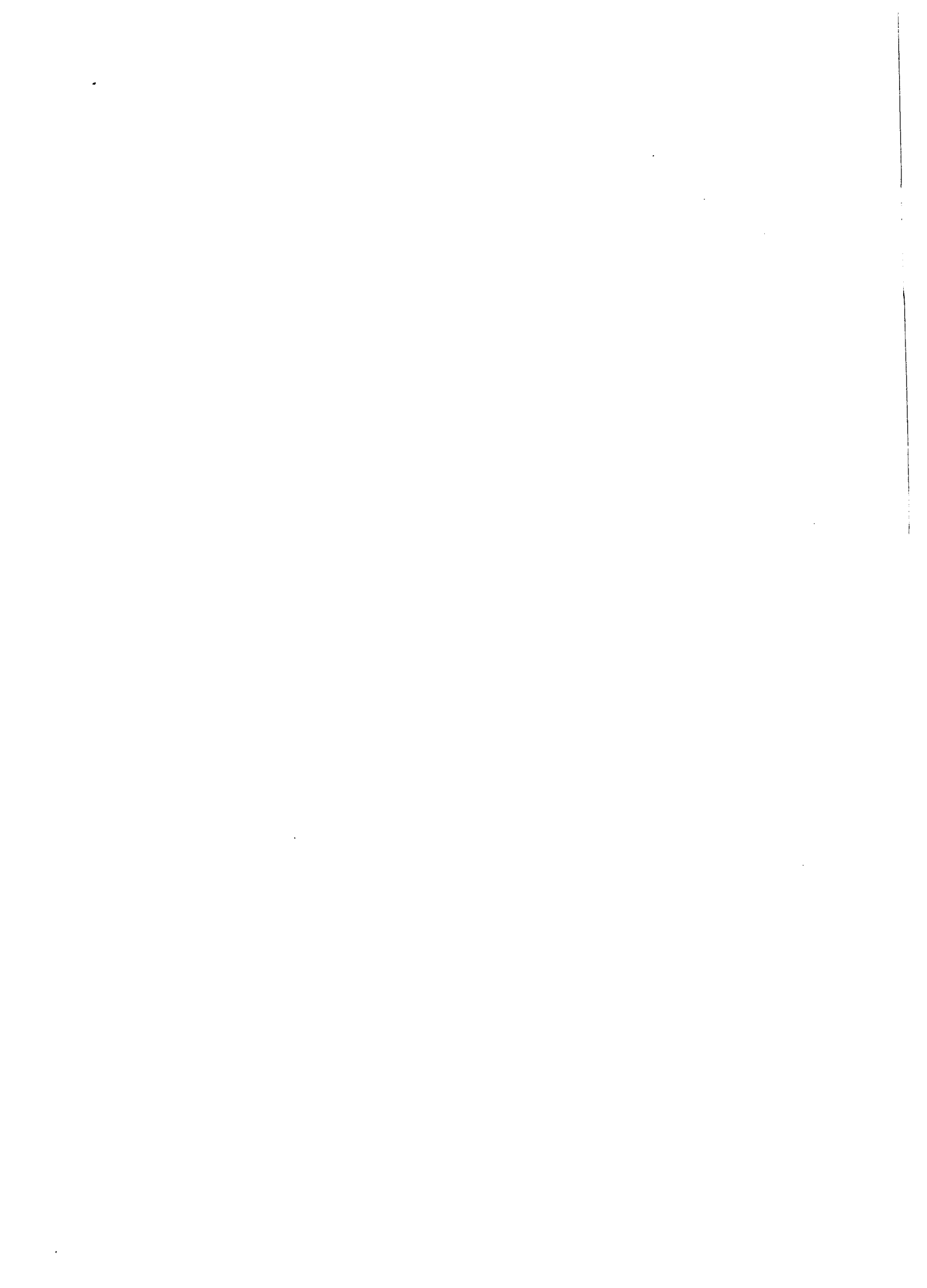


Figure 5. I-V Sweep Data During Emitter Temperature Transient



DISCUSSION

Speaker of paper C-2: R. C. HOWARD.

GUSKOV (USSR):

Were there pronounced temperature changes, thermal shocks, of the cathode during the experiments?

HOWARD (USA):

I believe there were about 80 sudden thermal shocks in which the reactor power was lost instantaneously. We never went up in power suddenly but we came down many times suddenly.

SCHOCK (USA):

Was the reactor neutron flux and hence the thermal power constant during the test?

HOWARD:

There were 5% fluctuations.

SCHOCK:

Was the position of the test specimen within the reactor always the same?

HOWARD:

Yes.

DEVIN (France):

We notice also quite generally a slow increase in efficiency during say the first 1000 hours of experience and we attribute this to the fact that some recrystallization occurs at the emitter surface and that this recrystallization leads to the increasing of the high work function grains. Thus the average work function of the emitters becomes higher. We generally notice also that we have to reduce the cesium pressure during the test, to keep the optimum performance.

HOWARD:

In this case at least for the first 5000 hours we did not see any general increase of efficiency. If any increase occurred it was very small.

DEVIN:

On slide 4 which contains the I-V data, are the data marks for steady state conditions? Is the IV curve for AC or steady state conditions?

HOWARD:

The curve is AC. The point that we were sweeping about was such that we

could sweep and then switch to the steady state. We did not sweep very wide as you noticed. There is very small difference in emitter temperature between the sweep and steady state points.

PEEHS (Germany):

Have you found some swelling effect after irradiation?

HOWARD:

Our results are not complete. We did the neutron-radiographs of the device before we removed the emitter and it looked like that there was a very small distortion of the emitter, not enough of course to cause a short. It was difficult to measure this distortion but it might have been a few mils. Of course you do not know whether to attribute that to fission gas pressure or just the fact that it is a cermet. Many cycles on a cermet generally cause some distortion. In fact with this number of cycles we would have expected much more serious distortion than we observed.

PEEHS:

Have you perhaps made a theoretical consideration of the swelling effect?

HOWARD:

Others have. Mr. RANKEN may discuss that when he gives his paper.

HARBAUGH (USA):

Was the cermet fuel outgassed at high temperatures prior to insertion into the converter?

HOWARD:

The fuel and the emitter were made at the same time by hot isostatic pressure bonding.

LONG TERM OPERATIONS OF IN-PILE AND OUT-OF-PILE THERMIONIC CONVERTERS*

by

J.W. Holland, M.K. Yates, D.E. Schwarzer and J. Kay

Gulf General Atomic Inc.
P.O. Box 608, San Diego, California 92112 (USA)ABSTRACT

Ten cylindrical geometry converters with series designation Mark VI have been life tested in-pile for a total of 20,034 hours, an average life of 2003 hours, and an average electrode power density of 7.2 W/cm². The longest test to date ran for 5369 hours at an average electrode power density of 10 W/cm². That test designated as IC-15 was fueled with UO₂ and achieved a burnup of 2×10^{20} fission/cm³.

Out-of-pile models of the Mark VI converters were life tested for a total of 51,542 hours, an average life of 6443 hours and an average power density of 7.9 W/cm². The longest test to date ran 10,406 hours at an average electrode power density of 8.6 W/cm². Both unfueled and fueled versions were tested.

* Part I is sponsored by the U. S. Atomic Energy Commission under Contract No. AT(04-3)-167, Project Agreement 14, and Part II is sponsored by the National Aeronautics and Space Administration under Contract No. NAS 3-8504.

PART 1

LIFE TESTS OF FISSION HEATED THERMIONIC CONVERTERS

INTRODUCTION

Development of fission heated cylindrical geometry thermionic converters, designated as the Mark VI series, has been in progress at Gulf General Atomic Incorporated since 1962. The first converters tested served to eliminate gross defects from the converter design and test apparatus. The first long term test was conducted in 1964 when 1006 hours were achieved on a 90UC-10ZrC fueled converter, designated as Mark VI IC-6. Including that test, a total of ten Mark VI IC-series converters have been life tested to date for a total operating time of 20034 hours. Nine of the ten converters were fueled with 90UC-10ZrC; one converter was fueled with UO₂. Because significant differences were observed between converters using the two types of fuel the test results will be presented according to fuel type.

CONVERTER DESIGN AND PARAMETERS

The configuration of the Mark VI in-pile converter is shown in Fig. 1. Significant design and material features are:

Fuel--UO ₂ or 90UC-10ZrC, 93% U ²³⁵	Collector material--wrought molybdenum
Emitter material--CVD (WF ₆) tungsten	Interelectrode spacing--0.020 cm hot
Emitter area--13 cm ²	Insulator seal--Litton design, Lucalox-Nb
Emitter diameter--1.64 cm	Cesium reservoir--2 grams liquid
Fuel clad thickness--0.1 cm	Fission product retention volume--20 cm ³

These converters were tested either in the Gulf General Atomic TRIGA or the General Electric Test Reactor. Waste heat from the conversion process was dissipated by way of gas gaps to reactor cooling water. Temperatures of the cesium reservoir and collector were adjustable by means of electrical heaters. Instrumentation included: chromel/alumel thermocouples for measuring cesium reservoir, collector and converter body temperature profiles; W/Re thermocouples located between the emitter wall and the fuel to measure

changes in the emitter temperature; voltage probes for measuring converter and electrode potentials; and a shunt for measuring the cell current.

Several parameters were calculated from the measured data. Changes in emitter temperature and values of relative power, P_r , and efficiency, η_r , were computed by means of a correlation that related changes in cell voltage to differences in plasma losses arising from cesium pressure changes required to maintain maximum cell voltage.¹ The relative power is defined as the fraction of the output that can still be produced at the initial operating conditions except for the cesium reservoir temperature which was optimized. The relative efficiency is defined similarly. Methods for calculating these parameters are described in Ref. 1. The initial emitter temperature was estimated by performance comparison with similar converters in which the emitter temperatures were accurately determined. Changes in emitter temperature were computed using the same correlation. The thermocouples in the fuel cavity were used only as a rough guide to the emitter temperature since they read as much as 200°C higher than the emitter temperature.

Deviations in the relative power from unity are interpreted to be caused by work function changes, alterations in the interelectrode gap or in the scattering of electrons by a foreign gas. Deviations in the relative efficiency from unity arise from the combined effects of changes in the relative power and changes in thermal transport such as would result from an electrode emittance change or from a change in electron waste heat. For these converters the external environment was an inert gas, either helium or argon, so that inleakage of these gases would also contribute to the thermal transport if such were to occur. Inleakage of fission gas from the fuel chamber into the converter is another possibility.

IN-PILE TEST SUMMARIES

A summary of the in-pile tests is presented in Table 1. Listed are the test designation, fuel and electrode materials, test durations, average electrode power density and emitter temperature, final relative power and efficiency, test termination date, burnup, and failure mode. Several

generalizations on this table are apparent. First, the highest average performance of 10 W/cm², and longest operation, 5369 hours, were obtained from the UO₂ fueled IC-15 converter. Also, the final power and efficiency relative to initial values were somewhat greater than unity. For the carbide fueled converters the average output powers were generally lower, ranging between 4 to 7 W/cm². The final relative power and efficiency were sometimes substantially below unity, and ranged down to as low as 0.45 in one case.

In all but three cells, IC-11, IC-12, and IC-15, the failure mode was related to envelope leaks which allowed inleakage of gas into the converter interior. Test IC-11 was terminated by contractual commitment and IC-12 and IC-15 by interelectrode shorting. The location of leaks in the envelope were not found in hot cell examinations, but from examination of similar out-of-pile converters the most probable locations were in the seal or in joints between dissimilar converter components. The IC-15 interelectrode short was found to have been caused by breakage of a getter ring during movement of the cell. The short found in IC-12 was related to a change in the emitter geometry due to a fuel interaction.

PERFORMANCE TREND IN UO₂ FUELED CONVERTER

The trends in relative power and efficiency of the UO₂ fueled Mark VI converter test IC-15 are shown in Fig. 2. The relative power factor varied between 1.00 and 1.10 over the 5369 hours of operation. The relative efficiency factor varied between 0.9 and 1.10. An upward trend in both the factors indicates the cell performance was improving. The reason for the improvement is attributed to the diffusion of oxygen through the fuel cladding. Experimentation has demonstrated that the bare emitter work function increases at emitter temperatures below 1800°C when oxide fuels are in contact with the inside wall of the emitter. The upward trend in the IC-15 performance was accompanied by a slight decrease in emitter temperature which is thought to have been responsible for the increase in performance.

PERFORMANCE TRENDS IN 90UC-10ZrC FUELED CONVERTERS

Relative power and relative efficiency factors are shown in Fig. 3 for IC-6 through IC-14, all fueled with 90UC-10ZrC. In examining these trends, several conclusions are reached. First, in the longest tests the relative powers were typically on the order of 80% by 2500 hours; and, second, there were additional thermal losses amounting to 10 to 25% as evidenced by the differences between the P_r and η_r factors. In the two cases of IC-10 and IC-13, P_r dropped below 80%, but these decreases were expected since they were accompanied by decreases in emitter temperature. This effect is discussed below.

A decrease in P_r by 15% was indicated in the carbide fueled emitter out-of-pile tests (Part II) so that there appears to be little added effect by the nuclear environment on the relative power.

The observed changes in relative power are interpreted to be the result of work function changes due to the diffusion of uranium to the emitter surface. Experiments investigating the effects of uranium (from non-stoichiometric UC-ZrC fueled emitters) on work function and thermionic performance have been conducted which showed that accumulation of uranium on the emitter surface lowered the emitter work function from 4.6 eV at 1800° C to as low as 3.5 eV at 1500° C. Decreases in emitter work functions yield significant decreases in performance. A decrease in emitter work function by 0.1 eV was found to have resulted in a 10% loss of output power. The cause for uranium diffusion to the emitter surface was attributed to the substoichiometric carbon content of the fuel.

The decrease in the relative efficiency appears to be significantly higher in-pile than out-of-pile. The cause for the higher thermal losses is not certain, but some insight is obtained in comparing the 2500 hour IC-11 test to the 3300 hour IC-12 test. In doing so, one observes an almost identical correspondence between the two results--that the relative efficiencies stabilized at the same values at about 2500 hours. This seems to rule out erratic phenomena such as inleakage of the helium containment gas into the

converters as the cause for the rather large decrease in efficiency. About half the effect could be explained if the emissivity of the collector changed from 0.15 to 0.8. Such an emissivity change could have been related to tarnishing of the collector surface by active gases or from the accumulation on the collector of fuel material or fission products. It is unlikely that enough fuel material could have collected on the emitter at its operating temperature to affect its emissivity. Surface roughening of the emitter could be a minor factor. Inleakage of fission gases from the fuel chamber on the other hand cannot in theory be eliminated as a causative factor since there is enough xenon buildup in the fuel chamber to give the observed results. Part of the added thermal loss may have been due to increased electron waste heat caused by an increase in effective collector work function or by an increase in kinetic energy of electrons entering the collector surface. It is estimated that such effects would have probably constituted less than 5% change in η_r .

CONCLUSIONS

The primary conclusion from these tests is that the oxide fueled converter presently represents the highest state of development as exhibited by its superior performance, stability and life. We speculate that the carbide fueled tests all suffered from a common difficulty of having employed a fuel substoichiometric in carbon. Future tests of carbide fueled converters with increased carbon content will determine the usefulness of the carbide fuel in its upgraded form.

As shown in Fig. 4, progress is being made in increasing the longevity of the tests. The increased longevity has been due to the combined efforts of improving the technology of fabricating converters, and the test environment. Our present goal of 10,000 hours of reproducible operation seems to be within reach in the next few years.

PART II

LIFE TESTS OF ELECTRICALLY HEATED THERMIONIC CONVERTERS

INTRODUCTION

As a companion effort to the in-pile program, development of an out-of-pile electrically heated Mark VI converter was undertaken for the purposes of determining: 1) the life and failure modes of the cells under high vacuum and outside of the nuclear environment, 2) the effects of fuel diffusion on the thermionic performance without the complications of fission products, 3) performance reproducibility, and, 4) effects of electrode material selection. To study the effects of fuel diffusion, slabs of fuel materials were imbedded within the emitter walls. Emitter thermocouples were also employed in the emitter walls to obtain accurate measurements of emitter temperature and hence direct determinations of the relative power. Since the input power was easily determinable, the relative efficiency was also directly derivable. Effect of electrode material selection on converter performance was studied in several converters by varying the crystal orientation of the tungsten emitter and by replacing the previously used molybdenum collectors with niobium.

To date eight of these life converters (LC-series) have been tested for a total time of 51,542 hours, an average life of 6443 hours, and an average power density of 7.9 W/cm². One converter is presently under test with 9353 hours of stable performance accumulated.

This part of the paper is organized according to the following subjects: Converter Design and Parameters; Test Summaries; Performance Reproducibility; Effect of Electrode Materials on Performance; Performance Trends; and Conclusions.

CONVERTER DESIGN AND PARAMETERS

The configuration of the Mark VI LC-series converter is shown in Fig. 5. It may be noted that the working part of the electrode configuration is essentially identical to the in-pile Mark VI. The main differences in

instrumentation were the inclusion of W/Re thermocouples in the emitter wall for a direct measurement of emitter temperature and the ability to directly measure the input power. When fuel slabs were contained within the emitter wall, they covered 53% of the surface area and were located at 0.1 cm from the emitter surface, the same clad thickness as used for the in-pile cells.

The converters were operated in ion pumped bell jars. Power to the emitter was supplied by means of electron bombardment. Collector and cesium reservoir heat sinks were fit onto the outside diameter of the collector structure and cesium reservoir and were either water or air cooled. Electrical heaters were used for automatic control of the collector and cesium reservoir. Both the cell and electrode potentials were measured as well as the cell current. For some of the converters, emitter and collector work functions were routinely measured to correlate work function alterations to changes in performance.

TEST SUMMARIES

A summary of the out-of-pile tests is presented in Table 2. Listed are the test designations, electrode and fuel materials, test durations, average electrode power density and emitter temperature, final relative converters contained W-60 v/o UO₂ cermets; three converters contained UC-ZrC in various molar percentages of 30-70, 50-50 and 90-10; one converter was unfueled. These converters all employed emitters fabricated by means of hydrogen reduction of WF₆ and used molybdenum collectors. The unfueled converters, LC-7 and LC-9 used different combinations of electrode materials.

With respect to performance the converters, with one exception, produced average output powers between 6.8 and 8.8 W/cm². That one exception was LC-6 which will be discussed in greater detail below. Conclusions regarding the final relative power and efficiency are made when the performance trends are discussed below.

The distribution of failure modes among the seven converters failed to date has been one short circuit and seven envelope leaks. One converter, LC-3, actually failed by envelope leak plus an interelectrode short caused by a

broken getter ring. The envelope leaks were generally located at the junction of two dissimilar converter components. Usually, the leaks were either in the final braze or the insulator seal.

PERFORMANCE REPRODUCIBILITY

Among the cells, six have used tungsten emitters, made by the hydrogen reduction of WF₆, and polycrystalline molybdenum collectors spaced at .008 in. from the emitter. The initial maximum power densities of these six cells are compared with each other to examine the degree of performance reproducibility achieved in these cells. For a comparator an earlier cell designated as OC-5² is used because it was performance mapped over a wide range of operating conditions and corresponds well with the performance of cells with similar materials and spacing-produced in other laboratories.

The initial performances mentioned above are compared in the table below where the comparative factor is the initial maximum output power of the cell divided by the output of OC-5 at the same current density, emitter temperature, and collector temperature as used for the compared cell but at optimum cesium pressures. In examining the results there is found close

<u>Out-of-Pile Converter Designation</u>	<u>Fuel</u>	<u>Po Po (OC-5) T_E, T_C, J, T_{Ropt}</u>
LC-1	30UC-70ZrC	0.77
LC-2	W-60 v/o UO ₂ Cermet	0.97
LC-3	W-60 v/o UO ₂ Cermet	0.97
LC-4	None	0.84
LC-5	90UC-10ZrC	0.98
LC-6	50UC-50ZrC	0.66

comparisons between OC-5 and LC-2, LC-3, LC-5, certainly within experimental errors. Converters LC-1 and LC-6 both contained UC-ZrC fuel material. Their low relative initial outputs of 0.77 and 0.66, respectively, were attributed to fuel diffusion to the emitter surface during processing which lowered the emitter substrate work function. The low relative output of the unfueled cell LC-4 of 0.84 was attributed to gaseous contamination of the electrodes.

Except for the effects of gaseous and fuel contamination in the cells, the out-of-pile cells have demonstrated reproducible performance. The effect of electrode materials on converter performance is discussed in the next section.

EFFECT OF ELECTRODE MATERIALS ON PERFORMANCE

One of the purposes of testing different combinations of electrode materials and crystal orientations was to determine performance advantages that might be gained through selection of electrode materials. The converters selected for comparison of electrode materials are:

<u>Converter Designation</u>	<u>Emitter/ Preferred Orientation</u>	<u>Collector</u>
LC-7	W/{100}	Nb
LC-9	W/{110}	Nb
OC-5	W/{100}	Mo

The LC-9 emitter surface was made by the hydrogen reduction of WCl_6 . The orientation was determined to be a partial {110}; its vacuum work function was 4.78 eV. By comparison, latest reported values³ for the {110} orientation range around 5.0 to 5.4 eV. The performance advantage to using emitters with work functions greater than obtained for LC-9 is discussed in Ref. 4. Electrode work function measurements on LC-7 and LC-9 are also presented in Ref. 4.

By comparing the performances of LC-7 and LC-9, both with niobium collectors, the advantage was determined for a converter using a 4.78 eV work function tungsten emitter over a 4.55 eV work function tungsten emitter. By comparing OC-5 and LC-7, the performance advantage was found for a polycrystalline molybdenum collector over the use of a polycrystalline niobium collector.

Maximum electrode power densities of LC-7, LC-9 and OC-5 are compared in Fig. 6 as a function of current density at an 1800°C emitter temperature. The cesium reservoir and collector temperatures were optimized at every

point on these curves. The results show that the improved emitter work function by 0.23 eV in LC-9 yielded a significant performance increase over the LC-7 performance. At 12 A/cm² LC-9 produced 21% more power than LC-7. The advantage diminished at low currents, but at higher currents the advantage grew larger. The optimum current density is shown to be higher for the higher performance converter. Comparing the output of LC-7 to the extrapolated output of LC-9 at optimum current densities, the maximum performance advantage of LC-9 is estimated to be 25%.

The increase in output resulting from use of molybdenum over niobium for the collector is found by comparing the OC-5 and LC-7 curves. The comparison is a little lopsided in favor of the molybdenum collector because the OC-5 hot spacing was .008 in., or .001 in. smaller than the LC-7 hot gap. Using correlation data⁵ to correct for the difference in spacing, OC-5 at a .009 in. spacing would have produced about 8% less power to make the real performance advantage of OC-5 29% at 12 A/cm². Again the advantage diminishes at low currents and becomes larger at higher currents. At optimum current densities the difference is about 40%.

PERFORMANCE TRENDS IN OUT-OF-PILE LIFE TEST CONVERTERS

Trends for the power and efficiency of eight out-of-pile life test converters relative to their initial values are shown in Fig. 7. In all of these tests the relative power exhibited fair stability and remained within $\pm 15\%$ of the initial value over their test durations with two exceptions: 1) the unfueled LC-4 showed a temporary 40% increase in power during the first 600 hours that was interpreted as being due to oxygen contamination remaining from the fabrication process; and, 2) the 50UC-50ZrC fueled LC-6 showed a very low initial performance due to a uranium contaminated emitter.

In all of the tests with the exception of LC-1 the relative efficiency closely tracked the relative power which indicates there were no significant added thermal losses. In LC-1 the relative efficiency was found to be about 10% less on the average than the relative power except near the end of the test. In the postoperational examination of LC-1 a defect in the emitter structure was found that had allowed a direct introduction of the carbide

fuel into the gap. From the operating data the defect was determined to have occurred 242 hours after the start of the test. The large decrease in η_r between 5000 and 7174 hours was attributed to leakage of atmospheric contaminants into the converter through an envelope leak which occurred at the time of a shutdown for thermocouple calibration.

The scatter in the LC-2 and LC-3 values is attributed to changing of oxygen contamination on the emitter resulting from fluctuations in the emitter temperatures. The fluctuations were due to varying input powers, changing operating parameters and shutdowns. In a separate experiment the source of contamination was attributed to the oxide fuel. Part of the scatter in the LC-2 and LC-3 values was the result of uncertainties in the determinations of P_r and η_r due to varying operating conditions employed in the test.

In the LC-5 test the relative power gradually decreased to about 0.85 over the first 3000 hours and then remained constant thereafter. The cause of the decrease was related to an accumulation of uranium on the emitter surface to lower its work function and decrease output power. The relative efficiency appeared to track the relative power within 5% which is within experimental uncertainties and thus no significant added thermal losses are indicated.

The very large changes in the power and efficiency of LC-6 were related to uranium diffusion to the emitter surface from the 50UC-50ZrC fuel. The main reason LC-6 showed such large changes was that the emitter temperature was operated at about 1650° C. At that temperature the emitter work function is lowered to about 4 eV by uranium accumulation. The cell output was about the level expected from an emitter with a 4 eV work function. In vacuum work function measurements on the emitter after it had been removed from the converter, it was found that if the emitter had been operated at 1800° C, the output would have been closer to the output of OC-5.

The relative power and efficiency factors for unfueled LC-7 and LC-9 tests showed no change throughout their operation, indicating completely stable performances.

In Fig. 8 relative powers of LC-1, -2, -3, -4, and -5 are normalized to the OC-5 performance, for the purpose of comparing LC-1 through LC-5 on an equal basis. In this way, the fact that LC-1 and LC-4 began at lower power densities than the rest of the cells can be factored into the comparison. Test data on LC-1, LC-4, and LC-5 are presented as curves while the LC-3 data are presented as a band $\pm 16\%$ wide, because of fluctuations in the relative power due to varying operating conditions employed during its test. The LC-2 test data are omitted since they fall within the LC-3 band. Converter LC-5 began 2% below OC-5 and was operating at an output power of 16% below OC-5 at 5500 hours at the time of the cesium leak. Converters LC-1 and LC-4 began 23% and 16% below OC-5, respectively, and ended (prior to cesium leakage) at 25% and 23% below OC-5, respectively.

The most significant observation is that in all cases the upper limit of loss in power density in these LC-series converters appears to be 25% as long as the emitter temperature is maintained in the region of 1800°C . A similar result was shown for the in-pile tests where the upper limit on power loss was about 20%. The explanation of this power loss limit is that once the collector became contaminated, additional accumulation caused little effect, and the emitter operated at a high enough temperature that gross accumulation of fuel or contaminants did not occur. The fact that LC-1 electrodes were heavily contaminated with fuel tends to support the theory of a 25% limit on loss of P_r for the operating conditions used in these tests.

CONCLUSIONS

The main conclusions reached from these tests were:

- 1) High work function emitters yielded a significant performance advantage.
- 2) Converters with niobium collectors exhibited completed stable performance but inferior performance to the molybdenum collector.
- 3) Carbide fuels in LC-1, LC-5, and LC-6 were most likely substoichiometric in carbon.
- 4) Operation of uranium rich carbide fueled emitters at temperatures below 1800°C leads to significant performance losses.
- 5) The added thermal loss mechanism observed in the carbide fueled in-pile converters was not found in the carbide fueled out-of-pile converters.

ACKNOWLEDGEMENT

The authors wish to acknowledge that the design, fabrication development and postoperational examinations of the Mark VI converters were performed by members of the Thermionic Conversion Program under the direction of Robert W. Pidd, Ling Yang, Albert. F. Weinberg, Joe T. Ream, and M. Harlan Horner.

REFERENCES

- 1) HOLLAND, J. W., "Diagnostic Procedure for Determining Emitter Temperatures, Relative Power and Relative Efficiency of Thermionic Converters in the Absence of Emitter Thermocouples," Thermionic Conversion Specialist Conference Proceedings, Houston, Texas, November 1966, p. 106.
- 2) HOLLAND, J. W., "Performance and Energy Transfer Measurements on Cylindrical Cesium Thermionic Converters," General Atomic Report GA-4729, November 13, 1963.
- 3) FOMENKI, V. S., Edited by G. V. Samsonov, Handbook of Thermionic Properties, Plenum Press Data Division, New York, 1966.
- 4) HOLLAND, J. W., "Performance of a Cylindrical Geometry Thermionic Converter with an Improved Work Function Tungsten Emitter," Thermionic Conversion Specialist Conference Proceedings, Palo Alto, California, October 30-November 1, 1967, p. 13.
- 5) RASOR, N. S. and KITRILAKIS, S. S., "Basic and Engineering Implications of Correlated Converter Phenomenology," Thermionic Conversion Specialist Conference Proceedings, Cleveland, Ohio, October 1964, p. 227.

TABLE 1
IN-PILE TEST SUMMARY

Test	Emitter/ Collector	Fuel	Hours	Average Electrode Power Density (W/cm ²)	Average Emitter Temperature (°C)	Final Relative Power	Final Relative Efficiency	Test Termination Date	Burnup (f/cc)	Failure Mode
IC-6	W/Mo	90UC-10ZrC	1006	7.3	1760	0.80	0.65	4/19/64	3x10 ¹⁹	Envelope leak-not found
IC-7	W/Mo	90UC-10ZrC	520	6.4	1720	0.90	0.80	6/28/64	NC	Envelope leak-no post-operational
IC-8	W/Mo	90UC-10ZrC	1552	6.3	1650	0.80	0.60	12/4/64	5x10 ¹⁹	Envelope leak-not found
IC-9	W/Mo	90UC-10ZrC	1105	6.8	1660	0.90	0.80	6/28/65	3x10 ¹⁹	Envelope leak-not found
IC-10	W/Mo	90UC-10ZrC	1552	6.9	1650	0.60	0.45	12/7/64	5x10 ¹⁹	Envelope leak-not found
IC-11	W/Mo	90UC-10ZrC	2506	6.9	1690	0.80	0.60	8/26/65	8x10 ¹⁹	None-contractual commitment
IC-12	W/Mo	90UC-10ZrC	3300	6.2	1670	0.80	0.50	6/3/66 [⊙]	1.6x10 ²⁰	Short due to growth on emitter
IC-13	W/Mo	90UC-10ZrC	1796	4.5	1490	0.70	0.50	6/30/66	7x10 ¹⁹	Envelope leak-not found
IC-14	W/Mo	90UC-10ZrC	1328	4.0	1620	0.95	0.85	6/30/66	NC	Envelope leak-no post-operational
IC-15	W/Mo	UO ₂	5369	10.0	1730	1.10	1.01	10/13/67 [⊙]	2x10 ²⁰	Short due to getter ring

⊙ Test interrupted for reactor shutdown of several months.

TABLE 2
OUT-OF-PILE TEST SUMMARY

Test	Emitter/ Collector	Fuel	Total Test Hours	Average Electrode Power Density (W/cm ²)	Average Emitter Temperature (° C)	Final Relative Power	Final Relative Efficiency	Test Termination Date	Failure Mode
LC-1	W/Mo	30UC-70ZrC	7174	6.8	1750	0.90	0.40	4/27/65	Envelope leak - cesium attack on insulator metallizing
LC-2	W/Mo	W-UO ₂ cermet	3235	7.8	1650	1.10	1.10	12/29/64	Envelope leak - crack in emitter stem at transition joint
LC-3	W/Mo	W-UO ₂ cermet	10406	8.6	1750	1.10	1.10	11/31/66	Envelope leak + short; leak not found; getter ring broken and shorted
LC-4	W/Mo	--	7345	8.7	1750	1.00	1.00	11/11/65	Envelope leak - final closure braze
LC-5	W/Mo	90UC-10ZrC	7558	8.8	1750	0.85	0.85	12/18/65	Envelope leak - cesium tube-collector braze
LC-6	W/Mo	50UC-50ZrC	2800	4.8	1650	1.18	1.13	8/10/66	Envelope leak - final closure braze
LC-7	W/Nb	--	3671	6.7	1800	0.99	0.99	7/13/67	Envelope leak - Cu-Nb weld in cesium reservoir
LC-9	*W/Nb	--	9353	7.9	1700	1.01	1.00		

+ Still operating as of 3/12/68

* Emitter from WC16

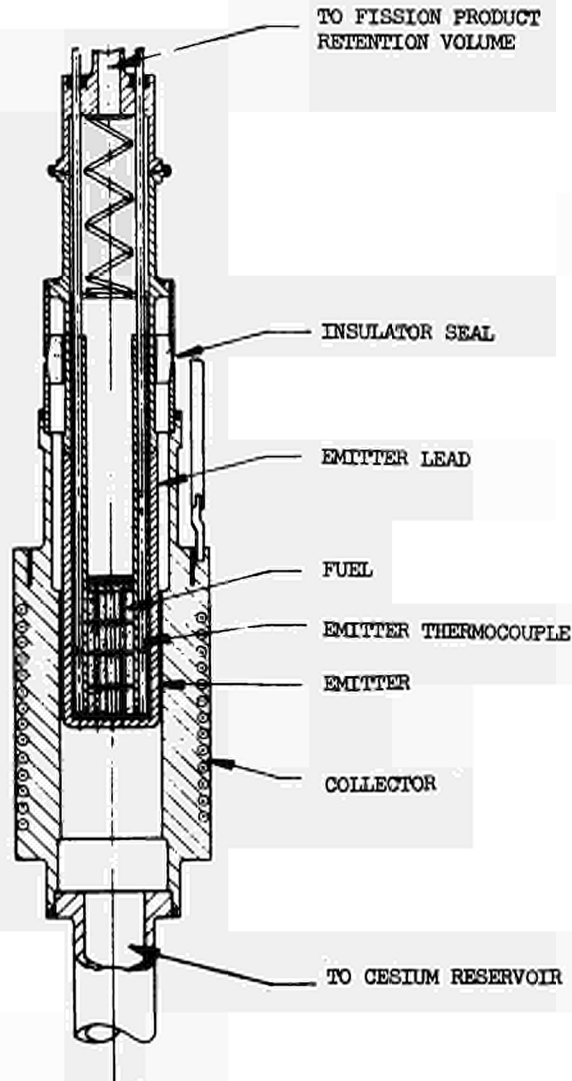


Fig. 1--Mark VI in-pile configuration

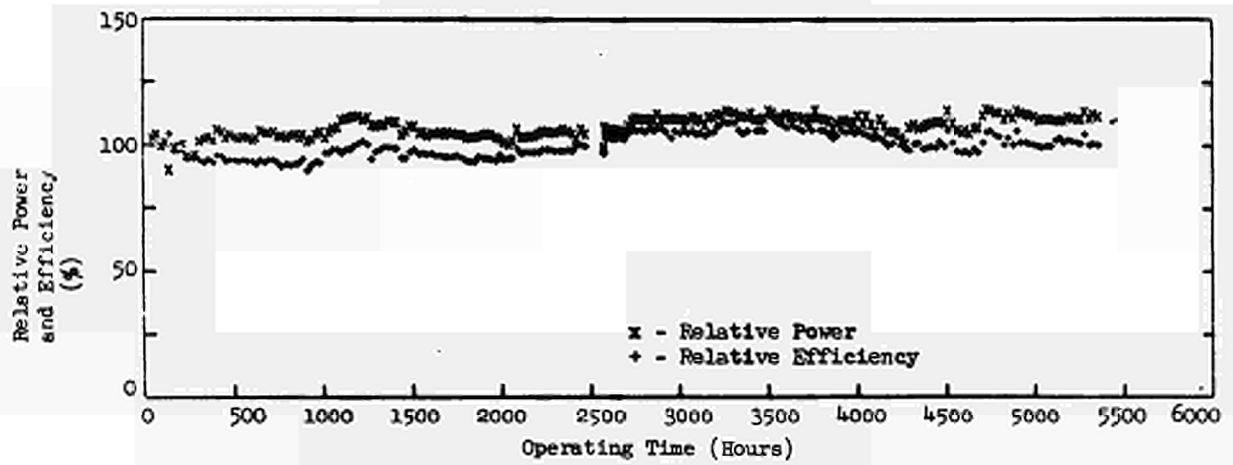


Fig. 2--IC-15 operating history

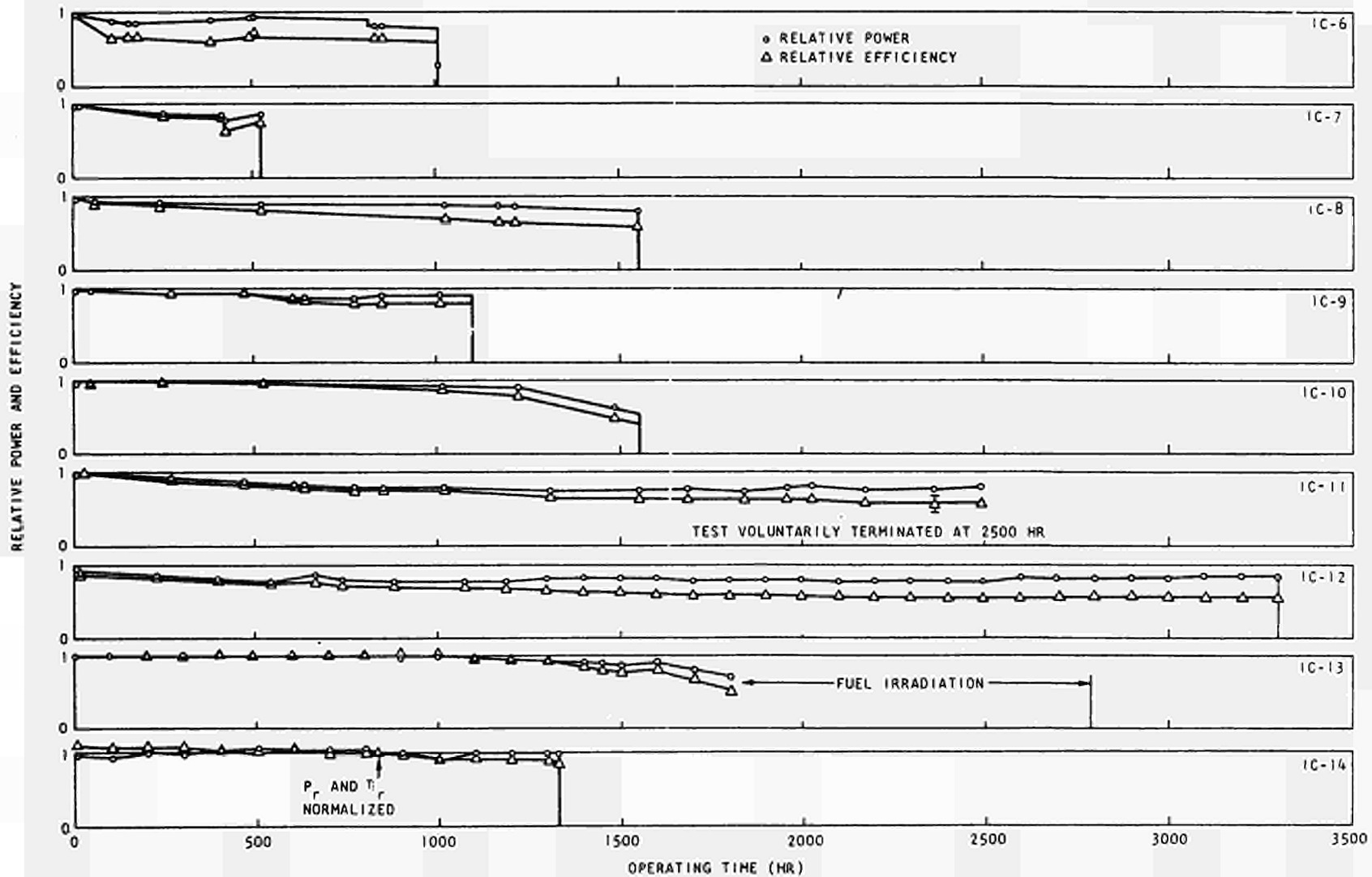


Fig. 3--Relative power and efficiency of carbide fueled in-pile converters

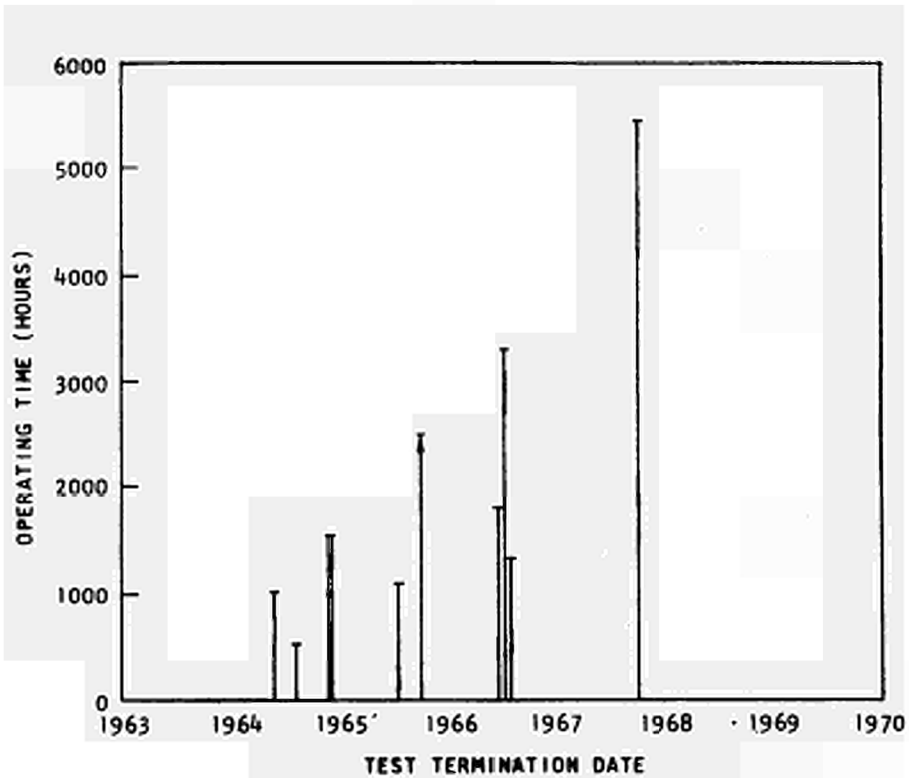


Fig. 4--In-Pile Mark VI converter tests

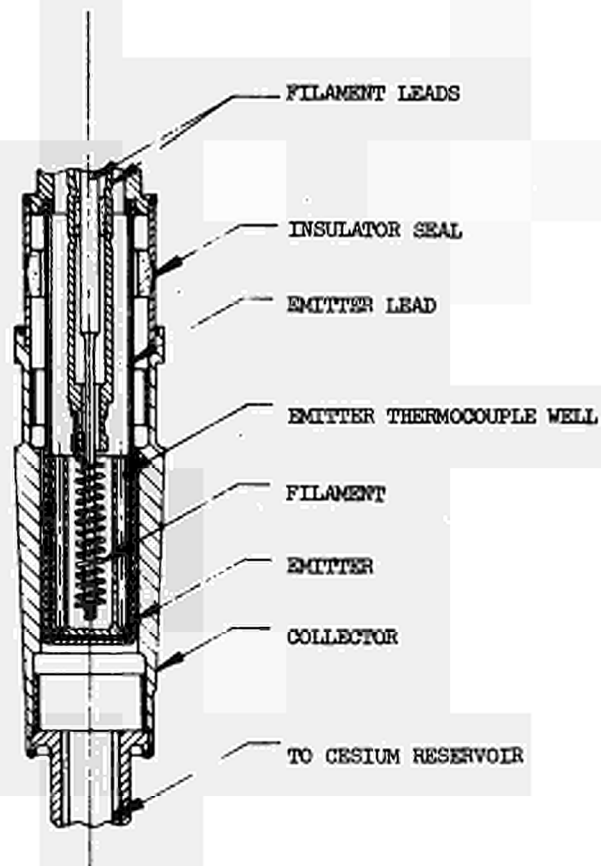


Fig. 5--Mark VI out-of-pile configuration

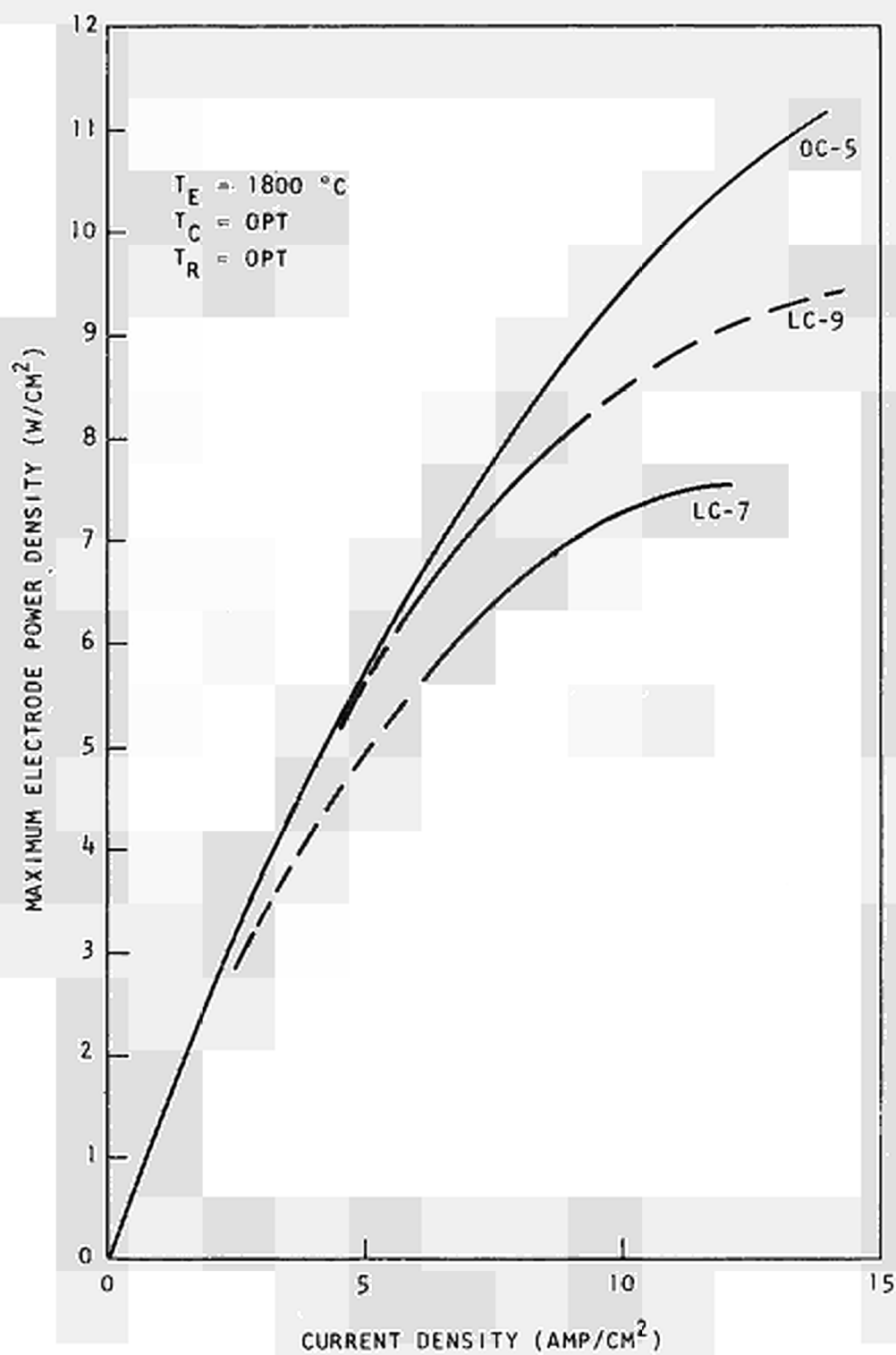


Fig. 6--OC-5, LC-9, and LC-7 performance comparison

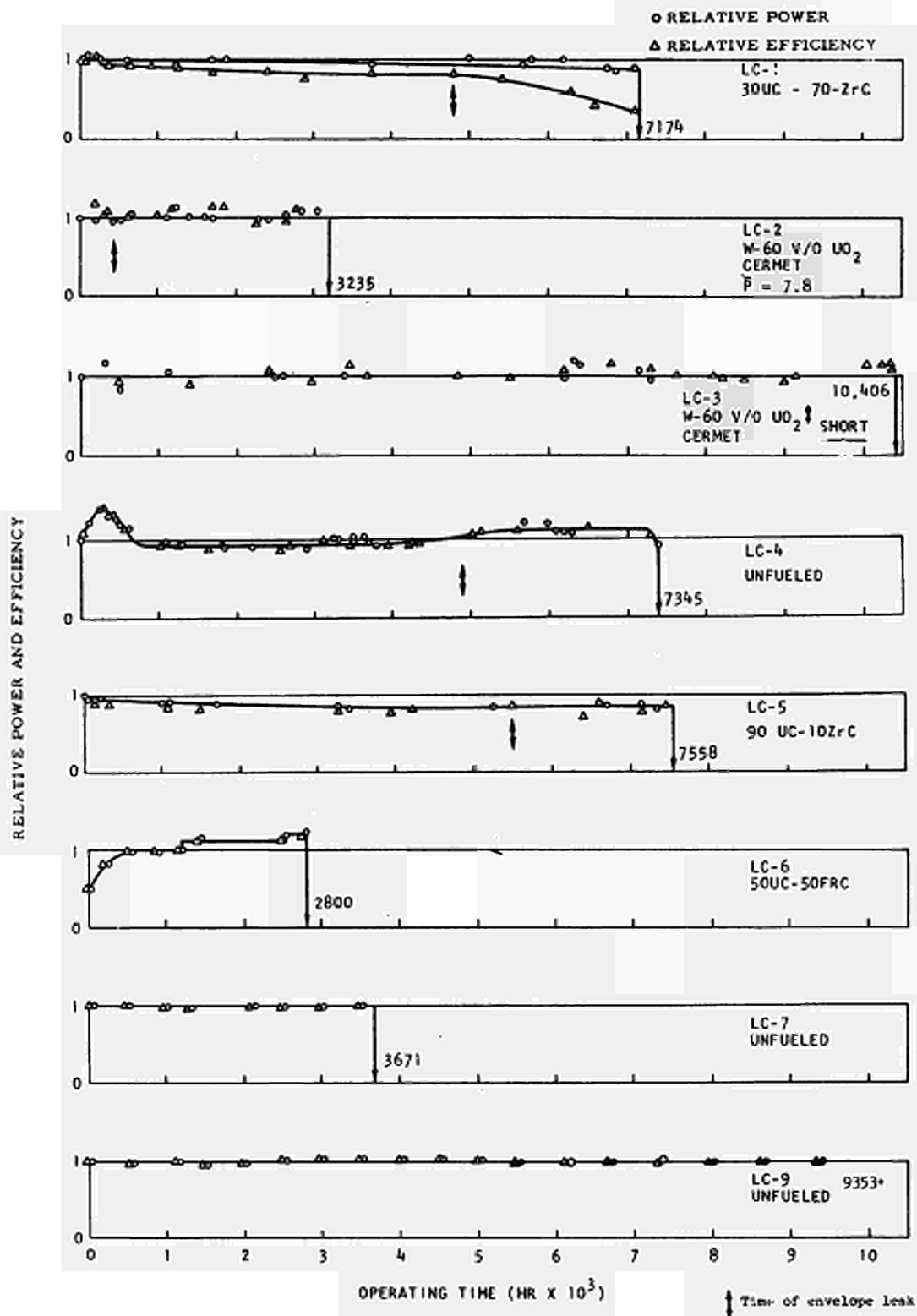


Fig. 7--Relative power and efficiency of out-of-pile converters

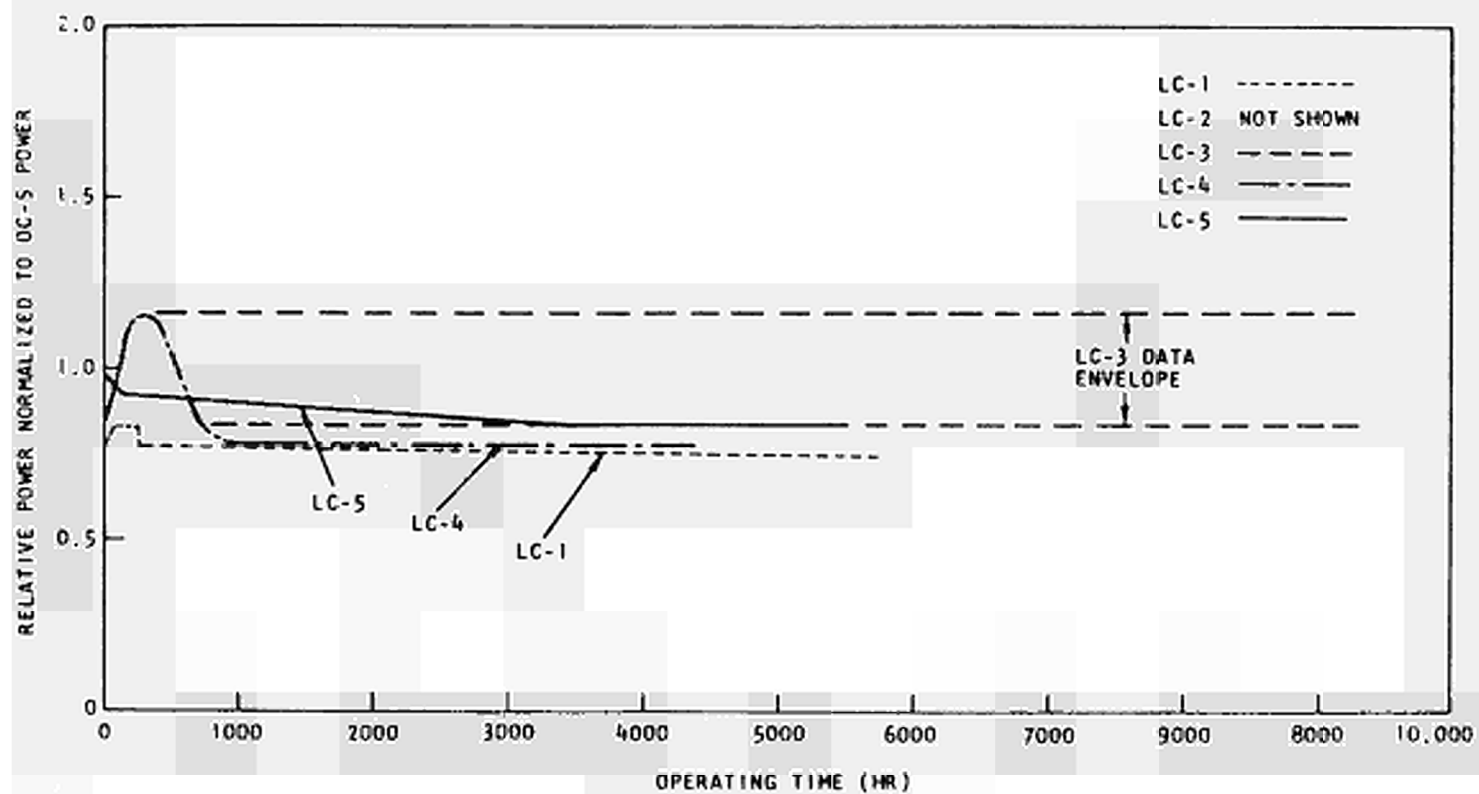


Fig. 8--Comparison of out-of-pile relative power data prior to cesium leakage

DISCUSSION

Speaker of paper C-3: J. W. HOLLAND.

UNGER (Germany):

What was the reason for choosing 90% UC and 10% ZrC?

HOLLAND (USA):

A series of compatibility experiments showed that this composition was adequate for at least gross compatibility effects. The additional zirconium is to raise the melting point. And the composition of 90/10 gives you a high melting point. You still have the zirconium present.

UNGER:

In what form was the fuel in the converter; was it sintered or was it a more solid structure?

HOLLAND:

All the fuel here was sintered.

UNGER:

How high was the percentage of theoretical density?

HOLLAND:

Generally the UO_2 started out at 90% theoretical. The (UZr)C was in various compositions, but I think the lowest percentages were about 80%.

UNGER:

Was there no pressure on the emitter, either by fission gas release or by swelling?

HOLLAND:

On our longest tests the fission product pressure did not exceed 1 atm.

UNGER:

And you do not have the effect of growth of the emitter?

HOLLAND:

No growth effects, no.

UNGER:

Within say one mil?

HOLLAND:

Yes.

HAUSNER (Euratom):

Did you seal the UO_2 -fuel into the emitter under vacuum and if so, did you find a redistribution of UO_2 outside the fueled region?

HOLLAND:

There was a UO_2 fuel converse, they were backed up with either Helium or Argon, and UO_2 was not found outside the emitter cabin.

STEHLE (Germany):

What was the stoichiometry of the fuel, that is, the oxygen/uranium ratio?

HOLLAND:

I don't know.

STEHLE:

What was the maximum centerline temperature of the UO_2 -fuel?

HOLLAND:

That was not measured. I would guess 2200°C .

STEHLE:

Have you finished your post-irradiation examinations?

HOLLAND:

No; this test was just completed.

SCHOCK (USA):

In your in-pile tests, what was kept constant, the heat input to the diode, or the emitter temperature?

HOLLAND:

It was our objective to keep the emitter temperature constant. But this did not always work out because of changes in neutron requirements for other tests at the same time. We were running three tests at one time on the same location.

SCHOCK:

How did the emitter geometry in your UO_2 test compare with practical designs for reactors, particularly with respect to the void volume available for fission gas accumulation?

HOLLAND:

I don't recall exactly how big it was, something like 50 cc. And this was just a means of keeping the atmosphere above the fuel separate from the atmosphere around the converter.

DEVIN (France):

Je voudrais savoir d'une part quelle a été la durée de vie des thermocouples tungstène-rhénium placés dans l'émetteur et d'autre part si la température optimale du réservoir de césium a dû être modifiée au cours de l'expérience.

HOLLAND:

The life time generally was around a 1000 hours. The changes in emitter temperature were calculated by means of a correlation with other parameters. On the UO_2 test, the one you are referring to, the variation of the optimum cesium reservoir temperature is negligible, a very slight increase. The reason for this is that the small performance improvement that we had was just offset by a decrease in the emitter temperature.

DANILOV (USSR):

What were the durations of the experiments; what were the maximum and minimum durations? What are the most typical reasons for the termination of the experiments?

HOLLAND:

The longest test was 5,400 hours, the shortest test was 520 hours. The average was 2,000 hours.

Concerning your other question, in these tests there was one termination due to the shorting of the electrodes and the rest were related to envelope leaks. These converters were tested in gas either helium or argon, so when the envelope leaked the gas went in.

DANILOV:

How does one explain the decrease of the power and the efficiency in the first 2,000 to 3,000 hours? Especially as in the preceding relation one could see even an increase of the power and efficiency. Could one explain this with the penetration of fission fragments into the inter-electrode gap?

HOLLAND:

The previous report where the performance improved was for a UO_2 fuel converter. The other converters where the performance decreased were fueled with UC/ZrC . The difference must be in the fuel.

LANGPAPE (Germany):

Did you find any corrosion of the emitter surface or an abnormal high evaporation rate of the emitter material due to oxygen diffusion through the emitter?

HOLLAND:

No corrosion was observed except a slight etching of the surface. But this was not any more than would have occurred with an unfueled emitter.

LANGPAPE:

Did you find an unusually large effect of collector temperature on the converter performance due to build-up of cesium oxide on the collector surface?

HOLLAND:

Yes.

RETENTION OF FISSION GASES IN THE UO_2 PHASE OF
Mo UO_2 CERMETS IRRADIATED AT HIGH TEMPERATURES*

W. A. Ranken, M. C. Chaney and A. J. Patrick
Los Alamos Scientific Laboratory
University of California
Los Alamos, New Mexico

ABSTRACT

Measurements have been made of the retention of xenon and krypton in the UO_2 phase of Mo UO_2 cermets for samples irradiated at average temperatures varying from 1800° to $2100^\circ K$ and at fission heating rates between 220 and $280 W/cm^3$. The measurements show that large fractions of the fission gases are released during irradiation from cermets having average UO_2 particle diameters of $\sim 22\mu$. The data is interpreted in terms of a gas bubble diffusion mechanism and effective diffusion coefficients are obtained. These values are among the lowest reported in the literature.

The fractional release from 125μ UO_2 spheres, also irradiated in the form of Mo UO_2 cermet, is only slightly less than for the 22μ UO_2 particles. This result is due to the collection of fission gas bubbles at the UO_2 grain boundaries. Gas release occurs when the fission gas pressure causes the UO_2 particles to crack along the weakened grain boundaries.

INTRODUCTION

Although a large body of literature describing theoretical and experimental investigations of fission gas migration and release in UO_2 now exists, the studies have been primarily concerned either with post-irradiation annealing experiments, the results of which cannot be extrapolated to long term irradiations at high temperature, or with long term irradiations of fuel forms where dimensions and temperature gradients are large. This paper reports measurements of gas release and retention made for UO_2 irradiated for long times at high temperature under conditions where both UO_2 dimensions and temperature gradients were small.

* Work performed under the auspices of the U. S. Atomic Energy Commission.

EXPERIMENTAL

The irradiation specimens consisted of Mo UO₂ cermet cylinders 0.63 cm in diameter and 2.54 cm long. These cylinders were clad with ~.01 cm of tungsten in order to prevent the evaporation of UO₂ from the cermet surface. The Mo UO₂ cermets were of two general types. In one of these the average UO₂ particle diameter was approximately 22 μ and no effort was made to surround each particle with the molybdenum matrix. This type of cermet is shown in Fig. 1. The other type of cermet consisted of 125 μ average diameter UO₂ spheres embedded in a matrix of molybdenum as is shown in Fig. 2.

The cermet specimens were irradiated in either the Materials Testing Reactor or the Omega West Reactor for times ranging from 5000 to 8000 hr at temperatures varying from 1800° to 2100°K and with fission power densities ranging from 220 to 280 watts per cubic centimeter of cermet. The temperature measurements were, with one exception, indirect and specimen temperatures decreased by as much as 200°K during irradiation for 8000 hr so that sample temperatures can only be quoted as averages with an error limit approaching 100°K. Power density values were obtained from radiochemical burnup determinations.

The techniques used to determine the quantity of krypton and xenon, which remained in the UO₂ particles is fully described elsewhere.¹ In brief, the procedure was to remove the molybdenum from the irradiated cermet samples by electrochemically dissolving it in 10 normal sodium hydroxide. Following this procedure the UO₂ particles were collected, washed and placed in a vacuum flask with a frozen solution of equal parts of hydrochloric and nitric acid. The solution was then heated to its boiling point and allowed to remain there for 30 minutes. The inert gases, which were liberated when the UO₂ particles dissolved, were driven from the solution and collected in a sample can immersed in a liquid nitrogen bath. Mass spectrometric analysis and Kr⁸⁵ counting were used to determine the quantity of inert fission gases collected. Radiochemical burnup measurements were used to calculate the amounts of these gases produced during irradiation and thus to obtain fractional retention and escape values.

RESULTS

Because of variations in irradiation time and average UO₂ particle size, the fractional retention data obtained for the UO₂ phase of the Mo UO₂

cermet fuels can best be represented in the form of an effective diffusion coefficient. Such a representation appears in Fig. 3 where effective diffusion coefficient values are plotted as a function of reciprocal temperature. The derivation of effective diffusion coefficients from fractional release data was based on a diffusion calculation assuming spherically shaped particles. Correction of the measured gas release values for recoil was straightforward in the case of the 125 μ spheres. For the case of the small particle cermet, the UO₂ was assumed to be in cylindrical form in so far as recoil effects are concerned. In making the diffusion coefficient calculations no consideration was given to trapping site theory. This is because trapping of fission gases into defects and bubbles takes place on a time scale much shorter than the irradiation times in these experiments so that the observed diffusion coefficients probably represent the motion of the trapping sites themselves, i.e., bubble diffusion.

The experimental points in Fig. 3 which were obtained for the small (22 μ) particle cermet (solid circles) show a spread of almost a factor of four in magnitude, a spread which may be largely due to the inaccuracy of the temperature determination. An estimate of the substantial error involved in fitting a curve to the data is given by the shaded region.

The measurements shown in Fig. 3 are specifically for Kr⁸⁵. However, in those cases where mass spectrometric measurements were made, the ratio of xenon to krypton was the same as the production ratio. This would indicate that the effective diffusion coefficient in Fig. 3 applies also to xenon and would fit a picture whereby xenon and krypton move together in diffusing bubbles.

The general range of diffusion coefficient vs temperature data shown in Fig. 3 is at the low end of the very wide spread in measured diffusion coefficients given by Belle.² It is generally recognized that this spread is as wide as it is because the values were based on post-irradiation annealing measurements at a time when the important effect of gas holdup in trapping sites was not recognized. However, the values in Fig. 3 are much higher than would be predicted by the post-irradiation annealing results of MacEwan and Stevens³ taken at 1673°K wherein the effect of trapping was indeed considered and was in fact the main point of the paper. This would suggest that results obtained from high temperature annealing of fuels irradiated at low temperature are not applicable in predicting gas release from fuels irradiated at high temperature.

It should be realized that the wide error range in the effective diffusion coefficient shown in Fig. 3 does not connotate a similarly wide variation in fractional release values from the UO_2 phase of the cermet. This is demonstrated by Fig. 4 where the shaded region in Fig. 3 has been converted to fractional release values to be expected in 10,000 hrs from UO_2 particles having a diameter of 22μ .

It is also important to note that the high fractional release values shown in Fig. 4 do not imply similarly high values for shorter irradiation times. The diffusion theory calculation predicts a time dependence which is shown in Fig. 5. Once again the shaded band represents the possible error in the diffusion coefficient measurements. It can be seen that fractional release values may be small for irradiation times less than 1000 hr. This would be especially true for large particles of UO_2 where sufficient gas pressure must build up in the grain boundaries to cause separation. The curve in Fig. 5 does not apply to this case.

Although fission gas fractional release values for small particles are indeed large, one might reasonably expect them to be much lower for cermets made with 125μ diameter particles since the diffusion model predicts that fractional release values scale as Dt/a^2 where D is the diffusion coefficient, t the irradiation time and a is the radius of the particle. Measured gas release fractions from the 125μ UO_2 particles do not show this behaviour and, in fact, are only slightly lower than the release fractions obtained for 22μ particles. The explanation for this behaviour can be seen in Fig. 2, which shows the appearance of the UO_2 particles after 3250 hr of irradiation. It is apparent that fission gas has collected at the UO_2 grain boundaries. Fig. 6 is an electron micrograph of an irradiated UO_2 particle showing a region where pullout during polishing has exposed what appear to be hemispherical depressions caused by gas bubbles at the grain boundaries. The collection of fission gas in bubbles at the grain boundaries simultaneously weakens the grain boundaries and exerts a pressure tending to separate the grains. Eventually grain boundary separation occurs and the fission gases escape. Thus the gas release from the UO_2 is governed by the UO_2 grain size rather than the UO_2 particle size. This effect is shown in Fig. 3 where the "x" point represents the effective diffusion coefficient calculated from a measured gas escape fraction of 62% when diffusion from a 125μ diameter sphere is assumed. The circled "x" is the diffusion coefficient

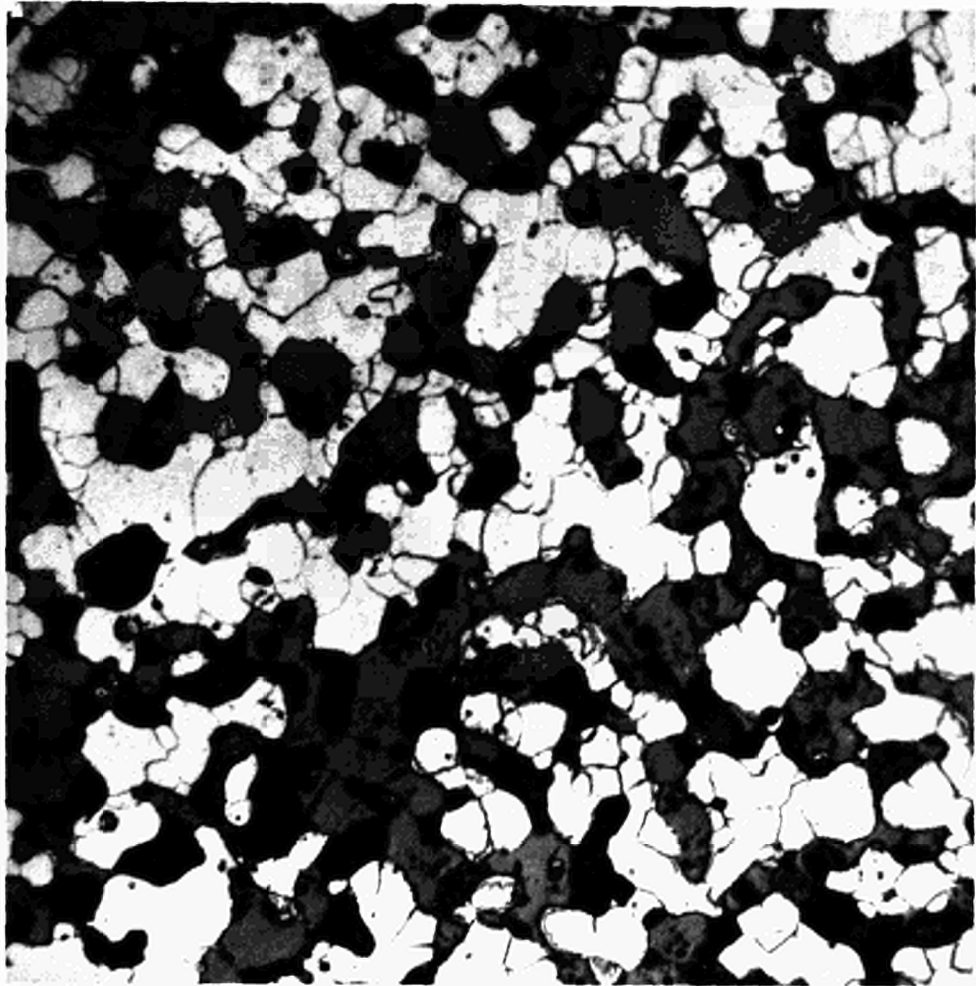
obtained from the same 125 μ particle gas escape data, but calculated on the basis that diffusion escape is determined by the grain size. The grain size was taken to be 28 μ based on photomicrographs such as Fig. 2. It can be seen that this procedure brings the diffusion coefficient obtained from the 125 μ particle irradiation into good agreement with those obtained from the irradiation of 22 μ particles.

CONCLUSION

It has been demonstrated that for long term irradiations significant fission gas release occurs from UO₂ at temperatures as low as 1700°K even under conditions where temperature gradients are relatively small; i.e., on the order of 100°C/cm. Release results can be interpreted on the basis of a diffusion model which postulates that gas escape occurs from UO₂ grains by the diffusion of small bubbles to the UO₂ grain boundaries where trapping, and eventual grain separation, occurs. Attempts to observe bubbles in the irradiated UO₂ grains by replica electron microscopy have not been successful. This may mean that the bubbles in the grain are too small to be detected with the 100-200 μ resolution attainable with the replicating technique.

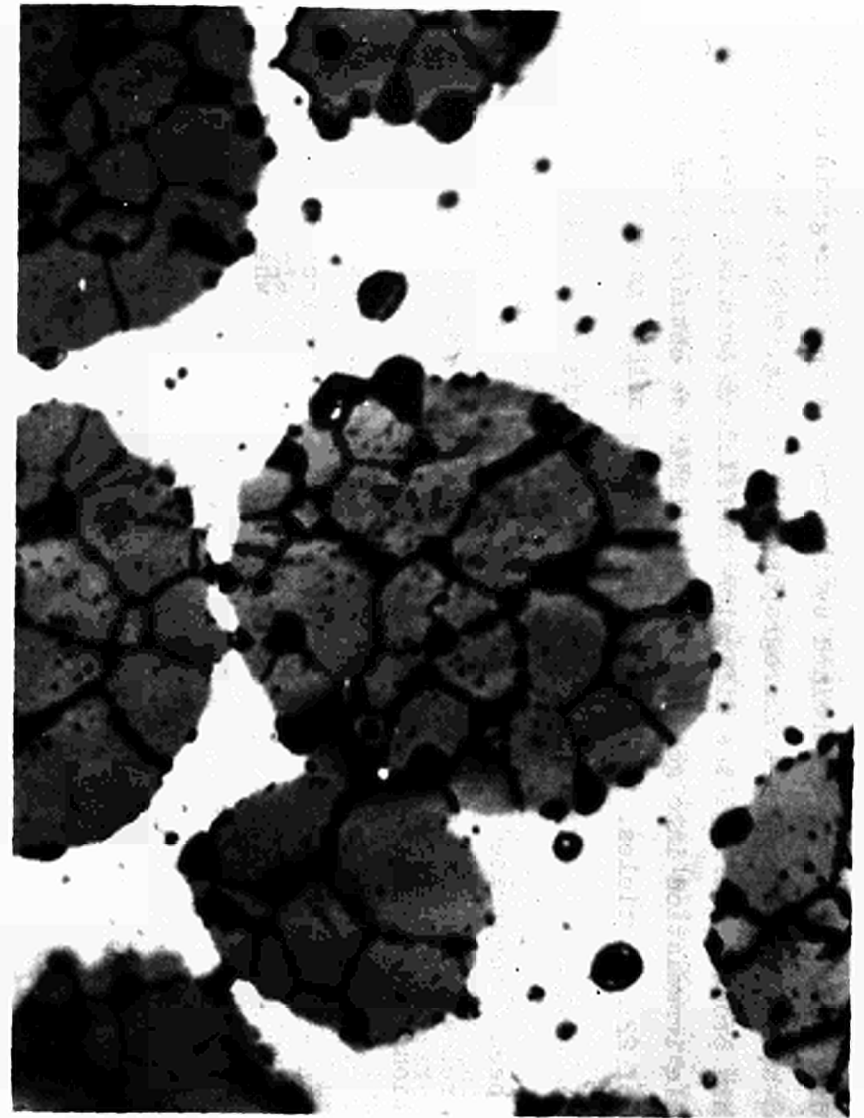
REFERENCES

1. PATRICK, A. P., "Gas-collection technique for measurement of fission gas retention in irradiated Mo UO₂ cermets," Los Alamos Scientific Laboratory Report LA-3718 (1967).
2. BELLE, J., Uranium Dioxide: Properties and Nuclear Applications, U.S. A.E.C., Government Printing Office, 1961, p 496.
3. MAC EWAN, J. R.; STEVENS, W. H., "Xenon diffusion in UO₂," J. Nucl. Mat. 11, (1964) 77.



←100μ→

Fig. 1 Photomicrograph of small particle Mo UO₂ cermet (etched).



←100μ→

Fig. 2 Photomicrograph of Mo UO₂ cermet containing 125μ diameter UO₂ spheres.

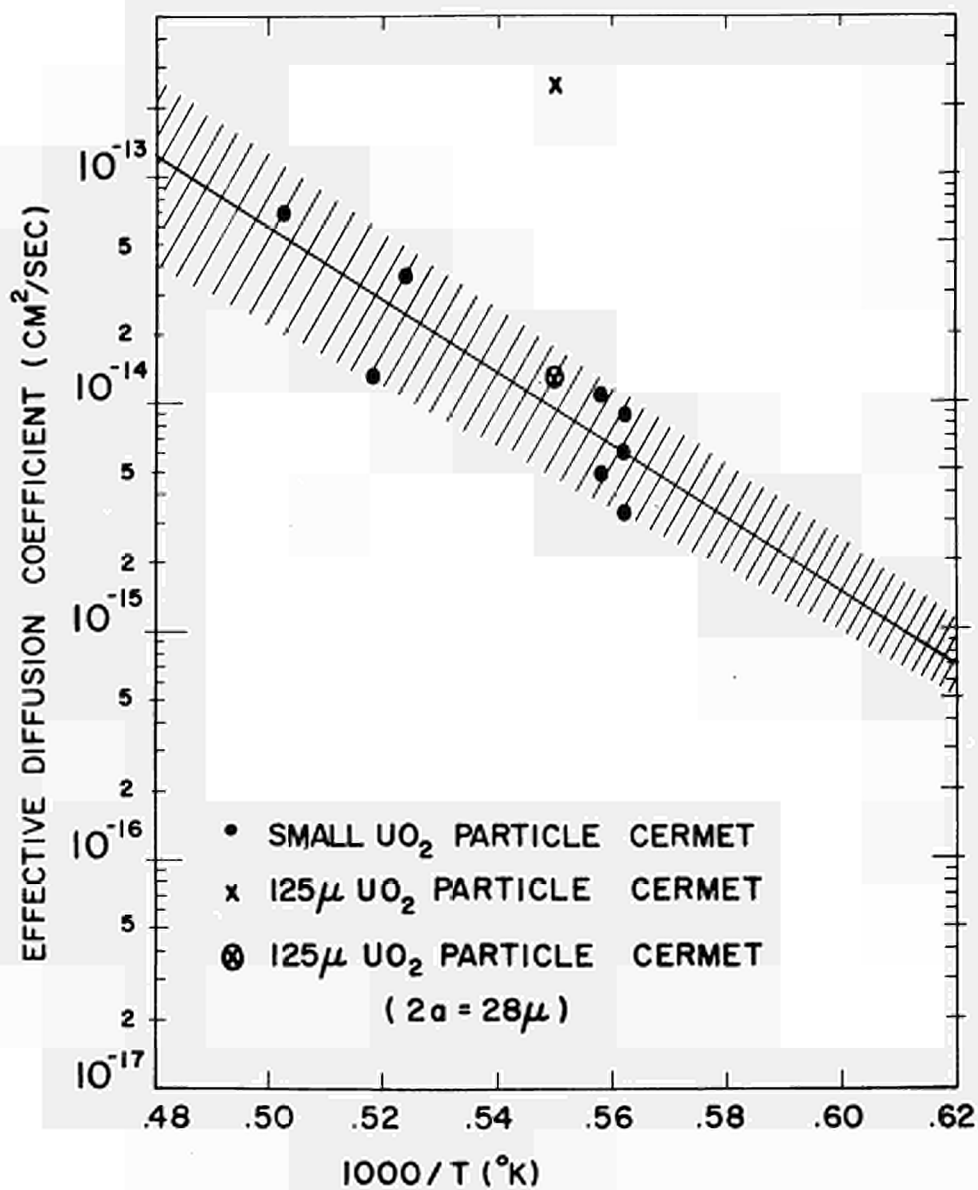


Fig. 3 Effective diffusion coefficient vs reciprocal temperature for small particle UO_2 irradiated in cermet form for 5000-8000 hr.

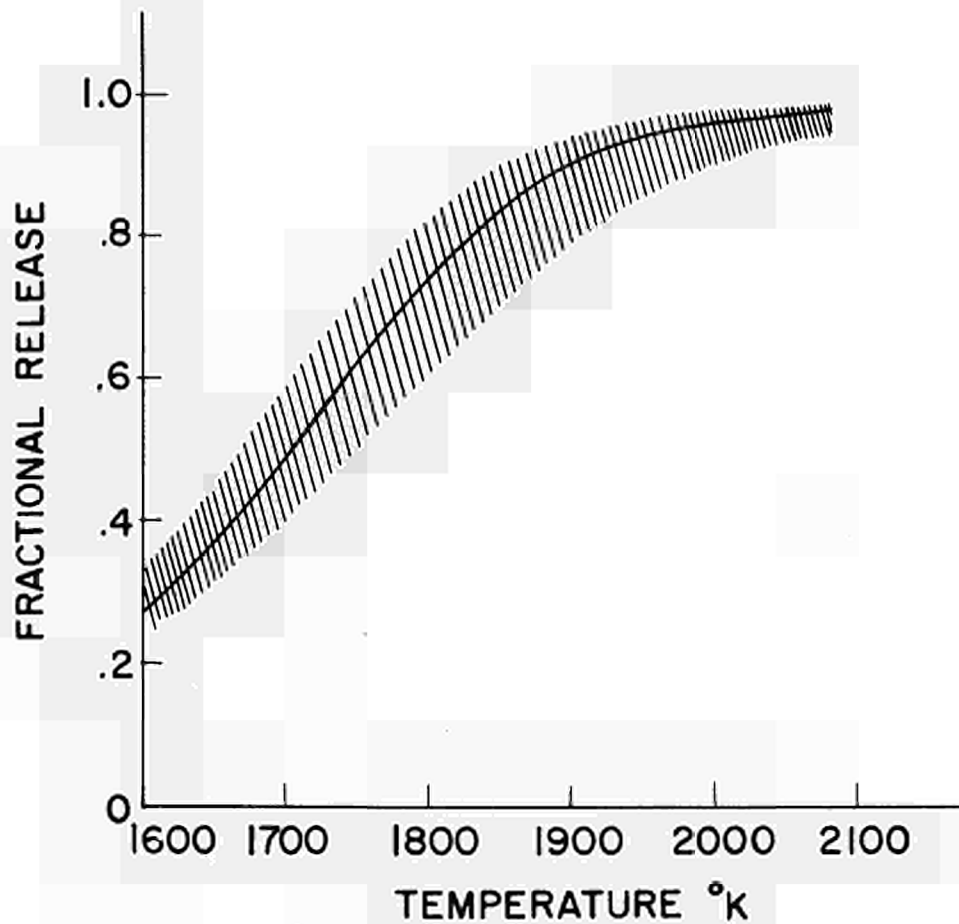


Fig. 4 Diffusion theory prediction of temperature dependence of fractional release of fission gas from 22μ UO_2 particles irradiated for 10,000 hr.

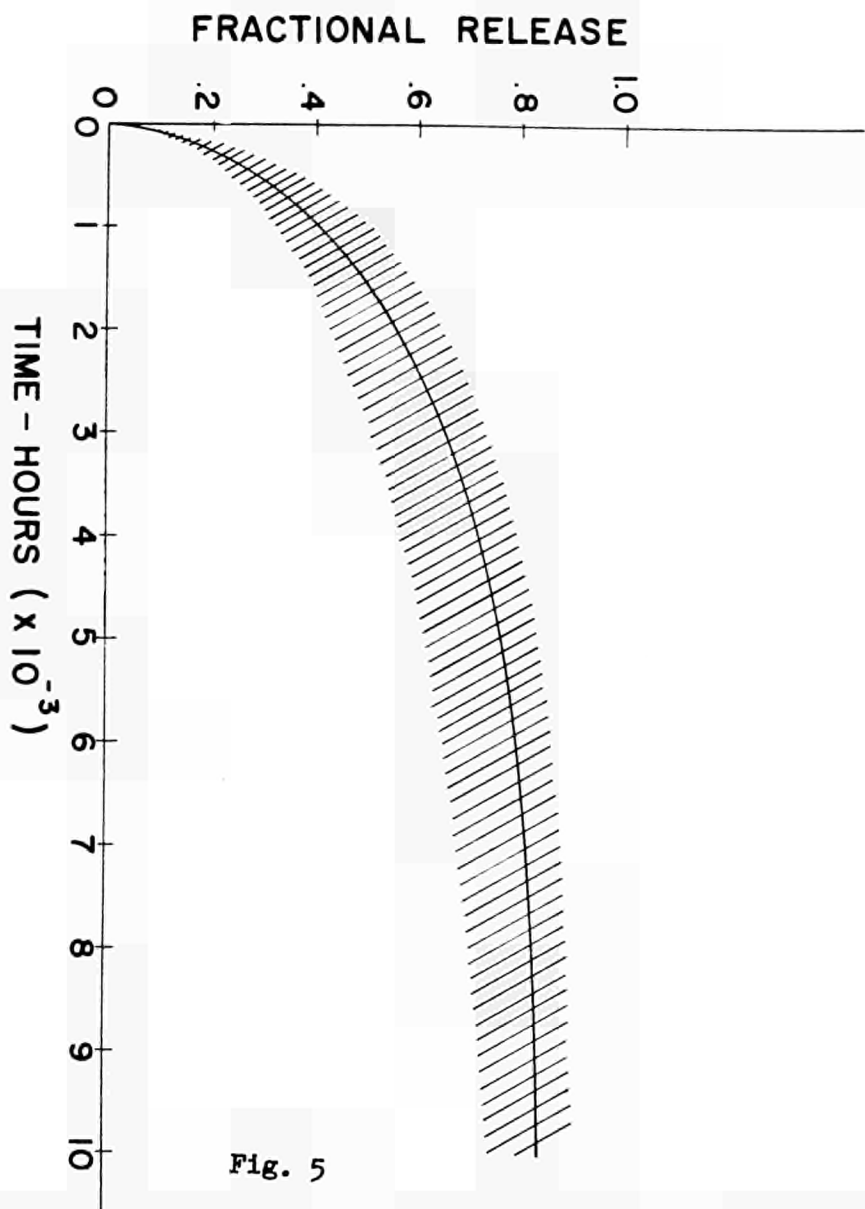
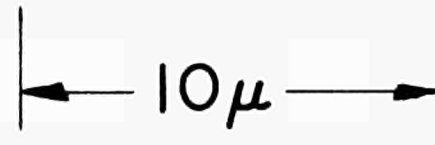


Fig. 5

Diffusion theory prediction of time dependence of fractional release of fission gas from 22 μ UO₂ particles irradiated at 1873°K.



Fig. 6



Electron micrograph of irradiated UO₂ showing evidence of fission gas bubble collection in UO₂ grain boundaries.

DISCUSSION

Speaker of paper C-4: W. A. RANKEN.

PEEHS (Germany): The recoil length of fission products is about $10/\mu$. Therefore, a good deal of fission gas must have escaped from the $20/\mu$ particles and have been injected into the Mo by recoil. How do you explain that you have found no differences between the little and the big UO_2 particles?

RANKEN (USA): The diffusion coefficients given in the paper have been corrected for the effect of recoil loss. The actual recoil loss from the $20/\mu$ particles is less than one would at first suspect because in the cermet form many of the UO_2 particles are contiguous to other UO_2 particles. Therefore atoms recoiling from one particle may be injected into another UO_2 particle. The actual recoil escape values for the small UO_2 particle cermets are approximately 35%.

PEEHS: We have found UO_2 -migration in a UO_2 -Mo-cermet by annealing out-pile for 500 h, e. g. the UO_2 -sites become round. Have you found the same effects after your irradiations?

RANKEN: We have found that there is indeed some further sintering of the cermet during the long term irradiations at high temperature.

PEEHS: Have you found any dimension changes during irradiation of your specimens?

RANKEN: Some dimensional change generally occurs with the amount depending on specimen temperature, irradiation time and a considerable number of other factors.

ROBERTSON (Canada): The paper quoted temperature gradient of $100^\circ C/cm$. Was this a macroscopic gradient or the microscopic gradient in the particles?

RANKEN: The temperature gradient quoted was the approximate total gradient. The maximum microscopic gradient in the fuel particles is about $60^\circ C/cm$ for the $125/\mu$ UO_2 particles and under $15^\circ C/cm$ for the small UO_2 particles.

ROBERTSON: Did Fig. 5, which is prediction, make any allowance for re-solution of the fission product gases? Such re-entry is required to explain the notable scarcity of fission product gasbubbles in irradiated UO_2 .

RANKEN: The actual measurements of gas released from the UO_2 gave values of 60-70% escape of the gas which remained in the UO_2 after recoil corrections had been made. This would indicate that re-solution is not effective in retaining gas in the UO_2 . However, it may be the mechanism that keeps gas bubbles small while they are diffusing towards the grain boundaries. It is not effective in keeping bubbles from growing at the UO_2 grain boundaries.

SCHOCK (USA): In your view, does the molybdenum matrix make any contribution to fission gas retention?

RANKEN: In our depicted cermet it does not.

SCHOCK: How does the ventability of your cermet compare with bulk UO_2 ?

RANKEN: That is a rather difficult question to answer. The comparison depends critically on the fuel temperature, the length of time the fuels have been irradiated and the magnitude of the thermal gradient in the bulk UO_2 fuel.

EXPERIENCES DE CONVERSION THERMO-IONIQUE "SIRENE" EN PILE

et

EXAMENS APRES IRRADIATION DU CONVERTISSEUR "SIRENE 302"

J. BLIAUX, M. CLEMOT, B. DEVIN et P. DUMAS

Service d'Electronique Physique - Centre d'Etudes Nucléaires de Saclay,
91 - Gif-sur-Yvette (France)Résumé -

On rend compte des expériences de durée de vie effectuées dans la pile piscine TRITON.

Les 3 convertisseurs présentés sont semblables et irradiés dans des capsules individuelles. La surface émettrice est de 20 cm^2 et comporte un revêtement pyrolytique de tungstène. L'espace interélectrodes est de 0,2 mm. La pression de césium est réglée soit par la température d'un bloc de graphite (qui est voisine de celle du collecteur) soit par la température d'un réservoir de césium classique.

Des durées de vie de l'ordre de 2 000 heures ont été obtenues. Les mesures effectuées pendant ces tests sont présentées dans cette première partie.

Dans la deuxième partie, on présente les résultats de l'examen, après irradiation du convertisseur SIRENE 302, effectué en cellule chaude : perturbation de la surface émettrice, réaction $\text{UO}_2\text{-Mo}$, transfert par évaporation de l'UO_2 , bon comportement du graphite et vérification du court-circuit émetteur-collecteur. Ces résultats confirment ceux obtenus précédemment en laboratoire.

1.1. Introduction.

On décrit dans la première partie les essais relatifs aux convertisseurs thermo-ioniques nucléaires SIRENE 302, SIRENE 29 et SIRENE 304* : mesures et durée de vie en pile (Réacteur TRITON, pile piscine de 6 MW).

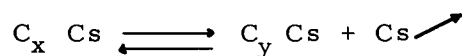
Dans la deuxième partie on donne les résultats des examens post-mortem du convertisseur SIRENE 302 effectués à SACLAY au LECI (Laboratoire d'Examen des Combustibles Irradiés).

1.2. Description de l'expérience.

Le schéma de l'expérience est représenté sur la figure (1) :

Le convertisseur est placé dans le bas d'une canne d'expérience qui est suspendue à un bras d'ascenseur pouvant se déplacer verticalement ; de ce fait le convertisseur reçoit un flux neutronique variable modifiant ainsi la puissance thermique injectée dans l'émetteur. Le refroidissement du collecteur est assuré par une circulation d'eau de pile sous pression. L'ajustement des températures de collecteur et du réservoir de césium est assuré par deux chaufferettes pouvant fournir au maximum 1 500 Wth et 500 Wth respectivement.

La pression de césium est déterminée par la température d'un bloc de graphite avec du césium comme produit d'insertion suivant l'équilibre $[\text{C}_x, \text{C}_y]$



* Convertisseurs fabriqués au titre des contrats CEA/CSF et CEA/CFTH-HB.

Les équilibres utilisés sont soit $[C_{10}, C_{24}]$, soit $[C_{24}, C_{36}]$ [1]. La température du réservoir est voisine de celle du collecteur.

La puissance électrique convertie est évacuée par la connexion du réservoir de césium et par l'embase d'émetteur (reliées successivement à deux tubes métalliques coaxiaux de forte section constituant la canne support) et connectées à la charge résistive par des câbles de très faible résistance.

La tension du convertisseur est prise entre le bas du collecteur et l'extrémité supérieure de l'embase d'émetteur.

Les températures sont mesurées par des thermocouples Chromel-Alumel à l'exception de celles du combustible et de l'émetteur mesurées par des thermocouples WRe 5 % - WRe 26 %.

Après irradiation la partie active contenant le convertisseur est désaccouplée de sa canne support, et transportée dans un château en plomb jusqu'aux cellules chaudes pour examens post-mortem.

1.3. Convertisseur SIRENE (fig. 2).

Le convertisseur thermo-ionique nucléaire SIRENE est de géométrie cylindrique. Il contient un cylindre d'oxyde d'uranium enrichi à 20 % (8 g. d' U_{235}). La surface émettrice est de 20 cm^2 et la distance interélectrodes de 0,20 mm à froid.

La géométrie des convertisseurs restant pratiquement identique (les écarts provenant des valeurs des résistances thermiques), les convertisseurs SIRENE 302, 29 et 304 ne diffèrent que sur les points importants suivants :

	SIRENE 302	SIRENE 29	SIRENE 304
Réservoir de césium	césium-graphite $C_{24}Cs \rightleftharpoons C_{36}Cs$	césium liquide	césium-graphite $C_{10}Cs \rightleftharpoons C_{24}Cs$
Emetteur	200 $\mu\text{W}/\text{Mo}$ (WF_6)	50 $\mu\text{W}/\text{Mo}$ (WF_6)	200 $\mu\text{W}/\text{Mo}$ (WF_6)
Collecteur	Nb-Zr 1 %	Mo	Nb-Zr 1 %
Centrage	non	oui	oui
Scellement métal-céramique	Lucalox//Ni-Ti// Nb-Zr 1 %	Alumine WESGO//W/ Cu-Ni//Nb	Lucalox//Ni-Ti// Nb-Zr 1 %

Montages annexes.

Le circuit de charge, l'équipement électronique et le fonctionnement autonome sans surveillance ont été décrits en détail dans une publication précédente [2].

1.4. Essais préliminaires.

Une expérience SIRENE 300 identique mais sans combustible a précédé les expériences effectives. Elle a permis de déterminer les valeurs du chauffage par rayonnement Υ dans les différents canaux et à différentes profondeurs.

Les puissances Υ dégagées dans les pièces massives du convertisseur interviennent

dans le bilan thermique (fig. 3), donc dans l'estimation du rendement.

Au début de chaque mise en pile d'un convertisseur, les résistances thermiques sont mesurées en injectant successivement des puissances connues dans l'élément chauffant du réservoir de césium puis dans celui du collecteur.

Les valeurs des résistances thermiques trouvées pour chacun des convertisseurs sont :

	SIRENE 302	SIRENE 29	SIRENE 304
R_1	5,7 °C/W	16,5 °C/W	4,7 °C/W
R_2	10,3 °C/W	17,0 °C/W	4,9 °C/W
ρ_1	0,11 °C/W	0,18 °C/W	0,376 °C/W
ρ_2	0,52 °C/W	0,52 °C/W	0,39 °C/W
r_1 r_2	$\left. \begin{array}{l} \\ \end{array} \right\} 3^\circ\text{C/W au total,}$ estimé d'après SIRENE 300	calculé $\left\{ \begin{array}{l} 1,14^\circ\text{C/W} \\ 3,1^\circ\text{C/W} \end{array} \right.$	$\left. \begin{array}{l} \\ \end{array} \right\} 3^\circ\text{C/W au total,}$ estimé d'après SIRENE 300

1.5. Rendement.

Le flux neutronique et le chauffage par rayonnement Υ engendrent une puissance ($P_{NE} + P_{\Upsilon E}$) dans l'émetteur. Le bilan thermique dans l'émetteur est

$$P_T = P_{NE} + P_{\Upsilon E} = P_o + P_{EB} + P_{EC} + P_{ER}$$

avec :

- P_T puissance injectée dans l'émetteur
- P_o puissance de sortie
- P_{EB} puissance évacuée de l'émetteur vers la base d'émetteur
- P_{EC} puissance évacuée de l'émetteur vers le pont thermique collecteur
- P_{ER} puissance évacuée de l'émetteur vers la connexion du réservoir de césium.

D'après les résultats de l'expérience SIRENE 300, la valeur de P_{CE} représente une fraction α de la puissance thermique transmise par l'émetteur, et dont la valeur est fonction des résistances thermiques, donc :

$$P_{EC} = \alpha [P_{EC} + P_{ER} + P_{EB}] \quad \text{soit :}$$

$$P_T = P_o + \frac{P_{EC}}{\alpha - \Delta\alpha}$$

L'imprécision sur le terme α provient surtout de l'imprécision sur la connaissance du chauffage Υ et sur le flux thermique évacué par l'embase d'émetteur.

Le bilan thermique du pont collecteur détermine P_{EC} , puisque :

$$P_{EC} + P_{PC} + P_{Y_{PC}} = \overline{\epsilon} \sigma S_{PC} (T_{PC}^4 - T_{PF}^4) + (T_{PC} - T_{PF}) \frac{1}{\rho_2}$$

avec :

P_{PC} puissance de la chaufferette du pont collecteur
 $P_{Y_{PC}}$ puissance Y dans le pont collecteur
 T_{PC} température du pont collecteur
 T_{PF} température de la paroi froide
 ρ_2 résistance thermique entre le pont collecteur et la paroi froide.

Le rendement est $\eta = \frac{P_o}{P_T} = \frac{1}{1 + \frac{P_{CE}}{P_o} \left(\frac{1}{\alpha + \Delta\alpha} \right)}$

Rendement des convertisseurs au point nominal :

SIRENE 302 (85 Wu)	(10,8 ± 1,0) %
SIRENE 29 (70 Wu)	(9,8 ± 0,9) %
SIRENE 304 (95 Wu)	(10,1 ± 1,1) %

1.6. Résultats de durée de vie.

Les convertisseurs avaient déjà subi des tests préparatoires en laboratoire ; le tableau suivant indique les différentes performances en laboratoire puis en pile :

	SIRENE 302	SIRENE 29	SIRENE 304
Durée préalable en laboratoire (h)	10	300	10
Puissance nominale en laboratoire (W)	100	60*	100
Durée totale en pile (h)	2 050	500	1 982
Durée sans dégradation en pile (h)	1 650	10	1 980
Cause de l'arrêt constatée ou présumée.	Court-circuit intermittent puis permanent	Court-circuit permanent et arc	Fuite dans la capsule ayant entraîné la destruction du convertisseur
Régime moyen de fonctionnement en pile (W)	85	70	90
Energie convertie en pile (kWh)	150	0,5	160

* Convertisseur de puissance nominale 100 watts, ayant été testé en laboratoire à puissance réduite.

Les courbes de durée de vie concernant les convertisseurs 302 et 304 sont représentées sur les figures 4 et 5.

1.7. Mesures.

Compte tenu des durées de vie ci-dessus, les mesures n'ont été effectuées que sur 2 convertisseurs :

Les examens sur SIRENE 29 ont porté surtout sur l'étude de la cause du court-circuit.

Les mesures plus complètes sur SIRENE 302 et SIRENE 304 sont représentées sur les figures ci-jointes.

Les thermocouples Chromel-Alumel ont fonctionné normalement; par contre les thermocouples WRe 5 % - WRe 26 % (fils nus montés dans des bifilaires de glucine) ont donné des indications de température variables en fonction du temps pour un même convertisseur. L'évolution des thermocouples émetteur et combustible a été plus rapide pour SIRENE 304 que pour SIRENE 302, surtout en ce qui concerne l'émetteur.

On retrouve par contre de grandes similitudes sur les caractéristiques Puissance de sortie en fonction de la puissance du réacteur (proportionnelle à la puissance injectée). Cette forme de caractéristique avait déjà été trouvée en laboratoire [3], les expériences en pile la confirment (fig. 6).

La valeur de la température du réservoir de césium semble moins critique que ne le laissaient prévoir les expériences fines de laboratoire : cela est sans doute dû aux hétérogénéités de températures du collecteur et aussi de l'émetteur.

Le réservoir de césium peut fonctionner à des températures variables suivant la quantité de césium introduite. Dans les expériences SIRENE 302 et SIRENE 304, le fait que le réservoir de césium ne soit pas isotherme (et ce pour des raisons de commodité structurale), conduit à une plage d'incertitude sur la température de l'élément du bloc de graphite où se définit la transition réversible C₂₄, C₃₆ ou C₁₀, C₂₄. Le convertisseur SIRENE 302 a fonctionné avec une température moyenne de graphite de 792 °C, et le convertisseur SIRENE 304 avec une température moyenne de graphite de 688°C (voir figures 7 et 8).

La puissance injectée théorique, déduite à partir de l'écart $T_{comb} - T_{émet}$ mesuré au début de l'expérience et de la dépression de flux [4], donne une valeur à 10 % près de la puissance thermique réelle obtenue à partir du bilan thermique. Bien que la puissance thermique de la pile (6 000 ± 150 kW) soit maintenue constante, le flux neutronique en un point varie au long du cycle du réacteur et en fonction des expériences voisines. Il est prévu dans les prochaines expériences de réguler la position du convertisseur en fonction d'un détecteur du type "neutron-électron" afin d'assurer une puissance injectée rigoureusement constante : sinon il semble très difficile de déceler les évolutions d'antiréactivité du convertisseur (produits de fission par exemple).

1.8. Causes d'arrêt.

Les causes d'arrêt présumées sont :

SIRENE 302 :	1) décollement couche W/Mo	(court-circuit intermittent)
	2) contact émetteur collecteur	(court-circuit permanent)
SIRENE 29 :	1) contact émetteur collecteur	(linéarité de la caractéristique I (V), voir fig. 9)
	2) arc dans le césium	(décrochement brutal de la caractéristique I (V) dans la partie négative du courant)
SIRENE 304 :	1) fuite dans la capsule étanche	(entraînant la destruction du convertisseur très rapidement, par réaction à haute température).

1.9. Références.

- [1] DEVIN B. ; LESUEUR R. ; SETTON R.. "Vapor pressure of cesium above graphite lamellar compounds" - Palo Alto Conf. 1967.
- [2] BLIAUX J. ; CLEMOT M. "In pile thermionic life test SIRENE 302" - Palo Alto Conf. 1967.
- [3] LANDROT J. P. "Etude des régimes transitoires des convertisseurs thermoioniques" Thèse de Docteur-Ingénieur - Paris 1967.
- [4] BLIAUX J. ; JAMET J. M. "Répartition des flux et des températures dans les convertisseurs thermoioniques SIRENE 50 et SIRENE 100" - Rapport CEA N° R 2792 - 1965.

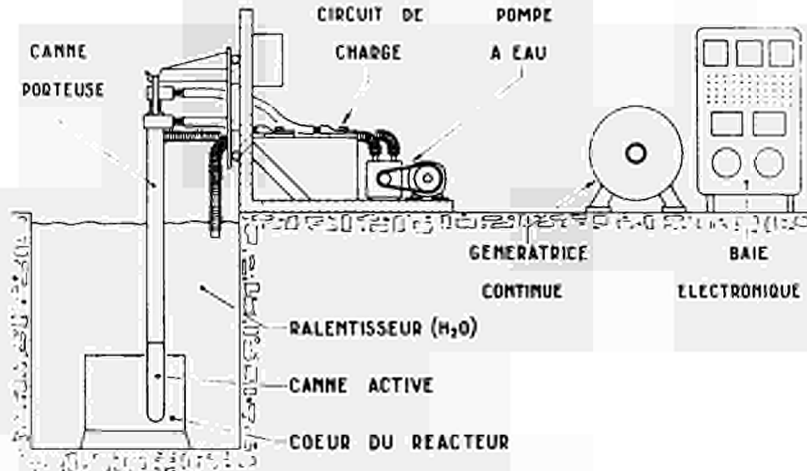


Fig. 1 - Montage d'expérience en pile

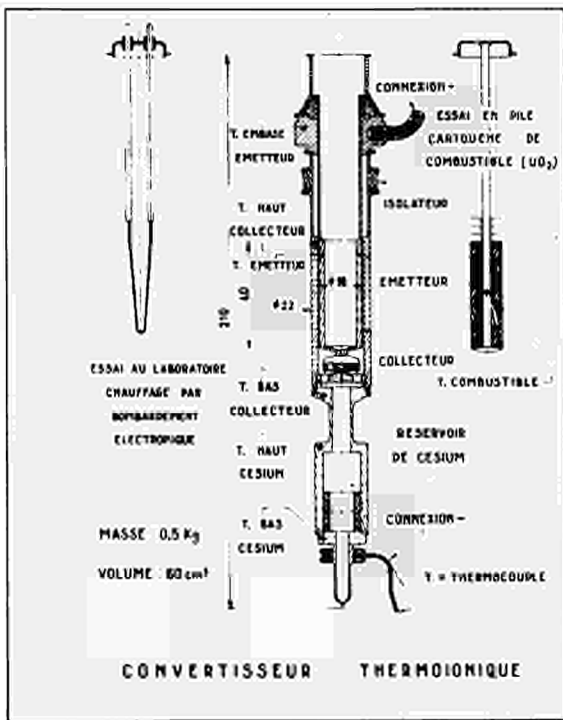


Fig. 2 - Coupe du convertisseur SIRENE

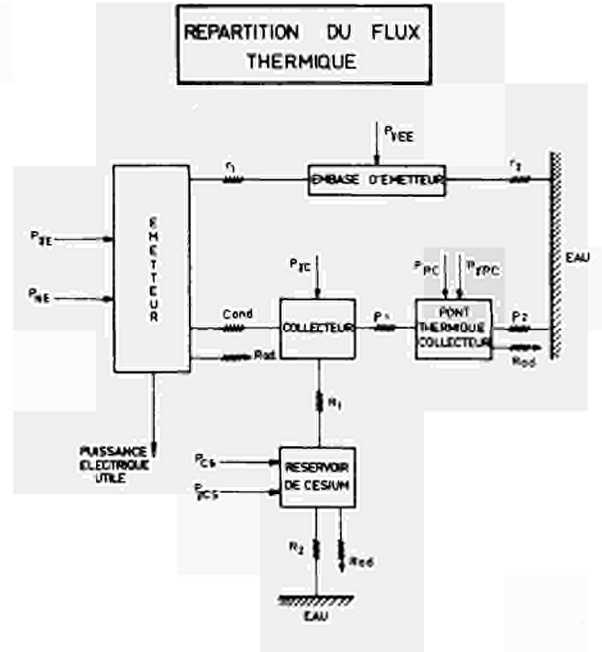


Fig. 3 - Bilan thermique

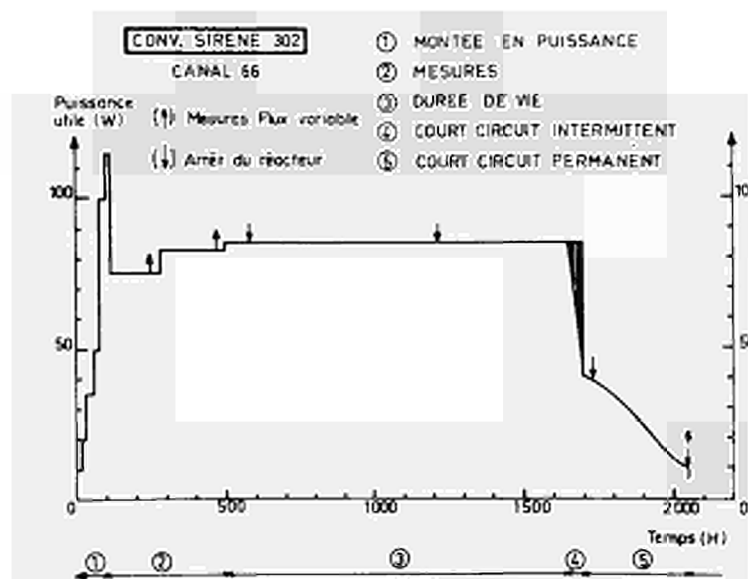


Fig.4 - Courbe de durée de vie SIRENE 302

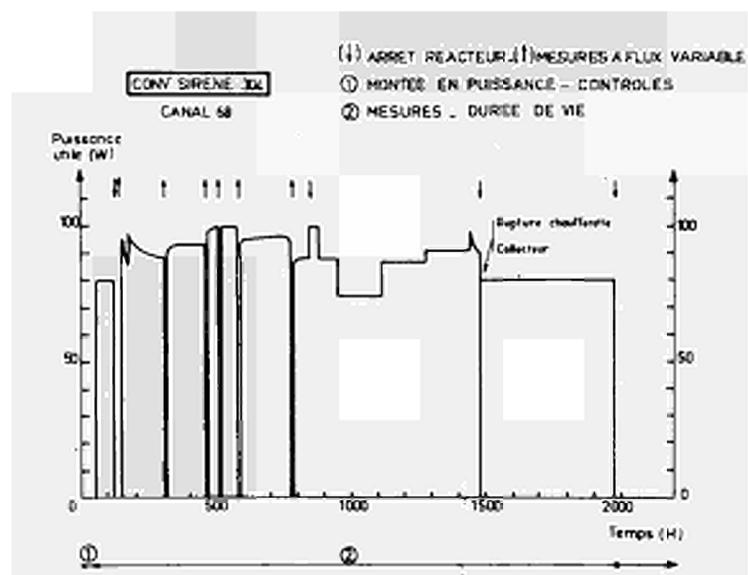


Fig.5 - Courbe de durée de vie SIRENE 304

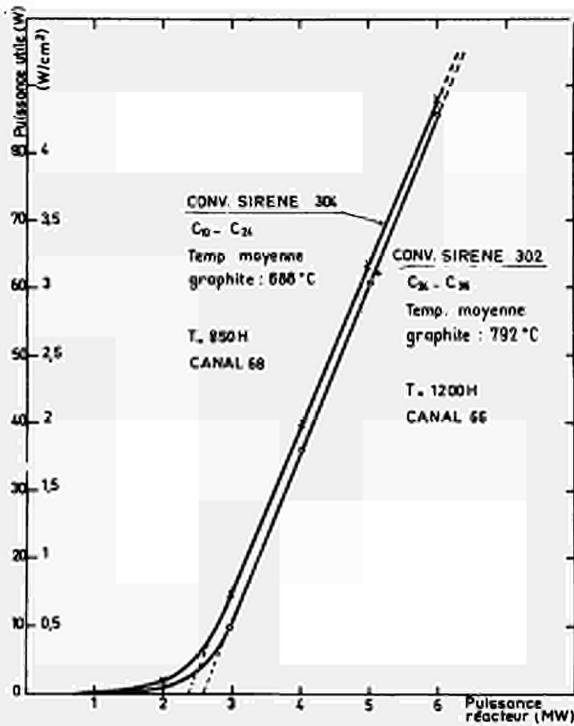


Fig. 6 - P_u en fonction de P_r

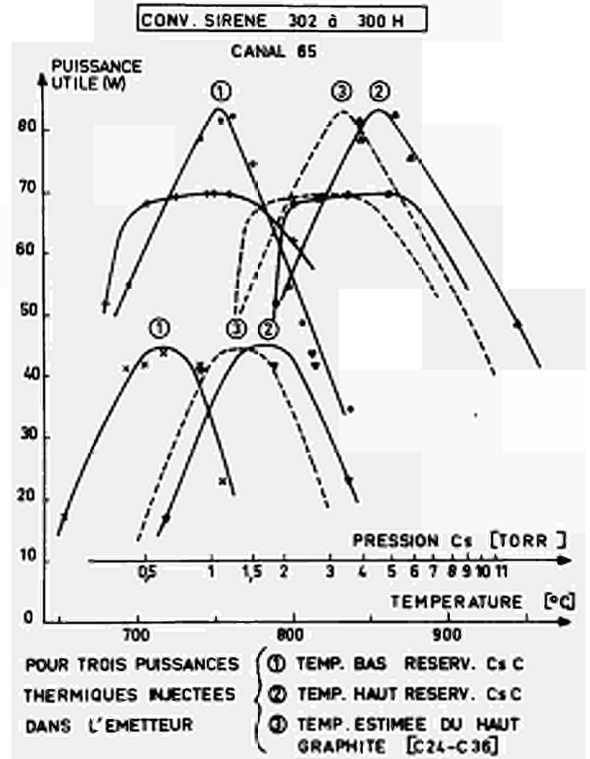


Fig. 7 - $P_u (T_{\text{graph.}})$ SIRENE 302

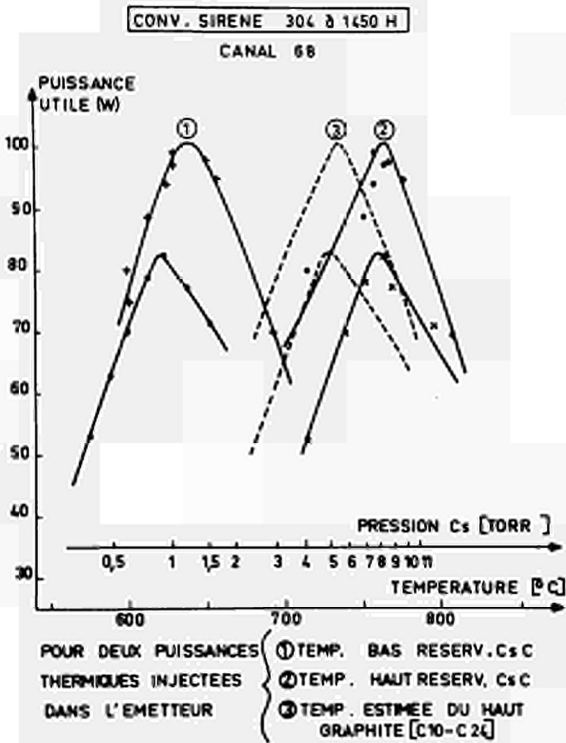


Fig. 8 - $P_u (T_{\text{graph.}})$ SIRENE 304

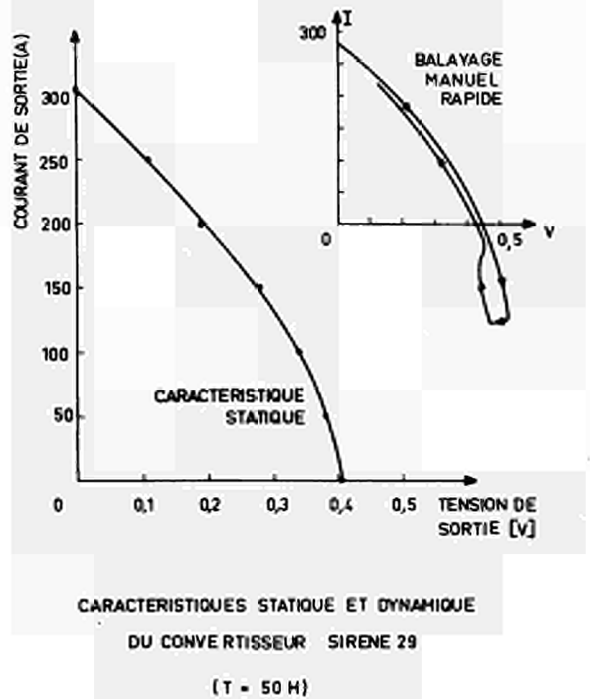


Fig. 9 - Caractéristique I(V) SIRENE 29

2. EXAMENS POST MORTEM SIRENE 302.

Le convertisseur SIRENE 302 a fonctionné en pile pendant 2 050 heures ; après une désactivation radioactive de six semaines, les examens en cellule chaude ont pu démarrer.

2.1. Convertisseur.

Après découpage de la partie active, le convertisseur a été extrait de son enceinte étanche (fig. 1). L'aspect extérieur du convertisseur (pièces non oxydées, chaufferettes en excellent état) a prouvé la qualité du vide autour du convertisseur. La figure 2 représente la courbe d'émission γ globale relevée sur le convertisseur [1] : les deux pics du Cs 134 prouvent que le césium est resté dans les deux blocs de graphite, les trois pics du Ta 182 correspondent aux colliers externes de prise de tension et de fixation du thermocouple, l'activité centrale correspond principalement à l'émission γ du combustible.

Le convertisseur a été découpé et les composants principaux ont été examinés.

2.2. Réservoir de césium.

Les deux blocs de graphite pyrolytique initialement introduits ont été retrouvés sous forme de six tores d'épaisseur 3 mm environ chacune, ayant conservé une bonne tenue mécanique malgré le gonflement dû à l'insertion du césium ; la fig. 3 représente l'un de ces tores. L'analyse du spectre γ dû au Cs 134 seul a montré un enrichissement en césium plus important aux extrémités supérieure et inférieure de l'ensemble des deux blocs.

2.3. Espace interélectrodes.

Dans l'espace interélectrodes a été recueillie une petite quantité de poudre noire dans laquelle l'analyse spectrographique a montré la présence de Cs 134 (réaction n, γ avec Cs 133), du Cs 137, du Ce 144, du Zr 95 et du Nb 95. Ces quatre derniers corps peuvent provenir soit d'impuretés contenues dans les matériaux constituants, soit de fissions d'uranium libre diffusé. On note également la présence de Ta 182, qui pourrait provenir d'une impureté de l'émetteur ou du collecteur (Mo ou Nb). La présence éventuelle de W n'a pu être mise en évidence par suite de la brièveté de la période (24 heures).

2.4. Emetteur.

Le cylindre émetteur (fig. 4) présente extérieurement quelques cavités et soufflures analogues à celles observées en laboratoire [2]. Une tache brune importante à l'extrémité de l'émetteur peut expliquer le court-circuit permanent qui mit fin à l'expérience.

Des coupes transversales de l'émetteur ont été effectuées dans les parties haute, moyenne et basse de l'émetteur, afin d'être soumises aux examens suivants :

- micrographie
- microdureté
- microsonde de Castaing
- mesure du travail de sortie sur la face émettrice.

A ce jour, seuls les résultats des deux premiers examens ont été obtenus. La figure 5 montre l'aspect de la couche de W et de la zone Mo-W pour la partie supérieure de l'émetteur : importantes coalescences de porosités à l'interface et nombreuses porosités dans la couche de W. Les figures 6 et 7 correspondent à une coupe médiane de l'émetteur : les porosités semblent s'être rassemblées aux joints de grains du W provoquant des arrachements jusqu'à la zone de liaison Mo-W. La zone de liaison Mo-W (importance de l'interdiffusion) n'a pu être estimée par microdureté, par suite des perturbations dues à ces cavités.

2.5. Combustible.

Le combustible était initialement constitué de 10 tores d' UO_2 enfilés sur un mandrin en W, de diamètre intérieur 3 mm et de diamètre extérieur 11,8 mm devant entrer dans la gaine émettrice de diamètre interne 12 mm. Après irradiation, le combustible s'est totalement modifié (fig. 8) : disparition de la partie centrale due à une évaporation importante de l' UO_2 qui est

venu se condenser principalement sur les écrans en Mo, provoquant ainsi leur détérioration partielle. La figure 9 représente la structure basaltique de l' UO_2 caractéristique d' UO_2 très chauffé. Aux points de contact UO_2 - Mo, on observe une zone correspondant vraisemblablement à une réaction UO_2 - Mo (épaisseur 160μ).

Au sein du combustible, on observe des inclusions blanches déjà identifiées [3] comme étant des produits de fission solides Mo, Ru, Cs et Zr.

2.6. Collecteur et scellement métal-céramique.

Actuellement en cours d'examen.

2.7.

Les examens sur le collecteur et sur le scellement métal-céramique ainsi que l'étude de l'ensemble UO_2 - Mo - W à la microsonde de Castaing et la mesure du travail de sortie (T.E.E.M.) de la surface émettrice permettront de compléter ces examens.

On espère ainsi mettre en évidence l'interaction UO_2 - Mo et connaître l'importance de la zone de diffusion Mo - W. Cette étude permettra également de rendre compte d'une diffusion éventuelle, à travers la gaine Mo - W, des produits de fission ou de l'uranium libre.

2.8. Références.

- [1] BAZIN, MANSARD, MONIER, VIGNESOULT, Rapport LECI/CEA à paraître - 1968.
- [2] ALLEAU, T. ; CLEMOT, M. ; HASSON, R. , "Post mortem examinations of thermionic emitters " - Palo Alto Conf. 1967.
- [3] BRADBURG, B.T. ; DEMANT, J.T. ; MARTIN, P.M. ; POOLE, D.M. "Electron probe micro-analysis of irradiated UO_2 " - Journal of Nuclear Materials, 17 - 1965.

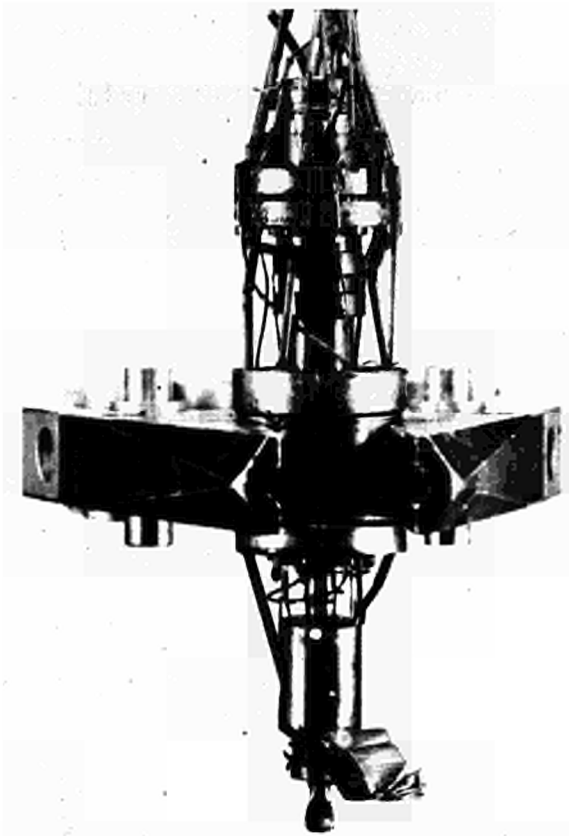


Fig.1 - Convertisseur SIRENE 302

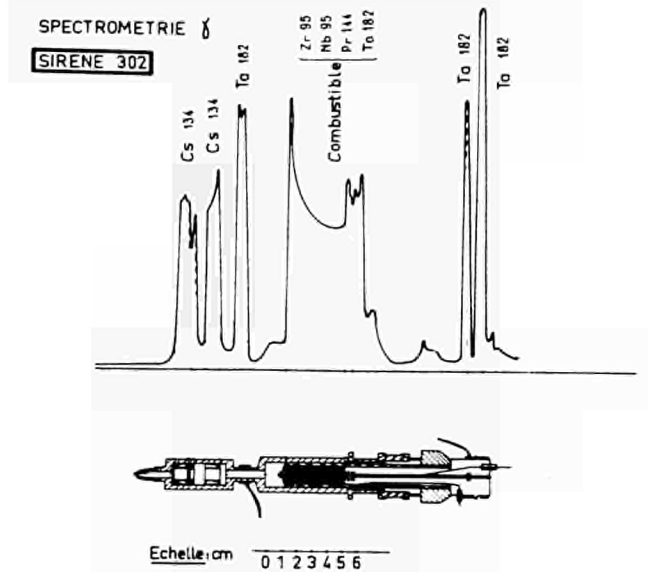


Fig.2 - Spectrométrie γ

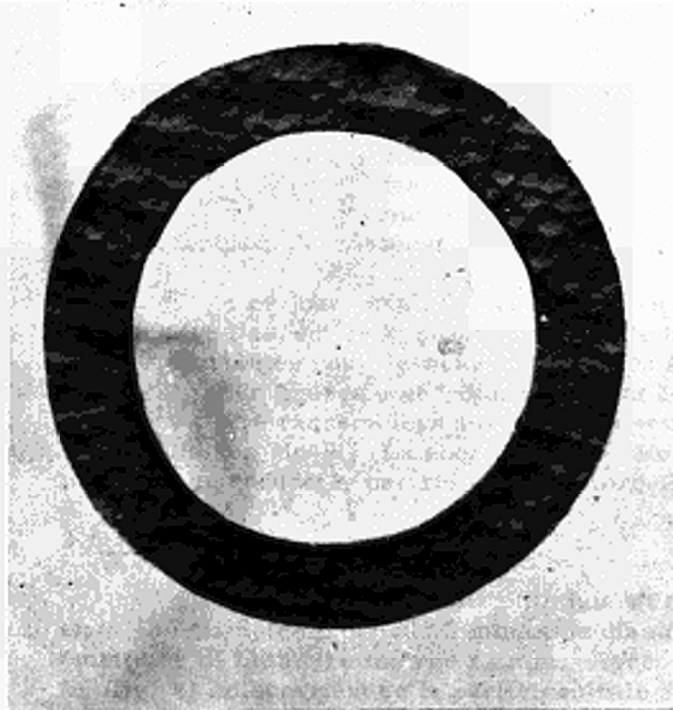


Fig.3 - Bloc graphite-césium



Fig.4 - Emetteur

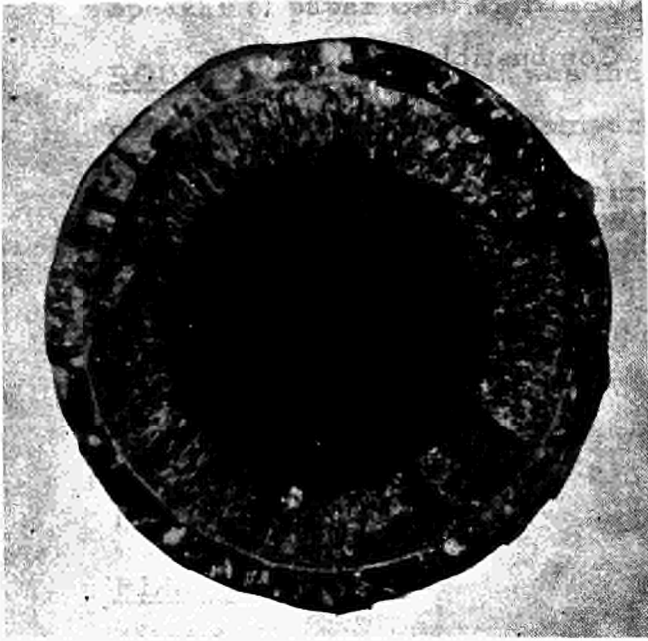


Fig. 5 - Coupe de l'émetteur

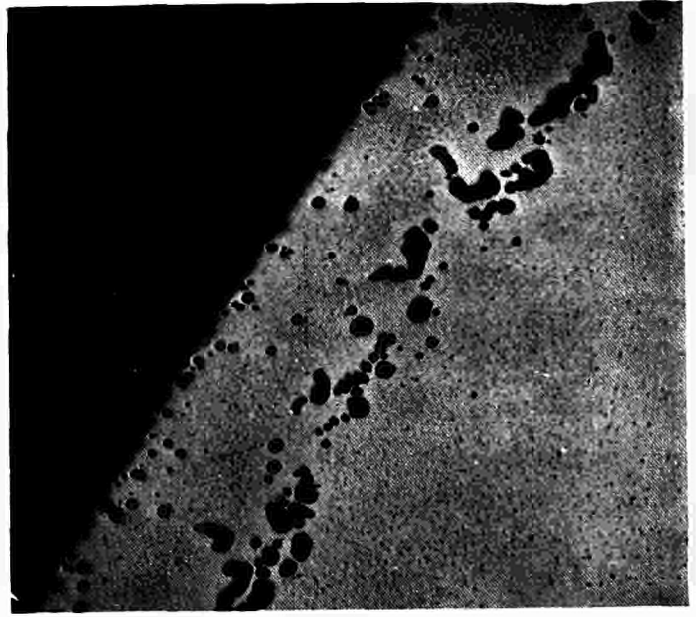


Fig. 6 - W - Mo - partie supérieure



Fig. 7 - W - Mo - partie centrale



Fig. 8 - W - Mo - partie centrale

Molybdène	Zone d'interaction	Combustible UO_2
-----------	-----------------------	---------------------------



Fig. 9 - Contact Mo- UO_2 - Structure basaltique du combustible

DISCUSSION

Speaker of paper C-5: J. BLIAUX.

ROUKLOVE (USA): What was the longest thermal shock time and did the converter revert to room temperature?

BLIAUX (France): Pendant l'arrêt du réacteur il est certain que le convertisseur a dû redescendre aux alentours de 16 à 20°C. Ce sont des arrêts qui durent 4 jours toutes les trois semaines, plus les durées de contrôles des résistances thermiques qui sont effectués hors-flux.

DEVIN (France): J'ai une question sur la durée de vie des thermocouples de l'émetteur et du combustible et sur le gradient thermique mesuré entre l'extérieur et l'intérieur.

BLIAUX: En ce qui concerne le gradient thermique on a pu mesurer dès le début de l'ordre de 450°C. En ce qui concerne l'évolution des thermocouples, dans l'expérience 302 le thermocouple émetteur a duré assez longtemps, mille heures. Dans l'expérience 304 dès le début les deux thermocouples ont évolués très nettement. La seule chance qu'il nous ait été donnée, c'est que les deux thermocouples ont évolués par hasard parallèlement, ce qui a permis de conserver le gradient et de faire des vérifications de flux thermique à travers l'émetteur pendant 200 à 300 heures.



LABORATORY LIFE TEST AND INPILE IRRADIATION STUDIES
OF CYLINDRICAL THERMIONIC CONVERTERS *)

A.Jester, F.Gross, H.Holick, R.Krapf and R.Zöller
Brown, Boveri & Cie, AG, Mannheim
Central Research Laboratory, 69 Heidelberg, Postfach 206

Summary

For the development of the ITR-project (Incore Thermionic Reactor) a preliminary test program has been started to demonstrate life time and performance of cylindrical thermionic converters.

A first generation of diodes has been tested in the Reactor Ispra I in cooperation with the Direct Conversion Division of the Ispra Research Center of Euratom. A second, more advanced version of diodes has been studied in the laboratory, where 5600 hours life time have been achieved, and in the FR 2 Reactor of the Karlsruhe Nuclear Research Center, with now 1250 hours of operation.

Typical design and operation data of the diodes are:

emitter area	: 20 cm ²
emitter material	: molybdenum
collector material	: molybdenum
electrode spacing	: 0.17 mm
fuel	: uranium dioxide 90 % enriched
emitter temperature	: 1800 ^o K - 1900 ^o K
collector temperature	: 900 ^o K
electrical output	: $\geq 5\text{W}/\text{cm}^2$
efficiency	: 10 %

* This work was supported by the German Bundesministerium für wissenschaftliche Forschung.

Introduction

For the development of the ITR-project [1] (Incore Thermionic Reactor) a preliminary test program has been started to demonstrate life time and performance of cylindrical thermionic converters.

With a first type of diodes series of laboratory tests and two irradiation experiments in cooperation with the Direct Conversion Division of the Ispra Research Center of Euratom were performed [2, 3, 4, 5]. A lot of experience in converter technology and physics was gained with this type of diodes. Hence, a more advanced version of cylindrical diodes could be developed and is being tested now in laboratory and inpile tests. 5600 hours of operation in the laboratory and 1250 hours in the FR 2 Reactor of the Karlsruhe Nuclear Research Center have been achieved. Both diodes are still operating satisfactorily. Further life tests in the laboratory with single diodes and irradiation tests of series connected diodes are scheduled to be started during the next few months.

Converter design and processing

A cross section of the first type of diodes is shown in Figure 1. The waste heat at the collector is removed by heat conduction across a heat bridge. The collector temperature can be controlled by means of additional coaxial heaters. For more details see [2, 3, 4, 5].

The above mentioned design has several disadvantages: To remove the waste heat from the collector to the copper block strain-free, to match the thermal expansion differences and to equalize the temperature profile along the collector axis, a rather complicated structure of flexible heat bridges was necessary.

The use of structure materials like copper limits brazing temperatures to less than 1000°C . During the processing of the diodes (machining, grinding etc.) it is difficult to keep all parts free from dirt, which makes it desirable to outgas them at temperatures as high as possible. Therefore the use of low melting materials is not very favorable.

These considerations yielded to a new version of diodes which is shown in Fig. 2. The waste heat is removed from the collector by heat radiation from 36 radially arranged molybdenum-fins to the same number of water cooled interlocking copper-fins. For better heat transport the emissivity of the molybdenum- and copper-fins is increased by coatings of zircon powder and nickel-oxyde powder respectively. This kind of heat rejection by radiation allows to vary the power throughput in a wide range with only small changes in collector temperatures because of Boltzmann's T^4 -law. Typical corresponding data are $T_c = 640^{\circ}\text{C}$ at 1050 W power throughput, and $T_c = 748^{\circ}\text{C}$ at 1515 W. Further advantages of this type of heat rejection are: constant temperature along the collector axis; no mechanical contact between collector and cooling system, i.e. no strains by different thermal expansions; possibility of cooling series connected diodes without insulating collector sandwich systems.

The emitter consists of polycrystalline molybdenum with 16 mm O.D. and 40 mm length, thus giving an emitter area of 20 cm^2 . Collector material is also molybdenum. Under operational conditions the electrode spacing is 0.17 mm. The centering of the emitter is accomplished at the upper end by a molybdenum tube which also serves as optimized emitter lead and at the lower end by a diaphragm free to slide in a ceramic ring.

In case of laboratory tested diodes, 4 black body holes of different depth are drilled into the emitter wall for pyrometrically measuring the emitter temperature profile. Nuclear heated diodes contain about 5-6 g uranium dioxide.

powder within 15 bore holes in the emitter wall, Fig. 3. The maximum density of the fuel in the holes is about 50 % theoretically possible.

The central hole of 9 mm diameter, allows the insertion of a tungsten filament, which was used for electrically heating the emitters of both laboratory and nuclear heated diodes. In the latter case the tungsten filament is also successfully used as resistance thermocouple to measure the emitter temperature during irradiation. Another method to determine the emitter temperature with an accuracy of $\pm 50^{\circ}\text{C}$ is based on plasma physical considerations suggested by N.S. Rasor and described in [4] .

The development of the metal-ceramic seal was proceeding in several stages. The alumina E 2 from Feldmühle, which is not resistant against cesium attack, was replaced by the high purity alumina E 37 from the same company. Cesium attack was also responsible for the change from the molybdenum-manganese metalizing to the more reliable tungsten metalizing. The ceramic ring is brazed by means of copper-2%nickel to 0.2 mm thick niobium sheets. The total design of the metal-ceramic seal includes heat resistances combined with heat capacities to protect the seal against temperature shocks.

Experience was gained, that with outgassing of the diode structure materials at elevated temperatures and operating the diodes itself under clean vacuum conditions (10^{-6} torr or better) reproducibility of converter output data and long life time is achieved. The finally assembled diodes are outgassed in an ion getter pumped all metal vacuum system with the vacuum pressure never exceeding 10^{-6} torr while increasing the electrodes temperatures above their finally operational temperature. After this outgassing process, which takes several days, the diode is closed and the connection to the cesium reservoir is opened in a single vacuum brazing step.

Laboratory studies

During the last year a total of 4 heat radiation cooled diodes have been life tested in the laboratory. The results are listed up in Table I.

Table I.

Diod.No.	T _E	[°C] Emitter-Material	Ceramic Seal	Life-Time [h]	Remarks
1	1600	sintered moly.	E2 Mo-Mn	300	ceramic destroyed, emitter shrinkage
2	1600	"	E2 Mo-Mn	300	vacuum diode, emitter shrinkage
3	1600	arc cast moly.	E37 Mo-Mn	1100	leak in metalizing
4	1600	"	E37 Mo-Mn	5600*	still operating

* valid for electrodes and ceramic seal, because of an exchange of the cerium reservoir at 3000 h.

Diode 1 failed after 300 hours because of a leak of the metal ceramic seal. Post operational examinations showed gross attack of the ceramic by cesium vapor. A check of the outer and inner emitter diameter yielded a 0.07 - 0.08 mm smaller value as before operation. No emitter material, however, could be found on the collector surface. Hence, the sinter molybdenum emitter obviously was shrinking during the operation. Diode 2, which was operated under the same conditions but as a vacuum diode yielded the same shrinking effect.

These experiments resulted in using arc cast molybdenum as structure material for the emitter instead of the sintered material and the high purity ceramic E37 instead of E2.

Diode 3 operated 1100 hours, producing about 100 W electrically without degradation, and failed after this time by loss of cesium through a leak in the metalizing of the ceramic seal.

A leak in the diode, allowing cesium to diffuse into the outer vacuum container can easily be detected: The tungsten filament heating the emitter by electron bombardment, is operated in the space charge mode. Cesium atoms reaching the central emitter hole are getting ionized by surface ionization and trapped near the negatively charged tungsten filament, causing a change in the current-voltage characteristic of the bombardment arrangement.

Diode 4, which was running under the same conditions as Diode 3, developed a leak in the final copper brazing joint after 3000 hours. A new cesium reservoir was welded to the diode, and after a new outgassing process, operation was started up again. Meanwhile 5600 hours of operation for the electrodes and the ceramic seal have been achieved.

With each diode to be tested, measurements of the vacuum work function of the emitter and of the electrical output for a number of emitter temperatures have been performed. All diodes yielded nearly identical data independent of the type of the molybdenum used as emitter material. The measured vacuum work functions range from 4,33 eV to 4,44 dependent on the emitter temperature. The electrical output data are shown in Fig. 4. The curves drawn in the figure are calculated power versus voltage curves. The data are taken from the envelopes of current-voltage characteristics with different cesium reservoir temperatures.

Irradiation Studies

Since 1966 three irradiation tests have been performed, which are listed in Table II.

Table II

Test No.	Reactor	Irradiation time [hours]	Remarks
1	Ispra I	30	leak in vacuum container
2	Ispra I	100	leak in vacuum container
3	FR 2 Karlsruhe	1250	still in operation

For the irradiation test to be performed in the reactor Ispra I two identical setups with diodes of the first generation have been built. The first test and its results are described in [4]. Because of the difficulties arising with an ion getter pump operating in the zone of high γ -flux the second setup was modified. The ion getter pump was taken out of the zone of high γ -flux by brazing it to the collector cooling tube at the lower end of the shielding plug. This arrangement showed improved performance when tested in November 1967, Test No. 2, Table II. After 100 hrs of successful operation the test failed by a leak in the vacuum container developing during the cooling period after an external reactor shut down. In both irradiation tests in Ispra no defect on the diodes could be observed. It was learned that the auxiliary experimental devices, such as the vacuum container with its feed throughs and demountable flanges and the pumping system, must be very carefully designed with respect to heat production by the γ -flux in the reactor.

For the inpile experiments to be performed in the Karlsruhe Nuclear Research Center the central irradiation channel of the FR 2 Reactor was available. With 130 mm diam. for the vacuum container and 200 mm diam. for the shielding plug, compared to 104 diam. of the Ispra irradiation channel, it was easier to design a relatively simple and therefore reliable test rig for the diodes.

Fig. 5a shows a cross section of the vacuum container with a heat radiation cooled diode inside. The waste heat from the collector and main part of the γ -heat is removed by the collector watercooling circuit. The high current feed-throughs, which are connected to the emitter base, are cooled by a separate electrically insulated water circuit. The nickel tubes of both water cooling systems serve also as high current leads. The vacuum container is pumped through a 1 1/2 "stainless steel tube by a watercooled ion getter pump (11 l/s), which is protected against γ -heating by a γ -shielding plug as can be seen in Fig. 5b. This device is connected to a main shielding plug; its lower end can just be seen in the figure. The FR 2 Reactor generally operates at a constant power of 44 thermal MW. As it is desirable to control the fission heat production in the emitter, the total experimental setup can be driven up and down within a range of 50 cm by a screw elevator. This arrangement allows to vary the heat production by a factor of ten. Riding with the emitter on the steep neutron flux slope results in neutron flux differences along the emitter axis of up to 20 %. The neat production in the emitter, however, will be equalized by sublimation of uranium dioxide along the bore holes to give constant fuel surface temperature [6] .

The emitter of the diode for Test 3 was fueled with 5,9 g 90 % enriched uranium dioxide with a bulk density of 48 %. The O/U ratio was determined to 2.003.

Results

The results of Test I have been described in [4]. Out of pile measurements of output data with electrically heating the emitters of the Test 2 and Test 3 diodes are shown in Fig. 6. The thin lines are I-V-curves for constant emitter temperatures taken with an AC-supply; the thicker ones are those with constant power input taken with a DC-supply. The dashed lines are measured efficiencies taking into account the total power input into the filament and the net power output at the cold ends of the electrodes. These output data are essentially higher than those obtained with unfueled laboratory type diodes (Fig. 4). The characteristic difference between fueled and unfueled diodes is the lower optimum cesium temperature for the fueled type, from which one can conclude that the bare work function of the fueled emitters is higher. Due to former measurements by L.N. Grossmann [7], it is assumed that excess oxygen is diffusing through the emitter wall and building up a cesium oxide layer on the collector surface, which acts then as an additive source. This assumption is confirmed by measurements taken during the Ispra Test 2 presented in Fig. 7. At constant power input and constant cesium reservoir temperature the emission characteristic of the emitter changed by varying the collector temperature, i.e. varying the additive pressure. This additive effect proved to be stable within the attained operation time of 1250 hours in Test 3 in Karlsruhe.

In pile Test 3 was started in March 1968 by stepwise diving the test rig into the reactor core until an output power of 100 W (0.65 Volt, 160 Amps.) was achieved. The corresponding temperatures of emitter, collector and cesium reservoir were 1600°C, 700°C and 350°C. Following to the starting up period the pressure reading of the vac-ion pumpmeter dropped to less than 10^{-7} torr. After 330 hours of operation the output power was reduced to 75 watts because of intermittent shuntings of

the leads outside the vacuum container, probably caused by a thermocouple sheet touching the emitter lead.

At the end of May 1250 hours of operation have been achieved with 110 KWh produced. This corresponds to a burn up of about 7800 MWd/to.

Acknowledgements

The authors wish to express their appreciation to Dr. H. Neu, Dr. C.A. Busse and Dr. H. Strub of the Ispra Nuclear Research Center of Euratom and to Dr. H. Oehme, Dr. W. Marth and Mr.G. Harbauer of the Karlsruhe Nuclear Research Center for supporting design and performance of the inpile experiments.

List of references

- [1] ANDRAE, H.; BUDNICK, D.; GROSS, F.; JAHNS, W.; JANNER, K.; JESTER, A., "The incore thermionic reactor as a space power source". This conference.
- [2] GROSS, F.; HOLICK, H. and JESTER, A., "Out pile test results of a cylindrical converter with a molybdenum emitter". Internation. Conference on Thermionic Electrical Power Generation, London 1965.
- [3] GROSS, F.; HOLICK, H. and JESTER, A., "Ein thermionischer Energiewandler mit zylindrischen Elektroden". BBC-Nachrichten Bd. 48 (1966) H.3.
- [4] JESTER, A.; GROSS, F.; HOLICK, H. and BUSSE, C.A., "A nuclear heated thermionic converter". Thermionic Conversion Specialist Conference, Houston/Texas, 1966
- [5] JESTER, A.; GROSS, F.; HOLICK, H.; KRAPP, R. und BUSSE C.A., "Bestrahlungsversuch an einem nuklear beheizten thermionischen Energiewandler". BBC-Nachrichten Bd. 49 (1967), H. 10.
- [6] GROSS, F. and WINKENBACH, H., "Irradiation studies with UO₂-fueled molybdenum emitters". Thermionic Conversion Specialist Conference, Houston/Texas, 1966.
- [7] GROSSMANN, L.N., "Uranium oxide fuel for thermionic energy conversion". AIME Conference on High Temperature Nuclear Fuels, Lake Lawn Lodge, Delavan, Wisconsin, Oct. 3.- 5, 1966.

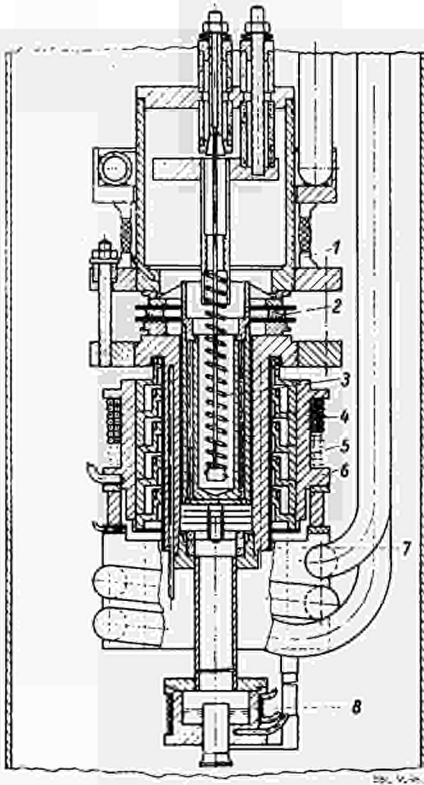


Fig. 1: Cross section of the first type of diodes

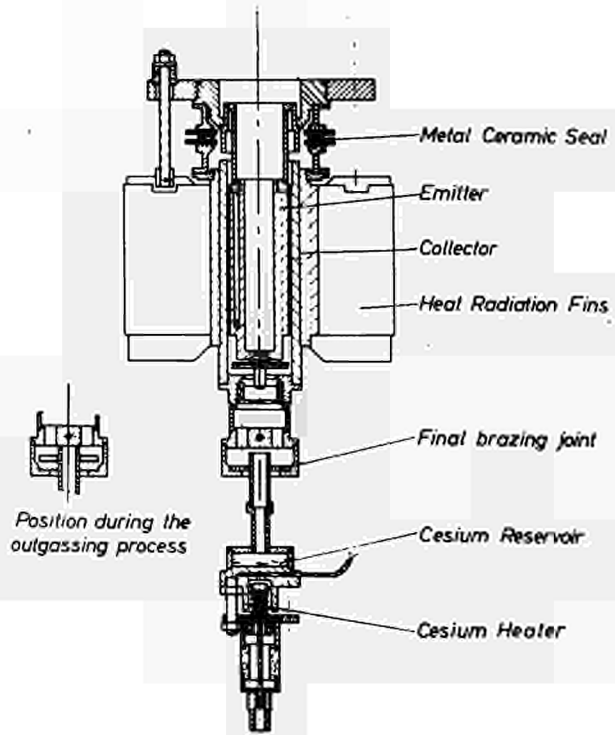


Fig. 2: Cross section of the second type of diodes

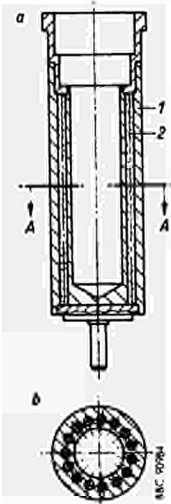


Fig. 3: Cross section of the emitter fueled with UO_2

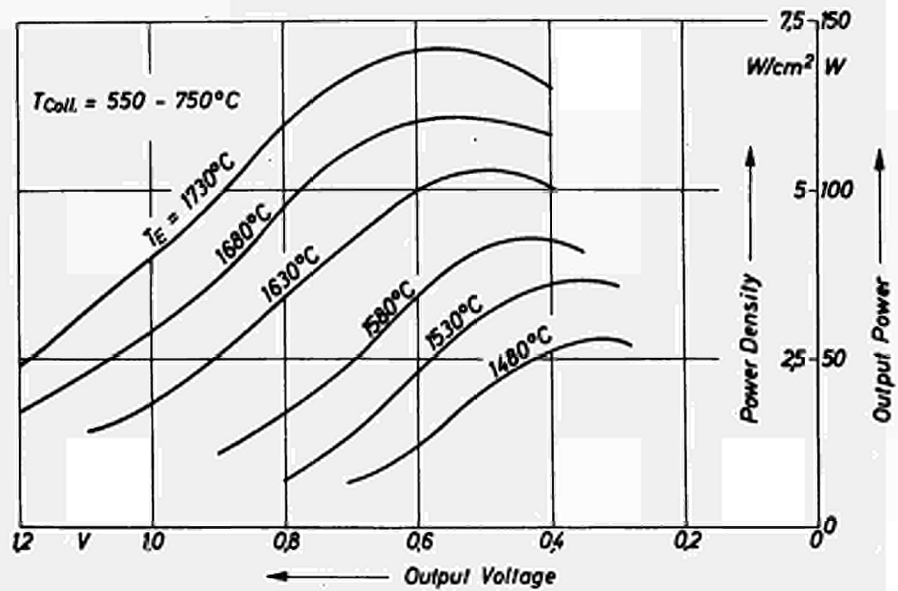


Fig. 4: Output power versus voltage curves optimized with respect to cesium temperature

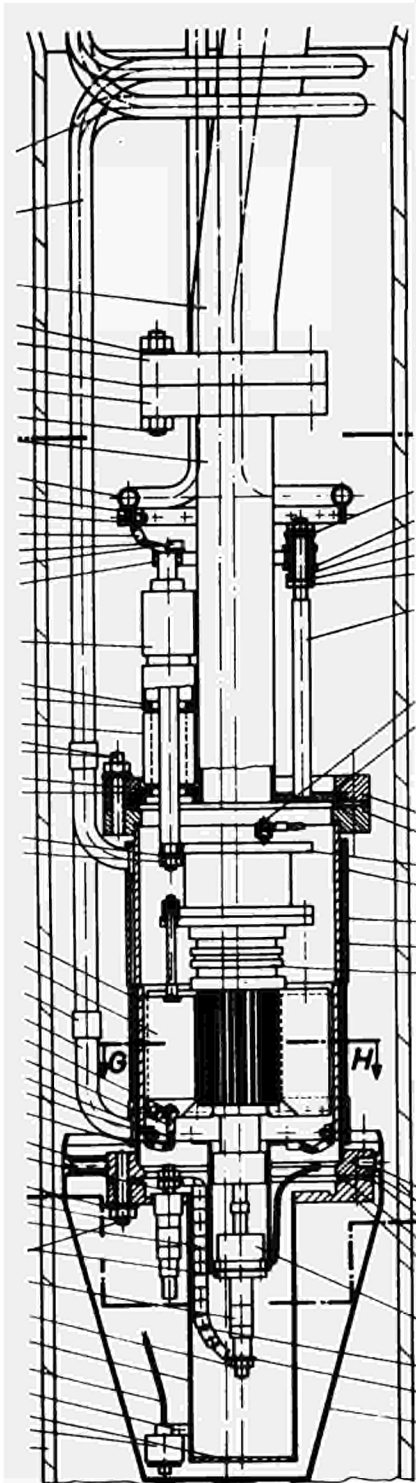
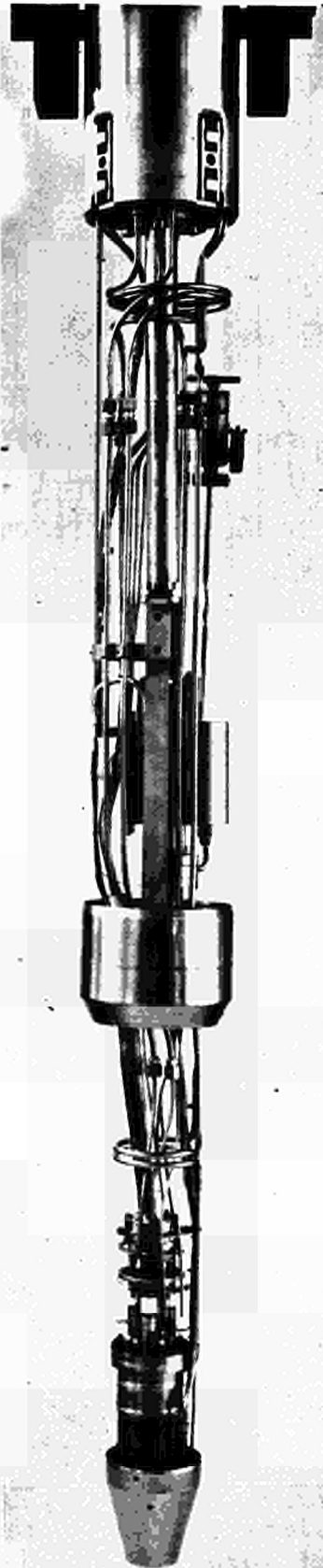


Fig.5a: Cross section of vacuum container with a diode inside



Main shielding plug

Watercooled ion getter pump

γ shielding plug

Vacuum container

Fig.5b: Photograph of the irradiation test rig with part of the main shielding plug

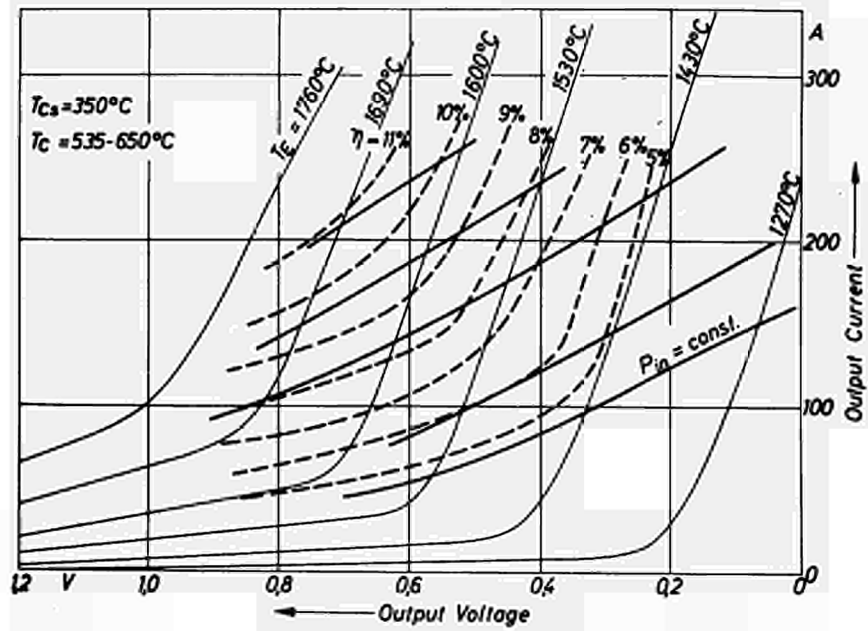


Fig. 6: I-V-curves for constant emitter temperature (thin lines); for constant power input (thick lines); curves of constant efficiency (dashed lines).

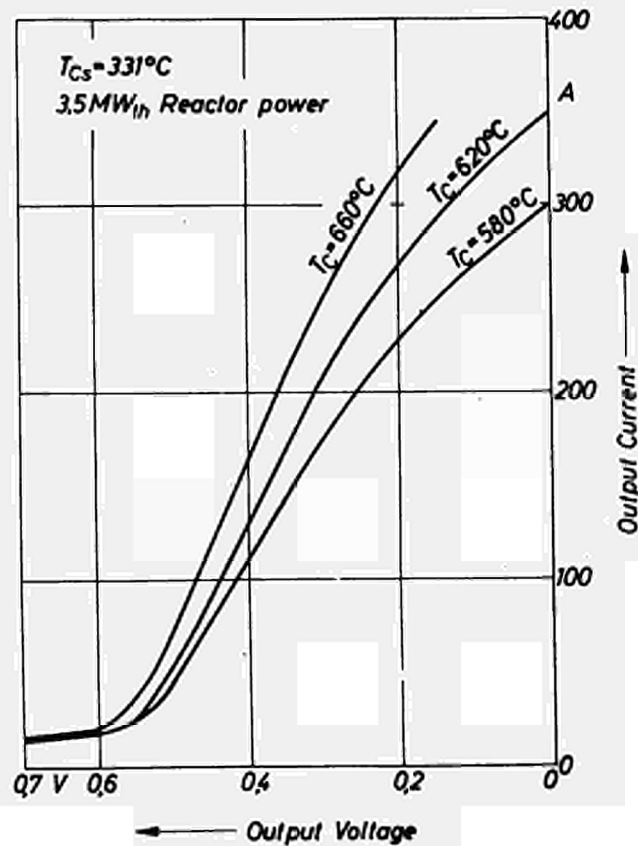


Fig. 7: I-V-curves at constant emitter and cesium temperature with varying collector temperature

DISCUSSION

Speaker of paper C-6: A. JESTER.

SCHOCK (USA): In your radiation cooled diodes how do you control the collector temperature?

JESTER (Germany): We don't control it, but because of the Boltzmann T^4 -law the collector temperature is a smooth function of power throughput. For a low emitter temperature you have a low collector temperature and this is also optimal for operation.

RASOR (USA): There was a larger fission product retention in the UO_2 than would be inferred from the other results that we heard this morning. Could you make the comparison and if it is different do you have an explanation for it?

JESTER: As far as I remember this was a 1200 hour test and if you look at RANKEN's data for 1200 hours you would not expect more than 60% fission gas release, which was measured.

CAMPBELL (USA): In your last slide you showed a set of I-V curves with the output power as a function of collector temperature. Was there any way during the test that you could separate out the effect of adjusting the collector temperature to optimize the collector work function for highest voltage output as distinguished from the possibility of returning oxygen to the emitter in the form of cesium-oxide? Are you able to distinguish between these two possibilities?

JESTER: With the second type of diodes we could not optimize the collector temperature; with the first type we tried it. But these diodes were all fueled so we could not distinguish these effects. I have some curves which show it much clearer which were taken in the laboratory. There you could see in the I-V curves that the saturation current is increased by increasing the collector temperature.

POST IRRADIATION INVESTIGATIONS OF UO_2 -FUELED
THERMIONIC EMITTERS*

F. Gross and R. Zöllner

Brown, Boveri & Cie, AG, Mannheim
Central Research Laboratory, 69 Heidelberg, Postfach 206

Summary

In a previous paper [1] two irradiation experiments with UO_2 -fueled molybdenum emitters and the preliminary post irradiation investigations were described (emitter I and IIa). In the meantime the investigations were completed by evaluation of released fission gases and and metallographic examinations of the second emitter in the second experiment (emitter IIb). The results are compared to an out of pile laboratory test (emitter III).

Operation conditions

In the first test one molybdenum emitter (emitter I), filled with UO_2 -powder, was irradiated for 200 hours at a temperature of 2000°K in an isotope loop of the reactor FR2 of the Nuclear Research Center Karlsruhe, showing no gross reactions between Mo and UO_2 .

In the second experiment two molybdenum emitters (emitter IIa + IIb), filled with molybdenum-coated UO_2 -particles, were irradiated for 1250 hours at 2000°K . It was expected that this fuel would give better results regarding to fission gas release and temperature rise in the fuel. Because most of the particles were damaged and deformed after irradiation, for comparison a third test with the same particles and emitter material (emitter III) at equal conditions (1250 h, 2000°K) was performed outside the reactor. The nuclear heat was simulated by

* This work was supported by the German Bundesministerium für wissenschaftliche Forschung

electrically heating the test emitter by a tungsten filament, inserted in a central hole. The fuel was filled in an annular slot.

By this set up similar temperature conditions as in the second reactor experiment were achieved, where the fuel was inserted in some bore holes in the emitter wall. But there exists a difference in heat production between both cases: in the reactor experiment the heat is generated in the inner particle region, producing a temperature gradient in the UO_2 from the center to the wall of the particles. In the laboratory experiment the heat is generated outside, giving rise to a radial temperature drop along the particle shell. In addition the temperature profile in the bore holes is parabolic, whereas in the annular slot it is of logarithmic kind. The temperature distribution in the fuel matrix cannot be calculated, because the thermal conductivity is not known. Heat transfer in the matrix is due to radiation between neighbouring particles and heat conduction along the touching points of the Mo-coatings. Because the number and size of the contact points change with time due to recrystallisation processes, no constant thermal conductivity can be given. The emitter geometry of the out of pile test was calculated, so that temperatures at the inner and outer wall of the slot are corresponding to those at the center and at the boundary of the holes in the second reactor experiment. Table I shows the conditions under which the experiments were performed. Some deviations arise from the previous published data, which are due to calculations, performed with more exact data for γ -heating of the emitters. It is assumed that γ -heating is proportional to the neutron flux and yields $0,3W/g$ at a neutron flux of $10^{13}n/cm^2$ sec. (In the previous paper [1], instead of the mean neutron flux the maximum neutron flux in the loop, was listed.) The emitters were run at $2000^{\circ}K$ ($\pm 50^{\circ}K$) in all cases, the O:U ratio being smaller than 2,005. The heat flux at the Mo-fuel interface was about $40 W/cm^2$.

Table I
Operation conditions

Emitter	Fuel	Enrichement	Power Watts	Time hours	Burn-up Mwd/toU	Mean N. Flux n/cm ² sec.
I	UO ₂ -pow- der	90% U-235	360	200	2200	0,75 · 10 ¹³
IIa	Mo-coated	} 35% U-235	250	1250	15000	2 · 10 ¹³
IIb	UO ₂ -par- ticles					
III			900	1250		

Post irradiation investigations

One part of the post irradiation investigations is described in the paper named above. For completeness the applied methods and the results are listed here.

After some weeks cooling time the emitters were photographed and the dimensions were controlled in hot cells of the Nuclear Research Center Karlsruhe.

Emitter I remained vacuum tight, the fission gas reservoir of emitter IIa was destroyed during dismantling the reactor thimble, so that no fission gas determination was possible. Emitter IIb showed little grooves at the upper end of the fission gas reservoir, probably causing fission gas leakage.

Molybdenum, dressed from the emitter surfaces, and material, dressed from the surrounding graphite cage, were examined radiochemically and by γ -spectroscopy for uranium and fission fragments. Qualitatively only Ta-182 and Co-60 could be detected at emitter I. Because the

fission yield of these fragments is very small ($\ll 10^{-5}$), the molybdenum must have been polluted by these materials. The contamination by Ta was due to Ta-mantled thermocouples. At emitter IIa and IIb Co-60 and Sc-46 was detected, which also can be explained by contamination of the emitter material.

By radiochemical analysis, using fluorimetric methods, no uranium diffusion through the molybdenum wall of the emitter within the limit of the method ($\ll 1$ ppm) could be detected.

Microprobe analysis of a coated particle at the emitter wall, taken of emitter IIb after irradiation, shows the same result. Figure 1 and 2 give photographs of integrated line-scannings compared to the image of absorbed electrons, figure 3. Point analysis, giving here a sensitivity better than 0,5 %, shows no uranium inside the Mo-coating.

The fission gases Kr and Xe, released or retained by the UO₂-fuel, were determined by gaschromatographic means. The limit of the method was given by the sensitivity of the γ -spectroscopy for Kr-85:

$$0,5 \mu\text{Ci} \hat{=} 0,01 \text{ mm}^3 \text{ Kr.}$$

Table II

	Emitter I (released gases)	Emitter IIb (retained gases)
Krypton	0,6 mm ³ \pm 5 %	27,5 mm ³ \pm 1,8 %
Xenon	3,8 mm ³ \pm 5 %	176,8 mm ³ \pm 0,5 %
Rare gases	4,4 mm ³ \pm 5 %	204,3 mm ³ \pm 0,6 %

Emitter I was pierced in a bell jar at a pressure of about 10^{-3} torr, the fission gas was swept out by helium and quantitatively measured. The results are shown in table II, giving the released or retended gases in mm^3 at normal conditions. With a theoretical production rate of $2,6 \cdot 10^{-5} \text{cm}^3$ for rare gases (1at, 0°C) per Watt and day the release rate yields 5,9 %. The deviation from 100 % is due to solution and adsorption of gases by the fuel.

To separate these two effects, fission gas determination of emitter IIb was performed in a heated, vacuum tight ceramic tube. After quenching off the fission gas reservoir, no fission gases could be detected, before and after heating the tube 4 hours at 1200°C . It was assumed that the channels between fuel holes and gas reservoir were jammed by diffused UO_2 . For that reason emitter IIb was suspended in a gas tight glass envelope and dissolved in nitric acid, until the fuel holes were open. Sweeping helium through the solution and gaschromatographic analysis of the gas mixture showed no fission gases. In a last stage a specimen, cut from emitter IIb, was dissolved and the retended rare gases were determined in the above mentioned manner. The results are also listed in Table II, corresponding to a fission gas retention of 61 % or gas release of 39 %. The free gases have probably leaked through the grooves at the upper part of the gas reservoir during the cooling time of about one year.

The metallographic examinations of emitter I and IIa are described in the previous paper [1]. In a similar manner metallographic cuts were taken of emitter IIb normal to the emitter axis. Figure 4 shows a fuel hole, filled with coated particles, after irradiation. Figure 5, 6 and 7 show enlarged views of some cuts (enlargement 200 x and 500 x). The coatings of the particles are partly destroyed, UO_2 has diffused and condensed at the wall of the fuel holes. The Mo-coatings have recrystallized, the grains of different coatings and the wall have grown together. By formation of thermal bridges the temperature increase in the matrix decreased. Due to formation of large crystal grains the tensile strength of the coatings has decreased, probably causing the damage. In the fuel, bubbles and cavities can be seen, the fuel is di-

vided in several separated districts, figure 5. The cavities probably retend most of the generated gases. The interfaces between fuel and Mo are sharp, no oxide phases or diffusion zones can be detected, figure 6. Some particles ($\sim 10\%$) showed neither UO_2 nor epoxy resin. (Epoxy resin is filled into the emitters before preparation and penetrates into empty and broken particles). This effect can be explained by removing the fuel during the cutting and polishing process. The generated fission gases cause a pressure build-up, by which the coatings are deformed. When grinding particles to less than a hemisphere the loose contact between fuel and coating permits the fuel to fall out.

These results are similar to those received with emitter IIa. But the particles of the latter were more damaged, and in consequence more fuel has condensed at the wall of the bore-holes. This is due to different neutron fluxes at emitter IIa and IIb.

The metallographic examinations of emitter III were also performed in hot cells of the Nuclear Research Center Karlsruhe. Figure 8 gives the cross section of emitter III, which has ruptured during preparation. Figures 9 and 10 show enlargements of different sections, as given in figure 11, which ran at different temperatures. At the hot zone (inner wall) nearly all particles are damaged, whereas at the cold zone (outer wall) the particles are attacked to a minor degree. The fuel has distilled to the outer wall. From figures 8, 9 and 10 it can be concluded, that the particles were damaged only under the influence of a thermal gradient. The Mo-coatings are sintered together and connected with the wall. They show large crystal grains. Oxide phases and diffusion zones at the Mo- UO_2 -interfaces cannot be detected, figure 12. The damage of the coated particles is probably due to a mass transport process, driving molybdenum from the hot side to the cold side of the slot. A diffusion of UO_2 through generated voids and grain boundaries of the coatings is connected with this process.

Conclusions

The results of the different examinations performed with different emitters agree in that:

1. no chemical reaction between Mo and UO_2 at the interfaces were detected.
2. no diffusion of U in Mo within the limits of the different methods was observed.
3. the fission gas build-up was lower than expected, caused by a high gas retention rate within the fuel.

Differences of the metallographic effects arise by the special operation conditions, for example different neutron fluxes at emitters IIa and IIb.

The performed tests have demonstrated the compatibility of the system UO_2 -Mo under reactor conditions up to a burn-up of 15.000 MWd/toU. For higher burn-ups, which must be obtained for operation times longer than one year, the pressure build-up by fission gases must be avoided. This can be done either by venting or providing large fission gas reservoirs.

The used coated particles seem not to give an improvement regarding gas retention, compared to pure UO_2 ; but it must be noticed, that different burn-ups are compared. The Mo-coatings did not stand the high thermal gradient during the in pile or out pile experiments, but were in both cases partially destroyed by a transport process.

Acknowledgements

The authors are indebted to the staff of the hot cells of the Karlsruhe Nuclear Research Center for performing the investigations of the hot probes.

References

- (1) GROSS, F.; WINKENBACH, H., "Irradiation Studies with UO_2 -Fueled Molybdenum Emitters". Thermionic Conversion Specialist Conference, Houston/Texas, 1966



Fig. 1 Electroprobe-micrograph of a coated particle (Uranium M_{β} -line, 350 x)

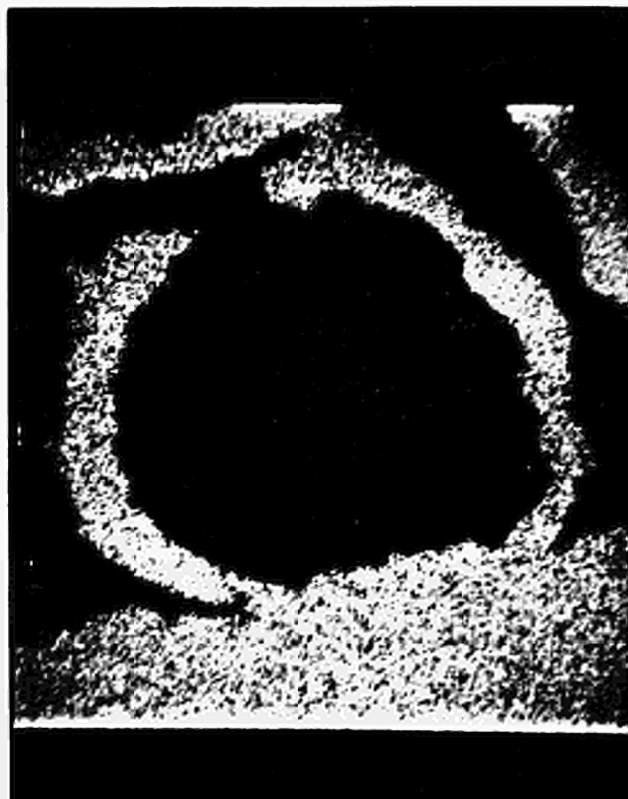


Fig. 2 Electroprobe-micrograph of a coated particle (Molybdenum L_1 -line, 350 x)

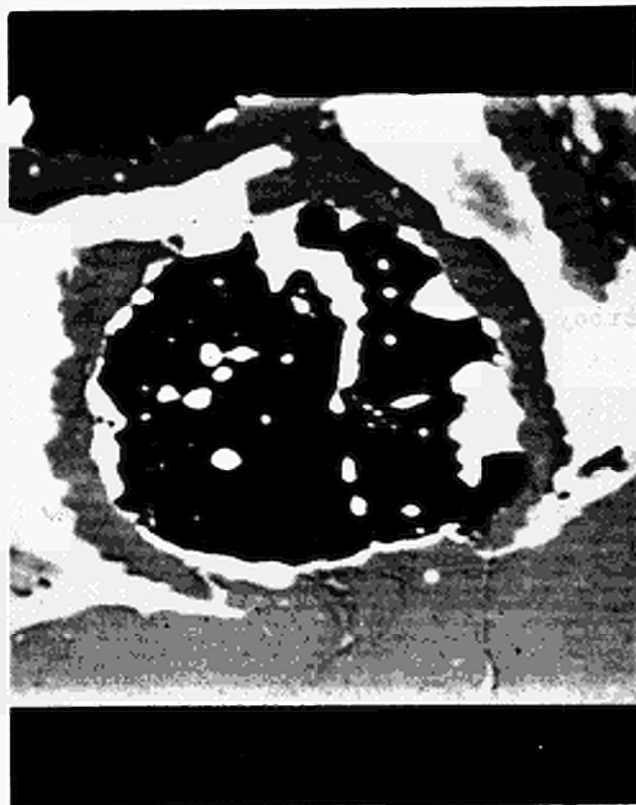


Fig. 3 Electron-micrograph of a coated particle (Mo and U, 350 x)

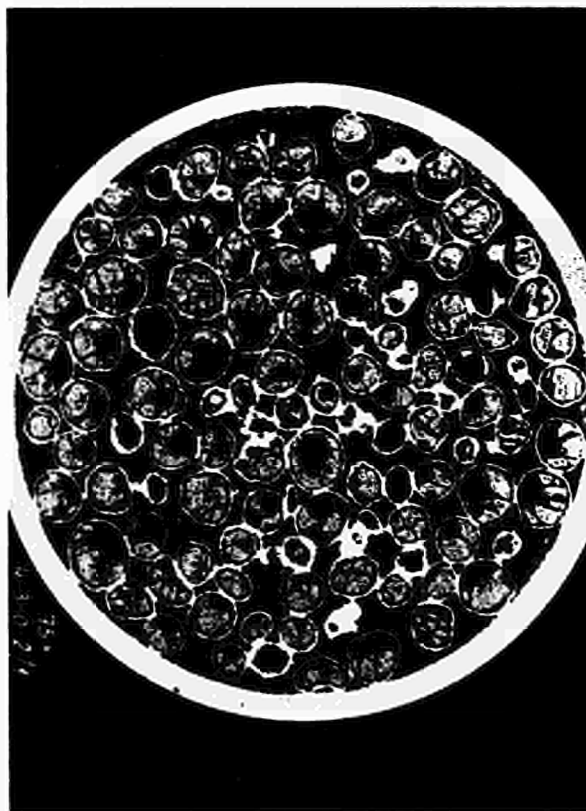


Fig. 4 Cross section of a fuel hole of emitter IIb after irradiation (50 x)



Fig. 5 Interface fuel-Mo (Section of fig. 4, unetched, 200 x)

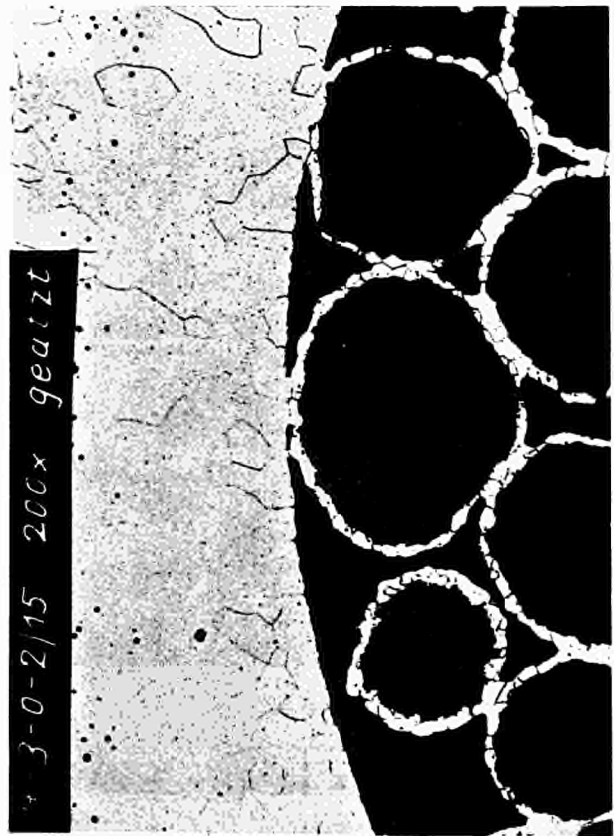


Fig. 6 Coated particles after irradiation, showing recrystallization of Mo-coatings (etched, 200 x)

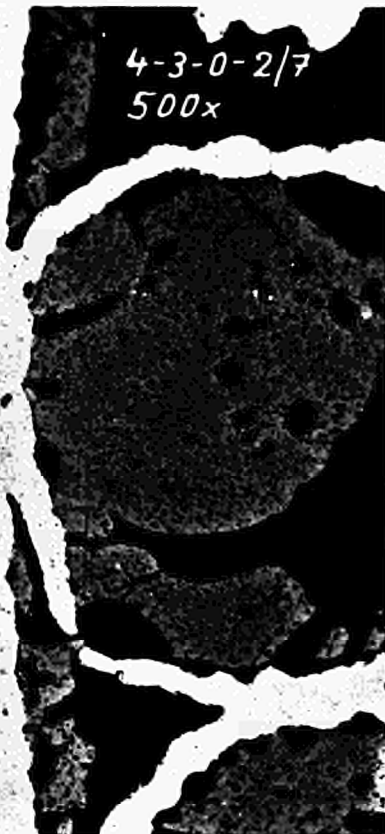


Fig. 7 Coated particle sintered to the emitter-wall (unetched, 500 x)

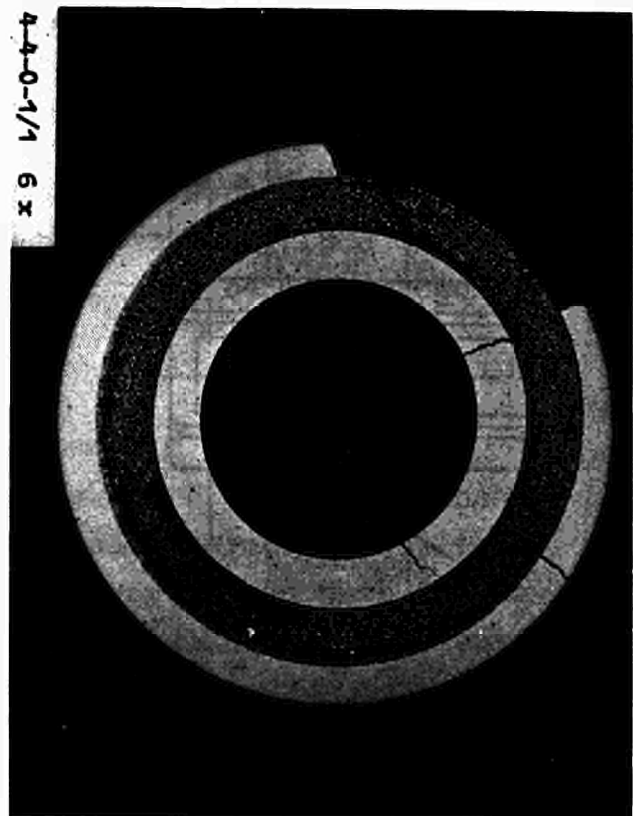


Fig. 8 Cross section of emitter III after heat treatment (4 x)

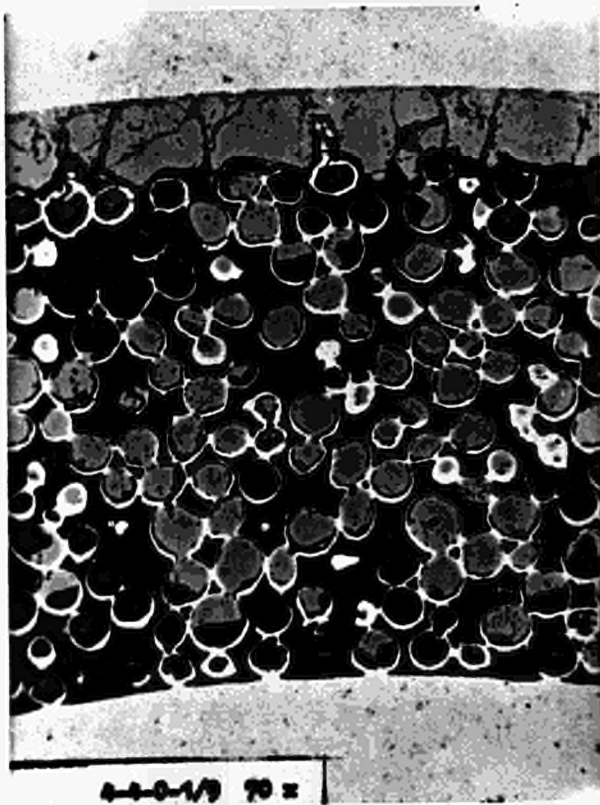


Fig. 9 Damage of coated-particles and distillation of UO_2 by influence of a temperature gradient (cut 4-4-0-1, fig.11)

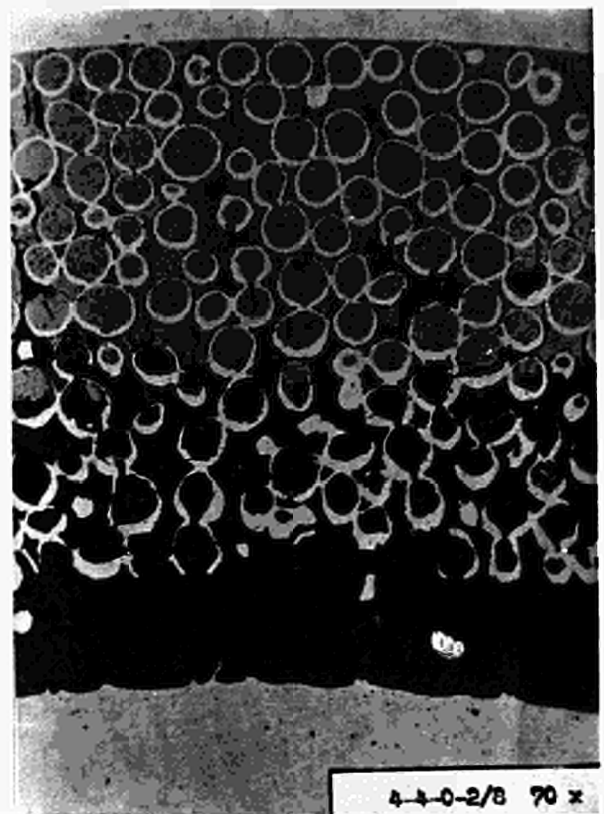


Fig. 10 Damage of coated-particles and distillation of UO_2 by influence of a temperature gradient (cut 4-4-0-2, fig.11)

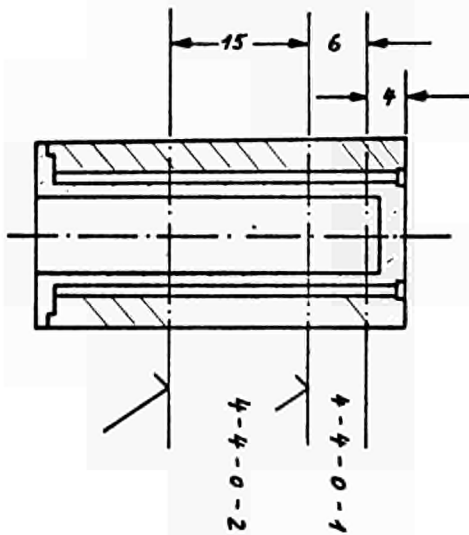


Fig. 11 Schematic of emitter III with positions of metallographic cuts

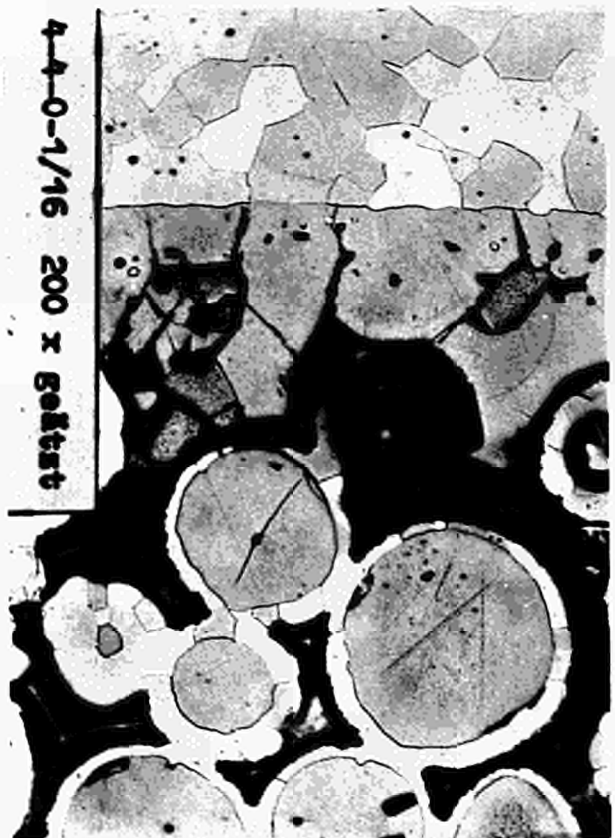


Fig. 12 Micrograph of the fuel-emitter-interface (etched, 200 x)

HEAT PIPE RESEARCH IN EUROPE *)

C.A. BUSSE
Euratom CCR, Ispra (Varese), Italy

INTRODUCTION

The heat pipe is a simple heat transfer device which can have an effective thermal conductivity a thousand times that of copper. This review deals with recent work on heat pipes in west european laboratories. Most of this work is somehow related to three practical questions:

- 1) How much heat can be transported with a heat pipe?
- 2) What is the maximum heating rate?
- 3) What is the life time of a heat pipe?

The different results will be discussed in this order.

HEAT TRANSPORT LIMIT

Fig.1 shows schematically a heat pipe. It consists of a vapor duct and a capillary structure saturated with a liquid. The heat is transported as latent energy in a two phase circulation: In the heated zone the liquid evaporates, the vapor flows along the heat pipe to the cooled zone where it condenses, and the condensate liquid returns through the capillary structure to the heated zone.

The heat transport limit of a heat pipe is characterized by insufficient return flow of condensate, resulting in a dry out of the heating zone. This transport limit can be calculated or measured.

Theory of the heat transport limit

To calculate the transport limit the pressure balance in the heat pipe has to be set up first. This balance means that the integral of the pressure gradient along any closed path in the heat pipe must be zero. The pressure integral consists essentially

*) Invited paper.

of three terms (see fig.1): They are the pressure drop in the vapor, the pressure drop in the liquid and the pressure differences across the curved liquid-vapor interfaces. This last term can easily be calculated from classical relations. What is more difficult to derive is the pressure drop in the liquid and in the vapor.

The liquid pressure drop depends on the capillary structure. Fig.2 shows some standard capillary structures:

- several layers of fine mesh screen fitted closely to the heat pipe wall
- open channels in the wall
- a screen at some distance from the heat pipe wall, leaving an annular space for liquid flow
- a screen inserted in corrugated form, so that the liquid flow channels become triangular
- channels in the wall covered with screen
- and finally a design, which is a combination of a tube for main liquid flow (the "artery") and a screen wick

Only the screen wick and the open channels present some difficulties in the calculation of the liquid pressure drop. In case of the screen wick, the problem is the complex structure of the wick. Therefore SCHMIDT (1967) has determined the pressure drop experimentally for a number of different screen wicks. Plotting a dimensionless pressure drop against the REYNOLDS number of the liquid, all data points fall on a single curve which corresponds to the general relation of BLAKE, KOZENY and ERGUN. From his data SCHMIDT derived a formula for the calculation of the pressure drop in screen wicks (see fig.3).

For open channels the difficulty in calculating the liquid pressure drop is the friction between the liquid and the vapor above the liquid, flowing in opposite direction. This problem has been analyzed by DI COLA (1968) (see fig.4). He found a linear relation between the liquid pressure drop and the friction pressure drop in the vapor. The proportionality factor in this relation is essentially the hydraulic diameter of the vapor channel divided by four times the depth of the liquid channel. This factor is generally large compared to one. This means that the pressure drop

in the liquid is generally much larger than the friction pressure drop in the vapor. Physically this can be understood as a sort of a hydraulic pressure transformation, which is due to the fact that the total cross section of the liquid channels is much smaller than the cross section of the vapor channel.

DI COLA's relation between the liquid pressure drop and the vapor shear on the surface of the liquid has experimentally been tested by BÄHR, BURCK and HUFSCHMIDT (1968) with water running down inclined rectangular channels. The vapor flow was simulated by blowing air over the channels in opposite direction to the water flow. For small flow velocities their data correspond closely to the theoretical relation of DI COLA. Deviations for larger flow velocities are provisionally explained by the authors by the formation of waves which they observed in the channels.

The third main term of the pressure balance is the pressure drop in the vapor phase. This term is theoretically the most difficult one, for a number of reasons. One reason is that the vapor flow is not a simple tube flow with a single velocity component, but is accompanied by evaporation and condensation on the tube wall. Therefore at least two velocity components have to be dealt with. Another reason is that both frictional forces and inertia forces occur in the vapor flow, and often neither force is negligible as compared to the other, so that both have to be taken into account. And finally, turbulence is important, and often practical heat pipes are operated close to the region of transition between laminar and turbulent flow.

While the theory of laminar vapor flow in heat pipes is sufficiently well advanced for most practical needs [7], little work has been done so far on turbulent heat pipe flow. Recently VAN ANDEL (1968) has made a synthesis of the theory of laminar heat pipe flow, of empirical relations for turbulent tube flow and of some turbulent heat pipe flow data (BOHDANSKY and SCHINS, 1965). He presented the result in the form of a diagram of the EULER number, shown in fig.5. The diagram permits to read the EULER number as a function of the REYNOLDS number and of the heat pipe geometry. The pressure drop in the vapor can hence be calculated very simply from the EULER number.

Having set up the pressure balance the heat transport limit of the heat pipe can be evaluated. This limit depends on the geometry of the capillary structure. Generally the capillary structure can be optimized for maximum heat transport. The result of such an optimization has been presented by VAN ANDEL (1968) in form of a useful nomogram (fig.6). It is based on the annular capillary structure consisting of a screen at some distance from the inner heat pipe wall and the (pessimistic) assumption that the liquid channel itself delivers the driving capillary force and not its screen cover made of relatively fine mesh. From the type of the working fluid, the operating temperature of the heat pipe, the effective length^{*)} and the diameter of the vapor channel the nomogram allows to determine easily the heat transport limit of the heat pipe. For instance, for a heat pipe of 2 cm diameter and 1 m effective length the heat transport limit for sodium at 800°C is 5 kW and for lithium at 1600°C 50 kw.

To conclude this discussion on the theory of heat transport limit, some work on the startup problems of heat pipes should be mentioned. When the temperature in the heating zone of a heat pipe is raised to the design value, there occurs frequently at lower temperatures a relatively large temperature drop along the heat pipe. At higher heating zone temperatures this non-isothermal mode of operation can change in two ways: Either the temperature drop decreases and the heat pipe enters a quasi isothermal mode of operation, or the temperature drop stays large and a dry out of the heating zone takes place. One of the start-up problems resides in the uncertainty of which of the last two operating conditions will occur. VAN ANDEL (1968) has shown that this depends essentially on the heat extraction from the heat pipe at a certain critical temperature; he derived a semi-empirical formula for the maximum tolerable heat flow at this critical temperature.

Finally, reference should be made to a useful critical collection of material data for the calculation of heat pipes (SCHINS, 1967).

^{*)} Effective length \approx half the length of the heating zone plus the length of the heat shielded zone.

Measurements of the heat transport limit

Experimental work on the heat transport limit has been done by BOHDANSKY, STRUB and VAN ANDEL (1966), by GAMMEL and WALDMANN (1967) and by SCHMIDT and SEMERIA (1968). These studies concerned sodium and lithium heat pipes, using as capillary structure either open channels or screen wicks.

In our laboratory we recently have measured a lithium heat pipe with channels covered by one layer of screen [8]. The results are shown in fig.7. The heat pipe was about 0.5 m long and had a cross section of less than 0.5 cm^2 . The maximum heat flow is plotted over the temperature of the heat pipe. The dots indicate the experimental values. At 1500°C the maximum heat transfer was about 7 kw, corresponding to a heat flow density of 15 kw/cm^2 . These data confirm the theoretically expected high performance of lithium heat pipes.

MAXIMUM HEATING RATE

If the heating rate of a heat pipe exceeds a certain value, boiling will occur in the capillary structure and hot spots may be formed in the heating zone in spite of the fact that the total heat input is still well below the transport limit of the heat pipe. Work on this effect has been done at the nuclear research center of Karlsruhe and in the Institut für Kernenergetik of the Technische Hochschule Stuttgart [12].

At Karlsruhe, DORNER, REISS and SCHRETZMANN (1967) used in their experiments sodium heat pipes, having as capillary structure open channels. The channels were 0.2 mm large and 0.4 mm deep and represented only 12% of the inner surface of the heat pipe. During operation of the heat pipe the channels were visible as slightly dark stripes. The heat pipe was heated with a very short RF coil. Using a transient method, DORNER, REISS and SCHRETZMANN determined for different heat pipe temperatures the power input where overheating just set in. Relating this power input to the surface of the liquid channels, they obtained the heat flux densities shown in fig.8. At 800°C , for example, overheating starts only at a heating rate of 2 kW per cm^2 of channel opening.

Boiling in a heat pipe with liquid channels was visually observed by BÄHR, BURCK and HUFSCHMIDT (1968) with an "inverse" heat pipe (fig.9), using water as working fluid. The inner wall of this heat pipe was a stainless steel tube with grooves on the outside, heated along the lower part and cooled along the upper part. The outer wall was formed by two concentric glass tubes between which hot air was vented to prevent condensation of water. The experiments showed that above a heating rate of 20 w/cm^2 bubbles and surface waves are formed and liquid is sprayed out of the channels. At still larger heating rates large bubbles occur and the channels dry out. After shut down the dried out channels are only rewetted when their temperature approaches the saturation value.

LIFETIME OF HEAT PIPES

Work on this question has mainly been done at Brown Boveri at Heidelberg, at CSF [1] and at our laboratory in collaboration with the Metallgesellschaft in Frankfurt [5,6,8]. We have studied heat pipes in the temperature ranges around 1000°C and 1600°C , aiming for a life time of 10.000 hours. In the 1000°C region no essential problem has been found so far. There is a number of very compatible heat pipe systems. For instance, in 1000 hour tests with Nb-1Zr/Na at 1100°C and Nb-1Zr/Cs at 1000°C , no corrosion of any type could be detected.

The situation in the 1600°C range is more problematic. For first screening tests we selected 3 wall materials and 5 working fluids (Nb-1Zr, Ta, W and Bi, Pb, Tl, Li, Ba). The resulting 15 combinations were life tested as heat pipes. In these first tests only two systems showed promise for a 10.000 hour operation, namely W/Li and W/Pb. But both are brittle and little suited for practical applications. All ductile heat pipes showed relatively strong corrosion.

The principal corrosion mechanism in heat pipes involves dissolution of wall material in the cooling zone and transport to the heating zone by the circulating working fluid. This wall material dissolution can be more or less selective. If it is not selective, the deposit in the heating zone has the same composition as the wall material. This is for instance the case in SGS-Ta/Tl heat pipes. One is shown in fig.10 after having been operated horizontally

for 2600 hours at 1600°C. This heat pipe is eroded in the cooling zone, and the mass deposit in the heating zone consists of tantalum. In this type of corrosion the heat pipe generally fails either because the capillaries in the heating zone got clogged or because the wall in the cooling zone got a leak.

If the dissolution process however is selective, only certain components of the wall material of the cooling zone are dissolved and accumulated in the heating zone. This process can come to a stand-still after the working fluid has extracted the critical components from the cooling zone. It can however happen that the accumulation of these components in the heating zone leads there to severe wall attack. This was observed with Li heat pipes and Nb-1Zr or Ta as wall material. These heat pipes fail at 1500°C or 1600°C often already after about 10 hours by wall perforation in the heating zone (see fig.10). We identified the critical wall material component in these two cases as oxygen. To inhibit this corrosion we tried three methods with success (see table 1).

Table 1 : Heat pipe life test results [8]

No.	wall material	filling	test conditions			observations
			temperature °C	time hr	heating rate w/cm ²	
1	deoxidized Nb-1Zr	Li	1500	1000	115	} no failure; Zr loss
2	Nb-1Zr	Li-13Ca	1500	1000	115	
3	SGS-Ta	Li	1600	1000	170	no failure

The first method was purification of the wall material. A heat pipe was built with Nb-1Zr, which was deoxidized down to an oxygen content below 1 ppm. This deoxidation was obtained making use of the corrosion process itself, which means that the heat pipe was built with the cooling zone material of another heat pipe which had already been operated, simply cutting away the defective heating zone. As a result this heat pipe did not fail after relatively few hours as before, but withstood a 1000 hour test.

As a second method it was tried to avoid the heating zone corrosion by trapping the extracted oxygen in the working fluid, adding to the Li some Ca, whose oxide has a very high free energy of formation.

Also this heat pipe withstood a 1000 hour test without failure. Though these tests demonstrate possibilities of corrosion inhibition, it seems doubtful whether Nb-1Zr can be considered as a construction material for long time operation at 1500°C (loss of Zr, large grain growth, some swelling).

The third method was to inhibit the oxygen extraction process. Here a very small addition of yttrium to tantalum proved to be very efficient. This material, known as SGS-Ta, showed no trace of oxygen corrosion at the end of 1000 hour test at 1600°C. There was only a very slight deposit of wall material in the heating zone (see fig.11). This heat pipe system is the most promising one for long life operation at 1600°C which we have found so far. If one takes into account that this heat pipe has been operated at a heating rate of 170 w/cm², and if one assumes that the mass deposit is proportional to the heating rate and the total time of operation, then one may hopefully extrapolate that in 10.000 hours at a heating rate of 50 w/cm² no serious clogging of the grooves would occur. However it has still to be demonstrated that no other problems arise in a 10.000 hour operation.

SUMMARY

If one tries to summarize the different results in the form of a rather general answer to the three questions put at the beginning of this review, one may say: Heat pipes allow to transport large amounts of heat with practically no temperature drop; heat transport rates up to 15 kw/cm² have been measured. Heat pipes can be heated at high heating rates without overheating, and there seems to be a good chance of finding ductile heat pipe systems with a life time of much more than 1000 hours, even at 1600°C.

REFERENCES

- [1] ARMAND, M., SHROFF, A.M.: "Résultats Préliminaires d'une Etude sur les Caloducs Haute Température", Proc. Second Int. Conf. on Thermionic Electrical Power Generation, Stresa (1968).
- [2] BAHR, A., BURCK, E. and HUFSCHMIDT, W.: "Liquid-Vapor Interaction and Evaporation in Heat Pipes", Proc. Second Int. Conf. on Thermionic Electrical Power Generation, Stresa (1968).
- [3] BOHDANSKY, J., SCHINS, H.E.J.: "Heat Transfer of a Heat Pipe Operating at Emitter Temperatures", Proc. First Int. Conf. on Thermionic Electrical Power Generation, London (1965).

- [4] BOHDANSKY, J., STRUB, H. and VAN ANDEL, E.: "Heat Transfer Measurements Using a Sodium Heat Pipe Working at Low Vapor Pressure", 1966 IEEE Conference Record of the Thermionic Conversion Specialist Conference, Houston (1966).
- [5] BUSSE, C.A., CARON, R., GEIGER, F. and PÖTZSCHKE, M.: "Performance Studies on Heat Pipes", Proc. First Int. Conf. on Thermionic Electrical Power Generation, London (1965).
- [6] BUSSE, C.A., GEIGER, F., QUATAERT, D. and PÖTZSCHKE, M.: "Heat Pipe Life Tests at 1600°C and 1000°C", 1966 IEEE Conference Record of the Thermionic Conversion Specialist Conference, Houston (1966).
- [7] BUSSE, C.A.: "Pressure Drop in the Vapor Phase of Long Heat Pipes", 1967 IEEE Conference Record of the Thermionic Conversion Specialist Conference, Palo Alto (1967).
- [8] BUSSE, C.A., GEIGER, F., STRUB, H., PÖTZSCHKE, M. and KRAFT, G.: "High Temperature Lithium Heat Pipes", Proc. Second Int. Conf. on Thermionic Electrical Power Generation, Stresa (1968).
- [9] DI COLA, G., EURATOM CCR Ispra (unpublished; the results are cited in [2]).
- [10] DORNER, S., REISS, F. and SCHRETZMANN, K.: "Experimentelle Untersuchungen an Natrium-gefüllten Heat Pipes", report KFK 512 (1967).
- [11] GAMMEL, G., WALDMANN, H.: "Messungen des maximalen Leistungsdurchsatzes von Wärmeleitrohren mit flüssigem Metall", in "Forschung über Direktumwandlung in elektrische Energie" Brown Boverie & Cie AG, Mannheim.
- [12] PRUSCHEK, R., SCHINDLER, M. and MORITZ, K.: "Das Wärmerohr (Heat Pipe)", Chemie-Ingenieur-Technik 39 (1967) 21.
- [13] REISS, F., SCHRETZMANN, F.: "Pressure Balance and Maximum Power Density at the Evaporation Gained from Heat Pipe Experiments", Proc. Second Int. Conf. on Thermionic Electrical Power Generation, Stresa (1968).
- [14] SCHINS, H.E.J.: "Liquid Metals for Heat Pipes; Properties, Plots and Data Sheets", report EUR 3653e (1967).
- [15] SCHMIDT, E.: "Détermination de la Perte de Charge dans des Milieux Capillaires Susceptibles d'être Utilisés dans des Caloducs", Centre d'Etudes Nucléaires de Grenoble, NOTE TT N° 265 (1967).
- [16] SCHMIDT, E., SEMERIA, R.: "Détermination Théorique et Expérimentale de la Puissance Thermique Limite Transférée par des Caloducs à Sodium", Proc. Second Int. Conf. on Thermionic Electrical Power Generation, Stresa (1968).
- [17] VAN ANDEL, E.: "Heat Pipe Design Theory", Proc. Second Int. Conf. on Thermionic Electrical Power Generation, Stresa (1968).

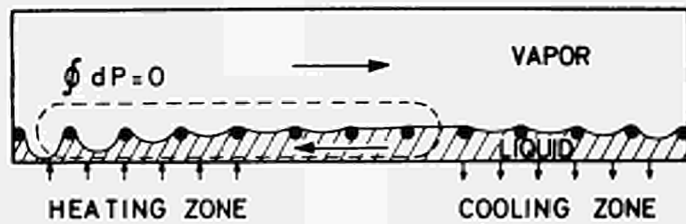


Fig.1: Principle of the heat pipe

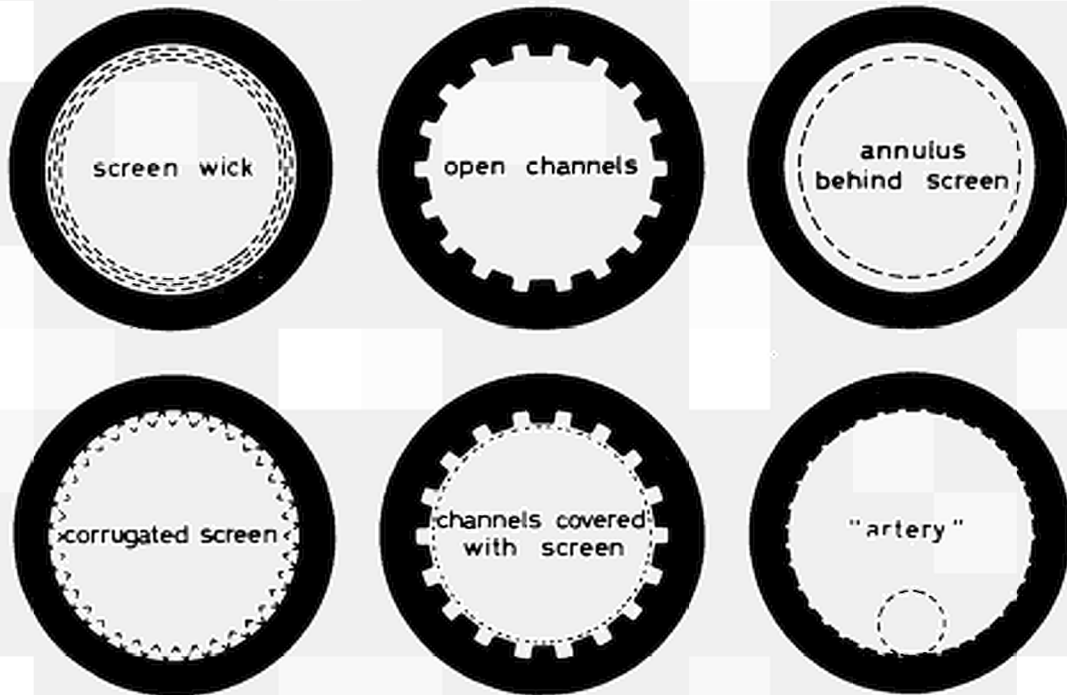


Fig.2: Capillary structures for heat pipes

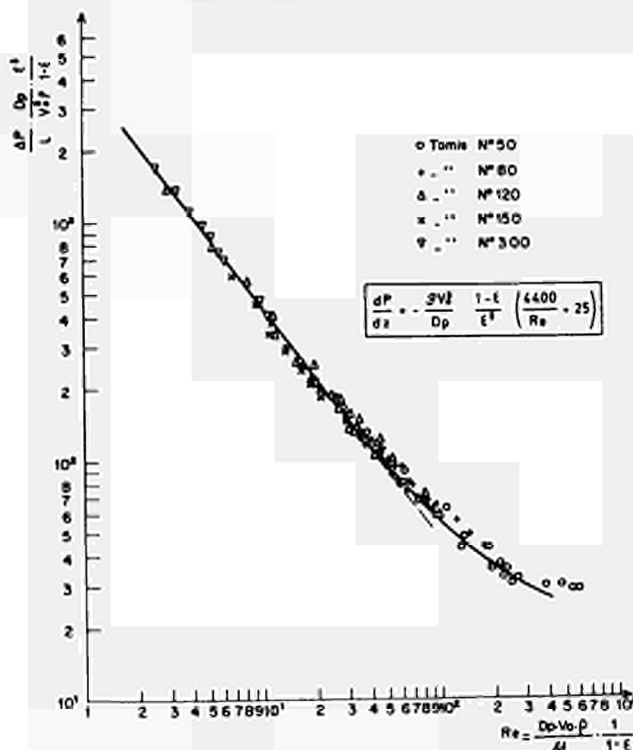


Fig.3: Pressure drop in screen wicks (E. SCHMIDT, 1967).

ΔP =pressure drop, l =length of wick, v_o =liquid flow velocity averaged over the total wick, ρ, μ =density and viscosity of liquid, ϵ =porosity of the wick = ratio of void to total volume of the wick, $D_p = 6$ times diameter of the screen wire, $dP/dz \cong \Delta P/L$

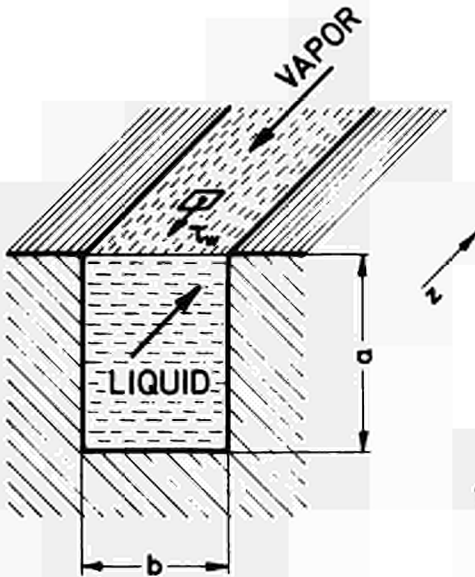


Fig.4: Vapor-liquid interaction in an open channel (after results from G. DI COLA, 1968).

$dP_1/dz, (dP_1/dz)_0$ =pressure gradient in the liquid with and without vapor friction, τ_w =shear stress on the liquid surface, d =hydraulic diameter of the vapor channel, dP_{vf}/dz =part of the pressure gradient in the vapor which is caused by wall friction

$$\tau_w = \frac{d}{4} \frac{dP_{vf}}{dz}$$

$a \geq b$, vapor duct diameter d :

$$\frac{dP_1}{dz} = \left(\frac{dP_1}{dz}\right)_0 - \frac{d}{4a(1-0.314 b/a)} \frac{dP_{vf}}{dz}$$

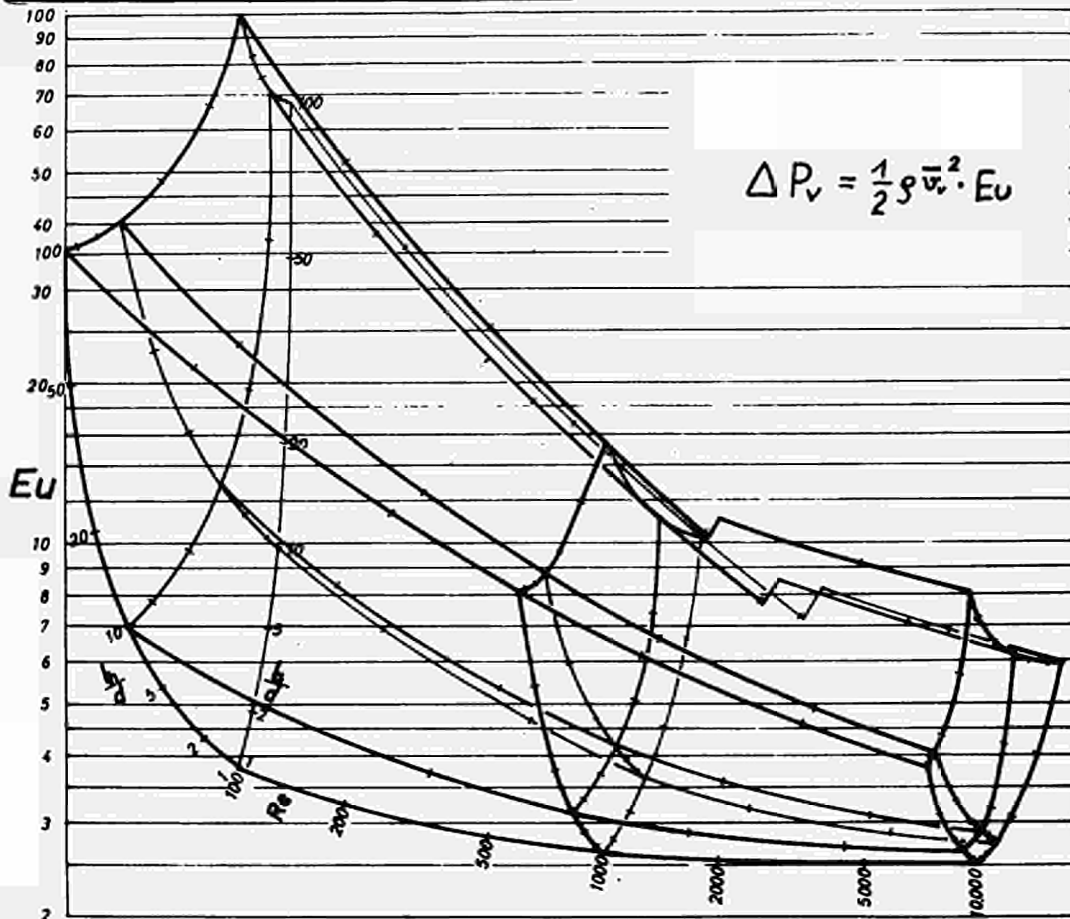


Fig.5: EULER number as a function of REYNOLDS number and heat pipe geometry (E. VAN ANDEL, 1968). l_h, l_s =length of heating zone and heat shielded zone, d =diameter of vapor channel, ΔP_v =pressure drop in heating zone plus heat shielded zone, ρ =vapor density, \bar{v}_v =vapor velocity averaged over the cross section of the vapor channel

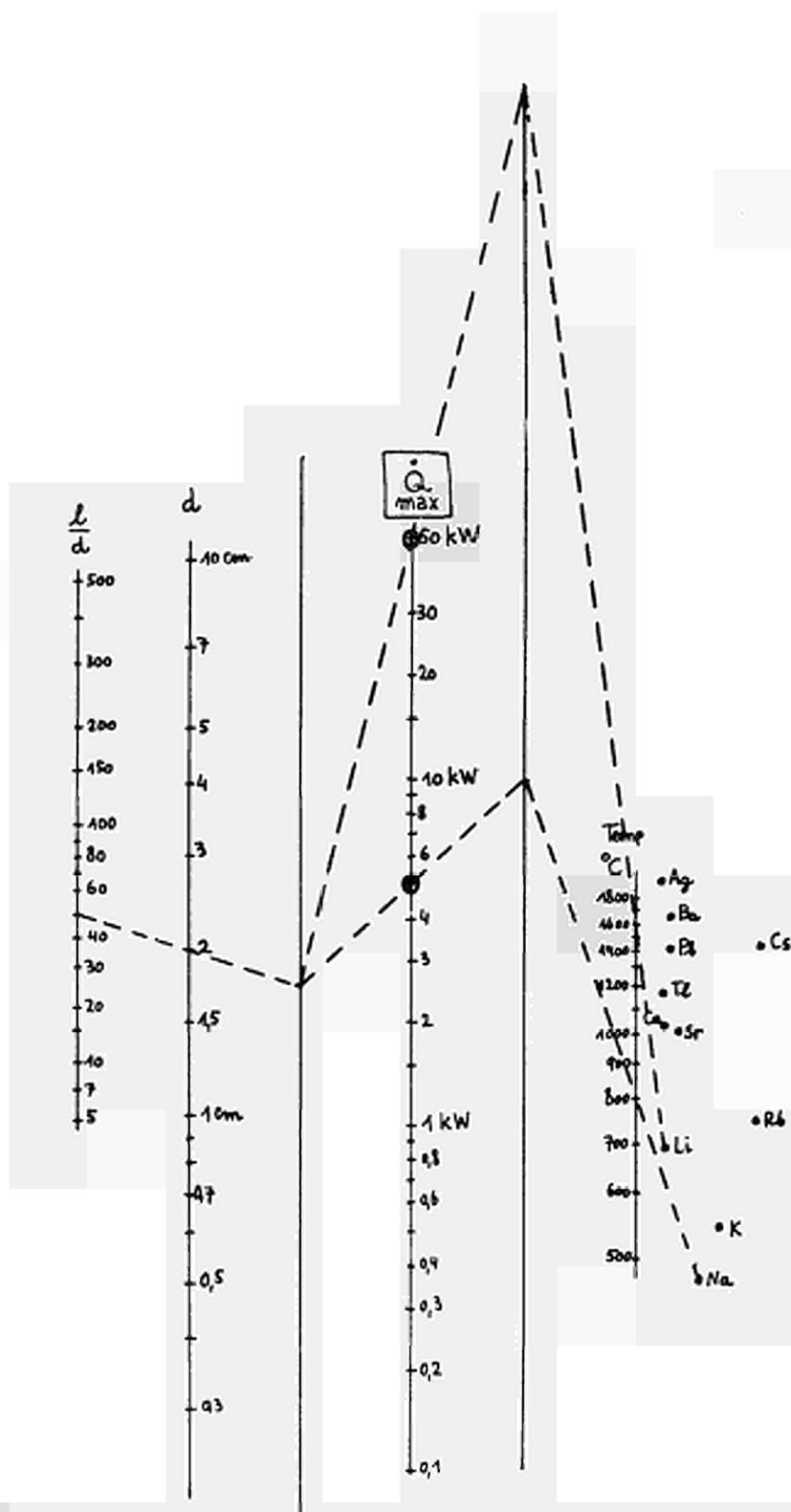


Fig.6: Heat transport limit of heat pipes with optimized annular capillary structure (E. VAN ANDEL, 1968). \dot{Q}_{max} = maximum heat flow, d =diameter of vapor channel, l =effective length \approx half length of heating zone plus length of heat shielded zone

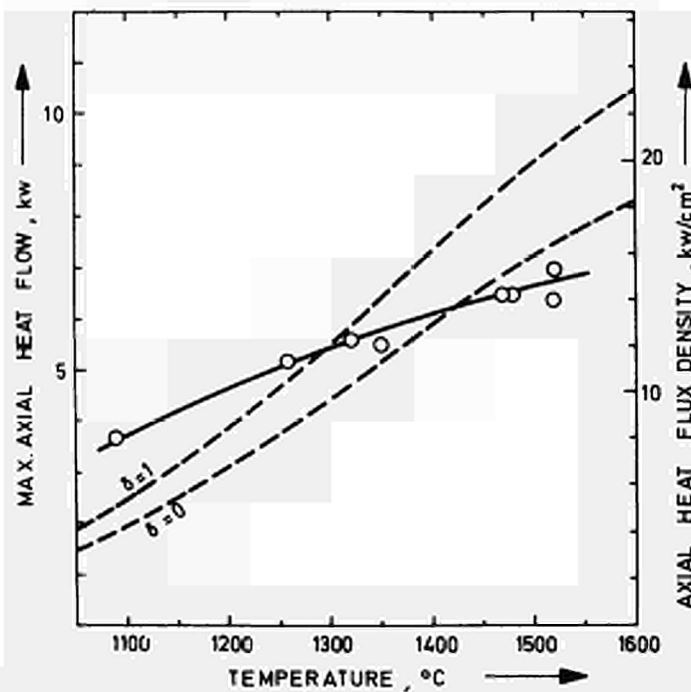


Fig.7: Heat transport limit of a lithium heat pipe (488 mm long, 0.76 mm i.d.) [8]

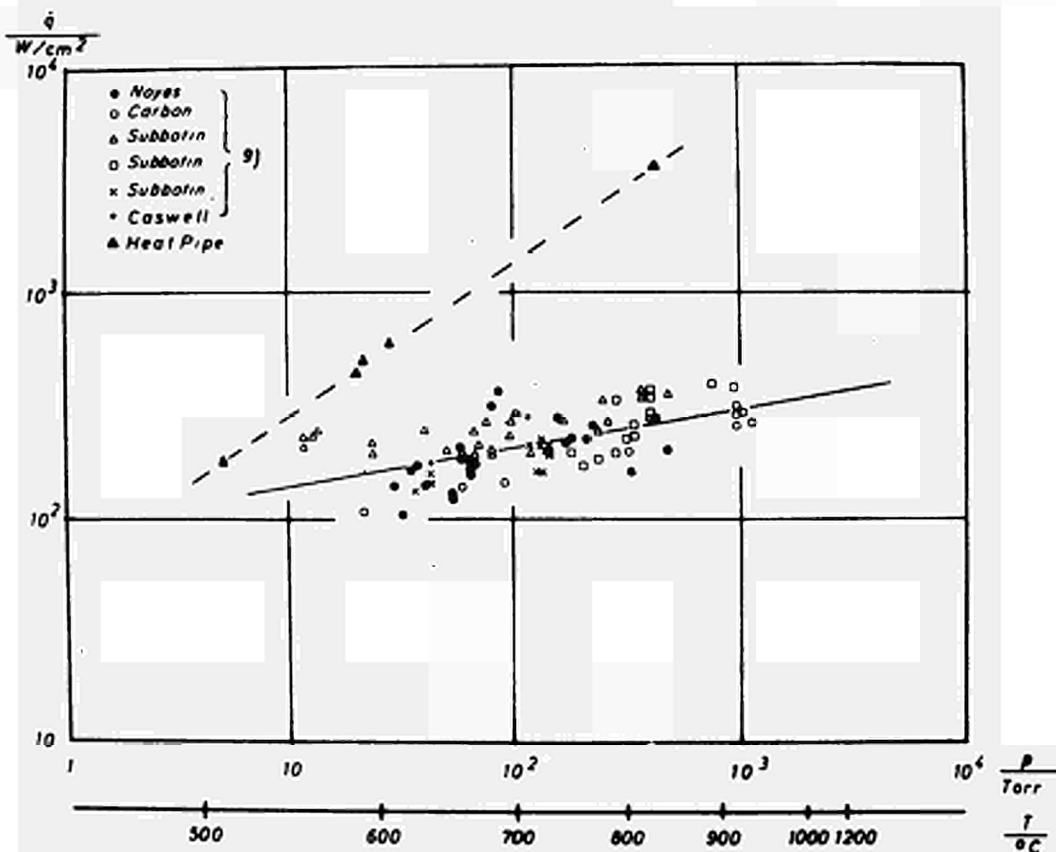


Fig.8: Maximum heat flux of evaporation in heat pipes (dashed curve) and burn-out heat flux in pool boiling (F. REISS, and K. SCHRETTZMANN, 1968)

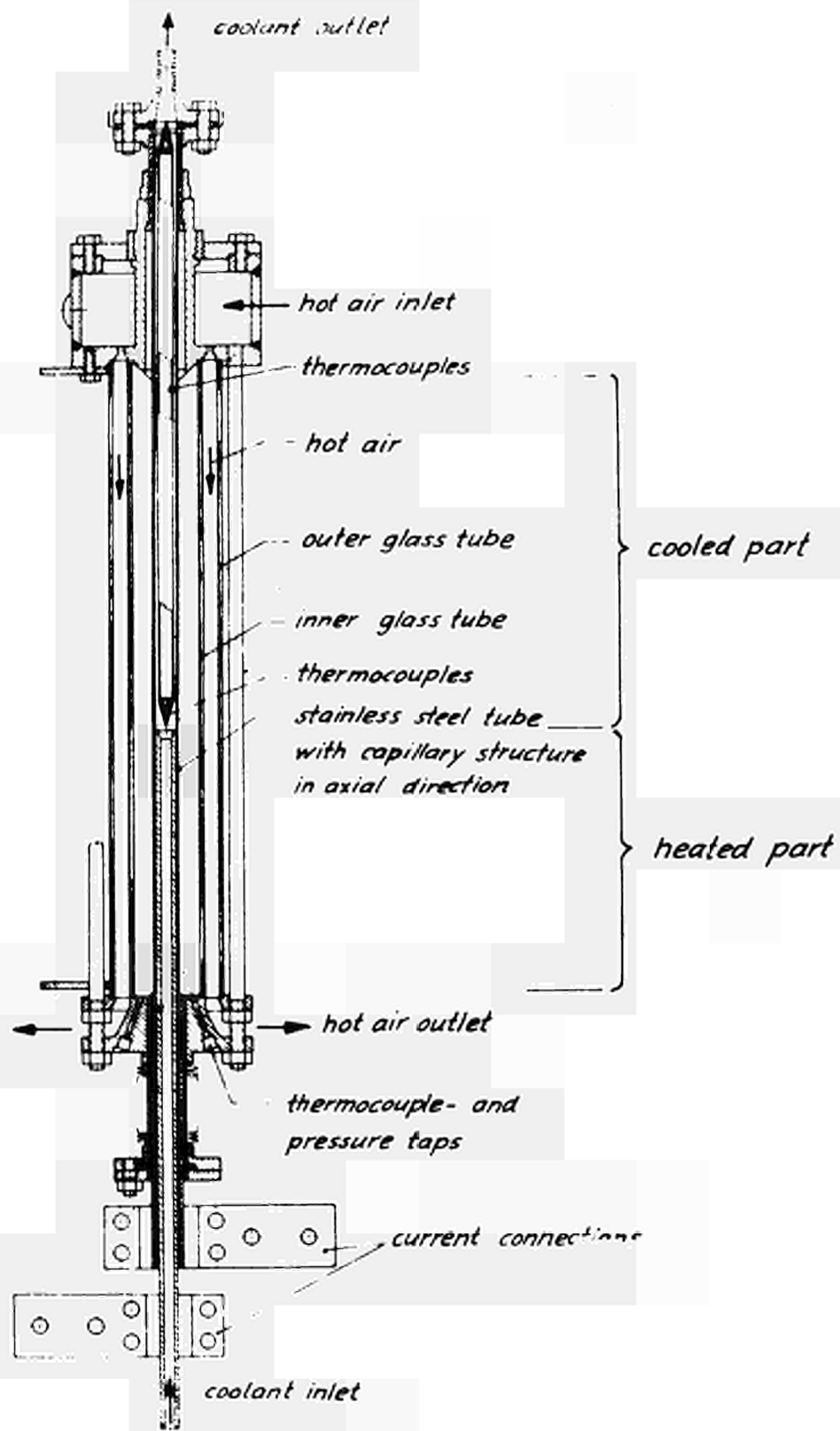


Fig.9: Visualization heat pipe
(A. BÄHR, E. BURCK and W. HUFSCHMIDT, 1968)



Mass transport (SGS-Ta/Tl, 2500 hours at 1600°C, heating rate 80 w/cm²)



Heating zone corrosion (Nb-1Zr/Li, 11 hours at 1500°C, heating rate 115 w/cm²)



Heating zone corrosion (Ta/Li, 9 hours at 1600°C, heating rate 155 w/cm²) [8]

Fig.10: Corrosion effects in heat pipes
(RF = position of heating coil)

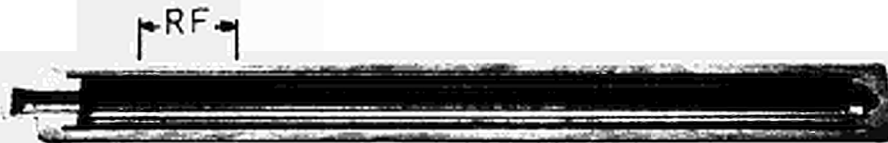


Fig.11: SGS-Ta/Li heat pipe after 1000 hours of horizontal operation at 1600°C, heating rate 170 w/cm² [8] (RF = position of heating coil)

ADVANCES IN HEAT PIPE TECHNOLOGY*

by

G. M. Grover, J. E. Kemme, and E. S. Keddy
Los Alamos Scientific Laboratory
University of California
Los Alamos, New Mexico 87544

ABSTRACT

Recent work on materials compatibility and work on maximum heat flux capability of heat pipes are reviewed. Experimental results on operational limiting factors such as sonic flow and liquid entrainment are given. The results of the orbital flight test of a water heat pipe confirm the operability of heat pipes in a zero-g environment.

Introduction

Heat pipes are structures exhibiting very high thermal conductance through the mechanism of convection of latent heat of vaporization of a working fluid. Liquid return of the working fluid is accomplished by capillary action. Many variations in form are possible and the range of application is therefore very large. We are interested here in the heat pipe problems associated with thermionic conversion and with the state-of-the-art relative to this field.

* Work performed under the auspices of the U. S. Atomic Energy Commission.

Materials Compatability

There are two temperature regimes of interest, the emitter range of 1400° to 2000°C and the collector range of 500° to 900°C. One may confidently say that for the lower range of temperatures, the compatability problem is satisfactorily solved for a rather wide variety of material combinations. The alkali metals with stainless steel, nickel, niobium-zirconium alloys and other refractory metals cover the temperature range adequately. As reported in reference 1, the longest test run has passed 16000 hours at 600°C. This heat pipe is made of nickel with potassium as the working fluid. Even beryllium (with potassium) is feasible where weight is of primary importance. A test was made in which a tube of beryllium was inserted between the wick and the wall of a heat pipe which were made of niobium-1% zirconium. With potassium as the working fluid, the pipe was operated at 750°C for 1200 hours. At the completion of this test, the beryllium was removed and compared with an untested specimen of this beryllium. The results of the analysis show that there was no attack or alloying and there was no evidence of mass transport. Recrystallization of the beryllium had occurred during the initial 1000°C bake out and considerable grain growth had occurred during the course of the test. Hardness tests showed the beryllium to be fully annealed. The strength of the material in this condition could limit its usefulness.

The compatability problems in the emitter temperature range is more trying. At the lower end of the range, Busse has reported on the use of lithium in a previous paper in this session.

At the other temperature extreme, vapor deposited tungsten heat pipes with silver as the working fluid show negligible mass transfer in one-thousand

hours at 1900°C. From the total mass flow, an upper limit to the solubility of tungsten in silver at this temperature can be set at 0.05 ppm.

Another candidate material for high temperature operation is rhenium. This has been used as the container material for two heat pipes. In the interest of expediency, tungsten was used as the wick material. With indium as the working fluid, after 1000 hours at 2000°C, considerable interdiffusion of tungsten with the rhenium wall had occurred and mass transport had displaced all of the tungsten wick into the evaporator section (Fig. 1). With silver as the working fluid, after about 300 hours, considerable interdiffusion of tungsten and rhenium had occurred together with considerable mass transport. There is some indication that the impurities and inclusions in the obtainable rhenium sheet stock may have contributed to the degradation of these high temperature heat pipes. Tests of rhenium as both container and wick material with silver and with indium are underway.

Operational Limits of Heat Pipes

There are a number of factors which must be considered in detail in the various practical applications of heat pipes. It would be desirable to have concise and complete parametric studies which would allow the selection of an optimized heat pipe for any particular application. Since these are unavailable, a review of the various limiting factors will be discussed as they are known at this time. Quantitative information is often unavailable and experimental evaluation is necessary in specific applications.

Factors of importance in heat pipes certainly include the following:

- a. Capillary forces available and their optimal utilization,
i.e., as in the use of composite wicks.

- b. Sonic limit of vapor flow.
- c. Startup dynamics.
- d. Vapor-liquid interface effects, specifically entrainment.

We believe the most significant step in the last year has been the proof of the operability of a composite wick. By definition, a composite wick is one in which the capillary pumping power is established by a fine porous structure such as a very fine mesh screen at the interface between the liquid and vapor flow passages. The return liquid flow occurs in a coarse mesh or open channel or annulus under the fine mesh cover. These experiments have been made in stainless steel pipes with sodium as the working fluid in the experimentally convenient temperature range below 900°C. Figure 2 shows such a pipe construction where a wick of pore size of less than 10 microns covers a annulus of about 0.15 millimeters radial thickness. Figure 3 shows this pipe in operation with the liquid returning against a gravity head of about 10^5 dynes/cm². If the capillary head had been established by the channel width, only 10^4 dynes/cm² would have been available and failure of the pipe would have occurred even neglecting any frictional flow impedance.

The upper limit of heat transfer ultimately occurs with choked flow at the exit of the evaporator. Figure 4 shows experimental data obtained by Kemme for both the sodium filled and the potassium filled composite wick heat pipes described above. The dashed line is the sonic flow limit heat transfer rate as calculated from the temperature at the beginning of the condenser zone. Of course, with mass addition flow through the heater zone, the central core can go supersonic while the flow near the walls is still subsonic. The maximum heat flow is in fair agreement with this sonic limit.

The departure from the sonic limit occurred when the limit of heat removal for this calorimeter was reached.

The importance of the investigation of heat pipe operation near this sonic limit arises from the fact that in gas-free heat pipes, the starting conditions usually involve the complete range of molecular flow, choked continuum flow and, finally, the chosen design conditions. All pipes must undergo startup conditions but probably few will be required to operate very close to the choked flow limit. A discussion of the transient modes of the startup of heat pipes is given in reference 2.

When heat pipes are operated in a mode in which the pressure drop in the evaporator is high due to acceleration of the vapor stream, a considerable recovery of this pressure drop is possible. The pressure recovery in the condenser section of the pipe described above is shown in Fig. 5. If the radial Reynolds number is high, i.e. > 10 , the flow is stabilized and one should recover all of the kinetic drop in the evaporator.^{3,4} However, in Kemme's experiments, although the average Reynolds number exceeded ten, only about 60% of the drop was recovered. The lack of complete recovery may be explained by non-uniform heat removal. A failure to stabilize the flow results in boundary layer separation and turbulent flow.

Another interesting limit of a heat pipe involves the interaction of the counterflowing vapor and liquid phases. When the vapor velocity is high, it is possible that entrainment of the liquid will occur. The interface between the liquid and vapor phase in a heat pipe is usually not smooth. The wick structure imposes a periodic pattern whose wave length is characterized in some manner by the wire size, spacing and weave. Because of the well-known dynamic instability of a vapor-liquid interface, for values of the Weber number⁵ greater than one, the theory shows that the

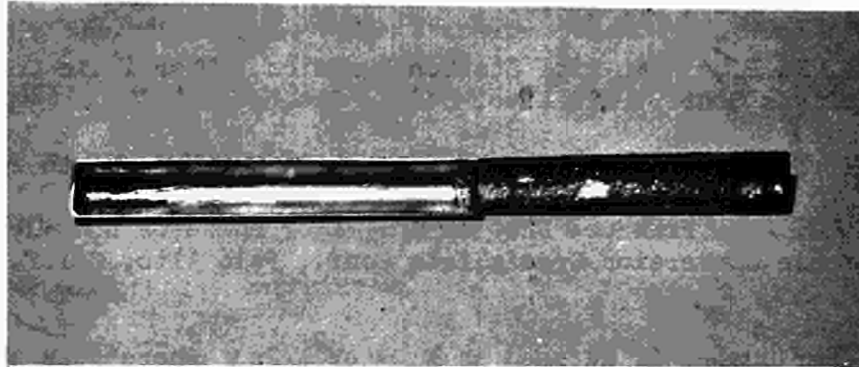
waves grow exponentially beyond the limits of the linear approximation. Presumably this growth results in droplets which detach from the wick and are entrained in the vapor flow. This increased liquid circulation rapidly exceeds the ability of the capillary forces to return liquid to the evaporator and failure occurs. Kemme's experiments show a rough correlation of this failure mode with center-to-center wire spacing and that a very fine screen suppresses entrainment.

Orbital Flight Test

In order to expedite the acceptance and use of heat pipes in problems of thermal control in space, an orbital flight test was made. These applications are concerned with distribution of heat loads in space structures, space suits, instrument packages and electrical components. The temperatures are such that water is a suitable working fluid. A water heat pipe electrically heated at one end was put into orbit, turned on four hours after launch, and its temperature profile along the pipe was monitored for forty-five hours. Figure 6 shows the experimental assembly and its test position on the aft rack of the Atlas Agena rocket and Fig. 7 shows the data obtained. As was expected no measurable difference from the laboratory calibration was detected. Further details on this experiment are available in reference 5. Presumably higher temperature heat pipes of interest in thermionic conversion will be accepted for space applications without too much difficulty.

References

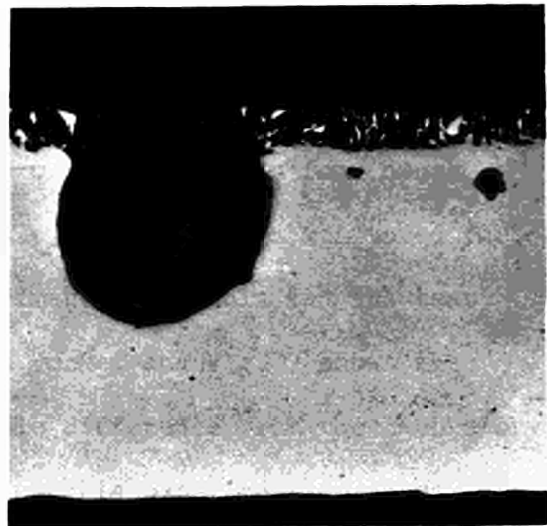
1. EASTMAN, G. Y., "The Heat Pipe," Scientific American, Vol. 218, No. 5, May 1968, pp. 38-46.
2. COTTER, T. P., "Heat Pipe Startup Dynamics," Thermionic Conversion Specialists Conf., Palo Alto, Calif, Oct. 30, 1967.
3. COTTER, T. P., "Theory of Heat Pipes," LA-3246-MS, March 26, 1965.
4. BUSSE, C. A., "Pressure Drop in the Vapor Phase of Long Heat Pipes," Thermionic Conversion Specialists Conf., Palo Alto, Calif., Oct. 30, 1967.
5. The Weber number is defined as $N_w = \rho V^2 \lambda / 2\pi \gamma$ where ρ is the density, V the velocity, γ is the surface tension and λ is a characteristic wavelength.
6. DEVERALL, J. E.; SALMI, E. W.; KNAPP, R. J., "Orbital Heat Pipe Experiment," LA-3714, June 22, 1967.



Lengthwise section of evaporator and condenser showing mass transport.



Evaporator section of pipe showing W-Re reaction layer and build-up of material in wick structure. (75X)



Section of pipe containing voids in rhenium wall. (100X)

Fig. 1
Re-W-In Heat Pipe After Testing

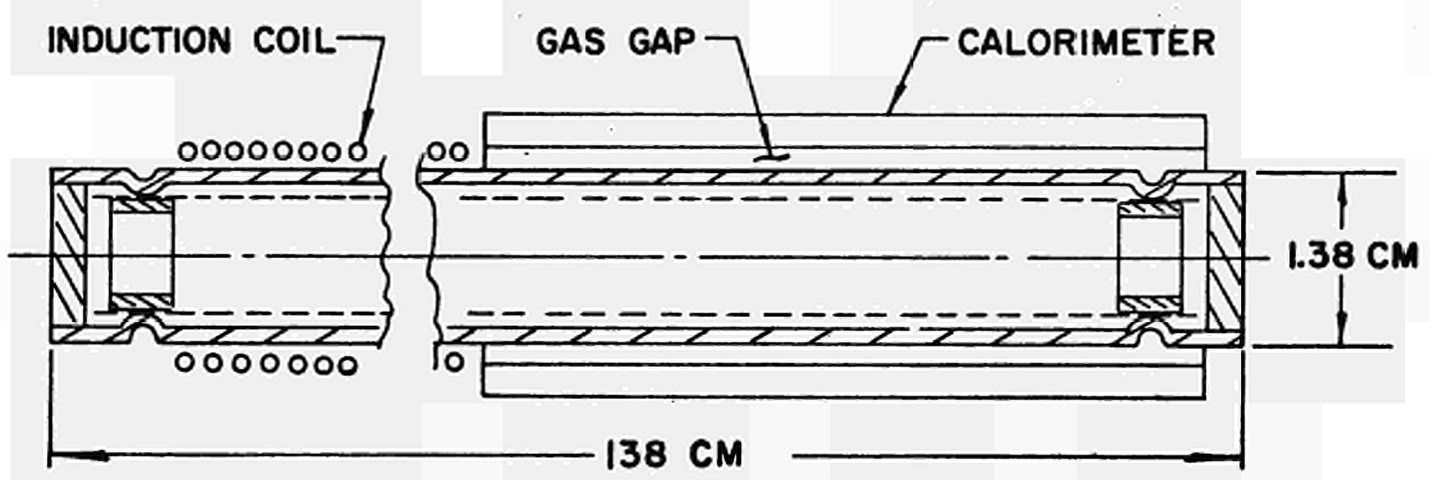
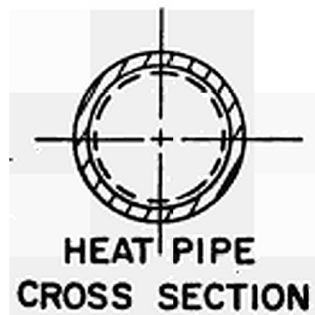


FIG. 2 ANNULAR RETURN HEAT PIPE



Fig. 3. Operation Against Gravity

X TEMPERATURES AT BEGINNING OF EVAPORATOR
• TEMPERATURES AT BEGINNING OF CONDENSER

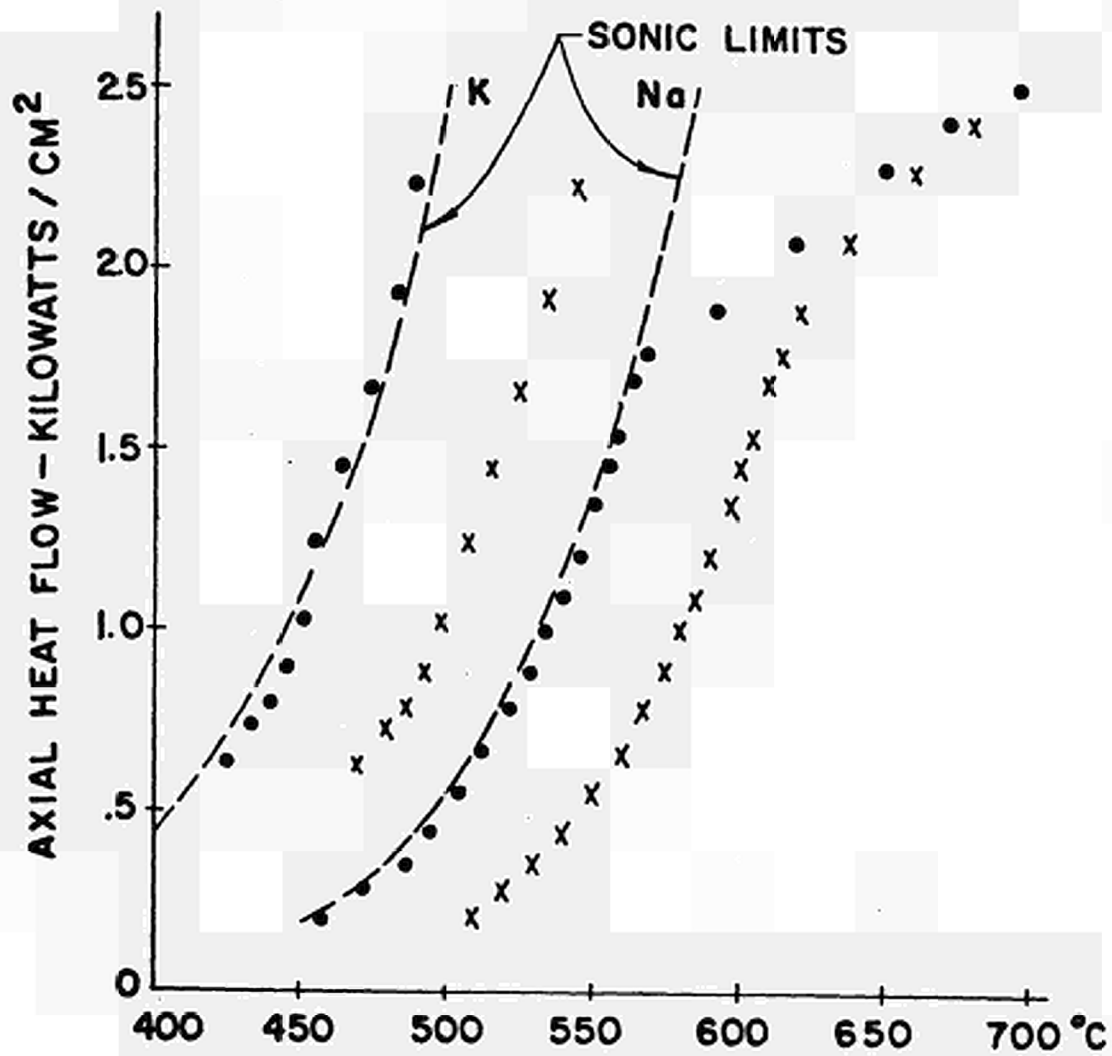


FIG.4 SONIC LIMITED HEAT FLOW
(SODIUM AND POTASSIUM)

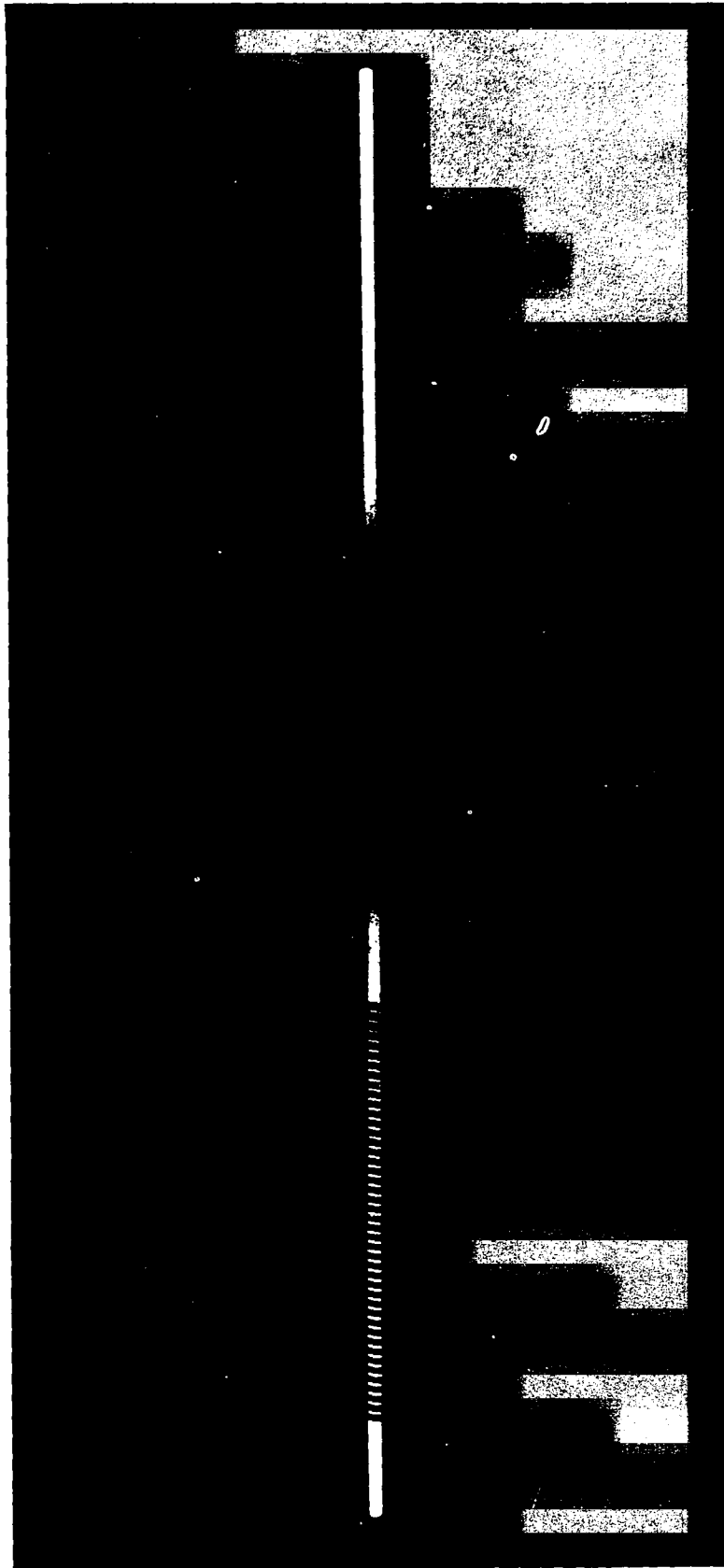


Fig. 5. Pressure Recovery in a Heat Pipe

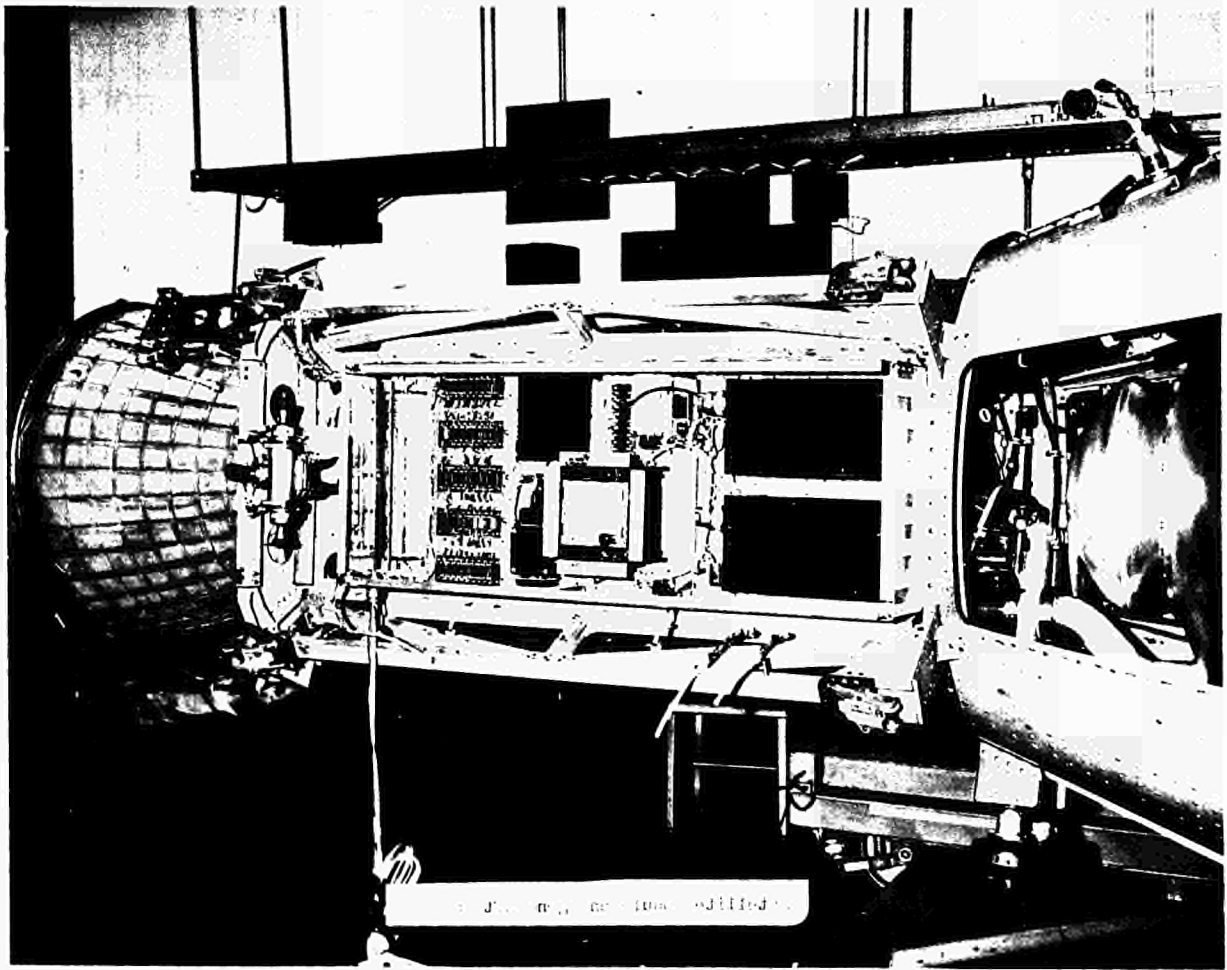
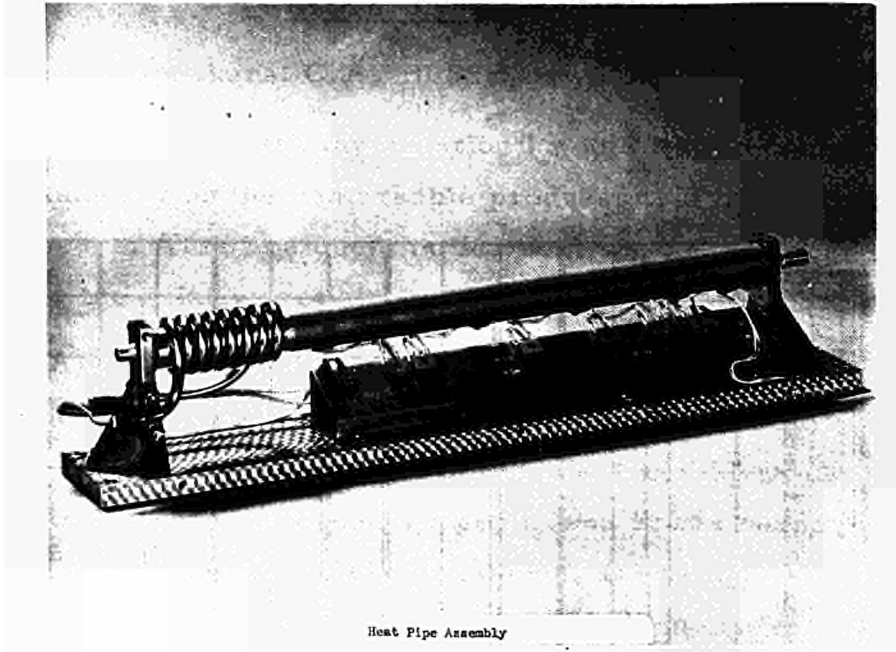
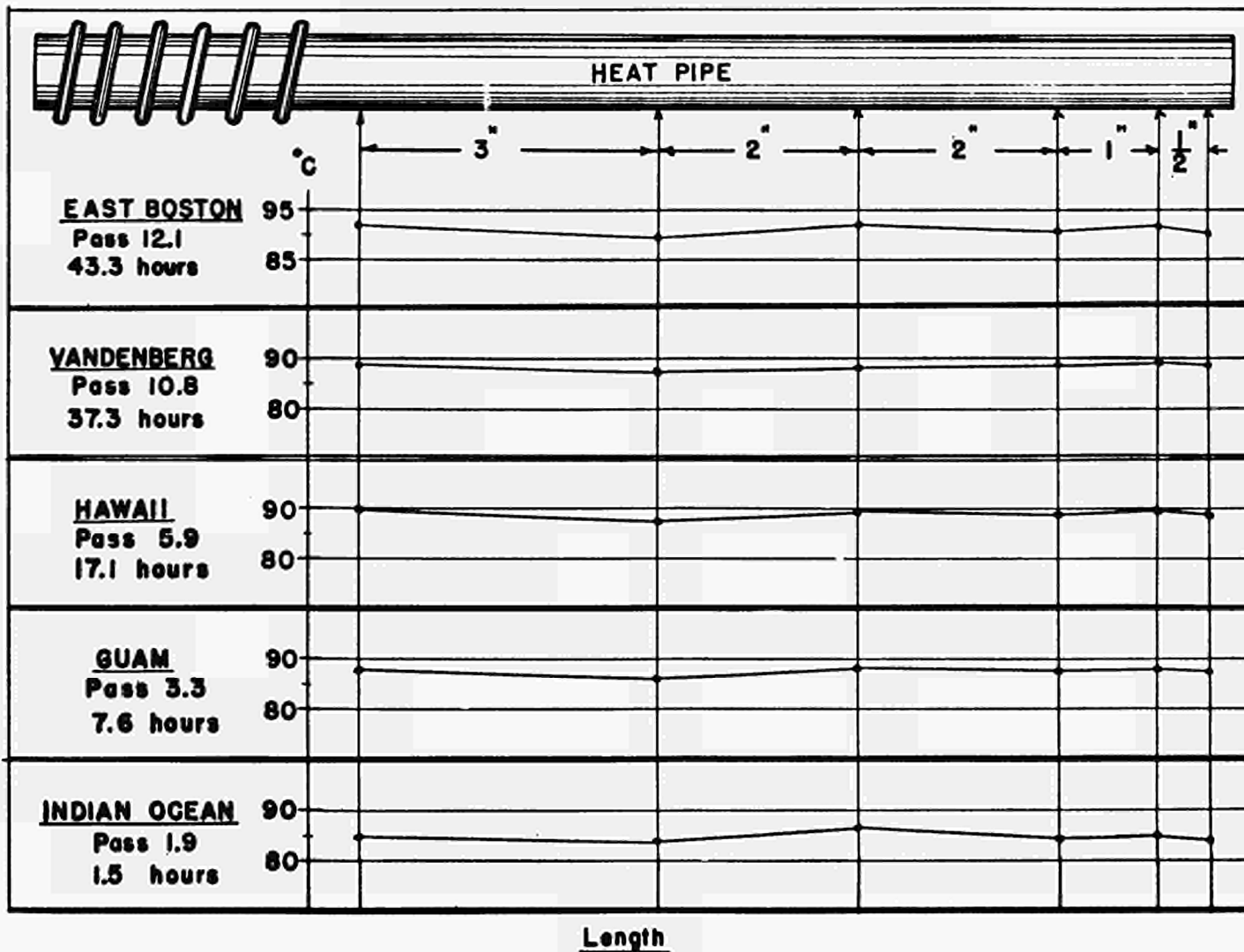


Fig. 6. Heat Pipe Assembly and Satellite Module on Agena Aft Rack

FIG. 7 SAMPLE DATA FROM
EACH TRACKING STATION



DISCUSSION

Session D Review speakers: C. A. BUSSE and G. M. GROVER.

SCHOCK (USA): Before I ask my question I would like to compliment the heat pipe community on the remarkable progress that has been achieved in the last few years. This is a question for both speakers. Other things being equal, what is the relative reliability of the different wick structures?

GROVER (USA): Once you have taken care of the compatibility problem, there does not seem to be a special problem of wick reliability. I might point out that the capillary structure of the annular return heat pipe was fabricated with 8 layers of screen swaged down. It was supported and sealed only at the ends, sagging freely elsewhere. It was not on center, of course. (As a matter of fact, one does not want it on center for best operation; it is better to produce an asymmetrical channel which has a lower flow impedance than a symmetrical channel). There was no sign of unwinding of the swaged screen or anything like this.

BUSSE (Euratom): I could add that mechanically very stable capillary structures (of the artery type, or consisting of channels covered with screen) can be made by bonding the screen to the wall. We have done this in a number of ways, for instance by sintering or by chemical vapor deposition which is a very efficient method for getting a good bond.

GROVER: In the water heat pipe that was operated in orbit the wick was pressed against the wall by swaging the wall down on the wick, and there was no other bonding. The heat pipe went through a complete shake test of course (the Saturn V vibration spectrum was used). There was no change in the operation. As a matter of fact, during vibration testing of another heat pipe of the same kind, an improved performance occurred. It was operated at a slight incline so that the water could not wet the complete wick, but the vibration filled all the pores and the heat pipe operated beautifully.

DESTEESE (USA): I have a question for Dr. BUSSE. Do you consider some observed corrosion in the heat pipe results from impurities in the working fluids?

BUSSE: At the beginning of our studies on lithium heat pipes we thought that impurities in the working fluid might cause the corrosion. But careful purification of the lithium and very clean filling techniques did not result in any improvement. Therefore in this case the corrosion was not caused

by impurities in the working fluid but, as we found out later, by the oxygen in the wall material. In general, of course, corrosion can be created by a sufficient amount of impurities in the working fluid.

DESTEESE: Can you quote the purity of the working fluids?

BUSSE: In the special case of lithium the nominal purity was 99.9%, which does not say very much because non-metallic impurities are not included in this figure. We purified this lithium by melting it first several times through a funnel in order to eliminate the major part of the oxygen, by hot getting it then for 10 hours at 800°C with zirconium sponge, and finally by distilling it into the heat pipe. I think that the amount of oxygen in this lithium was negligibly small compared to that in the wall material.

DESTEESE: I have one final question. May I ask, have you performed post-test chemical analyses of the working fluids?

BUSSE: No. Only the wall materials were analyzed.

PRUSCHEK (Germany): A question for Dr. GROVER. Since beryllium is a toxic material, are there severe handling problems during fabrication of beryllium heat pipes and during operation? Precaution would be necessary to prevent a heat pipe from burn-out during tests, otherwise a contamination by the evaporated beryllium might cause problems.

GROVER: It is beryllium oxide that is toxic, I believe. The metal can be handled with suitable precautions. We did not make a complete heat pipe of beryllium. What we did was merely take a cylinder of beryllium and slip it between the wick and the wall of a Nb-1 Zr assembly and test it as a heat pipe. If there had been mass transport, that is, had the beryllium not been compatible, we would have seen that transport.

HEFFELS (ESRO): I noticed two things in the presentations: (1) that all pipes were straight pipes and (2) that in all tests the heat input was away from the ends. Now the questions: 1) Are there any problems if the heat transfer takes place at the very end? and 2) Would bends or knees in the pipe introduce any problems?

GROVER: There is no problem with bends. There is an additional pressure drop and you have to take this into consideration. We have operated pipes in the shape of Z and they do fine. With regard to heating on the end: yes, you can heat on the end and that works perfectly satisfactorily. However, the heat removal from the other end that is a little different.

If there are any non-condensable gases in the system all of the non-condensable gases will be pushed to the condenser end of the heat pipe. If you are trying to take out heat at the end, then you might find that you have to take it out through a gas-film and that will give you a temperature drop.

BUSSE: The reason why we did not heat the pipes at the very ends was simply that heat pipes were supported at the ends, and we did not want to heat the support structure too much.

SCHOCK: A question for Dr. GROVER. How do you make a Z-shaped bend in a wick?

GROVER: In that case the performance required was very low and the wicks were merely butted against each other from one section into another.

HARBAUGH (USA): A question for Dr. BUSSE. In the experiments with the water heat pipes, what was the power density for the onset of nucleate boiling?

BUSSE: In the experiments of BÄHR bubble formation was observed at a heating rate of about 20 W/cm^2 .

HARBAUGH: My second question is to Dr. GROVER. Does the working fluid drop below the screen in composite wick structures when the pipe is driven hard, and does this cause catastrophic failure?

GROVER: Hot spots occur in the evaporator when the heat pipe is driven beyond the pumping power of the fine screen, and occasionally with catastrophic results.

HARBAUGH: How are your heat pipes processed?

GROVER: Liquid oxygen cleaning procedures are a good start, cleanliness is essential, and outgassing above operating temperature is desirable.

CONTZEN (ELDO): What was the type of motion of the vehicle carrying the heat pipe during the orbital test? Was the vehicle spun, attitude controlled or merely tumbled?

GROVER: It was tumbling very, very slowly, about 1 rev. per 3 hours or so, or something like that.

CONTZEN: Do you think that the spinning rate of a satellite could have an influence on the operation of an on-board heat pipe?

GROVER: Definitely.

ROUKLOVE (USA): I was just going to comment on the number of hours that Dr. GROVER quoted for the TZM/Li heat pipe which was operated between 1400°C and 1500°C. Actually the heat pipe failed after 10,526 hours.

VAN ANDEL (Euratom): I would address my question to Dr. GROVER. Did you find any other conclusive proof that in some heat pipes liquid metal entrainment by the vapor was the limiting factor in the heat flow?

GROVER: When we were specifically looking for liquid entrainment we had no other ready explanation for that type of failure and I must admit that the examination has been very sparse. I believe that the water experiments that Dr. BUSSE mentioned could be carried on a little further and get a much better determination of this entrainment.

LOCHKAREV (USSR): What is the feasible upper limit of the thermal power transmitted by a high-temperature heat pipe with the diameter of 1 cm?

GROVER: If I understand the question, the maximum heat transfer down a pipe would be given by the sonic limit. The maximum that has been measured corresponds to this and is around 15 kW/cm² for sodium at about 700°C. For lithium this sonic limit at higher temperatures would be extremely high and I don't know the numbers right off hand.

LOCHKAREV: What is the limit specific thermal power (W/cm²) in the active part of the heat pipe?

BUSSE: There are the data of DORNER, REISS and SCHRETZMANN. They measured the maximum heating rate for sodium with open channels as capillary structure and found values up to 2 kW per cm² of channel opening. With regard to the condensation zone, theoretically there are also limits, but experimentally no work has been done.

LOCHKAREV: Which part is more critical in relation to the magnitude of the specific thermal flow - the region of condensation or evaporation?

GROVER: I would believe the evaporation zone would be more critical. As Dr. BUSSE said, the condensation limits must exist, they are quite high, but none of us has made specific experiments towards this end to determine this.

HIGH TEMPERATURE LITHIUM HEAT PIPES

C.A. BUSSE, F. GEIGER, H. STRÜB
Euratom CCR, Ispra (Varese), Italy

and

M. PÖTZSCHKE, G. KRAFT
Metallgesellschaft AG, 6000 Frankfurt (Main) 1, Postfach 2609, Germany

Abstract

Corrosion in high temperature Nb-1Zr/Li and Ta/Li heat pipes can be caused by the oxygen content of the wall material. The corrosion mechanism consists in the extraction of oxygen from the wall material in the cooling zone and the transport to the heating zone, where the oxygen is accumulated in a relatively small region. By this enrichment phenomenon the oxygen concentration in the heating zone can reach values which are so high that rapid wall attack and penetration occurs, even if the initial oxygen content of the wall material is as low as about 100 ppm.

Promising results on corrosion inhibition have been obtained by using as wall material Nb-1Zr which had been deoxidized by a heat pipe process to below 1 ppm O, by adding Ca to a Nb-1Zr/Li heat pipe, and by using Ta with a small content of Y (SGS-Ta). The Nb-1Zr/Li heat pipes withstood tests of 1000 hours at 1500°C without failure, but considerable loss of Zr occurred. The best result was obtained with SGS-Ta/Li. After a test of 1000 hours at 1600°C with a heating rate of 170 w/cm² this heat pipe was completely free of impurity corrosion and showed only slight solubility mass transport.

Heat transfer measurements were made with a Li heat pipe about 50 cm long and with 0.46 cm² vapor flow area. The heat pipe had a composite wick (grooves covered with one layer of 150 mesh screen) and was made of Ta (wall) and Nb-1Zr (screen). At 1500°C a maximum axial heat flux density of about 15 kw/cm² was measured.

1. Introduction

Lithium is one of the most attractive working fluids for heat transfer with heat pipes in the temperature range around 1500°C. Present-day heat pipe theory indicates that of all elements with a vapor pressure of less than 10 atm at 1600°C Li should yield the highest axial heatflow densities [1]. In order to check these theoretical expectations, heat transfer measurements up to 1500°C were made with a Ta/Li heat pipe of composite wick structure (chapter 3).

The practical applicability of Li heat pipes depends strongly on the question whether mechanically reliable systems with long life time can be realized.

Promising life test results have been reported for Mo-0.8Zr-0.5Ti-0.03C(TZM)/Li (more than 9000 hours in vertical operation at 1475°C to 1500°C, heating rate 20 w/cm² [2]) and for W/Li (practically no corrosion after 1000 hours in horizontal operation at 1600°C, heating rate 70 w/cm² [3]). However, W is very brittle, and also TZM becomes brittle after heating for some hours to 1600°C. Life tests were therefore undertaken using Nb-1Zr and Ta as wall materials which remain ductile also after recrystallization. Details on heat pipe filling and testing methods as well as results of life tests and corrosion inhibition are reported in chapter 2.

2. Life tests

2.1 Corrosion mechanism in Nb-1Zr/Li and Ta/Li heat pipes

Early heat pipe life tests at 1600°C with Bi, Pb, Tl, Li, Ba as working fluid and Nb-1Zr, Ta and W as wall material had shown essentially two types of corrosion: (1) mass transport from the cooling zone to the heating zone, (2) local attack in the heating zone. While the first type was explained by the solubility of the wall material in the working fluid, it was suspected that the second type is caused by impurities [3] . Both Nb-1Zr/Li and Ta/Li heat pipes predominantly show this second type of corrosion which rapidly leads to wall penetration in the heating zone (after about 10 to 100 hours of operation in the 1500°C range). Fig. 1 is a typical photograph of a Ta/Li heat pipe which failed in this manner.

It is well known that in Nb-1Zr/Li and Ta/Li liquid metal systems corrosion can be caused by oxygen impurities (see e.g. [4]). We have found that filling a Nb-1Zr or a Ta heat pipe with deoxidized Li (hot gettered with Zr sponge) does not lead to a noticeable improvement in life time, that however the corrosion is caused by the initial oxygen content of the wall material. The corrosion mechanism consists in the extraction of oxygen from the wall material in the cooling zone and the transport to the heating zone, where the oxygen is accumulated in a relatively small region. By this enrichment phenomenon the oxygen concentration in the heating zone can reach values which are sufficiently high for rapid corrosion to occur (probably by the formation of a low melting O-Li-Nb resp. -Ta complex), even if the initial oxygen content of the wall ma-

terial is as low as about 100 ppm.

Having recognized the initial oxygen content of the wall material as the crucial impurity, three ways were tried for solving the corrosion problem: (1) deoxidation of the wall material prior to use, (2) inhibition of the corrosion process by adding strong oxygen getters to the working fluid or (3) to the wall material. All three tests resulted in a large improvement of the heat pipe life time, as will be discussed below.

2.2 Heat pipe filling technique

The heat pipe filling technique used in these experiments was basically always the same. In order to avoid oxygen contamination by introduction of the Li, a hot gettering step was generally included in the filling process. As getter Zr sponge with an average oxygen content of 400 ppm was used. The Zr quantity was chosen so that the sponge could suck up all the Li in the system (wt. of Zr \approx 30 times wt. of Li).

In fig. 2 the heat pipe with the getter container is shown. The entire unit was made of Nb-1Zr or Ta. The heat pipes themselves had a length of 116 mm. They were made of tube of 11 mm o.d. and 8 mm i.d., having in the inside wall 24 roughly square grooves of 0.5 x 0.5 mm. The end plugs were machined so that a radial clearance was left serving as capillary connection between the grooves.

The heat pipe preparation and filling procedure consisted of the following steps:

Preparation of refractory metal parts: Etching in aqua regia, followed by a treatment in HF+HNO₃ resulting in the removal of about 0.05 mm of wall material (in order to eliminate superficial Fe contamination which was found in the supplied tubes). Pre-outgassing for some minutes at 1650°C in a vacuum of about 10⁻⁵ torr. Joining by electron beam (leaving open the getter container). He leak test. Outgassing 5 min 1650°C at 10⁻⁵ torr. Transfer under vacuum into an argon glove box.

Preparation of Zr: Heating in high vacuum for 1 hour at 1500°C. Transfer under vacuum into the argon glove box.

Preparation of Li: Pre-cleaning by melting two or three times in a vacuum of 10^{-4} to 10^{-5} torr through a Ni funnel with a 1 mm opening, using the weight of a Ni piston to push the liquid metal through the funnel (Li_2O remains essentially in the funnel, so that a brilliant Li bead is obtained). Transfer of the Li bead under vacuum into the argon glove box.

Filling: In the argon glove box Zr sponge and Li are put into the getter container and the lid is inserted. After pumping down the glove box for two hours to about 10^{-5} torr the lid is welded tight by electron beam.

Gettering: The system as shown in fig. 2, with the getter container in downward position, is treated for 10 hours in a vacuum of about 10^{-5} torr heating the getter container to 800°C and keeping the rest of the system roughly 100°C hotter in order to ensure that the liquid Li is in the getter container. Afterwards (with the getter container in upward position) the Li is distilled over into the heat pipe by heating the getter container for 10 hours to about 800°C and keeping the temperature of the end of the heat pipe below the melting point of Li by means of water cooled Cu clamps.

Final processing: The narrow tube between heat pipe and getter, container (see fig. 2) is pinched together and cut through by electron beam. The heat pipe is then inserted into a quartz glass tube. After outgassing the heat pipe for some minutes at life test temperature as well as the total assembly for 10 hours at 400°C under a vacuum of 10^{-5} torr, the quartz container is sealed off with a propane-oxygen torch.

2.3 Test method

The sealed-in heat pipe ready for lifetesting is shown in fig. 3. The heat pipe is centered by the W pins of a Ta support. A movable Ta shield serves to keep a part of the quartz glass clean for pyrometric temperature measurement during the test.

Fig. 4 shows a heat pipe on the life test stand. All tests were made with the heat pipe in horizontal position, heating with a 13 mm long RF coil. Sensitive automatic shut down of the RF generator in case of heat pipe failure was provided by means of two photocells measuring separately the light output from heating zone and cooling zone. The difference of their signals was registered

on a millivolt recorder with a max and a min contact, which shut down the generator. Simple cooling control of the RF coil was made by means of a blackened piece of mica. It was suspended by a wire brazed with Rose's metal to the RF coil. If the coil became too hot, the braze melted and the mica piece dropped down between photocell and heat pipe thus releasing the shut down of the RF generator.

2.4 Life test results and discussion

Table 1 shows the results of the tests. Heat pipe No. 1 was made from Nb-1Zr which was deoxidized to below 1 ppm O by making use of the described oxygen transport process, i. e. building the heat pipe from the cooling zone material of another Li heat pipe having already been operated. For this purpose first a Nb-1Zr/Li heat pipe 200 mm long was filled and operated horizontally for 95 hours at 1500°C until a leak occurred in the heating zone. The rapid shut down by the photocell control system prevented most of the Li to escape from the heat pipe thus permitting the new heat pipe to be made in a simple way: The quartz glass tube was opened up in an argon glove box, the defective heat pipe pinched together in the cooling zone and welded tight by electron beam after evacuating the argon. The original heating zone was then cut away with a saw. The heat pipe was again sealed in quartz glass, after outgassing in a vacuum of 10^{-5} torr for some minutes at 1500°C and heating the quartz tube for 10 hours to 400°C. This heat pipe withstood a 1000 hour test at 1500°C without failure. After opening up, modest wall attack in the heating zone was found. It may have been caused by oxygen pick up after the initial deoxidation process and could presumably be avoided by some improvement of the processing. There was however another effect which may have serious consequences: During the test an electrically well conducting deposit (resistance < 1 ohm) formed on the inside of the quartz tube; it consisted mainly of Zr.

Table 1 : Lifetest results

No.	wall material	filling	test conditions			observations
			temperature °C	time hr	heating rate* w/cm ²	
1	deoxidized Nb-1Zr	Li	1500	1000	115	no failure; Zr loss
2	Nb-1Zr	Li-13Ca	1500	1000	115	
3	SGS-Ta	Li	1600	1000	170	no failure

Heat pipe No. 2 in table 1 was filled without hot gettering, but adding 46 mg of Ca to the Li. As the boiling temperature of Ca is well below that of Li, the Ca in heat pipe operation will probably be accumulated in the heating zone. There it should effectively trap the oxygen because CaO is among the oxides with the highest known free energy of formation. Also this heat pipe withstood 1000 hours of horizontal operation at 1500°C without failure. It shows however an anomalously strong deposit on the quartz tube in the heating zone (Ca diffusion?).

The last heat pipe in table 1 was built from SGS-Ta, which is a rather oxygen free Ta (~ 10 ppm O) containing a very small percentage of Y (whose oxide has a free energy of formation considerably larger than that of Zr). This heat pipe was filled using the described hot gettering process. After 1000 hours of operation at 1600°C this heat pipe did not show any wall attack in the heating zone. There were only some small deposits presumably caused by the usual solubility mass transport from the cooling zone to the heating zone (see fig. 5). The complete absence of oxygen corrosion may be due both to the relatively low oxygen content of the SGS-Ta and the action of the Y which seems to inhibit quite effectively the oxygen accumulation process.

If one takes into account that the SGS-Ta/Li heat pipe has been operated with a very high heating rate (170 w/cm²), and if one assumes that the mass depo-

* defined as the total radiated energy (outside the heating zone) divided by the area of the heating zone. This area was calculated as the surface of a cylinder having a diameter equal to the inner diameter of the heat pipe and a length equal to that of the RF coil.

sit per area is proportional to the heating rate and total time of operation (i. e., the total mass evaporated per area) [5], then one may hopefully extrapolate that in 10,000 hours at 1600°C with a heating rate of 50 w/cm² no serious clogging of the grooves would occur.

3. Heat transfer measurements

3.1 Apparatus

The maximum axial heat flow was measured with a heat pipe of composite wick structure (roughly rectangular grooves running axially and covered with screen). Table 2 shows the design data of the heat pipe.

Table 2 : Heat pipe design data

working fluid	Li
wall material	Ta
screen material	Nb-1Zr
diameter of vapor channel	7.6 mm
outer diameter	11.7 mm
total length	488 mm
length of heating zone	150 mm
length of cooling zone	204 mm
number of grooves	39 mm
average groove width	0.42 mm
average groove depth	0.96 mm
screen type	plain weave
number of screen layers	1
screen aperture	0.11 mm
screen wire diameter	0.06 mm

The problem of fixing the screen tightly on top of the indentation of the heat pipe wall was solved by making a spot welded screen tube which was inserted into the heat pipe; close contact between screen and heat pipe wall was then established by widening the screen by a hammering method. As hammer inside the heat pipe a loose W cylinder was used which was energized by vibrating the heat pipe in a round hammer machine.

The apparatus used for the heat flow measurement is shown in fig. 6. It consists essentially of two parts: a He filled one (left side), and an evacuated one (right side). The heating zone and a heat shielded zone are in the vacuum part, the cooling zone is in the He part. The vacuumtight separation between the two parts is made by a 0.2 mm thick Ta diaphragm, brazed with Nb by electron beam heating to the heat pipe, and clamped conically between a Cu piece and a stainless steel flange. The heat pipe was heated by an RF coil and cooled by water across a He gap of 0.4 mm width (cold value). The axial heat flow was measured by the flow rate and the temperature increase of the cooling water. The heat pipe temperature was controlled by two W-5Re/W-26Re thermocouples under the thermal shield and by an optical pyrometer at the beginning of the shielded zone.

The maximum axial heat flow was determined by simultaneously increasing the He pressure and the power input so that the heat pipe temperature remained essentially constant, until a hot spot appeared in the heating zone.

3.2 Results and discussion

The results of the axial heat transfer measurements are shown in fig. 7. Each data point represents an individually determined heat transfer limit. The measured maximum axial heat flux density of nearly 15 kw/cm^2 at 1500°C confirms the expected high performance of Li heat pipes.

Two theoretical curves (dashed) have been included into fig. 7. They were obtained by calculating the pressure drop in the vapor and the liquid phase from laminar theory [6, 7], equating the pressures in both phases at the beginning of the cooling zone and assuming as maximum capillary pressure P_c the pressure which would be developed by a partially filled groove, i. e.

$$P_c = 2 \left(\frac{1}{b} + \frac{\delta}{a} \right) \gamma$$

(b = width of groove, a = depth of groove, γ = surface tension of the working fluid). The parameter δ is introduced to make allowance for the fact that one side of the groove is not a solid wall but a screen; the maximum capillary pressure of a screen-covered partially filled groove should therefore be some-

where between that of a completely open groove ($\delta = 0$) and that of a groove closed by a solid wall ($\delta = 1$). The two curves in fig. 7 refer to these two limiting cases.

The data point at 1090°C lies nearly a factor two above the theoretical values. This seems to indicate that the maximum capillary pressure depends on the fine pores of the screen cover rather than on the size of the grooves themselves, this being in agreement with results of KEMME on Na heat pipes [8] . At higher temperatures, however, the data points in fig. 7 are closer to the theoretical curves. Partial destruction of screen and grooves in the heating zone may have lead to this result (the heat pipe, built without any provision for corrosion inhibition, failed by wall penetration in the heating zone shortly after the shown data points had been registered; the high value at 1090°C was in fact measured right at the beginning).

Conclusion

The SGS-Ta/Li system holds promise for realizing heat pipes with a lifetime of much more than 1000 hours at 1600°C and a heat transport capability well in excess of 10 kw/cm².

Acknowledgement

This investigation was aided considerably by the technical assistance of G. Kirchner. The authors would also like to thank D. Quataert for stimulating discussions.

References

- [1] VAN ANDEL, E., "Heat Pipe Design Theory", Proc. Second International Conference on Thermionic Electrical Power Generation, Stresa, 27-31st May, 1968.
- [2] RCA, note in C&EN, Aug. 21st, (1967) 16.
- [3] BUSSE, C.A., GEIGER, F., QUATAERT, D., PÖTZSCHKE, M.: "Heat Pipe Life Tests at 1600°C and 1000°C", 1966 IEEE Conference Record of the Thermionic Conversion Specialist Conference, Nov. 3rd and 4th, 1966, Houston, Texas, 149-158.
- [4] DiSTEFANO, J.R., HOFFMAN, E.E., "Corrosion Mechanisms in Refractory Metal-Alkali Metal Systems", in N.E. Promisel: "The Science and Technology of Tungsten, Tantalum, Molybdenum, Niobium and Their Alloys", Pergamon Press 1964, 257-288.

- [5] BUSSE, C.A., CARON, R., GEIGER, F., PÖTZSCHKE, M., "Performance Studies on Heat Pipes", Proc. Int. Conf. on Thermionic Electrical Power Generation, London, 20-24th Sept., 1965.
- [6] BUSSE, C.A., "Pressure Drop in the Vapor Phase of Long Heat Pipes", 1967 IEEE Conference Record of the Thermionic Conversion Specialist Conference, 30th Oct. - 1st Nov., 1967, Palo Alto, 391-398.
- [7] WEIZEL, W., "Lehrbuch der theoretischen Physik", Band I, 256, Springer Verlag 1955.
- [8] KEMME, J.E., "High Performance Heat Pipes", 1967 IEEE Conference Record of the Thermionic Conversion Specialist Conference, 30th Oct. - 1st Nov., 1967, Palo Alto, 355-358.



Fig. 1 - Failure of Ta/Li heat pipe by impurity corrosion (9 hours of horizontal operation at 1600°C, heating rate 155 w/cm²)



Fig. 2 - Heat pipe with getter container

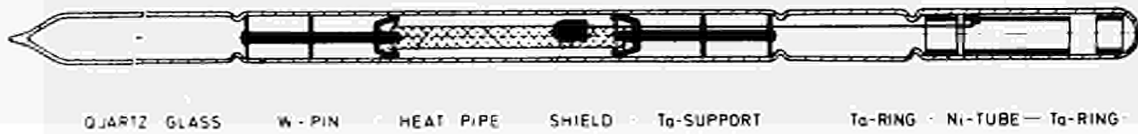


Fig. 3 - Heat pipe life test assembly

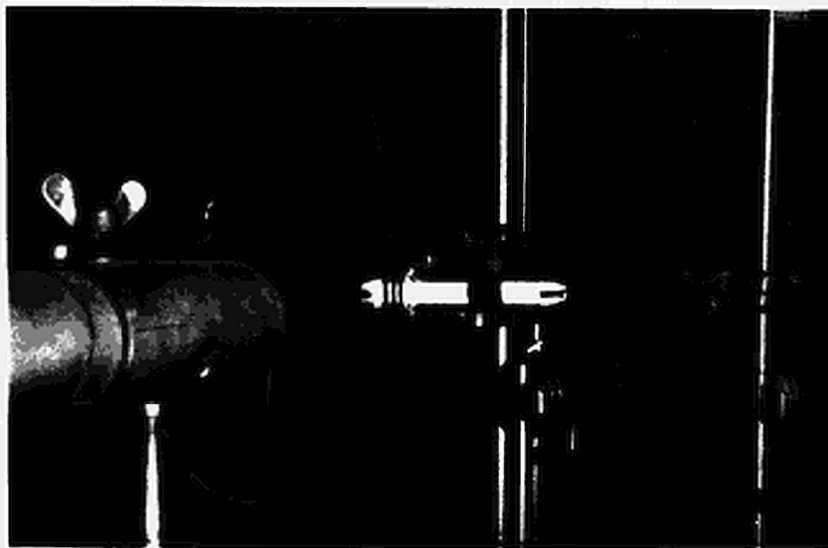


Fig. 4 - Heat pipe life test stand

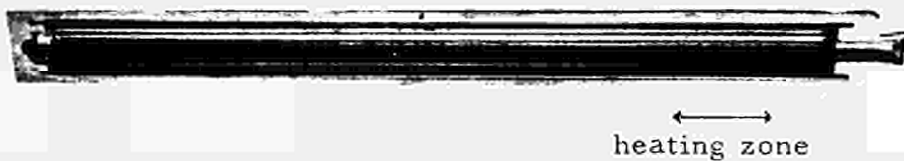


Fig. 5 - SGS-Ta/Li heat pipe after 1000 hours of horizontal operation at 1600°C (heating rate 170 w/cm²)

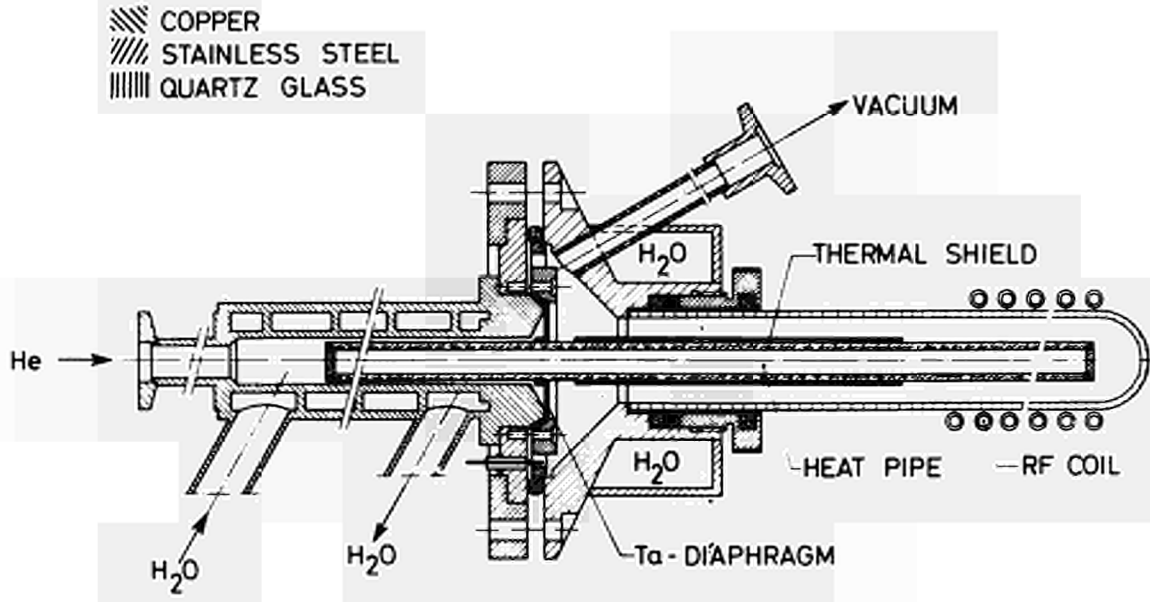


Fig. 6 - Apparatus for heat transfer measurements

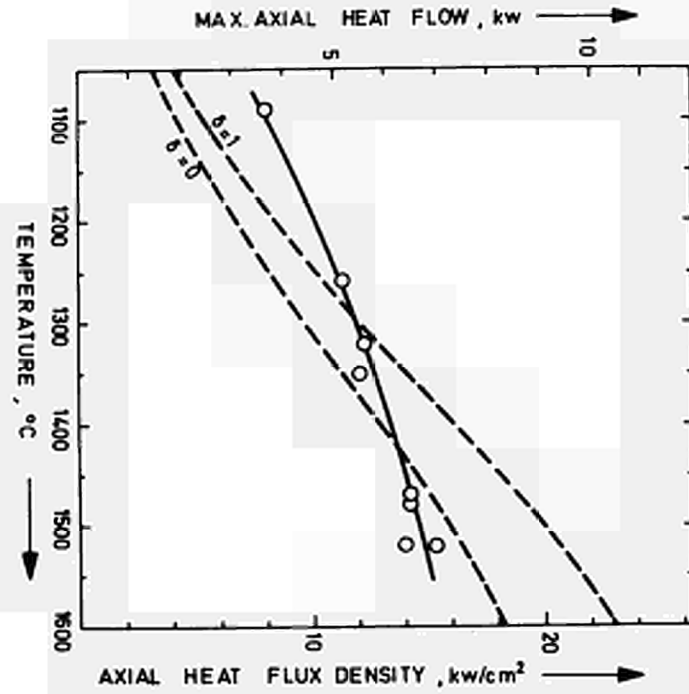


Fig. 7 - Heat transfer results

PRESSURE BALANCE AND MAXIMUM POWER DENSITY AT THE EVAPORATION GAINED FROM HEAT PIPE EXPERIMENTS

F. Reiss, K. Schretzmann

Institut für Neutronenphysik und Reaktortechnik
Kernforschungszentrum Karlsruhe, Germany

From capillary-lined evaporator surfaces very high heat flux densities can be removed. Data for the maximum attainable heat flux densities are derived from experiments preferably with sodium-filled heat pipes. Hydrodynamic and gaskinetic calculations are in accordance with measured data.

In the course of experiments with heat pipes we observed that the evaporation of fluids from capillary-lined evaporator surfaces allows much higher heat fluxes to be removed steadily than are possible with known technical evaporators ¹⁾. We tried to measure the maximum possible evaporation heat flux densities and their dependence on temperature. In this paper we give preliminary results at relatively low temperature and propose a simple model which serves to obtain the wanted heat flux quantities from experiments with sodium-filled SS-heat pipes and confirms the order of magnitude of the reduced data from gaskinetic consideration.

The bulk current of the fluid may be limited by the resistance of the vapor duct and of the capillaries for the streaming vapor and the fluid, respectively. The pressure drop that may be balanced by the capillary forces is relatively small. Since we wished to be independent of the hydrodynamic resistances as far as possible, we operated our heat pipes in vertical position, heating them at the lower end. If the bulk current in the streaming vapor decreases linearly to zero over the condenser length the pressure drop may be expressed as

$$\Delta P_s = \frac{\eta^2 l}{2 d^3 \rho} \cdot \frac{\int_0^{Re_0} \lambda(Re) Re^2 d Re}{Re_0} \quad (1)$$

η being the dynamical viscosity, l the length of the heat pipe, d the inner diameter of the vapor duct, ρ the vapor density, λ the dimensionless resistance number, Re the Reynolds number, and Re_0 the Reynolds' number at the beginning of the vapor stream. Re_0 may be calculated by

$$Re_0 = 4 Q_0 / \pi d L \eta \quad (2)$$

Q_o being the total heat power and L the heat of vaporization of the mass unit.

The resistance number λ depends only on the Reynolds' number and the roughness of the wall. Values of λ have been measured by PRANDTL²⁾ and NIKURADSE³⁾. With these values we calculated the integral

$$I = \int_0^{Re_o} \lambda Re^2 d Re / Re_o \quad (3)$$

The results are shown in Fig.1. With these I -values the vapor drop Δp_s may be written by

$$\Delta p_s = \gamma^2 \cdot l \cdot I / 2 d^3 \rho \quad (4)$$

We note that the formula is valid for all Reynolds' numbers and for the case that the vapor streams partly in turbulent manner and partly in laminar.

To check the formula we calculated from temperature drops ΔT measured on heat pipes¹⁾ the pressure drop Δp_d using the well known values of the equilibrium vapor pressure. The results are shown in Tab.1.

Tab.1. Calculated and measured pressure drops in the vapor duct of a sodium-filled heat pipe

$T_m / ^\circ C$	$\Delta T / ^\circ C$	Q_o / Watt	p_d / Torr	$\Delta p_d / \text{Torr}$	$\Delta p_s / \text{Torr}$
474	1	260	2.32	0.05	0.42
422	12	200	0.67	0.2	0.99
387	73	152	0.25	0.4	1.85

T_m means the mean temperature in degrees centigrade and p_d the mean vapor pressure. The values of Δp_d are distinctly lower than the values of Δp_s calculated from the hydraulic theory. The differences between Δp_d and Δp_s might come from an incompletely developed hydraulic stream caused by low pressure from the fact that admittance disturbances cannot decay in the short tube, that the edge sheet is peeled off by condensation, or from the inertia of the streaming vapor.

Further, the heat power and the heat flux in the evaporator are limited by gaskinetic laws. The maximum number of molecules j_m that may leave the surface unit is

$$j_m = n \bar{v} / 4 \quad (5)$$

n is the number density of molecules and \bar{v} the mean velocity in one direction. The highest possible bulk flux \dot{m}_m and the maximum evaporation power density \dot{q} are

$$\dot{m}_m = m n \bar{v} / 4 \quad (6)$$

$$\dot{q} = m n \bar{v} L / 4 \quad (7)$$

m is the mass of a molecule and L the heat of vaporization per unit mass. The heat flux cannot exceed the value of \dot{q} neither in the phase boundary nor in the vapor duct.

The value of \dot{q} is a very strong function of temperature since the number density of the vapor depends exponentially on temperature. Simple consideration shows that the maximum momentum flux possible in vaporization, i.e. evaporation into vacuum, gives rise to a reaction pressure equal to one half of the saturation vapor pressure p_d . This reaction pressure can be equated to the mass flow density \dot{m} times the mean velocity of the mass flow \bar{v} . The heat of vaporization L gives the maximum evaporation heat flux

$$\dot{q} = \dot{m} L = p_d L / 2 \bar{v} \quad (8)$$

We assume that the mean velocity at evaporation into vacuum is approximately the mean thermal velocity taken over equilibrium distribution function of the momentum component which is parallel to the direction of the mass flow. Fig.2 shows the result of this calculation for sodium. For the calculation up to 1200°C we used the values of the vapor pressure and heat of vaporization given by SCHINS⁴⁾. The dashed part of the curve is based on extrapolated values given by GMELIN⁵⁾. You see that q cannot exceed 230 W/cm² at 500°C but rises to 10⁵ W/cm² at 1000°C.

On the heat pipe the input heat power equals the heat losses in stationary state. The maximum evaporator heat power Q is given by

$$Q = \dot{q} \min \{ F_e, F_{vd} \} = \dot{q} F_m \quad (9)$$

\min being the lowest value of F_e and F_{vd} , F_e the mean evaporator surface, F_{vd} the vapor duct area, and F_m the lowest value of both areas. The maximum evaporator heat power and the heat losses increase with rising temperature. But \dot{q} increases by a higher power of the temperature than do the heat losses. The startup temperature is the temperature where the heat losses equal $\dot{q} F_m$. We had highly concentrated input heat fluxes in most of our experiments⁶⁾ and thus the evaporator area limited the total power.

In experiments, where "large" evaporators are used, where the thickness of the wall is much less than r , and where the heat pipes are cooled by radiation the following formula applies for isothermal mode

$$\pi r^2 \dot{q} \geq 2 \pi r l \epsilon \sigma T^4 \quad (10)$$

r being the inner radius of the tube, ϵ the emissivity, and σ the radiation constant. We have drawn the $2 \epsilon \sigma T^4 l/r$ -line on Fig.2 for $\epsilon = 0.5$ and $l/r = 50$. You see that the \dot{q} -line intersects the $2 \epsilon \sigma T^4 l/r$ -line at about 400°C . There should be no lower startup temperatures in sodium-filled heat pipes with $l/r = 50$ as is roughly confirmed by our experiments and by literature ⁷⁾. Some startup values are entered in Fig.2. Startup temperatures of 450°C follow from similar considerations if the sodium-filled heat pipe is cooled only in a small area at the opposite end of the evaporator ⁸⁾. Further, we have drawn the \dot{q} -line for lithium on Fig.2 and a startup temperature of a lithium-filled tube measured by us. l/r was about 30.

Fig.3 shows the distribution of the ratio of heat power per unit length to total heat power along the axis of inductively heated tubes. The values of Fig.3 are calculated and measured by two independent methods ⁶⁾. With a total heat power of about 3.5 kW we get a maximum heat flux of 300 W/cm^2 on tubes of 2 cm outer diameter.

Our tubes had 36 grooves with a groove-to-land ratio of 1 : 8. Since we can see the grooves on the outer side as more or less dark stripes when the heat pipe runs, we are sure that sodium evaporates only out of the grooves. We conclude that the heat current density at the phase boundary is at least 2000 W/cm^2 without the film boiling phenomena. Otherwise, there would have been a temperature difference of about 100°C between the tube wall and sodium vapor. Our measured values are marked in Fig.2. Their order of magnitude corresponds to the gaskinetic heat flux at lower temperatures. Fig.4 shows measured values of the burnout heat flux in pool boiling of sodium according to BALZHIESER ⁸⁾. Our values are two to ten times higher in the temperature region above 550°C .

In our opinion, there are two reasons for the limitation of the heat fluxes: At relatively low temperatures the reaction pressure p_r at the evaporation is comparable to the vapor pressure. If p_r is greater than the capillary pressure $p_c = 4 \sigma_o/D$ - σ_o being the surface tension, D the width of the grooves - the phase boundary recedes from the edge of

the groove to the bottom and into regions with a higher heat-source density. One may try to increase the maximum heat flux on the evaporator by reducing the width of the grooves and the partition walls. But there a limit is given by the breaking strength of the walls. At higher temperatures the temperature drop in radial direction and the drop of the equilibrium vapor pressure in the fluid from the outside to the inner regions is so great that it cannot be compensated by the friction pressure drop of the radially streaming fluid. Bubbles originate near the bottom of the groove, grow up, and cause it to dry up.

References

- (1) DORNER, S.; REISS, F.; SCHRETMANN, K., "Experimentelle Untersuchungen an Natrium-gefüllten Heat Pipes". Gesellschaft für Kernforschung, Karlsruhe, 1967, KFK 512.
- (2) PRANDTL, L., "Neuere Ergebnisse der Turbulenzforschung". Z. VDI 77 (1933) 105.
- (3) NIKURADSE, J., "Strömungsgesetze in rauhen Röhren". Forschungsarb. Geb. Ingenieurwesen 361 (1933).
- (4) SCHINS, H.E.J., "Liquid Metals for Heat Pipes, Properties, Plots and Data Sheets". EURATOM, JNRC Ispra, 1967, EUR 3653 e.
- (5) "Gmelins Handbuch der Anorganischen Chemie, 21, Erg.band, Lieferung 2". Verlag Chemie, Weinheim, 1965.
- (6) REISS, F.; SCHRETMANN, K., "Die axiale Verteilung der reduzierten Wärmeleistung auf induktiv geheizten, kreiszylindrischen Stäben". Int. Z. Elektrowärme 26 (1968), to be published.
- (7) KEMME, J.E., "Heat Pipe Capability Experiments". Los Alamos Scientific Lab., 1966, LA-3585-MS.
- (8) BOHDANSKY, J.; STRUB, H.; VAN ANDEL, E., "Heat Transfer Measurements Using a Sodium Heat Pipe Working at Low Vapor Pressure". 1966 IEEE Conference Record of the Thermionic Conversion Specialists Conference, Houston, 1966.
- (9) BALZHIESER, R.E. et al., "Investigation of Liquid Metal Boiling Heat Transfer". Air Force Propulsion Lab., Wright Patterson, ASB/Ohio, 1966, AFAPL-TR-66-85.
- (10) GROVER, G.M.; COTTER, T.P.; ERICKSON, G.F., "Structures of Very High Thermal Conductance". J. Appl. Phys. 35 (1964) 1990.
- (11) SEMERIA, R.; SCHMIDT, E.; "Compte Rendu des Travaux Concernant les Caloducs à Sodium". CEA, CEN de Grenoble, 1967, T.T. no.80.

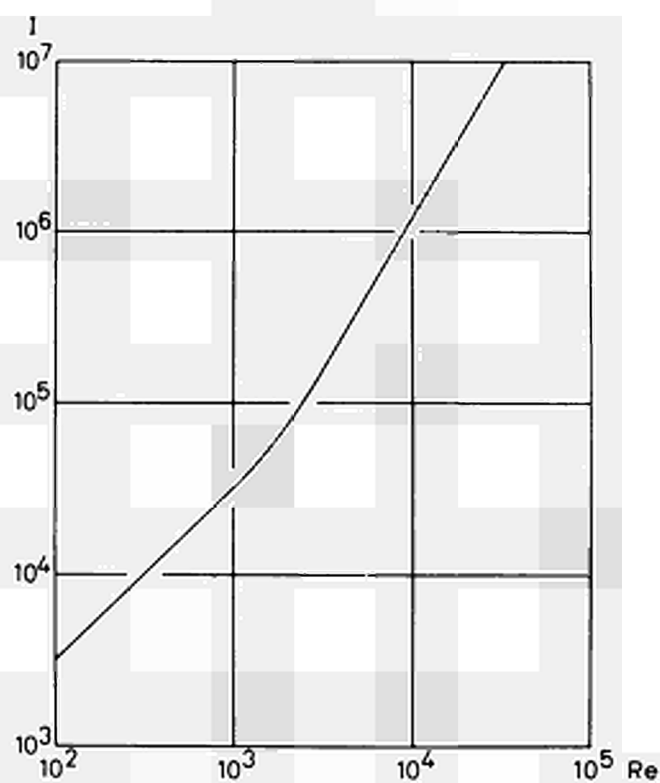


Fig.1. Integral I vs. Re

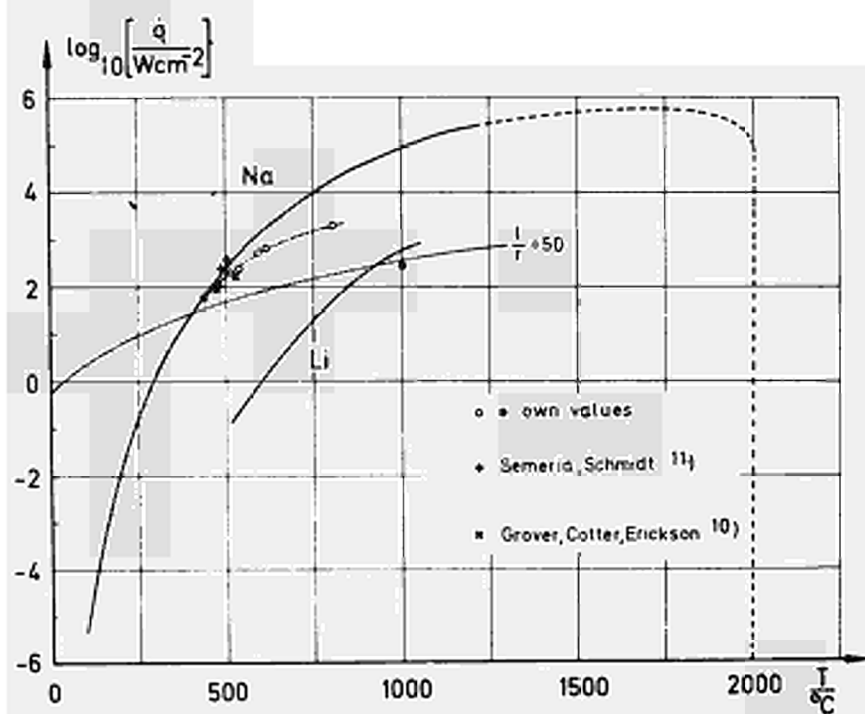


Fig.2. Evaporation power density vs. temp

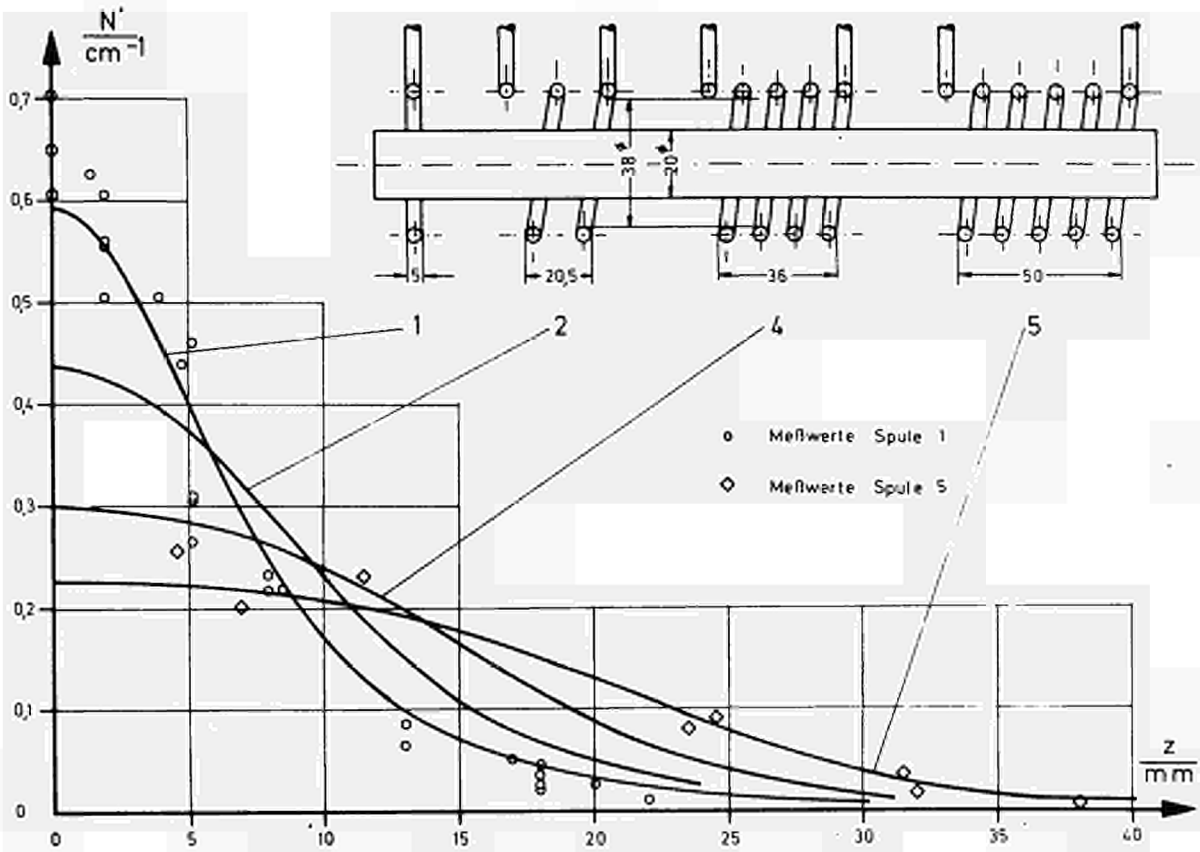


Fig.3. Distribution of the ratio of heat power per unit length to total heat power along the axis of inductively heated tubes

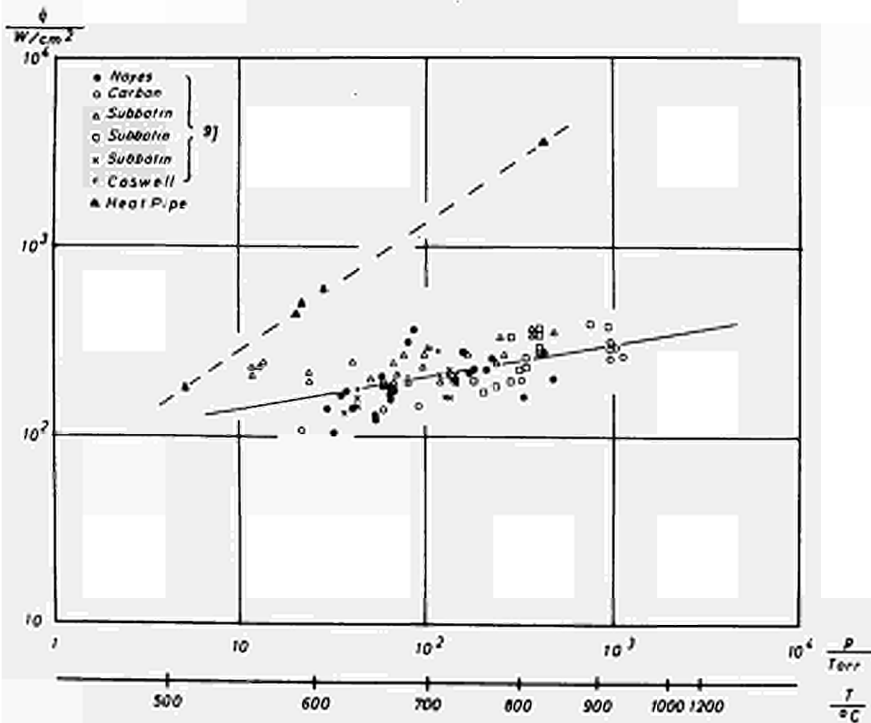


Fig.4. Maximum heat flux of evaporation in heat pipes and burn-out heat flux in pool boiling

DETERMINATION THEORIQUE ET EXPERIMENTALE DE LA
PUISSANCE THERMIQUE LIMITE TRANSFEREE PAR DES CALODUCS A SODIUM

E. SCHMIDT et R. SEMERIA *)

C.E.A. - Service Transferts Thermiques,
B.P. 269, Grenoble (France)

RESUME

Le présent rapport ayant comme but la détermination de la puissance thermique limite transférée par des caloducs à sodium comporte un modèle analytique et des résultats expérimentaux. La puissance thermique limite varie avec la géométrie du réseau capillaire, les dimensions du caloduc, l'angle d'inclinaison par rapport à la position horizontale et la température de fonctionnement.

Dans cette étude, on s'intéresse surtout au premier paramètre ; le réseau capillaire était constitué de quelques enroulements d'un tamis métallique à maille carrée. Dans plusieurs caloducs de même géométrie (diamètres : 21 x 25 mm, longueur intérieure : 200 mm), on a fait varier le vide de maille entre 0,055 mm x 0,055 mm et 0,36 mm x 0,36 mm ; la valeur optimale pour les caloducs travaillant contre la pesanteur a été trouvée égale à 0,21 mm x 0,21 mm ; la température optimale de fonctionnement est comprise entre 600°C et 750°C suivant l'inclinaison du caloduc. Pour des tamis plus fins, la perte de pression due à l'écoulement du liquide dans le réseau capillaire devient trop élevée ;

*) Cette étude a été effectuée au Commissariat à l'Énergie Atomique, Service des Transferts Thermiques, Centre d'Études Nucléaires de Grenoble - FRANCE, avec la participation financière de la Direction des Recherches et Moyens d'Essais.

pour des tamis plus gros fonctionnant contre la pesanteur, l'ascension capillaire devient insuffisante.

De plus, des essais d'amorçage ont été entrepris avec un caloduc à calcium.

0. INTRODUCTION

La puissance thermique transférée par un caloduc présente une limite supérieure due à l'assèchement de la zone de l'évaporateur qui subit alors une brutale élévation de température. Ce phénomène d'assèchement peut avoir deux origines différentes :

- 1) Caléfaction à l'évaporateur due à une trop grande densité de flux de chaleur ;
- 2) Interruption de la circulation du liquide caloporteur.

En ce qui concerne la première limitation, il ne semble pas que, pour des utilisations actuellement envisagées, la caléfaction risque de limiter les performances des caloducs.

La deuxième limitation peut être expliquée par le fait que les pertes de charge dues à l'écoulement du métal caloporteur à l'état liquide et gazeux plus éventuellement la pression hydrostatique ne doivent pas dépasser la pression motrice capillaire. Cette condition limitant le fonctionnement des caloducs fait l'objet de cette communication.

1. MODELE ANALYTIQUE

En négligeant la conduction thermique axiale dans l'enveloppe tubulaire, la puissance thermique transférée W est proportionnelle au débit massique m et à la chaleur latente de vaporisation \mathcal{L} du métal caloporteur.

La condition de fonctionnement pour un caloduc placé dans un champ de pesanteur est :

$$\Delta p_{\text{mot}} \geq \Delta p_l + \Delta p_v + (\rho_l - \rho_v) \cdot g \cdot L \cdot \sin \alpha$$

Les différents termes peuvent être calculés de la manière suivante :

Δp_{mot} : En ce qui concerne la force motrice capillaire, on peut supposer que, pour un tamis à maille carrée, les interfaces liquide-vapeur sont sphériques et on obtient pour la pression motrice :

$$\Delta p_{\text{mot}} = \frac{2 \sigma}{R_M} \cdot \cos \theta$$

où σ est la tension superficielle, R_M est le demi-côté du carré vide du tamis et θ est l'angle de contact. Pour les caloducs à sodium possédant du tamis à maille carrée comme réseau capillaire, nous proposons d'utiliser pour $\cos \theta$ une valeur de 0,5 - 0,6. Cette valeur a été déterminée expérimentalement et elle tient compte d'une part de l'angle de contact et, d'autre part, du fait que pour des tamis à maille carrée l'interface liquide-vapeur n'est pas purement sphérique.

Δp_1 : En ce qui concerne la perte de pression du liquide le long du réseau capillaire, nous écrivons la relation suivante qui a été établie à partir d'un coefficient de frottement [1] [2] :

$$\Delta p_1 = \frac{1}{C^3 \left(1 - \frac{0,317}{C}\right)^3} \cdot \frac{L}{(n - 0,5) R_M^3} \cdot \left[0,425 \frac{\mu_l}{\rho_l} \cdot \frac{1}{r + 1,32 R_M C (n - 0,5)} \text{ m} \dots \right. \\ \left. + 0,00182 \frac{1}{\rho_l} \cdot \frac{1}{[r + 1,32 R_M C (n - 0,5)]^2} \text{ m}^2 \right]$$

Cette relation a été vérifiée expérimentalement et elle est valable pour un écoulement laminaire ainsi que pour un écoulement turbulent.

On voit que Δp_1 varie essentiellement avec C. C'est le rapport entre l'épaisseur totale du réseau capillaire et l'épaisseur de n couches du tamis. On appelle C le facteur de foisonnement.

En plus, Δp_1 varie avec n, avec R_M et avec la longueur du caloduc L.

Δp_v

Si $Re_x < 1\ 500$, nous utilisons pour la zone de l'évaporateur une solution proposée par YUAN et coll. [3]. Pour le conduit de vapeur, on applique l'équation classique et on ajoute un terme supplémentaire (établi par SPARROW [4]) qui tient compte de l'établissement du régime d'écoulement ayant lieu à l'entrée du conduit de vapeur. Donc nous écrivons :

$$\Delta p_v = \left[0,125 \cdot \frac{1}{\rho_v} \cdot \frac{1}{r^4} m^2 + 1,689 \frac{\mu_v}{\rho_v} \cdot \frac{L_E m}{r^4} \right]_E$$

$$+ \left[2,55 \frac{\mu_v}{\rho_v} \frac{L_{cv}}{r^4} m + 0,388 L_{cv}^{0,435} \cdot \frac{\mu_v^{0,435}}{\rho_v} \cdot m^{1,565} \right]_{cv}$$

Dans la zone du condenseur, la condensation crée une certaine élévation de pression. Comme la pression dans la phase liquide ne peut pas être supérieure à celle dans la phase vapeur, on suppose que la pression est égale dans les deux phases à l'entrée du condenseur. Donc, on ne tient pas compte d'une variation de pression dans cette partie du caloduc [5].

Si $Re_x > 1\ 500$, nous utilisons pour la zone de l'évaporateur une relation établie expérimentalement par ECKERT et coll. [6] et pour le conduit de vapeur nous appliquons l'équation classique de BLASIUS. Pour la zone du condenseur, nous faisons les mêmes hypothèses que pour le cas de l'écoulement laminaire et nous écrivons :

$$\Delta p_v = \left[0,2255 \frac{1}{\rho_v} \cdot \frac{1}{r^4} m^2 \right]_E + \left[0,0107 \frac{\mu_v^{0,25}}{\rho_v} \cdot \frac{L_{cv}}{r^{4,75}} \cdot m^{1,75} \right]_{cv}$$

Finalement, on peut calculer le débit massique en fonction des dimensions des pores du tamis caractérisées par R_M .

Si le caloduc fonctionne contre la gravité, l'ascension capillaire et les pertes de charge dans la phase liquide varient en sens opposé. Il existe pour la puissance thermique limite une valeur optimale qu'on obtient pour $R_M \approx 0,009$ cm. On voit que au-delà d'une

valeur limite de R_M limite = 0,013 cm un fonctionnement contre la pesanteur n'est plus assuré (voir figure A).

Ces courbes ont été établies pour un caloduc à sodium, longueur totale 20 cm; longueur de la zone de l'évaporateur et celle du condenseur 4 cm, diamètre intérieur 2 cm, nombre de couches du tamis $n = 3$; $C = 1$ et la température de fonctionnement $t = 700^\circ\text{C}$.

Conformément à ces calculs préliminaires, nous avons choisi pour nos expériences cinq tamis à différente maille.

2. EXPERIENCES

Les essais ont été effectués avec des caloducs à sodium en acier inoxydable ayant les dimensions suivantes : longueur intérieure totale 20 cm, évaporation et condensation sur 4 cm, diamètre intérieur 2,1 cm. Le tamis en acier inoxydable était plaqué contre la paroi intérieure par un ressort hélicoïdal en fil d'acier inoxydable.

Le caloduc est chauffé par induction à l'aide d'un four à haute fréquence. Le réglage de la puissance thermique évacuée au condenseur était assuré par une résistance thermique variable constituée d'un espace annulaire entre le caloduc et l'échangeur à eau rempli d'un mélange de deux gaz à conductivité thermique très différente. Un bilan thermique sur l'eau nous donne la valeur de la puissance évacuée (voir figure n° 1).

Nous avons fait varier dans les cinq caloducs le numéro du tamis et le nombre d'enroulements comme indiqué dans le tableau suivant :

Caloduc N°	1	2	3	4	5
Tamis N°	50	80	120	150	300
Mesh size	45	75	100	120	270
Vide de maille $2 R_{\text{M}}$ (mm x mm)	0,36 x 0,36	0,21 x 0,21	0,141 x 0,141	0,125 x 0,125	0,055 x 0,055
Diamètre du fil d (mm)	0,20	0,14	0,09	0,06	0,04
Nombre de couches n	2	3	4	2	4

La puissance thermique limite a été déterminée en fonction de la température du caloduc et en fonction de l'angle d'inclinaison. Les cinq caloducs expérimentés montrent le même comportement caractéristique représenté sur la figure n° 2.

Ces valeurs ont été obtenues avec un caloduc possédant trois couches du tamis n° 80.

Nous pouvons constater que :

- la puissance thermique limite W_L varie nettement avec la température du caloduc t_c . Elle atteint une valeur maximale pour une température variant entre 650°C et 750°C selon l'angle d'inclinaison α .
- W_L varie avec α . En s'approchant de la position verticale, l'influence de la pression hydrostatique devient de plus en plus grande.

- le démarrage d'un caloduc à sodium se produit entre 450°C et 480°C, à condition qu'à cette température la résistance thermique au condenseur soit suffisamment élevée (pour les caloducs refroidis à l'eau, nous avons mesuré une valeur limite inférieure de la résistivité thermique de $\frac{1}{k} \approx 0,35 \cdot 10^3$ [cm °C/watt]).
- les valeurs calculées présentées en traits interrompus sont obtenues pour un angle de contact $\theta = 50^\circ$ et pour $C = 1$. Le facteur C a été déterminé par une radiographie faite à la température ambiante permettant de mesurer l'épaisseur du réseau capillaire. Pour des températures de fonctionnement peu élevées, on trouve un bon accord entre les valeurs calculées et mesurées, mais on constate qu'il y a un écart entre les deux courbes pour des températures élevées. Nous pensons que cette divergence peut être expliquée par un mauvais contact entre l'enveloppe tubulaire et le réseau capillaire dû à la dilatation différentielle du caloduc et du tamis.

Pour comparer les performances des caloducs étudiés, nous avons représenté la puissance limite maximale en fonction de la hauteur d'inclinaison (figure n° 3). Elle nous donne une idée de l'influence des propriétés caractéristiques de la structure capillaire (vide de maille, nombre d'enroulements).

Le caloduc n° 2 équipé de trois couches du tamis n° 80 et le caloduc n° 3 équipé de quatre couches du tamis n° 120 peuvent transporter les puissances les plus élevées.

Dans les différents caloducs, le nombre de couches varie entre 2 et 4 et le facteur de foisonnement entre 1,4

et 2,2, car notre système de fixation du réseau capillaire ne permet pas de plaquer les tamis contre la paroi d'une manière très rigide.

Pour obtenir une comparaison plus précise entre les différents tamis utilisés, nous avons calculé, à partir de ces résultats expérimentaux, la puissance limite maximale pour $n = 3$ et $C = 1$ (voir figure n° 4).

On voit que les caloducs possédant du tamis n° 80 transportent les plus grandes puissances contre la gravité.

Les caloducs avec le tamis n° 50 transportent des puissances thermiques encore plus élevées, mais leur fonctionnement est limité à 11 cm de dénivellation.

3. CONCLUSION

Les essais effectués avec cinq caloducs à sodium nous ont permis d'étudier leur fonctionnement et d'obtenir des valeurs pour la puissance thermique limite en fonction de la température, de l'angle d'inclinaison et des dimensions du réseau capillaire.

Nous avons montré que le démarrage et le fonctionnement d'un caloduc à sodium sont possibles dans toutes les positions, s'ils sont équipés d'une structure capillaire appropriée.

De plus, des essais d'amorçage ont été entrepris avec un caloduc à calcium fonctionnant normalement à 1 300°C dans la position verticale sans réseau capillaire et refroidi par rayonnement. Malgré la température de fusion élevée du calcium ($t_f = 850^\circ\text{C}$) et sa pression de vapeur

correspondante ($p_f = 1,99$ mm Hg), les essais préliminaires ont montré que l'amorçage était possible. L'étude détaillée sera publiée sous forme d'un rapport C.E.A. à paraître prochainement.

Nomenclature

g	accélération de la pesanteur
m	débit massique
n	nombre de couches du tamis
Δp	perte de pression
r	rayon du caloduc
t	température
C	facteur de foisonnement
L	longueur du caloduc
R_M	demi-côté du carré vide du tamis
Re	nombre de Reynolds
W	puissance thermique
θ	angle de contact
\mathcal{L}	chaleur latente
α	angle d'inclinaison
μ	viscosité dynamique
ρ	masse volumique
σ	tension superficielle

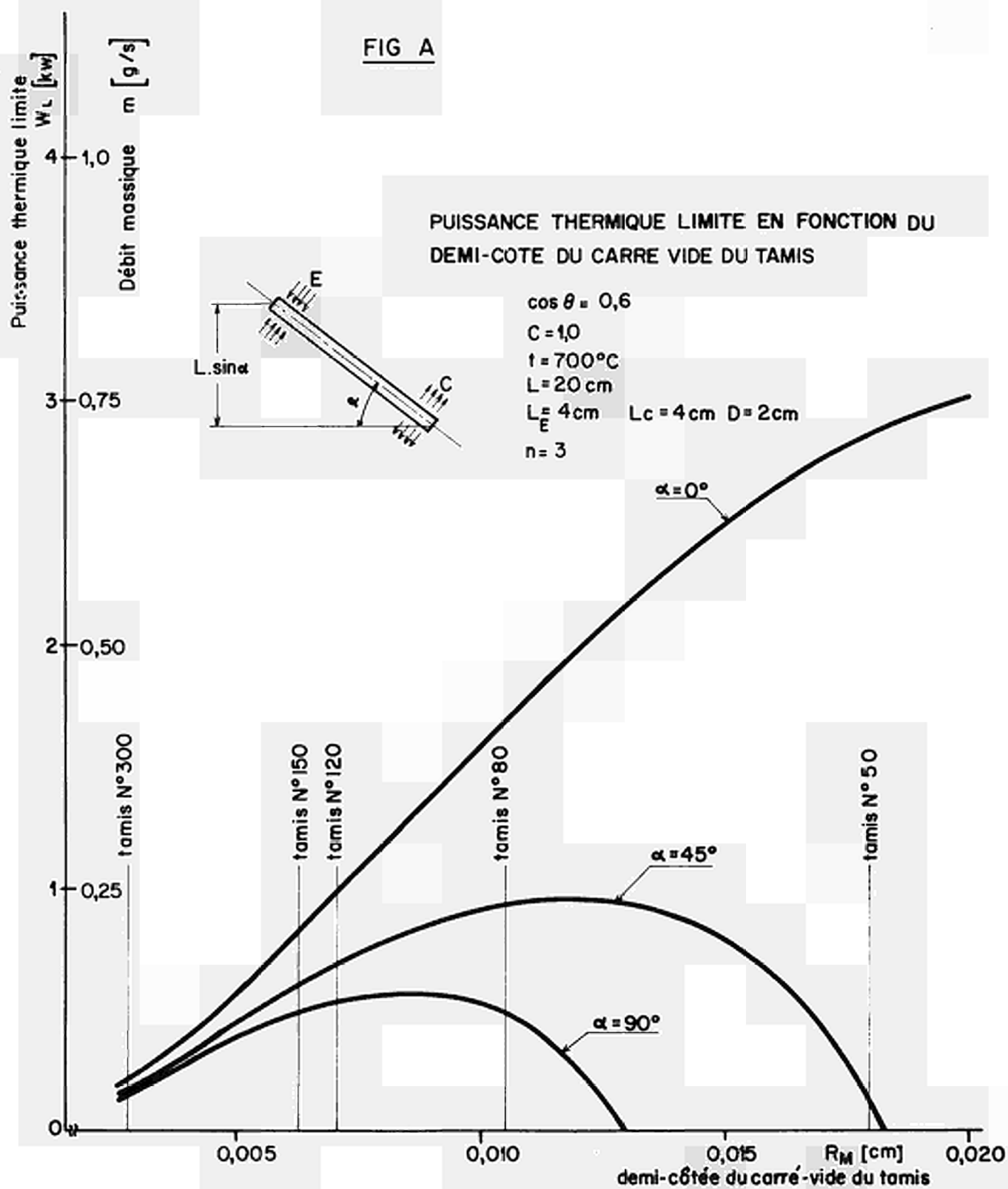
Indices

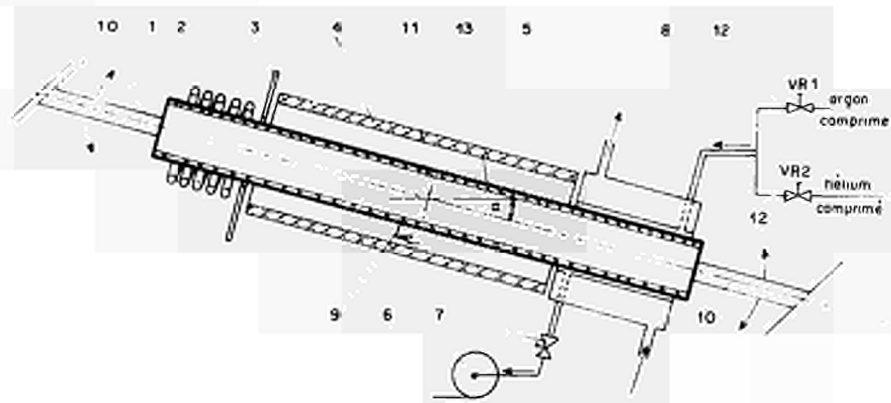
C	condenseur	l	liquide
CV	conduit de vapeur	mot	motrice
E	évaporateur	v	vapeur
L	limite	x	axial

BIBLIOGRAPHIE

- [1] SCHMIDT E.
Détermination de la perte de charge dans des milieux capillaires susceptibles d'être utilisés dans des caloducs
Note TT n° 265 - Avril 1967
- [2] BIRD R.B., STEWART W.E., LIGHTFOOT E.N.
Transport Phenomena
Department of Chemical Engineering
University of Wisconsin 1965
- [3] YUAN S.W., FINKELSTEIN A.B.
Laminar Pipe Flow with Injection and Suction through a porous Wall
TRANS. ASME - Vol. 78, 1956, pp. 719-724
- [4] SPARROW EKM, LIN S.H.
Flow Development in the Hydrodynamic Entrance Region of Tubes and Ducts
The Physics of Fluids, Vol. 7, n° 3, 1964
- [5] BUSSE G.A.
Pressure Drop in the vapor Phase of long Heat pipes
Communication presented at the thermionic Conversion Specialist Conference 30-10 - 1-11-67
- [6] OLSON R.M., ECKERT E.R.G.
Experimental Studies of Turbulent Flow in a Porous Circular Tube with Uniform Fluid Injection through the Tube Wall
J. of Appl. Mechanics, March 1966/67, p. 7-17

FIG A

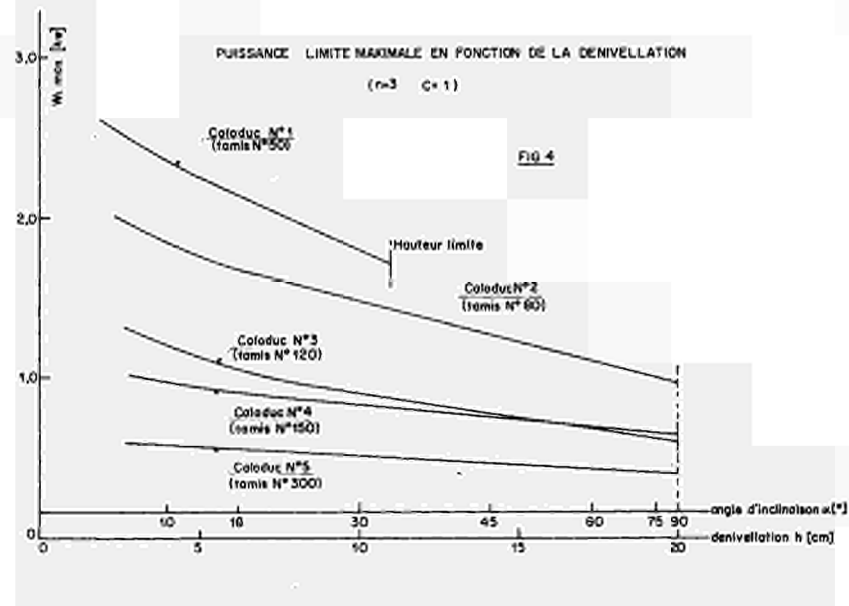
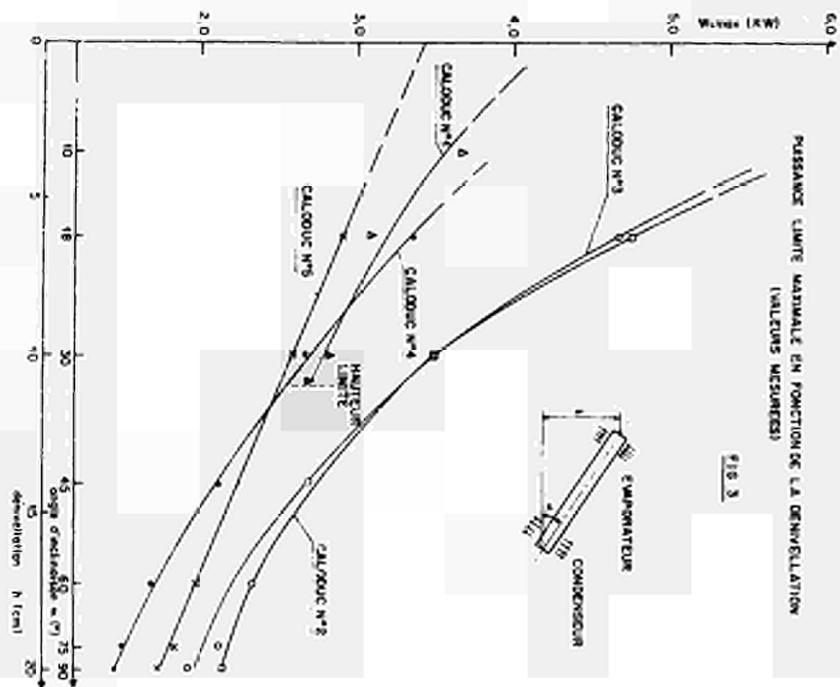
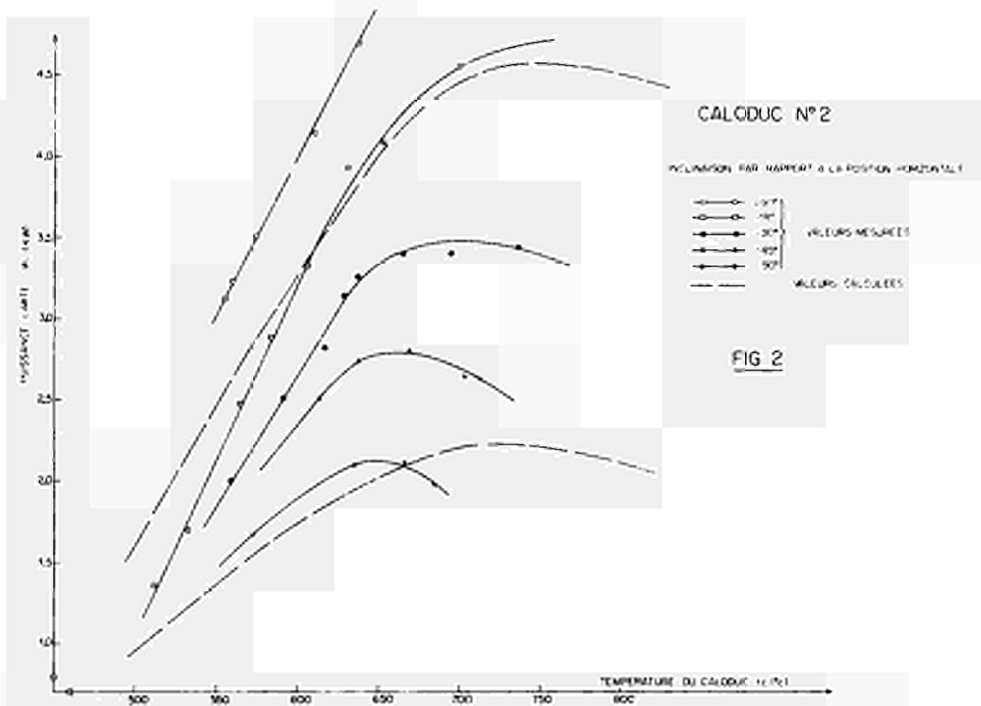




- | | | |
|----------------------|--------------------|------------------------|
| 1. Coloduc | 5. Echangeur à eau | 9. Thermocouple |
| 2. Bobine inductrice | 6. Pompe à vide | 10. Tige de suspension |
| 3. Déflecteur | 7. Vanne d'arrêt | 11. Axe de rotation |
| 4. Centrifuge | 8. Tube de mélange | 12. Vanne de réglage |
| | | 13. Réseau capillaire |

SCHEMA DU DISPOSITIF EXPERIMENTAL

Figure 1





HEAT PIPE DESIGN THEORY

E. van Andel - EURATOM CCR, Direct Conversion Division, Ispra, Italy

Abstract

A dimensionless approach is given for the calculation of maximum heat flow in heat pipes and optimization of the capillary structure. Parameters of twelve liquid metals in the temperature range of 600-2200 °K are given for use in the calculations. Nomogrammes for direct evaluation of heat pipe performance and optimum capillary dimension are presented.

1. Introduction

One of the tasks of a heat pipe theory is to predict the maximum heat flow in terms of known parameters. This is essentially a fluid flow problem, which has been treated by [1] and [2], and experimentally confirmed by [1] and [3]. A survey of relevant material constants [4] completes the basis for an engineering theory. This theory is expressed in a set of dimensionless parameters, which is common practice in transport physics.

2. Dimensionless Numbers

The following groups are chosen:

$$Re = \frac{\dot{Q} d}{\frac{\pi}{4} d^2 L \eta_v}, \quad \text{the Reynolds Number, proportional to the ratio of inertial to viscous forces in the vapor stream}$$

$$Hp = \frac{\dot{Q} \eta_v}{\frac{\pi}{4} d^2 L \rho_v \gamma}, \quad \text{the Heatpipe Number, proportional to the ratio of viscous forces in the vapor and capillary forces}$$

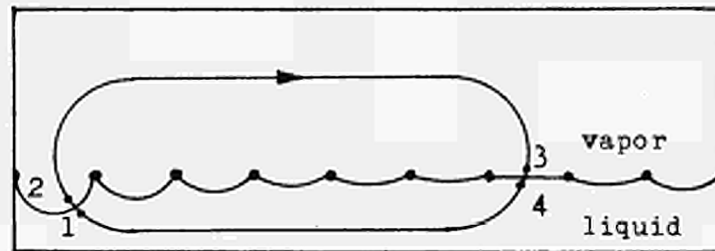
$$Eu = \frac{\Delta p_v}{\frac{1}{2} \rho_v v^2}, \quad \text{the Euler Number, or the effective vapor pressure drop, expressed in number of velocity heads}$$

$$\frac{\nu_l}{\nu_v} = \frac{\eta_l \rho_v}{\eta_v \rho_l}, \quad \text{the kinematic viscosity ratio, proportional to the ratio of viscous forces in liquid and vapor}$$

$$\frac{h}{h_c} = \frac{h \cdot r \cdot \rho_l \cdot g}{\gamma}, \quad \text{the ratio of gravity forces and capillary forces (Bond Number)}$$

The values of the groups of material constants, to be used for evaluating these numbers, are given in figs. 1 to 4.

3. Pressure Balance



The integral of the pressure along any closed path must be zero. The maximum capillary pressure drop acts [1] between two points: the dry point, where the curvature of the meniscus reaches its maximum at burnout condition, and the wet point, where the meniscus is flat and excess fluid assembles. So all other pressure drops must be calculated along a path that crosses the meniscus at these two points. The result is a balance between these pressure drops:

$$\Delta P_{v(a+f)}^{(2-3)} + \Delta P_l^{(4-1)} + \Delta P_g^{(4-1)} = \Delta P_c^{(1-2)} \quad (1)$$

and a criterium for the location of the wet point. We divide the equation through $\Delta P_c = \frac{\gamma}{r}$ and call the terms vapor term, liquid term, gravity term respectively:

$$p_v + p_l + p_g = 1 \quad (2)$$

These terms are now expressed with the dimensionless numbers.

3.1 The vapor term

From the definitions of the dimensionless numbers it is clear that the vapor term becomes:

$$p_v = \frac{r}{2d} Eu Hp Re \quad (3)$$

A vapor flow theory is needed to define Eu as a function of l_H/d ; l_S/d ; l_C/d and Re . In the case that there is sufficient pressure rise in the vapor in the cooled zone to shift the wet point to the end of the shielded zone, Eu is not dependent on l_C/d . For design purposes, Eu can be read from fig.7, when Re , l_H/d and l_S/d are known. The graph of fig. 7 contains four theories: (a,b,c,d)

a) For low Re values and long heatpipes, the theory of [2] is plotted. It can be written as:

$$Eu = \frac{16}{Re} \cdot \frac{2l_H + 4l_s}{d} + \frac{28}{9} - \frac{0,68 Re}{29l_H/d + Re} \cdot \exp\left(\frac{-60 l_s}{Re d}\right) \quad (4)$$

b) For higher Re values and shorter heatpipes, Eu is formally expressed as

$$Eu = f \cdot \frac{4l}{d} + 2 \frac{\sqrt{v}}{-v} \quad (5)$$

as a result of a momentum balance over the vapor cylinder. For the cosine profile which is in this case established, $2 v^2/\bar{v}^2 = \frac{\pi^2}{4}$ and f has been measured by [3] for Re values about 4000. For these heatpipes no sudden change from laminar to turbulent flow is observed [1].

We assume now that the amount of turbulency in the vapor stream increases steadily with increasing Re, and take for f the theoretical laminar value for the cosine profile, plus a turbulency term proportional with $Re^{-0,2}$:

$$f = \frac{2\pi^2}{Re} + \frac{0,03}{Re^{0,2}} \quad (6)$$

the value of 0,03 stemming from the experiments in [3]

c) For higher Re and very long heatpipes, the cosine profile decays in the shielded zone to the Blasius profile. In this region $2v^2/\bar{v}^2 = 2$ and for f is taken the value for a relative wall roughness of 1%. Here, of course, an abrupt change occurs from turbulent to laminar flow with decreasing Re value.

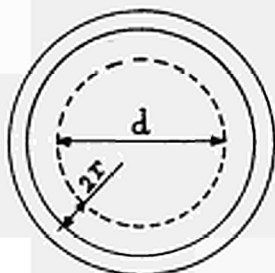
d) For low Re and very long heatpipes, the acceleration term can be neglected and

$$Eu = \frac{16}{Re} \cdot \frac{4l}{d} \quad (7)$$

3.2 The liquid term

We will impose self-priming on the capillary system, i.e. as maximum heat flow is considered that heat flow, with which an already existing dry spot will rewet itself. This means that the liquid channel itself delivers the capillary driving force, and not its relatively fine-meshed screen cover.

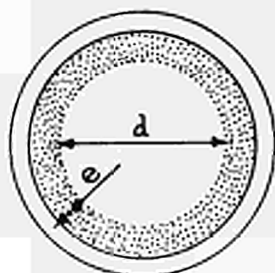
For a capillary system consisting of a permeable screen at a distance $2r$ from the inner wall, the liquid term becomes, when $r \ll d$:



$$p_l = 0,375 \frac{d l}{r^2} H_p \frac{v_l}{v_v} \quad (8)$$

When r is not much smaller than d , the term has a lower value, but this is compensated somewhat by the presence of spacer rods in the gap.

For layers of packed screen, or porously sintered particles, the resistance can be calculated with the Blake-Koseny equation. This gives:

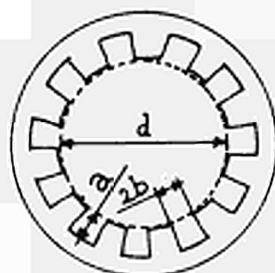


$$p_l = 1,18 \frac{d l}{e e r} H_p \frac{v_l}{v_v} \quad (9)$$

$$\text{where } r = \bar{d}_p \cdot \frac{e}{6(1-\epsilon)} \quad (9a)$$

\bar{d}_p is the mean particle diameter. For wires or screen, \bar{d}_p is 1,5 times wire diameter.

For N rectangular grooves, deep a , wide $2b$, and closed to the vapor steam by a permeable screen:



$$p_l = 1,18 \frac{d^2 l r}{a_{\text{eff}} b^3 N} H_p \frac{v_l}{v_v} \quad (10)$$

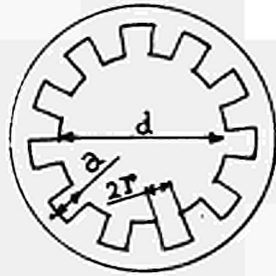
$$\text{with } r = \frac{a \cdot b}{a + 2b} \quad (10a)$$

$$\text{and } \frac{a_{\text{eff}}}{a} = a \left(1 - 2 \cdot \frac{192}{\pi} \frac{b}{a} \operatorname{tgh} \frac{\pi}{2} \frac{a}{2b} \right) \quad (10b)$$

the last being a form factor for laminar flow on rectangular channels.

For N rectangular grooves, deep a , wide $2r$, and open to the vapor stream,

$$p_l = 1,18 \frac{d^2 l}{a_{\text{eff}} r^2 N} H_p \frac{v_l}{v_v} \quad (11)$$



$$\text{with } \frac{a_{\text{eff}}}{a} = \frac{1 - \frac{192}{\pi^5} \frac{r}{a} \operatorname{tgh} \frac{\pi}{2} \frac{a}{r}}{1 + \frac{r}{2a} \left(\frac{r}{d}\right)^3 \cdot N \cdot \frac{f \cdot \operatorname{Re}}{v_l/v_v}} \quad (11a)$$

(11a) is an empirical correlation, stemming from a comparison of vapor friction-induced shearing stress and total shearing stress on the liquid in the channel. It explains very well the experimental data of [1].

3.3 The gravity term

The gravity term becomes simply

$$p_g = \frac{h}{h_c} \quad (12)$$

for horizontal heatpipes, $h = d$.

4. Other burnout mechanisms

When the maximum capillary pressure is γ/r , the heat pipe equation is (2). But the max. capillary pressure can be temporarily higher, for instance when an annular capillary gap is formed by very fine meshed screen, or when in such a structure nucleation causes burnout. In these cases (2) becomes

$$p_v + p_l + p_g = r/r' > 1 \quad (2a)$$

r' is then the effective capillary radius of the screen, or half the radius of the boiling nucleus. When these heatpipes develop a hot spot, the heat-flow must be lowered until ϵ_p becomes unity, and then the hot spot will vanish.

5. The optimized heatpipe

The heatpipe equation, for instance for an annular capillary structure, follows from (2), (3) and (8)

$$\frac{r}{2d} \operatorname{Eu} \operatorname{Hp} \operatorname{Re} + 0,375 \frac{d\ell}{r^2} \operatorname{Hp} \frac{v_l}{v_v} = 1 \quad (13)$$

It has been shown in (5) that r can be optimized to yield the largest maximum heat flow. For optimum r hold:

$$r_{opt} = (1,13 \text{ Hp} \frac{v_l}{v_v} d l)^{1/2} \quad (14)$$

$$\text{Hp}^3 \text{Re}^2 \text{Eu}^2 \frac{v_l}{v_v} \frac{l}{d} = 1,58 \quad (15)$$

(14) has been drawn in nomogram 2.

(15) can be made explicit in \dot{Q} when a Re invariant approximation is made for Eu, for instance (see (5))

$$\text{Eu} = 0,04 \frac{l}{d} + 2,5 \quad (16)$$

(16) holds for short heatpipes and Re about 4000. For l can be taken $\frac{1}{2} l_H + l_S$.

(15) becomes now: (drawn in nomogram 1)

$$\dot{Q} = \left(\frac{\pi^5}{648}\right)^{0,2} \left\{ \frac{d^8}{\frac{l}{d} (2,5+0,04 l/d)^2} \right\}^{0,2} \left\{ \frac{L^5 \gamma^3 \rho_v^2 l}{\eta_l} \right\}^{0,2} \quad (17)$$

the last factor in (17) is a material constant: a kind of quality factor for working fluids for short heatpipes, and is drawn in fig.5.

For very long heatpipes, for instance the kind that could be used for stabilizing temperature in a satellite skin, the approximation (7) is better. This leads also to an explicit expression for \dot{Q} , with a slightly modified quality factor.

Between these two limits, the calculation should be iterated. The nomogram 1 gives the starting value of \dot{Q} . With fig. 1 Re can now be calculated. Fig.7 gives Eu and (17), in which Eu is reinserted, gives the second value for \dot{Q} , with the help of fig. 5.

6. Heat pipe start up

In the process of bringing the heatpipe up to working temperatures by applying heat to the heated zone, another burn out criterium is to be observed. In this case the pressure in the colder part is practically zero. Burn out occurs when the saturation pressure in the heated zone exceeds the maximum capillary pressure. This determines the maximum temperature to which the heated zone can be heated, as function of r and the working fluid type. This temperature can be read from fig.6. The corresponding heatflow can now be calculated, assuming that the vapor expands adiabatically and friction in vapor and liquid can be neglected (closed capillaries). The theory of compressible flow yields for the mass flow density

$$\dot{M} = \left(\frac{2}{k+1} \right)^{\frac{1}{k-1}} \cdot \left(\frac{2k}{k+1} \right)^{\frac{1}{2}} \cdot \left(p_H \rho_H \right)^{\frac{1}{2}} \quad (18)$$

For metal vapors $k = 5/3$, so that the sonic heat flow density

$$\dot{Q}''_{\text{SONIC}} = 0,73 L (p_H \rho_H)^{1/2} \quad (19)$$

Experiments indicate that contraction of the vapor jet and friction effects reduce the theoretical value to about 40%. So:

$$\dot{Q}_{\text{START}} = 0,4 \cdot \frac{\pi}{4} d^2 \cdot 0,73 L \cdot (p_H \rho_H)^{1/2} \quad (20)$$

When the designer takes care that the cooled zone, is sufficiently insulated, at least during start-up, to reach the temperature of fig.6 with the heat-flow of (20), then the heatpipe can usually be brought in isothermal operation.

Acknowledgement

The author thanks Dr. H. Neu for the many heat pipe problems he gave to solve, which led to this more rapid way of calculating, and Dr. J. Bodansky and Dr. C.A. Busse for many correcting discussions.

References

1. J. Bohdansky, H. Strub, E. van Andel, "Heat Transfer Measurements Using a Sodium Heatpipe Working at Low Vapor Pressures" Thermionic Conversion Specialist Conference, Houston (1966)
2. C.A. Busse, "Pressure Drop in the Vapor Phase of Long Heatpipes" Thermionic Conversion Specialist Conference, Palo Alto. (1967)
3. J. Bohdansky, H.E.J. Schins, "Heat Transfer of a Heatpipe Operating at Emitter Temperatures" Proc. Int. Conf. on Thermionic Electrical Power Generation, London (1965)
4. H.E.J. Schins, "Liquid Metals for Heatpipes, Properties, Plots and Data Sheets" EUR 3653 e (1967)
5. G.M. Grover, J. Bohdansky, C.A. Busse, "The use of a new Heat Removal System in Space Thermionic Power Supplies", EUR 2229 e (1965)
6. C.A. Busse, R. Caron (1965) (unpublished)

a	(cm)	measured depth of capillary grooves
a _{eff}	(cm)	effective depth of capillary grooves
b	(cm)	half-width of closed capillary grooves
d	(cm)	internal or vapor channel diameter
\bar{d}_p	(cm)	mean particle diameter, i.e. the diameter of a sphere with the same volume-to-diameter ratio as all the particles in the bed together
e	(cm)	radial thickness of packed bed capillary system
f	(cm)	Fanning friction factor $f = \tau_w / \frac{1}{2} \rho_v \bar{v}^2$
g	(cm/s ²)	acceleration of gravity
h	(cm)	elevation of dry point over wet point
h _c	(cm)	rising height in capillary system
ℓ	(cm)	effective length for friction (mostly $\ell = \frac{1}{2} \ell_H + \ell_S$)
ℓ _H	(cm)	length of heated zone
ℓ _S	(cm)	length of shielded zone
ℓ _C	(cm)	length of cooled zone
L	(ws/g)	latent heat of evaporation
\dot{M}''	(g/cm ² s)	mass flow density
N	(-)	number of capillary grooves
ΔP_{va}	(dyne/cm ²)	pressure drop due to vapor acceleration
ΔP_{vf}	(")	" " " " " friction
ΔP_{lf}	(")	" " " " liquid friction
ΔP_g	(")	" " " " gravity
ΔP_c	(")	" " " " capillarity
\dot{Q}	(w)	maximum heat flow
r	(cm)	effective capillary radius: $\Delta P_c = \gamma/r$
\bar{v}	(cm/s)	mean vapor velocity: $\dot{Q} = \frac{\pi}{4} d^2 \cdot L \cdot \rho_v \cdot \bar{v}$
\bar{v}^2	(cm ² /s ²)	mean of square of vapor velocity at wet point location
γ	(dyne/cm)	surface tension
ε	(-)	void fraction of packed bed
η _{v,(l)}	(g/cm s)	dynamic viscosity of vapor (liquid)
μ	(-)	isentrop exponent $k = c_p/c_v$
ν _{v,(l)}	(cm ² /s)	kinematic viscosity of vapor (liquid)
ρ _{v,(l)}	(g/cm ³)	density of vapor (liquid)
P _H	(dyne/cm ²)	total vapor pressure in the zone
ρ _H	(g/cm ²)	vapor density in the heated zone

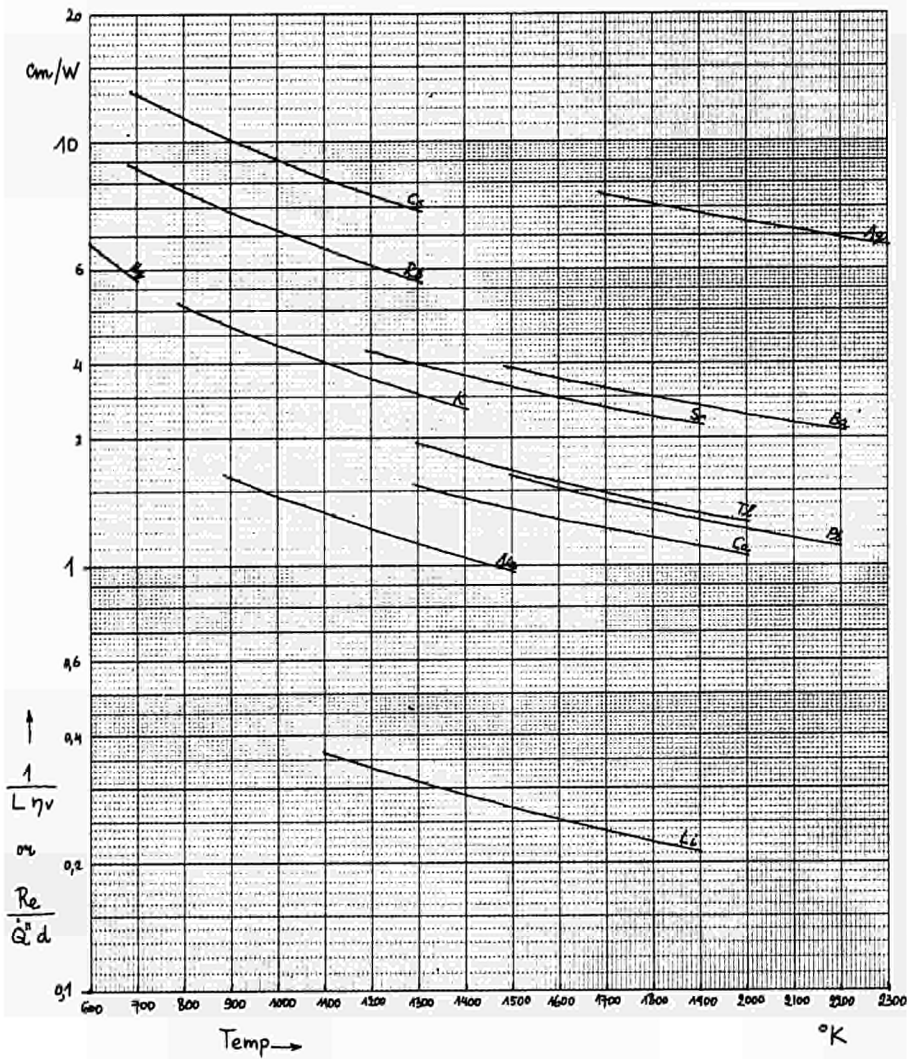


FIG. 1. Material Constants for Reynolds Number.

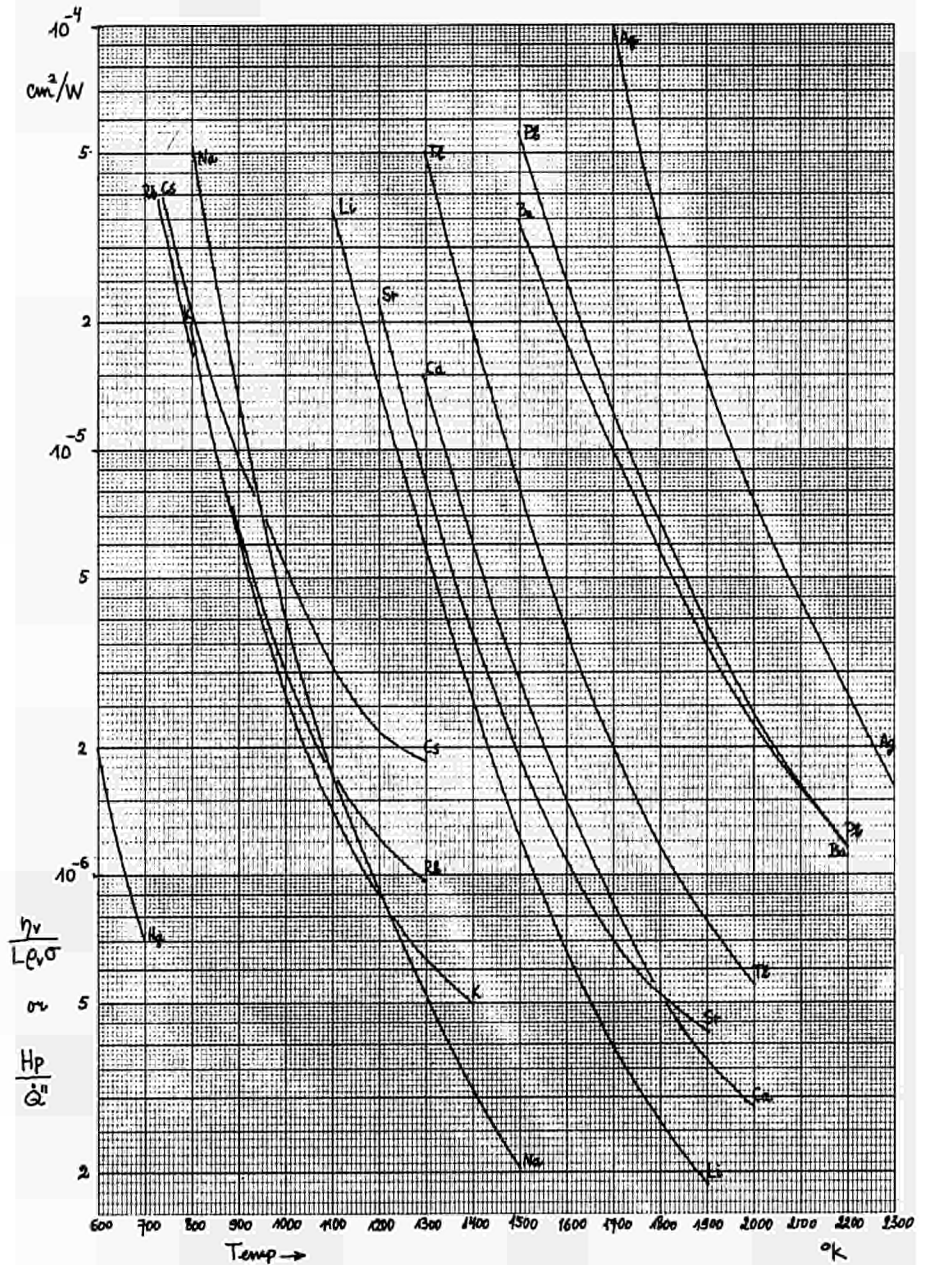


FIG. 2. Material Constants for Heatpipe Number.

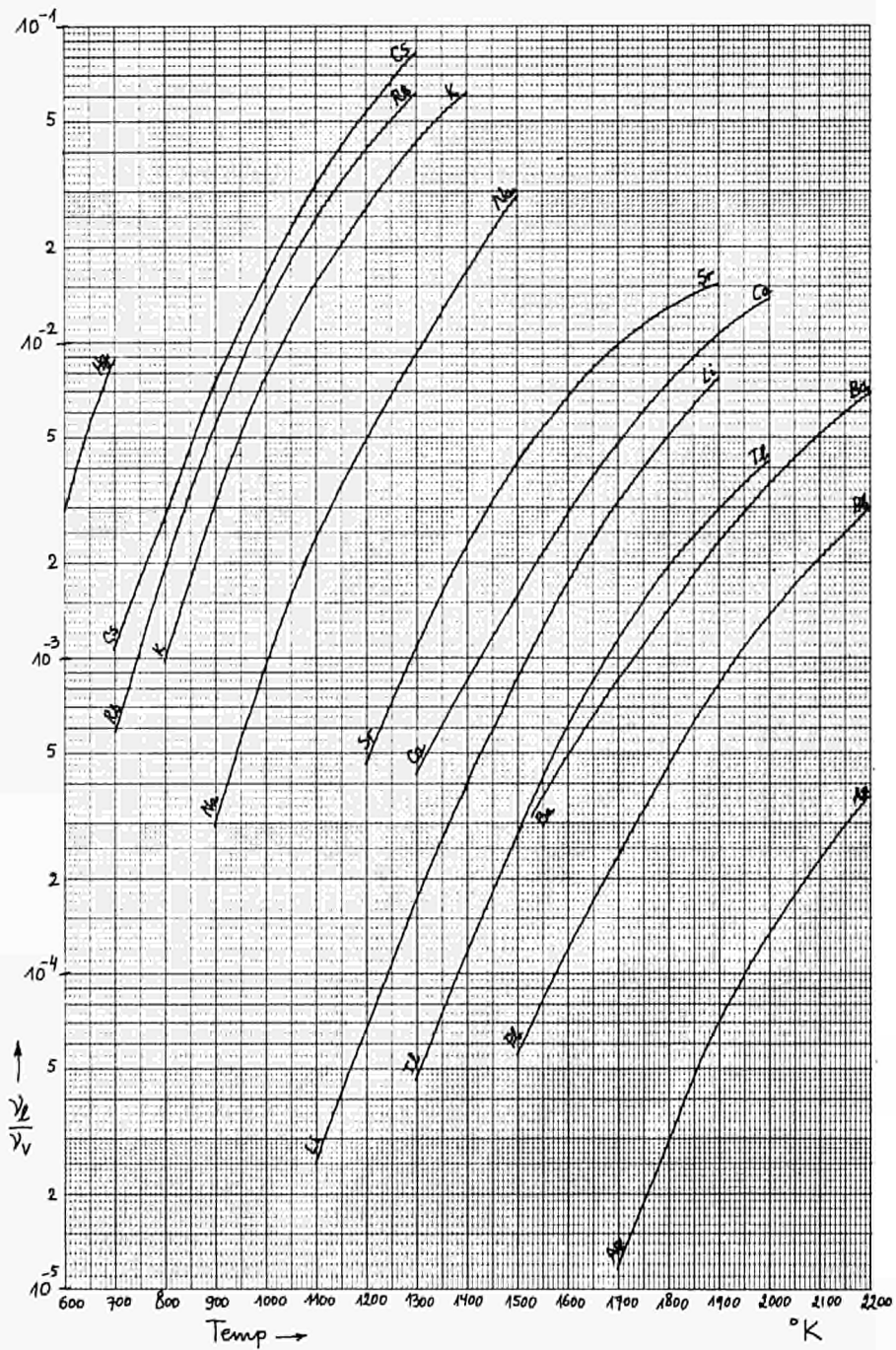


FIG. 3. Kinematic Viscosity Ratio.

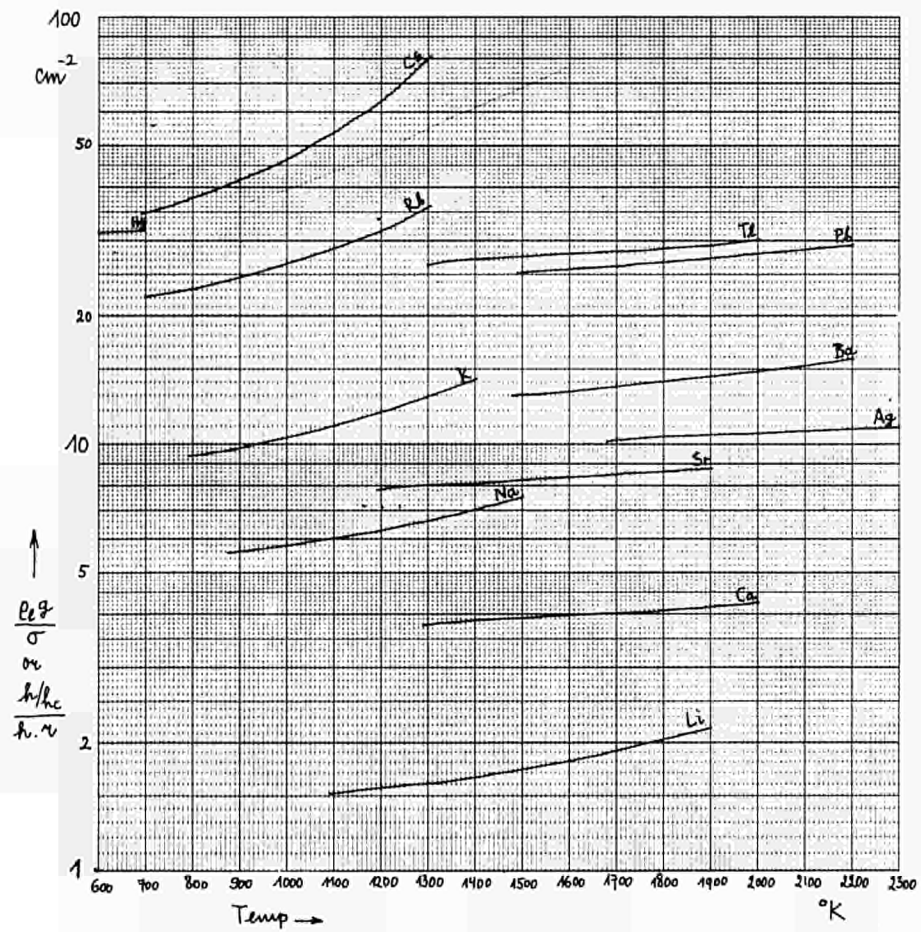


FIG. 4. Material Constants for Gravity Term.

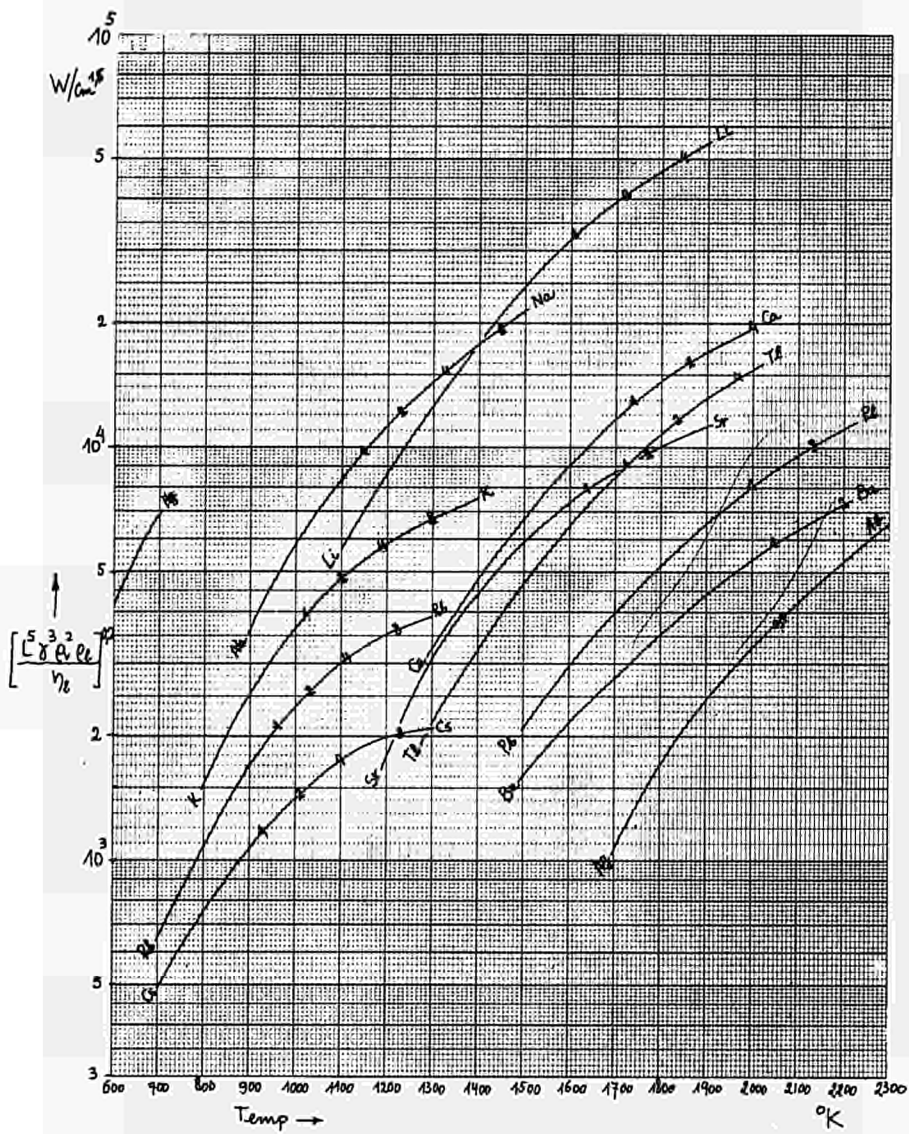


FIG. 5. Material Constants for Optimized Heatflow.

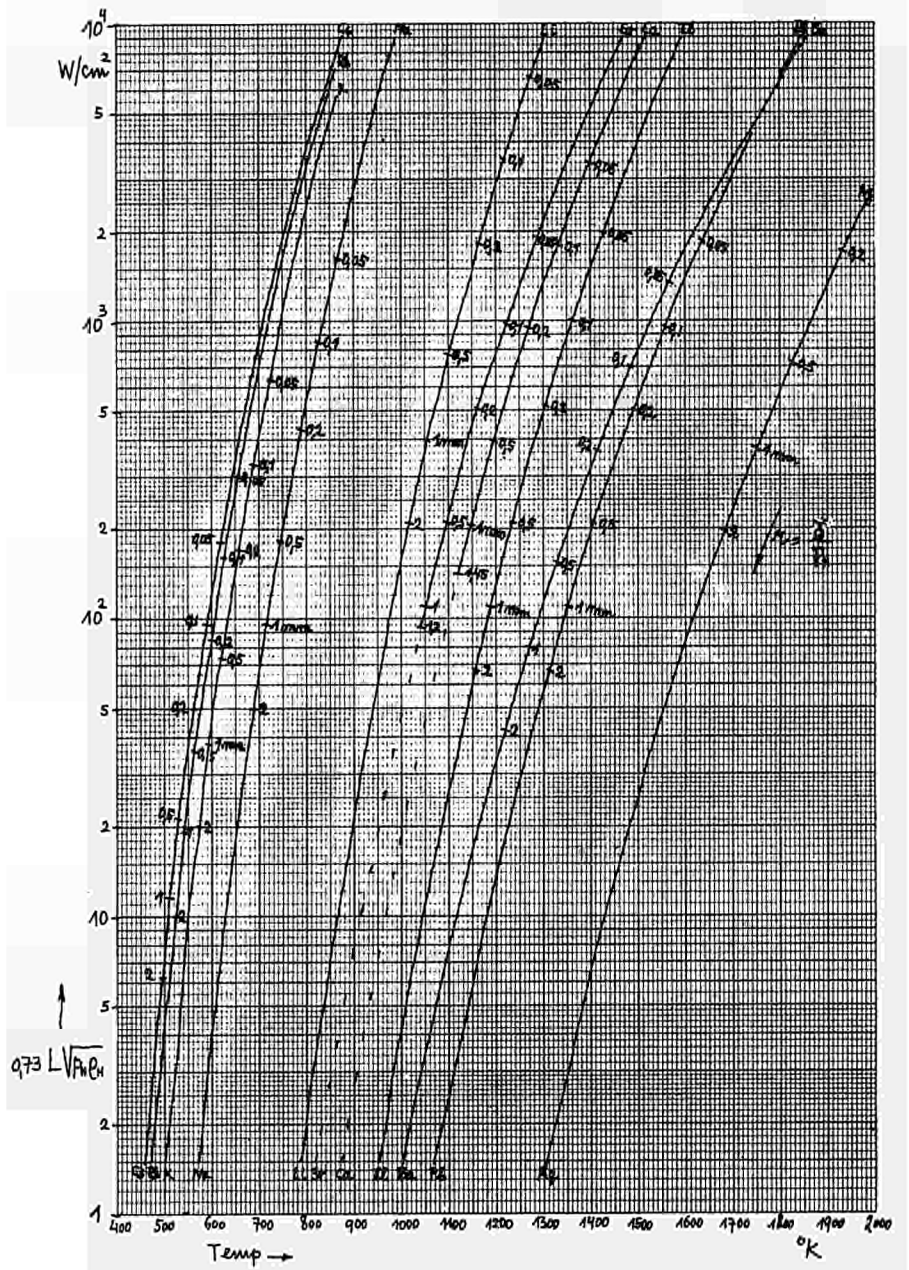


FIG. 6. Sonic Heatflow

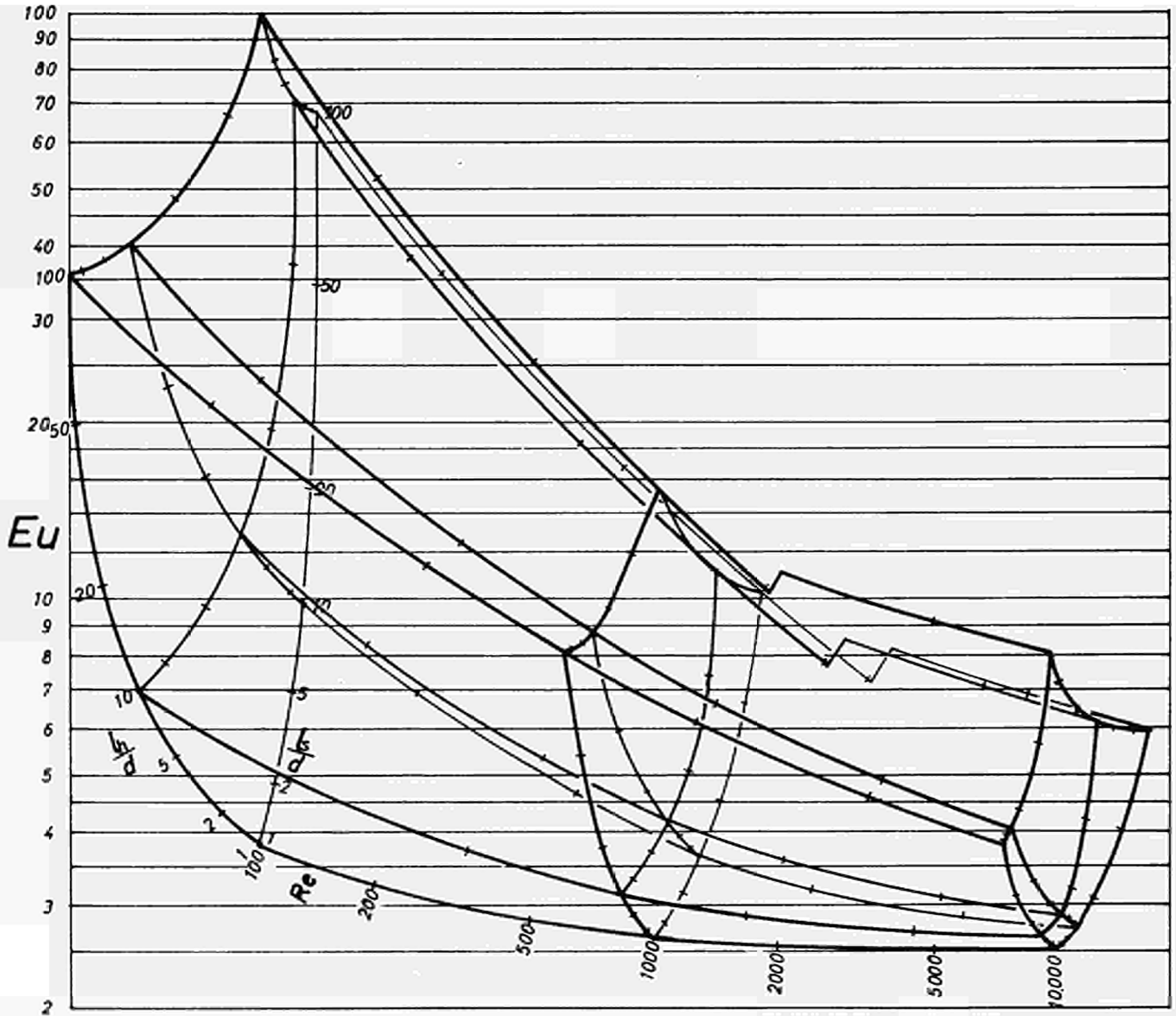
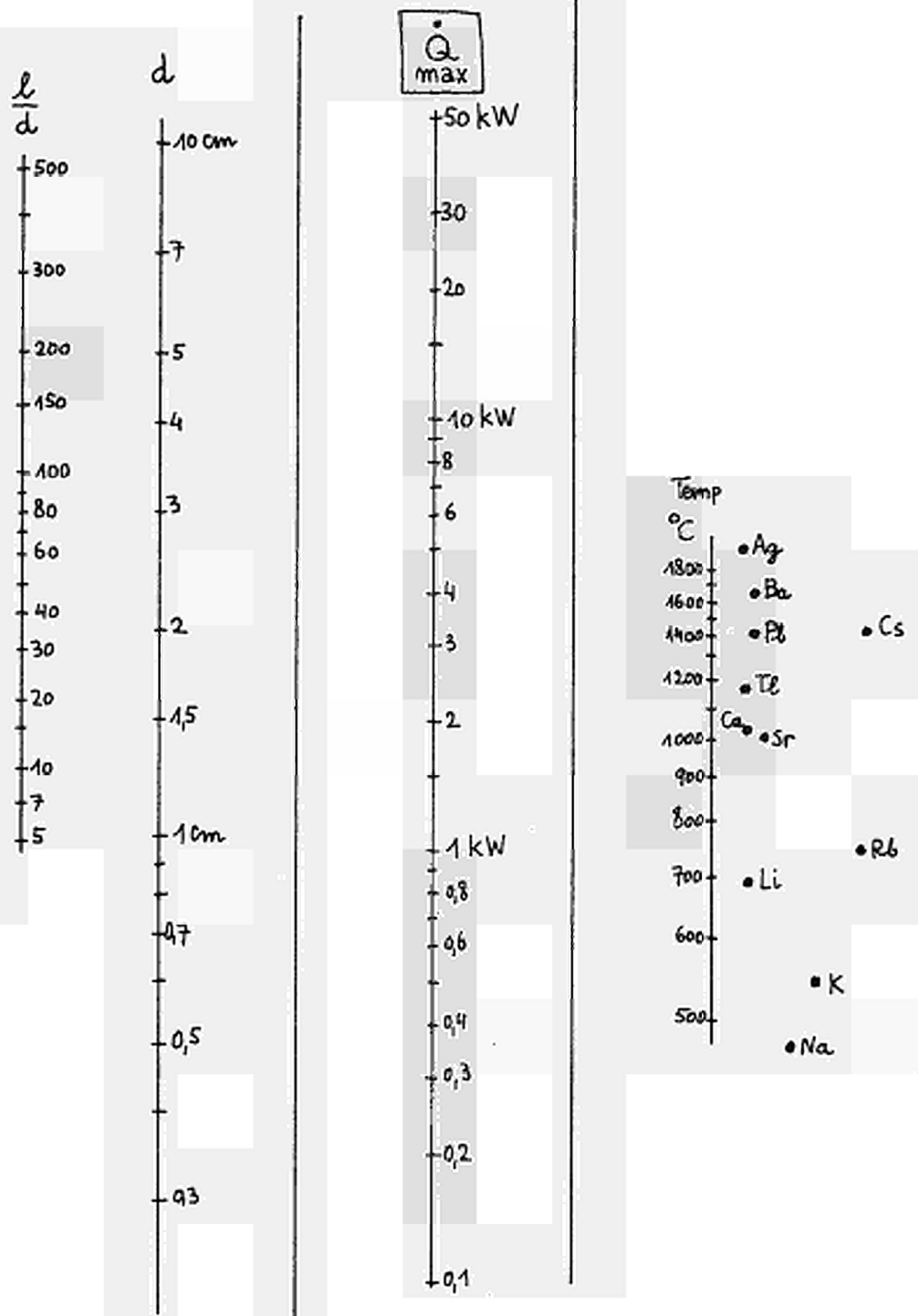
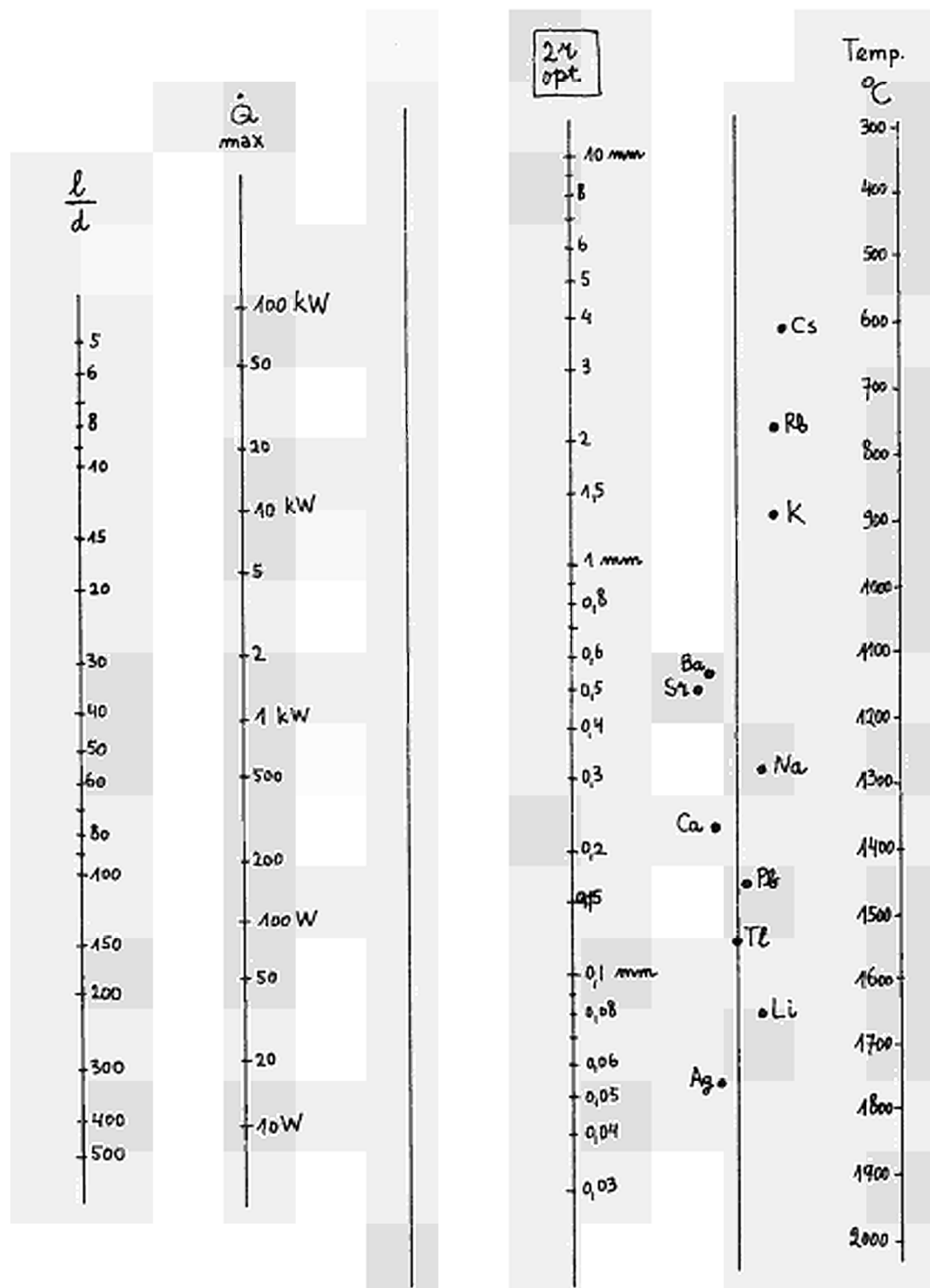


Fig. 7: The Euler number as a function of Reynolds Number and heat pipe geometry.



Nomogram 1. Max. Heatflow in Heatpipes with Optimized Annular Capillary System.



Nomogram 2. Optimum Gap Width for Heatpipes with Annular Capillary System.

LIQUID-VAPOUR INTERACTION AND EVAPORATION IN HEAT PIPES

by

A. Bähr, E. Burck, W. Hufschmidt

EURATOM, C.C.R. -Heat Transfer Division- Ispra, Italy.

Abstract

For heat-pipes having a structure of open capillaries in the transport section the vapour flow influences the mass flow rate of the liquid transported in the capillaries by the shearing at the liquid surface. The two-dimensional Navier-Stokes-equation of the liquid flow in the capillaries has been solved analytically by G. Di Cola [4]. The calculation of the friction factors of the fluid flow with and without gas shearing yields quantities in the order of 2 to 3 depending on the capillary geometry and a dimensionless shear stress at the surface. In a test loop plates with different capillary geometries have been studied experimentally with water as liquid in the open capillaries. The decrease of the transported water mass-flow by increasing air velocity has been measured and the results are compared with the analytical solution. In addition to these measurements the processes in the interior of a heat pipe have been observed visually. An inverse heat-pipe has been constructed with water as heat transporting medium. It consists of three concentric tubes, an inner stainless steel tube with a

capillary system at the outer surface and two involving glass tubes. The water is in the gap between the steel tube and the inner glass tube. The space between the two glass tubes is diffused by hot air to prevent condensation of water vapour at the inner glass tube. One part of the steel tube is heated electrically, the other cooled by a water flow. The investigations performed with this heat pipe concern: Liquid distribution along the capillaries, dry-out of the heated surface caused by bubble formation, asymmetrical liquid distribution and rewettability of the surface after dry-out. It is provided to continue these experiments with mercury as heat transporting medium.

Introduction

The total power of a heat pipe with a given transport medium and given operation temperature is limited by the transport capacity of the liquid in the capillaries. Theories of Cotter [1], Bohdanský et al. [2] and Busse [3] have not taken into account the influence of the gas shearing on the feed back of the liquid in the open capillaries at the inner surface of the heat-pipe by which the power will be reduced. Another limitation of the working method of a heat-pipe is the heat flux density which is determined by the evaporation process.

Influence of Momentum-Transfer Between Vapour and Liquid on Fluid-Flow in Open Capillaries.

For heat pipes having a structure of open capillaries in the transport section the vapour flow in the tube influences the mass flow rate of the liquid transported in contrary direction in the capillaries by the shearing at the liquid-vapour interface. Assuming laminar flow of the liquid in the capillaries of width $2r$ and depth a (see figure 1) the stationary two-dimensional Navier-Stokes-equation for the velocity v_x of the liquid in flow direction has been solved by Di Cola [4] by means of Fourier transformation for the boundary conditions that at the capillary walls the velocity is zero, in the symmetry line the velocity gradient is zero and at the free surface between liquid and vapour the shear stress τ_w of the liquid is equal to the value of the vapour and constant. This means that the

gas flow is not influenced by the liquid flow in the capillaries.
The solution yields:

$$\frac{f_l}{f_{LP}} = \frac{1}{2(1+\varphi)^2} \frac{3 + D \cdot \varphi^2 \left[1 - \frac{96}{\pi^4} \sum_{n=0}^{\infty} \frac{1}{(2n+1)^4} \operatorname{sech} \frac{(2n+1)\pi}{2\varphi} \right]}{1 - \frac{192}{\pi^5} \varphi \sum_{n=0}^{\infty} \frac{1}{(2n+1)^5} \operatorname{tgh} \frac{(2n+1)\pi}{2\varphi}} \quad (1)$$

where: $f_l = \frac{\Delta p \cdot d_h}{2 \rho_l \cdot \bar{v}_l^2 \cdot L}$ = real friction factor of liquid flow

$f_{LP} = \frac{16}{Re_l}$ = friction factor after Poiseuilles law

$\varphi = \frac{r}{a}$ = geometry constant

$D = \frac{a}{\mu_l \cdot \bar{v}_l} \cdot \tau_w$ = dimensionless shear stress at the surface.

($\Delta p / L$ = liquid pressure drop per unit length of capillary;
 $d_h = (4ar)/(a+r)$ = hydraulic diameter; \bar{v}_l = mean liquid velocity;
 ρ_l and μ_l = density and viscosity of liquid; $Re = (\bar{v}_l \cdot \rho_l \cdot d_h) / \mu_l$ = Reynolds number of liquid flow).

For a heat-pipe of diameter D_i and N capillaries in a distance $(s+2r)$ (fig. 1) gives:

$$D = \frac{4 \cdot Na^2 \cdot r}{\pi D_i^3} \cdot \frac{\nu_v}{\nu_l} \cdot f_v \cdot Re_v \quad (2)$$

where the Reynolds number Re_v of the vapour flow is defined in common manner $Re_v = (\bar{u}_v \cdot D_i) / \nu_v$ and f_v is the friction factor of vapour flow (mean velocity \bar{u}_v) which can be calculated either by the Blasius law ($= 0.079 \cdot Re_v^{-0.25}$ for turbulent flow) or the Poiseuilles law ($= 16 \cdot Re_v^{-1}$ for laminar flow). Substituting $N = \pi D_i / (2r+s) = \pi D_i / 2r (1+\omega)$ with $\omega = s/2r$ gives:

$$D = \frac{2}{(1+\omega) \varphi^2 (D_i/r)^2} \cdot \frac{\nu_v}{\nu_l} \cdot f_v \cdot Re_v \quad (3)$$

(ν_v and ν_l are the kinematic viscosities of vapour and liquid, respectively). For $\varphi < 0.5$ that means the capillary is deeper than wide equation (1) can be simplified:

$$\frac{f_l}{f_{lp}} = \left(\frac{f_l}{f_{lp}} \right)_0 \left(1 + \frac{\varphi^2}{3} \cdot D \right) \quad (4)$$

where

$$\left(\frac{f_l}{f_{lp}} \right)_0 = \frac{3}{2(1+\varphi)^2 (1 - 0.627\varphi)} \quad (5)$$

the friction factor ratio for $D = 0$ (zero gas shearing!) and which is constant for a given capillary geometry (φ). Equation (4) is a linear relationship between f_l and D and for a given heat pipe only a function of the vapour Reynolds number. In figure 2 the ratios

$(f_i / f_{iP})_0$ for $D = 0$ calculated after equation 1 are plotted against $1/\psi = a/r$. The dotted line indicates the values calculated after the simplified equation (5). As can be seen for $1/\psi > 2$ equation (5) can be applied without great errors.

The calculation of the ratios f_i / f_{iP} yields quantities in the order of 2 to 5 for heat-pipes depending on capillary geometry and the dimensionless shear stress D . (For a sodium heat pipe values of $D = 100 + 500$ can be reached - see Appendix). These rather great values make it necessary to investigate the influence of momentum transfer between vapour and liquid because of the uncertainty of the assumption that at the free liquid surface the shear stress is constant. Furthermore has been assumed that the liquid surface is smooth and no wave formation by the gas shearing occurs which have been observed by Cohen et al. [5] for a running liquid film along a plate with a gas-flow in contrary direction.

In a plexiglas channel of 240 x 85 mm cross section two plates with different capillary geometry (plate 1: $2r = 0.5$ mm, $a = 1.5$ mm, $s = 0.5$ mm, $N = 120$ capillaries; plate 2: $2r = 1.0$ mm, $a = 3.0$ mm, $s = 1.0$ mm, $N = 60$ capillaries; $L = 300$ mm) have been studied experimentally with water as liquid and air as vapour flowing in contrary direction over the brass plates with the capillaries. Different plate inclinations yielded the variations of the pressure drop Δp of the water flow in the capillaries. The decrease of the transported water mass-flow by increasing air velocity has been investigated and the results are compared with the analytical solution (4). The shear stress τ_w of the gas flow has been measured directly by means of two Preston tubes [6] situated next to the

capillaries. The readings of these tubes yielded the quantity D for the capillary plates in the test section.

In figure 3 the experimental results in form of f_l/f_{lp} are plotted against D. For the two plates the ratio $\varphi = 1/6$ and hence the ratio $(f_l/f_{lp})_0$ at zero vapour flow is 1.23 (see fig. 2). With the simplified equation (4) yields:

$$\frac{f_l}{f_{lp}} = 1.23 \left(1 + \frac{D}{108}\right) \quad (\text{for } \varphi = 1/6) \quad (6)$$

As can be seen in figure 3 the ratios f_l/f_{lp} follow well the predicted line at least for smaller plate inclinations (Δp). Greater values of Δp seem to give greater differences probably due to an increasing wave formation of the liquid surface with increasing air velocity (D). The measurement method, however, was very sensitive against disturbances in plate inclination and did not allow high accuracies especially at small values of Δp . The effect of wave formation could be found out by microscopic observation during the period in which air velocity has been increased from zero value and shall be followed up by high speed filming of the flow character in the capillaries. The studies are not finished and only preliminary results are published. For a first approximation the friction factor increase due to gas shearing can be calculated with equations (4) and (5).

Appendix: As to the quantity D a heat-pipe operating with sodium at 800°C (saturation pressure 450 mbar, kinematic viscosities of

vapour and liquid $\nu_v = 78 \cdot 10^{-6} \text{ m}^2/\text{s}$, $\nu_l = 0.238 \cdot 10^{-6} \text{ m}^2/\text{s}$) and the geometry: $D_i = 17 \text{ mm}$; $r = 0.25 \text{ mm}$; $a = 1.5 \text{ mm}$; $s = 0.5 \text{ mm}$ the D-value will be (equation 3):

$$D = 2.56 f_v \cdot \text{Re}_v$$

Assuming a vapour Reynolds number of $\text{Re}_v = 5000$ and for the friction factor Blasius law ($f_v = 0.079 \cdot \text{Re}_v^{-0.25} = 9.40 \cdot 10^{-3}$) yield: $D = 120$ and $f_l/f_{lP} = 2.60$. For the same heat-pipe with another capillary structure ($r = 0.5 \text{ mm}$; $a = 3.0 \text{ mm}$; $s = 1.0 \text{ mm}$) would give $D = 480$ and hence $f_l/f_{lP} = 6.70$.

Vapour Formation in a Heat-Pipe

In a normally working heat-pipe the vapour is formed only at the free surface between liquid and vapour space. The evaporation occurs without bubble formation continuously and in a rate corresponding to the heat transport to the liquid surface. The condition for the exclusive vapour formation at the free surface is that no part of the liquid is superheated in a degree that a bubble nucleus may be activated. The temperature of the liquid increases from the saturation value at the free surface to the value at the heated wall. The temperature rise depends on the heat flux, the thickness of the liquid layer and the thermal conductivities of the liquid and capillary structure. Liquid metals as common coolants for heat pipes may strongly be superheated before bubbles are formed and their good thermal conductivity relative to water or organic liquids limits the temperature rise in the liquid layer. In case of high heat flux

densities, however, e.g. 500 W/cm^2 and heat pipes with wicks or deep capillaries the activation temperature for the bubble nuclei may be reached and hence bubbles may be formed.

The bubble formation in a heat-pipe disturbs its function in several manner:

- 1) The liquid sprayed in the vapour space. That part of the sprayed liquid not reaching the opposite wall is carried away by the vapour flow in direction to the cooled end of the heat-pipe and lost for heat transport. The other part having received a velocity in vapour direction and reentering in the liquid layer slows it down. Furthermore the liquid distribution between different regions of the heat-pipe is disturbed.
- 2) The continuous liquid flow is disturbed by the bubbles and surface waves are formed. At higher heat fluxes the number of bubbles increases and finally the liquid flow is interrupted.

For direct visual observation of the vapour formation and liquid distribution an "inverse" heat-pipe has been constructed (figure 4) with water as heat transporting medium. It consists of three concentric vertically arranged tubes, an inner stainless steel tube with a capillary structure at the outer surface (tube 20 mm o.d., 90 grooves in longitudinal direction with rectangular cross-section, each 0.4 mm large and 0.6 mm deep), and two involving glass tubes. The water is in the gap between the steel tube and the inner glass tube. To prevent condensation of water vapour at the inner glass tube the space between the two glass tubes is diffused by hot air. The lower part of the steel tube is heated electrically and the upper part cooled by a hot

water flow. The evaporation under several conditions is studied by means of a high speed camera.

It could be observed:

- 1) Surface evaporation: Up to heat flux densities in the order of 20 W/cm^2 ^{x)} only surface evaporation occurs. The vapour velocity being slow the surface remains completely smooth.
- 2) Dry-out by lack of liquid: Increasing the heat flux density up to about 25 W/cm^2 many bubbles are formed and liquid is sprayed against the surrounding glass wall. Surface waves originating from bubble producing sites propagate in the capillaries. As soon as the liquid losses by spraying can no further be replaced by the liquid raising in the capillaries from the bottom of the heat-pipe dry-out occurs.
- 3) Dry-out by formation of big bubbles: Further sudden increase of the heat-flux density causes the formation of many bubbles agglomerating to big ones. The heated wall dries out also in the vicinity of the unheated part of the heat pipe. The temperature of the wall rises rapidly. In spite of liquid abundance the heated wall is not wetted due to the Leidenfrost phenomenon.
- 4) Rewetting of the superheated wall: Also after shut-down of the heating power the wall is not rewetted before its temperature approaches the saturation value. The hot wall being mainly cooled by thermal conduction between the wetted and the dry part the liquid front propagates slowly covering gradually the superheated spot.

x)

Using normal transport media in heat-pipes (liquid metals) the maximum heat flux density is much higher due to the higher values of thermal conductivity and greater propensity to superheating.

References

- [1] COTTER, T.P., Theory of heatpipes, LA-3246-MS (1965).
- [2] BOHDANSKY, J., STRUB, H., VAN ANDEL, E., Heat transfer measurements using a sodium heat-pipe working at low pressure. Proc. Thermionic Conversion Specialists Conf., Houston, Texas, Nov. 1966.
- [3] BUSSE, C.A., Pressure drop in the vapour phase of long heat-pipes. Thermionic Conversion Specialists Conf., Palo Alto, Calif., Oct. 1967.
- [4] DI COLA, G., Soluzione analitica, a mezzo della trasformata di Fourier, di un problema di flusso in un canale rettangolare. EURATOM C.C.R. Ispra (Italy), C.E.T.I.S. (1968).
- [5] COHEN, L.S., HANRATTY, T.J., Effect of waves at a gas-liquid interface on a turbulent air flow. J. Fluid Mech. 31 (1968) part 3, pp. 467-479.
- [6] PATEL, V.C., Calibration of the Preston-tube and limitations on its use in pressure gradients. J. Fluid Mech. 23 (1965), pp. 185-208.

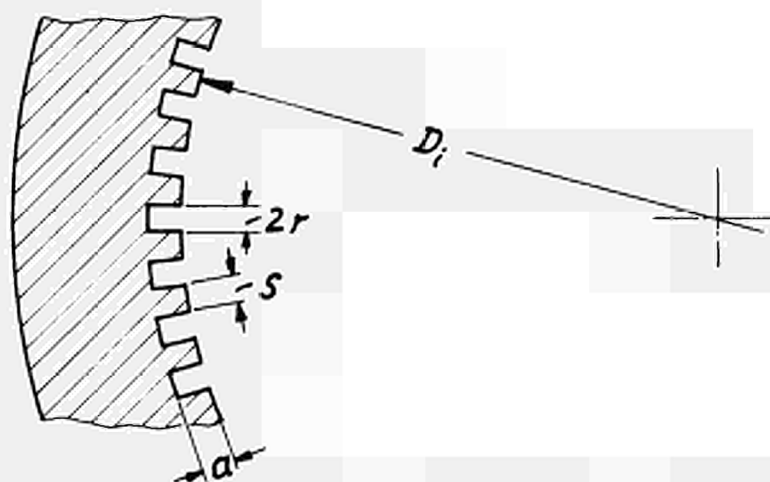


Fig. 1: Denotation of capillary geometry.

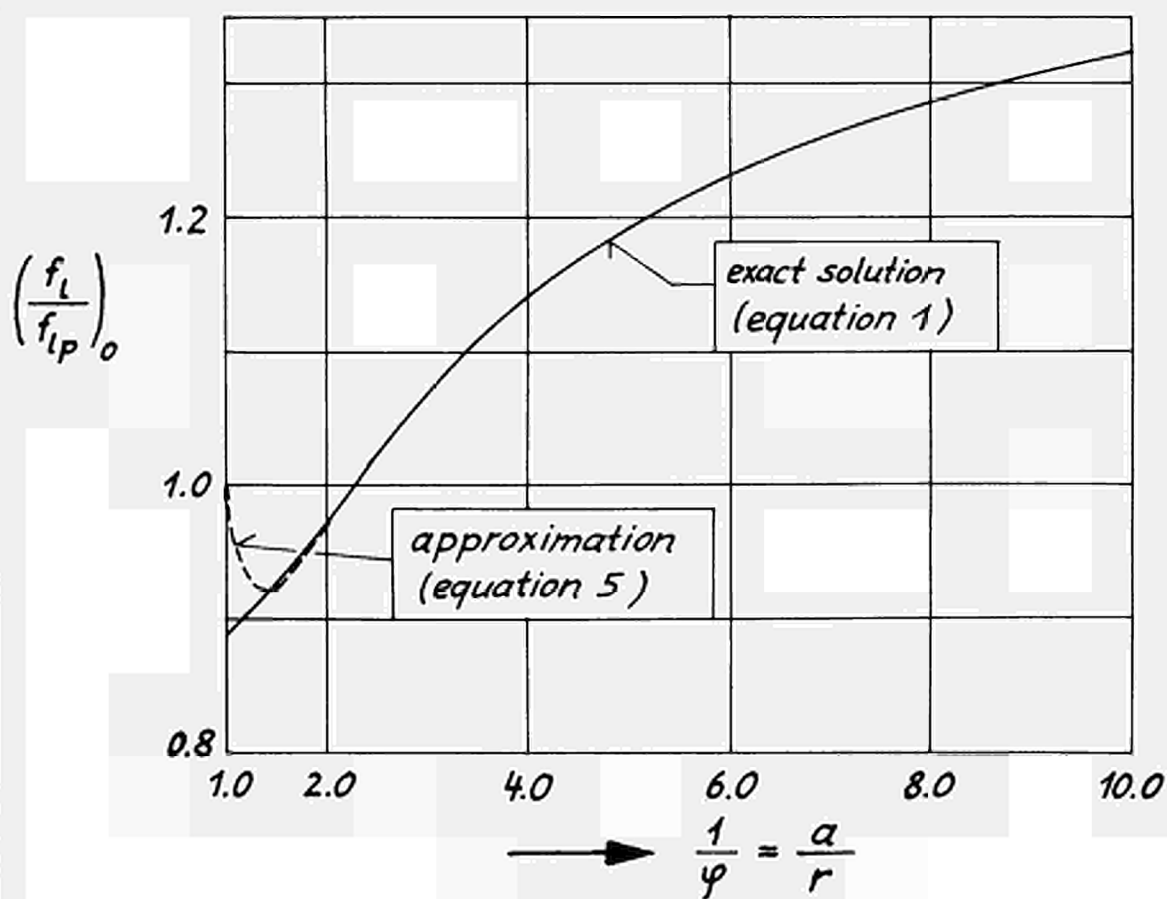


Fig. 2: Ratio $(f_l / f_{lp})_0$ of real friction factor of laminar liquid flow in capillaries to that after Poiseuille's law ($f_{lp} = 16 / Re$) for zero gas shearing ($D = 0$)

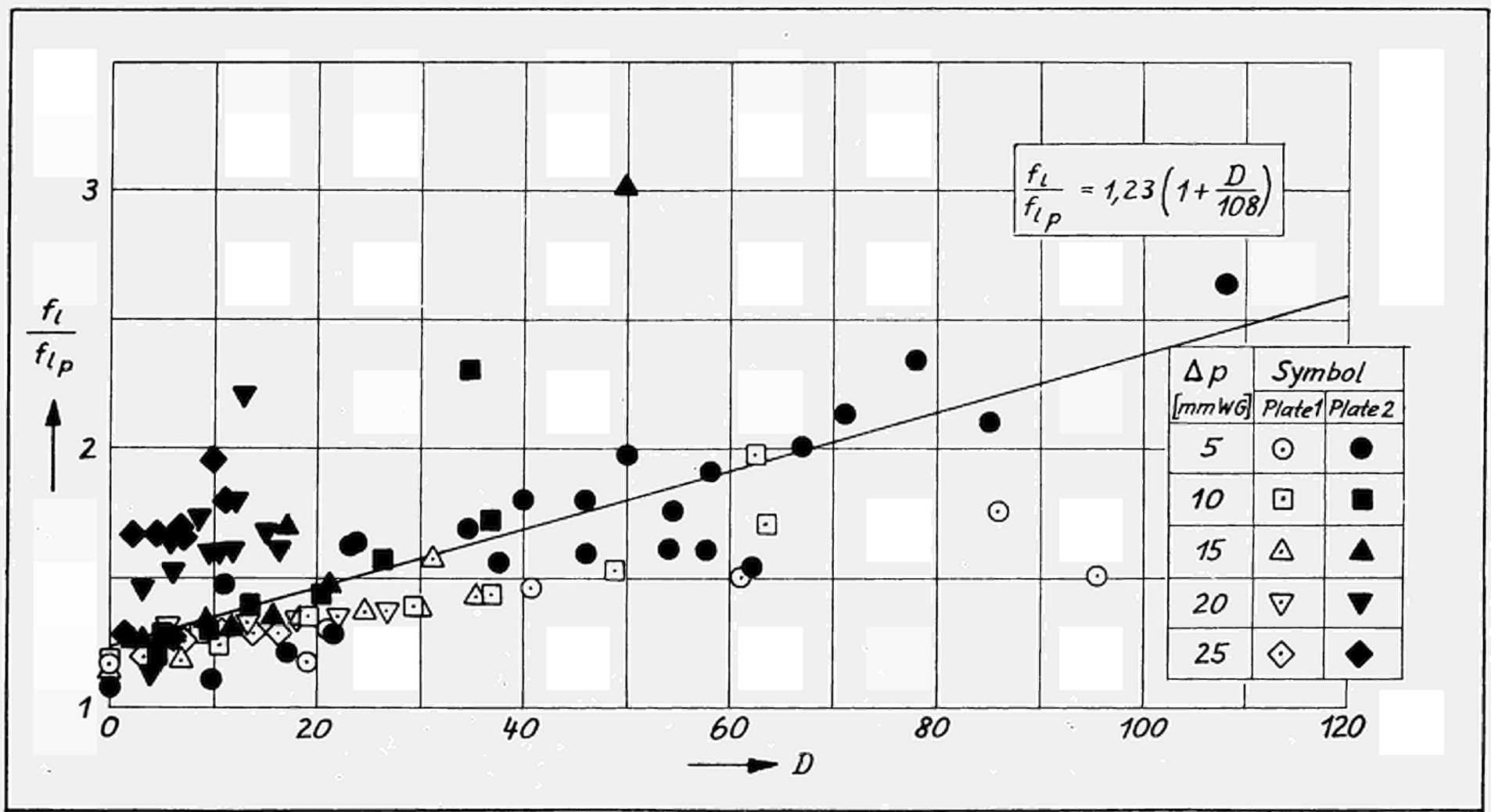


Fig. 3: Ratio f_l / f_{lp} of real friction factor of laminar liquid flow in capillaries to that after Poiseuilles law ($f_{lp} = 16 / Re$) against dimensionless shear stress at the surface $D = (a \cdot \tau_w) / (\mu_l \bar{v}_l)$ for $\varphi = r/a = 1/6$.

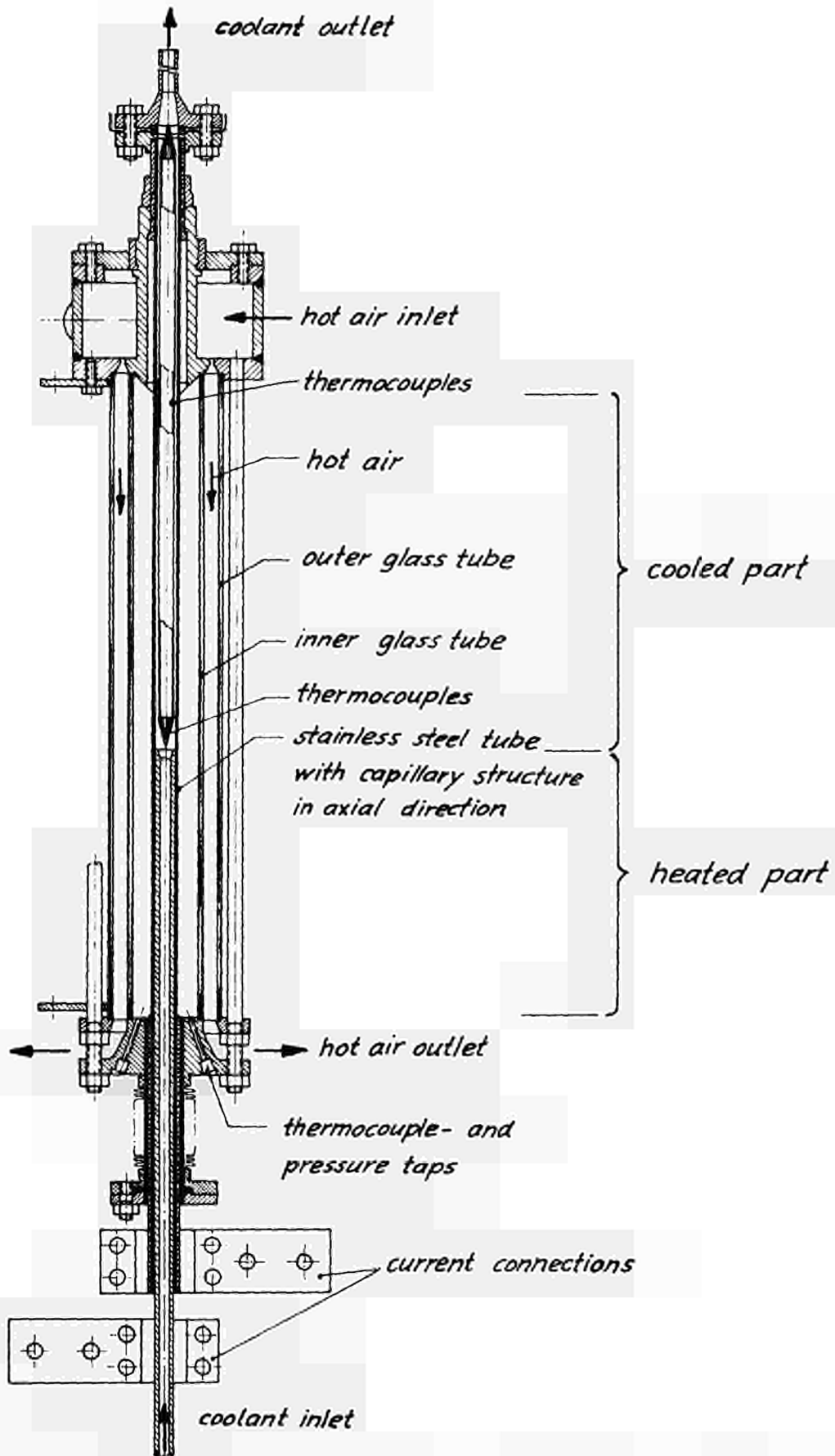


Fig. 4: Visualization heat-pipe with water as heat-transport medium.

RESULTATS PRELIMINAIRES D'UNE ETUDE SUR LES CALODUCS
A HAUTE TEMPERATURE

M. ARMAND et A.M. SHROFF
CSF - Compagnie générale de télégraphie Sans Fil,
Groupement Scientifique et Technique
Domaine de Corbeville, Orsay (France)

I n t r o d u c t i o n

Depuis la mise en avant par Grover et coll.⁽¹⁾ de l'idée d'utiliser la chaleur de vaporisation des fluides pour le transfert de chaleur sans chute de température, les principes de fonctionnement des caloducs ont pu être dégagés, tant du point de vue théorique que du point de vue expérimental.

Mettant à profit les résultats ainsi obtenus, nous nous sommes fixés pour objectif l'application de ce dispositif au cas des hautes températures, et en particulier au chauffage des émetteurs de convertisseurs thermoioniques. On connaît les divers avantages de ce mode de chauffage : excellente homogénéité de la température des émetteurs, possibilité de séparer la source de chaleur de la diode, ce qui peut être intéressant dans le cas du chauffage nucléaire.

De cet objectif, résultent les conditions que nous cherchons à obtenir :

- température de fonctionnement : 900° K
- puissance transportée 1 kW, avec une densité de 100 W/cm² recueillie au condenseur
- longueur 40 cm
- durée de vie plusieurs milliers d'heures.

Nous donnerons ici quelques résultats théoriques obtenus pour l'optimisation du système capillaire, ainsi que la résistance thermique à attendre. Nous décrirons ensuite les dispositifs expérimentaux utilisés pour évaluer les performances des caloducs. Enfin, dans une étude technologique, nous décrirons les matériaux utilisés, enveloppes et caloporteurs, les modes de réalisation et de formation des caloducs, et enfin les essais de durée de vie.

(1) G.M. Grover, T.P. Cotter, G.F. Erickson - J.N.P. Juin 1964, p. 1990 -

1 - Etude théorique

- a) Evaluation de la résistance thermique

On peut décomposer la résistance thermique d'un caloduc en 3 parties :

- une partie conduction dans la paroi et la pellicule de liquide à l'évaporateur et au condenseur, sensiblement indépendante de la température de fonctionnement.
- Une partie évaporation-condensation. Ces 2 phénomènes s'accompagnent d'une chute de pression :

$$\Delta p = \frac{\dot{Q}}{SL} \sqrt{\frac{2\pi RT}{M}}$$

- \dot{Q} puissance transférée
- S surface évaporateur ou condenseur
- L chaleur latente de vaporisation
- R constante des gaz parfaits
- T température absolue
- M la masse atomique.

Si la vapeur reste saturante, la résistance thermique correspondante est :

$$\left(\frac{\Delta T}{\dot{Q}}\right)_1 = \frac{RT^2}{S p M L^2} \sqrt{\frac{2\pi RT}{M}}$$

- Une partie perte de charge dans le conduit de vapeur. En régime de Poiseuille, la perte de charge vaut :

$$\Delta p = \frac{8}{\pi} \frac{\eta_v \ell \dot{Q}}{\rho_v r^4 L}$$

- η_v viscosité de la vapeur
- ρ_v densité de la vapeur
- ℓ longueur du caloduc
- r rayon du caloduc

Si la vapeur reste ici encore saturante la résistance thermique correspondante vaut :

$$\left(\frac{\Delta T}{\dot{Q}}\right)_2 = \frac{8}{\pi} \frac{\eta_v \ell}{r^4} \frac{R^2 T^3}{p^2 M^2 L^2}$$

On a représenté sur la courbe figure 1 les variations de ces 3 composantes de la résistance thermique avec la température, ainsi que leur somme, dans le cas d'un caloduc à plomb répondant aux conditions indiquées dans l'introduction; le rayon r a été choisi égal à 0,7 cm.

On voit que pour des températures assez basses correspondant à des pressions de vapeur inférieures à 20 Torr, la résistance thermique dépasse 100 degrés/kW.

- b) Optimisation du système capillaire mince

Bien que ne désirant transférer que 1 kW, il paraît intéressant de connaître la géométrie optimale des structures capillaires, ainsi que la puissance maximale transférable, à différentes inclinaisons et pour différents fluides caloporteurs. En effet, pour éviter le risque d'assèchement de la région évaporateur, il est souhaitable de faire fonctionner le caloduc à une puissance très inférieure à sa puissance maximale.

Pour ceci, nous considérerons d'abord le cas le plus simple à réaliser expérimentalement d'un système capillaire formé d'une seule couche de canaux parallèles de rayon x ; leur nombre est $N = \frac{2nr\alpha}{2x}$ où α est la porosité du système.

Le rayon laissé libre pour la vapeur est $r - 2x$. Si le caloduc est incliné d'un angle ϕ avec l'horizontale, compté positivement quand le caloduc travaille contre la pesanteur, la dépression capillaire devra vaincre, outre les pertes de charge, la pression hydrostatique

Si les capillaires sont séparés du conduit de vapeur par une toile métallique de maille assez fine, la dépression capillaire est voisine de $\frac{2\gamma}{x}$. En régime laminaire, le débit maximum \dot{m} est donc donné par :

$$\frac{8\dot{m}l}{\pi} \left(\frac{\eta_v}{\rho_v(r-2x)^4} + \frac{\eta_l}{\alpha\rho_l nr x^3} \right) + \rho_l g l \sin\phi = \frac{2\gamma}{x}$$

avec η_v viscosité de la vapeur
 ρ_v densité de la vapeur
 η_l viscosité du liquide
 ρ_l densité du liquide
 γ tension superficielle

g accélération de la pesanteur.

Posons $A = \frac{4l}{\pi\gamma} \frac{\eta_v}{\rho_v}$

$B = \frac{4l}{\pi\gamma} \frac{\eta_l}{\rho_l \alpha \pi}$

$C = \frac{\rho_l g l r}{2\gamma}$

et $u = \frac{x}{r}$

L'équation devient :

$$\frac{\dot{m}}{r^3} \left(\frac{A}{(1-2u)^4} + \frac{B}{u^3} \right) = \frac{1}{u} - C \sin\phi$$

L'optimisation de \dot{m} par rapport à u donne une relation entre la pression hydrostatique réduite $C \sin \phi$ et u :

$$C \sin \phi = \frac{1}{u} \frac{2B/A - \frac{u^3(1+6u)}{(1-2u)^5}}{3B/A - \frac{8u^4}{(1-2u)^5}}$$

relation qui permet de tracer la courbe (Fig. 2) donnant le rapport u optimum du rayon de capillaire au rayon du caloduc, en fonction de la pression hydrostatique à vaincre. Nous l'avons tracée pour le lithium, et nous donnons figure 4, courbe I, la puissance maximum transférable à chaque inclinaison.

- c) Réseau capillaire épais

Supposons qu'il soit possible de réaliser un réseau capillaire formé de plusieurs couches de canaux superposés, avec une épaisseur arbitraire, et cherchons sa forme optimale. Soit r_v le rayon laissé libre pour la vapeur. Le nombre de canaux est :

$$N = \frac{\alpha \pi (r^2 - r_v^2)}{\pi x^2}$$

L'équation du débit maximal sera alors :

$$\frac{8m \ell}{\pi} \left(\frac{\eta_v}{\rho_v r_v^4} + \frac{\eta_l}{\alpha \rho_l x^2 (r^2 - r_v^2)} \right) - \frac{2\gamma}{x} + \rho_l g \ell \sin \phi = 0$$

Posons : $A = \frac{4\ell \eta_v}{\pi \gamma \rho_v}$ $B = \frac{4\ell \eta_l}{\pi \gamma \rho_l \alpha}$ $C = \frac{\rho_l g \ell r}{2\gamma}$

L'optimisation de \dot{m} par rapport à r_v et x conduit à l'équation suivante pour r_v :

$$C \sin \phi \left(\frac{r_v}{r} \right)^3 + \frac{3}{2} \sqrt{\frac{A}{2B}} \left(\frac{r_v}{r} \right)^2 - \sqrt{\frac{A}{2B}} = 0$$

Cette relation permet à nouveau de tracer la courbe donnant la valeur optimale de r_v/r en fonction de l'inclinaison ϕ (Fig. 3).

Le débit optimum s'en déduit par :

$$\dot{m} = \frac{r_v^3}{\sqrt{8AB}}$$

et le rayon optimum des canaux :

$$x = \sqrt{\frac{B}{2A}} \frac{r_v^3}{r^2 - r_v^2}$$

Nous avons représenté figure 4, courbe II, la dépendance de la puissance maximum transférable en fonction de l'inclinaison, pour un caloduc à lithium.

On voit que lorsque le caloduc travaille contre la pesanteur, on a intérêt à augmenter la section du système capillaire aux dépens de la section du conduit de vapeur. La figure 4 montre en outre que le réseau capillaire épais autorise plus aisément le travail contre la pesanteur que le réseau mince.

2 - Etude expérimentale

- Formation des caloducs

En vue d'étudier le transfert de chaleur, nous avons réalisé plusieurs caloducs en molybdène, utilisant le plomb comme fluide caloporteur. Le retour de liquide s'effectue par gravité.

L'enveloppe est un tube de 14 x 16 mm et de 40 cm de long, fermé à la base, et pourvu au sommet d'un queusot de tantale. Cette enveloppe est chargée d'environ 20 g de plomb.

Cet ensemble est placé dans une cloche à vide, le queusot de tantale permettant de raccorder l'intérieur du caloduc au vide de la cloche par un intermédiaire de kovar et de verre. Au moyen de robinets, on peut mettre le caloduc en communication avec un système de remplissage de gaz rares (Fig. 5).

Le caloduc est alors dégazé, d'abord sous vide, puis en présence d'une contre-pression de gaz rare. On peut ainsi le dégazer à sa température de fonctionnement⁽²⁾. On scelle alors le queusot de verre, puis celui de tantale, par bombardement électronique.

Les caloducs ainsi formés ont été essayés à 1 900° K. La partie évaporateur, de même que la partie condenseur a une longueur de 5 cm. Un écran thermique protège le corps sur 30 cm. Le condenseur rayonne environ 15 W/cm², soit au total 375 watts; sa température est assez homogène, sauf l'extrémité, où l'on observe une chute d'environ 50°.

On a adapté à ces caloducs un radiateur à ailettes, qui prélève 100 W/cm² à 1 900° K; on observe alors une chute de température plus importante : 200° environ.

(2) J. Bohdansky et H.E.J. Schins, J. Phys. Chem. 71 (1967) 215 -

- Essais de durée de vie

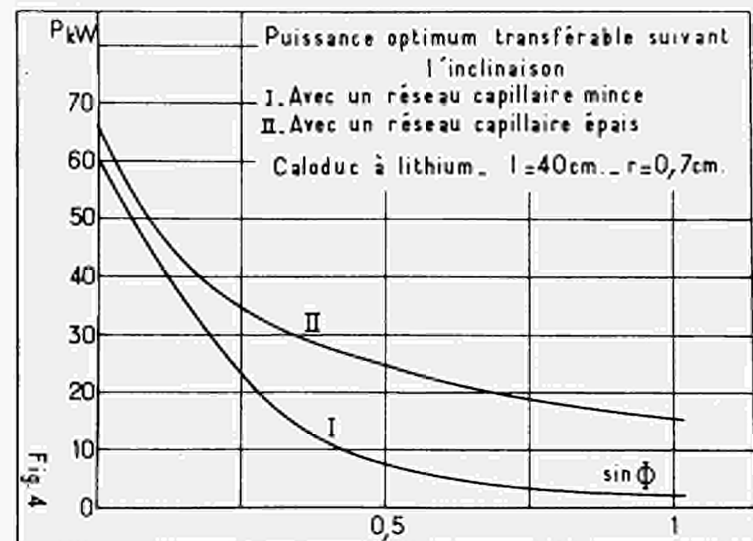
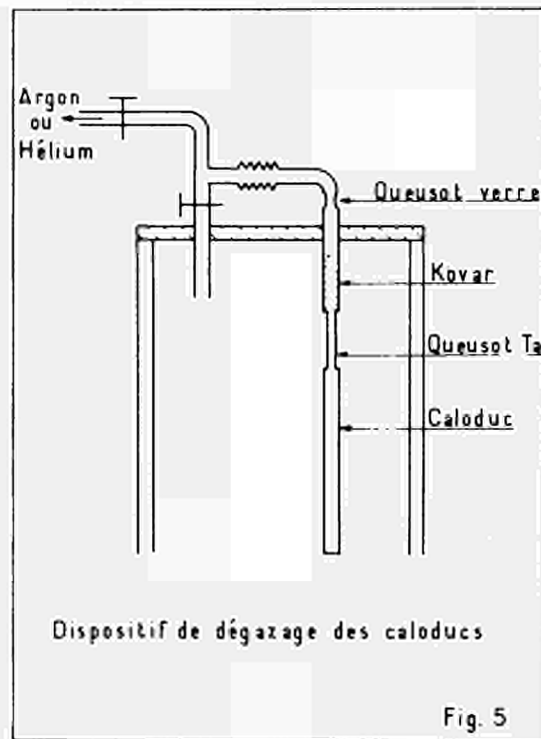
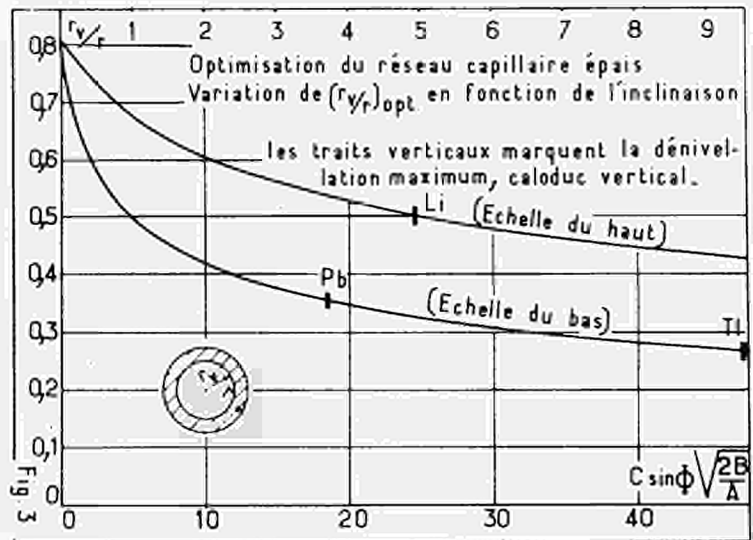
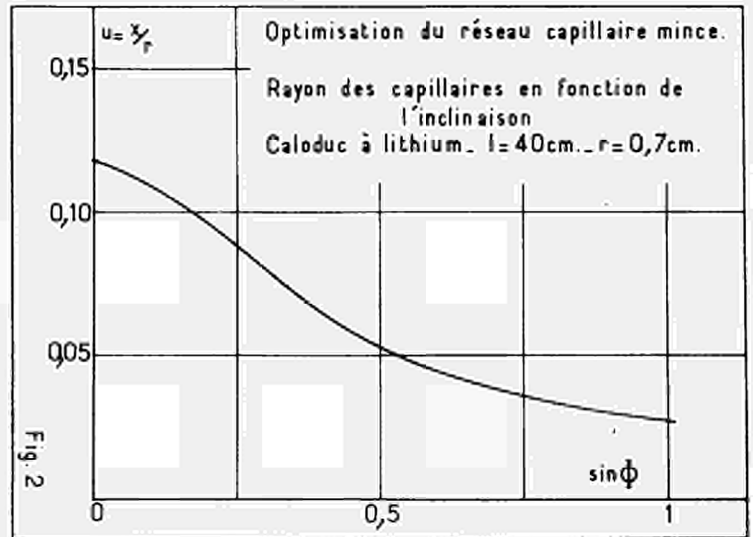
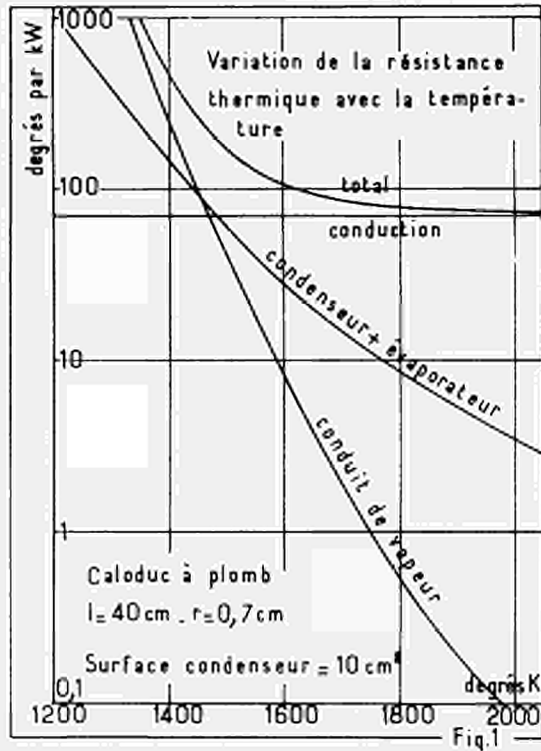
Pour l'étude de la compatibilité enveloppe caloporteur, on a réalisé plusieurs caloducs de dimensions plus petites : l'enveloppe est un tube de diamètre 8×10 mm, et de longueur 100 mm. Pour les fluides lourds (thallium, plomb), le retour s'effectue par gravité. Pour les fluides légers (lithium) le retour s'effectuera par capillarité.

Pour l'essai de durée, les caloducs sont montés en ampoule scellée, et chauffés par bombardement électronique. On injecte environ 200 W/cm^2 pour un total de 350 W. Un écran thermique protège le corps du caloduc sur 7 cm, et un radiateur adapté sur le condenseur prélève environ 100 watts à 900°K .

Actuellement, deux essais ont été menés à leur terme. Un caloduc molybdène-plomb, durée 110 heures, et un caloduc tantale-thallium, de durée 500 heures. Dans les deux cas, la mort des caloducs a été causée par une fuite du liquide caloporteur, les enveloppes étant fortement recristallisées. On peut donc tirer une première conclusion de ces essais, à savoir qu'il est indispensable d'utiliser des alliages, de préférence aux métaux purs.

Enfin, nous avons pu réaliser plusieurs caloducs en tungstène, obtenus par dépôts en phase vapeur. Cette technique nous a permis en particulier de réaliser des tubes rainurés intérieurement.

-----ooOoo-----



CHEMICAL VAPOR-DEPOSITION OF TUNGSTEN EMITTERS OF
{110} PREFERRED CRYSTAL ORIENTATION*

by

R. G. Hudson, T. Tagami and L. Yang

Gulf General Atomic Inc.
P.O. Box 608, San Diego, California 92112 (USA)

ABSTRACT

Studies have been carried out on the preferred crystal orientations and vacuum work functions of planar tungsten deposits formed by the hydrogen reduction of tungsten chloride, using the chlorination of fluoride tungsten chips to provide the tungsten chloride needed. Deposition conditions have been defined and the reproducibility of the results have been established for obtaining deposits of strong {110} preferred crystal orientation and vacuum work functions equal to 4.9-5.0 eV.

* This work is sponsored by the National Aeronautics and Space Agency under Contract NAS 3-8504.

INTRODUCTION

In the direct conversion of thermal to electrical energy by thermionic means, the performance of the converter depends strongly upon the vacuum electron work function of the emitter surface. Emitter surfaces of higher vacuum electron work function are more desirable since they require lower cesium pressure for optimum converter operation and therefore the loss of voltage output due to plasma impedance is reduced. Because of its compatibility with various nuclear materials at high temperature, tungsten is considered as one of the most promising emitter materials for fission heat conversion.^{(1),(2)} Chemical vapor deposition, which offers the best means for the fabrication of complicated shapes and the control of impurity contents, has been used exclusively for the forming of tungsten emitters in thermionic converters. Most of the tungsten emitters tested up to date were prepared by the hydrogen reduction of WF_6 , (referred hereafter as fluoride tungsten) which exhibit {100} preferred crystal orientation and vacuum work functions of 4.5 - 4.6 eV. Attempts have been made to raise the vacuum work function of fluoride tungsten by chemical or electrochemical etching.^{(3),(4)} Although such etching treatments may lead to an increase in vacuum electron work function up to a few tenths of an electron volt, the gain is unstable at high temperatures (e.g. 1800°C). It was found, however, that tungsten deposited by the hydrogen reduction of tungsten chloride may exhibit strong {110} preferred crystal orientation and a stable vacuum work function as high as 5 eV.^{(3),(4)} A cylindrical converter containing a chloride tungsten emitter of 4.8 eV vacuum work function⁽⁵⁾ and a planar converter containing a chloride tungsten emitter of 4.9 eV vacuum work function⁽⁶⁾ have both demonstrated performance superior to that of similar converters containing {100} oriented fluoride tungsten emitters. While the advantage of {110} oriented chloride tungsten emitters has been proven, the conditions under which {110} oriented tungsten deposits can be reproducibly obtained remained obscure. The purpose of this work is to explore the conditions under which {110} oriented tungsten deposits can be prepared in planar form for further evaluation of their metallurgical and thermionic emission properties at high temperatures.

EXPERIMENTAL

1. Preparation of Chloride Tungsten Deposits

Chloride tungsten deposits have been prepared by using either WCl_6 powder or the chlorination of fluoride tungsten chips to provide the tungsten chloride needed for the deposition process. Because of the hygroscopic and reactive nature of the WCl_6 powder, the handling of this tungsten source material proved to be very inconvenient and the tungsten flux in the reaction mixture was found to be difficult to control. The main effort was therefore devoted to the use of fluoride tungsten chips as a tungsten source material. Figure 1 illustrates schematically the experimental arrangements. The deposition chamber was made of quartz and had an inner diameter of 3.8 centimeters. The fluoride tungsten chips for generating the tungsten chloride needed were contained in a quartz reservoir located above the deposition chamber. The reservoir contained about 300 grams of fluoride tungsten chips of about 1 millimeter thickness and a few millimeters in other dimensions. Typical chemical analysis yielded: C, 10 ppm; O, 12 ppm; N, 1 ppm; F, 25 ppm. To remove any surface contaminations from the chips used, hydrogen was directed through the reservoir at the beginning of each experiment for 1 hour with the chips maintained at $900^{\circ}C$. Afterwards the temperature of the chips was brought to the desired value, the hydrogen flow was directed through the annular space between the reservoir and the quartz jacket, and chlorine was let into the reservoir for the initiation of the deposition experiment. The deposit was formed on a molybdenum mandrel of 1.9 centimeter diameter and 0.63 centimeter height. The temperature of the mandrel was determined during the deposition by sighting an optical pyrometer into a hohlraum located at its backside. A pressure of 5 torr or less was maintained at the exit end of the deposition apparatus. At the end of each experiment, the weight of the fluoride tungsten chips left in the reservoir was determined, from which the weight of the source material used and the tungsten flux in the reaction mixture during the run were deduced.

2. Determination of Preferred Crystal Orientation in the Deposit

After the completion of the deposition, the molybdenum mandrel containing the chloride tungsten deposit was separated from the ceramic support. The surface of the deposit was polished with fine emery paper and then

electropolished in an aqueous solution of NaOH. The nature of the preferred crystal orientation and the distribution of the orientation crystal lattice direction with respect to the normal to the surface of the deposit were then determined with a Norelco X-ray pole figure machine according to the techniques described previously.⁽³⁾

3. Determination of the Vacuum Work Function of the Deposit

For deposits the vacuum work functions of which were to be determined, the chloride tungsten deposits were separated from the molybdenum mandrel by dissolving the latter in a mixture of HNO₃ and HCl. A disc of 1.5 cm diameter was cored out of each deposit by electrical discharge machining. Remnants from the coring operation were used for determining the impurity contents and the microstructures of the deposit. The disc was ground to 1 millimeter thickness, polished with 1 micron diamond paste and then electropolished in an aqueous solution of NaOH. After outgassing at 1850°C for a period of 200 hours, the vacuum work function of the disc was measured at 1800°C in a vacuum emission cell used in our previous determinations of the vacuum work functions of thermionic emitter materials.⁽⁷⁾

RESULTS AND CONCLUSIONS

The results obtained are shown in Table 1 together with the conditions of deposition. In Fig. 2, the preferred orientation and the vacuum work function of each deposit obtained are plotted as a function of temperature of deposition and the mole ratio of hydrogen to tungsten in the vapor phase. Figure 3 and Fig. 4 show respectively the macroscopic appearance and the microstructures of a cross section of a {110} oriented chloride tungsten deposit. Analysis of these {110} oriented chloride tungsten deposits yielded the following ranges of major impurity contents: O, 0.5-1 ppm; N, < 1 ppm; C, 2-8 ppm; F, 9-17 ppm; Cl, 5-10 ppm; Al, 4-20 ppm; Fe, 10-20 ppm; Cu, 1-2 ppm; Mg 0.4-0.6 ppm; Si, 3-20 ppm.

From the data shown in Table 1 and Fig. 2, the following conclusions can be drawn for the deposition conditions studied.

1. Lower deposition temperature and lower H₂/W mole ratio in the vapor phase favor the development of {110} preferred orientation in the deposit.

2. Higher deposition temperature and higher H_2/W mole ratio in the vapor phase increase the deposition efficiency and favor the development of random or $\{100\}$ oriented deposits.
3. The Cl/W atom ratio in the vapor emerging from the tungsten chip reservoir is usually less than 6, indicating that the reaction product contains significant amounts of tungsten subhalides. At high chlorine flow rate, the Cl/W atom ratio becomes higher than 6, implying that a part of the chlorine gas passes through the tungsten column without reacting with the tungsten. The Cl/W atom ratio, however, does not seem to be a critical factor in determining the nature of the preferred crystal orientation in the deposit.
4. The temperature of the tungsten chips is the principal controlling factor for the tungsten flux and thus the Cl/W ratio and the H_2/W ratio in the gaseous reactant mixture. When the temperature of the tungsten chips is too low (e.g. $750^\circ C$), the efficiency of deposition is almost reduced to zero because of the low tungsten flux in the vapor surrounding the molybdenum mandrel.
5. Chloride tungsten deposits of vacuum work functions between 4.9 and 5.0 eV can be obtained at the following deposition conditions: mandrel temperature $1100-1150^\circ C$, hydrogen flow rate 140-160 c.c./min., chlorine flow rate 115-135 c.c./min., and tungsten chip temperature $830-875^\circ C$. The reproducibility of these results has been substantiated by the fact that ten chloride tungsten samples prepared at a mandrel temperature of $1100^\circ C$, a hydrogen flow rate of 140 c.c./min., a chloride flow rate of 115 c.c./min., and a tungsten chip temperature of $850^\circ C$, all exhibit vacuum work function of 4.9-5.0 eV. X-ray analyses indicate that for samples having vacuum work functions close to 5 eV, 90% of their $\langle 110 \rangle$ axes lie within about 7° from the normal to their emitting surfaces, and that for samples having vacuum work functions close to 4.9 eV, 90% of their $\langle 110 \rangle$ axes lie within 11° from the normal to their emitting surfaces.

Table 1

RESULTS OF CHLORIDE TUNGSTEN DEPOSITION

Run No.	Mo Mandrel Temperature (°C)	H ₂ Flow Rate* (c.c./min.)	Cl ₂ Flow Rate* (c.c./min.)	Time (min.)	W Chip Temperature (°C)	W Flux In Vapor (gm/hr.)	Atom Ratio of Cl to W in Vapor	Mole Ratio of H ₂ to W in Vapor	Thickness of Deposit on Top of Mo Mandrel (mils)	Efficiency of Deposition** (%)	Preferred Crystal Orientation	Vacuum Work Function (eV)
1	1350	70	350	180	850	25.7	12.24	1.22	33	24	(100)	4.55
2	1150	70	200	180	825	19.3	9.30	1.63	24	23	(110)	4.95
3	1250	70	200	180	850	22.6	7.92	1.39	39	32	(110)	4.80
4	1150	70	115	255	850	22.6	4.56	1.39	31	18	(110)	4.97
5	1150	140	115	240	830	22.0	4.70	2.86	63	43	(110)	4.88
6	1200	140	115	240	840	24.0	4.32	2.61	115	67	Random	4.57
7	1150	140	115	240	850	23.8	3.60	2.19	87	42	(110)	4.92
8	1200	100	60	180	820	16.0	3.36	2.80	53	61	Random	4.53
9	1220	100	60	240	825	16.7	3.23	2.61	80	66	(100)	4.52
10	1100	140	115	240	850	28.5	3.64	2.19	86	42	(110)	5.01
11	1050	140	115	240	875	31.2	3.32	2.01	46	20	(110)	4.85
12	1100	200	115	180	875	29.4	3.53	3.05	58	37	(110)	4.83
13	1100	160	115	180	875	31.2	3.32	2.29	60	36	(110)	4.89
14	1100	160	115	180	875	31.8	3.26	2.25	60	35	(110)	4.97
15	1100	140	115	180	850	26.4	3.93	2.37	46	33	(110)	5.00
16	1100	140	135	210	830	22.4	5.45	2.79	41	29	(110)	4.92
17	1100	280	115	72	850	27.9	3.71	4.55	31	52	Random	4.52
18	1100	140	115	200	750	4.5	22.7	13.39	1	0.4	-	-

*At 300°K and 1 atm.

**Defined as $\frac{\text{Weight of tungsten deposited on Mo mandrel surface X100}}{\text{Weight of tungsten intersected by Mo mandrel surface during the run}}$

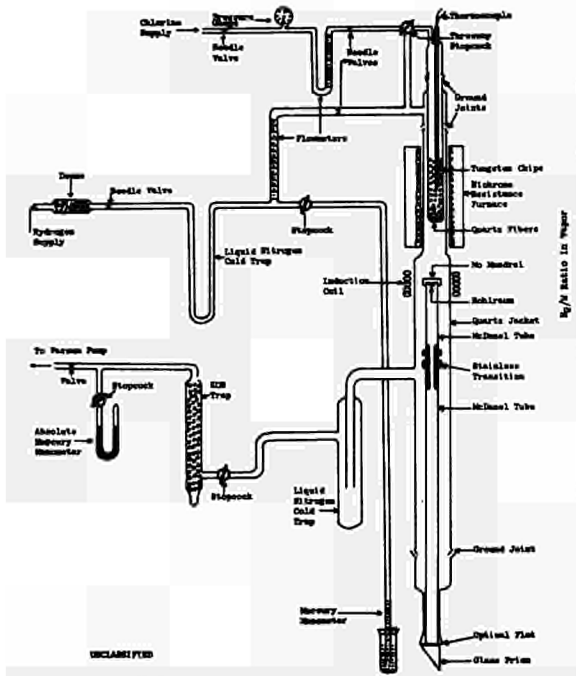


Fig. 1--(U) Chloride tungsten deposition apparatus using chlorination of tungsten chips to provide tungsten source material

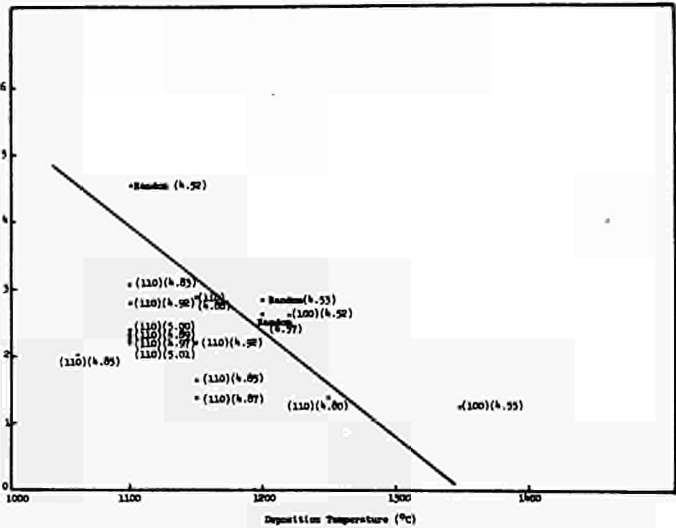


Fig. 2--(U) Preferred orientation and vacuum work function in chloride tungsten as a function of deposition conditions

The numbers in parentheses represent the lattice planes of preferred orientation and the vacuum work functions

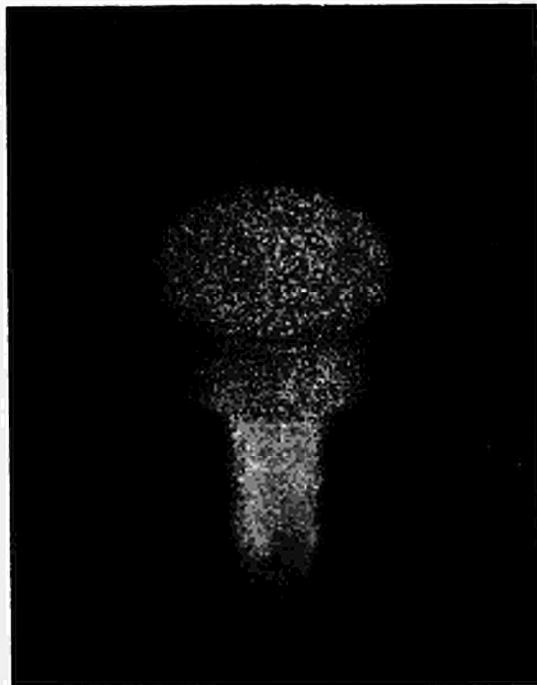


Fig. 3--(U) Macroscopic appearance of {110} oriented chloride tungsten deposit on molybdenum mandrel

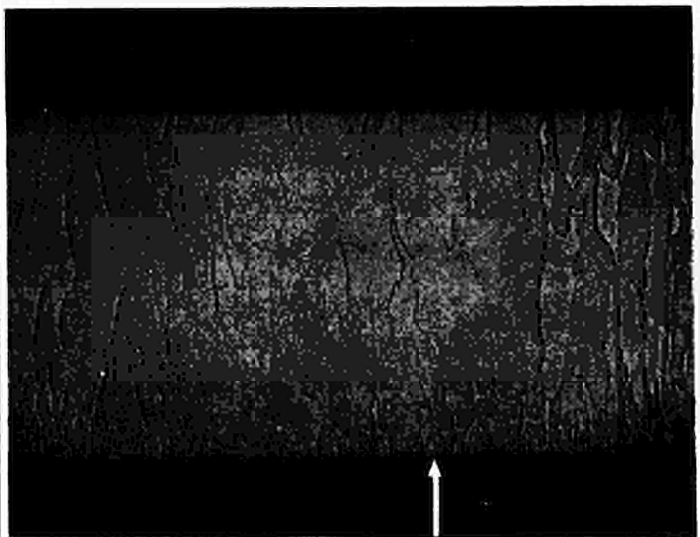


Fig. 4--(U) Microstructure of a cross section {110} oriented chloride tungsten deposit

REFERENCES

- (1) WEINBERG, A. F. and L. YANG, "Interdiffusion Between Uranium-Bearing Reactor Fuels and Refractory Metal Thermionic Emitters." *Advanced Energy Conversion*, 3, 101 (1963).
- (2) YANG, L., R. G. HUDSON, and F. D. CARPENTER, "Some High Temperature Diffusion Studies on Materials of Thermionic Interest." *International Conference on Thermionic Electrical Power Generation*, London (September 20-24, 1965).
- (3) YANG, L. and R. G. HUDSON, "Effect of Preferred Crystal Orientation and Surface Treatment on the Work Function of Vapor Deposited Tungsten." *Thermionic Conversion Specialist Conference*, Houston, Texas, pp. 395-404 (November 2-4, 1966).
- (4) YANG, L. and R. G. HUDSON, "Evaluation of Chemically Vapor Deposited Tungsten as Electron Emitters for Nuclear Thermionic Application." *Proceedings of the Conference on Chemical Vapor Deposition of Refractory Metals, Alloys, and Compounds*. Gatlinburg, Tennessee, pp. 329-348 (September 12-14, 1967).
- (5) HOLLAND, J. W. and J. KAY, "Performance of a Cylindrical Geometry Thermionic Converter with an Improved Work Function Tungsten Emitter." *Thermionic Conversion Specialist Conference*, Palo Alto California, pp. 13-15 (October 30-November 1, 1967).
- (6) HOWARD, R. C., L. VAN SOMEREN and L. YANG, "Preliminary Results on the Thermionic Performance of a Vapor-Deposited Tungsten Emitter Having {110} Preferred Orientation." *Thermionic Conversion Specialist Conference*, Palo Alto, California, pp. 10-11 (October 30-November 1, 1967).
- (7) HUDSON, R. G. and L. YANG, "Effect of Operating Temperature on the Vacuum Emission Stability of Vapor Deposited Tungsten Clad UC-ZrC and UO₂." *Thermionic Conversion Specialist Conference*, Houston, Texas, pp. 212-221 (November 2-4, 1966).

DISCUSSION

Speaker of paper E-1: R. W. PIDD.

SHROFF (France): Is there a critical thickness to have a stable (110) structure?

PIDD (USA): I don't think we know. We have made both what we call simplex structures (just one layer) and duplex structures (two layers). We have laid about of the order of 10 mils or so of chloride tungsten oriented (110) on an ordinary tungsten fluoride cylinder. It is very stable, but we have never pushed it to the limit to see how thin you could make it and maintain the work function.

FUEL AND FISSION PRODUCT TRANSPORT THROUGH
CHEMICALLY VAPOR-DEPOSITED FLUORIDE TUNGSTEN*

by

L. Yang and R. G. Hudson

Gulf General Atomic Inc.
P.O. Box 608, San Diego, California 92112 (USA)ABSTRACT

The transport rates of fuel components from 90UC-10ZrC, UO₂ and W-60 vol% UO₂ cermet through chemically vapor-deposited fluoride tungsten cladding were determined in the temperature range 1923-2273°K, using samples of both planar and cylindrical configurations. From the results obtained, it is estimated that the total amount of uranium transported through 40 mil thick fluoride tungsten cladding in 10,000 hours may vary from a few to 5000 monolayers, depending upon fuel composition, fuel stoichiometry and temperature. The uranium transport rate of UO₂ through fluoride tungsten cladding at 2273°K is many orders of magnitude higher than that reported for powder metallurgy or arc-cast tungsten cladding at the same temperature, implying the importance of cladding structure to uranium transport rate. It is shown that the carbon transport through fluoride tungsten cladding will not cause a significant change in fuel stoichiometry at 2073°K in 10,000 hours.

Measurements were made on the fission product recoil range and the diffusion constants of various fission products in fluoride tungsten. On the basis of the results obtained and an equation derived for the transport rates of primary fission products from fuels through cladding by both the recoil and the dissolution mechanisms, the total accumulations of various primary fission products outside the cladding were calculated as a function of time and temperature. It is shown that among the fission products studied the Ru isotopes constitute the major components of those diffusing through the cladding. Post-irradiation annealing studies substantiated this finding and showed that no significant transport of Xe¹³³ through 20 mil thick fluoride tungsten cladding at 2073°K in 1000 hours.

* This work is sponsored by the National Aeronautics and Space Agency under Contracts NAS 3-6471 and NAS 3-8504.

INTRODUCTION

The work function of a thermionic emitter surface is sensitive to the presence of a fraction of a monolayer of adsorbed impurity atoms. In a nuclear thermionic converter, the emitter consists of a refractory metal cladding in close contact with nuclear fuel materials at high temperatures in a neutron environment. If the transport rates of fuel components and fission products through the cladding are rapid, they may accumulate on the electrode surfaces and affect the thermal and electrical performance of the converter. To gain an insight of the problem involved, experimental measurements were made on the transport rates of fuel components through fluoride tungsten claddings of planar emitters fueled with 90UC-10ZrC and UO_2 and of cylindrical emitters fueled with 90UC-10ZrC and W-60 vol% UO_2 cermet. In addition, the fission recoil ranges and the diffusion constants of various fission products in fluoride tungsten were determined, from which their transport rates through fluoride tungsten claddings were deduced and compared with results obtained from post irradiation annealing studies made on planar emitters fueled with 90UC-10ZrC and UO_2 .

EXPERIMENTAL AND ANALYTICAL METHODS

1. Fuel Component Transport

Fuel component transport data were obtained by using both planar and cylindrical samples. The planar samples consisted of 90UC-10ZrC or UO_2 wafers of 20 to 40 mil thickness of 0.250 to 0.375 inch diameter clad with fluoride tungsten of 20 or 40 mil thickness. Each sample was heated at a certain temperature for a given period of time in vacuum by electron bombarding one of its flat surfaces. The uranium diffusing through the other flat surface was gathered on a water-cooled stainless steel collector and its amount determined by dissolving the deposit in dilute HNO_3 , irradiating the solution in Gulf General Atomic's TRIGA reactor at 250 kw for 1 hour, and counting the activity of the I^{134} formed. In some cases, the carbon content in the deposit was measured by oxidizing it to CO_2 with oxygen and Cu_2O at about $400^\circ C$ and determining the amount of CO_2 formed

by gas chromatographic techniques. The cylindrical samples consisted of 90UC-10ZrC and W-60 vol% UO₂ cermet fueled emitters in out-of-pile cylindrical converters which were life tested for periods from a few thousands to ten thousand hours. The uranium content in the deposit condensed on the collector surface was determined by the same radiochemical method described above.

2. Fission Product Transport

(1) Determination of fission product recoil range in fluoride tungsten.

Polished surfaces (to 0000 emery paper) of vacuum annealed (2073°K, 50 hours) fluoride tungsten discs 0.375 inch in diameter and 20 mil in thickness, were held in contact with a U²³⁵ source and irradiated in Gulf General Atomic's TRIGA reactor at ambient temperature at 250 kw for 1/2 hour. Thin layers were removed from the fission product impregnated surfaces either by mechanical polishing or by electrolytic dissolution. The concentrations of the fission products La¹⁴⁰, Ru¹⁰³ and Zr⁹⁵-Nb⁹⁵ in each layer were determined by radioactive counting techniques, and the thickness of each layer removed was determined by weighing. The recoil range of each of these fission product studied was deduced from its activity distribution in each tungsten disc.

(2) Determination of diffusion constants of fission products in fluoride tungsten.

The diffusion constants of Ru¹⁰³, Ce¹⁴¹, Zr⁹⁵, Ba¹⁴⁰, I¹³¹ and Te¹³² in fluoride tungsten were determined in the temperature range 1873° to 2123°K by the diffusion couple method. Each couple consisted of two fluoride tungsten discs 0.375 inch in diameter and 20 mils in thickness, each with one of its two flat surfaces prepared and impregnated with fission products according to the method described above. The impregnated discs were diffusion bonded in a vacuum hot press at the planned diffusion temperature and 5000 psi for 3 hours with the impregnated surfaces facing each other. The diffusion bonded couple was annealed in a tantalum resistance furnace

in vacuum at the desired temperature. After the diffusion anneal, the sample was mounted in plastic and sectioned by anodic dissolution in 10% NaOH solutions from one tungsten disc to the other tungsten disc across the interface. The Ru¹⁰³, Ce¹⁴¹, Zr⁹⁵, Ba¹⁴⁰, I¹³¹ and Te¹³² contents of the solutions obtained were determined by radiochemical techniques. The thicknesses of the tungsten layers dissolved were evaluated from the tungsten contents of these solutions. Since the initial fission product sources extend to a distance of only 5 to 6 microns (see the results on fission recoil range in tungsten below) at either side of the interface of the diffusion couple, the configuration of the sample can be treated as that of an infinite system containing an infinitely thin plane source at the interface,⁽¹⁾ provided the diffusion-anneal time is long enough to produce a diffusion distance much greater than 5 to 6 microns. For such a system, a straight line should result if $\log C$ is plotted against X^2 , when C is the concentration of the fission product at a distance X cm. from the interface. The diffusion constant D (in cm^2/sec) can be evaluated from the slope of such a straight line, which is equal to $\frac{1}{4Dt}$; where t is the diffusion time in seconds.

(3) Calculation of fission product transport through cladding from fission recoil range and diffusion constant.

A general equation was derived⁽²⁾ for a planar fuel-clad configuration to relate the transport rates of primary fission products (i.e. fission products formed either directly by the fission of U²³⁵ or from precursors of very short half-lives) through the cladding as a function of time during their continuous generation in the fuel material by taking into account the entry of the fission products into the cladding by both the recoil and the dissolution mechanism. The assumption was made that the diffusion of fission products from the fuel is such that a homogeneous concentration distribution in the fuel is maintained at all times. The equation is shown below together with the nomenclature of the symbols used (Table 1).

$$R(t) = R - \left\{ \frac{2D}{(b-a)^2} \sum_{n=1}^{\infty} \alpha_n \exp - \left[\left(\lambda + \frac{D \alpha_n^2}{(b-a)^2} \right) t \right] \right\} \times$$

$$\left\{ \frac{(b-a) S_1 + \frac{A(b-a)}{\delta_2} \left[-\phi \delta_2 + \frac{\beta(b-a)^2}{\alpha_n^2} - \frac{\beta(b-a)^2}{\alpha_n^2} \cos \frac{\delta_2 \alpha_n}{b-a} + \frac{\phi(b-a)}{\alpha_n} \sin \frac{\alpha_n \delta_2}{b-a} \right]}{\left[\lambda + \frac{D \alpha_n^2}{(b-a)^2} \right] \left\{ \left[\beta_1 (b-a) + \phi \right] \sin \alpha_n + \phi \alpha_n \cos \alpha_n \right\}} \right\} \quad (1)$$

where

$$R = \left\{ \frac{S_1 + \frac{A}{\delta_2} \left[-\phi \delta_2 + \phi \sqrt{\frac{D}{\lambda}} \sinh \sqrt{\frac{\lambda}{D}} \delta_2 + \beta \frac{D}{\lambda} \cosh \sqrt{\frac{\lambda}{D}} \delta_2 - \beta \frac{D}{\lambda} \right]}{\beta \cosh \sqrt{\frac{\lambda}{D}} (b-a) + \phi \sqrt{\frac{\lambda}{D}} \sinh \sqrt{\frac{\lambda}{D}} (b-a)} \right\} \quad (2)$$

The total accumulation of a given fission product outside the cladding at time equal to t_f is

$$M(t_f) = \int_0^{t_f} R(t) [\exp - \lambda (t_f - t)] dt \quad \text{atom/cm}^2 \quad (3)$$

(4) Post-irradiation annealing studies of fission product transport through fluoride tungsten cladding.

Fluoride tungsten clad (20 mil thick) 90UC-10ZrC and UO₂ wafers of 5% enrichment were irradiated in Gulf General Atomic's TRIGA reactor at ambient temperature to attain a total of 1×10^{14} fissions in each fuel wafer. Each irradiated sample was heated in vacuum at 2073°K for 1000 hours in water-cooled stainless steel enclosure connected to a liquid nitrogen cooled charcoal trap. Any Xe¹³³ diffusing through the cladding was collected in the trap and its activity in the trap was counted every few hours. The condensable fission products diffusing through the cladding were collected on the surface of a water-cooled stainless steel collector. The collector deposit was dissolved in dilute HNO₃ at the end of the experiment and the solution obtained was analyzed radiochemically for the total transport of various fission products through the cladding at 2073°K in 1000 hours.

Table 1
NOMENCLATURE OF SYMBOLS USED IN EQUATIONS (1) AND (2)

Symbol	Definition
$R(t)$	Fission product release rate from the outer surface of cladding at time t (atoms/cm ² -sec)
R	Fission product release rate from the outer surface of cladding at steady state condition, i.e., when the rate of fission product injection into the cladding is balanced by the rate of decay plus the rate of release (atoms/cm ² -sec)
D	Diffusion constant of fission product in fluoride tungsten (cm ² /sec)
b	Distance between the outer surface of the cladding and the center of the fuel body (cm)
a	Distance between the fuel-clad interface and the center of the fuel body (cm)
$(b-a)$	Thickness of cladding (cm)
α_n	Roots of the transcendental equation $\cot \alpha_n = [\phi/\beta(b-a)] \alpha_n$
ϕ	Ratio of fission product concentration in fuel to fission product concentration in clad at fuel-clad interface
β	Fuel-clad interfacial area per unit fuel volume (cm ² /cc)
λ	Disintegration constant of fission product (sec ⁻¹)
t	Time of diffusion (sec)
δ_1	Recoil range of fission product in fuel material (cm)
δ_2	Recoil range of fission product in tungsten cladding (cm)
S_1	Rate of increase of fission product source concentration in the fuel during the operation of the fuel element (atoms/cc-sec) = $Q - (\beta/4)\delta_1 Q$, where Q = rate of generation of fission product atoms in unit volume of fuel = 3×10^{10} PY (P = fission power in watts/cc and Y = fission yield), and $(\beta/4)\delta_1 Q$ = rate of loss of fission product atoms per unit volume of fuel due to fission recoil into tungsten cladding

Table I (Continued)
 NOMENCLATURE OF SYMBOLS USED IN EQUATIONS (1) AND (2)

Symbol	Definition
A	Rate of increase of fission product concentration in tungsten cladding at the fuel-clad interface due to fission recoil (atoms/cc-sec) = $1/2 Q(\delta_1/\delta_2)$, since the total number of atoms of fission product recoiled into the cladding is $1/4 (Q \delta_1)$ and this total number is distributed linearly in a zone of width equal to δ_2 in the cladding.

RESULTS AND CONCLUSIONS

1. Fuel Component Transport

The results are summarized in Table 2. In Fig. 1 the uranium fluxes shown in Table 2 for the various fuel materials are plotted as number of monolayer (each monolayer $\approx 5 \times 10^{14}$ atoms/cm²) transported through 40 mil thick fluoride tungsten cladding in 10,000 hours as a function of cladding temperature, assuming that the uranium transport is inversely proportional to cladding thickness and directly proportional to time. The results obtained by Kaznoff and Sanderson⁽³⁾ on uranium transport rates from UO_{2.004} through fluoride tungsten, powder metallurgy tungsten and arc-cast tungsten are included for comparison.

From the results shown in Table 2 and Fig. 1, the following conclusions can be drawn.

- (1) The uranium transport rate is affected by fuel composition and fuel stoichiometry. The transport rate from the oxide fuel, especially the cermet fuel, is less than that from the carbide fuel at equal temperature. For the carbide fuels studied, the carbon rich fuel has a lower uranium transport rate than the stoichiometric fuel, presumably due to the lower uranium activity of the carbon rich fuel.

Table 2

FUEL COMPONENT TRANSPORT RATES THROUGH FLUORIDE TUNGSTEN

Sample No.	Fuel	Cladding Thickness (mil)	Sample Configuration	Temperature (°K)	Time (hr)	Average Uranium Flux (gm/cm ² , hr)	Average Carbon Flux (gm/cm ² , hr)
1	UO _{2.004}	20	Planar	2273	1005	1.1 x 10 ⁻⁷	
2	UO _{0.90} Zr _{0.10} C _{1.02}	20	Planar	2223	820	2.5 x 10 ⁻⁷	
3		20	Planar	2173	1000	1.4 x 10 ⁻⁷	
4		40	Planar	2073	10146	1.2 x 10 ⁻⁸	1.6 x 10 ⁻⁹
5		40	Planar	2073	10000	1.1 x 10 ⁻⁸	1.8 x 10 ⁻⁹
6	U _{0.90} Zr _{0.10} C _{1.00}	40	Cylindrical	2023	7558	6.0 x 10 ⁻⁸	
7	W-60 vol% UO ₂	40	Cylindrical	2023	10406	3.6 x 10 ⁻¹⁰	
8		40	Cylindrical	1923	3235	6.0 x 10 ⁻¹¹	

- (2) At the normal emitter operating temperatures (1973-2073°K), the uranium transports through 40 mil thick fluoride tungsten cladding vary from about 5 to 500 monolayers in 10,000 hours for the various fuel materials studied. Whether such uranium transports would change the electrical and thermal performance of the electrodes in a thermionic converter depends upon the rate of evaporation of uranium from the emitter surface and the rate of diffusion of uranium into the collector bulk. These rates are affected by electrode temperature, nature of electrode material and the presence of other fuel components. One of the main objectives for testing fueled converters is to map out the operating conditions under which the converter performance is least affected by such finite rates of uranium transport.
- (3) The uranium transport rate through tungsten cladding is a strong function of the structure of the cladding. Transport rates through the equiaxial grains of powder metallurgy or arc-cast tungsten are much lower than that through the columnar grains of fluoride tungsten, as pointed out previously by Kaznoff and Sanderson.⁽³⁾
- (4) Although the carbon transport rate from the carbide fuel through the fluoride tungsten cladding is measurable, its effect on fuel stoichiometry is small. For instance, assuming the carbide contains 5 wt% carbon and has a density of 10 gm/c.c., for an emitter of 1/2 inch diameter and 40 mil cladding thickness, only 0.017% of the carbon content of the carbide fuel is lost in 10,000 hours by diffusion through the cladding.

2. Fission Product Transport

(1) Fission recoil ranges.

Studies were made on a total of six samples. The average values for fission fragments of mass 140, mass 103 and mass 95 are 5.2, 5.4 and 5.6 microns respectively.

(2) Diffusion Constants.

Studies were carried out at 1873°K, 1973°K, 2023°K, and 2123°K respectively. The variation of the diffusion constant D with temperature is expressed in the form $D = D_0 \exp \left[\frac{-Q}{RT} \right]$, with the D_0 and the Q values for the various fission products studied shown in Table 3.

Table 3
RESULTS FOR THE DIFFUSION OF FISSION
PRODUCTS IN FLUORIDE TUNGSTEN

Isotope	D_0 (cm ² /sec)	Q (cal./mole)
Ru ¹⁰³	5.70 x 10 ⁻²	41000
Ce ¹⁴¹	1.02 x 10 ⁻²	39600
Zr ⁹⁵	9.25 x 10 ⁻³	39400
Ba ¹⁴⁰	4.15 x 10 ⁻¹	49100
I ¹³¹	4.25 x 10 ⁻¹	49600
Te ¹³²	3.36 x 10 ⁻¹	49400

The metallic fission products studied have D values higher than that of the non-metallic fission products studied and Ru has the highest D value.

(3) Analytical evaluation of fission product transport through fluoride tungsten cladding.

A computer program was devised for the evaluation of the rate of transport R(t) and the total accumulation M(t) outside the cladding as a function of time according to Equations (1) and 3), using the fission recoil ranges and diffusion constants given above. Figure 2 shows the results on M(t) values as a function of time at a cladding temperature of 2073°K for both the radioactive and the stable Ru, Zr, Ce, Ba, I and Te primary fission product isotopes,

assuming $(b-a) = 0.1$ cm, $P = 500$ watt/cc, $\beta = 4$ cm²/cc, $\delta_1 = 6 \times 10^{-4}$ cm. $\phi = 1$ for the Ru, Ba, I and Te isotopes, and $\phi = 100$ for the Zr and Ce isotopes which form stable carbides and oxides. For the Ru isotopes, the calculations were extended to 1973°K and 1873°K and the results are shown in Fig. 3. It can be seen that Ru isotopes constitute the major components of fission products transported through the cladding. The total amount of Ru isotopes transported through the cladding in 10,000 hours is about 1000 monolayers at 2073°K, which decreases to about 100 monolayers at 1973°K and to about a few monolayers at 1873°K. Thus the Ru isotope transport is of the same order of magnitude as the uranium transport from a carbide fuel at the same temperature. It must be pointed out, however, that these calculations were made by assuming that the rates of diffusion of these fission products in the fuel material are not the limiting factor for the transport process through the cladding. In the event this is not true, then the observed transport should be less than that shown in Figs. 2 and 3.

(4) Post-irradiation annealing studies of fission product transport through fluoride tungsten cladding.

Two samples containing $U_{0.90} Zr_{0.10} C_{1.02}$ fuel wafers and two samples containing $UO_{2.005}$ fuel wafers were studied at 2073°K for 1000 hours, using the experimental method described above. In each case no Xe^{133} transport through the cladding was observed beyond the experimental detection limit ($\sim 10^7$ atoms), and Ru^{103} was the only radioactive fission product detected on the collector surface in amounts corresponding to 0.03% of the initial Ru^{103} contents of the carbide fuel and 0.18% of the initial Ru^{103} contents of the oxide fuel. Thus the results on Ru^{103} transport confirm the conclusion reached in the analytical evaluation made by using the measured fission recoil ranges and diffusion constants.

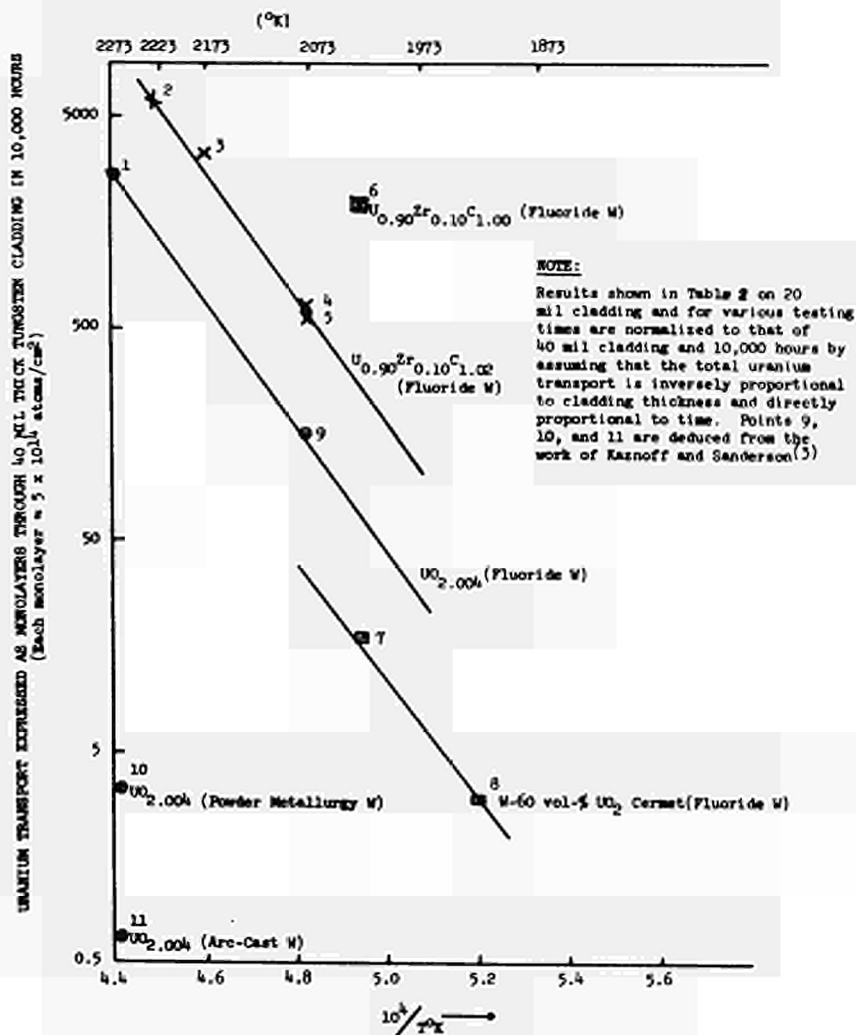


Fig. 1--(U) Uranium transport through 40 mil thick tungsten cladding in 10,000 hours at various temperatures

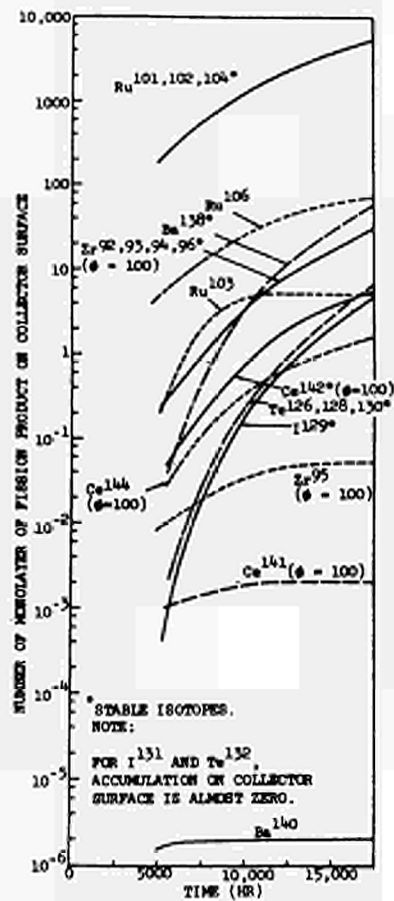


Fig. 2--(U) Number of monolayers of various fission product isotope accumulation on collector surface as a function of time. Temperature of tungsten cladding = 2073°K (assume 1 monolayer $\sim 5 \times 10^{14}$ atoms/cm²)

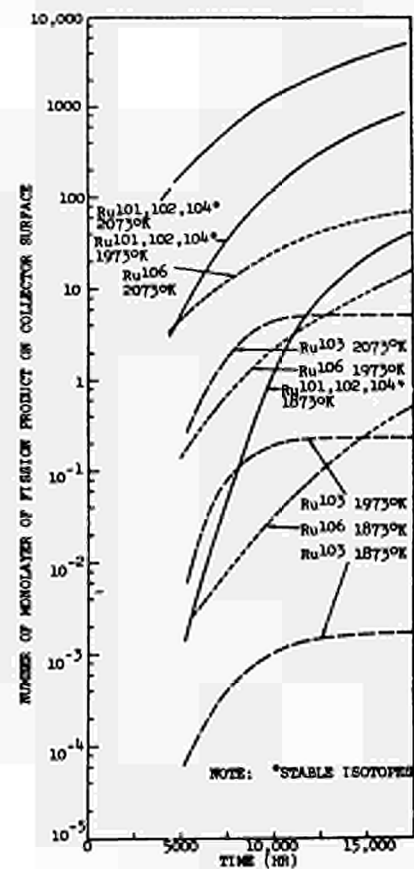


Fig. 3--(U) Number of monolayers of various Ru fission product isotope accumulation on collector surface as a function of tungsten cladding temperature and time (Assume 1 monolayer $\sim 5 \times 10^{14}$ atoms/cm²)

REFERENCES

- (1) "Diffusion in Solids, Liquids, Gases," p. 17, W. Jost, Academic Press Inc., New York, (1952).
- (2) Private Communication with B. W. Roos of Gulf General Atomic.
- (3) KAZNOFF, A. I., and M. J. SANDERSON, "Diffusion and Interactions in the Urania-Tungsten and Urania-Molybdenum Systems." International Conference on Thermionic Electrical Power Generation, London, (September 20-24, 1965).

DISCUSSION

Speaker of paper E-2: R. W. PIDD.

HOWARD (USA): Could you describe the technique that was used for the fission product diffusion experiments? In other words did you take metal and put it against tungsten or did you spread it out or what?

PIDD (USA): We performed experiments both with fuel and fission product transport through the cladding and used both pre-irradiation annealing and post-irradiation annealing techniques.

In the pre-irradiation annealing studies you have a piece of metal that has been heated while in contact with some fuel. The fuel passes into the metal, allowing a measure of the fuel transport.

In the post-irradiation annealing studies one irradiates metal-clad fuel wafers and heats them. The gaseous fission products which pass through the cladding are then passed to a nuclear counter where they are measured.

HOWARD: What about the ones that never leave the surface of the metal. They don't get swept by the gas. How do you count those?

PIDD: We have also dipped the tungsten in acid and we have found not only how much was on the surface but have measured densities as a function of depth for mil layers.

ROUKLOVE (USA): It is known that most of the products of fission do not react with the cesium. However, I think that iodine does. Did you observe what the effect of this reaction is?

PIDD: The work that I described here is simply concerned with the absolute amount of transport and not with what happens in the converter, or whether it helps the conversion process or harms it.

Dépôts par décomposition thermique
en phase vapeur de tungstène , rhénium
et niobium et d'alliage niobium tungstène

A.M. Shroff

CSF - Compagnie générale de télégraphie Sans Fil,
Groupement Scientifique et Technique
Domaine de Corbeville, Orsay (France)

I. - Introduction

Les problèmes posés par la conversion thermoionique, que ce soit dans la réalisation d'émetteurs d'électrons pour les diodes ou des conduits de chaleur pour les caloducs ou encore des revêtements pour les liaisons métal-céramique, ont nécessité l'étude et le développement de la technique de dépôt de métaux réfractaires en phase vapeur par réduction ou décomposition d'un de leurs halogènes. Parmi les différents métaux réfractaires connus, le tungstène et le rhénium sont ceux qui sont le plus communément utilisés comme émetteurs d'électrons, le niobium étant plus fréquemment employé comme métal de revêtement.

On a utilisé les halogénures de ces différents matériaux qu'on a réduits par l'hydrogène à haute température.

L'orientation cristalline dépend de la température, de la pression et de la composition du mélange gazeux utilisé.

En plus de la pureté, c'est la compacité des dépôts obtenus qui présentent un grand intérêt.

On décrit ici les dispositifs expérimentaux utilisés ainsi que les résultats obtenus.

II. - Dispositifs expérimentaux

On utilise la réaction de réduction à chaud par l'hydrogène soit à la pression atmosphérique, soit sous dépression.

Les dispositifs expérimentaux diffèrent suivant que l'on travaille à partir d'un produit gazeux, c'est le cas de l'hexafluorure de tungstène, ou dans un produit solide, c'est le cas de l'hexachlorure ou de l'oxychlorure de tungstène, du trichlorure de rhénium ou du pentachlorure de niobium.

A. - Cas d'un produit gazeux

La figure 1 montre schématiquement les dispositifs expérimentaux réalisés. La figure 2 montre un cliché photographique du dispositif expérimental réalisé pour les dépôts sous dépression.

L'hydrogène et l'hexafluorure sont mélangés puis introduits dans la chambre de réaction qui consiste soit en tube en quartz, soit en une cloche en dural. Le substrat à recouvrir est chauffé en haute fréquence, les gaz produits par la réaction de réduction ainsi que l'excès des autres gaz, sont évacués et neutralisés.

Les débits sont contrôlés à l'aide de débitmètres et la pression est mesurée à l'aide d'un baromètre à mercure. La température du substrat est mesurée à l'aide soit d'un pyromètre optique, soit d'un thermocouple.

B - Cas d'un produit solide

C'est le cas des chlorures de tungstène, du trichlorure de rhénium ou du pentachlorure de niobium.

On utilise en gros la même installation, mais on lui ajoute un évaporateur dans lequel le produit solide est introduit par petites quantités.

On utilise pour le tungstène et le niobium la réaction de réduction par l'hydrogène et pour le rhénium la réaction de décomposition. Dans tous les cas on travaille en dépression. Le dispositif utilisé est schématisé sur la figure 3.

III. - Résultats expérimentaux

Dépôt de tungstène et de niobium

Le dépôt de tungstène est réalisé par réduction de WF_6 , WCl_6 ou $WOCl_4$ par l'hydrogène; les différents paramètres intervenant dans la vitesse de dépôt sont : la température, le rapport stoechiométrique, la pression partielle.

On a vu que plus la température de dépôt était élevée et plus la vitesse de dépôt était grande à rapport stoechiométrique et pression constante. On a fait varier la température depuis $400^\circ C$ jusqu'à $1200^\circ C$. On s'aperçoit que la structure du dépôt dépend fortement de la température. On passe d'un dépôt à grains fins à un dépôt à gros grains en faisant varier la température entre 400 et $1200^\circ C$.

Le dépôt de niobium a été effectué à partir de la réduction par l'hydrogène ou le zinc du pentachlorure de niobium. Le domaine de température utilisé

est compris entre 300 et 1 200° C. Ici aussi la taille des grains dépend de la température. En dessous de 800° C il y a hydratation du dépôt, on utilise alors la réduction par le zinc.

Des essais de dépôt par décomposition de produits halogènes sous vide ont été effectués en vue de déposer le tungstène sur des substrats réactifs à l'hydrogène. La vitesse de dépôt et la structure du dépôt dépendent essentiellement de la pression partielle et de la vitesse d'évaporation du composé halogène.

IV. - Propriétés des dépôts en phase vapeur

IV.1. Propriétés mécaniques et physiques

Les premiers essais de flexion réalisés sur des éprouvettes parallélépipédiques ont montré que la résistance à la flexion d'un tungstène déposé en phase vapeur était comprise entre 80 et 100 kg/mm² alors qu'une éprouvette identique en tungstène déposé par schoopage est de 50 kg/mm² et un tungstène fritté de l'ordre de 120 à 140 kg/mm².

Afin de mesurer la densité on a réalisé des dépôts de tungstène de formes et d'épaisseurs variables sur substrats solubles, du cuivre par exemple. On a trouvé qu'elle se situait entre 98,5 et 99 % de la densité théorique. Ces chiffres sont supérieurs à ceux qu'on obtient par tous autres procédés de dépôt. Ceci montre que les dépôts de tungstène sont compacts et étanches au vide. Cependant du fait de la fragilité l'épaisseur minimum doit être de l'ordre de 150 μ .

Cette technique permet de réaliser des pièces et des revêtements étanches sur n'importe quel type de substrat.

IV.2. Examen de la structure des dépôts

L'examen des coupes métallographiques des différents dépôts montre dans tous les cas une croissance du type basaltique en général indépendante du substrat (Fig. 4). La taille des grains dépend de la température de dépôt. Plus cette température est élevée et plus les grains sont gros. L'examen au microscope électronique⁽⁴⁾ par la méthode des répliques au carbone platine de la

structure des dépôts révèle sur des coupes perpendiculaires à la surface une structure basaltique démarant de l'interface. La croissance s'effectue perpendiculairement à la microstructure du substrat. La figure 5 montre les différents clichés obtenus sur le tungstène déposé sur un substrat en molybdène. Si on examine maintenant la surface du dépôt, on remarque une série de petits trous qui débouchent à l'extérieur et dont le diamètre le plus grand est de l'ordre du 1μ . (Fig. 6).

IV.3. Etude aux rayons X des dépôts

- Dépôt de tungstène : L'étude a été effectuée à l'aide d'un diffractographe à rayons X Siemens. Le rayonnement utilisé est la raie $K\alpha$ du cuivre. Le tableau 1 résume les principaux résultats obtenus sur le tungstène déposé soit à partir des fluorures, soit à partir des chlorures. On observe que :

- Dans le cas des fluorures le plan qui apparaît le plus fréquemment est le plan $[100]$ dans un domaine de température compris entre 500 et 800° C.
- On remarque aussi que l'amplitude des pics $[100]$ passe par un minimum entre 900 et 1000° C; le plan $[110]$ devient alors plus important.

Cependant un recuit à 2100° K modifie sensiblement ces orientations. Les surfaces qui présentaient les plans $[110]$ ont une structure qui les rapproche plus de la structure du tungstène fritté, c'est-à-dire à égale répartition des plans $[100]$ et $[110]$.

- Le rapport H_2/WF_6 influe grandement sur l'orientation ainsi que la pression résiduelle lors du dépôt.
- Dans le cas des chlorures plus la température est élevée et plus le plan $[110]$ apparaît.

- Dépôt de niobium : En ce qui concerne le niobium, on observe que l'intensité des pics $[100]$ et $[110]$ sont presque identiques et qu'après recuit sous vide à 1500° C, l'orientation $[100]$ est prépondérante.

- Dépôt de rhénium : Pour les dépôts de rhénium on a toujours obtenu des structures sans orientation préférentielle. Après recuit il y a une tendance à l'orientation mais elle reste toujours faible.

IV.4. Etude de la répartition de l'émission électronique de dépôt de tungstène et de rhénium ⁽⁵⁾

Une étude de la répartition de l'émission électronique des dépôts de tungstène et de rhénium a été effectuée.

Le cliché figure 7 montre l'image électronique obtenue pour des dépôts de tungstène réalisés à partir de l'hexafluorure, de l'hexachlorure et de rhénium à partir du trichlorure.

On remarque la bonne homogénéité de la répartition de l'émission électronique. Le travail de sortie trouvé pour le tungstène est de 4,72 eV, ce qui correspond au plan [100] ce qui est en bon accord avec les résultats aux rayons X. De plus récents clichés montrent pour des échantillons réalisés à plus haute température l'apparition de plan [110] sur une grande partie de la surface.

IV.5. Modèle de travail

Le modèle de travail le plus vraisemblable compte tenu des différentes expériences réalisées, semble être le suivant :

la réaction de réduction de l'halogénure par l'hydrogène a lieu dans la phase vapeur avec précipitation des grains du métal à la surface du substrat. Dès que la température croît la nucléation s'effectue plus loin du substrat et les grains avant d'arriver en surface grossissent. L'épaisseur de la zone chaude à partir de laquelle la réaction peut avoir lieu est donnée par :

$$e = \frac{\lambda}{\rho v C_p}$$

pour un mélange $x \text{ WF}_6 + (1 - x) \text{ H}_2$, λ conductibilité thermique du mélange, C_p chaleur spécifique à pression constante, ρ densité du gaz, v vitesse du mélange à 1000° K. La zone à partir de laquelle la réaction peut avoir lieu est de l'ordre du centimètre.

La croissance cristalline dépendrait alors fortement de la température du substrat de façon analogue à l'évaporation sur un substrat chaud.

C o n c l u s i o n

Les dépôts de tungstène à partir de la réduction de WF_6 par l'hydrogène dans les conditions stoechiométriques conduisent à des structures cristallines en colonnes dont l'orientation à la surface dépend fortement de la température et des débits gazeux et de la pression résiduelle.

L'orientation $[110]$ a été obtenue pour des températures comprises entre 950 et 1100° C avec WF_6 .

Les dépôts à partir de WCl_6 par réduction dans l'hydrogène conduisent à des cristaux de plus grandes dimensions. La vitesse de dépôt est identique à celle obtenue par réduction de WF_6 toutes choses égales par ailleurs.

Le rhénium est obtenu par décomposition seulement; sa structure observée au microscope électronique est celle du matériau forgé.

Le niobium déposé à partir de $NbCl_5$ conduit à un matériau dense et de haute pureté dont l'orientation cristalline est $[100]$.

Les microporosités existent dans les dépôts effectués à la pression atmosphérique, elles ont tendance à diminuer lorsqu'on travaille sous vide.

La structure cristalline se maintient macroscopiquement après recuit à haute température, cependant que microscopiquement cette structure varie.

B i b l i o g r a p h i e

- (1) Proceedings of the Conference on Chemical Vapor Deposition of Refractory Metals, Gatlinburg, Tennessee - 12-14 Sept. 1967.
- (2) A.M. Shroff et al : "Dépôts pyrolytiques de tungstène et de rhénium" Thermionic Electrical Power Generation, London, Sept. 1965.
- (3) A.M. Shroff, Melle C. Dorromée : "Réalisation de dépôts de tungstène et rhénium par réaction solide-gaz" Varsovie, 27-29 Juin 1966.
- (4) A.M. Shroff, J. Guyonnet et R. Courtel : "Etude de la structure de dépôts de tungstène réalisés par réaction gaz-solide", à paraître.
- (5) T. Alleau et al : "The Study of the Work Function Distribution of Chemical Vapor Deposited Tungsten", San Diego, Thermionic Specialist Conference, 25-27 Oct. 1965.
- (6) L. Yang et R.G. Hudson : "Effect of Preferred Crystal Orientation and surface Treatment on the Work Function of Vapor Deposited Tungsten", Thermionic Conversion Specialist Conference, Houston, Texas,

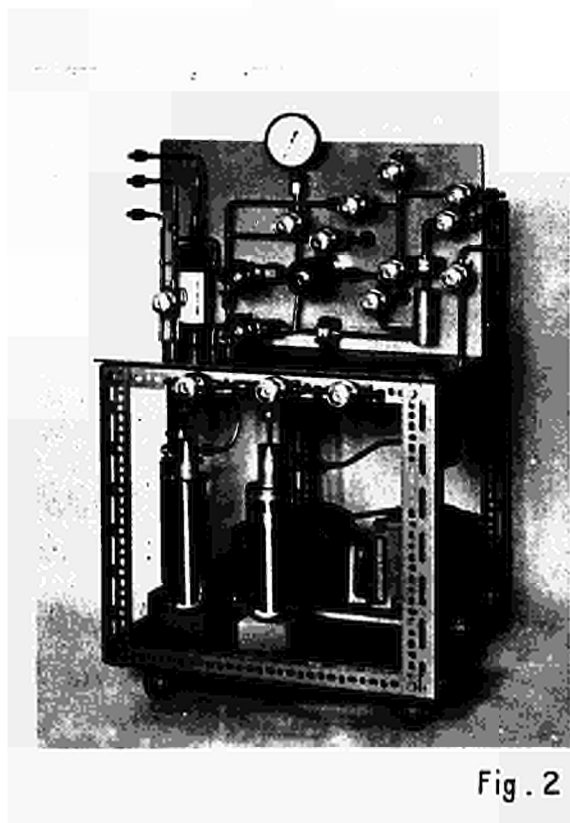
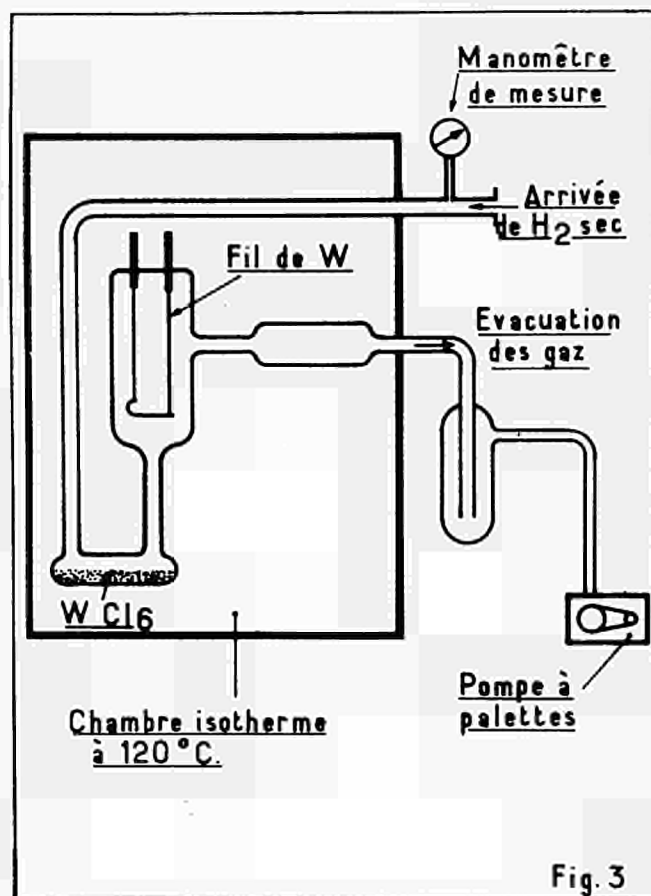
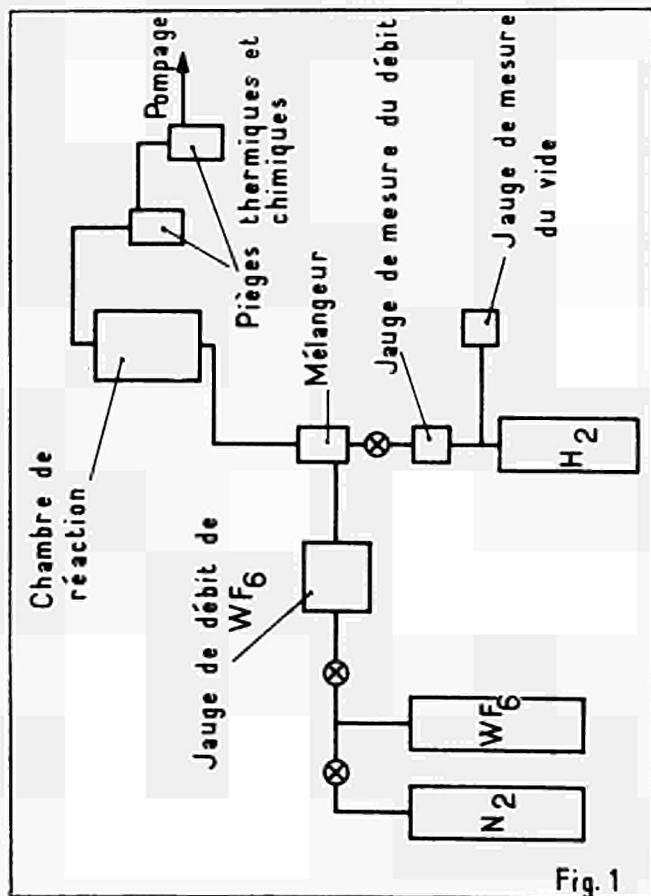
5f

Tableau 1

ETUDES AUX RAYONS X

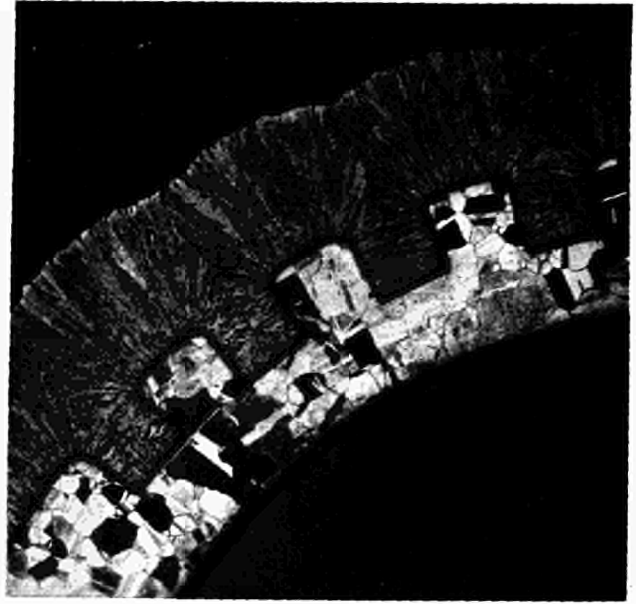
A) DEPOT A PARTIR DE WF_6	PLANS	P (mm Hg) / θ (°C)	1200	1100	1000	900	800	700	600
Composition $\frac{H_2}{WF_6} < 3$	< 100 >	760	4*	4	2	3	5	6	8
	< 110 >		2	2	4	2	1	1	0
	< 112 >			1	1	1	1	0	0
	< 111 >								
Composition $\frac{H_2}{WF_6} > 3$	< 100 >	760	DEPOT PULVERULENT					6	6
	< 110 >							0	0
	< 112 >							0	0
	< 111 >								
B) DEPOT A PARTIR DE WCl_6									
Composition $\frac{H_2}{WCl_6} < 3$	< 100 >	1			0	0			
	< 110 >				0,3	7,5			
	< 112 >				5	8,5			
	< 111 >				7	0,8			

* Intensité relative des pics

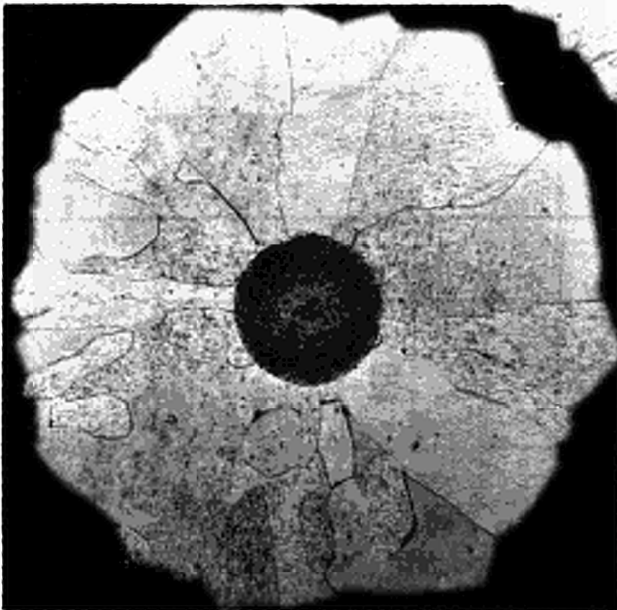




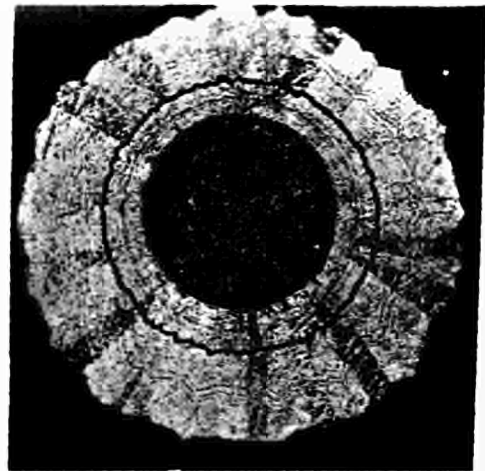
a



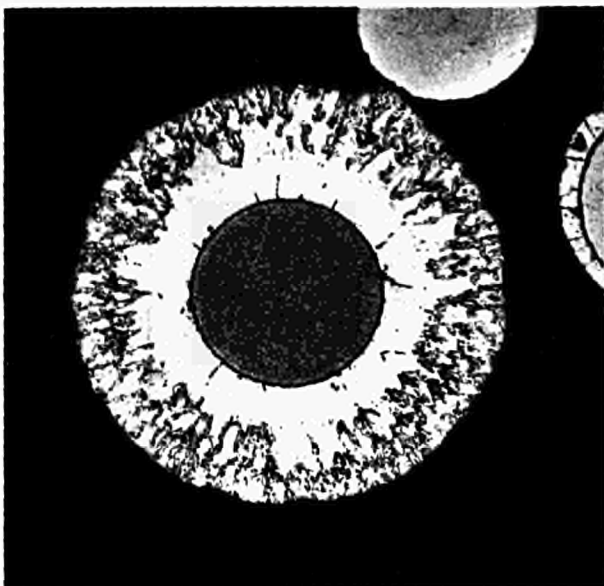
b



c



d



e

- a - Dépôt de tungstène à partir de WF_6
- b - Dépôt de tungstène à partir de WCl_6
- c - Dépôt de rhenium à partir de $ReCl_3$
- d - Dépôt de niobium à partir de $NbCl_5$
- e - Dépôt de niobium à partir de $NbCl_5$

Fig. 4

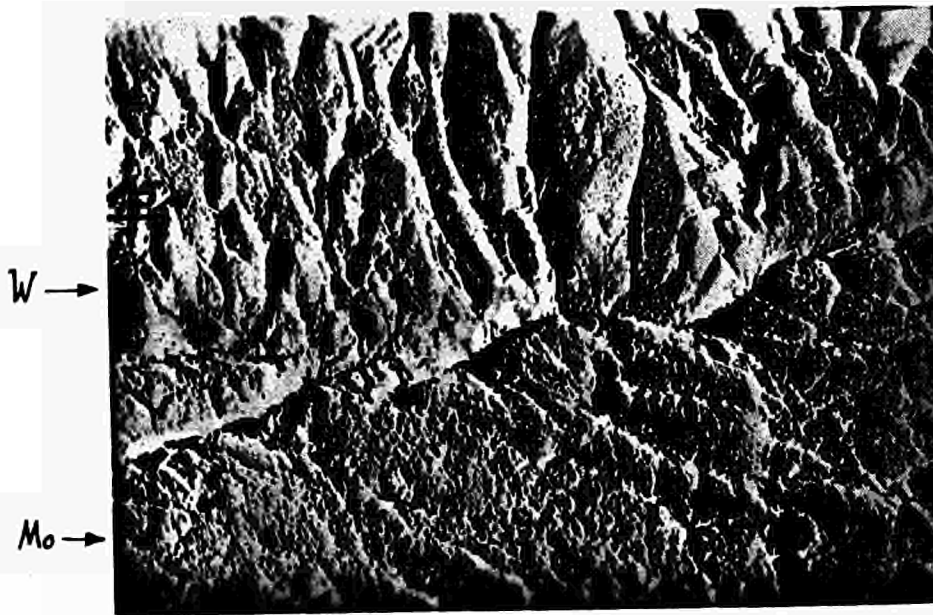
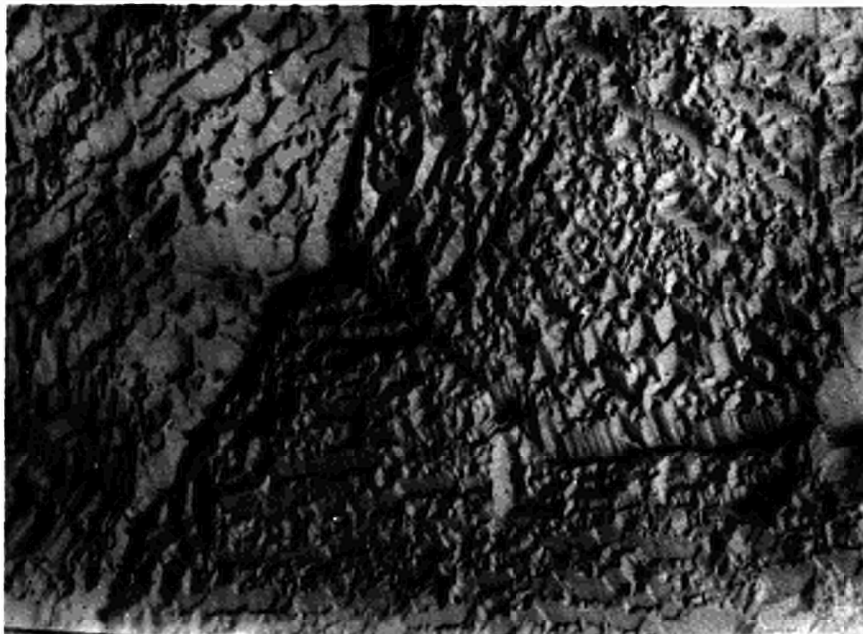


Fig. 5



(G x 2800)



(G x 3400)

Fig. 6

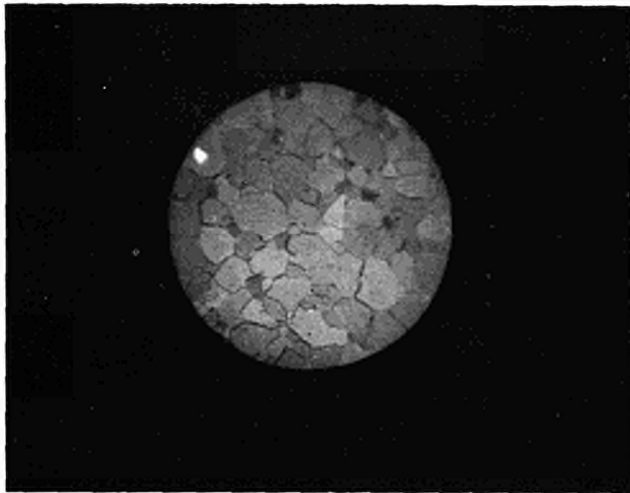


IMAGE ELECTRONIQUE D'UN
DEPOT DE TUNGSTENE A
PARTIR DE L'HEXAFLUORURE

G X 200

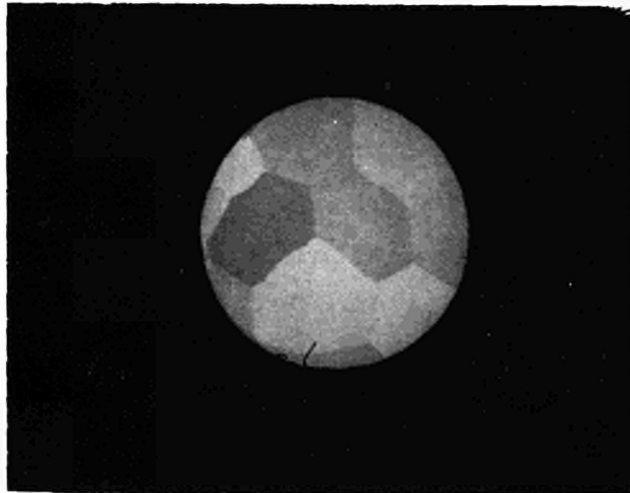


IMAGE ELECTRONIQUE D'UN
DEPOT DE TUNGSTENE A
PARTIR DE L'HEXACHLORURE

G X 200

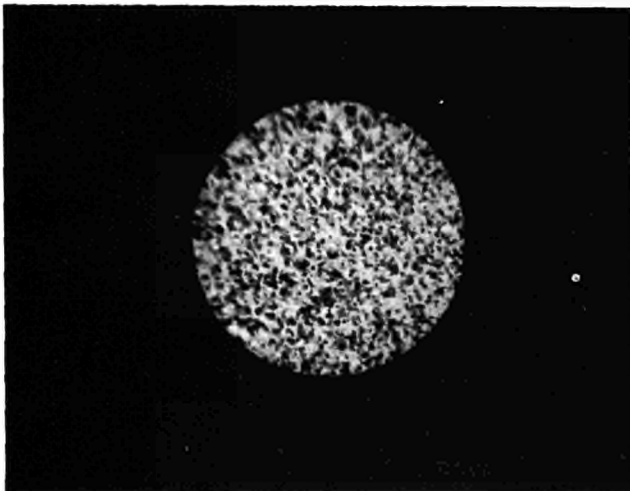


IMAGE ELECTRONIQUE D'UN
DEPOT DE RHENIUM A PARTIR
DU TRICHLORURE

G X 200

501-409-67
Fig.7

Deposition of Tungsten-layers
on Molybdenum and Interdiffusion

M. Peehs, H. Stehle
Siemens AG., Erlangen,
Zentrale Entwicklung und Forschung

Günther Scharowsky Strasse 2 (Deutschland)

Abstract

Molybdenum can be coated with Tungsten by high temperature pyrolysis of $W(CO)_6$. The microstructure of the deposited W-layers depends largely on the deposition temperature and rate. Porous layers on Mo, as produced by plasma spraying technique, can be densified. Properties of W-layers are described. The influence of the microstructure of the "transition zone" between Mo and W on interdiffusion has been investigated. Heat-treated samples up to 1600 h and $1860^\circ C$ have analysed by the microprobe method. An apparatus for coating thermionic emitters is described.

1. Introduction

In an Incore Thermionic Reactor (ITR) the fueled Mo emitter can be improved by applying a 200 μm thick tungsten layer on its e-emitting surface. The tungsten layer, which has a working temperature of approx. $2000^\circ K$, must remain stable and practically without any change in its properties during the 2 years operating period. The report below deals with the production and analysis of such layers.

2. Selection of method employed

The "Vapor plating" method has proved by far the best for depositing tungsten layers of high quality [1-5]. WF_6 , WCl_6 and $W(CO)_6$ are highly suitable base compounds. The halides can be reduced with H_2 at $600-900^\circ C$, whereas $W(CO)_6$ is decomposed pyro-

lytically in W and CO at temperature between 1100°C and 1700°C. The process temperature of the carbonyl method is 70 to 100 % that of the emitter operating temperature. Layers deposited in this way have little tendency to structure changes. Carbonyl pyrolysis is moreover a one-compound process, which is easy to conduct experimentally and for that reason was selected for the present case.

3. Coating equipment

Fig. 1 shows an overall view of the equipment. The parts to be coated are heated by high frequency induction. The actual reaction chamber (Fig.2) consists of two concentric glass tubes. The carrier gas (He) with the carbonyl ($W(CO)_6$) enters the inner tube from below. According to the special shape of the induction coil the gas flow is split into equal sub-flows, which are directed to the corresponding part of the surface. The carbonyl thus impinges uniformly on the object to be coated and coats it uniformly. The exhausted mixture emerges from the top centre opening of the inductor and is sucked out from between the outer and inner glass tube. The unexhausted carbonyl is trapped in a water-cooled baffle at the outlet opening of the reaction chamber.

4. W-deposition

The layers deposited on a dense, non-porous Mo-target by $W(CO)_6$ -pyrolysis have no pores and adhere very closely to the surface. The layers do not break away from the Molybdenum either during thermal cycling or machining (cutting, grinding, polishing). The deposition rate is between $5 \mu/h$ (1800°C) and $30 \mu/h$ (1200°C), depending on the operating temperature. The microstructure of the deposited layers is related to the deposition temperature. The average grain diameter increases with rising deposition temperature (Fig.3).

Porous base layers can also be coated. Porous W-layers produced by plasma spraying, for example, can be subsequently densified [6]. The layers then obtained contain small grain

sized material in the base layer, whereas the microstructure of the top layer corresponds to the deposition temperature (Fig.4). The pores of an Al_2O_3 base, which is applied thinly by plasma spraying on Mo, can also be filled up with W (Fig.5). W-layers produced on UO_2 -Mo cermets seal off the open pores of the cermet. The coating thickness therefore needed is about $40 \mu\text{m}$ [7].

5. Properties

Spectrographic surface analyses have revealed traces of Al, C, Ca, Fe, Mg, Mo and Si. Chemical analyses of the untreated Mo reveal 200 ppm C. Analyses of coated samples have not resulted in any higher carbon content. During very slow deposition, the Mo is even decarbonized due to the Boudouard reaction which takes place between the high sample temperature and cold inductor.

Gas release analyses of Mo samples coated with $200 \mu\text{m}$ W revealed that only 13.9 vppm gas is released at temperatures of up to 1800°C , whereas it can be assumed that pre-degassing takes place at a deposition temperature of 1300°C .

In the pertinent literature, vapor-deposited layers are described as being largely stable to recrystallization. Our observations confirmed this result in the layers under consideration. Only the combined vaporplated/plasma-sprayed coatings showed slight recrystallization in the fine grain-sized zone after 30 hours at 1800°C . The single vapor deposited coatings revealed only small changes in the substructure and migrations of the dislocations to the grain boundaries.

Fig. 6 shows the influence of deposition temperature on the surface orientation. The proportion of (110) orientation can be increased by raising the deposition temperature. The favourable deposition temperature of 1300°C furnishes predominantly (100) orientated surface. With slow coating and high deposition temperatures the W grows epitaxially on the Mo.

6. Diffusion

The diffusion performed is depicted in Table 1. High diffusion rates were found on epitaxial W-layers (Fig.7) in the form of a pronounced volume diffusion. Within a very short time a clear diffusion profile was measurable by a microprobe. Evaluation of the profiles resulted in a concentration-dependent diffusion coefficient between 10^{-8} - 10^{-9} cm²/s at 1750°C. The results are of the order of those determined by Kalinowitsch et al [8], but were considerably higher than those found by Larikow et al [9].

Quite better results are found by using the non-epitaxial transition zones. Two possibilities for disturbing the transition zones were investigated: 1) Interruption of crystal orientation and grain size distribution at the Mo/W-interface (Fig.8) and 2) covering the interface with a porous layer of Al₂O₃ approximately 30 μ thick, of which the pores are all filled with W (Fig.5). Both these methods force the volume diffusion below the sensitivity limit of the microprobe; the grain boundary diffusion, however, becomes so high that it is now clearly measurable. The grain boundary diffusion of the samples coated with Al₂O₃ was initially less than in the case of samples with non-epitaxial transition zones. This advantage is lost, however, by increasing the annealing time at 1860°C. At 1200 h the grain boundary diffusion of both is approximately the same.

As the annealing time increases, odd points with locally limited volume diffusion occur. This was observed for the first time at 400 h. As the annealing time increased, the number of points observed increased as well.

Table 1

Summary of diffusion analyses

No.	Annealing time [h]	Temperature [°C]	Microstructure of transition zone			Observed diffusion			
			epi- taxial	non-epi- taxial	with Al ₂ O ₃	Mo in W		W in Mo	
						Grain bound- ary diffusion	Vol. diffusion	Grain bound- ary diffusion	Vol. diffusion
1	2	1750	x			-	uniform	-	uniform
2	4	"	x			-	"	-	"
3	8	"	x			-	"	-	"
4	16	"	x			-	"	-	"
5	32	"	x			-	"	-	"
6	75	1830		x		20-25 μ	-	-	-
7	75	1860		x		"	-	-	-
8	75	"		x		"	-	-	-
9	75	"		x		"	-	-	-
10	75	"		x		"	-	-	-
11	75	1830			x	in places	-	-	-
12	84	1860		x		20-25 μ	-	-	-
13	84	"			x	in places	-	-	-
14	372	"		x		35 μ	in one place	35 μ	-
15	372	"			x	35 μ	-	-	-
16	372	"		x		"	-	10 μ	-
17	372	"			x	"	-	-	-
18	372	"		x		"	-	10 μ	-
19	372	"			x	"	-	-	-
20	400	"		x		15 μ	-	50 μ	-
21	400	"			x	"	-	"	-
22	720	"		x		30 μ	in places	60 μ	in places
23	720	"			x	"	-	30 μ	-
24	1200	"		x		"	in places	60 μ	in places
25	1200	"			x	"	"	16-30 μ	"
26	1600	"		x		16-65 μ	in places	16-65 μ	in places

References:

- [1] E.M.Gold "Simplified Vapor Plating of W"
ARS Journal, March 1962
- [2] Schmid, "Aufbringen von dichten Überzügen auf Hoch-
temperaturmetallen" BBC-Nachrichten, Sept. 1964
- [3] Flahkerty-Panisko, "Short Term Irradiation of UO₂-W-
Cermet-Rods", HW 76303, July 1964
- [4] Shroff-Boromé-Baro, "Depots pyrolytiques de W et
de Re", Thermionic Spec.Conf. 1965
- [5] Federer-Heestand-Patterson-Leitten, "Thermochemical
Deposition of Refractory Metals, Alloys and Compounds",
Thermionic Spec.Conf. 1965
- [6] Böhm-Jung-Peehs, "Entwicklung von thermionischen
Reaktorbrennelementen und Bau von Versuchszellen",
Report for the German Federal Ministry of Research
1965
- [7] Hübner-Janner-Peehs, "Entwicklung von Emittern und
Kollektormehrschichtsystemen", Report for the German
Federal Ministry of Research 1967
- [8] Kalinowitsch-Kowensky-Smolín, "Diffusion in der
binären Mo-W-Legierung", trans. from the Russian:
Pulvermetallurgie No. 4/28) 1965
- [9] Larikow-Taschkevitsch-Tschoma, "Untersuchung der
Diffusion von Re und Mo in W und dessen Legierungen",
trans.from the Ukranian: Ukr. Phys. Journal,
Volume 12/No. 6 1967

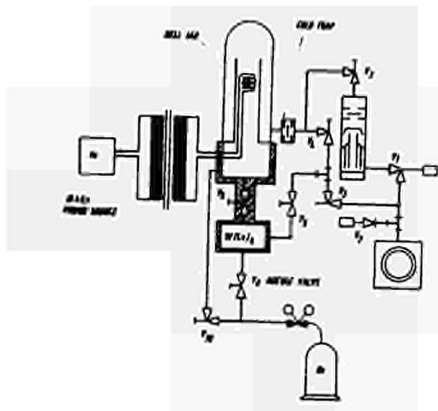


Fig. 1

Overall view of the equipment for Tungsten-deposition.

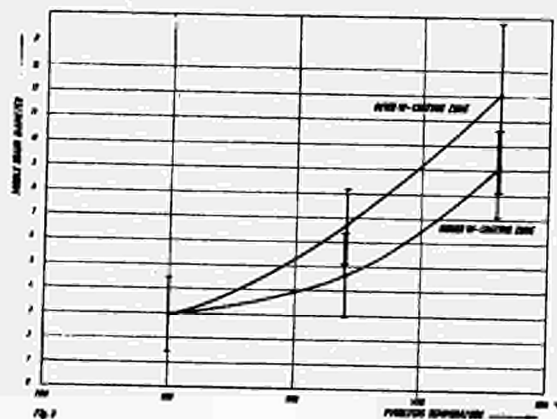


Fig. 3

Middle grain diameter as function of the pyrolysis temperature

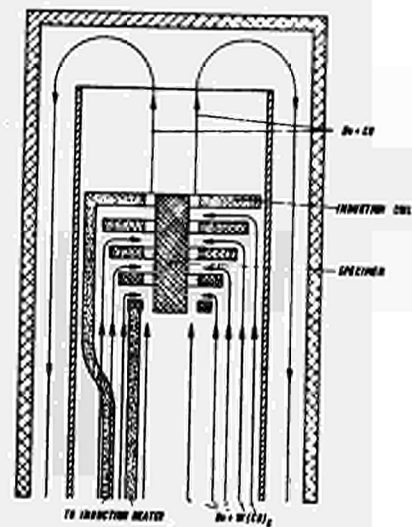


Fig. 2

Fig. 2

The reaction chamber



Fig. 4

Tungsten layer with a densified plasmasprayed zone

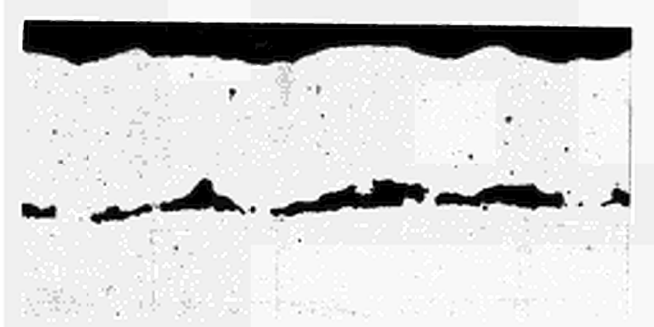


Fig. 5

Tungsten layer with a porous Al₂O₃ between Tungsten and Molybdenum



Fig. 7

Tungsten layer with an epitaxial transition zone between the layers and the Molybdenum target.

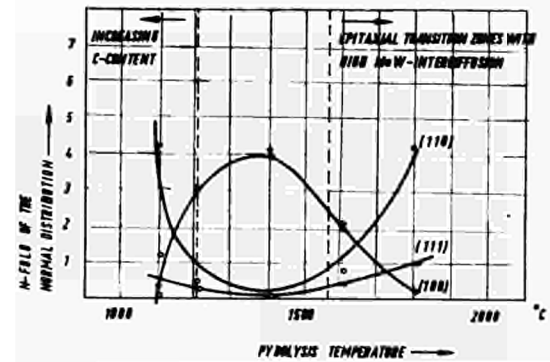


Fig. 6

Fig. 6

Surface orientation as function of the pyrolysis temperature

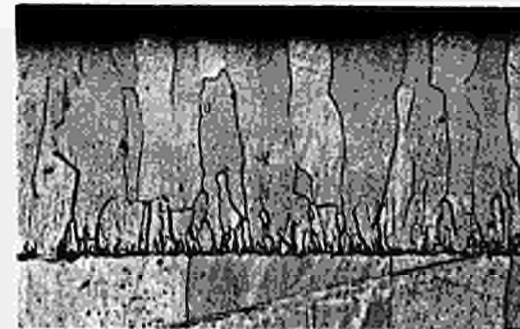


Fig. 8

Tungsten layer with a nonepitaxial transition zone between the layer and the Molybdenum target.

DISCUSSION

Speaker of paper E-4: M. PEEHS.

SCHOCK (USA): Have you tried carbonyl deposition of metals other than tungsten?

PEEHS (Germany): No, we have not. The possibilities are not very great e. g. with niobium and tantalum you have reactions with the CO which is produced during the pyrolysis of $W(CO)_6$ and you develop a carbide. The process is very good for tungsten and we have not done other work.

SCHOCK: Have you analyzed the carbon content of the W-deposit?

PEEHS: Yes, we have done this. We have found that we can decarborize the target by this process and this is due to the Boudouard-reaction which takes place between the hot target and the colder tube wall of the reaction chamber. You find the carbon on the tube wall.

HOLLAND (USA): Why are you putting the tungsten on the molybdenum?

PEEHS: Because we wanted to have very stable layers for the emitters of the thermionic converters.

HOLLAND: Have you measured the emitter work function thermionically at $1800^{\circ}C$ for extended durations?

LANGPAPE (Germany): The effective work function measured in vacuum was 4.6 eV. We did not demonstrate the stability of the work function. The duration of the experiment was only some hours.

GROSS (Germany): I would like to comment on diffusion of molybdenum through tungsten layers. We have made measurements on fluoride deposited tungsten on molybdenum. We found a diffusion line of molybdenum after 50 h. at $2500^{\circ}K$ within 2 mils from the tungsten-molybdenum interface.

PEEHS: Perhaps I may say that this is in relation to our experiments with non-epitaxial transition zones because the fluoride process produces non-epitaxial zones.

METAL-TO-CERAMIC SEALS FOR THERMIONIC CONVERTERS

C. M. CAPPELLETTI, C. A. BUSSE
Euratom CCR, Ispra (Varese), Italy, and

E. A. DÖRRE
Feldmühle AG, Werk Südplastik und Keramik,
731 Plochingen, Postfach 70, Germany

ABSTRACT

Thermionic converters require metal-to-ceramic seals for operating temperatures of about 1000°C, with an excellent compatibility with cesium vapor. To meet these requirements seals were studied utilizing the sintered metal-powder process. As ceramic a fine-grained high density pure alumina was chosen and as metal partner Nb-1Zr.

For metalizing, suspensions of W powder with small additions of TiO₂ or Y₂O₃ were tried. It was found that TiO₂ leads to grain growth and considerable weakening of the ceramic, while Y₂O₃ is free of this disadvantage. Factors affecting the bond strength were investigated, such as grain size of the W powder, amount of the additive, milling time of the suspension, temperature and time of firing, dew point of firing atmosphere. The optimum average adherence obtained with Cu-2Ni brazed samples is about 14 kg/mm².

High temperature brazing tests with alloys based on Pd and the active metals Ti, Zr and V were made. Brazing with Pd (at 1570°C) and V-30Nb-5Ti (at 1805°C) results in an average tensile strength of the metal-to-ceramic seal of about 10 kg/mm² and 8 kg/mm², respectively. These seals can be made both in planar and cylindrical geometry; problems of wall attack by Pd can be overcome by suitable seal design. The seals resist to 100 thermal cycles between 500°C and 1200°C, and they withstand a corrosion test of 1000 hours at 1000°C in cesium vapor of 20 torr practically without attack, without loss of vacuum tightness or change in tensile strength.

1. INTRODUCTION

Thermionic converters require vacuumtight metal-to-ceramic seals of high geometrical stability, which are resistant to Cs vapor at a pressure of about 10 torr. The operating temperature of these seals is necessarily higher than the condensation temperature of cesium at this pressure, i. e. roughly 400°C.

In practical designs, however, the seal has a much higher temperature which generally lies between the temperatures of emitter and collector. As the optimum collector temperature lies around 700°C , and in order to get some freedom in the design of the thermionic converter, a seal operating temperature of 1000°C was aimed at for the present development.

The sealing technique chosen utilizes the principle of the frequently employed sintered metal-powder process, which consists in applying a metalizing powder layer on to the ceramic, firing this layer and joining it to the metal partner by brazing. The following chapters deal with the different steps of this process. Chapter 2 contains a discussion of the arguments which lead to the choice of the ceramic. Chapter 3 shows the results of the metalizing studies on this ceramic, especially the dependence of the bond strength from parameters of the metalizing process. Chapter 4 deals with the selection of the metal partner. Chapter 5 contains a summary of the studies on high-temperature brazing of the metalized ceramic to the metal partner. Chapter 6, finally, deals with the properties of the obtained metal-ceramic assemblies; results are reported on tensile strength, thermal cycling and cesium corrosion.

2. CERAMIC COMPONENT

As ceramic an alumina of high purity, low porosity and small grain size was chosen (E37). The properties of this ceramic are shown in table 1, in comparison with a conventional alumina (E2).

E37 was chosen for several reasons. First, it is known that high purity low porosity alumina has an excellent Cs corrosion resistance [1, 2]. Second, when brazing of ceramic-metal seals is carried out at relatively high temperatures, considerable stresses on cooling can be generated due to different thermal expansion of metal and ceramic. These stresses do not only act at the brazing joint itself but also on the underlying ceramic layer. The mechanical properties of the alumina are therefore an important factor. It is known that these properties depend on the grain size [3 to 7]. The relationship between the average grain size and the compressive strength is given in fig. 1, showing that a slight increase in grain size results in a significant decrease of the compressive strength. In fig. 2 the flexural strength of pure

alumina ^{*}) is plotted versus the average grain size and temperature. It can be seen that when the grain size is sufficiently small, relatively high strengths can be obtained even at elevated temperatures.

Table 1 : Properties of alumina ceramics of different purity

		E37	E2
<u>General properties</u>			
Composition		99.7% Al ₂ O ₃ +0.25% MgO	97% Al ₂ O ₃ (rest silicates)
Average grain size	/μ	~ 4	~ 10
Density	g/cm ³	3.99	3.7
Residual porosity	%	0.2	7.2
Leak rate	torr. liter/sec	< 10 ⁻¹²	< 10 ⁻¹²
<u>Mechanical properties at 20°C</u>			
Compressive strength	kg/mm ²	450	300
Flexural strength	kg/mm ²	53	30
<u>Electrical properties</u>			
Volume resistivity			
at 100°C	ohm-cm	10 ¹⁴	10 ¹³
at 500°C	ohm-cm	10 ¹²	10 ¹¹
at 1000°C	ohm-cm	10 ⁷	10 ⁶
Dielectric strength at 20°C	kv/mm	30	18
Loss coefficient (tg δ) at 20°C and 4000 megacycles		1.10 ⁻⁴	14.10 ⁻⁴

Finally; the anisotropic effect also advocates a fine-grained structure. Al₂O₃ has a hexagonal structure and its thermal expansion depends on the crystallographic orientation (the coefficient of expansion in the c-direction

^{*}) The term "pure alumina" is generally used nowadays for Al₂O₃ with minor additions of MgO. Additions of oxides to Al₂O₃ generally result in a decrease in the strength, especially at elevated temperatures, because being situated at the grain boundaries they promote crystal slip thereby contributing to plastic flow. MgO is an exception to this rule; it leads to an increase of the strength of the ceramic by accelerating the sintering process and inhibiting excessive grain growth.

is 10-20% higher, depending on the temperature range, than in a direction parallel to the basal plane). In the event of two differently oriented grains meeting at a common grain-boundary, thermal stresses are created when a change in temperature occurs. These stresses are directly proportional to the contact area i. e. the grain size. They add to the total strain on the ceramic, thus leading to a decrease in mechanical strength.

The problem of producing a fine-grained high purity alumina was solved by reducing the sintering time to a minimum. In order to obtain nevertheless a high density, the original material is first wet ball-milled and then sintered in vacuum evacuating the air from the pores below the sintering temperature. Thus the pores close completely in spite of the short sintering time. By sintering for 10 minutes at 1900°C in a vacuum of 10^{-5} torr a product is manufactured with a density in excess of 99% of its theoretical value, a grain size below 10 microns and an average flexural strength of 53 kg/mm².

Fig. 3 shows the structure of the fine-grained high-strength alumina E37, together with a coarse-grained low-strength alumina of same purity (which was made by means of a higher sintering temperature and longer "soak" times). There is a slight advantage of the coarse-grained alumina with regard to light transmission, of which both ceramics are capable in the visible as well as the infra-red range up to a wavelength of approx. 7 microns. For thermionic converter applications, however, this difference does not matter.

3. METALIZING

A seal operating temperature of 1000°C being envisaged, only brazing alloys with a melting point above 1400°C were considered. This means that rather high firing temperatures had to be used for metalizing. With regard to the ceramic there is no problem, because E37 can be heated up to 1950°C without irreversible change in shape. Conventional metalizing processes however, for example the well-known Mo-Mn process, can not be used. Apart from the brazing temperature being too low, the ceramic must contain at least 1% SiO₂ for the process to function satisfactorily, but this SiO₂ content would render the ceramic susceptible to attack by cesium vapor.

It has already been tried to substitute the SiO₂ by the cesium resistant Y₂O₃ and this Y₂O₃-bearing alumina has successfully been metalized with pure

tungsten powder [8]. The Y_2O_3 addition results however in a significant drop of the mechanical strength of the ceramic due to the creation of cavities and structural imperfections. In order to avoid such unfavourable side-effects on the properties of the ceramic, metalizing promoters were not added to the ceramic itself but included in the metalizing suspension.

Tungsten was chosen as metalizing material. An initial study of different W powders showed that the quality of the metalizing layer depends strongly on the grain size of the powder used. The best results regarding vacuum tightness and bond strength were obtained with the two finest grained powders which were retained for all further investigations.

Fig. 4 is a photograph of the finest grained W powder having an average grain size of 0.05μ and a specific surface of $6.1\text{ m}^2/\text{g}$ ^{*}). Powder metallurgists are well aware of the fact that fine grained powders are more difficult to work with than coarser grained fractions. As a result, it was not possible to obtain a continuous coating by brushing on this powder. On sintering, cracks developed in the layer so that a second layer had to be applied and sintered in order to obtain a vacuum-tight seal. This difficulty was not encountered while using a slightly coarser powder (grain size between 0.1 and 1μ , specific surface $3.6\text{ m}^2/\text{g}$), which gave equally good results regarding vacuum tightness and bond strength. The metalizing suspensions with this powder were prepared by ball-milling in isoamylacetate for 250 hours. It was seen by x-ray diffraction that this treatment resulted in lattice strain, thus increasing the sintering activity of the powder.

As metalizing promotor additions of 0.5 to 7.5 w/o TiO_2 were used at first. The resulting ceramic-metal joints had however an average bond strength of less than $7\text{ kg}/\text{mm}^2$ which, according to past experience with other metalization processes, does not give a reliable high vacuum seal. It was furthermore noted that the bond strength decreased with increasing TiO_2 content, and that tensile tests samples generally fractured in the ceramic. Examination under the microscope showed that the grain size in the ceramic fracture

^{*}) In assessing the grain size from fig. 4 it should be noted that considerable agglomeration has occurred.

increases with increasing TiO_2 content in the metalizing suspension. This result was not particularly surprising as TiO_2 is an active grain growth promoter. In the present instance, the TiO_2 fraction of the metalizing layer diffuses along the grain boundaries into the ceramic matrix and causes the above mentioned grain growth. Figs. 6a and 6b are photographs of the ceramic areas in contact with the metalized layer. A TiO_2 content of 7.5 w/o in the metalizing mixture together with a firing of 20 minutes at 1900°C is sufficient to increase the grain size by a factor 20, i. e. grain diameters above 100 microns can be seen. This results in a drastic reduction in the mechanical strength (see chapter 2) accounting for the above mentioned observations of fractures in the ceramic and decreasing strength with increasing TiO_2 content.

Significantly better results were obtained when Y_2O_3 instead of TiO_2 was added to the tungsten powder. In contrast with TiO_2 , Y_2O_3 is not a grain growth promoter so that the structure as well as the mechanical properties of the ceramic remain practically unchanged during the firing of the metalizing layer. The Y_2O_3 content was varied between 0.5 and 5 w/o. The best results - bond strength between 13 and 15 kg/mm^2 - were obtained for a Y_2O_3 content of 2 w/o. Values of up to 18 kg/mm^2 were obtained with 5 w/o Y_2O_3 , but the results were not reproducible. (All bond strengths reported in this chapter were determined with Cu-2Ni brazed tensile test samples as shown in fig. 11; details regarding the test procedure are described in chapter 6).

Table 2 lists the bond strengths obtained with different firing conditions (time and temperature). These results show that the bond strength increases considerably with the firing temperature. A maximum value was not obtained. The firing time itself is of no significance in the investigated range.

Table 2 : Bond strength as a function of the firing temperature and time.

Metalizing : W + 2 w/o Y_2O_3

Firing atmosphere : wet N_2 + 20 v/o H_2 (dew point 18°C)

firing temperature, $^\circ\text{C}$	firing time, min	bond strength, kg/mm^2
1700	20	8.4
1900	10	13.4
1900	20	13.5
2000	10	15.7

In order to study the effect of the moisture content of the firing atmosphere on the bond strength, the dew point was varied between 18°C and 35°C, while firing temperature and time were kept constant. The result is plotted in fig. 5 which shows that the bond strength increases with decreasing dew point. This effect may be due to partial oxidation and evaporation of the tungsten layer with increasing moisture content.

In contrast to TiO₂-containing metalizing suspensions which lead to fractures entirely in the ceramic, additions of Y₂O₃ resulted in fractures in the metalizing layer, the braze as well as the ceramic. In the majority of cases, especially at high bond strengths, partial tearing out of a thin ceramic layer took place; the rest of the fractured surface showed remnants of brazing material and metalizing layer (see fig. 7). Occasionally the brazing material penetrated through the metalizing layer on to the ceramic surface.

4. METAL PARTNER

As metal partner of the seal Nb-1Zr was chosen, principally for the following reasons:

- Melting point: sufficiently high (2500°C)
- Thermal expansion: close to E37 (see table 3)
- Cs resistance: excellent, even to liquid Cs at 1000°C [9]
- Workability: good, can be spinned well

Table 3: Thermal expansion of Nb, Nb-1Zr and high purity alumina (E37) [10]*), [11]**)

Temperature range °C °C	Coefficient of average linear thermal expansion 10 ⁻⁶ /°C		
	E37	Nb-1Zr purity: 99.9%	Nb purity: 99.9%
20- 300	6.75	7.56	7.28
20- 400	7.05	7.63	7.41
20- 500	7.34	7.71	7.51
20- 600	7.61	7.78	7.62
20- 700	7.84	7.86	7.73
20- 800	8.05	7.96	7.84
20- 900	8.23	8.04	7.94
20-1000	8.39	8.11	8.04
20-1100	8.52	8.18	8.13
20-1200	8.7	8.2	8.2
20-1300	8.9	8.3	8.2
20-1400	9.0	8.4	8.3

*) Test Method: Dilatometer ADAMEL type DHT 60-2.

***) Test Method: Dilatometer LEITZ type Bollenrath

As can be seen from table 3, also Nb matches relatively well with the thermal expansion of E37; Nb-1Zr is preferred because of its higher strength and lower creep rates at elevated temperatures [12], and because there is much less grain growth during the high-temperature brazing cycle than in pure Nb.

5. HIGH TEMPERATURE BRAZING PROBLEMS

Because of the envisaged seal operating temperature of 1000°C and the optimum firing temperature of the metalizing layer between 1900 and 1950°C (see table 2), only brazing materials with a melting interval between 1400°C and 1900°C were considered. Among the properties, which an ideal brazing material should have, are the following ones:

- a) Resistance to Cs vapor.
- b) Good wetting of Nb-1Zr without serious attack.
- c) Good wetting of the metalizing layer, without deteriorating its adherence to the ceramic or the mechanical properties of the ceramic.
- d) Sufficient ductility so that foils and wires can be made.

Condition a) excludes the use of Au [13, 14], condition b) forbids higher percentages of Ni, Co and Fe in the brazing material because all three form low melting eutectics with Nb (1100°C [15], 1235°C [16] and 1372°C [15], respectively). By these restrictions the short list of conventional brazing materials in the 1400°C to 1900°C range becomes still shorter (see e. g. [17]). Therefore new brazing alloys had to be sought. Attention was mainly directed towards brazing materials based on Pd ($T_m = 1550^\circ\text{C}$) and the three active metals Ti ($T_m = 1707^\circ\text{C}$), Zr ($T_m = 1852^\circ\text{C}$) and V ($T_m = 1917^\circ\text{C}$).

A problem of all Pd based brazing materials, investigated so far, is that they attack the W metalizing layer. Fig. 8 shows a W metalized E37 disk on which some Pd was melted for 60 sec; the Pd has migrated in beads across the surface, taking up the W and leaving a track of uncoated ceramic behind. It was tried to decrease this attack by alloying the Pd, especially with W.

Table 4 contains some of the alloys tested. They all attack the metalizing layer more or less severely.

There is another problem with Pd brazing materials: they dissolve a relatively large quantity of Nb-1Zr. Table 4 shows some results of tests where a braze ring of 6 mm inner diameter, made of wire of 0.5 mm diameter, was melted on Nb-1Zr sheet.

Table 4 : Attack of Nb-1Zr sheet by braze rings (wire of ϕ 0.5 mm).

brazing material	temperature °C	time sec	depth of pene- tration, mm	remarks
Pd	1570	90	0.12	
		180	0.15	
Pd-10W	1570	90	0.20	partially melted
Pd-20W	1700	90	0.25	
Pd-8Mo	1630	90	0.20	partially melted
Pd-15W-2Ni	1620	180	0.28	
Pd-15W-5Ni	1620	180	0.33	
Pd-15W-2Cu-2Ni	1670	90	0.33	

If for example a seal geometry is chosen as shown in fig. 9a, the Pd is initially concentrated on a small region of the Nb-1Zr wall and, on melting, sometimes succeeds in perforating the wall. This problem can be overcome by taking care that the Pd in the molten state is never concentrated on a small area of Nb-1Zr surface. One solution is a plane seal geometry as shown in fig. 9b where the Pd is placed as a thin washer (50-70 μ) into the brazing gap. If however, a cylindrical geometry is desired, the problem of wall attack can be solved by using a seal design as shown in fig. 10. There the Nb-1Zr wall is protected against the Pd ring by one or several thin foils of a material, which is sufficiently resistant to Pd such as W, Mo or Ta; only after entering the brazing gap Pd gets into contact with Nb-1Zr. Some tests of this seal design were successfully made with pure Pd, using two layers of 25 μ W-foil.

In the group of high-temperature active metal brazes (Ti, V or Zr basis) work is still under way. The general impression so far is that these brazing alloys wet Nb-1Zr well without excessive attack. But they all react with the

ceramic, especially strongly if the ceramic is not metalized (erosion), reducing the mechanical strength in this reaction zone.

The best brazing material found so far in this group is V-30Nb-5Ti (brazing temperature 1805°C). It was derived from the minimum-melting-point-composition in the V-Nb-system (V-35Nb [16]), which could not be worked into wires unless its ductility had been increased by a 5 w/o Ti addition. V-30Nb-5Ti wets Nb-1Zr well without serious attack, but it penetrates through the W metalizing layer. The resulting seal can be considered as a compromise solution between a metalizing-plus-brazing joint and an active metal seal, with the metalization fulfilling two functions: it enhances the entry of the fused alloy into the brazing gap, and it protects the ceramic against too violent attack from the active components of the brazing alloy.

Summing up one can say that an ideal brazing material in the 1400°C to 1900°C range has not yet been found. With regard to the list of properties mentioned at the beginning of this chapter, none of the tested brazing materials fulfills condition c. This means that high temperature brazing will not result in the high seal strengths as obtained with Cu-2Ni brazing. However, the test results reported in the following chapter show that even with present non-ideal high temperature brazing materials seals of rather good quality can be made.

6. PROPERTIES OF HIGH TEMPERATURE METAL-TO-CERAMIC SEALS

The tests reported here concern vacuum tightness, tensile strength, thermal cycling and cesium corrosion of metal-ceramic assemblies, made from W metalized E37 and Nb-1Zr by brazing with Pd or V-30Nb-5Ti. The term "vacuumtight" will mean that the helium leakrate at room temperature is smaller than 10^{-9} torr.ltr/sec.

Tensile strength measurements were made with metal-ceramic assemblies as shown in fig. 11 in an exploded view. The test pieces were inserted in a ZWICK tensile test machine together with a cardan suspension which ensured that the samples were subjected only to tensile stress (fig. 12). Batches of 6 samples were used. The test results are shown in table 5, con-

taining of each batch the average tensile strength as well as the highest and lowest value.

Table 5 : Tensile strength of differently brazed E37/Nb-1Zr assemblies (at room temperature).

Metalizing: W + 2 w/o Y₂O₃, fired 20 min at 1950°C in wet N₂ + 15 v/o H₂ (dew point 20°C). All brazing done in high vacuum (10⁻⁵ to 10⁻⁶ torr).

braze washer	brazing conditions	number of vacuumtight samples	tensile strength of vacuumtight samples kg/mm ²		
			average	highest	lowest
Cu-2Ni, 60/μ thick	180 sec, 1150°C Mo furnace	5 of 6	14.3	15.6	12.6
P 60/μ thick	90 sec, 1570°C Mo furnace	6 of 6	9.6	11.0	8.3
	20 sec, 1570°C Mo furnace	5 of 6	10.0	13.6	6.8
V-30Nb-5Ti 80/μ thick	60 sec, 1805°C Ta furnace	3 of 6	8.4	8.6	8.1

As standard for comparison, the table begins with a batch of Cu-2Ni brazed samples showing an average tensile strength of 14.3 kg/mm²; the rupture of all 5 samples occurred completely in the ceramic. The table shows the data of two batches of Pd brazed samples with different brazing times. Both batches have an average tensile strength of about 10 kg/mm², but the batch with the shorter brazing time shows a larger scattering of the values. All Pd-brazed samples ruptured between ceramic and metalizing layer, leaving a clean and undamaged ceramic surface; only at the edges small ceramic pieces were broken off.

In the last line of table 5 are the results of a batch of V-30Nb-5Ti brazed samples which have a tensile strength somewhat above 8 kg/mm². In contrast with Pd-brazing, these samples ruptured in the ceramic, close (~0.5 mm) to the braze, indicating the weakening of the ceramic by the action of the active components of the brazing alloy.

Thermal cycling tests between 500°C and 1200°C were made in a high vacuum Mo furnace. The temperature-time-diagram of one cycle is shown in fig. 13. The heating speed was about 50°C/min, the cooling speed varied between 200°C/min and about 4°C/min. In table 6 are the results of the test. The last column shows that all samples withstood 100 cycles without failure.

Table 6 : Resistance to thermal cycling between 500°C and 1200°C.

Metalizing: same as in table 5.

seal design	brazing	number of vacuumtight samples after brazing	number of cycles	number of vacuumtight samples after cycling
plane (fig. 9b)	Pd foil 60 μ thick 20 sec at 1570°C	10 of 10	100	10 of 10
cylindrical (fig. 9 a)	V-30Nb-5Ti wire 0.8 mm ϕ 30 sec at 1805°C	11 of 14	100	8 of 8

Comparing the third columns of table 5 and 6 it can be seen that in the case of V-30Nb-5Ti brazing with a wire (cylindrical geometry) results in a much higher percentage of vacuumtight samples than brazing with a washer (plane geometry). This may be due to diffusion prior to melting leading to a change of the composition of the washer and resulting in incomplete liquefying and insufficient flowing at the brazing temperature. In case of a braze wire, this danger is evidently much smaller because of the smaller contact areas and the larger distances involved.

All components of the presently described seal and some complete metal-ceramic assemblies were subjected under rather clean conditions to a corrosion test of 1000 hours at $1000 \pm 10^\circ\text{C}$ in cesium vapor at about 20 torr (cesium reservoir temperature of $400 \pm 5^\circ\text{C}$). The apparatus is shown in fig. 14. The corrosion vessel was a welded Nb-1Zr container. After loading the container with the samples and outgassing it at about 1000°C for 10 hours in a vacuum of 10^{-5} torr, cesium (99.9) was introduced under argon (UPPA); after pumping down to 10^{-5} torr for 6 hours at room temperature, the container was sealed by electron beam. The 1000 hour test was performed pla-

cing the container (wrapped in Zr-foil) under dynamic high vacuum inside a sintered quartz tube which was surrounded by a tubular furnace. An appendix of the test vessel reached out of the heated zone and was adjusted so that its coldest part, serving as cesium reservoir, had a temperature of 400°C. Temperatures were measured with several thermocouples attached to the test vessel.

Table 7 shows some results of the corrosion test. There is practically no corrosion of the refractory metals (Nb, Nb-1Zr, W, Ta) and of the V-20Nb-5Ti braze, and only slight corrosion of the Pd- and Pt-brazes. The test confirmed the excellent Cs corrosion resistance of E37 [1].

Six metal ceramic tensile test assemblies as shown in fig. 11, of which 3 had been brazed with Pd and 3 with V-30Nb-5Ti, were also included into the corrosion test vessel. The metalizing in this case was of the early W + 5 w/o TiO₂ type. All samples were still vacuumtight after the test and, within the usual range of scattering, had the same tensile strength as samples of the same batch which were not subjected to the corrosion test.

Earlier work had shown that the chemical inertness of pure Al₂O₃ is a function of its grain size. It was therefore interesting to see whether the grain size also had an influence on Cs corrosion. For this purpose samples of E37 with normal and increased grain size were incorporated into the above test. No change in the surface of these samples could be detected under the optical microscope at magnifications up to 1000x. Further examination with an electron microscope at larger magnifications revealed small etch pits having a diameter of about 0.5 μ and a depth of about 0.1 μ (fig. 15). The observations with the electron microscope indicated that the surface of the fine grained structure was less attacked than that of the coarse one. Even for a single sample, as the fine grained one shown in fig. 15, the pitting attack can be seen to depend on the size of the individual grains. However, one may state with confidence that the above effects will not influence the physical properties of the ceramic body.

Table 7: Corrosion during 1000 hours at 1000°C in cesium vapor
(cesium reservoir temperature 400°C) [18]

material	origin (type)	density g/cm ³	sample weight g	weight change		comments
				total mg	per surface mg/cm ²	
Nb-1Zr	Heraeus		7.0702	+ 1.4	+0.08	no change in appear- ance (bright surface)
W	Plansee		1.6969	+ 0.2	+0.02	
Ta	Heraeus		13.3227	+ 0.4	+0.01	
V-20Nb-5Ti	Metallgesell- schaft		2.9766	+ 0.7	+0.05	bright, weak grain etching
Pd	Degussa		1.4050	- 14.2	-4.6	rough surface grain etching
Pt	Degussa		0.1879	+ 7.2	+3.6	formation of large grains, grain etching
BeO (> 99.5)	CGEC	2.85- 2.95	8.8703	- 0.8	-0.04	slightly dis- coloured at edges
Al ₂ O ₃ (99.7 Al ₂ O ₃ + 0.25 MgO)	Feldmühle (E37)	3.99	10.8926	- 2.5	-0.14	slightly grey
ZrO ₂ (97 stab.)	Degussa (Zr 23)	5.4	13.2949	+ 26.2	+1.4	grey
ZrO ₂ (93.7 ZrO ₂ + 5 CaO+Hf)	Berliner Quarz- schmelze (Thermal ZrO ₂)	4.5- 5.1	10.2109	- 7.6	-0.5	slightly grey
MgO·Al ₂ O ₃	Degussa (Sp 23)	3.3	8.4837	+ 45.5	+ 2.6	grey, par- tially meta- lized
MgO	Berliner Quarz- schmelze (Thermal ZrO ₂)	3.3- 3.4	9.0953			black, dis- integrated
MgO (99)	Koppers	3.0	7.0992	-36.7	-2.6	black and grey stains; sample porous

CONCLUSIONS

Metal-to-ceramic seals for high temperature applications having high strength and good resistance against Cs corrosion and thermal cycling can be made between the alumina E37 and Nb-1Zr by a sintered metal-powder process. The best adherence of the metalizing layer is obtained using a suspension of submicron W powder with 2 w/o Y_2O_3 in isoamylacetate, ball milled for 250 hours, brushed on to the ceramic and fired for 10 to 20 min between 1900°C and 1950°C in an atmosphere of wet $N_2 + 15$ v/o H_2 (dew point 20°C). High temperature brazing can be made with Pd (at 1570°C) and V-30Nb-5Ti (at 1805°C), both in planar and cylindrical geometry. Problems of wall attack with Pd can be overcome by suitable seal design.

ACKNOWLEDGEMENT

The authors are indebted to G. Kirchner for his technical assistance in the brazing operations.

REFERENCES

- [1] HALL, W. B. and KESSLER, S. W., "Cesium Compatibility of Thermionic Converter Structural Materials", Proc. Thermionic Converter Specialist Conference, Gatlinburg/Tenn. (1963).
- [2] HIGGINS, J. K., "Reaction of Alumina with Cesium Vapour", report AERE-R 4781, 1964.
- [3] KNUDSEN, F. P., "Dependence of Mechanical Strength of Brittle Polycrystalline Specimens on Porosity and Grain Size", J. Am. Ceram. Soc., 42 (1959), 376-387.
- [4] SPRIGGS, R. M. and VASILOS, T., "Effect of Grain Size on Transverse Bend Strength of Alumina and Magnesia", J. Am. Ceram. Soc., 46 (1963), 224-228.
- [5] SPRIGGS, R. M., MITCHELL, J. B., and VASILOS, T., "Mechanical Properties of Pure, Dense Aluminium Oxide as a Function of Temperature and Grain Size", J. Am. Ceram. Soc., 47 (1964), 323-327.
- [6] DAWIHL, W. and DÖRRE, E., "Über Festigkeits- und Verformungseigenschaften von Sinterkörpern aus Aluminiumoxid in Abhängigkeit von Zusammensetzung und Gefüge", Ber. Dtsch. Keram. Ges., 41 (1964), 85-96.
- [7] KLINGLER, E. A., and DÖRRE, E., "Neue Anwendungsgebiete für reines Aluminiumoxid in der Elektrotechnik und Elektronik", Ber. Dtsch. Keram. Ges., 44 (1967), 498-505.
- [8] BRUNDIGE, E. L. and HANKS, G. S., "Ceramic-to-Metal-Seals for High Temperature Operation", Report LAMS-2917 (1963).

- [9] BUSSE, C.A., GEIGER, F., QUATAERT, D., and PÖTZSCHKE, M., "Heatpipe Lifetests at 1600°C and 1000°C", 1966 IEEE Conference Record of the Thermionic Conversion Specialist Conference, Nov. 3-4, 1966, Houston, Texas, 149-158.
- [10] BEGHI, G., EURATOM, CCR Ispra, Metallurgy Division (unpublished data).
- [11] LANDES, C., EURATOM, CCR Ispra, Metallurgy Division (unpublished data).
- [12] MICHAEL, A. B. and GENTRY, W. O., "The Trend and Status of Development of Refractory Metal Alloys", in N. E. Promisel "The Science and Technology of Selected Refractory Metals", Pergamon Press, 1964, 111-129.
- [13] SMITH, R. G., HARGREAVES, F., MAYO, G. T. and THOMAS, A. G., "A Study of the Compatibility of Thermionic Converter Materials with Caesium", J. Nuclear Materials, 10 (1963) 191.
- [14] KEDDY, E. S., "Compatibility Evaluation of Materials with Caesium", report LAMS-2948, 1963.
- [15] ELLIOTT, R. P., "Constitution of Binary Alloys, First Supplement", McGraw-Hill 1965.
- [16] HANSEN, M., "Constitution of Binary Alloys", McGraw-Hill, 1958.
- [17] KOHL, W., "Electron Tubes", Reinhold Publishing Corp., 1960.
- [18] PÖTZSCHKE, M., RUDOLPH, G. and RÜHLE, M., "Entwicklung und Prüfung geeigneter Werkstoffe und ihrer Eigenschaften für thermionische Konverterzellen zur Verwendung im Reaktor", Bericht No. E 2528, EURATOM-Forschungsvertrag 007-64-5 CODD (10.-12. Vierteljahresbericht für die Zeit vom 1.10.1966 bis 30.6.1967).

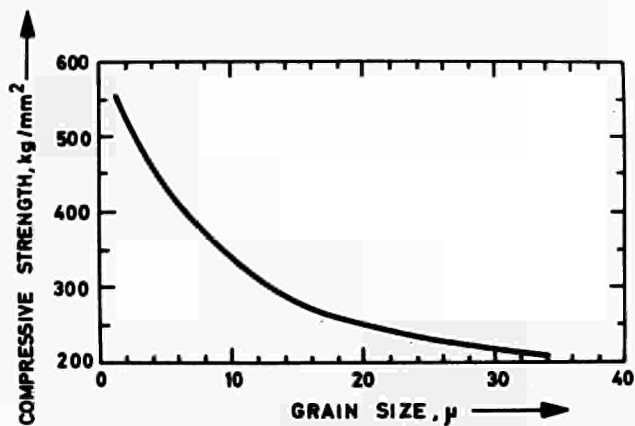


Fig. 1: Compressive strength of pure alumina versus grain size, at 20°C

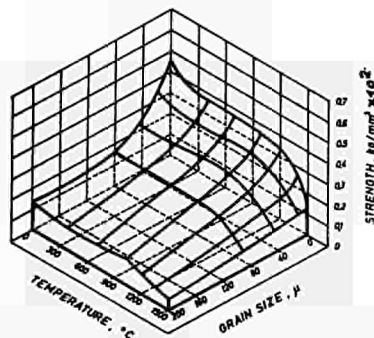
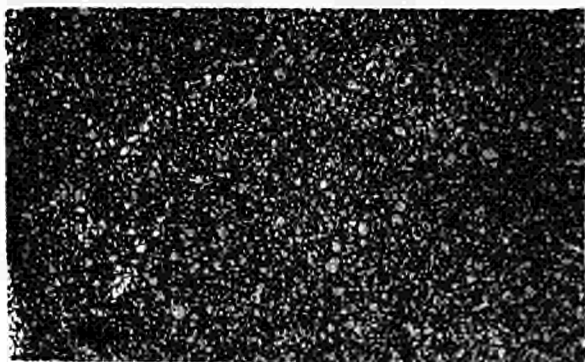
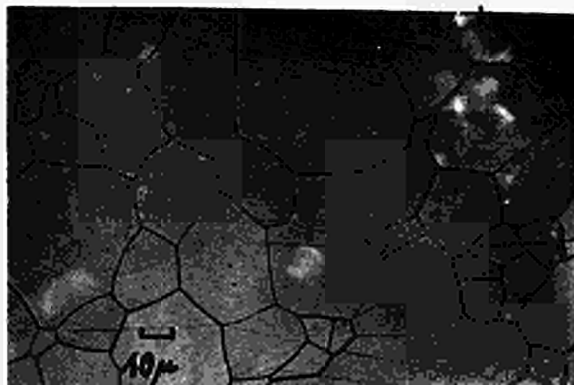


Fig. 2: Flexural strength of pure alumina versus grain size and temperature (after Spriggs et al.)



a
Av. grain size: ~4 μ
Flexural strength: 53 kg/mm²
Total transmission for visible light (thickness 0.5 mm): 89%



b
~50 μ
35 kg/mm²
91%

Fig. 3: Structure of Al₂O₃ + 0.25 w/o MgO samples of different grain size (density of both samples 99.8%)



Fig. 4: Tungsten powder (average grain size: 0.05 μ, spec. surface: 6.1 m²/g)

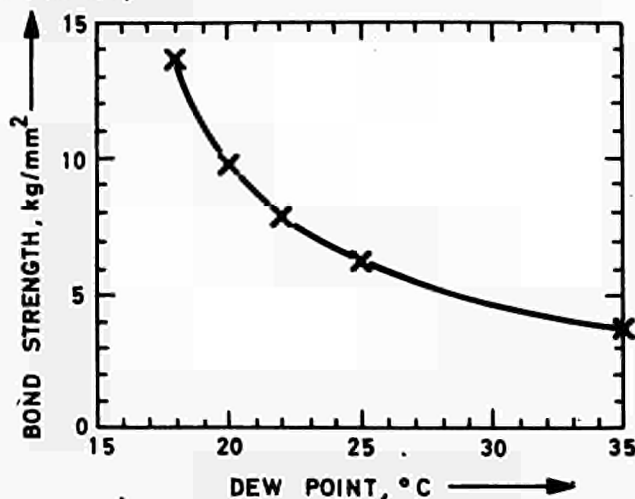
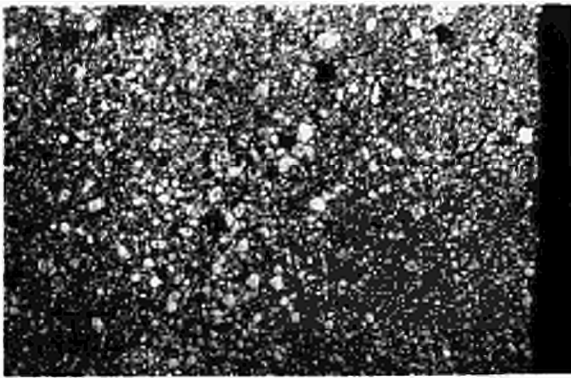
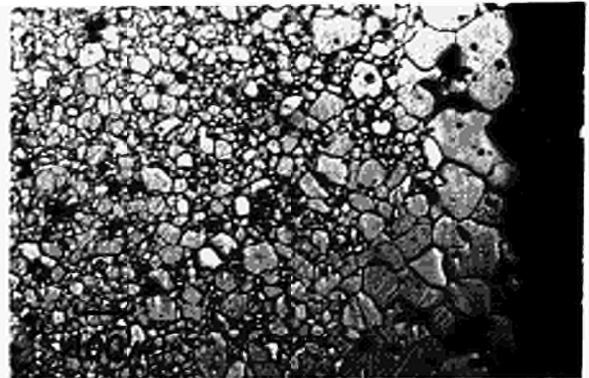


Fig. 5: Bond strength of W + 2 w/o Y₂O₃ metalizing versus dew point of firing atmosphere (firing of 10 min at 1900°C in N₂ + 20 v/o H₂)

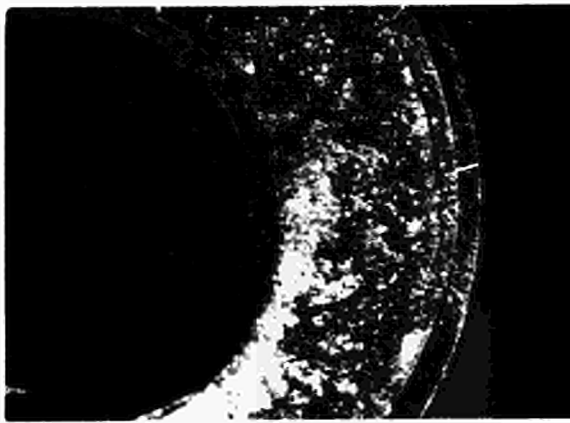


a: no TiO_2



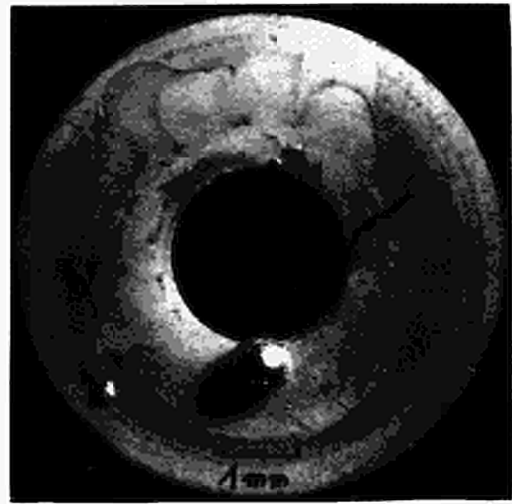
b: 7.5 w/o TiO_2

Fig. 6: Grain growth promoted by TiO_2 addition to the metalizing suspension (firing of 20 min at 1900°C)



1 mm

Fig. 7: Ceramic-metal fracture (view of Nb-1Zr surface)



1 mm

Fig. 8: W-metalized E37 after exposure to liquid Pd for 60 sec

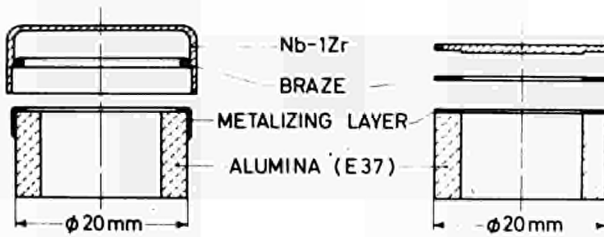


Fig. 9: Seal designs in cylindrical and planar geometry

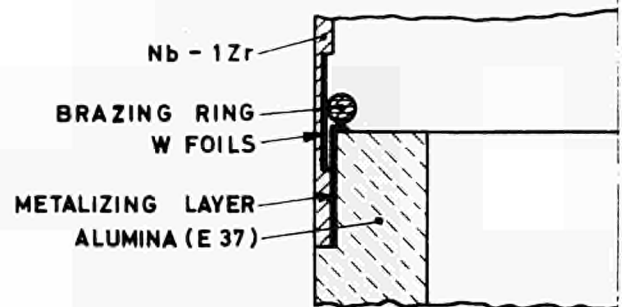


Fig. 10: Cylindrical seal for Pd-brazing

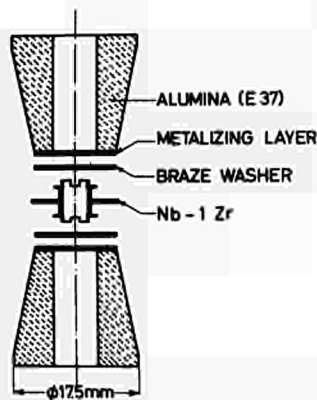


Fig. 11: Components of tensile test sample

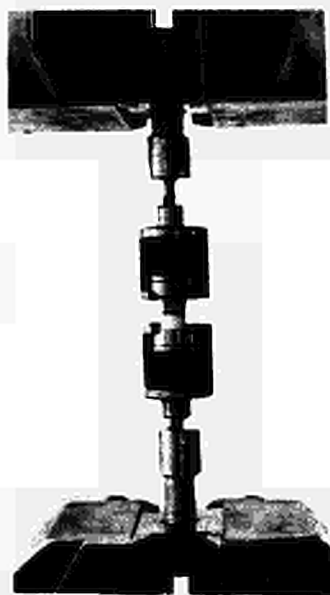


Fig. 12: Sample inserted in tensile test machine

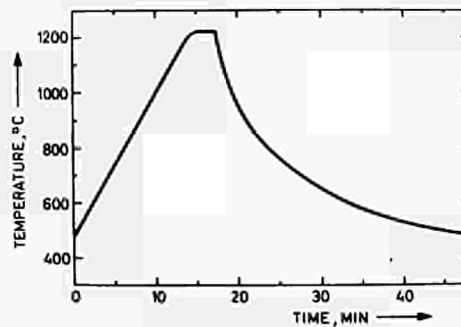


Fig. 13: Thermal cycle

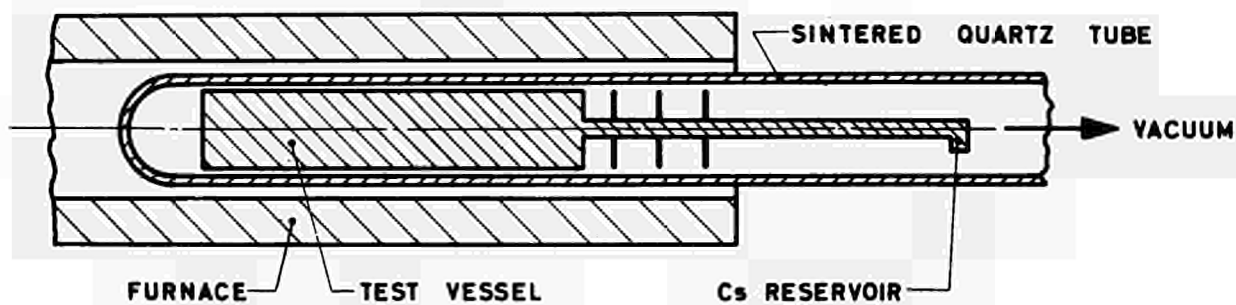


Fig. 14: Cesium corrosion test apparatus



a



b

Fig. 15: Surface of E37 after 1000 hours at 1000°C in cesium vapor of 20 torr.

DISCUSSION

Speaker of paper E-5: E. A. DÖRRE.

BUGL (Euratom): What was the sintering temperature and vacuum pressure to obtain the fine grain size of the Al_2O_3 ceramics?

DÖRRE (Germany): The sintering temperature was about $1900^{\circ}C$ and the vacuum pressure was about 10^{-6} Torr.

BUGL: Did you consider the possibility of obtaining this structure also by means of isostatic hot pressing?

DÖRRE: Yes, we did, but isostatic hot pressing is a very expensive process with restrictions in size and shape of the parts produced. The ceramic material E 37, here described, however, is a regular commercial high purity, high density alumina quality, used for many other applications with no restrictions in size or in shape.

SCHOCK (USA): How was the metallizing applied?

DÖRRE: By brushing.

SCHOCK: What is the liquid medium?

DÖRRE: The liquid medium is isoamylacetate..

SCHOCK: Did the Pd attack the metal during brazing, or during subsequent testing?

DÖRRE: During brazing.

SCHOCK: What was the time and temperature of the brazing process?

DÖRRE: They are dependent on the brazing alloy and are described in detail in the paper.

HARBAUGH: What was the brazing alloy used in the $1000^{\circ}C$, 1000 h test?

DÖRRE: The brazing materials in this case were copper-nickel, palladium and an active alloy consisting of niobium, vanadium, titanium.

HARBAUGH: Was any change in the alloy observed by cross-sectioning the seal?

DÖRRE: We did not observe any change.

SCELLEMENTS CERAMIQUE-METAL

A.M. Shroff et S. Esnaud

CSF - Compagnie générale de télégraphie Sans Fil,
Groupement Scientifique et Technique
Domaine de Corbeville, Orsay (France)

I - INTRODUCTION

La technologie des convertisseurs thermoioniques ainsi que celle des capsules d'irradiation nécessite l'emploi de matériaux et de scelllements, isolant-métal, fonctionnant à des températures allant jusqu'à 1 500° K, résistant à la corrosion par le césium, aux radiations, tout en restant étanches au vide.

Le présent article concerne les scelllements isolant-métal utilisant soit la technique de la métallisation préalable, soit la brasure directe.

On présentera quelques types de réalisation.

II - TECHNIQUE DES SCELLEMENTS

II.1. Scelllements directs

On entend par scelllement direct la liaison directe entre l'alumine et le métal à l'aide d'une brasure. Dans certains cas pour favoriser le scelllement on utilise un agent de liaison : de l'hydrure de titane par exemple. Le métal est en général recouvert de cuivre ou de nickel afin d'améliorer la mouillabilité de la brasure ou d'éviter la corrosion fissurante. Le tableau 1 donne les différentes possibilités de liaison.

II.2. Scelllements après métallisation de la céramique

Il existe plusieurs types de métallisation, qui ont un point commun, ils possèdent au moins un matériau réfractaire de base.

On peut métalliser de différentes manières :

- par sérigraphie,
- au pistolet,
- au pinceau,
- au trempé,
- par schoopage au pistolet à plasma,
- par évaporation,
- par dépôt en phase vapeur d'un composé halogène.

Dans tous les cas il est nécessaire de chauffer à haute température la céramique badigeonnée pour obtenir une bonne liaison entre le métal déposé et la base.

Le tableau 2 donne les différents types de métallisations associés aux alumines. En général les suspensions utilisées pour les dépôts au pinceau, au pistolet, au trempé ou par sérigraphie diffèrent entre elles par leur viscosité. Le liant organique composant la suspension le plus communément utilisé est à base d'acétate de butyle, de collodion et d'oxalate d'éthyle. Les épaisseurs de dépôts varient entre 10 et 20 μ pour le dimolybdate de lithium, 20 et 60 μ pour la métallisation au molybdène titane et sont de l'ordre d'une centaine de microns pour les métallisations au tungstène ou au niobium. On notera qu'après frittage, les métallisations subissent un retrait de l'ordre de 50 %, à l'exception de celles réalisées par phase vapeur.

Les brasures utilisées ainsi que les métaux auxquels sont raccordées les céramiques sont classés dans le tableau 3. On peut, pour améliorer le mouillage de la brasure, dans certains cas utiliser des dépôts de cuivre ou de nickel sur le métal de liaison. De la même manière on empêche la brasure de pénétrer dans la métallisation par un revêtement protecteur.

III - R É S U L T A T S

III.1. Essais de traction

Dans le cas des scelllements avec métallisation au molybdène titane et brasure au nickel or et au nickel cuivre or la résistance à la traction sur une éprouvette de forme cylindrique est comprise entre 2 et 4 kg/mm^{-2} . Dans le cas des scelllements directs la résistance à la traction est de l'ordre de 3 kg/mm^{-2} pour l'eutectique Ag-Cu. On a pour la brasure nickel titane des valeurs identiques.

III.2. Essai de durée sous l'effet de la corrosion sous tension

- a) Corrosion à l'air : Aucune corrosion apparente incompatible avec l'étanchéité a été décelée dans les deux types de scelllements, à l'exception des scelllements au niobium tantale fonctionnant à 700° C. En particulier les scelllements directs à l'eutectique argent-cuivre ont duré plus de 2 000 heures à 400° C. Les scelllements par métallisation dure brasés au nickel or cuivre,

à l'or cuivre et au cuivre métal ont dépassé 2 000 heures sans présenter de fuite.

- b) Corrosion au césium : Les scelllements comportant des brasures contenant des métaux nobles sont fortement corrodés. Seuls les scelllements au Cu-Ni ou au nickel titane résistent à la corrosion au césium (plus de 6 000 heures de durée à 700° C). Il faut aussi signaler que seules les alumines très pures résistent à la corrosion par le césium ainsi que les métallisations ne contenant pas de silicium ou de fer.

- c) Corrosion à UF₆ en phase vapeur : Les scelllements alumine, à l'eutectique argent cuivre sur inox ou titane ont résisté plus de 20 000 h à la température de 80° C environ.

- d) Corrosion par le sodium liquide : Les scelllements alumine brasés à l'argent cuivre sur l'inox revêtu d'un revêtement électrolytique protecteur de cuivre nickel n'ont pas présenté de fuite après plusieurs centaines d'heures de fonctionnement.

- e) Effet des radiations : Les scelllements du titane nickel, ainsi que ceux à l'eutectique Cu-Ni ont résisté plus de 2 000 h sous flux de neutrons.

IV - C O N C L U S I O N

Les scelllements avec ou sans métallisation préalable présentent un grand intérêt pour la réalisation d'enceintes étanches. Les brasures ne contenant pas de métaux nobles sont utilisables pour la réalisation de convertisseurs thermoioniques au césium. La tenue aux radiations ne semble pas être un problème dans le cas des scelllements au titane ou à l'eutectique argent cuivre.

Tableau 1
Scelllements directs

Alumine	Brasure	Métal de liaison	θ_f brasure	θ_{fonct}^{nt}
Alucer 99	Ag Cu	Titane massif Kovar + hydrure de titane	780° C	600° C
Wesgo	Ag Cu Pd	Inox + hydrure de titane Cuivre + hydrure de titane	810° C	
Coors	Ti Ni	Niobium	942° C	700° C
SRK	Cuivre nickel	Tantale	1050° C	
Lucclox				
Saphir	V	Niobium	1850° C	1500° C
Spinel				
Sintox				

Tableau 2

Alumine	Métallisation	Mode de dépôt	θ ° C frittage
94 %	Molybdène - titane	Sérigraphie Pistolet Pinceau Trenpe	1500° C
97 %	Molybdène - titane	"	
99 %	Molybdate de lithium Tungstène Niobium	Pinceau Pinceau Phase vapeur	1700° C 1800° C 1800° C

Tableau 3

Céramiques	Brasure	Métal de liaison	θ_f brasure	θ fonctionnement
Alucor 99	Ag Cu	Titane Kovar Cuivre	730	500
Wesgo	Ni Au	Kovar Cuivre	950	"
Coors S P K	Ni Au Cu	Kovar Cuivre Molybdène	910	"
Lucalox	Au Cu	Kovar Cuivre Nickel	1015	700
Saphir	Cu Ni	Niobium		
Spinel		Kovar	1100	700
Sintox	Pd Co	Niobium	1250	1000
	Pd	"	1550	1200
	Nb V	"	1810	1500

MULTI-FOIL THERMAL INSULATION
USING OXIDE PARTICLE LAYER SEPARATION

by

John B. Dunlay
Thermo Electron Corporation
85 First Avenue
Waltham, Massachusetts 02154

ABSTRACT

Current work is described on the development of multi-foil thermal insulation using oxide particle layer separation. The insulation consists of thin metal foils coated with high-purity refractory oxides. The metal foils act as thermal radiation shields, and the oxide coating prevents direct metal-to-metal contact between adjacent foils.

The heat-transfer characteristics of the insulation are discussed as a function of the heat source temperature and the oxide particle size. Cylindrical-to-planar edge configurations are described, and measured edge heat losses are presented.

The work described in this paper was sponsored by the United States Atomic Energy Commission under Contract No. AT(30-1)-3634.

INSULATION DESCRIPTION

Multi-foil thermal insulation consists of thin metal foils coated with oxide particles. The foils are closely spaced and act as radiation shields. Heat transfer through the insulation is primarily by radiation. The oxide particles form a thin, discontinuous coating on each foil. The small coverage of the particles, plus the interface contact resistances, results in minimum solid-conduction heat transfer. To eliminate gaseous conduction the insulation must be operated in a vacuum environment.

An insulation assembly is fabricated using basic sections of cylindrical and planar foils. These configurations are illustrated in Figure 1. The cylindrical section is formed by spirally wrapping a continuous length of foil. The planar or end sections consist of stacked foil disks. The foil thickness is typically 0.0005 inch, and the oxide particles are approximately 0.0005 inch in diameter. A thickness of 0.001 inch is therefore required for each foil layer in the insulation assembly.

The oxide particles are applied to the foils in the spray rig shown in Figure 2. Reproducibility of the spray conditions is achieved by means of a motor-driven conveyor belt and reel. The oxide particles are mixed with a binder for the spraying operation. After fabrication of the planar and cylindrical sections, the complete insulation assembly is fired in vacuum to remove the binder and outgas the insulation.

Refractory metal foils were investigated for high-temperature applications up to 1900°C. W, W(25%)Re, Ta, and Mo foils were tested in combination with ThO_2 and Y_2O_3 . No gross chemical reaction between the foil and the oxide was observed in any of the foil-oxide combinations. Varying degrees of bonding occurred, however, between the foils and oxides, and this bonding strongly affects the conduction heat-transfer component through the insulation. Ta and Mo in combination with both thoria and Y_2O_3 were found satisfactory for extended operation at temperatures up to 1600°C. Excessive bonding occurs above 1600°C. Combinations of W and W(25%)Re with ThO_2 and Y_2O_3 are satisfactory at operating temperatures of 1700°C. Some bonding occurs at 1900°C, however, after 2000 hours. In general, ThO_2 appears to be more resistant to bonding with the refractory metals than does Y_2O_3 .

Two different foil materials may be used for the insulation of heat sources operating at temperatures above 1600°C. W or W(25%)Re

is used for the insulation foils operating above 1600°C. As the temperature is reduced through the insulation, the foils can be changed to Ta or Mo. The use of Ta or Mo is generally desirable where possible from fabrication and availability considerations.

Pt, Ni, Cu, and Al are being investigated in combination with Al_2O_3 and ZrO_2 for low-temperature applications. Bonding studies indicate that ZrO_2 is consistently superior to Al_2O_3 . After 500-hour tests, the maximum operating temperatures for ZrO_2 -coated foils are: Pt - 1000°C, Ni - 1000°C, Cu - 600°C, and Al - 500°C.

THERMAL PERFORMANCE

Tests were performed to investigate the effects of oxide particle size on the heat-transfer characteristics of the insulation. These tests were carried out in a planar test assembly. The insulation samples are located between a calorimeter and an electrical heater block which forms the high-temperature heat source. The calorimeter measures the heat flowing from the heat source through the insulation sample to the calorimeter.

The results of these tests are presented in Figure 3. Only small changes in heat flux are observed for average particle sizes varying from 1 to 25 microns. The insensitivity of the results applies over the entire range of source temperatures investigated (800°C to 1750°C). These test data were obtained using Mo - ThO_2 insulation samples. Recent data obtained for other refractory-metal foils in combination with ThO_2 indicate very similar values of heat flux as a function of source temperature. Thus the curve shown on Figure 3 is generally representative of the refractory-metal foil insulation performance. Included in Figure 3 are the results of low-temperature tests using Ni - ZrO_2 insulation. These low-temperature data are consistent with

the high-temperature data and indicate that radiation is the dominant heat-transfer mechanism in the insulation, even at source temperatures as low as 200°C.

The average thermal conductivity of the insulation is shown in Figure 4. These values of thermal conductivity apply for sink temperatures of approximately 30°C, an insulation thickness of 0.0025 cm per foil layer, and a source temperature as indicated in the figure. The magnitude of the average thermal conductivity is in the 10^{-6} watts/cm-°C range and increases with increasing source temperature.

EDGE EFFECTS

In a complete multi-foil insulation assembly, discontinuities occur in the foil layers at the edge of the planar and cylindrical sections. These discontinuities can establish additional radiation and conduction heat-transfer paths through the insulation. Since heat transfer directly through the insulation is very small, the heat losses through the edge can represent a significant fraction of the total heat loss from a completely insulated heat source.

Three configurations have been tested to investigate edge heat losses. These configurations are illustrated in Figure 5. The overlap and taper configurations have proven to be very effective and are relatively easy to fabricate. Heat losses through each of the edge configurations are shown in Figure 6. The taper configuration exhibits the lowest heat loss, with a value of 0.25 watt/cm of edge for a source temperature of 1700°C.

SUMMARY

The multi-foil thermal insulation concept using oxide particle separation of the foils was proven to be very effective in reducing heat losses from high-temperature heat sources. Recent tests show that

the effectiveness of the insulation extends over a wide temperature range (200°C to 1700°C). Radiation is the primary heat-transfer mechanism through the insulation. The radiation heat-transfer characteristics plus the close foil spacing achieved by the use of oxide particle separation result in very low values of thermal conductivity. Where heat loss or insulation thickness is a dominant design parameter, this insulation concept offers the potential of significant improvement in system efficiency.

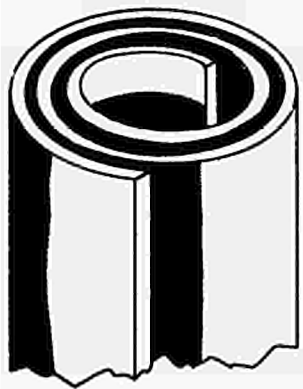
ACKNOWLEDGMENTS

The author would like to express his appreciation to co-workers on this program. They include R. Bishop, J. Carvalho, J. Fronduto, M. Paquin, V. Poirier, and L. van Someren.

INSULATION CONFIGURATIONS



PLANAR



CYLINDRICAL

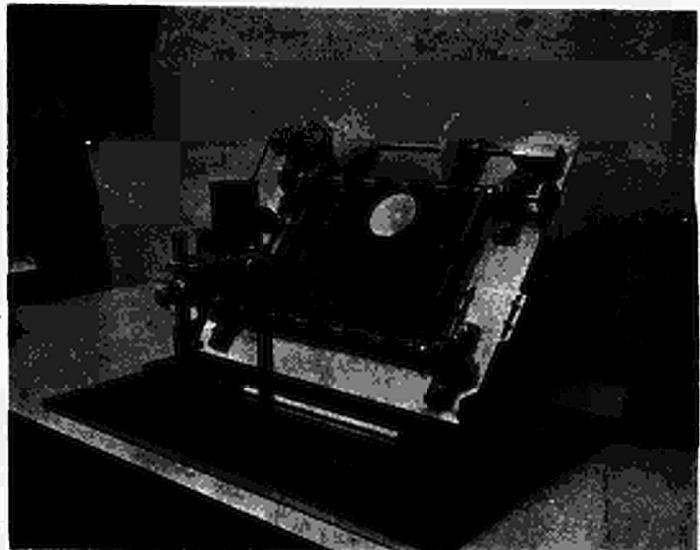


Figure 2. Spray Rig for Applying Oxide Particles

Figure 1. Insulation Configurations

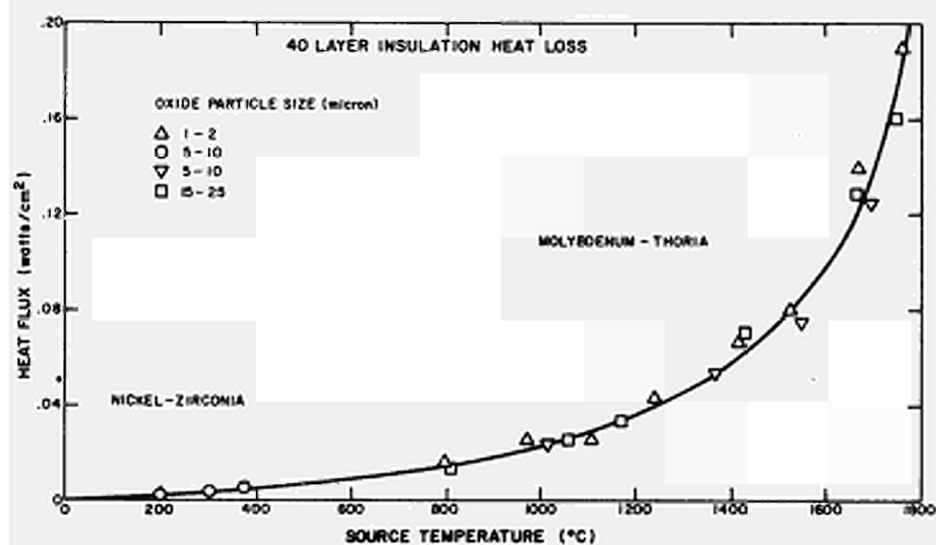


Figure 3. 40 Layer Insulation Heat Loss

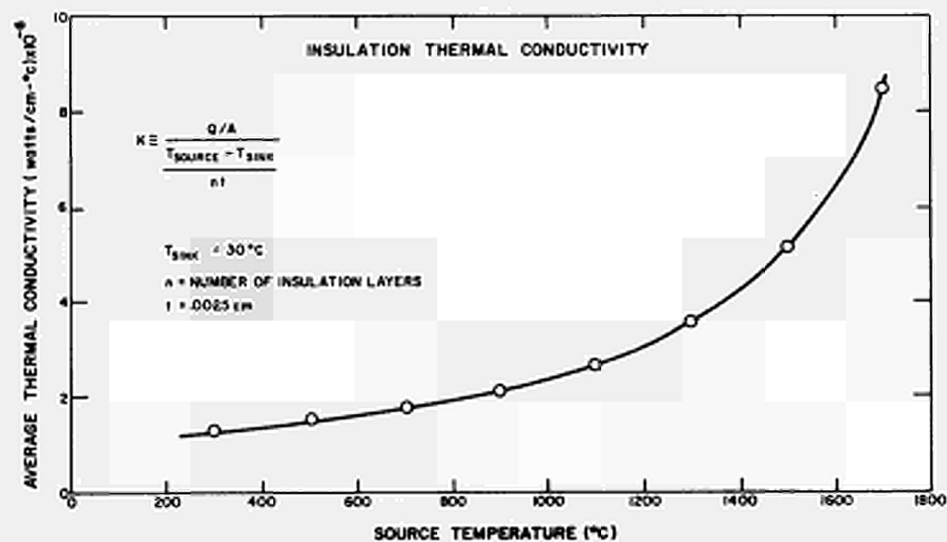


Figure 4. Insulation Thermal Conductivity

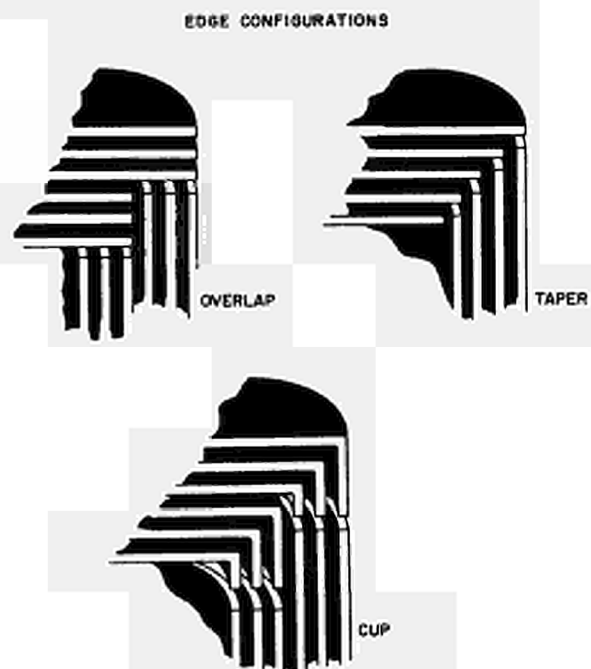


Figure 5. Edge Configurations

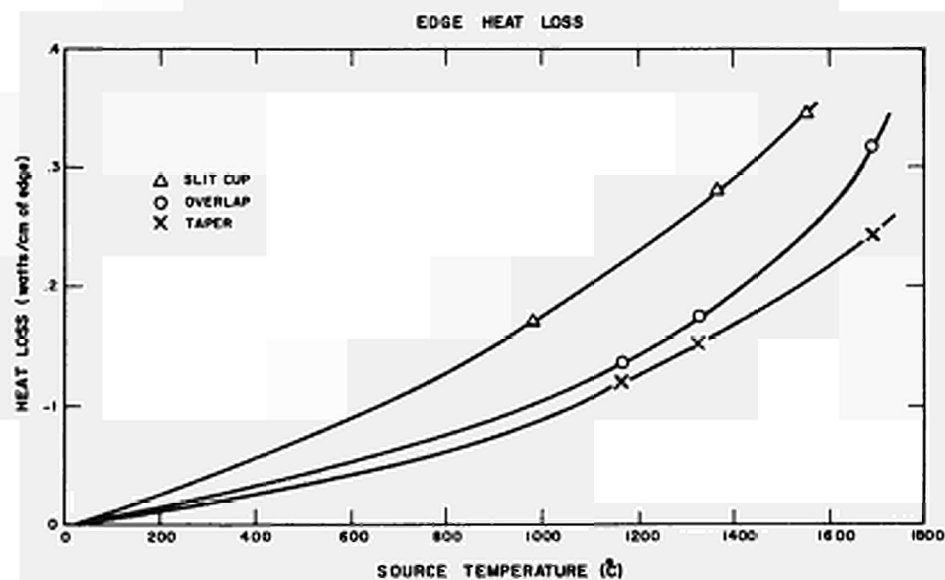


Figure 6. Edge Heat Loss

DISCUSSION

Speaker of paper E-7: J. B. DUNLAY.

GROSS (Germany): How is the stability of the layers with regard to time?

DUNLAY (USA): The material temperatures that I mentioned were based on compatibility tests, where we run materials together, typically for a test period of 2,000 hours. And the condition which establishes the maximum temperature that you can run at is where the two materials start to bond together to form thermal conduction paths.

GROSS: When did this happen? At about 2,000 hours?

DUNLAY: We made the test and if bonding occurs at the test temperature then we say that is too hot. Then we go to a lower temperature and evaluate at that much lower temperature.

RIABIKOV (USSR): Does the thermal resistance of similar multi-layer systems change after a series of thermal shocks?

DUNLAY: We have tested under vibration type conditions and we do not see any change in thermal performance. These are vibration conditions which are similar to launch conditions for space vehicles.

Also with thermal shocks we do not see any difference. We can build a device, heat it up, and cool it down many times and see no difference in thermal performance.

RASOR (USA): Do you have any new data on the load bearing abilities of the multifoil?

DUNLAY: We are making more load bearing measurements now. I do not have any of the data with me. Typically the insulation is restricted to fairly light loads in order to maintain its low value of thermal conductivity.

GUSKOV (USSR): Would you indicate the specific electrical resistance of the layers?

DUNLAY: We have not measured the electrical resistance.

SHROFF (France): Do you sinter the oxide layers or are they used as deposited?

DUNLAY: We do not sinter them, they are used as deposited.

SHROFF: Do you observe failures where the powder goes away when the system is heated up?

DUNLAY: No, we have not observed this type of phenomenon.

SHROFF: Have you made comparisons with the metallic spacing of layers?

DUNLAY: When we first started looking at insulation we looked at dimples, for example. We found that the oxide type separation works much better than the dimples.

SHROFF: In our particular case we did not find much difference between a very loose metallic spacing and the powder insulation between foils, for short periods of time.

A Special Technique for Manufacturing
Insulating Collector Multilayer Tubes

M. Peehs, H. Schörner, H. Stehle

SIEMENS AG., 852 Erlangen (Germany)
Zentrale Entwicklung und Forschung

Abstract

The paper describes development work for the manufacturing of multilayer tubes of low thermal resistivity ($\Delta T < 1^\circ\text{C cm}^2/\text{Watt}$) and high electric insulation properties. For depositing the insulating ceramic layers (Al_2O_3) on the outside of the inner Nb-collector tube plasma-spraying in an inert-gas atmosphere is used. Details of spraying technique to obtain ceramic layers of high density are described. To increase the thermal contact conductance between the ceramic layer and the Nb-surface metallic interlayers are employed. The outer Nb-tube is stretchformed onto the correspondingly prepared inner tube. The process may be improved by the application of a moving induction coil, producing a narrow hot zone. The highest thermal conductance is obtained by spraying a metal braze onto the Al_2O_3 , which melts during stretchforming in the hot zone. The physical properties of previously attained multilayers are described.

1. Introduction and problem presented

In designing the ITR plant (incore thermionic reactor), the collector system used consists of two concentric Nb tubes which are electrically isolated from each other by an Al_2O_3 layer. This system must be capable of functioning for approximately 2 years with outside contact to the Na coolant and inside contact to 4 Torr Cs vapor in the converter gap. The operating temperature is 700°C .

The specific temperature difference between the inner and outer tube wall must not exceed $1^{\circ}\text{C cm}^2\text{W}^{-1}$; the breakdown voltage should exceed 100 V at 700°C .

Besides the process described here for manufacturing sandwich tubes, the following ones are known to the authors.

a) Brazing of ceramic tubes [1]

In this process, a ceramic tube which is metallized on the cylindrical surfaces is brazed in between two concentric metal tubes. The gap caused by the clearance is closed by external pressure on the metal tube.

b) Pressing with interference fit [2]

In this case a ceramic tube which is metallized with copper on the outside is pressed into a Nb-tube; the ceramic tube is ground out to the desired ceramic layer thickness and copperplated again on the inside. A second metal tube is also pressed into the prepared metal ceramic assembly. The entire assembly is then subjected to diffusion bonding treatment at 1000°C .

The American TEECO Company also manufactures triple-layer sandwiches (metal-ceramic-metal) by a process which is not known to the authors.

The disadvantages of the mentioned methods are the limited finished length and the oxide layer thickness of 0.5 to 0.7 mm, which to all intents and purposes cannot be decreased. As shown in Fig. 1, this suggests that specific temperature differences must be anticipated, which are already at the upper limit for the present reactor design. The object of the work described below was to develop a method which is capable to manufacture multilayer tubes with very thin Al_2O_3 -layers and principally unlimited length.

2. Manufacturing principle

The manufacturing method consists of two basic steps:

- a) Applying the ceramic layer on the outside of the inner Nb tube by using the plasma spraying technique.
- b) Continuous zone-by-zone stretchforming of the outer tube onto the inner metal-ceramic assembly.

For plasma spraying Siemens equipment is employed. The work is performed in an inert gas chamber, since Nb cannot be heated in air without detrimental changes to its properties. Difficulties must be expected too in spraying Al_2O_3 in air [3]. For continuous zone-by-zone stretchforming, the outer tube is first slid over the inner metal ceramic assembly and then elongated at a suitably selected constant stretching rate. Deformation then occurs in a narrowly limited circular zone which is progressively heated to between 700 and 1000°C. The diameter contraction resulting from longitudinal stretching causes progressive zone-by-zone shrinking. Work is again performed in a vacuum chamber to prevent oxidation and gas absorption. Fig. 2 shows the principle of the stretchforming equipment.

3. Development work

Simple triple layer systems show a high specific temperature difference of 3 to 4.5°C cm²W⁻¹ at 700 to 800°C. Experiments have shown that this is primarily due to the poor thermal contact between the metal and Al_2O_3 and secondly to the porosity of the ceramic.

To completely melt the kernels of the Al_2O_3 powder which is used for plasma spraying, a power of 12 kW is used when the sieve range of the powder is - 270 mesh + 15 microns. This only can be reached with N₂ as working gas. But an Nb nitride layer then forms, which decomposes on cooling and leads to poor thermal contact since it produces a gap on

the interface Al_2O_3 -Nb. To prevent this effect, a thin Cu layer is first sprayed on with pure Ar as working gas. A Ni80/Cr20 layer (melting point 1440°C) is then applied with an admixture of N_2 to the Ar which still just prevents any significant coppernitride formation and allows to reach a sufficient high power density in the plasma. The Cu base layer melts briefly and thus wets the Nb as well as the NiCr. Al_2O_3 , with N_2 as a working gas, can now be applied to the NiCr without damaging secondary effects; the NiCr layer partly melts in this case and reveals relatively good wetting behaviour in contact with Al_2O_3 . The Al_2O_3 droplets occurring also melt somewhat into the metal layer. Due to the relatively good wettability, NiCr and then again Cu are applied to the Al_2O_3 . In zone-by-zone stretchforming at high temperatures, the Cu liquifies, ingresses into the pores of the NiCr layers, and brazes simultaneously with the outer Nb tube. This stage in the process enables excellent thermal contact to be established between the individual layers (Fig. 3) while at the same time avoiding nitride formation. The overall thickness of the $\text{CuNiCr-Al}_2\text{O}_3$ -NiCr-Cu layers is 0.2 to 0.3 mm. The Al_2O_3 comprises 0.15 to 0.2 mm of this.

To prevent porosity of the Al_2O_3 , only the section of the plasma jet which contains properly melted Al_2O_3 droplets can be used. The partially melted Al_2O_3 particles in the outer zone of the plasma jet are screened off by a gate. The Al_2O_3 droplets thus hit the target almost perpendicularly that the formation of pores through shadow effects are largely eliminated. Layers sprayed in this way reveal excellent structure (Fig. 4).

4. Properties

The tubes manufactured by the multilayer method enabled values for the specific temperature difference of 0.7 to $1^\circ\text{C cm}^2\text{W}^{-1}$ to be attained with high confidence. Measurements of the electrical properties were made at ambient temperature and at the designed operating temperature. The samples were

heated by high frequency induction at $p < 10^{-4}$ Torr to approximately 650°C . There was no flashover in the cold state at an applied voltage of 400 V. During heating up, the relationship between resistance and temperature was determined as shown in Fig. 5. After attaining the final temperature, outgassing of the plasma sprayed layers enabled an increase in the electrical resistance as a function of annealing time as shown in Fig. 6.

References

- 1 Fibelmann, Ispra; verbal information, 1966.
- 2 Böhm, Hübner, Janner, Peehs, Schörner,
report to the German Federal Ministry of Research, 1968.
- 3 A.Matting, B.Delventhal, Metalloberfläche 20, 1966,
Volume 10.

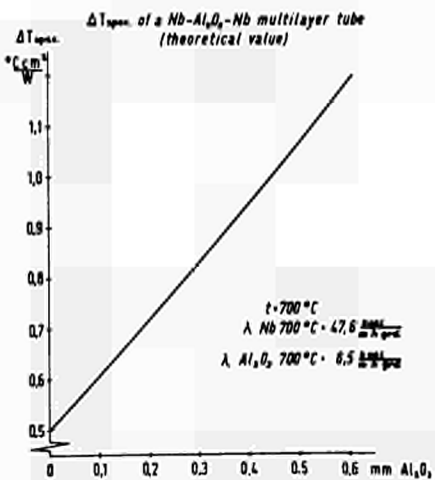


Fig. 1
 ΔT_{spec} of a Nb-Al₂O₃-Nb multilayer tube (theoretical value)

Fig. 1

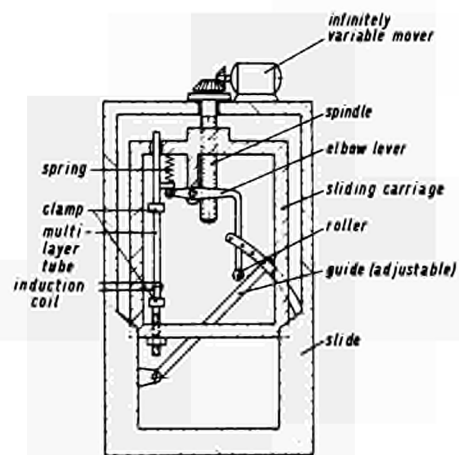


Fig. 2
 Principle of stretch forming equipment.

Fig. 2

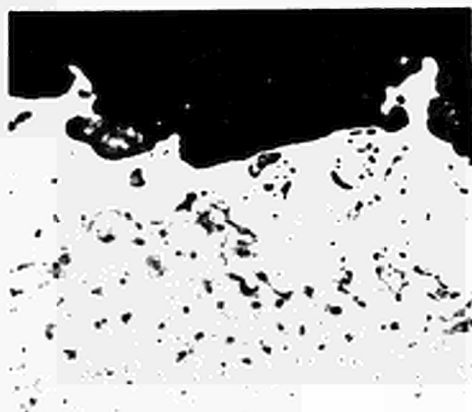


Fig. 3
 Transition zone between Nb and Al₂O₃ (500:1)

Fig. 3

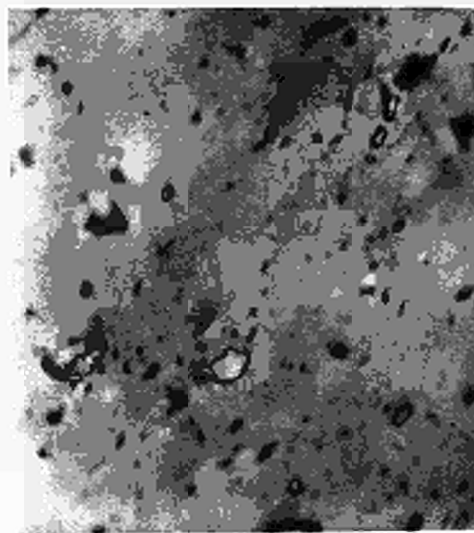


Fig. 4
 Microstructure of the plasma-sprayed Al₂O₃ (500:1)

Fig. 4

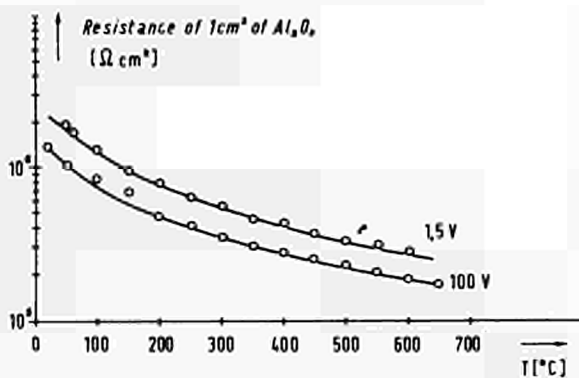


Fig. 5
 Electrical resistance of an insulating collector multilayer tube.

Fig. 5

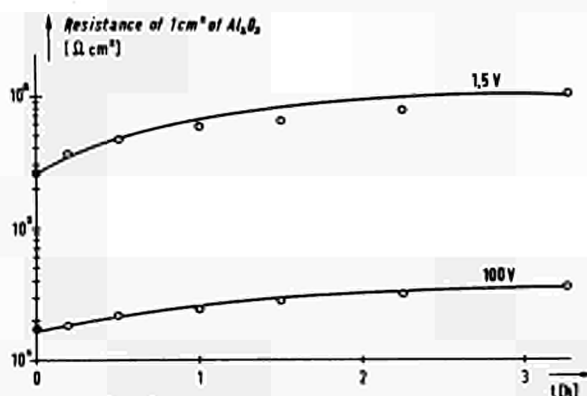


Fig. 6
 Electrical resistance during outgassing at 650^oC

Fig. 6

DISCUSSION

Speaker of paper E-8: M. PEEHS.

CAMPBELL (USA): What was the life time of your experiments which you indicated on the last slide?

PEEHS (Germany): We have times up to two weeks and we have no changes in electrical resistance with an applied voltage of 100 Volts DC. We have not made life time tests in heat transfer, but we have given shocks on the system and have found no influence.

CAMPBELL: At what temperature did your two weeks test run?

PEEHS: At 700°C.

DAVIS (USA): Am I correct in presuming that in fig. 6 this temperature is approximately 650°C at the $t = 0$ point? Is this totally outgassed?

PEEHS: This is totally outgassed. To obtain better sandwiches we now have an outgassing process before zone-by-zone shrinking in a good vacuum and I believe that values for these are much better than these given in the paper.

RIABIKOV (USSR): How great is the temperature drop Δt on your multi-layer system? And how does ΔT depend on the thermal flux supplied to the inner layer?

PEEHS: We made our measurements at heat fluxes up to 1 kW/cm² and we have then measured corresponding temperature drops to determine the heat conductivity values which are given in the paper. The ΔT decreases when thermal flow increases.

SCHOCK (USA): Why must one use nitrogen rather than an inert-gas for the plasma spray?

PEEHS: Only with the nitrogen working gas can we melt the alumina powder through, so that the individual droplets are properly melted. With argon we did not have as high an energy density in the plasma jet and so could not melt the alumina completely. In order to have a good structure to the alumina coating, we must melt up the powder completely.

DAVIS: I'm still a little confused about Fig. 5 and 6. At 700°C in Fig. 5, for example, there was some spread between the 1.5 and 100 Volt curves; then on Fig. 6, where the resistance is a function of outgassing time, the 0-point seems to be off. Which curve is correct?

PEEHS: These measurements refer to different specimens.

DAVIS: And there is that much spread from one tri-layer construction to another?

PEEHS: These values have spread to begin with. We hope that with this process of outgassing at beginning of the stringing, these values become better.

SCHOCK: Have you observed any reaction between the copper and the niobium?

PEEHS: Yes, when we hold the copper for 1 h perhaps at about 1000°C we found some diffusion zones, but the brazing process is finished in some 20 sec and in this case we have not found diffusion zones.

SCHOCK: What operational temperature for 10,000 hours you think this would be safe for?

PEEHS: For 700°C.

INSULATING MATERIALS OF THERMOEMISSION CONVERTERS

R.G. Belyanina, V.L. Bondarenko, A.A. Borisova,
I.N. Gorelov, V.A. Drozhin, Yu.V. Dubinskikh,
I.P. Zasorin, J.I. Ievleva, A.A. Korolyov,
A.D. Kunkina, N.P. Maximov, V.A. Malykh,
V.P. Sharov, I.M. Saratov, D.D. Yakovleva
L.V. Pavlinov, I.N. Prilezhaeva
Institute of Physics and Power
Engineering
Obninsk, USSR

The problem of efficient thermoemission converters construction is closely connected with the development of electroinsulating materials.

The following demands are made of electroinsulating materials:

- reliable electroinsulation;
- vacuum tightness;
- high thermomechanical strength;
- corrosion and radiation resistance.

Insulating material and technological procedure of insulating details fabrication are chosen according to these requirements. In the technological aspect at present it is possible to distinguish two main trends of works on electroinsulation fabrication for thermoemission converters:

a) creation of electroinsulating coating by spraying method;

b) fabrication of electroinsulating details.

The investigations carried out by the authors reveal that trend (b) provides:

- creation of electroinsulation with elevated complex of physical and mechanical properties, high electric and corrosion properties;

- comprehensive checking-up and thorough defectoscopy of fabricated electroinsulation details.

In this report some results of works on electroinsulating details fabrication of the following materials are presented:

a) oxide ceramics on the base of BeO and Al_2O_3 of higher purity;

b) homogeneous cermets on the base of BeO, Al_2O_3 and high-melting metals;

c) multilayer cermet systems on the base of BeO, Al_2O_3 and high-melting metals;

BeO and Al_2O_3 are known to have a complex of properties answering the principal requirements put to insulation materials for thermoemission converters. BeO and Al_2O_3 have high insulating properties maintained under operating conditions of thermoemission converters, satisfactory corrosion resistance in cesium vapours, high strength at operating temperatures of thermoemission converters. BeO has high thermal conductivity and resistance. BeO and Al_2O_3 are technologically similar to each other. Taking into account these well known properties the above oxides were chosen both for creation of purely ceramic electroinsulating materials and for fabrication of electroinsulation of cermet systems, the insulating properties of which are performed by ceramic base of BeO and Al_2O_3 .

Cermet systems are considered as perspective high-temperature insulating materials possessing higher thermomechanical properties, increased elasticity and thermal conductivity as compared to ceramics, which facilitate the problem of agreement

of thermal expansion coefficients when constructing vacuum-tight joints of electroinsulation with constructional metallic materials.

Cermet electroinsulating systems may be as follows:

a) Cermets on the base of BeO , Al_2O_3 with high-temperature metal content up to 45 wt. % homogeneously distributed in a ceramic matrix may be used for electroinsulating details fabrication. The cermets with higher metal content may be used for three-layer isolation where the isolating layers are made of cermet with metal content up to 45% and the external layers connected with metallic constructional materials are of cermet enriched with metal.

b) Multilayer cermet systems, where purely ceramic isolating layers of BeO , Al_2O_3 , 100 mc thick, alternate with metallic or cermet layers made of homogeneous cermets of the same thickness. Multilayer cermet systems can be made in such a manner that provides the gradual transition from a thin isolating layer to a pure metallic one through cermet layers of different metal content.

When making electroinsulating details of BeO and Al_2O_3 and cermets on their base, BeO and Al_2O_3 powders of higher purity (BeO - the total quantity of impurities is 0.1 wt.%, Al_2O_3 - $5 \cdot 10^{-4}$ wt.%) were used. To obtain the details of maximum strength and density the powders of high dispersity were used: BeO with particle size of 1 - 5 mc (specific surface - $2.85 \text{ m}^2/\text{g}$), Al_2O_3 - 1 - 5 mc (specific surface $2.6 \text{ m}^2/\text{g}$), Mo - with average particle size of 2.8 mc (specific surface - $0.35 \text{ m}^2/\text{g}$), Nb with average particle size of 5.6 mc (specific surface - $1.24 \text{ m}^2/\text{g}$).

The charge composition in wt. and vol.% and the index of experimental masses for homogeneous compositions are presented in Table I.

When fabricating cermet systems the homogeneous distribution of metal additions in BeO and Al_2O_3 was achieved by wet grinding of charges in planetary mills lined with the same metal as metallic component. Ethyl spirit was used as a medium for grinding. Additional grinding of components took place du-

ring the grinding operation. The fabrication of cermet test samples was made according to technological operating conditions developed for BeO and Al_2O_3 . Sintered samples characteristics are presented in Table II.

The complex of investigations carried out includes:

- a) The investigation of electroinsulating properties.
- b) The investigation of physical and mechanical properties.
- c) The investigation of corrosion resistance.

ELECTROINSULATING PROPERTIES INVESTIGATION

Insulating properties of ceramic and cermet materials used in thermoemission converters are of utmost importance. In this report the data on specific volume resistance of some materials on BeO, Al_2O_3 base, measured in vacuum and in cesium vapours are presented. For the investigation of insulating properties the samples of BeO, BeO + Mo (23 and 47 wt.%), Al_2O_3 + Mo (30 wt.%) were used.

The characteristics of the samples are presented in Table II. The measurements were carried out on tubular samples with screen electrodes by voltmeter-ammeter method. Mo coating 3 - 5 mc thick made by vacuum spraying were used as measuring electrodes. Mo coating was sufficiently porous and did not prevent from cesium penetration into samples. Before the measurements the samples were annealed in vacuum at $1000^{\circ}C$. during 2 - 4 hours. For determination of contact resistance effect upon the measurement results, the voltage-current characteristics were measured. These characteristics showed that the contact effect may be neglected.

INSULATING MATERIALS CONDUCTIVITY IN VACUUM

The measurements were carried out in dynamic vacuum 10^{-5} mm Hg within temperature range $200 - 1500^{\circ}C$. The measurement

results are given in Fig. 1. On the curve of BeO conductivity logarithm dependence inverse temperature there may be seen three sections of different slope angles. These sections evidently correspond to three conductivity ranges: impurity, transient and true ones. Introduction of 23 wt.% Mo into BeO increases its conductivity by about an order of magnitude at the temperature up to 700°C and by 1.5 - 2 orders at the temperature above 700°C. Mo content increase up to 47% results in a slight conductivity increase as compared to BeO with 23 wt.% of Mo. Al₂O₃ + Mo (30 wt.%) cermet provides the conductivity value within the range between BeO and BeO + Mo cermets.

THE RESISTANCE OF BERILLIUM OXIDE IN CESIUM VAPOURS

When studying insulating properties of BeO in Cs vapours a special working section was used. Cesium vapours were fed from the thermostat into the inner cavity of a tubular sample; there was vacuum outside the sample. High voltage electrode was outside the sample and the measuring one - within it. The measurements were performed within the temperature range 500 - 800°C. Cesium vapours pressure varied within 10⁻¹ - 7 mm Hg. The time of exposure at every point (t and P_{cs}) was 4 hours and more. The specific volume resistance of BeO in Cs vapours (Fig. 2) is by 3 - 4 orders lower than in vacuum. The Cs vapour pressure increase from 10⁻¹ to 7 mm Hg at constant temperature reduces the resistance within an order. During the time of sample exposure for 20 hours at 800°C and Cs pressure of 7 mm Hg the resistance did not change. The decrease of BeO resistance in Cs is evidently related with its penetration into pores and with effective thickness decrease. Besides, Cs may serve as a donor impurity increasing electronic conductivity.

PHYSICAL AND MECHANICAL PROPERTIES

HEAT EXPANSION

Heat expansion of BeO was measured on tubular samples along the axis by optical method, and that of cermets - on cy-

lindrical samples (d 8 - 10 mm, 16 mm long) on the quartz dynamometer in vacuum. The values of BeO average linear heat expansion coefficient as a function of temperature are presented in Table III. The spread of separate data does not exceed $\pm 0.4 \cdot 10^{-6}$ I/degree from the average value of heat expansion coefficient.

Temperature dependence of cermet linear expansion coefficient is presented by curves in Fig. 3 and 4. The data obtained confirm that thermal expansion of the cermets studied to be determined by the properties and quantitative ratio of the components. The character of thermal expansion temperature dependence of the cermets of the compositions studied is very similar to the temperature dependence of ceramic base thermal expansion.

MECHANICAL PROPERTIES

The strength of electroinsulating materials at different tests was characterized by maximum stresses under which the failure took place. The stresses were calculated by general formulas for an elastic body. Tensile tests of BeO were carried out on tubular samples at the room temperature. The ultimate tensile strength varied from 8 to 15 kg/mm² (for the samples with density of 2.83 - 2.96 g/cm³). The tensile strength is significantly effected not only by the grain density and size, but also by the uniformity of grain distribution over the sample cross section. A number of the samples tested revealed low density value because of the presence of a thin surface coarse-grain layer in spite of the high density value (2.94 g/cm³) and fine grain in the bulk of the sample (18 - 20 mm).

Compression tests of BeO and cermet samples were carried out on tubular samples 1.5 d high with ends fixed by plastic gaskets. The results obtained from BeO tests are presented in Fig. 5. Sample strength and data spread decrease with temperature use. Compression strength results for cermet samples are presented in Table IV.

From the data of Table IV it follows that BeO- and Al_2O_3 -based cermets with Mo addition have high compression strength value. The increase of cermet strength is apparently caused by fine-grain structure of ceramic base which results from introduction of Mo restricting BeO and Al_2O_3 grain growth. These data agree well with the results of microstructural analysis of the samples investigated and also with the data of the works [1] and [2].

The results of bending strength tests for tubular, plate and circular samples of BeO are presented in Fig. 6. Tubular and plate samples were tested according to the scheme of 4-point loading. The chart of bending moments at circular sample test was similar to the chart of 4-point loading. For all the cases the maximum tensile stress calculated by formulas for an elastic body was taken as the rupture stress. The results of the bending tests reveal an interesting feature of BeO, i.e. strengthening with temperature rise, which becomes apparent to a various degree on different samples. The material strengthening effect and maximum strength are achieved on tubular samples at higher temperatures than on plate and circular samples.

It is possible that the observed strengthening is connected with the stress redistribution, which in its turn, depends on the stress gradient value over the sample material grain.

Bending tests of cermet samples at room temperature were carried out on circular samples with a slit cut. The results of the tests are presented in Table IV.

THERMAL CONDUCTION

The results of thermal conduction investigation for cermet samples are shown in Figs. 3, 4. The character of temperature dependence of cermet thermal conduction coincides with the temperature dependence of ceramic base heat conduction. As it was to be expected the effect of heat conduction increase is appreciably manifested for Al_2O_3 -based cermets. The introduc-

tion of 30 wt.% Mo into Al_2O_3 increases heat conduction coefficient by 70% as compared to pure Al_2O_3 . For BeO-based cermets the heat conduction increase is less significant.

MICROSTRUCTURE

According to the type of their microstructure, the homogeneous cermets being studied refer to the materials with continuous oxide frame. Metallic phase is in the form of separate isolated inclusions. That is why the main cermet properties are determined by ceramic phase properties. This is confirmed by

χ - ray crystal analysis. For all the cermet systems of the compositions investigated there is noted fine-crystal structure of oxide phase. With metal content increase there may be observed the decrease of the grain size of oxide frame. Metal is in the form of grains of average 6 mc size. Among the great bulk of grains of rounded form there may be met some 5 - 10% of needle - shaped grains 15 mc long.

Microstructure of homogeneous and multilayer cermets is presented in Fig. 7. Microstructure of the multilayer cermet confirms the absence of sharp boundaries of transient layers from a purely ceramic layer to a pure metallic one through the intermediate cermet layers of various metal content.

CORROSION PROPERTIES

The tests of compatibility of BeO, Al_2O_3 samples and of the cermets on the base of these oxides with 30 and 40 wt.% of Mo with Cs vapours revealed good corrosion resistance of the samples. The tests were carried out at 700°C during 1000 hours. The appearance of samples did not change after the tests. The weight changes of some samples are within possible errors of weighing. Metallographic studies of ceramic and cermet samples did not reveal any interaction of the materials tested with Cs vapours. The absence of interaction is confirmed by χ - ray

crystal analysis.

CONCLUSIONS

1. Ceramic materials of BeO and Al₂O₃ pure oxides have a complex of properties meeting the main requirements put to electroinsulation of thermoemission converters.

2. BeO-, Al₂O₃-based cermet materials with addition of 30 - 40 wt.% high-melting materials in form of homogeneous and multilayer systems possessing high electroinsulating and improved mechanical properties may be considered as perspective materials for using as electroinsulation for thermoemission converters.

REFERENCES

- [1] N.I. Petch. Iron and Steel Inst. (1953) 174, 25 - 28.
- [2] C.O. McHugh, T.I. Whallen, M.Ir. Humenik. Dispersion-strengthened Aluminen Oxide. Journ. Amer. Ceram. Soc. (1966) 49, No. 9, 486 - 491.

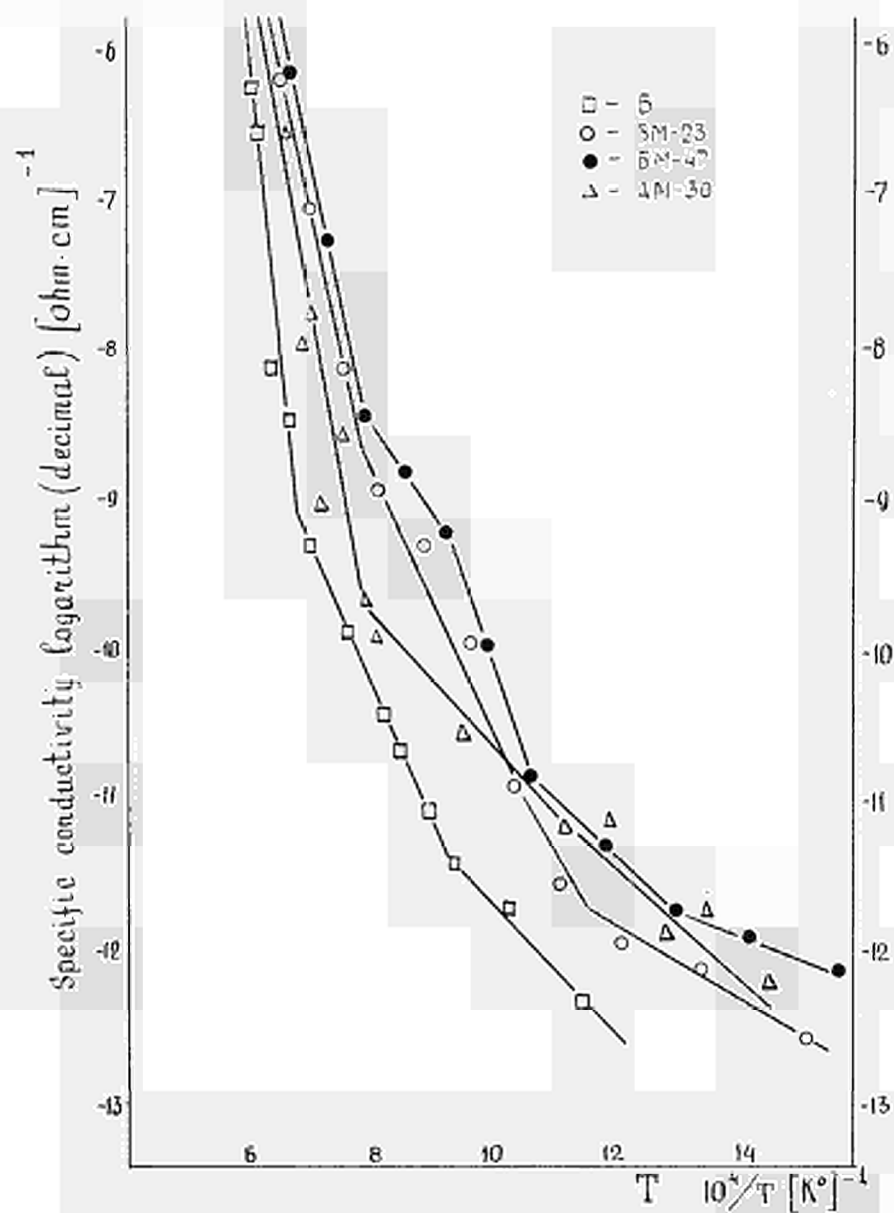


Fig. 1 Specific conductivity temperature dependence for insulating materials.

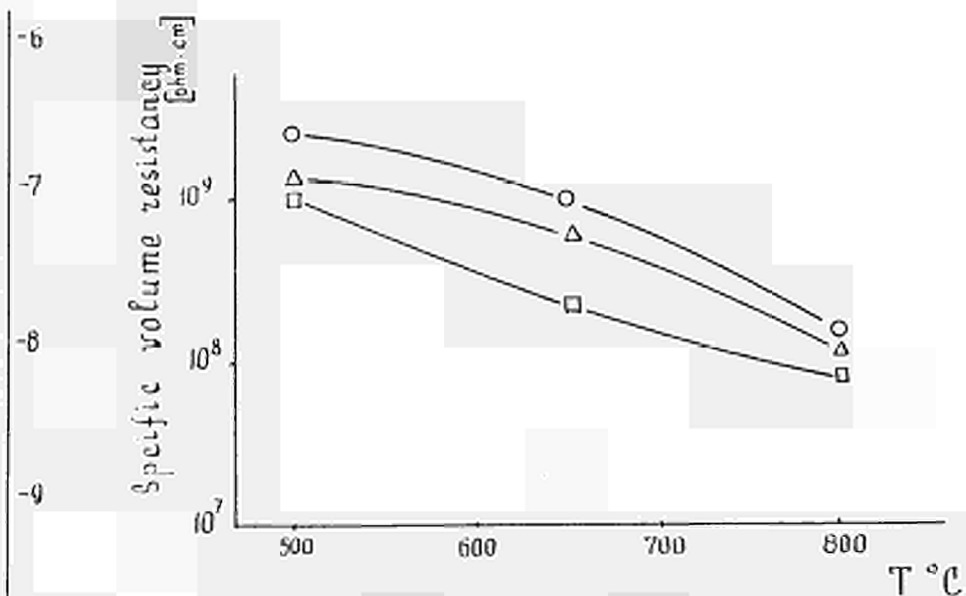


Fig. 2 Specific volume resistancy in Cs vapors.

\circ - 10^{-1} mm Hg
 \triangle - 1 mm Hg
 \square - 7 mm Hg

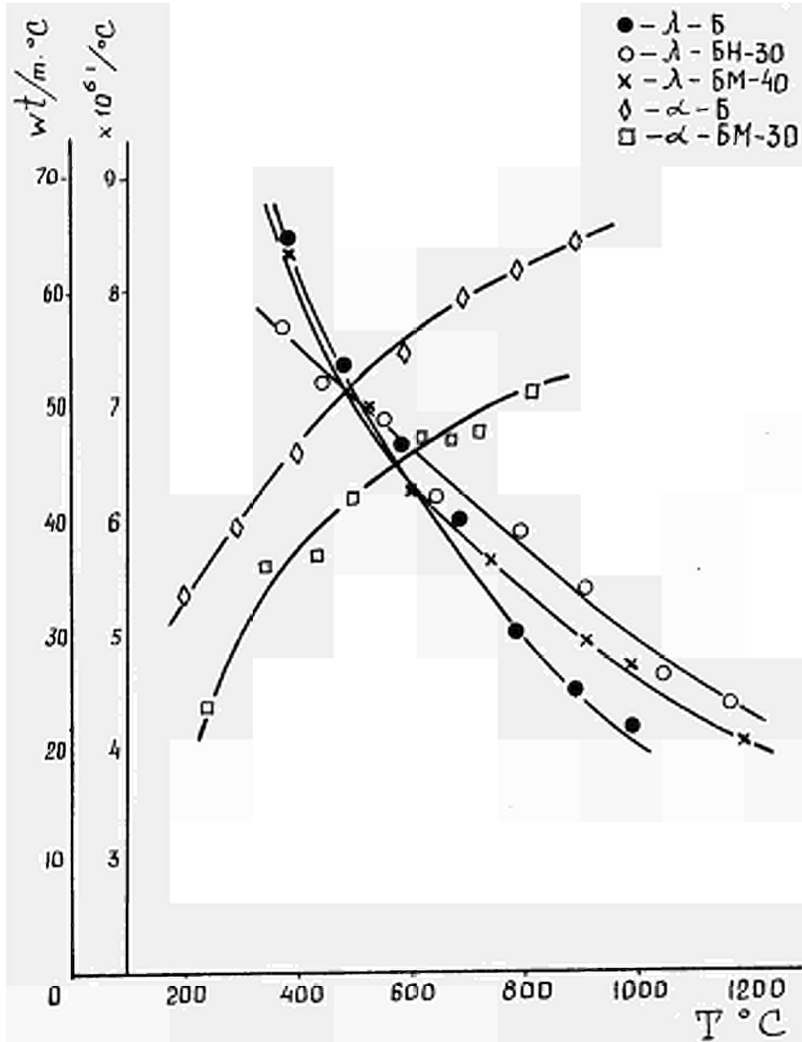


Fig.3 Temperature dependence of linear expansion coefficient and thermal conductivity.

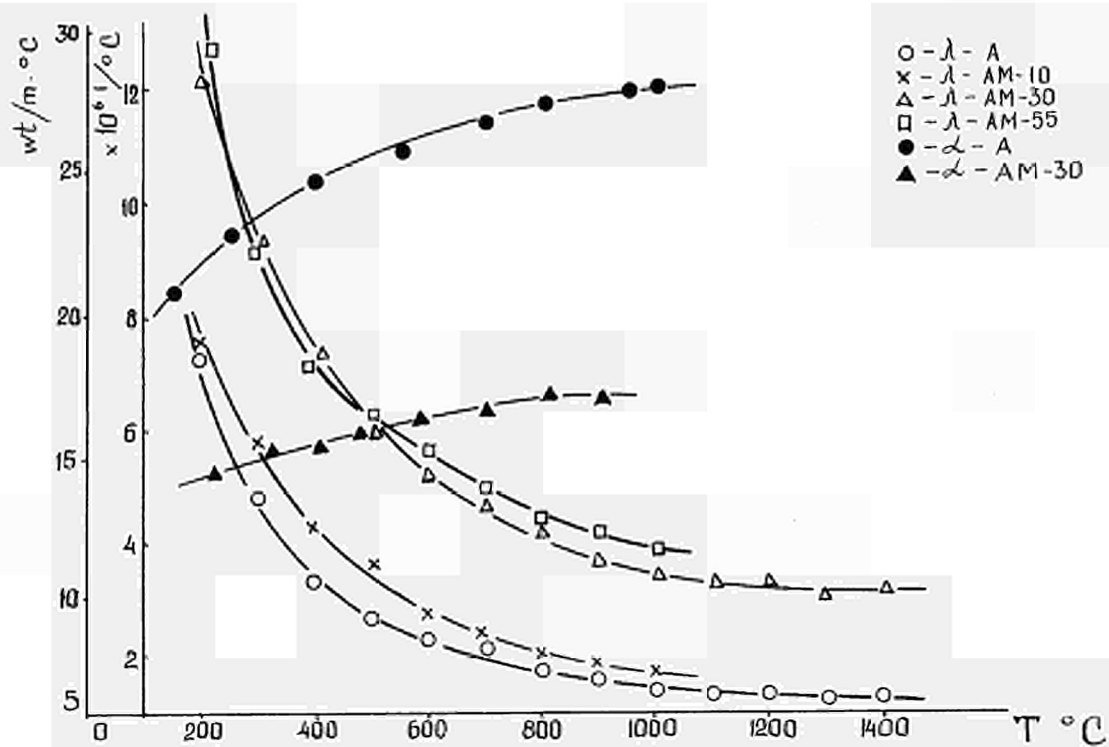


Fig.4 Temperature dependence of linear expansion coefficient and thermal conductivity.

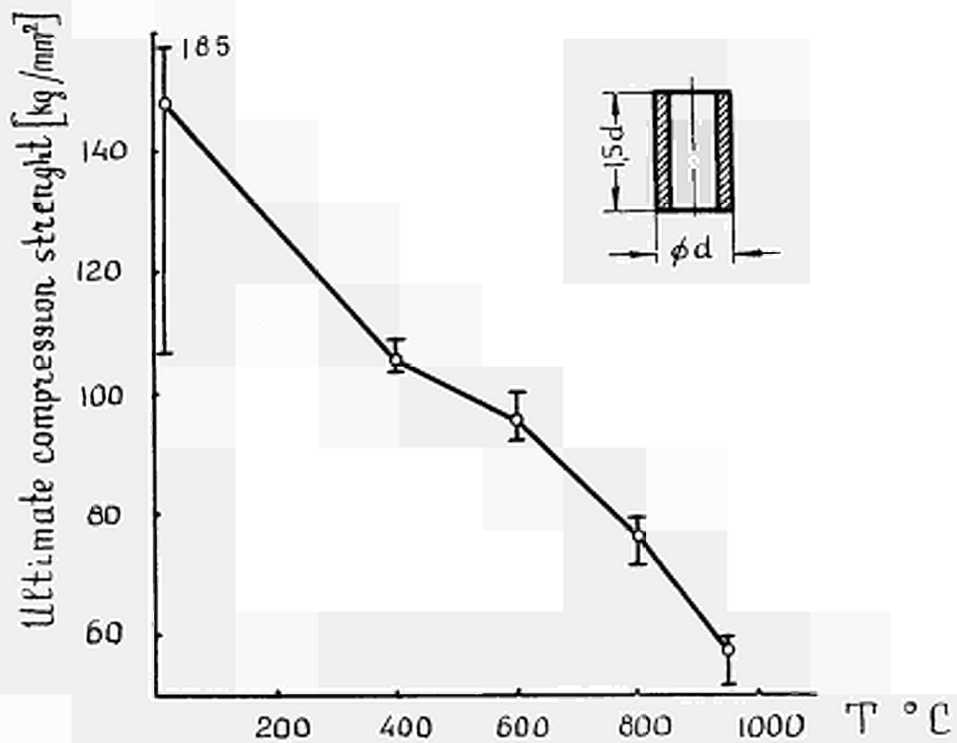


Fig 5. Temperature dependence ultimate compression strength BeO.

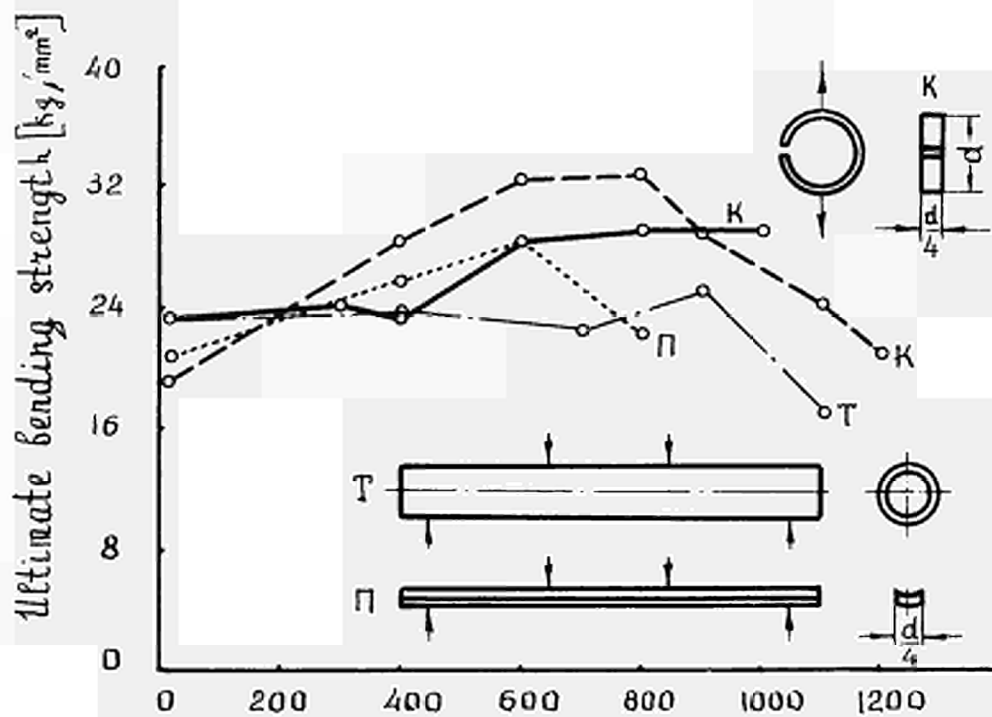


Fig 6. Temperature dependence ultimate bending strength BeO.

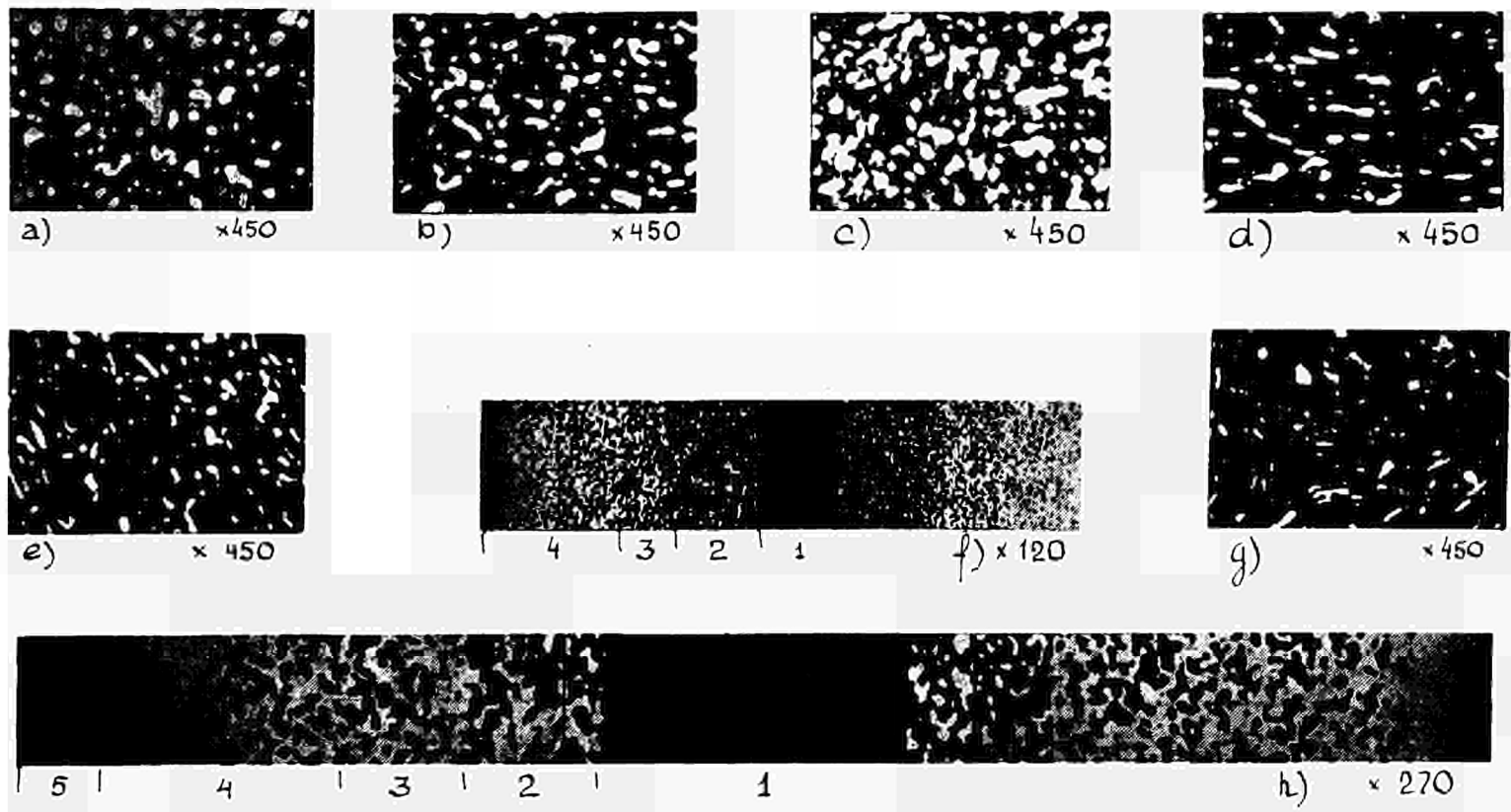


Fig.7. Microstructure of cermets.

a) BM-38; b) BM-47; c) BM-55; e) AM-40; d) AM-30 non-etched; g) AM-30 etched; f) photo of multilayer cermet; h) panoramic photo of multilayer cermet. Composition of multilayer cermet:
 1- BeO; 2- BeO+30% vol. Mo; 3- BeO+50% vol. Mo;
 4- BeO+70% vol. Mo; 5- Mo.

Table 1.

Charge composition and experimental mass index for cermet systems.

Index mass	Oxide	Metal	Volume zelation %		Weight zelation %	
			Oxide	Metal	Oxide	Metal
A	Al ₂ O ₃	—	100	—	100	—
AM-10	Al ₂ O ₃	Mo	95.7	4.3	90	10
AM-30	Al ₂ O ₃	Mo	85.3	14.7	70	30
AM-40	Al ₂ O ₃	Mo	78.0	22.0	60	40
AM-55	Al ₂ O ₃	Mo	66.8	33.2	45	55
Б	BeO	—	100	—	100	—
БН-23	BeO	Nb	90.2	9.8	77	23
БН-30	BeO	Nb	86.6	13.4	70	30
БН-46	BeO	Nb	76.3	23.7	54	46
БМ-23	BeO	Mo	92	8	77	23
БМ-38	BeO	Mo	84.5	15.5	62	38
БМ-47	BeO	Mo	79.0	21.0	53	47
БМ-56	BeO	Mo	72.0	28.0	44	56

Table 2.

Sintered samples characteristics.

Index of materials	Calculated density g/cm ³	Relative density %	Open porosity %	Average grain size μ
A	4.0	0.98	≤ 0.1	30
Б	3.01	0.98	≤ 0.1	35
AM-10	4.25	0.98	≤ 0.1	7
AM-30	4.89	0.97	0.1 ÷ 0.2	11
AM-40	5.26	0.98	< 0.1	6
AM-55	5.99	0.96	0.8	—
БН-23	3.50	0.98	0.5	11.0
БН-30	3.71	0.98	0.8	10.6
БН-46	4.23	0.97	0.9	11.4
БМ-23	3.46	0.98	0.5	6.0
БМ-38	4.10	0.98	0.9	5.5
БМ-47	4.5	0.97	0.8	5.0
БМ-56	4.9	0.96	1.1	3.6

Table 3

The values of average linear thermal expansion coefficient α_{BeO} .

$T - T_0$ °C	20-200	20-300	20-400	20-500	20-600	20-700	20-800	20-900
$\alpha \cdot 10^6$ 1/°C	5.4	6.0	6.6	7.1	7.5	7.8	8.15	8.45

Table 4

Compression and bending strength of cermet samples.

Index for materials.	Properties.	
	Compres. kg/cm ²	Bend. kg/cm ²
БН-23	12440	2800
БН-29	16390	3200
БН-46	15330	3600
БМ-23	22875	3500
БМ-38	19843	4410
БМ-47	17951	4320
БМ-56	16855	4626
АМ-30	35540	2845
АМ-40	40875	3435

On the Effect of Barium on Converter Materials

by R. Henne

Deutsche Versuchsanstalt für Luft- und Raumfahrt e.V.
Institut für Energiewandlung und Elektrische Antriebe
Stuttgart-Vaihingen, Allmandstr. 124

Abstract:

In a converter the addition of a second metal vapor to the cesium like barium vapor is expected to lead to smaller transport losses and therefore to a higher efficiency. As a further consequence the distance between the converter electrodes may be enlarged. On the other hand barium requires higher temperatures of the converter parts. Because of this and the chemical activity of the barium vapor increased corrosion of the materials is encountered. Different samples of materials, intended to be applied in our Ba-Cs-converter, have been tested at converter conditions. One series of experiments was aimed to show the compatibility of metals and ceramics in a barium atmosphere at high temperatures. In a second type of experiments the electrical conductivity of different ceramics, especially pure alumina was measured and the rate of attack by the barium vapor was observed. Thereby, temperature, residual gas and barium pressure were the parameters.

Introduction:

In order to diminish the transport losses in a cesium thermionic converter it was recently proposed to add a second metal vapor with a more electropositive character to the cesium vapor like barium, strontium or another alkaline earth metal. Here the cesium provides the ions for space charge neutralization, whereas the alkaline earth - we will restrict our work first to barium - is intended to modify the electrode work function. This principle of operation requires rather high temperatures of the converter parts. Because of this high temperature and the chemical activity of the barium vapor increased corrosion of the materials may be expected. Technological and engineering problems will be raised. There exists a considerable difference of opinion and experience in the use of alumina as an insulator in a Ba-Cs-converter. Some experiments indicated that the alumina, exposed to the vapor for a few hours, was covered with an electrically conducting layer. The conditions at which conducting layers build up or at which corrosion of the ceramic is possible were studied in our laboratory, likewise the suitability of several materials. In order to know the behaviour of the materials at converter conditions we had to simulate these in the test vessel. As a first step in our efforts we tested only the compatibility of the materials with barium vapor, at later times we will repeat the analysis at mixed vapors of Ba and Cs.

Experimental arrangement:

The reason for a series of experiments was the necessity, that the different converter materials, metals and ceramics, have to be compatible at the high temperatures, because they are in contact with a common atmosphere consisting of barium and cesium and also of vapors evaporated from the hot materials. Thus it is obvious, that there are interactions between the different parts of the converters. Therefore, several samples of oxide ceramics were tested in one vessel together with metals which we consider for use in our Ba-Cs-converter (fig.1). The samples are lined up on a pin in the barium vapor. To seal the stainless steel vessel a flat nickel ring was pressed between two edges. Thermocouples check the temperature which can be independently controlled from outside of the test vessel. In order to maintain a constant low residual gas pressure in the test vessel inspite of outgassing of the parts and in order to exclude the influence of these gases a VacIon pump had to operate continuously. The inevitable loss of barium by this operation was permissible because of an oversize barium reservoir and because of the large proportion between the liquid barium surface and the pump-out orifice (60:1). The same conditions were also in the second experimental arrangement we see in fig. 2.

A comparison of the free energies of formation of alumina and barium oxide - we see the characteristics in fig. 3 J.S.Elliot: "Thermochemistry for Steelmaking" - leads to the assumption, that barium will reduce the alumina to aluminium and that the insulating property of the ceramic will be destroyed. To see

the time dependence and the temperature effect on the surface we designed a second insert for the test vessel (fig.2), with which it was possible to measure continuously the electrical conductivity of the alumina at converter conditions during the time of heat up, of high temperature operation and cooling down. Two tantalum wires were squeezed in slits on two opposite points of the ceramic ring. Feedthroughs allow measurements from outside the vessel.

Test proceedings and conditions:

At room temperature a roughing and a diffusion pump lower the pressure in the test vessel under 10^{-4} torr; then a VacIon pump continues the procedure. A long time of outgassing at about 400 °C follows before the desired test conditions are slowly approached avoiding an excess of the residual gas pressure above $5 \cdot 10^{-6}$ torr. At the extreme case the samples had to stay 100 hours at 1000 °C at a barium pressure of about 5 torr. These may be considered the upper limits of the converter operation conditions, with the exception of the test duration, which in an actual converter may amount to many thousand hours.

Choice of the materials:

The conditions that the materials have to be useful at high temperature and in cesium atmosphere limit the choice severely. Therefore we choose for the hot electrodes refractory metals like W, Mo, Nb and Ta as test samples, and for the colder parts of the converter, samples of Ni, OFHC-Cu, stainless steel and "Vacon 70". - The coefficients of expansion of the refractory

metals and "Vacon 70", a Fe-Ni-Co alloy, are similar. - The usefulness of sapphire as windows for pyrometric temperature measurements was also of interest, but the main question was, which of the tested ceramics like extremely pure alumina, yttria, zirconia and $MgO \cdot Al_2O_3$ spinel would have the best features for use in Ba-Cs-converters.

Results:

Results of the integrated test with the different samples:

After opening of the vessel all parts were covered with a white, powdery layer, consisting of compounds of the condensed barium like barium oxide, barium hydroxide and barium carbonate which originates in contact with air. The surface beneath the powdery layer was more less attacked depending on the kind of contact with the barium.

Out of all "low temperature materials" stainless steel and Vacon 70 showed no or nearly no trace of attack. On the contrary nickel and OFHC-copper, useful in the Cs-converter, were very severely corroded. Ba and Cu have an eutectic mixture at 550 °C with 50 % Ba. Ni, at test temperature, has the high solubility of 20 % in the liquid Ba. The rate of attack on both materials is therefore a function of the barium pressure and depends on the kind of contact - with the liquid or vaporous barium. At points where even at high temperature a condensation of barium was possible, large parts of Ni and Cu disappeared. On these parts which had only contact with the barium vapor, the attack was restricted to the surface, but it was so severe as to exclude both metals for Ba-Cs-converters.

The refractory metals tungsten and molybdenum had no remarkable alteration of the surface after the corrosion test. In comparison with these tantalum and niobium were tarnished and slightly corroded, tantalum wires showed crystal textures and even dissolved parts. The use of Ta and Nb is not to be commended for long duration, especially at points where a condensation of barium may be possible.

Some remarks about the sapphire, an extremely pure monocrystal alumina are in order. Its use as a window is not promising because of the slight attack of the surface - smooth before, milky after the test - which influences the temperature, measurement with a pyrometer.

Beneath the powdery barium compounds, which can be dissolved with water, darker surfaces of the ceramics appear. Depending on the composition of the ceramic, the kind of contact and the test conditions a more or less pronounced, not easily removable surface layer was noted. In some cases small, metallic and electrically conducting spots or crystals were found. Some possible reasons will be explained later with the description of the alumina. MgO.Al₂O₃-spinnell showed a strong layer advancing from the outside to the inside with a relative sharp boundary. It possibly is an intermetallic phase between Ba and Al or Mg, formed by reduction of the ceramic by the Ba and stored up in the lattice of the spinel. A considerable alteration of the electrical and mechanical features could not be noted. Alterations of zirconiumoxide containing 3 % admixtures (binding materials) were evident. The original yellow ceramic

was bright black throughout. The specific electrical resistance decreased irreversibly. Resistance values in the range of 1 to 100 Ohms were found between points 1 cm apart. Therefore this ceramic is not recommended as an insulator.

The best results were obtained with yttrium oxide. The attack and the alterations were very slight. Unfortunately this ceramic is not so easy to obtain as pure alumina, which showed also good properties at particular conditions. Our efforts were directed especially towards the study of the behaviour of pure alumina. It is obvious that Ba-pressure and sample temperature would be of importance to the ceramic alteration, but our experiments showed that the residual gas pressure and its composition have the most effect on this. If provisions are taken to keep this pressure very low, the attack by the barium was only slight and no lasting conducting layer appeared as we see in fig. 4. - The white clouds are barium compounds. - At this conditions we observed with the arrangement shown in fig. 3, that the electrical conductivity of the alumina sample was reproducibly low and a function of barium condensation on the ceramic, i.e. only a function of barium pressure and sample temperature. As an example:

At 850 °C sample temperature and at a barium pressure of 10^{-1} Torr we could measure at the surface of the pure alumina sample between two points 1 cm apart a electrical resistivity of about 500Ω . If the VacIon pump after several hours of outgassing was switched off, i.e. if the residual gas pressure was permitted to rise, we could observe soon an irreversible

increase of the conductivity. The ceramic showed a metallic surface, which was even resistant at air access as we see in fig. 5 and 6. The process is not yet entirely understood, but we found by X-ray examination that this conducting layer consists mainly of compounds of Ba and Al with different concentrations. In one case it was Al_4Ba , an indication that at insufficient vacuum conditions the reduction of the alumina is intensified. At the same conditions we found with the integrated test some spots of molybdenum on the alumina. This can be explained by an oxidation cyclic process. Such an occurrence was observed at similar conditions with cesium. Supposedly, existing oxygen with Mo forms MoO_3 , which melts at about $860^\circ C$ and which has at test temperatures a considerable vapor pressure. It decomposes in contact with liquid barium in metallic molybdenum - building up a resistant conducting layer - as well as free oxygen, which is able to continue the destruction of the refractory metal. At favorable conditions - low residual gas pressure - no similar appearance could be noticed.

Conclusions :

The results of the tests showed, that the corrosion and the formation of conducting layers depends decisively on the quantity and the composition of the residual gas pressure. Under the following conditions, that

- 1.) there will be no difference between the behaviour of the materials in contact with barium alone and a

mixture of barium and cesium and

2.) that we have clean vacuum conditions and

3.) if the temperature of the ceramic is high enough
to avoid condensation of barium on the alumina,

we suppose, based on our experience, that pure alumina seems to be useful as insulator in a Ba-Cs-converter for several thousand hours. As electrode material we recommend W and Mo, and with certain restrictions Nb and Ta, and for the colder parts of the converter Vacon 70 and stainless-steel.

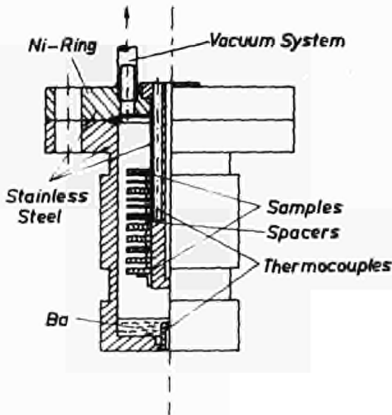


Fig. 1

Vessel for the Integrated Barium Compatibility Test

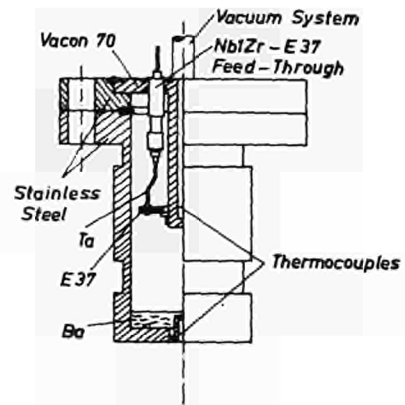


Fig. 2

Vessel for Continuous Measurement of the Electrical Conductivity

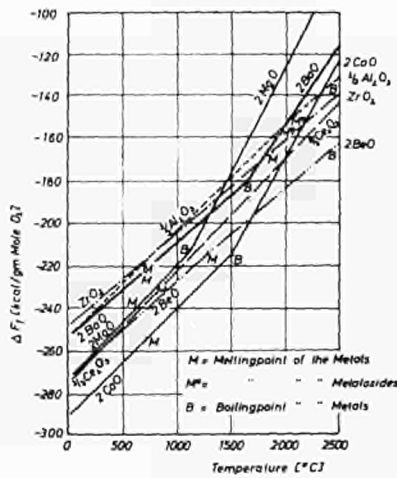


Fig. 3

Standard Free Energies of Formation of the Oxides per Gram-Mole of O_2

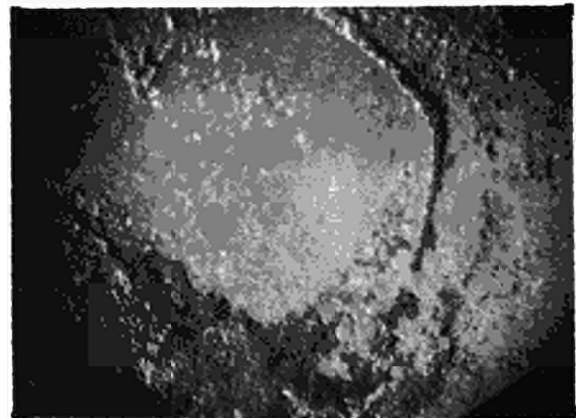


fig. 4: Al_2O_3 without reduction (10:1)

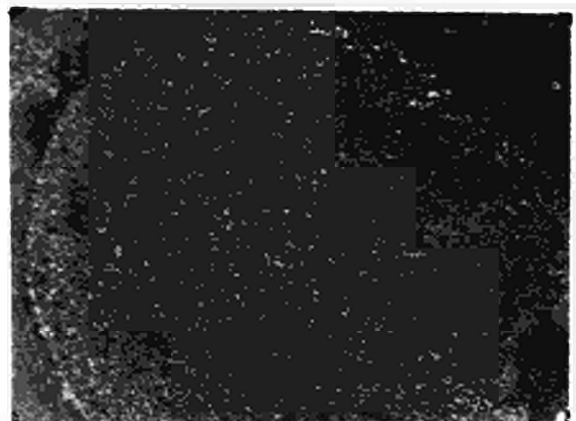


fig. 5: Al_2O_3 metallized by reduction (15:1)

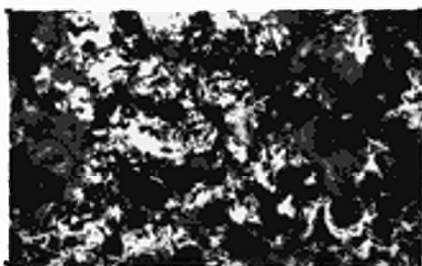


fig. 6: Part of fig. 5 enlarged (100:1)

DISCUSSION

Speaker of paper E-10: R. HENNE.

GUSKOV (USSR): Did you observe an influence of the barium vapor on the Al_2O_3 and on the contact points with the metal?

HENNE (Germany): Because of the high sample temperature we were able to keep the barium condensation on the Al_2O_3 very low. Therefore, there was only a weak attack on the surface by the barium; but it was important enough to exclude the use of sapphire windows in a barium-cesium converter. The surface was dull after the test. We found no reduction of the alumina to aluminium by the barium and no lasting metallic conducting layer, at favorable conditions, i. e. at very low residual gas pressure. At test conditions (850°C sample temperature and a barium pressure of 10^{-1} Torr) we measured a resistivity of about 500 Ohms between two points 1 cm apart, but at cold conditions this resistivity rose to 50,000 Ohms, the same value we had before the test. If we lowered the sample temperature and allowed the barium to build up a liquid phase on the sample, the electrical conductivity increased, and so did the attack.

GUSKOV: Did you observe an influence of barium on the solder which connects the metal with the ceramic or on the seal, if there is no solder?

HENNE: Until now we have not tested solders or seals in a barium atmosphere. In the second series of tests we used only feed-throughs with a palladium-nickel solder between Nb/Zr and the alumina. At the boundary of the solder we found a small hole in the alumina but the joint remained gastight.

Thermal Contact Resistance in Cylindrical Elements in
Thermionic Energy Converters

by

Yu. I. Danilov, V. K. Koshkin, T. V. Mikhailova, Yu. S.
Mikheev, S. A. Orlin

(Moscow Aircraft Institute, Moscow, USSR)

At present various types of thermionic converters are being studied. Most reactor-converters have cylindrical thermionic elements. In such reactor-converters there is usually the problem of contact between the cylindrical surfaces of individual parts. When there is radial flow through the contacting surfaces, thermal contact resistance arises. This happens when heat is transferred from the heat-emitting core to the cathode casing and among various elements of the anode pack, in which case the temperature difference reaches tens to hundreds of degrees. Since the electricity-generating elements are assembled at room temperature but operate at high temperatures (up to 1500-2000 °K), it becomes clear that the contacting elements must be designed in such a way that the temperature difference under operating conditions would be small and stable.

To solve this problem it may not be necessary to achieve uniformity of temperature drop with respect to the length of the element. On the contrary, it is entirely possible that by regulating the temperature drop in the contact area one can maintain the optimal operating conditions of thermionic converters, taking into account the non-uniformity of heat evolution with respect to the length of the reactor. Therefore the problem of temperature drop due

to contact is of great importance in the design of the reactor.

In this work a theoretical analysis and numerical calculations are made of the thermomechanical problem of contacting cylindrical surfaces. The analysis is based on the experimental studies by the authors concerning the thermal contact resistance of various high temperature materials (both ceramic and metallic) of plane geometry at various temperatures and pressures in the contact area.

Determination of Temperature Drop
 T_K and Pressure P_K at the Place
of Contact under Steady
Thermal Conditions

Let us consider the cylindrical contact pair (Fig.1).

The terms are defined as follows:

d_1, d_2 - diameters of the inner and outer cylinders respectively;

d_{noc} - diameter of the fit;

δ_0 - clearance or tightness at 0°C ;

α_1, α_2 - linear expansion coefficients;

E_1, E_2 - modulus of elasticity;

μ_1, μ_2 - Poisson coefficients

λ_1, λ_2 - thermal conductivity coefficients

q^* - heat flux per 1 m length (kcal/m·hr)

t_{w1} - temperature of the inner surface of the inner cylinder.

When the heat flux at a given value of q^* passes through the contact area between cylindrical surfaces, self-regulation of the fit takes place. This self-regulation is due, on one hand, to a decrease in the clearance and an increase in

tightness upon the increase in temperature difference Δt_K and, on the other, to a sharp decrease in the thermal contact resistance upon the increase in pressure on the contacting surfaces. The values for Δt_K and p_K are determined from the plot of two dependences (Fig.2);

1. the dependence of thermal clearance or tightness on temperature difference Δt_K (graph A);

2. the dependence of the thermal contact resistance R_K on clearance or tightness δ (graph B). Both dependences are plotted in the $(\Delta t_K, \delta)$ coordinates as follows.

The dependences of the clearance or tightness on the temperature difference of contacting surfaces Δt_K (graph A) are linear:

$$\delta = -\delta_0 + \delta_{noc} \left\{ \left[t_{w_1} + \frac{q^*(d_{noc}-d_1)}{2\lambda_1 \gamma_1 (d_{noc}+d_1)} \right] (d_1-d_2) + \alpha_2 \frac{q^*(d_2-d_{noc})}{2\lambda_2 \gamma_2 (d_2+d_{noc})} + \alpha_2 \Delta t_K \right\} \quad (1)$$

The position of dependence A on the graph can be varied within a wide interval by selecting materials having different α_1 and α_2 as well as different initial fit δ_0 values.

The temperature drop in the contact area, t_K , which is defined by the thermal resistance of the clearance or the contact area depending on δ (curves B in Fig.2) is determined as follows. In the presence of clearance ($-\delta$), thermal resistance is defined by the thermal conductivity of the medium λ_f which fills the gap and by radiant heat exchange. In the region of low clearance values the

radiation effect is small and the temperature drop becomes almost linear:¹

$$\Delta t_K = \frac{q^*}{\int_0^{\delta} \lambda f} \cdot \delta \quad (2)$$

In the case of media having different thermal conductivities, curves A have a common point m' , whose position is determined by the thickness of the equivalent clearance of the gap which depends on the microgeometry of the surfaces. Upon an increase in clearance, the role of radiation increases and the dependencies $\Delta t_K = f(\delta)$ deviate from linearity, asymptotically approaching the constant value

t_K in vacuo which depends only on the radiation coefficients of the surfaces C_1 and C_2 . The value of Δt_K in vacuo can be very high. The portions of curves B corresponding to the region of clearance can be constructed on the basis of experimental data or approximate calculation. The portions of curves B corresponding to the region of tightness ($+\delta'$) are constructed on the basis of experimental data on the dependence of thermal contact resistance on the stress in the contact area, the data being obtained for plane contacting surfaces.^[2,3]

For replotting the B curves in $(\Delta t_K; \delta')$ coordinates are used the following equation:

$$\Delta t_K = \frac{q^*}{\int_0^{\delta} \lambda f} \cdot R_K \quad (3)$$

and the relation between the contact pressure P_K and the tightness δ' based on the theory of elasticity.^[4]

$$P_K = \frac{(\delta / d_{noc})}{\frac{1}{E} \left[\frac{1 + \left(\frac{d_1}{d_{noc}}\right)^2}{1 - \left(\frac{d_1}{d_{noc}}\right)^2} - \mu_1 \right] + \frac{1}{E} \left[\frac{1 + \left(\frac{d_{noc}}{d_2}\right)^2}{1 - \left(\frac{d_{noc}}{d_2}\right)^2} + \mu_1 \right]} \quad (4)$$

The $P_K = f(\delta')$ dependence is also linear, if in the first approximation the temperature effect on the thermophysical characteristics of materials (λ, E, d, μ) is disregarded.

In some cases such a simplification is permissible in solving practical problems. When necessary one can obtain more precise relations by using reference data on the dependence of thermophysical parameters on temperature [5,6]

The dependences of „B” for various media filling the gap are shown schematically in Fig.2, together with thermal expansion characteristics of contacting cylinders (straight lines „A”). Apparently one should try to obtain a solution in the region of pressures close to the permissible maxima according to the strength of the materials by the correct selection of materials and the fit(δ'_0). In the process Δt_K will remain as small as possible..

Experimental Data on Thermal Contact Resistance

In Fig.3 are shown some experimental relations describing the contact thermal resistance of the following pairs: Steel type 1Kh18N10T + BeO; Steel type 1Kh18N10T + Al₂O₃; Mo + Al₂O₃ as the function of the load on the contacting surfaces at a constant average temperature in the contact area $R_K = f(P_K)$ at $t_K = \text{Const.}$

Based on a statistical treatment of the data and an

analysis of the experimental results, a semi-empirical equation is derived for the determination of the thermal contact resistance:

$$R_k = \frac{2(h_{cp1} + h_{cp2})}{\lambda_c \gamma K} + \frac{\pi d}{2\bar{\lambda}_M A (P_K / 3\sigma_8)^n} \quad (5)$$

where, $h_{cp1}; h_{cp2}$ - average height of micro-irregularities of contacting surfaces;

λ_c - thermal conductivity of the medium;

γ - relative thickness of the medium filling the gap;²

K - coefficient compensating for the undulation of the surface $K = 1.4$ -

d - diameter of the contact area;

$\bar{\lambda}_M$ - reduced thermal conductivity coefficient of the contacting surfaces:

$$\bar{\lambda}_M = \frac{2\lambda_{M1} \cdot \lambda_{M2}}{\lambda_{M1} + \lambda_{M2}}$$

A - coefficient compensating for the real geometry of the contacting surfaces;

P_K - specific load on the contacting surfaces

σ_8 - strength limit of the softer material;

n - exponent, $n = f(P_K)$ (Fig.4).

In Fig.5 are shown the results of the numerical analysis of a contacting cylindrical pair which can be used in designing the anode pack of a thermionic converter.

To simplify calculations the averaged thermophysical characteristics of the inner cylinder (under actual condi-

tions, a multi-layer cylinder) are used. The cylinder is considered monolithic with an outer surface made of Al_2O_3 . The material of the outer tube and its fit δ_0 are varied.

It was assumed that: $d_1 = 18$ mm, $d_f = 22.4$ mm, $d_2 = 23.2$ mm, $E_1 = 1.97 \cdot 10^6$ kg/cm², $\mu_1 = 0.3$, $\alpha_1 = 14.8 \cdot 10^{-6}$ deg⁻¹, $\lambda = 15.2$ kcal/m·hr, $q^* = 8500$ kcal/m·hr, $t_{w_1} = 775$.

The thermophysical data on the materials of which the outer wall is made ($d_2, E_2, \mu_2, \lambda_2$) are taken from the handbooks of Chirkin^[5] and Tumanov,^[6] taking into account their dependences on temperature.

From graphs (Fig.5) it can be seen that in the case of outer tube made of 1Kh18N10T steel ($d_2 = 18$) in the range of sliding fit ($\delta_0 = 0 - 40$ microm, graph A-1, A-2, A-3) very large temperature drops t_K are obtained in vacuo (up to 200°K and higher) at very low contact pressures P_K , whereas with argon as the medium the size of the gap is of the order 10 - 30 microm also at a high Δt_K . For the outer tube made of molybdenum (A-4, A-5, A-6) and niobium (A-7, A-8), much better contacting conditions

with tightness can be obtained, which results in a contact pressure up to 80 - 90 kg/cm² and considerably lower temperature drop, Δt_K , at the place of contact.

Below are given the results of a numerical analysis of contacting, which can be used in designing the cathodic pack of a thermionic converter (Fig.6). The calculation of the thermal expansion of inner rods made of uranium oxide was based on the averaged mass temperature t_{av} .

It was assumed that $d_f = 18$ mm, $d_2 = 19$ mm, $t_{w1} = 1700^\circ\text{C}$, volumetric heat evolution $q_v = 16 \cdot 10^6 \text{ kcal/m}^3 \cdot \text{h}$, for uranium oxide $\lambda_1 = 3.5 \text{ kcal/m} \cdot \text{hr} \cdot \text{deg}$, $\alpha_1 = 9 \cdot 10^6 \text{ deg}^{-1}$, $E_1 = 10^6 \text{ kg/cm}^2$, $\mu_1 = 0.3$, for the outer tube made of molybdenum $\lambda_2 = 100 \text{ kcal/m} \cdot \text{hr} \cdot \text{deg}$, $\alpha_2 = 5.5 \cdot 10^6 \text{ deg}^{-1}$, $E_2 = 2.5 \cdot 10^6 \text{ kg/cm}^2$, $\mu_2 = 0.3$.

The magnitude of the thermal contact resistance for uranium oxide and molybdenum was calculated according to the above-described semi-empirical equation. Results of the calculation are shown in Fig.7.

From graphs (Fig.7) it can be seen that by proper selection of the fit, δ_0 , one can obtain the most favorable conditions for contact with minimal Δt_K and permissible pressures, P_K , with respect to strength requirements, at the place of contact.

Influence of Reactor Radiation

In considering the performance of the electricity-generating element in the reactor it is necessary to take into account the effect of nuclear radiation on the thermomechanics pertaining to contact thermal resistance. The action of neutrons and fission fragments affects the physicomechanical properties of the construction materials, leading to the swelling of the materials, decrease in heat conductivity coefficient, changes in diffusion characteristics, and in particular it affects the creep threshold. In the case of low-power reactors, where the burn-up of the fission material is much less than 1%, these effects can be disregarded. To a lesser degree the radiation effects

would appear in anode pack elements; in this case neutrons are the only radiation source. With the burn-up efficiency up to 1% and higher, the substance, for example, uranium dioxide, undergoing fission inside the cathode pack becomes significantly changed in dimension, a fact which must be taken into account. Thus based on the experimental data of Zaimovsky, et.al. [8] it was determined that a 1% burn-up of the fission matter results in a linear increase in dimensions by approximately 0.33%. For the above-cited example, this linear increase would lead to an additional increase in the diameter by 60μ . The deformation of the cathode casing would exceed the strength limit. However, owing to high-temperature and radiational relaxation of stresses in the cathode and the gradual increase in dimension, it can be expected that the cathode casing will increase in dimension without being destroyed. This conclusion must be verified by special experiments. According to available experimental data, of much greater danger is the case where the temperature inside the heat-emitting element reaches the melting point of the core. Then radiation swelling increases 5-7 times, and the destruction of the cathode is possible.

Conclusions

1. The proposed procedure for the analysis of the conditions of contact between cylindrical surfaces makes it possible to determine the thermal resistance and pressure in the contact area.

2. The analysis of some versions of construction design of thermionic converter elements makes it possible to select such construction parameters that would provide minimal contact resistance under operating conditions with guaranteed tightness within the limits of the strength of the material.

3. Results show that in the design of elements it is necessary to take into account the radiation swelling of the cores of thermionic converters.

Literature

1. V. K. Koshkin, ed., Fundamentals of Heat Transfer in Aviation and Rocket Technology. Moscow: State Defense Publications, 1960.
2. Yu. P. Shlykov, "Calculation of Thermal Resistance Contact of Treated Metallic Surfaces," Teploenergetika, No.10, 1965.
3. V. S. Miller, Contact Heat Transfer in Elements of High-Temperature Machines. Kiev: State Publications, 1966.
4. S. D. Ponomarev, ed., Calculations of Strength in Mechanical Engineering, Vol. 2, Moscow: MEK State Publications, 1958.
5. V. S. Cherkin, Thermophysical Properties of Materials. Moscow, 1959.
6. A. G. Tumanov, Construction Materials. Moscow: USSR Academy of Sciences, 1965.
7. N. B. Demkin, Actual Shear Stress between Solid Surfaces. Moscow: USSR Academy of Sciences, 1962.
8. A. S. Zaimovsky, V. V. Kalashnikov, N. S. Golovin, Heat Emitting Elements of Atomic Reactors. Moscow: Atom. State Publications, 1966.

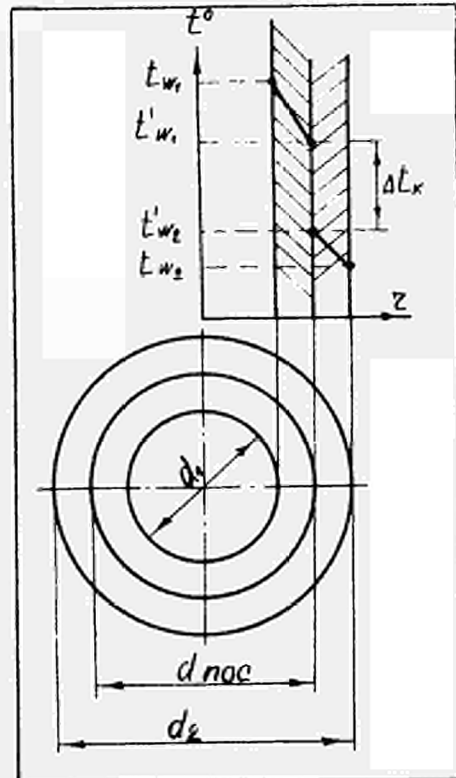


Fig1 Diagram of cylindrical contact pair and distribution of temperature along the radius.

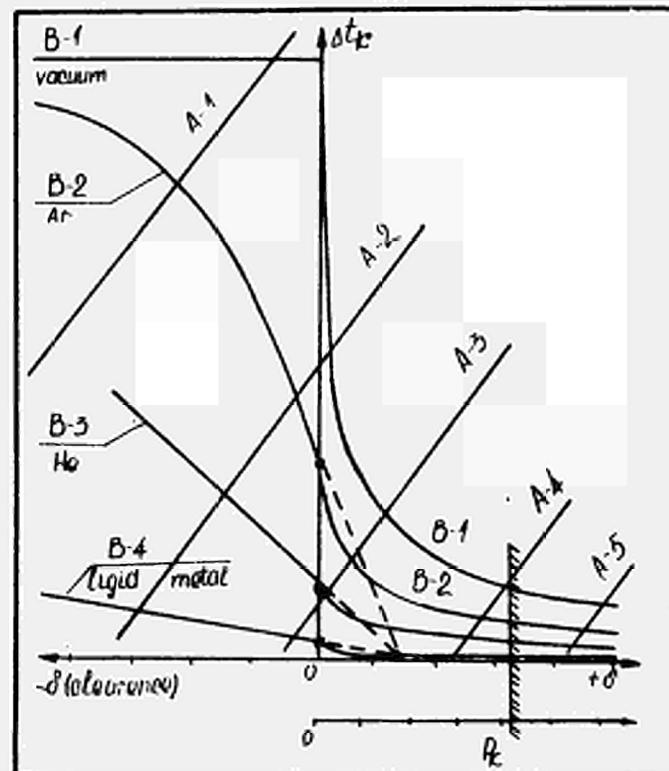


Fig2. Various operating conditions for contact pairs

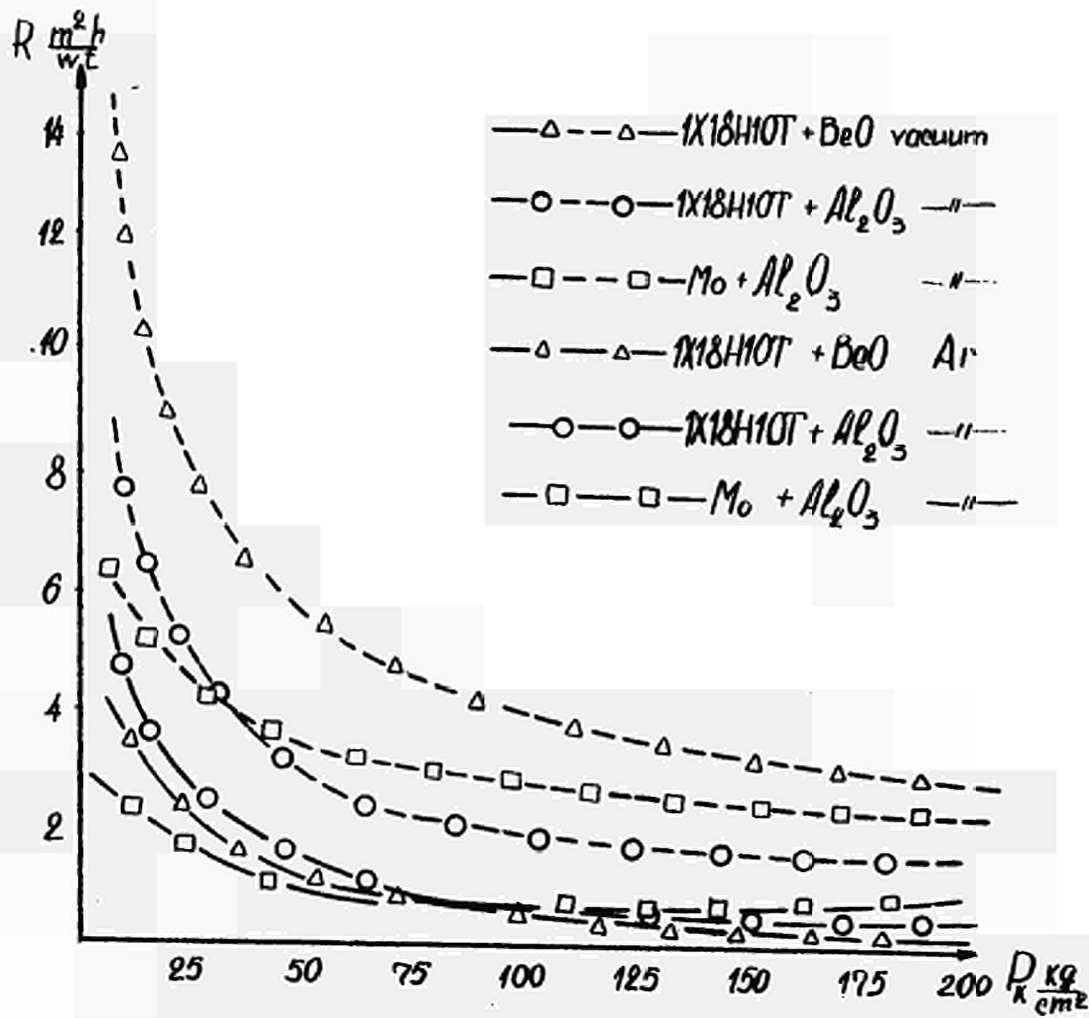


Fig3 Relation between thermal contact resistance and the load for different contact pairs at $t_k = 600^\circ C$

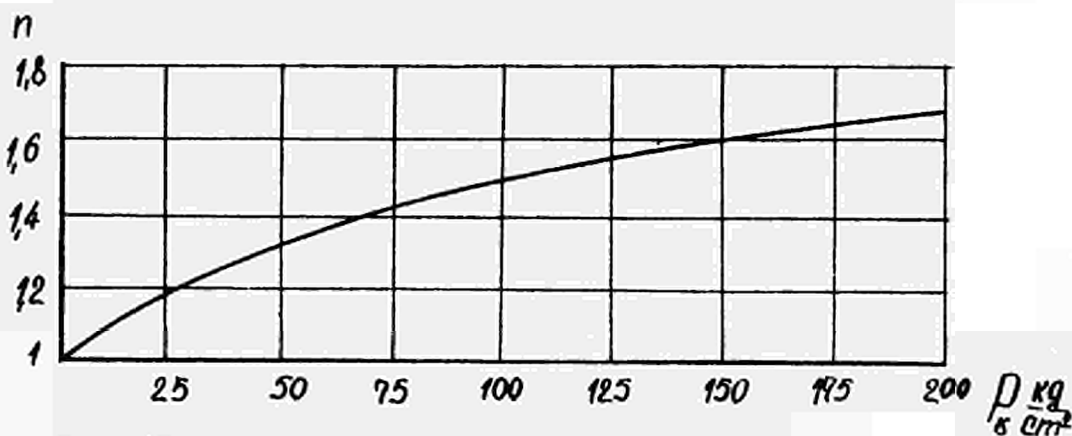


Fig4 The averaged values of the power index "n"

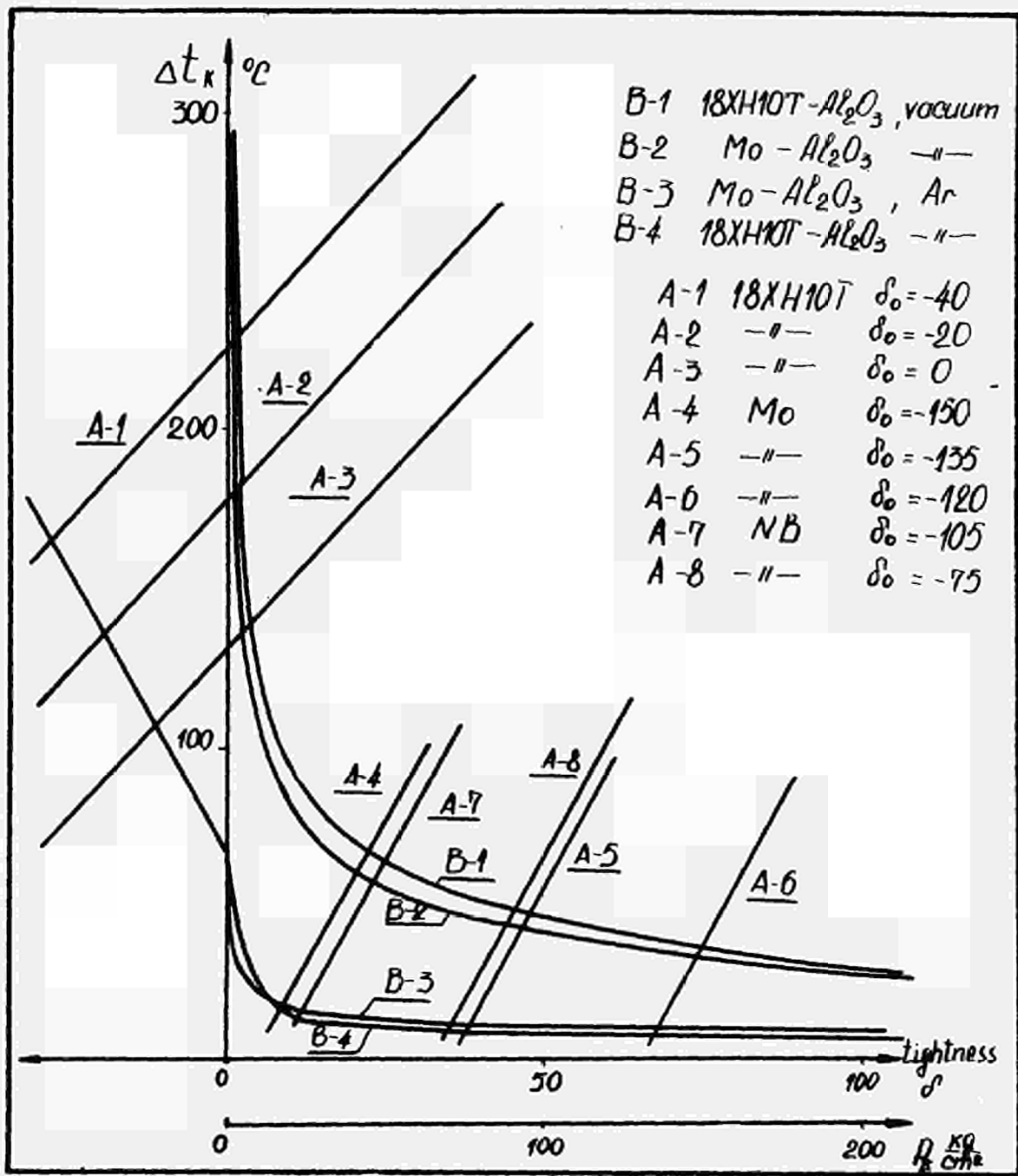


Fig5. Results of calculation of contact in the anode pack.

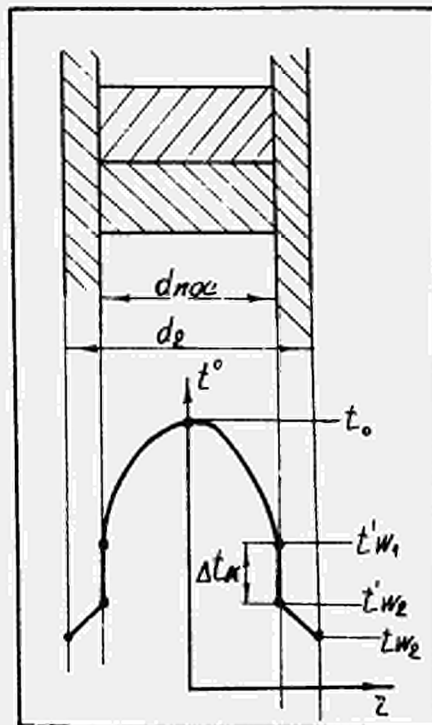


Fig6. The temperature distribution in the cathode puck.

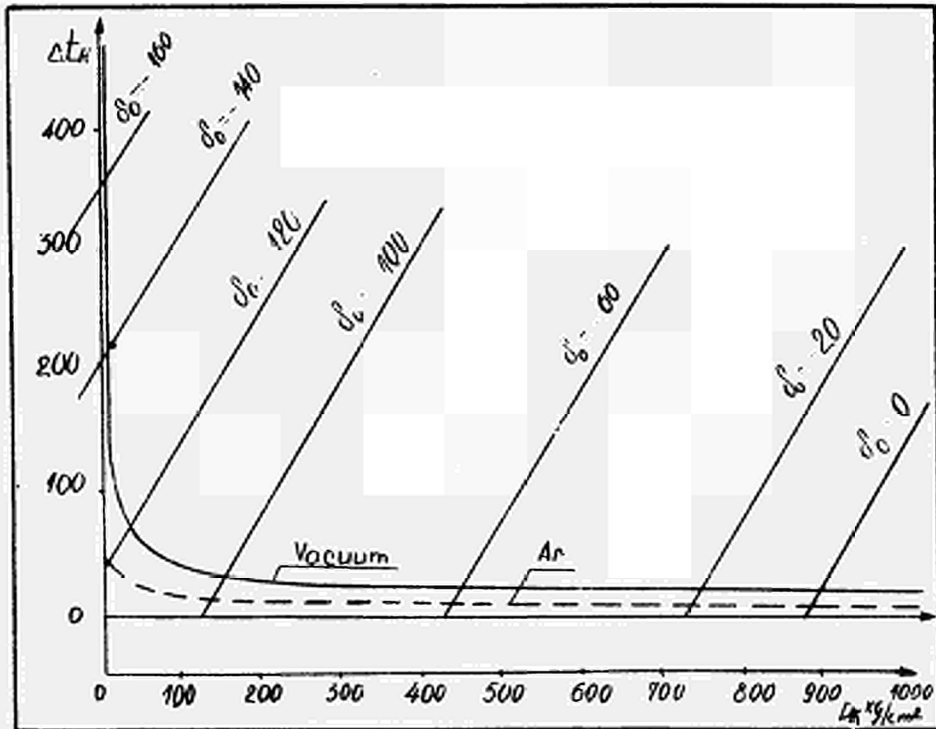


Fig7. Results of calculation of contact in the cathode puck

DISCUSSION

No speaker of paper E-11.

BEARD (USA): In your conclusion No. 2 in paper E-11 you mentioned that it is possible to select some construction parameters that would provide minimal contact resistance under operating conditions. I believe you are talking about contact resistance between the fuel and the emitter clad or the cathode as you call it. Is that correct?

KARETNIKOV (USSR): In the given case we performed experiments, but only thermal ones. How the electrical insulation behaves was not studied. But this problem was studied separately. One can find a condition when the electrical insulation is maintained.

We speak, first of all and basically of the thermal resistance of the anode assembly. But we have the same thermal picture between the emitter and the fuel. This problem is also considered in a shorter form.

BEARD: What do you do in the construction to provide for the swelling of the fuel, to maintain a minimal contact resistance and prevent swelling of the clad?

KARETNIKOV: When the burn-up of the fuel is not very great, with electrical powers 5, 10, 20, 100 kW, the mechanical expansion of the fuel is not important and can be fully compensated for by the plasticity of the emitter. It is assumed that the gas fragments must be withdrawn either into a separate volume or out of the heat-emitter element.

UTILISATION DES ALLIAGES DE TITANE EN CONVERSION THERMO-IONIQUE

M. CLEMOT, J. P. DURAND, S. E. P. Centre d'Etudes Nucléaires de Saclay

L. SEGURENS, S. R. N. A. Centre d'Etudes Nucléaires de Saclay

E. R. JOSSO, Société Métallurgique d'Imphy.

I. Introduction.

Afin d'améliorer la fiabilité des convertisseurs thermo-ioniques nucléaires, le Service d'Electronique Physique a développé le concept d'une structure entièrement métallique dans lequel "l'isolement" électrique émetteur-collecteur est assuré par un tube d'alliage à grande résistivité [1] (fig. 1).

Cette nouvelle structure impose que l'alliage ait :

- 1 - la résistivité électrique la plus élevée possible à la température de fonctionnement (600 °C à 800 °C),
- 2 - une capacité de déformation relativement importante pour réalisation de tubes étanches de faible épaisseur (0,2 à 0,3 mm),
- 3 - une inertie chimique vis à vis des vapeurs de césium,
- 4 - une aptitude à la soudure par bombardement électronique
- 5 - une faible section de capture neutronique.

Les critères 1 - 3 - 4 - 5 ont conduit à choisir le titane comme matériau de base.

Soixante alliages de titane furent élaborés en collaboration avec la Société Imphy-Kuhlmann. On indique les valeurs de résistivité et les propriétés mécaniques entre 20 °C et 1 000 °C. Les premiers essais d'obtention de tubes à parois minces sont également présentés.

II. Processus expérimental.

La phase exploratoire de l'étude s'est effectuée sur "boutons" de 35 à 45 grammes afin de connaître au point de vue résistivité, forgeabilité et résistance mécanique le plus grand nombre possible d'alliages.

Elaboration des boutons :

Ils sont élaborés au four à arc à électrode non consommable, sous pression partielle d'argon. Chaque bouton a subi jusqu'à 10 fusions successives. Le tableau 1 donne l'analyse des matières premières utilisées.

Métal	Référence	O ₂	N ₂	C	Fe	Si	Ta	W	Ni	Cr	Al	Cu
Titane	Ugine	-	322	380	T	T	-	-	-	-	-	-
Aluminium	Péchiney	-	63	60	T	T	-	-	-	-	-	-
Zirconium	Kroll	870	42	250	T	T	-	-	-	-	<20	-
	Van Arkel	20	-	140	40	<10	-	-	-	-	-	-
Molybdène	Kuhlmann	310	27	120	73	46	-	-	35	-	60	6
Vanadium	V214 brut	1400	260	490	700	1200	-	-	<30	<100	35	-
	VL2BE	1400	422	900	3000	220	-	-	-	<100	<20	-
Niobium	BE	<50	105	270	20	80	500	<100	-	-	-	-

Tableau 1 - Analyse des matières premières utilisées.

T : traces

- chiffres en p.p.m.

Forgeage :

Les boutons sont introduits dans une gaine en acier réfractaire fermée sous argon par soudure. Puis après chauffage au four, les échantillons sont écrasés en un seul coup de pilon. La gaine est alors retirée et l'échantillon est examiné. Après forgeage, les échantillons sont classés suivant l'importance des criques et des fissurations.

Investigations, mesures :

Dans chaque échantillon forgé, des barrettes sont prélevées pour les essais suivants :

- mesure de la résistivité à 20 °C et à chaud (jusqu'à 800 - 1 000 °C).
- détermination sur micro-éprouvettes des caractéristiques mécaniques de traction à 20 °C et à chaud,
- contrôle micrographique.
- Dans certains cas : étude du comportement aux vapeurs de césium.

Pour certains échantillons, les mesures de dureté et de résistivité à 20 °C sont effectuées aux divers états suivants :

- état brut de forgeage,
- état A : forgé, recuit sous vide 1 h à 900 °C, refroidissement four,
- état B : forgé, recuit sous vide 1 h à 900 °C, trempé huile,
- état C : forgé, recuit sous vide 1 h à 900 °C, trempé huile puis recuit sous vide 6 heures à 500 °C, refroidissement four.

III. Alliages binaires de titane : Ti + x (x = Zr, Si, Sn, Gd, Ce, Al).

Les alliages binaires étudiés figurent dans le tableau 2, on indique leur résistivité à 20 °C et leur dureté Vickers. En plus des éléments Zr, Si, Sn et Al, quelques alliages avec les terres rares Gd et Ce ont été étudiés, afin de perturber le réseau cristallin du titane et augmenter la résistivité de l'alliage. L'yttrium a également été retenu à cause de sa résistivité élevée : $\rho = 58 \mu.n.cm$ à 295 °K.

Au point de vue résistivité électrique les alliages Ti-Al présentent le plus grand intérêt. La résistivité des alliages augmente très sensiblement avec la teneur en Al, qui par ailleurs est la cause d'une diminution importante de l'aptitude au forgeage. La forgeabilité des alliages binaires est satisfaisante jusqu'à 6 % d'aluminium. Ceci est confirmé par les micrographies n° 2, 3, 4, 5, 6, 7 qui mettent en évidence la structure de l'alliage.

Alliages	Résistivité à 20 °C ($\mu . n . cm$)				Dureté Vickers VPN
	brut forgeage	Etat A	Etat B	Etat C	
Ti	55	-	-	-	-
Ti 10 Zr	75	76	72	-	-
Ti 90 Zr	76	77	76	-	-
Ti 1 Si	78	-	-	-	-
Ti 8,5 Si	83	-	-	-	-
Ti 4 Sn	78	-	-	-	-
Ti 6 Sn	82	-	-	-	-
Ti 8 Sn	115	-	-	-	-
Ti 1 Gd	56	-	-	-	225
Ti 3 Gd	59	-	-	-	231
Ti 1 Y	55	-	-	-	185
Ti 2 Y	53	-	-	-	162
Ti 1 Ce	58	-	-	-	244
Ti 2 Ce	58	-	-	-	216
Ti 2 Al	110	109	111	108	278
Ti 4 Al	138	138	139	137	227
Ti 6 Al	162	161	162	162	334
Ti 8 Al	175	174	176	174	348
Ti 10 Al	195	184	196	192	338
Ti 12 Al	-	-	-	-	349
Ti 15 Al	-	-	-	-	341
Ti 17 Al	224	192	224	213	324
Ti 20 Al	234	-	-	-	327

Tableau 2 - Alliages binaires de titane, résistivité à 20 °C,
Dureté Vickers,
(les pourcentages sont indiqués en poids).

Les alliages contenant plus de 6 % d'aluminium présentent un aspect pigmentaire qui laisse présumer l'existence de phases parasites sous forme de sphérules ou de bâtonnets. Ces phases peuvent être des carbures, nitrures ou xydes dus à la présence d'impuretés interstitielles. Leur étude systématique n'a pas été abordée.

IV. Alliages ternaires Ti-Al + y (y = V, Zr, Mo, Nb, Y, C, Sn, Ge, Si).

Alliages	Dureté Vickers	Résistivité 20 °C (μ.Ω. cm)	Alliages	Dureté Vickers	Résistivité 20°C (μ.Ω. cm)
Ti-6 Al-2V	348	160	Ti-6Al-0,5Sn	374	167
Ti-6Al-4V	348	169	Ti-6Al-1Sn	376	168
Ti-6Al-6V	348	161	Ti-6Al-2Sn	340	159
Ti-8Al-1V	339	188	Ti-6Al-4Sn	336	174
Ti-8Al-2V	348	189	Ti-6Al-6Sn	327	190
Ti-8Al-4V	348	181	Ti-6Al-8Sn	385	196
Ti-12Al-4V	402	170	Ti-6Al-0,25C	367	165
Ti-8Al-4Zr	348	177	Ti-6Al-0,5C	406	173
Ti-8Al-8Zr	353	189	Ti-6Al-1C	396	188
Ti-8Al-10Zr	395	188	Ti-6Al-2C	406	-
Ti-12Al-4Zr	378	-	Ti-6Al-0,5Ge	342	171
Ti-12Al-8Zr	394	196	Ti-6Al-1Ge	329	168
Ti-7Al-4Mo	368	176	Ti-6Al-2Ge	355	168
Ti-8Al-1Mo	365	172	Ti-6Al-0,5Si	365	168
Ti-8Al-2Mo	374	179	Ti-8Al-0,25Y	335	170
Ti-8Al-4Mo	348	173	Ti-8Al-0,5Y	287	183
Ti-12Al-4Mo	422	-	Ti-8Al-1Y	339	185
Ti-8Al-2Nb	348	182			
Ti-8Al-3Nb	336	183			
Ti-8Al-4Nb	348	186			
Ti-12Al-4Nb	348	-			

Tableau 3 - Alliages ternaires de titane, résistivité à 20 °C
Dureté Vickers.

Les alliages binaires Ti-Al présentant un grand intérêt au point de vue résistivité, l'élaboration d'alliages ternaires a pour but de trouver l'additif capable d'améliorer la résistivité et la forgeabilité des alliages très chargés en aluminium.

Le tableau 3 indique les alliages ternaires élaborés ainsi que leur résistivité à 20 °C et leur dureté Vickers.

Sur un même échantillon, la variation de la résistivité mesurée à 20 °C correspondant aux états bruts de forgeage, A, B, C est inférieure à 5 % (ordre de grandeur de l'erreur expérimentale), on n'indique donc que la valeur de résistivité correspondant à l'état brut de forgeage.

Le tableau 4 indique, pour les alliages les plus intéressants, les propriétés mécaniques à 20 °C, 600 °C et 800 °C.

Alliages	à température ambiante				à 600 °C sous vide				à 800 °C sous vide			
	E 0,2 kg/ mm ²	R kg/ mm ²	A %	∑ %	E 0,2 kg/ mm ²	R kg/ mm ²	A %	∑ %	E 0,2 kg/ mm ²	R kg/ mm ²	A %	∑ %
Alliages binaires												
Ti- 6Al	83,5	90,5	14	42,1	37,6	46,5	14	55	9,8	11,2	130	99
Ti- 8Al												
Ti- 4Sn	50	59	19	44	13	18	18	-	3	3,4	49	94
Ti- 6Sn	51	60	17	36	16	20	24	67	3,5	4,3	59	99
Ti- 8Sn	56	65	20	52	19	23	41	74	4,8	5,5	42	99
Alliages ternaires												
Ti- 6Al- 2V	85,8	94,2	16	41,4								
Ti- 6Al- 4V	89,6	101,5	10,4	36,7								
Ti- 8Al- 2V	91,2	104,9	17	42,7	55,9	62,1	20,3	67,6	14,6	17,5	89	99
Ti- 8Al- 4V	87,4	107,1	10,1	50,8								
Ti- 8Al- 4Zr	-	97	5,6	27,5								
Ti- 8Al- 8Zr	102,9	114,3	14,5	29,8	66,5	77,2	18,5	57	16,5	19,4	100	99
Ti- 8Al- 10Zr	92,3	103	5,7	13,7								
Ti- 8Al- 1Mo	90,1	100,3	10,4	35,8								
Ti- 8Al- 2Mo	95,7	106,5	8,7	30,5								
Ti- 8Al- 4Mo	92,8	100,2	12,7	35,8								
Ti- 7Al- 4Mo	100,1	108,7	10	34,9	62,2	70,2	13,7	68,5	16,9	20,3	47	99
Ti- 8Al- 3Nb	91	101,8	16,7	37,1								
Ti- 8Al- 0,25Y	82	89	14	20	50	60	17	37	12	13	75	65
Ti- 8Al- 0,5Y	80	85	9	40	49	60	15	35	11	12	54	60
Ti- 8Al- 1Y	85	88	1,4	6,8	52	60	1,5	4,4	11	14	46	46
Ti- 6Al- 0,25C	107,9	114	8,8	22	44,2	57,5	16,4	49,4	7	8,2	100	99
Ti- 6Al- 0,5C	108	111	1,4	3,9	48	61	11	40	10	12	73	-
Ti- 6Al- 1C	107	107	0,2	-	48	57	28	4	11	13	142	82
Ti- 6Al- 2C	-	49	-	-	54	62	1	-	11	13	90	-
Ti- 6Al- 0,5Sn	98	110	9	14	40	54	18	70	10	11	>106	n.r.
Ti- 6Al- 1Sn	96	102	10	-	37	51	16	51	8	9	>73	n.r.
Ti- 6Al- 2Sn	96	102	14	40	38	49	20	45	11	13	89	99
Ti- 6Al- 4Sn	82	86	16	49	39	50	16	53	13	14	100	99
Ti- 6Al- 6Sn	84	90	8	-	46	57	14	21	15	17	70	25
Ti- 6Al- 8Sn	-	91	-	-	61	73	13	24	18	23	71	99
Ti- 6Al- 0,5Ge	84	89	10	32	36	48	22	54	9	9	>104	n.r.
Ti- 6Al- 1Ge	87	93	16	32	39	49	20	29	10	11	>95	n.r.
Ti- 6Al- 2Ge	91	97	16	40	44	56	18	56	29	33	50	59
Ti- 6Al- 0,5Si	97	104,9	16	38,8								

Tableau 4 - Propriétés mécaniques des alliages de Titane.

n. r. = éprouvette non rompue.

V. Alliages quaternaires.

Cette étude exploratoire s'est poursuivie sur les alliages Ti-6Al 2V, Ti-6Al 4V, Ti 8Al 8Zr, Ti 8Al 2Mo, et Ti 7Al 4Mo par l'addition de 0,25 % C et 0,5 % Si. Cette addition n'a pas apporté de modification sensible de résistivité électrique à 20 °C. Par contre, la dureté a subi une augmentation de 5 à 10 %.

VI. Propriétés électriques et mécaniques des alliages de titane en fonction de la température.

Résistivité électrique :

La résistivité électrique de 34 alliages a été mesurée entre 20 °C et 1 000 °C (figures 8, 9, 10, 11, 12, 13). La résistivité maximum est obtenue entre 500 °C et 750 °C, température de fonctionnement de l'alliage dans le convertisseur thermo-ionique. Des résistivités de l'ordre de 200 $\mu\Omega\cdot\text{cm}$ sont obtenues pour l'alliage binaire Ti-6Al (courbe 5) et pour les alliages ternaires Ti-6Al-8Sn (courbe 30), Ti-6Al-4Sn (courbe 28) et Ti-8Al-1Y (courbe 24).

Des valeurs supérieures à 200 $\mu\Omega\cdot\text{cm}$ sont obtenues pour les alliages binaires Ti-Al contenant plus de 6 % d'aluminium (courbes 4, 5, 6) ainsi que pour les alliages possédant une teneur en carbone supérieure à 1 % (courbes 7 et 18). Mais ces alliages sont difficilement forgeables (alliages Ti-Al avec teneur en Al supérieure à 6 %) et se révèlent extrêmement fragiles à cause de leur dureté élevée (alliages à forte teneur en C).

Propriétés mécaniques :

Les figures 14 et 15 indiquent les valeurs des caractéristiques mécaniques :

- résistance à la traction
- limite élastique
- allongement
- striction,

mesurées entre 600 °C et 800 °C (température de fonctionnement dans les convertisseurs thermo-ioniques) pour les alliages Ti-6Al et Ti-7Al 4 Mo.

VII. Tenue des alliages de titane aux vapeurs de césium.

Des échantillons Ti-7Al-4Mo, Ti-6Al, Ti-8Al-8Zr, Ti-8Al-2V, Ti-4Sn, Ti-8Sn ont été soumis à l'action des vapeurs de césium sous une pression de 10 torr à la température de 800 °C. Des examens micrographiques et analyses effectués après 150 et 600 heures d'exposition ont révélé une parfaite résistance de ces alliages à la corrosion par le césium.

VIII. Fabrication des éléments tubulaires.

Afin d'être utilisables dans une structure thermo-ionique, les tubes d'alliages doivent avoir une épaisseur de l'ordre de 0,2 mm à 0,3 mm. Les premiers essais de filage ont donc eu pour but d'approcher au mieux ces dimensions afin de limiter les opérations d'usinage. Les 2 critères de qualité visés dans cette première phase furent d'obtenir pour l'alliage Ti 7Al 4Mo par filage, un tube de mince paroi avec géométrie correcte. Compte tenu du schéma de fabrication disponible, les conditions technologiques de gainage et de filage sont consignées dans le tableau 5.

Des tubes de dimensions 18,8 x 21 ont été obtenus (fig. 16). Ces tubes présentent des ondulations transversales dues vraisemblablement à une inhomogénéité du matériau de base.

Gainage			Acier doux	Inox	Inox 16 NCD 13				Inox 30 NCD 16	
			XC 10f	18/8						
Outil-lages	∅ filière	mm	27,4	27,4	27,4	27,4	27,4	27,4	27,4	27,4
	∅ aiguille	mm	18,6	18,6	18,6	18,6	18,6	18,6	18,6	18,6
Pré-chauffage	Mode				s/argon	s/argon	s/argon	s/argon	s/argon	s/argon
Chauf-fage	Durée	mn			30	30	30	30	30	30
	Mode		s/argon	bains sels	bains sels	bains sels	bains sels	bains sels	bains sels	bains sels
	Tempé-rature	°C	975	1 050	1 050	1 050	1 100	1 100	1 050	1 100
Lubri-fication			MoS ₂ graphite	MoS ₂ graphite	MoS ₂ graphite	MoS ₂ graphite	MoS ₂ graphite	MoS ₂ graphite	MoS ₂ graphite	MoS ₂ graphite
Rapport filage So/Si	ρ		13,03	13,03	13,03	13,03	13,03	13,03	13,03	13,03
Pression filage (contrainte axiale)	hbar		73	86	52	52	56,5	65	68	62
Vitesse filage	m/s		-	1,9	1,45	1,8	1,07	2	1,7	1,65
Résistance plas-tique à la dé-formation	hbar		30,25	35,70	21,6	21,6	23,4	27,3	28,20	26

Tableau 5 - Conditions de filage et gainage.

IX. Conclusion.

En ce qui concerne leur application aux convertisseurs thermo-ioniques, les alliages Ti-Al que nous avons étudié montrent une limite supérieure de 200 μ.Ω. cm pour la résistivité électrique. Cette valeur semble ne pas pouvoir être dépassée aisément si l'on désire conserver à l'alliage des possibilités de transformation métallurgiques. Des convertisseurs thermo-ioniques ont été réalisés avec des tubes obtenus par un filage à chaud suivi d'une passe de rectification interne-externe.

Actuellement des recherches sont poursuivies dans la voie des alliages titane-étain, avec contrôle de la teneur en oxygène.

Références.

- [1] M. CLEMOT, D. BORDE, Liaison métallique résistante à l'usage des convertisseurs thermo-ioniques - Int. Conf. thermionic electrical power generation, London, Sept. 1965.

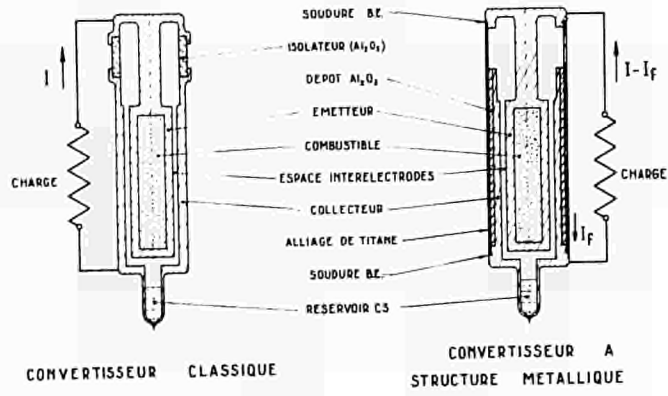


Fig. 1



Fig.2 - Ti - 4 Al
(Etat A)



Fig.3 - Ti - 4 Al
(Etat B)



Fig.4 - Ti - 6 Al
(Etat A)



Fig.5 - Ti - 8 Al
(Etat A)



Fig.6 - Ti - 10 Al
(Etat A)



Fig.7 - Ti - 17 Al
(Etat A)

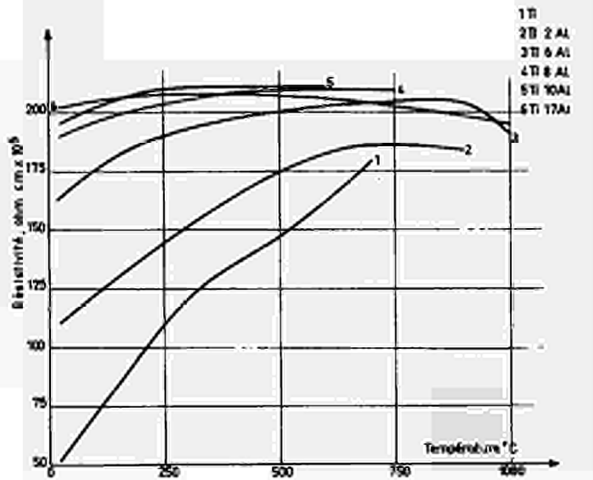


Fig. 8

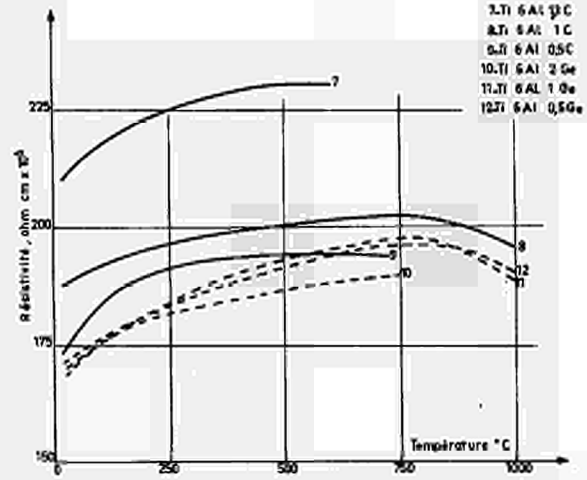


Fig. 9

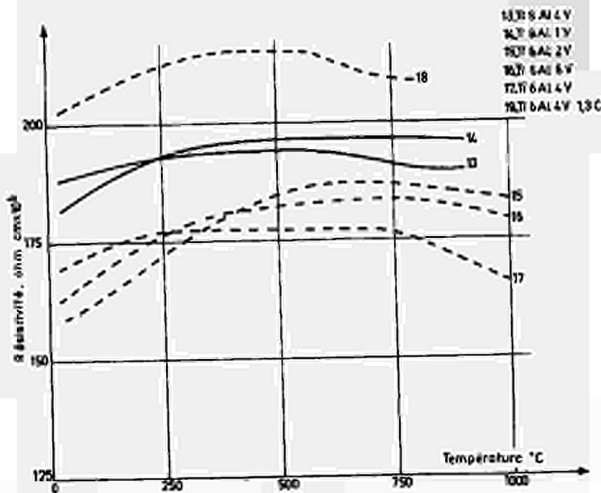


Fig. 10

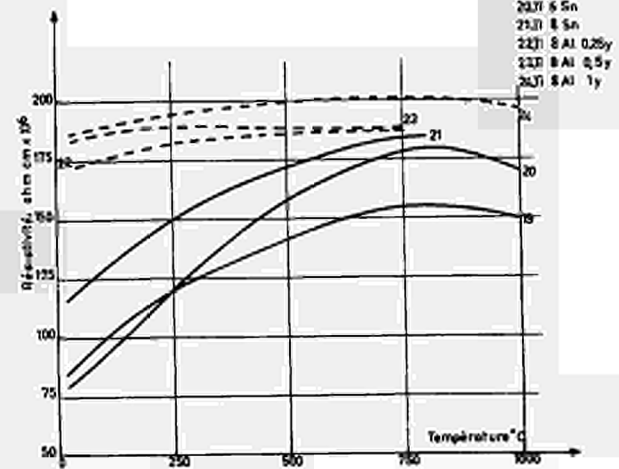


Fig. 11

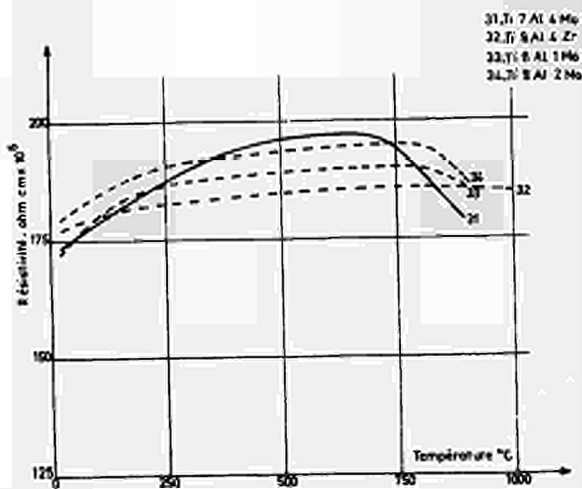


Fig. 12

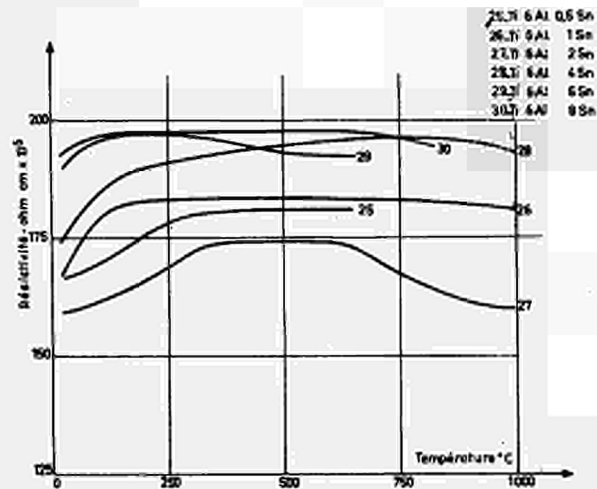


Fig. 13

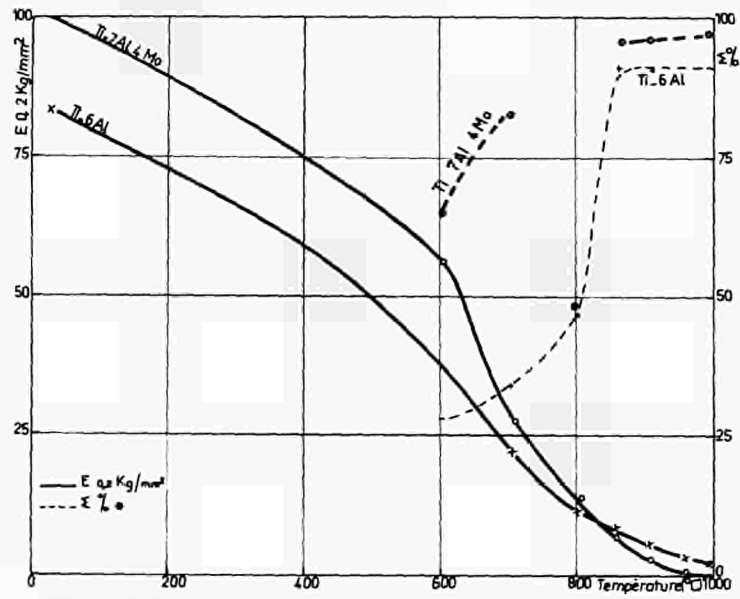


Fig. 14

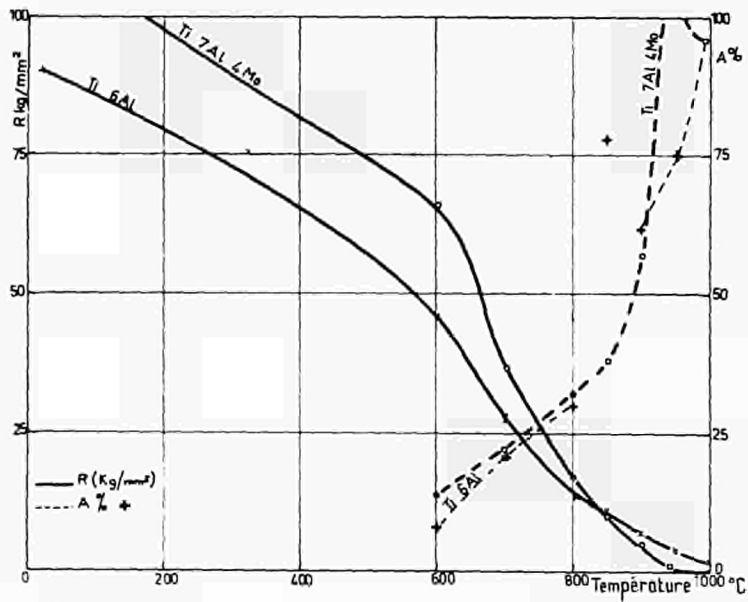


Fig. 15

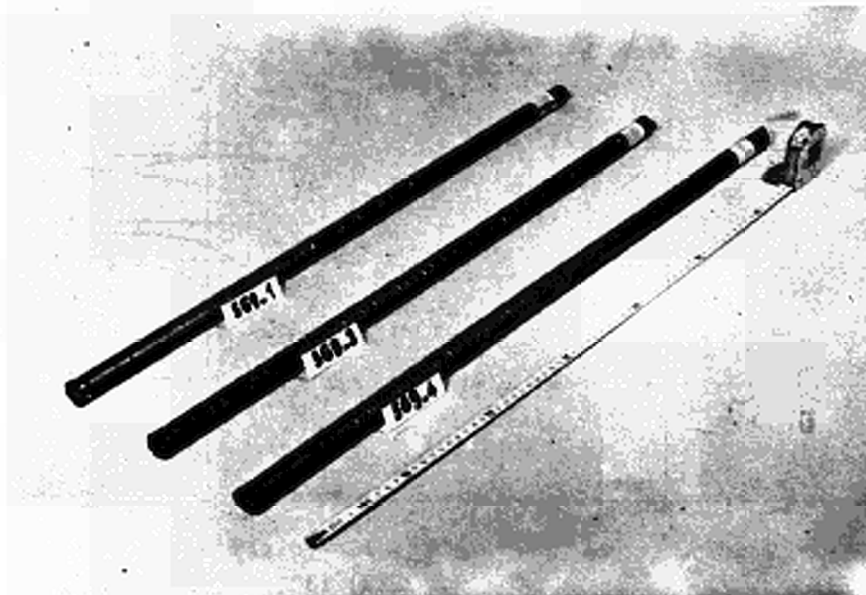


Fig. 16 - Tubes de Ti-7 Al - 4 Mo obtenus par filage

DISCUSSION

No speaker of paper E-12.

SCHOCK (USA): What is the thermal expansion coefficient of these alloys? How do they compare with Al_2O_3 , with which they are in contact?

DEVIN (France): There is no significant change in expansion coefficient due to the aluminium content of the titanium alloy, so you can use the expansion coefficient of titanium.

DAVIS (USA): Have any brazing investigations been made?

DEVIN: They were intended to be welded by electron beam welding. Brazing seems to be quite difficult because titanium and copper are an eutectic at rather low temperatures.

A low swelling, oxide fueled thermionic emitter

H. Hübner, K. Janner, M. Peehs, H. Stehle

SIEMENS AG. , 852 Erlangen (Germany)
Zentrale Entwicklung und Forschung

Abstract

Two possibilities may be considered, to overcome the problems arising from fission gas induced swelling: Either the use of fission gas retaining material, which compensates the pressure in gas bubbles by surface tension, or the ventilation of the gaseous fission products.

An attempt to solve the problem by the first idea can be made by employing a cermet containing uranium dioxide of very fine grained particle size. In this case the magnitude of swelling depends on whether the recoiled fission products diffuse back the uranium dioxide sites or form new pores

The second method of venting the gaseous fission products could be tried by using coated particles. The dimensions of kernel and coating then have to be selected so that a high fraction of fission products escape from the particle by recoiling and diffusion. Out-pile investigations, however, have shown that molybdenum coatings of adequate thickness are not stable at converter temperatures. Another way is to use sintered uranium dioxide pins. The design of the emitter must take into consideration the problems connected with fission gas venting and with uranium dioxide migration due to thermal gradients in the emitter.

A specially adapted capsule for irradiation tests with vented fuel is described and the design problems outlined. The irradiation time can be shorted by observing special conditions.

1. Introduction

The concept of the Incore Thermionic Reactor necessitates that the fuel [1] meets special requirements. A burn-up of nearly 27 000 MWd/tU must be attainable at an operating temperature of approximately 2000 °K and a power density of approximately 40 W/gU without the emitter being deformed by swelling caused by gaseous or solid fission products. The fuel and molybdenum - which is used as structural material - must also be compatible. Uranium dioxide is the best-known fuel, the properties of which suggest that it is capable of meeting the requirements. The possibilities of using uranium dioxide as a fuel in a thermionic emitter are therefore discussed below.

2. Uranium dioxide-molybdenum-cermets

The creep rate of the molybdenum at 2000°K is relatively high [2, 10]. The usual uranium dioxide-molybdenum cermets are therefore not suitable for the burn-up foreseen in the present application since an impermissibly high swelling effect due to internal fission gas pressure would result [2]. High-temperature experiments have moreover shown that a given uranium dioxide distribution in a cermet does not remain stable for long periods. We may expect the surface tension to compensate for the fission gas pressure adequately, however, if the uranium dioxide particles with a grain size $\leq 0.5 \mu\text{m}$ can be incorporated in a stable configuration.

The fission gas atoms produced during the burn-up are primarily distributed uniformly in the lattice by the recoiling effect. Since the uranium dioxide particles form ideal condensation nuclei for fission gas atoms, however, the fission gases may

be expected to be trapped at the uranium dioxide. Whether a homogeneous bubble formation also occurs depends largely on the resulting concentration of the fission gas atoms in the molybdenum matrix [3-4]; this in turn is related to the diffusion coefficient of the fission gases in molybdenum, which is up to now unknown. It is difficult to estimate theoretically the swelling effect caused by additional heterogeneous bubble formation at lattice defects, since little can be predicted about crystal imperfections of the suggested cermet.

The gas bubble distribution may be disturbed by the growth of a few bubbles in such a way that the surface tensions can no longer compensate the fission gas pressure due to the increasing bubble radius. Because of the foregoing facts, in-pile testing must be used to decide if this version is feasible.

One possibility for manufacturing the cermets described above was lined out by NUKEM [6]. A fine uranium dioxide-molybdenum mixture can be manufactured by chemically decomposing uranium-paramolybdate and subsequently reducing the molybdenum dioxide in H_2 ; this material can then be processed further by pressing and sintering.

3. Coated Particles

The emitter design requires approximately 30 vol% uranium dioxide. Fig. 1 shows the coating thickness as a function of the "uranium dioxide kernel" diameter. With a uranium dioxide diameter of 200 μm , the coating thickness is 10 μm , so that the greater part of the fission gas remains primarily in the uranium dioxide. Biersack predicts two periods of the fission gas release: the initial release period and the following steady-state release period [7]. Calculating the swelling effect results that these particles swell after the initial release period, which lasts about 100 h. But with a kernel diameter of 20 μm -with a corresponding molybdenum coating

thickness of 3 μm - the major part of the fission gas is recoiled into the coating material. If the fission gas diffusion coefficient is large enough for suppressing the homogeneous bubble formation, the fission gases will diffuse primarily to the outer surface and will be released there.

We investigated various types of coated particles to determine whether molybdenum coatings of 3 μm thickness remain stable on uranium dioxide at temperatures around 2000°K [9]. Since particles of the proposed dimensions were not available, larger particles with 3 and 5 μm thick coatings were used. The originally smooth surface was roughened already after a short period of annealing at 2000°K in a vacuum. This was determined by hot stage microscopy and also by metallographic examination after annealing. The roughening of the surface was accompanied by the particles sintering into a fritter. Annealing experiments lasting up to 239 hours caused the surfaces to roughen so heavily that some of the coatings were perforated. Figs. 2 and 3 illustrate particles in their initial state and after annealing. Activation analyses of the evaporated substance resulted in more than 99 % molybdenum. Similar effects have also been observed by other authors after in-pile experiments [8].

Since a coated particle fuel for a reactor with a predominantly thermal neutron spectrum necessitates the use of molybdenum for the metallic coating, the employment of metal coated uranium dioxide particles does not appear very promising to us.

4. Solid Uranium Dioxide

Fig. 4 shows a uranium dioxide fueled molybdenum emitter with fission gas ventilating. The electron-emitting surface is coated with a 200 μm thick tungsten layer; this reduces metal evaporation from the emitter surface and permits favourable converter data to be obtained. The uranium dioxide is in bore holes which are interconnected with a system of fission-gas ventilating channels to prevent a build-up of the fission pressure.

In order to avoid swelling of the emitter due to fission gas pressure it is important to keep open the venting system. According to Biersack [7], approximately 90 % of the fission gases generated can be expected to be released when the operating temperature of the fuel is somewhat over 2000°K.

The emitter contains the uranium dioxide in form of little sintered pins with a low smeared density. During operation the uranium dioxide relocates due to well known effects, forming axial voids. The surface of the upper annular space will be coated with uranium dioxide too. Since the inner uranium dioxide surface forms in the equilibrium state isotherms, the channels of all fuel holes converge in the annular space.

In order to ensure that the uranium dioxide does not block the inlet of the fission gas venting capillary tube, the nozzle temperature must always be kept higher than that of the isothermal uranium dioxide surface. For this purpose, the top of the nozzle is surrounded by a canned annular fuel pellet, not participating in the evaporation equilibrium. The heat produced by this extra fuel creates the required temperature drop. To minimize uranium dioxide vapour losses through the fission gas tube, its inside diameter tapers down towards the fuel chamber.

It may be expected that at 2000°K, the radially relocation of the uranium dioxide will be completed after 500 h at the latest. However, it is believed that axial temperature gradients need much larger times for being smoothed by fuel relocation. Additional fuel is therefore provided in the area above the upper annular space in order to compensate for the thermal losses at the support and of the emitter.

It is in principle impossible to avoid swelling of the uranium dioxide due to solid fission products and due to fission gas trapped in pores which consist in dynamic equilibrium in the

uranium dioxide. Because the creep rate of uranium dioxide at 2000°K in the range of low stresses is higher than that of molybdenum [2], the uranium dioxide creeps into the inner voidage with little deformation of the emitter.

5. In-pile testing of the emitter

The proposed alternatives for the emitter and the various fuels should be tested by in-pile experiments, the object of which is to evaluate the feasibility of the emitter design, the fuel relocation and the fission gas venting system in long time experiments at thermionic operating temperature (2000°K).

Measurable swelling effects of the emitter, if any, are only expected to occur close to the end of the lifetime. This is due to the fact that the molybdenum creep rate is strongly stress dependent ($\dot{\epsilon} \sim \sigma^4$) and that the stress responsible for the swelling of the emitter is built up proportionally with irradiation time.

The emitters are operated at double heat rating to shorten the in-pile time for the given target burn up. The temperature-dependent creep rate of the molybdenum is therefore doubled by raising the temperature by 45°C. This strong temperature dependence of creep rates necessitates that the emitter temperature in the reactor must be measured as accurately as possible and carefully controlled.

An irradiation capsule with the following characteristics was thus developed:

- a) Two vented emitters can be irradiated simultaneously. The pressure in the fission gas collecting system and emitter does not exceed 150 Torr.

- b) The heat is dissipated from the emitter surface (100 W/cm^2 at 1750°C) via a helium-filled gas gap (helium pressure 100 Torr, gap width 0.6 mm).
- c) The emitters are suspended in such a way that no external stresses are exerted and swelling deformation caused by irradiation can proceed unimpeded.
- d) The emitters are each instrumented with 2 WRe tungsten-rhenium thermo-couples.
- e) The emitter temperature is kept constant by additional electrical heating compensating any changes in the emitter heat rating caused by changing nuclear heat production.

A first long time in-pile experiment is to start this year in FR 2 and will last 9 months, so that a burn-up condition equivalent to 18 months operating time of the thermionic reactor will be attained.

References:

- 1) Budnick, Janner, Jung, Oldekop, Peehs
"Thermionische Kernreaktor-Energieversorgungsanlagen für einen Leistungsbereich von 5-50 kWe"
DGRR Monographs, Vol. 2, 1966
- 2) Böhm, Jung, Peehs
"Entwicklung von thermionischen Reaktorbrennelementen und Bau von Versuchszellen"
- 3) Greenwood, Boltax
"The role of Fissions Gas Re-Solution during Post-Irradiation Heat Treatment"
J. Nucl. Nat. No. 2, (1962)
- 4) Greenwood, Foremann, Rimmer
"Role of Vacancies and Dislocation in the Nucleation and Growth of Gas Bubbles in Irradiated Fissile Material"
J. Nucl. Nat. 4 (1959)

- 5) Agranowich, Mikhlin, Semenov
"Kinetics of Swelling Produced in Fissionable Materials
by Supersaturation of the Gaseous Phase from a Supersaturated
Solid Solution"
Soviet Atomic Energy 15,5 (63)
- 6) Liebmann, Hackstein, Huschka
Private Communication
Oct. 1965
- 7) Biersack
"Blasenwanderung und Spaltgasabgabe aus UO_2 "
Nukleonik, Issue No. 8, Vol. 8
- 8) Winkenbach, Heidtmann
"Untersuchungen an bestrahlten mit UO_2 gefüllten
Mo-Emittern"
BBC-Nachrichten Vol. 49, 1967
- 9) Hübner, Janner, Peehs
"Entwicklung von Emittern und Kollektormehrschicht-
systemen"
Report for the German Federal Ministry of Research, 1965
- 10) General Electric Material Testing Report
GEMP 270 A, 1964

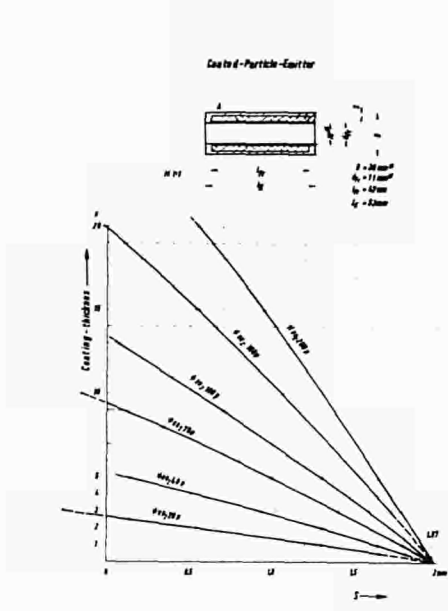


Fig. 1
Coating thickness of the coated particles as function of the emitter wall thickness.

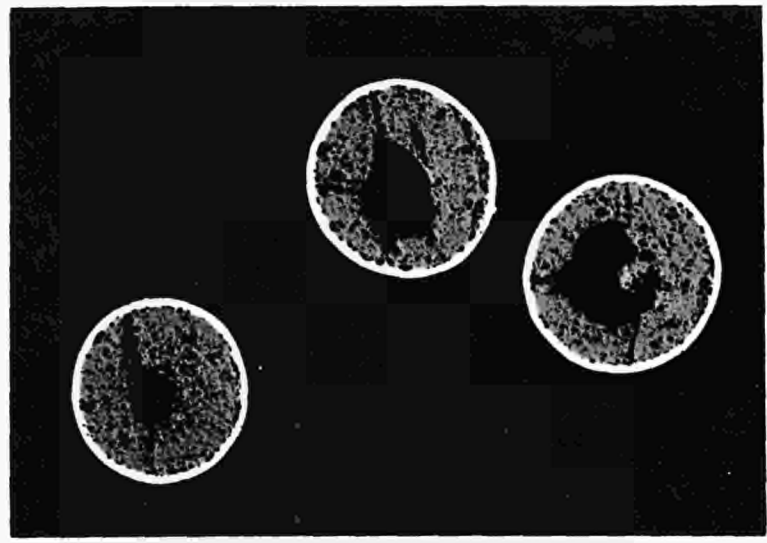


Fig. 2
Coated particles before heat treating (200:1)

200:1

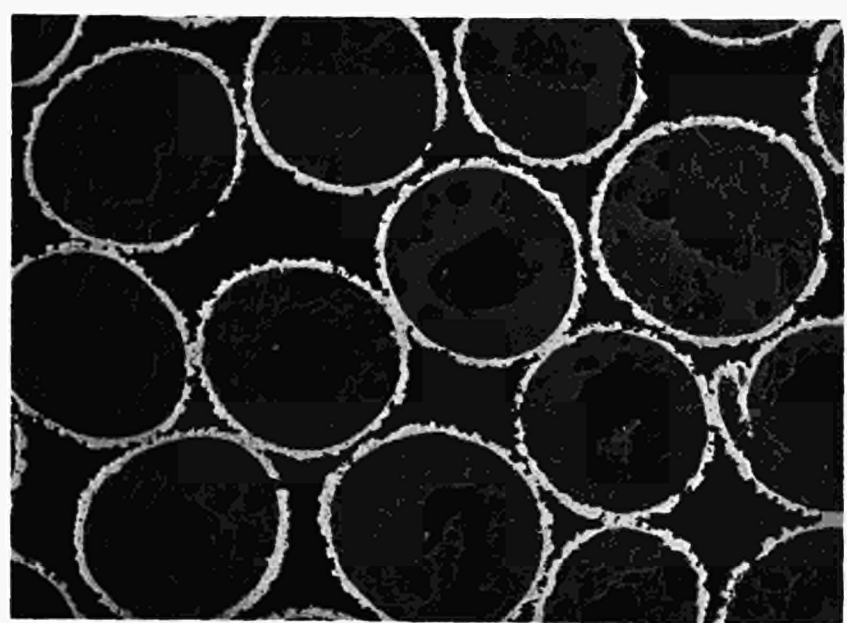


Fig. 3
Coated Particles after 239 h annealing at 1860°C

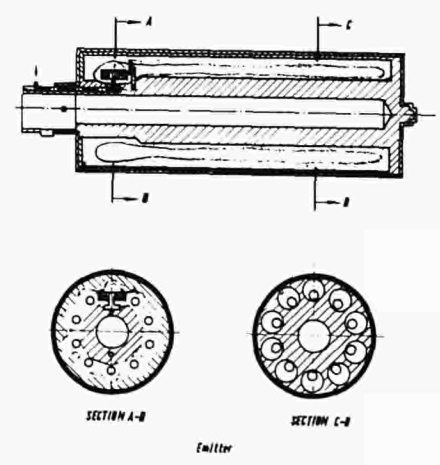


Fig. 4
Emitter design

200:1

DISCUSSION

Speaker of paper E-14: M. PEEHS.

HAUSNER (Euratom): You mentioned that it is necessary to have a UO_2 -particle size of approximately 0.5μ in order to retain fission gases. Is it possible to keep this dimension after densification or after a heat treatment at high temperatures?

PEEHS (Germany): Since this is one of the great problems, I have mentioned in the paper that we have found by annealing cermet that UO_2 distribution is not stable at converter temperature and much work must be done to fix the UO_2 at the uranium distribution.

Concerning the vented UO_2 -emitter with MO_2 -pellets, I want to make a remark. The problem which we have is to vent fission gas at a hot hole and not to have a cold hole in the emitter, for we must have little distance between the active emitter lengths.

SCHOCK (USA): Are you saying that it is easier or harder to have a hot vent hole rather than a cold vent hole? And why?

PEEHS: I believe the hot vent hole is not so easy, for UO_2 can migrate through and come to the venting system and may perhaps block the venting system. That is a difficulty we have.

THERMAL RESISTANCE OF MULTILAYER CYLINDRICAL
ELEMENTS IN THE THERMIONIC CONVERTERS

E.S.A. Arkin, S.F. Kukushkin,
H.A. Murinson, B.G. Ogloblin,
P.Z. Cherepanov, V.S. Chekhovich.
The Academy of Sciences,
Moscow, the USSR.

Thermal converter operation and performances depend on temperatures and stresses arising in the elements. The influence of various factors on the temperatures and stresses in the main elements of the thermionic converter (collector and emitter multilayer cylindrical elements) is considered below.

As the heat flux passes through the multilayer cylindrical elements during the operation, the temperature gradient between the inner and outer layers appears, which depends on the heat flux value and the sum of layer material and layer contact thermal resistances.

Thermal resistance of the contact depends on the mechanical properties and fineness of machining of the contacting surfaces and contact forces.

These forces are influenced by the initial clearance or tightness values and the layer temperature strains.

Under high operation temperatures and extensive life-time the creep strains in certain layers can reduce contact forces and increase thermal resistance.

In the devices, where numerous start-ups take place, the difference between residual strains can cause the lamination of the system; that will be followed by the appearance of additional contact surfaces and consequently by the growth of thermal resistance.

To provide the required stable thermal resistance and to prevent the cylindrical elements lamination under the thermal cycling, it is necessary to choose properly the layer materials, their thicknesses, fineness of contacting surfaces machining and the initial clearance or tightness values.

The influence of various factors on the thermal resistance of the multilayer cylindrical elements and on its stability during the operation can be described by the system of equations, including:

the temperature strain equation;

the thermal conductivity equation considering the thermal resistance of the layers and their contacts;

creep equation.

As an example a concept of composite collector system is considered. (see fig.1). The inner cylinder tube (collector) with an insulating layer on the outside and a special coating for reduction of the contact thermal resistance, is inserted in the outer tube (casing) securing an initial clearance or tightness. The heat flux, passing from the collector to the casing, is taken off by the coolant.

In this case the equation system is as follows

$$\left\{ \begin{aligned} & \alpha_c z_2 \left(\frac{T_2 + T_1}{2} - T_H \right) + \frac{z_2}{E_c(z_2^2 - z_1^2)} \left\{ 2p_1 z_1^2 - p_2 [(1 - \mu_c) z_2^2 + (1 + \mu_c) z_1^2] \right\} - \\ & - \alpha_d z_2 \left(\frac{T_2 + T_3}{2} - T_H \right) - \frac{z_2}{E_d(z_2^2 - z_3^2)} \left\{ p_2 [(1 - \mu_d) z_2^2 + (1 + \mu_d) z_3^2] - 2p_3 z_3^2 \right\} = 0 \\ & \alpha_d z_3 \left(\frac{T_2 + T_3}{2} - T_H \right) + \frac{z_3}{E_d(z_3^2 - z_2^2)} \left\{ 2p_2 z_2^2 - p_3 [(1 - \mu_d) z_3^2 + (1 + \mu_d) z_2^2] \right\} - \delta - \\ & - \alpha_f z_3 \left(\frac{T_4 + T_3'}{2} - T_H \right) - \frac{z_3'}{E_f(z_4^2 - z_3'^2)} \left\{ p_3 [(1 - \mu_f) z_3'^2 + (1 + \mu_f) z_4^2] - 2p_4 z_4^2 \right\} = 0 \\ & T_4 = T_g + q_1 \frac{z_4}{z_1} \frac{1}{k_g} \\ & T_3' = T_4 + q_1 \frac{z_4^2 - z_3'^2}{2z_1 \lambda_f} \\ & T_3 = T_3' + q_1 \frac{z_3'}{z_1} \frac{1}{\frac{2 \cdot 10^4 p_3 \frac{2\lambda_f \lambda_m}{\lambda_f + \lambda_m} + \lambda_w}{3\sigma_B} + \frac{\lambda_w}{h}} \\ & T_2 = T_3 + q_1 \frac{z_3^2 - z_2^2}{2z_1 \lambda_d} \\ & T_1 = T_2 + q_1 \frac{z_2^2 - z_1^2}{2z_1 \lambda_c} \\ & \frac{z_3'}{E_f(z_4 - z_3')} \frac{dp_3}{d\tau} + \frac{z_2}{E_c(z_2 - z_1)} \frac{dp_2}{d\tau} + \alpha_c \frac{dT_2}{d\tau} - \alpha_f e^{\beta_f T_3'} \left(\frac{z_3' p_3}{z_4 - z_3'} \right)^{n_f} - \alpha_c e^{\beta_c T_2} \left(\frac{z_2 p_2}{z_1 - z_1} \right)^{n_c} = 0 \end{aligned} \right.$$

where

- α is the linear expansion factor of the layer material;
- T is the temperature on the layer surface;
- E is the modulus of elasticity of the layer material;
- p are the specific forces, acting upon the layer surface;
- μ is Poisson's ratio of the layer material;
- δ is the initial clearance (tightness) value; $\delta = z_3' - z_3$,
- q_1 is the heat flux value through the collector inner surface;
- k_g is the heat transfer factor between the casing and the coolant;
- λ is the thermal conductivity factor of the layer material;
- λ_m is the thermal conductivity factor of the special

coating material;

λ_w is the thermal conductivity factor of the media between the contact surfaces (assumed to be λ_w^2

$$= 2,5 \cdot 10^{-3} \frac{\text{K cal}}{\text{m} \cdot \text{hour} \cdot ^\circ\text{C}}) ;$$

h is the average value of the contact surface roughness;

σ_0 is the minimum value of the ultimate strength of contact surface materials (special coating and casing);

a, b, n are the empirical factors, characterizing the material creep rate under the variable temperature and stress;

τ is time.

The investigation is carried out on the following assumptions.

1. The collector system with uniform heat supply is infinitely long;
2. No thermal resistance between the insulation and collector and between the insulation and special coating exists during the operation.

The main initial data.

1. The initial coolant and layers temperature $T_{\text{H}} = 20^\circ\text{C}$.
2. The operational coolant temperature $T_{\text{O}} = 600^\circ\text{C}$.
3. $\tau_1 = 10 \text{ mm}$, $\tau_2 - \tau_1 = 0,8 \text{ mm}$, $\tau_4 - \tau_3 = 0,4 \text{ mm}$
4. The collector and casing material is the stainless steel.
5. The contact surfaces are in vacuum.

The characteristic charts of thermal resistance and contact stress plotted against the various parameters are shown in fig.2 - 6. In fig.2 - 5 the characteristic curves of thermal resistance (ΣR) and contact stress (P_s) in the

cylindrical elements of the collector system under consideration are plotted against the initial clearance (tightness) under the following conditions:

Fig. 2. The contact surfaces are of stainless steel and nickel, the fineness machining is of $\sqrt{5}$, $\sqrt{7}$ and $\sqrt{9}$ th classes, heat flux $q_1 = 2 \cdot 10^5 \frac{\text{k cal}}{\text{m}^2 \cdot \text{hour}}$, the insulation thermal conductivity factor

$$\lambda_d = 1,0 \frac{\text{k cal}}{\text{m} \cdot \text{hour} \cdot \text{OC}} ;$$

Fig. 3. The contact surface materials are stainless steel - nickel, stainless steel - copper, stainless steel - aluminium, the fineness of machining is of the $\sqrt{7}$ th class, $q_1 = 2 \cdot 10^5 \frac{\text{k cal}}{\text{m}^2 \cdot \text{hour}}$

$$\lambda_d = 1,0 \frac{\text{k cal}}{\text{m} \cdot \text{h} \cdot \text{OC}} .$$

Fig. 4. The contact surface materials are stainless steel and nickel, the fineness of machining is of the $\sqrt{7}$ th class. Heat flux values are $2 \cdot 10^5$, $4 \cdot 10^5$ and $6 \cdot 10^5 \frac{\text{k cal}}{\text{m}^2 \cdot \text{hour}}$; $\lambda_d = 1,0 \frac{\text{k cal}}{\text{m} \cdot \text{h} \cdot \text{OC}} .$

Fig. 5. The contact surface materials are stainless steel and nickel, and the fineness of machining is of the $\sqrt{7}$ th class.

The insulation thermal resistance $R_d = \frac{z_1 - z_2}{\lambda_d}$ values are

$$0; \quad 4,5 \cdot 10^{-4} ; \quad 9 \cdot 10^{-4} \left(\frac{\text{m}^2 \cdot \text{h} \cdot \text{OC}}{\text{k cal}} \right) ,$$

$$q_1 = 2 \cdot 10^5 \frac{\text{k cal}}{\text{m}^2 \cdot \text{hour}} .$$

In fig. 6 the thermal resistance of the system and contact stresses are plotted against the time of operation under the various initial contact forces. The contact surface materials are stainless steel - nickel and stainless steel - aluminium, the fineness of machining is of the $\sqrt{5}$ th class,

$$q_1 = 2 \cdot 10^5 \frac{\text{k cal}}{\text{m}^2 \cdot \text{hour}}, \quad \lambda_d = 1,0 \frac{\text{k cal}}{\text{m} \cdot \text{h} \cdot ^\circ\text{C}}.$$

Under the assumed initial data the tangential stresses in the casing and collector are related to the contact stresses as follows

$$\begin{aligned} \sigma_f &\cong 30 P_3 \\ \sigma_c &\cong 13 P_3 \end{aligned}$$

and under the allowable stresses

$$[\sigma_f] = 14 \frac{\text{kg}}{\text{cm}^2} \text{ and } [\sigma_c] = 10 \frac{\text{kg}}{\text{cm}^2}$$

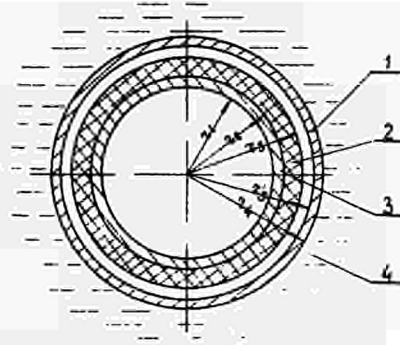
the contact stress value P_3 can be as high as $P_3 \cong 35 \frac{\text{kg}}{\text{cm}^2}$ which considerably exceeds the value $P_3 \cong 2 \frac{\text{kg}}{\text{cm}^2}$, corresponding to the operational conditions with the stabilized thermal resistance.

The analysis of obtained data for the design under consideration permits to draw the conclusions, valid for rather wide variety of multilayer cylindrical elements, operating under the high-temperature conditions.

1. Thermal resistance stability of cylindrical, multilayer collector or emitter system during the operation is determined by the layer strain rate. The layer stresses determining the creep strain safe value, are a few times less than those determining the construction strength.

2. The improvement of machining fineness of the contact surfaces, lowering of the separate layers thermal resistance, and especially using of more plastic and heat conductive materials in contact results in the lowering of thermal resistance. At the same time it is necessary to choose the value of initial clearance (tightness) between the layers properly in order to provide for the performance stability.

3. In such thermionic converters where the limitations of material thickness and of thermal resistance are required, it is necessary to use for interlayer contact the materials of high plasticity including liquid metals and gases.



1-casing (f), 2-insulation (d);
3-collector (c); 4-coolant (g)

Fig 1. Schematic representation of the multilayer cylindrical element of a thermionic converter.

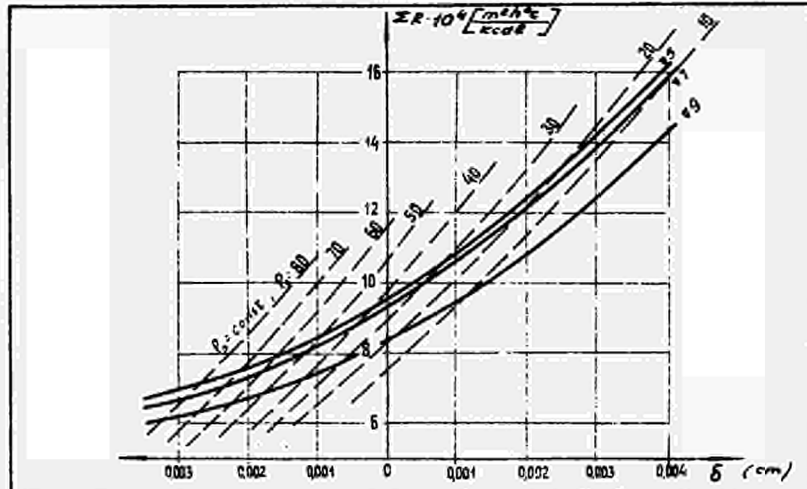


Fig 2. Dependence of ER and P₃ on δ and contact surface fineness of machining; contact surface materials are stainless steel and nickel

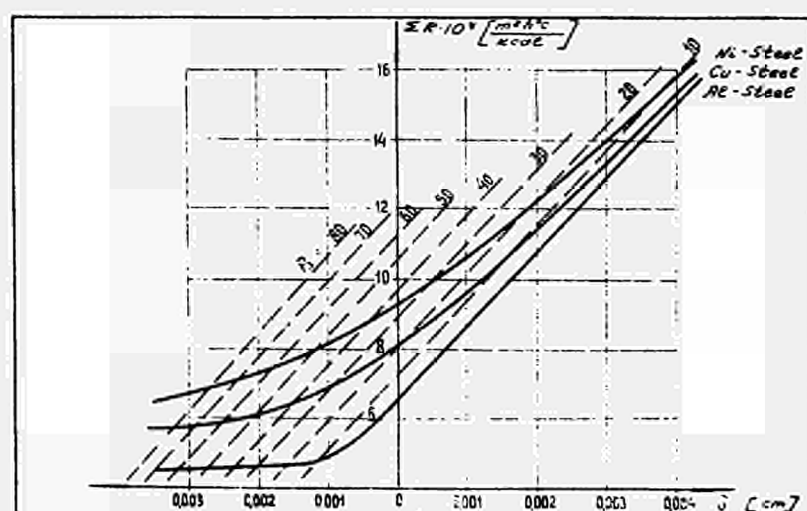
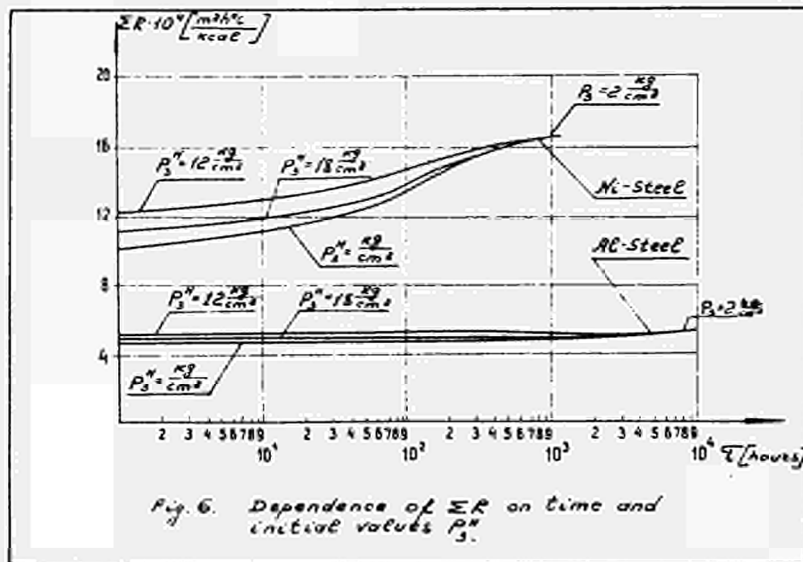
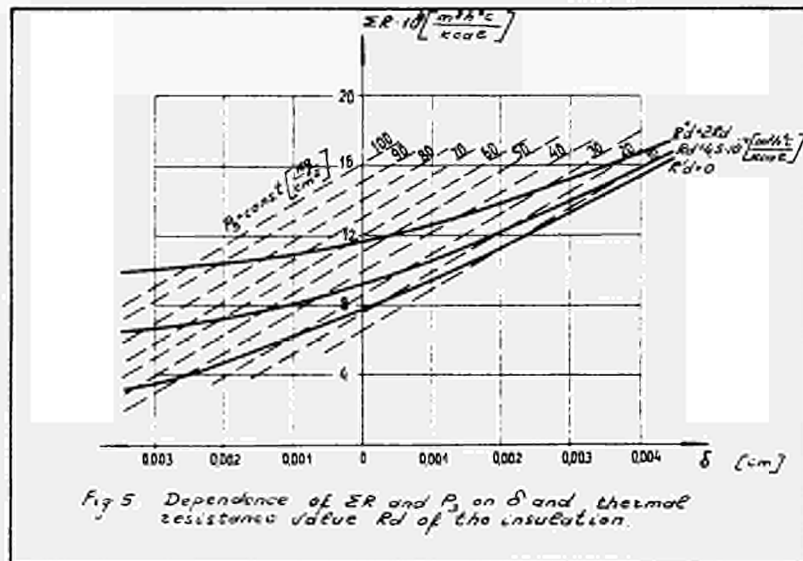
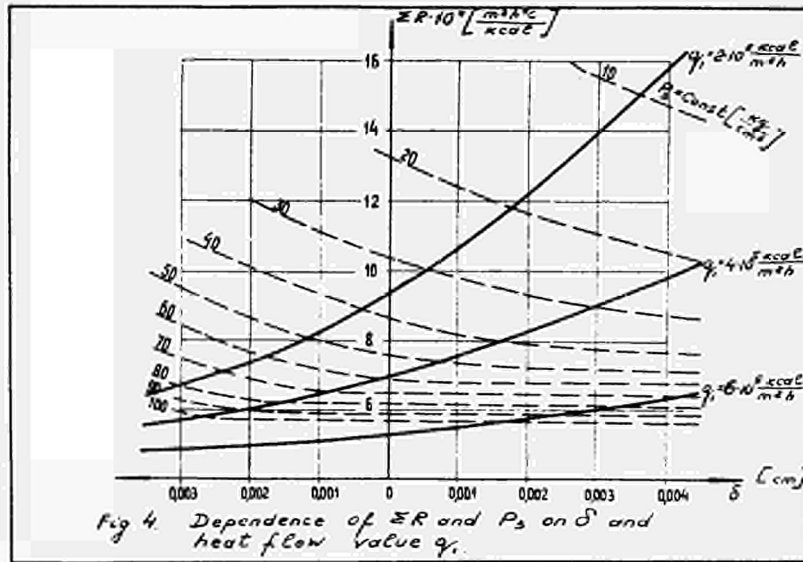


Fig 3. Dependence of ER and P₃ on δ and materials in contact



DISCUSSION

No speaker of paper E-15.

ROUKLOVE (USA): In your remarks 2 and 3 and in your conclusion, when you say that you sometimes need to use a clearance and if I understand properly even some gases for the insulation in order to adapt the cooling systems, is it only in case of laboratory tests or is it also during the operation of the devices?

KARETNIKOV (USSR): Permit me to give a clarification. The paper E-11 and the paper E-15 are devoted to one subject, and this paper concerns the practical realization of thermionic converters. We consider that in a real construction the anode or collector must be separated from the heat transfer agent which takes the heat from the anode, and here we are considering different variants of the implementation of this contact either with clearance or with a gap.

If the external pipe cooled by a metal is put on the anode with a clearance, the temperature drop in the contact may be rather small in the order of 20, 30, 50^o, but in order to ensure this clearance one must either make a hot fitting in the beginning, or compute the mutual thermal tensions of the external jacket and the inner anode assembly with the insulator. This problem is not easily resolved and in the papers E-11 and E-15 this problem is analyzed in all the possible range of clearances and gaps. It is shown that, if there is no clearance, but a gap, and the gap is not filled with gas, (that is, there is a vacuum gap) then the temperature drops can be very large, 200, 300^oC. If we want to construct a space assembly, then such a temperature drop will cause a considerable increase of the dimensions of the radiator. This is undesirable. Therefore one must fill the gap with a good thermal-conducting gas, and keep the gap small. It would be better, if one could fill the gap with a liquid metal. In this case the difficulties are in sealing the ends of the channel. Finally, a simple conclusion: if it were possible to make a continuous connection of the anode, the insulation and the external jacket, and to overcome the problem of the foliation of the assembly during the thermal pulsations and thermal shocks, this would be the best solution. This approach turns out to be the most interesting. It allows one to obtain minimal losses due to the temperature drop.

ROUKLOVE: Did you perform some tests, and in this case what materials or gas mixtures did you use?

KARETNIKOV: We examined pure gases, argon and helium. We did not consider gas mixtures. For materials we examined aluminum oxide and beryllium oxide in contact with various metals: molybdenum, niobium, heat-resistant steels and some alloys.

GYFTOPOULOS (USA): Could you please discuss briefly the type of converter design you are describing?

KARETNIKOV: We consider a cylindrical thermionic channel: The fuel, the emitter, the gap, the collector. The collector is separated from the cooled jacket by an insulator of which I have already spoken. We are now speaking of the gap or clearance i. e. of the contact-thermal resistance at this point.

SCHOCK (USA): Is the Al_2O_3 insulator applied to the outside of the collector as a coating?

KARETNIKOV: The Al_2O_3 layer is applied by plasma coating and is therefore firmly connected to the collector. The external jacket is connected to the anode by different methods.

SCHOCK: If you have stacked diodes within one fuel element, then there are axial gaps between the joining collectors. Do you coat those too?

KARETNIKOV: The coating is between the fuel and the emitter.

SCHOCK: Have you considered the danger that cracks in the Al_2O_3 will be filled with liquid metal, shorting the collector to the sheath?

KARETNIKOV: Here we consider a scheme consisting of one element over the entire length of the reactor.

HIGH TEMPERATURE COMPATIBILITY OF REFRACTORY METALS IN CONTACT
WITH REFRACTORY MATERIALS*

J-J. HUET - J. VANGEEL

Centre d'Etude de l'Energie Nucléaire, Mol, Belgium

* Work performed by C.E.N./S.C.K., Mol, under Euratom contract
n° 021-65-10 CODB

1. INTRODUCTION

Nuclear fuel elements consisting of ceramic spherical particles coated with pyrolytic carbon are applied with success in high temperature reactors [1 - 5] . The same concept was proposed here as a fuel for thermionic converters. It is known that the usual UC based fuel shows swelling phenomena after some time of irradiation at temperatures above 1400°C. Irradiation tests made in several laboratories confirm that the coating can withstand the high pressure of fission gases so that the swelling is avoided.

Application of coated particles to the thermionic converters involves a working temperature several hundred degrees higher than in conventional high temperature reactors but the principal difference lies in the refractory metal sheath necessary to provide a good emitter surface.

2. SAMPLE FABRICATION

The samples consisted of a thick refractory metal tube filled with coated UC₂ fuel particles (in a few cases uncoated UO₂ and UN fuel particles were used). To try to prevent interreaction of the carbon coated particles on the can, as well as to improve the thermal conductivity, different filler materials were used.

After vibrocompaction of particles and filler material, the tubes were closed by a cap which was sealed by means of an electron-beam weld (6).

3. CHOICE OF FILLING MATERIAL

The different filling materials tested were chosen amongst the most thermodynamically stable compounds having a melting point above 2200°C. They also were selected so that any reaction occurring with the four refractory metals would give products with melting points well above 2000°C (7 - 8). The final selection was ZrC, SiC, TaC, CeS, Zr_6Si_5 , AlN.

4. COMPATIBILITY

A programme was set up to investigate the four refractory metals Mo, W, Nb and W as canning materials, allied with a variety of filling materials with high melting points (above 2200°C) and high formation energies. All the tests were done in a vacuum furnace ; the working pressure being between 10^{-4} and 10^{-5} mm of Hg.

4.1. Study of zirconium carbide as a filling material

4.1.1. Molybdenum behaviour

Two molybdenum cans were filled, one with ZrC and pyrocarbon coated particles, the other with ZrC alone, and then treated for ten hours at 2000°C. Fig. 1 and 2 show the difference of the carbon diffusion into the can wall in both cases. With ZrC alone, the penetration was 85 μ m ; when pyrocarbon coated particles were included, the penetration was 240 μ m. Other qualities of ZrC do not change the reaction with molybdenum, but the quality of the pyrocarbon coating has been found to be a very important factor on the carburization rate of the can.

A heat treatment was also carried out at 1800°C, which was more representative for thermionic emitters. The aspect of the

reaction band remained the same ; after ten hours its thickness was approximately 100 μm . If a square root of the time law is applied, after one year, the reaction thickness would be of the order of 3 mm.

X-ray diffraction of the inner side of the Mo can, shown in Fig. 1, detected the presence of Mo, Mo_2C and ZrC. It can thus be explained that the molybdenum carburization was due to the formation of a carbon deficient ZrC ; the homogeneity range of ZrC is indeed very large.

The sample shown in Fig. 2 was analysed by electron microprobe analysis. The dark phase in the reaction band is molybdenum metal and the light phase is Mo_2C ; the molybdenum plates are probably produced by precipitation on cooling from a high temperature solid solution. The Mo_2C penetrates into the molybdenum grain boundaries.

4.1.2. Tungsten behaviour

The compatibility tests were carried out at 2000° and 1800°C. Results of the 2000°C test are shown in Fig. 3 ; the mean thickness of the reaction zone was 250 μm and the layer was very similar to the one with molybdenum. The concentration gradient of tungsten platelets in the W_2C is more typical of a re-precipitation of tungsten from a high temperature solid solution containing a concentration gradient. Micrographic analysis of the coated particles after the test showed nearly complete dissolution of the outer layer of the coating.

The results of the compatibility test at 1800°C for ten hours were similar ; the mean thickness of the penetration band was 40 μm . Applying again a square root of the time law, a penetration thickness of 1 mm could be expected after one year.

The appearance of the carbide layer was somewhat different from the one found after the 2000°C test ; there were no tungsten platelets in W_2C ; the solubility of tungsten in W_2C is significantly higher at 2000°C than at 1800°C.

4.1.3. Niobium behaviour

The compatibility tests were run for 200 to 1000 hours at 1700°C. Dissolution of the pyrocarbon coating in ZrC was evident after 200 h and nearly complete after 500 h. There was no carbide layer on the inside of the can but the carbon diffusion proceeds along grain boundaries throughout the whole thickness of the can.

4.1.4. Tantalum behaviour

Tantalum behaves in a manner similar to niobium. However, a reaction layer could be seen on the inside of the tantalum capsule (Fig. 4), but the carbon diffusion proceeds also along grain boundaries and the whole thickness of the can was passed through.

4.2. Study of silicon carbide as a filling material

Silicon carbide can be very easily applied as a second coating on pyrocarbon coated particles and is perfectly compatible with graphite and pyrocarbon : some tests have shown that duplex SiC - PyC coated particles can withstand a heat treatment at 2200°C for several hours without damage.

The four refractory metals Mo, Nb, Ta and W respectively were placed in contact with pyrocarbon coated particles and SiC filling material. Only tungsten withstood a ten hour test at 2000°C. Fig. 5 shows the diffusion zone, identified micrographically as W_2C ; its thickness was 760 μm . The molybdenum capsule produced a liquid phase shortly after reaching 2000°C. Niobium and tantalum were very strongly attacked after four hours at 2000°C. ; carburization proceeded throughout the wall mainly along the grain boundaries.

4.3. Study of cerium sulfide as a filling material

A molybdenum capsule was filled with CeS plus pyrocarbon coated particles and heat treated for 10 h at 2000°C. The failure was not complete but the reaction proceeded to such an extent that the whole thickness of the can was penetrated. In the same time, the pyrocarbon coating was severely attacked, and for this reason the other refractory metals were not tested.

4.4. Study of zirconium silicide as a filling material

Zirconium silicide was prepared by melting pure zirconium and silicon metals in a non consumable electrode arc furnace. Metallographically, at least two phases were detected and the product obtained was thus a mixture of two or more of the following compounds : Zr_6Si_5 , $ZrSi$ (decomp. 2095°C), Zr_3Si_2 (decomp. 2225°C) or Zr_5Si_3 (decomp. 2210°C) (7 - 8)

When treated for 10 h at 2000°C, most of the pyrocarbon coated particles dissolved completely in the surrounding silicide. Molybdenum forms a eutectic with the filler. The capsule melted after 6 min at 2000°C. The reactions with tantalum for 10 h, and with tungsten for 4 h at 2000°C were severe.

4.5. Study of tantalum carbide as a filling material

4.5.1. Molybdenum behaviour

A very strong reaction was detected with the typical Mo_2C formation. This behaviour can be attributed to the presence of pyrocarbon coated particles because the metallographic inspection of the capsule showed that the carburization depth was a function of proximity of the coated particles to the capsule.

4.5.2. Tungsten behaviour

A reaction was also found with the tungsten can after 10 h at 2000°C. A typical carbide formation was observed.

Fig. 6 shows the influence of the proximity of a particle on the carbide penetration thickness in the can. Tungsten platelets were found in the W_2C . The mean thickness of the layer was 175 μm .

4.6. Study of aluminium nitride as a filling material

4.6.1. Behaviour of niobium and tantalum

In tests at 2000°C, where AlN alone was in contact with niobium or tantalum, complete melting occurred by formation of a eutectic. In an other test, where pyrocarbon coated particles were present as well in the can, complete melting did not happen. However the niobium can was completely penetrated and the tantalum can strongly attacked. The absence of melting could be explained by a slightly lower temperature reached in the latter tests ; The precision on the temperature measurement with the optical pyrometer reading was certainly not better than $\pm 50^\circ C$ at 2000°C. The eutectic formation can thus be fixed very near to 2000°C.

4.6.2. Behaviour of molybdenum

No diffusion could be observed microscopically in molybdenum when it had been in contact with AlN alone for 10 h at 2000°C. Only small grain boundary precipitates and an irregular grain growth, not unexpected for molybdenum at that temperature, could be detected.

When pyrocarbon coated particles were added to the AlN powder, only a thin irregular reaction band on the inside of the can was noticed after 10 h at 2000°C (Fig. 7). The X-ray diffraction analysis showed that the phases present in this capsule after heat treatment were Mo, Mo_2C ; AlN, UC_2 and C. A thin reaction band on the external layer of the pyrocarbon could also be observed.

From the two preceding experiments, it could be concluded that AlN was compatible with molybdenum at 2000°C but the presence of carbon in the capsule should be avoided. After these tests UN and UO₂ were suggested as possible fuels. Uranium nitride was used as uncoated ground powder ; it was mixed with aluminium nitride powder and filled directly into a molybdenum can. There was no visible influence of the uranium nitride on the compatibility at 2000°C. The same test was performed with UO₂, and again no influence of this material was found. Fig. 8 shows a typical aspect of molybdenum after being in contact with AlN at 2000°C for 10 h ; the irregular grain growth and the grain boundary precipitate can be observed. The few patches of white phase in the inside of the grain are probably the grain boundary precipitate left over by boundary movement.

4.6.3. Tungsten behaviour

The same series of tests were carried out with tungsten and the same general behaviour was observed. If AlN powder was tested alone, no reaction was visible, and the grain size remained small after 10 hrs at 2000°C.

If pyrocarbon coated particles were added to the AlN powder, only very local carbide formation could be observed ; this occurred probably only when a particle was in the immediate vicinity of the can (Fig. 9). A very small quantity of a second phase was precipitated mainly along the grain boundaries, but hardly more than in the case of tungsten and filler alone, heat treated in the same conditions. Some of the coated particles were very slightly attacked during the test. The aluminium nitride did not stop completely the carbon diffusion from the particle coating, and, after a long time, the tungsten would also probably be carburized.

Compared to the behaviour of tungsten in contact with AlN alone, the addition of UN or UO₂ powder did not change the micrographic aspect of the can after 10 h heat treatment at 2000°C. Fig. 10 shows the result of the test with UN and AlN mixed powders and is typical of the aspect of tungsten after these tests.

5. CONCLUSIONS

- a) All compatibility tests between pyrocarbon coated particles and refractory metals have shown that the can will not withstand one year at 1800°C without undue carburization occurring
- b) Tantalum and zirconium carbides alone are compatible with tungsten and molybdenum ; this compatibility is destroyed in the presence of pyrocarbon
- c) The use of oxide or nitride fuels could probably solve the compatibility problems. Some other problems may arise and the tests carried out in this study are not sufficient to ascertain this statement.

ACKNOWLEDGEMENTS

The authors wish to thank Messr. H. NEU and D. QUATAERT for helpful discussions and they are grateful for the assistance of :

G. BOMBERNA and G. BREUGELMANS for the heat treatment and the coating of particles.

Mrs. M. HEYLEN with the technical assistance of L. DRIESEN, P. BODDOU, M. PHILIPS, L. NICASY and V. GIJBELS for the metallographic work.

The other main collaborators were F. GORLE (fabrication of spherical particles), Ph. VAN ASBROECK (vibratory compaction of powders), M. MEULEMANS (welding of refractory metals).

REFERENCES

- 1 L.R. SHEPHERD et al
"Review of research and development work for the Dragon Project"
A/Conf. 18/P.122
 - 2 R.W. DAYTON et al
"Ceramic coated particle nuclear fuels"
A/Conf. 28/P.235
 - 3 D.V. RAGONE
"Fuel fabrication technique for high temperature gas cooled reactor
fuels"
G.A. 5399 (May 1965)
 - 4 N.O. HORMS and D.B. TRAUGER
"Fabrication variables, performance and cost considerations for H.T.G.R.
coated particle fuels"
ORNL-TM-1129 (April 1965)
 - 5 J.B. SAYERS et al
"The irradiation behaviour of coated particle fuel"
"Symposium on carbides in nuclear energy" Harwell, November 5-7, 1963
 - 6 Fabrication and tests of nuclear fuel elements for thermionic converters
Final reports - J-J.Huet - S.C.K./C.E.N. D/411/65 and R.2431
 - 7 G.V. SAMSONOV
"High temperature materials" - Properties index
Plenum Press - New York, 1964
 - 8 P.T.B. SHAFFER
"High temperature materials" - Material index
Plenum Press - New York, 1964
-

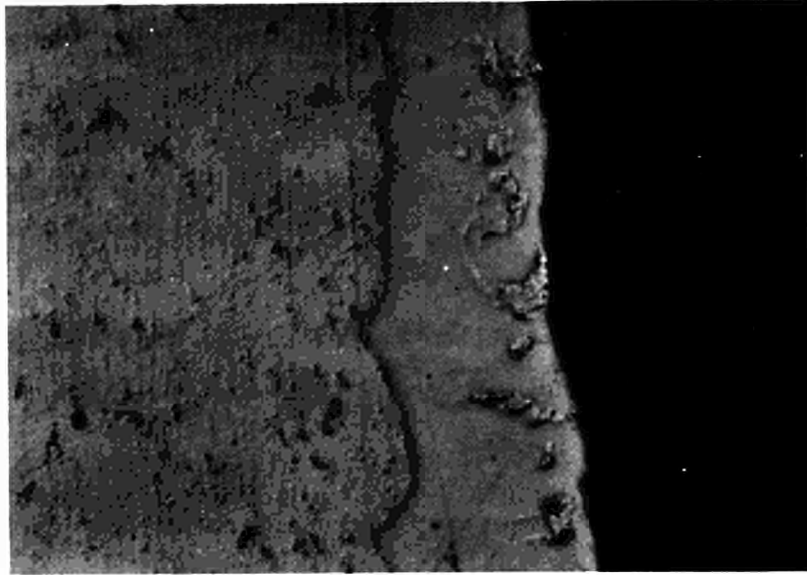


Fig. 1 Detail of a Mo can filled with ZrC powder only, after 10 hours at 2000° C. (x 250)



Fig. 2 Detail of a Mo can filled with ZrC and pyrocarbon-coated particles after 10 hours at 2000° C. (x 250)

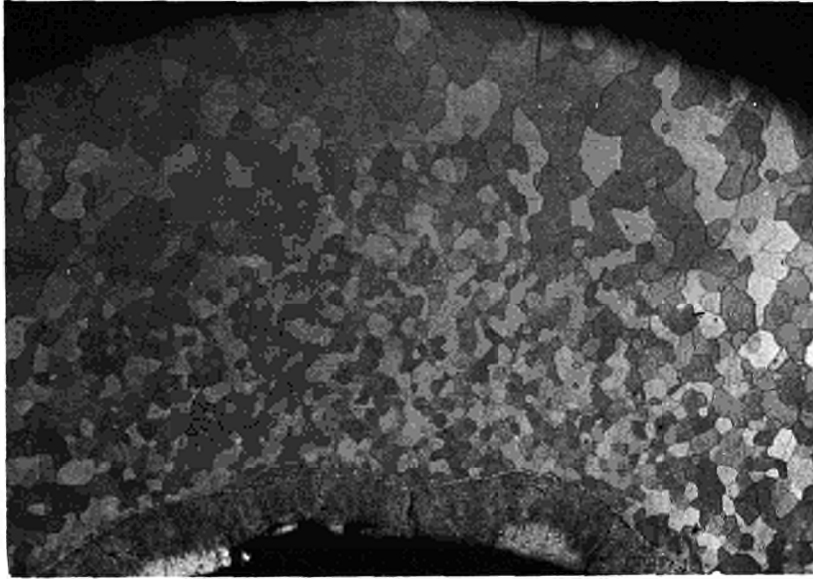


Fig. 3 (T_{30}) Detail of a W capsule filled with ZrC powder and PyC-coated uranium carbide particles after a heat treatment of ten hours at 2000°C (mean thickness of reaction ring: $250\ \mu\text{m}$. (x 29)

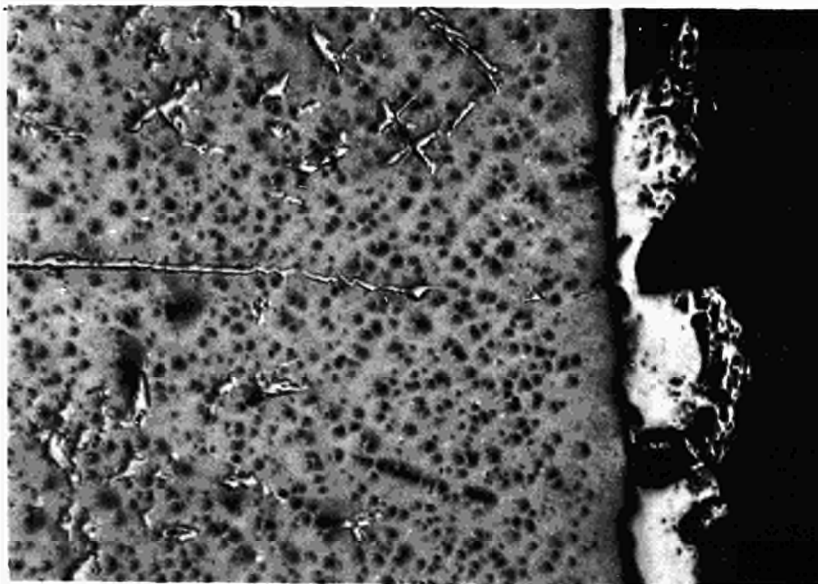


Fig. 4 Detail of a Ta capsule filled with ZrC powder and PyC-coated uranium carbide particles after a heat treatment of 10 h at 2000°C . (x 250)

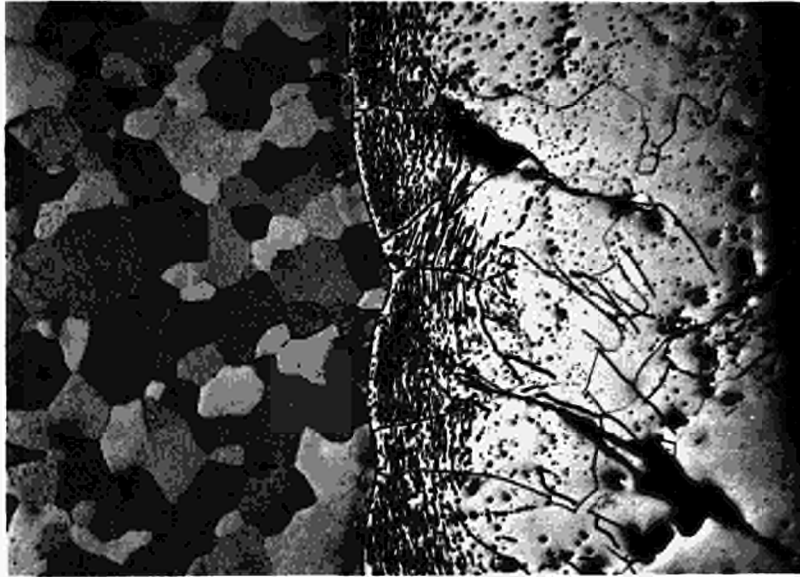


Fig. 5 Detail of a tungsten can filled with SiC powder and PyC-coated particles after ten hours at 2000°C , showing the contact zone between W metal and the reaction band (x75)



Fig. 6 Detail of a W can filled with TaC powder and PyC-coated uranium carbide particles after ten hours at 2000°C , showing the influence of the proximity of a particle. (x75)



Fig. 7 Detail of a molybdenum can filled with AlN powder and pyrocarbon-coated particles after ten hours at 2000°C. (x29)

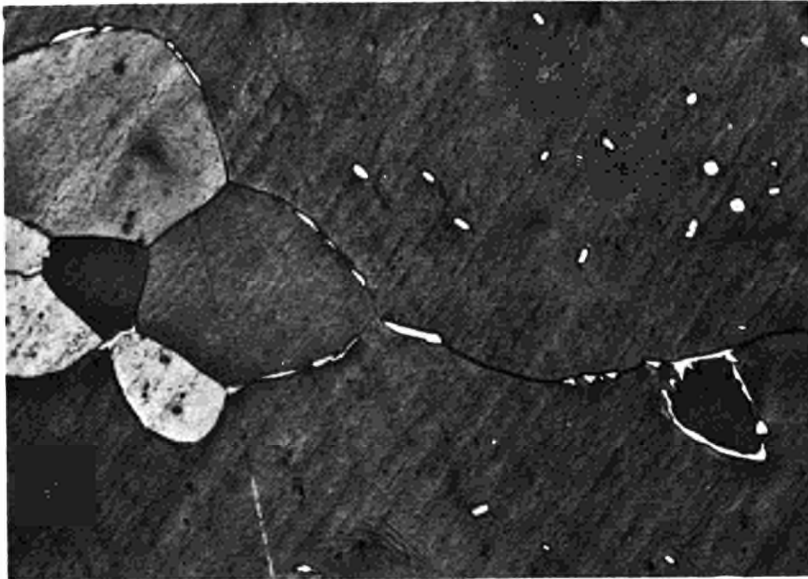


Fig. 8 Micrograph of a molybdenum can filled with AlN and UO₂ powder after ten hours at 2000°C, showing grain boundary precipitates. (x 250)

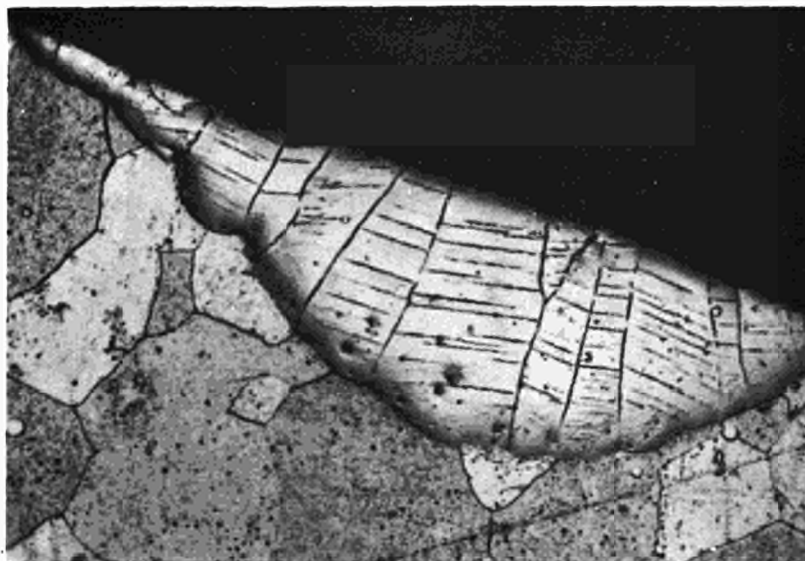


Fig. 9 Micrograph of the tungsten capsule containing AlN and PyC-coated particles heat treated during ten hours at 2000°C , showing the carbide formation. (x 250)

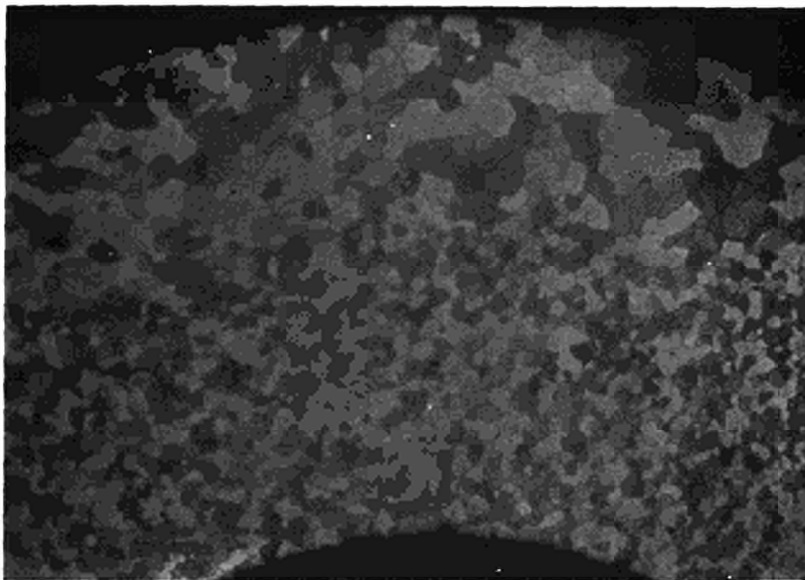


Fig. 10 Detail of a W can filled with AlN powder and uncoated UN powder after ten hours at 2000°C . (x 29)

DISCUSSION

No speaker of paper E-16.

BUGL (Euratom): How has the uranium nitride been fabricated?

VANGEEL (Belgium): The uranium nitride was made by nitrating uranium powder.

BUGL: Did you observe free uranium in your uranium nitride?

VANGEEL: We did not analyze it for this purpose, because it was only at the end of the study that we did some experiments with the nitride.

BUGL: In your paper you came to the conclusion that the use of oxide or nitride fuel could solve the compatibility problems.

As it concerns the oxide I agree to a certain extent; with respect to the nitride I would like to make the limitation "as long as you have stoichiometric UN" This is, however, as one sees from the phase diagram which has been published a few years ago by A. BAUER and myself, rather difficult to obtain.



ETUDE DE SOUDURE PAR DIFFUSION DU MOLYBDENE.

G. FUSTIE, B. JACQUIN
Société BOCUZE, LES ECHETS, France.

M. CLEMOT, J.P. DURAND,
Service d'Electronique Physique, Centre d'Etudes Nucléaires de Saclay
91 Gif-sur-Yvette (France)

Introduction.

Les moyens classiques de soudure des métaux réfractaires nécessitent ou bien la fusion locale (bombardement électronique) qui entraîne une recristallisation et une fragilisation importante, ou bien la présence d'un matériau intermédiaire (brasure) qui nécessite une succession d'opérations délicates et limite nécessairement la température d'utilisation et les propriétés mécaniques de l'ensemble.

Le Service d'Electronique Physique du Commissariat à l'Energie Atomique avec le concours de la Société BOCUZE a développé une étude de soudure par diffusion qui évite ces inconvénients car elle s'effectue sans intermédiaire à une température inférieure à celle de fusion des matériaux de base. Elle présente en outre l'avantage de conduire à des zones de jonction de grandes dimensions. Dans le présent article, on donne les premiers résultats obtenus pour la réalisation de jonctions molybdène-molybdène.

Ensemble expérimental.I - Appareillage. (fig. 1)

Il comprend :

- 1 - une enceinte à vide (pression inférieure à 10^{-5} T) ;
- 2 - un resistor en tungstène en hélice ;
- 3 - un vérin hydraulique avec passage étanche du piston à travers l'enceinte à vide.

La mesure de la température se fait soit par pyrométrie optique soit par thermocouple tungstène-rhénium 5-26 %.

La température maximum de fonctionnement est de l'ordre de 1 800 °C.

La force appliquée par le vérin est réglable de 0 à 1 000 Newtons.

II - Les éprouvettes. (fig. 2)

La forme et les dimensions ont été choisies de façon à pouvoir :

- 1 - traiter plusieurs échantillons ensemble ;
- 2 - faire des essais de traction sur les jonctions sans réusinage ;
- 3 - faire des tests d'étanchéité ;

- 4 - mesurer la température de l'échantillon en cours d'expérimentation (trou de thermocouple).

III - Processus expérimental.

Les éprouvettes sont empilées par deux ou trois, et sont tenues en position par l'application d'une légère pression. L'ensemble est mis sous vide. On procède alors à "l'accrochage de diffusion" sous pression à chaud.

Les échantillons subissent ensuite un recuit de diffusion dans un four sous vide annexe.

Paramètres de l'étude.

Les principaux paramètres de l'étude sont :

- 1 - l'état de surface de l'échantillon - ceci comprend à la fois l'aspect chimique (présence d'oxyde, gaz occlus) et l'aspect mécanique (rugosité, planéité) ;
- 2 - la température de "l'accrochage" ;
- 3 - la durée de mise sous pression en température ;
- 4 - la pression appliquée ;
- 5 - la température de recuit de diffusion ;
- 6 - la durée du recuit.

Examens.

Sur le matériau de base, ils portent sur :

- 1 - l'analyse chimique - dosage des impuretés ;
- 2 - la détermination de la structure micrographique ;
- 3 - la mesure de la rugosité et de la planéité des surfaces à souder ;
- 4 - la détermination de la charge de rupture à froid .

Sur les pièces d'essai assemblées, ils portent sur :

- 1 - la mesure de l'étanchéité ;
- 2 - l'examen de la structure micrographique de la liaison éventuelle ;
- 3 - la mesure de la résistance à la rupture ;
- 4 - après arrachement, examens des surfaces de rupture dans le cas où celle-ci se produit au niveau de la zone de jonction (cas général).

Essais effectués.

I - Matériau de base.

Tous les échantillons ont été prélevés dans des barres de molybdène BOCUZE préparé par frittage.

L'analyse chimique du produit fini donne :

Eléments	Mn	Cu	Fe	Ni	Co	W	B	O ₂	H ₂	N ₂	C	SiO ₂	Al ₂ O ₃	CaO	Pb
Teneur en p.p.m.	4	8	62	21	4	< 100	0	65	2	42	70	75	37	28	2

L'examen micrographique montre des grains uniformés dans toute la masse du matériau, ils présentent une forme allongée parallèle à l'axe de martelage (figure n° 3).

A 20 °C la résistance à la rupture est de 45 Kg/mm².

II - Influence de la préparation de surface

Dans ces essais, les paramètres de pressage ont été figés aux valeurs suivantes :

- Nettoyage chimique : dégraissage - rinçage - séchage ;
- Température de pressage 1 600 °C
- Durée 1 h.
- Pression 330 Kg/ cm².

A) Facteur mécanique.

Les divers préparations d'échantillons sont résumées sur le tableau ci-dessous.

Nature	Rugosité	Planéité	n° figure
Pièce tournée rodée "marbre" (1) *	≤ 10 μ	très bonne	5
Pièce tournée polie "diamant" (2)	≤ 0,5 μ	mauvaise: surface ar- rondie	6
Pièce tournée rodée "alumine" (3)	≤ 1 à 2 μ	bonne	7
Pièce tournée	≤ 20 μ	bonne	
Pièce tournée et rectifiée	≤ 1 μ	-	4

Les examens micrographiques montrent que les accrochages sont sensiblement identiques, exception faite pour les pièces rodées diamant où l'arrondi de la surface empêche toute jonction autre que sur la ligne de contact.

La figure 8 est une micrographie au grossissement 76, correspondant à l'accrochage réalisé avec des pièces brutes de tour.

En conclusion, la planéité semble indispensable, la rugosité tant qu'elle reste faible (inférieure à 10 μ) influence peu la liaison.

* (1)- Les pièces sont rodées face contre face avec de la poudre de carbure de silicium, ce qui explique la très bonne planéité.

(2)- Les pièces sont polies l'une après l'autre avec des poudres de diamant de différentes granulométries.

(3)- Même technique que le polissage marbre mais avec de l'alumine en suspension aqueuse.

B - Facteur chimique.

On a étudié l'influence des traitement chimiques de surface suivants :

- 1 - Elimination des traces d'oxydation par attaque chimique.
- 2 - Traitement thermique (800 °C) en atmosphère réductrice (H₂).
- 3 - Dégazage à chaud sous vide des surfaces à souder avant mise en contact.

Les opérations 1 et 3 n'ont pas eu d'influence sensible sur la soudure ; l'opération 2 semble être néfaste et nuire à la croissance ultérieure des grains de molybdène lors des opérations de recuit. Elles n'ont pas été maintenues pour les essais suivants.

III - Température de l'accrochage.

Les essais de soudure ont été faits aux températures suivantes : 1 300 °C - 1 400 °C - 1 500 °C et 1 600 °C pendant une heure sous une pression de 330 Kg/ cm².

Au-dessous de 1 400 °C, les liaisons sont dans l'ensemble mauvaises, (fig. 9 et 10) ; on commence à observer des bons résultats à 1 500 °C (fig. 11). A 1 600 °C (fig. 14) l'accrochage est excellent avec disparition presque complète des porosités qui restaient sur la ligne de jonction dans les cas précédents .

IV - Influence de la durée du pressage.

Les essais ont porté entre 1 heure et 4 heures, à une température donnée, elle est pratiquement sans effet.

V - Influence du recuit de diffusion.

Sur les structures accrochées à basse température (< 1 500 °C), un recuit à température élevée (1 800 °C) durant 4 heures de façon à permettre un léger grossissement des grains améliore les résultats (figure n° 12 et 13) , sans pour cela faire disparaître complètement les porosités, quelle que soit la durée du recuit.

Sur les soudures effectuées à 1 600 °C, le recuit se traduit par un grossissement des grains de jonction, et par suite à une homogénéisation du matériau ; la ligne de jonction alors disparaît complètement (fig. n° 14 et 15).

VI - Les essais de traction.

Sur les échantillons traités à 1 600 °C, dont les micrographies sont excellentes, les essais de traction donnent des profils d'arrachement avec des rugosités supérieures à 100 μ (fig. n° 16 et 17).

L'absence de rotule dans la transmission de la pression sur les échantillons ne permet pas de corriger les défauts de parallélisme du montage. La pression n'est pas uniforme sur la totalité de la surface à souder, c'est pourquoi les essais de traction n'ont pas donné pour l'instant les résultats que l'on pouvait escompter - vu la qualité micrographique des liaisons obtenues.

Conclusions.

Au cours de cette étude, on a réalisé pour l'instant cinquante essais. Vu le grand nombre de paramètres, on ne peut encore donner de conclusions formelles. Cependant il semble définitivement établi que :

- 1 - la planéité des échantillons est indispensable ;
- 2 - la rugosité peut varier sans grande incidence sur la qualité des jonctions ;

3 - la température minimale d'accrochage se situe à 1 600 °C, quelle que soit la durée de la tenue sous pression ;

4 - Un recuit de diffusion à plus haute température (1 800 °C) est nécessaire pour homogénéiser la jonction.

Bibliographie.

- [1] DANNESSA A. T.
"Diffusion bonding beryllium molybdenum and tungsten." *Metal Progress* .
- [2] NEALE E. , ORROK,
"Application of diffusion bonding" *metal progress*, June 66.
- [3] "Investigation of diffusion barriers for refractory metals"
Technical documentary report NR-ASD(TDR 62-432)
- [4] BONNIN P.
"Etude bibliographique sur les procédés de jonction par diffusion"
Bibliographie CEA n° 44.

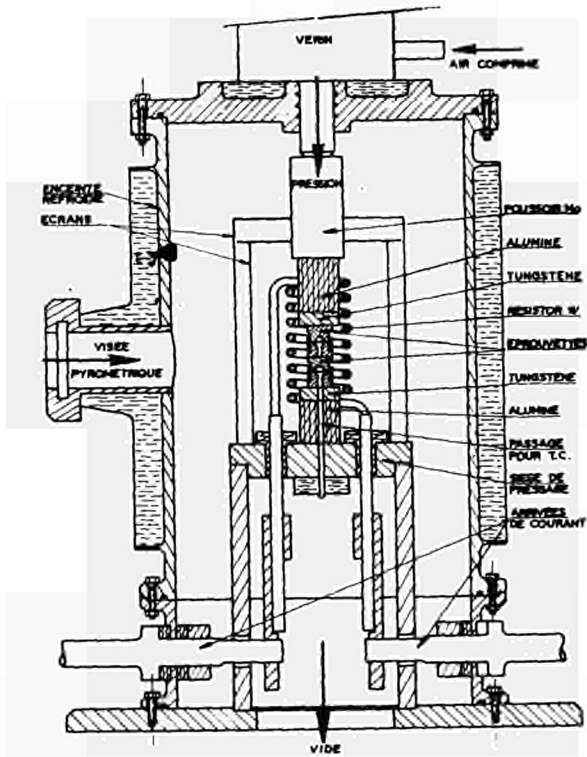


Fig. 1 - Dispositif expérimental

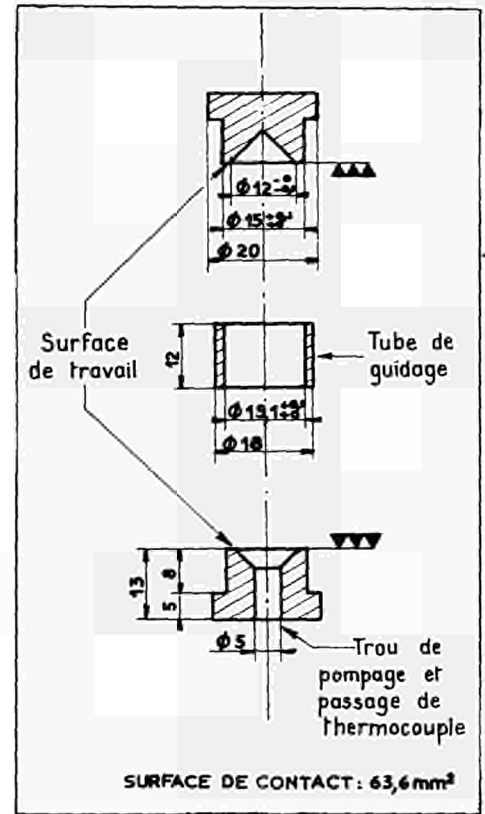


Fig. 2 - Eprouvettes



Fig. 3 - Aspect micrographique du molybdène utilisé

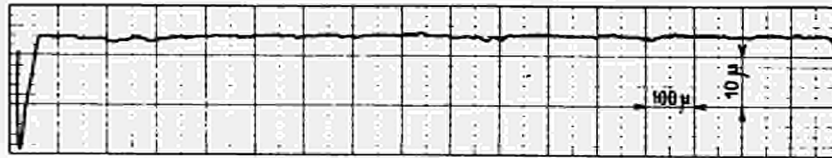


Fig.4 - Pièce tournée rectifiée

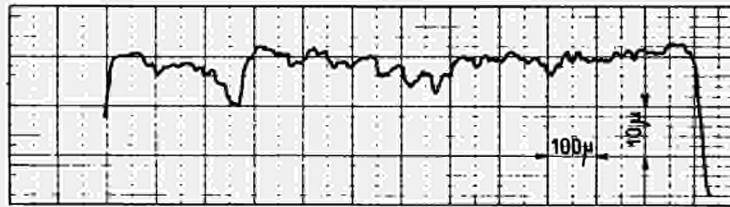


Fig.5 - Pièce tournée rodée "marbre"



Fig.6 - Pièce tournée poli "diamant"

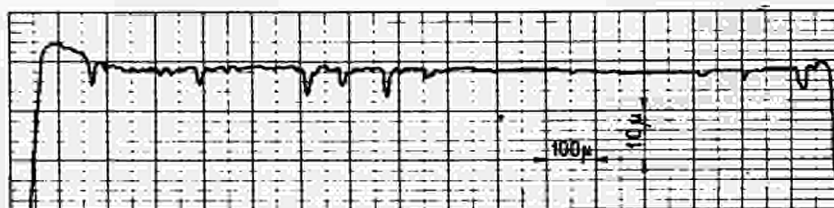


Fig.7 - Pièce tournée rodée "alumine"

PREPARATION DES SURFACES



Fig. 8 - Pièce tournée, $T = 1600^{\circ}\text{C}$,
 $t = 1$ heure, $P = 330\text{kg}/\text{cm}^2$



Fig. 9 - Pièce rodée "marbre", $T = 1300^{\circ}\text{C}$,
 $t = 1$ heure, $P = 330\text{kg}/\text{cm}^2$



Fig. 10 - Pièce rodée "marbre"
 $T = 1400^{\circ}\text{C}$, $t = 1$ heure,
 $P = 330\text{ kg}/\text{cm}^2$

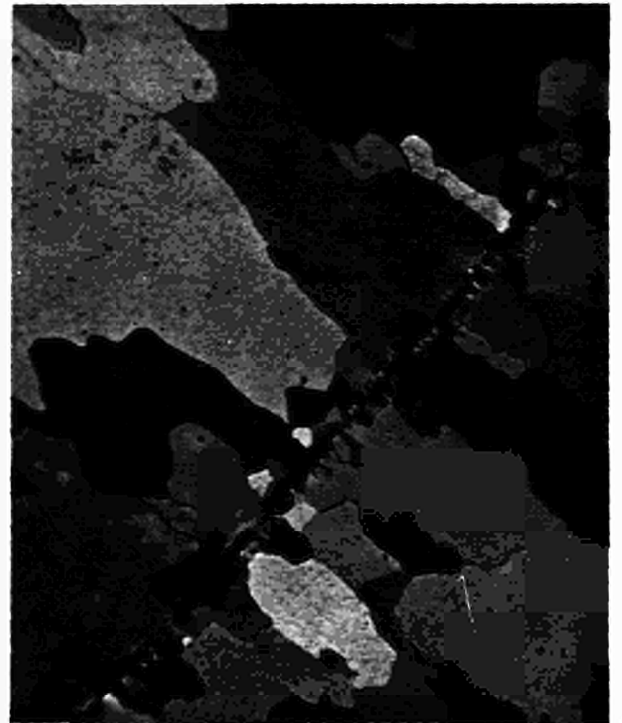


Fig. 11 - Pièce rodée "marbre"
 $T = 1500^{\circ}\text{C}$, $t = 1$ heure,
 $P = 330\text{ kg}/\text{am}^2$



Fig. 12 - Pièce polie Al₂O₃ ,
T = 1400°C, t = 1 heure ,
P = 330 kg/ cm²



Fig. 13 - Pièce polie Al₂O₃ (T = 1400°C,
t = 1 heure, P = 330 kg/ cm² +
4 heures recuit 1800°C)

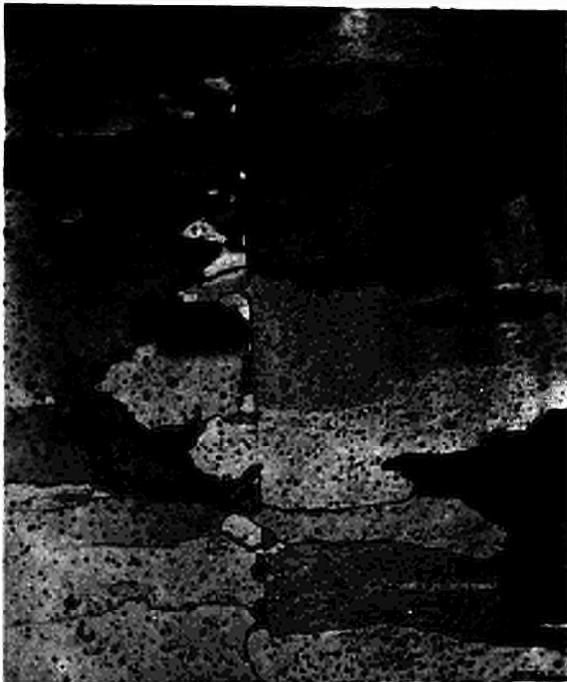


Fig. 14 - Liaison effectuée avec pièce
rôdée "marbre", T = 1600°C,
t = 1 heure, P = 330kg/ cm²

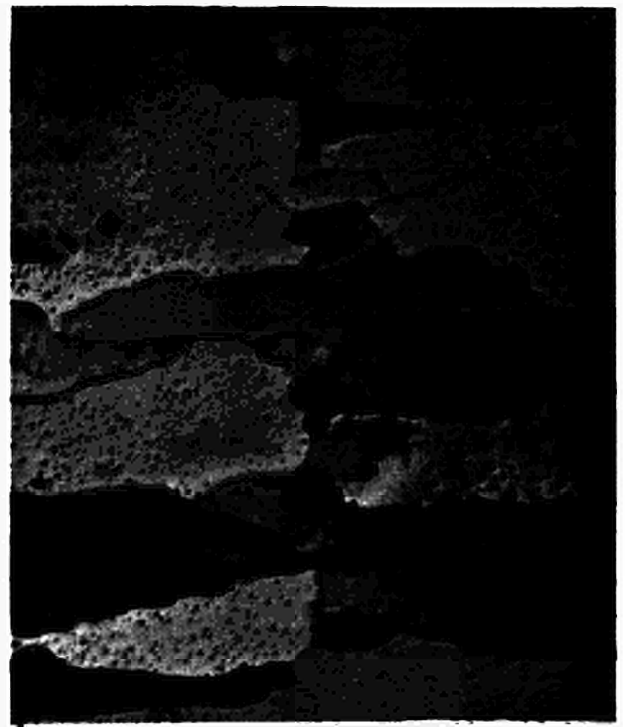


Fig. 15 - Liaison avec pièce rodée "marbre"
T = 1600°C, t = 1 heure, P = 330kg/
cm² = 4 heures recuit 1800°C

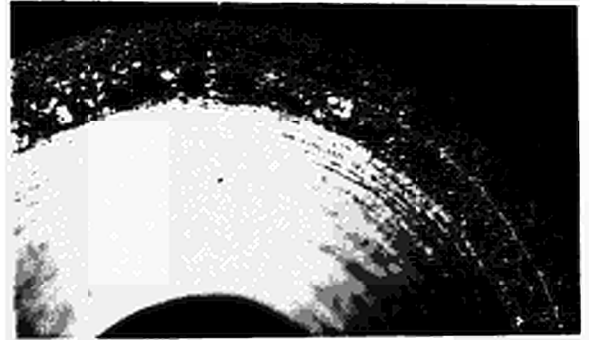
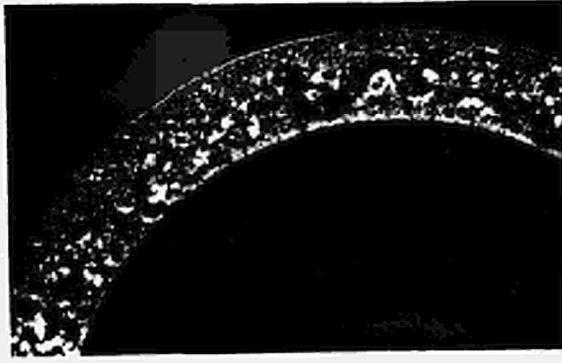


Fig.16- Surfaces après arrachement . (Pièce polie "marbre", $T = 1600^{\circ}\text{C}$,
 $t = 1$ heure , $P = 330 \text{ kg/ cm}^2$)

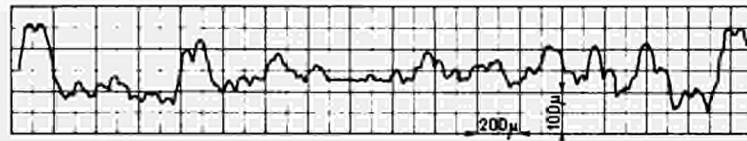
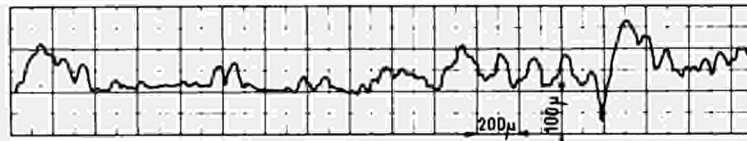


Fig. 17 - Profil des surfaces après arrachement (Pièce polie "marbre", $T = 1600^{\circ}\text{C}$,
 $t = 1$ heure , $P = 330 \text{ kg/ cm}^2$)

DISCUSSION

Speaker of paper E-17: B. JACQUIN.

SCHOCK (USA): Your pressure would be applied mechanically, not by isostatic gas, do I understand that correctly?

JACQUIN (France): Oui, la pression est appliquée mécaniquement. La pression pneumatique sert uniquement à actionner le vérin.

SCHOCK: I wonder whether you could clarify how you propose to utilize this method in the application of the diode.

JACQUIN: Nous ne fabriquons pas de diodes, nous faisons simplement des essais pour savoir si par la suite dans la diode il sera possible d'utiliser ce procédé. Pour la fabrication des diodes on utilisera certainement un autre dispositif. Pour le moment il s'agit de déterminer les paramètres de bonne soudure par diffusion.

BUSSE (Euratom): I think the aim of the study was to avoid the embrittlement by recrystallization, during welding. Did you test how far you avoided embrittlement by your method? I understand your temperatures are rather high.

JACQUIN: Oui, la température était élevée mais le grossissement des grains est certainement nettement inférieur à celui observé lors d'une soudure par bombardement électronique, puisqu'il n'y a pas de fusion du matériau de base.

BUSSE: Did you consider going to lower temperatures and higher pressures, so that you can avoid this grain growth?

JACQUIN: Non, pas pour le moment, parce que trop peu d'essais ont été réalisés. Avec une pression comme celle indiquée (330 kg/cm^2) et à des températures inférieures à 1600°C il n'est pas possible d'obtenir un bon accrochage de diffusion.

CAMPBELL (USA): What material was your ram made of? What effect had the mechanical pressure on the parts of the ram?

JACQUIN: Le vérin lui-même est en acier. Il est équipé, en bout, d'un poussoir en molybdène qui appuie sur des pièces en alumine qui servent d'isolant thermique. Le vérin lui-même est dans une zone froide.

ROUKLOVE (USA): What precaution did you take that the pressure would

be equally distributed along all the surface of the part?

JACQUIN: Tout simplement, un bon usinage de pièces, un bon montage du dispositif expérimental, mais il a été prouvé qu'il n'était pas possible, sans emploi d'une rotule, de pouvoir appliquer, d'une manière uniforme, la pression sur les pièces.

INVESTIGATION OF DIFFUSION INTERACTION AND
STRUCTURAL STABILITY OF CATHODE MATERIAL

V.N.Bykov, L.V.Pavlinov, Yu.A.Gorban, M.I.Zakharova,
A.A.Korolev, V.A.Malykh, I.P.Mukhin, A.I.Nakonechnikov,
B.A.Nevzorov, A.V.Frolov, A.S.Shatalin

When selecting material of cathode assembly of nuclear energy thermionic converter, one must take into account the chemical interaction processes of contacting materials which occur at operational temperature ($\geq 1500^{\circ}\text{C}$) including cesium vapours, evaporation and mass transfer through gaseous phase, creep, structural changes and others which can result in undesirable changes of the complex of physical-mechanical characteristics and the construction as a whole. At that, the material selection is limited by the requirement of necessary nuclear properties and thermionic characteristics. Those requirements are satisfied to a considerable extent with molybdenum, tungsten and uranium dioxide, used as cathode and fission composition shells, respectively. In present report the results are given describing the investigations of diffusive interaction and uranium dioxide and cesium compatibility with refractory metals, high molybdenum strength in cesium vapours, evaporation and uranium dioxide composition changes and structural changes of monocrystal samples of molybdenum and tungsten cathodes by annealing.

I. Evaporation and Changing the Uranium Dioxide Composition

Examination of Uranium dioxide evaporation was carried out by the differentiation of Knudsen's method. The assembly gave the possibility to cover 30 targets in series with uranium dioxide without $\sim 10^{-6}$ mm Hg vacuum unhermeticity. The condensate amount was measured by natural uranium α -activity. Original powdery uranium dioxide consisted of the following components (weight %): U-86.79; O-12.76; H₂O-0.357; Fe, Mn, Al and others- the rest. The oxygen content corresponds to the UO_{2,20} formula. Roentgenographic analysis shows only the presence of strongly broadened UO_{2+x} phase lines with the lattice parameter $a=5,460$ Å which corresponds to the UO_{2,09} formula.

After 5 hours holding at 460°C U₄O_{9+y} phase lines appeared at the roentgenograms. The result of changing uranium dioxide with the temperature are shown in Fig.I. When increasing the temperature, U₄O_{9+y} is enriched with oxygen while UO_{2+x} loses it approaching a stoichiometric composition at 2170°C. The U₄O_{9+y} phase presents till about 1120°C (it is shown by the arrow in Fig.I). Fig.I illustrates also changing the ratio O/U with the temperature for the condensate formed and stoichiometric uranium dioxide, places into the chamber without contact with the base sample (curves 2 and 3, respectively). As the paper I shows vapour pressure above uranium dioxide depends on oxygen excess. For stoichiometric uranium dioxide the dependence of vapour elasticity on the temperature in the range of 1600-2300°C is described by the following equation:

$$\lg P_{\text{mm}} = - \frac{32258}{T} + 12,183,$$

which corresponds to heat of evaporation:

$$\Delta H_v = 147500 \pm 500 \frac{\text{cal}}{\text{mol}}$$

2. Structural Changing the Monocrystal Samples of Molybdenum and Tungsten Cathodes by annealing By means of methods of microscopy and X-ray analysis

there was carried out the investigation of dislocated structure and structural imperfection distribution in molybdenum and tungsten depending on the method of obtaining monocrystals and those imperfections behaviour during the monocrystal cathodes annealing under a vacuum of $(5 \cdot 10^{-5} \text{ mm Hg})$ for 500 hours in the temperature range of $1400-2000^{\circ}\text{C}$.

There was shown that the degree of perfection and the character of the monocrystal dislocated structure depend essentially on the method of their obtaining. One can observe nonuniform placing of dislocations in molybdenum which was obtained from the gaseous phase and by the method of electronic beam melting: aggregates forming dislocated grids on the planes $\{110\}$ and aggregates forming dislocated "sockets" around micropores on the planes $\{100\}$, respectively.

Monocrystals obtained by the method of zone electronic beam melting are the most perfective: (angles of disorientations between subgrains do not exceed $20''$), dislocations are uniformly placed in the field of subgrains; the sample rotation during the melting promoted the formation of the most uniform dislocated structure without subgrained boundaries with dislocation density $\sim 9 \cdot 10^6 \text{ cm}^{-2}$.

Such a difference in original sample structures effects further dislocation behaviour at annealing.

In that case when dislocations placed as aggregates one can observe the redistribution of dislocations results in increasing the disorientation angles between original subgrains from $30'' - 2'$ to $1^{\circ} - 4^{\circ}$ and the fragmentation of original subgrains to smaller ones [2].

Voltages of monocrystal cathode shells and thermocycling promote more intensive fragmentation and increasing the disorientation angle of substructure grains. Hence, mechanical and emissive properties are respectively changed. Monocrystal samples of molybdenum and tungsten formed by the method of zonal electron beam melting for the uniform dislocation distribution have the most stable structure during annealing.

3. Uranium Dioxide Interaction With Refractory Metals

The interaction of uranium dioxide having the $UO_{2.20}$ composition with molybdenum was investigated for 1000 hours at the temperature of $1500^{\circ}C$ and for 100 hours at $1,600, 1,700, 1,800, 1,900$ and $2,000^{\circ}C$. The interaction of uranium dioxide having $UO_{2.00}, UO_{2.10}$ and $UO_{2.20}$ compositions and the composition of $UO_{2.10} + 40$ weight%W with tungsten was investigated for 930 and 800 hours at the temperatures of 1700° and $1850^{\circ}C$, respectively. In present work there were used molybdenum and tungsten the purity of which was equal to 99,98%. The samples were enclosed into hermetic and open molybdenum containers. After isothermal annealing under the conditions above there were conducted metallographical, roentgenostructural, roentgenospectral and radiometric analyses of molybdenum and tungsten samples. Those results pointed out the absence of interaction with new oxide phases which agree with the results of thermodynamic calculations and experimental data [3,4]. Uranium dioxide loses oxygen excess at high temperature annealing and its composition approaches stoichiometry. That is confirmed by the measurement of the uranium dioxide crystal lattice parameter and by the "swelling" of hermetic molybdenum containers during annealing at $1850^{\circ}C$.

The radiometric analysis helped to detect uranium diffusion into molybdenum depth penetration of which was equal 300μ for 1000 hours at 1500° . So, there were conducted systematical investigations of uranium diffusion into molybdenum and tungsten from the uranium dioxide and thin uranium layer covered the samples by a dispersion in vacuum. To investigate uranium diffusion from dioxide there were used uranium dioxide in the form of fine-dispersive powder enriched to 36% with U-235 isotop, and molybdenum and tungsten samples having form of rectangulars of $7 \times 10 \times 15$ mm annealed beforehand for 100 hours at $2000^{\circ}C$. Those samples pressurised to the uranium dioxide powder in molybdenum containers under the pressure of 4000 kg/cm^2 . The containers

were welded by electronic beam welding and were annealed at the temperatures of 1600-2000°C in a vacuum furnace. After annealing plano-parallel layers were taken down the sample surface and integral α -activity was measured. The diffusion coefficient was calculated using the equation of Fick's second law for the case of a constant concentration at a surface:

$$\frac{I}{I_0} = 1 - \operatorname{erf} Z,$$

where I - is the integral sample activity after taking down a thickness layer;

I_0 - is the integral sample activity at $x = 0$;

$\operatorname{erf} Z$ - is the probability integral, $Z = \frac{x}{2} \sqrt{Dt}$,

D - is the diffusion coefficient;

t - is the duration of diffusive annealing.

The temperature dependence of the diffusion coefficient is given in plots as $\lg D$ versus $1/T$. That dependence can be analytically described by the expressions: for molybdenum

$$D = 7.60 \cdot 10^{-3} \exp(-76400/RT) \text{ cm}^2/\text{sec}^*)$$

$$D = 0.34 \cdot 10^{-5} \exp(-60000/RT) \text{ cm}^2/\text{sec}.$$

Uranium diffusion data from dioxide into molybdenum are in good agreement with the result for the uranium diffusion from a thin layer [5]. The plot in Fig.2 shows that the difference between uranium diffusion coefficients from dioxide and momentary source into molybdenum is within the range of experimental errors. The temperature dependence equation of the uranium diffusion coefficient into molybdenum for the momentary source has the same form as eq. (*)

4. Cesium Diffusion into Molybdenum

The investigation of cesium diffusion into molybdenum was carried out using radioactive cesium isotope Cs-134 at plane polycrystal samples and monocrystals in the direction of $\langle III \rangle$. Polycrystal hot-forged samples were tested both in unannealed and annealed forms for 100 hours at 1200° and 1600°C.

A diffusive saturation of samples with cesium was carried

out from a vapour phase in hermetic molybdenum containers containing except samples chloride of cesium-134 isotope and the diluent that is nonradioactive cesium chloride.

A cesium distribution was determined by the method of taking down layers and measuring their thickness both weighing and direct measuring using an optical longmeter with the accuracy of 1μ .

Integral β -activity of the sample was measured by a scintillation method and a concentrated curve $c \approx f(x)$ was drawn accounting the radiation absorption correction of sample material.

The diffusion coefficient was obtained by the method of a standard curve using the equation for a constant concentration at a boundary. Diffusion coefficient experimental values are given in coordinates $\lg D - \frac{1}{T}$ in Fig.3. The temperature dependence of the diffusion coefficient for monocrystal and polycrystal unannealed samples is described by the following equations:

$$\begin{aligned} \text{for monocrystal } D &= 8.52 \cdot 10^{-9} \exp(-39800/RT) \text{ cm}^2/\text{sec} \\ \text{for polycrystal } D &= 3 \cdot 10^{-11} \exp(-15500/RT) \text{ cm}^2/\text{sec} \end{aligned}$$

Diffusion coefficients for polycrystal molybdenum thermo-treated at 1200° and 1600°C have intermediate values at a considerable spread.

Data obtained points out a considerable diffusion contribution of structure defects to a general diffusive cesium flow in polycrystal molybdenum. Material annealing at 1200° and 1600°C decreases the diffusion coefficient. A typical concentration curve is given in Fig.4. For all the temperatures and all the sample types an excess cesium concentration at a molybdenum surface is shown compared with that following from a standard curve. For unannealed samples anomal large cesium concentrations after taking down the layers are typical which corresponding to predicted decreasing the cesium concentration by 15-20 times.

The first fact must be probably explained by physical processes at a sample surface and the second one confirms a considerable effect of structure defects on the cesium diffusion in molybdenum.

Autoradiography of samples saturated with cesium in all cases fixes cesium aggregates in the form of point and linear objects, located either along grain boundaries or in grainbodies directly. Nowhere cesium penetration was observed along interface planes between grains as along the plane of a final thickness.

The results obtained point out that a preliminary high temperature treatment of molybdenum articles intended for the operation in cesium vapours can be useful for decreasing a cesium content in material that must correspondingly improve its characteristics of long-time strength and plasticity.

5. Molybdenum Long-Time Strength in Cesium Vapours

The long-time strength investigation of molybdenum with small additions of titanium (0.4%) and zirconium (0.2%) was conducted in vacuum of 10^{-5} mm Hg and in cesium vapours under the pressure of 4-8 mm Hg at the temperature of 1600°C .

The alloy results are given in plots in logarithmic coordinates of stress and time before failure (Fig.5). The dependence coordinates of stress and time before failure can be expressed by the following equations:

$$\text{(for vacuum)} \quad \lg \sigma = 0,248 \lg T + 0,833$$

$$\text{(for cesium vapours)} \quad \lg \sigma = -0,263 \lg T + 0,784$$

The results show a somewhat decreasing the alloy rupture strength when investigating in cesium vapours. Increasing the time before failure, one can increase a relative decreasing of the alloy rupture strength when investigating in cesium vapours.

Maximum creep rate was observed for samples investigated in cesium vapours and here a relative deformation during short periods of investigations (below 50 hours) has the greatest importance. Increasing the test interval before failure results in decreasing the sample elongation (Fig.6). Metallographical and X-ray analyses did not reveal the corrosive effect of cesium vapours on stressed alloy. Cesium traces were detected in the

alloy surface layer with spectral analysis. Molybdenum holding in cesium vapours for unstressed state does not practically change its mechanical properties.

Conclusions

1. High temperature annealing of uranium dioxide with oxygen excess ($UO_{2.20}$) results in the oxygen excess loss and approaching the stoichiometry composition ($UO_{2.00}$).
2. Annealing of monocrystal molybdenum samples and tungsten at temperatures exceeding the recrystallization temperature results in appearing the substructure and grain fragmentation which are explained by the dislocation redistribution. Mechanical and emissive properties are changed by that.
3. At the temperatures till $2000^{\circ}C$ uranium dioxide does not interact with molybdenum and tungsten forming new oxide phases. However when contacting uranium dioxide with molybdenum and tungsten the replacing uranium diffusion within a solid solution takes place at the temperature above $1500^{\circ}C$.
4. The investigations conducted point out the cesium diffusion from a gaseous phase to molybdenum. A cesium concentration on the surface and a diffusion depth depend on molybdenum structural state.
5. Rupture strength and a relative molybdenum elongation (the alloy with 0.4 Ti and 0.2% Zr) at the temperature of $1600^{\circ}C$ in cesium vapours (4-8 mm Hg) are less than in vacuum. Molybdenum holding in cesium vapours for unstressed state does not practically change its mechanical properties.

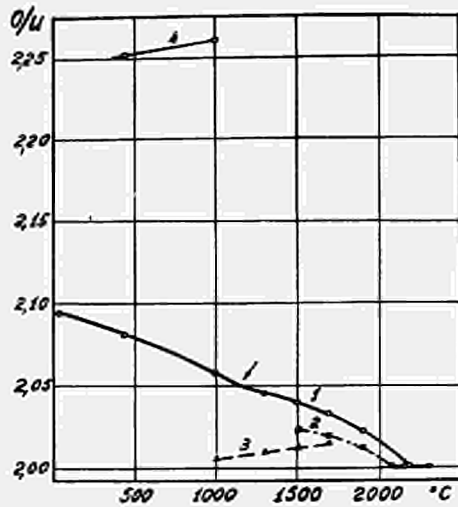


Fig. 1. Dependence of the UO_{2+x} composition on the temperature. 1. Original material; 2. Condensate in the chamber; 3. $UO_{2.00}$ placed into the chamber; 4. U_4O_{9+y}

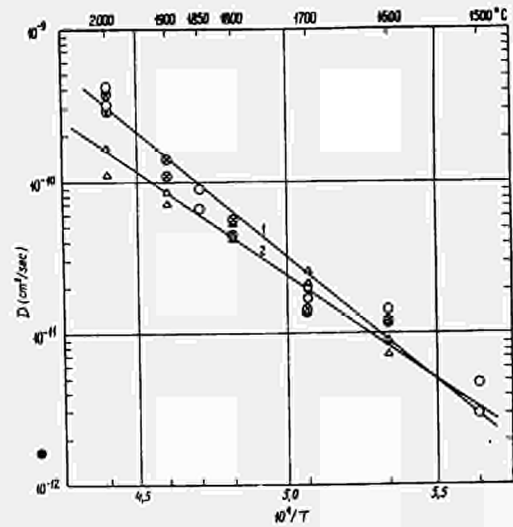


Fig. 2. Temperature dependence of uranium diffusion coefficient into molybdenum (1) (O - diffusion from dioxide, ⊗ - momentary source); into tungsten (2) - (Δ)

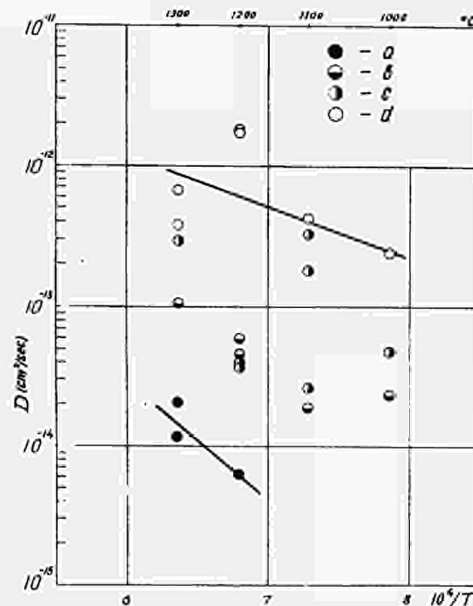


Fig. 3. Temperature dependence of cesium diffusion coefficient into molybdenum. a) Monocrystal molybdenum; b) Polycrystal molybdenum annealed at $1200^{\circ}C$; c) Polycrystal molybdenum annealed at $1600^{\circ}C$; d) Polycrystal unannealed molybdenum.

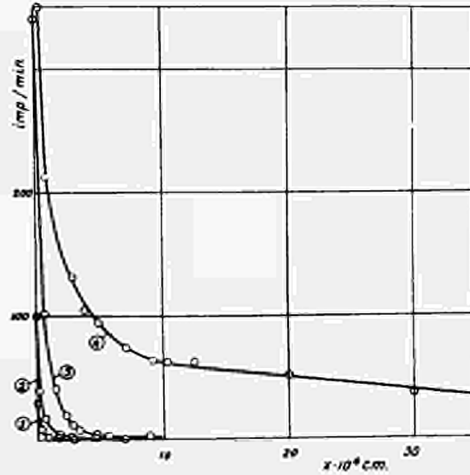


Fig. 4. Cesium distribution in molybdenum holding in CsCl vapours for 72 hours, 1200°C
1) Monocrystal molybdenum; 2) Polycrystal molybdenum annealed at 1600°C; 3) Polycrystal molybdenum annealed at 1200°C; 4) Polycrystal unannealed molybdenum.

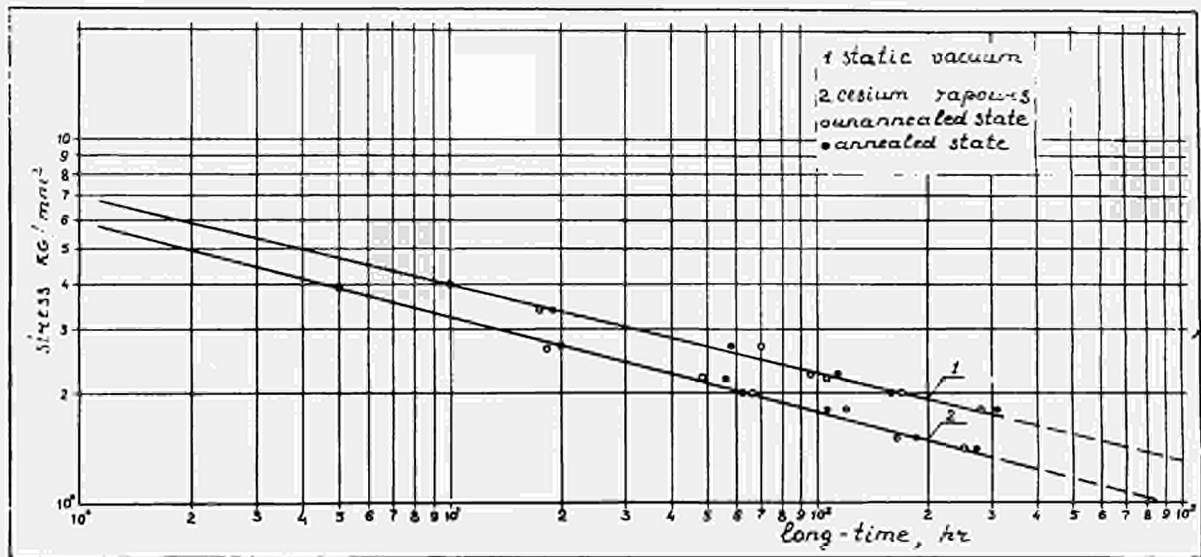


Fig. 5. Molybdenum long-strength in vacuum and in cesium vapours at 1600°C.

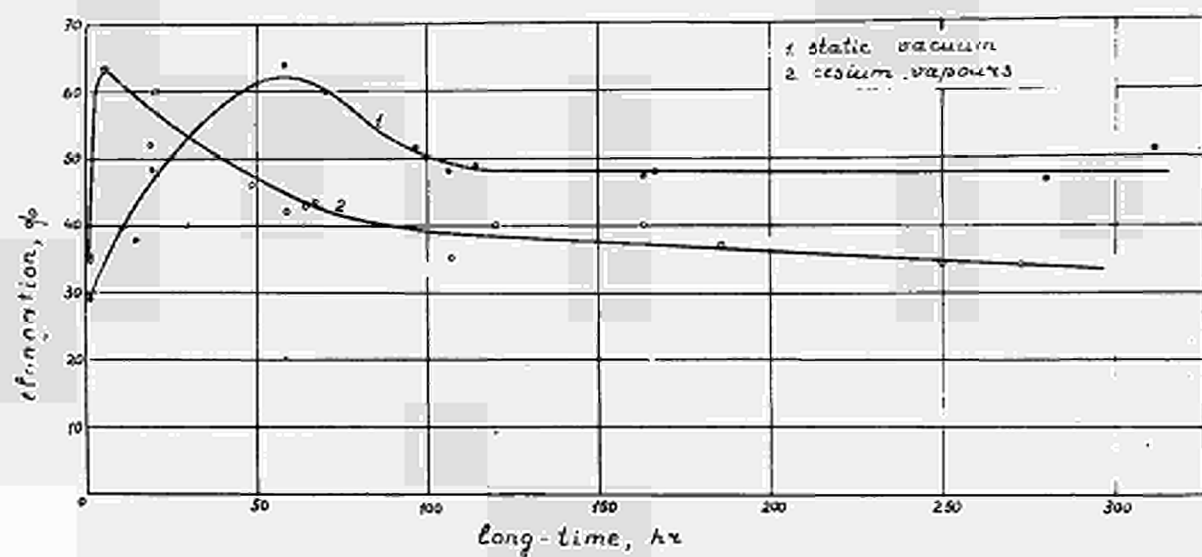


Fig. 6. Dependence of molybdenum plasticity change in vacuum and in cesium vapours at 1600°C.

R E F E R E N C E S

1. Gorban Yu.A., Pavlinov L.N., Bykov V.N. *Atomnaya Energiya*, 22, 6, p.p.465 (1967).
2. Bykov V.N., Rudenko V.A., Zakharova M.I. *Fiz. Metal.Metalloved.* 19, 1, p.145 (1965).
3. Weinberg A., Yang L. *General Atomic (G.A. 3124)*, 1962.
4. *Quarterly Progress Report, General Electrical Co. (G.E.S.R. 2006)*, 1962.
5. Pavlinov L.N., Nakonechnikov A.I., Bykov V.N.;, *Atomnaya Energiya*, 19, 6, p.p.521-23, (1965).

Cermets as Material for Thermionic Emitters

by

D.Schmidt *; G.Ondracek ** ; E.Gebhardt ***

- * Deutsche Versuchsanstalt für Luft- und Raumfahrt e.V.
Institut für Energiewandlung und Elektrische Antriebe
Stuttgart-Vaihingen
- ** Kernforschungszentrum, Institut für Material- und
Festkörperforschung, Karlsruhe
- *** Max-Planck-Institut für Metallforschung, Institut
für Sondermetalle, Stuttgart

Abstract :

Cermet electrodes for a low Temperature range ($\text{Ba}_2\text{-Ca}_{0,55}\text{WO}_6\text{-W}$) and for higher operating temperatures ($\text{UO}_2\text{-Mo}$) were manufactured with reproducible properties. The following parameters proved to have an influence on the work function : the operating temperature and the operating time, the gas at the surface of the emitter and its partial pressure, the combination of the emitter material and the addition of small portions of further metals. On the assumption that the degree of coverage of the surface is a measure for the emission current all the temperature functions of the work function of the two systems can be explained by a model.

The efficient operation of thermionic generators demands that the material of the emitter fulfills certain requirements, which can be met to a large degree by the use of a combination of ceramic and metallic components, i.e. by cermet electrodes. Such requirements are, for example, high electrical conductivity, low rate of evaporation, insensibility against ion attack and contamination by gases, mechanical and chemical stability.

With aspect to the geometrical structure one can classify electrodes as coated electrodes, capillary- and matrix electrodes. Regarding the chemical composition one differentiates between oxide, sulfide, nitride, carbide and boride electrodes. Neglecting the influence of the metallic phase for a moment, the composition of the ceramic phase determines the properties of the electrode. For example, if the Ba-concentration in the compounds barium strontium tungstate and barium calcium tungstate falls below a certain limit a strong increase of the work function takes place (fig. 1). The presence of calcium in such an electrode increases its life without changing the other properties [1, 2, 3, 4]. Therefore we tried to prepare barium calcium tungstate with a barium content of at least 20 at-% for use at lower temperatures. On the other hand the use of fission heat in thermionic emitters results in higher operating temperatures (UO_2). The powder characteristics, the conditions for mixing and densification have been studied

in order to manufacture cermet electrodes with reproducible properties. The desired samples ($\text{Ba}_2\text{Ca}_{0,55}\text{WO}_6\text{-W}$, $\text{Ba}_2\text{Ca}_{0,55}\text{WO}_6\text{+Al+W}$ and $\text{UO}_2\text{-Mo}$) could be produced from these electrode materials. For comparison of the different electrodes the effective work functions were measured in high vacuum with a planar geometry.

After the initial heating of the combination (supporting and the emitter material) relatively high emission currents were measured. At the end of several hours (> 24 h) operating time the current density reached a steady state and the emission properties of the electrodes did not change further during the test time (50 - 400 h). All data reported here were therefore obtained with emitters that had operated for a longer period (> 50 h).

The following parameters proved to have an influence on the work function:

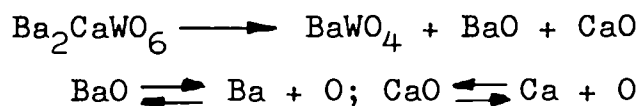
operating temperature and operating time,
the gas at the surface of the emitter and its partial pressure,
the combination of the emitter material and
the addition of small portions of further metals.

The temperature dependence of the work function showed a minimum at a certain critical temperature which varied with the material. Fig. 2 shows such functions for three different samples.

Inert gases (Ar, He) did not alter the work function. At small partial pressures (10^{-5} torr) the measurements were

carried out in the presence of the gases. At higher partial pressures (30 torr) ^{this} effect could only be detected by measurements in vacuum before and after introducing the gas. On the other side the addition of small portions of air increased the work function of all the emitters at least up to the critical temperature. With increasing partial pressure of air the minimum shifted to higher temperatures. Its absolute value was also higher (figs. 3 and 4). In the case of UO₂-Mo even a partial pressure of 2.10⁻⁶ torr air was not sufficient to shift the minimum of the work function.

The combination of the emitter materials proved to be another important parameter. With increasing fraction of the metallic component higher work functions were measured and the minimum moved to higher temperatures (figs. 5 and 6). A probable explanation of the variation of the temperature minimum as well as the temperature dependence of the work function of the Ba₂Ca_{0,55}WO₆-W cermet electrodes lies in the change of the emitter material after a long heating time (300 h). The trace of BaWO₄ (< 0,5 Vol-%) originally found by X-ray methods increased with increasing temperature and time. This confirmed the analogy with pure barium tungstate and its expected reactions [5]:



These very slow reactions continually supply material to form a thin film at the surface of the emitter. The thickness and

homogeneity of the film seems to be dependent on the following parameters supply of alkaline earth metal oxides or their components, their transport and distribution over the surface and finally evaporation [6]. In Fig. 7 each of these parameters is shown as a function of the electrode temperature. In the first region the restricting parameter is supply of material. The particles that come to the surface have enough time to spread over the surface before they evaporate. With increasing temperature the coverage increases until the surface is fully covered. Evaporation is the restricting parameter in this zone II up to the temperature where the parameters diffusion and evaporation intersect. From this point onwards the supplied particles do not have sufficient time to spread over the entire surface before they evaporate (zone III). If we now decrease the supply parameter ($1 \rightarrow 1'$ in fig. 7), the zone II will be more and more restricted till it finally disappears. Further reduction of the supply will shift the temperature with a relative high coverage - the border of zone I' and III' - to higher temperatures and reduce the amount of coverage. On the assumption that the degree of coverage of the surface is a measure of the emission current [7, 8, 9, 10], all the temperature functions of the work function of the system can be explained by this model.

For example the addition of small portions of aluminium to the $\text{Ba}_2\text{Ca}_{0,55}\text{WO}_6$ -W cermet electrodes increased the parameter supply to the surface. With increasing fractions of aluminium the minimum of the work function shifted to lower temperatures

and to lower values of that function (fig. 8).

The trend of the work function of the Al-rich electrode (6 Vol-% Al) indicates that the zone II of the model may be reached.

Literature:

- 1 J. Levi: J. of appl. Phys. 26, 5, May 1955
- 2 J. Brodie: J. Electronics 2, 457, 1957 .
- 3 A. I. Melnikov et. al: Izvest. Akad. Nauk. SSR,
Ser Fiz 22, 613, 1958
- 4 A. I. Melnikov et. al: Radio Eng. and El. 3, 3, 11, 1958
- 5 E. S. Rittner et. al: J. appl. Phys. 28, 1468, 1957
- 6 R. F. Hill, F. E. Gifford: Therm. Conv. Spec. Conf. NY 1963
- 7 B. Ch. Dyubua et. al: Radio Eng. and El. 5, 8, 56, 1960
- 8 L. V. Reshelnikova: Radio Eng. and El. 8, 1918, 1963
- 9 Y. P. Zingermann et. al: Sov. Phys. Solid State 4, 1618,
1963
- 10 Ya. V. Zubenko et. al: Sov. Phys. Solid State 3, 1133, 1961

Acknowledgement

Prof. Thümmeler was the principle adviser to this work. His assistance was highly appreciated. To him the authors wish to express their thanks. The authors also gratefully acknowledge the encouragement by Prof. Knoernschild.

Fig. 1 : Work funktion of barium tungstates as function of other alkaline earths.

(x Sr · Ca)

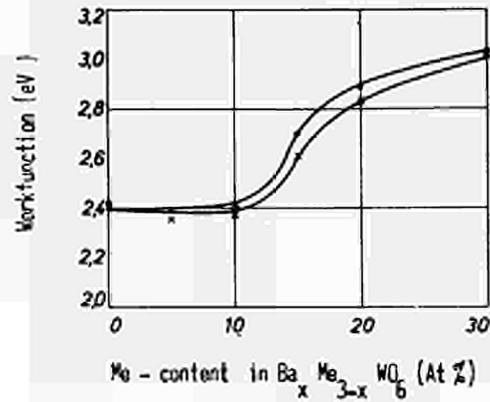


Fig. 2 : Temperature dependence of the workfunktion of pellets with varying electrode material

- △ 30 % (Ba₂Ca_{0,55}WO₆ + 3 Al) + 70 % W
- × 100 % Ba₂Ca_{0,55}WO₆
- 95 % UO₂ + 5 % Mo

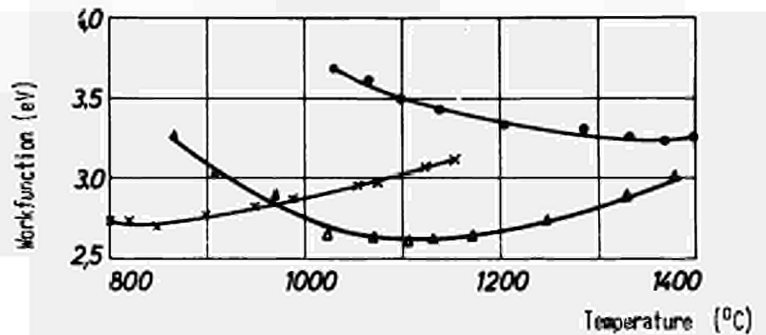


Fig. 3 : Temperature dependence of the workfunktion of pellets with varying partial pressure of air.

- □ 30 % (Ba₂Ca_{0,55}WO₆ + Al) + 70 % W
- ■ 10 % Ba₂Ca_{0,55}WO₆ + 90 % W
- ● 3 × 10⁻⁷ Torr, □ ■ 2 × 10⁻⁶ Torr

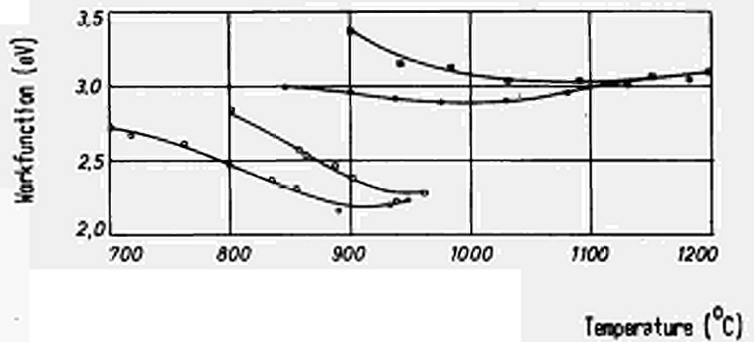


Fig. 4 : Temperature dependence of workfunktion of UO₂ - Mo- pellets with varying partial pressure of air.

- □ 75 % Mo + 25 % UO₂
- ■ 5 % Mo + 95 % UO₂
- ■ 3 × 10⁻⁷ Torr, ○ ● 2 × 10⁻⁶ Torr.

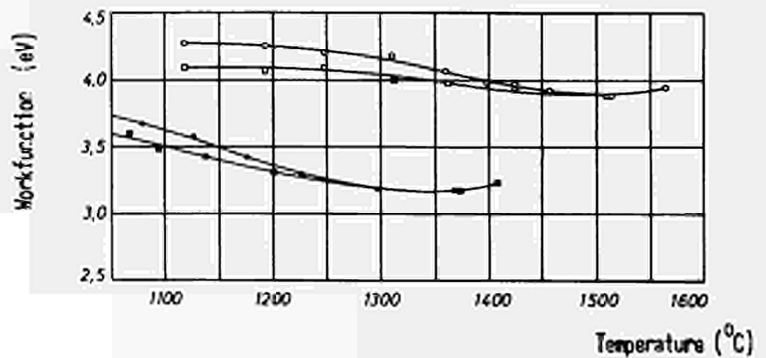


Fig. 5 : Temperature dependence of the workfunction of $Ba_2Ca_{0,55}WO_6$ - W pellets with varying W - content.

• 0% W, x 10% W, ° 20% W,
 △ 30% W, ▽ 70% W,
 □ 90% W
 partial pressure 2×10^{-7} Torr.

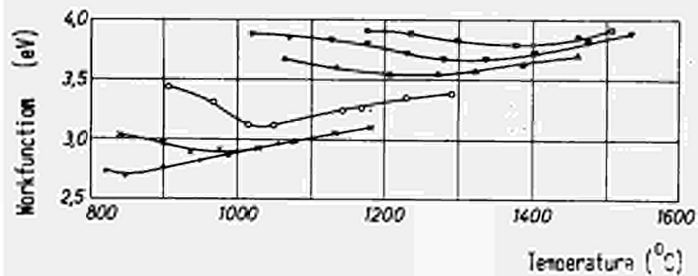


Fig. 6 : Temperature dependence of the workfunction of UO_2 -Mo pellets with varying Mo - content.

o 5% Mo, x 30% Mo, • 75% Mo, □ 50% Mo
 partial pressure 3×10^{-7} Torr air.

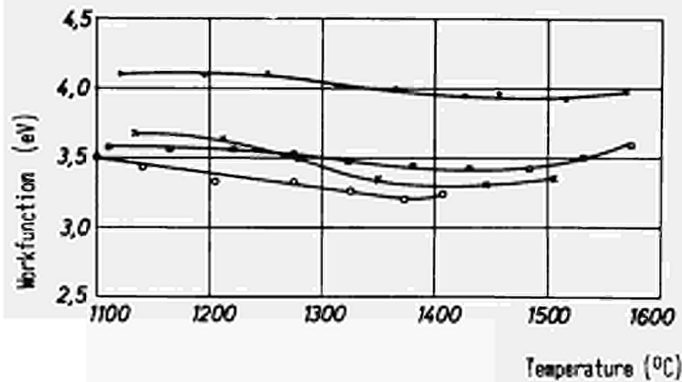


Fig. 7 : Parameter for the film thickness at the emitter surface:

- 1 supply
- 1' reduced supply
- 2 evaporation
- 3 transport

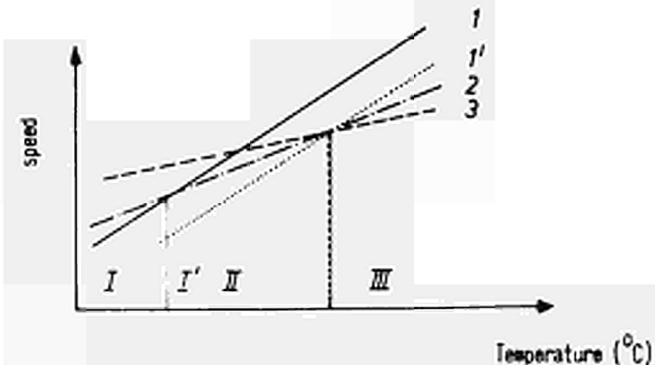
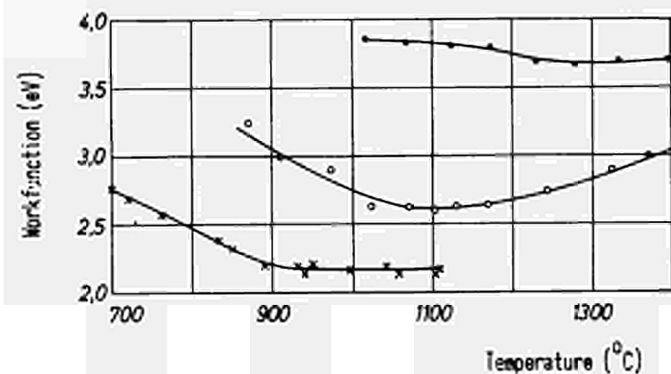


Fig. 8 : Temperature function of the workfunction of $Ba_2Ca_{0,55}WO_6$ - W - pellets with varying Al - content.

• 0% Al
 o 3% Al
 x 6% Al
 partial pressure 3×10^{-7} Torr air.



DISCUSSION

Speaker of paper E-19: D. SCHMIDT.

GROSS (Germany): What were the vacuum conditions under which the work function measurements were performed? As I see in Fig. 2, you have a rather high temperature coefficient of the work function.

SCHMIDT (Germany): On Fig. 2 the work functions were measured at 3×10^{-7} Torr.

GROSS: Our measurements showed that the work functions depend rather strongly on the influence of oxygen. You must have a vacuum better than 10^{-9} to 10^{-8} Torr in order to get good work function measurements.

SCHMIDT: We also made our first measurements at 1×10^{-8} and 5×10^{-9} Torr. But considering that the vacuum condition in a converter cannot be maintained at these extreme values, we made the measurements reported here at pressures of approximately 10^{-7} Torr. In order to see that the conditions do not alter, we operate the electrodes for a long time, that is to say at least for 50 hours at the same conditions. After every change of either temperature or partial pressure of air it took about one hour till we again got steady conditions of the emission current. I think this agrees with your measurements.

SCHOCK (USA): Did you check the emitters for compositional changes after the test?

SCHMIDT: We did measure the changes of the composition by X-ray studies. Let me take the example of barium-calcium-tungstate. After a testing time of 300 to 400 hours we noticed an increase of the amount of basic barium-tungstate $BaWO_4$. Out of this reaction that may lead to BaO and CaO we can see that the composition of the combination will alter very slowly. In the beginning we had $BaWO_4$ with a percentage of about 0.5% and after 400 hours operating time we had about 3%.

GROSS: What is the activation time of the cathode?

SCHMIDT: If you take as activation time that time until we obtain constancy of the current under DC current condition, I would say it is at least 24 hours. Mostly we waited up to 100 hours before we started the measurements. We noticed the same effect with the evaporation rate which was not reported here. The evaporation was higher at the first 20 hours and de-

creased up to 100 hours. It remained steady from 200 hours on.

RASOR (USA): Have you considered the adverse effect that the evaporation of the emitter, however slight, might have on the work function of the collector?

SCHMIDT: All electrode materials will evaporate slightly. Up to now we are only concerned with specific effects of the emitter material. We therefore measured all work functions of the electrodes at high vacuum and did not use them yet in a converter.

Gulf General Atomic Inc.
P.O. Box 608, San Diego, California 92112 (USA)

CESIUM SORPTION IN MATERIALS FOR THERMIONIC CONVERTERS*

M. K. Yates and G. O. Fitzpatrick

ABSTRACT

Materials for sorption reservoirs in thermionic converters were characterized as to their purity and BET surface area. Five samples were selected and loaded with cesium over a range of 600-1000°C sample temperature, 0.1-30 torr cesium vapor pressure, and 0-1000 mg Cs/gram sample cesium loading. In addition, the cesium loadings of five porous tungsten samples were measured at 800°C and 10 torr cesium vapor pressure. Cesium sorption in the Al₂O₃, tungsten and carbon samples tested depended primarily on adsorption and were in general agreement with their BET surface areas. The cesium loadings in a W-10 W/o Ta sample were approximately 100 times that expected from surface area considerations, but these results were shown to be at least partly due to cesium sorption in the tantalum. The cesium sorption in the graphite samples tested depended primarily upon compound formation and were in good agreement with earlier work.

INTRODUCTION

Materials for sorption type cesium reservoirs were investigated for use in thermionic converters. Earlier work had identified three interesting groups of materials: porous metals,⁽¹⁾ high surface area carbons or charcoals,^(2,3) and graphite.⁽⁴⁻⁹⁾ A fourth group, porous alumina was added, primarily because certain types are known to be compatible with cesium and the refractory metals normally found in thermionic converters.⁽¹⁰⁾ The work included surveying for candidate materials and characterization of these materials. Out of 45 samples, 6 samples of porous tungsten, 2 samples of graphite, and 1 sample each of carbon and alumina were chosen for further characterization with respect to their cesium loading and pressure-temperature response.

* This work is sponsored by the U. S. Atomic Energy Commission under Contract No. AT(04-3)-167, Project Agreement No. 14.

EXPERIMENTAL APPARATUS AND PROCEDURE

The apparatus for measuring the pressure-temperature loading characteristics consisted of an isothermal sample oven, a liquid cesium reservoir which provided the required cesium and established the cesium pressure over the sample, and a gamma ray counting system to monitor the cesium loading (Cs^{134}) in the sample. The design of the apparatus is shown in Figure 1, the sample oven is shown in Figure 2. The counting system was calibrated with a cesium standard that was irradiated along with the cesium metal. Temperature accuracy was considered to be $\pm 2^\circ C$.

The P-T curve used for the cesium was that recommended by Nottingham and Breitwieser⁽¹¹⁾ as that giving the best fit to the experimental vapor pressure data.

Chemical cleaning was used to remove contaminants introduced during sample preparation, but high vacuum outgassing at temperatures around $1200^\circ C$ was relied upon for the final preparation prior to cesium loading.

SAMPLE SELECTION

The first five sample materials tested were chosen from those listed in Table I on the basis of superior purity, high surface area, sintering stability, and/or structural characteristics. The five samples selected and the reasons (in order of importance) are listed below:

<u>GROUP</u>	<u>SAMPLE SELECTED</u>	<u>BASIS FOR SELECTION</u>
Porous Tungsten	EOS W-10 Ta	Sintering Stability ⁽¹²⁾
Carbon	Pure Carbon FC-50	High Surface Area, High Purity, Structural Characteristics
Graphite --Isotropic	CARB-I-TEX 700	Minimum Surface Area, Structural Characteristics
--Anisotropic	Gulf General Atomic Sample	Structural Characteristics
Alumina	ALSIMAG 548	High Surface Area, High Purity

COMPARATIVE SUMMARY

Table 2 compares the cesium loadings of the samples tested at $800^\circ C$ and 10

TABLE I, SAMPLE CHARACTERIZATION

DESCRIPTION OF MATERIAL	DENSITY g/cm ³	% OF THEOR.	Surf. Area m ² /g	IMPURITIES ppm								
				Cr	Fe	Mg	Cn	Ti	Sr	Zn	Si	
Al₂O₃												
Coors AD-995 (L32)			0.1±.05	4000	600	600					400	
WESCO AL-300	97.60%	3.67										
WESCO AL-1009	99.85%	3.15	79.1	0.1±.05	400	60					400	
Silk City SC-99P	99.94%	1.34	83.9	<.1	400	80			400		600	
Technical Ceramics #1002		3.9	72.9	0.17	800	800	1000	200			>1%	
American Lava ALSIMAG 548												
99.8%	2.49	62.7	0.2±.05		200						100	
BeO												
Brush 15	99%	82	<.1		100	400					>1000	
Brush 9	99%	80	<.2		60	200		200			>1000	
Brush 35	99%	61	<.2		80	100		200			>1000	
CARBON & CHARCOAL												
					Al	Fe	Mg	Ca	Na	Ni	Cu	Si
Carborundum Carbon Felt, felt	97.8%	0.07	0.8									
Carborundum Carbon Fiber CY-2F, fiber	99.5%											
Gulf General Atomic B-204		0.75	.588		>1000	800		100				>1000
Gulf General Atomic #60		1.05	1.01	0.20 ¹	80	1000		80	400	100	80	80
Speer Carbon #37		1.33	0.32 ²		200	200	40	100	400	60	6	40
Speer Carbon HP-5		1.23	14.7		10	40	40				20	100
Speer Carbon HP-10		1.26	1.3		8	40	10				20	40
Witco Carbon #337, Granular	99.5%	.45	.874		<.1	200	<.5	<20	200		4	<10
					Al	Fe	Mg	Ca	Na	Br	Ba	Si
California Carbon Activated Charcoal, Granular					100	20	100	1%	800	100	20	80
Pittsburgh Activated Carbon, Granular		.5	1050.N		>1%	>1%	200	>1%	800	400	100	>1%
Pittsburgh Activated Carbon, Granular		.5	1050.N		>1%	>1%	100	>1%	1000	600	100	>1%
Pittsburgh Activated Carbon, Granular		.5	1050.N									
Pure Carbon FC-14	99.9%	.90	6.8		6	>1000	2	40	100	ND	2	8
Pure Carbon FC-50	99.7%	.85	347		60	200	20	60	80	ND	20	800
Pure Carbon FC-22	95%		600.N		800	800	40	200	>1000	40	20	>1000
GRAPHITE												
					Al	B	Mg	Fe	Ca	Cu	V	Si
General Electric, foamed pyrolytic												
Union Carbide BSCR		1.633	.57		20	2	1					40
Speer 370-L		1.376	.75		1		1	4	<20			<10
Speer 3499B	99.9%	1.617	2.28			1	1	1	<20	.5		40
Speer 105G		1.447	2.23			2	1	<.1	40	.5		40
Carborundum Graphite Felt	99.0%	7x10 ⁻²	.23									
Carborundum GSGY2-30 Graphite Yarn	99.97%											
Carborundum CARB-I-TEX 700		1.44	.39		2	.5	1	8	40	.5		10
Speer HPG-10		1.12										
Graphite Flake, Pitch Binder			0.5					<.5				
Pyrolytic Graphite, GCA, annealed at 3000°C/15 min.		2.08	0.8					<.5				
POROUS TUNGSTEN												
					PORE DENSITY x10 ⁶ /cm ²	HOTTEST TIME	SINTER TIME	IMPURITIES ppm				
TRW Pure W		14.6	76	.035		2 hr.	1900 or 2000					
EOS F-7A, Pure W												
EOS 7102, Pure W		15.2	79	.018	2.	1 hr.	2000°C		19	30		
EOS 6269, W-10 W/o Ta		15.1	78.5	.023	2.9	1 hr.	2100°C			30	40	
EOS 5253, Pure W		15.2	78.8	<.3	2.2	1 hr.	2000°C			3	20	
EOS 7103, W-2 W/o B ang.pwdr.		12.2	63.5		3.9	.5 hr.	1800°C	91	200	200	70	
ASTROMET 210-7, Pure W												
ASTROMET 105, Pure W ang.pwdr.		12.96	67.5	.042								
EOS Misc. Pieces		14.20		.01±.01								
Phillips, Pure W ang.pwdr.		12.82	67.0	.05								

1. 0.41 after 1200°C Bakeout
2. 0.78 after 1200°C Bakeout

N = Nominal

torr cesium pressure, a typical operating point. As shown, the cesium loadings per square meter of surface area of the carbon, alumina, and at least three of the six tungsten samples are between 1.1-2.0 mg Cs/m². These quantities correspond roughly to 1-2 monolayers based on a cesium cross-sectional area of 28(Å)². Therefore, the cesium sorption in these cases is primarily one of adsorption. However, the cesium loadings of the graphite, W-10 w/o Ta, and EOS W samples suggest another mechanism. The mechanism in graphite was assumed to be compound formation as discussed in references 4-9. The mechanism in the W-10 Ta sample was shown to be partly due to the presence of tantalum and is discussed more fully later. The reasons for the high loadings of the EOS W sample have not been determined. The test durations are also listed in Table 2. No significant changes in the cesium loading characteristics of any of the materials tested were observed over the duration of the tests, which lasted from 250-1200 hours. However, the carbon and both of the graphite samples were broken up during testing. The maximum loadings achieved in these three samples were approximately 1g Cs/g.

Carbon Sample, Pure Carbon FC-50

Isotherms for the carbon sample are shown in Figure 3. No significant hysteresis was observed except that lower loadings were observed on the first sorption curve than were later seen. These first results were probably due to the replacement of sorbed gases by cesium on the high surface area carbon. The Freundlich isotherm equation⁽¹³⁾ produced a satisfactory fit to the data. Lines of constant loading (isosteres) versus 1/T are plotted in Figure 4. These curves give the pressure-temperature relationship which would exist in a small volume thermionic cell.

The isosteric heat of adsorption was calculated from the relationship:

$$q = -R \frac{\Delta (\ln p)}{\Delta (1/T)}$$

Where R is the gas constant, 1.987 cal/deg mole

p is the pressure in torr

T is the sample temperature in degrees K

The variation of q with respect to loading is shown in Figure 5. q is essentially constant at approximately -33 Kcal/mole until the loading exceeds approximately 500 mg Cs/g carbon and then begins decreasing. This break in the curve is thought to occur near the formation of the first monolayer.

Graphite Samples, CARB-I-TEX 700 and Annealed Pyrolytic Graphite

Isotherms for the graphite samples are shown in Figures 6 and 7. Also plotted in the figures is the 700°C isotherm based on Salzano and Aronson's work on the cesium-graphite lamellar compounds.⁽⁷⁾

For the CARB-I-TEX sample, Figure 6, there was a knee in the curve on the 700°C isotherm where the transition from CsC_{24} to CsC_{10} should occur. However, as the cesium vapor pressure was increased the loading did not increase to the expected CsC_{10} level but instead rose uniformly with the cesium pressure.

Isotherms for the pyrolytic graphite sample, Figure 7, show several well defined plateaus, particularly those corresponding to the transitions between $C_{36}Cs$ -- $C_{24}Cs$ and $C_{24}Cs$ -- $C_{10}Cs$. In both samples, the loadings involved were generally less than expected from Salzano and Aronson's work.⁽⁷⁾

Figure 8 is a Clausius-Clapeyron Plot of all the graphite data. There is good agreement between this experiment and the previous work, particularly in the two highest loading transitions studied.

W-10 Ta and Tungsten Samples

Isotherms at 600, 800, and 1000°C are shown in Figure 9. The three isotherms show hysteresis effects and don't appear consistent.

The cesium loadings that were obtained were approximately 100 times higher than those expected from the measured BET surface area. Two possible explanations for the observed loading were considered. First, some type of chemical reaction could be involved, perhaps with the tantalum in the sample. Microprobe analysis of the W-10 Ta sample was

done after the test in cesium (final loading approximately 1 mg Cs/g) and proved that areas of high cesium concentration correlated directly with areas of high tantalum concentration. In addition, presence of a fourth constituent (possibly oxygen) in the areas of high cesium concentration was indicated, since the fractional parts of W, Ta, and Cs added up to only approximately 75 atom per cent of the total.

The possibility that capillary condensation had been occurring was also considered, particularly since a loading of 7 mg Cs/g W corresponded to enough cesium to fill 60% of the sample's pore volume.

In an attempt at reproducing the W-10 Ta result, five tungsten samples were selected and then loaded with cesium at 800°C and 10 torr. Then points were taken at 30 torr at 600°, 1000°, and 600°C in order to load and unload the samples. When the conditions of the first data point were repeated, no hysteresis was observed. Therefore, the oven was cooled down, retaining the cesium in the samples. The samples were then removed from their oven and counted separately. The cesium contents of these samples have been listed in Table 2.

The highest loading observed in mg Cs/g on the five samples was less than one tenth that of the W-10 Ta piece. Since the pore structures were roughly the same in all samples, it is improbable that the capillary condensation mechanism can be made to account for the high loadings. The last three samples all held about the same amount of cesium per square meter of surface area, an amount which is about equivalent to a monolayer coverage.

TABLE 2
COMPARISON OF CESIUM LOADING ALL SAMPLES TESTED

SAMPLE	DURATION OF TEST (hr)	PORE DIA	BET Surface Area m ² /g	CESIUM LOADING @800°C, 10 torr mg Cs/g	CESIUM LOADING @800°C, 10 torr mg Cs/m ²
Pure Carbon FC-50	450	--	347.	505.	1.75
Carborundum CARB-I-TEX 700 Graphite	1000	--	0.39	400.	1002.
Pyrolytic Graphite	500	--	0.8	420.	525.
EOS W-10 Ta	1200	2.79	0.023	2.1	91.
EOS W Misc. pcs.		--	< 0.02	0.17	< 9
EOS W 5253		3.44	< 0.3	0.12	> 0.4
Phillips W angular pwdr. 100		3N	0.05	0.062	1.2
Astromet, W 105		5N	0.042	0.054	1.3
TRW, W		2N	0.035	0.038	1.1
ALSIMAG 548, Al ₂ O ₃	250	--	0.2	0.4	2.0

Al₂O₃ Sample - American Lava ALSIMAG 548

Isotherms for the alumina sample are shown in Figure 10. The scatter in the data is primarily due to the low count rate from the sample. The highest loading attained, approximately 1 mg Cs/g, corresponds to approximately 2.5 mg/cm³ of alumina. Based on the measured BET surface area of 0.2 M²/gram and a cesium cross-sectional area of 28(Å)², one monolayer coverage amounts to approximately 0.2 mg Cs/g alumina. Actual loadings greater than five times this amount were achieved.

CONCLUSIONS

Although all of the materials tested appear useful in thermionic converters, advantages and disadvantages exist for each. The low loading samples, alumina and tungsten, are compatible with the other materials in a thermionic cell and dimensionally stable. However, the stability of their surface area has yet to be demonstrated for times of interest for thermionic diodes (5000-10,000 hours).

The high loading carbons and graphites have yet to be proven to be compatible with thermionic cells and are not dimensionally stable at the loadings to which they were subjected in this study. In addition, the sintering stability of the high surface area carbons has to be demonstrated.

The choice of which material would make the best reservoir depends to a large extent upon what amount of cesium is expected to be lost during cell operation. Work on this subject has been published⁽¹⁴⁾ and has found that total cesium losses to tungsten, molybdenum, tantalum, niobium and Al_2O_3 in two of the three cells studied were less than 20 μg . Those two cells were operated for 7558 and 10,406 hours. On the basis of these low magnitude cesium losses, all of the materials tested appear attractive.

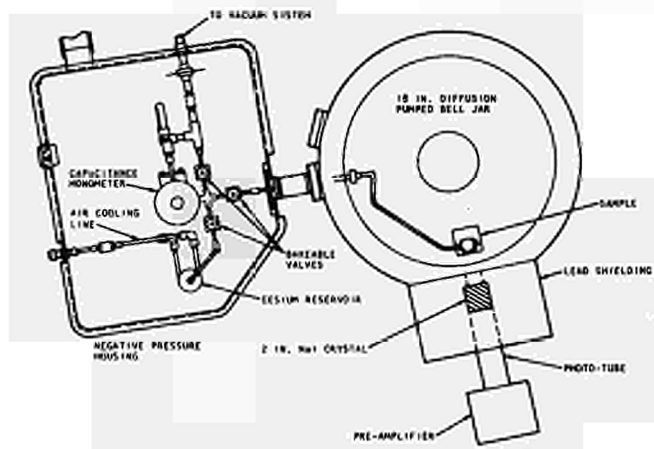


Figure 1 Plan View of Pressure-Temperature-Loading Apparatus

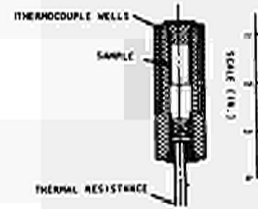


Figure 2 Double Mounting

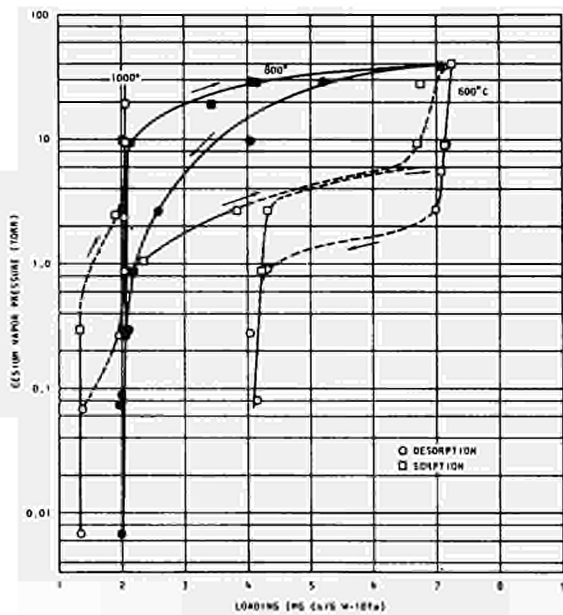


Figure 3 Pressure-Loading Isotherms for W-22 Sample

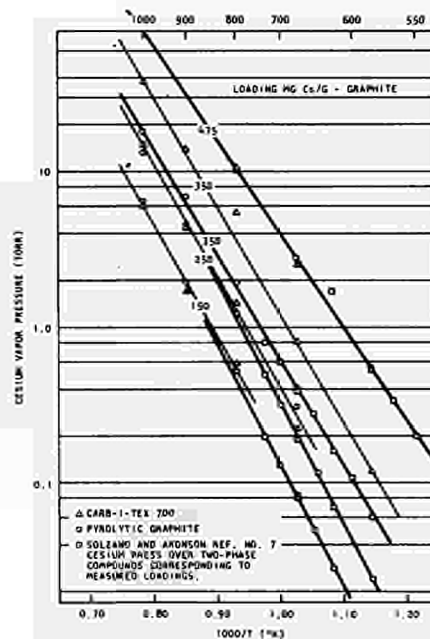


Figure 4 Desorption-Adsorption Pairs for Graphite Samples

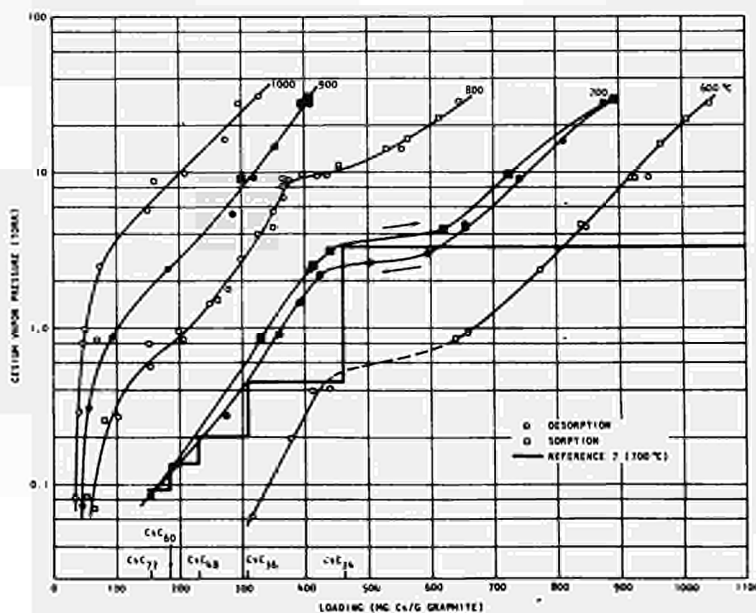


Figure 5 Pressure-Loading Isotherms Carbonized CARB-1-TEX 700

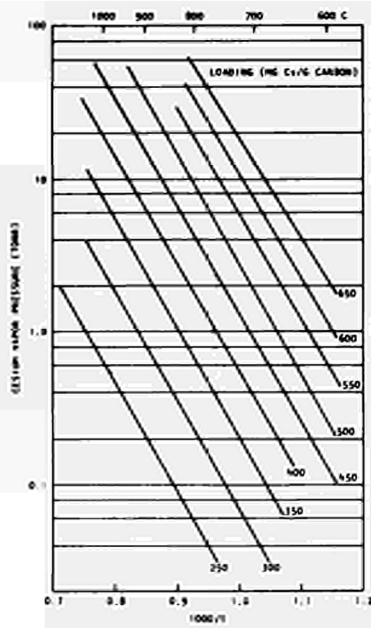


Figure 6 - Cesium-Capacitor Test For Graphite (within limits)

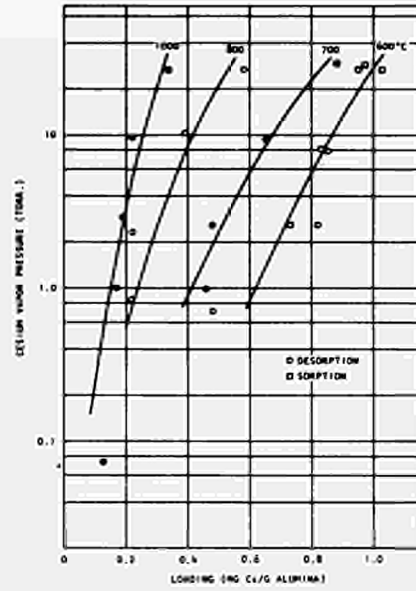


Figure 10 - Pressure-Loading Curves for Alumina-Absorber (also K27860-54)

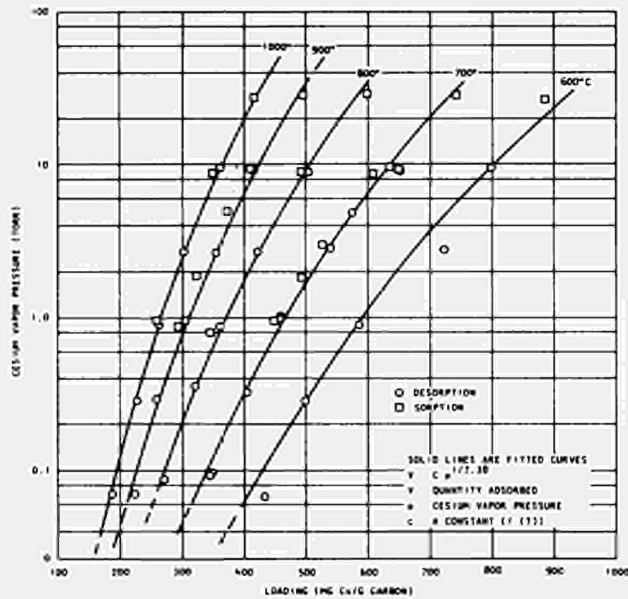


Figure 7 - Pressure-Loading Curves for Pure Graphite (PC-10)

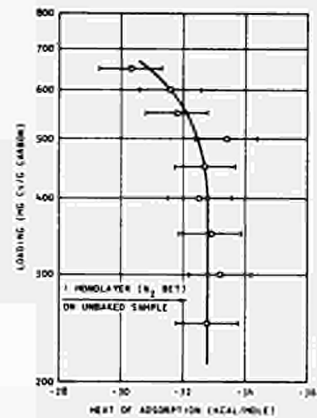


Figure 5 - Isotherm Heat of Adsorption for Pure Graphite (PC-10)

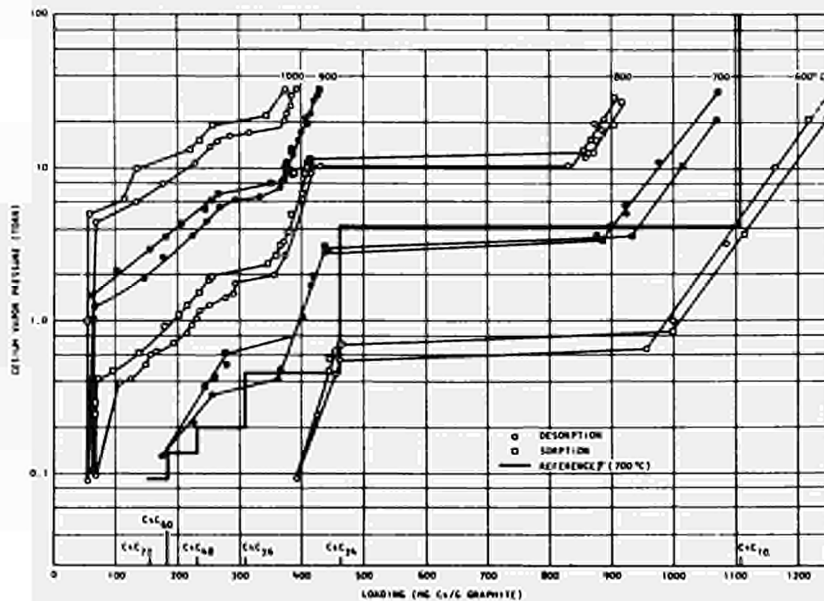


Figure 7 - Pressure-Loading Curves for Pyrolytic Graphite

REFERENCES

1. RCA, "The Development of an Adsorption Cesium Reservoir," Summary Technical Report, NYO-3642-4, December 1966.
2. C. E. MILSTEAD, A. B. RIEDINGER, L. R. ZUMWALT, "Cesium-Graphite Sorption Isotherms Determined by an Isopiestic Method," General Dynamics/General Atomic Division Report No. GA-6415 (Rev.), November 1965.
3. E. E. ANDERSON, G. L. WESSMAN, L. R. ZUMWALT, "Fission Product Trapping--Sorption of Cesium by Activated Charcoal," Nuclear Science and Engineering, No. 12, April 1961, p106.
4. A. HEROLD, "Recherches sur les composés d'insertion du graphite," Bull.Chem.Soc., France, 1955, p999.
5. S. ARONSON, F. J. SALZANO, "Some Experimental Observations in the Caesium-Graphite System," Journal of Inorganic and Nuclear Chemistry, Volume 26, January 1964.
6. S. ARONSON, F. J. SALZANO, "Kinetic Study of the Decomposition of Cesium-Graphite Lamellar Compounds," J.Chem.Phys., Volume 42, No. 4, February 1965, p1323.
7. S. ARONSON, F. J. SALZANO, "Thermodynamics Properties of the Cesium-Graphite Lamellar Compounds," J.Chem.Phys., Volume 43, No. 1, July 1965, p149.
8. S. ARONSON, F. J. SALZANO, "On the Bonding Energy in Cesium-Graphite Compounds," J.Chem.Phys., Volume 44, No. 11, June 1966, p4320.
9. S. ARONSON, F. J. SALZANO, "Stability of Phases in the Cesium-Graphite System," J.Chem.Phys., Volume 45, September 1966, p2221.
10. L. N. GROSSMAN, "Insulator Materials for Nuclear Thermionic Power Conversion," Thermionic Electrical Power Generation Conf., Proceedings, 1965 (London) Session 7b.
11. R. BREITWIESER, W. B. NOTTINGHAM, "Theoretical Background for Thermionic Conversion Including Space-Charge Theory, Schottky Theory and the Isothermal Diode Sheath Theory," NASA TN D-3324, March 1966.
12. K. BUTLER, G. KUSKEVICS, M. LACHANCE, B. THOMPSON, H. TODD, "Development and Testing of Porous Ionizer Materials," NASA/CR-54707, EOS Report #6650 Summary, Part I, September 1966.
13. J. W. MCBAIN, "The Sorption of Gases and Vapours by Solids," (London), 1932, p5.
14. G. BIZZELLI, R. G. HUDSON, L. YANG, "Post-Operational Determination of Cesium Contents in Life-Test Converter Components," Thermionic Conversion Specialist Conference, Proceedings, 1967 (Palo Alto), p271.

DISCUSSION

Speaker of the paper E-20: J. W. HOLLAND.

DAVIS (USA): For stability analysis it would be quite interesting to know what the kinetics of the absorption and desorption are, that is, the pressure response timewise to a change in the reservoir temperature. Did you get any indication of that? Was it relatively fast, or relatively slow?

HOLLAND (USA): Most of these samples other than that tungsten-tantalum are fast. They were so fast that you could not track them because of the thermal inertia of the system that you are measuring. But tungsten-tantalum generally took on the order of hours to come to complete equilibrium.

SUR LES APPLICATIONS, AUX ETUDES DES EMETTEURS THERMO-IONIQUES,
D'UN NOUVEAU REACTIF DU MOLYBDENE.

R. HASSON

Département de Physico-Chimie, Service d'Etude des Barrières et de l'Hexafluorure
d'Uranium, Centre d'Etudes Nucléaires de Saclay
91 Gif-sur-Yvette (France)

Résumé -

Après avoir mis au point un réactif micrographique colorant les grains de molybdène en relation avec leur orientation cristalline, nous avons pu observer et mettre en évidence les propriétés physiques et métallurgiques des orientations du métal.

Appliqué aux études de soudure et de diffusion des métaux réfractaires, ce réactif a mis en évidence la grande réactivité des grains présentant l'orientation cristalline (100).

I. Introduction.

Les études micrographiques des convertisseurs thermo-ioniques, nous ont conduit à la mise au point d'un réactif colorant les grains de molybdène en fonction de leur orientation cristalline [1], dont nous résumons la composition :

Fe Cl_3^* : 40 à 60 cc

H Cl à 22° B^e : 25 cc

$\text{C}_2\text{H}_5\text{OH}$ à 95° : 75 cc.

Les conditions d'utilisation de ce bain sont les suivantes :

- température ambiante,
- durée d'immersion : 2 à 3 minutes,
- rinçage à l'eau courante.

Les colorations obtenues sont :

- | | | |
|-----------------------|---|------------------------------|
| - plan (100) | - | jaune d'or |
| - plan (110) | - | bleu foncé |
| - plan (111) | - | bleu foncé à violette |
| - plan (111) \pm 2° | - | bleu foncé à violette |
| - plan (112) | - | bleu clair à bleu très clair |
| - plan (116) | - | jaune d'or |

Utilisé au début uniquement pour révéler le molybdène et identifier les orientations cristallines des grains de ce métal, ce réactif micrographique a ensuite été appliqué à l'étude métallographique du molybdène pur et des assemblages de ce métal avec d'autres métaux réfractaires.

* solution à 1 300 g de Fe Cl_3 par litre - densité 1,26.

II. Applications du réactif.

a) Identification chimique.

Ce réactif, ne colorant que le molybdène pur, permet de localiser rapidement cet élément dans les assemblages complexes et de révéler les inclusions de composés (fig. 1) ou de métaux (fig. 2) étrangers, et aussi les revêtements (fig. 3).

b) Influence de l'orientation cristalline sur les propriétés physiques et chimiques du molybdène.

L'orientation cristalline étant révélée par une simple immersion dans le réactif micrographique, il devient aisé de déterminer les propriétés du molybdène en fonction des orientations cristallines.

Nous avons pu ainsi observer la croissance exagérée des grains présentant une orientation (100) de couleur jaune d'or, et (110) de couleur bleu foncé (fig. 4).

Les grains présentant le plan (100) ont des propriétés nettement différentes de celles des autres grains. On met en effet en évidence l'aptitude de cette orientation à donner des grains immenses au cours des traitements thermiques (fig. 5).

On constate aussi qu'aux frontières de ces grains particuliers les liaisons obtenues soit par soudage (fig. 6 et 7), soit par diffusion intermétallique (fig. 8) sont beaucoup plus intimes.

On note également, à leur surface, une densité de porosités plus élevée.

Enfin, on a observé, lors d'examen de convertisseurs thermo-ioniques après fonctionnement, que seule cette orientation cristalline présentait des ségrégations de grains.

Signalons enfin, pour conclure, que les porosités semblent accélérer nettement la vitesse de diffusion intermétallique.

Cette caractéristique a été mise en évidence sur un émetteur thermo-ionique molybdène-tungstène (fig. 9).

REMERCIEMENTS.

Au Département de Physico-Chimie du Commissariat à l'Energie Atomique, nous tenons à remercier tout particulièrement Madame CHARPIN pour les études en Rayons X, Madame DAGOURY et Monsieur CALVET pour leur aide, au Laboratoire de Métallographie.

Nos remerciements vont aussi à Monsieur le Professeur OUDAR, de la Faculté des Sciences de Paris, pour les conseils qu'il nous a si souvent prodigués.

REFERENCES BIBLIOGRAPHIQUES.

- [1] R. HASSON - Sur la métallographie en couleurs du molybdène - Symposium de Microscopie, Cambridge, Août 1967.



Fig. 1 - (x 800) - Composés en inclusions dans le molybdène.



Fig. 2 - (x 460) - métal (tungstène) en inclusion dans le molybdène.

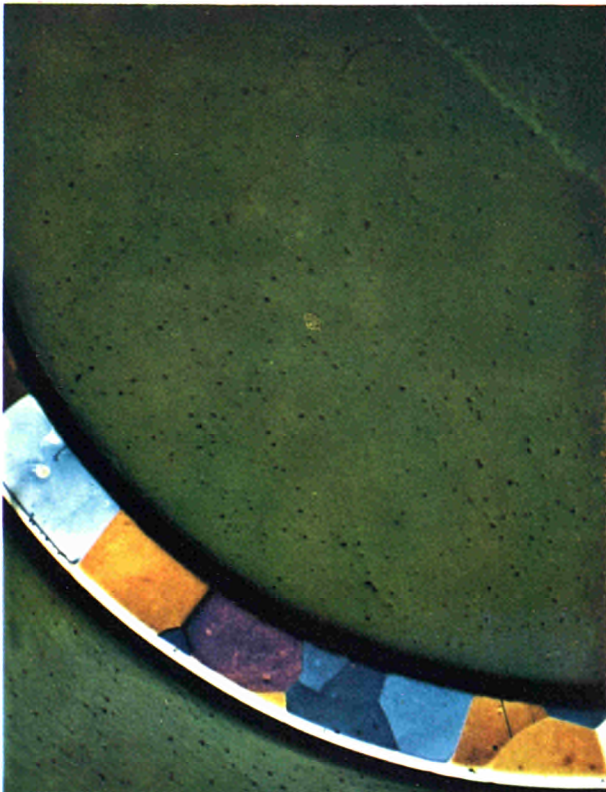


Fig. 3 - (x 14) - revêtement de rhénium (en blanc) sur du molybdène.

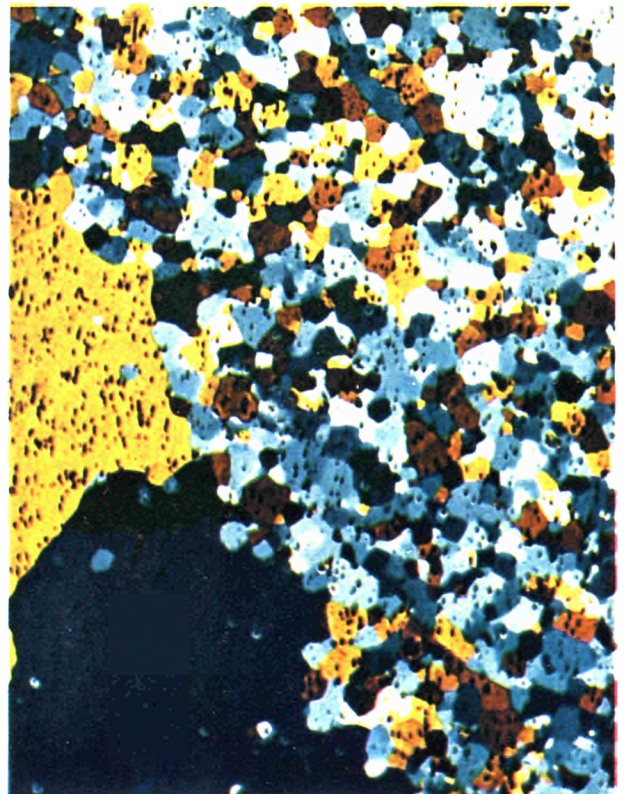


Fig. 4 - (x 76) - croissance exagérée des grains (100) et (110) .



Fig. 5 - (x 76) - monocristal de molybdène obtenu par un maintien de 3 heures à 1750° C.

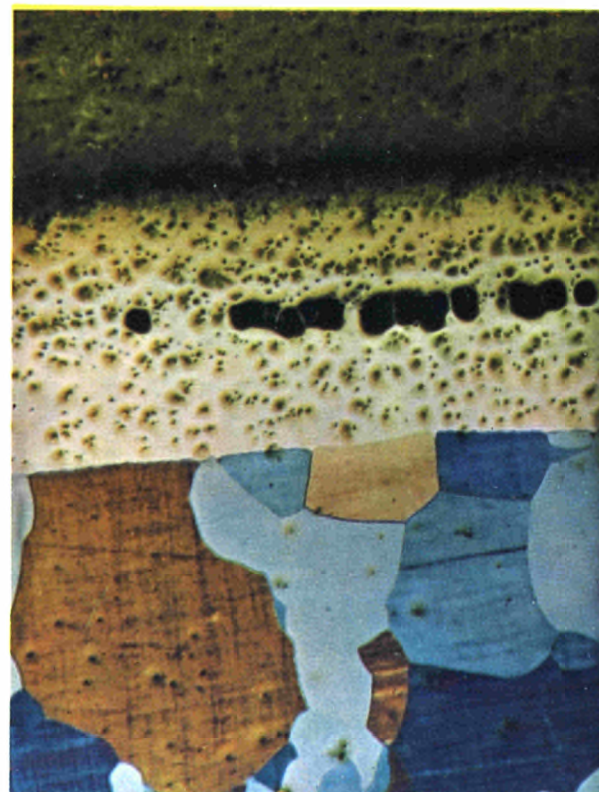


Fig. 6 (x 76) - jonction molybdène-titane.



Fig. 7 (x 76) - jonction molybdène-tantale.



Fig. 8 (x 90) - diffusion intermétallique molybdène - rhénium.

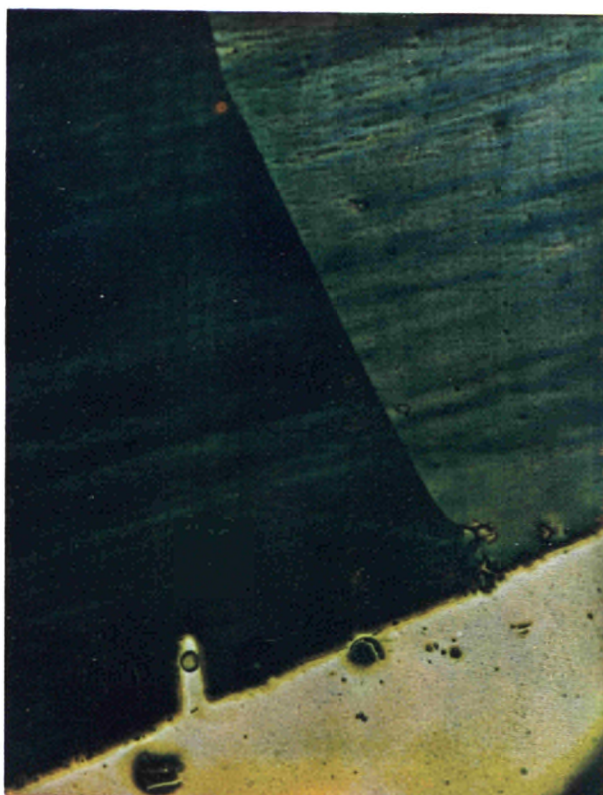


Fig. 9 (x 460) - migration dans le molybdène d'une porosité du revêtement de tungstène.

THEORY OF THERMIONIC CONVERTER OPERATION
WITH APPLICATIONS TO THERMIONIC REACTOR ANALYSIS

D. R. Wilkins, C. D. Sawyer, P. R. Hill
General Electric Company, Pleasanton, California
United States of America

ABSTRACT

Fundamental principles of molecular chemistry, statistical mechanics, and plasma physics are used to derive theoretical output current and efficiency characteristics of vapor thermionic converters. The results are obtained in terms of basic physical parameters which describe the converter electrodes and interelectrode gas and are in good agreement with corresponding experimental measurements for a broad range of converter operating conditions.

The theoretical formalism is employed to study the thermal and electrical performance characteristics of a nuclear thermionic fuel element. It is shown that, with realistic axial fission profiles, fuel void fractions, and temperature limits, over-all fuel element efficiencies in the vicinity of 12 to 14% can be achieved.

INTRODUCTION

A theoretical description of thermionic converter operation is important in developing thermionic power plants. In particular, accurate converter theory greatly facilitates the design, testing, and evaluation of prototype converters, and is fundamental in analytical studies which lead to an optimum power plant design.

An analytical description of the thermionic converter which adequately fulfills these needs must incorporate three key features: (1) be formulated in terms of basic data which characterizes the converter materials and operating conditions; (2) be applicable to the entire domain of practical thermionic converter operation; (3) yield results which are in agreement with experimental data.

The development of a useful analytic description of thermionic converter performance requires that due consideration be given to both electrode surface and interelectrode volume phenomena and to Schottky effects which occur at the electrode surface - interelectrode volume interfaces. Phenomena in each area have been separately considered in previous theoretical studies, many of which are cited in the literature.^(1, 2) These studies have served to isolate and to clarify many of the individual physical processes which are significant in thermionic converter operation. No attempt has been made, however, to combine and extend the previous analyses to provide a unified, practical theoretical description of thermionic converter operation.

In this study, a unified theoretical description of thermionic converter performance characteristics is developed, programmed for digital computer studies, and the theoretical results compared with appropriate experimental data. Significant features of the analysis are that it: (a) simultaneously accounts for the influence of surface and volume phenomena and Schottky effects on converter operation, (b) contains no restrictions concerning the "mode" of converter operation, (c) deals with the plasma sheath polarities self-consistently, (d) applies to converters with elevated collector temperatures, (e) provides for the determination of converter efficiency, and (f) is not restricted to Cs converters. Theoretical output current characteristics

are obtained for a W emitter, Mo collector converter and exhibit good agreement with corresponding experimental characteristics for a broad range of emitter and Cs reservoir temperatures, and interelectrode spacings.

As an illustrative practical application, the theoretical formalism is employed to optimize the thermal and electrical performance characteristics of a nuclear thermionic fuel element (TFE). The influences of different design constraints on the optimized performance characteristics are discussed.

THERMIONIC CONVERTER THEORY

VOLUME PHYSICS

The neutral interelectrode plasma in a thermionic converter may be analyzed by using a previously derived set of transport differential equations.⁽³⁾ Since plasma electron temperatures are nearly uniform,⁽⁴⁾ these equations may be written in the well-known approximate form:

$$(dJ_e/dx) = (dJ_i/dx) = e(\nu_i n - \beta_r n^3) \quad (1)$$

$$J_e = -e\mu_e [\theta_e (dn/dx) + nE]; J_i = -e\mu_i [\theta_i (dn/dx) - nE] \quad (2)$$

where J_α , μ_α , and θ_α are the current density, mobility, and temperature (in electron volts) for the electrons ($\alpha = e$) and ions ($\alpha = i$), respectively; n is the charged particle density; E is the electric field; ν_i is the ionization frequency; and β_r is the three-body recombination coefficient.

The source terms in Eq. (1) describe a multistage volume ionization-recombination process. The recombination coefficient for Cs is assumed to have a form similar to that for hydrogen,⁽⁶⁾ since both atoms have a valence of unity and similar binding energies for the higher excited states. The ionization frequency ν_i is computed from the recombination coefficient β_r to satisfy certain thermodynamic equilibrium requirements.⁽²⁾

The electron and ion mobilities in Eq. (2) are computed by using relations previously developed for three-component plasmas.⁽³⁾ Both charged particle and charged particle - neutral particle collisions are accounted for in the electron and ion mobilities. The former collisional processes are represented by a Coulomb interaction potential, while the latter are described in terms of effective hard sphere cross sections. The plasma electron temperature, which is assumed to uniform, must satisfy the energy balance equation

$$q_{e1} - q_{e0} = JV_P - (J_{i1} - J_{i0}) V_i \quad (3)$$

where q_e is the electron kinetic energy flux; V_P is the voltage drop across the interelectrode plasma, and the subscripts "0" and "1" are used to denote a quantity evaluated at the emitter and collector edges of the plasma, respectively.

Equations (1) and (2) are integrated to yield, in terms of Jacobi elliptic functions, the charged particle density and electrostatic potential distributions in the interelectrode plasma.⁽²⁾ The integration constants which arise and the electron kinetic energy fluxes q_{e0} and q_{e1} are evaluated from sheath analyses as discussed in the following paragraphs.

The electrostatic sheaths at the plasma-electrode interfaces are analyzed by writing electron and ion current and electron kinetic energy flux balances across the sheaths; i. e., between each electrode and the adjacent edge of the interelectrode plasma. The exact form of these balances for a given sheath depends upon its polarity, which is referred to here as accelerating or retarding if the sheath accelerates or retards, respectively, an electron traveling toward the collector. Electron and ion current and electron kinetic energy flux balances are given in Table 1 for accelerating and retarding emitter and collector sheaths. In this table, J_M and I_M are the electron and ion emission current densities, respectively, for the emitter ($M=E$) and collector ($M=C$); V_M are the sheath voltage drops at the emitter ($M=E$) and collector ($M=C$) edges of the plasma; and J_r and I_r are the electron and ion random current densities, respectively, in the interelectrode plasma. Note that the sheath voltage drops are treated as negative and positive for accelerating and retarding sheaths, respectively. The equations presented in Table 1 contain terms, derived from first order transport theory, to account for the non-Maxwellian, anisotropy of the plasma electron and ion distribution functions. These terms become appreciable if the net particle currents near the sheaths are comparable to the corresponding random currents.

The electron and ion emission current densities from the emitter and collector (Table 1) are governed by surface phenomena and Schottky effects. The theoretical determination of these quantities is discussed in the following two sections.

SURFACE PHYSICS

The field-free, electron work function ϕ_M of a substrate metal (M) partially coated by an adsorbate film depends upon the substrate and adsorbate properties, the substrate temperature T_M , and the adsorbate reservoir temperature T_R . In other words, for a specified substrate and adsorbate: $\phi_M = \phi_M(T_M, T_R)$. The theoretical prediction of this relation for thermionic emitters ($M=E$) and collectors ($M=C$) is the objective of thermionic converter surface physics studies.

TABLE 1. Emitter and Collector Sheath Analyses

ACCELERATING EMITTER SHEATH ($V_E \leq 0$)	ACCELERATING COLLECTOR SHEATH ($V_C \leq 0$)
1. $J_{e0} = J_E - (J_{r0} - 1/2 J_{e0}) \exp(V_E/\theta_e)$	1. $J_{e1} = (J_{r1} + 1/2 J_{e1}) - J_C \exp(V_C/\theta_C)$
2. $J_{i0} = I_E \exp(V_E/\theta_E) - (I_{r0} - 1/2 J_{i0})$	2. $J_{i1} = (I_{r1} + 1/2 J_{i1}) \exp(V_C/\theta_C) - I_C$
3. $q_{e0} = 2 J_E (\theta_E - \theta_e) + J_{e0} (2 \theta_e - V_E)$	3. $q_{e1} = 2 J_{r1} (\theta_e - \theta_C) + J_{e1} (\theta_e + \theta_C)$
RETARDING EMITTER SHEATH ($V_E \geq 0$)	RETARDING COLLECTOR SHEATH ($V_C \geq 0$)
1. $J_{e0} = J_E \exp(-V_E/\theta_E) - (J_{r0} - 1/2 J_{e0})$	1. $J_{e1} = (J_{r1} + 1/2 J_{e1}) \exp(-V_C/\theta_e) - J_C$
2. $J_{i0} = I_E - (I_{r0} - 1/2 J_{i0}) \exp(-V_E/\theta_E)$	2. $J_{i1} = (I_{r1} + 1/2 J_{i1}) - I_C \exp(-V_C/\theta_C)$
3. $q_{e0} = 2 J_{r0} (\theta_E - \theta_e) + J_{e0} (\theta_E + \theta_e)$	3. $q_{e1} = 2 J_C (\theta_e - \theta_C) + J_{e1} (2 \theta_e + V_C)$

Notes

1. Electron Current Balance 2. Ion Current Balance 3. Electron Kinetic Energy Flux Balance

In this analysis, the recently developed Steiner-Gyftopoulos formalism⁽⁷⁾ is employed to determine the field-free, emitter and collector work functions. This formalism is an extension of earlier work⁽⁸⁾ and is based upon principles of molecular chemistry and statistical mechanics; it yields the relation $\phi_M = \phi_M(T_M, T_R)$ once a set of parameters which characterize the substrate and adsorbate are specified.

SCHOTTKY EFFECTS

The field-free work functions do not always prevail at the emitter and collector electrodes in a thermionic converter. In particular, if the emitter sheath is accelerating or the collector sheath is retarding, the electric field at the corresponding electrode surface depresses the effective electrode work function as shown in Fig. 1.

The effective lowering of an electrode work function by an imposed electric field (Fig. 1) was first analyzed by Schottky who obtained

$$\Delta \phi_M = \phi_M - \phi'_M = \sqrt{[e/(4\pi\epsilon_0)] E_M} \quad (4)$$

where ϕ_M and ϕ'_M are the field-free and effective work functions of electrode M, respectively, e is the electronic charge, ϵ_0 is the vacuum permittivity, and E_M is the magnitude of the electric field existing at the surface of electrode M.

Hansen^(9,10) employed Eq. (4) to demonstrate the importance of Schottky effects in thermionic converters. The analyses were performed for limited domains of converter operation, and they cannot readily be extended to apply to the broad range of converter operating conditions under present consideration. Therefore, an alternate approach to the analysis of Schottky effects in thermionic converters is utilized here. Significant features of the present analysis are that it is mathematically simple, and yet can be expected to yield reasonably accurate results for the entire range of converter operating conditions of practical interest.

In applying Eq. (4) to the present problem, some uncertainty exists concerning the electric field, E_M , since the exact potential distribution within the electrostatic sheath is unknown. Generally, the sheath voltage drop occurs within several plasma electron Debye lengths of the electrode. Hence, it is reasonable to expect that the electric field at the electrode surface can be accurately approximated by

$$E_M = k_S |V_M| / L_M \quad (5)$$

where L_M is the electron Debye length at the edge of the plasma adjacent to the sheath; and k_S is a dimensionless constant of order unity.

Equations (4) and (5) are used in this analysis to describe the Schottky reduction of the emitter work function caused by an accelerating emitter sheath, and of the collector work function caused by a retarding collector sheath. The field-free work functions ϕ_M (M=E, C) are computed from surface physics considerations; Eq. (4) and (5) then yield the effective work functions ϕ'_M (M=E, C). When the emitter sheath is retarding or the collector sheath is accelerating, no Schottky correction is applied to the corresponding electrode work function; i. e., $\phi'_M = \phi_M$.

Once the effective work function ϕ'_M is determined, emission current densities of electrons and ions from a thermionic converter electrode M (M=E, C) follow directly from the Richardson and Saha-Langmuir equations, respectively. In particular:

$$J_M = A T_M^2 \exp(-\phi'_M/\theta_M); \quad \theta_M = k T_M/e \quad (6)$$

$$I_M = e p_g (2\pi m_g e \theta_M)^{-1/2} (1/2) \exp [-(V_i - \phi'_M)/\theta_M] \quad (7)$$

where A is the Richardson constant and m_g is the mass of the adsorbate atoms. Equation (7) is an approximate form of the Saha-Langmuir equation which is valid provided the surface ionization probability is small compared to unity. This condition is always fulfilled for practical thermionic converter operating conditions.

THERMIONIC CONVERTER PERFORMANCE

The thermionic converter output voltage V for a specified output current density J is obtained by summing the voltage drops between the emitter and collector Fermi levels. Thus,

$$V = \phi'_E + V_E - V_P + V_C - \phi'_C \quad (8)$$

The several terms in this relation follow directly from the preceding analyses.

The intrinsic efficiency η_i of a thermionic converter is defined as the efficiency in the absence of electrode, lead, and structural support losses. This efficiency is independent of detailed converter design considerations and is given by

$$\eta_i = P/(Q_e + Q_i + Q_r + Q_g) \quad (9)$$

where $P = JV$ is the output power density; and Q_e , Q_i , Q_r , and Q_g are the heat fluxes removed from the emitter by electrons, ions, radiation, and gas conduction, respectively. The first three heat fluxes are given by

$$Q_e = J_{e0} (\phi'_E + V_E) + q_{e0} \quad (10)$$

$$Q_i = -J_{i0} (\phi'_E + V_E) + J_{i0} V_i \quad (11)$$

$$Q_r = \sigma (\epsilon_E T_E^4 - \epsilon_C T_C^4) \quad (12)$$

where σ is the Stefan-Boltzmann constant, and ϵ_E and ϵ_C are effective emissivities. An expression for the interelectrode gas conduction term Q_g for Cs has been given by Kitrilakis, et al. (11) Note that Eq. (9) is readily modified to compute device efficiencies for specific converter designs by including terms to account for electrode, lead, and structural support losses.

COMPARISON OF THEORY WITH EXPERIMENT

NUMERICAL CALCULATIONS

A digital computer code has been written which incorporates the volume physics, surface physics, and Schottky effect analyses described here. The code input includes the physical parameters which characterize the converter electrodes and interelectrode gas and the converter operating conditions. With this input, the code obtains iterative solutions of the equations which

describe the surface and volume phenomena. In these computations, self-consistent sheath polarities are determined for each set of converter operating conditions; Schottky corrections are applied to the electrode work functions if appropriate. The code returns the converter output current and efficiency characteristics and other operating parameters of practical interest.

EXPERIMENTAL DATA

The experimental data chosen for comparison is a set of output current characteristics obtained by TECO⁽²⁾ for a thermionic converter with a heat-treated W emitter and polycrystalline Mo collector. The characteristics encompass a broad range of converter operating conditions and are divided into three groups to exhibit the effects of independent variations in emitter temperature, Cs reservoir temperature, and interelectrode spacing (Fig. 2).

THEORETICAL INPUT PARAMETERS

The input parameters used to compute output current characteristics for comparison with the experimental data are presented elsewhere.⁽²⁾ It is shown that the values employed for the key parameters are in satisfactory agreement with the available, but sometimes limited and inapplicable, independent data.

THEORETICAL RESULTS

The theoretical output current characteristics in Figure 2 are computed for the indicated operating conditions by using the techniques and data reported here. The results are in excellent qualitative and good quantitative agreement with corresponding experimental measurements for the entire range of converter operating conditions. Even better agreement could be anticipated, however, with slight adjustments of certain input parameters.

Note that both the computed and measured output current characteristics in Fig. 2 exhibit an abrupt rise in the output current density as the output voltage is decreased and the converter enters the ignited mode of operation. The theory of this transition from the extinguished to the ignited mode has not been previously presented.

Another significant feature of the theoretical results in Fig. 2 is the nonsaturation of certain output current characteristics at low output voltage; e. g., curve 4 of Fig. 2a. The significant increase in the output current density as the output voltage is decreased is due to Schottky effects and ion currents at the emitter surface.

THERMIONIC FUEL ELEMENT ANALYSIS

In this section the theoretical formalism is employed in an investigation of the thermal and electrical performance characteristics of a nuclear TFE. The influence of fuel center and emitter temperature constraints on the performance of the fuel element is shown.

FUEL ELEMENT DESCRIPTION

A nuclear TFE is shown in Fig. 3; it consists of N series-connected cells contained within an insulated sheath tube and serviced by a single cesium reservoir. Each cell is loaded with an

identical volume fraction of UO_2 fuel, and receives a fraction f_n ($1 \leq n \leq N$) of the total TFE thermal power. In general, the f_n 's are unequal because of the nonuniformities in the axial fission profile. The fuel element is cooled externally by a liquid metal coolant.

COMPUTATIONAL PROCEDURE

The operating state of a multicell TFE is completely defined by specifying the thermal power, axial power distribution, electrical current, cesium reservoir temperature, coolant inlet temperature, and over-all coolant temperature rise. Figure 4 shows the logical structure of a digital computer program which employs this information to yield a cell-by-cell and over-all description of the TFE electrical and thermal performance characteristics. This program incorporates the thermionic converter analysis as a subroutine. Other major subroutines describe heat transfer within the fuel-emitter body, through the tri-layer collector-insulator-sheath structure, and from the TFE sheath to the liquid metal coolant.

TFE PERFORMANCE CHARACTERISTICS

A 12-cell TFE with a coolant inlet temperature of 800°K and over-all coolant temperature rise of 100°K is discussed. The axial fission profile, which is typical for a small, fast spectrum, thermionic reactor, is shown in Table 2. Note that this profile exhibits a peak-to-minimum fission ratio of 1.2 to 1.0.

TABLE 2. Axial Fission Profile

<u>Cell, n</u>	<u>Fractional Power, f_n</u>	<u>Cell, n</u>	<u>Fractional Power, f_n</u>
1	0.08020	7	0.09071
2	0.07434	8	0.08858
3	0.07933	9	0.08463
4	0.08502	10	0.07945
5	0.08899	11	0.07490
6	0.09099	12	0.08288

A summary of the performance characteristics of the 12-cell fuel element for a thermal input power P_{th} of 14.9 kWt is given in Fig. 5. Shown versus electrical current density are: (a) the optimum cesium reservoir, T_r^{opt} , (b) the cesium optimized electrical power, P_e , (c) the highest prevailing emitter temperature, T_e^{max} , and (d) the highest prevailing central fuel cavity temperature, T_f^{max} . The latter quantity is shown for several fuel void fractions, V . Note that the maximum electrical output which can be achieved for the 14.9 kWt thermal input is 2.24 kWe; which corresponds to an over-all TFE efficiency of 15%.

The influence of design constraints on the fuel and emitter temperatures is readily deduced from Fig. 5. Suppose, for example, that the cell emitter temperatures are to be operated below 2073°K . This temperature restricts the permissible output current densities to values in excess of 10.6 A/cm^2 . The maximum electrical output consistent with this constraint is 2.02 kWe which corresponds to a TFE efficiency of 13.5%. For a specified fuel void fraction, constraints on the central fuel cavity temperature may be applied in a like manner.

Plots of the type shown in Fig. 5 have been computed for other TFE thermal power levels. For each thermal power, an optimum electrical output exists for a given set of design constraints.

Figure 6 shows the fully optimized TFE electrical output versus thermal input for different design limitations on the emitter and central fuel cavity temperatures. In Fig. 6 Curve 1 represents an upper limit which is achieved in the absence of temperature limitations. Curves 2 through 5 reflect the influence of both a 2073°K emitter temperature limit and a 2850°K central fuel cavity temperature limit on the results for different fuel void fractions. Note that when such temperature limits are imposed the electrical output does not increase monotonically with thermal input.

The results shown in Fig. 6 indicate that, with realistic axial fission profiles, fuel void fractions, and temperature limitations, TFE efficiencies in the vicinity of 12 to 14% can be achieved. The determinations of over-all thermionic reactor efficiencies require further optimizations involving fuel loading fractions and radial fission distributions, and is beyond the scope of this paper. Results of the type presented in Fig. 6, however, are important in such determinations.

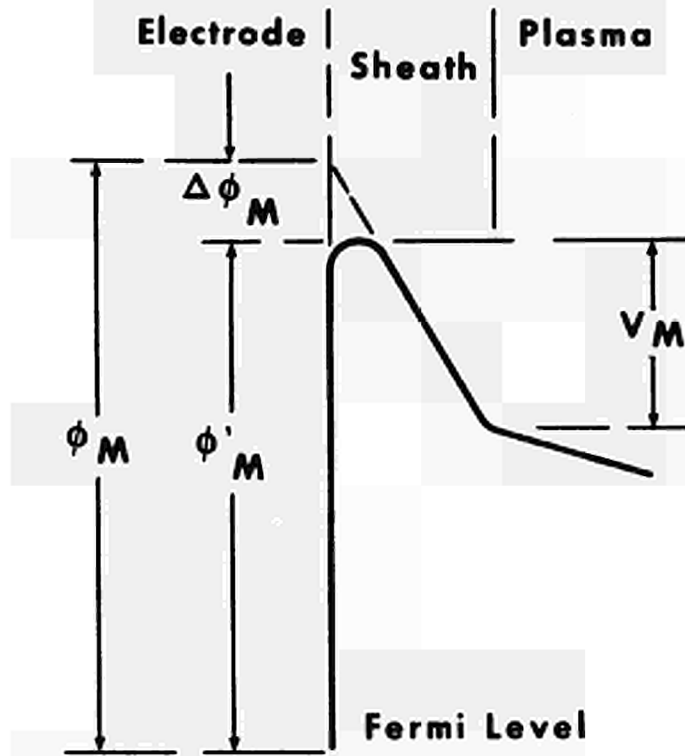
SUMMARY AND CONCLUSIONS

A unified theoretical description of thermionic converter performance characteristics is presented. The analysis simultaneously accounts for the influence of surface phenomena, volume phenomena, and Schottky effects on converter operation; and yields theoretical output current characteristics which are in good agreement with experiment data for a very broad range of converter operating conditions. The analysis has practical applications for converter physics studies, converter performance evaluations, and thermionic power plant design.

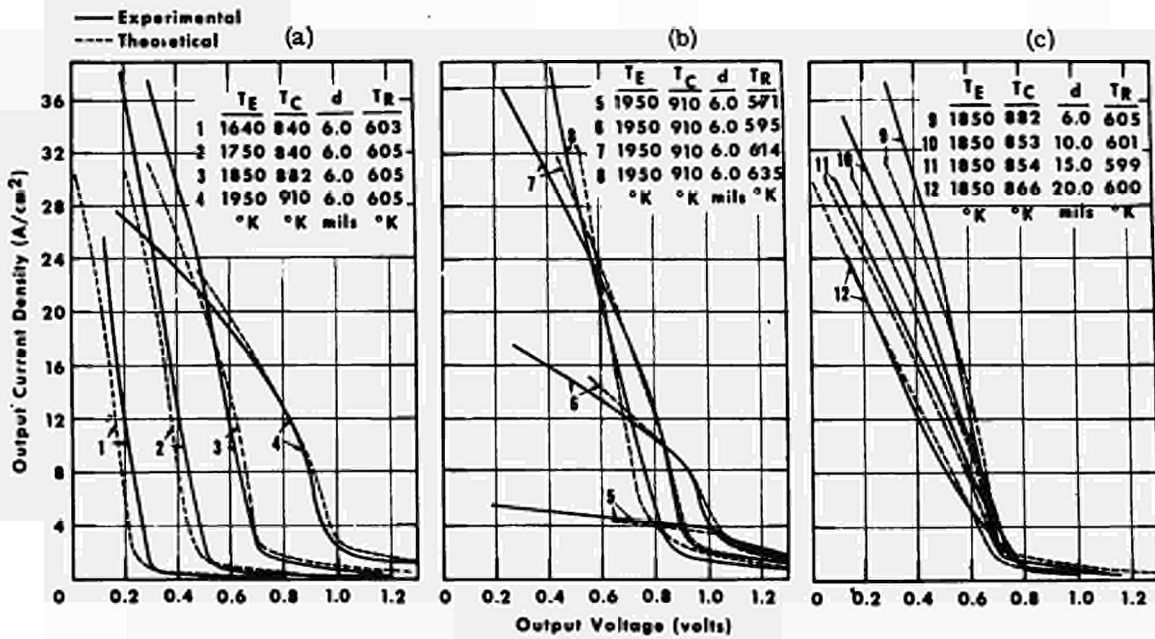
The electrical and thermal performance characteristics of a 12-cell nuclear thermionic fuel element are described. It is shown that, with realistic axial fission profiles, fuel void fractions, and fuel and emitter temperature limitations, TFE efficiencies in the 12 to 14% range can be realized.

REFERENCES

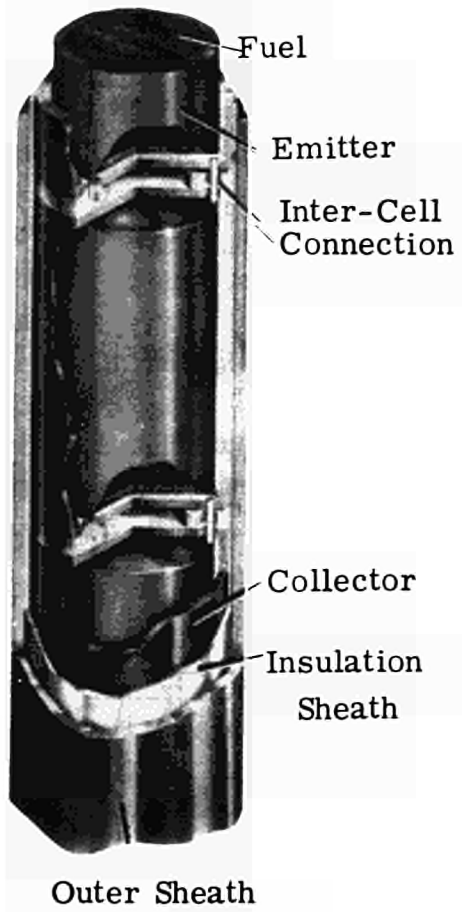
1. Bullis, R. H., et al., Therm. Conv. Spec. Conf., San Diego, Calif., October 1965.
2. Wilkins, D. R., to be published, J. Appl. Phys., (1968).
3. Wilkins, D. R. and Gyftopoulos, E. P., Proc. Int. Conf. on Therm. Elec., Power Gen., London, England, September 1965.
4. Reichelt, W. H., Proc. Int. Conf. on Therm. Elec. Power Gen., London, England, September 1965.
5. Wilkins, D. R. and Gyftopoulos, E. P., Proc. Therm. Conf., San Diego, Calif., October 1965.
6. Hinnov, E. and Hirschberg, J. G., Phys. Rev. 125 (1962) 795-801.
7. Steiner, D. and Gyftopoulos, E. P., Proc. 27th Ann. Phys. Elec. Conf., Cambridge, Mass., March 1967.
8. Levine, J. D. and Gyftopoulos, E. P., Surface Science, 1 (1964) 171-193, 225-241, 349-360.
9. Hansen, L. K., Proc. 25th Ann. Phys. Elec. Conf., Cambridge, Mass., March 1965.
10. Hansen, L. K., Proc. Therm. Conv. Spec. Conf., San Diego, Calif., October 1966.
11. Kitrilakis, S. and Meeker, M., J. Adv. Energy Conv., 3 (1963) 59-68.
12. Howard, R., Thermo Electron Corp., Waltham, Mass., private communication, March 1966.



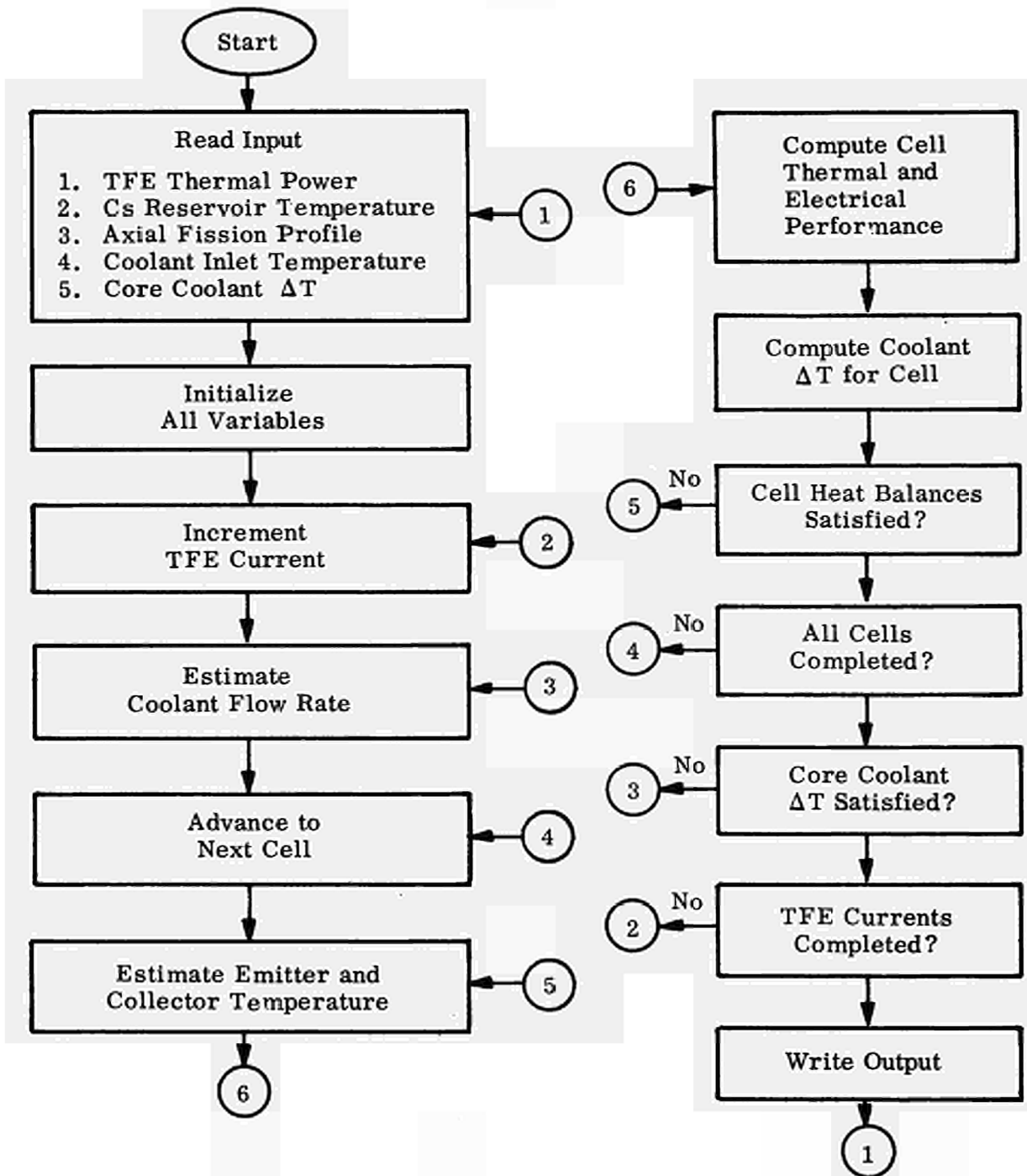
1 Influence of Electrostatic Sheath on Work Function of Thermionic Converter Electrode



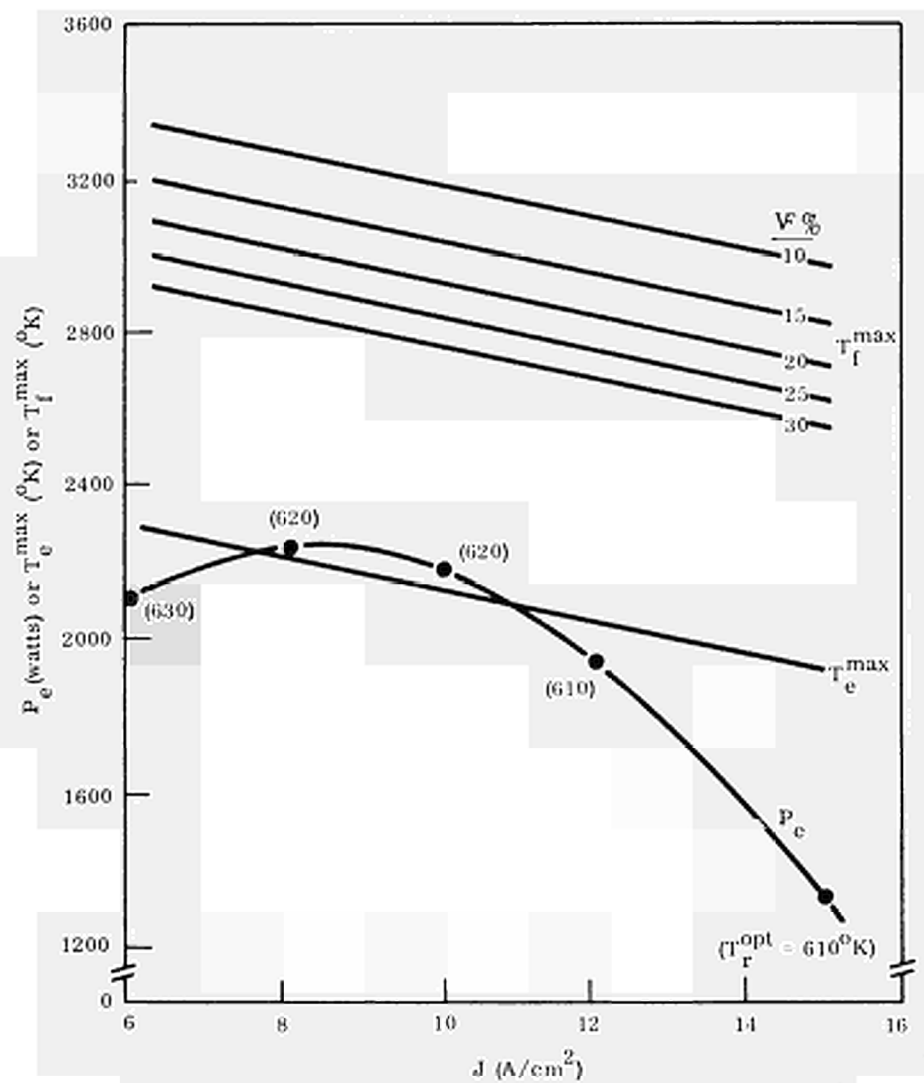
2 Comparison of Computed and Measured⁽²⁴⁾ Output Current Characteristics For Several (a) Emitter Temperatures, (b) Cesium Reservoir Temperatures, and (c) Interelectrode Spacings



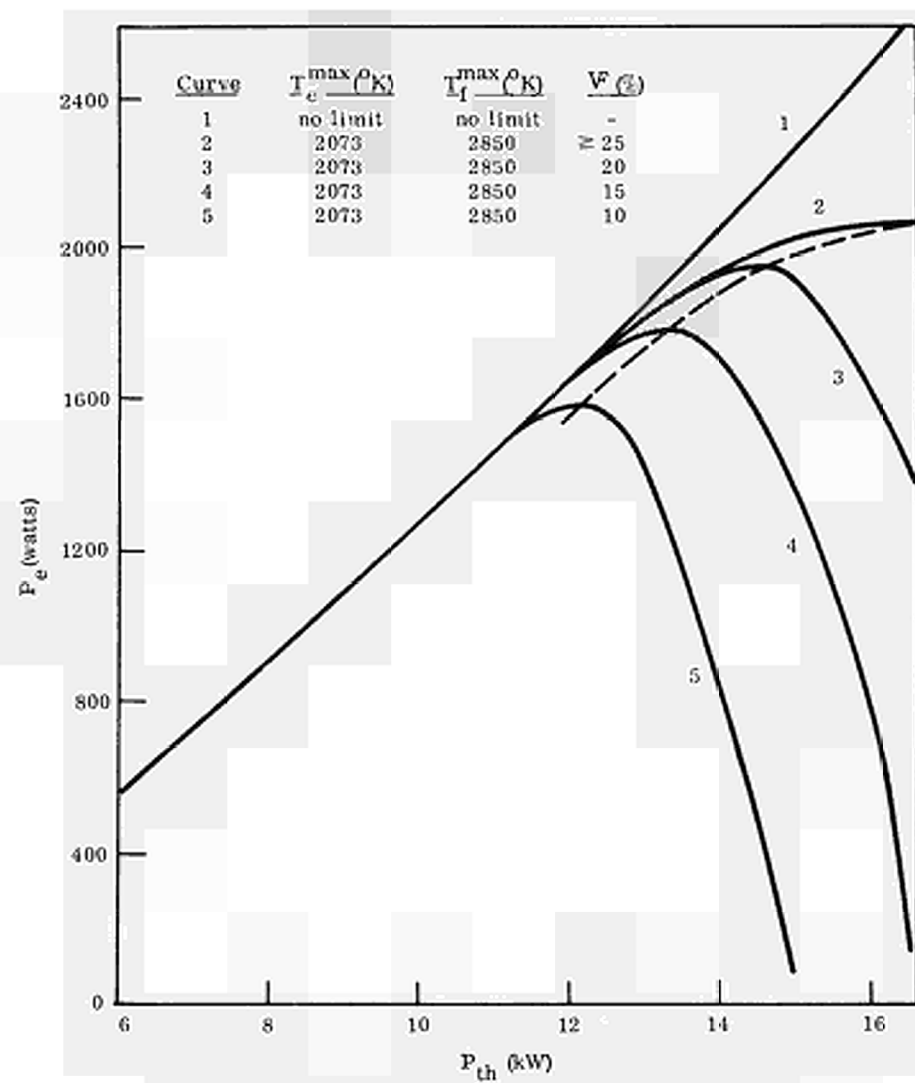
3 Nuclear Thermionic Fuel Element



4 Logical Flow Diagram for TFE Performance Computation



5 TFE Performance Characteristics for $P_{th} = 14.9$ kW



6 Fully Optimized TFE Performance Characteristics

DISCUSSION

Speaker of paper F-1: P. HILL.

MUSA (Rumania): First question: In the diffusion equation you have assumed that the electron mobility is independent on x . The diffusion coefficient for electrons depends on mean free path and electron temperature both of which depend directly on x .

Second question: Why in equation 5 have you assumed the constant k_s to be about one. What physical meaning supports this assumption? This constant must be higher than 1, maybe about 10 or more.

HILL (USA): I would first like to explain that the first portion of this work represents the work of Dr. WILKINS of our organisation and I am not fully qualified to answer to full particulars the questions that you have asked. I will however say a few words about what I do know about that.

First, we have taken a heuristic view of this calculation. We have asked ourselves the question, how well with this theory can we predict experimentally measured curves, regardless of theoretical inadequacies in the equations.

We have found that in simulating existing sets of experimental data we are able to do quite well and we have done this at this time for more than one set of experimental thermionic measurements. At this time we are unfortunately not able to predict thermionic converter behaviour. The theoretical demands of predicting performance are considerably greater. More attention to plasma-physics and especially to the physics of the surfaces would be required to predict performance. In the plasma physics model the reason for the selection of the constant electron temperature, and all of the things that theoretically result from that selection, was made primarily from the point of view of obtaining an analytic solution to the equations.

In the selection of the parameter k for the Schottky-effect, we recognized the fact that the value of unity is somewhat arbitrary and as a matter of fact we have some evidence of our own that this is not always the proper selection. It does, nevertheless, for the converter data that we have analyzed to date (the high pressure regime) seem to represent a good choice from a purely heuristic sense.

WARNER (USA): Do you include the possibility of an emitter double sheath?

HILL: At the present time, no. We are investigating that effect at this time, however. We do not know what influence that would have on the model.

LOCHKAREV (USSR): In the paper it is assumed that the effective work function of the cathode is related to the electric field at the cathode according to theory of the normal Schottky-effect. In view of the fact that the comparison of the experimental data with monocrystalline cathodes gave a good correspondence with the theory, can one consider that for the monocrystalline cathodes the influence of the anomalous Schottky-effect, and hence also the patch-effect is irrelevant?

GYFTOPOULOS (USA): First, let me clarify that the reported work was not for a monocrystal. It was for a polycrystalline surface. Second, no Schottky-effects related to surface-patches were taken into account. Third, the Schottky-effect we are talking about is that introduced by the plasma sheaths. Fourth, there was one condition that was imposed in all the calculations, namely that the minimum number of input parameters would be used to describe a large amount of data.

RASOR (USA): A more detailed and rigorous analysis of the Schottky-effect in thermionic converters has been published recently by L. K. HANSEN (J. Appl. Phys., 38, 4345 (1967)).

Dr. HANSEN is present at the meeting. I suggest you discuss this question with him.

COMPARISON OF METHODS FOR CALCULATING RADIATIVE HEAT TRANSFER *

A. Schock and M. J. Abbate
 Republic Aviation Division of Fairchild Hiller Corporation
 Farmingdale, New York

Abstract

Various approximations for calculating radiative heat transfer between parallel surfaces are evaluated. This is done by applying the approximations based on total emissivities to a special case of known spectral emissivities, for which exact heat transfer calculations are possible. Comparison of results indicates that the best approximation is obtained by basing the emissivity of the receiving surface primarily on the temperature of the emitter. A specific model is shown to give excellent agreement over a very wide range of values.

Accurate computation of radiative heat transfer in thermionic converters is of great importance for predicting the conversion efficiency and the open-circuit temperature rise.

The diffuse radiation heat transfer rate from a plane emitter E to a parallel collector C is given by

$$q = \int_0^{\infty} [q_E(\lambda) - q_C(\lambda)] d\lambda, \quad (1)$$

where $q(\lambda) d\lambda$, the radiant energy flux in the wavelength interval λ to $\lambda + d\lambda$, leaving each surface is given by the sum of the emitted and reflected radiation:

$$q_E(\lambda) d\lambda = \epsilon_E(\lambda, T_E) \frac{2\pi h c^2 \lambda^{-5} d\lambda}{\exp(hc/\lambda k T_E) - 1} + [1 - \epsilon_E(\lambda, T_E)] q_C(\lambda) d\lambda, \quad (2)$$

$$q_C(\lambda) d\lambda = \epsilon_C(\lambda, T_C) \frac{2\pi h c^2 \lambda^{-5} d\lambda}{\exp(hc/\lambda k T_C) - 1} + [1 - \epsilon_C(\lambda, T_C)] q_E(\lambda) d\lambda. \quad (3)$$

Here h and k are Planck's and Boltzmann's constants, c is the speed of light, and $\epsilon(\lambda, T)$ denotes the hemispheric emissivity at wavelength λ and surface temperature T . Solving Eqs. (2) and (3) for $q_E(\lambda)$ and $q_C(\lambda)$ and inserting the results in Eq. (1), we obtain

* Work supported by U. S. Atomic Energy Commission.

$$q = 2\pi hc^2 \int_0^\infty \left\{ \left[\exp\left(\frac{hc}{\lambda kT_E}\right) - 1 \right]^{-1} - \left[\exp\left(\frac{hc}{\lambda kT_C}\right) - 1 \right]^{-1} \right\} \left[\frac{1}{\epsilon_E(\lambda, T_E)} + \frac{1}{\epsilon_C(\lambda, T_C)} - 1 \right]^{-1} \frac{d\lambda}{\lambda^5} \quad (4)$$

It is now convenient to let $\bar{\epsilon}$ denote an effective emissivity, defined by

$$\bar{\epsilon} = \frac{\int_0^\infty \left\{ \left[\exp\left(\frac{hc}{\lambda kT_E}\right) - 1 \right]^{-1} - \left[\exp\left(\frac{hc}{\lambda kT_C}\right) - 1 \right]^{-1} \right\} \left[\frac{1}{\epsilon_E(\lambda, T_E)} + \frac{1}{\epsilon_C(\lambda, T_C)} - 1 \right]^{-1} \frac{d\lambda}{\lambda^5}}{\int_0^\infty \left\{ \left[\exp\left(\frac{hc}{\lambda kT_E}\right) - 1 \right]^{-1} - \left[\exp\left(\frac{hc}{\lambda kT_C}\right) - 1 \right]^{-1} \right\} \frac{d\lambda}{\lambda^5}} \quad (5)$$

Combining Eqs. (4) and (5) and integrating, we obtain the usual expression

$$q = \sigma \bar{\epsilon} (T_E^4 - T_C^4), \quad (6)$$

where σ is the Stephan-Boltzmann constant defined by

$$\sigma = 2\pi^5 k^4 / 15 c^2 h^3. \quad (7)$$

Equations (5) and (6) permit accurate computation of radiative heat transfer when experimental measurements of emissivity versus temperature and wavelength are available for both surfaces. For most surfaces, however, the only available data are not the spectral emissivity $\epsilon(\lambda, T)$ but the total emissivity $\epsilon(T)$, defined by

$$\epsilon(T) = \frac{\int_0^\infty \left[\exp(hc/\lambda kT) - 1 \right]^{-1} \lambda^{-5} \epsilon(\lambda, T) d\lambda}{\int_0^\infty \left[\exp(hc/\lambda kT) - 1 \right]^{-1} \lambda^{-5} d\lambda} \quad (8)$$

In such cases, it is customary to approximate the effective emissivity in terms of the total emissivities of the two surfaces, using an expression of the form

$$\bar{\epsilon} = \left[\epsilon_E(T) + \epsilon_C(T) - 1 \right]^{-1} \quad (9)$$

The crucial question, to which this paper addresses itself, is what temperatures to use in the arguments of Eq. (9). In general, the options considered include the use of the emitter temperature T_E , the collector temperature T_C and the geometric mean temperature

$$T_G \equiv (T_E T_C)^{\frac{1}{2}}, \quad (10)$$

in various combinations. To determine which recipe yields the most accurate approximation of the actual heat transfer, we shall examine a special case (tungsten emitter and collector) for which sufficient measurements of spectral emissivity are available⁽¹⁾ to permit exact calculations. As shown by Figure 1, the spectral emissivity of tungsten is essentially a linear function of temperature, so that

$$\epsilon(\lambda, T) = a(\lambda) + b(\lambda)T. \quad (11)$$

Figure 2 presents a plot of the coefficients a and b as a function of λ .

To ensure complete consistency between the exact and the approximate calculations, the above set of emissivity data was used throughout. For the exact calculations the effective emissivity was computed from Eq. (5), while for the approximate calculations the total emissivities of the emitter and collector (presented in Figure 3) were computed from Eq. (8). It should be pointed out that the integration range in Eqs. (5) and (8) had to be truncated, because of the lack of experimental data below 0.25 and above 10.0 microns. However, the range covered included all but a small fraction of the radiant energy, since the Planck weighting function drops off rapidly at small and large wavelengths. Moreover, since the integration ranges in the numerator and denominator of Eqs. (5) and (8) are equally truncated, the resultant error in their ratio should be negligible.

Effective emissivities using four different approximations were computed for comparison with the exact solution:

$$\bar{\epsilon}_{\epsilon c} = \{[\epsilon_{\epsilon}(T_{\epsilon})]^{-1} + [\epsilon_c(T_c)]^{-1} - 1\}^{-1} \quad (12a)$$

$$\bar{\epsilon}_{\epsilon} = \{[\epsilon_{\epsilon}(T_{\epsilon})]^{-1} + [\epsilon_c(T_0)]^{-1} - 1\}^{-1} \quad (12b)$$

$$\bar{\epsilon}_{\epsilon \epsilon} = \{[\epsilon_{\epsilon}(T_{\epsilon})]^{-1} + [\epsilon_c(T_p)]^{-1} - 1\}^{-1} \quad (12c)$$

$$\begin{aligned} \bar{\epsilon}_{\epsilon gc} = & \{[\epsilon_{\epsilon}(T_{\epsilon})]^{-1} + [\epsilon_c(T_0)]^{-1} - 1\}^{-1} [1 - (T_c/T_{\epsilon})^4]^{-1} \\ & - \{[\epsilon_{\epsilon}(T_0)]^{-1} + [\epsilon_c(T_c)]^{-1} - 1\}^{-1} [(T_{\epsilon}/T_c)^4 - 1]^{-1}. \end{aligned} \quad (12d)$$

The last of these had been recommended by a recent study⁽²⁾ devoted to the same question as the present paper. That study had been based on a theoretical model rather than experimental data to describe the dependence of emissivity on wavelength.

The results of the present study, illustrated by Figure 4, showed that over the temperature range of interest in thermionic converters ($850 \leq T_c \leq 1150^\circ\text{K}$, $1700 \leq T_e \leq 2400^\circ\text{K}$) the third approximation ($\bar{\epsilon}_{eE}$, Eq. 12c) gives by far the best agreement with the exact solution (Eq. 5). Thus, while Reference 2 is correct in stating that the relatively crude approximation $\bar{\epsilon}_{eC}$ gives values that are 10-15% lower than $\bar{\epsilon}_{eGC}$, the present results indicate that $\bar{\epsilon}_{eGC}$ is still 10-15% below the actual value of the effective emissivity, and that a much better approximation is provided by model $\bar{\epsilon}_{eE}$.

In conclusion, a plausible qualitative argument can be offered for basing the receiver emissivity primarily on the emitter temperature: Spectral emissivity depends rather strongly on wavelength, but only weakly on temperature; in fact, as shown by Figure 1 the direction of the latter dependence reverses with wavelength. The principal reason why the total emissivity of a surface varies with temperature is the latter's effect on the spectral distribution. Therefore, the total emissivities used in calculating the heat transfer should be based not on the temperature of the surface, but rather on that temperature which best characterizes the spectral distribution of the predominant radiation reflected between the electrodes. Because of the fourth-power dependence, the dominant radiation in a thermionic converter is clearly that which originally emanated from the emitter. It is therefore not surprising that basing both emissivities on the emitter temperature yields the better approximation.

A still better approximation can be obtained by giving predominant, but not sole, weight to the temperature of the radiation source, with much lighter weight given to the temperature of the receiver. To determine the best way of doing this, exact heat transfer calculations were carried out over a very wide range of emitter and collector temperatures. Examination of the results indicated that they could be quite well approximated by the purely pragmatic equation:

$$q = \sigma \left[\frac{T_e^4}{\epsilon_e(T_e) + \epsilon_c(.8T_e + .2T_c) - 1} - \frac{T_c^4}{\epsilon_e(.2T_e + .8T_c) + \epsilon_c(T_c) - 1} \right]. \quad (13)$$

The computed results are presented in Table I. For each set of emitter and collector temperatures, the three numbers shown are respectively the exact heat flux (Eq. 4), the approximate heat flux (Eq. 13), and the percent error. As can be seen, this approximation exhibits remarkably good agreement over a thousand-fold variation in heat flux.

		Emitter Temperature, °K											
		3000	2800	2600	2400	2200	2000	1800	1600	1400	1200	1000	800
Collector Temperature, °K	400	81.886 81.199 -0.8	58.944 58.754 -0.3	41.198 41.299 0.2	27.822 28.069 0.9	18.044 18.341 1.6	11.156 11.441 2.6	6.516 6.754 3.7	3.555 3.732 5.0	1.788 1.903 6.4	0.814 0.878 7.9	0.327 0.356 8.8	0.110 0.119 8.6
	600	82.437 81.685 -0.9	59.432 59.158 -0.5	41.615 41.624 0.0	28.163 28.319 0.6	18.309 18.522 1.2	11.350 11.562 1.9	6.646 6.825 2.7	3.632 3.765 3.7	1.822 1.908 4.7	0.819 0.866 5.7	0.314 0.334 6.3	0.087 0.093 6.4
	800	82.865 82.072 -1.0	59.805 59.468 -0.6	41.923 41.859 -0.2	28.401 28.483 0.3	18.478 18.621 0.8	11.452 11.604 1.3	6.689 6.821 2.0	3.627 3.724 2.7	1.780 1.842 3.5	0.752 0.784 4.3	0.232 0.244 4.9	
	1000	83.072 82.262 -1.0	59.964 59.587 -0.6	42.025 41.907 -0.3	28.441 28.465 0.1	18.456 18.543 0.5	11.371 11.474 0.9	6.557 6.648 1.4	3.452 3.520 2.0	1.575 1.616 2.6	0.528 0.545 3.3		
	1200	82.892 82.092 -1.0	59.746 59.351 -0.7	41.760 41.608 -0.4	28.124 28.106 -0.1	18.085 18.130 0.2	10.951 11.015 0.6	6.094 6.153 1.0	2.956 2.998 1.4	1.058 1.078 1.9			
	1400	82.086 81.319 -0.9	58.913 58.521 -0.7	40.890 40.722 -0.4	27.212 27.168 -0.2	17.131 17.146 0.1	9.959 9.994 0.4	5.070 5.103 0.6	1.910 1.929 1.0				
	1600	80.335 79.623 -0.9	57.146 56.776 -0.6	39.099 38.931 -0.4	25.391 25.334 -0.2	15.280 15.276 -0.0	8.080 8.094 0.2	3.171 3.184 0.4					
	1800	77.245 76.604 -0.8	54.052 53.718 -0.6	35.991 35.836 -0.4	22.265 22.206 -0.3	12.135 12.121 -0.1	4.919 4.921 0.0						
	2000	72.350 71.791 -0.8	49.163 48.874 -0.6	31.098 30.964 -0.4	17.363 17.311 -0.3	7.223 7.209 -0.2							
	2200	65.118 64.643 -0.7	41.944 41.706 -0.6	23.881 23.777 -0.4	10.144 10.110 -0.3								
	2400	54.952 54.564 -0.7	31.793 31.613 -0.6	13.737 13.673 -0.5									
	2600	41.195 40.903 -0.7	18.051 17.944 -0.6										
	2800	23.134 22.961 -0.7											

Table 1. Radiative Heat Transfer in w/cm² between two tungsten surfaces

exact solution Eq. 4
 approximation Eq. 13
 percent error

References

- (1) GUBAREFF, G.G., JANSSEN, J.E., and TORBORG, R.H., "Thermal Radiation Properties Survey," Honeywell Research Center, Minneapolis, Minnesota, 1960.
- (2) McCANDLESS, R. J. and HILL, P. R., "Radiation Heat Transfer Calculations," 1967 IEEE Conference Record of the Thermionic Conversion Specialist Conference, p.370.

Fig. 1: Spectral Emissivity of Tungsten

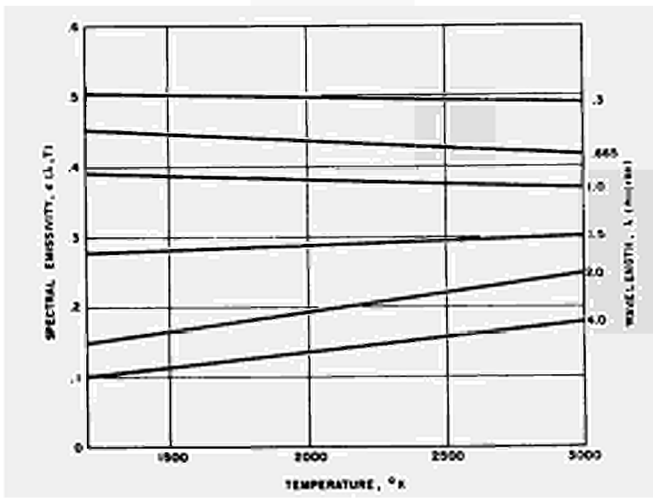


Fig. 2: Curve-Fit Constants $a(\lambda)$ and $b(\lambda)$

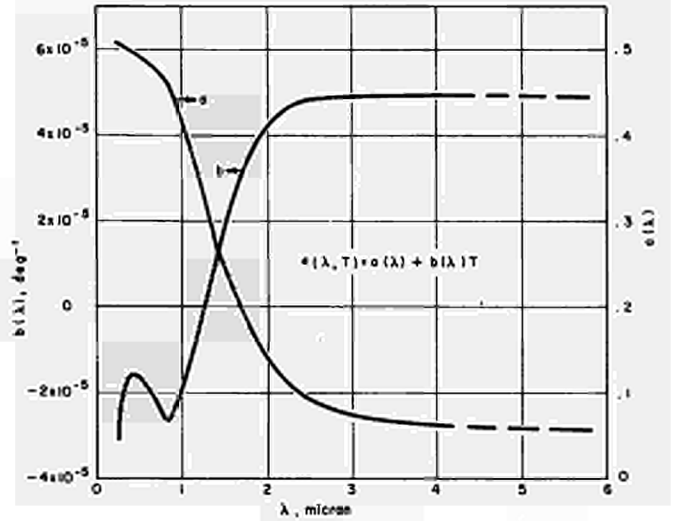


Fig. 3: Total Emissivity of Tungsten

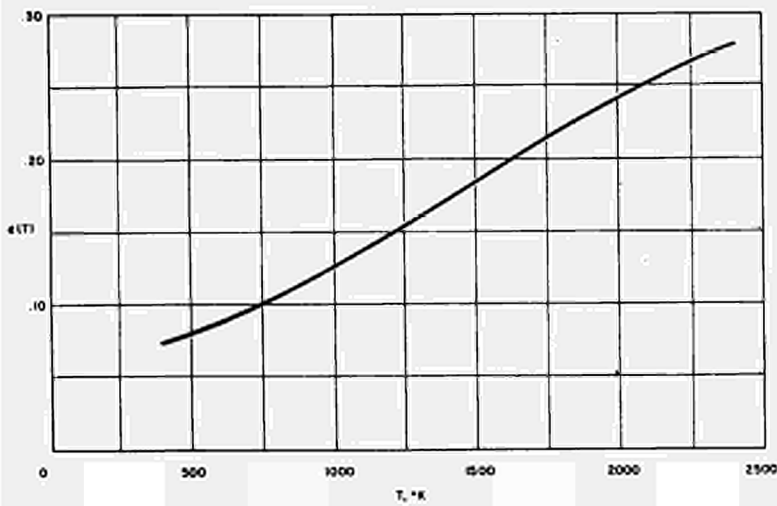
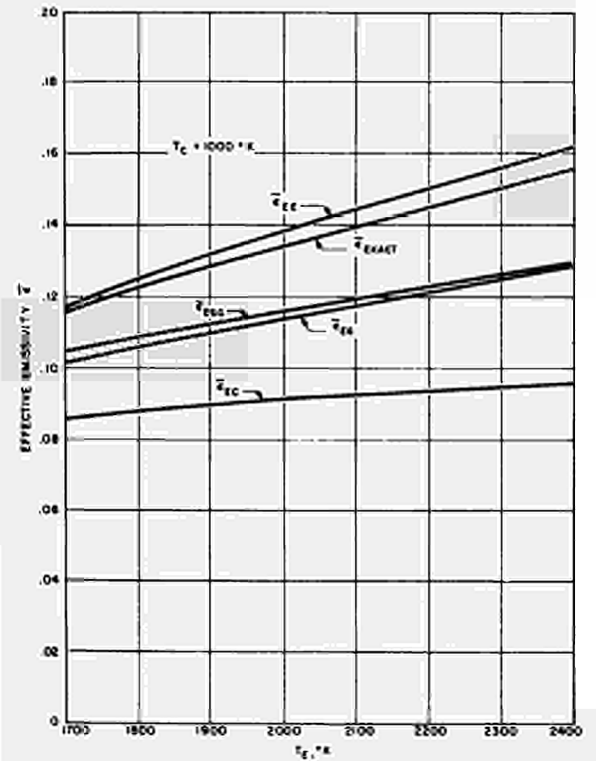


Fig. 4: Comparison of Approximations with Exact Solution





METHODS OF CALCULATION AND OPTIMIZATION
OF THERMIONIC ELECTROGENERATING ELEMENTS

I.S.Mosevitsky

I.V.KURCHATOV INSTITUTE OF ATOMIC ENERGY, Moscow, USSR

INTRODUCTION

The electrogenerating element (EGE) is an individual thermionic converter in the general circuit of the direct conversion installation. There are different non-uniformities in EGE (temperature, potential) which impair characteristics of the element and therefore methods both for test and variant calculations and for optimization of EGE have to be developed. The calculation methods are defined by formulation of the problem and accuracy required and vary from simplified calculations and estimations to general numeric solution of the problem depending on different stages of the development of the installation.

In the present paper the EGE model with one-dimensional linear geometry is considered, for example EGE with the cathode as a thin wall cylindrical sheath without azimuthal non-uniformity. The EGE may be switched into the general circuit with one or both its ends. The approximate analytic methods of calculation and optimization (in linearized approach) and one of the

possible numerical methods for the digital computer are discussed in the present paper.

2. BASICAL EQUATIONS AND SIMILARITY CRITERIA.

In the EGE scheme under consideration let us assume the thermal flow delivered to the cathode $q_0 \cdot \phi(x)$; $\phi(0)=1$ to be given and not depending on cathode temperature distribution. Since variations in anode temperature around its optimal value alters weakly on the converters characteristics, let us consider the anode temperature given and constant in length as well as cesium vapour pressure. Under these assumptions the cathode temperature distribution $T(x)$ is to be the solution of Eq.(1).

$$\frac{d}{dx}(\lambda \delta \cdot \frac{dT}{dx}) = q_s - q_0 \cdot \phi(x) - q_r; \quad 0 \leq x \leq l; \quad (1)$$

$$\left(\frac{dT}{dx}\right)_0 = \frac{\Lambda}{\lambda \delta} (T_0 - t_0)^x; \quad \left(\frac{dT}{dx}\right)_1 = -\frac{\lambda_k}{K \cdot \lambda \delta} (T_1 - t_1) + \frac{\rho_k K}{2 \lambda \delta} \cdot J_p^2;$$

where $q_s = q_r + q_e + q_t$ is the thermal flow from the cathode surface due to radiation ($q_r = \epsilon \sigma (T^4 - t_a^4)$), "electron cooling" ($q_e = j(x) \cdot \psi(T; \rho_e)$, $\psi(T; \rho_e) = \psi(T; \rho_{e0}) + 2 \frac{k}{\delta} T$) and thermal conductivity of interelectrode medium ($q_t = \alpha (T - t_a)$) and $q_r = \frac{\rho}{\delta} \left[\int_0^x j(x) dx \right]^2$ is the ohmical heat output in the cathode. l , δ and K are length and thickness of the cathode and the ratio of commutation length to its thickness, respectively. Coefficients λ , ρ , λ_k , ρ_k , ψ , α , ϵ and Λ are in general case functions of $T(x)$. The boundary conditions define heat flow from the cathode over the commutation ($x=l$) and over a certain gap-fixing component (retainer) with effective thermal conductivity Λ on the component with temperature t_1 and t_0 . It is assumed that through all the length of EGE there are no local heat leakages. The commutation is considered to be "small" since it is not necessary to calculate it as a system with distributed parameters.

Distribution of potential $U(x)$, which is equal to the difference of cathode and anode potentials (fig.1), is found from the equation

$$\frac{d}{dx} \left(\frac{1}{\frac{\rho}{\delta} + \left(\frac{\rho}{\delta}\right)_A} \cdot \frac{dU}{dx} \right) = -j(x); \quad \left(\frac{dU}{dx}\right) = \xi \cdot \left(\frac{\rho}{\delta}\right)_A \cdot J_p = -\xi \left(\frac{\rho}{\delta}\right)_A \cdot \left(\frac{\delta}{\rho}\right)_A \cdot \left(\frac{dU}{dx}\right)_1; \quad (2)$$

The parameter ξ is determined by the scheme of switching of the X). And, ρ_1 denote parameter values at $x=0$ and $x=l$; ρ_k and ρ_A denote commutation and anode parameters

element into the outer circuit: at one- and two-way schemes $\xi=0$ and $\xi=1$, respectively.

The element current J_p (per a perimeter unit) and input voltage V are

$$J_p = \int_0^l j(x) dx; \quad V = U_0 - \int_0^l \int_0^x j(x) dx dx - (1-\xi) \cdot \left(\frac{l}{\delta_A}\right) \cdot \int_0^l \int_0^x j(x) dx dx \quad (3)$$

To close the equation set (1)-(2) the relation between current density $j(x)$ at any point of the element and other parameters has to be shown. The simplest assumption, which is used in the present paper, is to consider j depending on other parameters at the same point along the EGE length, particularly, on T and U . Such a additivity principle is likely to be valid enough for operating conditions (by temperature, current and cesium vapour pressure) of most of EGE, but limits of its using have to be refined. When this principle is disturbed over a small range, corrections on this "disturbance" can be introduced according to the relations presented below.

The dependence $j(U;T)$, which most often is obtained experimentally, may be presented as a set of curves $j(T)_{U=const}$; in the same coordinates $j-T$ another set of curves may be built, since at given t_A and P_{CS} : $q_s = \beta(T) \epsilon (T^4 - t_A^4) + j(u;T) \cdot \psi(T) + \alpha(T) \cdot x(T - t_A) = q_s(u;T) = q_s(j;T)$. After connecting points with similar specific power $W_s = j \cdot u$ one obtains a unified electrical and thermal characteristic of the elementary converter, which will be called $j-T$ diagram (figure 2). The region of the most advantageous operating of such a converter will be limited at the top by the line of maximum specific powers $\max[W_s]$ and at the bottom by the line of maximum efficiencies $\max[\eta]$.

In this form the problem of EGE calculation is solved by numerical methods. Dependence of coefficients on cathode temperatures was assumed to be linear and the characteristic $j(U;T)$ was introduced as a two-dimensional table.

The analytical solutions of the problem may be obtained after some simplifications. If the coefficients λ, ρ , etc. mentioned above are assumed to be constant Eqs.(1)-(2) may be written as follows

$$\frac{1}{\alpha_\lambda} \cdot \frac{dT}{dx^2} = q_s(u;T) - q_0 \cdot \phi(\bar{x}) - \alpha_p \cdot \left[\int_0^{\bar{x}} j(u;T) \cdot dx \right]^2;$$

$$\left(\frac{dT}{dx}\right)_0 = N_0 \cdot (T_0 - t_0); \quad \left(\frac{dT}{dx}\right)_1 = -N_1 (T_1 - t_1) + \frac{F}{2N_1} \cdot \alpha_p \cdot \sqrt{\alpha_\lambda} \cdot \left[\int_0^1 j(u;T) dx \right]^2 \quad (4)$$

$$\frac{1}{\alpha_p} \cdot \frac{d^2 u}{dx^2} = -(1+A) \cdot j(u; T); \quad \left(\frac{du}{dx}\right)_0 = -\xi A \cdot \left(\frac{du}{dx}\right)_1; \quad (5)$$

These equations contain a relative coordinate $0 \leq \bar{x} = \frac{x}{\ell} \leq 1$ and six complexes: $\alpha_\lambda = \frac{\ell^2}{\lambda \delta}$; $\alpha_p = \frac{\rho \ell^2}{\delta}$; $N_0 = \frac{\Delta \ell}{\lambda \delta}$; $N_1 = \frac{\lambda_k \ell}{K \cdot \lambda \delta}$; $A = \left(\frac{\rho}{\delta}\right) \cdot \frac{\delta}{\rho}$; $F = \frac{\lambda_k \rho}{\lambda \delta}$

They determine similarity of electrogenerating elements in geometrical size and thermal and electrical properties of materials. Output characteristics—mean current density \bar{j} in EGE and voltage— \bar{v} :

$$\bar{j} = \int_0^1 j(u; T) d\bar{x}; \quad \bar{v} = U_0 - \alpha_p \cdot (1+A - \xi A) \cdot \int_0^1 \int_0^{\bar{x}} j(u; T) d\bar{x} d\bar{x} - \frac{F}{N_1} \cdot \alpha_p \cdot \bar{j};$$

and distribution of parameters $T(\bar{x})$ etc. are determined by values of these complexes, dependences $q_s(u; T)$, $j(u; T)$, $\phi(\bar{x})$ and EGE operating conditions which (at given t_A , t_0 and t_1) will be determined by q_0 and U_0 . This way of setting of the operating conditions "binds" local parameters to a certain region of j - T diagram and makes it possible to obtain simpler solution while setting of \bar{v} (instead of U_0) leads to more difficulties in solving the problem. A point in j - T diagram corresponding to $U=U_0$ and $q_s=q_0$ let us call the EGE operation point (OP).

The next stage of problem simplification is linearization of dependences $q_s(U; T)$ and $j(U; T)$ around a certain point — linearization center (LC) with parameters U^* , j^* , q_s^* , T^* . In test calculations it is convenient to make coincident LC with OP. The set of curves $j(T)$ usually has good linearity. For ignited-mode conditions typical dependences $j(T)$ are linear enough on the ascending part of the characteristics. The linearized equations and boundary conditions written in the form

$$\frac{d^2 \theta}{dx^2} = \theta - 1 + G_1(U-1) - G_0 [Q_0 \phi(x) - 1]; \quad \left(\frac{d\theta}{dx}\right)_0 = M_0 Q_0 \left(\frac{d\theta}{dx}\right)_1 = -M_1 Q_1; \quad (7)$$

$$\frac{d^2 V}{dx^2} = -H \cdot I(x) = -H [1 + G_2(\theta - 1) + G_3(U - 1)]; \quad \left(\frac{dV}{dx}\right)_0 = -\xi A \cdot \left(\frac{dV}{dx}\right)_1; \quad (8)$$

contain dimensionless variables $\theta(x) = \frac{T(x) - T_0}{T^* - T_0}$; $V(x) = \frac{U(x) - U^*}{U^*}$; $I(x) = \frac{j(x)}{j^*}$;

$Q_0 = \frac{q_0}{q_s^*}$; $0 \leq x \leq L$ and constants being similarity criteria. Some of them determine relations which are the most specific ones for the problem under consideration. These are:

$L = \ell \sqrt{\frac{1}{\lambda \delta} \cdot \left(\frac{\partial q_s}{\partial T}\right)_{U^*}}$; $M_0 = \frac{N_0}{L} = \frac{\Delta}{\sqrt{\lambda \delta} \left(\frac{\partial q_s}{\partial T}\right)_{U^*}}$; $M_1 = \frac{N_1}{L} = \frac{\lambda_k}{K \sqrt{\lambda \delta} \left(\frac{\partial q_s}{\partial T}\right)_{U^*}}$; $H = (1+A) \frac{\rho \lambda}{\left(\frac{\partial q_s}{\partial T}\right)_{U^*}} \cdot \frac{j^*}{U^*}$
 L is equal to the ratio of the cathode length to the characteristic length $x_0 = \sqrt{\lambda \delta \left(\frac{\partial T}{\partial q_s}\right)_{U^*}}$, where the "longitudinal thermal

resistance" $\frac{x_0}{\lambda_s}$ is equal to the "transverse thermal resistance" $\frac{1}{x_0 \cdot \left(\frac{\partial T}{\partial x}\right)_u}$. The criteria M_0 and M_1 are equal to the ratio of the "longitudinal thermal resistance" to the thermal resistance of the commutation $\frac{K}{\lambda_k}$ or retainer $\frac{1}{\Lambda}$; since on the x_0 length the greatest drop of the cathode temperature will take place due to heat leakage at the cathode ends, these criteria characterize the ratio of this fall to temperature drop on the commutation or retainer and in the simplest case are equal to it. The complex HL^2 is the ratio of electrical resistivity of EGE electrodes to the load resistance of the ideal EGE (having $\lambda = \rho = \lambda_k = \rho_k = \Lambda = 0$) of the same length, whose OP coincides with LC; thus HL^2 determines the relative contribution of the electrode resistance losses. Other criteria

$G_0 = \frac{q_s}{T^* - t_0} \cdot \left(\frac{\partial T}{\partial q_s}\right)_u$; $G_1 = \left(\frac{\partial q_s}{\partial u}\right)_T \cdot \left(\frac{\partial T}{\partial q_s}\right)_u \cdot \frac{u^*}{T^* - t_0} = -\left(\frac{\partial T}{\partial u}\right)_q \cdot \frac{u^*}{T^* - t_0}$; $G_2 = \left(\frac{\partial j}{\partial T}\right)_u \cdot \frac{T^* - t_0}{j^*}$; $G_3 = \left(\frac{\partial j}{\partial u}\right)_T \cdot \frac{u^*}{j^*}$; determine the similarity of the linearized j-T diagrams.

3. ANALYTICAL METHODS OF APPROXIMATE CALCULATIONS AND ESTIMATIONS.

Taking into account both coefficient errors and those due to linearization, it is advantageous to use approximate solutions of Eq.7 and 8 since the precision solution involves difficulties in the examination of the problem. For this purpose we shall use a simplified calculation model of EGE(adiabatic model) that has no heat leakage over the cathode, equations (4,7) turn to algebraic ones: $q_s(u_a; T_a) = q_0 \cdot \phi(x) + q_R$. ²⁾ The values of θ_{oa} , I_{oa} , U_o , and Q_o parameters of such a model coincide with parameters at the operation point. Represent Eqs.(7,8) in the following form

$$\frac{d^2 \theta}{dx^2} = \theta - \theta_{oa} + F_\theta(x); \quad \frac{d^2 U}{dx^2} = \alpha^2 (U - U_o) - H [I_{oa} + F_U(x)]; \quad (9)$$

Let us assume $F_\theta(x)$ and $F_U(x)$ to be non-explicit functions of the coordinate, and α^2 to be a positive constant. At $F_\theta = F_U = 0$ and $\alpha^2 = -HG_3$, solutions of the first approximation of $\theta_1(x)$ and $U_1(x)$, not taking into account mutual influence of θ and U and possible non-uniformity of heat supply, will be obtained. For the adiabatic model

$$\theta_a(x) = \theta_{oa} + G_0 \cdot Q_0 \cdot \Delta \phi(x) - G_1 [U_a(x) - U_o]; \quad F_U(x) = G_0 G_2 Q_0 \cdot \Delta \phi(x); \quad \alpha^2 = H(G_2 G_2 - G_3).$$

As from the physical point of view $F_\theta(x) = G_0 \frac{\Delta q_s}{Q_0} = G_0 G_2 Q_0 \cdot \Delta \phi(x)$ and

2) Index a denotes parameters for EGE adiabatic model.

$F_v(x) = \frac{\Delta I}{I}$ they may be considered as disturbances defined by factors not considered in the equations for example by interrelation between θ and U etc. Since non-explicit functions enter into the equations linearly, the solution may be represented as $\theta(x) + \Delta\theta(x)$, $U(x) + \Delta U(x)$, where the first items are solutions of the first or adiabatic approximation, and the second are solutions of equations $\frac{d^2 \Delta\theta}{dx^2} = \Delta\theta + F_\theta(x)$; $\frac{d^2 \Delta U}{dx^2} = \alpha^2 \Delta U - H \cdot F_v(x)$ with boundary conditions $(\frac{d\Delta\theta}{dx})_0 = M_0 \cdot \Delta\theta_0$; $(\frac{d\Delta\theta}{dx})_L = -M_1 \cdot \Delta\theta_1$; $\Delta U_0 = 0$; $(\frac{d\Delta U}{dx})_L = -\xi \cdot A \cdot (\frac{d\Delta U}{dx})_L$. The Laplace transformation makes it possible to obtain solution of these equations at arbitrary form of $F_\theta(x)$ and $F_v(x)$ functions, which may be even δ -functions. This method of non-explicit functions allows to estimate influence of any disturbances which may be represented as disturbances of heat flow or current density. Let us estimate the temperature drop at the cathode ends by the first approximation. For sufficiently "long" EGE conditions at one end do not influence practically on the temperature distribution near the other end; in this case

$$\theta_1(x) = \theta_{\infty} \cdot [1 - \frac{M_0}{1+M_0} \cdot e^{-x} - \frac{M_1}{1+M_1} \cdot e^{x-L}]; \quad \theta_{01} \approx \theta_{\infty} \cdot \frac{1}{1+M_0}; \quad \theta_{11} \approx \theta_{\infty} \cdot \frac{1}{1+M_1};$$

This solution and those considered below may be used at $L \geq 3 \div 4$ since in this case the maximum relative error $\theta(x)$ will be

$$\leq 5 \div 2\%. \text{ For the given } F_\theta(x) \text{ the solution } \Delta\theta(x) \text{ is}$$

$$\Delta\theta(x) = -\frac{1}{2} \int_0^L F_\theta(\tau) \cdot \exp[-|x-\tau|] \cdot d\tau - D_0 \cdot e^{-x} - D_1 \cdot e^{x-L};$$

Here the first item shows indirect influence $F_\theta(x)$ on temperature shift, and two others influence of boundary conditions changed due to $F_\theta(x) \neq 0$. For practical estimations in the case of sufficiently smooth and weakly varied function $F_\theta(x)$

$$D_0 \approx \frac{1-M_0}{2(1+M_0)} \int_0^L F_\theta(\tau) \cdot e^{-\tau} \cdot d\tau; \quad D_1 \approx \frac{1-M_1}{2(1+M_1)} \int_0^L F_\theta(\tau) \cdot e^{\tau-L} \cdot d\tau.$$

If for large values of L exponents are substituted by δ -functions; then

$$\Delta\theta_p(x) = -F_\theta(x) + F_\theta(0) \cdot \frac{M_0}{1+M_0} \cdot e^{-x} + F_\theta(L) \cdot \frac{M_1}{1+M_1} \cdot e^{x-L} \approx -F_\theta(x) \cdot [1 - \frac{M_0}{1+M_0} e^{-x} - \frac{M_1}{1+M_1} e^{x-L}].$$

In the second approximation the temperature distribution has the form:

$$\theta_{\frac{1}{2}}(x) = \theta_1(x) + \Delta\theta(x) = \theta_2(x) \cdot [1 - \frac{M_0}{1+M_0} e^{-x} - \frac{M_1}{1+M_1} e^{x-L}],$$

where $\theta_2(x)$ takes into account influence of potential and heat supply change according to the adiabatic model.

Solutions of the equations for the potentials

$$U(x) = U_0 - I_{\infty} \frac{H}{\alpha^2} \cdot [ch\alpha x - 1 - \xi \frac{A \cdot sh\alpha L}{1+A \cdot ch\alpha L} \cdot sh\alpha x]$$

$$\Delta U_F(X) = -\frac{H}{\alpha} \left[\int_0^X F_v(X-\tau) \cdot sh \alpha \tau \cdot d\tau - \xi \cdot \frac{A \int_0^L F_v(L-\tau) \cdot ch \alpha \tau \cdot d\tau}{1+A \cdot ch \alpha L} \cdot sh \alpha X \right]$$

have to be calculated at $\alpha^2 = H(G_2 \cdot G_2 - G_3)$ assuming initial approximation to be adiabatic; and for the second approximation

$$F_v(X) = G_2 \left[G_0 Q_0 \Delta \phi(X) - \theta_{oa} \left(1 - \frac{M_0}{1+M_0} e^{-X} - \frac{M_2}{1+M_2} e^{X-L} \right) \right]$$

The current density distribution is defined as $I(X) = I_a(X) + \Delta I_f(X)$ where $\Delta I_f(X) = F_v(X) - \frac{\alpha}{H} \cdot \Delta U_f(X)$. At uniform heat supply ($\Delta \phi(X) = 0$)

$$I(X) = I_{oa} \left\{ ch \alpha X - \left[\xi \frac{A \cdot sh \alpha L}{1+A \cdot ch \alpha L} + \frac{\theta_{oa} \cdot G_2}{I_{oa} \cdot L} \left(\frac{M_0}{1+M_0} - \xi \frac{M_0 \cdot A \cdot ch \alpha L}{1+M_0 \cdot (1+A \cdot ch \alpha L)} - \xi \frac{M_2 \cdot A}{1+M_2 \cdot (1+A \cdot ch \alpha L)} \right) \right] sh \alpha X - \frac{\theta_{oa} \cdot G_2}{I_{oa}} \left(\frac{M_0}{1+M_0} e^{-X} + \frac{M_2}{1+M_2} e^{X-L} \right) \right\}$$

Assuming $\Delta I_f(X) \approx F_v(X)$, at $\Delta \phi(X) = 0$ one can obtain conditions limiting the range of permissible solutions with positive values of current density over the whole length of EGE, i.e. the conditions under which $I(0) \geq 0, I(L) \geq 0$:

$$\frac{1}{M_0} \geq \frac{\theta_{oa}}{I_{oa}} \cdot G_2 - 1; \quad \frac{1}{M_2} \geq \frac{\theta_{oa}}{I_{oa}} \cdot G_2 \frac{1 + \xi A \cdot ch \alpha L}{ch \alpha L + \xi A} - 1.$$

At the linear variation of heat supply $\Delta \phi(X) = \Delta \phi(L) \cdot \frac{X}{L}$ the distribution of current increase over the length will be

$$\Delta I_f(X) = \Delta \phi(L) \cdot G_0 G_2 Q_0 \cdot h_{j\xi} \cdot \frac{sh \alpha X}{\alpha L}$$

The average value of the current density over the EGE length is expressed by the value of the current density in OP (I_{oa}) and a number of coefficients:

$$\bar{I} = \frac{1}{L} \int_0^L I(X) dX = I_{oa} \cdot h_j; \quad h_j = h_{j\xi} h_{j\phi} - h_{j_0} - h_{j_1} + h_{j\phi}$$

These coefficients take into account the total uniformity of current (h_j) and each of them takes into account the influence of different factors—potential variations due to ohmic losses ($h_{j\xi}$), connection of the element ($h_{j\phi}$), edge current fall (h_{j_0} and h_{j_1}) and non-uniformity of heat supply ($h_{j\phi}$). They are expressed in the following way

$$h_{j\xi} = \frac{sh \alpha L}{\alpha L}; \quad h_{j\phi} = 1 - \xi \frac{A(ch \alpha L - 1)}{1 + A \cdot ch \alpha L}; \quad h_{j_0} = \frac{\theta_{oa} \cdot G_2}{I_{oa} \cdot L} \cdot \frac{M_0}{1+M_0} \left(1 - \frac{1 - h_{j\xi} \cdot ch \alpha L}{L} \right); \quad h_{j_1} = \frac{\theta_{oa} \cdot G_2}{I_{oa} \cdot L} \cdot \frac{M_2}{1+M_2} \left(1 - \frac{1 - h_{j\xi}}{L} \right).$$

For the linear heat supply $h_{j\phi} = \Delta \phi \cdot G_0 \cdot G_2 \cdot \frac{Q_0}{I_{oa}} \cdot h_{j\xi}$.

The input voltage is defined in accordance with Eq. 6:

$$V = \frac{U}{U_0} = U_0 - \bar{I} \cdot HL^2 \left[\left(1 - \xi \frac{A}{1+A} \right) \cdot h_v + \frac{F}{N_2} \cdot h_j \right]; \quad h_v = \frac{1}{j_{oa}} \int_0^L j(X) dX = \frac{1}{I_{oa} \cdot L^2} \int_0^L I(X) dX.$$

For $\alpha^2 L^2 \ll 20$ and $L \geq 3+4$: $h_v = h_{vR} - \theta_{j_0} - h_{j_1} + h_{v\phi}$; $h_{vR} = \frac{1}{2} - \xi \frac{A \cdot sh \alpha L}{6(1+A \cdot ch \alpha L)}$; $h_{v\phi} = \frac{1}{3} h_{j\phi}$.

The obtained solutions of linearized problem take into account main interrelations and mutual dependences of the parameters. In a number of cases h_j and h_v may be considered as constant values with further, if required, refinement. Then the output characteristics of electrogenerating elements for approximate calculations may be represented as the simplest dependences on j_{oa} and U_0 .

$$\bar{j} = j_{oa} \cdot h_j ; \quad v = u_o - \bar{j} \cdot \bar{l}_s = u_o - \bar{j} \cdot \bar{l}_p. \quad (9)$$

where $\bar{l}_s = \alpha_j \left[(1+A-3A) \frac{h_k}{h_j} + \frac{E}{N_k} \right]$ is the normalized specific resistance of EGE, $\bar{l}_p = \frac{1}{\epsilon} \cdot \bar{l}_s$ is the total normalized resistance:

$\bar{l}_p = \bar{l}_{pe} + \bar{l}_{pk}$; $\bar{l}_{pe} = \frac{\rho \ell}{\delta} (1+A-3A) \cdot \frac{h_k}{h_j}$; $h_{pk} = \rho_k \cdot K$
 The values of h_j and \bar{l} may be found not only from the expressions given above but also from the results of more precision calculations by Eq.(9)

4. APPROXIMATE METHODS OF EGE OPTIMIZATION.

Problems of EGE optimization may be quite different in their definition. The most typical are the following:

- 1) Determination of matched electrical load, or voltage optimization;
 - 2) Optimization of geometrical size of EGE;
 - 3) Optimization of operating conditions by P_{cs} and T^{\max} (or q_o)
- In these problems the mean specific power $\bar{W}_s = \bar{j} \cdot v$ or total power $W_p = \bar{j} \cdot v$ or efficiency of the element are maximized. The second problem includes the first one, i.e. the condition of load matching; for both of them the j-T diagram is assumed to be given.

Consider the first problem and some kinds of problems of the second type, that will be solved on assumption that output characteristics can be represented in the form of (9). Since usually it is T^{\max} or q_o that are given, let us linearize the real current-voltage characteristic $j(u)_{T^{\max}}$ or $j(u)_{q_o}$ in the region of the optimum expected: $j_{oa} = j_k \left(1 - \frac{u_o}{E} \right)$; where j_k and E are density of the short-circuit current and electromotive force of this linearized characteristic.

To solve the first problem let us find the optimal parameters maximizing W_s at given geometrical sizes of EGE from the condition $\frac{\partial W_s}{\partial v} = \bar{j} + v \cdot \frac{\partial \bar{j}}{\partial v} = 0$.

They may be represented in the following form:

$$v^{\text{opt}} = \frac{E}{2} ; \quad u_o^{\text{opt}} = \frac{E}{2} \cdot \frac{1+2S}{1+S} ; \quad j_{oa}^{\text{opt}} = \frac{j_k}{2} \cdot \frac{1}{1+S} ; \quad S = Z_s \cdot \bar{l}_s = Z_p \cdot \bar{l}_p$$

The complex $Z_s = \frac{\bar{l}}{E} \cdot h_j$ determines the slope of the current-voltage characteristic and takes into account the non-uniformity of current density by the coefficient h_j ; $Z_p = l \cdot Z_s$. It is interesting to note that in the suggestions presented the

resistance of electrodes and commutation does not alter the optimal value of the output voltage, which is equal to the optimal voltage of the ideal EGE, but only decreases the value of the current due to the shift of u into the region of larger values. The maximized \bar{W}_s^m equal to $\bar{W}_s^m = W_s^m \cdot h_w^{opt}$ where $W_s^m = \frac{1}{2} j_k \cdot E$ is the maximum specific power according to the linearized characteristic, and $h_w^{opt} = \frac{h_i}{1+S}$ is the coefficient of power loss due to "not ideal" EGE. Since the least variable value at different $j(u)$ is E , it is convenient to represent dependence of \bar{W}_s^m on other parameters in the form

$$\frac{\bar{W}_s^m}{E^2} = \frac{Z_s}{4(1+Z_s \cdot l_s)} \quad (10)$$

As one of the problems of the second type let us consider the problem of definition of the optimal commutation (i.e. parameter K) for obtaining $\max[\bar{W}_s^m]$ at a constant length of EGE and given temperature T_{oa} . The condition $\frac{\partial h_w}{\partial K} = 0$ leads to $h_j \cdot Z_p \cdot \rho_k \cdot \frac{\partial K}{\partial h_j} = -1$ since both Z_p and l_p depend on K . If solutions of linearized problem and corresponding expression for $h_j \approx \frac{\theta_{oa} \cdot G_2 \cdot M_2}{I_{oa} \cdot l \cdot (1+M_2)}$ is used the optimal value of the parameter K is defined from

the expression $\frac{l_{pk}^{opt}}{C_o} = \left(\frac{1}{M_2}\right)^{opt} = \sqrt{2 \frac{\theta_{oa} \cdot G_2 \cdot \frac{1}{h_j} \cdot \frac{1+Z_p \cdot l_{pe} - Z_p \cdot C_o}{Z_p \cdot C_o}}{I_k \cdot l} - 1}$; $C_o = \frac{\rho_k \cdot \lambda_k}{\sqrt{\lambda \delta \cdot \left(\frac{\partial \lambda_k}{\partial T}\right)_{j_k}}}$; $I_k = \frac{j_k}{j^*}$
 In this case it is assumed that the values h_j, h_v directly entering into this expression may be given beforehand. After having calculated l_{pk}^{opt} can find the value h_{j1} and improve h_j, h_v and then l_{pk}^{opt} ; such an iteration is usually quite sufficient. Then $S, l_o^{opt}, j_{oa}^{opt}, j$ and \bar{W}_s^{mm} optimized over K and V are calculated.

In order to find the maximum of the total power $W_p = J \cdot U_p$ let us transform Eq.(10) into

$$\frac{W_p^m}{E^2} = \frac{Z_p}{4(1+Z_p \cdot l_p)} = \frac{Z_p}{4(1+Z_p \cdot l_{pe} + Z_p \cdot l_{pk})}$$

This dependence is shown in Fig. 3. When only 1 changes parameters $\frac{W_p^m}{E^2}, Z_p$ and l_{pe} will change in accordance with the motion of the point in a straight line which is at the angle ψ to the Ω -axis and crosses it at the point $l = l_{pk} \cdot \frac{j_k}{E} \cdot \frac{\delta}{\rho(1+A-\delta A)} \cdot \frac{h_i^2}{h_v}$

The maximum $\frac{W_p^m}{E^2}$ is reached at the point of contact of this line with the line $\frac{W_p^m}{E^2} = \text{const}$; the condition $\frac{\partial}{\partial l} \left(\frac{W_p^m}{E^2}\right) = 0$ give relations for optimal values: $l_{pe}^{opt} = \sqrt{\text{ctg } \psi}$; $Z_p^{opt} \cdot l_{pe}^{opt} = 1$.

Thus if values defining ψ are given, the optimal length of the element $l^{opt} = \sqrt{\frac{E \cdot \delta}{\mu \cdot g(U+A-\xi A)} \cdot b_v^{-1}}$. Since l^{opt} does not depend on K, the values l^{opt} and K^{opt} may be determined in succession with iteration improvement of values b_j and b_v .

As for optimization of operating conditions of EGE it should be noted only that if j-T diagram has the form shown in Fig.2, the optimum power value P_{cs} has to be such that OP on the line $U=U^{opt}$ were on the ascending slope a little to the left from the maximum j. If it is on the maximum or to the right from it the pressure of cesium vapour should be increased.

5. NUMERIC CALCULATIONS OF EGE.

For the numeric solution of the set of equations (1),(2) they, together with boundary conditions, are represented in the form of difference algebraic equations, which may be written as follows $f_i(\vec{z}) = \delta_i$; $\vec{z} = \{z_1, \dots, z_j, \dots, z_n\}$; $\vec{\delta} = \{\delta_1, \dots, \delta_i, \dots, \delta_m\}$.

Here $i=1; 2; \dots, m$ is the number of the equation; \vec{z} is the vector of computer variables which differ from the real variables $\vec{U} = \{U_1, \dots, U_j, \dots, U_n\} = \{z_1 M_1, \dots, z_j M_j, \dots, z_n M_n\}$ in the scale of M_j ; $\vec{\delta}$ is the vector of error of the set of equations (if \vec{z} is the root of the set of equations components of $\vec{\delta}$ are zero). Such a system is solved by the numeric method [1] proposed for investigation of a set of equations of the most general kind by means of successive calculation of the increase of dependent variables:

$\Delta \vec{y} = [D] \cdot \Delta \vec{x} - [F_j] \cdot \vec{\delta}$ here $[D]$ and $[F_j]$ are the matrixes whose elements are partial derivatives calculated numerically. The vector of the increase of independent variables $\Delta \vec{x}$, as well as division of variables in dependent ones y and independent ones x , is given depending on the type of the problem, for example, $\Delta \vec{x} = 0$ at searching of the root or $\Delta \vec{x} = h \cdot \vec{a}_v$ at searching of the extremum y , (\vec{a}_v is the v -th line of the matrix $[D]$ which is the vector-gradient; h is the step).

For searching of the root three or four iteration are usually required. Divergency takes place in few cases when the characteristic $j(U, T)$ has a sharp winding, and values of parameters in a node vary around it, or when at a sufficiently large number of nodes (≈ 10) the initial vector is given very

rough.

The optimization problems are usually solved with an automatic selection of h depending on the ψ angle of revolution of the vector-gradient. It is assumed that $h \times 2$ at $\psi < \psi_2$; $h : 2$ at $\psi > \psi_2$; $\psi_2 \approx 5 \div 10^\circ$; $\psi_2 \approx 15 \div 30^\circ$. On each gradient step searching of the root may be performed with a required precision. The selection of scales is of importance as it allows to deform the variable space in such a way that "ravines" on the surface of y , eliminate and the level surfaces approaches the pseudosphere. In Fig.4 the simplest case of searching $\max[\bar{W}_g]$ in K and U_0 is displayed; it can be seen that due to a "ravine" on the variable K at scales equal to 1, the solution found differs sharply from the real optimum which is found to a sufficient degree of accuracy using the automatic selection of scales.

LITERATURE

- 1 . Mosevitsky J.S., Eljukim S.B. On one problem of a nonlinear programming. AN USSR, Techn. Cybernetica N4, 1965, 192.

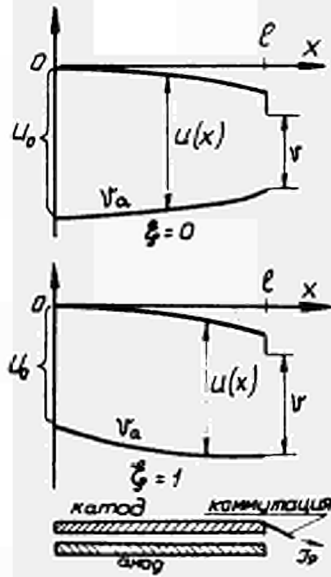


Fig. 1. - Distribution of electrode potentials and EGE scheme.

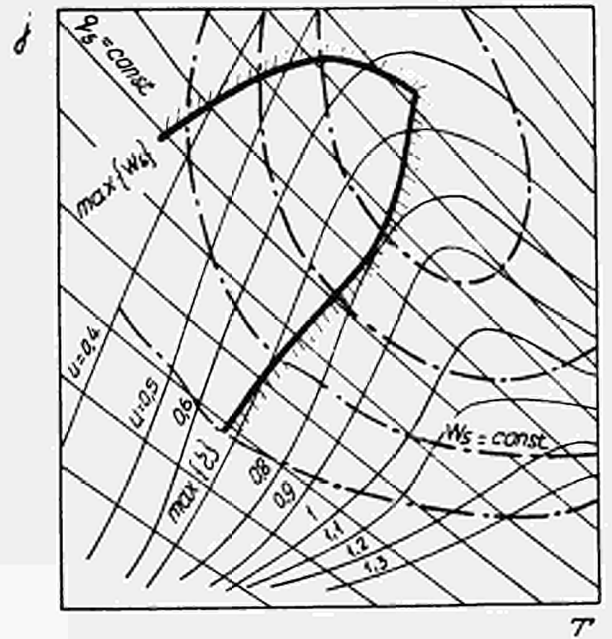


Fig. 2. - i-T - diagram.

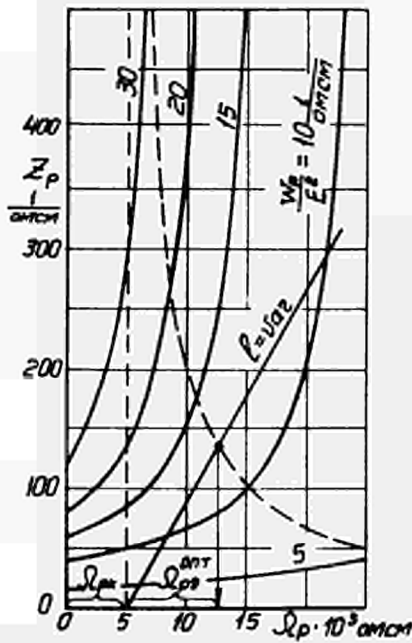


Fig. 3. - Optimization of EGE length.

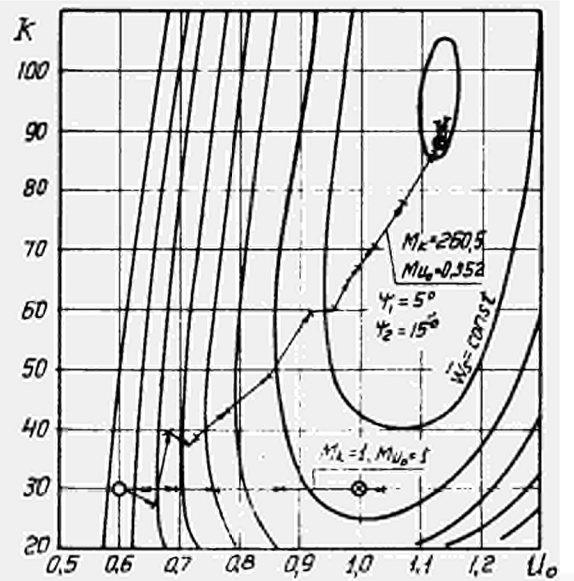


Fig. 4. - An example of optimization of EGE parameters.

THERMIONIC CONVERTER ELECTRICAL CHARACTERISTICS
WITH MATRIX CIRCUIT CONNECTIONS

Gutshin G.I., Kolmakov A.P., Pereslavytsev E.B.,
Pupko V.Ya., Subbotin V.I., Chernukhina G.M.,
Yur'ev Yu.S.

The Institute of Physics and Power Engineering,
Obninsk, USSR

I. Introduction

A practical application of thermionic converters (TC), operating together with nuclear reactors as electrical energy sources, necessitates the investigation of such system behaviours for different operational stages, reaction to different load changes, behaviour in the case of beginning different circuit failures.

Principle and constructive limits putting to power and output voltage of one thermionic converter require to connect them in series-parallel circuits. Creation of large matrix circuits raises a problem to determine optimal commutation and to find out methods of increasing system reliability consisting of relative unreliable assemblies. In matrix circuits of TC connections in the case of failure element accident the role of that element performs adjacent TC parallel to it.

The present paper deals with the investigation of thermionic converter electrical characteristics with matrix circuit connec-

tions for different operational conditions in the presence of electrical failure of one or some elements taking into account modelling of real voltage-current characteristics.

At the same time it should be useful to consider current cartograms for matrix branches to evaluate the ranges of possible failure spreading.

Model investigations are supplemented with calculations and theoretical considerations of dependences for output characteristics of such systems under deviating converter parameters from nominal.

2.Method and Equipment

For matrixes amount to hundred and more elements the using of computers becomes problematical particularly for those cases where more accurate considerations of voltage-current characteristics are demanded. The using of analog technique in that case does not arise principle difficulties and gives acceptable accuracy. Usually practical interest have matrix circuit connections of thermionic converters in the form of a plane network considered in [1,2] or a volume network formed by rolling up a plane surface as "a cylinder" or circuits commutated as "a star" (Fig.I) considered in a given report. As a base of a generator matrix circuit there was taken R-network of USM-I analog computer permitting to carry out connections and investigations pointed above. The most accurate consideration of practical voltage-current characteristics of TC

formed the general difficulty of modelling. The character of a real voltage-current dependence is explained by a converter construction and depends on cathode and anode operational temperatures, cesium vapour pressure and other factors. Thus by modelling the circuit it is desirable to have a number of electrical generators possessing definite voltage-current characteristics.

Typical voltage-current dependences for different operational TC ranges and the circuits modelling them are given in Fig.2. In d,e circuits putting diode valves in operation gave the possibility to get fractures of linear characteristics. Putting nonlinear varistors into and their corresponding locations (b,c circuits) permitted to obtain more smooth fractures of characteristics.

For the sources modelling TC operation must be separated, they are supplied from separate windings of a general feeding transformer. It permit to increase the accuracy of relative measurements. Electrical resistances of cathode, anode and commutational arrangement between TC were modelled by resistors taking into account a corresponding modelling coefficient. Integral voltage-current characteristics of system (Fig.3) were obtained by changing the load resistance from open circuit regime to short circuit regime at different resistances of R_c commutation.

3. Determination of Integral Characteristics of Generator Matrix Circuit in Different Failure Regimes

Three types of failures were possible: broken circuit (Bc), short circuit of converter electrodes one to another (Sc), short circuit of electrodes to support structure which is partly equivalent to puncture of anode electroisolation, and their possible combinations. The possibility of one or other failure depends on TC construction, technology of manufacture and operational conditions.

The carried out investigations of voltage-current characteristics for circuits under different emergency conditions allow to determine the value of generator output power losses at local failures against commutation resistance (see Fig.4). With an assumed probability of the failures of every kind the value of optimum commutation resistance (R_{c0}) may be obtained from Fig.4. For equally probable local failure the optimum commutation value is determined by intersection of the curves for broken circuit and short circuit. Fig. 4 shows the optimum commutation value for an "elongated" matrix to be some more than the internal resistance value for commutated converters. In Fig.5 the relative power of matrix system is plotted against the number of failures under optimum loading conditions. The dependence of N/N_0 on the failure number allows to find the probability of this relation at the end of life time to be not less than some given value. This probability is determined from binomial function distribution for spurious failure combinations [I] :

$$P_n(m_1, m_2) = \sum_{k=0}^{m_1} C_n^k p_1^k p_2^{n-k}; \quad m_1 + m_2 = n.$$

P_1 and P_2 - the probability of the 1st and 2nd event, respectively.

m_1 and m_2 - the number of the 1st and 2nd events, respectively, taking place during some fixed period of time.

Then BC and SC events are assumed to be independent.

Such treatment of results allows to obtain quantitative estimation of thermionic converter reliability, if the reliability implies the probability of its power at the end of life time being not less than some given designed power. In Fig.6 the matrix system reliability of a TC is presented as a function of relative power for three reliability values of separate TC-s: 0.9, 0.95, 0.99.

The reliability of star-connection converter scheme (Fig.I) must be higher theoretically, because current redistributions at a separate element failure are distributed uniformly over a larger number of neighbour cells. However, in practice the reliability calculation (at optimum R_c) carried out for a star connection didn't differ much from the analogous one for a cylinder connection. Just so the general character of power losses dependences on commutation resistance at local failures proved to be substantially the same both for the converters with the refined trend of voltage-current characteristic and for the idealized: converters with linear characteristic.

4. Current Diagrams and Failure Spreading Range

In case of a broken circuit the lack of converter cathode cooling by electron emission considerably increases the cathode temperature. There is also some change of operating conditions in adjacent TC-s. In the case of short circuit failures the defect converter becomes a load if the commutation resistances are not large. The most serious and therefore intolerable type of failure is simultaneous shorting to the structure of two or more elements. Depending on their arrangement the system may lose practically all its useful net power cutting off many franchises of the connected unfailed converters. Fig.4 illustrates current change in a

failed branch as a function of R_c/R_{in}

Current value may vary depending on failed converter position. This shape of curve results in considerable reverse currents at $R_c/R_{in} \leq 0,7$ that may cause further TC failure. Fig.7 shows the distribution of currents over matrix commutations at BC. In this figure the current transformation may be seen as a function of commutation resistance.

In Figs. 8 and 9 the diagrams of distribution of relative currents in commutations and parallel branches of matrix system at BC and two failures of a SC type in one of the branches. In these diagrams some critical relative current value in matrix branches is noted. If the current of less than critical value passes through the TC then that converter is considered to be under emergency conditions. Therefore this critical value defines the range of failure spreading.

5. Perturbation Theory Application

To study the influence of small deviations of thermionic converter parameters upon the generator output characteristics the device of conjugate functions and perturbation theory was used, it is widely worked out in [3,4]. For this purpose a reactor-converter discrete two-dimensional nm-matrix (Fig.1) consisted of elementary thermionic converters with characteristics

$$E_{i,j}; \tau_{ij}; R_{i,j}; R_{u,i,j} \quad (1 \leq i \leq n; 1 \leq j \leq n)$$

was transformed into electric generating cylindrical cell with corresponding continuous parameters:

$$E(\zeta, \varphi); \tau(\zeta, \varphi); R(\zeta, \varphi); R_u(\zeta, \varphi)$$

The differential equation of potential distribution is:

$$\frac{\partial}{\partial \zeta} \left(\sigma_\zeta \frac{\partial U}{\partial \zeta} \right) + \alpha^2 \frac{\partial}{\partial \varphi} \left(\sigma_\varphi \frac{\partial U}{\partial \varphi} \right) - \omega^2 \sigma_u U = \frac{\partial}{\partial \zeta} (\sigma_\zeta E) = -q \quad (I)$$

Here, potential U , open circuit voltage E and conductances $\sigma_\zeta, \sigma_\varphi, \sigma_u$ refer to mean thermionic converter parameters:

$$\sigma_\zeta = \tau_0 / \tau; \sigma_\varphi = R_0 / R; \sigma_u = R_u^0 / R_u; E = E_0 / E_0; U = \frac{U}{m E_0}$$

The 1st boundary condition following from the problem symmetry is a usual condition of the joining of solutions of U function and its derivative on both sides from an arbitrary cell

cross-section along the generating line:

$$u(\xi, \varphi) = u(\xi, \varphi + 2\pi k); \quad k = 1, 2, 3, \dots \quad (2)$$

The second boundary condition is derived from the potential constancy at $\xi = 0$ and $\xi = 1$, i.e. on the reactor-converter leads, and the constancy of an external load regime R_L .

$$u|_{\xi=0} = u_0 = \text{const} \quad u|_{\xi=1} = u_1 = \text{const} \quad (3)$$

$$u_1 - u_0 = \frac{H}{2\pi} \int_0^{2\pi} \left[\left(\varepsilon - \frac{\partial u}{\partial \xi} \right) \sigma_{\xi} \right]_{\xi=0} d\varphi = \frac{H}{2\pi} \int_0^{2\pi} \left[\left(\varepsilon - \frac{\partial u}{\partial \xi} \right) \sigma_{\xi} \right]_{\xi=1} d\varphi \quad H = R_L \frac{n}{2\omega m}$$

Potential equation (I) with the boundary conditions (2) and (3) is lightly integrated at parameter constancy

$$\sigma_{\xi} = \sigma_{\varphi} = \sigma_u = \varepsilon = 1 \quad u = \frac{1}{2 \left(\frac{1}{H} + \frac{\omega}{2 \operatorname{tg} \frac{\omega}{2}} \right)} \frac{j h \frac{\omega}{2} (1 - 2\xi)}{j h \frac{\omega}{2}} \quad (4)$$

In case if parameters $\sigma_{\xi}, \sigma_{\varphi}, \sigma_u, \varepsilon$ are the given functions of coordinates ξ, φ the solution of (I) with the boundary conditions (2) and (3) may be obtained only by numerical methods or electric modelling (see above).

Let's write down formally the equation which is conjugated with Eq (I)

$$\frac{\partial}{\partial \xi} \left(\sigma_{\xi} \frac{\partial u^*}{\partial \xi} \right) + \omega^2 \frac{\partial}{\partial \varphi} \left(\sigma_{\varphi} \frac{\partial u^*}{\partial \varphi} \right) - \omega^2 \sigma_u u^* = -P \quad (5)$$

It is possible to shown that the left parts of equation (I) and (5) are really conjugated of the boundary conditions analagous to (2) and (3) take place for the conjugated potential :

$$u^*(\xi, \varphi) = u^*(\xi, \varphi + 2\pi k) \quad k = 1, 2, 3, \dots \quad (6)$$

$$u_1^* - u_0^* = \frac{H}{2\pi} \int_0^{2\pi} \left[\left(\varepsilon - \frac{\partial u^*}{\partial \xi} \right) \sigma_{\xi} \right]_{\xi=0} d\varphi = \frac{H}{2\pi} \int_0^{2\pi} \left[\left(\varepsilon - \frac{\partial u^*}{\partial \xi} \right) \sigma_{\xi} \right]_{\xi=1} d\varphi \quad (7)$$

and then $\varepsilon(\xi=0) = \varepsilon(\xi=1) = 0$

One notes that taking $\varepsilon(\xi=0) = \varepsilon(\xi=1) = 0$ under boundary condition, we obtain two δ -shaped sources in the right equation part: $-q = \delta(\xi=1) - \delta(\xi=0)$ (8)

Applying the conjugivity condition one may obtain

$$\frac{1}{2\pi} \int_0^{2\pi} \int_0^1 q u^* d\xi d\varphi = \frac{1}{2\pi} \int_0^{2\pi} \int_0^1 P u d\varphi d\xi = J \quad (9)$$

After ordinary operations of the perturbation theory we get the connection of the variation functional J with the

perturbations of the parameters of the thermionic converter linkage matrix circuit

$$\begin{aligned} \Delta J = & \frac{1}{2\pi} \int_0^{2\pi} \int_0^1 (\rho' u' - \rho u) d\varphi dz = \frac{1}{2\pi} \int_0^{2\pi} \int_0^1 \Delta \varepsilon \delta_z \frac{\partial u^*}{\partial z} d\varphi dz + \\ & + \frac{1}{2\pi} \int_0^{2\pi} \int_0^1 \Delta \delta_z \frac{\partial u^*}{\partial z} (\varepsilon - \frac{\partial u'}{\partial z}) d\varphi dz - \frac{1}{2\pi} \int_0^{2\pi} \int_0^1 z^2 \Delta \delta_\varphi \frac{\partial u^*}{\partial \varphi} \frac{\partial u'}{\partial \varphi} d\varphi dz - \\ & - \frac{1}{2\pi} \int_0^{2\pi} \int_0^1 \omega^2 \Delta \delta_u u^* u' d\varphi dz \end{aligned} \quad (I0)$$

u' - denotes the solution of Eq.(I) at its parameter perturbation:

$$\Delta \varepsilon = \varepsilon' - \varepsilon; \Delta \delta_z = \delta_z' - \delta_z; \Delta \delta_\varphi = \delta_\varphi' - \delta_\varphi; \Delta \delta_u = \delta_u' - \delta_u$$

Depending on a mode, i.e. physical essence of the functional J (we are interested in) conjugated equation (5) must be solved with respective right part $P(z, z', \varphi, \varphi')$

If, for instance, we choose P in the form:

$$-P = \delta(z=1) - \delta(z=0) \quad \text{then} \quad P = q; \quad u^* = u \quad (II)$$

In this case J means the potential difference of the thermionic generator (or load), and ΔJ is the variation of this potential difference proportional to the variation of current and the output power. From formula (I0) we obtain in the 1st approximation, using (4) and (II), a relative variation of $\Delta f, \Delta \delta_z, \Delta \delta_u$ in presence of small defects in single TC

$$\frac{\Delta J}{J} = \frac{\Delta \varepsilon}{nm} f_\varepsilon(z') + \frac{\Delta \delta_z}{nm} f_\delta(z', H) - \frac{\Delta \delta_u}{nm} f_u(z', H) \quad (I2)$$

Fig.I0 shows "functions of danger" $f_\varepsilon, f_\delta, f_u$ depending on the coordinate of "defect module" z' and it follows that the puncture of anode electric isolation, for example, are the most dangerous at the ends of series assembly (curve 5). It must be noted that while lowering electric resistance of the whole anode isolation we obtain from perturbation theory formula (I0) the following ratio:

$$\frac{\Delta J}{J} = \frac{\omega^2}{12(1 + 1/H)} \Delta \delta_u \quad (I3)$$

which may be directly derived from the solution of "non-perturbation" problem (4).

Conclusions

1. For determining the electric characteristics of matrix circuits of TC connection the electric modelling method proposed is obvious and operative.
2. Power losses after local failures (broken circuit and short circuit) may be lowered if one uses an optimum commutation in any of the thermionic converter connection circuit considered (planar, "cylinder", "star"). The change of the operating conditions of the neighbouring thermionic converters is in this case negligible.
3. The reliability of the thermionic reactor-converter may be essentially raised by using the optimum commutation in matrix, more reliable thermionic converters and reserve ones.
4. The study of the differential equation of potentials by the perturbation theory method revealed the possibility to plot the defect "functions of danger" as the defect thermionic converter location.

R E F E R E N C E S

1. A.M.Palovko. "Osnovy teorii nadejnosti" Nauka, 1964.
2. I.W.Holland. "Thermionic Reactor Network Reliability". London, 1965.
3. G.I.Marchuk, V.V.Orlov. "K teorii sopryajennykh funktsii". Neitronnaya fizika, 1961.
4. V?Ya.Pupko. Inj. Fiz. Jor. V.XI, No.2, 1966.

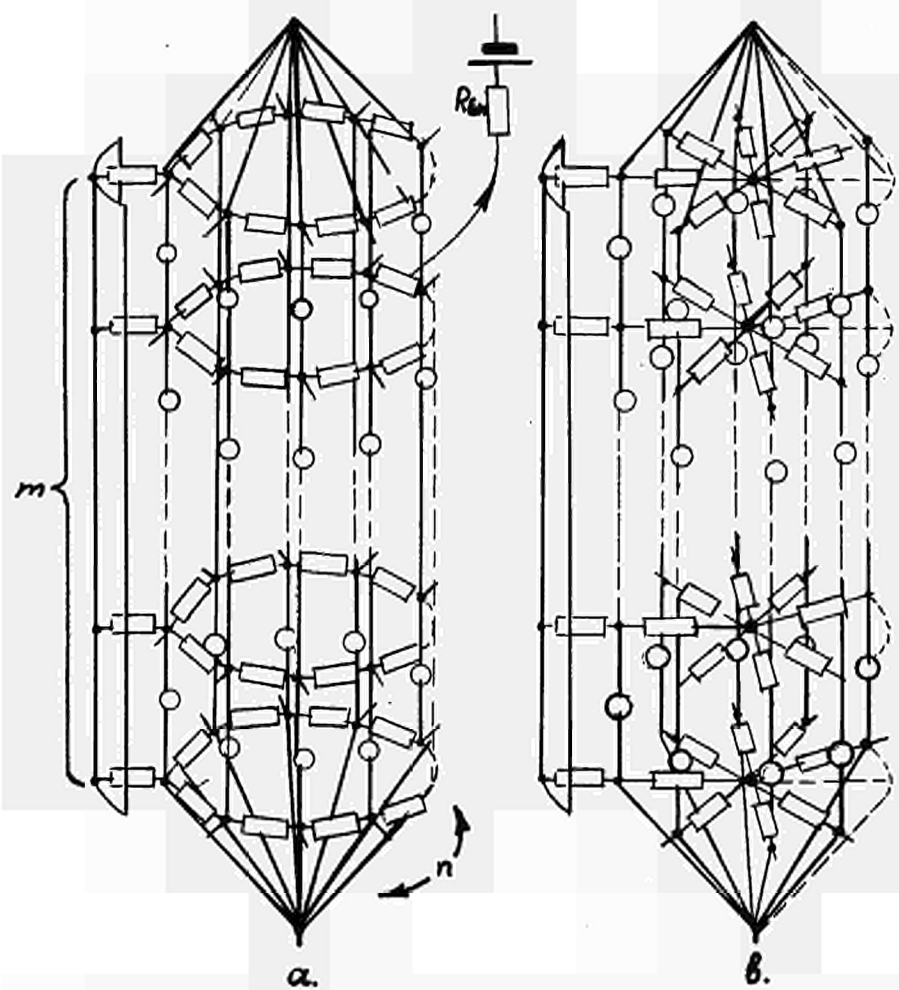


Fig. I. Matrix Circuits of TC Connection
 a) "cylindrical" b) "star"

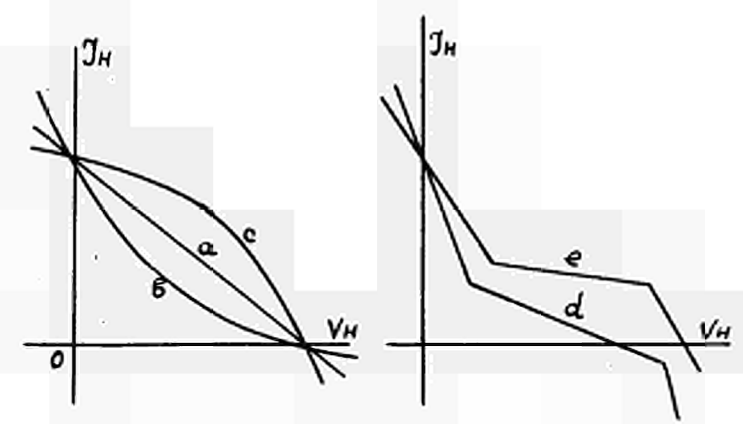


Fig. 2. VA-Dependence and their Modelling Circuits

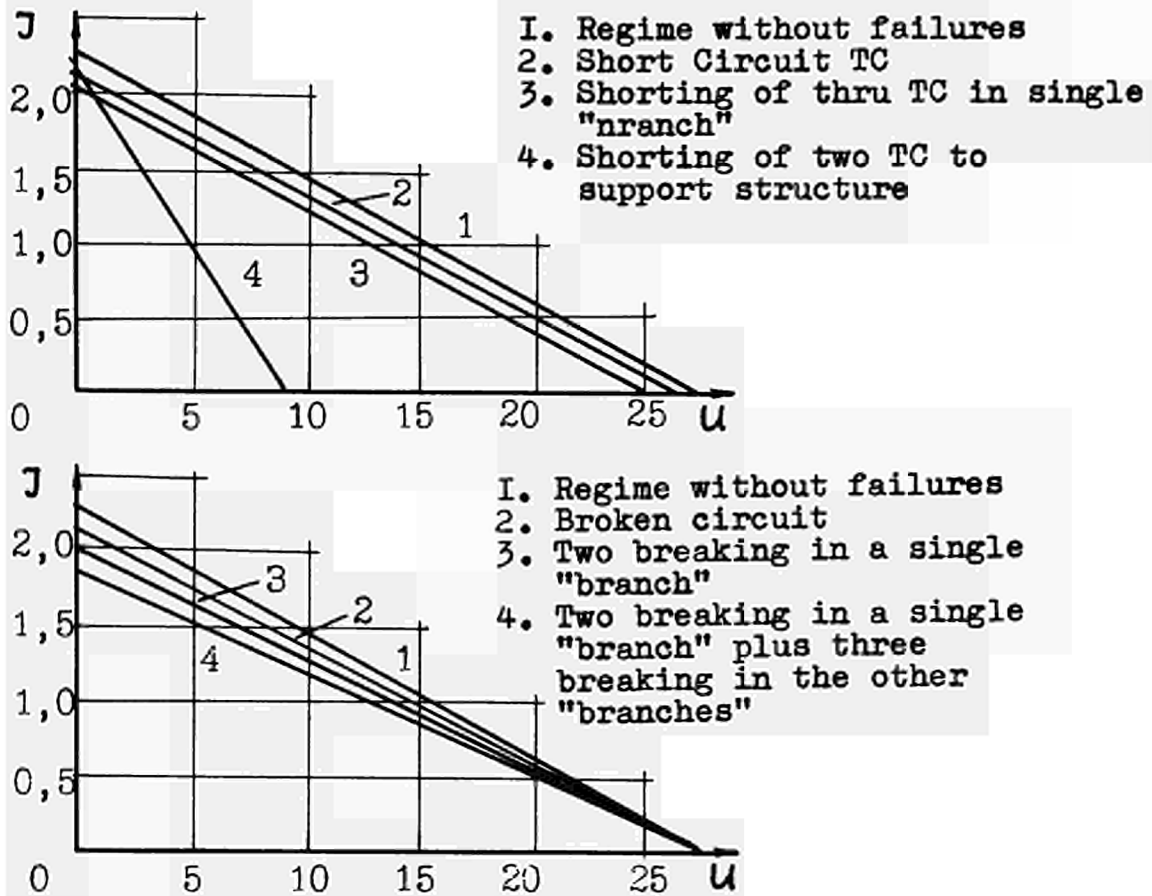


Fig.3. Integral Characteristics of Matrix System in Different Failure Regimes

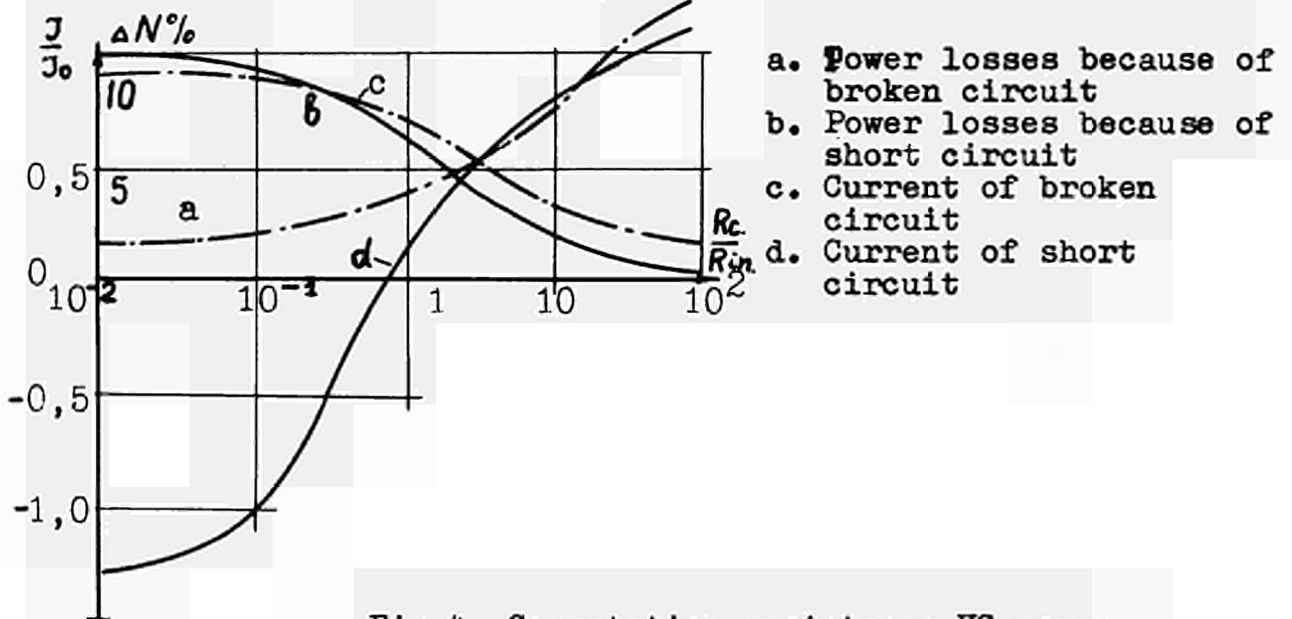


Fig.4. Commutation resistance VS power losses and relative current changing in failure cell.

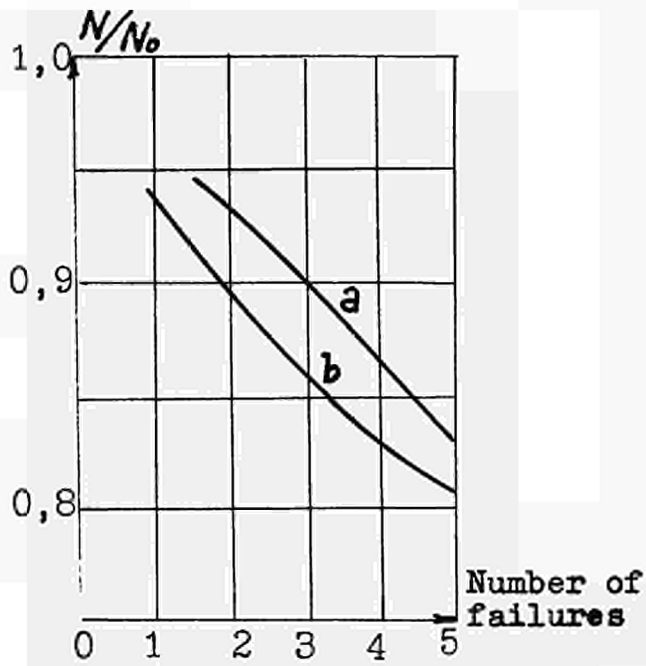


Fig.5. Relative power losses:
a) broken circuit
b) short circuit

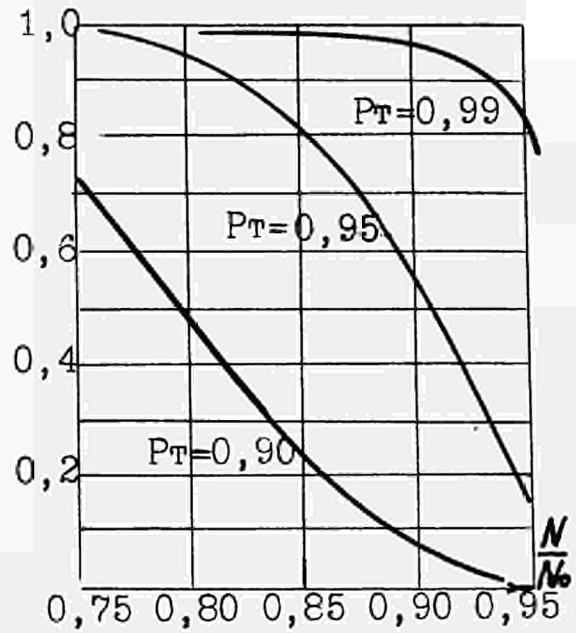


Fig.6. Matrix circuit
Reliability

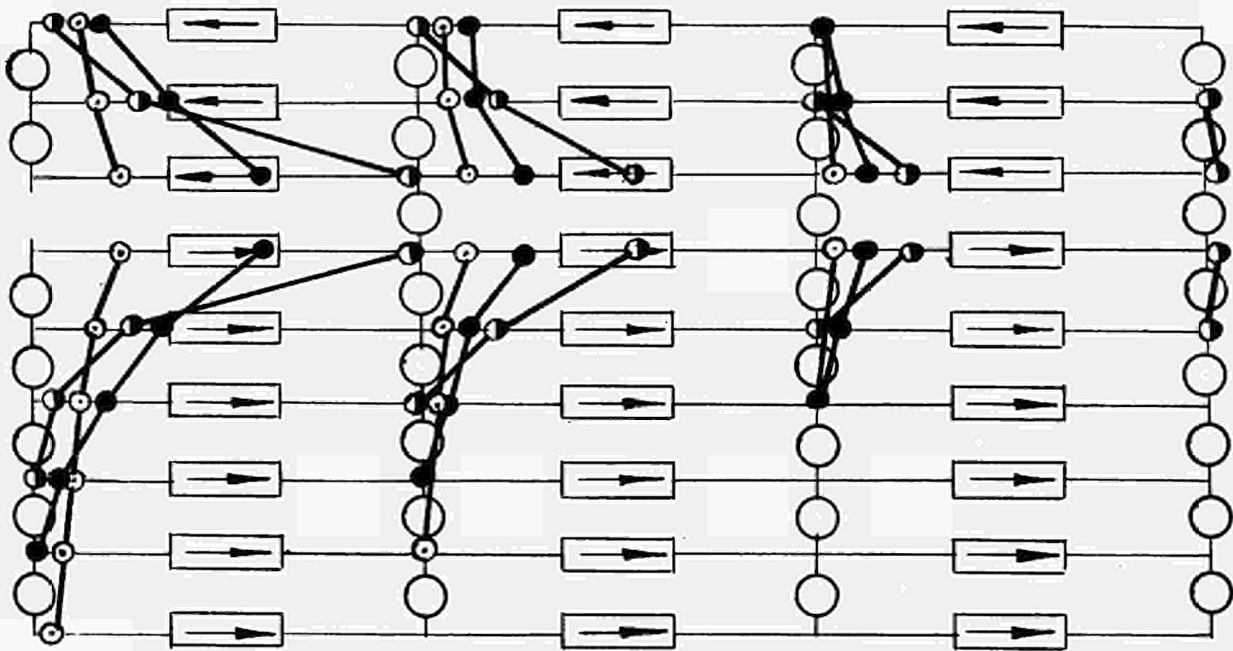


Fig.7. Current Redistribution along commutation resistances when the circuit is broken

$$\text{---} \bullet \text{---} \frac{R_c}{R_{in}} = 10^2; \quad \text{---} \bullet \text{---} \frac{R_c}{R_{in}} = 1; \quad \text{---} \bullet \text{---} \frac{R_c}{R_{in}} = 10^{-2}$$

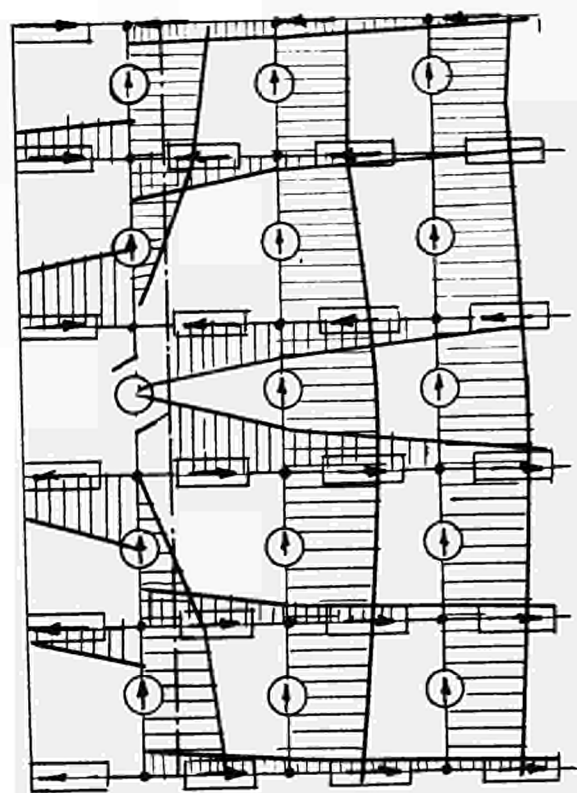


Fig.8. Diagram of relative Current Maghitudes because of Failure "BC"

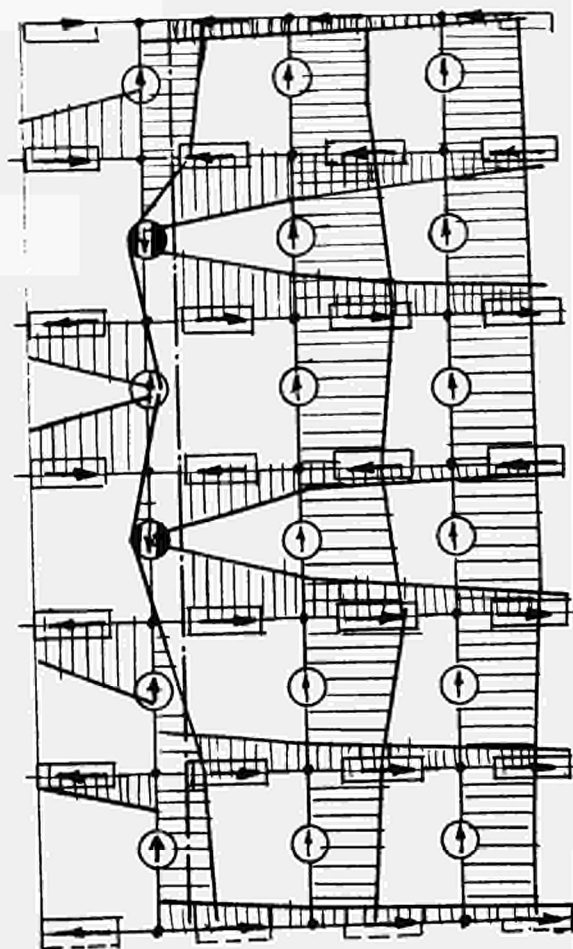


Fig.9 Diagram of relative Current Maghitudes because of two Failures SC

— Critical maguitude of current relative magnitude

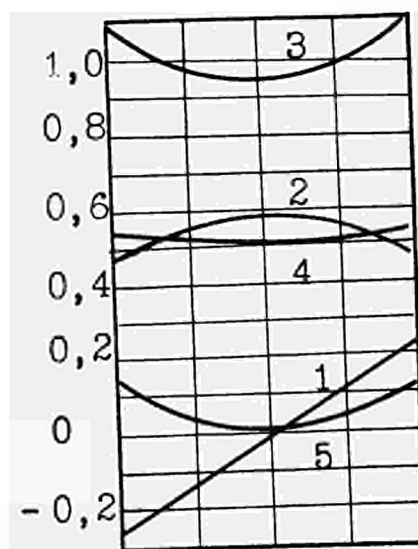


Fig.10. "Functions dangerous" distribution when $H=1; \omega=1$;
 1. potential
 2. current along circuit
 3. "function dangerous" of lowering module EMF (f_a);
 4. "Function dangerous" of raising module inner resistance (f_b);
 5. "function dangerous" of lowering resistance of anode electrical isolation module (f_u);

THEORETICAL STUDY OF TRANSIENT THERMAL CONDITIONS
DURING THE START-UP OF A THERMIONIC CONVERTER

E.S.A. Arkin, A.N. Luppov,
H.A. Murinson, B.G. Ogloblin,
P.Z. Cherepanov.

The Academy of Sciences,
Moscow, the USSR.

Among the various thermionic converter designs those ones, consisting of coaxial cylindrical electrodes, (the cathode being an inside cylinder) are the most applicable. The clearance between the cathode and the anode is to be done sufficiently small in order to get good performance. Besides the technological limitations the different thermal expansion of cathode and anode prevents from obtaining the small clearance.

During the start-up period the cathode and anode temperatures grow up disproportionately. Then due to thermal expansion the clearance reduction and even its disappearance can take place. As there are spacing insulators in this clearance preventing the electrode contact, it is obvious

that such expansion may be a possible reason of converter failure.

The increase of the designed clearance size to provide for the heating process makes the converter performance worse. In addition the cathode gets then excessive freedom of displacement inside the anode, which also leads to undesirable effects.

Besides the above mentioned considerations it is interesting to determine the cathode longitudinal expansion in relation to the anode. In case of a long thermionic converter these relative expansions may be considerable and pose additional requirements to cathode - anode connection and commutation elements.

Thus for working out the converter design it is necessary to know the cathode and the anode temperatures during heating process. Then the problem of longitudinal expansions can be solved by a constructive way, and for solving the radial expansions problem it is most convenient to choose a proper law of thermal energy source capacity variation. It is obvious that thanks to the slow enough heating the considerable decrease of the difference between the cathode and the anode expansions can be get. However the thermionic converter heating time is often limited. This necessitates to choose such source capacity variation law, that provides for the converter heating in a given time and minimum reduction of interelectrode clearance.

The objective of the present study is the determination of the cathode and the anode temperatures during their heating under the different laws of heat source capacity growth.

Mathematical representation of the problem and the solution procedure.

The temperature distribution along the radius only is considered. Heat escape in axial direction is neglected.

It is assumed for simplicity that the heating proceeds with no gas in the interelectrode space, i.e., the heat transfer from cathode to anode is by radiation only and the electronic cooling and heat transfer by thermal conductivity are neglected.

Mathematical representation of the problem gives the following differential equations.

$$\frac{\partial T_1(z, t)}{\partial t} = \frac{\alpha_1}{z} \frac{\partial}{\partial z} \left(z \frac{\partial T_1(z, t)}{\partial z} \right) + \frac{w(t)}{c_1 \gamma_1}; \quad z \in [0, R_1] \quad (1)$$

$$\frac{\partial T_2(z, t)}{\partial t} = \frac{\alpha_2}{z} \frac{\partial}{\partial z} \left(z \frac{\partial T_2(z, t)}{\partial z} \right), \quad z \in [R_1, R_2] \quad (2)$$

$$\frac{\partial T_3(z, t)}{\partial t} = \frac{\alpha_3}{z} \frac{\partial}{\partial z} \left(z \frac{\partial T_3(z, t)}{\partial z} \right); \quad z \in [R_3, R_4] \quad (3)$$

under the initial conditions

$$T_1(z, 0) = T_2(z, 0) = T_3(z, 0) = T_0$$

The first equation describes the temperature field in the fuel element, the second one - in the cathode and the third one - in the anode assembly (with the average thermo-physical parameters). The boundary conditions are:

$$\frac{\partial T_1}{\partial z} \Big|_{z=0} = 0 \quad (4)$$

$$T_1(R_1, t) = T_2(R_1, t); \quad -\lambda_1 \frac{\partial T_1}{\partial z} \Big|_{R_1} = -\lambda_2 \frac{\partial T_2}{\partial z} \Big|_{R_1} \quad (5)$$

$$-\lambda_2 \frac{\partial T_2}{\partial z} \Big|_{R_2} = \sigma \varepsilon [T_2|_{R_2}^4 - T_3|_{R_3}^4]; \quad -\lambda_2 R_2 \frac{\partial T_2}{\partial z} \Big|_{R_2} = -\lambda_3 R_3 \frac{\partial T_3}{\partial z} \Big|_{R_3} \quad (6)$$

$$-\lambda_3 \frac{\partial T_3}{\partial z} \Big|_{R_4} = \alpha (T_3|_{R_4} - \vartheta(t)) \quad (7),$$

where $\vartheta(t)$ is the coolant temperature¹⁾

λ_i - the layer thermal conductivity factor,

1) The temperature $\vartheta(t)$ is given or determined by solving the problem, external in respect to considered one.

σ - Stephan - Boltzman constant,

ϵ - the thermal emissivity factor

α - the heat transfer factor

Instead of perfect heat contact condition (5) it is possible to consider heat transfer through the clearance. When studying the experimental devices with electric heater the heat flow is given instead of the equation (1) and boundary conditions (5). For more detailed studying of the heating process it is possible to consider the equation (3) in each layer of the anode assembly separately, making the boundary conditions on the layer contacts similar, for example, to the conditions (5).

The most suitable solutions of this problem are the net procedure, connected with changing differential equations for finite-difference ones, and the presentation of the solution as a series of cylindrical functions. Here the second procedure is used.

By introducing some unknown time functions as a heat flow values on the layer boundaries it is possible to subdivide this problem into three boundary problems of the form

$$\frac{\partial T_i}{\partial t} = \frac{\alpha_i}{\tau} \frac{\partial}{\partial z} \left(\tau \frac{\partial T_i}{\partial z} \right) + A_i(t) \quad (8)$$

$$T_i(\tau, 0) = T_0; \quad -\lambda_i \frac{\partial T_i}{\partial z} \Big|_{R_{i-1}} = \varphi_i(t); \quad -\lambda_i \frac{\partial T_i}{\partial z} \Big|_{R_i} = \psi_i(t).$$

Here $A_i(t)$ - are known functions and $\varphi_i(t)$ and $\psi_i(t)$ - introduced unknown time functions.

The solution of each such problem is as follows:

$$T_i(\tau, t) = \sum_{k=0}^{\infty} c_k^i(t) Z(\mu_k^i \tau) \quad (9)$$

where $Z(\mu_k^i z)$ are the natural functions of Sturm-Liouville's problem, corresponding to the problem (8). These functions are the linear combinations of Bessel functions of the I and II type. Multiplying the equations (8) by $Z(\mu_k^i z)$ and integrating in the interval $[R_i, R_{i+1}]$, we derive the expressions for $c_k(t)$ as functions of $\varphi_i(t), \psi_i(t)$ and their integrals. To determine the introduced unknown functions, it is necessary to use the boundary conditions (4) - (7). We obtain the integral equation system for φ_i, ψ_i . One of these equations is non-linear. To solve the system the time pitch is chosen, and within each interval the functions φ_i and ψ_i are assumed to be linear. Thus within each pitch we get the algebraic system, which is solved by means of Newton's method. Having determined φ_i and ψ_i the temperature distribution in each layer is found from the formula (9).

Results.

In fig. 1 it is shown as an example the typical cathode and anode temperature curves plotted against time under the constant heat source capacity, coolant temperature being determined from joint solution of the problem (1) - (7) and the equations for the coolant circuit.

Cathode heating consists of two basic stages. The first one is quick heating up to nearly nominal temperature

at low anode temperature. The second one is the slow temperature rise up to its nominal value due to anode temperature growth.

The characteristic parts of the anode temperature curve are:

a) OA - the heating delay because of low value of heat flow from the cathode ($Q \sim T^4$). This part on the curve is

determined by the rate of cathode temperature rise.

b) AB - the anode temperature growth when the coolant is cold. The duration of this period depends on thermal inertia of the coolant circuit. For the low-inertia circuits the duration of this period is small. But in those devices, where the coolant practically is not heated and the operational anode temperatures are attained due to low thermal conductivity of the anode assembly, the interval AB is the end of their heating.

c) BC - the anode temperature rise up to nominal value when coolant circuit is heated through.

As it was already noted, the interelectrode space reduction can be slowed down by decrease of the source capacity growth rate. In fig. 2 is shown the relationship between the relative value of the space maximum reduction under the same conditions and total time t_p of the converter heating, from time t_1 of capacity growth to nominal value. It is assumed, that

$$w(t) = \begin{cases} w_{\text{HOM}} \frac{t}{t_1}; & t \leq t_1 \\ w_{\text{HOM}}; & t > t_1 \end{cases}$$

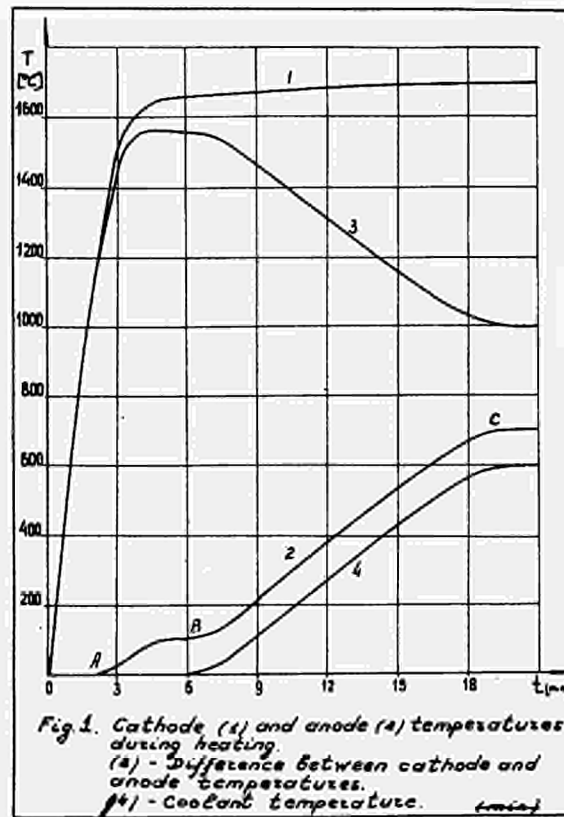
The anode heating time t_p to 95% of the nominal value is assumed to be the total heating time, and the heating time at $w(t) = w_{\text{HOM}}, t > 0$ (see fig. 1) is assumed to be the unit of time.

It is seen that the desire to reduce the cathode and the anode expansion difference leads to quick growth of the converter heating time. Choosing more complicated law of capacity growth as compared with linear law it is possible to get more favourable relation between these values. However if it is not possible to prolong the start up period, the difference between the cathode and the anode thermal expansions remains to be considerable and is to be allowed for in the design.

Conclusions.

1. The difference between the cathode and the anode temperatures during the start up may be considerably higher than under the normal operational conditions. The designed value of the clearance between the spacing insulators and one of the electrodes is to be chosen on account of the supposed start up conditions.

2. In case of the limited heating time it is reasonable to minimize the cathode and the anode expansion difference by proper choice of the law of energy source capacity variation.



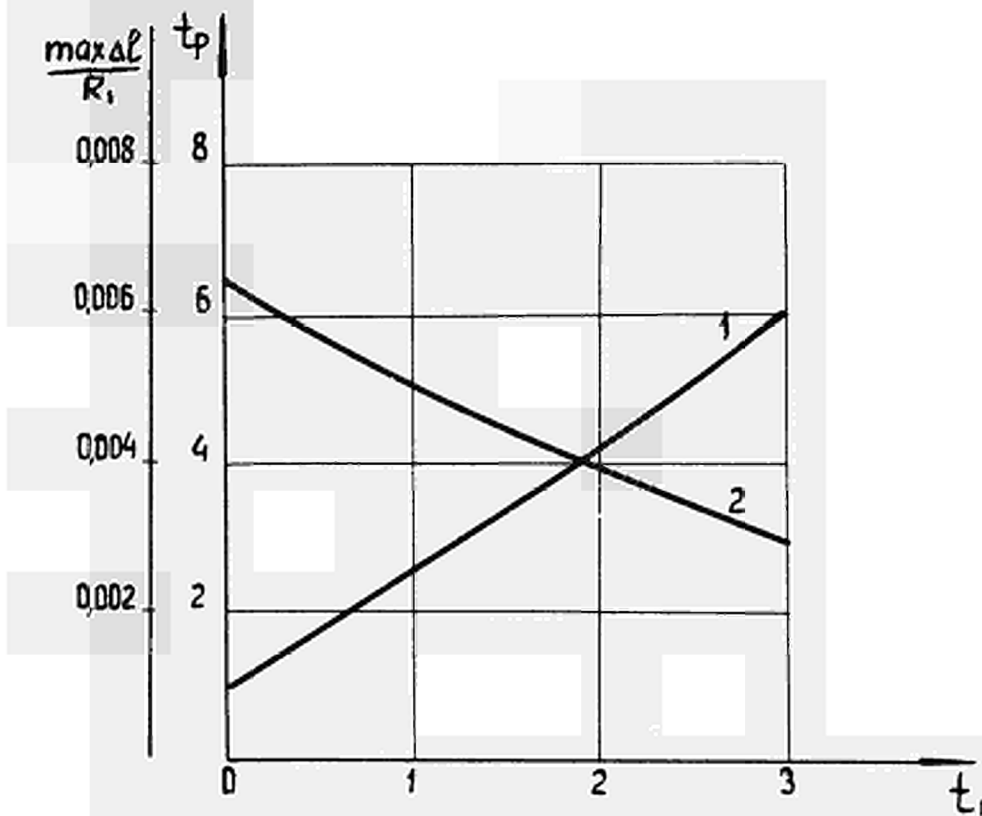


Fig. 2. Converter heating time (1) and relative value of the space maximum reduction (2) versus time of capacity growth.

FAILURE MODELS AND RELIABILITY ANALYSIS OF THERM-
IONIC CONVERTER COMPONENT PARTS

Diakov B.B.

A.F. Ioffe Physical Technical Institute , Leningrad,
Academy of Sciences of the USSR

Abstract

The failure model intended for reliability evaluation which is considered in this work postulates connection between physical nature of failures and mathematical calculation methods. Failures are treated as a result of accumulating irreversible changes in a structure of an investigated material i.e. as so-called irreversible defects (point , linear or volume defects).

Random character of defect distribution in the volume or at the surface of material testifies to *probabilistic* nature of failures.

Finite relationships describing probability of damage are obtained for thermionic converter component parts characterized by failure criteria which may be expressed by maximum permissible concentration of defects belonging to one or several types.

Problem of reliability of certain component materials under mechanical load is treated separately.

Failure model accounting for quantity or accumulating defects may be extended to the case of simultaneous action of several failure mechanisms.

Introduction

Thermionic network reliability is connected usually with simple failure modes of thermionic module: short and open circuits and so-called failure propagation /1/. The module failure is a random event with respect to both location in the network and time and its reliability is a function of time: $R = R(t)$.

Simultaneously reliability is determined by the degradation processes of device materials and fundamental properties of cathode, anode, fuel, envelope with vacuum tight seals, isolation and others.

With this attitude the model "short circuit-open circuit" has the operationable significance only just as the failures occur due to natural laws of material changes.

The formalism describing these processes and establishing a direct connection with conventional probability parameters is presented below as mathematical model to use the knowledge of physical processes in component parts of thermionic converter with purpose of the reliability evaluation.

Presentation of Failure Model

First introduce basic terms and notations. Let any com-

ponent part of thermionic converter be called a physical system of volume V under stress H . Let H be unique and constant for simplicity.

The failure will result from irreversible change accumulation in system and minimal value of this change will be called "defect" (point, linear, surface or volume ΔV).

The defect concentration or their total number defined by one variable X is a basic parameter to determine the failure. Its maximal value: $X_{\max} = V/\Delta V$ and failure limit: $X_{\lim} (X_{\lim} < X_{\max})$.

Then in absence of other processes and consequently of defects of other type from elementary considerations the probability of single defect formation per unit time is equal to

$$q = \frac{dX/dt}{X_{\max} - X(t)} \quad (1)$$

For sufficiently small time interval Δt it can't arise other than one defect with probability $q \Delta t$.

The failure is complex random event involving a summation of the defects (its number or concentration) up to X_{\lim} and having the probability for time interval Δt :

$$dQ = \frac{P_{X_{\lim}-1}(t) q \Delta t}{\sum_i^{X_{\lim}-1} P_i(t)} \quad ; \quad (2)$$

as a conditional probability.

The values of $P_i(t)$ are obtained from the equations of the next type:

$$\frac{dP_i}{dt} = q P_{i-1}(t) - q P_i(t) \quad ; \quad (3)$$

(3)

with initial data:

$$P_i(t=0) = \begin{cases} 1 & \text{for } i = 0 \\ 0 & \text{for } i = 1, 2, 3, \dots, X_{\text{lim}} - 1 \end{cases}$$

For example, if $q = \text{const}$, the system (3) has well-known solution

$$P_i(t) = \frac{(qt)^i}{i!} \exp(-qt). \quad (4)$$

Substituting (4) in the formula (2) we have

$$dQ = \frac{(qt)^{X_{\text{lim}}-1} \cdot q dt}{(X_{\text{lim}}-1)! \sum_i \frac{(qt)^i}{i!}} \quad (5)$$

In practice the reliability value R is evaluated as a ratio of number of operationable devices to total number of device under test:

$$R(t) = 1 - \frac{N_{\text{otk}}}{N_0} \quad (6)$$

where N_{otk} denotes the number of failures, N_0 and N_{otk} being great enough for reliable value of R .

Since the number of failures for dt is equal to

$$dN_{\text{otk}} = (N_0 - N_{\text{otk}}) dQ \quad \text{with } N_{\text{otk}}(t=0) = 0$$

then

$$N_{\text{otk}} = N_0 \left[1 - \exp\left(-\int_0^t dQ(t)\right) \right], \quad (7)$$

the value of R being obtained from (6).

In this form the failure model oversimplifies the natural processes of failure and so it demands several improve-

ments. In particular the number of possible defect realizations in volume $-X_{\max}$ is limited by initial condition $X(t=0) = 0$. For different volume zones of physical system this number can be different, hence, value X_{\max} in (1), too. It is necessary to divide total V into n zones each having the volume δV_{κ} ($\kappa = 1, 2, \dots, n$) great enough in comparison with ΔV . Every zone has its proper characteristic value of X_{\max}^{κ} , X_{\lim}^{κ} , $X^{\kappa}(t=0)$. The value of αQ^{κ} is determined from (2) as shown above with these constants.

The probability of component part failure is determined as in /2/, by approximate relation

$$\alpha Q = \sum_{\kappa}^n \alpha Q^{\kappa} \quad ; \quad (8)$$

if
$$\sum_{\kappa}^n (\alpha Q^{\kappa})^2 \ll 1 ;$$

which is realized first of all for system with high reliability. Real physical systems may not possess similar work conditions for all zones δV_{κ} . This additional nonuniformity cannot be described by a set of parameters X_{\max}^{κ} , X_{\lim}^{κ} and $X^{\kappa}(t=0)$ and must be taken in account by substitution of new functions $\frac{\alpha X}{\alpha t}$ and $X(t)$ into (1) and also other external stress parameters varying from zone, as temperature T and mechanical load $\bar{\sigma}$ etc.

The clear example of real physical system division on zones mentioned above is appointment of regions near interfaces or system boundaries. For removing the restriction introduced

above: $H = \text{const}$, we approximate the variations of H by suitable function of time having the steps as H changes at moment T_s . The values of X obtained after each step will be considered as the initial data for determining of failure probability Q at subsequent steps.

Failure Model Development

Failure model is complicated if the defects have not similar influence on system state. Let evaluate this nonuniformity by different values of damage y inserted by each defect in parameter A determining the system state and write it as a distribution function of $f(y)$ with density function $r(y)$ and generalized function $\pi(s)$, where s - auxiliary parameter.

At moment t total damage Y depends on number (or concentration) of arising defects $X(t)$, every defect having its value of damage y from $f(y)$.

Under such conditions Y has also certain distribution function $F(Y)$ at moment t described by generalized function $\Pi(\pi(s))$ if the probability of defect arising at t has generalized function $\pi(s)$ /3/.

If, for example, we have the defect number distribution in form of (4), having the producing function

$$\Pi(s) = \exp(-qt + qts)$$

and variable y is described by Gaussian distribution

$$f(y) = \frac{1}{s\sqrt{2\pi}} \exp\left(-\frac{(y-\bar{y})^2}{2s^2}\right)$$

with mean \bar{y} and variation σ^2 , the producing function of total damage distribution at t is equal

$$\Pi(\pi(s)) = \exp \left\{ -qt + qt \exp \left[-\bar{y} \ln s + \frac{(\ln s)^2}{2} \right] \right\} \quad (9)$$

Substituting in (13) e^{-pY} for S where p is auxiliary parameter we obtain none other than Laplace transform of unknown function $F(Y)$:

$$\int_0^{\infty} F(Y) \exp(-pY) dY = \exp \left\{ -qt + qt \exp \left[p\bar{y} + \frac{p^2}{2} \right] \right\} \quad (10)$$

which can be served for its determination.

Instead of Laplace inversion necessary approach to the function $F(Y)$ may be obtained by its moment computation. For our example we have the first moment: $\mu_1 = \bar{y}qt$ and the second one: $\mu_2 = (qt\bar{y})^2 + qt(\bar{y}^2 + \sigma^2)$ whence the distribution function of total damage of parameter A has the mean: $\bar{Y} = \bar{y}qt$ and the variation: $\sigma_Y^2 = (qt)^2(\bar{y}^2 + \sigma^2)$.

In any case after this model the failure probability for time interval dt can be expressed as

$$dQ = \frac{F(Y) f(y) q dt}{\int_0^{Y_{lim}} F(Y) dY} \quad (11)$$

where Y_{lim} - total damage limit determined from parameter A . Expression (11) is obtained taking in consideration the fact that for time interval dt it may be arised single defect (with probability qdt) or none (with probability $1 - qdt$). Reliability evaluation is performed after expressions (6) and (7).

Discussion of Failure Model Application to
Thermionic Converter Component Parts

Theoretically to use the failure model exposed in previous sections for thermionic converter component parts is possible if the natural terms analogous to the defects introduced above can be found. For practical study of reliability it is necessary to obtain information on physical processes in form of $\frac{dX}{dt}$ and $X(t)$, as in principal relation (1). Consider with this attitude several converter component parts.

If one adopts as a defect of material the microfissures arising in it under stress, accumulation of which leads to cracks formation and body destruction then described model is suitable for any converter element under mechanical load.

For example, taking X as a crack length with critical value for certain material

$$X_{lim} = L_{lim} = L \left(1 - \bar{\sigma} / \bar{\sigma}_{lim} \right)$$

where L denotes the thickness, $\bar{\sigma}$ - stress and $\bar{\sigma}_{lim}$ - strength limit, λ - elementary defect, we obtain the crack growth rate (without corrosion) /4/:

$$\frac{dX}{dt} = \lambda_{const} \exp \left(\frac{\gamma \bar{\sigma}}{[1 - X/L] k_B T} \right) \quad (12)$$

where γ is constant and k_B - Boltzman constant.

If a pore having minimal volume ΔV is considered as a defect then porosity of vacuum seal material can be taken for a variable X changed under chemical reaction of seal material or its admixtures with active medium (for example Cs).

In this case $\frac{dX}{dt}$ will be rate of chemical reaction leading to pore formation.

The cathode thickness diminution because of material evaporation can be described by the model the cathode being divided into two zones: superficial and internal. The evaporation rate is expressed as linear measure as in /5/:

$$\frac{dX}{dt} = g = g_0 \exp\left(-\frac{\Delta\phi}{k_B T}\right) \quad (13)$$

where g_0 and $\Delta\phi$ denotes the cathode material constants. If cathode life is improved by superficial film of other material the film reliability is evaluated. In particular, for the disperse cathode the defect formation rate is equal to the differences between the rate of evaporation of film atoms and their migration rate. As a result the disperse substance supply is diminished, i.e. $(X_{\max} - X)$ in terms of the model.

Another example is a converter electrical isolation resistivity of which is inverse to change carrier concentration. The latter is considered as a variable X . The degradation rate is determined more often by diffusion of metal surrounding the isolation layer:

$$\frac{dX}{dt} = aD \exp\left(-\frac{t}{\tau}\right); \quad (a, D, \tau - \text{const}) \quad (14)$$

Conclusion

The difference between the failure model for reliability analysis considered above and reliability evaluation by statis-

tic testing consists in obtaining of necessary information. Statistic tests provide us with the information consisting either in the form of number of failure devices N_{otk} , substituted in (6), or as a set of lifetimes of tested devices up to the test end. The model considered above provides us with the information consisting in experimental functions $\frac{dX}{dt}$ and $X(t)$.

When statistical tests are being carried out it is essential to provide for all tested devices the equal work conditions whereas in failure model presented here variations of these conditions signify only the change of initial data for X . The natural processes being approximated as above these variations are described by the set of X_{max}^* , X_{lim}^* , $X^*(t = T_3)$.

REFERENCES

1. HOLLAND J.W., "Thermionic Network Reactor Reliability". Proc. Int. Conf. on Thermionic Energy Conversion, London, 1965.
2. GNEDENKO B.V., BELYAEV Yu.K., SOLOV'EV A.D., Mat. metody v teorii nadezhnosti. Nauka, M. 1965
3. FELLER W., Vvedenie v teoriyu veroyatnosti i eje prilozheniya. Mir, M., 1967
4. BARTENEV G.M., RAZUMOVSKAYA J.V., KARTASHOV E.M., "Phys.-tech. mekhanika materialov" 3, (1967), 592
5. RAZOR N.S., Advanced Energy Conversion, March, 1963

DISCUSSION

Speaker of papers F-10 : B. DIAKOV.

HOWARD (USA): The speaker said that most of the failures observed were shorts. What were the causes of these shorts?

DIAKOV (USSR): The converters referred to were laboratory converters, not in-pile converters. The shorts were between emitter and collector.

DAVIS (USA): In addition to electrode shorts within a converter, have you also considered the effects in the reliability analysis of shorts of the converter to ground, to the liquid metal cooling circuit?

DIAKOV: In our calculations the failures due to shorts were for many reasons. The shorts concerned not only the electrodes, but also, as you have just mentioned, the liquid metal coolant circuit. Since we did get these results in the laboratory, we can expect the same to occur in actual practice. Particularly, one can expect leaks after a long period of time.

DAVIS: Would it not be so that the effect of an internal short and the effect of a short to the liquid metal cooling circuit would have totally different effects to the power degradation of the system. It is not clear from the paper that these could really be treated similarly. Would not an independent type of analysis be necessary for these two types of shorts?

DIAKOV: The reliability analysis requires consideration of all important probabilities. For these analyses to be more complete, more comprehensive, we must take into account all possibilities of failure.

SCHOCK (USA): I am intrigued by your statement that in your laboratory work you have observed short-circuit failures far more frequently than open-circuit failures. This differs from the experience of other laboratories, and the infrequency of open-circuits suggests that you must have some very reliable joining techniques. Could you tell us what methods you employ for joining metals to metals and to ceramics? Do you use brazing or electron-beam welding? Also, could you tell us something about the typical duration of your laboratory tests, and the configuration, size, and electrode spacing of the diodes which experienced short-circuit failure?

DIAKOV: The details of our reliability analysis are based on theoretical or rather mathematical considerations. In certain experiments we did have certain failures. However, we can evaluate the real probability of meeting

these failures in the reactor only once we have tested a large number of diodes. But we have not studied enough experimental cases. As you know the number will have to be very large, to be statistically valid, several hundreds of samples for example. We are now trying to perform a sufficient number of experiments; we have not made that number yet.

ANALYSIS AND OPTIMIZATION OF "FULL-LENGTH" DIODES*

by

Alfred Schock

Republic Aviation Division of Fairchild Hiller Corporation
Farmingdale, L. I., New YorkAbstract

A method of analyzing the axial variation of the heat generation rate, temperature, voltage, current density and emitter heat flux in a thermionic converter is described. The method is particularly useful for the case of "long" diodes, each extending over the full length of the reactor core. For a given diode geometry and fuel distribution, the analysis combines a nuclear solution of the axial fission density profile with the iterative solution of four differential equations representing the thermal, electrical, and thermionic interactions within the diode. The digital computer program developed to solve these equations can also perform a design optimization with respect to lead resistance, load voltage, and emitter thickness, for a specified maximum emitter temperature. Typical results are presented, and the use of this analysis for predicting the diode operating characteristics is illustrated.

Introduction

A thermionic reactor design study⁽¹⁾ currently under way is based on the concept of using long, cylindrical diodes, each extending over the full length of the reactor core. In such a design, accurate knowledge of the diode's axial voltage and temperature profiles is vital, since the optimum converter length represents a compromise between minimum neutron leakage and minimum ohmic loss.

Earlier ohmic loss calculations have usually assumed a uniform emitter current density, an assumption that is clearly inaccurate since the existence of significant voltage variation must necessarily lead to a redistribution of the diode current. Similarly, thermionic system studies have frequently treated each diode as isothermal, even though the rather substantial emitter lead heat loss must result in correspondingly large temperature gradients near the end(s) of

* Work supported by U. S. Atomic Energy Commission.

the emitter. With an axially uniform heat generation rate, this effect can be shown to lead to appreciable temperature non-uniformities, extending over a significant fraction of the total emitter length. The resultant penalty in diode power is important not only in the full-length design discussed above, but also in the shorter diodes used in conventional designs. In the case of full-length diodes, however, it is possible to compensate for the emitter's end losses and improve its temperature uniformity, by using a combination of axial reflectors and fuel zoning to produce a skewed fission profile. Thus, a detailed axial analysis is particularly important in full-length diodes.

Such an analysis must provide close coupling between the various nuclear, electrical, thermal, and thermionic equations because of their mutual interdependence, particularly the effect of local diode voltage and emitter temperature on current density and electron cooling. In the present study, the relationship between these variables was obtained from an extensive set of thermionic performance data that had been generated by the recently developed⁽²⁾ SIMCON computer code. These data extend over a wide range of emitter temperatures (1700 to 2400°K), collector temperatures (850 to 1150°K), and cesium reservoir temperatures (550 to 690°K). A specialized "thermionic correlation" subroutine TICORR, capable of performing multi-dimensional interpolations, was employed to compute the local current density and emitter heat flux.

Analysis

Within each diode, a complete thermal and electrical analysis should really be three-dimensional (or two-dimensional in the case of axisymmetric converters). However, since the axial dimension of a full-length diode is much larger than the transverse dimensions, and since current flow is primarily in the axial direction, we shall simplify the problem by treating it as one-dimensional.

The first step of the analysis is to compute the axial fission density profile $f(z)$ for the assumed fuel distribution. This is done by means of the ANISN⁽³⁾ one-dimensional, multi-group, multi-zone neutron transport code, with transverse leakage represented by appropriate buckling terms. Beyond the actual core, additional zones are included to provide a realistic representation of axial reflectors and various diode components (e. g. , power leads, seals, coolant

plenums). The computed fission density $f(z)$ is normalized to unity at $z = 0$, the reactor midplane.

To carry out the thermal and electrical analysis of the fuel-emitter structure, it is convenient to employ four simultaneous first-order differential equations, describing the variation of the axial heat flow rate Q and current I_E , the emitter temperature T and the local diode voltage V . The axial heat flow Q in the fuel-emitter assembly varies because of heat generated by fissions, heat lost at the emitter surface $r = r_E$, and ohmic heating:

$$dQ/dz = A_F Q_O''' f(z) - 2 \pi r_E q_E(V, T) + I_E^2 / A_E \sigma_E' \quad (1)$$

Here, A_F and A_E respectively denote the cross-sectional areas of the fuel and emitter, Q_O''' is the volumetric heat generation rate in the fuel at the reactor midplane ($z = 0$), q_E represents the emitter heat flux at the local voltage V and temperature T , and σ_E' is the effective electrical conductivity of the emitter. The latter includes not only the actual conductivity of the emitter, but also the possible contribution of a conductive fuel. Moreover, in the case of the external-fuel design⁽¹⁾ where the fuel surrounds the emitter, the outer sheath may also contribute to conduction if an electrical path exists between sheath and emitter. Thus, the effective emitter conductivity σ_E' is defined in its most general form by:

$$A_E \sigma_E' \equiv A_E \sigma_E + A_F \sigma_F + A_S \sigma_S \quad (2)$$

Since we shall strive for an isothermal emitter, the effect of temperature on conductivity will be ignored within the diode.

Next, the axial current I_E in the fuel-emitter assembly varies because of electrons leaving the emitter surface. Thus

$$dI_E/dz = 2 \pi r_E J(V, T), \quad (3)$$

where J is the thermionic current density at the local diode voltage V and emitter temperature T . The axial variation of T is defined by the usual conduction equation,

$$dT/dz = -Q/A_E K_E' \quad (4)$$

where the definition of the effective thermal conductivity K_E^* , in its most general form, is analogous to Eq. (2):

$$A_E K_E^* \equiv A_E K_E + A_F K_F + A_S K_S. \quad (5)$$

Finally, to derive the fourth differential equation, we note that the local diode voltage V is the difference between the emitter and collector voltages,

$$V = V_E - V_C. \quad (6)$$

These are related to the corresponding currents by Ohm's law:

$$dV_E/dz = - I_E / A_E \sigma_E^*, \quad (7)$$

$$dV_C/dz = - I_C / A_C \sigma_C. \quad (8)$$

We must now differentiate between two types of diode connections. If the emitter lead is connected to one end of the diode and the collector lead to the opposite end, the currents I_E and I_C flow in the same direction, and their sum equals the diode current I_D :

$$I_E + I_C = I_D. \quad (9a)$$

In that case the diode voltage variation, obtained by combining Eqs. (6), (7), (8), and (9a), is given by:

$$dV/dz = - I_E / A_E \sigma_E^* + (I_D - I_E) / A_C \sigma_C. \quad (10a)$$

If, on the other hand, the emitter and collector leads are connected to the same end of the diode, then the currents I_E and I_C are of opposite direction and equal magnitude:

$$I_E + I_C = 0. \quad (9b)$$

In that case, combining Eqs. (6), (7), (8) and (9b) yields:

$$dV/dz = - [(A_E \sigma_E^*)^{-1} + (A_C \sigma_C)^{-1}] I_E. \quad (10b)$$

The present study assumes the use of double-ended diodes, with a set of emitter and collector leads at each end of the converter. This arrangement minimizes ohmic losses, since such a converter is electrically equivalent to two single-ended diodes of half the length. Equation (10b) therefore constitutes our fourth differential equation.

Boundary Conditions

The system of Eqs. (1), (3), (4), and (10b) requires a total of four boundary conditions. Because of symmetry about the reactor midplane, we conclude that the axial heat flow Q and current I_e are each zero at $z = 0$. To define the other two boundary conditions, we must first relate the net diode voltage V_D to the heat flow Q_1 , current I_1 , voltage V_1 , and emitter temperature T_1 at $z = z_1$, the junction of the emitter and the emitter lead.

In general, the lead may have a non-uniform cross-sectional area $A_L(z)$, and its cold junction operates at the collector temperature T_c . Moreover, since T_1 and T_c differ considerably, the temperature dependence of its electrical and thermal conductivities should not be ignored. For an emitter lead passing a current I_1 , the temperature and heat flow gradients (neglecting radiation) are given by

$$dT/dz = - Q/A_L K_L(T), \quad (11)$$

and

$$dQ/dz = I_1^2/A_L \sigma_L(T). \quad (12)$$

The emitter lead conductivities K_L and σ_L are assumed to obey the Wiedemann-Franz law,

$$K_L/\sigma_L = \frac{1}{3}(\pi k/e)^2 T, \quad (13)$$

where k is Boltzmann's constant and e the electronic charge. Dividing Eq. (12) by (11) and combining the result with (13), we obtain the separable equation,

$$dQ/dT = - \frac{1}{3} (\pi k I_1/e)^2 (T/Q). \quad (14)$$

Since the emitter lead neither consumes nor produces energy, it must satisfy the energy balance

$$I_1 V_1 + Q_1 = I_1 V_D + Q_c, \quad (15)$$

where Q_c is the heat flow from lead to collector.

Integrating Eq. (14) from $T = T_1$, $Q = Q_1$ to $T = T_c$, $Q = Q_c$ and solving for the net diode voltage, we obtain:

$$V_D = V_1 - [(Q_1/I_1)^2 + \frac{1}{3}(\pi k/e)^2 (T_1^2 - T_c^2)]^{\frac{1}{2}} \quad (16)$$

Finally, the emitter lead resistance R_L must, of course, obey Ohm's law:

$$R_L = (V_1 - V_0) / I_1 \quad (17)$$

Equations (16) and (17) constitute the required third and fourth boundary conditions. Thus, for a diode of given geometry and fission density profile $f(z)$, the operating point is completely defined, at least in principle, by specifying the central heat generation rate Q_0''' , lead resistance R_L , and a single parameter to characterize the load, such as the voltage V_0 , current I_1 , or resistance V_0 / I_1 . In practice, however, solutions can only be found for a limited range of parameters, because of the limited extent of the available SIMCON⁽²⁾ data needed by the TICORR subroutine to compute the emitter current density $J(V, T)$ in Eq. (3) and the emitter heat flux $q_\epsilon(V, T)$ in Eq. (1).

Computer Program

In the course of the present study, a digital computer program TET(thermal, electrical, thermionic) was developed for solving the set of four differential equations. Since two of the required boundary conditions apply to the reactor mid-plane ($z = 0$) and the other two to the emitter-lead junction ($z = z_1$), a two-level trial and error procedure must be employed; e. g., by guessing at the midplane voltage V_0 and emitter temperature T_0 . Each trial requires numerical integration of the four equations, with the use of TICORR for thermionic data interpolation at each mesh point. The trials are repeated until boundary conditions 3 and 4 are satisfied.

In actual practice, rather than specify the heat generation rate Q_0''' and solve for the central emitter temperature T_0 by trial and error, it was found more efficient to solve for Q_0''' after first specifying T_0 (which is usually, though not always, the maximum emitter temperature).

In addition to finding solutions for specified values of the emitter temperature T_0 , lead resistance R_L , and load voltage V_0 , the TET program also provides the option of optimizing the leads and load, i. e., finding the values of R_L and V_0 which maximize the net diode power $P_0 = 2I_1 V_0$. Moreover, if desired TET can also determine the optimum value of the emitter cross-sectional area A_ϵ , i. e. the value which maximizes the diode's volumetric power density,

$$P_0''' = I_1 V_0 / (\pi r_\epsilon^2 + A_\epsilon) z_1 \quad (18)$$

Finally, the TET program also solves for the net conversion efficiency,

$$\eta = I_1 V_D / A_F Q_0''' \int_0^{z_1} f(z) dz \tag{19}$$

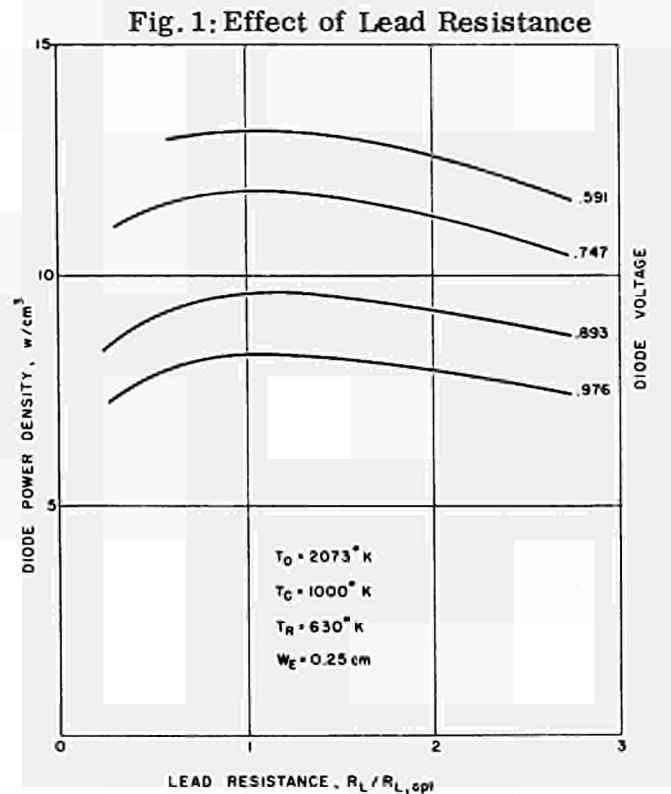
Results and Conclusions

A large number of TET optimizations were carried out, covering a range of emitter diameters (1.25 to 2.5 cm), diode lengths (20 to 25 cm), and fuel distributions (flat and zoned). The problems generally postulated a maximum emitter temperature of 2073°K, a collector temperature of 1000°K, a reservoir temperature of 630°K, and a 0.025cm electrode spacing.

We have assumed tungsten emitters and sheaths, with bulk UO₂ fuel wafers (normal to the diode axis), separated by tungsten fins occupying from 15 to 50% of the fuel chamber volume. These fins serve to reduce the maximum fuel temperature, and their thickness can be varied to adjust the axial fission density profile. The fuel chamber itself was generally assumed to occupy 40% of the total core volume. Actually, the results are virtually independent of this assumption, since UO₂ has no electrical conductivity and very little thermal conductivity. In the case of a conductive cermet fuel, however, the fuel volume fraction would be an important parameter.

Design Optimization

The emitter lead resistance was found to have a very broad optimum. As illustrated by Figure 1, the lead resistance can be varied over a surprisingly wide range without incurring excessive performance penalties. This is fortunate, since it permits structural and mechanical considerations to influence the lead design. The high currents generated in full-length diodes favor the use of very thick leads.



The net diode power was found to be a far more sensitive function of the diode voltage V_0 , as illustrated by Figure 2 (for optimized lead resistance). It was found that the optimum load voltage is essentially independent of the emitter's diameter, length, or cross-sectional area; it does depend on cesium pressure and maximum emitter temperature.

Fig. 2: Effect of Diode Voltage

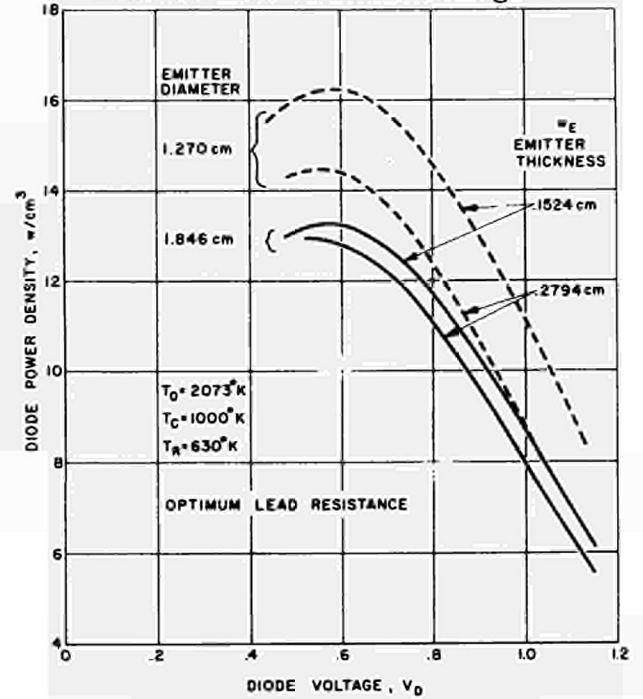
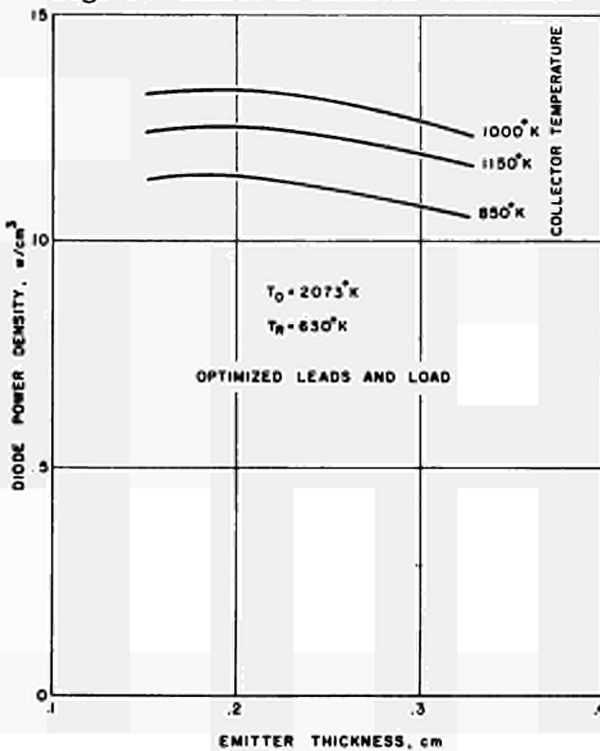


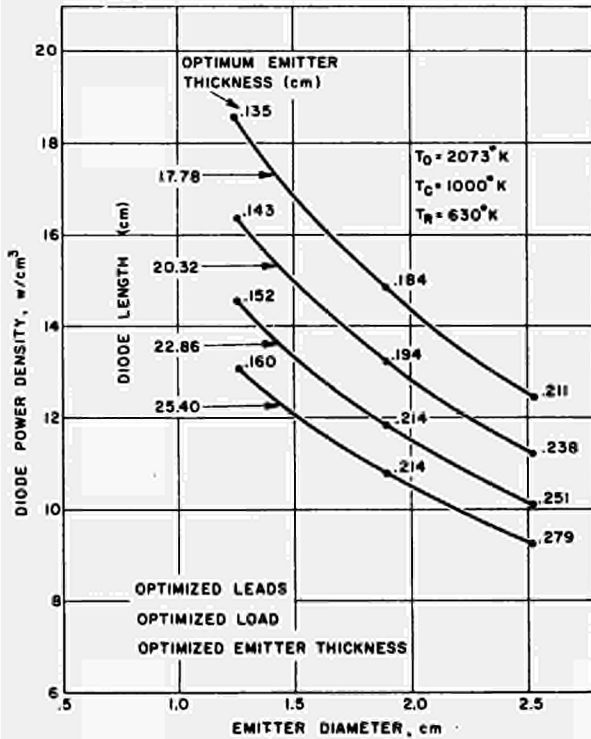
Fig. 3. Effect of Emitter Thickness



The effect of varying the emitter's cross-sectional area is illustrated by Figure 3, for optimized lead and load conditions. The figure also illustrates the weak effect of collector temperature, with 1000°K giving the best results. The emitter thickness was consistently found to optimize at rather low values, in spite of the fact that these correspond to high ohmic losses. However, the optimum is seen to be quite broad, permitting the choice of thicker emitters to reduce ohmic losses and enhance the diode's structural integrity. Thus, the use of a 0.25 cm-thick emitter only results in a relatively small penalty in net power density.

Figure 4 shows the effect of emitter diameter and length on the diode's net volumetric power density, with optimized lead resistance, load voltage, and emitter thickness. Over the range investigated, the power density increases monotonically with decreasing emitter diameter, which should therefore be sized at the lowest value consistent with the requirement for structural integrity and dimensional stability.

Fig. 4: Effect of Emitter Diameter and Length



Similarly, the volumetric diode power density can be increased by reducing the diode length, because of reduced ohmic loss. However, this length reduction increases the axial neutron leakage, and therefore raises the fuel volume required to maintain criticality. Thus, while there is no optimum length from the viewpoint of diode power density, there is an optimum with respect to the reactor power density. Extensive design calculations⁽¹⁾ revealed this to be about 20 to 25 cm, over a very wide range of reactor power levels.

Finally, Figures 5 and 6 display detailed axial solutions for two identical diodes, to illustrate the effect of fuel zoning. Figure 5 assumes a uniform fuel, with UO₂ occupying 85% of the fuel chamber volume. In the second case, as shown by Figure 6, the fuel is divided into 12 axial zones, with an average UO₂ content in the fuel chamber of 66% (varying from 50% in the center to 85% near the ends).

Both cases assume the same axial reflectors, including seals, power leads, coolant plenum, and 10 cm of BeO. The resultant fission density profiles, as computed by ANISN, ⁽³⁾ are shown in Figures 5 and 6. The remaining curves (showing the axial variation of emitter temperature, current density, voltage, and power density) are self-explanatory. The principal data about the two cases are summarized in Table I.

Fig. 5: Axial Profiles with Uniform Fuel

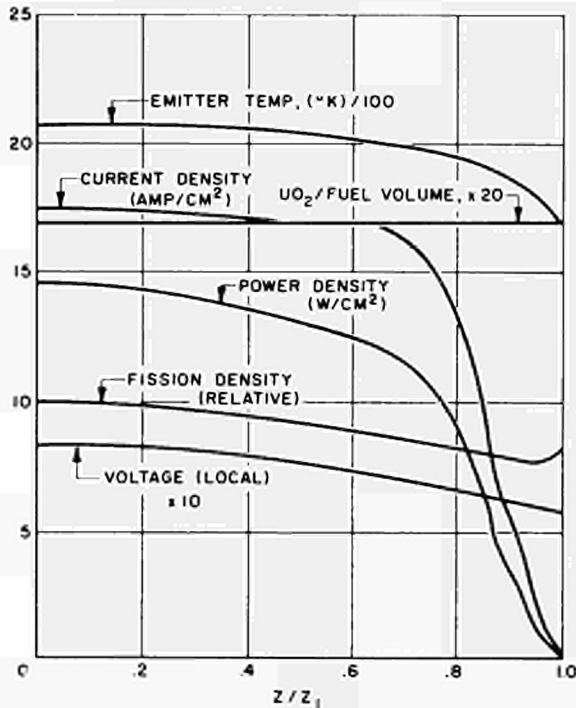
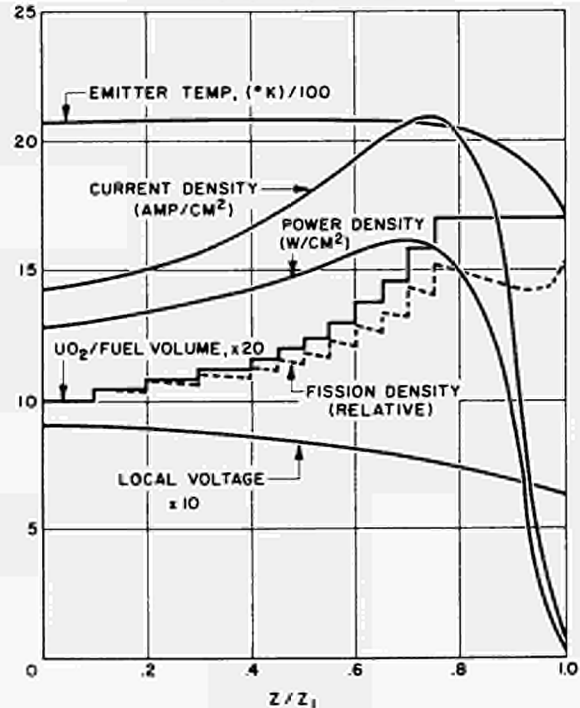


Fig. 6: Axial Profiles with Zoned Fuel



As can be seen, a flat fuel distribution leads to a highly non-uniform temperature profile, primarily because of heat losses to the emitter leads. Since converter performance is very sensitive to emitter temperature, the last 20% of the diode is relatively ineffective.

It should be noted that this problem also applies to conventional, short diodes. It can be shown that the heat lost to the emitter leads (expressed as a fraction of total heat generation) and the extent of the resultant temperature depression (expressed as a fraction of total diode length) are essentially the same for short and long diodes. In the latter case, however, considerable improvement can be achieved by axial fuel zoning.

The particular zoning illustrated in Figure 6 is not necessarily optimum; other calculations have shown that almost the same improvement can be achieved using just three coarse zones. Note, however, that the goal should be to produce a skewed rather than a flat fission profile, to compensate for heat losses at the ends of the diode. With such a fission profile it is seen that the emitter temperature can be maintained near its maximum value over a much larger fraction of the total diode length.

As shown by the overall performance summary in Table I, the use of fuel zoning raises the optimum diode voltage from 0.531 to 0.601 volt, the net diode power from 930 to 1154 watts, and the net conversion efficiency from 12.7 to 13.9%. However, it must be kept in mind that this improvement is only achieved at the price of lowering the UO_2 volume fraction in the fuel chamber from 85% to 66%. Thus, axial fuel zoning makes it possible to achieve a given reactor power output with fewer diodes, but with each diode having a larger fuel chamber. Consequently, the overall effect of zoning on critical core size must be determined for each specific case, and cannot be predicted a priori.

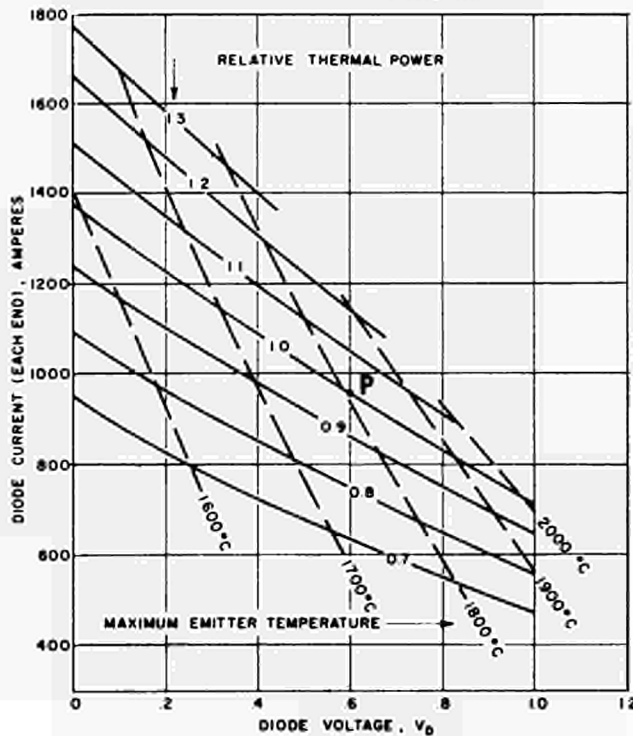
TABLE I: Effect of Fuel Zoning on Diode Performance

	Figure 5	Figure 6	
UO₂ Volume Fraction in Fuel Chamber			
Maximum	0.85	0.85	
Minimum	0.85	0.50	
Average	0.85	0.66	
Fission Density (Relative to Midplane)			
Maximum	1.000	1.502	
Minimum	0.771	0.999	
Average	0.904	1.220	
Diode Design			
Length	20.32	20.32	cm
Emitter Diameter	1.85	1.85	cm
Emitter Thickness	0.25	0.25	cm
Collector Thickness	0.42	0.42	cm
Optimum Lead Resistance	0.049	0.047	mΩ
Temperatures			
Central Emitter Temperature	2073	2073	°K
Maximum Emitter Temperature	2073	2077	°K
Collector Temperature	1000	1000	°K
Reservoir Temperature	630	630	°K
Voltages			
Optimum Diode Voltage	0.531	0.601	volt
Lead Voltage Drop	0.043	0.045	volt
Electrode Voltage	0.574	0.646	volt
Thermal Performance			
Heat Generation Per Unit Length at Midplane	398	334	watt/cm
Total Heat Generation	7320	8300	watt
Emitter Lead Heat Loss (each end)	442	528	watt
Electrical Output			
Diode Current (each end)	877	960	amp.
Diode Power	930	1154	watt
Diode Power Density	10.52	13.05	watt/cm ³
Net Emitter Power Density (Average)	7.90	9.79	watt/cm ²
Net Conversion Efficiency	12.7	13.9	%

Diode Characteristics

Thus far our discussion has dealt with the use of the present analysis to optimize the diode dimensions and choose the best operating point. However, the same analytical program (without the optimization options) can also be used to determine the current-voltage characteristics for a diode of fixed design. Figure 7 presents such a set of characteristics, for the same diode design represented in Figure 6. The solid curves are for constant thermal power of the reactor, while the dashed lines are for constant maximum emitter temperature. The thermal power is expressed in relative terms, where unity represents the heat generation rate (8300 watts per diode) given in Table I.

Fig. 7: I-V Characteristics at Constant Heat Input



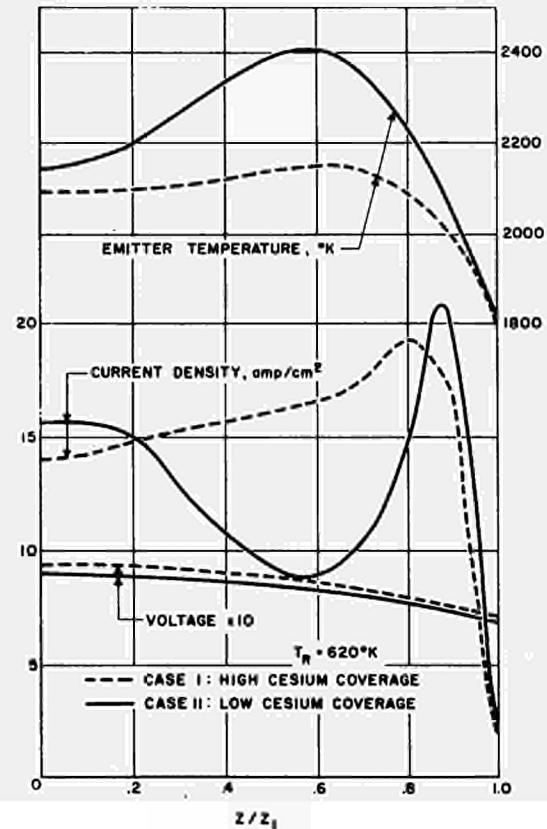
The curves shown in Figure 7 are of practical value not only for designing the reactor and its control system, but also for assessing the electrical effect of open-circuit failures on total reactor power. To minimize the effect of open-circuits (including loss of cesium) it is desirable to connect diodes in parallel groups, before connecting these groups in series. In that way, when a particular diode is open-circuited its group-partners can make up the current deficit, although at the penalty of operating at a lower (possibly even negative) output voltage.

The significant fact illustrated by Figure 7 is that this voltage penalty is much greater in the case of constant thermal power input than would be predicted from the constant temperature diode characteristics usually shown. This is so because raising the diode current results in increased electron cooling; at constant heat input this lowers the emitter temperature.

For example, for the design point depicted in Figure 6 and represented by point *P* in Figure 7, increasing the diode current by 45% above its design value lowers the maximum emitter temperature by 215°K and reduces the output voltage to zero. It appears questionable whether very substantial current increases beyond this point could be achieved, because of the rapidly decreasing emitter temperature. Since any reliability analysis must contemplate the occurrence of more than one open-circuited diode per parallel group, this places a lower limit on the number of diodes per group to ensure continued system operation in spite of such multiple failures. A detailed discussion of this point is beyond the scope of the present paper.

Finally, it was found that under certain conditions the TET equations and boundary conditions may be satisfied by more than one axial solution. This condition arises because the emitter current density and heat flux can actually diminish at higher temperatures, as a result of cesium desorption. The phenomenon is illustrated by Figure 8 for the same diode design, heat input, and fission profile represented by Figure 6, but with a 620°K cesium reservoir and a 0.535-volt load. The axial variation of temperature, voltage, and current density for the high and low cesium coverage solutions is represented in Figure 8 by the dashed and solid curves, respectively. Comparison of the two solutions shows that Case II has a 260°K higher maximum emitter temperature, and a 16% lower output current.

Fig. 8: Example of Dual Solutions



This co-existence of more than one possible operating point is similar to a phenomenon in the case of isothermal, isopotential diodes. By analogy, we infer that still a third solution of the TET equations exists, but at extremely high temperatures, beyond the range of the SIMCON data. A detailed discussion of this phenomenon, which can have considerable practical significance, is presented in another paper. ⁽⁴⁾

Acknowledgments:

The author wishes to express his appreciation for valuable help given by C. L. Eisen and M.J. Abbate, and for the SIMCON-generated thermionic performance data tabulations furnished by D. R. Wilkins.

References:

- (1) M. J. ABBATE, C. L. EISEN, B. RAAB, and A. SCHOCK, "External-Fuel Thermionic Reactors," Proceedings of the Second International Conference on Thermionic Electrical Power Generation, May 1968.
- (2) D. R. WILKINS, "An Improved Theoretical Description of Thermionic Converter Performance Characteristics," Report on Twenty-Seventh Annual Physical Electronics Conference, " M. I. T. , Cambridge , Mass. ,
- (3) W. W. ENGLE, Jr. , " A Users Manual for ANISN, A One Dimensional Discrete Ordinates Transport Code with Anisotropic Scattering," United Carbide Corporation, Nuclear Div. , Report K-1693, March 30, 1967.
- (4) A. SCHOCK, "Effect of Cesium Pressure on Thermionic Stability," Proceedings of the Second International Conference on Thermionic Electrical Power Generation, May 1968.

DISCUSSION

Speaker of paper F-12: A. SCHOCK.

GUSKOV (USSR): How does the current density vary through the converter? Do you have any data concerning the fuel element?

SCHOCK (USA): I believe that in my paper there were some very specific characteristics with regard to fuel distribution, fission density distribution, currents, voltages, temperatures. I'm referring specifically to Table 1 and to Fig. 5 and 6 corresponding to Table 1.

GUSKOV: But was there a drop in the value of the density of the current?

SCHOCK: If you would look at Fig. 6, one of the curves is marked current density (Amps. per sq. cm.) and it is plotted against axial position, the left side being the center of our double-ended diode and the right side being the joint for the emitter-lead. I could add one comment. Of course our analysis was carried out for externally fueled converters as described in the paper B-6. We had actually a modification of the same computer program for full-length internally fueled converters which, if I understood correctly in the session of Tuesday-afternoon, is a design-concept, some of the Soviet-investigators are pursuing.

Our analysis of internally fueled full-length converters shows that this concept is not too promising in the sense that either you must go to quite short lengths to keep ohmic losses down or you must provide such thick emitters and collectors that the fuel volume fraction in the reactor is necessarily quite limited, which would make it difficult to achieve criticality. I would appreciate hearing any comments from any one of the Soviet-delegation, who would have information to this problem.

RIABIKOV (USSR): First question. Did you take into consideration the decrease of the output characteristics under the influence of the proper magnetic field, which can be considerable for "long" elements.

Second question. Did you examine the interaction of the plasma with the magnetic field of the current passing through the electrodes, which can cause a considerable gradient or so-called magnetic pressures along the gap and a deterioration of the output parameters of the element?

SCHOCK: I think I understood the first question better than the second. As far as magnetic field effects are concerned and their influence on current transmission, it happens that I did a fair amount of work on this subject a

few years ago. I think you are probably familiar with some of the theoretical papers that were published in the Journal of Applied Physics, but you may not be aware that there was a paper on the experimental results of magnetic field effects published in the International Journal of Advanced Energy Conversion. This was in 1963. The general conclusions were that magnetic field effects are important at low cesium pressure and diminish as you go up in cesium pressure where the mean free path gets shorter. At around 300°C cesium reservoir temperature the effect is almost negligible. You would need really enormous fields, I don't recall the precise numbers, to have any noticeable effect. I might point out incidentally that in our design there is no accumulative field effect, in other words each converter sees the magnetic field generated by its own current, but outside the diode the magnetic field is zero and therefore you don't build up accumulative magnetic fields from all the other diodes. As far as the second part of your question is concerned, I don't have an answer. Of course, you know in any theoretical calculation you can only get out what you put in, and since we have not put in any correction term for the type of effect you refer to, we can not see it. As far as experimental measurements are concerned, there we only see the gross macroscopic effects, not what is going on inside the plasma. The actual variation in the magnetic field is zero at the center of our converter and reaches a maximum near the terminals.

RLABIKOV: Why is there an optimum thickness for the cathode, particularly in Fig. 3? In the analysis, what concurrent effects enable you to determine this optimum?

SCHOCK: We are talking about an in-core thermionic reactor. Therefore, the axial converters (other than the fuel) are a diluent in the reactor. The greater the diode volume, the greater the fuel needed to achieve criticality and produce a certain power. The larger the reactor gets, the heavier it gets, and the heavier the neutron shield gets. These are the controlling factors. We are trying to maximize the net electrical power output per unit converter volume.

COMMENTS ON PLASMA THEORIES FOR CESIUM DIODES*

George N. Hatsopoulos
Thermo Electron Corporation
85 First Avenue
Waltham, Massachusetts 02154

INTRODUCTION

In the past few years, research and development activities in thermionic energy conversion in the world have concentrated on "high pressure" cesium diodes. The qualification "high pressure" has not been formally defined but it has come to mean that the product of the cesium pressure times the interelectrode spacing is more or less greater than 10 mil-torr. Under this condition, it is generally accepted that electrons experience several collisions as they move from emitter to collector.

The present paper attempts to make a partial assessment of the current state of the knowledge about the electron transport phenomena involved in high pressure cesium diodes. The analyses that have been reported in the literature about these diodes involve a large number of assumptions. The present paper describes and attempts to evaluate the most common of these assumptions.

THE REFERENCE SET OF ASSUMPTIONS

In most analyses of high pressure cesium diodes, the following assumptions concerning the boundaries of the interelectrode space are made.

- a. The interelectrode gap-width d is much smaller than any of the dimensions of the electrode surfaces.
- b. The emitter temperature T_E and the collector temperature

T_C are uniform over the respective electrode surfaces.

- c. The emitter work function and the collector work function are uniform over the respective electrode surfaces.
- d. The emitter and collector work functions are solely functions of the cesium pressure and the temperature of the corresponding electrode surface.

The validity of these assumptions is of great importance when comparing the results of a theory with experimental data. If these assumptions are not satisfied, many discrepancies between theory and experiment may arise. In the present paper, the above assumptions are taken for granted and the discussion is restricted to the transport phenomena that take place once the boundary conditions of the inter-electrode space are fixed.

In what follows, a reference set of assumptions concerning the transport phenomena in the interelectrode space is given. A discussion of these assumptions is presented in the next section.

I. General Assumptions

1. The conditions in the interelectrode space, e. g. particle densities, particle temperatures, electrostatic potential, and fluxes, are solely a function of the distance x from the emitter surface; in other words, the problem is one-dimensional.
2. The interelectrode space may be separated into three regions: an emitter sheath region, a plasma region, and a collector sheath region.

II. Assumptions Concerning the Sheaths

3. The width of the sheaths in the x-direction is negligible.
4. The sheaths are collisionless.
5. The electrostatic potential in the sheaths varies monotonically with x.

III. Assumptions Concerning the Plasma

III a. On the nature of the thermodynamic state in the plasma:

6. The plasma consists of a mixture of three species: neutral atoms, ions, and electrons.
7. The neutral atoms, the ions and the electrons in the plasma each possess a quasi-static (near equilibrium) distribution corresponding to temperatures T_a , T_i , and T_e and to densities n_a , n_i and n_e , respectively.
8. Each of the species in the plasma is a perfect gas.

III b. On the relations between thermodynamic properties:

9. The plasma is neutral at each point, that is

$$n_e = n_i = n$$

10. The atom temperature equals the ion temperature, namely,

$$T_a = T_i$$

11. The temperatures of the atoms and the ions are independent of x, namely

$$T_a = T_i = \text{const.}$$

12. The electron temperature varies with x , namely

$$T_e = T_e(x)$$

IV. On the Transport Equations

13. The linearized Boltzmann equation applies to all particle transport processes in the plasma.

V. On the Values of the Transport Coefficients

14. The coefficients of the temperature gradients in all particle transport equations are zero. This means that all thermoelectric effects in the plasma are neglected.

15. The coefficient of the electron temperature gradient in the energy equation, namely the thermal conductivity of the electrons, is assumed finite and different than zero.

VI. On the Ionization Process

16. The rate of ionization (reaction rate) is given by the relation

$$\frac{d J_e}{d x} = \beta n - \alpha n^3 \quad (1)$$

where J_e is the electron current density, and the coefficients α and β are functions of both n and T_e , namely

$$\alpha = \alpha(n, T_e) \text{ and } \beta = \beta(n, T_e).$$

17. The rate equation (1) yields the Saha equation as n approaches its equilibrium value at temperature T_e

This assumption means that

$$\lim_{n \rightarrow n_{\text{equ.}}} \beta / \alpha = \left(\frac{2 \pi m_e k T_e}{h^2} \right)^{3/2} \exp \left(\frac{V_i}{k T_e} \right)$$

where m_e is the electronic mass, k is the Boltzmann constant, h is Planck's constant, and V_i is the ionization potential energy.

18. Radiation in the plasma is trapped.

DISCUSSION OF THE ASSUMPTIONS

I. General Assumptions

1. The possibility that the discharge in a high pressure cesium diode may not be one-dimensional in character was advanced in 1963^{1, 2} with reference to the work of E. O. Johnson³ on the ball-of-fire mode. Subsequently, visual observations by Rasor indicated that indeed in some parts of I-V curves of a cesium diode the discharge is three-dimensional in character.⁴ Other experimenters^{5, 6} have also observed such a behavior. For conditions of current density and cesium pressure that are important to thermionic energy conversion, however, the discharge is, to within a good approximation, one-dimensional in character.

2. For the discussion of assumption 2, consider the definitions of a sheath and a plasma. The general definition of a sheath is the region of an ionized gas in which space charge effects are important. In this region, therefore, the electrostatic potential varies rapidly with distance as required by the Poisson equation. The general definition of a plasma is the region of an ionized gas in which approximate charge neutrality prevails. Again, because of the sensitivity of the second derivative of the electrostatic potential on net charge, as required by the Poisson equation, and the difference in mobilities of the charged species, near neutrality in the plasma does not mean that the electrostatic potential is uniform; it just means it varies less abruptly in

the plasma than in the sheath.

If one limits the definitions of the sheaths and the plasma to those given above, it is always correct to state that the interelectrode space may be divided into three regions: two sheaths and a plasma. If, however, one is to qualify further the description of the sheaths by assuming they are collisionless and that of the plasma by assuming that the particles in the plasma possess quasi-static distributions of energy, as is done in assumptions 4 and 7, the division of the interelectrode space in three such regions may not always be valid.

The range of validity of assumptions 4 and 7 will be discussed later. Here we shall restrict ourselves to discussing the problems associated with the matching of a sheath to a plasma.

At the boundary between a sheath and a plasma, the following conditions must be satisfied: (a) continuity of particle fluxes, (b) continuity of energy fluxes, (c) continuity of electrostatic potential, (d) continuity of momentum fluxes, and (e) continuity of entropy fluxes. If the sheath is collisionless, the energy distribution of particles in it will be summations of half-Maxwellian distributions. If the plasma is quasi-static, the energy distribution of particles in it will be quasi Maxwellian. Under these conditions, it is only possible to satisfy three of the five continuity relations.⁷ All authors satisfy the first three and fail to satisfy the remaining two. To justify this, one must make the following assumption: there is a region between the sheath and the plasma, which may be called transition region, which is sufficiently wide to allow collisions for momentum

exchange and the production of entropy, but sufficiently narrow so that no appreciable ionization takes place in it and the electrostatic potential in it is uniform. Such an assumption is of doubtful validity.

To allow for momentum exchange and entropy production the transition region must have a width of at least one mean-free path and is probably wider than that. Moreover, the potential distribution in it probably varies much more than in the plasma due to the highly non-equilibrium nature of the energy distribution of the contained particles. It appears, therefore, that in many cases of practical importance, it may be necessary to take into account transition regions in analysing high pressure cesium diodes.

II. Assumptions Concerning the Sheaths

Assumptions 3, 4, and 5 are intimately related and will be discussed concurrently.

Most authors assume that the width of the sheath is negligible. This assumption is usually based on the hypothesis that the sheath width is equal to the Debye length given by the relation

$$L_D = 6.9 \left(\frac{T_e}{n} \right)^{1/2} \text{ cm} \quad (2)$$

This quantity is indeed very small in most cases and generally much smaller than the mean free path. Thus the sheaths may be assumed collisionless.

Study of experimental data led Razor to advance the theory that a double sheath forms near the emitter under some conditions.⁴ He termed this mode of operation the obstructed mode. Hansen and Warner claim that under some conditions they were unable to find solutions to their transport equations⁸ unless they postulated the existence of a double sheath at the emitter. On the other hand, Wilkins who used similar transport equations,⁹ maintains that these equations always possess solutions with simple sheaths which vary monotonically with distance. For this reason, Wilkins concludes that it is not necessary to introduce an obstructed mode for the interpretation of current-voltage characteristics.

The present author agrees with Wilkins in that the transport equations always admit solutions with simple sheaths. He also agrees with Hansen and Warner in that a double sheath may exist at the emitter under some conditions. A double sheath may also exist at the collector. The questions as to when a double sheath exists and when it does not may be answered only through a space charge analysis of the sheaths.

In general, a near-zero width of the sheath would lead to the conclusion that the potential distribution in it would be monotonic and would rule out the possibility of a double sheath. A simple approximation of the space charge equation applied to a sheath having a width equal to the Debye length also rules out the possibility of a double sheath for cases for which it is claimed that a double sheath exists. There is, however, no reason to assume that the plasma extends up to within a Debye length from the emitter surface. In fact, the plasma probably begins one or more mean-free paths beyond the surface. If now one were to assume that the emitter sheath extends over one or two mean-free paths, it is more likely for a solution of the Poisson equation to indicate a double sheath.

The question still remains as to how can the potential distribution in a sheath vary beyond a Debye length. The answer lies in the fact that the Debye length is computed for equilibrium conditions not prevailing in a thermionic diode. To illustrate the point, consider a plasma at temperature T in equilibrium with a surface at temperature T as shown in Fig. 1.

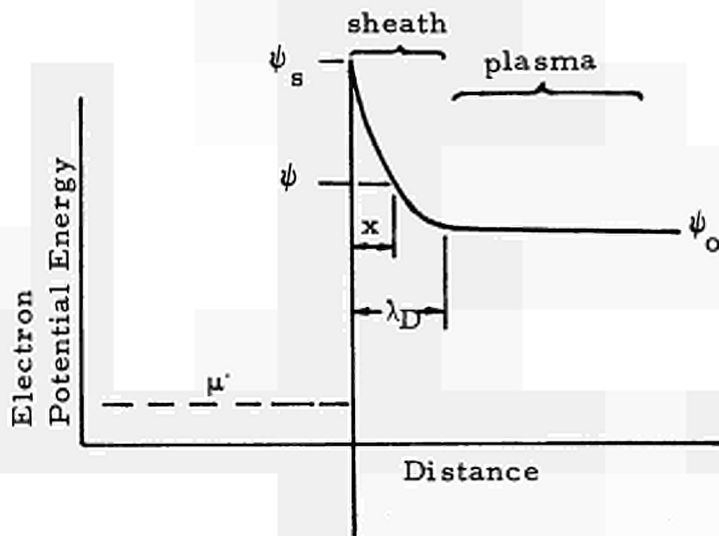


Figure 1.

Let ψ_0 be the potential of the plasma and ψ_s the potential just outside the surface. (An analysis of this equilibrium may be found in Ref. 10.) At any position x in the sheath the potential ψ will be greater than ψ_0 . Equilibrium, therefore, requires that the electron density at x be smaller than that at the plasma and the ion density larger than that at the plasma. The resulting space charge causes the potential distribution to bend sharply upward as required by the Poisson equation. Further rise of the potential at a point closer to the surface will cause even sharper increase of the slope of the potential distribution. The net effect of all this is that regardless of the

difference between ψ_o and ψ_s the thickness of the sheath cannot exceed the Debye length.

Suppose now the emission from the surface exceeded the current from the plasma as it does in a thermionic diode. Then the positive space charge at any point x in the sheath will be less than that at equilibrium causing the potential distribution to be less steep. In fact, for sufficient electron emission, the sheath may acquire a negative space charge at some point, in which case a double sheath would form. Anyway, the effect of the non-equilibrium emission from the surface would be the widening of the sheath. We conclude, therefore, that the Debye length is not a proper measure of sheath width in a cesium diode.

An exact sheath width calculation may be done by means of a space charge analysis and by neglecting collisions. Such an analysis, however, may result in a width which is greater than a mean-free path and may raise questions about the assumption of a collisionless sheath.

An instructive discussion of sheaths is given in Ref. 11.

III. Assumptions Concerning the Plasma

III a. On the nature of the thermodynamic states in the plasma:

Assumption 6 may be improved by adding excited atoms to the analysis. This has been done in the literature.¹² Except, however, for the effect of excited atoms on the ionization rate,¹³ excited atoms seem to be unimportant in the electron transport rates.

Assumption 7 (quasi-equilibrium) is a key assumption in most

analyses of high pressure cesium diodes. It has been commonly assumed that the criterion for its validity is the value of the product $P_{cs}d$. Specifically, it is generally accepted that assumption 7 is valid if

$$P_{cs}d > 10 \text{ mil-torr.}$$

Such a criterion is not quite valid over a wide range of conditions. The product $P_{cs}d$ is a measure of the number of collisions that the various particles experience per unit of time in the interelectrode space. On the other hand, the departure from the equilibrium distribution that particles assume in a steady state rate process, such as that occurring in a diode, depends both on the number of collisions per unit of time as well as the rate of the process as measured by both particle fluxes and energy fluxes. For example, as the fluxes decrease and approach zero, the energy distribution of particles will approach the equilibrium distribution regardless of how few collisions take place per unit of time. A better criterion on the validity of assumption 7 is the ratio $\frac{P_{cs}d}{S}$, where S denotes the rate of entropy production in the process.

Nevertheless, probe^{14, 15} and spectrographic¹⁶ measurements as well as comparison of theory^{17, 18} with experiments indicate that assumption 7 is fairly good for most operating conditions of practical importance.

Assumption 8 is probably the most valid assumption made in thermionic conversion. This is so because of the very low density of the gases considered.

III b. On the relations between thermodynamic properties:

Assumptions 9 through 11 have been discussed in the literature¹⁹ and appear to be reasonable for most conditions of operation.

As for assumption 12, it has been frequently proposed in simplified analyses of the high pressure cesium diode to assume a uniform electron temperature. Computer solutions^{20, 21, 14} of the plasma transport equations, however, have shown that electron temperature varies significantly with x . Moreover, since the ionization rate of cesium depends exponentially with temperature, an artificial imposition of a constant electron temperature will dramatically distort the description of the phenomena that take place in a plasma. Nevertheless, some simplified analyses that use a uniform electron temperature have successfully described experimental I-V curves. This paradox will be discussed in a later section.

IV. On the Transport Equations

Assumptions 7 and 8 insure the applicability of the linearized Boltzmann equation to a cesium diode plasma. These transport equations have also been confirmed by means of thermodynamic arguments in Ref. 22.

V. On the Values of the Transport Coefficients

Thermoelectric effects are definitely present in a cesium plasma but their overall contribution is probably less than 0.1 volt.

On the other hand, there is so much uncertainty about the analysis of high pressure cesium diodes concerning the values of the transport coefficients that probably no theory is accurate to within

0.1 volt. Thermoelectric effects may, therefore, be justifiably neglected from the transport equations, in accordance with assumption 14. Thermoelectric effects in a plasma are discussed in Refs. 23 and 24.

It has been shown by Lieb and Bornhorst²¹ that electronic conductivity affects significantly the electron temperature distribution in a plasma, and through it the rate of ionization. Assumption 15 is, therefore, important.

VI. On the Ionization Process

Much discussion has been presented in the literature about the ionization mechanisms that prevail in a cesium diode. This subject is too involved to be reviewed here. The following simple comment, however, may be helpful in assessing the situation.

There is experimental evidence that indicates that at least part of the plasma is near Saha equilibrium corresponding to the electron temperature. This means that it is important in any analysis of the plasma to take into account both a multi-stage ionization process and a recombination process. Only then would the resulting ionization equation be in the limit consistent with thermodynamic equilibrium. Such an equation must have the form of Eq. (1) and satisfy Eq. (2). Norcross and Stone¹³ have derived such an equation. It has been used by Hansen and Warner²⁵ in their numerical calculation of characteristics of the high pressure diode. Wilkins⁹, Lieb and Bornhorst,²¹ Baksht et al¹⁷ and Sonin¹² all use similar equations in their numerical calculations. In addition, they all assume total trapping of the emitted radiation. The range of validity for this last assumption has not yet been established.

It is at present nearly impossible to form a judgment about which of the equations proposed and which satisfy conditions (1) and (2) are more applicable to cesium diodes. Analysis of experimental data obtained under practical conditions of operation of the diodes will continue to involve so many assumptions that no accurate quantitative conclusion will probably result for some time. A more fruitful approach will probably be further analytical work, of the type performed by Norcross and Stone, using techniques developed in chemical kinetics.

SIMPLIFIED TRANSPORT THEORIES

Several simplified transport theories have been proposed and have successfully correlated experimental data. Since the simplified assumptions used in these theories vary significantly from one to the other, it appears surprising that they all seem to be consistent with experiment.

The explanation of this apparent paradox probably lies in the facts that: (1) the values of the Saha equation and the transport coefficients are sufficiently uncertain that by their proper adjustment one can easily compensate for errors introduced by the simplifying assumption; (2) the experimental results used are many times valid over a small range of parameters; and (3) integral experimental data such as I-V curves, are not sensitive to the details of the transport phenomena.²⁶

If one considers that in addition to the uncertainties about the rate equations and the transport coefficients, there are significant uncertainties about the electrode work functions corresponding to a particular experimental I-V curve, it does not appear sound to base the proof of the validity of a simplifying assumption on the ability of the

theory to correlate a particular experiment. Instead, it is more dependable to compare the results of a simplified theory utilizing a given simplified assumption to those of a theory as identical as possible to the first but not utilizing the simplified assumption. If the two theories agree, the assumption is justifiable. If not, the simplified theory is not justifiable even though it may correlate data better than the more complex theory.

An example of this process is the work of Lieb and Bornhorst²¹ on electronic thermal conductivity.

CONCLUDING REMARKS

The assumption regarding the quasi-static nature of the particle distribution functions in a cesium diode is the basis of all analyses advanced so far. This assumption appears to be sound for the conditions of operation of cesium diodes encountered presently in practice. Better emitter materials, however, have steadily led in the past to lower cesium pressure requirements for obtaining a given emitter work function. It is possible, therefore, that in the future it might be advantageous to operate some diodes at such low pressures that the quasi-equilibrium assumption is no longer valid. Analysis of such diodes would require a complete restructure of the current theories.

REFERENCES

1. Hernqvist, K. G., Proceedings of the IEEE, 51, 748, (1963)
2. Kitrilakis, S. S., Shavit, A., and Rasor, N. S., "The Departure of the Observed Performance from the Idealized Case in Cesium Thermionic Converters." Report 24th Annual Conference on Physical Electronics, Cambridge, (March, 1964) p. 171
3. Johnson, E. O., RCA Review XVI, 498, (1955)
4. Rasor, N. S., "Analytical Correlation of Cesium Diode Phenomenology." Report International Conference on Thermionic Electrical Power Generation, London, (September, 1965)
5. Warner, C., Hansen, L. K., (unpublished report AI-7979, 1962). See also Journal of Applied Physics, 38, 3425, (1967)
6. Saggau, B., Strecker, H., "The Voltage Drop of the Ignited Mode as a Function of Current Density." Report 2nd International Conference on Thermionic Electrical Power Generation, Stresa, Italy, (May, 1968). Paper No. G-4
7. Adt, R. R., Jr., Sc. D. Thesis, June, 1967, Dept. of Mech. Eng., Massachusetts Institute of Technology, "A Study of the Liquid-Vapor Phase Change of Mercury Based on Irreversible Thermodynamics"
8. Hansen, L. K., and Warner, C., "Computer Solution of Thermionic Converter Transport Equations." Report 27th Annual Conference on Physical Electronics, Cambridge, (March, 1967) p. 308
9. Wilkins, D. R., "An Improved Theoretical Description of Thermionic Converter Performance Characteristics." Report 27th Annual Conference on Physical Electronics, Cambridge, (March, 1967) p. 341
10. Hatsopoulos, G. N., and Keenan, J. H., Principles of General Thermodynamics, Wiley & Sons, New York, (May, 1965) p. 554
11. Baksht, F. G., Moizhes, B. Ya., and Nemchinskiy, V. A., "On the Plasma Sheath Theory." Report 2nd International Conference on Thermionic Electrical Power Generation, Stresa, Italy, (May, 1968). Paper No. G-2

12. Sonin, E. B., "Theory of the Low-Voltage Arc in the Cesium Thermionic Converter." Report 2nd International Conference on Thermionic Electrical Power Generation, Stresa, Italy, (May, 1968). Paper No. G-2
13. Norcross, D. W., and Stone, P. M., "Non-Equilibrium Populations in Cesium Discharges." Report 26th Annual Conference on Physical Electronics, Cambridge, (March, 1966) p. 96
14. Djuzhev, G. A., Martsinovskii, A. M., Moizhes, B. Ya., Pikus, G. E., Kaplan, V. B., Shahnazarova, G. A., and Yurjev, V. G., "The Probe and Spectral Investigations of Dense Plasma Thermionic Converters." Report 2nd International Conference on Thermionic Electrical Power Generation, Stresa, Italy, (May, 1968). Paper No. I-3
15. Bullis, R. H., and Wiegand, W. J., "Plasma Properties in a Thermionic Converter." Report Thermionic Specialists Conference, Cleveland, (October, 1964) p. 211
16. Reichelt, W. H., "Spectrographic Investigation of the Ignited Mode of Thermionic Converter Operation." Report International Conference on Thermionic Electrical Power Generation, London, (1965)
17. Baksht, P. G., Djuzhev, G. A., Kaplan, V. B., Korobova, I. L., Martzinovskii, A. M., Moizhes, B. Ya., Shahnazarova, G. A., and Yuriev, W. G., "Theoretical and Experimental Investigation of Low-Voltage Arc in Thermionic Converter." Report 2nd International Conference on Thermionic Electrical Power Generation, Stresa, Italy, (May, 1968). Paper No. I-1
18. Nighan, W., "Charged Particle Production and Energy Loss Rates in Thermionic Converter Plasmas." Report Thermionic Conversion Specialists Conference, Palo Alto, (October, 1967) p. 198
19. Wilkins, D. R., and Gyftopoulos, E. P., Journal of Applied Physics, Vol. 37, No. 9, p. 3533, (August, 1966)
20. Warner, C., "Theoretical Considerations of the Ignited Mode." 2nd International Conference on Thermionic Electrical Power Generation, Stresa, Italy, (May, 1968). Paper No. G-5

21. Lieb, D., and Bornhorst, W., "Analysis of the Diffusion-Dominated Thermionic Converter Plasma." Report Thermionic Conversion Specialist Conference, Palo Alto, (October, 1967) p. 191
22. Hatsopoulos, G. N., and Bornhorst, W., "The General Linear Transport Equations for the Three-Component Plasma in a Thermionic Converter." Report Thermionic Conversion Specialist Conference, Houston, (November, 1966) p. 287
23. Lewis, H. W., and Reitz, J. R., "Efficiency of the Plasma Thermocouple." Journal of Applied Physics, Vol. 31, 723, (1960)
24. Boffi, V. C., Molinari, V. G., and Parks, D. E., "Electron Temperature Distribution in a Plasma Diode." Report International Conference on Thermionic Electrical Power Generation, London, (1965)
25. Warner, C., and Hansen, L. K., "Computer Solution of Thermionic Converter Equations II." Report Thermionic Conversion Specialist Conference, Palo Alto, (October, 1967) p. 184
26. Wilkins, D. R., and Gyftopoulos, E. P., "Thermionic Converters Operating in the Ignited Mode, Part I: Theoretical Output Current Characteristics", Journal of Applied Physics, 37 (1966) p. 2888

THE SPACING EFFECT IN THE IGNITED MODE DIODE ⁺

Lorin K. Hansen ⁺⁺

Institute for theoretical Physics
Ruhr-University Bochum
463 Bochum - Querenburg (Germany)
Buscheystrasse

Abstract

The inverse current of the ignited mode diode has been shown experimentally to be a linear function of spacing^{1, 2)} This effect has also been derived from a simplified theoretical description of the ignited mode diode,¹⁻³⁾ which is intended to be appropriate for very wide space diodes. In the present paper it is pointed out that although some of the assumptions of this derivation are justified, the derivation is still inadequate. The effect of spacing on the ignited mode is derived using current theoretical descriptions of the narrow space diode. It is found that the assumption of a double sheath at the emitter allows the derivation of an effect similar to that observed experimentally.

⁺
This work was supported in part by the Office of Naval Research, U.S.N. and in part by the Land Nordrhein-Westfalen, Landesamt für Forschung.

⁺⁺
On leave from Atomics International, Canoga Park, California, U.S.A.

Introduction

If the inverse current for the ignited mode diode is plotted (for particular voltages) as a function of spacing, one obtains linear plots with a single point of intersection. This effect was discovered by Rasor^{1, 2)} An example of Rasor's data is shown in Figure 1. The data appear to be well correlated by the expression⁴⁾

$$J_R/J = 1 + A(1 + Bpd) \exp\left(\frac{eV_0}{kT_e}\right) \quad (1)$$

where J is the diode current, p the cesium pressure, d the diode spacing and V_0 the output voltage. The quantities J_R , T_e , A and B are constants. In a simplified derivation of eq. (1) Rasor associated the first two of these with the electron Richardson emission at the emitter and the electron temperature in the plasma, respectively.

In the present paper the effect of spacing on diode current is derived using current theoretical description of the narrow space diode ($5\lambda_e < d < 25\lambda_e$, where λ_e is the electron mean free path). However, before the discussion is specialized to the case of the narrow space diode, the more general results of the derivation are used to evaluate some of the assumptions for Rasor's derivation, above, for the very wide space ($d > 100\lambda_e$) diode.

Transport Equations

We assume that the particle transport in the ignited mode plasma can be described adequately by the equations⁴⁾

$$\frac{\Gamma_e}{\mu_e} + \rho en(\Gamma_e - \Gamma_p) = n \frac{dV}{dx} - \frac{kT_e}{e} \frac{dn}{dx} \quad (2)$$

$$\frac{\Gamma_p}{\mu_p} - \rho en(\Gamma_e - \Gamma_p) = -n \frac{dV}{dx} - \frac{kT_p}{e} \frac{dn}{dx} \quad (3)$$

where Γ_e and Γ_p are the electron and ion fluxes, μ_e and μ_p the electron and ion mobilities, T_e and T_p the electron and ion temperatures, n the plasma density, V the plasma potential, and ρ the plasma resistivity due to electron-ion interactions. The latter is given by⁵⁾

$$\rho = 6.5 \times 10^3 T_e^{-3/2} \ln \Lambda_0 \quad \Omega \text{ cm.} \quad (4)$$

where T_e is given in degrees Kelvin and Λ_0 is the order of 10. Some of the approximations involved in equations (2) and (3) are discussed in reference 4). It should be mentioned in addition, however, that we are assuming quasi-neutrality and are ignoring temperature gradients. The latter assumption is not too difficult to remove, but is convenient to retain to assist in bringing out certain qualitative features of the spacing effect.

Diode With Unipolar Sheaths

For the boundary conditions, we assume a positive sheath at the collector, but consider two possibilities at the emitter, a positive single sheath and a double sheath. We consider the single sheath first. The potential distribution in this case is shown qualitatively in Figure 2 . From this figure we see that the diode voltage drop, V_d , is given by

$$V_d = V_E - V_C + V_P \tag{5}$$

We assume the boundary conditions for such a potential distribution to be given by

$$\Gamma_e(x=0) = \Gamma_{e0} = \frac{v_e - n_0 v_e}{4} \exp\left(-\frac{eV_E}{kT_e}\right) \quad \Gamma_e(x=d) = \Gamma_{e1} = \frac{n_1 v_e}{4} \exp\left(-\frac{eV_C}{kT_e}\right) \tag{6a, b}$$

$$\Gamma_p(x=0) = \Gamma_{p0} = -\frac{n_0 v_p}{2} \quad \Gamma_p(x=d) = \Gamma_{p1} = \frac{n_1 v_p}{2} \tag{7a, b}$$

where v_e is the electron emission from the emitter, v_e and v_p the average electron and ion velocities and n_0 and n_1 , the plasma densities near the emitter and collector. We have neglected ion emission and will assume the sheaths to be of negligible thickness.

If eq. (2) is integrated for the plasma drop, V_p , we obtain

$$\frac{eV_p}{kT_e} = \ln\left(\frac{n_1}{n_0}\right) + \rho \frac{e^2 \Gamma d}{kT_e} + \frac{1}{De} \int_0^d \frac{\Gamma_e}{n} dx \tag{8}$$

where we have used $De = \frac{\mu_e kT_e}{e}$ and

$$\Gamma = \Gamma_e - \Gamma_p = \text{const.} \tag{9}$$

Eqs. (6a, b) and (8) can then be substituted into eq. (5) to give

$$\frac{v_e}{\Gamma_{e1}} + \frac{\Gamma_n}{\Gamma_{e1}} = 1 + \exp \left\{ -\frac{eV_d}{kT_e} + \rho \frac{e^2 \Gamma d}{kT_e} + \frac{1}{De} \int_0^d \frac{\Gamma_e}{n} dx \right\} \tag{10}$$

We have used the relation

$$\Gamma_{e1} - \Gamma_{e0} = \Gamma_{p1} - \Gamma_{p0} = \Gamma_n \tag{11}$$

which follows from eq. (9). Using eq. (10) we can calculate the inverse diode current (v_e / Γ_{e1}) due to variation of diode voltage, due to electron-ion interaction, and due to electron and ion collisions with neutrals. These three effects are contained respectively in the three terms of the exponent. Special cases of eq. (10) are now considered.

Wide Space Diode

An adequate derivation of the spacing effect for the very wide space diode has not yet been developed. One of the main difficulties in obtaining such a derivation is the difficulty of ob-

taining an expression for the plasma density distribution, so the last term in the exponent of eq. (10) can be evaluated.

In the derivation for this case by Rasor^{1, 2)} and that by Wilkins and Gyftopoulos³⁾ which is very similar to that by Rasor, the assumption is made that the plasma is not a net source of ionization ($\nabla \cdot \Gamma_e - \nabla \cdot \Gamma_p = 0$). This assumption, used with the particle transport equations, infers a linear density distribution for the plasma. And it is easy to show that such a distribution used in eq. (10) leads essentially to Rasor's result. However, such a derivation is not very satisfying, in two respects. First, the zero-source assumption should not be valid in the emitter region of the plasma. Also, in the case of negligible net source, one would expect the plasma density distribution to be determined more by the local balance of ionization and recombination than by the transport equations. It should be added, however, that near linear distributions in the plasma column have been observed experimentally⁶⁾.

Rasor and Wilkins also assume zero electric field in the plasma. However, this assumption was not essential for their result. Significant fields occur in the plasma⁷⁾, but the net potential across the plasma is small, as can be shown using eq. (8). It is only the latter quantity which is used in the derivation. Finally, Rasor neglects electron-ion interactions. One might be concerned about this assumption considering the importance of these interactions to the transport processes⁸⁾. However, from eq. (10) it is evident that the approximation $\rho = 0$ is reasonable. In fact, if we drop the last term of the exponent in eq. (10) and plot the result we obtain a figure very much like Figure 1, but with spacings a factor of 20 - 30 too large.

Narrow Space Diode With Unipolar Sheaths

Although a general expression for the plasma density distribution has not been obtained for the very wide space diode, such expressions have been proposed for the narrow space diode. Thus, we now evaluate the spacing effect for this case. Following the concepts currently proposed for describing the narrow space diode we assume that recombination can be ignored and assume that the ionization coefficient, α , is constant through the diode. Particle conservation is then given by

$$\frac{d\Gamma_e}{dx} = \frac{d\Gamma_p}{dx} = \alpha n_g n \quad (12)$$

where n_g is the neutral atom density. Calculated values for α have been suggested by Norcross and Stone⁹⁾ and by Moizhes, Baksht and Melikiya¹⁰⁾.

Adding eqs. (2) and (3) and using eq. (12) we obtain

$$\frac{d^2 n}{dx^2} + \gamma^2 n = 0 \quad (13)$$

where

$$\gamma^2 = \frac{e}{k(T_e + T_p)} \left(\frac{1}{\mu_e} + \frac{1}{\mu_p} \right) \alpha n_g \quad (14)$$

so that the plasma density has the distribution

$$n = c_1 \cos(\gamma x + c_2) \quad (15)$$

Also, in adding eq. (2) and eq. (3) we find that ion current in the diode is zero at $x = x_0$ where

$$-\frac{k}{e}(T_e + T_p) c_1 \gamma \sin(\gamma x_0 + c_2) + \frac{\Gamma}{\mu_e} = 0 \quad (16)$$

Thus from eqs. (12), (15) and (16) we have

$$\Gamma_{p0} = -\alpha n_g \int_0^{x_0} n dx = -\alpha n_g c_1 \left[\frac{e \Gamma}{k(T_e + T_p) \mu_e c_1 \gamma} - \sin c_2 \right] \quad (17)$$

$$\Gamma_{p1} = \alpha n_g \int_{x_0}^d n dx = \alpha n_g c_1 \left[\sin(\gamma d + c_2) - \frac{e \Gamma}{k(T_e + T_p) \mu_e c_1 \gamma} \right] \quad (18)$$

These equations can be combined with eqs. (7a, b) to give

$$\begin{aligned} \frac{\gamma d}{2} \tan \frac{\gamma d}{2} &= \frac{v_{pd}}{4} \cdot \frac{e}{k(T_e + T_p)} \cdot \left(\frac{1}{\mu_e} + \frac{1}{\mu_p} \right) \\ &\approx \frac{1}{2} \left(\frac{2T_p}{T_e + T_p} \right) \frac{3d}{4\lambda_p} \end{aligned} \quad (19)$$

We are only considering the collision dominated plasma, so we have

$$\frac{\gamma d}{2} = \frac{\pi}{2} - \epsilon \quad (20)$$

where

$$\frac{1}{\epsilon} = \frac{1}{\pi} \left(\frac{2T_p}{T_e + T_p} \right) \frac{3d}{4\lambda_p} \gg 1 \quad (21)$$

The electron temperature is given by a solution of eqs. (14), (20) and (21). Since ϵ is small electron temperature is almost independent of spacing and position on the I-V-curve.

By eliminating c_1 , in eqs. (17) and (7a) we obtain

$$\frac{\gamma d}{2} \tan c_2 = -\frac{1}{2} \left(\frac{2T_p}{T_e + T_p} \right) \frac{3d}{4\lambda_p} \left(\frac{R-1}{R} \right) \quad (22)$$

where $R = \left| \frac{\Gamma_{p0} \mu_e}{\Gamma_{e0} \mu_p} \right|$. Since $\gamma d \approx \pi$ we have

$$c_2 = -\frac{\pi}{2} + \delta \quad (23)$$

where

$$\frac{1}{\delta} \approx \frac{1}{\pi} \left(\frac{2T_p}{T_e + T_p} \right) \frac{3d}{4\lambda_p} \left(\frac{R-1}{R} \right) \quad (24)$$

The condition that the plasma density is everywhere positive gives us

$$2 < R < \infty \quad (25)$$

Thus, eq. (24) will be a reasonable approximation. Using eqs. (2), (3), and (15) we also find

$$\frac{\Gamma_{e0}}{c_1 D_e \gamma} = \left(\frac{T_e + T_p}{T_e} \right) (R-1)^{-1} \quad (26)$$

We can now evaluate the last term in the exponent of eq. (10). Using eqs. (15), (20), (21), (23), (24) and (26) we find

$$\begin{aligned} \frac{1}{D_e} \int_0^d \frac{\Gamma_e}{n} dx &\approx \frac{\Gamma_{e0}}{c_1 D_e \gamma} \ln \left\{ \frac{\tan \left(\frac{\gamma d}{2} + \frac{C_2}{2} + \frac{\pi}{4} \right)}{\tan \left(\frac{C_2}{2} + \frac{\pi}{4} \right)} \right\} \\ &= 2 \left(\frac{T_e + T_p}{T_e} \right) (R-1)^{-1} \ln \left\{ \frac{2}{\pi} \left(\frac{2T_p}{T_e + T_p} \right) \frac{3d}{4\lambda_p} \left(\frac{R-1}{\sqrt{R^2 - 2R}} \right) \right\} \end{aligned} \quad (27)$$

Here we have used the approximation $\Gamma_e \approx \Gamma_{e0}$. Therefore, eq. (10) becomes

$$\frac{\nu_e}{\Gamma_{ei}} + \frac{\Gamma_n}{\Gamma_{ei}} = 1 + \exp \left\{ -\frac{eV_d}{kT_e} + \frac{\rho e^2 \Gamma_d}{kT_e} \right\} \cdot \left[\frac{2}{\pi} \left(\frac{2T_p}{T_e + T_p} \right) \frac{3d}{4\lambda_p} \left(\frac{R-1}{\sqrt{R^2 - 2R}} \right) \right]^{\left(\frac{T_e + T_p}{T_e} \right) \frac{2}{R-1}} \quad (28)$$

The parameter R can be obtained from energy balance considerations. If we neglect radiation losses and diffusion of excited atoms to the electrodes, the energy balance for the diode becomes¹¹⁾

$$\nu_e 2k(T_E - T_e) + e\Gamma_{ei}V_d - \Gamma_n (eV_E + eV_i + 2kT_e) + e\Gamma_{pi}V_p = 0 \quad (29)$$

where T_E is the emitter temperature and V_i the ionization potential for cesium. The last term of eq. (29) is negligible. Also, for the cases of interest we have $V_i \gg V_d$ and $V_d \approx V_E$. Thus, we can write

$$\frac{\Gamma_n}{\Gamma_{ei}} = \frac{\nu_e/\Gamma_{ei} \cdot 2k(T_E - T_e) + eV_d}{eV_d + eV_i + 2kT_e} \quad (30)$$

or, by using eq. (11)

$$\frac{\Gamma_n}{\Gamma_{e0}} = \frac{\nu_e/\Gamma_{ei} \cdot 2k(T_E - T_e) + eV_d}{eV_i + 2kT_e - \nu_e/\Gamma_{ei} \cdot 2k(T_E - T_e)} \quad (31)$$

Using eqs. (15), (7a, b) and (11) we also obtain

$$R = 1 + \frac{1}{2} \frac{\Gamma_n}{\Gamma_{e0}} \frac{\mu_e}{\mu_p} \quad (32)$$

Thus, R is given by eqs. (31) and (32). In many features the above model for the narrow space diode is similar to the description presented by Stakhanov and Kasikov¹²⁾.

Two examples of eq. (28) are plotted in Figure 3. (In this and subsequent plots we use $kT_e/e = .23 \text{ eV}$; $kT_p/e = .10 \text{ eV}$; $kT_E/e = .155 \text{ eV}$ and $\rho = 0$) It is immediately evident from this figure that the predicted spacing effect for the above model is not like that observed experimentally (for example Figure 1) except in the region $v_e/\Gamma_{e1} \approx 1$. The "turn back" in the plots for constant V_d is associated with a negative resistance predicted for the I-V curve. The origin for the latter can be seen in eq. (32). We always have $\Gamma_n > 0$; thus, as diode current decreases (v_e/Γ_{e1} increases) the term eV_d must increase to balance the $v_e/\Gamma_{e1} \cdot 2k(T_e - T_E)$ term. Physically this means that a larger diode voltage drop is needed to overcome the energy losses associated with electrons which are emitted into the plasma, and heated up before leaving the plasma.

There are more efficient ways for the discharge to operate at low currents. One way would be for the discharge to constrict. In fact, whenever negative resistance has been observed experimentally there has been an associated discharge constriction¹³⁾. This suggests that constriction is minimizing losses that would occur without this mechanism. We will not consider the effect of constriction on the spacing effect, but will now examine another possibility for low current operation, the possibility of a double sheath at the emitter.

Narrow Space Diode With An Emitter Double Sheath

Whether or not an emitter double sheath exists in a thermionic diode is still an open question. It was assumed to exist in many early diode theories, and recently it has been found to be consistent with computer solutions of diode equations¹⁴⁾. However, the possibility of ion trapping in such a sheath puts the concept in question¹⁵⁾. Since the above narrow space diode theory, without a double sheath, is at variance with experiment in the low current region it is of interest to consider this possibility.

The potential distribution for this case is shown qualitatively in Figure 4. Most of the previous results still apply. For example, in eqs. (10) and (29), V_d must be replaced by V_D

$$V_d = V_E - V_C + V_P - V_B = V_D - V_B \quad (33)$$

and v_e must be interpreted as the electron emission over the double sheath barrier.

$$v_e = v_R \exp\left(-\frac{eV_B}{kT_e}\right) \quad (34)$$

where v_R is now the Richardson emission. Thus, we write eqs. (28), (30) and (31) as

$$\frac{v_e}{\Gamma_{ei}} + \frac{\Gamma_n}{\Gamma_{ei}} = 1 + \exp\left\{-\frac{eV_D}{kT_e} + \frac{\rho e^2 \Gamma_d}{kT_e}\right\} \cdot \left[\frac{2}{\pi} \left(\frac{2T_p}{T_e + T_p}\right) \frac{3d}{4\lambda_p} \left(\frac{R-1}{\sqrt{R^2-2R}}\right)\right] \left(\frac{T_e + T_p}{T_e}\right)^{\frac{2}{R-1}} \quad (35)$$

$$\frac{\Gamma_n}{\Gamma_{ei}} \approx \frac{v_e/\Gamma_{ei} \cdot 2k(T_e - T_c) + eV_D}{eV_D + eV_i + 2kT_e} \quad (36)$$

$$\frac{\Gamma_n}{\Gamma_{eo}} \approx \frac{v_e/\Gamma_{ei} \cdot 2k(T_e - T_c) + eV_D}{eV_i + 2kT_e - \frac{v_e}{\Gamma_{ei}} \cdot 2k(T_e - T_c)} = \frac{\mu_p 2(R-1)}{\mu_e} \quad (37)$$

An additional boundary condition is required to specify the double sheath. For simplicity we neglect ion emission from the emitter, electron backscatter from the plasma and ion trapping. The double sheath condition then becomes the Langmuir relation

$$\left| \frac{\Gamma_{po}}{v_e} \sqrt{\frac{M}{m}} \right| = 1 \quad (38)$$

This may also be written

$$R = \frac{v_e}{\Gamma_{eo}} \frac{\Delta e}{\lambda_p} \sqrt{\frac{T_p}{T_e}} = \frac{v_e}{\Gamma_{ei}} \left(1 + \frac{\Gamma_n}{\Gamma_{ei}}\right) \frac{\Delta e}{\lambda_p} \sqrt{\frac{T_p}{T_e}} \quad (39)$$

Eqs. (35), (36), (37) and (39) can be solved for v_e/Γ_{ei} , V_D , and R as functions of $3d/4\lambda_p$. Such a solution is shown in Figure 5. For various V_D , V_B is then obtained from eq. (33) and v_R/Γ_{ei} obtained from eq. (34). Some plots of the latter quantity are shown in Figure 6. It is interesting that with the assumption of a double sheath we now obtain a spacing effect like that observed experimentally. We also find, however, that there is a maximum current for the existence of the double sheath. Thus there appears to be a region in the I-V curve from the knee down to about 1/2 to 1/3 the Richardson emission that is not interpreted by either of the above models. The transition between the two models, however, requires more careful attention to some of the approximations we have used. This transition region is particularly sensitive to extra plasma losses and to changes in the Langmuir relation. A study of this transition has not been carried out yet.

The author would like to express appreciation to Professor G. Ecker for helpful discussion.

References

- (1) RASOR, N.S., 25th Annual Conference on Physical Electronics, Cambridge 1965 (Oral presentation, not included in report).
- (2) RASOR, N.S., International Conference of Thermionic Electrical Power Generation, London, September 1965.
- (3) WILKINS, D.R.; GYFTOPOULOS, J. Appl. Phys. 37, 2892 (1966). (In addition to a derivation which closely follows that of Rasor this reference also presents Rasor's unpublished data of reference (1)).
- (4) ECKER, G., "Gas Discharge Theory" in Advanced Plasma Theory, M.N. Rosenbluth, ed., Academic Press, New York, 1964, p.97 .
- (5) SPITZER, SR., L., Physics of Fully Ionized Gases, Interscience Publ., 1956.
- (6) REICHELDT, W., H.,; KRUER, W.L., Report on Thermionic Conversion Specialist Conference, San Diego, 1965 (IEEE), p. 129.
- (7) BULLIS, R.H.,; WIEGAND, W.J., Report on 24th Annual Conference on Physical Electronics, Cambridge 1964 (Technology Press, Cambridge, Mass.) p. 224.
- (8) NIGHAN, W.L., Report on Thermionic Conversion Specialist Conference, San Diego, 1965 (IEEE), p. 84.
- (9) NORCROSS, D.W.; STONE, P.M., Report on 26th Annual Conference on Physical Electronics, Cambridge 1966 (Technology Press, Cambridge, Mass.) p. 96.
- (10) MOIZHES, B.Ya.,; BAKSHT, F.G.; MELIKIYA, M.G., Soviet Physics - Technical Physics 11, 234 (1966).
- (11) HANSEN, L.K., J. Appl. Phys. 38, 4345 (1967).
- (12) STAKHANOV, I.P.; KASIKOV, I.I., Report FEI 17, Obninsk Physical Energetic Institute. Translation appears in Post Conference Report (1967) by IEE for the International Conference on Thermionic Electrical Power Generation, London (1965).
- (13) HANSEN, L.K.; WARNER, C., Report on Thermionic Conversion Specialist Conference, Cleveland, (1964) (IEEE) p.310.
- (14) HANSEN, L.K.; WARNER, C., Report on 27th Annual Conference on Physical Electronics, Cambridge 1967 (Technology Press, Cambridge, Mass.)
- (15) BEDNARZ, R; DAVIS, M.V., Report on Thermionic Conversion Specialist Conference, Palo Alto, 1967 (IEEE).

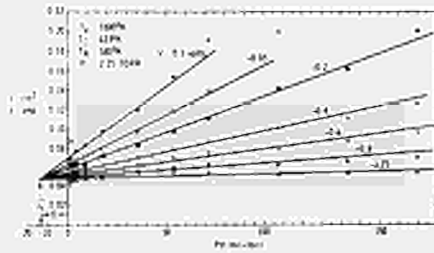


Fig. 1: Spacing Effect Observed by Razor

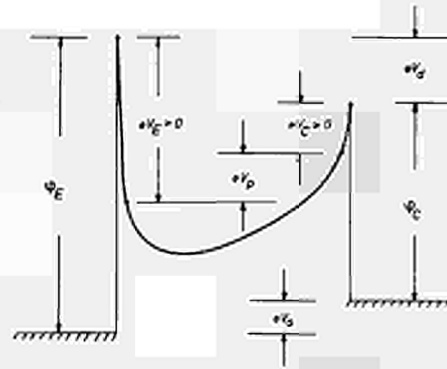


Fig. 2: Potential Distribution with Unipolar Sheaths

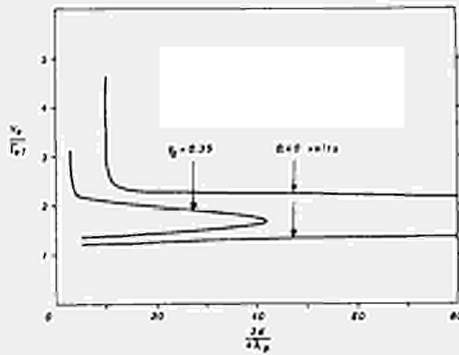


Fig. 3: Spacing Effect Expected with Unipolar Sheaths

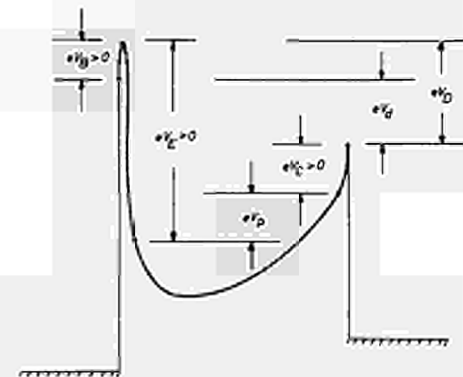


Fig. 4: Potential Distribution with Emitter Double Sheath

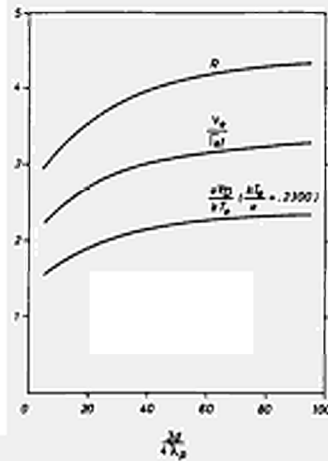


Fig. 5: Solutions for Double Sheath Case

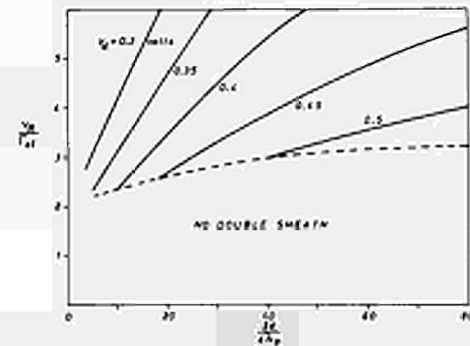


Fig. 6: Spacing Effect Expected with Emitter Double Sheath

DISCUSSION

Speaker of paper G-1: L. K. HANSEN.

MUSA (Rumania): First question: Dr. HANSEN's equations for ion production assume direct ionization. How is this justified? It is not known exactly how the ions are produced, stepwise, by molecular ions and so on.

Second question: What is the double sheath's thickness?

HANSEN (Euratom): I assume a uniform coefficient for ion-generation. This does not say that the ionization process is assumed to be single-stepped, it does not say that it is assumed to be multi-stepped. In fact in the work of NORCROSS and STONE where a multi-stage process of ionization is considered, it is evident that one can use an approximate effective ionization coefficient like I have assumed here.

Concerning the second question, the thickness of the double sheath: With the densities that we have in the ignited mode and the spacings we are working with, I don't think this thickness will be very important. As far as these calculations are concerned it was assumed to be of negligible thickness.



THEORY OF THE LOW-VOLTAGE ARC IN THE CESIUM
THERMIONIC CONVERTER

Sonin E.B., Institute of semiconductors, Academy of sciences of USSR, Leningrad.

The current-voltage characteristics (the I-V curves), the electron temperatures T , the electron densities N_e and the plasma potentials ϕ were determined in the cesium thermionic converter operating in the ignited mode. The transport equations with volume ion production were computed, the following processes being taken into account: the elastic and inelastic electron-atom collisions, the ionization by electron impact and the three body recombination, the radiation and the diffusion of excited atoms to the electrodes, the electron-ion collisions.

The transport equations with volume ion production were used for the cesium low-voltage arc by Moizhes B.Ya., Baksht F.G. and Melikiya M.G. [1] They neglected the radiation and the diffusion of excited levels and proposed a multistage process for ion production.

It was assumed that the high excited levels down to the level 7S inclusive are in Saha equilibrium with free electrons. But it was shown in author's article [2] that this assumption is valid only for much higher levels

(above 11S) and overestimate the value of ion production (see References [3,4] too). This value is low enough for the low excited levels up to level 7S inclusive to be in equilibrium with the ground state provided the radiation and diffusion of excited levels neglected. The collisions of electrons with atoms at these levels made the electron energy distribution to be Maxwellian even if the electron-electron collisions are rare. Therefore large deviations from Maxwellian distribution received in Reference [1] for the case of rare electron-electron collisions can not take place in cesium plasma.

A numerical solution of the moment equations for the electron distribution function in author's article [5] showed that deviations from Maxwellian distribution take place near the electrodes, but they are not essential for determining plasma potentials ψ , densities N_e and temperatures T in conditions under consideration ($pd = 1 \text{ torr} \times \text{mm}$ where p is the pressure, d is the interelectrode spacing). Therefore Maxwellian electron energy distribution is assumed in this report. Equations to be solved were obtained from more general moment equations [5]. It needs to computer non-linear differential equations with non-linear boundary conditions on the emitter and the collector. Used numerical methods were reported before [6]

If radiative deexcitation from the first excited level is essential, the space derivatives of the ion current I_i , of electron current I_e and of the electron kinetic energy flux P_e are given by:

$$\frac{1}{e} \cdot \frac{dI_i}{dx} = \frac{1}{e} \frac{dI_e}{dx} = Q v N_e N_0 \left[\frac{N_1}{N_1^B} - \left(\frac{N_e}{N_s} \right)^2 \right] \quad (1)$$

$$\frac{dP_e}{dx} = -I_e \frac{d\psi}{dx} - E_{ion} \frac{dI_e}{dx} - \frac{N_1}{\tau_1} E_1 \quad (2)$$

where Q is the cross-section of ionization [2], $v = \left(\frac{8kT}{\pi m} \right)^{1/2}$ is the mean electron velocity, N_0 and N_1 are the densities of atoms at the ground level 6S and the first excited levels 6P, E_{ion} is the ionization potential, E_1 is the

first excitation potential, $N_1^B = \frac{g_1}{g_0} N_0 \exp(-\frac{E_1}{kT})$
 - Boltzmann equilibrium density at the first excited level, g_0 and g_1 are the statistical weights of the ground and first excited level,
 $N_s = \left\{ 2 \left(\frac{2\pi m k T}{h^2} \right)^{3/2} \frac{N_0}{g_0} \exp\left(-\frac{E_{ion}}{kT}\right) \right\}^{1/2}$ is
 Saha equilibrium density of free electrons, τ_1 is the de-excitation time at the first excited level 6P.

The last two terms in Equation (2) are energy losses in inelastic electron-atom collisions. They vanish if the ionization and the radiation are neglected.

The density N_1 is given by the particle balance equation for the first excited level.

$$Q_{01} N_0 N_e v = Q_{10} N_1 N_e v + \frac{N_1}{\tau_1} + \frac{1}{e} \frac{dI_1}{dx} \quad (3)$$

where Q_{01} and Q_{10} are the cross-sections for the electron impact transitions $6S \rightarrow 6P$ and $6P \rightarrow 6S$, averaged over Maxwellian electron energy distribution. The term $\frac{1}{e} \frac{dI_1}{dx}$ was omitted in Equation (3) because $Q_{01} N_0 N_e v \gg \frac{1}{e} \frac{dI_1}{dx}$ [2]. If the term $\frac{N_1}{\tau_1}$ is omitted too ($\tau_1 \rightarrow \infty$), the density N_1 is equal to equilibrium density N_1^B and Equation (1) is identical to the equation for $\frac{1}{e} \cdot \frac{dI_1}{dx}$ in Reference [2]. Performed there calculations of the cross-section Q includes all the transition between about fifty excited levels. The obtained dependence of Q upon the temperature T can be approximated by the formula:

$$Q = A \exp\left(-\frac{\Delta}{kT}\right) \quad (4)$$

where $A = 0,603 \cdot 10^{-12} \text{ cm}^2$ and $\Delta = 2,98 \text{ e-v}$.

The consideration of the radiation absorption and the diffusion of excited atoms requires much more complex equations than Equations (1)-(3), but these processes were taken into account approximately substituting time τ_1^* instead of deexcitation time τ_1 :

$$\tau_1^* = \tau_1 \frac{J_{20}}{J_2 + J_d} \quad (5)$$

where $J_d = \frac{1}{4} N_{1E} v_a$ is the flux of excited atoms to the emitter, N_{1E} is the density N_1 near the emitter, v_a is the mean velocity of atoms, J_{r0} is the summary photon flux to the emitter and the collector if the absorption being neglected, J_r is the same flux if the absorption being taken into account.

It was assumed that $N_1 = N_{1E} \exp(-\frac{x}{L})$, where x is the distance from the emitter, and length L was determined after calculating of space distributions of the density N_1 . Then J_r J_{r0} are given by:

$$J_r = \delta \frac{8\pi^2}{3\lambda^2} \frac{N_{1E}}{N_0} \frac{g_0}{g_1} \Delta\nu \left[\operatorname{erf}\left(\sqrt{\frac{d}{L}}\right) - i \operatorname{erf}\left(i\sqrt{\frac{d}{L}}\right) \exp\left(-\frac{d}{L}\right) \right] \sqrt{\kappa L} \quad (6)$$

$$J_{r0} = \frac{N_{1E}}{\tau_1} L \left(1 - \exp\left(-\frac{d}{L}\right)\right) \quad (7)$$

where d is the interelectrode spacing, λ is the wavelength, κ is the absorption coefficient in the center of line, $\Delta\nu$ is the linewidth, δ is the reflection coefficient of electrode surfaces.

Equation (6) was derived before [7] for the uniform plasma ($L \rightarrow \infty$).

The value of $\Delta\nu$ is determined by resonance broadening [8].

The value τ_1^* given by Equations (5)-(7) was averaged over two sublevels $6P_{1/2}$ and $6P_{3/2}$. For the case $d=0.5\text{mm}$ calculations gave $L=0.1\text{mm}$ and $\frac{\tau_1^*}{\tau_1} \approx 40$.

On solving transport equations the mean free path of ions and of electrons (L_i and L_e) were assumed to be independent upon an energy and to be equal.

$$L_i = \frac{1}{N_0 \sigma_{ia}} \quad L_e = \frac{1}{N_0 \sigma_{ea} + N_e \sigma_{ei}} \quad (8)$$

where σ_{ei} is the electron-ion collision cross-section for the electron energy $\mathcal{E} = \frac{3}{2} \kappa T$, σ_{ia} and σ_{ea} are the ion-atom and electron-atom collision cross-sections. They were assumed to be equal $\sigma_{ia} = 7 \cdot 10^{-14} \text{cm}^2$ and $\sigma_{ea} = 3.5 \cdot 10^{-14} \text{cm}^2$ as in Reference [9].

The boundary conditions in References [1] and [4]

assumed the accelerating field for the emission electrons near the emitter. One can evaluate the field E near the emitter by means of formula for E^2 in Talaat's article [10]. It was shown in Reference [11] that the value E^2 can become negative when the potential drop in the emitter sheath decreasing. It means that the accelerating field can not exist and a double-sheath appear near the emitter, i.e. the emitter sheath is divided into two regions: with retarding (near the emitter) and accelerating field for emission electrons. This is an obstructed mode. In this case it is useful to introduce a so-called virtual emitter. The surface of this emitter is the boundary surface between two regions of the emitter sheath, where the potential have the maximum value. The work function χ_v of the virtual emitter is the work function χ_E of the real emitter plus the height of retarding barrier, which is equal to the potential difference between surfaces of the real and the virtual emitter. The boundary conditions for accelerating field are invalid in the obstructed mode, but they become valid if to replace the work function χ_E by the work function χ_v [11]. χ_v is determined so that the condition $E^2=0$ was fulfilled near virtual emitter which is the point of maximum potential.

Below are reported only the results for the very weak surface ionization, i.e. if $\chi_E < \mathcal{M}$ (the electron-rich emission). Here \mathcal{M} is the plasma chemical potential determined for the emitter temperature T_E . The cases $\chi_E < \mathcal{M}$ and $\chi_E > \mathcal{M}$ were studied in Reference [11] by using the simplified model of the ignited mode. Similar models were used in References [12] and [13]. If $\chi_E > \mathcal{M}$ the extinguished and ignited regions of the theoretical I-V curve were regions of one continuous curve with a positive slope in agreement with experiment. But if $\chi_E < \mathcal{M}$ the extinguished and ignited regions were disjointed by the band of forbidden currents. This was interpreted as a cause of current jumps on the experimental I-V curves. The bounda-

ry point between regions of the positive and negative slope was compared with the experimental point of extinction. It was the case $\chi_E < \chi_V$ in which above simplified model appeared to be not quite content. The more rigorous calculations reported here have shown that the region of negative slope appear on I-V curves in the ignited mode only if losses of the energy of electrons, related with the radiation and the diffusion of excited atoms (we shall refer them as radiation losses) are taken into account. These losses are more essential for the lower currents.

Theoretical I-V curves are presented in Fig 1. for various electron emission currents I_{eE} . Solid lines show I-V curves if assuming an accelerating field near the real emitter. They are valid only above points where $E^2=0$. These points are the dotted line V. If assuming the virtual emitter (the obstructed mode) theoretical points are on the curve V for any emission current I_{eE} . This assumption is valid until $\chi_E < \chi_V$. Therefore the I-V curves coincide with solid lines until $E>0$ and with the dotted line V until $\chi_E < \chi_V$. The points where $E=0$ and $\chi_E = \chi_V$ are break points on theoretical I-V curves. Arrows in Fig 1 show the I-V curves for $I_{eE} = 9,1 \frac{A}{cm^2}$ and $I_{eE} = 0,66 \frac{A}{cm^2}$

The region of the line V below the point C have a negative slope. It was assumed the point C for $I_{eE} = 9,1 \frac{A}{cm^2}$ and the point d for $I_{eE} = 0,66 \frac{A}{cm^2}$ to correspond with experimental extinction points. In these points a transverse contractation of the arc was observed [11]. The theoretical I-V curves for $I_{eE} = 9,1 \frac{A}{cm^2}$ and $I_{eE} = 0,66 \frac{A}{cm^2}$ are in accordance with the I-V curves with two break points (points b and c) observed at large I_{eE} and with the I-V curves with one break point (point d), observed at small I_{eE} . Thus reported calculation have confirm proposed in Reference [11] an interpretation of regions between two break point for large I_{eE} as an obstructed region with a double-sheath near the emitter.

The curve V was obtained using the formula for E from Reference [10]. This formula is approximative and overestimate the value E . Therefore it may be that for $I_{eE} = 0,66 \frac{A}{cm^2}$ the point where $E_e = 0$ is below the point g in the region of a negative slope of the solid line. Then the extinction point is the point g where $E \rightarrow 0$ and $\frac{dI}{dV} = \infty$. Regions of negative slope on solid lines as on the dotted line V are caused by radiative losses which are inessential for large currents. The I-V curve for $I_{eE} = 9,1 \frac{A}{cm^2}$ have a positive slope down to point a , where the potential drop in the emitter sheath is equal to zero. The I-V curves in Fig.2 were obtained for constant χ_E . The Schottky effect, reducing the work function χ_E at large voltages, was considered in Reference [11]. There it was shown that regions of negative slope appear on theoretical I-V curves at large voltages owing to the Schottky effect. This leads to jump increase of the current and the saturation do not take place at large voltages.

Theoretical and experimental dependences of the internal voltage V_1 upon current j_1 at the first break point (the point b for $I_{eE} = 9,1 \frac{A}{cm^2}$ and the point d for $I_{eE} = 0,66 \frac{A}{cm^2}$) in Fig.1) are shown in Fig.2. An internal voltage V_1 is equal to output voltage V plus the contact potential $\chi_E - \chi_c$ (χ_c is the collector work function). Experimental values V_1 were obtained by A.M.Martsinovskiy and V.G.Yuziev (unpublished) for various emitter temperatures T_e in accordance to the S-type dependence j_1 upon T_e [11] similar to the dependence I_{eE} upon T_e . Theory and experiment demonstrate a slow increase of V_1 when T_e decreasing. The increase of V_1 at small currents is related with the radiation losses and increase of V_1 at large currents is caused by the recombination and the electron collisions.

The theoretical I-V curves are curves with two break point if the current j_1 is more than the current j_1 at

the point g (Fig.2). This current is equal $1 \frac{A}{cm^2}$ at $T_E = 1500^\circ K$ and $2,15 \frac{A}{cm^2}$ at $T_E = 900^\circ K$.

The corresponding experimental values are $\sim 3,5 \frac{A}{cm^2}$ at $T_E = 1670^\circ K$ and $\sim 8 \frac{A}{cm^2}$ at $T_E = 1150^\circ K$.

Theoretical space distribution of potentials ψ , densities N_e and electron temperatures T_e were compared with that obtained by probe measurements [14]. An example of this comparison is shown in Fig.3.

REFERENCES.

1. B.Ya.Moizhes, F.G.Baksht and M.G.Melikiya, J.T.F 35 9 (1965) 1621
2. E.B.Sonin, JTF 37 10 (1967) 1840
3. V.A.Abramov, Teplofizika vysokiyh temperatur 3 1 (1965) 23
4. L.M.Biberman, V.S.Vorobiev, I.T.Yacubov, Teplofizika v vysokiyh temperatur 5 2 (1967) 201
5. E.B.Sonin, JTF, 38 3 (1968) 434
6. E.B.Sonin, Prikladnaya mehanika y tehnikeskaya fizika 4 (1966) 60
7. V.A.Abramov, Ya.A.Tarasov, Teplofizika vysokiyh temperatur 2 2 (1964) 160
8. A.W.Ali, H.R.Griem, Phys. Rev. 140 (1965) A1044; 144 (1966) 366
9. G.A.Djuzhev, A.M.Martzinovsky, B.Ya.Moizhes, G.E.Pikus, V.G.Yuriev, JTF 36 (1966) 692
10. M.E.Talaat, Advanced Energy Conversion, 2 (1962) 447
11. G.A.Djuzhev, A.M.Martzinovsky, G.E.Pikus, E.B.Sonin, V.G.Yuriev. JTF 37 10 (1967) 1825

12. N.S.Rasor, Intern. Conf. on Thermionic Electrical Power Generation, London, (1965)
13. L.K.Hansen, Intern. Conf. on Thermionic Electrical Power Generation, London, (1965).
14. G.A.Djuzhev, Dissertation, Institute of semiconductors, Academy of Sciences of USSR, Leningrad (1967)

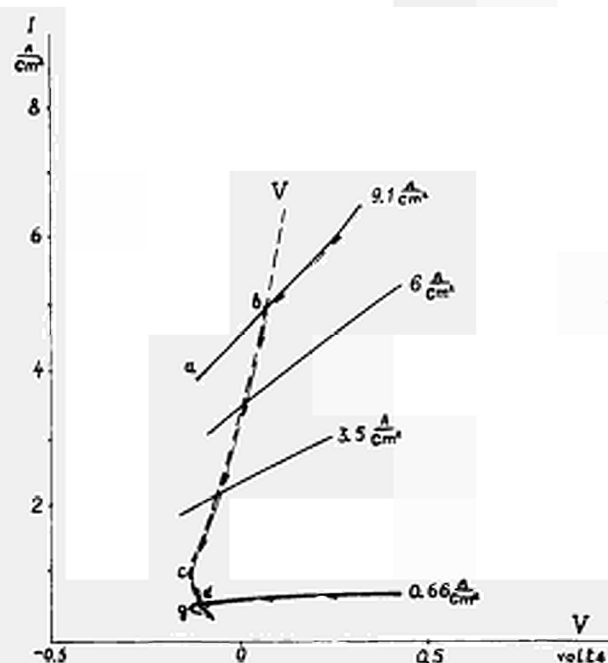


Fig. 1. Theoretical I-V curves for various electron emission currents $I_e E$.
 $p = 1$ torr, $d = 0.5$ mm, $T_E = 1500^\circ\text{K}$,
 $T_C = 700^\circ\text{K}$, $\chi_C = 1.7\text{e-v}$.

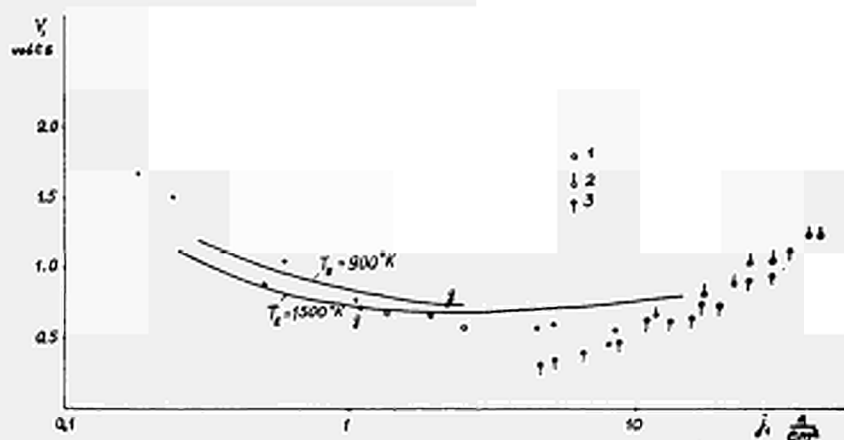


Fig. 2. Theoretical and experimental dependences of internal potential V_1 upon current j_1 at the first break point. $p = 1$ torr, $d = 0.5$ mm.
 Experimental points for I-V curves with one break point: 1 - the right side of curve $j_1 = f\left(\frac{1}{T_E}\right)$ (small T_E).
 Experimental points for I-V curves with two break points: 2 - the right side of curve $j_1 = f\left(\frac{1}{T_E}\right)$
 3 - the left side of curve $j_1 = f\left(\frac{1}{T_E}\right)$ (large T_E).

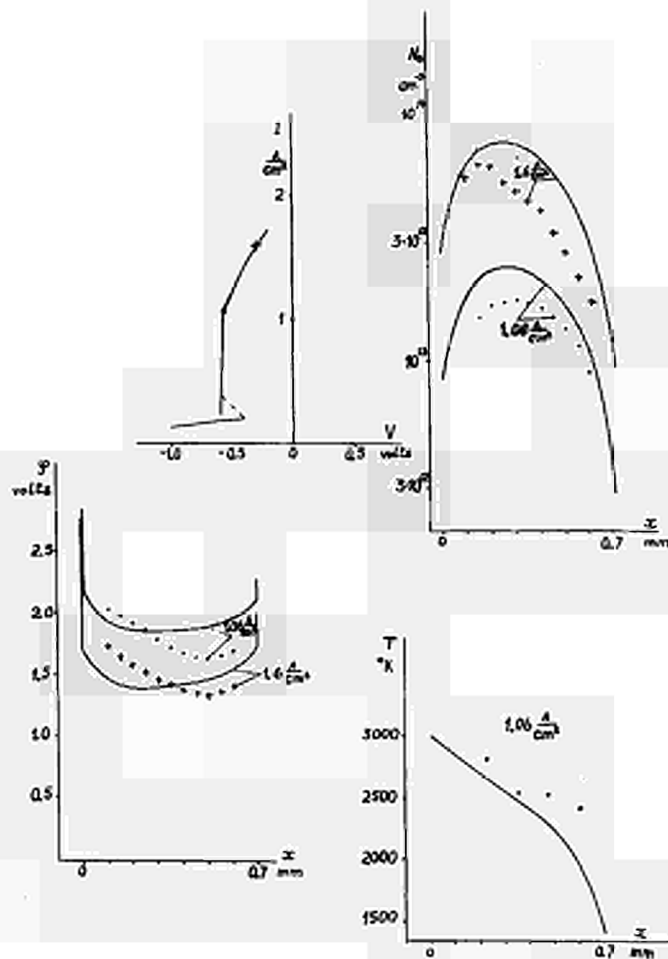


Fig.3. Comparison of potentials ϕ , electron densities N_e and electron temperatures T obtained by calculations (lines) and by probe measurements (points).

$$\rho = 1 \text{ torr}, T_E = 1680^\circ \text{K}$$

THE VOLTAGE DROP OF THE IGNITED MODE AS A
FUNCTION OF CURRENT DENSITY

by B. Saggau, H. Strecker

(Institut für Gasentladungstechnik und
Photoelektronik, Universität Stuttgart,
Breitscheidstrasse 2 (Germany))

Abstract

Experiments on low voltage arcs (ignited mode) of a Cesium diode have shown, that the plasma voltage drop U_{NB} is not only a function of pressure - spacing product pd (Johnson 1955, Rasor 1964/65), but also a function of current density j_E :

1. The ignited mode needs a minimum value of j_E in order to sustain itself.
2. U_{NB} is at a minimum at an exactly defined height of j_E .

Our measurements, carried out at a Cs-diode with plane geometry, show that the behavior of the low voltage arc corresponds to Hehl's Law of a glow discharge, at which the covered cathode surface due to the discharge is proportional to the discharge current, remaining $j_E = \text{const}$, a consequence of Point 2.

In determining the covered cathode surface by photos of the arcs, it was found, that the current is carried by two plasma parts: A bright plasma zone in the center and a relatively dark zone surrounding the bright center with a constant thickness.

Introduction

Visual observations¹⁾²⁾ of the plasma of the ignited mode in Cs-vapor have shown, that, with increasing converter current the bright plasma expands transversely - beginning with a small "ball of Fire" - to cover more of the emitter area F_E .

When the emitter area is entirely covered, the output voltage of a converter decreases, i. e. the plasma voltage drop U_{NB} rises with increasing current. A relatively simple theoretical model for the ignited mode³⁾⁴⁾ implies no current dependency on U_{NB} . But it is experimentally evident that 1. the ignited mode must have a minimum value of j_E (current density) in order to sustain itself, otherwise the arc jumps into the so-called "anode glow mode"; and that 2. at a defined value of j_E U_{NB} is at a minimum.

Experiment

The experimental device used was a Cs-diode with plane geometry. The Molybdenum emitter was indirectly heated and its surface F_E was 1.77 cm^2 .

I-U-characteristics were taken from the Cs-diode for different values of pressure-spacing product pd .

Fig. 1 shows a typical I-U-curve at $pd = 0,058 \text{ Torr.cm}$ given in a semilogarithmic plot. At constant emitter temperatures, the Boltzmann line gives the values of the total emitter work function as a function of j_E . The total emitter work function is the sum of the real emitter work function plus the negative emitter sheath barrier. In the region of the ignited mode we found a highly constant output voltage between 0.23 and 2.5 A. When, at the same time, we measure the area of the emitter, which is covered by the arc plasma, we note that here the current density is constant too. This behavior corresponds to Hehl's Law of a glow discharge, at which the covered cathode surface extends with increasing discharge current; remaining a current density $j_E = \text{const}$.

The covered area of the emitter was determined by photos of the arc. By evaluating these photos we discover that the converter current is carried by two plasma parts:

1. A current zone in the center of the arc, where the current

- density is constant, and where the plasma is bright, and
2. a current zone surrounding this region, where the plasma is relatively dark and where the values of current density are smaller than in the inner part.

Fig. 2 shows the converter current I as a function of the covered area F_{NB} of the emitter ("core" plus "shell"). Whilst the area of the bright "core" is won from the photos, the area of the dark "shell" having a constant thickness is so normed that F_{NB} is then equal to F_E when the voltage drop U_{NB} begins to rise. In the range of $0.7 < F_{NB} < 1.77 \text{ cm}^2$ the curve is a straight line, what means a constant current density in the "core" of $j_n = 2.1 \text{ Acm}^{-2}$. ($F_{NB} > F_E$ does not mean that here the plasma area is larger than the geometric emitter surface, but that the thickness of the "shell" becomes smaller).

Therefore, the straight line in the area range given above demonstrates that U_{NB} is constant as long as the current density of the proper arc - without the dark surrounding zone - is constant, i. e. as long as the emitter surface is not entirely covered by the total arc plasma.

From Fig. 1 and Fig. 2 we get U_{NB} as a function of current density j_E , as given in Fig. 3. U_{NB} , the voltage drop without the negative emitter sheath barrier, has a minimum at $j_E = 2.1 \text{ A/cm}^2$. This value is approximately that of the Richardson emission of the emitter. (The exact Richardson emission density, taken from S-curves, is not available due to a unclean-ness of the emitter surface).

Comparison with theory

At first we tried to compute $U_{NB \text{ min}}$ and j_n with the same equations used for Hehl's Law of the glow discharge by substituting the secondary emission coefficient $\gamma = 0.1$ by $\gamma = \sqrt{\frac{M}{m}} = 492$. But the calculated values are in great disagreement with the experimental results.

Recently Hansen and Warner⁵⁾ presented computer solutions for the ignited mode. Especially they gave results for varying current densities. At these solutions the entire voltage drop (U_{NB} + negative emitter sheath barrier) is a monotonously increasing function of the increasing j_E . But U_{NB} itself has a minimum value at a current density smaller than the Richardson emission.

Most recently, Djuzhev et al.⁶⁾ have also investigated the current density dependence of the ignited mode. They found also a region of the U-I-characteristic where the current density is constant. They conclude that the increase of the voltage drop at small current densities is related to the radiation losses, and the increase at high current densities is caused by recombination and electron-ion collision losses.

In conclusion we want to point out that the Hehl'Law, which is found for the low voltage arc, is related directly to the appearance of a minimum voltage for a defined current density.

References

- (1) RASOR, N. S., "Int. Conf. on Thermionic Electrical Power Generation", London, Sept. 1965.
- (2) WARNER, C.; HANSEN, L. K., (unpublished Rep. AI-7979 1962) see also J. Appl. Phys. 38, 3425 (1967).
- (3) JOHNSON, E. O., RCA Rev. 16, 498 (1955).
- (4) KIKRIDAKIS, S.; SHAVIT, A.; RASOR, N. S., Rep. on 24th Ann. Conf. on Physical Electronics, Cambridge, Mass., 1964.
- (5) WARNER, C.; HANSEN, L. K., Rep. on Thermionic Conv. Spec. Conf. Palo Alto, Cal. 1967, p. 184.
- (6) DJUZHEV, G. A.; MARTZINOVSKY, A. M.; PIKUS, G. E.; SONIN, E. B.; YURIEV, V. G., JTF 37 10 (1967) 1825.
Engl.: Sov. Phys. Techn. Phys. 12 (10) 1336 (1968).

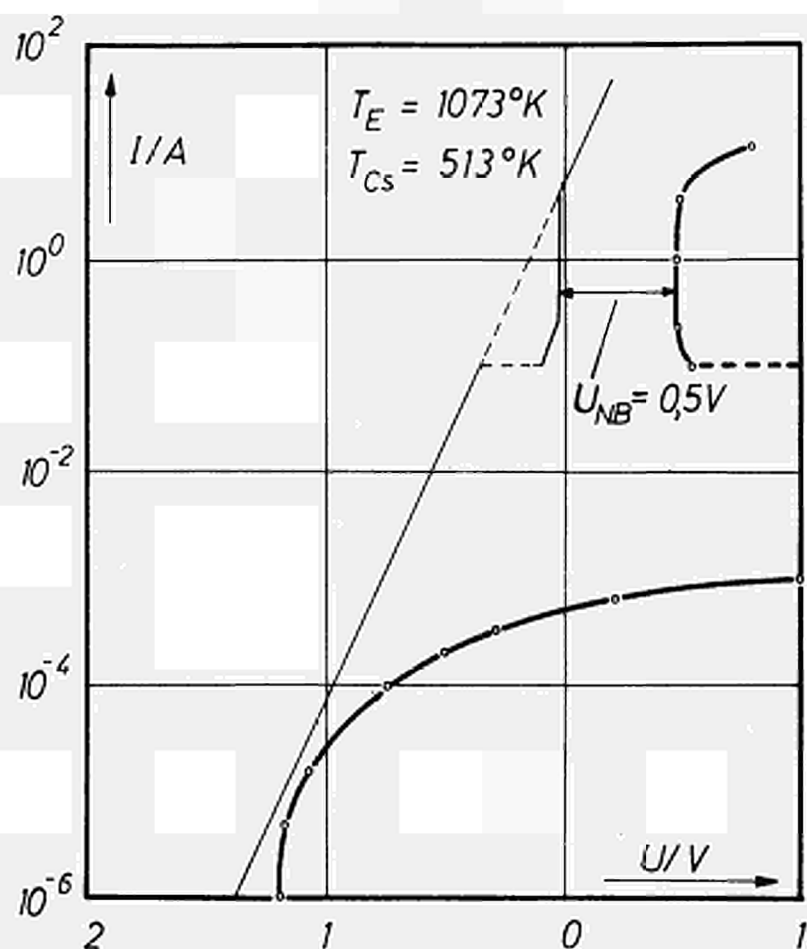


Fig. 1. I - U -characteristic of a converter with plane geometry

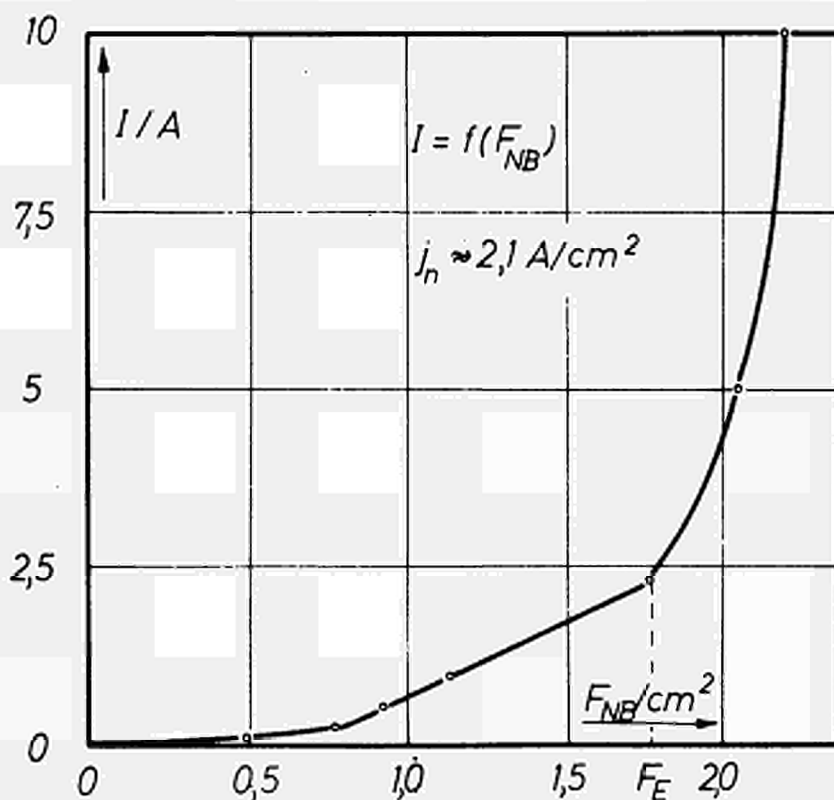


Fig. 2. Converter current as a function of the normed covered area of the emitter

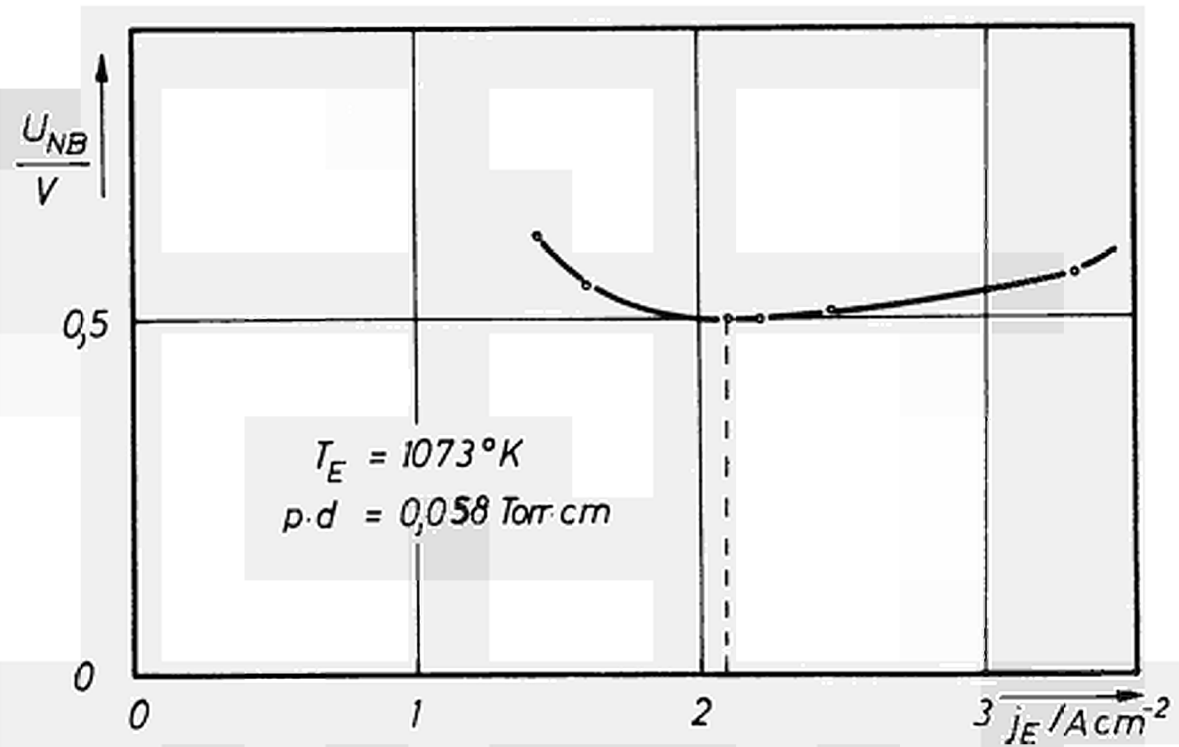


Fig. 3. Voltage drop U_{NB} of the ignited mode - without emitter sheath barrier - as a function of current density (Exper., converter with plane geometry)

DISCUSSION

Speaker of paper G-4: B. SAGGAU.

RASOR (USA): I believe it is important to recognize that in this region of the characteristics, i. e. in the ball-of-fire region, the behaviour of the volt-ampere curve is very strongly dependent on the ratio of the spacings to the diameter of the electrodes. The process here presumably is dominated by ion and other losses from the edges of the discharge to the outside walls of the chamber. Since your results describe devices in which such effects are of dominant importance, you certainly should qualify these results by specifying the ratio of the spacing to the diameter in your device.

SAGGAU (Germany): That is true for the region of high current when the plasma is fully extended over that electrode area. But in the range of low current I think the spacing is small enough that the boundary of the walls has no effect on this, that is, that the rising of the voltage at low current densities is not affected by spacing.

RASOR: What was the electrode spacing and diameter in your device?

SAGGAU: The spacing was 2 mm. The diameter of the electrodes was 1.5 cm.

RASOR: There indeed is a significant area at the edge of the plasma through which ions can be lost, relative to the electrode area.

SAGGAU: Yes, but we have a great range where the voltage drop is constant and so have no effect on the boundary of the electrodes.

DJUZHEV (USSR): I want to make a brief communication. We are studying the physical processes occurring on different ranges of the volt-ampere characteristic. It was discovered that:

1. On the volt-ampere characteristic there exists a vertical range in which the current in the converter increases along with the cathode surface involved in the discharge. Here, as probe and spectral measurements have shown, the parameters of the plasma inside the discharge filament remain unchanged, and at the cathode a monotonic distribution of the potential is realized.

2. The probe measurements have shown that with large cathode emission currents ($j > 10 \text{ A/cm}^2$) the existence of a double layer at the cathode is possible (the so-called virtual cathode) for a monocrystalline surface, or

the existence of a strong anomalous Schottky-effect for polycrystalline surfaces. This differs somewhat from the statements made in Dr. HANSEN's paper.

THEORETICAL CONSIDERATIONS OF THE IGNITED MODE*

C. Warner

Atomics International
A Division of North American Rockwell Corporation
Canoga Park, California

Abstract

A theory of the ignited mode is developed in terms of five differential equations corresponding to ion and electron particle transport, electron energy transport, and continuity of ion flux and electron energy flux. This system of equations with boundary conditions has been solved on an analog computer. The multistage ionization calculations of Norcross and Stone¹ have been used. Electron-ion collisions are included in the manner developed by Nighan². The analog solutions yield spatial profiles of the five dependent variables: plasma density, electron temperature, ion flux, electron energy flux, and electrostatic potential. The sheath potentials are also obtained. Typical solutions are given and general conclusions stated. Comparison with experiment is good at small spacings. Difficulties at wider spacings are discussed.

Introduction

In the past, the transport equations for the thermionic energy converter have been solved under various simplifying assumptions such as vanishing plasma electric field, vanishing electron temperature gradient, negligible ion-electron collisions, existence of local thermodynamic equilibrium, and one- and two-step ionization mechanisms. These models have been useful in a qualitative way and have done much to develop a general understanding of thermionic diodes. More recently, numerical or computer solutions have been obtained without the preceding assumptions. An early example of such an approach is the work of Moizhes, Baksht and Melikiya³ who represent the dependent functions as polynomials in the distance. By the method of moments, they obtain a set of simultaneous transcendental equations which are solved numerically. We have used a different approach^{4,5}, solving the

* This work was sponsored by the Office of Naval Research

differential equations on an analog computer. Lieb and Bornhorst⁶ have done similar work with a digital computer. Nighan^{7,8} has developed transport equations which take account of experimental results for the electron-atom cross section and also include electron-ion scattering. Nighan has used these equations and the experimental data of Reichelt and Kruer⁹ for the spatially varying plasma density and electron temperature to obtain the spatially varying ion flux, electrostatic plasma potential, electron energy flux and net ionization rate.

The present paper will describe first the transport equations and boundary conditions employed; some typical results will be presented and some general conclusions obtained. Secondly, our results will be compared with the experimental data of Kitrilakis et al¹⁰ (used by Rasor in his London Paper¹¹). The agreement with experiment is fairly good at close-spacings. Further difficulties at wide spacings will be discussed in an attempt to continue Nighan's analysis of the Reichelt-Kruer⁹ data across the ion production region to the emitter.

Transport Equations and Boundary Conditions

The plasma will be described by five first order equations for the five quantities: the plasma density $n(x)$; the plasma potential $V(x)$; the electron temperature $T_e(x)$; the electron total energy flux $Q_e(x)$; and the ion flux $\Gamma_p(x)$. The electron flux Γ_e is assumed spatially constant, but could easily be added as a variable.

The first two equations are obtained from the electron and ion transport equations, neglecting thermal diffusion

$$\frac{dn}{dx} = - \frac{T_e}{T_e + T_p} \left[\frac{\Gamma_e}{D_e} + \frac{T_p}{T_e} \frac{\Gamma_p}{D_p} \right] \quad (1)$$

$$\frac{dV}{dx} = \frac{T_e}{T_e + T_p} \cdot \frac{T_p}{ne} \left[\frac{\Gamma_e}{D_e} - \frac{\Gamma_p}{D_p} \right] \quad (2)$$

where T_p is the ion temperature; D_e and D_p , the electron and ion diffusion coefficients. The importance of electron-ion collisions has been shown by Nighan² who presented graphically effective transport coefficients which include this effect and an energy dependent electron-atom cross section,

all consistent with experimental data. We approximated his original results as

$$D^{*-1} = D_e^{-1} n_g^{-1} = 0.15 \times 10^{-20} + 0.53 \times 10^{-18} n n_g^{-1} \quad (3)$$

where n_g is the gas density. This approximation neglects a weak electron temperature dependence, and was used in the section, "Typical Results and General Conclusions". A slight modification was used to approximate Nighan's more recent results⁷.

$$D^{*-1} = (0.158 \times 10^{-20} + 26.9 \times 10^{-20} \frac{n}{n_g}) \frac{2500}{T_e} \quad (3')$$

This modification was used in the last section, "Comparison with Experiment." We have not used Nighan's ion transport equation⁸ which includes ion-electron collisions.

The third equation is the transport equation for the electron total energy flux, Q_e

$$\frac{dT_e}{dx} = \frac{1}{2nkD_e} \left[\Gamma_e (2kT_e - eV) - Q_e \right] \quad (4)$$

The fourth equation is that of continuity of ion flux, Γ_p

$$\frac{d\Gamma_p}{dx} = f(n, T_e) = Snn_g - \alpha n^3 \quad (5)$$

The net ionization rate $f(n, T_e)$ has been taken from the multistage ionization results of Norcross and Stone. Our approximation to $\alpha(n, T_e)$ and $S(n, T_e)$ are given in Reference 4.

An alternative ionization theory has been given by Moizhes, Baksht, and Melikiya³. A means of including the non-Maxwellian electron distribution function of Moizhes, et al within the calculation of Norcross and Stone has been described¹² but was not used in the present calculations.

The final equation represents continuity of total energy flux

$$\frac{dQ}{dx} = -eV_1 f(n, T_e) \quad (6)$$

The assumption that energy losses due to radiation, elastic collisions and diffusion of excited atoms are negligible, is open to question. The analysis of Nighan⁸ shows the importance of radiation losses and elastic losses at wide spacings. We shall avoid these regions in our analysis.

The boundary conditions on the electron flux are

$$\Gamma_e = \Gamma_{r1} \exp\left(\frac{-eV_C}{kT_{e1}}\right) \quad (7) \quad v_E - \Gamma_{r0} \exp\left(\frac{-eV_E}{kT_{e0}}\right) = \Gamma_e \quad (8)$$

where v_E is the Richardson flux; Γ_r the electron random flux; V_E and V_C the emitter and collector sheath drops; the subscripts 0 and 1 denoting the emitter and collector edges of the plasma.

The boundary conditions on the ion flux are

$$\frac{\Gamma_{p0}}{2} = -\frac{n_0 v_p}{4} \quad (9) \quad \frac{\Gamma_{p1}}{2} = n_1 \frac{v_p}{4} \quad (10)$$

Finally, $V(0) = 0$. These boundary conditions must be modified for a double sheath at the emitter or a negative collector sheath. The modified double sheath equations resulting from a solution of Poisson's equation with electrons and ions from both emitter and plasma are given in Reference 4. Trapped ions were not included, but can be important according to Bednarz and Davis¹². Trapped ions are expected to affect our results only at very low currents.

Summarizing, there are five first order equations for the five unknowns; n , V , Γ_p , T_e and Q_e . The seven boundary conditions take account of the two additional unknowns, V_E and V_C . For the calculations, the above equations were expressed in dimensionless form with the variables

$$z_1 = \frac{n}{n_E} \quad z_2 = \frac{eV}{kT_E} \quad z_3 = \frac{T_e}{T_E} \quad z_4 = \frac{Q_E}{v_E kT_E} \quad z_5 = \left(\frac{\Gamma_p}{\frac{n_E v_p}{4}} \right)$$

$$\xi = \frac{x}{L} \quad \bar{\Gamma} = \frac{\Gamma_e}{v_E} \quad v_E = \frac{n_E v_E}{4} = \frac{n_E}{4} \sqrt{\frac{8kT_E}{m}}$$

where T_E is the emitter temperature and L , the diode spacing.

Typical Results and General Conclusions

Many calculations^{5,12} have been made under the following conditions: $v_E = 10 \text{ amps/cm}^2 = 6.24 \times 10^{19} \text{ cm}^{-2}\text{-sec}^{-1}$; $T_E = 1800\text{K} = 0.155 \text{ ev}$; $\lambda_p = 2.87 \times 10^{-4} \text{ cm}$; $T_p \text{ (ave)}/T_E = 0.75$ with the associated values $v_E = 2.63 \times 10^7 \text{ cm-sec}^{-1}$; $n_E = 9.49 \times 10^{12} \text{ cm}^{-3}$; $n_g = 2.9 \times 10^{16}$; $\sigma_p = 1200 \text{ A}^2$; and $T_{cs} = 592\text{K}$. The value for T_{cs} assumes an average gas temperature of 1300K and constant gas pressure throughout the system. Work function vs T/T_{cs} plots indicate that the emitter has a bare work function $\phi_0 \cong 4.4 \text{ ev}$ corresponding to molybdenum. Some typical results will now be given.

The plasma density profile for various currents $\bar{\Gamma}$ are shown in Figure 1 for a spacing of $L = 0.01 \text{ cm} = 3.94 \text{ mils}$. The emitter double sheath starts at about $\bar{\Gamma} = 0.53$. The profiles in this region are not shown, but decrease only slightly below the $\bar{\Gamma} = 0.55$ curve. The plasma density thus varies strongly with current above the knee of the volt-ampere curve and slowly below it. The ion current varies approximately in proportion to dn/dx according to equation (1) and the net ion production rate as the second derivative d^2n/dx^2 . Examination of Figure 1 shows that the net ionization is appreciable only on the emitter side of the plasma, even at the small $pd \cong (3.9)(3.94) = 15.4 \text{ mil-torr}$.

An example of $\Gamma_p(x)$ and the net ionization rate $f(x)$ are shown in Figure 2. The ionization region is very small. The maximum of the ion production curve was found to occur at $x = 0.013 \text{ mm}$ for $0.004 \text{ cm} < L < 0.020 \text{ cm}$. If extrapolation were possible to wide spacings (e.g., $L = 0.1 \text{ cm}$), the region of net ion production and the maximum in the plasma density would be unobservable experimentally (contrary to experiment). Further difficulties with widespaced solutions will be discussed later. The electron temperature z_3 varies appreciably across the diode as seen in

Figure 3 for $L = 0.01$ cm. If the Saha density is calculated from these electron temperatures and the gas density n_g , it is seen that very strong departures from LTE occur over almost all the space. An example is given in Figure 4 at $\bar{\Gamma} = .7$ and $L = 0.01$ cm. The steady state density is that predicted by Norcross and Stone with no diffusion losses. The plasma potential z_2 for $L = 0.01$ cm is shown in Figure 5 for various $\bar{\Gamma}$. The electric field is retarding over most of the interelectrode space at these close spacings. At wider spacings, Nighan's analysis⁸ shows the electric field to be accelerating as it must certainly be for very wide spacings of a conventional arc. The motive diagrams at $L = 0.01$ cm are shown in Figure 6 as a function of current $\bar{\Gamma}$. The emitter sheath drop varies strongly with current, until the double sheath sets in. The volt-ampere curves are shown in Figure 7 where $\Delta\eta = \eta_E + z_2(1) - \eta_c - \Delta\phi$, $\Delta\phi$ being the double sheath barrier. The points in Figure 7 (and also Figure 8) are calculated points. The output voltage V is thus $\phi_E - \phi_c - \Delta\eta kT_E$. At the knee of the curve, the maintenance voltage is 0.42 volts. This voltage is reasonable in contrast to results from models with one- or two-step ionization. Finally, Figure 8 shows the electron temperature $z_3(0)$ as a function of spacing for fixed current. The curve is reminiscent of the Paschen curve and perhaps similar in explanation. More results can be found in our previous work. Experimental checks on $n(x)$, $T(x)$ and $V(x)$ are not available at close spacings. At large spacings, the analog program (based on a shooting method) is unstable and there are indications of more fundamental difficulties.

Comparison With Experiment

To obtain a check with experiment, we have chosen the TEECO V-I data¹⁰ used by Rasor¹¹ at the London conference. We used the following input parameters: $v_E = 20$ amps/cm²; $T_E = 1800K$; $\lambda_p = 3.82 \times 10^{-4}$ cm. Since we use $\sigma_p = 1200$ A², this λ_p -value implies $n_g = 2.18 \times 10^{16}$ cm⁻³, which is actually about 20% too high to be consistent with $p_{cs} = 2.25$ torr. This discrepancy is not expected to affect our results appreciably since we choose v_E rather than calculate it. The diffusion constant of equation (3') is used in our calculations. The quantities $z_1(0)$ and $z_3(0)$ are guessed for fixed $\bar{\Gamma}$ until the collector boundary conditions are satisfied. This procedure leads to the accumulation of data for various spacings L . The data was then plotted to obtain results for $L = 3, 4, 6, 8$ and 10 mils.

The resulting volt-ampere curves are shown in Figure 9. The experimental results are shown in Figure 10. The dashed lines in Figure 9 are extrapolations. The transition point (knee of I-V curve) was determined from the calculations but that portion of the curve below the transition was drawn to roughly parallel the experimental data. A comparison of Figure 9 and 10 shows that the agreement is better than qualitative. The theoretical maintenance voltages are about 0.1 volts too large, where we use Rasor's estimate of the collector work function, $\phi_c = 1.9\text{v}$. The variation of the curves with L differs quantitatively. Thus, in Figure 11 the theoretical current Γ at short circuit decreases more rapidly with spacing than in the experimental case. The discrepancy between theory and experiment appears to be increasing with spacing. A Rasor $1/\Gamma$ vs L plot for the $V = 0.0\text{v}$ and $V = 0.15\text{ v}$ yielded straight lines which were consistent with an intersection at $1/\Gamma = 1$ and $L = -2.3$ mils. Contrary to Rasor's theory, the quantity $\eta_c - z_2$ varied rapidly with spacing for fixed Γ , as the double sheath transition point was approached. The emitter sheath is similarly varying rapidly in this region as seen in Figure 12. It is thus very difficult to extrapolate η_E at the transition point. The electron temperatures $z_3(0)$ and $z_3(1)$ are shown in Figure 13. The $z_3(1)$ values all lie close to one curve independent of Γ . The $z_3(0)$ values depend on both Γ and L. In conclusion, the close spacing results appear in fair agreement with experiment, although better agreement appears necessary if useful predictions are to be made.

In order to investigate wide-spaced solutions and take advantage of the Reichelt-Kruer data⁹, we have tried to obtain solutions in the near electrode or ionization region. We use the data for $p = 1.95$ torr, $L = 2.0$ mm and $\Gamma = 4$ amps/cm² ($\bar{\Gamma} = .4$ assumed). Nighan's analysis just enters this region from the plasma side. Since including the electron temperature gradient in equation (4) led to difficulties, we took the electron temperature to be constant, as indicated experimentally. We obtain solutions with the experimental values of n and dn/dx at $x = 0.4$ mm by integrating backward to the emitter for various T_e . We found the following difficulties. The solution, which satisfied the emitter boundary condition (9) had $z_1(0) = 1.4$ and $z_3(0) = 1.52$ ($n(0) \cong 1.4 \times 10^{-2}$ cm⁻³; $T \cong 2630\text{K}$) and thus implied an unphysically small emitter sheath drop, .24 volts. While the theoretical $n(x)$ is below the experimental values,

the electron temperature is close to the experimental $T \approx 2480\text{K}$. A second solution was found with $z_1(0) = 12$ and $z_3(0) = 1.49$ ($n(0) \approx 1.2 \times 10^{13} \text{ cm}^{-3}$ and $T \approx 2560\text{K}$) which fit the $n(x)$ data. This solution did not satisfy equation (9) since the backwards integration yielded $z_5(0) = -2.2 \neq -24$. These difficulties are being further studied.

Acknowledgement

The author wishes to thank A. Presson for performing the analog computations.

REFERENCES

- (1) NORCROSS, D. W. and STONE, P. M., Report on 26th Annual Conference on Physical Electronics, MIT (1966) p. 96.
- (2) NIGHAN, W. L., Report on Thermionic Conversion Specialist Conference, San Diego (1965) pp. 84-100.
- (3) MOIZHES, B. Ya.; BAKSHT, F. G.; and MELIKIYA, M. G., Soviet Physic-Technical Physics 10, p. 1252 (1966).
- (4) HANSEN, L. K., and WARNER, C., Report on 27th Annual Conference on Physical Electronics, MIT (1967) p. 308
- (5) WARNER, C., and HANSEN, L. K., Report on Thermionic Conversion Specialist Conference, Palo Alto (1967), p. 184.
- (6) LIEB, D., and BORNHORST, W., Report on Thermionic Conversion Specialist Conference, Palo Alto (1967), p. 191.
- (7) NIGHAN, W. L., Report on Thermionic Conversion Specialist Conference, Houston (1966) p. 276; J. of Appl. Phys. 39, 223 (1968).
- (8) NIGHAN, W. L., Report on Thermionic Conversion Specialist Conference, Palo Alto (1967), p. 198
- (9) REICHELT, W. H., and KRUEER, W. L., Report on Thermionic Conversion Specialist Conference, San Diego, (1965), p. 129.
- (10) RUFEB, F., RASOR, N., LEIB, D., WEINSTEIN, J., and KITRILAKIS, S., Thermo Electron Report No. TE 67-65, March 1965.
- (11) RASOR, N. S., International Conference on Thermionic Electrical Power Generation, London, Sept. 1965.
- (12) WARNER, C., and HANSEN, L. K., Atomic International Report AI-67-155, Oct. 1967.
- (13) BEDNARZ, R., and DAVIS, M. V., Report on Thermionic Conversion Specialist Conference, Palo Alto (1967), p. 207.

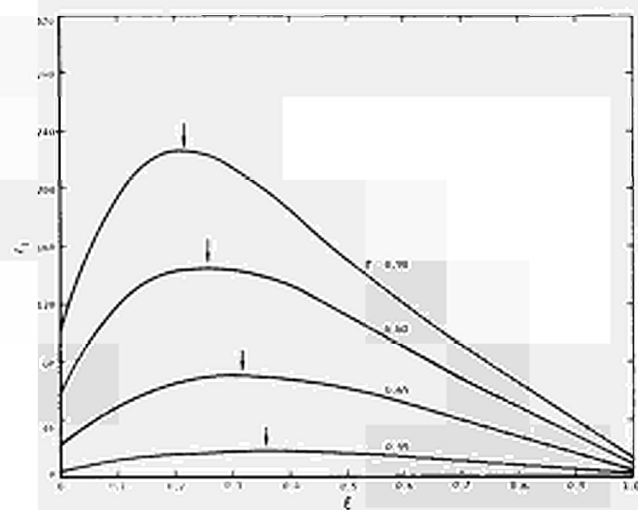


Figure 1. Plasma Density Profile vs $\bar{\Gamma}$

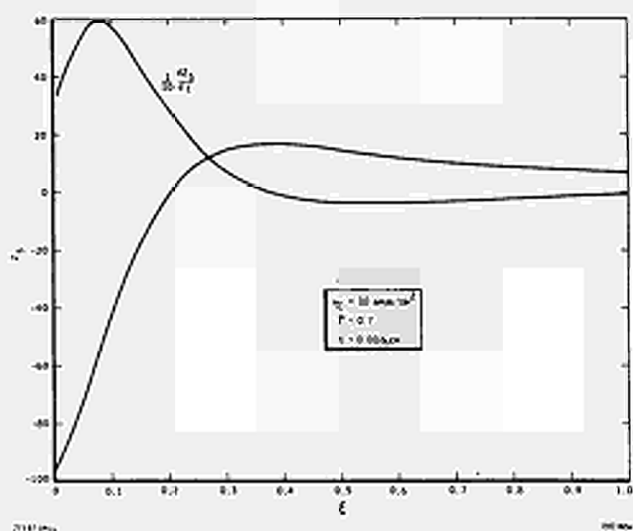


Figure 2. Ion Flux and Net Ion Production Rate at $L = 0.016$ cm

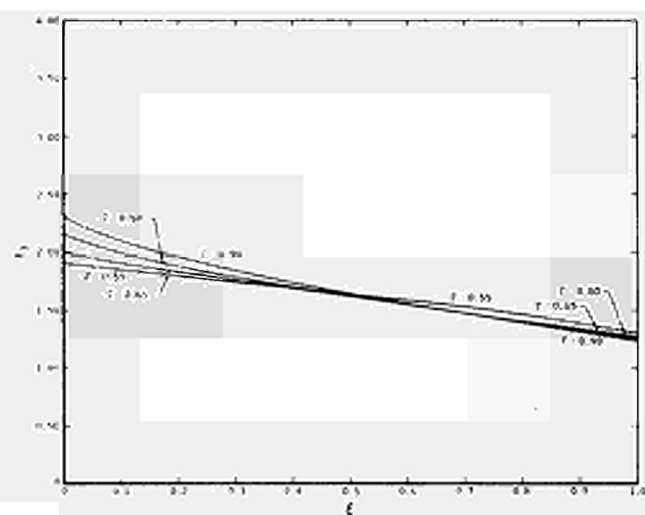


Figure 3. Electron Temperature Profile vs $\bar{\Gamma}$

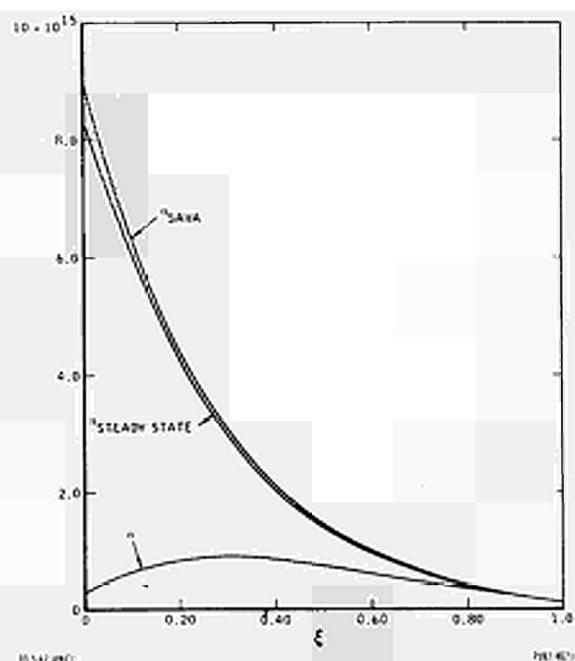


Figure 4. Departure from LTE

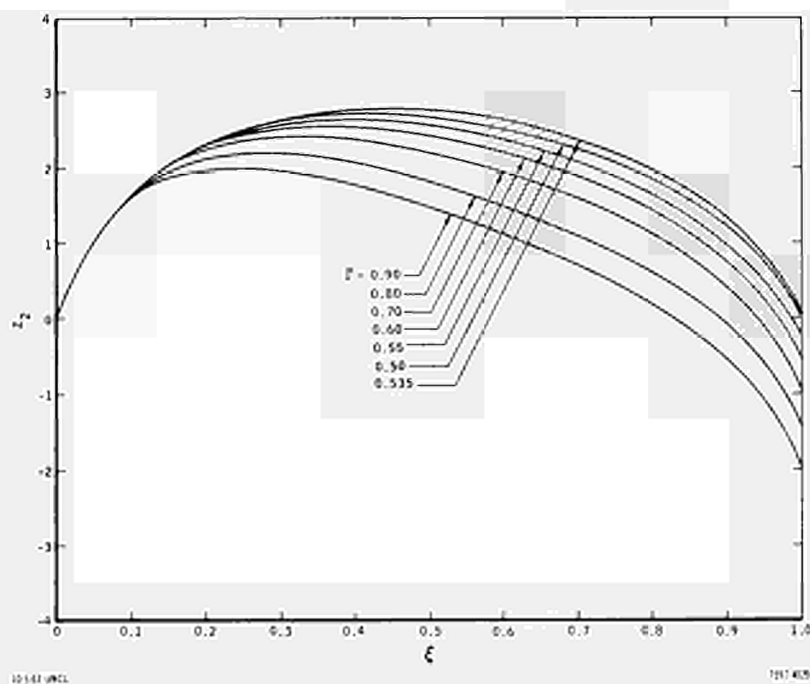


Figure 5. Plasma Potential Profile vs $\bar{\Gamma}$

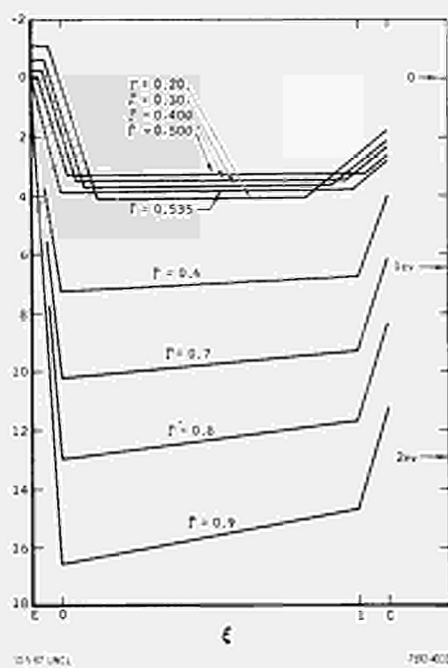


Figure 6. Schematic Potential Diagrams vs $\bar{\Gamma}$

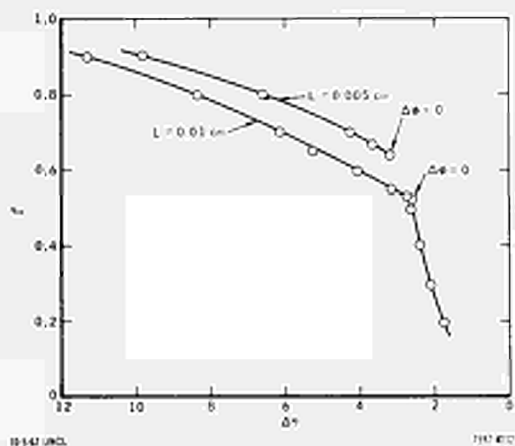


Figure 7. Volt-Ampere Curve

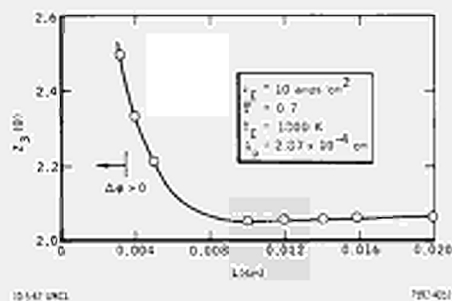


Figure 8. Electron Temperature $z_3(0)$ vs Spacing

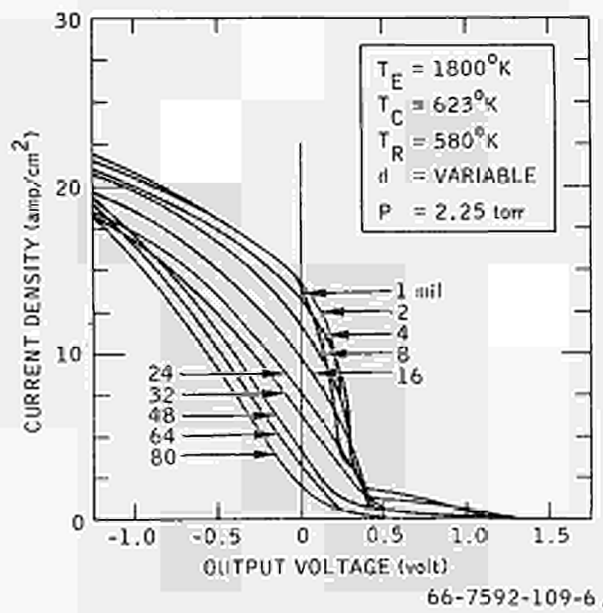


Figure 9. Theoretical V-I Curves

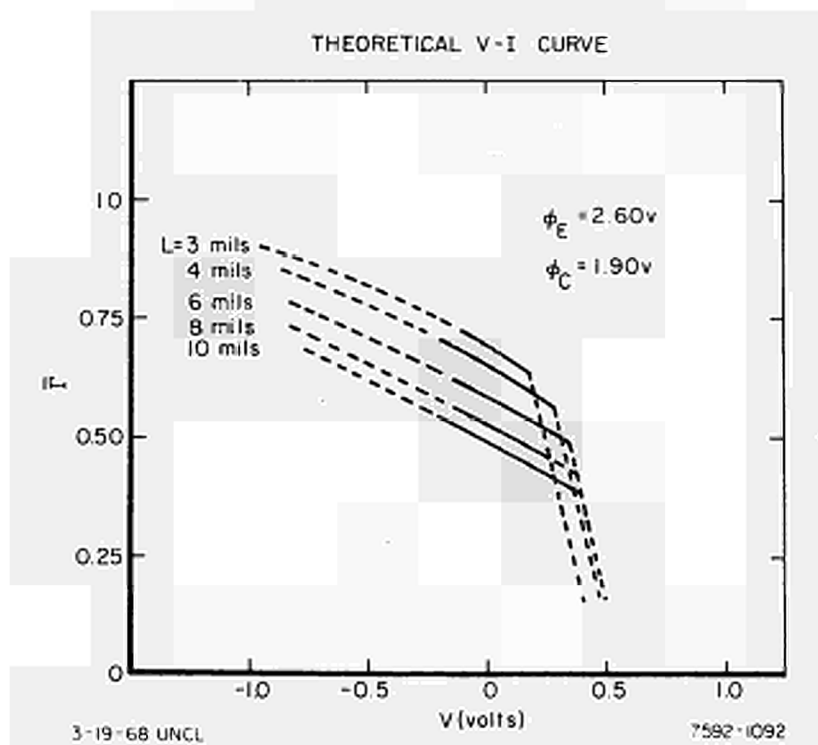


Figure 10. TEECO V-I Curves

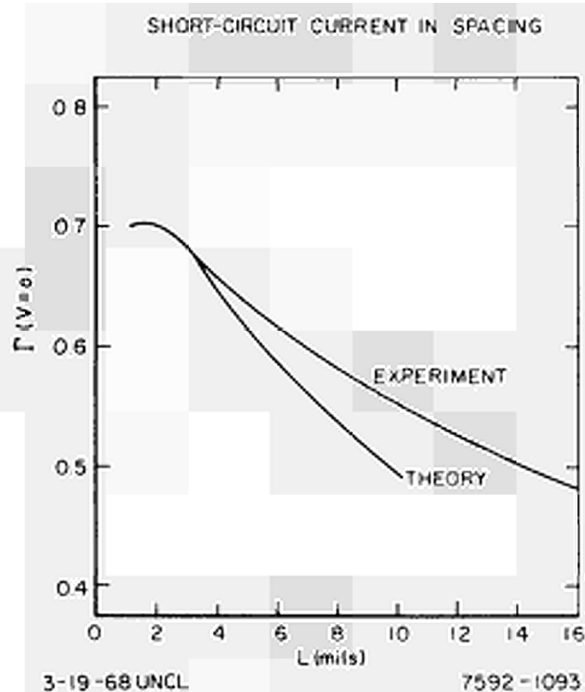


Figure 11. Short Circuit Current vs Spacing

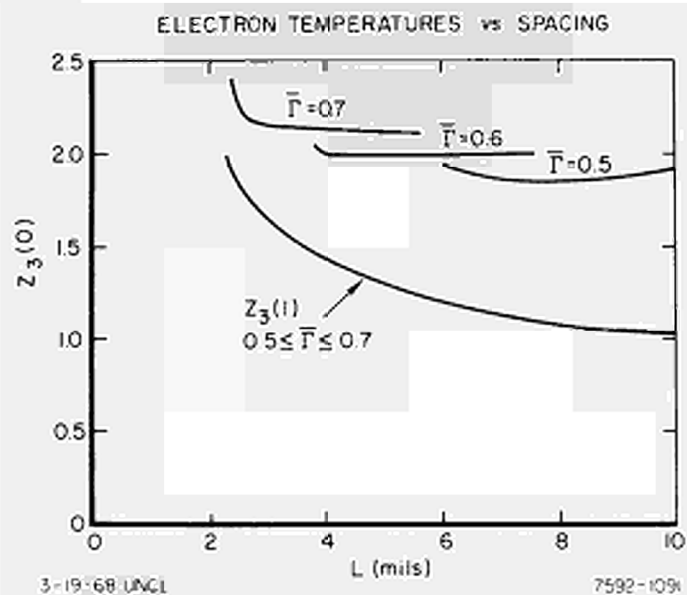


Figure 13. Electron Temperatures vs Spacing

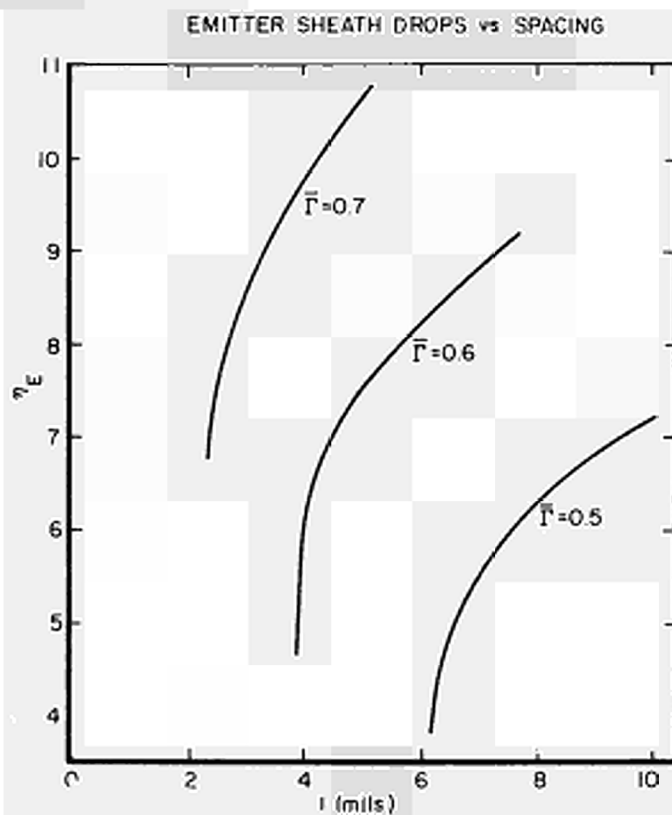


Figure 12. Emitter Sheath Drop vs Spacing

DISCUSSION

Speaker of paper G-5: Ch. WARNER.

HATSOPOULOS (USA): I'm a little bothered by the fact that we keep using the same data to prove the various theories. In particular, the data that are presented here are already 2.5 years old. But there is a tremendous wealth of newer data. Not all of it is so well behaved as that particular set of data used at the London Conference, but we have a need to extend our analysis and compare it with the data that is not so well behaved. I would like to make a point that the WILKINS-analysis is compared with some of the TEECO-data, and WARNER and HANSEN use some other set of TEECO-data, and the data are taken in different regions. For example, the behaviour changes somewhat when you go to higher temperatures where you have considerable ion-emission from the emitter. The data changes when you have some operating conditions at the converter where it appears that there may be some non-equilibrium situations. I'm not posing that as a criticism because we do need to find where some of the theories apply, to be sure, but I'm posing it as a caution that we should realize that there are regions of important data where at least we don't have a complete definite answer.

WARNER (USA): I would like to ask, where are all these data?

HATSOPOULOS: A few samples of these data are included in the paper A-1. These data were taken from a much broader library of data, which was printed on Jet Propulsion Lab-reports. You used the results of NIGHAN on the ion-electron scattering. This indicates that for the equations you use, this has a substantial effect. Judging from what HANSEN just said, he believes that this may not have a large effect and I wonder if you could comment on that.

WARNER: I have not had a chance to compare my results with HANSEN's. Also I am not so sure how important the electron-ion collisions are in my calculations. I never took them out of my calculations to check it in that fashion.

HANSEN (Euratom): In the work I reported I mentioned that the electron-ion collisions were not important for this one particular effect, the linear dependence of inverse current on spacing. I did not mean to imply that it is not important if you consider it from some other aspect of the volt-ampere curve, for example the diode internal voltage drop.

ON LOW-VOLTAGE ARC IN CESIUM VAPOR

I.P. Stakhanov, I.I. Kasikov

Institute of Physics and Power
Engineering

Obninsk, USSR

I N T R O D U C T I O N

It is the purpose of this paper to obtain with the help of rather a simple model the main qualitative characteristics of low voltage arc charge in cesium vapor.

As it is generally known [1] , [2] , at low temperatures and at rather high pressure the ignition is followed by a region of negative resistance on volt-ampere characteristic and by hysteresis (Fig. 1). At high temperatures these phenomena disappear and the arc ignition is followed only by the characteristic change (Fig. 2). The potential qualitative characteristic within the interelectrode space is given in Fig. 3. For the low voltage arc the large potential drop is characteristic in Langmuir's cathode layer and also the anode potential drop retarding the electrons leaving the plasma. The potential

change in the interelectrode space is comparatively small and non-monotonous with the maximum approximately in the middle of the interelectrode space [3] , [4] .

The electron temperature in the interelectrode space change rather little decreasing to the cathode by 500°K. Later on we shall assume the electron temperature constant and equal to some mean temperature T_e . Strictly speaking slight temperature changes lead to highly sufficient ionization rate change within the interelectrode space which appear maximum near by the cathode. However, these changes do not influence sufficiently volt-ampere characteristics. In this connection we shall assume that the ionization rate is defined by the equation

$$Q = \alpha n \quad (1)$$

where Q - the ion quantity appearing in the unit of volume per time unit; n - the plasma density; α - the ionization coefficient determined at the temperature T_e

2. ENERGY BALANCE

Let us assume the Fermi level in the cathode the beginning of the potential count. Then the energy carried by the emission electrons into the plasma is equal to

$$j_0 \left(W' + \frac{2T'}{e} \right)$$

where j_0 - the emission current density; W' - the cathode work function; T' - the cathode temperature in energy units; e - the electron charge.

The energy carried by the electrons out of the plasma into the cathode is

$$(j_0 - j) \left(W' + \frac{2T_e}{e} \right)$$

So we obtain the cathode differential energy flow

$$\Delta \varepsilon' = j \left(W' + \frac{2T_e}{e} \right) - j_0 \left(W' + \frac{2T_e - T'}{e} \right) \quad (2)$$

As the anode does not emit the electrons the energy differential flow from the plasma near by the anode will be

$$\Delta \varepsilon'' = (J + j) \left(W' - \Delta V + \frac{2T_e}{e} \right) \quad (3)$$

where j - the electron current increase owing to the ionization; ΔV - the potential drop in the plasma (including the layers near by the electrode).

The energy balance for electron gas in the interelectrode space will be

$$\Delta \varepsilon' = \Delta \varepsilon'' + S \quad (4)$$

where S - energy losses in the interelectrode space. Since elastic electron-atom collisions do not result in energy change, the value S is determined by nonelastic collisions only. The value of S will be given by

$$S = S' + S'' \quad (5)$$

where S' - the losses due to the ionization; S'' - other losses caused by radiation output and diffusion of excited atoms:

$$S' = jQ \quad (6)$$

where Q - energy losses during the ionization event.

$$Q = E_i + \varphi = E_i - W + E' \quad (7)$$

where E_i - the ionization potential in volts; φ - the electron gas potential; E' - potential drop near by the cathode. Substitution of Equations (2), (3), (5) + (7) in (4) (Equation of energy balance) yields

$$J \Delta V = 2 \frac{T_e - T_i}{e} J_0 + j \left(E_i - \Delta V + E' + \frac{2T_e}{e} \right) + S'' \quad (8)$$

3. ELECTRON TEMPERATURE

Neglecting temperature gradients of electrons and ions we obtain for electron and ion current the following equations

$$J_e = -e D_e \frac{dn}{dx} + e u_e n \frac{d\varphi}{dx} \quad (9)$$

$$J_i = -e D_i \frac{dn}{dx} - e u_i n \frac{d\varphi}{dx} \quad (10)$$

where $D_{e,i}$; $U_{e,i}$ - diffusivity and mobility coefficients for electrons and ions; n - the plasma density.

Owing to the volume ionization

$$\frac{dJ_i}{dx} = q \quad (11)$$

Since one can consider that the volume ionization does not influence the electron current value, it follows that

$$J_e \approx \text{const} = J$$

From Equations (9) - (11) we obtain

$$\frac{d^2 n}{dx^2} = -\frac{q}{D_a} \quad (12)$$

where

$$D_a = D_i \left(1 + \frac{T_e}{T_i}\right) \quad (13)$$

where T_i - the ion temperature taken constant while obtaining Equation (12).

Neglecting the surface ionization in comparison with the volume one and considering that near by electrode barriers let the ions from the plasma to the electrodes freely we obtain the boundary conditions: on the cathode ($x=0$)

$$-J_i' = e D_a \left. \frac{dn}{dx} \right|_{x=0} + \frac{u_i}{u_e} J = \frac{1}{2} n' \alpha_i e \quad (14)$$

on the anode ($x=L$)

$$J_i'' = -e D_a \left. \frac{dn}{dx} \right|_{x=L} - \frac{u_i}{u_e} J = \frac{1}{2} n'' \alpha_i e \quad (15)$$

where $\alpha_i = \sqrt{\frac{8T_i}{\pi M}}$; the values near the cathode are marked with one stroke, with two - near the anode.

Using (1) we write the solution of Equation (12) as

$$n = n'' \cos \gamma x + \frac{n'' - n' \cos \gamma L}{\sin \gamma L} \sin \gamma x \quad (16)$$

where

$$\gamma = \sqrt{\frac{\alpha}{D_a}} \quad (17)$$

L - the interelectrode space.

Using Equation (16) we obtain from Equations (14), (15)

$$\left(D_a \gamma \frac{\cos \gamma L}{\sin \gamma L} + \frac{1}{2} \sigma_i - \frac{D_a \gamma}{\sin \gamma L} \right) (n' + n'') = 0 \quad (18)$$

As $n' + n'' = 0$ do not satisfy the requirement of positive density one must adopt that

$$D_a \gamma \frac{\cos \gamma L}{\sin \gamma L} + \frac{1}{2} \sigma_i - \frac{D_a \gamma}{\sin \gamma L} = 0 \quad (19)$$

It is worth considering that Equations (14), (15) regarding Equation (16) present the system of linear algebraic equations relative to n' and n'' , Equation (19) causes zero determinant of this system and may be presented as follows:

$$\frac{\gamma L}{2} \operatorname{tg} \frac{\gamma L}{2} = \frac{\sigma_i L}{4 D_a} \quad (20)$$

The same result one can obtain from the condition of ion balance:

$$\frac{1}{2} n' \sigma_i + \frac{1}{2} n'' \sigma_i = \alpha \int_0^L n dx \quad (21)$$

in which (16) is necessary to be used while calculating the integral in the right-hand part.

As $\frac{\sigma_i L}{4 D_a} \approx \frac{3}{8} \cdot \frac{L}{\ell_i} \gg 1$ (ℓ_i - the ion free path length), the average value of the first root of (20) has the form:

$$\gamma L = \pi \left(1 - \frac{4 D_a}{\sigma_i L} \right) \quad (22)$$

Equation (22) can be used for determination of electron temperature (T_e) which appears to be independent upon current.

Since γ depends on temperature exponentially it results that

T_e decreases logarithmically with increasing L and pressure.

These results are confirmed with the experimental data [3], [4].

It should be mentioned that in reality electron temperature T_e

rises when current increases. However, this increase occurs very slowly. According to [3] when current increases from 2 to 10 a/cm² temperature rises only by 200° from 2600°K to 2800°K

($T' = 1565^\circ\text{K}$, $p = 2$ mm Hg). The same conclusion about the weak dependence of electron temperature upon current was drawn by

Rasor [5].

4. ENERGY LOSSES CALCULATION

Considering the fact that the potential drop in the volume is small one may assume that $E' - \Delta V \approx E''$, where E'' - potential drop at the anode (Fig. 3). The magnitude $E'' \approx (1 \div 2) \frac{T_e}{e}$. Since $E_i \gg \frac{T_e}{e}$ the expression for energy losses in Equation (8) can be written in the form:

$$j(E_i + (2 \div 3) \frac{T_e}{e}) + S'' \quad (23)$$

Further S'' is not considered, assuming that the ionization losses prevail. Thus the problem reduces to determination of the dependency of j on electron current (J) and voltage. Note that

$$j = \frac{1}{2} (n' + n'') v_i e \quad (24)$$

From (14), (16) and (19) it follows that:

$$n' - n'' = j \frac{u_i}{u_e} \frac{\sin \gamma L}{D_a \gamma e} \quad (25)$$

using (22) we obtain from (25)

$$n' - n'' = j \frac{u_i}{u_e} \frac{4}{v_i e} \quad (26)$$

For determination of n' and n'' we use the boundary conditions for electron current

$$J_0 - J = \frac{1}{4} n' v_e e \exp(-\frac{eE'}{T_e}) \quad (27)$$

$$\frac{1}{4} n'' v_e e = J \exp(-\frac{eE''}{T_e}) \quad (28)$$

Multiplying member by member (27) and (28) and using (26) we obtain:

$$n' = \frac{(J_0 - J) j \frac{4}{v_i e} \frac{u_i}{u_e}}{J_0 - J [1 + \exp(-\frac{e\Delta V}{T_e})]} \quad (29)$$

$$n'' = \frac{j^2 \frac{4}{2i} \frac{u_i}{u_e} \exp\left(-\frac{e\Delta V}{T_e}\right)}{j_0 - j \left[1 + \exp\left(-\frac{e\Delta V}{T_e}\right)\right]} \quad (30)$$

where neglecting the potential drop we assume $E' - E'' \approx \Delta V$

Taking into account (29), (30) and (24) the ionization losses will be written in the form:

$$S = \frac{1}{e} T_e \varepsilon j \frac{j_0 - j \left[1 - \exp\left(-\frac{e\Delta V}{T_e}\right)\right]}{j_0 - j \left[1 + \exp\left(-\frac{e\Delta V}{T_e}\right)\right]} \quad (31)$$

where

$$\varepsilon = 2 \frac{u_i}{u_e} \frac{E_i + \frac{5}{2} \frac{T_e}{e}}{\frac{T_e}{e}}$$

5. VOLT-AMPERE CHARACTERISTICS

Note that in (31) the coefficient $\varepsilon \ll 1$ because $\frac{u_i}{u_e} \sim \sqrt{\frac{m}{M}}$. So when the denominator of (31) differs from zero the ionization losses in Equation (8) can be neglected. As a result we obtain

$$j\Delta V = \text{const} \quad (32)$$

where

$$\text{const} = 2 \frac{T_e - T'}{e} j_0 \quad ($$

Equation (32) represents a branch of a volt-ampere characteristic with negative resistance. Since $\varepsilon \ll 1$, the ionization losses (S) will be significant only in the case when the denominator of (31) is close to zero, i.e. at

$$j \approx \frac{j_0}{1 + \exp\left(-\frac{e\Delta V}{T_e}\right)} \quad (33)$$

Formula (33) may be considered as an approximate volt-ampere characteristic at large ionization losses. It corresponds to the normal branch of a positive resistance volt-ampere characteristic.

In general case using (8) and (33) and neglecting S'' we get the following quadratic equation for the volt-ampere characteristics:

$$I^2 [\Delta U (1 + e^{-\Delta U}) - \varepsilon (1 - e^{-\Delta U})] + I [\varepsilon - (1 + e^{-\Delta U}) \tau - \Delta U] + \tau = 0 \quad (34)$$

where

$$\Delta U = \frac{e\Delta V}{T_e}, \quad I = \frac{j}{j_0}, \quad \tau = 2 \frac{T_e - T'}{T_e}$$

The dependency I on ΔU , obtained from the solution of this equation at different values of ε , is given in Fig. 4. At $\varepsilon \neq 0$ the point of turning on the characteristic can be found from the condition that the discriminant of Equation (34) equals to zero. At $\varepsilon = 0$ two solutions of Equation (34) coincide correspondingly with (32) and (33) (see dash-line in Fig. 4). These curves cross at the point $j = 0.78 j_0$, $e\Delta V = 1.27 T_e$.

At high temperatures the ignition occurs under the conditions of sufficient overcompensation when the current in the predischage condition can be compared to j_0 in value. If the magnitude of this current surpasses the value of the current at the point of turning of the volt-ampere characteristics the branch with negative resistance vanishes (compare Fig. 2). The volt-ampere characteristics given in Fig. 4 have the saturation as the emission current was assumed constant in the calculation. As a matter of fact, with the increase of cathode drop the emission current increases (Schottky effect).

The consideration of this phenomenon leads to the volt-ampere characteristics shown in Fig. 5.

R E F E R E N C E S

- 1 Стаханов И.П., Пашенко В.П., Гуськов Ю.К., Лебедев М.А.
"Состояние исследования физических процессов в термоэмиссионных преобразователях энергии" Доклад на I Международную конференцию по термоэмиссионному преобразованию энергии Лондон 1965г.
- 2 Г.А.Дожев и др. "Исследование вольт-амперных характеристик термоэмиссионных преобразователей" ЖТФ 35 II /1965/ 2054
- 3 Г.А.Дожев и др. "Зондовые исследования плазмы в термоэмиссионных преобразователях с высоким давлением паров цезия" ЖТФ 36 4 /1966/ 679
- 4 Г.А.Дожев и др. "Зондовые исследования плазмы в термоэмиссионных преобразователях с высоким давлением паров цезия" ЖТФ 36 9 /1966/ 1685
- 5 N.S. Rasor. Conf. Thermoionic Electrical Power Generation London (1965).

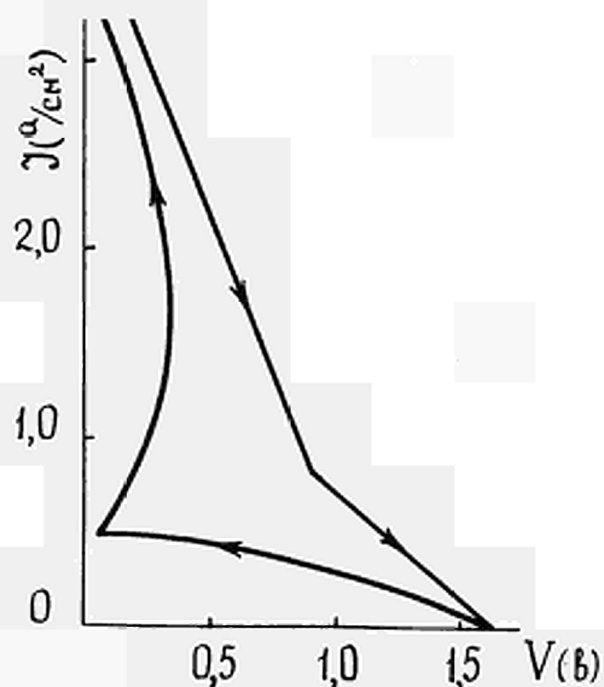


Fig. 1. Arc ignition at low cathode temperatures ($\rho = 2$ mm Hg, $T^c = 1710^\circ\text{K}$).

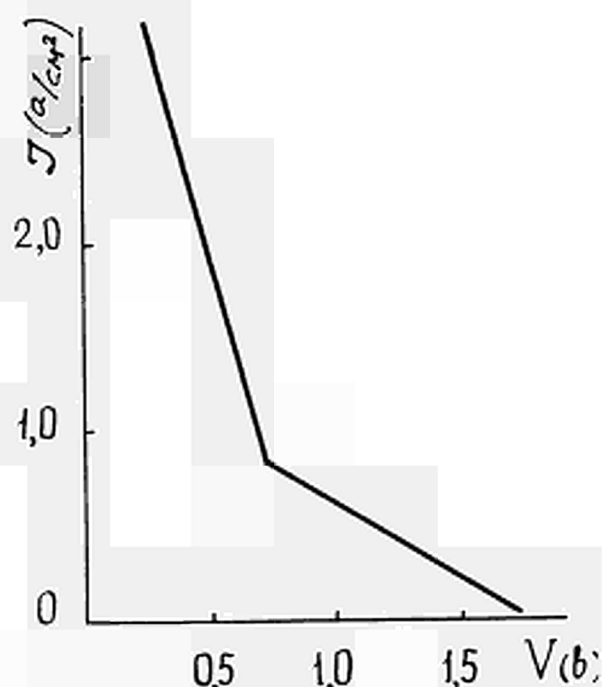


Fig. 2. Arc ignition at high cathode temperatures ($\rho = 2$ mm Hg, $T^c = 1760^\circ\text{K}$).

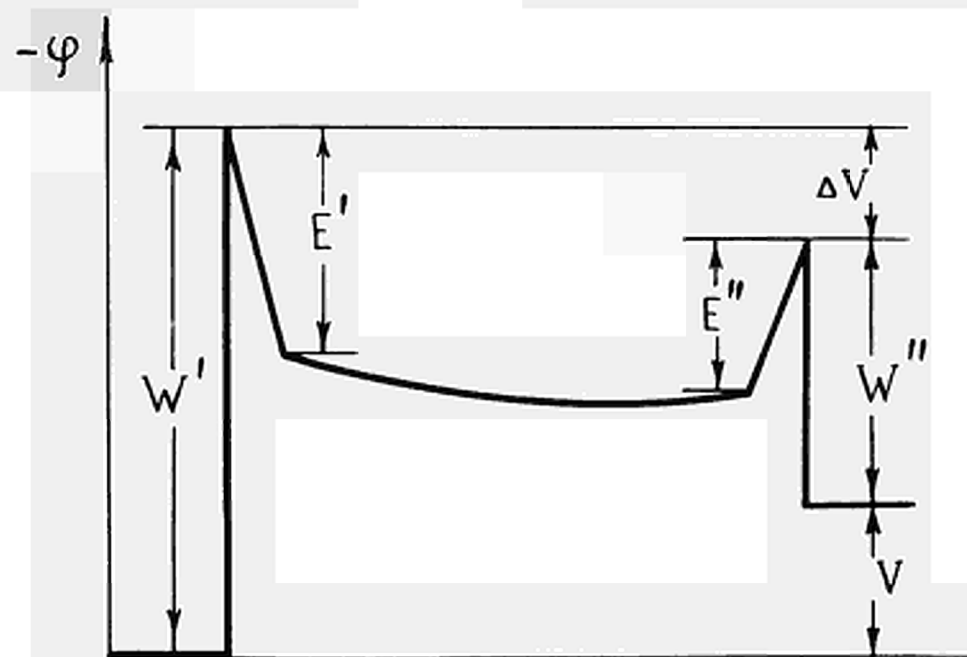


Fig. 3. Schematic potential distribution in the interelectrode space

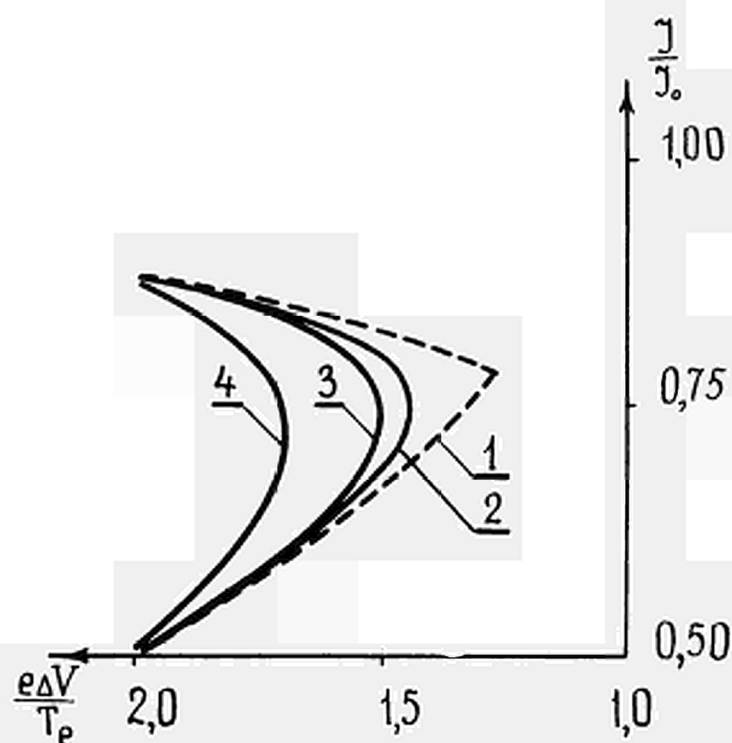


Fig. 4. Volt-ampere characteristics of low voltage arc calculated according to (34) for different ε : curve 1 $\varepsilon=0$; curve 2 $\varepsilon=0.02$; curve 3 $\varepsilon=0.04$; curve 4 $\varepsilon=0.10$.

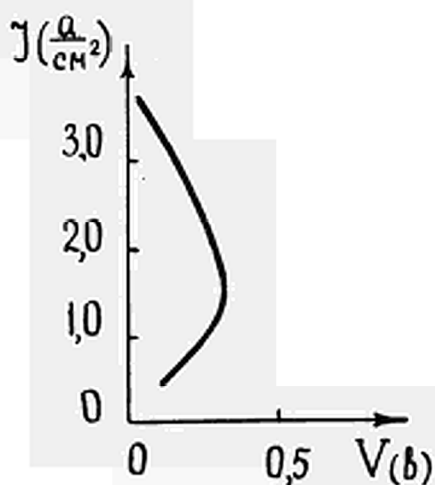


Fig. 5. Volt-ampere characteristics calculated with consideration of Schottky effect.



TWO TYPES OF POTENTIAL DISTRIBUTION IN COLLISIONLESS
MODE OF THERMIONIC CONVERTER OPERATION IN THE PRESENCE
OF A TRANSVERSE MAGNETIC FIELD

A.Ender

A.F. Ioffe Physical Technical Institute, Academy of
Sciences of the USSR , Leningrad , USSR

In the collisionless mode of thermionic converter operation considerable losses resulting from magnetic field effect are observed.

This phenomenon was investigated in detail by A.Shock (see J.Appl.Phys. 31 ,1960, 1978). In the paper mentioned it was assumed that the potential distribution across a gap is given beforehand and corresponds to constancy of the electric field.

Now , in a general case the potential distribution between any point in an interelectrode gap and the cathode may belong to two types: Type A , when the number of electrons , reaching the point in question , doesn't depend on distribution pattern , and Type B , when such a dependence exists. We obtained intermediate (relative to Types A and B) distribution of potential for arbitrary coordinates of point considered on the potential plot and arbitrary magnetic field.

Obtaining general solution of the self-consistent

task in the presence of magnetic field presents great difficulties. Nevertheless, for the majority of conditions observed in a converter operating in the collisionless mode this task as we managed to prove may be completely solved.

In the collisionless mode of thermionic converter operation plasma is generated on a cathode, electrons being supplied by thermionic emission and ions-by surface ionization. In /3/ it is shown that the electrode sheaths which are present during the operation of the converter in a transverse magnetic field can influence to a considerable extent its current-voltage characteristics. In particular, it is shown that in the presence of the electron retarding anode sheath, i.e. the plasma potential exceeds the anode potential, the current passing through the converter doesn't depend on the plasma potential and is determined by that of the anode. Note that the number of electrons reaching the anode, doesn't depend on the electron pre-history, i.e. it remains the same for a whole group of potential distributions.

Examples of such distributions equivalent for the passing current (see /3/) are shown in Fig. 1; the cathode is taken for the origin of coordinates, z-axis is directed to the anode, y-axis coincides with the direction of the magnetic field and the potential axis - φ is directed downward.

If there exists an electron accelerating sheath at the anode, in the presence of a magnetic field in the con-

verter the current passing through the converter doesn't depend on the anode potential and it is determined by the plasma potential on the boundary of the anode region.

Consequently , there exist such potential distributions at which the current passing through the converter essentially depends on the distribution pattern.

One may ask , what is the shape of the potential distribution intermediate between the two types of those described above. Such a question is valid not only for the anode but also for any point $-z$ placed in the interelectrode gap. Indeed the potential distribution between the point considered and the cathode may belong to one of the two types, namely: the potential distribution of the A-type , when the number of emitted electrons reaching the chosen point is determined only by the strength of the magnetic field and by the potential difference between this point and the cathode; the potential distribution of the B-type which differs from the A-type in that the number of electrons reaching the point in question strongly depends on the pattern of the potential distribution between the point and the cathode.

Let us find now the potential distribution $\tilde{\varphi}(z)$ intermediate between A- and B-types provided that the point considered is placed on the anode. Let's suppose that we have a potential distribution $\varphi(z)$ which can be approximated by a certain number of segments with constant electric field strength. Accordingly , we'll denote the dividing points as $0, 1, 2 \dots n$, k -th point having coordinates (Z_k, φ_k) and

n-th point being placed on the anode.

The electron velocity at each point of division will be defined in terms of velocity in the immediate vicinity of the cathode (see /3/). For the point 1 we have

$$\begin{aligned} V_{z_1}^2 &= V_{z_0}^2 - (\omega z_1)^2 + 2\omega z_1 V_{x_0} + \frac{2e\varphi_1}{m} \\ V_{x_1} &= V_{x_0} - \omega z_1 \end{aligned} \quad (1)$$

Here V_{x_0} , V_{z_0} , V_{x_1} , V_{z_1} are components of the electron velocity at the zero point and the first point, respectively, φ_1 is the potential of the point 1, $\omega = \frac{eH}{m}$. The point will be reached by the electrons the velocities of which at the cathode belong to the region Ω_1

$$V_{z_0}^2 - (\omega z_1)^2 + 2\omega z_1 V_{x_0} + \frac{2e\varphi_1}{m} \geq 0 \quad (2)$$

If the electron has reached the point 1, its velocity at this point may be taken for an initial velocity when it moves towards the point 2 and consequently we can define the electron velocity at the point 2 in terms of its velocity at the point 1

$$\begin{aligned} V_{z_2}^2 &= V_{z_1}^2 - \omega^2 (z_2 - z_1)^2 + 2\omega (z_2 - z_1) V_{z_1} + \frac{2e}{m} (\varphi_2 - \varphi_1) \\ V_{x_2} &= V_{x_1} - \omega (z_2 - z_1) \end{aligned} \quad (3)$$

Using (1), one can define the electron velocity at the point 2 in terms of its velocity at the cathode

$$\begin{aligned} V_{z_2}^2 &= V_{z_0}^2 - \omega^2 z_2^2 + 2\omega z_2 V_{x_0} + \frac{2e\varphi_2}{m} \\ V_{x_2} &= V_{x_0} - \omega z_2 \end{aligned} \quad (4)$$

Hence it follows that the point 2 will be reached by those electrons passing through the point 1, the velocities of which belong to the region Ω_2

$$V_{z_0}^2 - \omega^2 z_2^2 + 2 \omega z_2 V_{x_0} + \frac{2e\varphi_2}{m} \geq 0 \quad (5)$$

Similarly, for the k-th point we may define Ω_k

$$V_{z_0}^2 - \omega^2 z_k^2 + 2 \omega z_k V_{x_0} + \frac{2e\varphi_k}{m} \geq 0 \quad (6)$$

This region has the following meaning: if the electron has passed all the preceding points of division, including k-1, and if its velocity at the cathode belongs to Ω_k , it will reach the k-th point.

Evidently, if each preceding region contains each succeeding region, i.e. the condition

$$\Omega_n \subset \Omega_{n-1} \subset \Omega_{n-2} \subset \dots \subset \Omega_2 \subset \Omega_1 \quad (7)$$

is satisfied, the number of electrons emitted from the cathode getting in a certain point of division, doesn't depend on the electron prehistory, i.e. the potential distribution is of A-type for all the points in the interelectrode gap. If the condition (7) is satisfied, the current passing through the converter will be determined only by the region Ω_n :

$$V_{z_0}^2 - (\omega D)^2 + 2 \omega D V_{x_0} + \frac{2e}{m} \varphi_c \geq 0 \quad (8)$$

Here $D = z_n$ is the distance between the cathode and the anode, $\varphi_a = \varphi_n$ is the anode potential. The current will depend only on the anode potential even in case when a less stringent condition

$$\Omega_n \subset \Omega(z) \quad (9)$$

is satisfied for all the values of z.

It can be shown that the above expression implies the following inequalities

$$\frac{1}{2\omega z} \geq \frac{1}{2\omega D} \quad \text{and} \quad \frac{\omega z}{2} - \frac{e\varphi(z)}{m\omega z} \leq \frac{\omega D}{2} - \frac{e\varphi_c}{m\omega D} \quad (10)$$

The first of these inequalities is fulfilled automatically and the second one when it becomes an equality, determines the needed potential distribution $\tilde{\varphi}(z)$, i.e. the boundary distribution intermediate between numerous potential distributions of the A- and B- types relative to the anode

$$\tilde{\varphi}(z) = \varphi_c \left[\frac{z}{D} + \delta \sigma\left(\frac{z}{D}\right) \right] \quad (11)$$

Here $\delta = \frac{\omega^2 m D^2}{2e\varphi_a}$ and $\sigma\left(\frac{z}{D}\right) = \left(\frac{z}{D}\right)^2 - \frac{z}{D}$

If H is measured in oersteds, D - in mm and φ_a in volt we'll get $\delta = \frac{9 \cdot 10^{-4} H^2 D^2}{\varphi_a}$ for dimensionless parameter.

Fig. 2 represents the relationship $\tilde{\varphi}(z)$ at $\varphi_a = 0.9$ v and for three values of δ : $\delta = 0.1$ ($H \times D = 10 \text{ oe} \times \text{MM}$); $\delta = 1$ ($H \times D = 33 \text{ oe} \times \text{MM}$); $\delta = 10$ ($H \times D = 100 \text{ oe} \times \text{MM}$).

Thus, if at a given anode potential and at constant strength of an external magnetic field condition $\varphi(z) \geq \tilde{\varphi}(z)$ is satisfied, the current passing through the anode doesn't depend on the potential distribution

In an overcompensated mode of the thermionic converter the potential distribution belongs to the A-type either for all the points in an interelectrode gap (at small anode potential values, $\varphi_a < \varphi_p$) or for the majority of points in an interelectrode gap with the exception of a narrow anode sheath (at large values of anode potential $\varphi_a > \varphi_p$).

In the first case the current passing through the converter is determined by the anode potential , in the second case it is determined by the plasma potential at the boundary of the anode sheath. Therefore , in order to get current-voltage characteristics of the converter in a transverse magnetic field one should calculate the potential of a point placed at the anode sheath boundary.

For a potential distribution of the A-type electron concentration at any point may be determined in a general form from the concentration of emitted electrons in the immediate vicinity of a cathode (only the electrons emitted from the cathode are taken into account). Magnetic field practically doesn't influence ions , hence , their concentration depends only on potential of the chosen point.

The plasma potential may be calculated on the basis of the plasma neutrality condition for any region except narrow sheaths near electrodes. In particular , it may be calculated for the anode region boundary.

After the calculations mentioned above the current passing through the converter is determined by means of relatively simple expressions.

Current-voltage characteristics have been drawn for several values of the magnetic field strength and several values of overcompensation ratio γ , the latter being equal to the ratio of ion and electron concentrations at the cathode. In Fig. 3 current-voltage characteristics of the converter are presented corresponding to constant magnetic

field strength ($S=2$) and to several values of the overcompensation ratio. Here $S = \frac{eHD}{(2mkT)^{1/2}}$

The distinguishing feature of current-voltage characteristics in a magnetic field when collisionless plasma is present in the interelectrode gap is the dependence of saturation current on the magnetic field strength.

On the basis of a great number of calculated current-voltage characteristics the dependence of saturated current on the magnetic field strength at different values of the overcompensation ratio was obtained (Fig. 4).

Owing to strong dependence of the curves obtained on this parameter we may experimentally determine ion flow from the cathode surface directly in a working mode of the thermionic converter.

REFERENCES

- (1) SHOCK A.J., J.Appl.Phys. 31 (1960) , 1978
- (2) KAGANOV M.I., KUCHEROV R.Ya., RICKENGLAZ L.E. ,
MTΦ 31 , (1961) , 588
- (3) ENDER A.Ya. MTΦ (to be published)

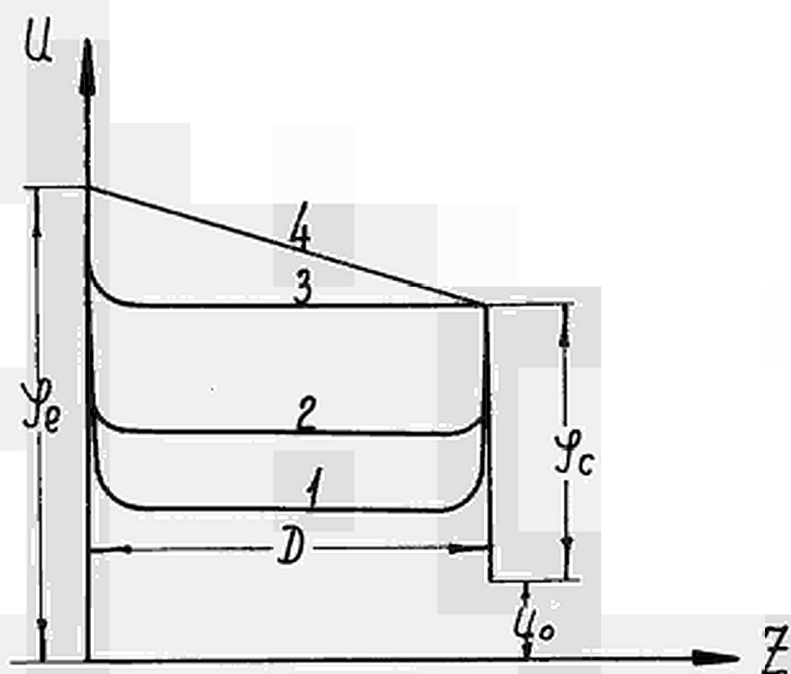


Fig.1

Examples of different potential distributions which are characterized by the same value of current in the presence of a magnetic field.

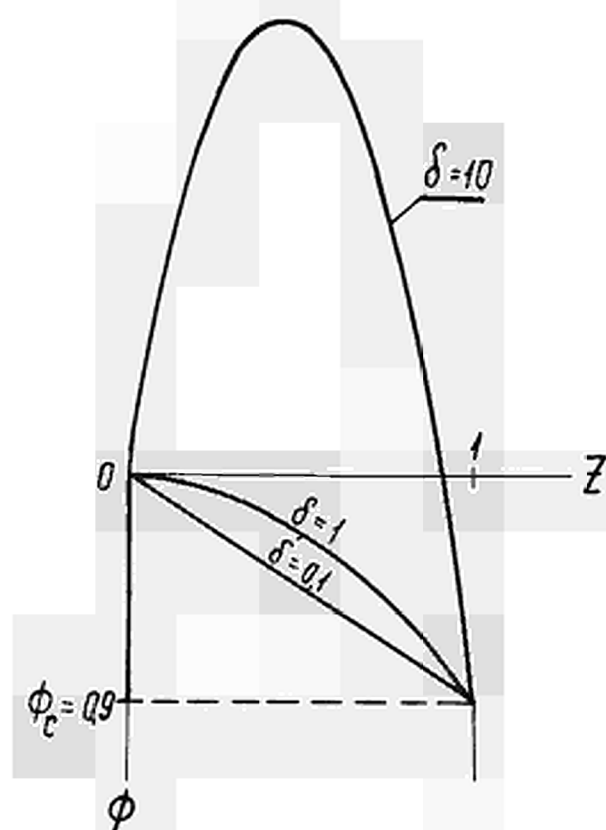


Fig. 2

Potential distribution $\tilde{\varphi}(z)$ intermediate between potential distributions of the A- and B-types for three values of the parameter δ .

($\delta = 0.1$; $H \times D = 10$ oersteds \times mm
 $\delta = 1$; $H \times D = 33$ oersteds \times mm
 $\delta = 10$; $H \times D = 100$ oersteds \times mm)
 and $\varphi_c = 0.9$ V

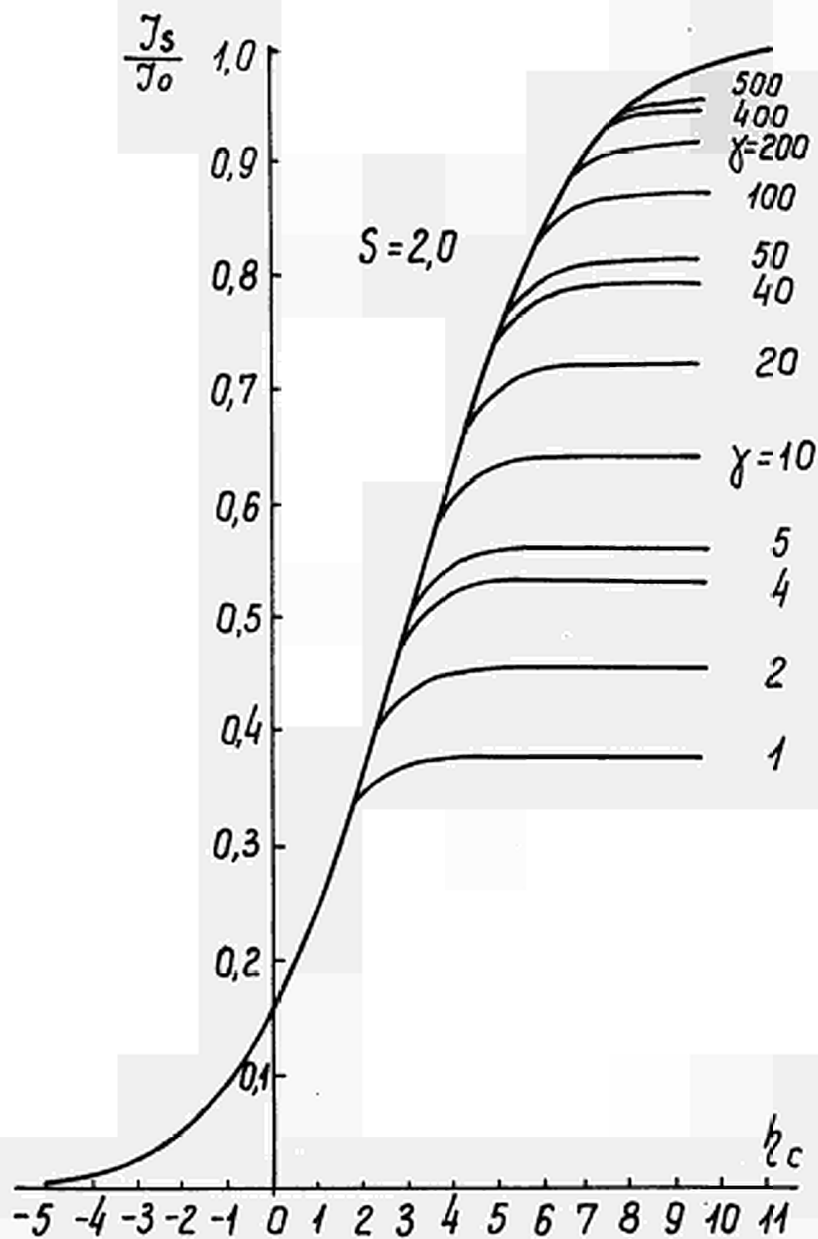


Fig. 3

Theoretically computed current-voltage characteristics of the ideal collisionless thermionic converter placed in a transverse magnetic field $S = 2$, at different values of γ ; $\eta_c = \frac{e \Phi_c}{\kappa T}$

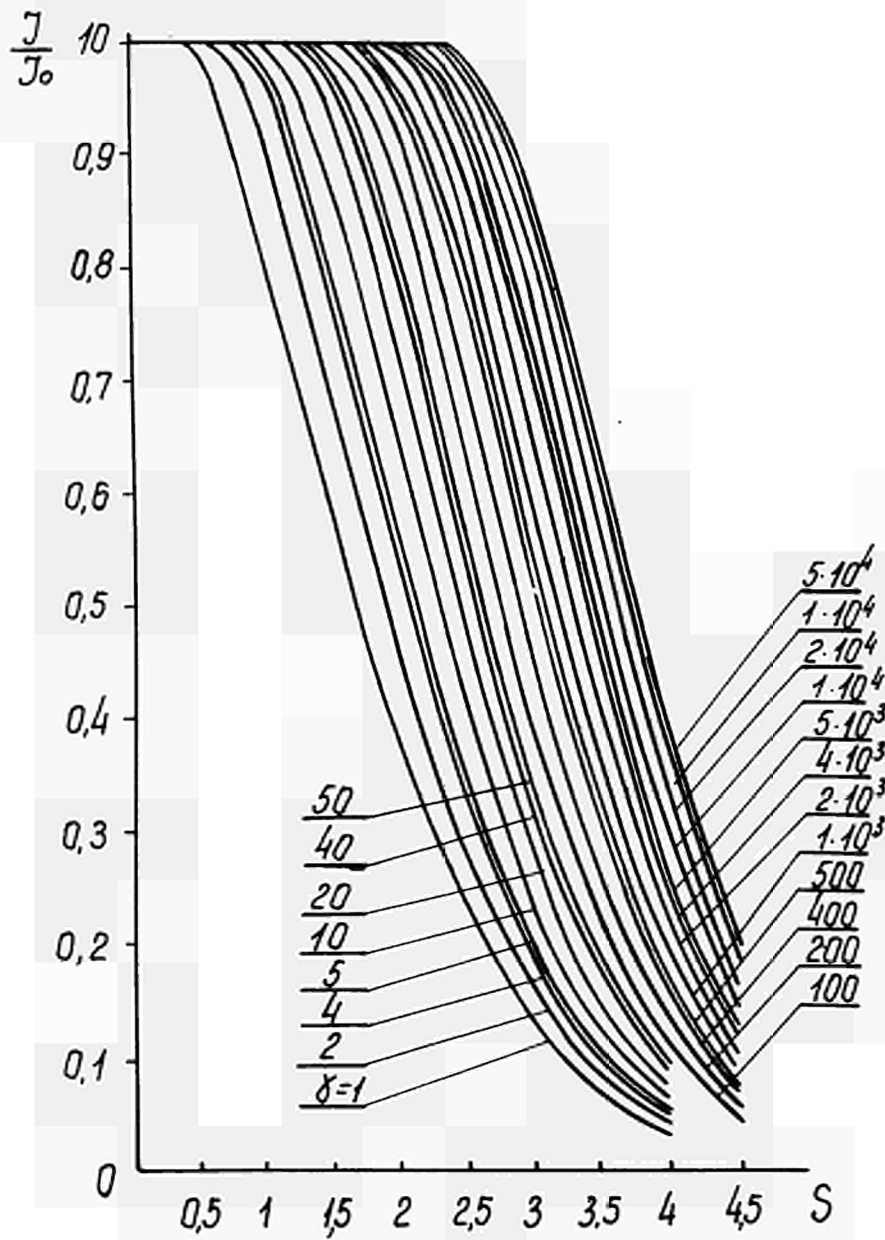


Fig. 4

Dependence of dimensionless saturation current ($\frac{J_s}{J_0}$)
in a magnetic field on S at various values of γ

I_0 - emission current from the cathode

EFFECT OF CESIUM PRESSURE ON THERMIONIC STABILITY*

A. Schock
Republic Aviation Division of Fairchild Hiller Corporation
Farmingdale, New York

Abstract

It is shown that under certain conditions of heat input, reservoir temperature, and load voltage or resistance a thermionic converter can equilibrate at two radically different operating points, corresponding to conditions of high and low cesium coverage. Moreover, abrupt transitions between these operating regimes, accompanied by a temperature rise of hundreds of degrees, can occur whenever the critical heat generation rate for a given reservoir temperature is exceeded. To provide adequate safety margin against such an occurrence, thermionic systems must be operated at relatively high cesium pressures, even though this may cause some performance degradation.

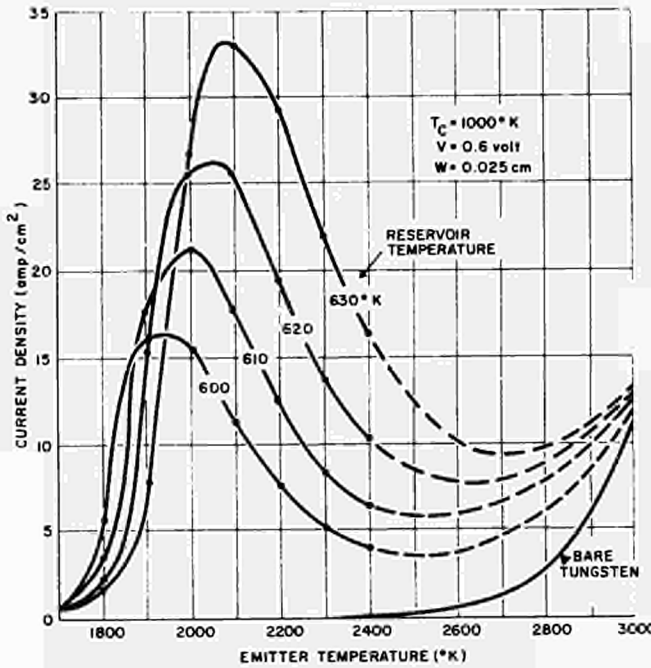
It is customary for thermionic system designers to choose the optimum operating point by maximizing some figure of merit, such as power density, efficiency, or power per unit weight. The present paper seeks to demonstrate that the choice of operating parameters, particularly the cesium reservoir temperature, must also take account of a factor we shall refer to as "thermionic stability." In fact, under certain conditions this factor must dominate over other considerations in order to achieve a stable system and avoid excessive temperature excursions.

In practical applications, thermionic converters typically operate under conditions of constant voltage or constant load resistance. Under these conditions relatively small perturbations of load or heat input can lead to extensive desorption of cesium, with a consequent large rise in emitter temperature. We designate this phenomenon as "thermionic burnout" because of its similarity to burnout in boiling heat transfer. This condition had been postulated by the author in an earlier paper⁽¹⁾ on the basis of purely qualitative arguments. The recent development of the SIMCON code⁽²⁾ for the theoretical extrapolation of thermionic performance data over a very wide range of temperatures has made it possible to demonstrate this effect on a quantitative basis.

* Work supported by U.S. Atomic Energy Commission

To clarify the subsequent discussion, let us first examine typical curves of current density versus emitter temperature, as illustrated by Figure 1. All data are for a tungsten emitter (with a 4.75-ev bare work function) and a 1000°K - molybdenum collector, separated by a 0.025-cm gap. The bottom curve represents the saturated emission of the bare tungsten emitter. The other curves are for a fixed converter potential of 0.6 volt, and represent constant cesium reservoir temperatures of 600, 610, 620, and 630°K, respectively.

Fig. 1: Effect of Temperature on Current Density



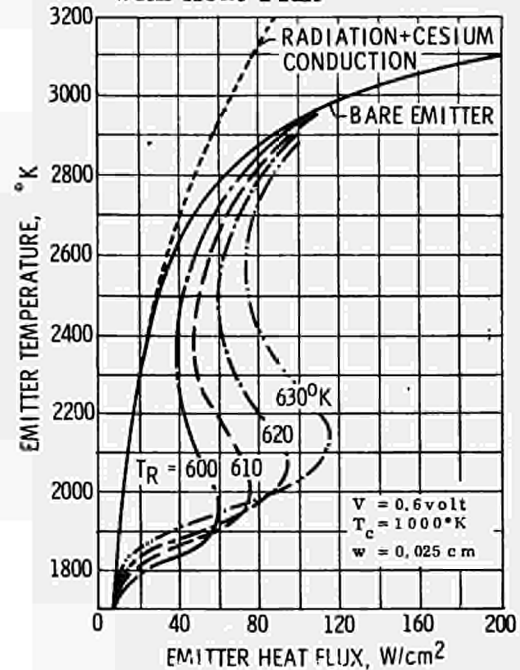
For emitter temperatures up to 2400°K, the curves were produced by a special "thermionic correlation" (TICORR) computer code. The program operates on a large array of SIMCON-generated⁽²⁾ current-voltage heat flux data, covering a wide range of emitter temperatures (1700-2400°K), collector temperatures (850-1150°K), and reservoir temperatures (550-690°K). TICORR performs multi-dimensional interpolations, and automatically produces a wide variety of cross-plots, not only of the above six parameters but also of power density, efficiency and specific load conductance.

Construction of the curves above 2400°K was based on the fact that each curve must asymptotically approach the "bare emitter" curve at sufficiently high temperatures. Since the subsequent discussion is primarily concerned with the qualitative nature of the effect, it is sufficient to draw smooth transitions between the TICORR plots and the "bare emitter" curve, as illustrated by the dashed curves in Figure 1.

Each of the constant cesium pressure curves passes through a maximum and a minimum. As in the case of Langmuir S-curves, this comes about because cesium desorption increases the emitter work function at higher temperatures.

Figure 2 presents a plot of emitter temperature versus heat flux, corresponding to the data shown in Figure 1. The left-most curve represents the emitter heat flux due to radiation and cesium conduction. (Actually, cesium conduction varies with reservoir temperature, but this variation is generally small compared with the total heat flux.) The curve marked "bare emitter" contains the additional heat flux due to saturation-current electron cooling from the uncesiated tungsten surface. As can be seen, at very high temperatures this makes a quite appreciable contribution.

Fig. 2. Variation of Temperature with Heat Flux



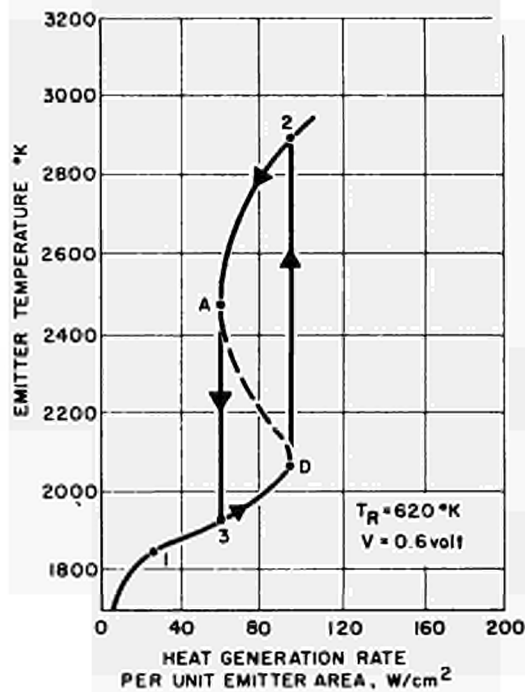
Finally, the constant cesium pressure curves contain the electron cooling heat flux corresponding to the current densities depicted in Figure 1. Each curve again passes through a maximum and a minimum. As would be expected, the temperature at which the maximum heat flux occurs increases with cesium pressure, as does the magnitude of the maximum heat flux.

Before proceeding to the principal subject of this paper, it should be noted that Figure 2 provides a very graphic illustration of the open-circuit temperature rise, which results from loss of electron cooling. The curves reveal that there is a rather substantial difference between a literal open-circuit, i.e. a complete break in the diode-to-load circuit, and the much more likely nominal "open-circuit", i.e. loss of cesium due to a small leak (as long as sufficient cesium remains for space charge neutralization, $\sim 10^{-5}$ torr). This can be seen by comparing the "bare emitter" and the "radiation and conduction" curves in Figure 2.

The distinction, however, is somewhat academic, since the curves show that both a literal and a nominal "open-circuit" would lead to an excessively high temperature rise. This demonstrates the importance of designing the fuel-emitter configuration to provide an alternative cooling mechanism in the event of this type of failure.

To appreciate the significance of the curve shapes shown in Figure 2, let us examine a single such curve, as illustrated in Figure 3. Only this time the abscissa could be interpreted not as the emitter heat flux, but as the heat generation rate per unit emitter area. As can be seen, for any heat generation rate between points A and the various SIMCON equations⁽²⁾ are satisfied at three distinct emitter temperatures, corresponding to high, medium, and low cesium coverage. However, only two of these represent stable operating conditions, since the middle point will be shown to be inherently unstable. At which of the two outer points the converter operates must depend on its previous history.

Fig. 3: Effect of Varying Heat Generation Rate



Consider a converter starting from equilibrium at point 1, whose heat generation rate is increased in a series of small steps, with sufficient time intervals between steps to allow the system to equilibrate. Each increase in heat generation produces a small increase in emitter temperature, until point D (the cesium desorption point) is approached. Any further increase in heat generation, however small leads to a condition in which the generated heat exceeds the heat leaving the emitter, resulting in a steady temperature rise. As the emitter temperature rises, its heat loss rate (which follows the dashed portion of the curve) diminishes. This further increases the lack of equilibrium, causing the temperature rise to accelerate.

Clearly, the temperature will continue to go up until point 2 on the low-cesium-coverage branch of the curve is reached, where equilibrium is re-established. Any further increase in heat generation will cause the operating point to follow the upper branch in a normal fashion.

Conversely, when the heat generation rate is decreased from point 2, the operating point will follow the upper branch until point A (the cesium adsorption point) is reached. Any further decrease in heat generation will cause an abrupt drop in temperature, until equilibrium is re-established at point 3 on the high-cesium-coverage branch of the curve. Thus, the overall cycle is seen to exhibit a hysteresis effect, completely by-passing the middle(negative slope) branch of the curve.

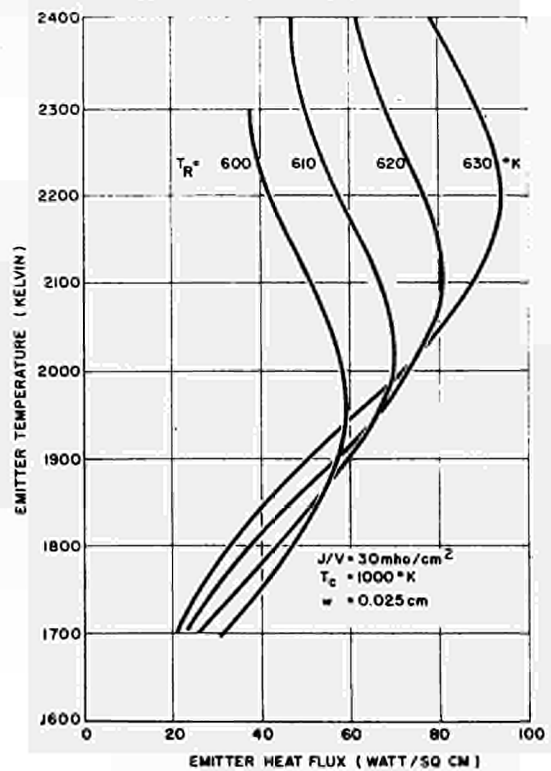
Although it might be possible, by some transient maneuver, to bring the converter to equilibrium at some point on the middle branch of the curve, such equilibrium would be inherently unstable, since even a slight perturbation of the heat generation rate (or load resistance) would drive the converter to either the upper or lower branch of the curve.

The principal significance of the phenomena discussed above is that they introduce an additional constraint in choosing the converter operating point. For example, with a maximum emitter temperature of 2000°K and a 0.6 volt load, Figure 2 shows that it is not practical to employ reservoir temperatures at or below 610°K, even though such temperatures may yield the highest conversion efficiencies.

Even a reservoir temperature of 620°K would provide scant margin for safety, since the diode operating point could be shifted to the high temperature (3000°K) branch of the curve by a minor increase in heat generation rate (e.g., from 87 to 93 watt/cm²). Such small deviations, either spatial or temporal, would be very difficult to avoid in a thermionic reactor. It therefore appears that to operate at 2000°K with a fixed 0.6-volt load one should employ a reservoir temperature of 630°K or more. In that case the "burnout" condition, i.e., the cesium desorption point, is not reached until the heat generation rate increases from 89 to 116 watt/cm², providing a comfortable 30% safety margin.

The precise numbers in the above discussion would vary somewhat for different load voltages, or for a fixed-resistance rather than fixed-voltage load. However, the general principles discussed above would still apply. This is illustrated by Figure 4 for a constant load conductance of 30 mho per cm² of emitter.

Fig. 4: T-q Variation at Constant Load Resistance



Finally, it is of interest to examine the dynamic behavior of a thermionic reactor passing through the cesium desorption point. To do so, we make use of a specialized digital transient analysis code developed at Republic Aviation. The code combines a zero-dimensional nuclear analysis using six delayed neutron groups with a 2-dimensional (rz) thermal analysis of a single thermionic fuel element. The program uses the TICORR code to compute the instantaneous emitter heat flux. It permits step changes in reactivity, separate fuel and emitter temperature feedback coefficients, and ramp insertion of scram rods with programmed time delay.

The code automatically produces plots of heat generation and heat loss rates per unit emitter area; also of reactivity, emitter temperature and maximum fuel temperature. Such computer-produced plots are shown in Figures 5 and 6. Both figures portray the behavior of an open-loop reactor following a 2-cent reactivity step change, and are based on the identical converter geometry (the details of which are not important for the present discussion). The reactivity feedback coefficients were taken to be $+0.001 \phi / ^\circ\text{K}$ for the fuel and $-0.020 \phi / ^\circ\text{K}$ for the emitter, with a 1-microsecond prompt neutron lifetime. Both figures assume a constant collector temperature of 1000°K , and initial equilibrium at an emitter temperature of 2000°K . (The difference between the heat generation and loss rates during the transient has been shaded in both figures, to bring out the net heat surplus or deficit.)

The principal difference between the figures is the postulated cesium reservoir temperature, which is 630°K in Figure 5 and 620°K in Figure 6. In the former case, it is seen that, as the result of the 2-cent reactivity step, the heat gain and loss rates slowly rise from 88 to 113 watt/cm², where a new thermal and nuclear equilibrium is established. During this process, which occurs over a period of several minutes, the emitter temperature rises by approximately 95°K , without any temperature overshoot. Note that the new emitter temperature is still below the cesium desorption point for a 630°K reservoir.

By contrast, consider the effect of the same reactivity perturbation in the case of a 620°K reservoir temperature, shown in Figure 6. As before, the stepped up reactivity produces a prompt jump in heat generation; this causes a gradual rise in temperature, which in turn lowers the reactivity and raises the heat loss rate. However, after 1.5 minutes the cesium desorption point D is passed, and the subsequent loss in cesium coverage causes a sharp drop in the emitter cooling rate. This continues until point A is passed at $t=3.4$ minutes, when the heat loss starts to rise again.

Fig. 5: Effect of 2-Cent Step with 630°K Reservoir

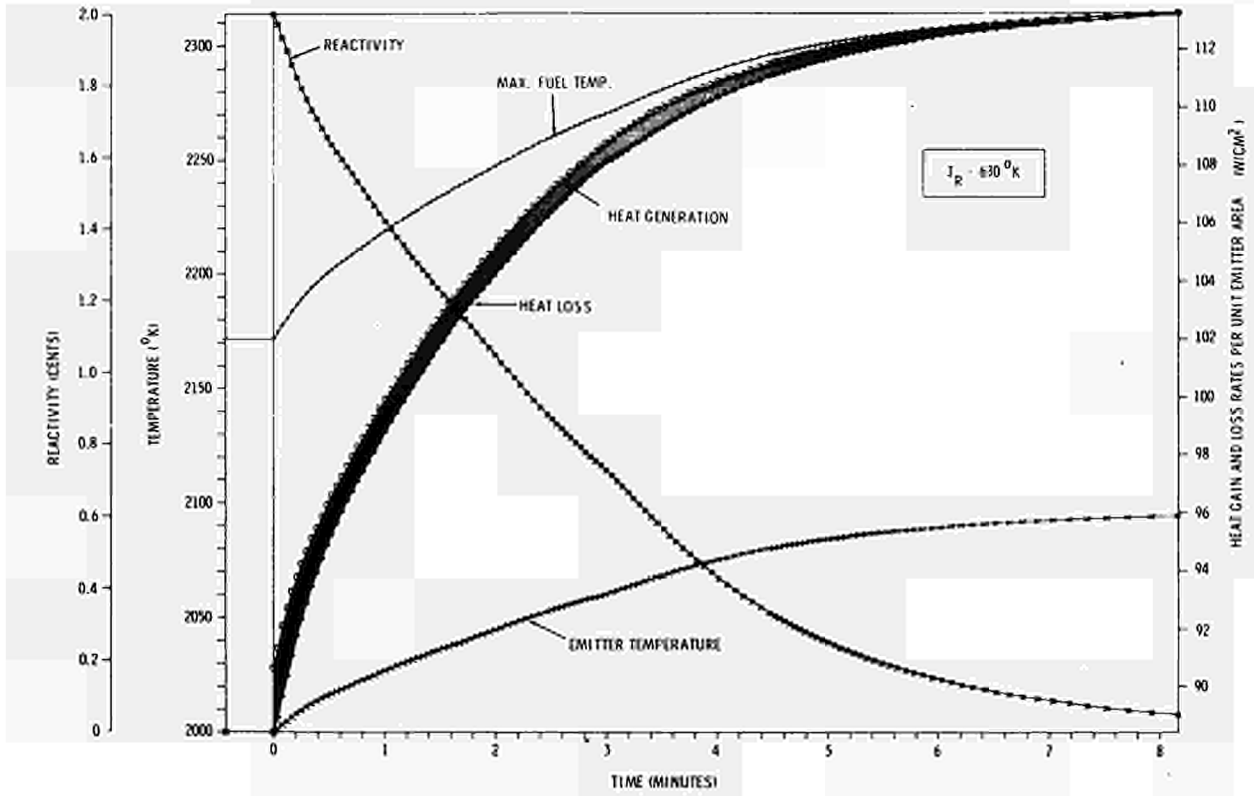
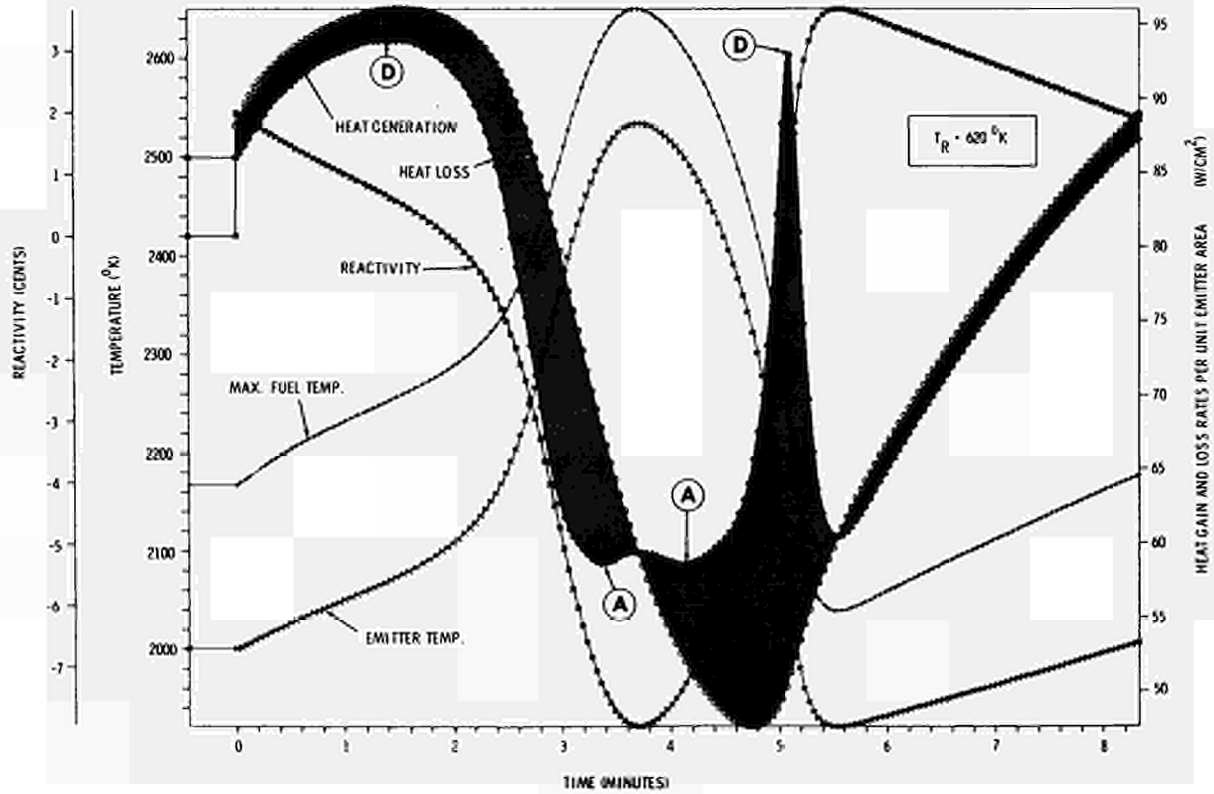


Fig. 6: Effect of 2-Cent Step with 620°K Reservoir



Meanwhile, because of the large heat surplus, the emitter and fuel temperatures have risen by hundreds of degrees. As a result of the emitter feedback coefficient, the reactivity drops sharply (passing through the criticality point at $t = 1.9$ minutes), leading to a decrease in the heat generation rate. Eventually, at $t = 3.7$ minutes, the heat gain and loss rates cross, the emitter and maximum fuel temperatures peak at 2534 and 2650°K respectively, and the reactivity bottoms at -7.98 cents.

The subsequent heat deficit causes the temperature to diminish slowly until, at $t = 4.1$ minutes, the cesium adsorption point A is passed again. After this, the increased cesium coverage produces a sharp increase in the heat loss rate, with a corresponding drop in temperature.

At $t = 5.1$ minutes point D is passed, and the heat loss rate drops abruptly, until it crosses the rising heat production curve at $t = 5.5$ minutes, at which point the emitter temperature reaches a low point of 1920°K and the reactivity peaks at +3.5 cents. Although Figure 6 is cut off at 8 minutes, extended computations have shown that the cycle essentially repeats indefinitely. Within the assumptions of the particular problem, there is no damping mechanism and the system would never reach equilibrium.

In a sense, the results presented are somewhat reassuring, since they show that the various changes occur quite slowly, allowing ample time for the control system to react. This relative sluggishness arises from the high heat capacity of the fuel-emitter assembly. It may therefore be argued that the problem is not really of practical interest, since the type of transients described above would be prevented by the control system. The argument is flawed for two reasons: Even if it is feasible to do so, it is not very desirable to operate a basically unstable system, where the control system must be constantly active to prevent small perturbations from causing large temperature excursions.

Moreover, even if it were practical to avoid the above type of transients for the reactor as a whole, this still would leave the problem of undetected "burn-out" in individual converters. That would be a danger if the design operating point were close to the cesium desorption point, since some variation among converters is unavoidable. The transient studies therefore confirm the desirability of operating at a higher cesium pressure, i. e., 630°K in the present instance, to provide a reasonable margin of safety.

Acknowledgments:

The author wishes to express his thanks to Mr. C. L. Eisen for his valuable help, particularly in the construction of the transient analysis program, and to Dr. D. R. Wilkins for furnishing the tables of SIMCON-generated thermionic performance data.

References

- (1) SCHOCK, A. , "Effect of Non-Uniform Heat Generation on Thermionic Reactors," Proceedings of the Thermionic Conversion Specialist Conference , November 1966.
- (2) WILKINS, D. R. , "An Improved Theoretical Description of Thermionic Converter Performance Characteristics," Report on Twenty-Seventh Annual Conference Physical Electronics, M.I.T. , Cambridge, Massachusetts, March 1967.

ON THE THEORY OF ELECTRODE LAYER OF PLASMA [1]

I.P. Stakhanov, P.P. Scherbinin

Institute of Physics and Power
Engineering
Obninsk, USSR

1. Within Langmeur's cathode layer at the arc regime there is a drop of the potential which retards the electrons leaving the plasma. The value of this cathode drop E_0 is well above the heat energy both of ions (T) and electrons (T_e). Because of this the electron distribution function near by the cathode is very close to the Maxwellian distribution except the high energy region $E \geq E_0$ where the electron function is perturbed by the cathode. The ions leaving the plasma are not retarded by Langmeur's layer and, thereby, the ion function may differ from the Maxwellian one essentially. The relaxation of the ion function to the equilibrium function must be over the distances of an order of a free path length. We shall assume that the free path length is well above the width of Langmeur's layer " a ".

2. In case of the plasma ionisation low rate in the region close to the cathode the ion-atom collisions will prevail. Therefore the atom distribution function may be considered rather accurately equal to the Maxwellian function (with the temperature T). Then a kinetic equation for the ion function can be written as the following:

$$v \frac{\partial f}{\partial x} + \frac{e}{M} \mathcal{G} \frac{\partial f}{\partial v} = \frac{n f_0 - f}{\tau} \quad (1)$$

where v - the velocity along x axis,

$$n = \int_{-\infty}^{\infty} dv f(v, x) \quad (2)$$

$$f_0 = \left(\frac{M}{2\pi T} \right)^{\frac{1}{2}} e^{-\frac{Mv^2}{2T}} \quad (3)$$

τ - the relaxation time of the ion function which we assume independent on the velocity.

So in (1) it has been assumed that the atoms of the plasma are like a reservoir absorbing ion energy and impulse.

As it has been said above the electron function is very close to the equilibrium one; then electron density and the electric field in the plasma are bound with the barometer formula. From this it follows that in the quasineutrality region next equation is available:

$$\mathcal{G} = -\frac{T_e}{e} \frac{1}{n} \frac{dn}{dx} \quad (4)$$

In the case of the arc the surface ionisation on the cathode can be neglected when comparing with the volumetric one. Then the ion flow into the plasma may be put equal to zero, namely

$$f(v, 0) = 0, \quad v > 0 \quad (5)$$

3. If the electric field is not taken into account then the equations (1), (2) are simply one linear integro-differential equation with an unknown function $f(v, x)$. Making Fourier's transformation in the halfspace $x \geq 0$ and using the boundary condition (Eq. (5)) one can reduce Eqs. (1), (2) to a singular integral equation:

$$f(u)\lambda(u) = \frac{e^{-u^2}}{\sqrt{\pi}} \int_0^{\infty} \frac{dt t f(t)}{t-u} \quad (6)$$

where

$$\lambda(u) = 1 + \frac{u}{\sqrt{\pi}} \int_{-\infty}^{\infty} \frac{dt e^{-t^2}}{t-u}, \quad (7)$$

$$f(u) \equiv f(u, 0)$$

$$u = -\frac{v}{v_0}, \quad v_0 = \sqrt{\frac{2T}{M}}$$

Moreover, it is proved that the distribution function of the ions going out of the plasma $f(u)$ is bound with $N(k)$ (Fourier's transformation of the ion density) with the following equation:

$$f(u) = \frac{\sqrt{2} e^{-u^2}}{u} N\left(\frac{i}{u}\right) \quad (8)$$

Equation (6) can be reduced to the Riemann-Hilbert problem the solution of which gives:

$$f(u) = \sqrt{\frac{2}{\pi}} n(0) \frac{e^{-u^2}}{X(-u)} \quad (9)$$

where

$$X(-u) = \frac{1}{u} \exp \left[\int_0^{\infty} \frac{dt}{t+u} \left(\frac{1}{\pi} \operatorname{Arctg} \frac{\sqrt{\pi} t e^{-t^2}}{\lambda(t)} - 1 \right) \right] \quad (10)$$

The functions $f(u)$ and $X(-u)$ are plotted in Fig. 1. For the ion flow (j) the next equation is received:

$$j = - \frac{n(0) \bar{v}}{4} \cdot \sqrt{2\pi}, \quad (11)$$

where $\bar{v} = \sqrt{\frac{8T}{\pi M}}$ - the velocity along x axis, $n(0)$ - the ion density at the boundary.

Calculating some momenta of the distribution function (9) one finds mean ion energy corresponding to x velocity component equal to $0.7T$ at the boundary instead of $\frac{T}{2}$ in the case of the equilibrium distribution. The mean energy carried out of the plasma by an ion is equal to $2.27T$. Let us notice here that for $u > 1$ the function (9) is well approximated by the function

$$f(u) \approx \sqrt{\frac{2}{\pi}} n(0) (u+1) e^{-u^2}$$

The momenta of this function are close to those of function (9) with the precision more than 0.5%.

4. The electric field influence is possible to be taken into account by replacing in the nonlinear term of Eq. (1) the function $f(v, x)$ by its equilibrium expression $n f_0$. Then Eq. (1) can be reduced to the linear one and solved by the method described previously. In this approach the electric field does not influence the ion function at the boundary. Because of this Eqs. (9), (11) do not change. However, the electric field changes the space behavior of the ion function. The latter can be obtained by replacement in Eq. (8) the function $f(u)$ by the function

$$f(u) + \frac{T_e}{T} n(0) f_0(u)$$

It results in:

$$n(\xi) = \frac{n(0) \sqrt{2}}{1 + \frac{T_e}{T}} \left[\xi + 1,016 + \frac{T_e}{\sqrt{2} T} - n_2(\xi) \right], \quad (12)$$

where $\xi = \frac{x}{v_0 \tau}$. The function $n_2(\xi)$ is shown in Fig. 2. The electric field can be calculated from Eqs. (4), (12). The space potential distribution is plotted in Fig. 3. The potential drop at the distances of about the free path length ($v_0 \tau$) near by the cathode is equal to T_e approximately (Fig. 3). At the large distances (the diffusion region) from the cathode the potential drop is more than T_e . If $v_0 \tau \approx 10^{-3}$ cm (ions of Cs), $T_e = 0.2$ eV, $\frac{T_e}{T} \approx 1$ at the distances of $\xi \approx 0.5 + 1$ the electric field intensity is about 100 v/cm.

From Eq. (12) one obtains for an extrapolation length L :

$$L = 1,016 + \frac{1}{\sqrt{2}} \frac{T_e}{T} \quad (13)$$

Of course, the account of the electric field described above is a very approximate one. However it proved possible to indicate the correction upper limit caused by the electric field. Obviously, it may be found if Eq. (1) is solved with assuming the electric field space constant and equal to the field near by the cathode. This gives for $\frac{T_e}{T} = 1$ the next results:

$$|j| < \frac{n(0) \bar{v}}{4} \sqrt{2\pi} \cdot 1,5$$

the mean energy of an ion $< 1.26 T$, the mean energy carried out by an ion from the plasma $< 2.46 T$.

5. Let us consider now the behavior of the electron function in the region of high energies $E \geq E_0$. We assume that the free path length l_k for the electron-electron collisions is more considerable than the free path length l for the electron-atom ones. The elastic electron-atom collisions taken into account, it is enough to study the one-velocity case. Then the kinetic equation for the electron function is:

$$-\mu \frac{\partial f}{\partial y} + f = \frac{1}{2} \int_{-1}^1 d\mu f(\mu, y) \quad (14)$$

where $x = ly$ - the coordinate orthogonal to an electrode,
 μ - the angle cosine between external normal to the plasma boundary and the velocity of an electron.

For the electrons with $E \geq E_0 \gg T_e$ in the quasineutrality region the electric field can be neglected. But Langmuir's layer electric field may be taken into consideration in the form of the boundary condition as:

$$f(\mu, 0) = \begin{cases} g(\mu) & -1 < \mu < -\mu_0 \\ f(-\mu, 0) & -\mu < \mu < 0 \end{cases} \quad (15)$$

where $\mu_0 = \sqrt{\frac{E_0}{E}}$. Namely, the electrons with $E\mu^2 < E_0$ are reflected back into the plasma.

Equation (14) together with the boundary condition (15) can be reduced to the singular integral equation of the form:

$$\Lambda(\mu) f(\mu) = \frac{1}{2} \int_0^1 \frac{dt t f(t)}{t-\mu} + \frac{1}{2} \int_0^{\mu_0} \frac{dt t f(-t)}{t+\mu} + \frac{1}{2} \int_{\mu_0}^1 \frac{dt t g(t)}{t+\mu}, \quad (16)$$

where

$$f(\mu) \equiv f(\mu, 0), \quad \mu > 0; \quad (17)$$

$$\Lambda(\mu) = 1 - \frac{\mu}{2} \ln \frac{1+\mu}{1-\mu}$$

6. It can be shown that the angular distribution function of the particles leaving the plasma is readily the isotropical one if the angular distribution function of the particle going into the plasma is the same. In this sense the angular distribution problem is not interesting (if the Maxwellization process is enough slow: $l_k \gg l$). Therefore let us consider the case of not emitting electrode ($g(\mu) \equiv 0$). In the right hand side of Eq. (16) there is the nonsingular integral term. Owing to this the formal solution of the Rie-

mann-Hilbert problem corresponding to Eq. (16) leads to the Fredholm's integral equation of the second kind:

$$f_1(\mu) = \frac{\sqrt{3}}{2} \frac{1}{Y(-\mu)} \left[1 - \mu\sqrt{3} \int_0^{\mu_0} \frac{dt f_1(t)}{(t+\mu)Y(-t)} \right] \quad (18)$$

where $f_1(\mu)$ is the function $f(\mu)$ with the unit zero momentum. The solution of this equation is shown with different values of μ_0 in Fig. 4 (dots). If $\mu_0=0$ the found solution coincides with the known solution of the Miln's problem. As it is seen in Fig. 4 the exact solution of Eq. (16) is enough well approximated by the straight lines (with accuracy more than 2.5%).

7. Finally, let us consider the electron flow through the potential barrier E_0 assuming the Maxwellian velocity distribution for the electrons and approximating their angular distribution by the following formula (see Fig. 4):

$$f_1(\mu) = \frac{1}{2} + \frac{1-\mu_0}{1+\mu_0^2} \mu \quad (19)$$

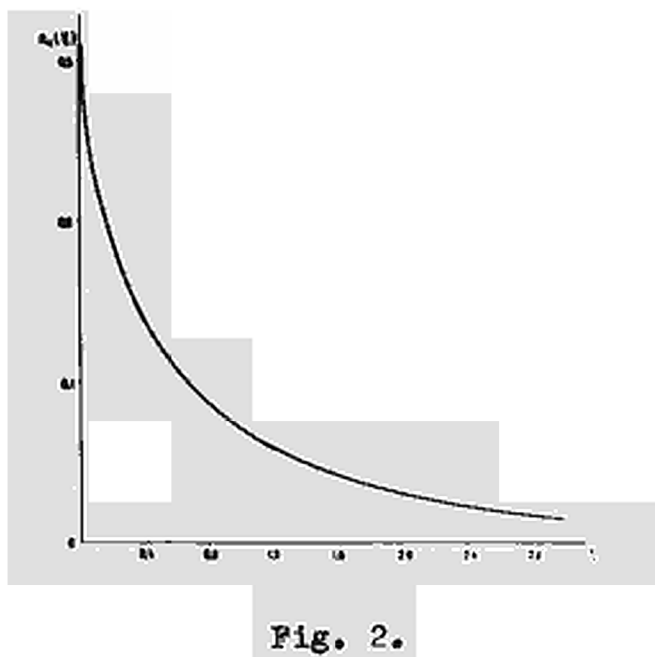
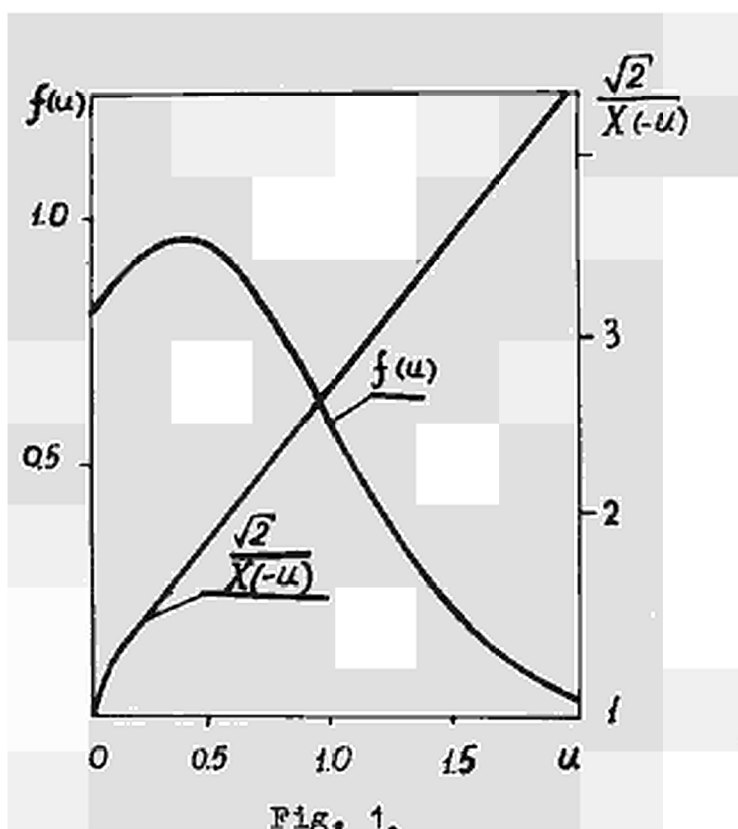
It is proved that between the flow of the electrons and their density n at the boundary there exists the relation:

$$j = \frac{1}{n} \bar{v}_e e^{-\frac{E_0}{T_e}} \chi\left(\frac{E_0}{T_e}\right) \quad (20)$$

where $\bar{v}_e = \sqrt{\frac{8T_e}{\tau m}}$. The function $\chi(t)$ is plotted in Fig. 5. For $t=0$ $\chi(0)=2.33$; but for $t \gg 1$ $\chi(t) = 1 + \frac{1}{t} - \frac{3}{2t^2}$. The extrapolation length has been calculated for the electrons $\mathcal{L}(\mu_0)$ (See Fig. 6).

R E F E R E N C E

- [1] И.П. Стаханов. ЖТФ 37 II (1967) 2067



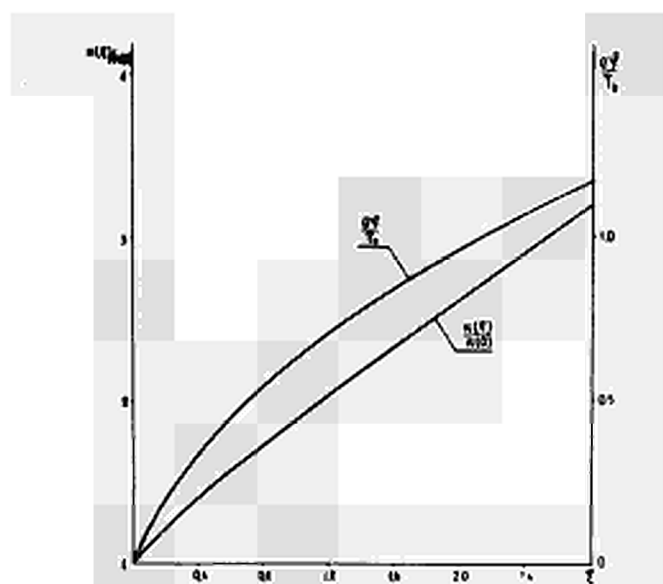


Fig. 3.

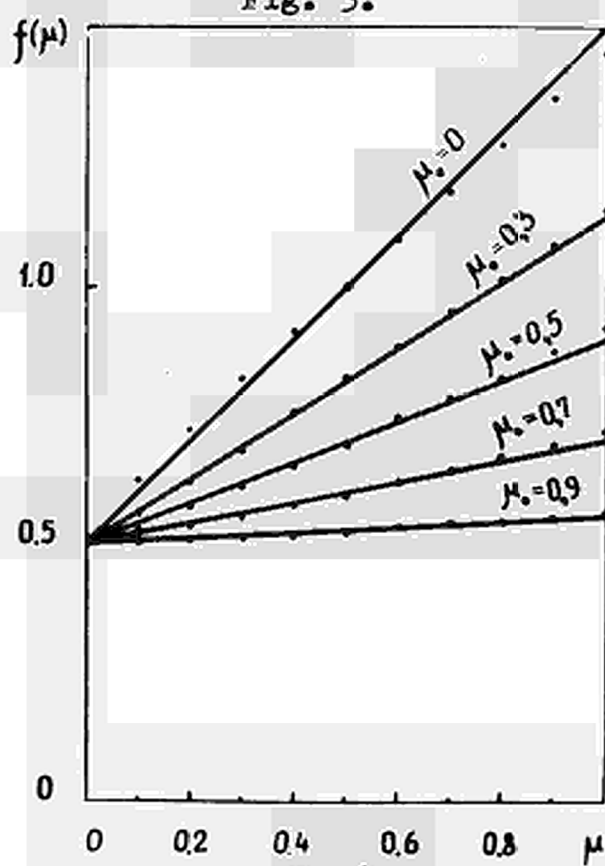
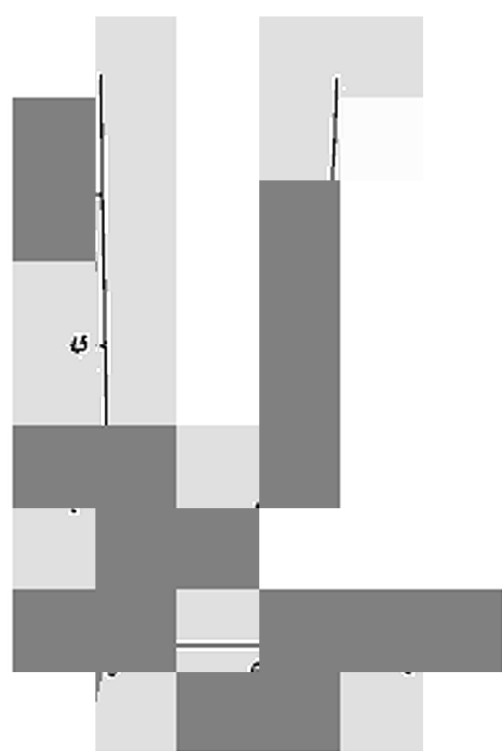


Fig. 4.



CALORIMETRIC MEASUREMENTS WITH A HEAT PIPE
THERMIONIC CONVERTER

J. Bohdanský and E. van Andel

Euratom CCR, Direct Conversion Group, Ispra (Varese), Italy

Abstract

A planar diode has been constructed with a collector- and a guard ring heat pipe. In this construction the central collector tube is surrounded by an annular shaped guard ring heat pipe. Both pipes are operated at equal temperature (established by an inert gas layer of equal pressure) to avoid any losses of heat energy from the central tube. The generated heat energy at the collector is measured by the heat flow through the collector pipe with an accuracy of about 2%.

The spacing between the Re emitter and the Nb collector is variable between 0.05 mm and 1 mm. Emitter temperature and Cs-temperature are controlled by electronic means (better than 0.5%).

Measurements have been performed at 1800^oK emitter temperature and different spacings (0.05 mm, 0.2 mm and 1 mm) and collector temperatures (900^oK, 1000^oK, 1100^oK). These experiments allow an experimental definition of generated electrical power density and of the electrode electrode efficiency. Both values are important for practical converter design.

The most significant result of the measurements is the behavior of the heat production at the collector as a function of cell current. At low collector temperature (900^oK) the well known linear relation between cell current and heat production exists. At high collector temperature (1100^oK) the heat production is considerably reduced for cell currents up to 10 A/cm². Therefore, the highest electrode efficiencies (14%) have been measured at those collector temperatures (1100^oK). The maximum power density has been measured at lower collector temperature (1000^oK) in accordance with other data, referred to in literature.

Introduction

Electrical power generation and heat generation at the collector of a thermionic converter are the most important values for the application of these devices. Measured data of both quantities are needed for practical cell design as well as for a physical interpretation of discharge and electrode surface conditions. Electrical power generation is measured usually in test diodes with a guard ring collector to relate this quantity directly to the electrode system.

Measured values of heat production at the collector also should be related to the electrode system in order to use this data in practical cell design. Unfortunately, only few measurements exist where this quantity has been investigated [1, 2]. In most of these experiments diodes with guard ring structure were used. The collector lead was constructed as a thermal bridge and the heat generation of the collector was measured by the heat flow across this bridge. Uncontrolled side losses of heat energy and the not very well known behavior of thermal conductivity of the lead material limited the accuracy of such measurements.

In this paper a cell construction is described, where electrical power generation and heat generation can be measured with sufficient accuracy. In this construction the collector is cooled by a heat pipe and the heat flow through the pipe is defined calorimetrically. Radiation and conduction losses from the pipe to the guard ring are practically avoided.

This kind of devices also allows a direct measurement of the electrode efficiency, which is normally calculated making some assumptions about irreversible losses [3] .

Cell construction

The cell construction is given in fig. 1. A Re-emitter is joined (by hot pressing) to a small Ta-heat pipe (working fluid Ag) to establish constant temperature across the emitter surface. The emitter-collector spacing can be adjusted by three micrometer screws between 0.05 mm and 1 mm.

The collector guard ring construction consists of two heat pipes whereby the central collector tube is surrounded by an annular shaped guard ring heat pipe. Both tubes are operated with an inert gas layer of equal pressure [4]. Therefore, the temperature in both pipes is equal and independent of all discharge parameters. The vapor-gas transition zone has been kept in the shielded part (see fig. 1 dotted line) for all reported measurements in order to avoid also radiation losses to the guard ring heat pipe. Both pipes are cooled at the upper end by water cooled copper cones. The heat flow through the collector tube is measured with an accuracy of 2% by the usual technique in heat pipe research [5].

Emitter- and Cs-temperature are controlled by electronic means (stabilization better than 0.5% during a run).

Measurements

Generated electrical power and heat energy produced at the collector have been measured at 1800°K emitter temperature but different spacing, collector and Cs-temperature.

In a separate run heat transfer has been measured also at open circuit conditions to measure the radiation losses of the collector system as well as to prove the reliability of the collector heat pipe construction. A typical result of the latter measurements is given in fig. 3. Heat generation at the collector is indicated as a function of Cs-reservoir temperature. The expected relation for the heat flow through the cell has been found [3] with reasonable values for the effective emissivity of the electrode system ($\epsilon^1=0.15$) and the thermal conductivity of the Cs-vapor ($\lambda_m = 6.7 \cdot 10^{-5} \text{ W/cm}^{\circ}\text{K}$).

A typical result for power and heat generation is given in fig. 2. Both values are measured as a function of cell current and related to unit electrode area. The measured power generation shows the typical and well known behavior with two maxima in the ignited and unignited discharge mode.

Two regimes of operation are also indicated by the heat generation at the collector. A sudden change in power generation occurs at the ignition point

due to a change in surface potential and arc radiation. Unexpected is the behavior of heat generation in the ignited regime. A very weak increase of heat energy in the current interval up to 10 A/cm^2 has been measured. This increase depends on collector temperature indicated in fig. 6. Measured data at fixed spacing and Cs-temperature are plotted in this figure. At low collector temperature (900°K) the expected linear relation was found between heat production and cell current. However, at high collector temperature a significant deviation from this relation has been measured leading to a reduced heat production. Therefore, the electrode efficiency is higher at high collector temperature as indicated in fig. 4 in spite of the reduced power generation. This quantity, which may be defined by

$$\eta_1 = \frac{W_e}{W_e + W_c} \quad (1)$$

(W_e electrical power generation per unit area
 W_c heat generation at the collector per unit area)

can be measured in such a device.

Measured data of power density and efficiency are plotted for different spacings in fig. 5.

The highest electrode efficiency has been measured at a spacing of 0.2 mm. The reduction in efficiency at a closer spacing (0.05 mm) can be explained by the higher heat conduction through the Cs-vapor.

Discussion

The measured data presented in the foregoing section should show the possibility to measure also heat production and electrode efficiency with the described heat pipe converter. The knowledge of these quantities in addition to the power generation for different electrode systems may give a better basis for practical converter design. This is of special importance for the construction of isotope fueled thermionic converters, where the efficiency is of extreme importance. The discussed behavior of the heat production at the collector should be considered as a preliminary result. More data at different emit-

ter temperatures and for different electrode materials are needed to learn whether this effect is of importance also for other discharge conditions or not. Moreover, a converter analysis should be based on more data than those reported here. Nevertheless, the reported results indicate the importance of those measurements also for a theoretical interpretation of the conversion process.

Acknowledgement

The authors would like to acknowledge the assistance of R. LEBOURG in converter construction and data taking.

References

- [1] KITRILAKIS, S. and BROSENS, P., "Proc. Thermionic Conversion Specialist Conference", San Diego 1965, p. 316
- [2] PAQUIN, M. L., "Proc. Thermionic Conversion Specialist Conference", Palo Alto 1967, p. 51
- [3] BLOCK, F.G., HATSOPOULOS, G.N., WILSON, V.C., "Proc. Thermionic Conversion Specialist Conference", San Diego 1965, p. 379
- [4] BOHDANSKY, J., SCHINS, H.E.J., "J. Appl. Phys." 36 (1965)
- [5] BOHDANSKY, J., STRUB, H., VAN ANDEL, E., "Proc. Thermionic Conversion Specialist Conference", Houston (1966), p. 144

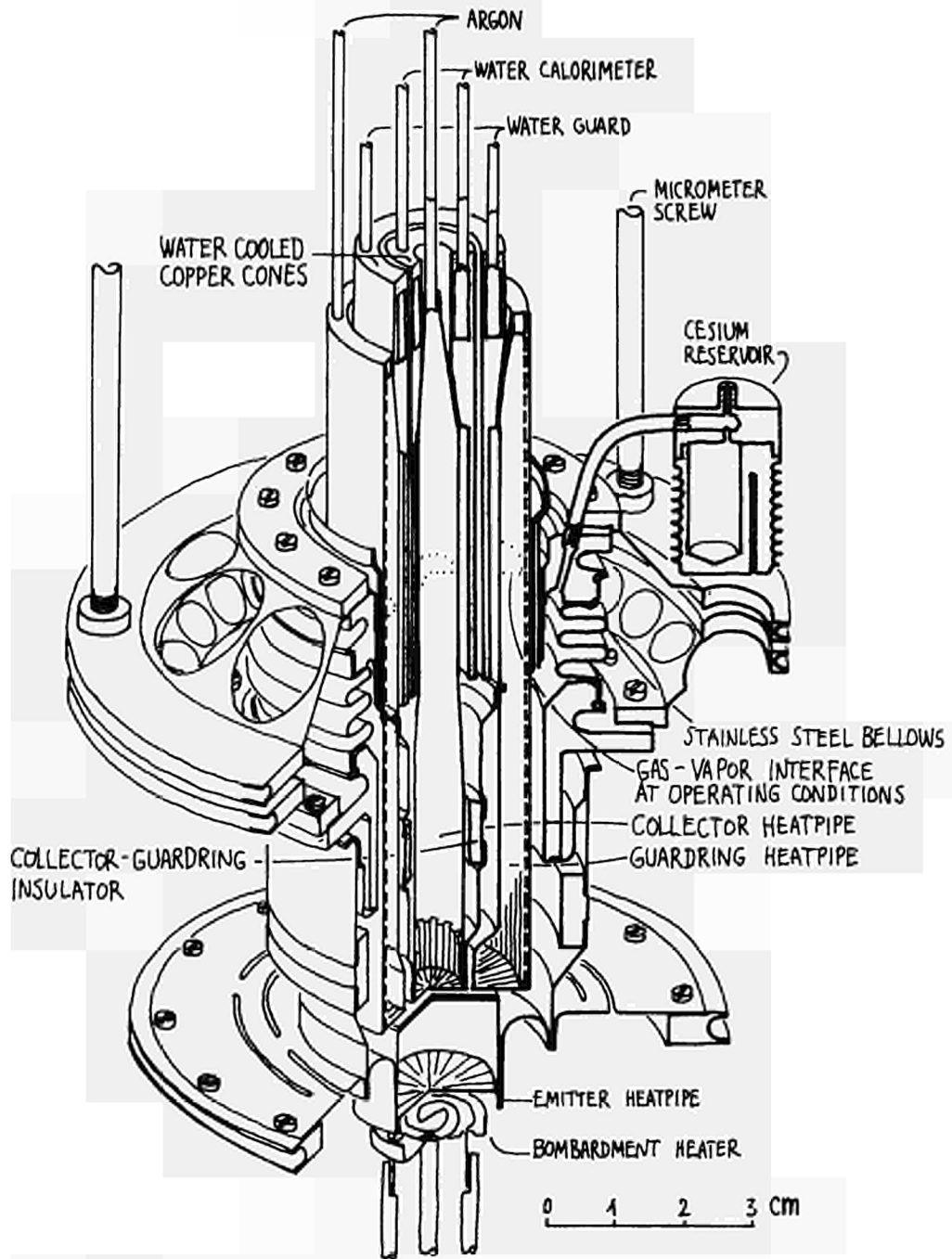


FIG. 1.
CALORIMETRIC CONVERTER WITH THREE HEATPIPES

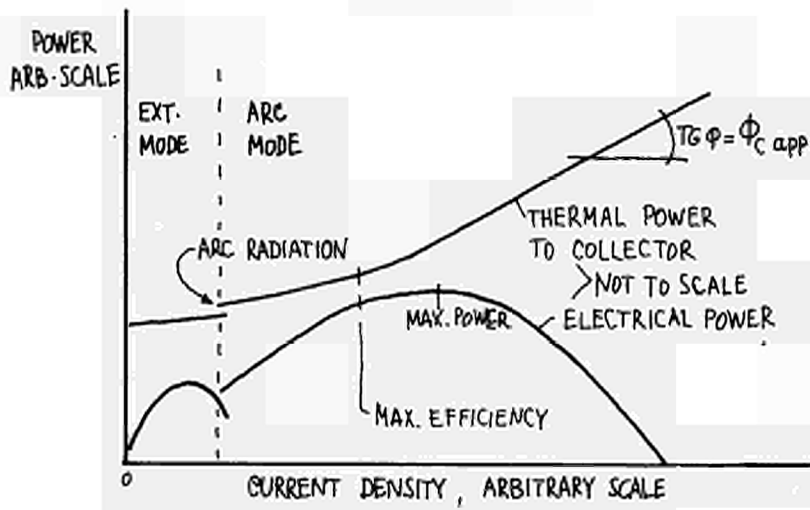


FIG. 2. TYPICAL EXPERIMENTAL RESULT

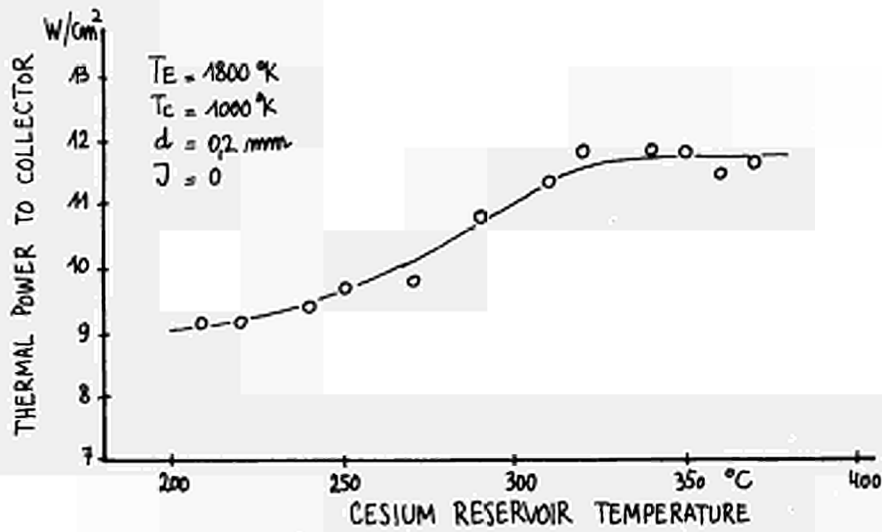


FIG. 3. POWER SHIFT DUE TO Cs VAPOR CONDUCTION

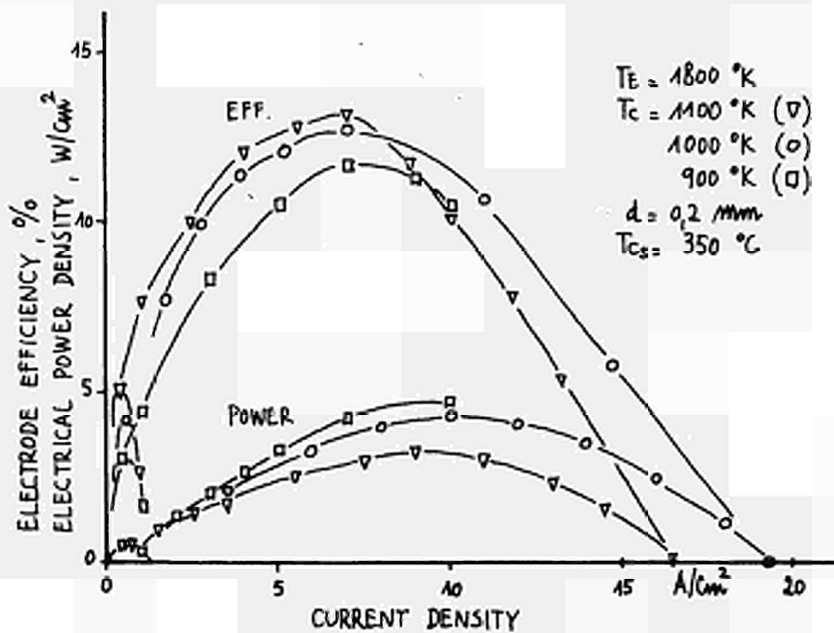


FIG. 4. POWER DENSITY AND EFFICIENCY WITH DIFFERENT COLLECTOR TEMPERATURES

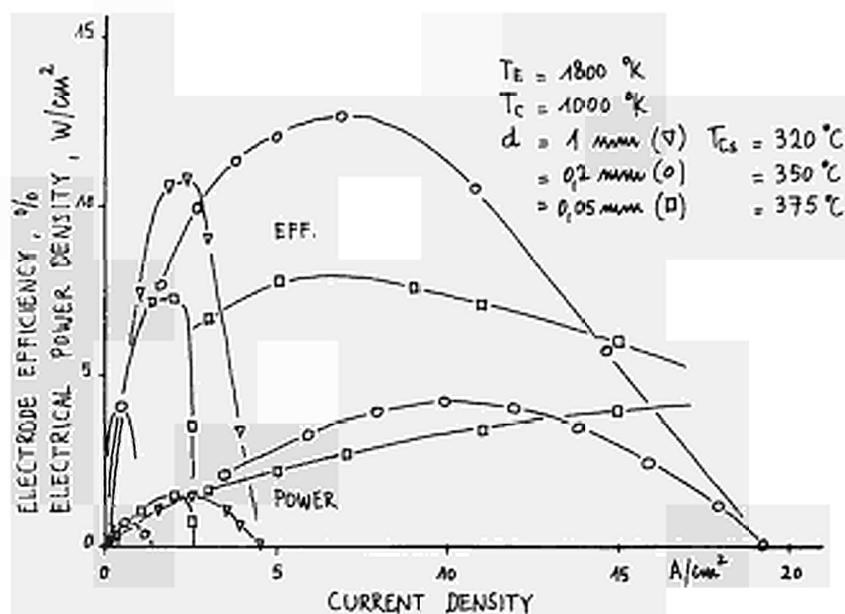


FIG. 5. POWER DENSITY AND EFFICIENCY WITH DIFFERENT SPACINGS

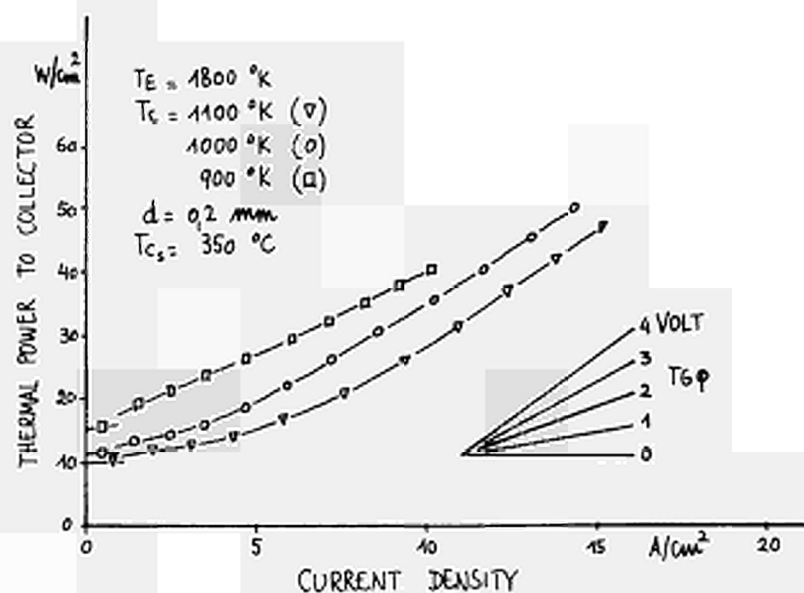


FIG. 6. COLLECTOR DISSIPATION.

DISCUSSION

Speaker of paper H-2: J. BOHDANSKY.

SAGGAU (Germany): Do you believe that you can measure quantitatively the radiation from the plasma by this method?

BOHDANSKY (Euratom): Three effects occur at the ignition point. One is of course the change in radiation of the plasma. The second is a change in the plasma sheaths. And third, the conductivity of the plasma may change. Therefore, it is difficult to say how much the radiation change contributes to the change in heat flow. The sensitivity of the calorimeter of course is sufficient to measure the change in the radiation.

THE CHARACTERISTICS OF THERMIONIC
CONVERTERS FILLED WITH VAPOUR MIXTURE

V.D.Bondarenko, Yu.K.Guskov

Institute of Physics and Power Engineering, Obninsk,
USSR

The interest in studies of mixtures to cesium effect upon thermionic converter characteristics is caused first of all by the attempt to raise the cesium metal film cathode electron emission in the cathode high-temperature range under optimum cesium vapour pressure.

Another important cause drawing attention to these investigations is the possibility of fission fragment build-up in the interelectrode spacing during converter operation within nuclear reactor.

As it was been shown in [1,2] to obtain the output characteristics of optimum converter performance at the given cathode temperature it is necessary that the cathode work function (φ) and the cesium vapour pressure satisfy the definite conditions.

Under operating conditions without volume ionization cesium vapour optimum pressure (P_{op}) is determined by the relationship

$$[2] \quad P_{op} = \frac{3\pi}{8\sqrt{2}} \gamma \frac{T}{L G_1} \text{ or } \frac{l_e}{L} \sim 1 \quad (I)$$

where T' is the cathode temperature in energy dependent units,

G_1 is the scattering cross-section for electrons on cesium atoms; L is the interelectrode spacing;

l_e is the electron mean free path; γ is the factor

averaging the temperature over the interelectrode spacing which varies usually within I-2.

The cathode work function must then satisfy the condition:

$$\varphi' \leq \mu + \frac{T'}{e} \ln \left(\frac{1}{\sqrt{2}} + \frac{8L}{3\pi y l e} \right) \quad (2)$$

where μ is the plasma chemical potential near the cathode.

The second term in the right part of the inequality (2) is equal to about $0.5 T'$ under cesium vapour optimum pressure.

It follows from (2) that in the cathode temperature region of about 2000°K , the interelectrode spacing ~ 0.5 mm and the cesium vapour optimum pressure the cathode work function will be equal to ~ 3 ev.

In arc mode the optimum pressure is determined by the condition [3]: $\frac{L}{e} \sim 10-20$

Choosing the emitter work function in an arc mode one must consider the necessary values of output current potentials and the converter efficiency as the most significant.

It is known from [4,5] that due to low cesium evaporation heat from the main refractory metal surface (Nb, Mo, W, Re, Ir and others) one cannot provide the optimum conditions in the converter with ~ 0.5 mm spacing and at cathode temperature 2000°K . Basing on the estimates for this purpose one needs the material with ~ 6 ev work function.

We shall dwell on the use of different additions to cesium vapours to raise the electron emission of the converter cathode. There are two trends in the question. The 1st one is the use of electric positive additions with great absorption energy on a refractory metal surface to obtain the necessary work function of the cathode at high temperatures [6]. And secondly, the introduction of electric negative elements into the interelectrode spacing increase the absorption capability of the cathode base to cesium [7,8].

In Fig. I it is shown the work function of W in the vapours of the most active electron positive elements Cs, Ba, Sr, Ca, Mg,

Th depending on the ratio of the cathode temperature and the filler thermostat one (T_{fil}) calculated from the data [9-13]. As it is seen from the figure, with these elements one may obtain the necessary cathode work function. However, Ca as well as Cs may be used at cathode high temperature only under great vapour pressures. The same is referred to Sr at the cathode temperature above 2000°K. While using Th as the addition to cesium one need high temperatures of the anode and the thermostat with thorium due to low vapour pressure.

Besides, while using the additions out of vapour phase for the cathode activation one must take into consideration their influence upon the anode work function (φ''). The absorption energy of the given additions is higher than that of cesium, and from Fig.1 the minimum work function in these elements vapours is in the range of 2-3 ev. Therefore, the anode work function will be determined by the introduced addition as according to [14] cesium slightly influences upon the base work function at about 1000°K and the base work function of 2-3 ev.

Great anode work function will lead to essential decrease of the output voltage and converter power.

That is why apparently barium serves as the most suitable addition to cesium for thermionic converters.

The use of barium as an addition reveals the possibility (see Fig.2) to use actually all the known refractory metals as cathodes. The curves of Fig.2 are plotted from the data [13,15].

Fig.3 shows the influence according to [7,16] of electric negative elements of fluorine and oxygen upon Mo and W absorption properties. In presense of fluorine and oxygen Cs absorption energy on Mo and W substantially raises. In this case Mo becomes equivalent by its absorption properties to Ir having the work function 5.5 ev and tungsten - to the material with the work function ~ 6 ev in presence of oxygen.

The introduction of the additions to cesium will lead not only to the change of the cathode and anode work function, but also to the increase of the interelectrode spacing diffusion resistance, to the change of concentration of plasma and its separate components, especially when using electric negative

elements which form low mobile negative ions.

Let us consider the influence of additions upon the transport processes and plasma generation in the converter in diffusion approximation without volume ionization.

For this purpose the transport equation system for three-component plasma [17] must be added with the equations for new components and solved then with the boundary conditions taking into account the generation and leakage of all plasma components.

Then we shall have the following system of transport equations

$$\begin{aligned} J_e &= -D_e \nabla n_e + n_e U_e \nabla \varphi \\ J_i &= -D_i \nabla n_i - n_i U_i \nabla \varphi \\ J_{i_2} &= -D_{i_2} \nabla n_{i_2} - n_{i_2} U_{i_2} \nabla \varphi \\ J_{i_3} &= -D_{i_3} \nabla n_{i_3} + n_{i_3} U_{i_3} \nabla \varphi \end{aligned} \quad (4)$$

where J, D, n, U - is the current, the diffusion factor, concentration and mobility of separate plasma components, respectively;

φ is the plasma potential, indexes e and i are referred to electrons and ions, respectively, and indexes 1, 2 and 3 - to cesium, electric positive and electric negative additions.

In this case we suppose that the generation of all charged plasma components takes place on the cathode.

The boundary conditions on the cathode and anode are written down for under compensating conditions ($\Delta \varphi' < 0$) since under these conditions the converter output characteristics are optimum and close to thermodynamic equilibrium [2, 3]. Besides, we shall consider the region of currents close to saturation current, i.e. when the near-anode potential barrier is positive ($\varphi'' > 0$) and the converter had the maximum output voltage. Then for the case of electric positive addition it will be:

$$\begin{aligned} \Delta \varphi' < 0 \quad J_i e^{\frac{e \Delta \varphi'}{T_i}} - \frac{1}{4} n_i' V_i' &= \frac{1}{2} J_e \\ J_e - \frac{1}{4} n_i' V_i' e^{\frac{e \Delta \varphi'}{T_i}} &= J_i (1 - \frac{1}{2} e^{\frac{e \Delta \varphi'}{T_i}}) \\ J_{i_2} - \frac{1}{4} n_{i_2} V_{i_2} e^{\frac{e \Delta \varphi'}{T_{i_2}}} &= J_{i_2} (1 - \frac{1}{2} e^{\frac{e \Delta \varphi'}{T_{i_2}}}) \end{aligned} \quad (5)$$

$$\begin{aligned} \Delta \varphi'' > 0 \quad J_e &= \frac{1}{2} n_e'' V_e'' \\ J_i (1 - \frac{1}{2} e^{-\frac{e \Delta \varphi''}{T_i}}) &= \frac{1}{4} n_i'' V_i'' e^{-\frac{e \Delta \varphi''}{T_i}} \\ J_{i_2} (1 - \frac{1}{2} e^{-\frac{e \Delta \varphi''}{T_{i_2}}}) &= \frac{1}{4} n_{i_2}'' V_{i_2}'' e^{-\frac{e \Delta \varphi''}{T_{i_2}}} \end{aligned} \quad (6)$$

For the case of electric negative addition

$$\begin{aligned} \Delta\varphi' < 0 \quad J_2 e^{\frac{e\Delta\varphi'}{T_2}} - \frac{1}{4} n_e' V_e' &= \frac{1}{2} J_e \\ J_c - \frac{1}{4} n_i' V_i' e^{\frac{e\Delta\varphi'}{T_1}} &= J_i (1 - \frac{1}{2} e^{\frac{e\Delta\varphi'}{T_1}}) \\ J_3 e^{\frac{e\Delta\varphi'}{T_3}} - \frac{1}{4} n_{i3}' V_{i3}' &= \frac{1}{2} J_{i3} \end{aligned} \quad (7)$$

$$\begin{aligned} \Delta\varphi'' > 0 \quad J_c &= \frac{1}{2} n_e'' V_e'' \\ J_i (1 - \frac{1}{2} e^{-\frac{e\Delta\varphi''}{T_1}}) &= \frac{1}{4} n_{i1}'' V_{i1}'' e^{-\frac{e\Delta\varphi''}{T_1}} \\ J_{i3} &= \frac{1}{2} n_{i3}'' V_{i3}'' \end{aligned} \quad (8)$$

where J_2, J_c are Richardson and Saha-Langmuir currents when the surface ionization are either positive or negative, V - is the velocity of separate plasma components ' and '' indexes are referred to the values near the cathode and anode, respectively.

While solving equations (4) we shall assume that the temperature of all the plasma components is constant over the spacing and equal to the cathode temperature.

From equations (4) for the case of electric positive addition we shall obtain with a good approximation the following expression for the saturation current ($J_{i1} = J_{i2} = 0$)

$$J_e^0 = \frac{2D_e \sqrt{n_1^{02} + n_2^{02}}}{L(1 - 4\sqrt{2}D_e)} \quad (9)$$

In quasivacuum regime $\frac{L}{V_e} (e_e \gg L)$ we shall have

$$J_e^0 = \frac{V_e \sqrt{2(n_1^{02} + n_2^{02})}}{4} \quad (10)$$

where $n_1^0 = \sqrt{\frac{16J_2 J_c}{V_e V_i}}$ is the plasma equilibrium concentration near the cathode for cesium; $n_2^0 = \sqrt{\frac{16J_2 J_{c2}}{V_e V_{i2}}}$ is the plasma equilibrium concentration near the cathode for the addition.

Thus, the addition introduction led to the growth of the near-cathode plasma concentration.

Equation (9) gives the dependence of the converter current on cesium vapour and the addition pressure.

In general case equation (9) has no absolute maximum relative to cesium and addition pressure. From (9) it is possible to find the relative maximum for one component pressure when there is fixed value of the other component pressure.

From (9) we obtain the following expression for cesium vapour optimum pressure depending on the addition pressure:

$$P_{on Cs} = P_2 \left[\frac{\sigma_2}{\sigma_1} - 2e \frac{e(V_{i1} - V_{i2})}{T_1} \right] + \frac{4\sqrt{2} T}{3L\sigma_1} \quad (II)$$

Substituting (II) into (9) we get the expression for the converter saturation current at the cesium optimum pressure and the arbitrary pressure:
$$j_{e,max} = \frac{2A}{6L\sigma_1 \sqrt{\frac{4\sqrt{2} T}{3L\sigma_1} + \frac{P_2}{T_1} \left[\frac{\sigma_2}{\sigma_1} - e \frac{e(V_{i1} - V_{i2})}{T_1} \right]}} \quad (I2)$$

where $A = \sqrt{e} \left(\frac{Ne}{2} \right)^{1/2} e^{-\frac{V_{i1}}{2T_1}}$, Ne is the density of electron states.

As it is seen from (I2) the introduction of the addition to cesium may cause either maximum current decrease or its increase. Here the criterion is ratio $\frac{e^{-\frac{V_{i1}}{2T_1}}}{\sigma}$, the filter efficiency, which is proportional to the probability relation of the atom ionization to the electron scattering probability on it.

If the addition efficiency is lower than the cesium efficiency, then the converter current will be decreased but the cesium optimum pressure increase. Vice versus, if the addition efficiency is higher than cesium one, the maximum current will raise but the cesium optimum pressure fall.

Figures 4 and 5 give the dependences of the saturation current for Cs + Ba system on the cathode temperature at different cesium and barium vapour pressures for the converters with Mo and W cathodes. In the same pictures there are dependences of the saturation current for purely cesium converter.

It is seen from the curves obtained that the saturation current dependences on $\frac{1}{T}$ at different pressure ratios of cesium and barium vapours are close to straight lines with a slope somewhat lower than $\frac{V_{i1}}{2}$. Figure 4 shows the cathode work function does not actually depend on cesium vapour pressure (see the cathode temperature region > 1100 K).

Figure 6 shows the dependences of the saturation current on the cesium vapour pressure at the cathode constant tempera-

ture. In these experiments the barium vapour pressure was chosen optimum so that the cathode work function was equal to plasma chemical potential. In the same picture there given calculated values of the saturation current for the purely cesium converter, the cathode work function satisfies the condition (2).

As it is seen from the relationships given in the regions of small cesium vapour pressures, the barium addition leads to some converter current increase, as follows from (10) As the cesium pressure increases the barium contribution - to the converter current decreases, and in the region of the cesium vapour optimum pressure barium serves only for providing the necessary cathode work function.

The fact that barium introduction into the converter does not cause the converter current decrease at the optimum cesium pressure, reveals that the barium efficiency $\frac{e^{-\frac{eV_c}{T}}}{\sigma}$ is close to the cesium efficiency.

For the case of electric negative addition we obtain solving equation system (4) with the boundary conditions (7) and (8) the following dependence of the saturation current of negative charges of the converter ($J_i = 0$) on the cesium and the addition pressures

$$J_{e+i_3}^0 = J_e^0 + J_{i_3} = \frac{2De n_{i_1}}{L(1 + \frac{4\sqrt{2}De}{L V_e})} - J_{i_3} \left[\frac{\frac{2De}{D_{i_3}} + \frac{4\sqrt{2}De}{L V_{i_3}}}{1 + \frac{4\sqrt{2}De}{L V_e}} - 1 \right] \quad (I3)$$

where $n_{i_1} = \sqrt{n_1^{02} + n_3^{02}} = \sqrt{\frac{16J_e J_{i_1}}{V_e V_{i_1}} + \frac{16J_e J_{i_3}}{V_{i_1} V_{i_3}}}$ is the plasma equilibrium concentration near the cathode. For quasivacuum regime ($e \gg L$) we obtain

$$J_{e+i_3}^0 \approx \frac{n_{i_1} V_e}{2\sqrt{2}} - J_{i_3} \frac{V_e}{V_{i_3}} \quad (I4)$$

As it is seen from (I3) and (I4) the electric negative addition introduction leads also to some increase of the plasma concentration near the cathode. However, due to occurrence of the second terms in the right part of equations (I3) and

(I4) it does not lead to the converter raise but vice versus to its fall. In this case the S-shaped curve with the addition will be displaced relative to the S-shaped curve of the purely cesium converter in the range of lower currents.

As the pressure of the electric negative addition grows the converter current will fall. Fig. 7 shows two S-shaped curves for the cesium converter with Mo cathode in the inter-electrode spacing of which one introduced iodine vapours through the anode. To determine the range of equilibrium regime ($\varphi' < 0$) the emission currents were taken from this device under an arc mode and hence its work function was estimated. The same figure shows the dependence of the saturation current and Richardson current for purely cesium converter at cesium pressure of 1 torr.

As it is clear from Fig. 7 the dependence of the saturation current on the cathode temperature in presence of iodine is of S-shape. However, the equilibrium part of the saturation current is displaced in the range of lower currents. Then the converter current decreased by 1 - 2 orders.

The equilibrium parts of S-shape curves with iodine addition are close to the line with the slope of about 3.3 ev. The increase of cesium pressure at constant flow of iodine atoms influences slightly on S-shaped curve of the saturation current and the emission current from the cathode.

Thus, the iodine introduction led to the cathode emission current decrease, to very essential decrease of the converter saturation current under equilibrium and arc modes.

At low iodine additions ($\sim 10^{-6}$ torr) one observes slight increase of the converter parameters under an arc mode.

Solving the equation system (4) with the boundary conditions (5 - 8) one may obtain the equation of the converter voltage-current characteristic in presence of additions. Then one obtains too complex expressions. Analysing them we see that the converter work function under equilibrium conditions decreases as because of near-cathode concentration growth as

well as because of the growth of diffusion resistance spacing. This decrease of the work function is low and may be compensated by the anode work function decrease, especially when introducing electric negative additions.

Reference

1. Маев А. и др. ЖТФ, 37, 1079 (1967).
2. Гуськов Ю.К. и др. ЖТФ, 37, 1090 (1967).
3. Волков Н.В. и др. ЖТФ, 36, 1475 (1966).
4. Гуськов Ю.К. и др. Изв. АН СССР серия физ. 28, 1530 (1964).
5. Юрьев В.Г. Диссертация, ФТИ им. А.Ф.Иоффе (1962).
6. Psaronthakis J. "Thermionic energy conversion with mixed vapors". Conf. Thermionic electrical power generation. London (1965).
7. Aamodt P. et al. J. Appl. Phys., 33, 2080 (1963).
8. Langpape Pr. and Minor A. "The influence of a cesium fluoride additive on the emitter work function and power output of cesium diodes with various emitter materials". Conf. Thermionic electrical power generation. London (1965).
9. Зингерман Я.И. и др. ФТТ, 3, 1044 (1961).
10. Becker J. Trans. Farad., 28, 151 (1932).
11. Марчук П.М. РИЭ, 2, 1479 (1957).
12. Дюбуа Б.Ч., Попов Б.Н. Электроника, 9, 98 (1960).
13. Дюбуа Б.Ч. РИЭ, 10, 1161, (1965).
14. Rasor Ned., Werner C. J. Appl. Phys., 35, 2589 (1964).
15. Дюбуа Б.Ч., Попов Б.Н. РИЭ, 7, 1566 (1962).
16. Langmuir J. and Kingdon K. Phys. Rev. 21, 380 (1923).
17. Мойжес Б.Я., Пикус Г.Е. ФТТ, 2, 856 (1960).

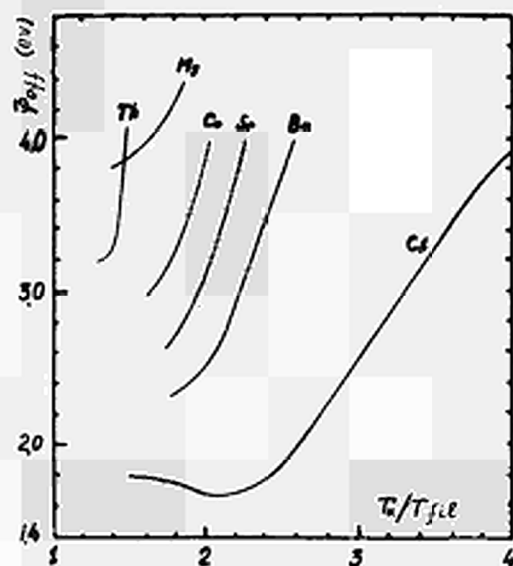


Fig.1. Work function W in vapours of Cs, Ba, Sr, Ca, Mg, Th.

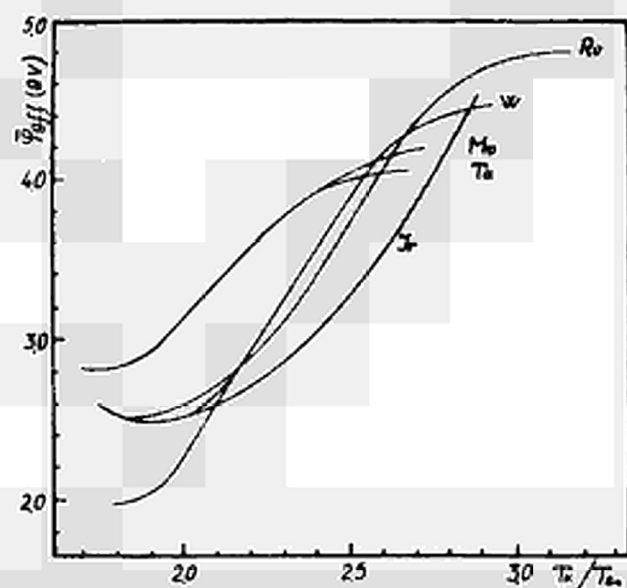


Fig.2. Work function Ta, Mo, W, Ra, Ir in barium vapour.

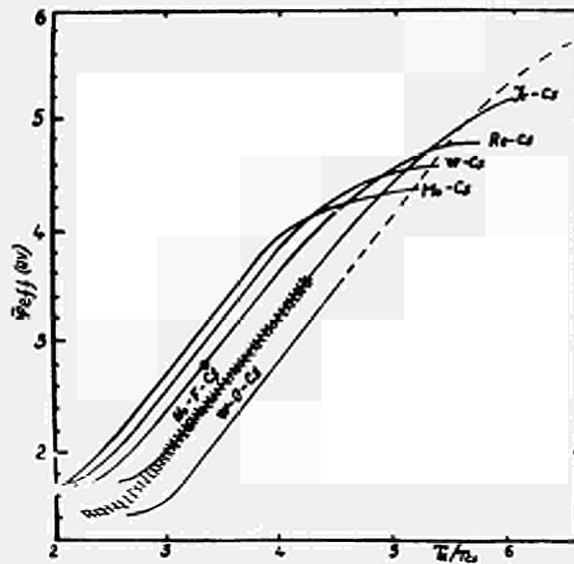


Fig.3. Influence of F_2 and O_2 upon the work function of Mo and W in cesium vapour.

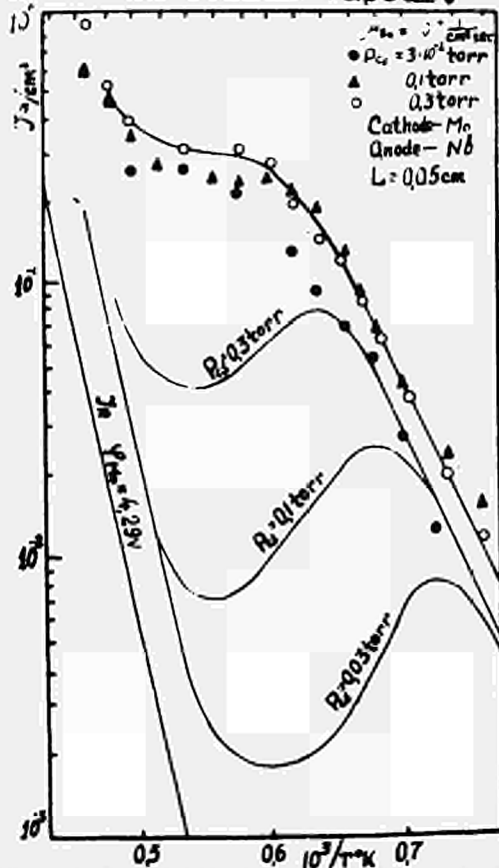


Fig.4. Dependence of the saturation current of the converter filled with Ba and Cs on Mo cathode temperature.

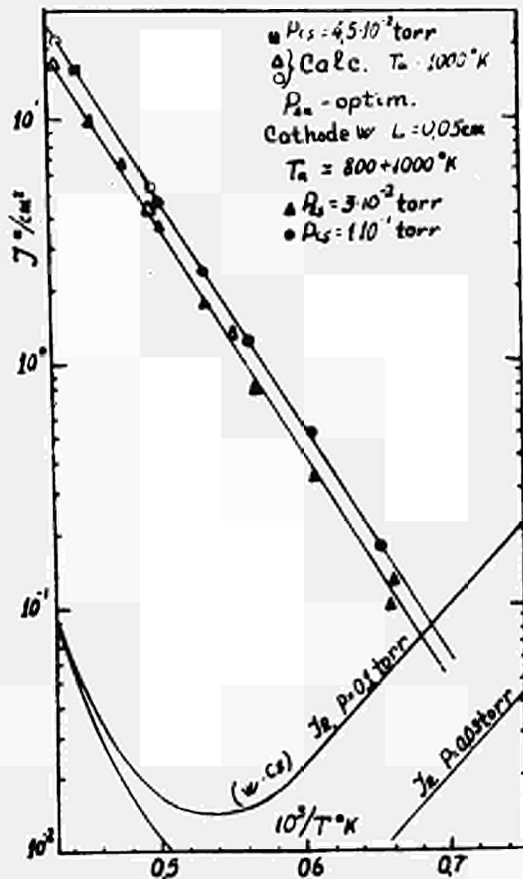


Fig.5. Dependence of the saturation current of the converter filled with Ba and Cs on W cathode temperature.

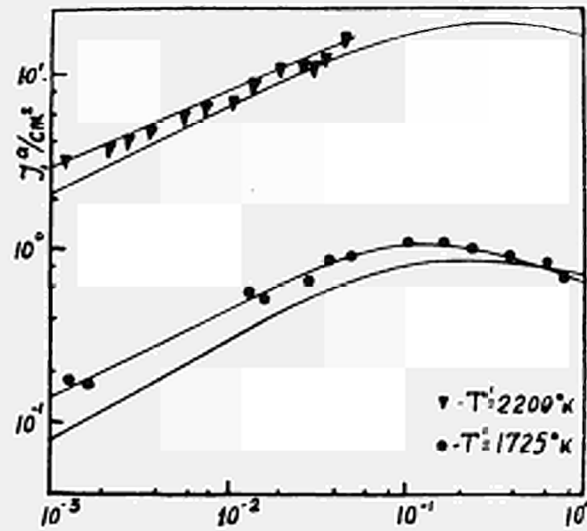


Fig.6. Dependence of the saturation current of the converter filled with Ba and Cs on cesium vapour pressure.

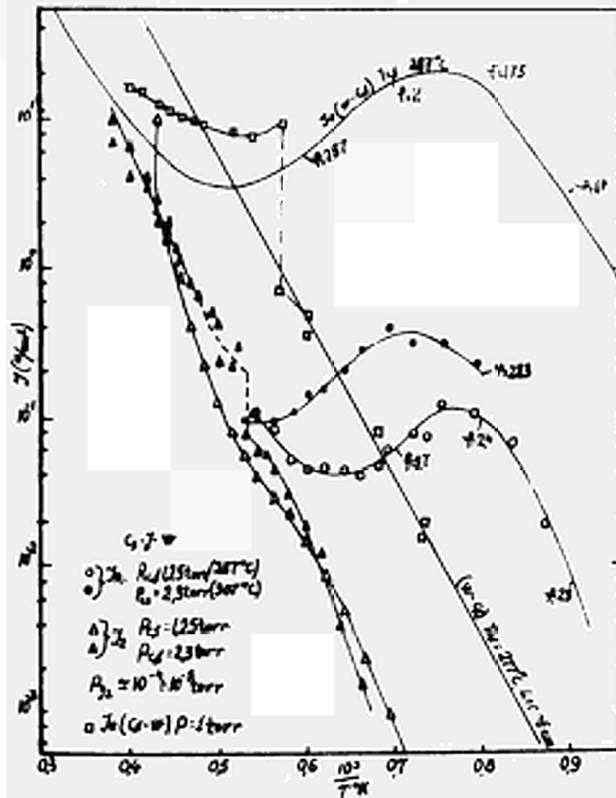


Fig.7. Dependence of the saturation current of the converter filled with Cs and I on the cathode temperature.

UNIGNITED MODE CONVERTER DIAGNOSTICS WITH REGARD TO EMITTER
WORK FUNCTION PATCHES

E. Wolf, R. Mayer and M. Schindler

Institut für Kernenergetik der Universität Stuttgart (Germany)

Abstract

From measured electron saturation currents in the electron rich unignited mode electron-cesium momentum transfer cross sections are calculated. The measurements were performed on a cylindrical cesium-converter with Ta-emitter and stainless steel collector.

Particle transport is described in the diffusion approximation. In the momentum transfer collision integrals the velocity dependence of the scattering cross sections reported in the literature is taken into account. For electron-cesium collisions this yields an electron temperature dependent correction factor for the diffusion constant definition, because of the complicated Ramsauer-like structure of the scattering cross section.

Improved ion boundary conditions are used in the few-collision case.

The computed cross sections show a systematic dependence on the emitter and reservoir temperatures which, in part, is explained by emitter patch effect.

List of Symbols

A-Richardson constant; b-mobility; d-plasma length; E-electric field; g-relative velocity charged particle-atom; I-ionization potential; j-particle current density; m-particle mass; n-particle density; Q-momentum transfer cross section; V_E -emitter sheath potential; v-particle velocity; μ_a -Cs-arrival rate on the emitter; Φ, Φ -emitter work function. Indices: a-atom; C-collector; E-emitter; e-electron; i-ion; R-from Richardson equation (Φ_R), Reservoir (T_R); SL-from Saha-Langmuir equation; 1,2-emitter, collector edge of the plasma.

Experimental Apparatus

The measurements of unignited mode current-voltage characteristics were performed on a cylindrical Cs-converter (Fig.1) with polycrystalline Ta-emitter and stainless steel collector (spacing 0,36 mm (hot)). A large emitter area of 10 cm² was chosen in order to diminish the influence of leakage currents and field inhomogeneities at the converter edges on the converter performance. The emitter is heated by a coaxial radiator along its entire axis. The heater consists of a graphite tube with a concentric tantalum return wire for magnetic field compensation of the heater's current. With this kind of heating and with heat dams on the emitter body a constant emitter temperature (± 10 °K) is achieved along the active emitter surface. The emitter temperature is measured pyrometrically in a radial black-body hole which is visual through a heated sapphire window and a radial collector bore. Collector and reservoir temperatures are held constant within $\pm 0,75$ °K respectively.

The current-voltage characteristics were dynamically measured by means of a 50-cps-sweep-generator and a sampling system. A typical set of unignited mode characteristics is shown in Fig.2. Similar measurements were performed with $T_E=1300$ °K to 1800 °K $T_R=498$ °K to 648 °K and $T_C=670$ °K¹. Several runs with the same parameters gave a good consistency of the measuring values.

Parts of this work were supported by the Bundesministerium für wissenschaftlicht Forschung of the Federal Republic Germany.

Theory

The diffusion approximation of the Boltzmann equation is used for electron and ion transport in the plasma:

$$j_e = -D_e \frac{dn}{dx} - b_e n E ; \quad j_i = -D_i \frac{dn}{dx} + b_i n E \quad (1)$$

If the diffusion constants D are defined as $\lambda \bar{v} / 3$, where $\bar{v} = \sqrt{8 kT / \pi m}$, the particle mean free paths λ in the Cs-gas are related to the momentum transfer cross sections $Q(\bar{g})$ (\bar{g} is arbitrarily chosen as reference velocity) by the equation

$$\lambda = \frac{\alpha \beta}{n_a Q(\bar{g})} ; \text{ where } \alpha = \left(1 + \frac{m}{m_a}\right) \frac{\bar{v}^2}{\bar{g}} / \frac{\bar{g}^2}{\bar{g}} \quad \text{and} \quad \beta = \frac{\bar{g}^2 \bar{g}^2 Q(\bar{g})}{\bar{g} \bar{g}^2 Q} \quad (2)$$

are derived from the momentum transfer collision integrals in the diffusion approximation.

For a Maxwellian distribution of the charged particle and neutral atom velocities the average \bar{F} of an arbitrary function F(g) is

$$\bar{F} = \frac{4}{\sqrt{\pi}} \left(\frac{m}{2k(T + \frac{m_a T_a}{m})} \right)^{3/2} \int_0^\infty F(g) \exp\left(-\frac{m g^2}{2k(T + \frac{m_a T_a}{m})}\right) g^2 dg \quad (3)$$

$\alpha = 1$ for electron-cesium collisions; $\alpha = \sqrt{2}$ for ion-neutral collisions with equal masses and temperatures. β may be calculated if the shape of $Q(g)$ is known. For a velocity dependence $Q(g) = Q(\bar{g}) \bar{g}^v / g^v$ one has

$$\beta(v) = \frac{9\pi}{32} \left(\frac{\pi}{4}\right)^{v/2} \Gamma\left(\frac{6-v}{2}\right) ; \quad (\text{Fig. 3}) . \quad (4)$$

For electron-cesium collisions $Q(g)$ has a rather complicated Ramsauer-like structure^{2,3}. In this case β is electron temperature dependent (Fig. 4).

In the continuity conditions of the particle currents at the boundaries between the plasma and the collision-free electrode sheaths the 1st order transport approximation is used^{4,5}. Contrary to the 0th order approximation (random current) in these boundary conditions the linear anisotropy of the velocity distribution is considered, consistent with the diffusion approximation in the plasma.

The electron temperature is assumed to be constant in the plasma $T_e = T_E$. For the ion temperature $T_i = T_a = (T_E + T_C) / 2$ is used in the plasma equations (1). In the few-collision case the effective ion temperature T_{i1} in the ion boundary condition for an electron rich emitter sheath, is determined by the equation

$$j_{SL} = \frac{1}{4} n_1 \bar{v}_{i1} \exp\left(-\frac{eM_E}{kT_{i1}}\right) = \frac{1}{\chi} \int_0^1 \frac{1}{4} n_1 \bar{v}_i(\xi) \exp\left(-\frac{eM_E}{kT_i(\xi)}\right) \exp\left(-\frac{\xi d}{\lambda_a}\right) d\xi ; \quad (5)$$

with $\chi = \int_0^1 \exp\left(-\frac{\xi d}{\lambda_a}\right) d\xi ; \quad \xi = \frac{x}{d} ; \quad j_i = 0$

and the assumption $n(\xi) = n_1$ over 2 to 3 ion mean free paths from the emitter.

The right hand side of eq (5) sums up all the ions at their corresponding temperatures coming from the plasma to the emitter. In the transmission probability $\exp(-\xi d / \lambda_a)$ the mean free path of Cs-atoms λ_a ($Q_a = 110 \text{ \AA}^2$ hard sphere) instead of λ_i is used because of the large charge exchange cross section. For a linear temperature drop between emitter (T_E) and collector (T_C) one obtains

with the mean-value theorem:

$$T_{i1} = T_E - \gamma \frac{\lambda}{d} (T_E - T_C), \quad (6)$$

where in the interesting range $1 < d/\lambda_a < 10$ γ varies between 0,3 and 1, and is weakly dependent on V_E, T_E and T_C (Fig.5).

The electron saturation current density for a converter with electron rich emitter sheath is

$$j_{e,sat} = \frac{2 \sqrt{j_R j_{SL}} \cdot \sqrt{\frac{m_i}{m_e}} \sqrt{\frac{T_E}{T_{i1}}} \left[j_R / \left(j_{e,sat} \left(1 + \frac{3}{8} \frac{4T_E}{3T_E + T_C} \frac{d}{\lambda_e} \right) \right) \right]^{\frac{T_E - T_{i1}}{2T_{i1}}}}{\sqrt{\left(1 + \frac{3}{4} \frac{4T_E}{3T_E + T_C} \frac{d}{\lambda_e} \right) \left(2 + \frac{3}{4} \frac{4T_E}{3T_E + T_C} \frac{d}{\lambda_e} \right)}} \quad (7)$$

Similar expressions were derived earlier from Bohdanský and Langpape⁶, Warner and Hansen⁴, Maev et al.⁷, Wilkins and Gyftopoulos⁸. The differences between the models mainly concerning the boundary conditions (0th and 1st order), the definition of the diffusion constants and the assumptions about the particle temperatures may cause discrepancies of a factor 2 in the numerical results.

Results and Discussion

The momentum transfer cross sections $Q_e(\bar{g}_e)$ calculated from saturation current measurements of converter Ta4 show a systematic dependence upon the emitter and reservoir temperatures (Fig.6). From published^{3,4} experimental and theoretical electron-caesium cross sections a decrease of the cross section to a Ramsauer minimum with increasing electron temperature is indicated for the temperature range in Fig.6. There is a rather good agreement between the high reservoir temperature values and the extrapolated momentum transfer cross sections given in Ref.3. In the following an attempt is made to explain the splitting and the shape of the curves at different reservoir temperatures.

According to Ref.3, electron-ion scatterings cause an increase of the cross section with increasing degree of ionization. In Fig. 6 for $T_E=1436$ °K the degree of ionization at the emitter edge of the plasma n_1/n_a is decreasing from $4 \cdot 10^{-5}$ at $T_R=513$ °K to $6 \cdot 10^{-6}$ at $T_R=648$ °K, but $Q_e(\bar{g}_e)$ is increasing. At the collector edge n_2/n_a is about 0,5 n_1/n_a and 0,02 n_1/n_a respectively. Therefore, we may assign a secondary role to the degree of ionization effect.

Kundsen law instead of ideal gas law for calculation of the Cs-density n_a in the converter at low Cs-pressure may also be shown to give a contrary effect.

The cross sections in Fig.6 were calculated assuming a uniform emitter work function distribution ($\phi_{SL} - \phi_R$). From a patchy emitter surface electrons are chiefly emitted from the low work function patches, while ionization particularly takes place at the high work function patches. Therefore, in eq. (7) we have ($\phi_{SL} \lesssim I - 2 kT_E$)

$$\sqrt{j_R j_{SL}} = \sqrt{\frac{A T_E^2}{e} \cdot \frac{1}{2} \mu_a \exp\left(-\frac{I}{kT_E}\right) \exp\left(\frac{\phi_{SL} - \phi_R}{2kT_E}\right)} \quad (8)$$

where the "patch factor" $\exp((\phi_{SL} - \phi_R)/2kT_E)$, (≥ 1), depends on the patch distribution and the emitter temperature. The patch distribution function $f(\Psi)$ is influenced by the Cs-coverage; additionally space charge fields and patch fields⁹ will disturb the patch distribution function in a complicated way.

In the case of independent patches (patch fields and space charge fields negligible) ϕ_R and ϕ_{SL} are easily calculated^{10,11} from the equations'

$$A T_E^2 \exp\left(-\frac{\phi_R}{k T_E}\right) = \int_0^{\infty} A T_E^2 \exp\left(-\frac{\phi}{k T_E}\right) f(\phi) d\phi; \frac{\mu_a}{2 \exp\left(\frac{1-\phi_{SL}}{k T_E}\right) + 1} = \int_0^{\infty} \frac{\mu_a f(\phi) d\phi}{2 \exp\left(\frac{1-\phi}{k T_E}\right) + 1} \quad (9)$$

Haas¹² and Xuan-Phuc et al.¹³ have shown for Cs-free surfaces, that for the calculation of the electron emission current at different emitter temperatures the measured patch distributions may be substituted in a good approximation by Gaussian functions. In Fig.7 the temperature dependence of the patch factor is shown, calculated from Gaussian distributions at different half widths and from measurements for which the assumption of independent patches holds. For refractory metals in Cs-atmosphere the mean value of the work function distribution depends on T_E and T_R . With the theory of Rasor and Warner¹⁴ for Cs-covered surfaces we may expect approximately constant widths of the patch distribution if T_E/T_R is in the linear range of the $\phi(T_E/T_R)$ -plots, i.e. the patch factor should have the same emitter temperature dependence as the Gaussian patch factors at constant half width for all reservoir temperatures. For the patch distribution measurements of Ref. 15 of a vapor deposited electropolished Re-surface at various T_E/T_R by means of electron beam scanning method the agreement is reasonably good (Fig.7).

It is also possible to obtain the patch factors more directly by calculating ϕ_{SL} and ϕ_R from ion and electron emission current measurements of the same emitter^{16,17}. The patch factors calculated from Breitwieser's measurements¹⁶ (110-W-emitter) have strong reservoir temperature dependence (Fig.7), although all T_E/T_R are in the linear range of the Rasor-Warner-plots. The magnitude and the shape of the curves cannot be explained by a Gaussian-like patch distribution. If the modified Saha-Langmuir equation (9b) holds, there must be spots of high work functions between ϕ_R and the substrate work function ϕ_0 , where a large part of the ions are produced. These spots could have even sizes much below the resolution of the electron beam scanning techniques.

From unignited mode saturation current measurements the patch factors can be calculated for given momentum transfer cross sections (eqs. (2,7,8)). Because of the complicated electric fields near the emitter surface and the poor knowledge of adequate cross sections the results are only qualitative.

Patch factors are calculated from the Ta4 saturation current measurements (Fig.8) using the "asymptotic" cross sections at $T_R=648$ °K shown in Fig.6. These patch factors have reservoir temperature and emitter temperature dependences similar to the data calculated from Breitwieser's measurements in Fig.7 and could be explained by the above mentioned arguments. This implies in Fig.6, that at low emitter and reservoir temperatures the momentum transfer cross sections computed from the unignited mode measurements with the assumption $\phi_R = \phi_{SL}$ are considerably distorted by the emitter patch effect.

For the ion saturation current and ion rich emitter sheath a similar formula as eq. (7) can be derived. From ion current measurements of Houston¹⁸ (thoriated W-emitter) patch factors are calculated using hard sphere collision model ($\beta=9\pi/32$ in eq. (2)) (Fig.9). A good fit to the Gaussian patch factors is obtained with $Q_1 \sim 800$ A² ($b_1=0,08$ cm²/Volt sec at $T_1=1240$ °K, normalized to $n_a=2,69 \cdot 10^{19}$ Cs-atoms/cm³).

Acknowledgement

The assistance of E. Maier in the construction and operation of the experimental apparatus and of R. Rühle and his programmer group in preparing the computer programs, is gratefully acknowledged. The authors wish to thank to Dr. L.K. Hansen for a fruitful discussion.

References

- (1) MAIER, E., Institut für Kernenergetik der Universität Stuttgart, Diplomarbeit 5-47d (1967).
- (2) STONE, P.M., REITZ, J.R., Phys. Rev. 131, 2101, (1963).
- (3) NIGHAN, W.L., Therm. Conv. Spec. Conf., San Diego, Oct. 1965, p. 84.
- (4) WARNER, C.; HANSEN, L.K., J. Appl. Phys. 38, 491 (1967).
- (5) INGOLD, J.H., Therm. Conv. Spec. Conf., Houston, Nov. 1966, p. 306.
- (6) BOHDANSKY, J.; LANGPAPE, R., 6th Conf. on Ionization Phenomena in Gases, Paris, 1963, IV, P. 543.
- (7) MAEV, S.A.; STAKHANOV, I.P.; GUSKOV, Yu.K.; ZYUKOV, V.I.; PASHCHENKO, V.P., Soviet Phys.-Tech. Phys. 12, 778 (1967/68).
BONDARENKO, I.I., et al., Geneva Conf. Sept. 1964, P/317.
- (8) WILKINS, D.R.; GYFTOPOULOS, E.P., J. Appl. Phys. 38, 12 (1967).
- (9) HANSEN, L.K., J. Appl. Phys. 37, 4498 (1966).
- (10) HERRING, C.; NICHOLS, M.H., Rev. Mod. Phys. 21, 185 (1949).
- (11) KAMINSKY, M., Physikalische Verhandlungen 1962, Heft 1/2, Seite 60.
- (12) HAAS, G.A., THOMAS, R.E., J. Appl. Phys. 34, 3457, (1963).
- (13) XUAN-PHUC, N.; HUTZLER, B.; ALLEAU, T., Int. Conf. on Therm. Elect. Pwr. Gen., London, Sept. 1965.
- (14) RASOR, N.S.; WARNER, C., J. Appl. Phys. 35, 2589, (1964).
- (15) VAN SOMEREN, L.; LIEB, D.; MISKOLCZY, G.; KITRILAKIS, S.S., J. Adv. Energy Conv. 7, 201, (1968).
- (16) BREITWIESER, R., Therm. Conv. Spec. Conf., Galtlinburg, Oct. 1963, p. 17.
- (17) BREITWIESER, R.; RUSH, W., Therm. Conv. Spec. Conf., San Diego, Oct. 1965, p. 218.
- (18) HOUSTON, J.M., 24th Phys. Elect. Conf., MIT, March 1964, p. 211.

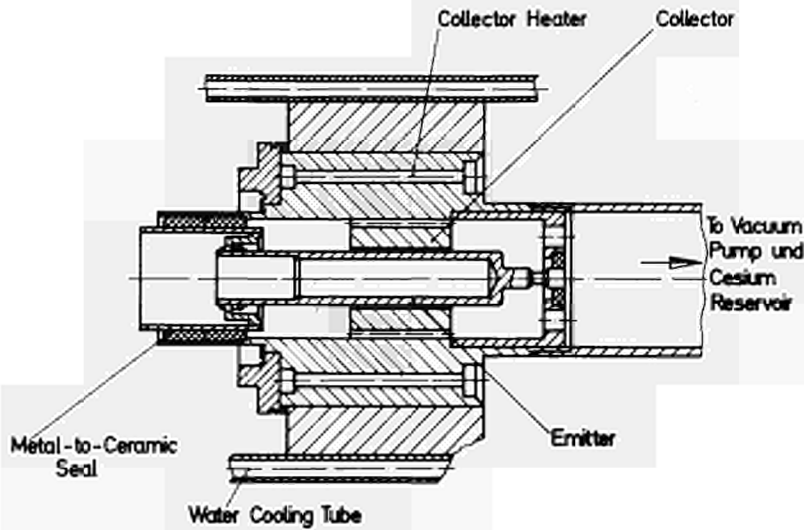


Fig.1.
Experimental
Converter Ta4

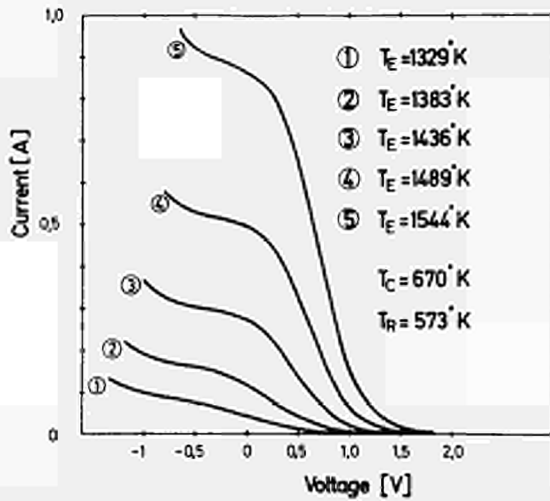


Fig.2. Typical Characteristics in the Unignited Mode (Converter Ta4)

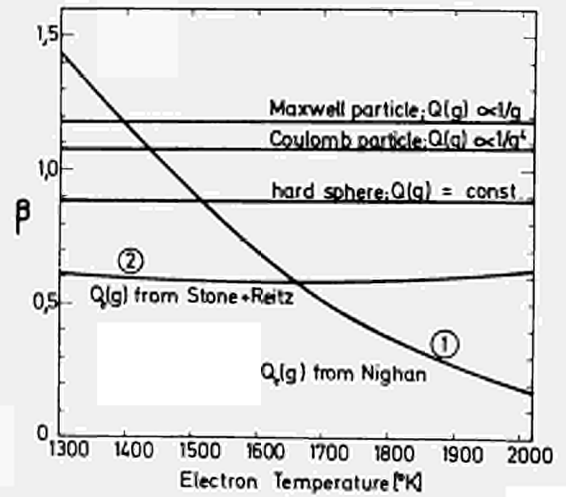


Fig.4. β for Electron - Cesium Collisions, eq. (2)

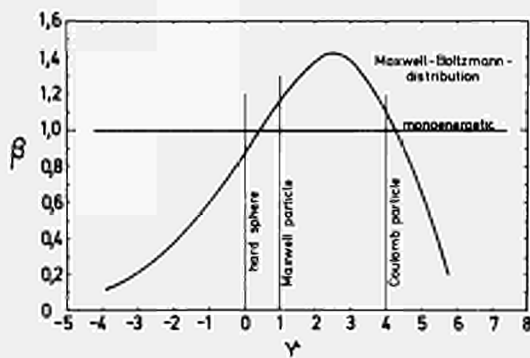


Fig.3. $\beta(\nu)$, eq. (4)

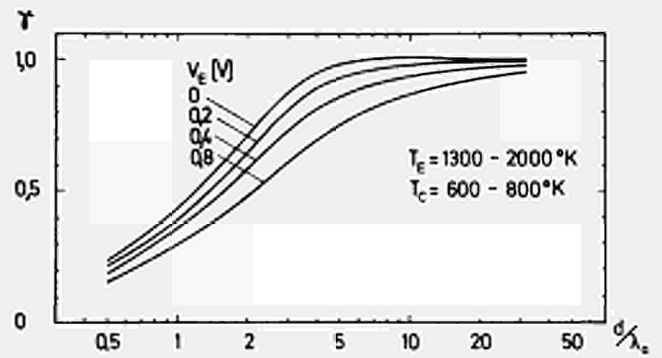


Fig.5. $\gamma(d/\lambda_0)$; Parameter V_E ; eqs. (5), (6)

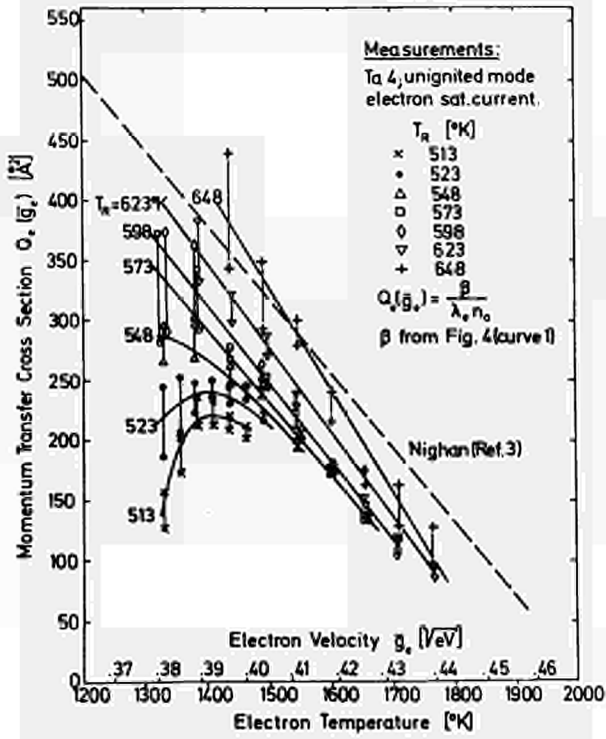


Fig. 6. Electron - Cesium Atom Momentum Transfer Cross Section

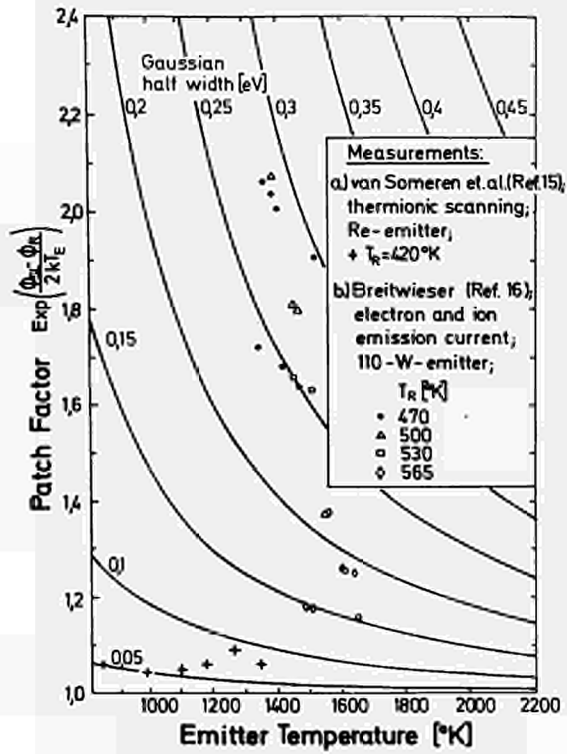


Fig. 7. Emitter Patch Factor

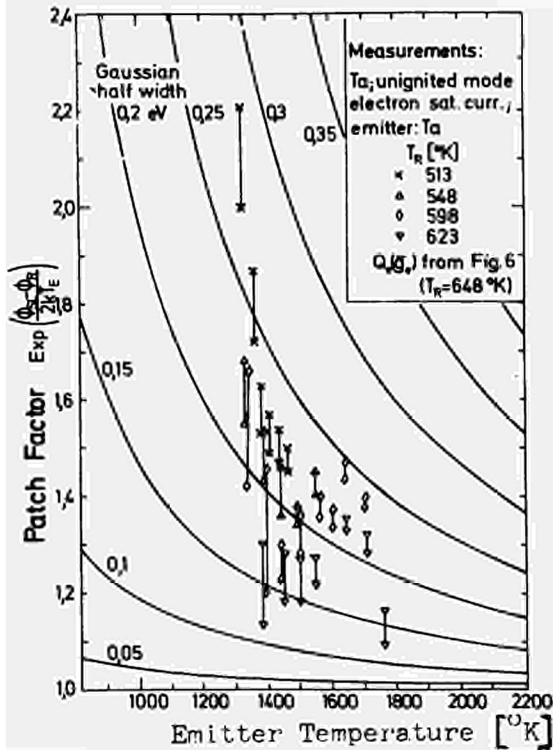


Fig. 8. Emitter Patch Factor

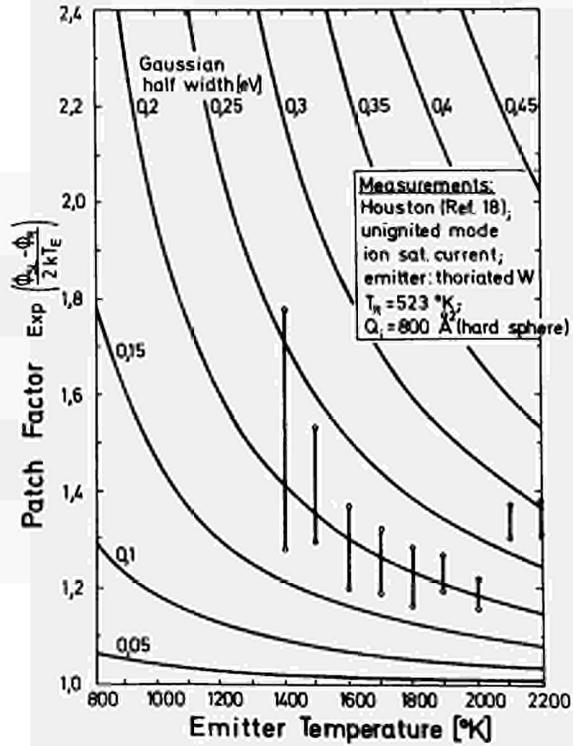


Fig. 9. Emitter Patch Factor

DISCUSSION

Speaker of paper H-4: E. WOLF.

GUSKOV (USSR): Did you take into account when determining these scattering cross-sections of the electrons and the atoms, the additional scattering by plasma fluctuations and how would you differentiate one from the other?

WOLF (Germany): We considered the emitter patch effect as an attempt to explain the fact that the cross sections calculated from our saturation current measurements are apparently pressure-dependent. We assumed that the patches are independent, that the patch fields can be neglected, and that the emitter sheath is homogeneous and has no fluctuations.

RASOR (USA): There may be a misunderstanding here. Dr. GUSKOV, I believe, is asking about the scattering by fluctuations in the plasma, and not about the fluctuation of the field at the surface due to patches. Therefore, I believe, the answer to the question is that Mr. WOLF is operating always under electron-rich conditions, under-compensated.

And under these conditions the electrons are not injected into the plasma through an accelerating sheath. The emitted electrons therefore are nearly in equilibrium with the plasma electrons, so there is no highly non-equilibrium electron beam disturbing the plasma to cause significant fluctuations. I believe that is the answer to the question.

WOLF: Yes.

SOME PECULIARITIES OF I-V CURVES OF THE THERMIONIC
CONVERTERS IN CESIUM VAPOR AT THE PRESSURE 10^{-2} - 5 TORR

Borzenko V.L., Drobjazko S.V., Drobjazko L.A., Knizhnikov V.N.
I.V. Kurchatov Atomic Energy Institute, Moscow, USSR

ABSTRACT

I-V curves of the thermionic converters in the regimes of the quasi-saturation and of the deep acceleration are considered. In these regimes the plasma density was measured by the single Langmuir probe. Influence of the normal and the anomalous Schottky effects to the emission from the patch emitter, and conditions of the existence of the space charge barrier is discussed.

INTRODUCTION

The power output and the efficiency of the thermionic converters are strongly influenced by the emissivity of the cathode.

The measurements of the emissivity of the different cathodes in the presence of cesium vapour. ("S" curves) were made for the low cesium vapour pressure ($\leq 10^{-2}$ Torr) only. For these pressures the electrical field at the emitter reached the value of the order 10^4 - 10^5 v/cm and the fields of patches disappeared. The volume ionisation did not occur in these cases [1,2,3] .

When cesium vapour pressure is increased, the volume ionisation and the dense plasma are developed. In this case the electrical field at the emitter depends upon properties of the plasma.

Currents in the power quadrant and in the short circuit are not likely to be the emission currents, because saturation of the currents is not reached [4,5,6] .

In the present paper attempt was made to analyze the reasons of the deviation of the currents in the power quadrant from the emission currents, when temperature of the emitter and cesium vapour pressure were ranged in the typical region for thermionic converters.

APPARATUS AND EXPERIMENTAL TECHNIQUE

A cross-section of the experimental device with 30 mm diameter plane-parallel electrodes is shown at the Fig.1. The lateral surfaces of the electrodes are covered by Al_2O_3 to remove the false discharge. Such coverage allowed to operate at the sufficiently high external voltage up to 10v whereas the emission's area remained constant. The spacing was ranged within 0,1-15 mm. The location of the electrodes was determined by the optic cathetmeter through the sapphir

window. The electrodes were heated by the electron beams, and temperature of the emitter was varied from 700 to 1700°C. The Optical pyrometer used for taking a measurement.

An oil-free vacuum of the order $5 \cdot 10^{-7}$ Torr in metallic container with temperature about 400°C was produced by sorption pump. I-V curves were measured in pulse regime, so that the emitter temperature did not change within the impulse. Single Langmuir probe with guarding to remove the false current was used to measure the plasma density and the temperature of the electrons.

EXPERIMENTAL RESULTS

Typical I-V curves with Mo emitters in the various regimes shown at the Fig.2. It is seen that the complete saturation of the converter current exist when temperature of the emitter low $T_{\text{em}}=800-1000^{\circ}\text{C}$. Growth of the current behind knee I-V curve presents when temperature increase. Current is 1,5-2 times increase, when voltage raise to 5-7v. It is seen from Fig.3, that with low temperature the current of the saturation remained constant, when the interelectrode space changed.

At Fig 4 the regimes in which the plasma density was measured is noted by point at the I-V curves. The plasma density near emitter for each point of the I-V curve is plotted at Fig 4 also.

The plasma density near emitter and the temperature of the electrons which were measured by the several authors [4,7,8] are tabulated in the Table I.

DISCUSSION

It is affirmed [4,5,6] that complete saturation of the converter current in the regimes of the quasisaturation and of the deep acceleration should be failed due to three causes: I) electron back emission from plasma is being reduced due to

emitter sheath height increasing, 2) increasing ion current, generated by the electrons, accelerated on the growing emitter sheath, 3) the emitter work function is reduced via the normal and the anomalous Schottky effects.

The first suggestion should be essential when emitter sheath is low. It is evident that this effect should be low in the regimes of the short circuit and with external voltage.

It is seen from the Table I, that ion current is 1-20% from total converter current. In the paper [8] it is demonstrated that plasma density near emitter varies directly proportional to converter current. It is seen from Fig. 4 that, when the converter current has reached the saturation, plasma density varies slightly. Therefore neither the first nor the second mechanisms are not capable to explain the growth of current in the regime of deep acceleration". Let us consider the influence of the normal and the anomalous Schottky effects to the growth of current. In the Hansen's paper [9] there is the solution of the Poisson's equation at the emitter sheath of the thermionic converter,

The field at the emitter with the assumption, that the plasma field at the beginning of the sheath is zero, is

$$E^2 = 7,6 \cdot 10^5 \cdot V_s^{1/2} \left[J_p \left(\frac{M}{m} \right)^{1/2} \left(1 - \alpha \frac{T_e}{T_e} \right) - e V_e (1 - 2\alpha\beta) \right] \quad (1)$$

All notations is such as in the Hansen's case.

Electrical field at the emitter is zero, if

$$J_p \left(\frac{M}{m} \right)^{1/2} \left(1 - \alpha \frac{T_e}{T_e} \right) = e V_e (1 - 2\alpha\beta) \quad (2)$$

In this case

$$J_{emax} = J_p \left(\frac{M}{m} \right)^{1/2} \frac{\left(1 - \alpha \frac{T_e}{T_e} \right)}{(1 - 2\alpha\beta)} \quad (3)$$

If the emission from the cathode is higher than I_{\max} the space charge barrier (virtual cathode) develops in the front of the emitter. This double sheath limits the current from the emitter down to I_{\max}

In this case as well as in the case of the vacuum diode the current from emitter is independent on the emissivity of the cathode. But this case differs from the vacuum diode one by the fact that the increasing of the sheath potential can not increase the current higher than I_{\lim}

$$J_{\lim} = J_p \left(\frac{M}{m} \right)^{1/2} \quad (4)$$

Transition from the regime with space charge barrier to the regime with accelerating field with variation of the plasma density occurs very roughly because the derivative of the current with respect to plasma density is infinite in the point where the electric field at the emitter is zero, and emission current at the knee of the curves I versus n more than I_0 .

At the Fig.5 current from emitter is plotted versus the plasma density for parameters $I_0=1, 10, 100 \text{ A/cm}^2$ with $V_s=1v$, $T_E=0, 1, 9 \text{ ev}$ $T_e=0, 25 \text{ ev}$, $P_{cs}=1 \text{ Torr}$.

Straight line (ABC) corresponds to the case of space charge barrier and at the parts of the curves AA', BB' and CC' the current enhancement due to normal Schottky effect is shown. Current enhancement due to ion current is shown by dotted lines.

At the Fig.6 the current from Mo emitter is plotted versus plasma density the cesium vapour pressure being 1 Torr. Emission currents were taken from the paper [2].

From these figures it is seen that current enhancement due to normal Schottky effect is not over than 70%, when the plasma density is 10^{15} cm^{-3} .

From Table I it is seen that maximum value of the plasma density near emitter is never exceeded $4 \cdot 10^{14} \text{ cm}^{-3}$.

In the case when the surface of the emitter compose of patch with different work function and the size of the patches considerably more than Debay length, the patches with different work function is possible to consider as independent [10]. In this case the full current from such emitter will equal to the sum of the currents from different patches.

In the our experiments size of patches was of the order of 20μ . If the plasma density was higher than 10^{12}cm^{-3} , the Debay length was considerably less than size of patches.

The difference of work function of different patches is small, when the coverage of emitter by cesium atoms is high. Such surface is near uniform when $T_E/T_R < 2,6$ [11]. When the plasma density near such emitter is sufficient in order to remove the space charge barrier, the growth of the emission current can be caused by the normal Schottky effect only.

In our experiments when plasma density changed slightly, Fig.4, the complete saturation of the converter current was reached Fig.2. However, when the lateral surfaces of the electrodes are not cover, current saturation is absent even in the case in which the guard screens are used.

When the temperature of the emitter increased $T_E/T_R < 2,6$, the difference of the work function of different patches might become $0,5-1 \text{v}$ [11]. In this case the plasma density is not sufficient in order to compensate the space charge barrier near patch with low work function.

It is seen from Fig.5 that small increasing of the plasma density caused the large enhancement of the emission current. In this case the complete saturation is not reached Fig.2.

In order to receive the total emission current it is necessary to increase the plasma density near emitter considerably. It is likely that the increasing of the voltage is no enough in order to increase the plasma density near emitter.

CONCLUSIONS

1. If the coverage of the emitter by cesium atoms is high the complete saturation of the converter current obtained. When the coverage is decreased the saturation of the current is not took place.

2. Ion current is less than 20% from converter current and can not explain the growth of the current in the regimes of the quasi-saturation and of the deep acceleration

3. The growth of the current due to the normal Schottky effect is not excede 70% when the plasma density increase up to 10^{15}cm^{-3} .

4. With the low coverage that fact, that the current saturation is not reach, is explain by the plasma density near emitter is unsufficiently in order to compensate emission from patches with low work function.

TABLE I

P_{cs} [Torr]	T_E °K	V [volt]	J [$\frac{A}{cm^2}$]	n_p [cm^{-3}]	T_e °K	J_p/J	$\frac{n_p}{N\alpha}$	Authors
1	1730	-0,2	4	$2 \cdot 10^{14}$	2600	0,2	$2 \cdot 10^{-2}$	W.H.Reichelt at al [7] .
1	1730	+0,7	8,5	$4 \cdot 10^{14}$	2800	0,2	$4 \cdot 10^{-2}$	
2	1730	-0,42	4	10^{14}	2300	0,1	$5 \cdot 10^{-3}$	
3	1730	-0,1	4	$1,5 \cdot 10^{14}$	2400	0,15	$5 \cdot 10^{-3}$	
0,7	1150	+0,7	1,4	$8 \cdot 10^{12}$		$2,3 \cdot 10^{-2}$	10^{-3}	E.K.Kosyrev at al [8]
0,7	1150	+0,8	2,8	$1,2 \cdot 10^{13}$		$1,7 \cdot 10^{-2}$	$1,7 \cdot 10^{-3}$	
0,7	1150	+1	4,7	$5 \cdot 10^{13}$		$4 \cdot 10^{-2}$	$7 \cdot 10^{-3}$	
0,7	1150	+1,2	5,7	$7 \cdot 10^{13}$		$5 \cdot 10^{-2}$	10^{-2}	
1	1405	+0,6	6,3	$3,7 \cdot 10^{13}$	2400	$2,3 \cdot 10^{-2}$	$3 \cdot 10^{-3}$	G.A.Dyuzhev at al. [4]
1	1405	+0,9	13,8	$1,8 \cdot 10^{14}$	2600	$3,4 \cdot 10^{-2}$	10^{-2}	
2	1685	-0,24	1,3	$1,8 \cdot 10^{13}$	2300	$5,5 \cdot 10^{-2}$	10^{-3}	
2	1685	+0,05	3,6	$6,4 \cdot 10^{13}$	2400	$7,1 \cdot 10^{-2}$	$3 \cdot 10^{-3}$	
2	1685	+0,24	5,1	$3,7 \cdot 10^{13}$	2300	$7,6 \cdot 10^{-2}$	$5 \cdot 10^{-3}$	
10^{-1}	1573	+0,3	0,8	$1 \cdot 10^{13}$		$5 \cdot 10^{-2}$	10^{-2}	
10^{-1}	1573	+1,2	1	$3,5 \cdot 10^{13}$		0,14	$3,5 \cdot 10^{-2}$	Results of authors of this paper.
10^{-1}	1373	+1	1	$3 \cdot 10^{13}$		0,12	$3 \cdot 10^{-2}$	
10^{-1}	1173	+2	2	$5 \cdot 10^{13}$		0,2	$5 \cdot 10^{-2}$	

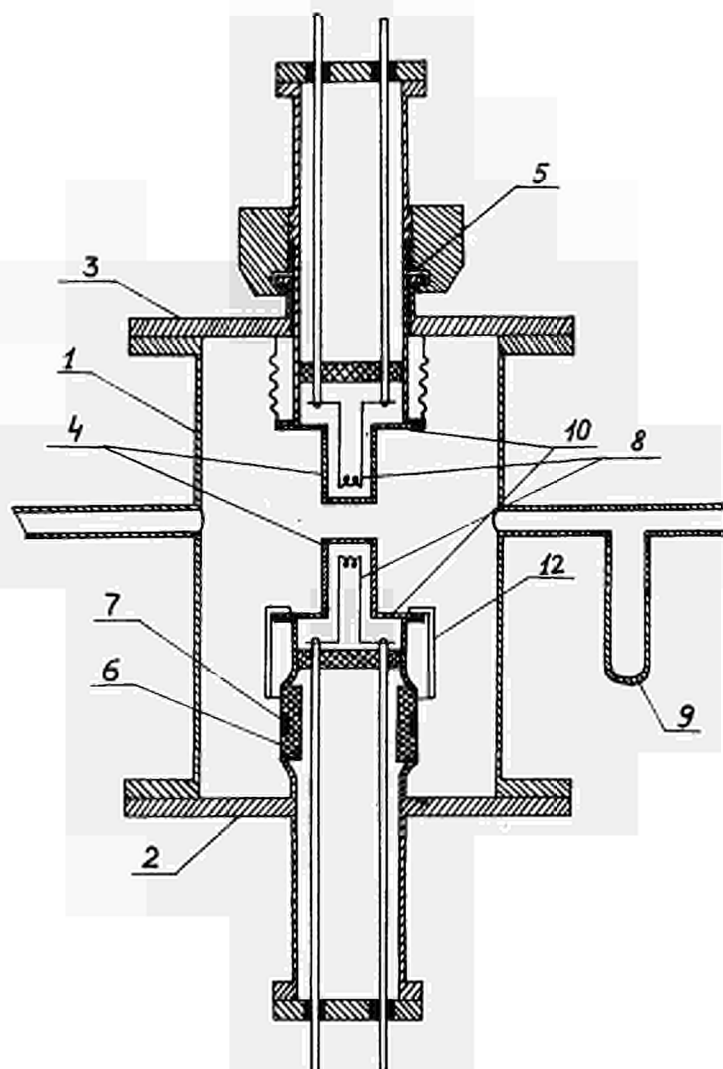


Fig.I. Experimental device

- 1 - the Container,
- 2,3 - the flanges
- 4 - the electrodes,
- 5 - the mechanism of the displacement,
- 6 - the insulator,
- 7 - the guard ring at the insulator,
- 8 - the heaters,
- 9 - the cesium reservuar,
- 10,11 - the surfaces and screen, which cover by Al_2O_3 .

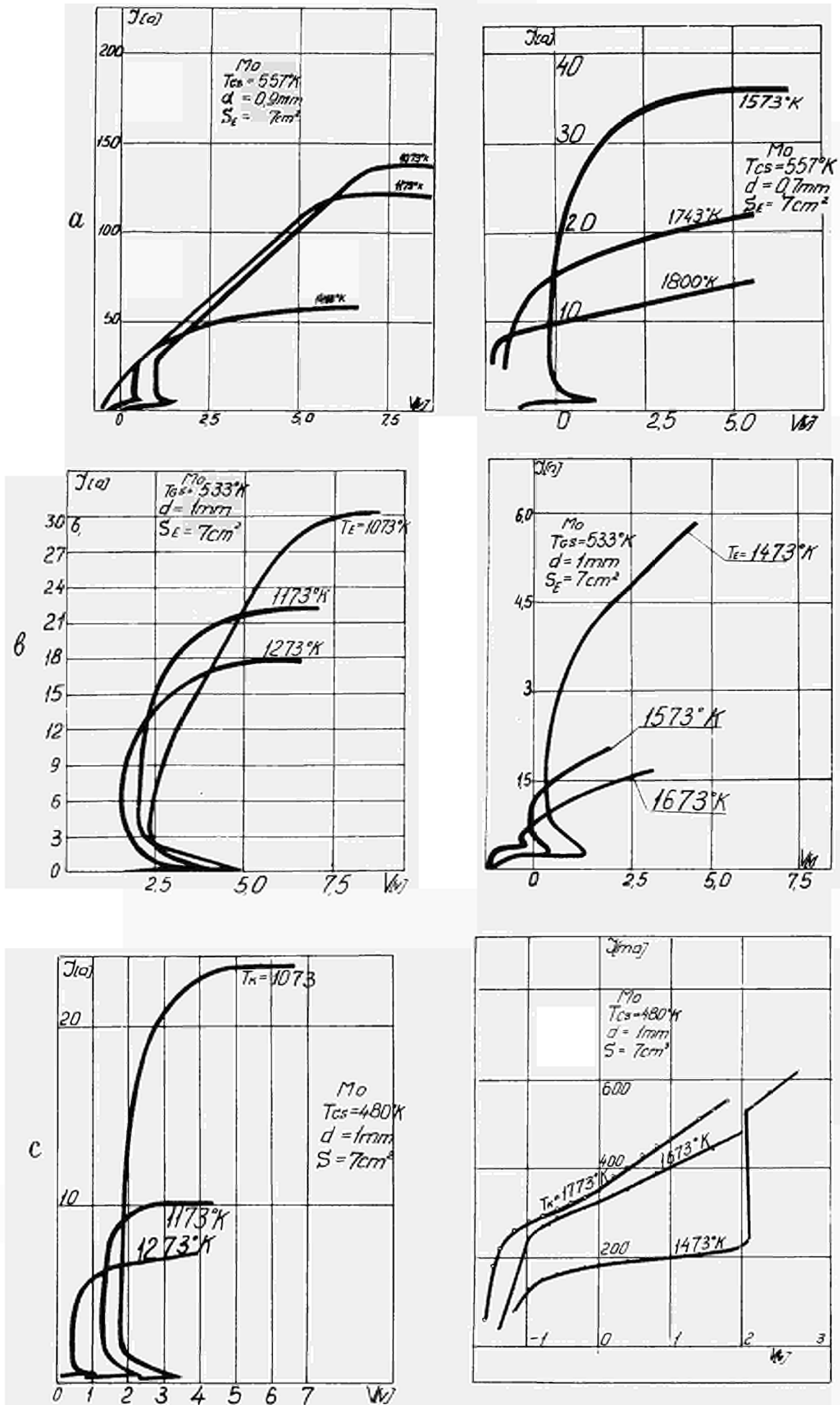


Fig.2. The I-V curves.

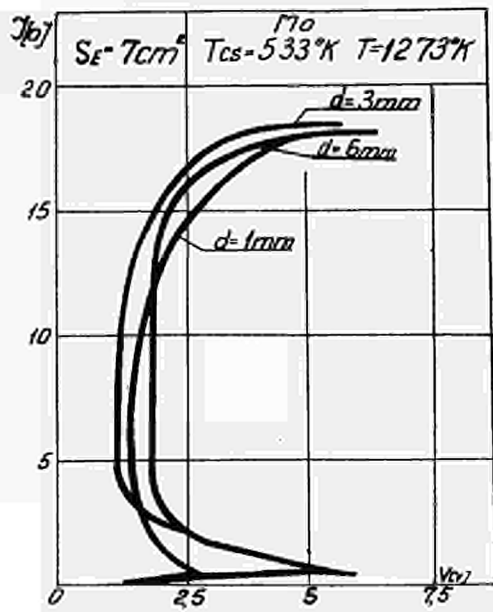


Fig. 3. The I-V curves for different space.

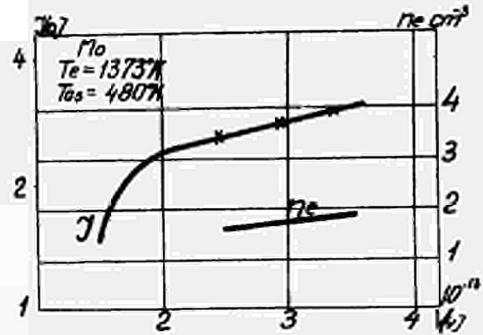


Fig. 4. The plasma density near emitter at each point of the I-V curve.

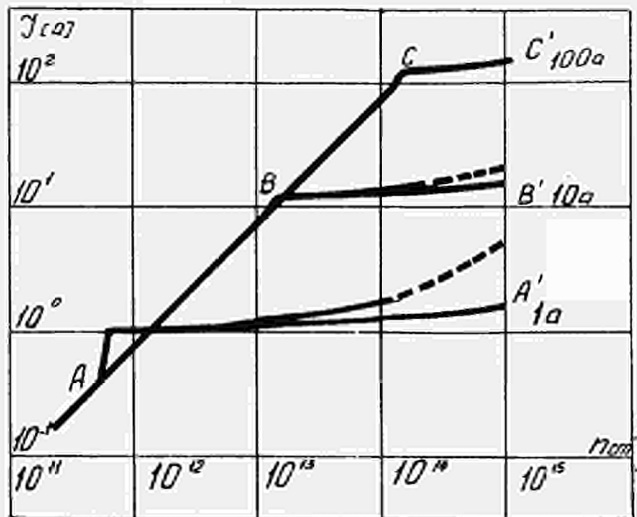
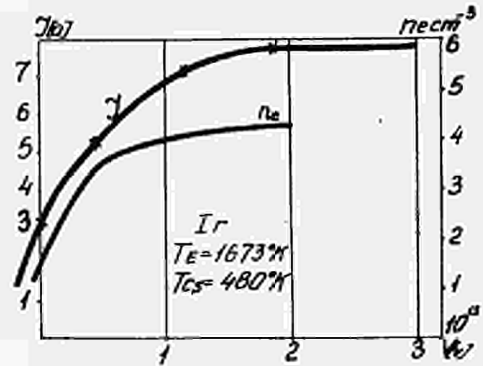


Fig. 5. The current from emitter as a function of the plasma density.

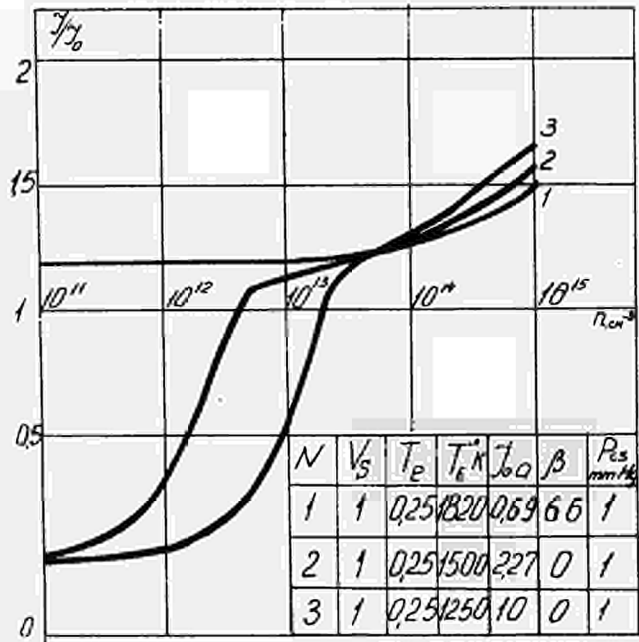


Fig. 6. The current from Mo emitter as a function of the plasma density.

REFERENCES

- I. J.Langmuir. Phys.Rev.44, 433 (1933).
2. R.L.Aamodt at al. J.Appl. Phys.33, 2080 (1962).
3. R.G.Wilson, J.Appl.Phys.37, 3161 (1966).
4. Г.А.Дюжев. и др.ЖТФ,36, 692 (1966).
5. R.H.Bullis at al. Proceedings of Thermionic Conversion Specialist Conference (San Diego, October, 1965).
6. Г.А.Дюжев и др.ЖТФ 37, 1823 (1967).
7. W.H.Reichelt and W.L.Kruer. Proceedings of Themionic Conversion Specialist Conference (San Diego, October, 1965).
8. F.K.Kosyrev, these proceedings.
9. L.K.Hansen. J.Appl.Phys.38, 4345 (1967).
10. N.S.Rasor at al. *Advanced Energy Conv.* 2, (1963)
- II. N.S.Rasor. J.Appl.Phys.35, 2589 (1964).

EXPERIMENTAL VERIFICATION ON THE RASOR PHENOMENOLOGICAL
THEORY OF THE ARC MODE REGIME OF A CESIUM THERMIONIC
CONVERTER.

F.V.Kondratiev, G.V.Sinyutin.

I.V.KURCHATOV INSTITUTE OF ATOMIC ENERGY, Moscow, USSR.

A sufficiently strict theory of the arc mode regime for a cesium thermionic converter was proposed by B.Moizhes et al, [1]. One of the important conclusions of this theory is the fact that under the arc mode regime, ions are generated mostly near the cathode while in the other area of the interelectrode spacing, the generation function rapidly decreases with respect to the coordinate. Main disadvantage of the theory is associated with the complicated equations which are difficult to solve even by electron computers.

Arc mode regime theory of a thermionic converter developed by I.Stakhanov [2] assumes that ionization should occur within the entire thermionic converter volume, the ionization rate being proportional to the charge density while the ionization coefficient being independent of the plasma density. In later works [3,4] it was, however, shown that the ionization rate in the gap would rather rapidly drop as the distance from the cathode surface increases. The area of volume ionization is evaluated as an area of the width $(10-15)\lambda$, where λ is the free path length of electron scattering by cesium atoms.

The phenomenological theory of the arc mode regime suggested by N. Rasor [5] can be considered as another case compared with [2]. This theory assumes that space ionization should occur within a narrow region of the cathode potential drop, and the charge transfer should be of a purely diffusion character within the rest interelectrode space. Here, the character of the boundary conditions is similar to that of [1, 2].

According to this theory the current-voltage characteristic can be written as

$$\frac{J_s}{J} = 1 + A(\rho\delta + D) e^{\frac{eV}{kT_{ex}}},$$

where

$$A = \frac{3}{4} \cdot \frac{1}{\rho\lambda} e^{-\frac{e}{kT_{ex}}(\varphi_k - \varphi_a + V_a)}; \quad D = \frac{4}{3} \rho\lambda \cdot (e^{\frac{eV_a}{kT_{ea}}} - 1); \quad (1)$$

φ_k, φ_a are the cathode and anode work functions; T_{ek}, T_{ea} are the electron temperature near the cathode and anode, V_a the anode potential drop; p is the cesium vapour pressure; J_s is the saturation current (the cathode emission current with the effective work function φ_k); J, V are the converter current and voltage (since under the working conditions $V < 0$, in Eq.(1), V implies $-V$).

Eq.(1) must describe the current-voltage characteristic within the range of the converter working voltages from 0 to a certain value V' which practically coincides with V_{opt} . With further increase, the $V > V'$ characteristic breaks down, and the current should drop exponentially due to appearance of a double electric layer near the cathode

$$J(V) = J(V') e^{\frac{e(V' - V)}{kT_k}} \quad (2)$$

$J(V')$ satisfying Eq.(1).

The present paper deals with the comparison of experimental output characteristics of the converter with the calculated ones. The measurements were performed with flat electrode converters. The dimensions of the cathodes were 2,5 cm²,

they were made of different materials: tantalum and molybdenum were obtained by means of the powder metallurgy technique, and molybdenum and tungsten by vacuum fusion. The arc mode regimes were investigated for various cathode temperatures, cesium vapour pressures and electrode gaps for:

$$\begin{aligned}t_k &= 1400^\circ - 1800^\circ\text{C}, \\t_{cs} &= 220^\circ - 380^\circ\text{C} \quad (p=0,17-12 \text{ mm Hg}), \\ \delta &= 0,1 - 2 \text{ mm}.\end{aligned}$$

Analysis of a family of the current-voltage characteristics taken for various δ for fixed electrode temperatures and cesium vapour pressures allow determination of the constants J_s , A , D , and T_{ek} in Eq.(1), and thus we were able to plot a theoretical current-voltage characteristic. The possibility of such a treatment was shown in the papers [6,7] .

Using this method all the experimental data on the arc mode regime were treated.

Fig.1 a gives an illustration of one of the arc mode regimes ($t_k=1600^\circ\text{C}$, $t_a=700^\circ\text{C}$, $t_{cs}=320^\circ\text{C}$) where the solid lines show the measured current-voltage characteristics of a converter with the cathode made of vacuum fused tungsten. The characteristics were taken for various electrode gaps, and the output power corresponding to these values was

$$W = JV. \tag{3}$$

Dashed lines show the values calculated by Eq. (1).

The effect of the double-layers potential near the cathode calculated by Eq.(2) is shown by chain-dotted lines in the same plot (here V_{opt} represents V').

Comparison of the characteristics shows that Eq.(1) is valid for greater values of V , than it was predicted by the theory, and the shape of the current-voltage characteristics indicates that there should not appear a double electric layers near the cathode . According to our data, this note can be applied to those regimes at which the cesium vapour pressures are near optimum. At the same time in a number of cases the characteristics could be described by total Eqs. (1) and (2).

For example, Fig.2 presents the measured and calculated

current-voltage characteristics and output powers of a converter having the cathode made of vacuum fused molybdenum for $t_k=1600^\circ\text{C}$, $t_a=700^\circ\text{C}$, and $t_{cs}=300^\circ\text{C}$. The cesium pressure for this regime is lower than optimum, and one can see an area in the characteristics which shows the presence of the double layer potential. The same areas were present in the characteristics taken at pressures which were sufficiently higher than the optimum ones.

The data presented in Fig.2 are also of interest due to the fact that they allow evaluation of the width of the space ionization region. According to the theory of Ref. [5] this region is assumed to be very narrow. In practice, however, it has the finite dimensions of $(10-15)\lambda$ [3,4].

When $\delta = 0.1$ mm and 0.25 mm the calculated values of $\frac{\delta}{\lambda}$ were ~ 1.5 and ~ 4 respectively. The developed arc mode regime was not realized, and the characteristics observed greatly differ from those predicted by the theory. For $\delta \geq 0.5$ mm the ratio $\frac{\delta}{\lambda} \geq 10$, a developed arc mode regime will be realized in a converter, and the experimental characteristics become close to the calculated ones.

Fig.1 b shows the converter currents and powers as a function of the interelectrode spacing. It is seen that under a developed arc mode regime the dependence $J(\delta)$ is in fact described by a fraction-linear function of Eq.(1). Hence one can arrive at a practically important conclusion that the output power slightly depends on the gap in the range of small values of δ (when the cesium vapour pressure are fixed). The optimum voltage of the converter can be found from the condition

$$\frac{\partial W}{\partial V} = 0,$$

which is equivalent to the equation $e^{-u} = \xi(u-1)$, where $u = \frac{(4) eV}{kT_{ex}}$

$\xi = A(\rho\delta + D)$. For the maximum power one obtains the expression

$$W_{max} = J_s \left(V_{opt} - \frac{kT_{ex}}{e} \right).$$

If experimental and calculated values of W_{\max} are plotted on the coordinate axes then in the cases of their coincidence the points corresponding to each regime should lie on the angle bisector between the axes. For all other regimes (except those when due to the smallness of $\rho\delta$ one observed increase in the current with the gap) the values W_{\max} were obtained using Eq. (5). The greatest relative difference between the experimental and calculated values of power was observed for $t_k=1400^\circ\text{C}$ for large $p \sim 10$ mm Hg and $\delta \geq 1\text{mm}$. In other cases the difference between W_{\max}^{calc} and W_{\max}^{exp} was smaller than 10 per cent, their best agreement being within the halfwidth of the curve $W_{\max}(t_{cs})$. Fig.3 shows such a comparison made for four cathode materials (the points are taken within a halfwidth of the curve $W_{\max}(t_{cs})$).

The theory allows the cathode potential drop and the cross section of electron scattering by cesium atoms to be determined from the experimental data for different regimes within $\sigma_s = (0.1 - 1) \cdot 10^{-14} \text{ cm}^2$ which are in agreement with other experimental data cited in literature.

The total data allow a conclusion about experimental evidence of the Rasor theory for the above range of the cesium vapour pressures, and about the possibility of describing the most interesting region of a current-voltage characteristic in Eq.(1).

ADDITION

It is known from the experimental data that under an arc mode regime, the dependence of currents and powers of a cesium converter upon the anode temperature t_a has its maximum when $t_a \approx 600^\circ - 700^\circ\text{C}$ (for example, [7]).

Probe measurements carried out with a low voltage cesium arc in a converter with the molybdenum electrodes [8] made with the aim of elucidation of the phenomenon mechanism proved that there appeared a potential barrier near the anode. The barrier slows down electrons leaving interelectrode plasma towards the anode, however, it does not prevent the anode emission electrons. As the anode temperature increases the charge concentration also increases, and the plasma electron temperature becomes higher. These effects should result in the current growth. Decrease in the current with further rise in the anode temperature

could be attributed to increasing of the anode emission current.

In our experiments, the cathode was made of molybdenum, and the anode was made of nickel.

A balance condition for the anode current can be written as

$$J = \frac{en_a v_a}{4} e^{-\frac{eV_a}{kT_{ea}}} - J_{sa}, \quad (6)$$

where J_{sa} is the current of the anode emission, n_a , v_a are the concentration and thermal velocity of the electrons near the anode.

Since with the increase in the anode temperature n_a , $v_a \sim \sqrt{T_{ea}}$ and T_{ea} also increase, the current J should correspondingly increase. According to calculations carried out using the data of Ref. [9] the emission current J_{sa} from the nickel anode is not great for the temperature range under investigation. Therefore, in forming the maximum in the curves $J(t_a)$ an important part should be played by the dependence of the anode potential drop V_a on t_a .

A great number of current-voltage characteristics taken under regimes when the application of the Rasor theory was valid, were treated by the methods of Ref. [5]. Fig.4 presents short circuit current J_{K3} , and maximum output power W_{max} as a function of the anode temperature observed experimentally.

The magnitude of the anode barrier (in terms of the electron temperature) can be found from the equation

$$f(y) = \beta,$$

$$\text{where } f(y) = -\frac{2y}{2+y} + \ln(e^y - 1), \quad y = \frac{eV_a}{kT_{ea}}, \quad \beta = \ln AD + \frac{e(\varphi_k - \varphi_a)}{kT_{ex}} \quad (7)$$

Since all the values appearing in the expression for β can be determined directly from an analysis of the current-voltage characteristics, the parameter β is a known constant for each regime. The values of $\frac{eV_a}{kT_{ea}}$ determined from Eq.(7) are also in the plots of Fig.4 together with calculated errors

As is seen from the plots when the anode temperature varies the value of $\frac{eV_a}{kTe_a}$ goes through the minimum at the point which is close to the optimum anode temperature. Here, as follows from Eq.(6) the magnitude of the current in this temperature range should pass through the maximum. This is in good agreement with the experimental data.

Since the electron temperature near the anode slightly increases with the anode temperature the shape of the dependence $\frac{eV_a}{kTe_a}(t_a)$ should mainly depend on the character of the variation in the anode potential drop V_a with the increase in t_a .

Appearance of appreciable anode emission current J_{sa} can cause a shift in the optimum anode temperature towards lower values of t_a compared with the position of the curve minimum $\frac{eV_a}{kTe_a}(t_a)$.

REFERENCES

1. Б.Я. Мойжес, Ф.Г. Бакич, М.Г. Меликян, ЖТФ, 35/9 (1965) 1621.
2. И.П. Стаханов, И.И. Касиков, Препринт ФЭИ-17 (1965).
3. И.П. Стаханов, ЖТФ, 37/7 (1967) 1277.
4. И.П. Стаханов, ЖТФ, 37/7 (1967) 1286.
5. N.S.Razor, Intern. Conf. on Thermionic Power Generation. London (1965).
6. S.S.Kitrilakis, F.Rufeh, Intern. Conf. on Thermionic Power Generation. London (1965).
7. Ф.В. Кондратьев, Г.В. Синдтин, В.Ф. Тихонов, Атомная энергия, 23 9 (1967) 208.
8. Г.А. Дожев, А.М. Марциновский, Б.Я. Мойжес, Г.Е. Пикус, В.Г. Дрьев, ЖТФ, 37 6 (1967) 1155.
9. R.G.Wilson, J. Appl. Phys, 37 8 (1966) 3161.

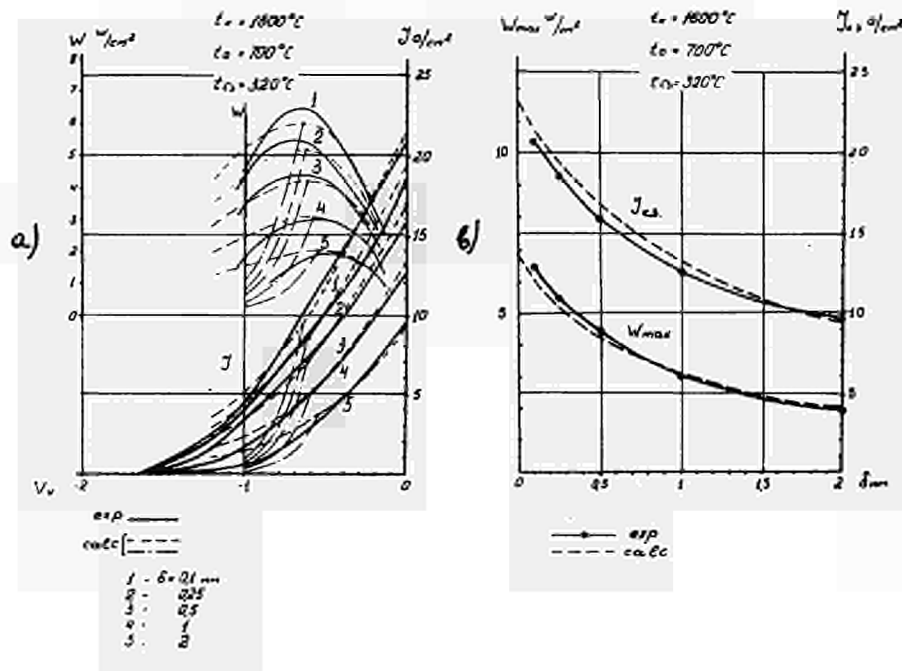


Fig.1. Comparison of experimental and calculated characteristics of the converter (the tungsten cathode).

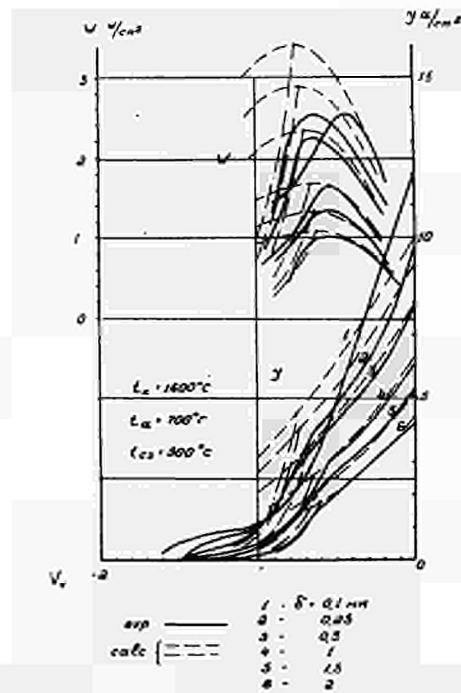


Fig.2. Comparison of experimental and calculated characteristics of the converter (the molybdenum cathode).

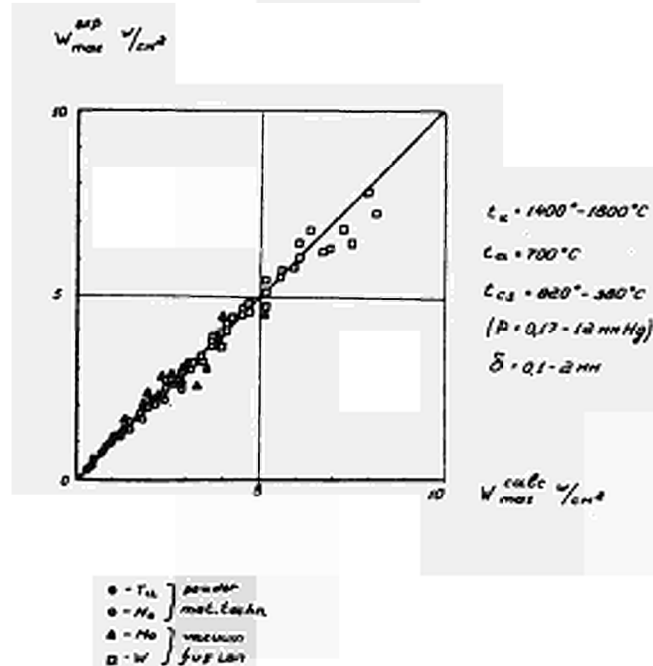


Fig.3. Comparison of experimental and calculated power of the converter.

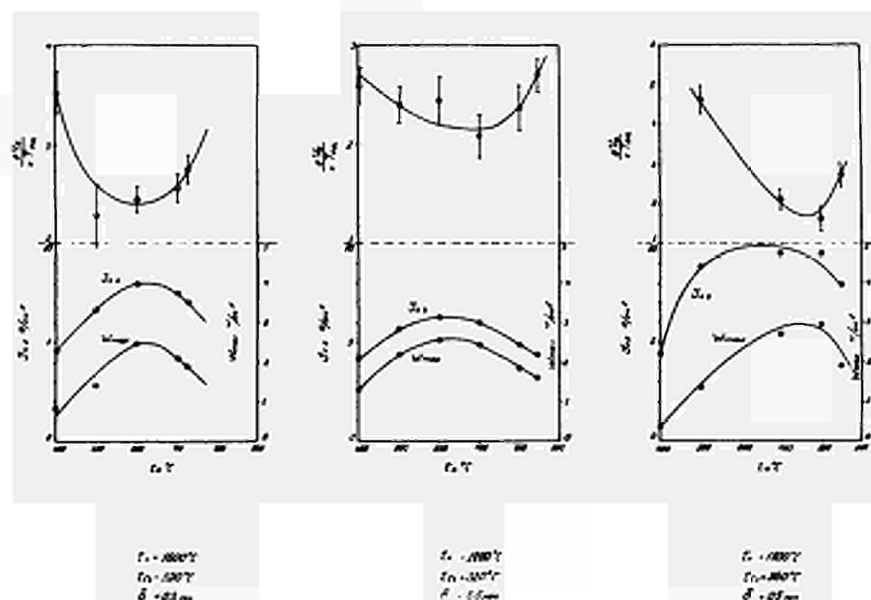


Fig.4. Short circuit current, maximum power, and anode potential barrier (in terms of the electron temperature) as a function of the anode temperature.

IONIZATION STATE OF CESIUM THERMIONIC
CONVERTER PLASMA

Kosyrev F.K., Kosyreva N.P., Lunev E.I.

I.V.Kurchatov Atomic Energy Institute
Moscow, USSR

One of the main unsolved problems in the investigation of arc conditions for the work of thermionic converter is the consideration of physical processes occurring in the interelectrode space plasma. The most important problem consists in the way for realization and support of the ionization in a volume with $T_e > T_E$

In a number of available works (for instance [1,2,3,4] the authors take certain ionization mechanisms in the converter space. It is known that ion generation in Cs is caused by step ionization through 6P state. Atom excitation from the basic state to 6P one is due to fast electrons

with the energies higher than the first excitation potential. These are either the electrons accelerated at the cathode fall [1], or fast electrons of "the tail" of Maxwell distribution [2,3,4]. Depending on the relation between the processes causing population and devastation of Cs atom energetic levels one can observe in plasma both the presence of ionization equilibrium (electron density is associated with Saha equation electron temperature) and the deviation from it. Ionization equilibrium disturbance may be caused by the following reasons: 1) non-Maxwellian function of electrons distribution; 2) radiation (especially a resonance one) going beyond the boundaries of the system; 3) particle diffusion to the walls. Apparently, in a real thermionic converter a deviation from ionization equilibrium can exist, which is associated with any of above-mentioned reasons. Ionization equilibrium in a thermionic converter is usually observed either at high electron densities [5] or at rather large distances [6]. One can judge on the presence of ionization equilibrium in plasma by Saha equation validity, which can be controlled by a simultaneous measurements of temperature and electron concentration. In such a case the electron "temperatures" measured by various optical methods, should coincide. When ionization equilibrium disturbs, electron "temperatures" measured by various optical methods and quite different by their values, can give a valuable information on the space ionization state. Most full information on plasma ionization state one can obtain while measuring the absolute populations values in a wide range of excitation energies. Unfortunately, as it is known, such measurements for the case of cesium plasma were carried out under the discharge tube condition [7]. In the present work an attempt was made to realize such measurements under the conditions of a thermionic converter with a narrow space.

Experimental apparatus

The experiments were carried out at the apparatus consisting of a plane-parallel diode with a changeable space (0-5mm) and 30 mm electrode diameter (fig.I). Temperature in the cesium reservoir was changing up to $T=400^{\circ}\text{C}$. Cathode maximum temperature $T\sim 2000^{\circ}\text{C}$, anode temperature was changing within $400-900^{\circ}\text{C}$. Small ohmic losses at the anode terminal ($R\sim 10^{-6}$ ohm) and a set of shunts from $5\cdot 10^{-5}$ to 2 ohm allowed to obtain volt-ampere characteristics in a converter condition directly under the loading without application of any additional feeding sources. In order to take characteristics under a non-energetic quadrant a possibility is provided for switching on an additional feeding source into the scheme. Optical measurements of plasma, measurements of cathode temperature and of the interelectrode distance value were performed through 4 sapphire windows soldered into removable flanges. Cathode temperature was measured by an optical pyrometer on a cavity radiation in the cathode body, modelling "black body" while the gap value was measured by an optical cathetometer.

To avoid any contamination, the sapphire windows were closed with metallic screens during the process of the cathode degassing and during the intervals between the measurements. The apparatus is fully dismountable, the available metallic gaskets provide a long work under the temperature up to 500°C .

For optical measurements of plasma parameters a grating spectrograph with linear dispersion of $5,5 \text{ \AA}/\text{mm}$ and with photoregistration, as well as a prism spectrograph with photoelectrical registration, were used.

These devices provide the accomplishment of rather wide spectroscopic investigation of the converter plasma. Application of one-lens optical system and a narrow diaphragm allowed to obtain rather a great depth in the image sharpness.

Measurements of spectral lines and recombination continuum absolute intensities, of spectral lines profiles, and of reversal temperatures for diffusion series lines were performed. During absolute and relative measurements the calibration was made by means of a standard band lamp. During photographic registrations the calibrated spectrum of the standard lamp and the observed discharge spectrum were being photographed on the same film. Photographing of plasma spectra and standard lamp radiation was performed at several expositions. Schwarzschild constant was neglected. During calculations the values of recombination cross-sections obtained in [7] were used, while for the calculations of transition possibilities the data of [8] were used. If the interelectrode space was not fullfilled with plasma, the discharge diameter was measured on the photographs taken by a narrow-band filter for the wavelength 4560 \AA .

Experimental results

Plasma parameters measurements were made in wide range of cathode temperatures and cesium pressures under the converter conditions and with applied voltage. Originally, plasma parameters behaviour was studied in a diode with electrodes heated to the same temperatures. The form of L-V characteristics and a visual picture of discharge development in these conditions are in accord with the description given in the work [4]. Fig.3 L-V characteristics in a discharge region, as well as the electron density behaviour near the cathode at different discharge currents. At the current-voltage characteristic one can clearly see the region of discharge development (voltage are nearly constant), plasma occupying only a part of the cathode area. When current is above 10-15a the voltage are sharply increasing with the discharge current. Electron density near the cathode (curve 2, fig.3).behaves analogous to the voltage: in the regime of discharge broadening the electron concentration remains practically constant. It is

important to emphasize that the full electron number (i.e. $N_e S$ I/cm, where S cm² is the arc cross-section near the cathode) in the whole region of the discharge current changes is continuously increasing (curve 3, fig.3). Electron density behaviour in plasma distanced from the cathode is analogous.

Fig.4 presents the curves of electron temperature distributions across the interelectrode gap, measured by means of various methods. Temperature of the diffusion series lines reversal 9-10/D-6P (T_D) and electron temperature were measured on relative intensity of recombination continuum T_e . Electron density was measured, and ionization temperature T_{Saha} was calculated too. As it is seen from the given curves, electron temperatures measured by two independent methods, are in a practical accord with that calculated from Saha equation in the whole space, except the region near the cathode. Plasma parameters behaviour near the cathode makes us to suppose the anomaly in population value of excited cesium levels. To study the atoms distribution by the excited states, the measurements of absolute values of cesium levels populations in the space center at two interelectrode gap values were performed. The first d -value is equal to the distance at which a deviation in "temperatures" values (fig.4) can be observed. Besides that, the given value at the pressure $p=1$ mm Hg nearly corresponds to the optimal value on pd 4. If the space value $d=3$ mm, one can wittingly expect the ionization equilibrium to be valid in the space center [6].

Measurement results are given on fig.5. The curves are built on the results of measurements of absolute intensities of forbidden transitions (5-6) D-6S (points with excitation energies 1,8 and 2,8 eV) and absolute measurements of sharp series lines (9-14) S-6P. In addition the data were obtained on absolute intensity of recombination 6P-continuum

(take in consideration the superposition of 5D-continuum) and on broadening of the fundamental series lines. The curve I obtained in the converter regime ($U_p = -0,1v$), while the curve 2 - under the applied voltage $+0,8 v$. As it was expected, when the interelectrode gap value is 3 mm, the points lie down on the stright line with an inclination corresponding to the temperature measured on the recombination continuum relative intensity. Saha equation is observed to be precisely valid. For $d=0,4$ mm an essential deviation from the linear behaviour of levels population as well as from Saha equation (curve 2) is observed. In the whole excitation energy range the curve 2 lies lower than the corresponding Boltzmann curve (a-a). Curve inclination at low excitation energies corresponds to the electron temperature measured on the recombination continuum.

Discussion of the results

Electron distribution is in equilibrium with all bound and free energetic states in plasma, i.e. it strongly obeys to Saha and Boltzmann equations with the same temperature, if the detailed equilibrium of all shock and radiation processes take place. In such a case the distribution of electrons and heavy particles by their velocities is a maxwellian one. Radiation escape from plasma, disturbance of temperature components equality, particles diffusion cause the deviation from the equilibrium. But, if the probabilities for shock processes prevails over the effective probabilities for radiation processes and diffusion role is unessential, then the distribution on exitation levels will be close to an equilibrium distribution with temperature of that

component of the plasma, which determine the shock processes frequency. So, if in this case the majority of collisions occurs with electrons participation, then the distribution on levels will be close to that equilibrium with electron temperature. This problem is thoroughly considered in the works [9, 10, 11]. Estimations show that in the investigated regimes ($d=0,4$ mm, $N_e=2 \cdot 10^{13}$ I/cm³) radiation escape cannot cause a visible deviation from equilibrium distribution. On the other hand, only one of the rest two factors to be able to disturb equilibrium distribution, is studied in detail; namely - the particles diffusion upon the walls [10, 11]. These show that essential electrons and ion escape from the considered volume cause the deviation from upper levels equilibrium population (on the contrary, radiation escape influences mainly on the lower levels population). Estimations show that for the case given on fig.5 curve 2, the diffusion may give an essential deviation from equilibrium distribution. Really, as one can see from the given experimental data, if the space is 0,4 mm, then an essential deviation of $\lg Ni/Gi$ value behaviour from the linear law is observed. Apparently, the authors of [12] ran into analogous phenomena during T_e measurements by the lines relative intensity. When using this method the relative intensity is usually measured at those lines which correspond to the transitions from upper levels. For our case " T_e " determined by this method, correlates with the inclination of the straight line b-b. This seems to give an extremely understated result, having no likeness with the real electron temperature. (By the way, "the temperature" determined on the relative intensity of those lines which correspond to the transitions from rather low levels, gives a precious T_e value [7]. This result is confirmed in our work too).

Returning to fig.5, we note that neither electrons and ions diffusion, nor radiation escape can explain the lowered population of our levels as compared to the Boltzmann one. It remains to suppose that this effect is caused by nonmaxwellian distribution function. In an unequilibrium plasma the electron-electron collisions are responsible for the equilibrium distribution establishment while electron interactions with ions and atoms cause its disturbance. The presence of a significant electron flow along the atomic energy levels in a discrete spectrum, as well as in a continuous spectrum, may cause electron distribution function deviation from an equilibrium one, especially, if electron energy is higher than the first excitation potential. On the other hand, the estimations shown that under the curve 2, fig.5 conditions the length of maxwellian distribution establishment for the electrons with energy higher than 1,4eV [13] is more than the space magnitude. Inside the space the equilibrium electrons distribution can establish for much lower energies

It is necessary to emphasize in conclusion that the anomaly of the levels population leads to some difficulties in ions generation, i.e. to the "ion price" increase.

It is possible that Vd increase during pd parameter decrease is associated with a sharp growth of levels populations deviation from equilibrium ones.

In conclusion the authors express their gratitude to G.A.Kasabov for fruitful discussions.

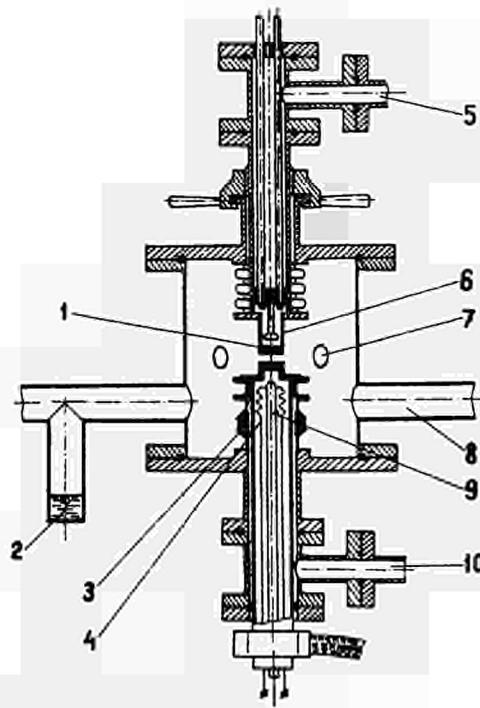


Fig. I. Experimental diode.

1. Emitter. 2. Cesium reservoir. 3. Insulator.
4. Collector heater. 5. Vacuum pump of heater
volume. 6. Emitter heater. 7. Sapphire windows.
8. Vacuum pump of device. 9. Cooling gas. 10. Vacuum
pump of collector volume.

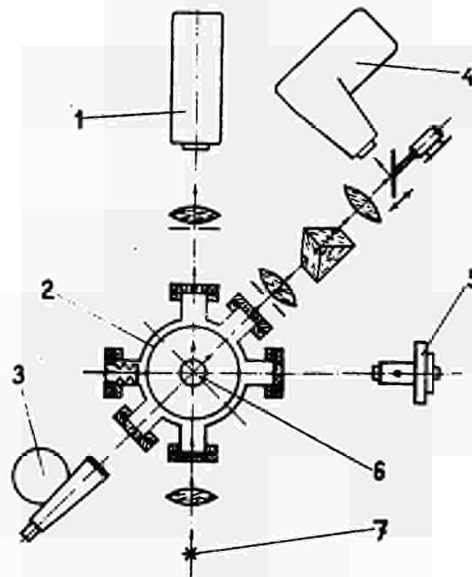


Fig. 2. Sketch of optical measurements.

1. Grating spectrograph. 2. Screens. 3. Cathotometer.
4. Prism spectrograph. 5. Pyrometer. 6. Emitter of the
diode. 7. Standard band lamp.

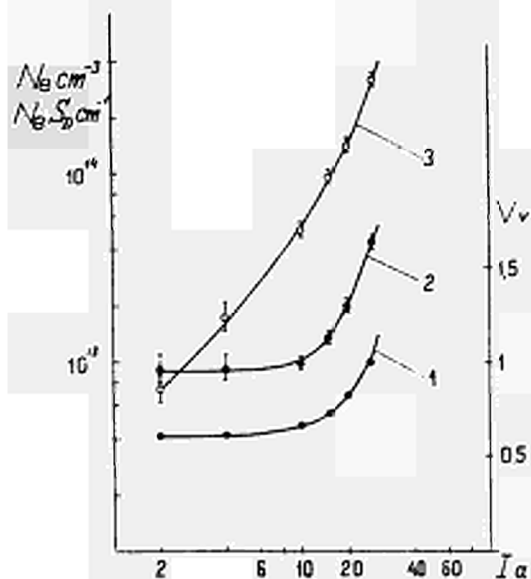


Fig.3. Electron density near the emitter.
 $T_e = T_c = 1160^\circ\text{K}$ $P_{cs} = 0,7$ mm Hg. Materials of Emitter and Collector are molibdenum. $d = 2,15$ mm.
 1. Voltage-current characteristic. 2. Electron density (N_e I/cm³). 3. Full electron number ($N_e \cdot S$ I/cm).

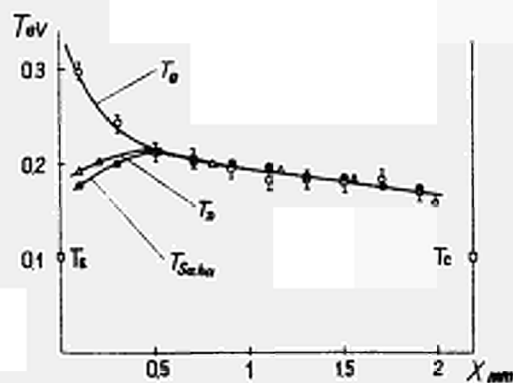


Fig.4. Curves of electron "temperatures" distribution across the interelectrode gap.
 $T_e = T_c = 1160^\circ\text{K}$ $P_{cs} = 0,7$ mm Hg $d = 2,15$ mm $J = 20\text{a}$.

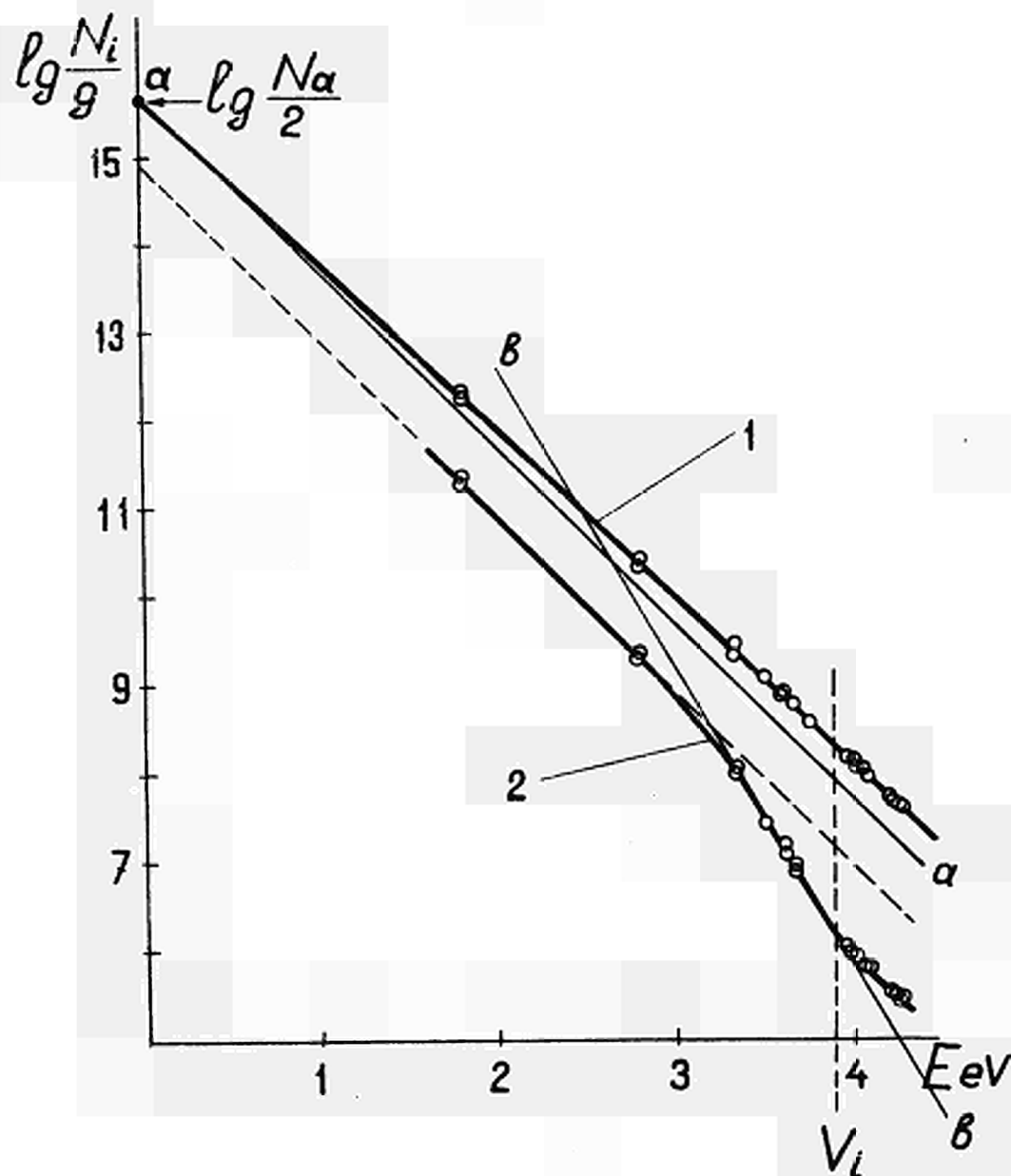


Fig.5. Absolute values of cesium levels population in the center of interelectrode space.

$T_{\text{B}} = 1440^{\circ}\text{K}$ $T_{\text{c}} = 970^{\circ}\text{K}$ $j = 2$ a/cm $P_{\text{CS}} = 1.0$ mm Hg.

1. $d = 3$ mm $N_{\text{e}} = 2 \cdot 10^{14}$ I/cm³ $T_{\text{e}} = 0.23$ ev

2. $d = 0.4$ mm $N_{\text{e}} = 2 \cdot 10^{13}$ I/cm³ $T_{\text{e}} = 0.22$ ev.

REFERENCES

1. Стаханов И.П. ЖТФ, II, 1967.
2. Ф.Г.Бакшт, Б.Я.Мойжес ЖТФ XXXV 2, 1965, 266.
3. Мойжес Б.Я. et al. ЖТФ XXXV 9, 1965, 1621.
4. N.S.Rasor. Proc.of Int.Conf.on Thermionic Pwr. Gen. London, 1965.
5. Agnew L., Summers C. Advanced Energy Conv.2, 1963.
6. Kosyrev F.K., et al. Proc.of VIII Conf. on Phenomena in Ionized Gases (Vienna, 1967).
7. Gridneva S., Kasabov G. Proc.of the Int.Symp.on MHD Electr. Power Generation (Salzburg) 1966.
8. Gridneva S., Kasabov G. Proc.of the VII Int.Conf.on Phenomena in Ionized Gases (Belgrad), 1966.
9. Биберман Л.М., Ульянов К.М. Оптика и спектроскопия 16, 3, 1964
10. Биберман Л.М. et al. ТВИ, 2, 1967, 201.
11. Сонин Э.Б. ЖТФ XXXVII, 1967, 1840.
12. Дунаев Ю.А. et al. ЖТФ, 36, 1966, 533.
13. MacDonald W.M. et al. Phys. Rev., 107, 350, 1957.

DISCUSSION

Speaker of papers H-5, H-6, H-7: D. V. KARETNIKOV.

WARNER (USA): Have the deviations from a Maxwellian distribution shown in Fig. 5 of H-7 been explained theoretically?

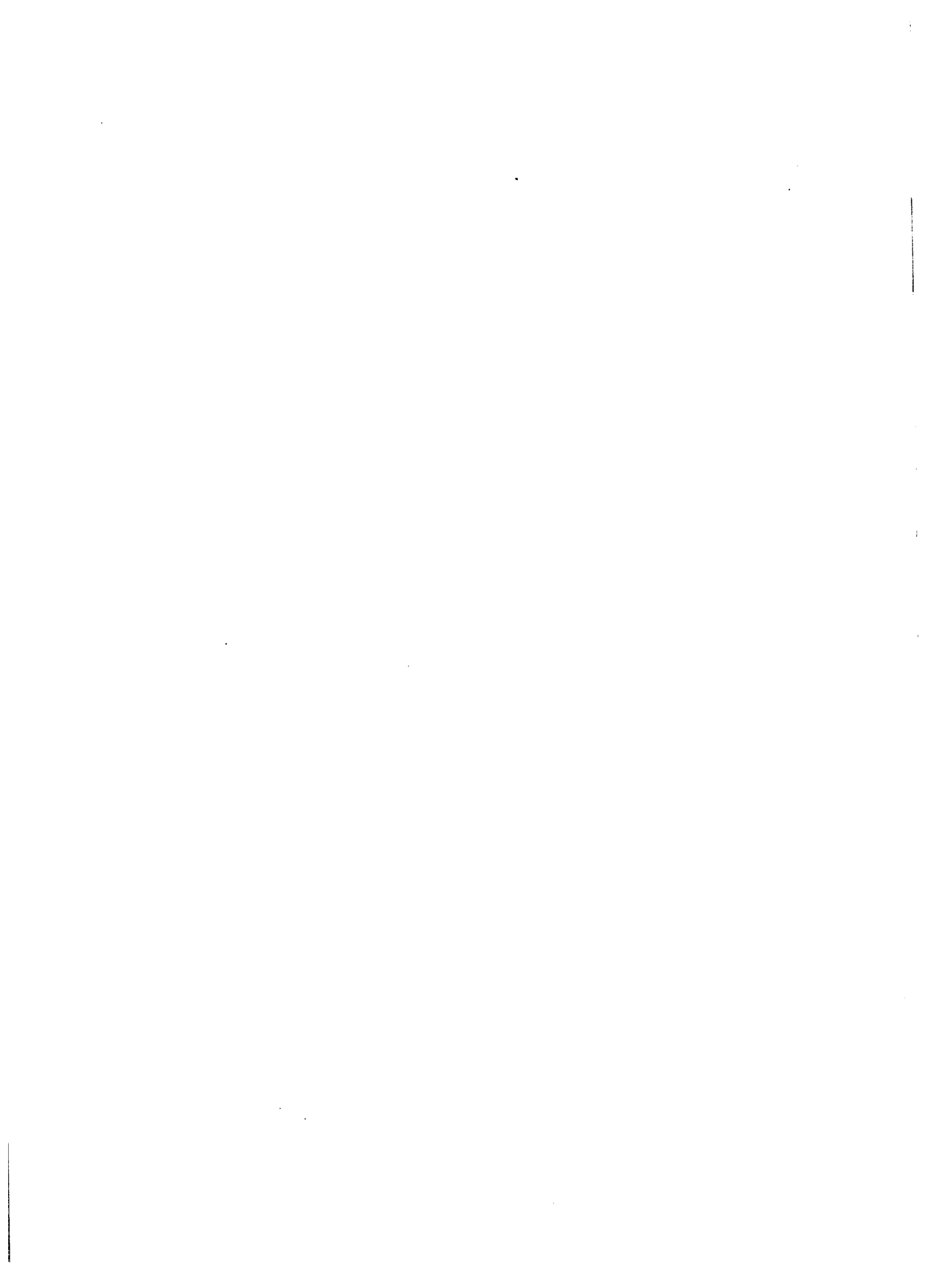
KARETNIKOV (USSR): The theory of the thermionic diode where the plasma is in a state of equilibrium was reported on last year at the Vienna Conference, There we showed that in that case those laws did apply, the ones discussed in this report today. The resulting deviation of the populations of the lower levels from the Boltzmann-law is a new result which has not yet been given a theoretical explanation. The deviation of the population of the upper levels from Boltzmann has been pretty well considered in theoretical work by RAVIOLA, SORINA and other Soviet physicists.

SCHOCK (USA): How did you introduce axial variation in the heating rate in your long diode test? Did you use multiple heaters?

KARETNIKOV: Our emitter had been made fairly thick, so that we could disregard the linear temperature drops. Our experience showed that, when the temperature profile was changed on the heater, there was in practice no change in the current flow.

SCHOCK: Is your test designed to simulate a non-uniform axial fission profile in the reactor?

KARETNIKOV: We had two different heaters. There were different profiles of heat emission, in one case there was a 50° drop and in the other, about a 200°. We noticed a considerable difference with regard to the instability depending on whether our heater was more homogeneous or with a temperature drop along the emitter of about 200°C.



ON THE DEVELOPMENT OF A LOW VOLTAGE ARC IN
A THERMIONIC DIODE WITH EXTENDED ELECTRODES

Derbilov V.I., Karetnikov D.V.,
Kosyreva N.P., Nastojashchy A.F.,
Turundajevsky V.B.

I.V.Kurchatov Institute of Atomic Energy, Moscow, USSR

INTRODUCTION

Real conditions of thermionic converter exploitation can differ to a great extent from ideal ones. The differences are connected, in particular, with following factors:

i) Temperature changes along the working parts both of the emitter and the collector due to heat source inhomogeneity and thermal losses on the different apparatus components.

ii) Voltage drops along the emitter and the collector due to their electrical resistance.

iii) Gap changes in different parts of the converter owing to mechanical inaccuracies and deformation during the work.

iiii) The detail maintaining the gap value, providing they are used.

iiii) Different constructive features. The effect of these factors can be seen most clear in the converters with extended or lengthy electrodes. The effect of any difference or their combination must influence in the first place the distributions both the current and plasma density in the converter.

In the present work some experiments on the studies of only one source of "nonideality" (the others being removed) are reported. (It should be noted, that the same experimental device may be used in complex measurements too). In fact development of a low voltage arc in cesium vapor in the thermionic diode with lengthy electrodes in the presence of the temperature variation along the emitter was investigated. The curves of plasma and current densities distribution along the diode are presented. In particular, the stable striation of the discharge was found is thought to have an ionization instability origin. The theory of instability is suggested.

EXPERIMENTAL APPARATUS

The sketch of the experimental diode is given on the fig. 1. The thick cross-shaped molybdenum tube had four plane areas (1,4 x 10 cm), one of which was used as the emitter, and others were covered with the heat screens. The coaxial electrical heater was put into the tube. The heater cavity was continuously pumped out during the experiments. The main heating took place in the thin plasma sprayed tungsten film, isolated from niobium current leading tube by alumina. The profile of the heating (and, hence, the emitter temperature) was ensured by profiling the thickness of the tungsten film. The temperature on the most heated part of the emitter was varied in the experiments from 900 to 1500°C. Two emitter temperature profiles were used: 1) "isothermal" with the total temperature drop on the whole emitter length $\Delta T \leq 50^\circ\text{C}$, the temperature from left to right side on fig. 1 being increased; 2) nonisothermal, with $\Delta T \geq 200^\circ\text{C}$ and decreasing the temperature to right side.

The temperature distribution along the emitter was controlled through one of the six sapphire windows by precision optical pyrometer, using blackbody cavities.

The thick molybdenum bar, having two current leads on the both sides, was used as the collector. In the current density distribution measurements the collector pictured on fig. I was used. It consisted of the plasma sprayed molybdenum film 1 mm thick, which was isolated by alumina layer from molybdenum base. This collector had 2 current and 11 potentiometrical leads, which were apart 1 cm one from another. The nonworking parts of the collector surfaces were covered by alumina. The cathetometer controlled value of the interelectrode gap d could be changed during the experiments.

In experiments visual observation of the arc was carried out; the photographs of the discharge in typical regimes were taken with polarisable filter; the current-voltage curve, plasma and current density distributions along the diode were measured. The I-V curves was point by point measured, the emitter temperature being constant. The plasma density was measured, using absolute intensity of the radiation of 6P - recombination continuum ($\lambda = 4820 \text{ \AA}$). The image of the discharge gap was formed with objective and then by electrically driven rotary mirror the successive parts of the image were directed to the entrance slit of the monochromator. The other movable slit was placed in front of and perpendicular to the first one. This slit 0,1 mm width allowed to measure the radiation from the different parts across the gap. Most measurements were carried out at the distance from the emitter, nearly equal to 0,5 gap value. In display the results the constant electron temperature (0,2 eV) in any part of the discharge was assumed [1].

In current density distribution measurements the well known equation (see, for example [2]) was used

$$j(x) = - \frac{1}{7b} \frac{d^2U}{dx^2} \quad (1), \text{ where}$$

b - diode width,

r - electrical **resistance** per unit **length**, which was equal in our case to the collector resistance between the adjacent potentiometrical leads.

Measuring step-by-step the potential difference per unit collector length dl/dx and differentiating the results once, we obtain in accordance to eq.(I) the current density distribution. The value r was calibrated before the run.

RESULTS

The I-V curves of lengthy electrodes diode (fig.2) are rather like to ones of the isothermal diodes with a small electrode dimensions. The visual picture of arc **ignition** and development on the early growth stages is also similar to one described before [3]. There are, however, many differences in details. For example, even at a large temperature drop along the emitter ($\Delta T > 200^\circ\text{C}$) the spot of "ball-of-fire" initiation depended both on the cesium vapor pressure and on the magnitude of emitter temperature. At high temperatures (1400-1500 $^\circ\text{C}$) and low vapor pressures ($T_{\text{cs}}=255^\circ\text{C}$ -) the arc was **ignited** near the "cold" end of the emitter. If the pressure increased, the spot of ignition was passed to more hot end. For the isothermal emitter ($\Delta T \leq 50^\circ\text{C}$) there was not some regular correlation between the spot of "ball-of-fire") **ignition** and diode parameters. The further stages of discharge development revealed as was known in the "ball-of-fire" **germination** to the electrodes with further spreading along the gap. However sometimes, for example, at high temperatures and high cesium vapor pressures the ball-of-fire) maintained its form and dimensions when the current increased, but near it the new plasma cloud appeared and spreaded along the **gap**.

It should be noted some important features of discharge development, which may be seen at the curves of longitudinal

plasma density distribution (fig.3). Firstly, there was irregular stationary plasma striating, which it seems not to bind with patch effect. The plasma layers (strata) arranged perpendicularly to the electrodes and had the typical dimensions of some millimeters. The striating took place practically in all regimes, if the arc was well developed. The modulation depth at some cases raised up to 20-30%. We suppose, that this striating was the final result of ionization instability development, the nature of which will be discussed in the next chapter. Secondly, at some cases (fig.3c, for instance) parallel with the low-scale strata there was the large-scale striating too. This big strata had the dimensions of the order of some centimeters, the density modulation being up to 50%. At the present time we cannot propose the complete model of this phenomenon. It seems to take place, if the Richardson emission current at the middle of emitter is larger, than that at the ends. For example, in diode with $\Delta T \approx 50^\circ\text{C}$ the discharge was attached to the left side of the diode at the low cesium vapor pressure (T_{Cs} up to 280°C), but it was attached to the right side at more high pressures.

Along the nonisothermal diode there was strong nonuniform current density distribution (fig.4), which is in a good accordance with plasma density distribution (fig.5). It may be seen, that the most part of the total current concentrated roughly on one half of diode area, if ΔT was equal to 200°C .

DISCUSSION. MODEL OF IONIZATION INSTABILITY

The reasons of ionization striating may be as follows. In the stationary state the magnitude of plasma density and its distribution in the interelectrode gap depend on the ionisation (and recombination) sources and ion losses due to the diffusion to the electrodes. Suppose, that the parameters

of stationary state are known. In order to investigate the stability of this state we must consider the plasma density time-variation given by equation:

$$\dot{n} = \text{div} (D \text{grad } n) + S(y; n) \quad (2), \text{ where}$$

D - coefficient of ambipolar diffusion,
S (y, n) - the rate of ion generation.

The chosen co-ordinate system is showed fig.6. We shall consider two-dimensional case, supposing the plasma in a Z - direction to be uniform. Averaging (2) in limits from y=0 to y=d and using the ordinary boundary conditions for the plasma density, one obtains

$$\langle \dot{n} \rangle = \langle S(y; n) \rangle - \frac{1}{2d} \bar{v}_i [n(0) + n(d)] + D \frac{d^2 n}{dx^2} \quad (3)$$

where \bar{v}_i - average ion thermal velocity; the angular brackets signify the result of averaging. The right hand terms have an simple physical sense:

$\frac{1}{2d} \bar{v}_i n(0)$, $\frac{1}{2d} \bar{v}_i n(d)$ - ion losses at the electrodes
 $D \nabla_x^2 n$ - the losses owing to diffusion in x - direction.

The instability will take place, if the right side of (3) more than 0.

For small density perturbations $\delta n, \delta j \propto e^{ikx}$. Suppose, that the plasma density distribution in y - direction remain quasistationar one (the dimension of strata $kd \ll 1$). When $\delta n(y) \propto n(y)$ and

$$\langle \delta \dot{n} \rangle = [(\alpha - 1) \langle S \rangle - k^2 D] \delta n \quad (4)$$

and hence the criterium of instability growth is

$$\alpha = \frac{d \ln S}{d \ln n} > 1 \quad (5)$$

It should be noted that the result obtained previously in the work [7] corresponds to the case of $\alpha \gg 1$.

The nature of instability is, therefore connected with the mechanism of ionization. The value Δ in (4) may depend on wave vector $\Delta = \Delta(k)$, if on take in account, that the current fluctuation in the external circuit $\delta J = \int_0^L \delta j dx$ must result in change of the arc voltage.

May be two limiting cases:

1. The big strata, $kL \ll 1$. The instability result in a jamping of the whole discharge in a new regime, the total current being change too. This instability take place only if the differential resistance of the discharge $\delta U / \delta J < 0$.

2. Low-scale strata, $kL \gg 1$. Consequently, $\delta J \approx 0$. The appearing of instability depends strongly on the ionisation mechanism, but only slowly on the external circuit parameters.

It may be showed, that the arc with ionization equilibrium [4] is stable. Instability may take place in a discharge, where the ionization is maintained by the stream of fast electrons [5,6].

The instability with the change of full current, are possible, if the temperature of slow electrons, which determine the potential distribution, $T > 2T_e$. The small-scale strata in the absence of volume ionization may take place already by $T > T_e$. The volume recombination make the discharge more stable and the instability boundary heaves to higher T . The nature of this instability connected essentially with the emitter neighbourhood (fig.6). The increasing of plasma density in a some region result in increasing the cathode voltage drop there. This, in one's turn must, according to [6] result in a exponential ionization growth. The development of instability in the case, when virtual cathode take place, must be the same. In our experiments there was the intermediate case between the ionization equilibrium arc [4] and the discharge with beam fast electrons [5]. The length of

electron energy relaxation was estimated to be $l_E \approx 0,3 \div 0,5 d$. Using the fast electron discharge model, it may estimate the low-scale strata dimension, which depend only slowly on the discharge conditions:

$$\lambda \approx \sqrt{\frac{2\pi^2 \kappa l_E}{j}} \quad (6), \text{ where}$$

κ - heat conductivity due to electrons

j - current density.

The estimation using formula (6) give the results, which accord with the experiments.

The modulation depth is determined by increment and must only slowly depend on current (if $\lambda \gg d$ and the ionisation mechanism is not changed). For a more complete comparison between the theory and experiments, the further detailed investigation is necessary, which must include the measurements of electron temperature and electrode voltage drops. This experiments is now in progress.

CONCLUSION

The preliminary results of investigation of arc discharge development in cesium non-onedimensional thermionic diode with lengthy electrodes and with longitudinal emitter temperature variation are reported.

In particular, the phenomena of large - and low-scale plasma striating were observed. The mechanism of low-scale striating, which seems to have an ionization origin is discussed in detail. The existence of these phenomena call in question the possibility of such diodes calculation on the basis of one-dimensional models.

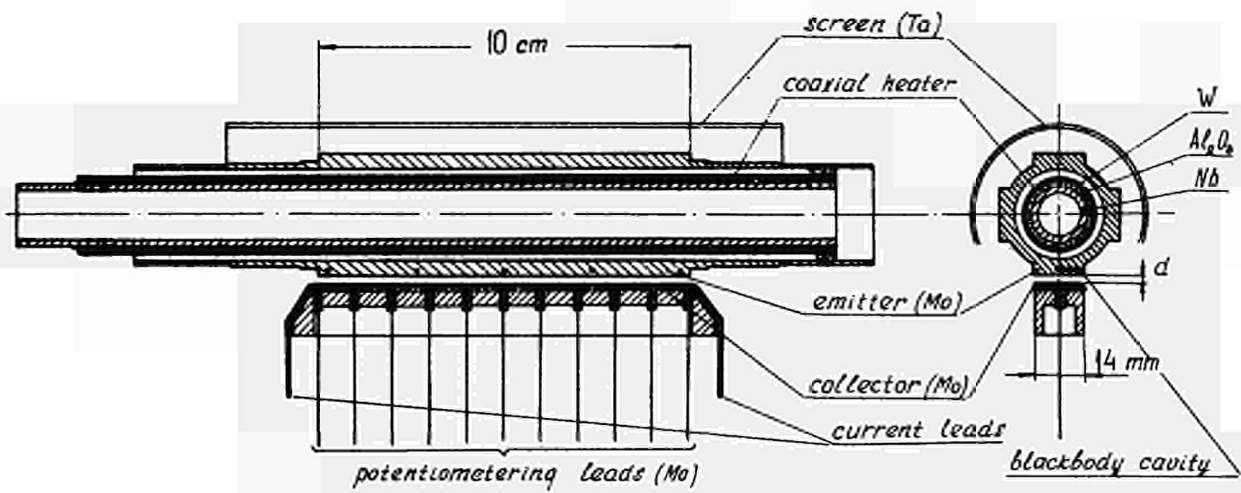


Fig. 1. Experimental diode.

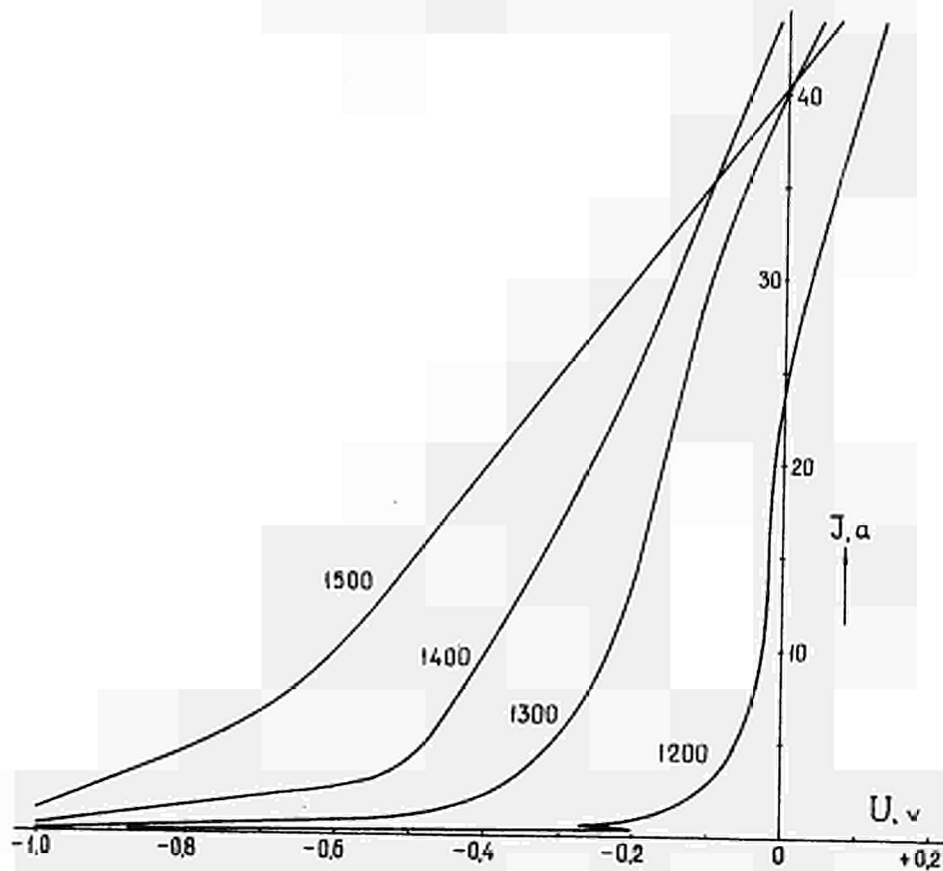


Fig. 2. Current-voltage curves (isothermal emitter-)

Emitter Mo
Collector Mo
 $d=0,45$ mm
 $T_{cs} = 330^{\circ}C$

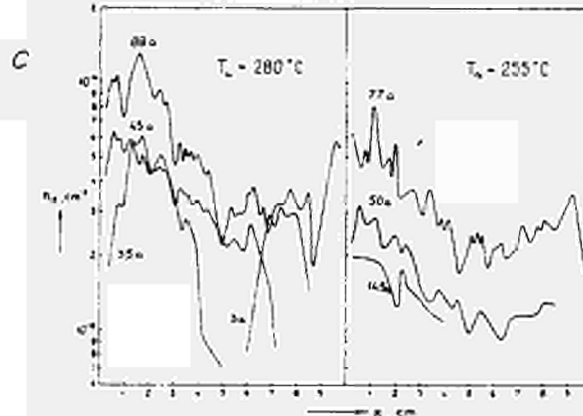
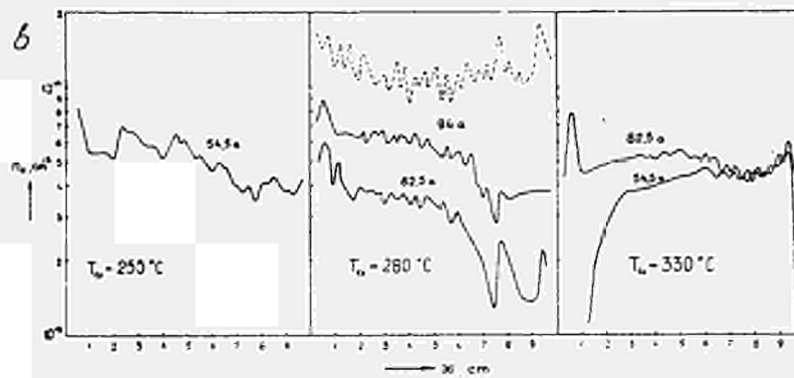
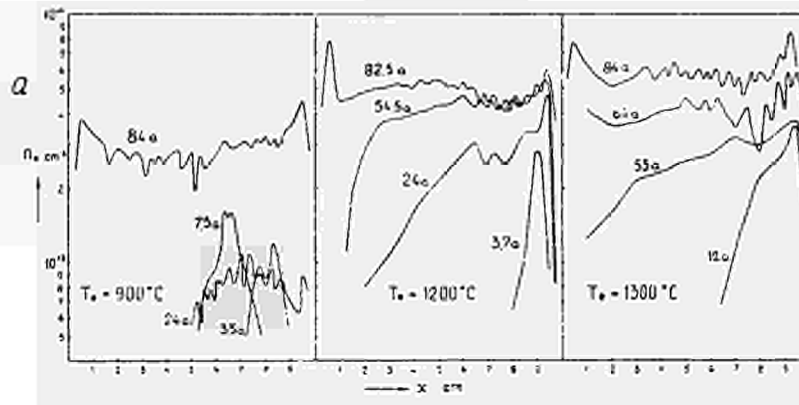


Fig.3. Plasma density distribution along the diode at different discharge currents:

- a) Isothermal emitter $\Delta T=25-50^{\circ}\text{C}$, $T_{cs}=330^{\circ}\text{C}$, $d=0,45\text{mm}$.
- b) Isothermal emitter $\Delta T=50^{\circ}\text{C}$, $T_e = 1200^{\circ}\text{C}$, $d=0,45\text{mm}$
- c) Nonisothermal emitter $\Delta T=110^{\circ}\text{C}$, $T_e \approx 1000^{\circ}\text{C}$, $d \approx 0,45 \text{ mm}$.

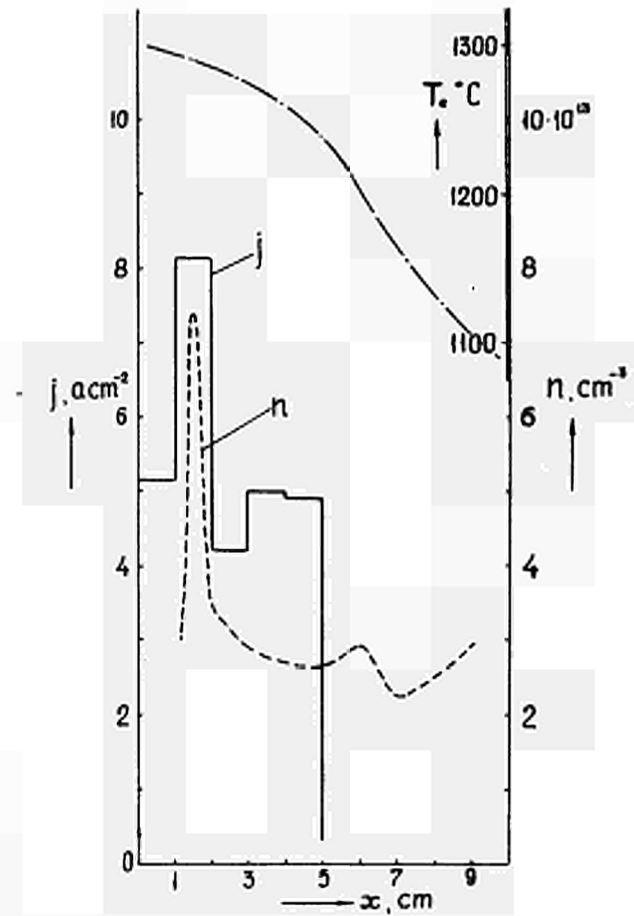
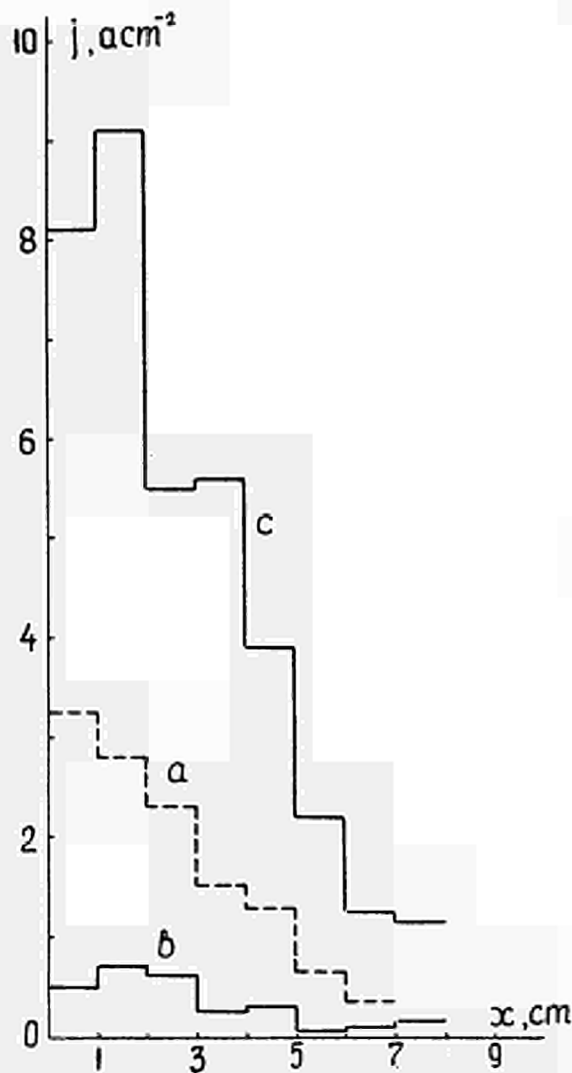


Fig.4. Current density distribution along the diode (monisothermal emitter)

$T_{e, \text{max}} = 1300^{\circ}\text{C}$, $T_c = 550-600^{\circ}\text{C}$, $T_{cs} = 280^{\circ}\text{C}$.

a) Preignited mode ($I_{\text{total}} = 0,77a$, 10-mal augmentation).

b) Obstructed mode ($I_{\text{total}} = 4,5a$)

c) Quasi-saturation mode ($I_{\text{total}} = 66a$).

Fig.5. Current density, plasma density and emitter temperature distributions along the diode (non-isothermal emitter).

$T_{e \text{ max}} = 1300^{\circ}\text{C}$, $T_0 \leq 600^{\circ}\text{C}$, $T_{cs} = 330^{\circ}\text{C}$, $d = 0,83\text{mm}$.

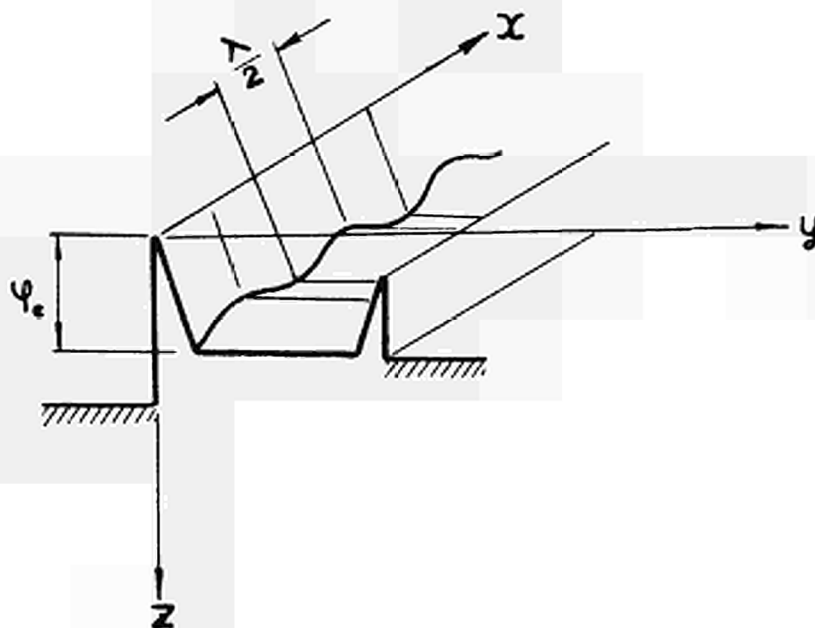


Fig.6. Diagram of the potential energy of electrons in a gap.

REFERENCES

- F.K.Kosyrev, N.P.Kosyreva, E.I.Lunev.
The report on present Conf.
W.C.Reichelt. Proc.Thermionic Conv.Spec.Conf.
Cleveland, 1964.
2. R.R.Hile. Proc.I Int.Conf.on Thermionic El.
Power. Gen.London, 1965.
 3. N.S.Rasor. Proc.I Int.Conf. on Thermionic El.
Power Gen.London, 1965.
 4. F.K.Kosyrev. N.P.Kosyreva, E.I.Lunev,
A.F.Nastojashchy. Proc.VIII Int.Conf. on
Phen.in Ionized Gases, Vienna, 1967.
 5. A.F.Nastojashchy. TBT, 2 6, 927, 1964.
 6. R.J.Kutshjerov. A.F.Nastojashchy. The
report on present Conf.
 7. A.F.Nastojashchy. TBT, 3 5 (1965).

KINETIC THEORY OF KNUDSEN ARCS IN THE MIXTURE
OF INERT GASES WITH CESIUM VAPOUR

R. Ja. Kucherov⁺, A.F. Nastrojashchy^{**}

⁺Physical-Technical Institute, State Committee
of Atomic Energy, Sukhumi (USSR)

^{**}I.V. Kurchatov Atomic Energy Institute, Moscow (USSR)

"beam" of the relatively fast particles. It is supposed that the main part of electrons passes to the anode without scattering. Nevertheless, rare collisions of these electrons essentially affect the processes in plasma:

I- Inelastic collisions with atoms secure the ion generation necessary to support the discharge.

II- Rare collisions of the fast electrons with plasma particles result in the electron capture in an electrostatic trap.

As a matter of fact, trapped electrons don't take part in the current-carrying process. However, they play the definite role in the potential distribution in the gap, since their density usually exceeds the beam density. The slow particles at the potential wells bottom make the major part of these electrons.

Since the Coulomb scattering cross section rapidly increases with the energy decrease, the average free path of these electrons can be even less than the gap. Inelastic collisions of these electrons with atoms can play an essential role in transitions between highly excited states of atoms during the step-by-step ionisation.

In the present paper intending to understand the main features of the phenomenon, we did not tend to the accurate mathematical description and in some cases used the simplified physical models.

1. THE ELECTRON DISTRIBUTION FUNCTION.

The fast electrons in the Knudsen arc plasma can be divided into two groups: the beam electrons and the electrons trapped by the potential well as a result of elastic collisions

The beam electrons distribution in the case of absence of the anode emission and reflection from electrodes has been obtained in the paper [2] by solving Vlasov equation. It gives:

$$f_1 = \frac{1}{2} \frac{m^2 j_e}{\pi \tau_e^2} e^{-\frac{\epsilon}{T_0}}, \quad \epsilon = \frac{mv^2}{2} - \varphi, \quad \epsilon_x = \frac{mv_x^2}{2} - \varphi \quad \left(\begin{array}{l} \epsilon_x > 0 \\ v_x > 0 \end{array} \right) \quad (1)$$

where: φ -the potential, j_e -the emission current density,

T_e - the cathode temperature. The rest denotations are commonly used.

The distribution of fast electrons, trapped as a result of rare elastic collisions, has been obtained in the paper [3] by solving the approximated kinetic equation which describes the balance between these and the beam electrons during the collision:

$$f_2 = \frac{m^2 j_e}{4\pi T_e^2} e^{-\frac{\epsilon}{T_e}} \left[1 - \frac{\sqrt{\varphi} - \sqrt{\varphi - \varphi_a}}{\sqrt{\epsilon + \varphi} - \sqrt{\varphi - \varphi_a}} \right] \quad (2)$$

In the deduction of equation (2) it was assumed that the potential well had a rectangular shape, and that the elastic collisions took place more often than Coulomb collisions. We shall use the expression (2) assuming here and further that the well potential change is small relatively to its depth.

There is a gap $0 < \epsilon < \varphi_a$ in the impulse space between the fields occupied by trapped and untrapped electrons. In this gap the electrons are practically absent. And really, according to the condition $l \gg a$ (l is the length of electron's free path), the electrons which fall after the collision into this gap, immediately go to the electrodes. The edges of this gap will be somehow smeared because of Coulomb collisions.

A mechanism leading to the filling of the potential well by slow electrons is provided by inelastic collisions of fast electrons with the atoms, and also by short distance Coulomb collisions, when the electrons lose considerable energy during a single collisions process. In the case of plasma high densities and small φ_a the electron beam diffusion through the energetic gap due to the long distance Coulomb collisions may play a certain role.

Further we shall consider the particle capture as a certain source of electrons of intensity $q(x, \theta, v)$.

The problem of mathematical investigation becomes essentially simplified with the fact that the collisions between the slowest electrons take place more often than with the beam electrons. Because of that the distribution of these particles making the major part of the slow electrons will be close to the Maxwell distribution. The electron distribution in the upper part of the well where the collisions are rare,

considerable differs from Maxwell distribution as a result of the existancee of the sources and the parttical exit from the well; it must be found from the solution of kinetic equation.

According to foregoing the Coulomb integral of the collisions in kinetic equation can be simplified because one can assume that field particles are distributed by Maxwellian function. To describe the elastic collisions with neutral atoms we shall use the Lorentz model. Using the variables ξ and $\theta = \arccos \frac{|v_x|}{v}$ ($0 \leq \theta \leq \frac{\pi}{2}$) and designating the distribution functions of particles with $V_x > 0$ as f^+ and with $V_x < 0$ as f^- we put down the kinetic equation in the following form: .

$$\begin{aligned} \pm \cos \theta \frac{\partial f^\pm}{\partial x} \pm \frac{\sin \theta}{2(\epsilon + \varphi)} \frac{d\varphi}{dx} \frac{\partial f^\pm}{\partial \theta} &= \frac{\alpha n}{2(\epsilon + \varphi)} \frac{\partial}{\partial \epsilon} \left(T \frac{\partial f^\pm}{\partial \epsilon} + f^\pm \right) + \\ + \frac{\alpha n}{4(\epsilon + \varphi)^2} \left(1 - \frac{T}{\epsilon + \varphi} \right) \frac{\partial}{\partial \theta} \sin \theta \frac{\partial f^\pm}{\partial \theta} &+ \frac{1}{\pi l} \left[f^\pm - \frac{1}{2} \int_0^{\pi/2} (f^+ + f^-) \sin \theta d\theta \right] + \\ + \frac{q^\pm(x, \theta, \epsilon)}{\sqrt{2m(\epsilon + \varphi)}} ; \quad \alpha &= 4\pi e^4 L, \quad l^{-1} = \sigma n_a \end{aligned} \quad (3)$$

where n is the density of the slow electrons, T is their temperature assumed to be constant along the gap, n_a is the atom density, σ - is the cross-section of elastic scattering. For the trapping electrons in the upper part of the potential well we can approximately take: $\cos \theta \approx \sqrt{\epsilon_x + \bar{\varphi}} / (\epsilon + \bar{\varphi})$ where $\bar{\varphi}$ is a certain average range depth of the well, since for these electrons the variation of θ during their motion, due to the relatively small change of φ

is not large. In this approximation ξ and θ are the invariants of the movement. Allowing for the fact that for the electrons near the well edge $l \gg a$ is valid, we shall look for the solution of the equation in the form:

$$f^\pm = f^{\pm(0)} + \frac{a}{l} f^{\pm(1)} + \dots \quad (4)$$

Then, as it is well known [4], $f^{\pm(0)}$ depends only on the invariables ξ and θ and can be found by averaging the kinetic equation over X -coordinate. Further we shall expand $f^{\pm(0)}$ by Legendret polynoms:

$$f^\pm = f_0^\pm(\epsilon) \pm f_1^\pm(\epsilon) \cos \theta + \frac{1}{2} f_2^\pm(\epsilon) (3 \cos^2 \theta - 1) + \dots \quad (5)$$

After substituting the expansion (7) into the averaged kinetic equation it appears that $f_1(\varepsilon) = 0$; and as a result of the condition $l \ll l_c$ also $f_2(\varepsilon) \ll f_0(\varepsilon)$, (where l_c is the Coulomb free path). Solving the equation for the spherically symmetric part of the distribution function f_0 , and equalling the flux of particles flowing out from the well to the source integral efficiency, we obtain:

$$f_0(\varepsilon) = f_0(\varphi_a) + e^{-\frac{\varepsilon}{T}} \int_{\varepsilon}^{-\varphi_a} \frac{e^{\frac{\varepsilon'}{T}}}{T} d\varepsilon' \int_{-\varphi}^{\varepsilon'} \frac{\bar{q}}{\bar{v}} d\varepsilon'' \quad (6)$$

where
$$\bar{q} = \int_{x_1}^{x_2} \frac{q_0 dx}{\sqrt{2m(\varepsilon + \varphi)}} \quad , \quad \bar{v} = \alpha \int_{x_1}^{x_2} \frac{v dx}{2(\varepsilon + \varphi)} \quad (7)$$

(x_1, x_2 - are the turning points)

Taking into account the smallness of $f_0(\varphi_a)$ and that in the case of large ε f_0 tends to the Maxwellian distribution function we find:

$$\int_{-\varphi_m}^{-\varphi_a} \frac{e^{\frac{\varepsilon'}{T}}}{T} d\varepsilon' \int_{-\varphi_m}^{\varepsilon'} \frac{\bar{q}}{\bar{v}} d\varepsilon'' = n_m \left(\frac{m}{2\pi T} \right)^{3/2} e^{-\frac{\varphi_m}{T}} \quad (8)$$

where φ_m - is the potential maximum, $n_m = n(\varphi_m)$ - is the maximum density of plasma.

The source of the particle capture into the well due to the Coulomb collisions $q_k(x, \varepsilon)$ between the fast and slow electrons is calculated neglecting the thermal part in the velocities ($T, T_k \ll \varphi$)

$$dq_k(\varepsilon) = \frac{4\pi e^4}{\varphi} n \alpha_j e \left[\frac{\psi(-\varepsilon - \varphi_a)}{\varepsilon^2} + \frac{\psi(\varepsilon + \varphi_a)}{(\varepsilon + \varphi)^2} \right]; \quad \psi(x) = \begin{cases} 1 & \text{at } x > 0 \\ 0 & \text{at } x < 0 \end{cases} \quad (9)$$

(α - is the fast electrons / density of the beam electrons)

The second term includes the possible exit of the electrons from the well if they got the energy exceeding the magnitude of anode barrier.

The flow of particles into the well due to the inelastic collisions is equal to:

$$q_{in}(\varepsilon) = \sum_{i, \kappa} \left[\varphi(\varepsilon + \varphi + \varepsilon_{i\kappa}) n_{a i} \bar{v}^+ \sqrt{\frac{2(\varepsilon + \varphi + \varepsilon_{i\kappa})}{m}} - f(\varepsilon) \bar{v} n_{a \kappa} \sqrt{\frac{2(\varepsilon + \varphi)}{m}} \right] \quad (10)$$

$\varphi = f_1 + f_2 \quad ; \quad i, \kappa = 0, 1, 2$

where δ^+ and δ^- are the cross-sections of excitation and extinction, respectively; n_{ai} - is the number of the atoms on the level i ; ϵ_{ik} - is their transition energy between the levels i and k .

The slow particles energy balance in the well consists of influx Q^+ or loss Q^- of the energy due to the capture (or exit) of particles; loss the energy on the excitation (extinction) of the atoms and heating due to the Coulomb interactions with the fast electrons $d\mathcal{E}/dt$:

$$\int_0^a \left\{ \frac{d\mathcal{E}}{dt} + Q^+ - Q^- - g(\epsilon_{\infty} - \epsilon_2) - K(\varphi - \varphi_a) \right\} dx = 0 \quad (11)$$

where K is the density of particles flux out from the well.

Above it was taken into account that when resonance radiation was trapped (see the following section) the energy losses of slow electrons are equal to the product of the ionization velocity g and the potential of atoms ionization from the second level, from which the excitation by slow electrons becomes dominating.

Using the expression for the velocity of energy losses by the "test" particle due to its scattering on the "field" particles having Maxwell distribution with the temperature T , and taking into account the energy distribution function for the fast electrons we obtain:

$$\frac{d\mathcal{E}}{dt} = \frac{2\pi e^4 L}{\varphi} n_{\infty} j_e \quad \left(\frac{\varphi}{T} \gg 1 \right) \quad (12)$$

(n_{∞} - is the ratio of the fast electrons total density to the density of electrons in the beam).

2. THE VELOCITY OF IONIZATION IN PLASMA

We shall now consider the arc discharge in cesium vapour.

The main mechanism of the ion generation in such an arc is the step-by-step ionization of atoms. Populations densities of excited states are determined by the atom excitation and extinction due to the electron impacts and optical transitions. The process is described by the system of chained equations of the following type:

$$\sum_{m \neq k} \left[n_e (n_k j_{km} - n_m j_{mk}) + (n_k a_{km} - n_m a_{mk}) \right] = D$$

(m, k = 0, 1, 2, ... S; e) (13)

Indices $0 \leq k; m \leq S$ concern to the bound electrons; index e to the continuous spectrum so that n_e is the free electrons density; j_{km} are the probabilities of atoms excitation ($k < m$) or extinction ($k > m$) by electron impact with the transition from the state k into the state m , averaged with distribution function of free electrons; a_{km} - are the probabilities of the optical transitions with the absorption ($k < m$) or radiation ($k > m$) of photon with the energy ϵ_{km} . For excitations with the considerable energy variation $\epsilon_{km} > \varphi - \varphi_a$, only the collisions with the fast electrons are essential; and at the same time all the free electrons can equally take part in the extinction processes.

The probabilities of optical transitions of and of the transitions due to electron impact are proportional to the oscillator strengths for the given transition f_{km} .

The Table 1 shows the oscillator strengths for some cesium atom transitions calculated in the paper [6]. However the data for the transitions 7 P - 5 D (with the main quantum number change to two) in this paper probably are too large. For this transitions we shall use the results obtained in the more recent work [7].

As the Table shows, the transitions from the level 5 D to the upper one can be neglected, because this path for the electrons is closed. Though the impact transition cross-sections between the levels 6P - 6S and 6P - 7S are comparable in magnitude, but the transitions by the excitations are provoked only by the fast electrons while extinction is carried out by all the electrons. Therefore the levels 6S - 6P - 5D may be assumed to be closely bound.

Generally speaking, for the level 7S it is necessary to take into account both the transitions to the levels 6P and to levels of large energy - 7P. As to the level 7P, for the of calculation simpleness we shall assume it to be in equilibrium with the continuous spectrum x).

Thus we pass to some three-level model of Cs atom. The population densities $n^{(1)}$, $n^{(2)}$, $n^{(3)}$ of the states 6P, 7S in this model are equal to:

$$n^{(1)} = n^{(0)} \frac{n_e j_{01} + a_{01}}{n_e j_{10} + a_{10}}, \quad n^{(2)} = \frac{n^{(1)}(n_e j_{12} + a_{12}) + n^{(3)}(n_e j_{32} + a_{32})}{n_e (j_{21} + j_{23}) + a_{21} + a_{23}}$$

where $n^{(0)}$ and $n^{(3)}$ are population densities of the states 6S, 7P. Hence the rate of ionization (recombination) can be determined in the following way:

$$g = (n_e j_{12} + a_{12}) n^{(1)} - (n_e j_{21} + a_{21}) n^{(2)} \quad (I5)$$

The formulas derived allow further simplifications. The estimates show that in the cases we are interested in, optical transitions a_{12} , a_{23} , $\dots\dots a_{r1}$ hardly probable compared to impact transitions. As to the optical transitions a_{01} , its corresponding line is highly reabsorbed, so that the effective life time of the 6P state is mainly defined by electron impacts at the density $n_e > 10^{12} \text{ cm}^{-3}$.

Concrete calculations have been carried out using the Born approximation which gives the cross sections larged at about three times compared to experimental ones [9]. The averaging of transitions probabilities has been carried for the transitions 6S - 6P and 6P - 7S by the fast electrons distribution function, and for the rest transitions by all the free electrons. As a result we have :

$$g = \frac{x e^4}{\epsilon_{12}^2} \frac{x^2 j_e}{n \bar{v}_e} f_{12} \left[F_{01} \cdot F_{12} - \frac{n^4}{4 N_e} \bar{v}_e^2 e^{\frac{\epsilon_{00} - \epsilon_2}{T}} \right] \quad (I6)$$

$$F_{km} = \begin{cases} 2 \left[1 - \sqrt{\frac{\varphi}{\epsilon_{km}}} - \frac{2 T_K}{\epsilon_{km}} \left(1 - \frac{3}{2} \sqrt{\frac{\varphi}{\epsilon_{km}}} \right) \right] e^{\frac{\varphi - \epsilon_{km}}{T_e}} & \text{at } \varphi < \epsilon_{km} \\ \frac{\epsilon_{km}}{\varphi} \left[1 - \frac{\epsilon_{km}}{\varphi} + \frac{T_K}{\varphi} \left(1 + \frac{\epsilon_{km}}{\varphi} \right) \right] & \text{at } \varphi > \epsilon_{km} \end{cases} \quad (I7)$$

where \bar{v}_e - the average velocity of electron, N_e - is the density of free electrons levels.

x) In the case of high rate of ionization in the upper levels the deviations from the equilibrium distribution may arise [8], which are related to exponential fall of the population density with the increase of the level energies. The consideration of this fact can be carried out within the limits of the model discussed.

3. THE DISTRIBUTION OF POTENTIAL AND PLASMA DENSITY IN THE INTERELECTRODE SPACING.

To describe the distribution of plasma density we use the ambipolar diffusion equation:

$$\frac{d}{dx} D \frac{dn}{dx} + g(x;n) = 0 \quad (D = \frac{1}{3} (\tau + \tau_e) l_i \bar{v}_i) \quad (18)$$

with the boundary conditions at the plasma edges :

$$D \frac{dn}{dx} \Big|_{x=+0} = \gamma n \bar{v}_i, \quad D \frac{dn}{dx} \Big|_{x=a-0} = -\gamma n \bar{v}_i \quad (19)$$

where D - is the ambipolar diffusion coefficient, m_i - is the mass of ion, l_i - is the length of ion's free path. Let's assume the coefficient γ to be equal to $\frac{1}{2}$.

The ambipolar diffusion equation's applicability follows from the Boltzmann distribution of slow electrons which determine the density of plasma .

$$n = n_m e^{\frac{\varphi - \varphi_m}{T}} \quad (20)$$

Solving the equation (18) together with boundary conditions (19), substituting the ionization rate from the formula (17) and taking into account (20), we obtain the expressions for the plasma density and φ_m :

$$v_m^{p+1} = 1 + \frac{3}{8} \frac{p+1}{\theta+1} \frac{n(0) \bar{v}_i}{g(0) l_i} \quad \left(p = \frac{d \ln g}{d \ln n}, \quad \theta = \frac{T}{T_e}, \quad v = \frac{n(x)}{n(0)} \right) \quad (21)$$

$$\pm \int_1^v \frac{dv}{\sqrt{v_m^{p+1} - v^{p+1}}} = \frac{3}{2} \frac{1}{\sqrt{v_m^{p+1} - 1}} \frac{x}{l_i (\theta+1)} \quad (22)$$

Further substituting the obtained value of n_m into the formula (8) we obtain the equation relating φ_m and φ_a .

Now it's left to consider the distribution of potential in the cathode-side region. Two cases are possible:

i) The field near the cathode is positive $\varphi'_k > 0$ and the total emission current flows through the diode; ii) $\varphi'_k < 0$, the current is limited by so called virtual cathode. Solving Poisson equation in the range of $0 \leq x \ll l_1$ and matching this solution with the solution for the plasma region we find the field φ'_k for the first case and the cathode side jump value and the virtual

cathode potential Δ_k for the second case:

$$i) \quad \varphi_k' = \sqrt{8\pi e n(o) (1-\beta) (\sqrt{(\varphi_k + T_e) T_e} - T_e)} \quad (23)$$

$$ii) \quad \varphi_k = \left[\left(1 + \frac{1}{2(1-\beta)} \frac{T}{T_e} \right)^2 - 1 \right] T_e, \quad \Delta_k = T_e \ln \frac{j_s}{j_e} \quad (24)$$

where $\beta = 2j_e/n(o)\bar{v}_e$ - is the ratio of the slow electrons' density to the ions density on the boundary between the plasma and the cathode; j_s - is the current of Richardson's emission from the cathode.

Preliminary calculations were made to find how inert gas additions influence on processes occurring in the Knudsen arc. The distribution potential in the arc at $\varphi_k' < 0$ in the region $x > 0$ doesn't depend on the current. It is shown in fig.1; the voltamper characteristics of thermionic converters are given by $V(j_e) = \Delta\chi + \Delta_k(j_e) - \varphi_a$, where $\Delta\chi$ is contact difference potential.

Insertion of inert gas additions into the gap results in 1) increasing of the absolute value of plasma density and that of plasma distribution over the gap; 2) changing of potential distribution; 3) decreasing of arc burning voltage, as shown in fig.1. At $a \sim (3 - 5)l_i$ the voltage decrease is $\Delta\varphi_a \sim (1 - 2) T_e$.

This result becomes obvious if one uses expressions (21) and (22) of plasma density as well as eq.(8) which after substituting sources (9) has the following form:

$$n_m \left(\frac{m}{2\pi T} \right)^{3/2} e^{-\frac{\varphi_m - \varphi_a}{T}} = \frac{m^2 \alpha j_e}{8\pi L \bar{\varphi}} \frac{\varphi_m - \varphi_a}{\varphi_m \varphi_a} \quad (25)$$

where $\bar{\varphi}$ is the mean value of potential in plasma.

The inert gas favour retention of ions in the volume and thus lead to increasing of plasma density what, in its turn, is to increase the anode barrier, according to eq.(25). The absolute values of arc burning potential are sensitive to cross section values (ionization etc.), which may be given only with a certain degree of accuracy.

The calculations show, that the Knudsen arc in mixture of inert gases with cesium vapour may be of interest from the point of its application in thermionic converters. In this case providing of necessary electron emission from the cathode becomes the most important problem.

CONCLUSIONS.

The theory of the Knudsen arcs is discussed where electron processes are described on the base of a kinetic approach and an ion motion on the base of a hydrodynamic model. The theory can be applied to the discharges in the mixture of inert gases with cesium vapour.

REFERENCES.

1. Byrdin Ju.A., Lubimov B.Ja., Nastrojashchy A.F.
High Temperatures (USSR), 5 I (1967) 25.
2. Kaganov M.I., Kucherov R.Ya., Ricenglas L.E.
Journal of Technical Physics (USSR), 31 5 (1961) 588.
3. Kucherov R.Ja., Shuander Ju.A.
Journal of Technical Physics (USSR), 34 I(1964) 66.
4. Budcker G.I., Belaev S.T. Plasma Physics and Problems
Controlled Thermonuclear Fusion (USSR), 2(1958) 330
5. Trubnicov. B.A. Plasma Theory Review (USSR), I(1963) 98.
6. Stone P. Phys. Review, 127 3(1962) 1151.
7. Anderson E.M. Zylitis V.A. Opt. and Spectr. (USSR), 16 3
(1964)
8. Biberman L.M., Vorobjev V.S., Jacobov I.T.
High Temperatures (USSR), 5 2(1967).
9. Zapesochny I.P., Shimon A.L. Opt. and Spectr.(USSR), 16
6(1964).

APPENDIX I.

Table of oscillator strenghts for Cs atom [6] .

Transition	f_{km}	Transition	f_{km}
6P _{1/2} -6S _{1/2}	0.394	7S _{1/2} -6s _{1/2}	$2.84 \cdot 10^{-5}$
6P _{3/2} -6S _{1/2}	0.814	7P _{3/2} -6S _{1/2}	$1.74 \cdot 10^{-2}$
5D _{3/2} -6P _{1/2}	0.251	7P _{1/2} -5D _{3/2}	$1.2 \cdot 10^{-2}$ [7]
5D _{3/2} -6P _{3/2}	0.021	7P _{3/2} -5D _{3/2}	$2.4 \cdot 10^{-3}$ [7]
5D _{5/2} -6P _{3/2}	0.204	7P _{3/2} -5D _{5/2}	$1.44 \cdot 10^{-2}$ [7]
7S _{1/2} -6P _{1/2}	0.28	7P _{1/2} -7S _{1/2}	0,556
7S _{1/2} -6P _{3/2}	0.171	7P _{3/2} -7S _{1/2}	1.115

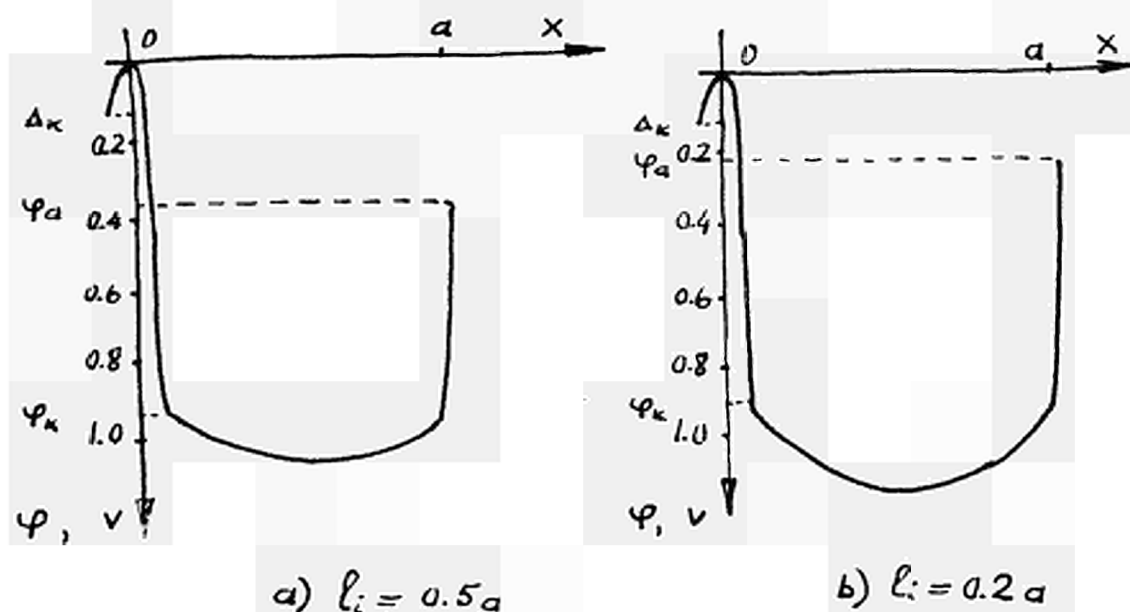


Fig.I. Potential distribution in interelectrode space:
 a) in pure cesium vapour; b) in mixture of cesium with inert
 gases. $T_e = 1750^\circ K$, $n_a = 5 \cdot 10^{14} \text{ cm}^{-3}$, $a = 2 \cdot 10^{-2} \text{ cm}$
 ($j_e = 0,4 j_s$)

CURRENT OSCILLATIONS AND ELECTROMAGNETIC RADIATION
IN LOW-PRESSURE THERMAL-EMISSION CONVERTERS.

I.G.Gverdtsiteli, V.Ya.Karakhanov, R.Ya.Kucherov, Z.A.Oganezov,
V.K.Tskhakaya.

Physical-Technical Institute, State Committee on Utilization
of Atomic Energy, Sukhumi (USSR)

Current oscillations in the circuits of cesium thermal-emission converters have been experimentally investigated in a number of papers. It has been shown that there were two regions of the device parameters where the oscillations have been observed /1,2/ in the case of low pressures ($p < 5 \cdot 10^{-2}$ torr) of cesium vapours and the cathode temperature of $T_k \geq 1800$ K ; and in the case of higher pressures of $5 \cdot 10^{-2} < p < 0,6$ torr and the cathode temperature of $1100 + 1600^\circ\text{K}$. The oscillation frequency in low-pressure region is $10^5 + 10^6$ c.p.s., the oscillation period being of the order of the time of flight across the interelectrode gap L by cesium ions. It has been found that τ is proportional to L and increases with the applied voltage growth /3,4/. The oscillation amplitude reaches 50% of the constant constituent of the current and some cases the current appears to be completely modulated/3/.

Initially it has been thought that the oscillations took

place only in the case of the potential negative jump at the cathode and were related to the oscillations of ions or ion clusters trapped in the potential well/1,3/. On the basis of the current-voltage characteristics analysis the paper /5/ has shown that the oscillations have been mainly observed in such modes when there was no potential well for ions the oscillations always leading to the decrease of the current constant constituent.

The oscillation theory based on the analysis of the plasma interaction with the beam of electrons accelerated in the cathode sheath has been developed in the paper /6/. However, the formula obtained in the small amplitude approximation can not explain a number of experimentally observed trends which are, no doubt, of nonlinear type. The paper /7/ gives the oscillation theory based on the beam instability onset near the cathode and the propagation of damping longitudinal ionic-sound waves towards the anode. Apparently this theory correctly treats the processes observed at relatively low cathode temperatures and high pressures ($l_e \gg L$) of cesium vapours, but it fails in the case of processes taking place in a collision-free plasma.

Recently there appeared the papers /8,9/ which give the modellings of diode operation instable modes using the high-speed computer. The potential distributions obtained, being consequent in time, show that the current oscillations arise as a result of electron lock-up by the potential barrier. In order to treat the computer-obtained results the authors consider "temporary states of the direct current" which are stationary for electrons but instable for ions. According to the authors, these states are more probable than completely stationary ones calculated in the papers /10+12/. Transitions into these states and their development during the ion motions result in the generation of the barrier limiting the electron current.

The paper /4/ gives some experimental data which agree with the results obtained in a computed model.

The present paper gives the experimental investigation results on the oscillation period dependence on the diode main parameters in pure cesium and the mixture of cesium with inert gases - argon and xenon. An empiric formula has been obtained

for the oscillation period dependence on the gap and voltage; the h.f. electromagnetic radiation has been measured. The results are in accordance with the computed model data.

The Experimental Apparatus. The measurements have been carried out in the glass diode with plate-geometry electrodes. The tantalum cathode of the diameter of 15mm has been heated by electron bombardment. The interelectrode gap has been regulated from 0 to 5mm by the transfer mechanism. The cathode temperature has been measured by tungsten-rhenium thermocouple and sustained with the accuracy of $\pm 2^\circ \text{C}$ of the electron stabilization circuit. A high-temperature rectifier allowed to perform dosed fillings of inert gases (argon and xenon) during the diode operation. The measurement techniques for direct and alternating constituents of ion and electron current are described in the paper /5/.

The electron and ion saturation currents I_{se} and I_{si} have been defined by direct measuring the currents flowing through the diode on the electron and ion plateaus of the current-voltage characteristics (+550 and -10 volts, respectively). If to neglect the possible influence of Shottki effects hence we can determine the compensation parameter $\alpha = \frac{I_{si}}{I_{se}} \sqrt{\frac{m_i}{m_e}}$. The oscillation shape and frequency have been recorded by the oscillograph and the spectrum analyser. The electromagnetic radiation has been accepted by a dipole or horn-type antennas and recorded by the measuring receivers of sensitivity of 10^{-12} wt in the range of frequencies: 400 + 4000 MS. At the receivers' exit there was an envelope of the s.h.f. radiation which after preliminary enhancement became directed onto the control-electrode of the oscillograph electron-image tube cathode. This gave us the opportunity to obtain the time momenti in the form of light-spot on the oscillograph traces of oscillations when the s.h.f. radiation of frequency, corresponding to the receiver adjustment was recorded.

The Current Oscillations in Cesium. The detailed investigations of the oscillation period dependence on the interelectrode space L and the applied voltage V have been performed under the conditions analogous to the experiments carried out in the work /4/ ($T_k = 2130^\circ \text{K}$, $I_{se} = 6,7 \cdot 10^{-2} \text{A}$ $L = 0,5 \div 5 \text{mm}$ and Debye spacing $\lambda = 1,4 \cdot 10^{-2} \text{mm}$) with three values of the compensation parameter: $\alpha = 0,3; 0,5; 3$. Fig. 1 and 2 give the dependence of τ on the gap size

and the anode voltage for $\alpha = 0,3$ and $\alpha = 0,5$. The line dependence $\tau(L)$ has been earlier noted by a number of authors. The slope angle of straight lines $\tau(L)$ reduces with the voltage growth. If we assume that the ion mean velocity v_i slightly depend on V and corresponds to the cathode temperature, then the slope decrease can be related to the reduction of the plasma-occupied region by the value of Δ according to Burger model/9/. The dependence Δ on the voltage calculated from the data of Fig. 2 is given in Fig.3. It appears that in the case of fixed voltage the ratio $\frac{\Delta}{L}$ does not depend on L . In Fig.3, the dotted line corresponds to the values of $\frac{L-\Delta}{L}$ against the voltage. For comparison, Fig.3a gives the values of $\frac{L-\Delta}{L}$, obtained as a result of Burger's numerical calculations /4/ in the form of vertical segments at $V = 4, 8, 12$ and 16 volts for ion energies from 1 to 5 kT. In the case of large α ($\alpha > 3$) the oscillation frequencies in the range of $0,5 < V < 10$ volts do not depend on the voltage (Fig.3c). In order to find the type of the dependence of Δ on the voltage the dependences of Δ on $(V-V_0)^{3/4}$ and $(V-V_0)^{1/4}$ are distinguished in the case of $\alpha = 0,3$. V_0 is the voltage at which Δ turns into zero. In the case considered $V_0 = -1,8$ volts. From this figure it is evident that there are two regions for which the dependence Δ on $V-V_0$ is various.

$$\begin{aligned} \Delta &= B_1 L (V-V_0)^{3/4} \text{ at } V \lesssim 2,2 \text{ volts} \\ \Delta &= B_2 L (V-V_0)^{1/4} \text{ at } V \gtrsim 2,2 \text{ volts} \end{aligned} \quad (1)$$

where the coefficients $B_1 \approx 0,1$ and $B_2 \approx 0,25$ B coefficients at $\alpha < 0,5$ slightly depend on α . Hence for the oscillation period in the case of $\alpha < 1$ we can obtain the following empiric formula:

$$\begin{aligned} \tau &= \frac{L[1-B_1(V-V_0)^{3/4}]}{v_i} \text{ at } V \lesssim 2,2 \text{ volts} \\ \tau &= \frac{L[1-B_2(V-V_0)^{1/4}]}{v_i} \text{ at } V \gtrsim 2,2 \text{ volts} \end{aligned} \quad (2)$$

Table 1 gives the comparison of τ values obtained in the experiments by Guttler and Burger /4/ with the computed values obtained using Eq.(2). From the Table it is clear that using Eq.(2) we obtain good agreement with experimental values of the oscillation period.

Investigations of voltage and gap regions of oscillations have

shown that there were instable oscillations of noise type in the case of $0,4 \leq L \leq 0,7 \text{ mm}$, and there were no oscillations in the case of $L < 0,4 \text{ mm}$. Above $L \sim 0,7 \text{ mm}$ the oscillations become regular.

The voltage-region oscillations appear at $V \approx -2,2$ volts in the region of $-2,2 \text{ v} < V \leq -1,8$ volts they are of the noise-type. The oscillations disappear with the voltage growth at $V \approx 150 \text{ v}$. A typical view of the oscillation spectrum is shown in Fig 5

Current Oscillations in the Cesium-Inert Gas Mixture. The experiments have been carried out on oscillations in the medium filled by the mixture of cesium and some inert gas (argon or xenon). As a result of Ramsauer effect these gases - intensely scattering the ions do not affect the electron component of the plasma (i.e. $l_e \gg L \sim l_i$) up to the pressures of the order of 10 torr. The measurement results are given in Fig. 6.

The oscillations have been observed up to the pressures of 3 torr in argon and 1,5 torr in xenon. The oscillation period has increased with the gas pressure growth, however, more slowly than it can be assumed from the increase of the ion motion time towards the anode. With the argon pressure growth, the reduction of the sum of the current constant constituent and the amplitude value of the alternating constituent has been observed too /Fig 7/. Since at $l_e \gg L$ and the potential is nowhere in the diode this sum must not vary /5/, it can be assumed that there appeared the potential barrier retarding electrons in the diode. The formation of such a barrier near the anode can be understood if to take into account the temperature decrease from the cathode to the anode related to the filling gas thermal conductivity. Such a distribution of the temperature leads to the ion density increase near the anode and this, in turn, leads to the potential decrease from the cathode to the anode (at sufficiently high potentials of the anode when the ion current towards the anode is negligible) and can result in the barrier for electrons at the anode. The electron reflection by this barrier prevents the current oscillation development.

The Diode Electromagnetic Radiation. Together with the current oscillations the electromagnetic s.h.f. radiation has been measured. At $L \approx 3$ nearly continuous spectrum of the radiation of inten-

sity 10^{-12} - 10^{-10} wt has been found over the frequency range of 500 - 3000 Mc/s. However, the time-sweeping of the s.h.f. radiation envelope has shown that the radiation continuous spectrum was related to the oscillations of plasma parameters in the diode. Fig.8 shows typical oscillograph traces of the current including the s.h.f. radiation envelope (light spot) supplied from the receiver (The receiver transmission band being 5Mc/s). On readjusting the receiver the spot moves on the oscillograph trace in accordance with the radiation frequency variation in various phases of the current oscillations.

If we presume that the plasma electromagnetic radiation is related to the nonlinear interactions of longitudinal Langmuir and relatively low-frequency ionic-sound waves, then from the radiation frequency we can roughly estimate the plasma average density variation during the oscillating cycle development. The results of such estimates are shown in Fig.9.

The electron density change nearly by an order of magnitude indicates the fact that the current oscillations are accompanied with large-amplitude oscillations of the plasma potential, resulting in the considerable decrease of the electron beam density because of its acceleration.

TABLE 1

The Comparison of Experimental Values of τ with calculated ones using the equation (2).

L, cm	V volts	V+(V ₀)	$\tau_{calc.}$ $\mu sec.$	$\tau_{exp.}$ $\mu sec.$	notes
0,1	0	1,8	1,65	1,75	$\alpha = 0,3$
	2	3,8	1,45	1,4	
	5	6,8	1,2	1,15	
0,3	0	1,8	4,95	5	$\alpha = 0,5$
	2	3,8	4,35	4,3	
	5	6,8	3,6	3,65	
0,8	1	2,8	12,4	10	exper. /4/
	2	3,8	11,6	9	
	5	6,8	9,5	6	
1,2	1	2,8	18,6	15,3	exper. /4/
	2	3,8	17,5	14	
	5	6,8	14,3	12,5	

Note: In the experiment /4/ the value of α is not indicated (at which the measurements have been carried out); therefore, in the course of calculations, the values of B_1 and B_2 coefficients, obtained in our experiment are used.

R E F E R E N C E S

1. Левитский С.М., Грошев И.Н. Радиотехника и Электроника
8. (1963) 612
2. Караханов В.Я., Татишвили Д.Г. Радиотехника и Электроника
9 (1964) 138.
3. Zollweg R.J., Gottlieb M. Proc. IEEE 51 (1963) 754
4. Guttler W.H., Burger P., J.Appl.Phys., 37 (1966) 2867
5. Караханов В.Я., Кучеров Р.Я., Татишвили Д.Г. ЖТФ 34 (1964)
326
6. Chivian J.S. J.Appl.Phys., 35 (1964) 302
7. Стаханов И.П., Степанов А.С. ЖТФ 35 (1965) 132
8. Norris W.T., J.Appl.Phys., 35 (1964) 3260
9. Burger P., J.Appl. Phys., 36 (1965) 1938
10. Каганов М.И., Кучеров Р.Я., Рикенглаз Л.Э. ЖТФ 31 (1961) 588
11. Кучеров Р.Я., Рикенглаз Л.Э. ЖТФ 32 (1962) 1275.
12. McIntyre R.G., J.Appl.Phys. 33 (1962) 2485
13. Johnson F.M., RCA Rev., 22 (1961) 21.



Fig.1. - The oscillation period dependence on the voltage and the interelectrode gap for $\omega = 0,5$.

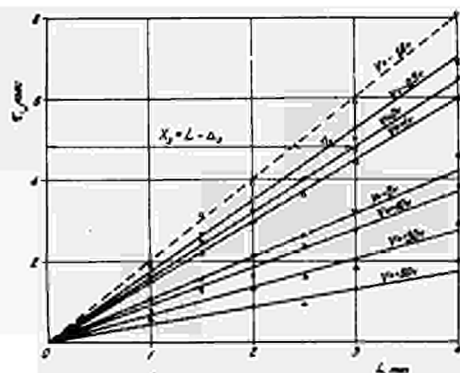


Fig.2. - The oscillation period dependence on the voltage and the interelectrode gap for $\omega = 0,3$ ($\lambda = 1,4 \cdot 10^{-10} m, E_k = 2750^\circ K$); (the dotted line corresponds to the time of flight of an ion over the gap L with an average velocity equal to the cathode temperature).

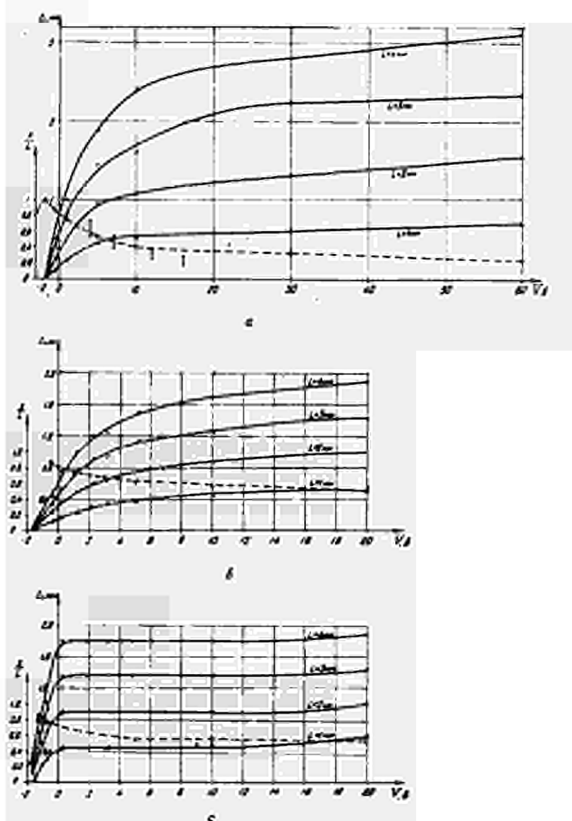


Fig.5. - The anode-side region Δ and the ion penetration depth $x = L - \Delta$ (dotted) dependence on the applied voltage.
a) $\alpha = 0,3$; b) $\alpha = 0,5$; c) $\alpha = 5$.

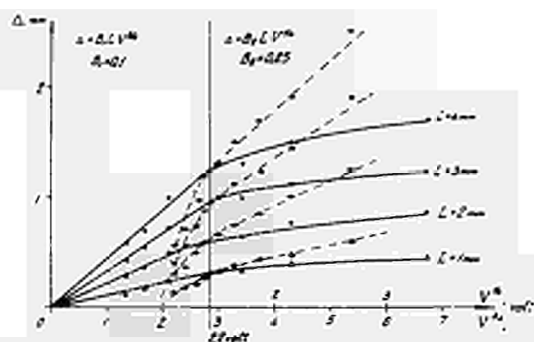


Fig.6. - Graphical search of the anode-side region dependence Δ on the voltage and the interelectrode gap.



Fig.5. - Typical oscillation spectra, a) $V=0$ volts; b) $V=-2,2$ volts.

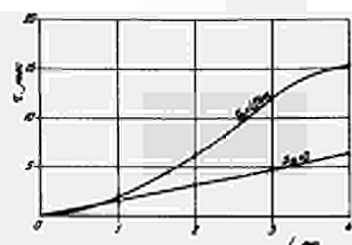
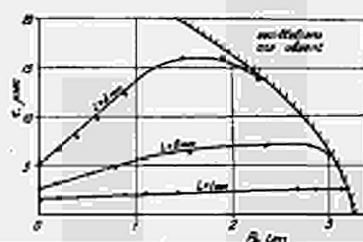


Fig.6. - The oscillation period dependence on a) the argon pressure and b) the interelectrode gap. $T_k=2130^\circ\text{K}$, $\alpha=1,5$.

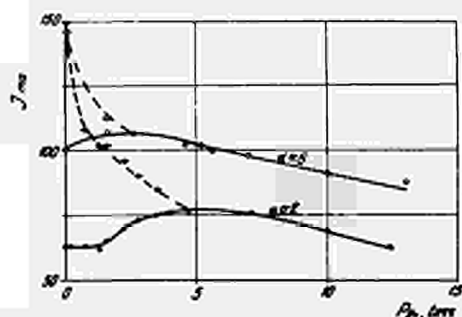


Fig.7. - The influence of argon on total current $J_k = J_0 + J_1$ (dotted) at $V=0$. The solid curve represents the constant component of the current. $T_k=2130^\circ\text{K}$, the saturation current $J_k=150$ mA, $S=2,25$ cm, $L=2$ cm.

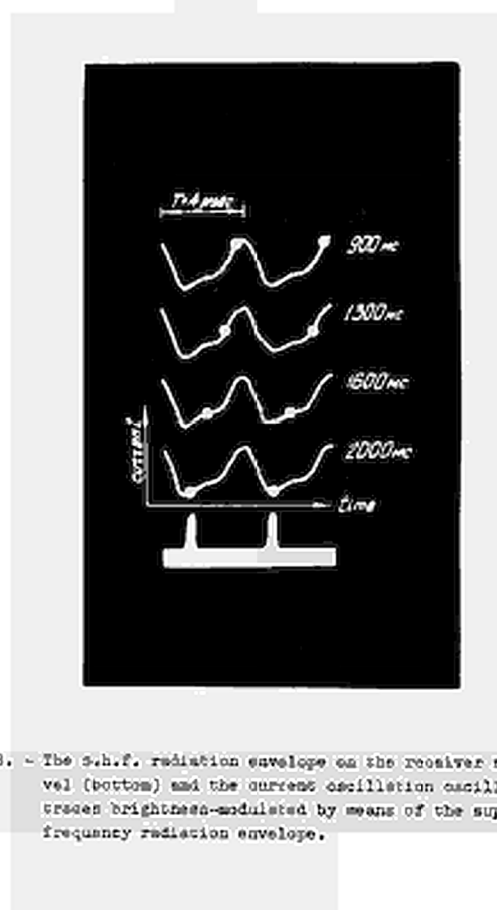


Fig. 8. - The s.h.f. radiation envelope on the receiver noise level (bottom) and the current oscillation oscillograph screen brightness-modulated by means of the super high frequency radiation envelope.

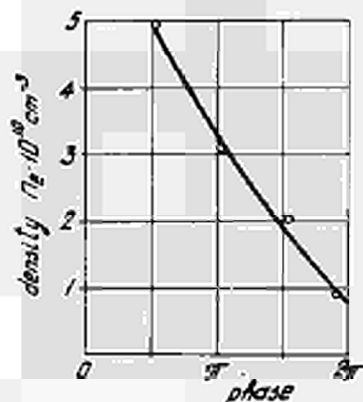


Fig. 9. - The n_e density variation during the oscillation cycle development.

LOW-VOLTAGE ARC IN THE CESIUM-BARIUM
MIXTURE

I.G.Gverdtsiteli, R.Ya.Kucherov, G.I.Tkeshelashvili,
V.K.Tskhakaya.

Physical-Technical Institute, State Committee on
Utilization of Atomic Energy, Sukhumi (USSR)

It has been shown in the paper /1/ that the thermal emission converter filling by the cesium-barium mixture allows us to essentially improve its characteristics in the surface ionization regime thanks to the separation of the cathode work function decrease (barium) and the space charge neutralization (cesium) functions.

In the present paper the experimental investigations of the converter filled by the cesium-barium mixture in the arc mode are described.

The experimental apparatus is represented by a plate-parallel diode with the controllable size of the interelectrode gap, and separate containers for cesium and barium. Metallic barium is placed into the container directly connected with a high-temperature operating chamber where the electrodes are situated; a thermostat filled with liquid cesium is connected with this chamber by a capillar.

The emitter is made of tungsten with the predominating orientation of the face /110/, and the collector - of polycrystal molybdenum. In order to prevent parasitic discharges out of the interelectrode space, the electrodes are surrounded by the ceramical isolation.

The stabilization system allowed us to sustain the cathode and the cesium and barium containers temperature during the experiment with the accuracy of $2-3^\circ$. The current-voltage characteristics have been recorded by means of the two-coordinate potentiometer.

Fig.1 shows the emission current dependence in the bending point of the arc current-voltage characteristics upon the cathode reverse temperature for pure cesium and the cesium-barium mixture. According to the paper /2/ this dependence reflects the shape of S-type curves. The curve maximum in the case of the cesium-barium mixture is displaced in the direction of much higher temperatures and corresponds by an order of magnitude to the high-valued current.

Hence it is evident that the optimum modes for the cesium-barium arc lies in the cathode temperature range of $1900-2200^\circ$ K. In the case of lower temperatures the contact potential difference between the anode and the cathode decreases to such a level that the external source of e.m.f. is necessary to sustain the discharge burning.

Fig.2 shows the current-voltage characteristics taken at the emitter temperature of 2100° K and various pressures of cesium and barium. A low-voltage arc is observed at the filling gas pressures above 10^{-3} torr. At the pressures of the order of 10^{-2} torr the characteristics pass into the negative voltage region. The pressure increase is accompanied with the growth of short-circuiting currents and the minimum discharge current. At the cesium pressures of the order of 10^{-4} torr the transition into the discharge mode is performed continuously at the voltages of 0,7 - 0,8 volts.

The given current voltage characteristics have been obtained in the case of the interelectrode gap of 0.7 mm. How-

ever the discharge parameters up to $5 \cdot 10^{-2}$ torr do not actually change with the interelectrode gap increase from 0.6 to 2mm. At $L < 0.5$ mm the short-circuiting current fall and the arc ignition and extinction potential growth are observed. /See fig.3,4/.

Similar results have been obtained in the apparatus with the cylindric geometry of electrodes.

Thus in the converters filled by the cesium-barium mixture the discharge is observed at the filling gas pressures lower by an order of magnitude than in the case of pure cesium. In this discharge much higher current densities can be reached and the discharge is slightly sensitive to the interelectrode gap variation.

REFERENCES

- [1] John Psarouthakis, Thermionic Energy Conversion with mixed Vapors.
International Conference on Thermoionic Electrical Power Generation. London, september, 1965.
- [2] Г.А.Дюжев и др. ЖТФ XXXV II (1965) 2054

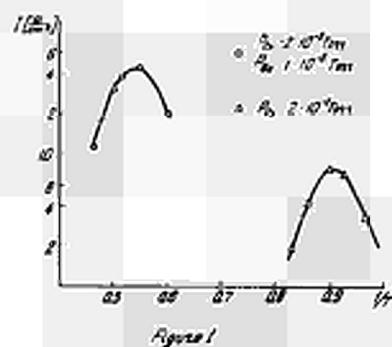


Fig.1 - S-shaped curves for cesium and cesium-barium mixture.



Figure 2. Experimental J-V curves for Ba-Cs operation
 a) $P_{Ba} = 4 \cdot 10^{-4}$ Torr, $P_{Cs} = 3 \cdot 10^{-4}$ Torr
 b) $P_{Ba} = 4 \cdot 10^{-4}$ Torr, $P_{Cs} = 1 \cdot 10^{-4}$ Torr
 c) $P_{Ba} = 7 \cdot 10^{-4}$ Torr, $P_{Cs} = 1 \cdot 10^{-4}$ Torr
 d) $P_{Ba} = 7 \cdot 10^{-4}$ Torr, $P_{Cs} = 2 \cdot 10^{-4}$ Torr

Fig.2- Current-voltage characteristics, taken in the case of cesium-barium filling of the diode.

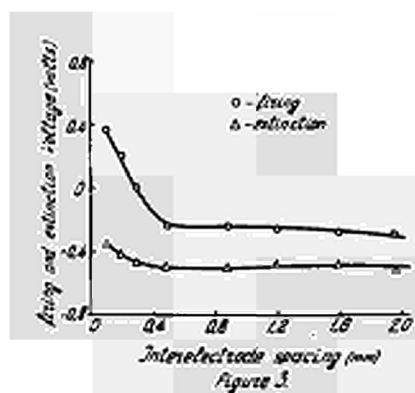


Fig.3- The arc ignition and extinction potential dependence on the inter-electrode gap.

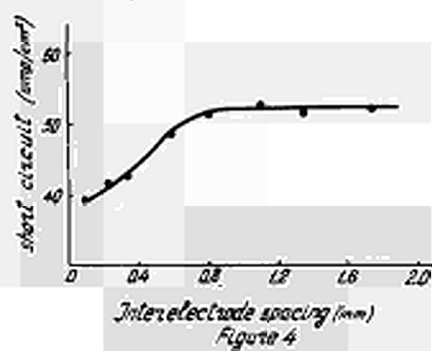
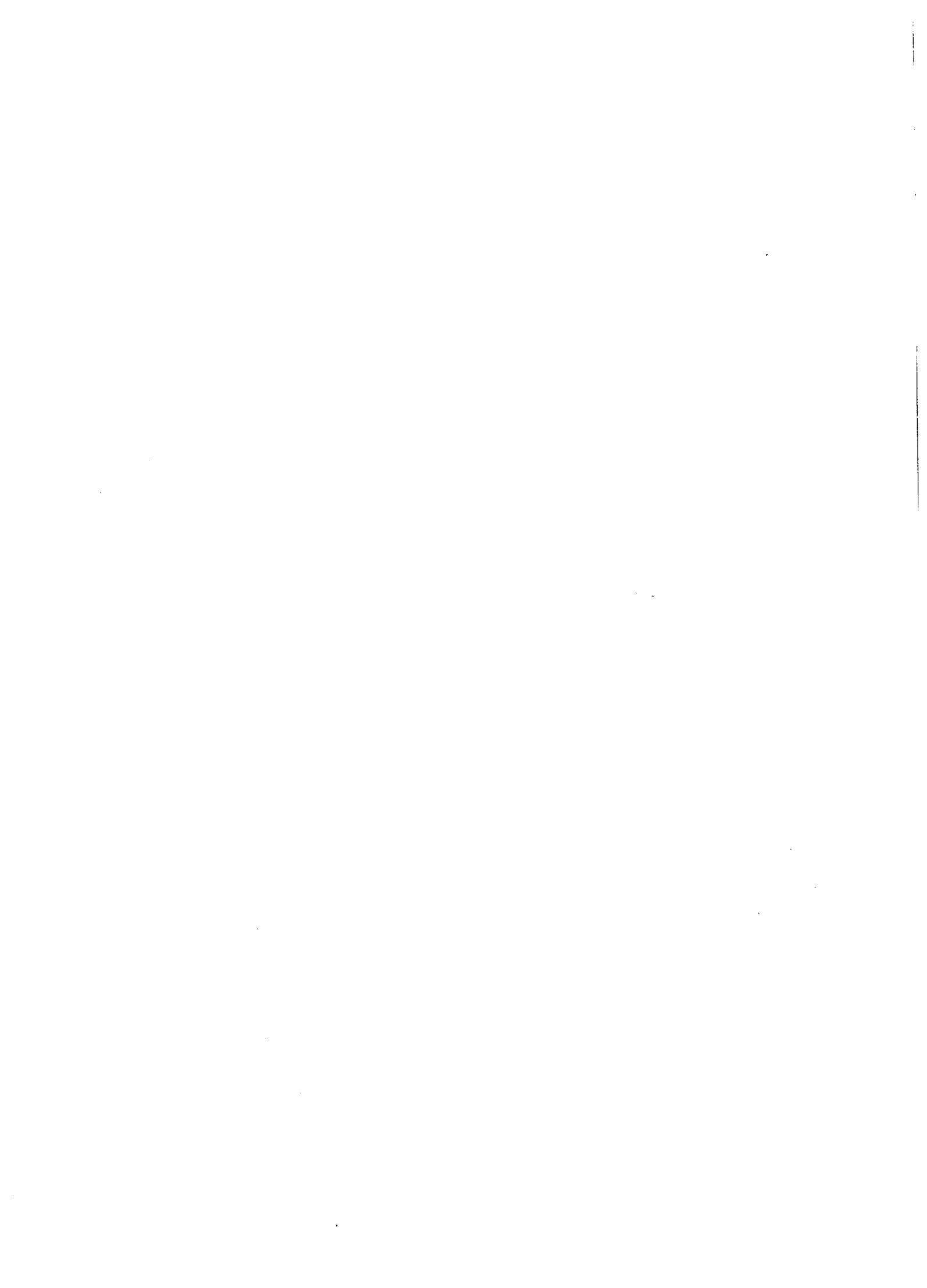


Fig.4- The short-circuiting current dependence on the inter-electrode spacing.



LOW-VOLTAGE KNUDSEN ARC IN THE CESIUM-INERT GAS
MIXTURE.

I.G.Gverdtsiteli, V.Ya.Karakhanov, R.Ya.Kucherov,
G.I.Tkeshelashvili, V.P.Tsiberev, V.K.Tskhakaya.

Physical-Technical Institute, State Committee on
Utilization of Atomic Energy, Sukhumi (USSR)

A low-voltage arc in cesium vapours is the most promising prospect for their practical use in the thermal-emission converters. The ions necessary to compensate the space charge form as a result of step-by-step ionization of cesium by plasma electrons heated by passing of the potential cathode-side jump. The arc is observed in the gap between the hot cathode and relatively cold anode under the conditions when the mean length of the particle free path l is much less than the interelectrode space L . The arc-burning at small cesium pressures is prevented by the fast escape of forming ions and excited atoms towards the electrodes; this results in the ion density decrea-

se in size and the potential jump fall to the magnitude which is no more sufficient to supply the energy necessary to excite cesium atoms to the electrons.

The escape velocity of ions and excited atoms to the electrodes may be essentially reduced by filling the discharge gap by the cesium-inert gas vapour mixture. As a result of the great difference between cross sections of ion and electron scattering by the inert gas atoms ($\frac{\sigma_e}{\sigma_i} \sim 10^3$) we can form a medium which is practically transparent for electrons but highly scatters cesium ions ($l_e \gg L; l_i \ll L$). The ions necessary to compensate the space charge can be formed either as a result of surface ionization on the cathode, or by rare inelastic collisions of electrons with cesium atoms. In the last case a Knudsen arc arises in the interelectrode gap. / I /.

In the experiments carried out the discharge gap between the plate-parallel electrodes has been filled by the cesium - argon mixture. Both electrodes have been made of tungsten. The gap between electrodes can be varied from 0 to 4mm. A special care was taken to avoid the parasitic discharge formation outside the interelectrode gap.

Fig. I shows the current-voltage characteristics corresponding to the cathode temperature of 2050°K, the anode temperature-900°K, the cesium vapour partial pressure of 10^{-2} torr and the interelectrode gap of 0.7mm. On increasing the interelectrode gap to 4mm the current-voltage characteristics do not actually change. The argon addition results in the essential decrease of the voltage at which the arc burns and in the mode

when the ion volume generation is absent it leads to a marked rise in current. Similar curves have been obtained on changing the cesium vapour partial pressures from 10^{-4} to 10^{-1} torr. At higher pressures of cesium (1 torr) the discharge current-voltage characteristics in the cesium-argon mixture and in pure cesium arc nearly same.

Fig.2 gives the dependences of the arc ignition and extinction potentials upon the argon pressure for the cesium vapour partial pressures of 10^{-3} torr.

The analysis of the current-voltage characteristics shows that in such experiments the Knudsen arc has been really observed. In contrast to the ordinary low-voltage cesium arc, the current is carried here by relatively fast electrons accelerated on entering the plasma to the energy of ~ 1 eV. Since the Coulomb scattering cross-section rapidly falls with the energy, the condition $l_e > L$ can be kept at sufficiently high value of the current density. The collector barrier does not prevent the current pass and its height is defined only by the balance of trapped electrons.

The plasma investigations in the Knudsen arc have been carried out by taking probe characteristics and measuring the the electromagnetic radiation.

T-shaped cylindrical probe with the diameter of 0.15mm, has been introduced into the apparatus through the anode of plate-parallel diode with molybdenum electrodes. The stabilization system allowed us to compare probe characteristics of the pure cesium plasma with that of cesium-inert gas (xenon) mixture

plasma at fixed diode parameters. In order to avoid the probe overheating the measurements have been performed in the following range of the cathode temperatures: 800-1500°K. To support the discharge burning it is necessary to apply an external voltage to the anode.

However, the main physical trends were the same as in the operating mode.

The analysis of the probe characteristics ionic branch allows us to build energetical diagrams for electrons. Fig. 5 gives the comparison of such diagrams at same currents flowing through the diode filled by pure cesium and cesium-xenon mixture. The xenon addition leads to the decrease of the cathode-side potential jump and the external anode voltage by 0,4-0,8 volts.

The plasma density defined from the probe characteristics exceeds the fast electron density more than by an order of magnitude. The trapped electron temperature in the potential well was 7000-10000°.

At the cesium pressures of the order of 10^{-3} torr the probe measurements display a beam of fast electrons at the cathode which relaxes as it moves towards the anode. Simultaneously we fix fairly intense electromagnetic radiation of the diode. At the cesium pressures above 10 torr we failed to obtain the fast electron beam on the basis of the probe characteristic analysis. The electromagnetic radiation intensity considerably relaxes under such conditions.

The beam fast relaxation may be related to the beam instability in the plasma.

REFERENCES

I.R.Ya.Kucherov, A.F.Nastoyastchi. Kinetic theorie of the Knudsen arc. The report presented on the Second International Conference on Thermoionic Electrical Power Generation.

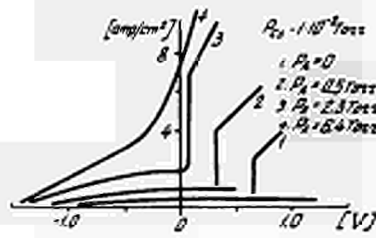


Fig. I. Experimental current-voltage characteristics of the diode, taken on the cesium-argon mixture.

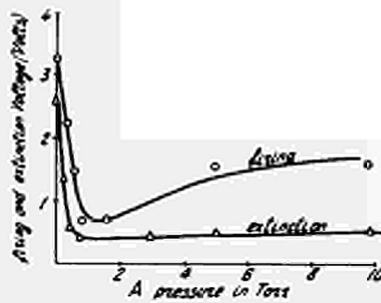


Fig. 2. The arc ignition and extinction potential dependence on the argon pressure.

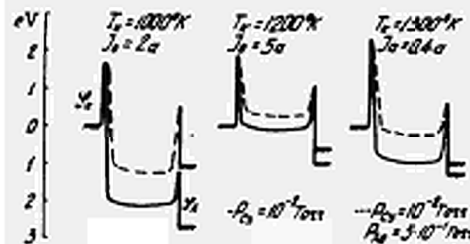


Fig. 3. Energetic diagrams for electrons, taken on filling the diode by cesium and the cesium xenon mixture.

DISCUSSION

Speaker of papers H-9, H-10, H-11 and H-12: R. Ja. KUCHEROV.

HATSOPOULOS (USA): In connection with your data with the inert gases and your question about the possible influence of oxygen in the data, I would like to make the following comments.

In paper H-16 we report some extensive experiments that we conducted with Xenon, Krypton and Argon. In the beginning of a several months period, we were observing an enhancement of the performance characteristics, although we took great care in having pure gases. Actually what happens is that one part in 10^6 of oxygen will produce an enhancement in these characteristics. We had to go to quite an elaborate refluxing system to clean the gases in cesium vapor to eliminate all oxygen, and, after we did this and after we took the data, we found that the enhancement had completely disappeared and that any addition of an inert gas just contributed to the diffusion losses of electrons in the converter.

KUCHEROV (USSR): We too were very worried about the influence of oxygen. It was for this reason that I only took a few data points from our tests, since we did have some where we thought we did not have the oxygen influence. Later on it was always present so we degassed and we worked with pure argon again. With argon we did not see an increase in current. We consider that this demonstrates that the oxygen was almost entirely absent there. Then in H-16 you spoke about adiabatic characteristics. Of course if we increase the cesium pressure, we increase the current and get better results with fairly high pressure, but the test I mentioned only worked with very low voltages and the results discussed were with the same pressure. The current was low and I wonder whether we should or should not create a Knudsen-arc. Otherwise, I don't see how we are to obtain the arc which will be required.

HATSOPOULOS: I agree with your comments. As a matter of fact at very low cesium pressures we might have observed a beneficial effect, but it was in such a low cesium pressure that it was not of very practical importance. There is one point of a caution I want to point out. That is, when dealing with an inert gas, it is very difficult to estimate the pressure of cesium in the converter due to diffusion, Soret-effects, and other effects of this kind. For this reason we dealt with cesium optimized envelopes which presumably are independent of the cesium level of pressure and that

is how we made comparisons. When we tried to make comparisons in a constant cesium pressure, we found great discrepancies because of the difficulties associated with reproducing the same cesium pressure in the presence of an inert gas.

KUCHEROV: I agree with you. We too had some difficulties. We had to make a very short tube for the cesium reservoir. It was fairly wide we thought, and we carried out a number of tests before we got a change and we think that the cesium pressure remained constant during that period.

INVESTIGATIONS ON NOBLE GAS CONVERTERS

H. Albrecht, B. Saggau, H. Strecker *)

(Institut für Gasentladungstechnik und
Photoelektronik, Universität Stuttgart,
Breitscheidstrasse 2 (Germany))Abstract

The ability of an auxiliary discharge to compensate the negative space charge with an optimum efficiency is investigated by some experiments. The use of an auxiliary cathode permits that the "quality" of the auxiliary discharge power can be varied, so that either an auxiliary discharge with high voltage drop and low current or another one with low voltage drop and high current can be maintained.

The output current divided by the auxiliary power was measured as a function of auxiliary discharge power and its "quality".

In a second part of the paper the method of the auxiliary discharge for space charge compensation is compared with the converter operation in the ignited mode in Cesium vapor, and conditions were found where either the one or the other mode can be more advantageous.

Introduction

The present work deals with the modes of two different kinds of plasma: The auxiliary discharge mode¹⁾²⁾ and the low voltage arc mode.

In order to test the applicability in thermionic noble gas converters, the ability of an auxiliary discharge to compensate the negative space charge with an optimum efficiency is investigated by some experiments.

1. Auxiliary Discharge in Noble Gas

Operation with an auxiliary discharge has to meet two require-

ments: First the negative space charge has to be compensated, on the other hand the plasma between the electrodes has to be well conducting, that means its electrical resistance must be kept at low values because losses in the interelectrode space mean a lower output voltage.

For the testing of the effectiveness of an auxiliary discharge in noble gas the experimental tube (Fig. 3) was filled with Xenon having a pressure in the range from 0.1 to 0.6 Torr.

The emitter consists of an indirectly heated cylindrical Molybdenum tube which was covered by a 1 mm Tungsten coating impregnated with Ba-Ca-aluminate by Philips Metalonics, Mount Vernon, N.Y. The emitter has an area of 23 cm^2 and its current density is about 10 A/cm^2 at temperatures of appr. 1450°K .

The collector is made of stainless steel.

Two Tungsten wires of 0.3 mm diameter, mounted in the middle of the emitter-collector spacing, that is 0.4 cm, were used as auxiliary cathodes. The electron emission of the wires could be varied by direct heating.

As a result of measurements at a constant output voltage the emitter current density as a function of the auxiliary power (Fig. 1) is obtained.

During these measurements, first the auxiliary voltage was kept at a constant value of 40 V while the auxiliary current was varied. At very low emitter current densities, the curve (- -) is nearly proportional to the auxiliary discharge current, yet then bends aside and rises only little at current densities of $> 0.5 \text{ A/cm}^2$ when the auxiliary current is raised. It seems as if the saturation emission of the main emitter were reached.

Quite a similar behavior is shown by the diagram at which the auxiliary discharge current is kept constant at a value of 20 mA and the power consumed in the auxiliary discharge

is varied by means of the auxiliary voltage.

As a result, the effectiveness of auxiliary discharge for space charge compensation only depends on the power consumed in the auxiliary discharge; above the ionization potential it is obviously of no importance whether the voltage is increased at constant auxiliary current or vice versa the current at constant auxiliary voltage. Apparently, an auxiliary discharge with high voltage drop and low current is not more effective in plasma generation than one with low voltage drop and high current.

No essential raise in the emitter current density is achieved when the same auxiliary power is bisected on two auxiliary emitters - even if by this geometric conditions are possibly improved.

When we look at the ratio of the output current to the auxiliary power necessary to obtain this space charge compensation, we find that the function $(\text{---}) I/N_{\text{aux}} = f (N_{\text{aux}})$ has a maximum at low current densities and drops down when the current density increases. The optimum ratio of emission current to auxiliary power is obtained at emitter current densities below 0.3 A/cm^2 and no reasonable output power can be reached.

There remains a negative emitter sheath that is hard to remove by increasing the auxiliary power. On principle, the reaction can be attributed to two features: Either the ion density is not proportional to the power of the discharge or - if so - the positive ions cannot get near the emitter. Probe investigations at which the ion saturation current of the probe was measured as a function of the power put into the discharge show the similar "saturation characteristic" like the curves in Fig. 1.

This result permits to conclude that the first assumption is correct, i. e. that already the ion density does not increase proportionally with the discharge power and that by this the

current density for higher auxiliary powers only rises slowly when the auxiliary density is raised.

Obviously the balance for high particle densities becomes more and more disadvantageous.

2. Comparison of the Auxiliary Discharge with the Ignited Mode

Both, the auxiliary discharge and the low voltage arc need a fraction of electric output power of a converter. If we spend about 10 % of output power to maintain an auxiliary discharge, we obtain an emitter current density of scarcely more than $\approx 0.5 \text{ A/cm}^2$ as found above. The ignited mode of a Cesium plasma has a voltage drop of 0.4 - 0.6 V in the minimum of p.d (p = vapor pressure, d = emitter-collector spacing). This value is nearly irrespective of current density, so that high emitter current densities can be realized.

Considering the aspects following from the experimental results, we can now compare the two modes of space charge compensation under the following assumptions:

- a) We only consider low temperature converters having emitter temperatures up to 1600°K .
- b) We postulate, that an optimum emitter can be realized for each emitter temperature (for each emitter temperature, to the optimum efficiency an optimum emitter work function is assigned to, which can be regulated by Cs-vapor pressure).
- c) For the calculation of losses of thermal radiation, we lay down an emissivity of $\epsilon = 0.3$. The emitter lead is optimized as far as thermal and electrical conduction is concerned.

The maximum converter efficiency as a function of the remaining variable, i. e. collector work function ϕ_C is given by Fig. 2.

The curve representing the auxiliary discharge mode intersects

the range of the ignited mode in two domains:

In the upper domain, the converter efficiency with the ignited mode is more advantageous, and in the lower one, the efficiency is more disadvantageous than this one of a converter operated with an auxiliary discharge mode.

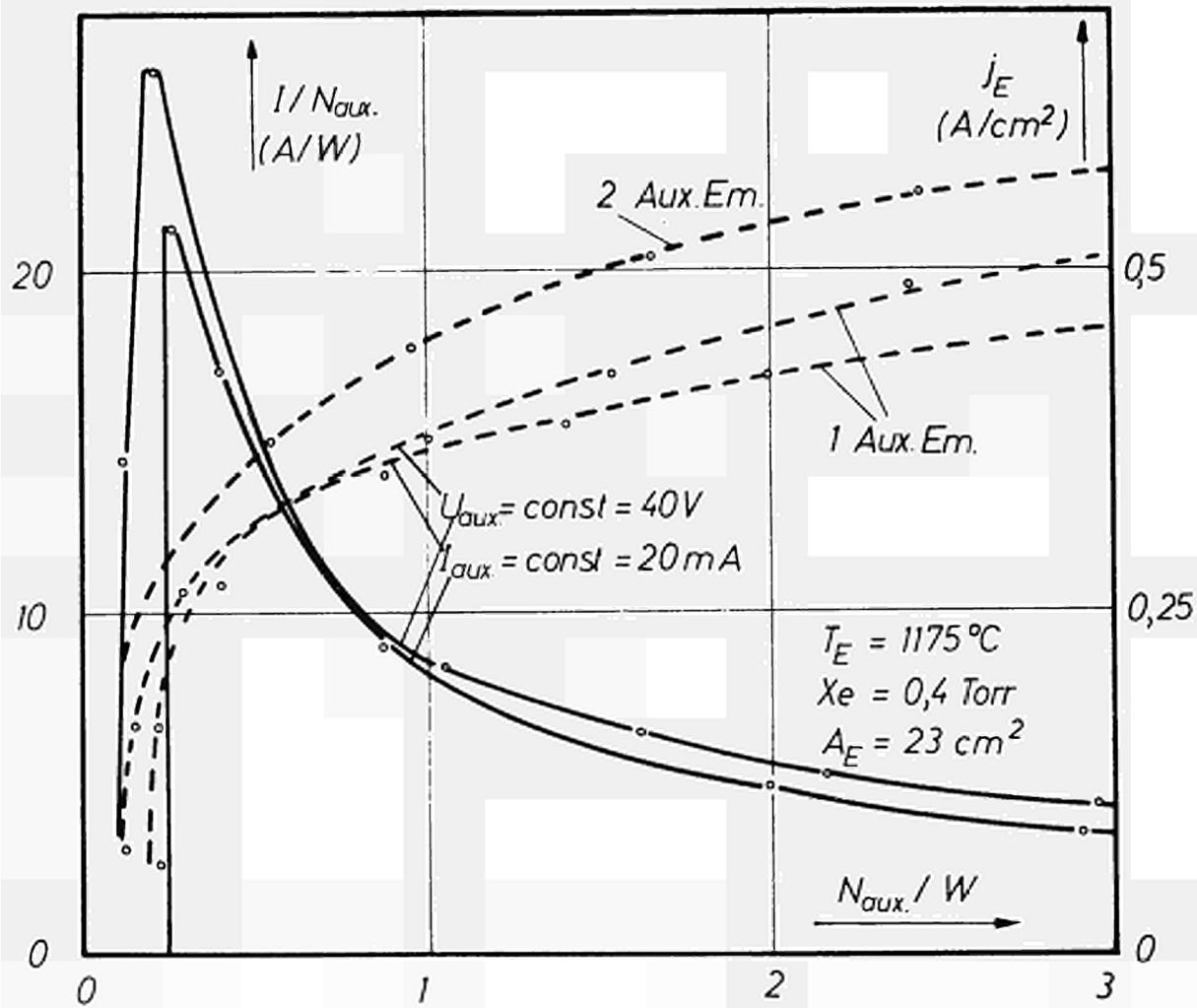


Fig. 1. Converter Current (—) and Converter Current Density (---) per Auxiliary Power

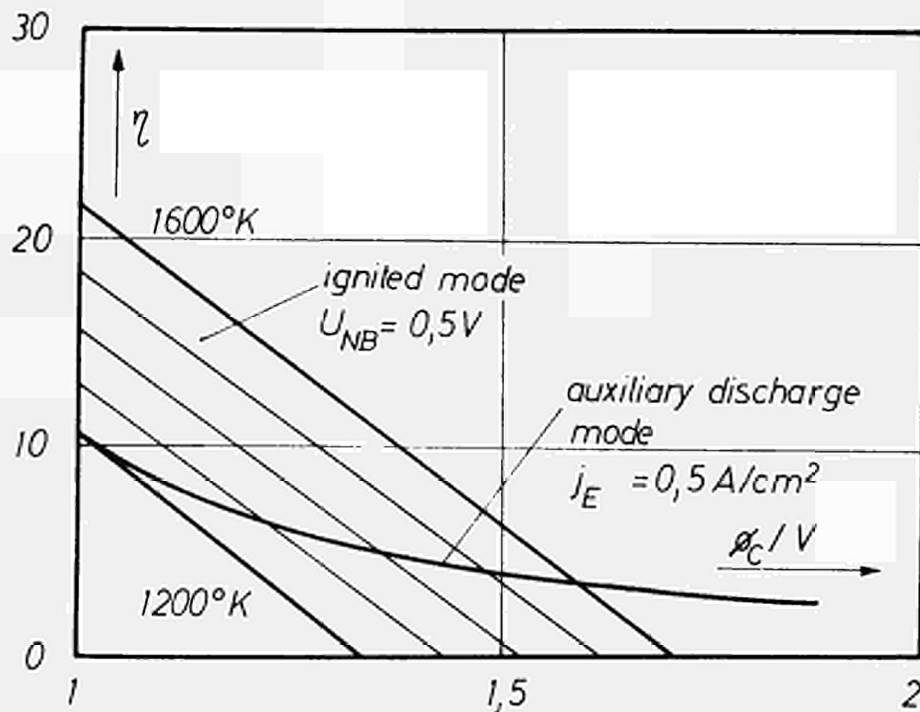


Fig. 2. Maximum Converter Efficiency as a Function of Collector Work Function ϕ_c

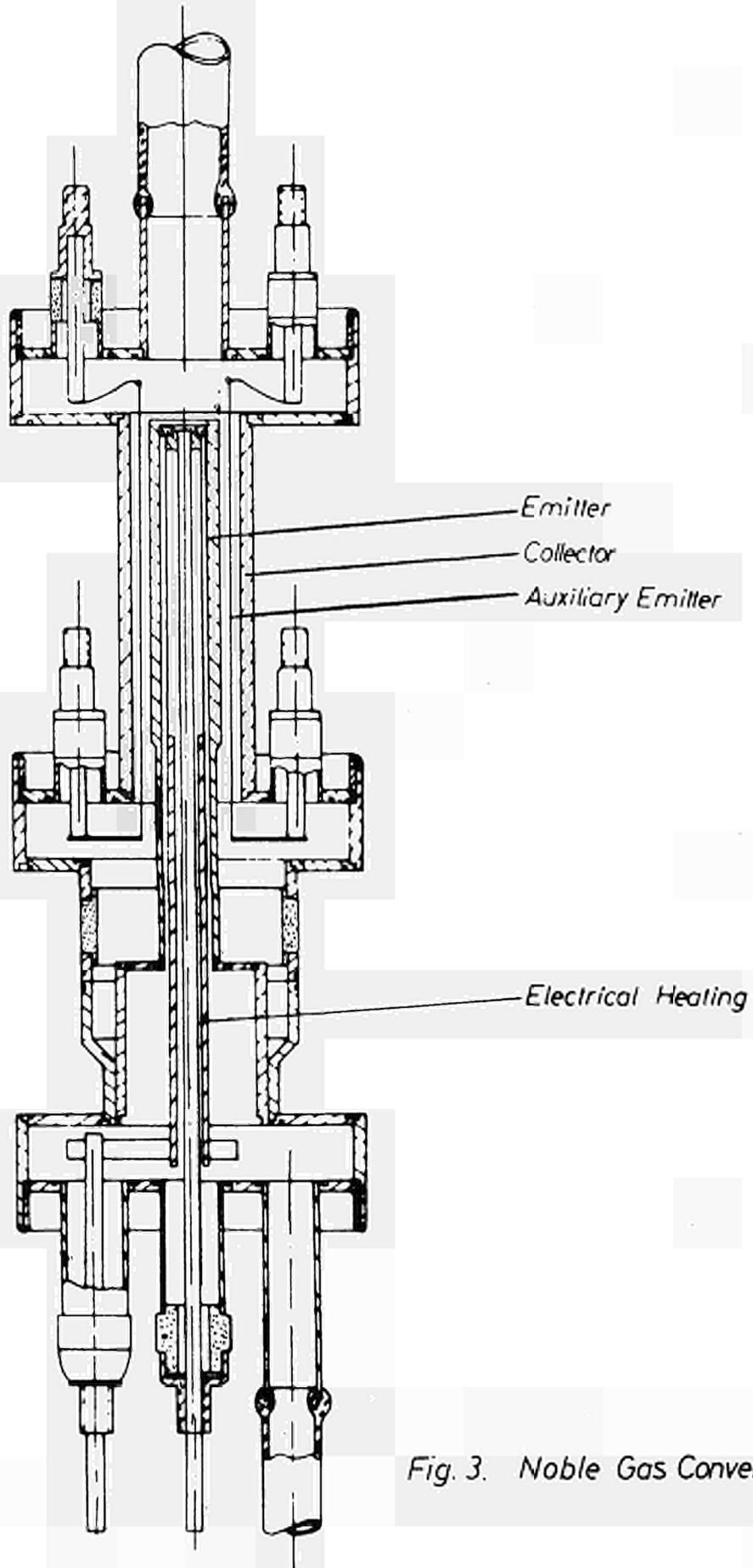


Fig. 3. Noble Gas Converter

DISCUSSION

No speaker of paper H-13.

Mrs. BACAL (Rumania): What, in the opinion of the authors, is the explanation of the fact that the collector current and also the ion density does not increase proportionally with the auxiliary discharge currents?

SAGGAU (Germany): The insufficient space charge compensation at high auxiliary discharge currents is an important point. It is a question of either the ion diffusion to the emitter sheath is not proportional to the produced ion density or the produced ion density itself is not proportional to the auxiliary power. Probe measurements have shown that the latter is the case because of more essential ion losses at higher ion densities.

Mrs. BACAL: Well, I wanted to comment on why at some auxiliary discharge current, these losses should increase and further why there is not a proportionality of the electron current to the collector with auxiliary discharge current. Perhaps at some critical value of the auxiliary discharge current there may occur a transition from an electron-rich potential distribution in the diode to an ion-rich one, which should increase the ion losses to the electrodes. I think that this should be verified by experiments.

LOW-VOLTAGE CESIUM ARC IN THERMIONIC CONVERTER WITH
EXTENDED CATHODE SURFACE

M.B. Barabash, E.P. Busigin, V.G. Grigoryants,

I.P. Yavor

A.F. Ioffe Physical Technical Institute ,
Academy of Sciences , Leningrad , USSR

Abstract

To study possible mechanism of current enhancement from excess cathode area two series of experiments were performed. The first one was carried out on two similar devices with different cathode surfaces: a smooth one and a slotted surface. Measurements data carried out on these two devices were compared at equal total currents passing through diodes.

Electron concentration and temperature distribution across interelectrode space as well as across the slots were determined spectroscopically. Relationship between these values showed that current enhancement in the device with extended surface cathode was due to increase of total emission current drawn on the cathode.

To study contributions of different surface regions of a separate cathode cavity in emission process were conducted the second series of experiments on a device with electrodes simulating a cathode with rectangular slots. Depth of plasma penetration into the cavity was measured spectroscopically

and visually (by means of optical cathetometer) as a function of pressure , current passing through the device and cavity width. It was found that current enhancement when applied voltage increased was due at first to the depth increasing of plasma penetration (h) into the cavity.

Introduction

A number of published works [1-3] testify to the fact that cathode surface extension is one of possible methods for increasing of thermionic converter effectiveness. In spite of certain contradictions in the results obtained data analysis shows that current gain is not proportional to geometric increase of cathode surface in collisional modes of thermionic converter operation at large extension coefficients.

To study some qualitative and quantitative relationships of this process in arc mode operation two series of experiments were carried out on the models of thermionic converters with smooth and extended cathode surface and on a rectangular slot model.

Experimental method

Experiments were performed on evacuated and sealed-off glass devices. To compare characteristics of extended and smooth cathodes measurements were made on two devices of similar design having different molybdenum cathodes. One of the cathodes had a smooth and polished surface , another

had an extended surface. Extension of surface was obtained by the use of narrow rectangular slots, which are shown schematically in Fig. 1. Extension coefficients, i.e. ratio of total working cathode surface to corresponding surface before extension, was equal to 5.

Arrangement of electrodes in the device simulating a single slot of extended surface cathode is shown in Fig. 2. Heaters (3) and cathode plate surfaces (2) facing them were shielded by sapphire screens (4) which decreased current to anode drawn from these surfaces. One of cathode plates was movable. Replacement of this plate relative to fixed plate allowed to vary cathode cavity width within 0 - 2.5 mm.

Each device was equipped with two sapphire windows in opposite walls of a cylindrical glass envelope.

Temperature measurements were carried out using optical pyrometer. Indirect heating scheme employed in the experimental devices allowed to maintain working cathode temperatures amounting to 1600°K. Cesium vapour pressure varied within 0.1 - 1.0 Torr. Spectrometer having linear dispersion 3 Å/mm was used for spectral measurements. During measurements radiation flows from plasma layers whose width didn't exceed 0.1 mm were recorded. Electron concentration was determined from Stark-broadening of nF-5p lines, electron temperature was determined from the shape of cesium 6P-recombination continuum [4-5]

Results and Discussion

Comparative estimation of emission properties of extended cathode can be made on the basis of current-voltage performances, shown in Fig. 3. Dotted line represents current density level corresponding to total current equal to 1 ampere. In the case of extended surface cathode this level is attained at a lower voltage value (voltage is by 0.2 v less than the value for the smooth cathode). Under similar conditions and at equal currents electron concentration and temperature distributions essentially coincide. Therefore it may be assumed that density of current drawn from frontal regions of extended cathode fins is equal to current density

j_p drawn from the smooth cathode. In this case density of current j_s drawn from frontal area of slots ($S_s = S_o - S_p$) is:

$$j_s = \frac{i - j_p \cdot S_p}{S_s} \quad (1)$$

where i - total current from extended cathode, S_o - frontal area of the cathode, S_p - frontal area of the extended cathode fins. This expression is used to obtain curve 3 in Fig. 3. It may be seen that ratio of current drawn from the slot to total inner surface of the slot proves to be less than current density of the smooth cathode. It means that inner surfaces of the extended cathode slots must markedly contribute to its emission. It is clearly confirmed by experiments which permitted to observe plasma penetration into the slots. Electron concentration distributions are given in Fig. 4; they were measured both in the interelectrode space and in the

slots for two values of current.

Qualitative conclusion about greater emissivity of extended cathode in arc mode of operation can be derived from comparing ratios of total anode current and back electron current from plasma to the cathode in two devices having smooth and extended cathodes. Since plasma parameter distributions are similar in both devices random electron currents in corresponding interelectrode regions are similar too. Therefore, in these two devices potential drop in plasma and retarding anode sheath values, equal to

$$\Delta U_a = \frac{k T_{ea}}{q_e} \ln \frac{n_{ea} \sqrt{k T_{ea}}}{j_a \sqrt{2 j_{me}}} \quad (2)$$

are the same. Both anodes have equal work functions due to equivalence of their heat regimes. Hence, extended cathode sheath value must be less by 0.2 v than the value for smooth cathode which means that the back current from plasma to extended cathode exceed that to smooth cathode. At equal total currents passing through two devices it results in larger emission currents of extended surface cathode. If one introduces effective thermionic emission constants for extended cathode, analysis of potential distribution and I-V plots for smooth and extended cathodes shows that emission current gain of extended surface cathode corresponds to increased Richardson's constant A, work function remaining unchanged.

Contribution of different surface regions inside a single cathode cavity to emission process was investigated on the rectangular slot model. Current dependence on cathode

cavity width is shown in Fig. 5 for two fixed anode potentials. These curves can be used for calculating current densities as functions of cavity width assuming that current corresponding to zero width is determined by insufficient shielding of non-working areas of cathode plates. This background current doesn't depend on cavity width at constant voltage. Therefore, density of current drawn from the cavity is

$$j_s = \frac{i - i_b}{\delta l} \quad (3)$$

where i - total current to the anode, i_b - background current, l - cathode plate width. Curves, calculated with the use of this expression, are shown in Fig.6. When cavity width is equal to width of extended cathode slot ($\delta = 0,07$ mm), calculated current density agrees within 25% with the results of measurements on extended surface cathode. Consequently, increasing cavity width results in increase of cavity current while decreasing its density. On the basis of Fig.6 we can evaluate maximum current gain brought about by the use of cathode surface extension under given conditions. It is evident, that extended cathode current can exceed current from smooth cathode not more than by 3-4 times, even in case of very thin walls between adjacent slots.

Main contribution to electron emission is provided by those regions of cathode plate inner surface, which are in the most intimate contact with luminous plasma. Hence, dimensions of these regions are determined by depth of plasma penetration h into the cavity. Dependencies of h from

anode current value are shown in Fig.7. At large currents these dependencies tend to saturate. Average density of current from surfaces being in contact with plasma approximately corresponds to density of current, obtained from smooth cathode under similar conditions. Evidently, current increase comparing to current from smooth cathode must occur at $h > \frac{\delta}{2}$. As may be seen from Fig. 7, these conditions can be satisfied more easily at lower cesium vapour densities. Process of plasma "extrusion" from the cavity at decreasing cavity widths is clearly illustrated by curves of Fig. 8, representing 6354\AA line intensity as function of cavity width.

Resuming, we may state, that increase of current from extended cathode in arc modes of operation is due to plasma penetration into the slots and to increase of total surface area contributing to electron emission.

REFERENCES

- (1) SCHNEIDER R.T., DUNLOP J.D., Appl.Phys.Letters, 3, 73 (1963)
- (2) QUINTELLA S.G., SOO S.L., Int.Conf.of Therm.Power Generation, London, 1965
- (3) BADAREU E., POPOVICI C., SOMESAN M., Rev.Romanic de Phys. 12, 3 (1967)
- (4) AGNEW L., SAMMERS C., Adv.Energy Conversion,3, 79(1963)
- (5) AGNEW L., SAMMERS C., VII Int. Symposium on Ionization Phenomena in Gases, Beograd, 1965

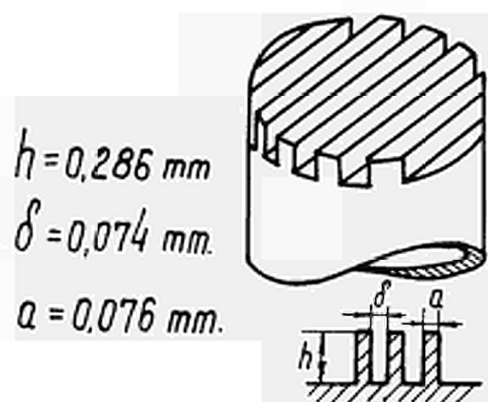


Fig.1. Extended Surface Geometry

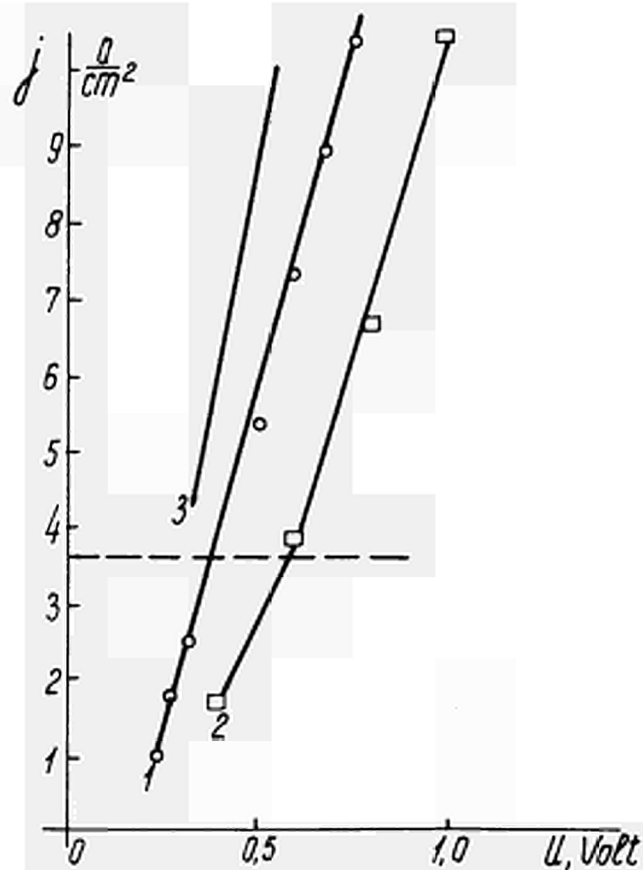


Fig.3. Comparison of I-V Performances between the Extended Cathode Device (1) and the Smooth Cathode Device (2); (3) -Current Density from Eq. 1.
 $P_{ca} = 0.5 \text{ Torr}$, $T_c = 1360^\circ\text{K}$, $d = 2.0 \text{ mm}$

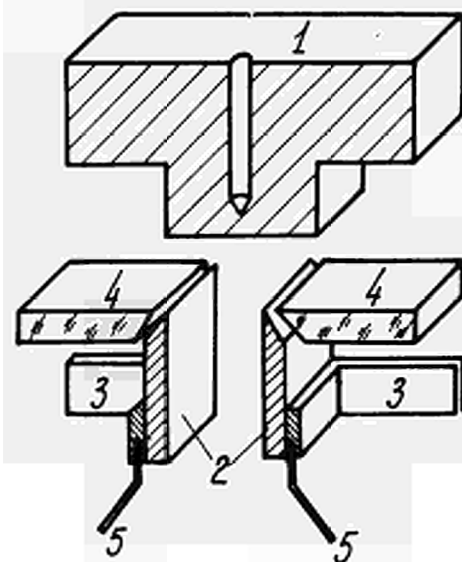


Fig.2. Schematic Diagram of Device with Cavity Type Cathode
 1-anode, 2 -cathode plates, 3-heaters, 4-sapphire screens, 5-potential leads.

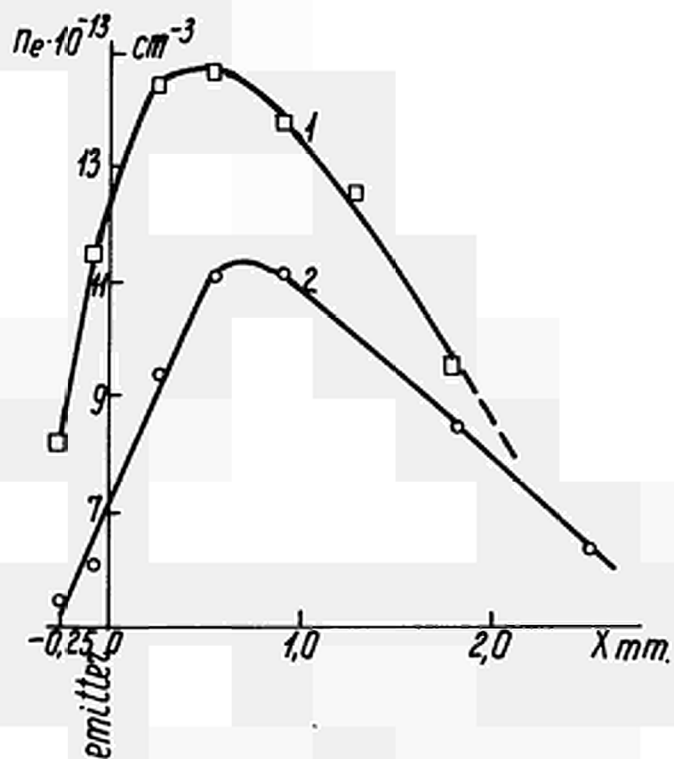


Fig. 4. Electron Density Distribution along the Gap and between Filaments of Extended Cathode.

1- $i=2.4a$, 2- $i=1.2a$

$P = 1.0$ Torr, $T_c = 1360^\circ K$

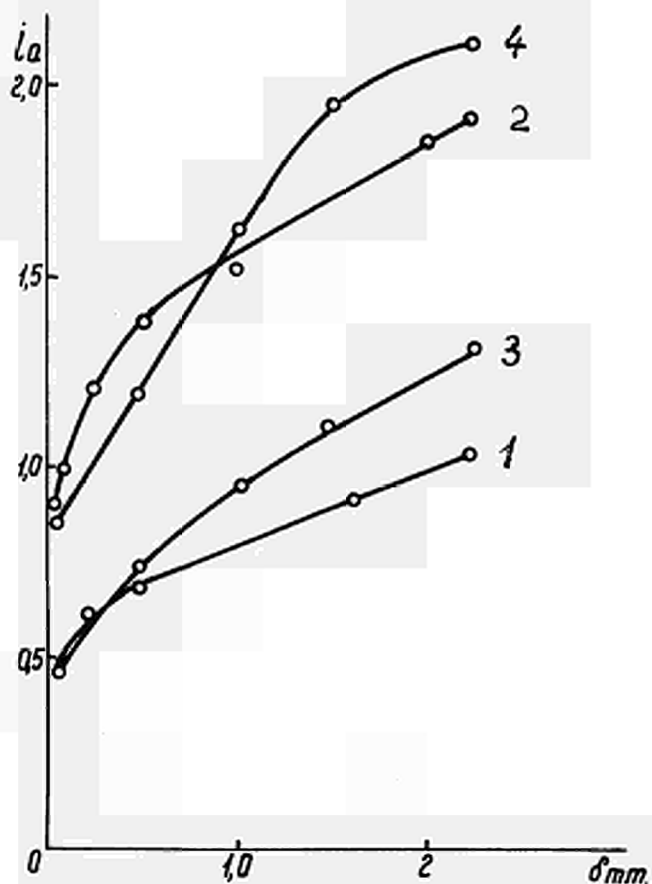


Fig. 5. Anode Current as a Function of Cavity Width

1- $U=0.7$ v, 2- $U=1.0$ v, $P_{0g}=0.5$ Torr;

3- $U=0.7$ v, 4- $U=1.0$ v, $P_{0g}=0.15$ Torr;

$T_c=1360^\circ K$

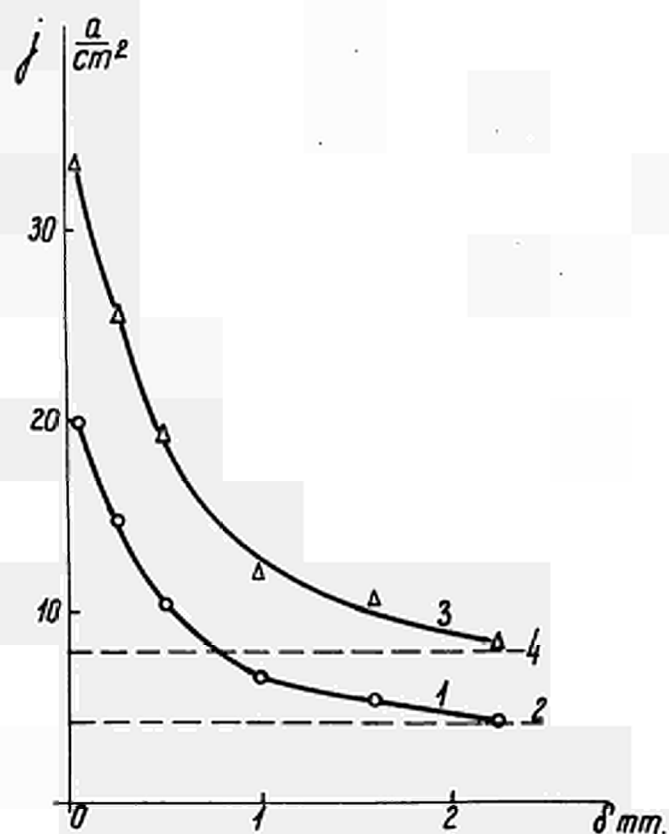


Fig. 6. Current Density as a Function of Cavity Width, $P_{0g} = 0.5$ Torr, $T_c = 1360^\circ K$, $U=0.7$ v, 1-cavity, 2-smooth cathode, $U=1.0$ v, 3-cavity, 4-smooth cathode,

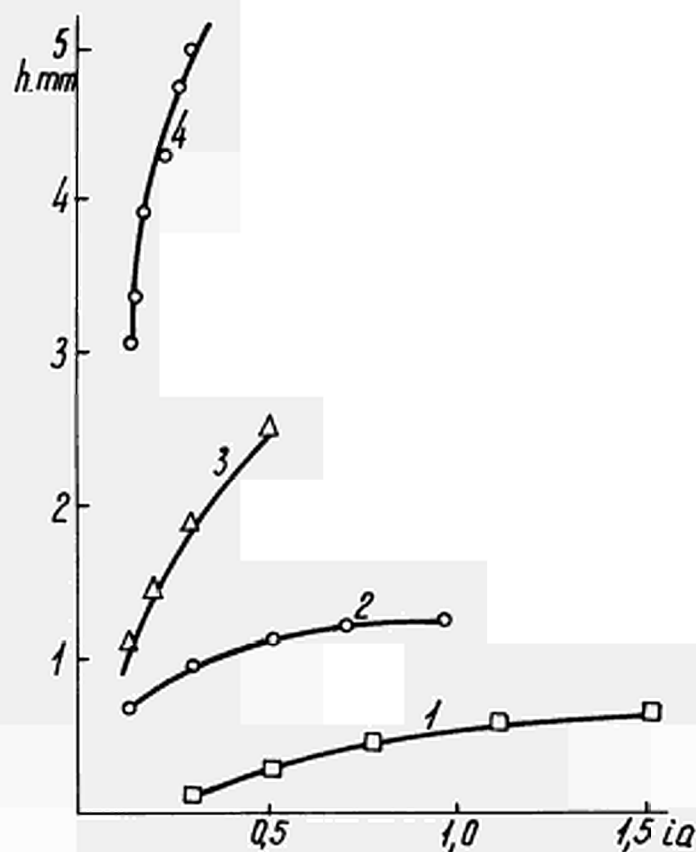


Fig. 7. Plasma Depth Penetration as a Function of Anode Current. $T_c = 1360^\circ\text{K}$, $\delta = 0.3$ mm; 1- $P_{c0} = 0.5$ Torr, 2-0.15 Torr, 3-0.15 Torr, 4-0.05 Torr

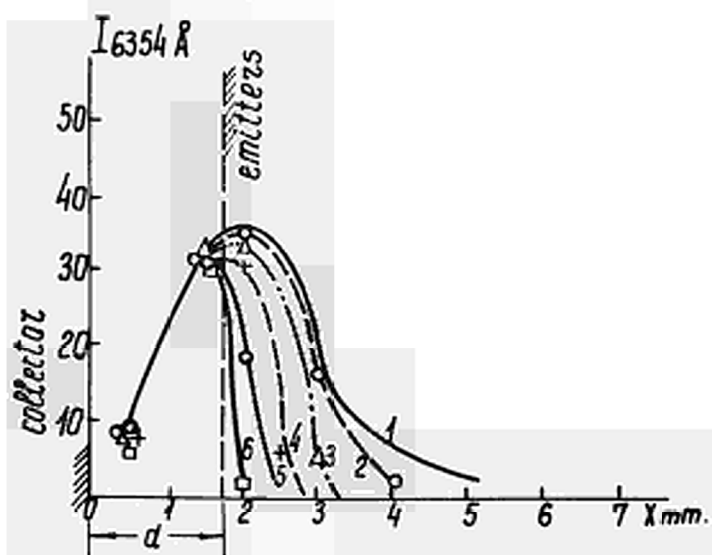


Fig. 8. Line Intensity Distributions as a Function of Cavity Width. $T_c = 1360^\circ\text{K}$, $P_{c0} = 0.5$ Torr, $U = 0.7$ v.
 1- $\delta = 2.25$ mm ($i = 1.0$ a), 2-1.6mm ($i = 0.42$ a),
 3- 1.0 mm ($i = 0.76$ a), 4- 0.5 mm ($i = 0.7$ a)
 5- 0.25 mm ($i = 0.62$ a), 6- 0.05 mm ($i = 0.46$ a)

ELECTRON SCATTERING IN THERMIONIC CONVERTERS

BY XENON, KRYPTON AND ARGON^{*}

F. Rufeh and D. Lieb

Thermo Electron Corporation
Waltham, Massachusetts

ABSTRACT

The effect of argon, krypton and xenon on volt-ampere characteristics was investigated in a thermionic converter. A consistent decrease in performance was observed as the inert-gas pressure was increased in the range of 0 to 200 torr. This data contradicts the results of other studies, in which a substantial improvement in performance was reported when inert gases were introduced into converters. The improvement in performance reported by others was probably caused by oxygen contamination in the inert gas.

EXPERIMENTAL APPARATUS

In this work special precautions were taken in order to minimize oxygen contamination in the inert gas. Oxygen impurities, even at a level of 1 part per million, can appreciably change the emitter work function and therefore the emission characteristics. The converter used in the experiments is described in Reference 1. It is equipped with a re-fluxing cesium reservoir which allows the introduction of inert gases into the diode during operation. The gas injection system is shown in Figure 1. The valves and fittings are all metal and are bakable up to 600°K. The pressure was measured with an accuracy of ± 0.2 torr by the expansion of a metal capsule. A hot cesium trap

* Supported by the Air Force Cambridge Research Laboratory under Contract F19628-67-C-0091.

was incorporated in this system to minimize oxygen contamination. It will be shown later that the trap was quite effective for this purpose. Two water-cooled blocks were used to prevent the escape of cesium vapors from the trap.

The gas injection procedure is as follows: With valve No. 1 closed, valve No. 2 is opened momentarily to introduce the desired pressure of inert gas into the trap. The gas is kept in the hot cesium vapor for about 20 hours, and then it is injected into the converter by opening valve No. 1. The gas pressure in the converter is continuously monitored by the pressure gauge.

EXPERIMENTAL RESULTS AND CONCLUSIONS

The volt-ampere characteristics were monitored as the inert gases were introduced into the converter. Each time the cesium temperature was changed, a time interval of one to thirty hours was required to establish pressure equilibrium between the cesium reservoir and the interelectrode space. Inert gases impede the transport of cesium atoms and cause poor communication of cesium between the cesium reservoir and the interelectrode space. Even after pressure equilibrium is established, the cesium pressures in the reservoir and in the interelectrode space are not necessarily the same. Cesium atoms must diffuse through the inert gas from the reservoir to the emitter surface. This process takes place in the presence of a temperature gradient which causes the cesium pressure in the interelectrode space to be higher than that in the reservoir and is called the Soret Effect.²

Because of these considerations, the data in this experiment are in the form of variable-cesium-temperature families of volt-ampere characteristics. Such a family is obtained by changing the cesium reservoir temperature while all the other converter parameters are held constant; an envelope is formed that represents the optimized

performance with respect to cesium temperature. The effectiveness of the trap in eliminating oxygen contamination was established by the following procedure: An envelope obtained before introduction of the inert gas was compared with an envelope obtained after the gas was introduced and removed from the converter. The two envelopes were in good agreement within $\pm 2\%$.

The effect of the inert gas was evaluated by a comparison of the envelopes obtained at various inert-gas pressures. The emitter temperature and interelectrode spacing chosen for this comparison was 1800°K and 10 mils. A typical family and its envelope are shown in Figure 2, and a summary of the cesium envelopes obtained for the argon pressure range of zero to 200 torr is shown in Figure 3. Similar data for krypton and xenon are shown in Figures 4 and 5. A consistent decrease in output current is observed when the inert-gas pressure is increased. This finding contradicts the results of other studies, in which a substantial improvement in performance was reported when inert gases were introduced into converters.³⁻⁶ The improvement in performance reported in the references cited was probably caused by oxygen contamination in the inert gas.

These data can be presented in an alternate form by plotting the current density at a given voltage as a function of pressure (Figure 6). This figure shows the decrease in output current at 0.10 volt due to inert-gas pressure. In Figure 7 inverse current at 0.10 volt is plotted as a function of pressure. For xenon and krypton there is an approximate linear relationship between inverse current and gas pressure. This is consistent with most plasma theories. The curve for argon, however, crosses that of xenon. This is believed not to be caused by experimental errors, but is probably related to the scattering cross section of these gases. Several sets of data taken, using two gas injection systems, showed good reproducibility (Figures 8 through 10).

ACKNOWLEDGMENT

The authors wish to express their appreciation to H.L. Hirsch for assistance in taking the data.

REFERENCES

- (1) RUFEB, F.; LIEB, D.; VAN SOMEREN, L., "Summary of Applied Research," presented at this conference.
- (2) HATSOPOULOS, G.N.; KEENAN, J.H., Principles of General Thermodynamics, John Wiley and Sons, Inc., New York, 1965.
- (3) FENDLEY, J.R. Jr., "Gas Analysis and Gas Dosing of Cesium Vapor Diodes," Proceedings of Thermionic Conversion Specialist Conference, Gatlinburg, 1963.
- (4) KAPLAN, C.; MERZENICH, J.B., "Xenon Addition Experiment in a Thermionic Converter," Proceedings of Thermionic Conversion Specialist Conference, Cleveland, 1964.
- (5) BEKMUKHAMBETOV, E.S., et al., "Thermionic Converter Operation in the Presence of Krypton and Xenon," Sov. Phys. - Tech. Phys., 10, 1318-1321 (1966).
- (6) KONDRAT'YEV, F.V.; SINYUTIN, G.V.; TIKHONOV, V.F., "The Influence of a Xenon Admixture on the Operation of a Cesium-Vapor-Filled Thermionic Converter," Atomnaya Energiya, 23:3, 213-218 (1967).

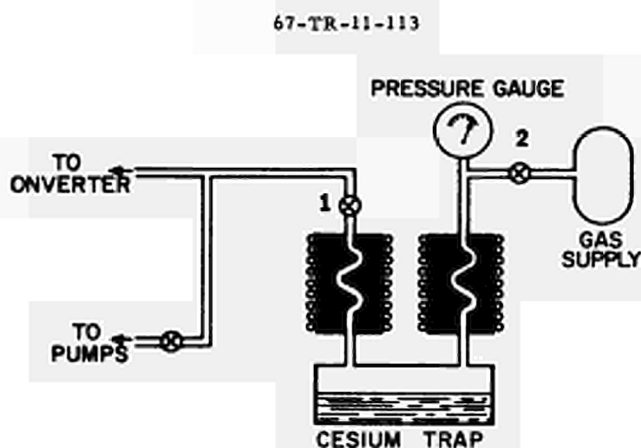


Figure 1. Schematic of Gas Injection System.

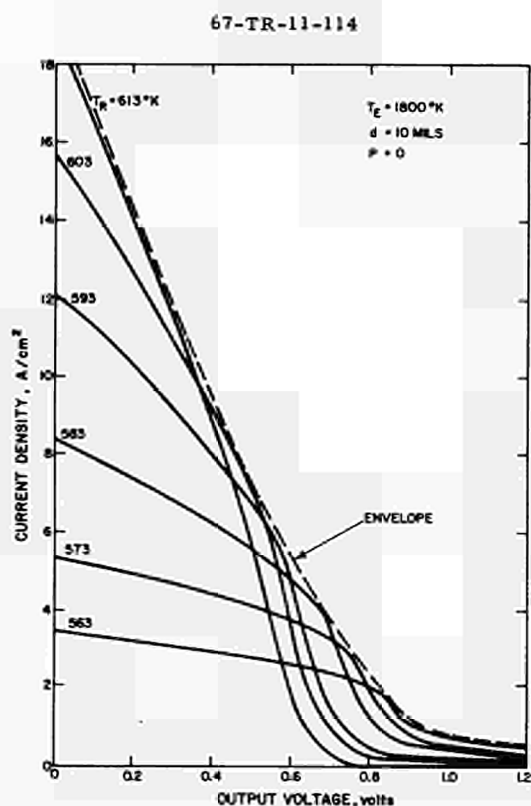


Figure 2. Typical Family of Volt-Ampere Characteristics.

68-TR-2-22

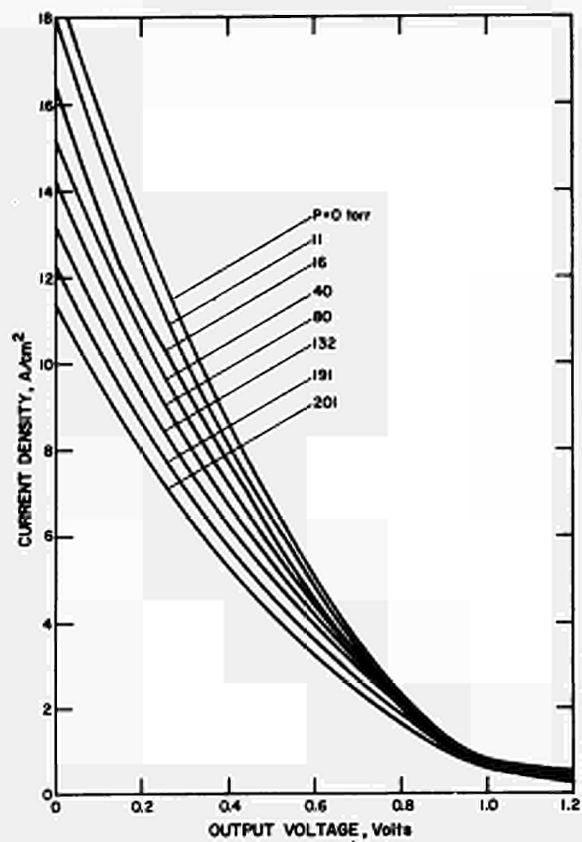


Figure 3. Cesium Optimized Envelopes for Several Pressures of Argon.

68-TR-3-2

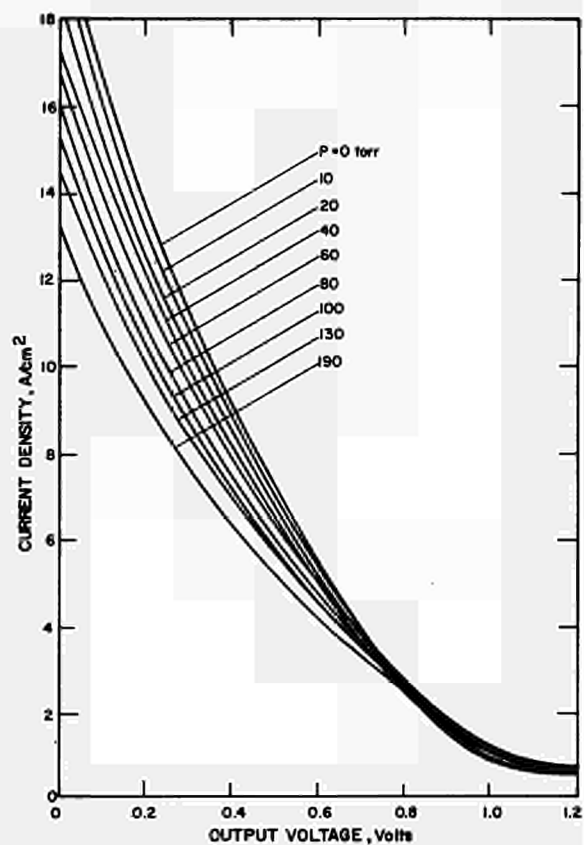


Figure 4. Cesium Optimized Envelopes for Several Pressures of Krypton.

68-TR-3-5

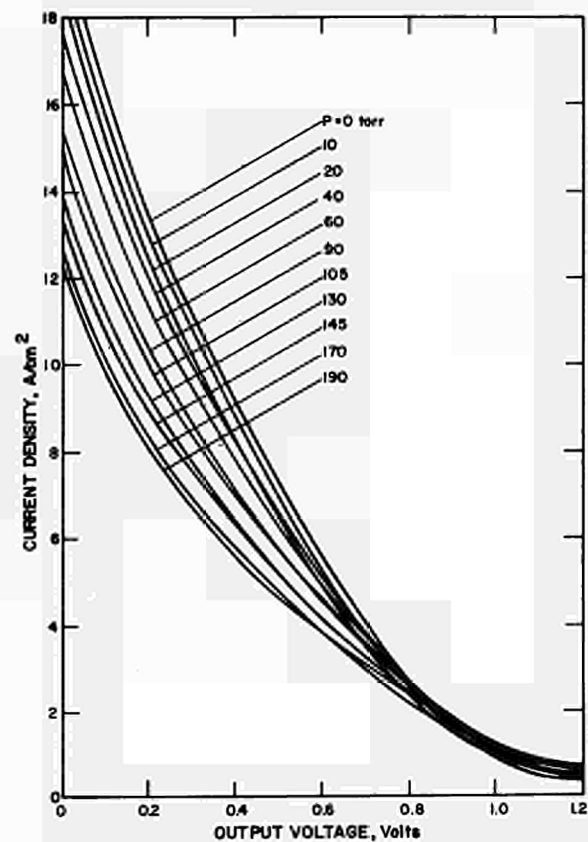


Figure 5. Cesium Optimized Envelopes for Several Pressures of Xenon.

68-TR-3-12

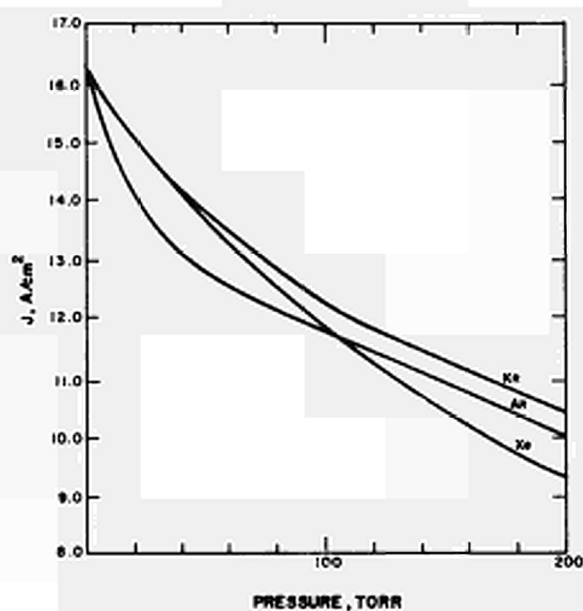


Figure 6. Cross Plot of Figures 3, 4 and 5 at $V = 0.10$ Volt, Showing the Current Attenuation by the Inert Gases.

68-TR-3-13

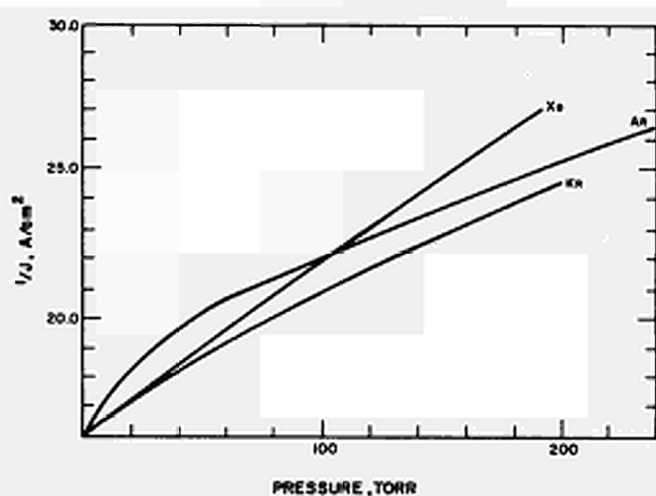


Figure 7. An Alternate Cross Plot of Figures 3, 4 and 5 at $V = 0.10$ Volt.

68-TR-2-25

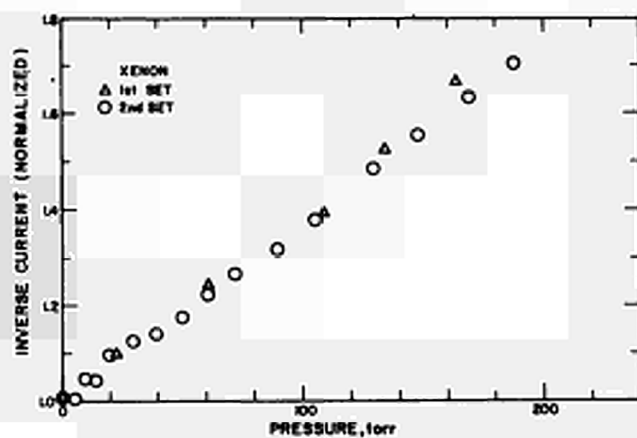


Figure 8. Raw Data Showing the Attenuation of Output Current by Argon.

68-TR-3-8

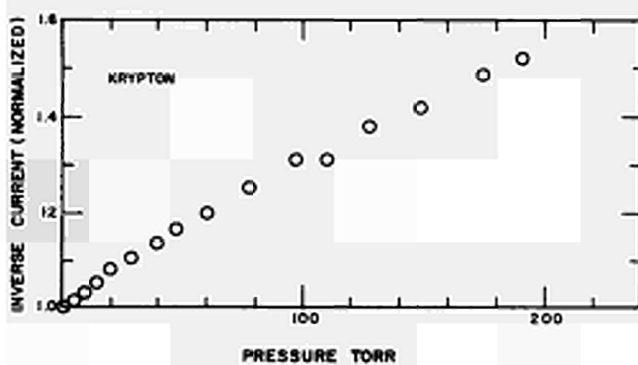


Figure 9. Raw Data Showing the Attenuation of Output Current by Krypton.

68-TR-3-4

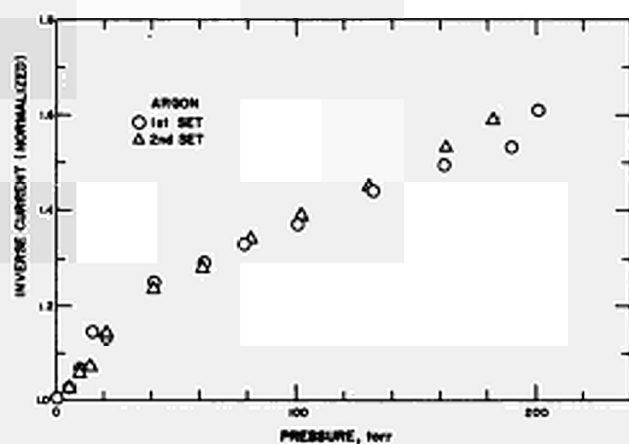


Figure 10. Raw Data Showing the Attenuation of Output Current by Xenon.

PULSE INVESTIGATION ON THERMIONIC CONVERTERS

by

V.Orlinov, T.Doncev and B.Gorancev

Institute of Electronics, Bulgarian Academy of Sciences,
Sofia, Bulgaria

and

G. Musa

Institute of Physics, Academy of the Roumanian Socialist
Republic, Bucharest, Roumania,

Summary. With the help of pulse ionization the decay time for the cesium ions τ_i in thermionic converter is investigated in gas-kinetic mode of operation. A dependence of τ_i on interelectrode potential distribution is established. In ion rich mode of operation τ_i almost does not depend on T_k while in electron rich emission mode of operation τ_i rapidly increase with the decrease of T_k . Qualitative explanation of the obtained results is given.

1. Introduction

Pulsed ionization of the interelectrode space was reported in some papers as a method to improve the performances of the Cs thermionic converters [1], [2], expecting that needed electrical power to sustain the pulsed discharge is much lower than the output power increase of the diode. This expectation is reasonable because the rise-time of the discharge at pulse application is usually shorter for a Cs diode than the ions life-time in the

emitter-collector space. The decay times of the ions were measured and the presence of two kind of Cesium ions (Cs^+ and Cs_2^+), was assumed [2] .

In connections with these results we must note that the investigations were not systematic and complete, containing some contradictions. For example in [1] , a value of the decay time for ions $\tau_i \approx 100 \mu s$ was obtained, not depending on pressure and as pointed in [3] not depending on experimental conditions too. In [2] , two decay times were observed ($\tau_i' \approx 30 \mu s$ and $\tau_i'' \approx 1 \mu s$) and associated these with two kinds of Cesium ions.

In this preliminary report, experimental results are given convincingly illustrating ion decay time dependence on the interelectrode potential distribution of the thermionic converter. The obtained results are useful for the optimization of the pulse ionization method as well as a new possibility to study physics of thermionic diode.

2. Experimental set-up

The experimental glass-metal device is shown in fig.1. It consists of a flat molybdenum cathode (1), heated by electron bombardement (2). The cathode temperature is measured by Ta-W thermocouple (4). A stainless-steel guard ring (5) ensures parallel plane geometry of the cathode-anode system. The anode (6) made of stainless -steel is

provided with a moving system (7) for interelectrode distance changing.

Two additional tungsten wire electrodes (8) are placed in anode-cathode space at 2 mm from the cathode. These electrodes are ceramic insulated except the end of the wires (1 mm)

The schematic diagram of the circuit is given in fig.2. In order to avoid the measurement difficulties encountered in [1] and [2], the pulse discharge circuit as shown in fig.2, is separated from the circuit for the ion decay time measurements.

The typical oscilloscope curves are given in fig.3, where a indicates the shape of the pulse applied between the cathode and the additional electrodes (the pulse distortion is due to the discharge which appears between these electrodes during the pulse), and b the changing of the drop voltage on the load resistance R_L , registered after the pulse.

The positive ions formed during the discharge neutralize the negative space charge and increase the electron current of the converter. The decrease in time of converter current conditionally gives us the life time of the Cesium ions.

3. Experimental results and discussions

The aim of the present experimental investigation was, to establish whether the ion decay time depends on the interelectrode potential distribution of the thermionic converter.

As is known for „gas kinetic" mode of operation of the diode, i.e, electron mean free path λ_e is of the same order of magnitude as interelectrode distance d_{ak} ($\lambda_e \simeq d_{ak}$), is characterized by two possible interelectrode potential distribution as shown in fig.4. In the case of electron rich emission mode of operation (fig.4a) the drop voltage at the cathode limits the emitted electrons. ($\Delta\phi' > 0$), and in the case of ion rich emission mode of operation (Fig.4b) the drop voltage at the cathode accelerates the emitted electrons ($\Delta\phi' < 0$). The potential distribution is shown by solid lines for short circuit and by dashed ones for open circuit.

It is obvious that the potential distribution corresponding to short circuit in electron rich mode of operation (Fig.4a) is a potential t_{gap} for the positive ions. That is why the ion decay time should be longer compared with the ion-rich emission mode of operation where potential distribution permits free ion loss. For the open circuit (Fig.4a) the potential t_{gap} at the anode side disappears and shorter ion decay times must be expected.

In order to prove these assumptions we carried out following investigations. At $T_{Cs} = 423^{\circ}K$ and interelectrode space $d_{ak} = 4mm (\lambda_e \approx 1,3mm)$ i.e, we are in gaskinetic condition ; $(\lambda_e \approx d_{ak})$.

We measured the dependence of the converter current I_a on the cathode temperature T_k at an output voltage $U_a = 0,5V$ in the low temperature maximum range (Fig.5a).

According to the results reported in [4] , the temperature where the curve has a maximum almost correspond to $\Delta\varphi' = 0$, i.e., to the point of transition from the electron-rich emission to the ion-rich emission mode of operation..

By dashed curve on the figure 5a is given the same dependence I_a versus T_k but in the presence of pulsed ionization with a repetition frequency of $f_p = 1 Kc/sec$ pulse width $\tau_p = 10\mu s$ and pulse amplitude $U_p = 8,5 V$.

As should have been expeted, to the left of the maximum (electron rich emission region) the influence of the additional pulse ionization is considerably, while in the right of the maximum (ion rich emission region) this influence is negligible.

The dependence of the decay time for the ions τ_i of T_k was measured in short circuit conditions ($U_a = 0,05V$) at pulse parameters $U_p = 8-8,5V$, $\tau_p = 10-12, \mu s$ and $f_p = 600 c/s$

All calculations of τ_i were made at $1/e$ level of the exponent of the type shown in Fig.3b.

In fig.5b such a dependence is given by a solid line, averaging the results of four series of measurements.

The obtained results are in agreement with the above mentioned considerations on the influence of the interelectrode potential distribution of the converter on the ion life-time. The increase of T_k in the condition of electron rich emission mode of operation leads to a sharp drop of τ_i due to the decrease of the depth of the potential gap and of the ion retarding field at the cathode. This dropping continues till to cathode temperatures close to the maximum of the dependence $I_a(T_k)$, (given in fig.5a), where

$\Delta\varphi'$ becomes equal to 0 and the potential distribution pass from electron rich emission (Fig.4a) into ion rich emission mode of operation (fig.4b). In the case of higher T_k , $\tau_i \approx \text{const} \approx 20-30 \mu\text{s}$, as should have been expected. Indeed, in ion rich emission operation there is no ion potential gap, the ions being lossed by free movement to the cathode, and τ_i should remain constant.

The slight increase of τ_i for higher T_k may be explained by the rapid increase of electron emission and consequently by the transition into the second region of electron rich emission mode of operation.

The computation of τ_i with the assumption that ion kinetic energy is given by thermal energy only at $T_i = 423^\circ\text{K}$ and that the ions are lossed by free movement gives at $d_{ak}=4\text{mm}$, $\tau_i \approx 19 \mu\text{s}$ which is in good agreement with

our experimental values for the τ_i in ion rich emission mode of operation.

4. Conclusion

In the present investigations the dependence of the decay time for the Cesium ions τ_i on the interelectrode potential distribution in thermionic converter has been experimentally established for the first time. Investigations on the dependence of τ_i on the remaining parameters of the converter, and also for the clarification of the question of the presence of two decay times and in how far they actually correspond to two types of Cesium ions - Cs^+ and Cs_2^+ , are in progress.

References

- [1] R.A. Laubenstein, C.Kaplan, S.Schneider and J.Creedon. Advanced Energy Conversion v.3, 351 (1963)
- [2] C.Kaplan, Thermionic Conversion Specialist Conference, Cleveland, Ohio, 326 (1964)
- [3] T.E.Firle, 21st Ann.Conf.Phys.Electron, Mass.Inst. Techn.March (1961)
- [4] I.P.Stakhanov, Yu.K.Gus'kov, V.P.Paschchenko, M.A. Lebedev, Report on The International Conference on Thermionic Electrical Power Generation, London 1965.

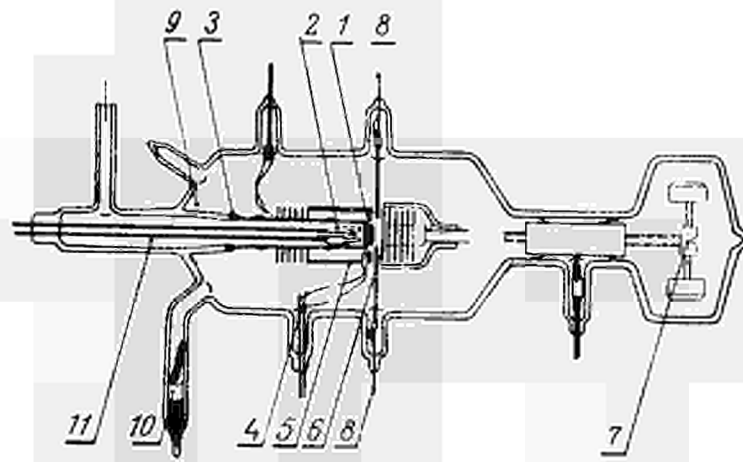


Fig. 1 -

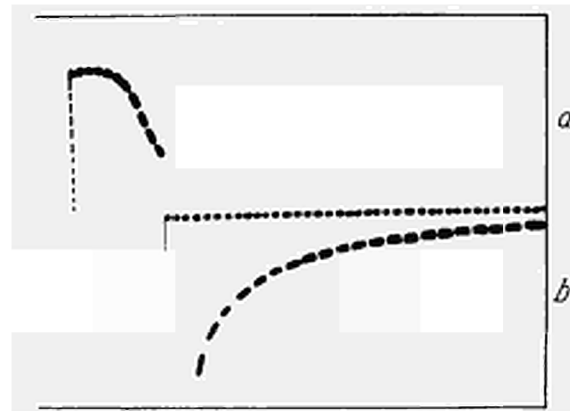


Fig. 3 -

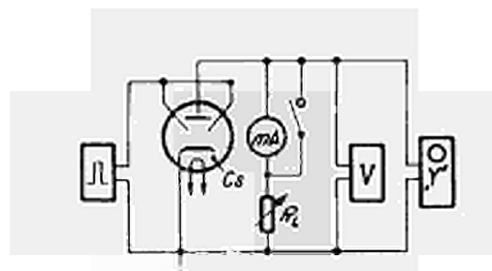


Fig. 2 -

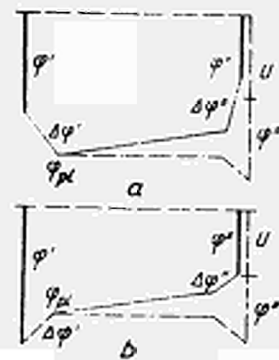


Fig. 4 -

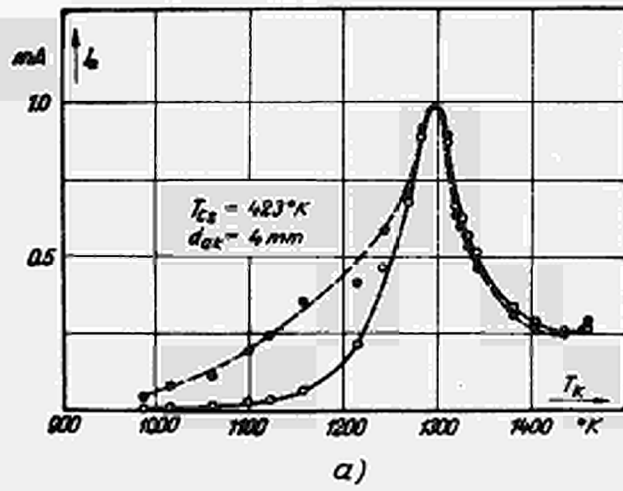


Fig. 5 -

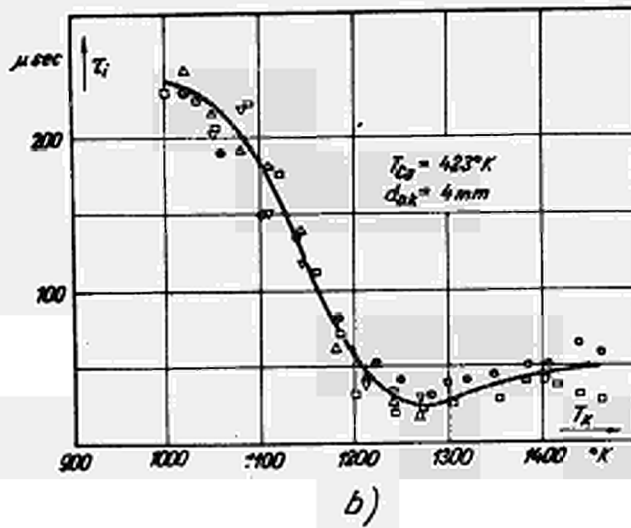


Fig. 6 -

Pre-ignition and Ignition Characteristics of Cesium Thermionic Diodes*

Katsunori Shimada

Jet Propulsion Laboratory, California Institute of Technology

Pasadena, California

ABSTRACT

Pre-ignition volt-ampere curves for thermionic cesium diodes exhibit non-saturation characteristics when the diodes are operated at low temperatures under electron-rich emission conditions. The current through diodes under those conditions increases exponentially, exhibiting two straight lines as asymptotes in semi-log plots of the volt-ampere curves. The slopes of these curves for diode voltages immediately above the knee of the volt-ampere curve (Schottky-like region) were found to be determined by the emitter temperature. For diode voltages larger than those in the Schottky-like region but smaller than the diode breakdown voltage (avalanche region), the current increased at a rate that was an order of magnitude larger than that in the Schottky-like region. The rate of current increase in the avalanche region was determined by the cesium reservoir temperature.

An abrupt ignition follows the avalanche as the applied voltage reaches a certain value—the breakdown voltage—at which the current increases many orders of magnitude above that in the pre-ignition region. We have examined the breakdown voltages for emitter temperatures up to 1900°K and for pressure-distance product $P \cdot D$ between 0.2 and 200 mil-torr. Paschen-type curves were obtained for the breakdown voltage V_B as a function of $P \cdot D$. Breakdown voltages as small as 0.8 volts were observed for $P \cdot D$ values between 20 and 100 mil-torr.

Pre-ignition Volt-Ampere Curves

A SET-type thermionic energy converter was operated at relatively low emitter temperatures T_E (1120°K - 1560°K) and cesium reservoir temperatures T_{Cs} (433°K - 513°K). The diode had basically plane-parallel electrode geometry with an interelectrode distance of 0.028 inch (0.712 mm), and an effective emitter area of 2.67 cm². At a cesium reservoir temperature $T_{Cs} = 463°K$, the electron-neutral mean-free-path was approximately equal to the interelectrode distance; therefore the diode operated in a collisionless regime for $T_{Cs} < 463°K$. Furthermore, the combination of temperatures T_E and T_{Cs} was selected to be such that the emission was either strongly electron-rich or weakly ion-rich. Under these conditions the volt-ampere curve prior to the ignition of the diode exhibited its non-saturation characteristics very clearly. As is shown in Fig. 1, the current increased quite rapidly just before cesium breakdown. From such volt-ampere curves, the normalized current—that is, the ratio of the measured current I to the current I_0 at the knee of a particular volt-ampere curve—was calculated. The normalized current increased exponentially in the manner shown in Figs. 2 and 3 as the diode voltage increased. Two different slopes are evident in Fig. 2: the lower and higher parts of the curve represent the Schottky-like region and the avalanche region of the volt-ampere curve respectively. Curves for a given emitter temperature yielded the same slope in the Schottky-like region for all cesium reservoir temperatures used, whereas the slopes in the avalanche region depended upon the cesium reservoir temperature. Obviously the current in the lower part of the curve was governed by the negative space-charge barrier rather than by the true Schottky barrier. The current I increased exponentially as the applied voltage increased; this finding is somewhat in contradiction to those reported elsewhere.^{1,2}

The normalized current can be related to the applied voltage V by an

empirical expression:

$$I/I_0 = A_1 \exp k_1(V - V_1) + A_2 \exp k_2(V - V_2). \quad (1)$$

The first term is dominant for voltages V less than 1 volt; the second term is dominant for voltages above 2 volts. The constant k_1 was first determined from the asymptotic slope of the lower part of the semi-log volt-ampere curve. Then the asymptote was extrapolated to larger voltages and the current on the asymptote was subtracted from I/I_0 measured at the same voltage. The reduced current thus obtained indeed lay along another straight line on a semi-log plot. From this line, representing the second term in Eq. (1), the constant k_2 was determined. The constant k_1 was found to depend on the emitter temperature T_E but not on the cesium reservoir temperature. An empirical expression for k_1 is

$$k_1 = 0.5 \times 10^{-3} \exp(8.7 \times 10^3/T_E) \text{ per volt}, \quad (2)$$

where T_E is the emitter temperature in degrees K. A theoretical model in which it is assumed that all the electrons and ions that are generated at the emitter surface subsequently drift toward the collector yields a trend for k_1 similar to that given by Eq. (2). Further studies are required to clarify the correlation between k_1 and T_E .

As the applied voltage increased above approximately 1.5 volts, the current increased at a much faster rate than in the Schottky-like region. The constant k_2 that describes this rate was in the range 3.0 to 5.0 per volt. The rate also increased as the cesium reservoir temperature increased. This behavior is attributed to those ions generated near the collector by impact ionization processes. As ions drift back toward the emitter, they will modify the potential minimum in the motive in such a way as to increase the electron flow. The resulting feedback mechanism causes an avalanche and an eventual cesium breakdown.

Ignition Characteristics

As the voltage across the diode reaches a certain value—the breakdown voltage—the diode current increases discontinuously over that in the pre-ignition region. The breakdown voltages were measured for a wide range of cesium pressure and emitter temperature. Moreover, the breakdown voltages were measured in two different diodes, a conventional diode (No. 1) and a non-conventional diode (No. 2) that was equipped with a cavity emitter.³ Diode No. 2 has two interelectrode regions: one between the collector and the bottom of the cavity (an 18-mil gap), the other between the collector and the remainder of the emitter (a 2-mil gap). The breakdown voltage V_B was determined by adding the contact potential between the cesiated tantalum emitter and the molybdenum collector to the measured breakdown voltage. Results are shown in Fig. 4 for diode No. 1, which has a planar geometry with a uniform interelectrode gap of 28 mils. For small values of pressure-distance product $P \cdot D$, the breakdown voltage was nearly equal to the ionization potential of cesium. As $P \cdot D$ increased from 1 to 10 mil-torr, V_B generally increased again except at high emitter temperatures. The minimum of V_B occurred for $P \cdot D \cong 10$ mil-torr. Note that the output voltages of thermionic energy converters are the highest for $P \cdot D$ values between 10 and 20 mil-torr. The breakdown voltages for diode No. 2 are shown in Fig. 5 as a function of the $P \cdot D$ values calculated using an interelectrode distance of 18 mils. In this diode the increase in V_B for $P \cdot D > 10$ mil-torr was negligible. Since this diode has narrow gap regions (2 mil) as well, the breakdown is apt to occur there for larger cesium pressures. The minimum breakdown voltage was approximately 0.8 volt at $T_E = 1900^\circ\text{K}$.

Another representation of the breakdown curves is shown in Fig. 6 in which $\ln(V_B/P \cdot D)$, instead of V_B itself, is plotted as a function of $P \cdot D$.

In this representation, $\ln (V_B/P \cdot D)$ depends linearly on $P \cdot D$ over three decades for diode No. 2, indicating that V_B is proportional to $(P \cdot D)^\alpha$ with α slightly less than minus 1. This type of plot may be useful in determining the interelectrode distance and the parallelism of the electrodes in hardware converters once a standard curve has been obtained.

Conclusion

Pre-ignition volt-ampere curves for a thermionic cesium diode that was operated at low temperatures exhibited Schottky-like and avalanche regions prior to the ignition. The current increased exponentially with the diode voltage at different rates in the two regions. The rate in the Schottky-like region was determined by the emitter temperature, whereas that in the avalanche region was determined by the cesium reservoir temperature.

Cesium breakdown voltages, at which the diode current increased abruptly above that in the avalanche region, were measured as a function of the pressure-distance product. A Paschen-type dependence was evident except that the breakdown voltage lowered as the emitter temperature increased. Results were in agreement with those of Gibbons⁴ for large $P \cdot D$ values.

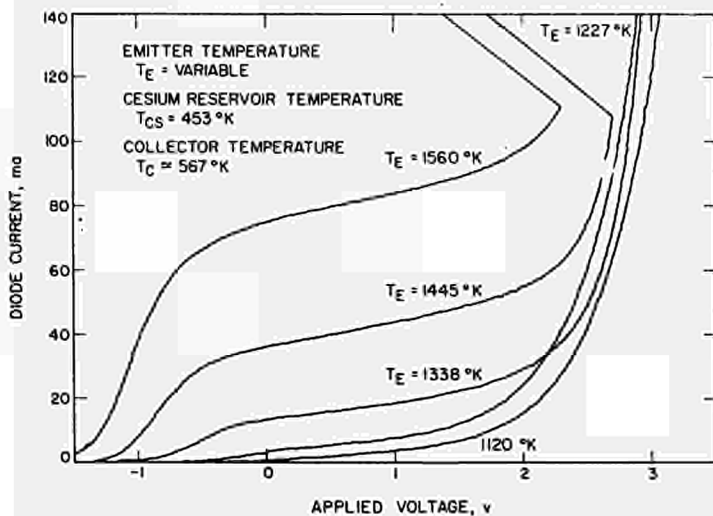


Fig. 1. Typical volt-ampere curves.

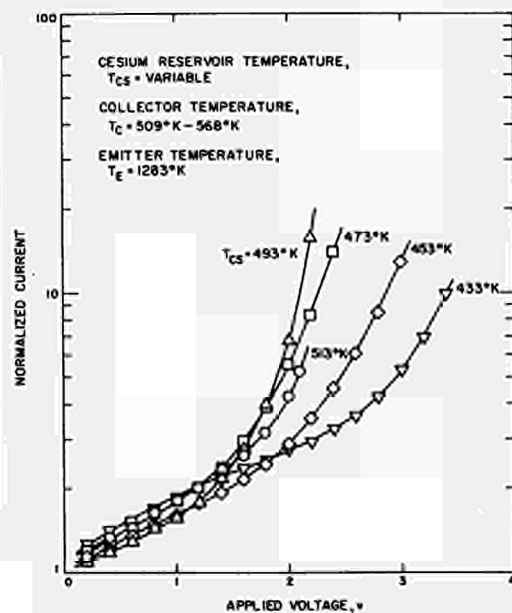


Fig. 2. Normalized current vs applied voltage for $T_E = 1283^\circ\text{K}$.

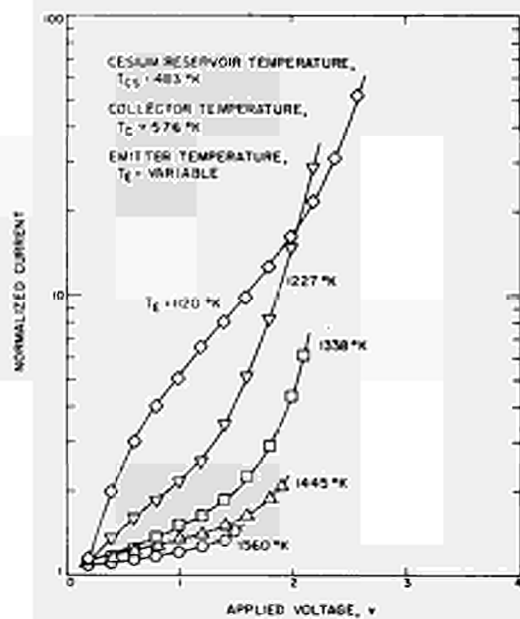


Fig. 3. Normalized current vs applied voltage for $T_{CS} = 483^{\circ}K$.

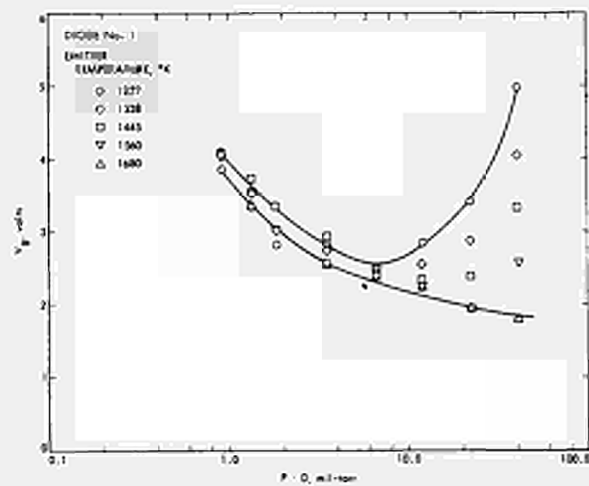


Fig. 4. V_B vs $P \cdot D$ for diode No. 1 with a planar emitter.

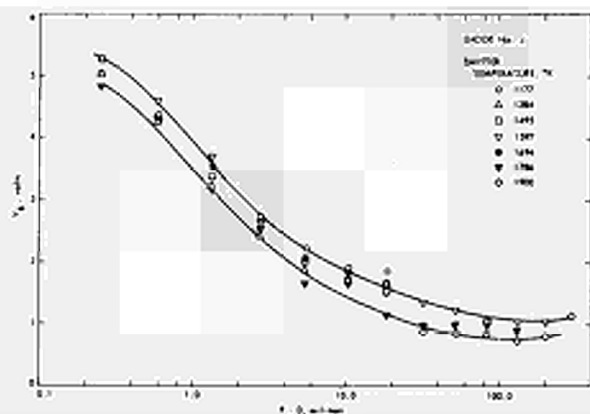


Fig. 5. V_B vs $P \cdot D$ for diode No. 2 with a cavity emitter.

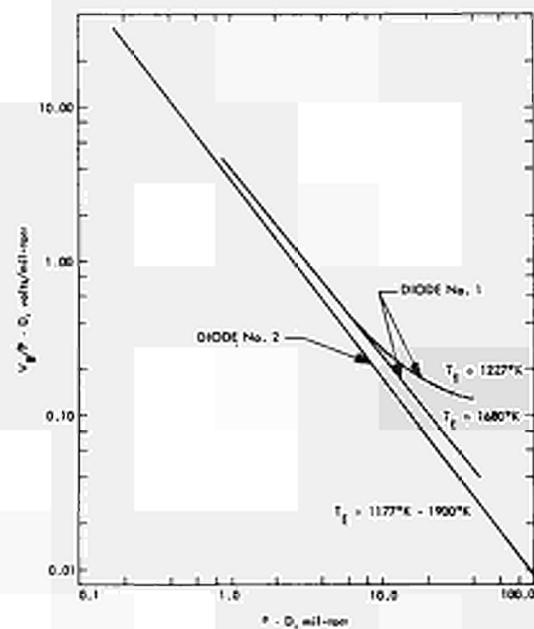


Fig. 6. $\ln(V_B/P \cdot D)$ vs. $P \cdot D$.

References

- * This paper presents the results of one phase of research performed at the Jet Propulsion Laboratory, California Institute of Technology, sponsored by the National Aeronautics and Space Administration under contract NAS 7-100.
- (1) Auer, Peter L., "Potential Distributions in a Low-Pressure Thermionic Converter," J. Appl. Phys. 31, No. 12, 2096-2103 (1960).
 - (2) Warner, C. and Hansen, L. K., "Transport Effects in the Electron-Rich Unignited Mode of Cesium Diodes," J. Appl. Phys. 38, No. 2, 491-500 (1967).
 - (3) Shimada, Katsunori, "Apparent Work Function of Cavity Emitters," 1967 IEEE Conference Record of the Thermionic Conversion Specialist Conference, 29-32 (October/November 1967).
 - (4) Gibbons, M. D., "Experimental Studies of the Emission and Discharge Characteristics of the Ta-Cs System," ADVANCED ENERGY CONVERSION (Pergamon Press, Great Britain, 1962), Vol. 1, pp. 527-543.



THEORETICAL AND EXPERIMENTAL INVESTIGATION OF LOW-VOLTAGE
ARC IN THERMIONIC CONVERTER

F.G.Baksht, G.A.Djuzhev, V.B.Kaplan, I.L.Korobova,
A.M.Martzinovskiy, B.Ya.Moizhes, G.A.Shahnasarova,
V.G.Yuriev.

Semiconductor Institute of the Academy of Sciences of USSR.
Leningrad

Introduction

At present there are considerable data on the experimental [1-3] and theoretical [3-6] research of the low-voltage arc (LVA) in thermionic converter (TC) with caesium vapour. The experimental data, obtained by us, and the theoretical computation carried on enable us to take not only a qualitative, but also a quantitative comparison between the theory and the experiment. Such comparison shows a possibility of the correct physical description of main phenomena in gas - discharge plasma of TC by solving a system of differential equations without using any arbitral parameters.

§1. Basic equations and boundary conditions

Theoretical plasma parameters distribution is found from the solution of transfer equations of electron j_e , ion j_i currents and of electron energy flux Q_e .

$$j_e = -u_e n \left[q \frac{d\varphi}{dx} + \left(\beta - \frac{3}{2} \right) \kappa \frac{dT_e}{dx} \right] - q D_e \frac{dn}{dx}, \quad (1)$$

$$j_i = -u_i n \left[q \frac{d\varphi}{dx} - \frac{1}{2} \kappa \frac{dT_i}{dx} \right] + q D_i \frac{dn}{dx}, \quad (2)$$

$$Q_e = j_e \left(\beta \frac{\kappa T_e}{q} + \varphi \right) - \alpha D_e n \kappa \frac{dT_e}{dx} \quad (3)$$

$n, q\varphi, T_e$ are the parameters to be found - electron concentration, potential energy and electron temperature; u is a mobility, $D = \frac{\kappa T}{q} u$ is a diffusion coefficient of charged particles. The constants α and β in (1) and (3) depend on the type of electron scattering: $\alpha_{ea} = \beta_{ea} = 2$ (electron - atom scattering); $\alpha_{ei} = 1,6, \beta_{ei} = 3,2$ (electron - ion scattering [7]). In the intermediate case we used the interpolation formulas

$$\alpha = \frac{\alpha_{ea} u_{ea}^{-1} + \alpha_{ei} u_{ei}^{-1}}{u_{ea}^{-1} + u_{ei}^{-1}} \quad \beta = \frac{\beta_{ea} u_{ea}^{-1} + \beta_{ei} u_{ei}^{-1}}{u_{ea}^{-1} + u_{ei}^{-1}}$$

where

$$u_{ea} = \frac{q}{3\kappa T_e} l_{ea} \bar{v}_e \quad u_{ei} = \frac{1,47 (\kappa T_e)^{3/2}}{\sqrt{2\pi} n \sqrt{m_e} \lambda q^3}$$

(l_{ea} - the electron atom mean free path, λ - Coulomb logarithm [8]). Equations (2) and (3) are supplemented with the continuity equations for fluxes of particles and energy

$$\frac{dj_i}{dx} = - \frac{dJ_e}{dx} = - q \Gamma(x), \quad (4)$$

$$\frac{dQ_e}{dx} = [q\varphi(x) - E_i] \cdot \Gamma(x), \quad (5)$$

where E_i is the ionization energy, $-q\varphi$ is the potential energy of generated ion and $\Gamma(x)$ is the ionization rate - the number of ionization acts in unit of volume per unit of time. In working conditions of TC the gap voltage drop is less than ionization potential. Therefore the change of electron current is relatively small, and we shall neglect it, considering the left part of (1) as a constant. At the same approach we must neglect the term $-q\varphi(x)$ in brackets in (5).

The boundary conditions for equations (1-5) bind the fluxes of particles and energy, carried over the near electrode potential barrier, with values n, T_e and φ at the plasma - electrodes boundaries.

$$j_e = j_{es}^{(c)} - \frac{1}{4} q n_e \bar{v}_e \exp\left(-\frac{q\varphi_c}{\kappa T_{ee}}\right), \quad (6)$$

$$j_{ic} = \frac{1}{4} q n_e \bar{v}_i - j_{is} \exp\left(-\frac{q\varphi_c}{\kappa T_e}\right), \quad (7)$$

$$Q_{ec} = \frac{j_{es}}{q} 2\kappa T_c - \frac{1}{4} n_c \bar{v}_e \exp\left(-\frac{\varphi_c}{\kappa T_{ec}}\right) \cdot 2\kappa T_{ec}, \quad (8)$$

$$j_e = \frac{1}{4} q n_e \bar{v}_e \exp\left(-\frac{q\varphi_a}{\kappa T_{ea}}\right) - j_{es}^{(a)}, \quad (9)$$

$$j_{ia} = -\frac{1}{4} q n_a \bar{v}_i, \quad (10)$$

$$Q_{ea} = \frac{1}{4} q n_a \bar{v}_e \exp\left(-\frac{q\varphi_a}{\kappa T_{ea}}\right) \left[\frac{2\kappa T_{ea}}{q} - \varphi_0\right] - j_{es}^{(a)} \left[\frac{2\kappa T_a}{q} - \varphi_0\right] \quad (11)$$

where $j_{es}^{(c)}$ and j_{is} are the currents of electron and ion emission from cathode, $j_{es}^{(a)}$ is the electron emission current from anode, T_c is the cathode temperature, φ_c and φ_a are the cathode and anode potential barriers, φ_0 is the voltage drop across the gap. Indexes c and a label the plasma parameters near cathode and near anode respectively. The boundary conditions for j_e and Q_e are written for Maxwellian distribution function of electrons, leaving the plasma, because in the ordinary discharge conditions the deviation of electron distribution function from Maxwellian one is usually not essential, owing to sufficiently large concentration of free electrons. [9] This problem is considered in detail in [10]. The distribution function and the drift velocity of ions in the near - electrode layer require a special consideration [11]. However the change of the ion velocity at the plasma - electrode boundary leads only to the redistribution of the voltage between the volume of plasma and the near - electrode layer of the thickness of about the mean free path of ion. In this paper we assume the drift velocity of ion at the boundary to be equal

$$v_{d2} = \frac{1}{4} \bar{v}_i = \frac{1}{4} \left(\frac{8\kappa T_i}{\pi m_i}\right)^{1/2}$$

§2. The ionization rate in gas discharge caesium plasma

The theoretical consideration [10] and probe measurements show [11], that in ordinary LVA discharge in TC the maxwellization length of electrons (including fast electrons with en-

ergy about the threshold of Cs atom excitation to the first level) is usually small in comparison with the gap. Therefore the energy distribution of free electrons may be assumed to be Maxwellian one. The Cs ionization rate for Maxwellian electron distribution was computed in [12,13]:

$$\Gamma = n \bar{v}_e \zeta_0(T_e) n_a \left[1 - \frac{n^2}{n^2(T_e)} \right], \quad (*) \quad (12)$$

where n_a is a concentration of Cs atoms, $n(T_e)$ is the equilibrium Saha concentration of free electrons at temperature T_e and $\zeta_0(T_e)$ is the effective ionization cross-section, depending on the electron temperature T_e .

The values of ion current $j_i(x)$ and ionization rate $\Gamma(x)$ may be calculated from the probe and optical measurements. The results of measurements in the near-cathode layer, where the ionization essentially prevails over recombination, were used for the experimental determination of $\zeta_0(T_e)$. At Fig. 1 the experimental values of effective ionization time

$\tau_0 = [\bar{v}_e \zeta_0(T_e) n_a]^{-1}$ are depicted by points. At the same figure the calculated curves, obtained with different excitation cross-sections, are shown: curve 1 is obtained with cross-sections in Bethe-Born approximation [13], curve 2 is obtained with Thomson cross-sections [12]. It is evident, that satisfactory agreement exists between the theoretical and experimental results. In our calculations we used the expression, obtained in [13].

§3. The voltage - current characteristics of the thermionic converter and general features of low-voltage gas discharge [16].

The numerical integration of the differential equations

(*) In the case of large values of ψ_c and $j_{eS}^{(c)}$, when the intensive electron beam is injected into plasma, the nonequilibrium ionization may be essential in addition to above mentioned so called equilibrium ionization.

The beam ionization is considered in [10].

(1-5) was carried out by the electronic computer. The equations were solved about the derivatives and then were integrated with some arbitrary values of any two parameters (e.g. ψ_c and n_c). On the other end of plasma the corresponding discrepancies in the boundary conditions were obtained. These discrepancies were reduced to zero according Newton's method by changing ψ_c and n_c .

At Fig.2 the typical v-c characteristics are shown. The form of characteristics and their changes with change of cathode temperature T_c , cathode work function χ_c and interelectrode distance d are in a good agreement with the experimental data [14]. E.g. it is seen from Fig.2, that the nonstable part of v-c characteristics decreases and vanishes, if T_c increases. As the computation shows, such manner of changing of the v-c characteristics is connected with the fact, that, at low cathode temperature, it is necessary to have sufficient volume voltage drop in plasma to receive the high electron temperature. Therefore the arc is ignited near anode - in the region of the highest electron temperature.^(xx)

The arc ignition leads to concentration increase and to forming the potential maximum at the place of the most intensive ionization. The potential difference on the plasma volume increases and this leads to the further increase of electron temperature.

Owing to the rapid (exponential) rise of ionization with increase of T_c , plasma passes into the nonequilibrium state, in which the volume ionization is not balanced by ion fluxes to the plasma boundaries. The potential difference must decrease for the electron temperature stabilisation, and from solution of the system of equations one receives the unstable part of the v-c characteristics, where the ionization moves to the near - cathode plasma region and concentrates near

(xx) Before the arc ignition, in diffusion mode of operation [15], only the limited potential difference may be applied to the plasma volume. Therefore, when the cathode temperature T_c is sufficiently low, the plasma electron temperature T_e may be insufficient to arc ignition. Then the arc is ignited by ionization on the near + anode potential barrier.

electrode(~~xxx~~), while in the other plasma volume the ionization is balanced by recombination, which usually regulates the dimension of ionization layer near cathode.

At high cathode temperature and accelerating near - cathode barrier, there is a sufficiently high electron temperature already in the diffusion mode of operation, and diffusion mode of operation passes continuously into the discharge one.

At the stable part of the discharge characteristics nearly the whole increase of the external voltage falls on the near - cathode barrier. However the electron temperature T_e in the discharge increases comparatively little owing to the large ionization energy losses. T_e is also affected by the resonance radiation, carrying out from plasma. In ordinary discharge conditions the radiation energy losses are usually small in comparison with ionization losses. However near the minimum discharge current the radiation, carrying out from plasma, may be essential for energy balance. The comparison between computed and experimental characteristics requires to take into account Shottky effect on cathode. In intensive discharge the spatial ion charge prevails in Langmuir layer near cathode. Therefore the electric field strength on cathode may be evaluated by the 3/2 law for ion current from plasma to the cathode: $E_c^2 = 16 \pi j_{ic} \varphi_c^{1/2} \left(\frac{29}{m_i}\right)^{1/2}$ At Fig.2 (curve 2') the V-C characteristic, computed with Shottky effect, is given. It is seen, that even normal Shottky effect leads to the marked change of v-c characteristics form. However anomalous Shottky effect is essential for the full comparison between characteristics. Therefore the theory will be compared with the experiment mainly at the constant values of j_e . In this case lack of the full emissive cathode characteristics does not prevent the experimental verification of the theory.

(~~xxx~~) As probe and spectral measurements show, near the point of discharge extinguishing the contraction of discharge occurs, the concentration, current density and other parameters being constant.

§4. Comparison of calculated and experimental data
on the plasma parameters distribution

At Fig.3 the calculated and experimental data on n , φ and T_e distributions are depicted for points of V-C characteristic, given at Fig.2. Though the cathode emission current was considered to be constant in the calculation, the agreement (not only qualitative, but ^{also} quantitative (for n and φ)) between the theory and the experiment is received.

The comparison between the calculated and experimental plasma parameters was carried out at the different gaps d at constant current j_e . At Fig.4 the experimental probe results for n , φ and j_i distributions are shown. The same concentration distribution is also carried out from the spectral measurements. It is seen, that, when gap increases, the concentration maximum increases also and slightly moves aside the cathode, the concentration falling down nearly linearly behind maximum. At Fig.5 the calculation results are shown for different gaps at the constant current j_e . The general character of calculated parameters distribution agrees well with the experiment. At Fig.5 the calculated values of the ionization rate $\Gamma_i = n\bar{v}_e \sigma_i(T_e) n_e$ and recombination rate $\Gamma_r = n\bar{v}_e \sigma_r(T_e) n_a \frac{n^2}{n^2(T_e)}$ are given separately ($\Gamma = \Gamma_i - \Gamma_r$) for two gaps 0,4 mm and 0,8 mm. At the same figure the electron concentration to its equilibrium value $n(T_e)$ ratio is given. When gap increases and concentration rises, j_i stops to change noticeably still in that region, where the electron temperature is high. The ion current constancy in the central part of the gap is connected not with the ionization lack, but with recombination.

It is interesting to investigate the mode of operation with a considerable electron emission from anode. The main experimental fact is that the plasma parameters distribution in the gap remains practically unchanged (Fig.6), when the anode temperature T_a and electron emission current from anode $j_{es}^{(a)}$ change in the large diapason. The results of theoretical calculation leads to the same conclusion: when $j_{es}^{(a)}$ increases, the anode barrier decreases and then changes the sign, the

parameters distribution in the volume of plasma being nearly unchanged. (Fig.7). This result is partly connected with relatively low value of plasma electron temperature near anode. Therefore the appearance of "cold" anode electrons in the near-anode region perturbs plasma comparatively little. As the computation shows, in these conditions two different values of anode emission $j_{es}^{(a)}$ and near - anode potential barrier φ_a may correspond to the same plasma parameters distribution.

Conclusion

As the experiment and the theory show, plasma in thermionic converter is essentially inhomogeneous. Rather peculiar plasma parameters distribution in TC is connected mainly with the conditions of the best ions moving away from plasma to the electrodes. Therefore in the near- cathode region, where the main ionization takes place, the field component of electron current prevails. In the near - anode region electron current flows mainly owing to the diffusion in retarding electric field.

The presence of ionization maximum in the near-cathode region leads to the electron temperature maximum occurrence at the same place, that is observed in the experiment. The computation shows, that it is impossible to apply the considerable electron accelerating field to the plasma volume, because it would increase the electron temperature and would move the ionization maximum deep into plasma. When TC current increases, the near - cathode potential barrier and electrons heating increase. Therefore the electron temperature increases also, though the increasing is slow. In consequence of this, plasma behind the ionization region approaches to the state of the local ionization equilibrium, in which the concentration is connected to electron temperature by Saha formula. In this regime the length of ionization equilibrium establishment must be small in comparison with the gap. To maintain such mode of operation, the temperature must be high enough ($T_e \geq (2700-2800)^\circ K$). This conclusion agrees well with the experimental results.

Thus plasma in TC is different from homogeneous plasma, in which the current flows under the influence of electric field, and heat is transmitted from electrons to atoms, radiates and so on.

Therefore plasma in narrow gap is fairly peculiar object, which has an independent physical interest.

Literature

1. Г.А.Дожев, А.М.Марциновский, Б.Я.Мойжес, Г.Е.Пикус, Б.И.Циркель, В.Г.Юрьев. ЖТФ 36 (1966) 679
Г.А.Дожев, А.М.Марциновский, Б.Я.Мойжес, Г.Е.Пикус, В.Г.Юрьев ЖТФ. 36 (1966) 692
Г.А.Дожев, Ф.Г.Бакшт, А.М.Марциновский, Б.Я.Мойжес, Г.Е.Пикус, В.Г.Юрьев. ЖТФ 36 (1966) 1685
2. В.Б.Каплан, Б.Я.Мойжес, Г.Е.Пикус, Г.А.Шахназарова, Г.В.Юрьев ЖТФ 36 (1966) 1901
3. Г.А.Дожев, А.М.Марциновский, Г.Е.Пикус, Э.Б.Сонин, В.Г.Юрьев. ЖТФ 37 (1967) 1825
4. Б.Я.Мойжес, Ф.Г.Бакшт, М.Г.Меликия. ЖТФ 35 (1965) 1621
5. В.Ya. Moizhes and F.G.Baksht. Proc. 7th. Int. Conf. Phenomena in Ionized Gases (Beograd. 1965). p.557.
6. R.H.Bullis, J.M.Houston, M.F.Koskinen, N.S.Rasor. Journ. Appl. Phys. 38 (1967) 3425
7. L.Spitzer, Jr.R.Harm. Phys.Rev. 89 (1953) 977
8. C.Longmire "Elementary Plasma Physics". Willey, New York. 1963
9. Ф.Г.Бакшт, Б.Я.Мойжес, В.А.Немчинский. ЖТФ 37 (1967) 729
10. F.G.Baksht, В.Ya.Moizhes, V.A.Nemchinskiy. "Electron Energy Distribution Function in the Near - Electrode Layer of Slightly Ionized Plasma and the Rate of Nonequilibrium Ionization in Thermionic Converter" (report on Conf).

11. F.G.Baksht, B.Ya.Moizhes, V.A.Nemchinskiy "On the Plasma Sheath Theory" (report on Conf.).
12. Э.Б.Сонин. ЖТФ 37 (1967) 1840
13. F.G.Baksht, B.Ya.Moizhes, V.A.Nemchinskiy. Contributed Papers. 8th Int. Conf. Phenomena in Ionized Gases (Vienna 1967) p.284.
14. Г.А.Дожев, А.М.Марциновский, Г.Е.Пикус, Б.И.Циркель, В.Г.Юрьев. ЖТФ 35 (1965) 2054
15. Б.Я.Мойжес, Г.Е.Пикус. ФТТ 2 (1960) 756
16. Г.А.Дожев, А.М.Марциновский, В.Б.Каплан, Б.Я.Мойжес, Г.Е.Пикус, Г.А.Шахназарова, В.Г.Юрьев. "Зондовые и спектральные исследования плотной плазмы ТЭП" Доклад на настоящей конференции.

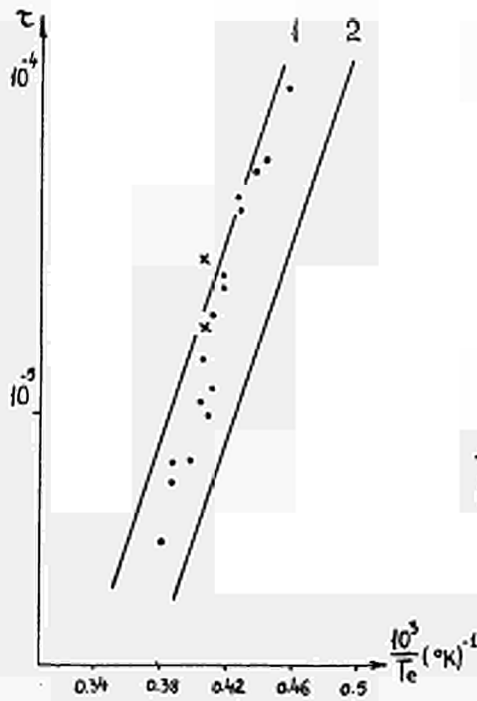


Fig. 1

Temperature dependence of the ionization time.

• - probe measurements,
 x - spectral measurements.

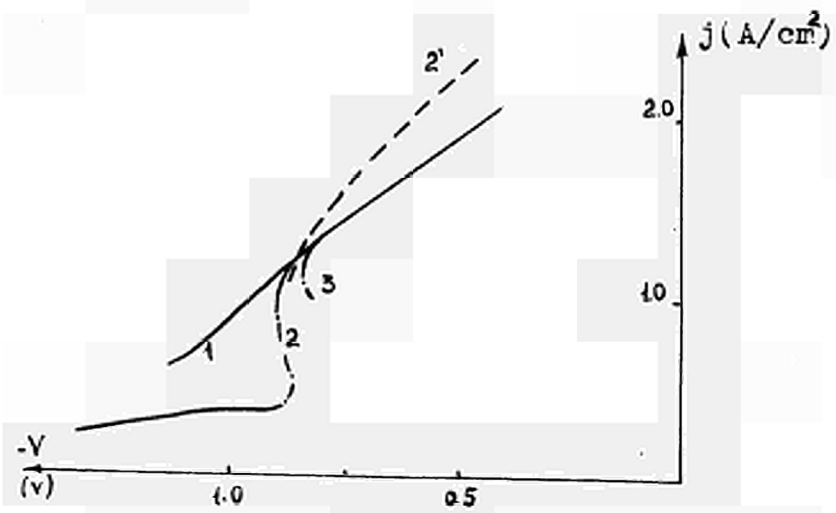


Fig. 2

Calculated voltage-current characteristics $P_{cs} = 2,0$ torr, $d = 0,6$ mm, emission current $2,4$ A/cm².

curve 1 - $T_f = 2260^\circ\text{K}$ } without
 2 - $T_f = 1830^\circ\text{K}$ } Shottky
 3 - $T_f = 1500^\circ\text{K}$ } effect

curve 2' - $T_f = 1830^\circ\text{K}$ - with Shottky effect.

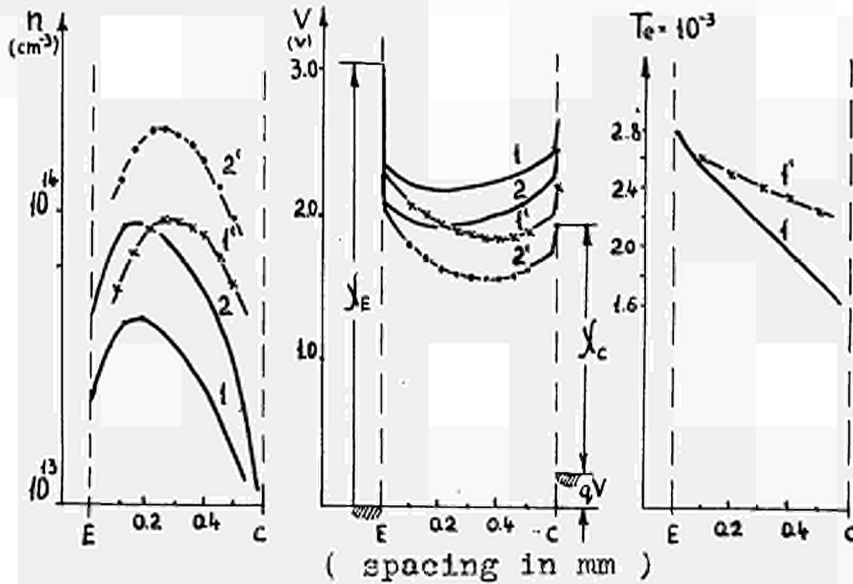


Fig. 3

The Comparison of experimental and calculated plasma parameters.

$P_{cs} = 2,0$ torr, $T_f = 1830^\circ\text{K}$.

curve 1 - calculated } $j = 1,18$ A/cm²
 1' - experimental }
 curve 2 - calculated } $j = 1,49$ A/cm²
 2' - experimental }

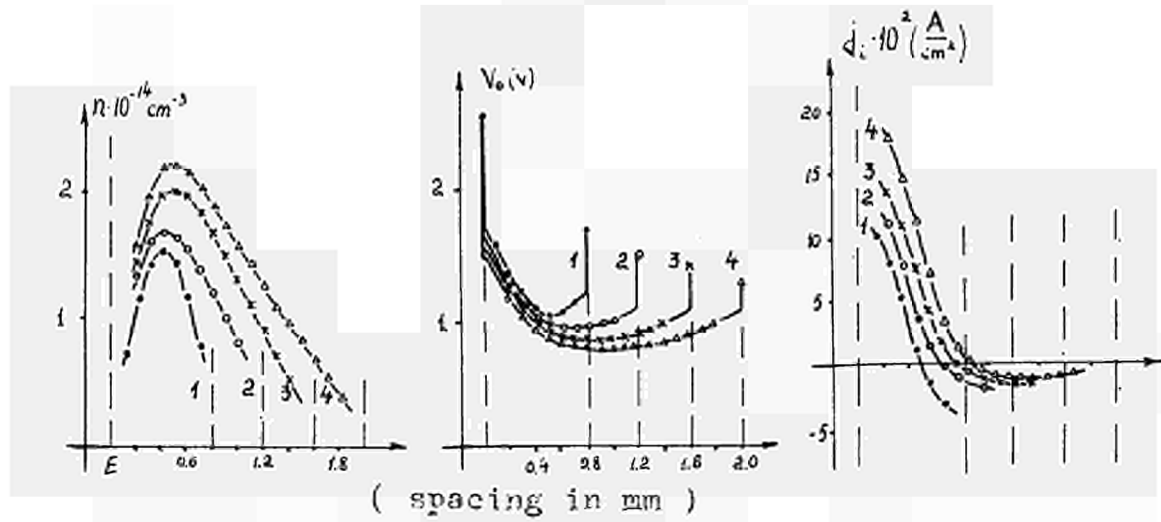


Fig.4

The dependence of plasma parameters on interelectrode gap.

$T_e = 1680^\circ\text{K}$, $P_{cs} = 1,0 \text{ torr}$, $j = 1,7 \text{ A/cm}^2$.

Curves: 1-0,8mm, 2-1,2 mm, 3-1,6 mm, 4-2,0 mm.

(n -concentration, V_0 -potential, j_i -ion current)

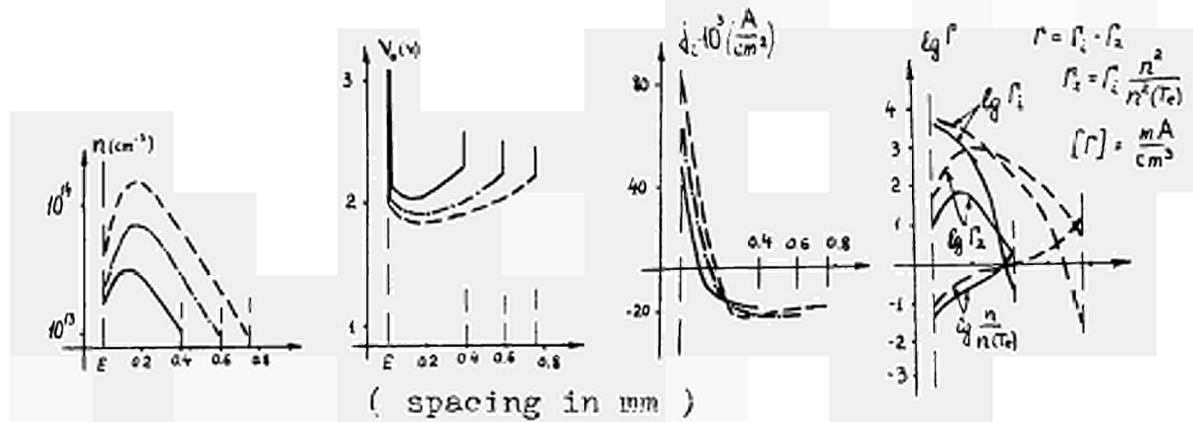


Fig.5

Calculated plasma parameters as a function of the interelectrode spacing. $P_{cs} = 2,0 \text{ torr}$, $T_e = 1830^\circ\text{K}$, $j = 1,49 \text{ A/cm}$.

r_1 - rate of ionization, r_2 - rate of recombination
 $n(T_e)$ - equilibrium (Saha) concentration of electrons.

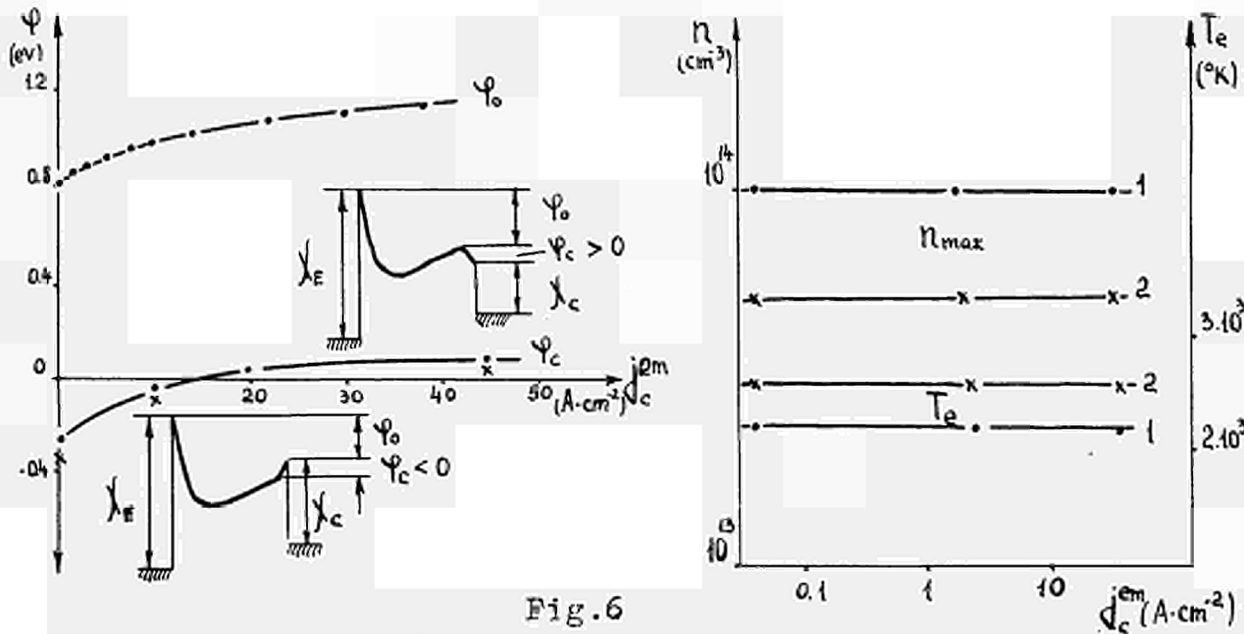


Fig. 6

The dependence of plasma parameters on the collector emission current near the maximum of electron concentration.

$P_{c3} = 1$ torr, $T_f = 1240^\circ\text{K}$, $d = 1,5$ mm.

• - probe measurements, * - spectral measurements.

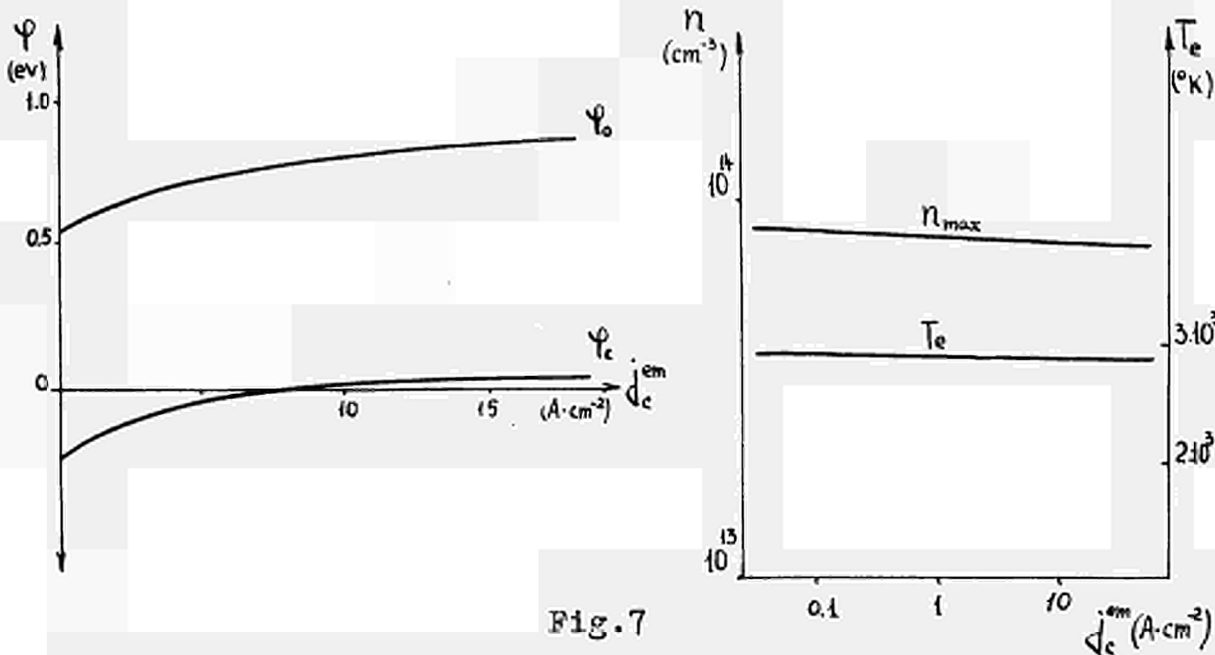


Fig. 7

The calculated plasma parameters distributions at the various collector emission currents near the maximum of electron concentration.

$P_{c3} = 2$ torr, $T_f = 1830^\circ\text{K}$, $d = 0,6$ mm.

THE ELECTRON ENERGY DISTRIBUTION FUNCTION
AND THE RATE OF NONEQUILIBRIUM IONIZATION IN THE
NEAR-CATHODE LAYER OF THE THERMIONIC CONVERTER

F.G.Baksht, B.Ya.Moizhes, Y.A.Nemchinskiy

Semiconductor Institute of the Academy of Sciences of USSR.
Leningrad

When considering the phenomena in the thermionic converter (TC), one must often calculate the electron energy distribution function (DF) near the electrode, negatively biased with respect to plasma. This problem is essential for calculation of the electron beam produced ionization near the cathode, the reverse electron current from plasma to electrode etc., as well as for potential and temperature evaluation from the results of probe investigations.

Introduction

In low-voltage arc in TC the Debye length is always small with respect to the mean free path l_{ea} of electron, colliding with C_0 neutral atoms, and one may consider the near electrode potential barrier as rectangular one (Fig.1), when calculating the electron DF in plasma.

The degree of ionization in plasma is small [1], and the randomization of the electron DF, which is due to the electron-atom collisions, occurs before the interelectron collisions and the collective effects in plasma will change the energy spectrum of electrons. Therefore one may consider the electron motion as diffusion. The electron concentration in the beam, injected to (or extracted from) plasma, is usually small compared with concentration of thermal plasma electrons. Therefore one can neglect the interaction between the fast electrons and consider the collisions between the fast and

thermal electrons only. Owing to the quick randomization, the DF is stable, and one may consider the interelectron interaction as pair collisions, i.e. as diffusion in energy space (in Fokker-Plank approximation).

§1. The fundamental equation and the boundary conditions

Thus one may consider the electron motion as two-dimensional diffusion (in coordinate and energy spaces) and write the kinetic equation as differential one. [2]

$$\frac{\partial^2 n(E, z)}{\partial z^2} + \frac{E_0}{L_0^2} \left[\kappa T \frac{\partial^2 n(E, z)}{\partial E^2} + \frac{\partial n(E, z)}{\partial E} \right] = 0, \quad (1)$$

where $L_0 = (DT_0)^{1/2}$ - the energy relaxation length. $D = \frac{1}{3} l_{ea} \left(\frac{2E_0}{m} \right)^{1/2}$ - the diffusion coefficient of fast electrons, E_0 - near electrode potential barrier ($E_0 \gg kT$).

$$\tau_0 = \frac{m^{1/2} E_0^{3/2}}{2^{3/2} \pi q^4 n_0 \lambda} \quad (2)$$

the energy relaxation time due to the interelectron collisions [2]. n_0 - the concentration of the thermal electrons. λ - Coulomb logarithm, q and m - the electron charge and mass.

The boundary conditions near the electrode ($z=0$) are

$$-D \left. \frac{\partial n(E, z)}{\partial z} \right|_{z=0} = \frac{J_{es}}{q} \frac{E-E_0}{(\kappa T_E)^2} e^{-\frac{E-E_0}{\kappa T_E}} - \frac{E-E_0}{4E_0} \left(\frac{2E_0}{m} \right)^{1/2} n(E, 0), \quad (E > E_0) \quad (3)$$

$$\left. \frac{\partial n(E, z)}{\partial z} \right|_{z=0} = 0, \quad (E < E_0) \quad (4)$$

where J_{es} - electron emission current from cathode, T_E - cathode temperature. (3) is the balance of currents over the potential barrier, electron DF being symmetric near the boundary, that is true, when solid angle for the electrons, emitted from plasma to cathode, is small compared with 4π : $\frac{E-E_0}{4E_0} \ll 1$. (4) signifies, that the current is zero, when $E < E_0$. If $z \rightarrow \infty$,

$$n(E, z) \rightarrow n_M(E) = \frac{2E_0^{1/2}}{\pi^{1/2}(\kappa T)^{3/2}} \cdot n_0 e^{-\frac{E}{\kappa T}} \quad (5)$$

where $n_M(E)$ is Maxwellian DF, n_0 and T are the concentration and temperature of the plasma electrons in the near-electrode layer.

The solution of the equation (1) may be written in the form

$$n(E, z) = n_1(E, z) + n_M(E) - n_2(E, z) \quad (6)$$

where the nonequilibrium additions $n_1(E, z)$ and $n_2(E, z)$ are the solutions of equation (1) with boundary conditions:

$$-D \frac{\partial n_1(E, z)}{\partial z} \Big|_{z=0} = \frac{j_{es}}{q} \cdot \frac{E-E_0}{(\kappa T)^2} \cdot e^{-\frac{E-E_0}{\kappa T}} - \frac{E-E_0}{4E_0} \left(\frac{2E_0}{m}\right)^{1/2} n_1(E, 0), \quad (E > E_0) \quad (3a)$$

$$-D \frac{\partial n_2(E, z)}{\partial z} \Big|_{z=0} = \frac{E-E_0}{4E_0} \left(\frac{2E_0}{m}\right)^{1/2} n_M(E) - \frac{E-E_0}{4E_0} \left(\frac{2E_0}{m}\right)^{1/2} n_2(E, 0), \quad (E > E_0) \quad (3b)$$

$$\frac{\partial n_{1,2}(E, z)}{\partial z} \Big|_{z=0} = 0, \quad (E < E_0) \quad (7)$$

$$n_{1,2}(E, z) \rightarrow 0 \quad (z \rightarrow \infty) \quad (8)$$

$n_1(E, z)$ - is the DF of the electrons of beam, injected into plasma; $n(E) - n_2(E, z)$ - is the DF of the electrons near the non-emitting electrode, the negative term $-n_2(E, z)$ corresponding the deviation of DF from Maxwellian one due to the electron emission from plasma to electrode [2]. The total DF is the sum of these two solutions. The electric field is omitted in equation (1), because the potential drop in neutral plasma near Langmuir sheath $\sim \kappa T/q$ [3] and affects little the motion of fast electrons.

§2. Electron distribution function and electron current on the plasma-electrode contact

One usually writes the electron current over the potential barrier (Fig.1) in the form

$$j_e = j_{es} - \frac{1}{4} q n_0 \left(\frac{8kT}{\pi m} \right)^{1/2} e^{-\frac{E_0}{kT}} \quad (9)$$

This formula is valid, if the two conditions are satisfied: electron loose energy before they return from plasma to electrode after collisions with neutral atoms; the DF of plasma electrons near the barrier is Maxwellian one.

These conditions may be actually not satisfied. E.g. let n_f be a concentration of injected fast electrons with energy $E > E_0$ at the boundary $z=0$. Their energy dispersion $\Delta E = E - E_0 \approx kT_e$, and they must loose this energy ΔE to be "captured" by plasma. Their current into plasma $\sim D n_f / L^*$, where $L^* = L_0 \sqrt{kT_e/E_0} = \sqrt{2T_0 kT_e/E_0}$ is the length of relaxation of energy $\sim kT_e$. In order to escape from plasma to electrode, electron must be reflected in small solid angle $\sim \frac{kT_e}{E_0}$ after collision with neutral atom. Therefore the reverse electron current $\sim \frac{kT_e}{E_0} n_f \left(\frac{2E_0}{m} \right)^{1/2}$. The ratio of these two currents is determined by parameter

$$p(T_e) = \left(\frac{kT_e}{E_0} \right)^{3/2} \left(\frac{L_0}{l_{ea}} \right)^{1/2} \quad (10)$$

If $p(T_e) \gg 1$ and $p(T) \gg 1$, the energy relaxation of fast electrons is slow, electrons return to electrode before they loose energy $\sim kT_e$, and formula (9) is not valid. In this case one must solve the above mentioned problem to calculate the true value of boundary current.

In opposite limit case, when $p(T_e) \ll 1$ and $p(T) \ll 1$, the energy relaxation is quick, and probability of electron reflection from plasma is small. In its turn, in this case the generation of fast electrons by plasma itself due to the interelectron collisions is very intensive, and emission from plasma doesn't disturb the tail of plasma Maxwellian DF. In this case formula (9) is actually valid.

If $p \gg 1$ one can neglect the left side of (3), (3a) and

(3b) and obtain a priori the boundary values $n_1(E, 0)$ and $n_2(E, 0)$ for $E > E_0$. In this case electrons, injected into plasma, are in equilibrium with cathode at the plasma boundary $z=0$, if $E > E_0$, and electron current may be regarded as zero in first approximation. This case corresponds to slightly ionized plasma. Because the boundary conditions at $z=0$ contain unknown functions, if $E > E_0$, and derivatives of these functions, if $E < E_0$, the problem must be solved by Wiener-Hopf (WH) technique [4].

In opposite limit case, when $p \ll 1$, one may neglect the electrons, reflected from plasma, i.e. the last terms in right sides of (3a) and (3b). Then boundary conditions contain only derivatives $\frac{\partial n(E, z)}{\partial z} \Big|_{z=0}$ both for $E > E_0$ and $E < E_0$, and the problem may be solved simply by Fourier transformation. In this case the solution of problem is interesting only for the evaluation of non-equilibrium part of DF, because, in spite of quick relaxation of injected beam, the non-equilibrium part of DF may be important, if the ratio of cathode emission current to equilibrium emission from plasma

$$\gamma_0 = \frac{j_{es}}{\frac{1}{4} q n_0 \left(\frac{8kT}{\pi m} \right)^{1/2} e^{-E_0/kT}} \quad (11)$$

is larger than 1.

The dependence of parameter p upon the concentration of plasma electrons for $l_{ea} = 2,5 \cdot 10^{-3}$ cm ($p_{cs} \approx 2$ torr) at various E_0 and T is demonstrated at Fig.2. In usual conditions of TC [1] $p < 1$. The case, when $p > 1$, is rare one and corresponds to high Cs pressures. But we shall describe both limit cases in order to explain the physical sense of results.

If $p(T_e) \gg 1$ and $p(T) \gg 1$, the equation (1) with boundary conditions was solved analytically. The results are

$$n_1(E, z) = \frac{j_{es}}{q} \frac{(8m E_0)^{1/2}}{(kT_E)^2} \exp \left\{ - \left(\frac{E_0}{4kT} \right)^{1/2} \left[\left(\frac{z^2}{L_0^2} + \frac{(E-E_0)^2}{E_0 kT} \right)^{1/2} + \frac{E-E_0}{(E_0 kT)^{1/2}} \right] \right\} \times \quad (12)$$

$$\times \operatorname{Re} W \left\{ i \left(\frac{E_0}{4kT} \right)^{1/4} \left[\left(\left(\frac{z^2}{L_0^2} + \frac{(E-E_0)^2}{E_0 kT} \right)^{1/2} - \frac{E-E_0}{(E_0 kT)^{1/2}} \right)^{1/2} \left(\frac{T}{E} \right)^{1/2} + \right. \right.$$

$$+ i \left\{ \left(\frac{z^2}{L^2} + \frac{(E-E_0)^2}{E_0 kT} \right)^{1/2} + \frac{E-E_0}{(E_0 kT)^{1/2}} \left(\frac{T}{T_E} - 1 \right)^{1/2} \right\} ,$$

$$n_2(E, z) = \frac{2n_0 E_0^{1/2}}{\pi^{1/2} (kT)^{3/2}} e^{-\frac{E}{kT}} \left\{ 1 - \operatorname{erf} \left[\sqrt{\left[\frac{(E-E_0)^2}{(2kT)^2} + \frac{E_0}{4kT} \left(\frac{z}{L} \right)^2} \right]^{1/2} - \frac{E-E_0}{2kT}} \right] \right\} . \quad (13)$$

$$W(z) = e^{-z^2} \left(1 + \frac{2i}{\sqrt{\pi}} \int_0^z e^{-t^2} dt \right)$$

is the probability integral of complex argument, tabulated in [5].

The electron current over potential barrier is

$$j_e = \int_E^\infty j(E) dE = -qD \int_{E_0}^\infty \left. \frac{\partial n(E, z)}{\partial z} \right|_{z=0} dE . \quad (14)$$

From (6), (12), (13) and (14) we conclude, that j_e may be regarded as difference of two terms, each term being small as compared to analogous terms in (9):

$$j_e = \frac{4}{3} \frac{\rho_{ca}}{L_0} \left[\left(\frac{E_0}{kT_E} \right)^{3/2} j_{es} - \left(\frac{E_0}{kT} \right)^{3/2} \frac{1}{4} q n_0 \left(\frac{8kT}{\pi m} \right)^{1/2} e^{-\frac{E_0}{kT}} \right] . \quad (15)$$

In TC at the cathode boundary $\gamma_0 > 1$. But, under condition $E-E_0 > kT > kT_E$, the total nonequilibrium part of DF may be positive or negative, because, if $T > T_E$, the number of electrons, emitted from plasma with given energy E , may be larger or smaller, than the number of injected ones.

E.g. we show at Fig.3 the values $n_1(E, z)$, $n_2(E, z)$ and $n(E, z)$, calculated by formulas (12), (13) and (6) at the constant electron energy E . Curve 1 corresponds to the total DF $n(E, z)$ to Maxwellian one $n_M(E)$ ratio. Curve 2 corresponds to injected electron DF. Curve 3 corresponds to electron concentration diminution due to the emission from plasma.

$n_1(E, z)$ is non-monotonous function of z , because of the interaction of beam electrons with relatively small energy dispersion kT_E with plasma electrons with larger energy dis-

persion kT . This interaction increases the part of fast electrons in electron beam.

In opposite case, when $p < 1$, that usually corresponds to the low-voltage are in TC, there is an appreciable gradient of concentration in near-cathode layer [1]. The concentration distribution may be usually regarded as linear one along the distance $\sim L_0$: $n_{pl}(z) = n_0(1 + \alpha x)$, where $\alpha = \text{Const} \sim 1$, $x = \frac{z}{L_0}$. The energy DF is calculated as Fourier integral

$$n_1(E, z) = \frac{j_{es} L_0 (E_0 kT)^{1/2}}{2\pi q \beta (kT_E)^2} (1 + \alpha x)^{-1/4} e^{-\alpha y} \int_{-\infty}^{\infty} \frac{\exp[-i\alpha y - (d^2 + x^2)^{1/2} \omega(x)]}{(x_0 - i\alpha)^2 (d^2 + x^2)^{1/2}} dx, \quad (16)$$

where

$$x = \frac{1}{2} \left(\frac{E_0}{kT} \right)^{1/2}; \quad x_0 = x \left(2 \frac{T}{E} - 1 \right); \quad y = \frac{E - E_0}{\sqrt{E_0 kT}}; \quad \omega(x) = \frac{2}{3} \alpha^{-1} \left[(1 + \alpha x)^{3/2} - 1 \right] \quad (17)$$

In order to define more exactly the criterion of application of formula (16), we calculated the "kinetic coefficient of electron reflection" [2] from plasma boundary $r = j_- / j_{es}$, where

$$j_- = \left(\frac{2E_0}{m} \right)^{1/2} \cdot \frac{1}{4E_0} \int_{E_0}^{\infty} (E - E_0) n_1(E, 0) dE, \quad (18)$$

- is the reverse current: Calculating the value of r , we may neglect the plasma inhomogeneity, because r is a function of L^* (but not of L_0) and concentration change at L^* is usually not essential. From (16) and (18) we deduce

$$r(T_E) = \frac{8}{\pi} \left(\frac{kT_E}{E_0} \right)^{3/2} \cdot \frac{L_0}{l_{ea}} \cdot \Psi \left(\frac{T}{E} \right), \quad (19)$$

where

$$\Psi(\tau) = \frac{3(6\tau - 5) l_{ea} [2\tau - 1 + 2\sqrt{\tau(\tau - 1)}]}{64(\tau - 1)^{3/2}} + \frac{3\tau^{1/2}(4\tau - 5)}{32(\tau - 1)} + \frac{\tau^{3/2}}{8} \quad (20)$$

- is a function describing that electron plasma temperature T is larger than cathode temperature T_p (Fig. 4). In TC plasma near cathode $\tau \approx 1,5$ [1], and $\Psi(1,5) \approx 1,15$. It can be shown from

Fig.2 and Fig.4, that in TC low-voltage are plasma $r(T_e)$ and $r(T)$ are usually small and we may utilize the ordinary form of boundary condition (9) in near-cathode layer [1] and the ordinary method of electron part probe characteristics analysis [6].

In intermediate case, when $p \sim 1$, one must retain all the terms in boundary conditions (3a) and (3b). Neglecting the energy dependence of emission solid angle on electron energy, one may replace $\frac{E-E_0}{\sqrt{E_0}}$ by $\frac{E_{pe}-E_0}{\sqrt{E_0}}$, where E_{pe} is constant value. Then the problem may be solved by WH technique [4]. It is convenient to describe the result of calculation as a function of parameter.

$$P_0 = \frac{3}{2} \frac{L_0}{L_{ca}} \frac{(E_{pe}-E_0)(kT)^{1/2}}{E_0^{3/2}} \quad (21)$$

If $E_{pe}-E_0 \approx kT$, $P_0 \sim P$ (see (10)). Formula (12-13) and (16) may be calculated as the limit cases for large and small values of P_0 . We show the dependence of DF on P_0 at Fig.5 in order to explain the physical sense of results. These results were calculated at the distance $z \gg L_0$ from cathode. One can see, that the energy relaxation increases and electron concentration n_1 diminishes when value P_0 decreases.

§3. Nonequilibrium Ionization in the Near-Cathode Layer of TC.

The rate of nonequilibrium ionization (NI) in TC was previously calculated in [7] under following assumptions: 1) the rate of ionization is equal to the rate of excitation to the first level; 2) the injected fast electrons are in equilibrium with the cathode at the plasma boundary. The calculation, recently carried out [8,9], shows, that the stepwise ionization of excited atoms occurs slowly and the concentration of excited to the first level atoms must be deduced under assumption of equality between excitation and deexcitation rates. Furthermore experiments show [1], that degree of ionization in plasma is large and it is necessary to use formula (16) instead of (12) (see §2). Both the factors lead to the diminu-

tion of the rate of NI. Utilizing (16) and experimental linear dependence of excitation cross-section on the electron energy difference $E-E_1$, E_1 being the threshold of excitation [10], one obtains the concentration of atoms, excited to the first level

$$n_1^{(c)} = n_a \frac{g_1}{2} e^{-\frac{E_1}{kT}} V_1^{(c)}$$

$$V_1^{(c)} = \frac{\int_{E_1}^{\infty} (E-E_1) n_1(E, z) dE}{\int_{E_1}^{\infty} (E-E_1) n_M(E, z) dE}, \quad (22)$$

where $V_1^{(c)}$ is the excited atoms concentration to equilibrium one ratio. Because of exponential increase of $n_M(E)$ with energy decrease, the transitions between the other levels are usually due to Maxwellian plasma electrons, and we may utilize the results, obtained in [9], in order to calculate the rate of ionization of excited atoms:

$$\Gamma(z) = n_{pe}(z) \bar{v}_e \sigma_i(T) n_a \frac{g_1}{2} e^{-\frac{E_1}{kT}} \left[1 + V_1^{(c)} - \frac{n_{pe}^2(z)}{n^2(T)} \right], \quad (23)$$

$$\sigma_i(T) = 4,8 \cdot 10^{-13} e^{-\frac{1,81eV}{kT}} \text{ cm}^2, \quad (24)$$

where $n(T)$ is the equilibrium Saha concentration. In the case of equilibrium ionization, when the DF is Maxwellian one, $V_1 = 1$ [8,9]. Therefore V_1 characterizes the relative number of ions, generated by the non-equilibrium part of electron DF.

The values V_1 are shown at Fig.6 for the highest point of calculated V-C characteristic, depicted at Fig.2 (curve 2') in [1]. At this point $E_0 \approx E_1$, and NI is more essential than at the other points. It is obvious, that NI is ^{not} significant in the case, described in [1].

In situations, when NI is essential, one may calculate analytically the addition to ion current by formulas (22-24) replacing $n_{pe}(z)$ by the mean quantity \bar{n}_{pe} . Then

$$j_{ic} = \bar{n}_{pe} \bar{v}_e \sigma_i(T) n_a \frac{g_1}{2} e^{-\frac{E_1}{kT}} \int_0^{\infty} V_1^{(c)}(z) dz. \quad (25)$$

The integral in (25) is calculated, and we obtain

$$j_{ic} = j_{es} \cdot 3g_1 \cdot \frac{L_0^2 n_e \sigma_i(\tau)}{l_{ea}} \left(\frac{kT_E}{E_0} \right)^2 \varphi\left(\frac{\tau}{T_E}\right), \quad (26)$$

$$\varphi(\tau) = \frac{\tau^4}{2(\tau-1)^2} \left[1 - e^{-\frac{E_1-E_0}{kT_E} \cdot \frac{\tau-1}{\tau}} \cdot \frac{E_1-E_0(\tau-1)+4\tau-3}{\tau^4} \right] e^{-\frac{E_1-E_0}{kT_E \cdot \tau}} \quad (27)$$

The function $\varphi(\tau)$ is shown at Fig.7.

Literature

1. F.G.Baksht, G.A.Djuzhev, V.B.Kaplan, I.L.Korobova, A.M.Martzinovskiy, B.Ya.Moizhes, G.A.Shahnasarova, V.G.Yuriev. "Theoretical and Experimental Investigation of Low-Voltage Arc in Thermionic Converter". (report on Conference):
2. Ф.Г.Бакшт, Б.Я.Мойжес, В.А.Немчинский. ЖТФ. 37 (1967) 729.
3. F.G.Baksht, B.Ya.Moizhes, V.A.Nemchinskiy. "On the Plasma Sheath Theory" (report on Conference).
4. B.Noble "Methods Based on the Wiener-Hopf Technique for the Solution of Partial Differential Equations". Pergamon Press 1958.
5. В.Н.Фаддеева, Н.М.Терентьев "Таблицы значений интеграла вероятностей от комплексного аргумента". ГИТД. Москва 1954.
6. G.A.Djuzhev, V.B.Kaplan, A.M.Martzinovskiy, B.Ya.Moizhes, G.E.Pikus, G.A.Shahnasarova, V.G.Yuriev. "The Probe and Spectrum Investigation of Dense Plasma of Thermionic Converter" (report on Conference).
7. И.П.Стаханов ЖТФ. 37 (1967) 1277; 37 (1967) 1286
Ф.Г.Бакшт, Ю.Л.Игитханов ЖТФ. 37 (1967) 1298
8. Э.Б.Сонин "Журнал технической физики - ЖТФ" 37 (1967) 1840
9. F.G.Baksht, B.Ya.Moizhes, V.A.Nemchinskiy. Contributed Papers 8th Int. Conf. Phenomena in Ionized Gases. (Vienna 1967) p.284.
10. J.F.Wolan, A.N.Phelps. Bull. Am. Phys. Soc. 8 (1963) 445.

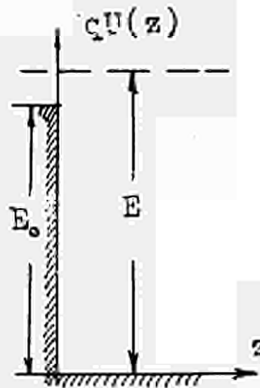


Fig. 1

Electron potential energy $qU(z)$ distribution near the electrode.

E_0 - potential barrier
 E - electron energy.

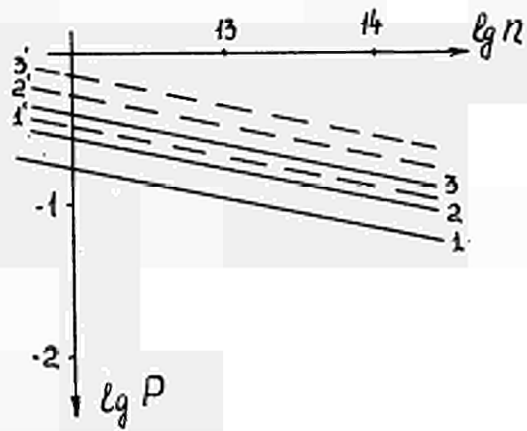


Fig. 2

Dependence of the value of parameter p upon the electron concentration at various E and kT .

- | | |
|-------------------------|--------------------------|
| $E = 1,5\text{eV}$ | $E = 1,0\text{eV}$ |
| 1) $kT = 0,15\text{eV}$ | 1') $kT = 0,15\text{eV}$ |
| 2) $kT = 0,20\text{eV}$ | 2') $kT = 0,20\text{eV}$ |
| 3) $kT = 0,25\text{eV}$ | 3') $kT = 0,25\text{eV}$ |

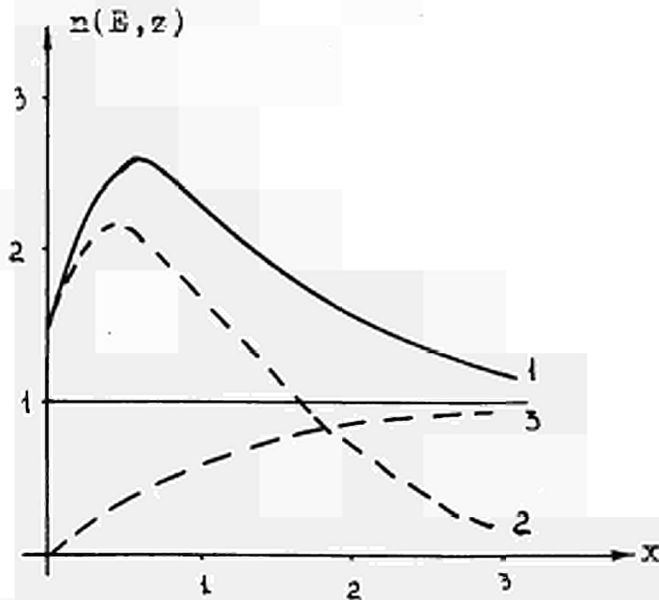


Fig. 3

Dependence of the electron distribution function $n(E, z)$ upon the distance $x = \frac{z}{L_0}$ at the constant electron energy. $E = \text{const.}$

- 1) $\frac{n(E, z)}{n_M(E)}$, 2) $\frac{n_1(E, z)}{n_M(E)}$, 3) $\frac{n_M(E) - n_2(E, z)}{n_M(E)}$,
 $T = 2T_F$, $E - E_0 = 2,3kT$, $E_0 = 4kT$, $\gamma_0 = 3$.

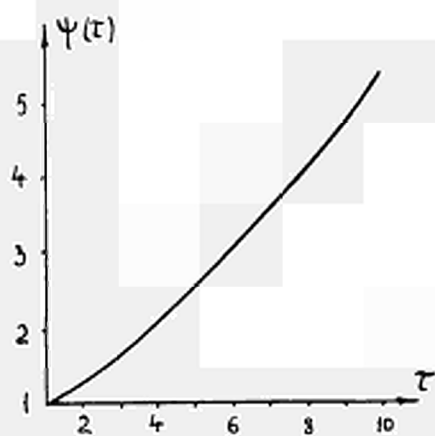


Fig.4

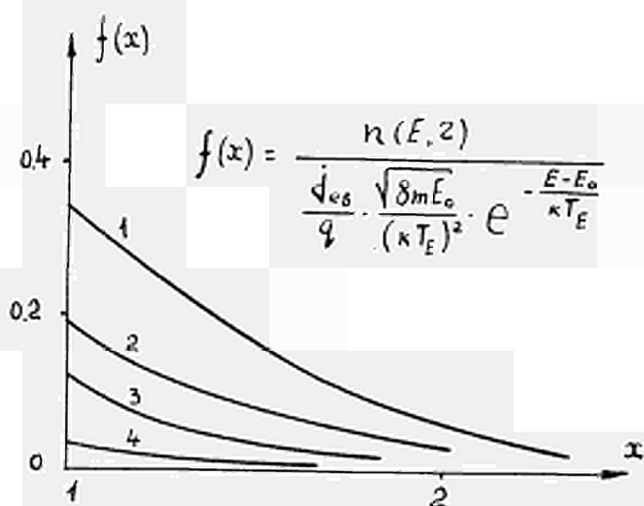


Fig.5

Dependence of the electron distribution function upon the value of parameter p .

$T=1,5T_E$; $Z=1,1$; $E-E_0=2,3kT$; $E_0=4kT$.

1) $P_0 \gg 1$; 2) $P_0 = 1$; 3) $P_0 = 0,66$;
4) $P_0 \ll 1$.

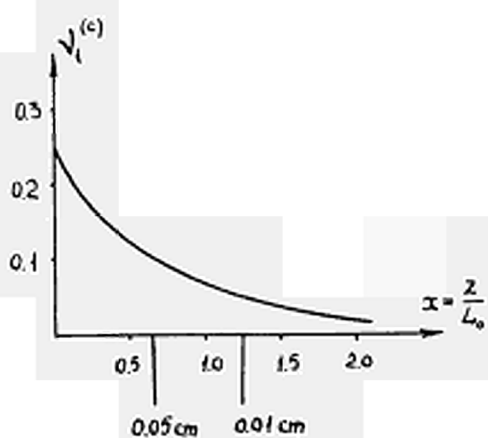


Fig.6

Nonequilibrium population of the first excited level.

$E_0=1,34\text{eV}$; $E_1=1,4\text{eV}$; $n_{pe}(0)=1,1 \cdot 10^4 \text{ cm}^{-3}$;
 $Z=0,25$; $L_0=7,8 \cdot 10^{-3} \text{ cm}$; $j_{es}=3 \text{ A/cm}$;
 $T=2900^\circ\text{K}$.

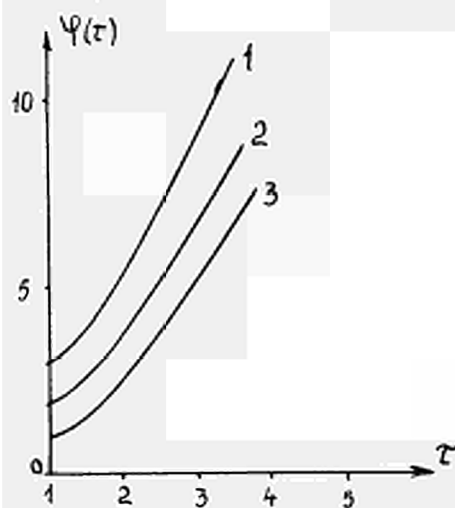


Fig.7

1) $E_1 - E_0 = 0$
2) $E_1 - E_0 = kT_E$
3) $E_1 - E_0 = 2kT_E$

THE PROBE AND SPECTRAL INVESTIGATIONS OF DENSE
PLASMA THERMIONIC CONVERTERS

G.A.Djuzhev, A.M.Martsinovskii, B.Ya.Moizhes, G.E.Pikus,
V.B.Kaplan, G.A.Shahnazarova, V.G.Yurjev.

Institute of semiconductors, Academy of Sciences of USSR.
Leningrad

It is necessary to use various methods of plasma diagnostic for investigation of various processes in the dense plasma of the thermionic converter. In this report a probe and a spectroscopical methods were used.

The Construction of experimental Devices and Method
of measurements.

The investigations were fulfilled on a flat system of electrodes with area $0,8\text{cm}^2$ in glass envelope. A special system of sapphire guarding rings (screen) was used to decrease the edge effects from the side surface of the electrodes. The probe was able to move by means of a silfon junction. One model of devices used is represented in fig.1. The manylayer insulation system of probe supporters [1] was used to prevent the penetration of the plasma current in measuring circuit. The equipotential defence was used to exclude the probe-electrode leakage currents. The cooling of the supporters reduced the thermionic current from the probe into plasma to a necessary minimum. The envelope had a sapphire window for the radiation passing. The electrical scheme of probe measurements was constructed to receive directly the distributions of potential, concentration and dependence of the tempera-

ture of electrons upon the location of the probe in the gap. The impulse measurements were used to decrease the heating of probe and to expand the limit of measured concentration up to $2 \cdot 10^{15} \text{ cm}^{-3}$. The photoelectrical registration of the plasma radiation was used. The optical system permitted to measure the width of the spectral lines. The calibration for the continuum radiation was done directly in the experimental apparatus with the aid of a block cavity in the cathode [2].

The Method of Determination of the Plasma Parameters and their Control

Firstly it was necessary to develop the theory of probes in the dense plasma, when the probe diameter is larger, than free path of electrons and ions in the plasma and to take into account that the length of the cylindrical probe is longer than the distance between electrodes. The theory used the approximate boundary conditions on the electrodes [3,4]. The concentration of the electrons was determined from the electronic ($n \leq 10^{12} \text{ cm}^{-3}$) or ionic ($n > 10^{13} \text{ cm}^{-3}$, when the electronic part of the characteristics is distorted) saturation current

$$n = \frac{j_{ei}^s}{\gamma q \bar{v}_{e,i}} \left[1 + \frac{3\gamma \ln R/a}{1 + T_e/T_i} \cdot \frac{a}{l_i} \right], \quad \text{where } R = \frac{2d}{\pi} \sin \frac{\pi b}{d}$$

Here a - is the probe radius, d - the gap between electrodes, R - distance between the probe and one of the electrodes, l - the free path. According to [4] we put $\gamma=1$. The space potential V_0 may be found from the potential V_1 , where the total probe current is equal to zero ($j_e = |j_i|$).

$$V_0 = \chi_s + V_1 + \frac{\kappa T_e}{q} \left\{ \ln \left[1 + \frac{3\gamma \ln R/a}{1 + T_e/T_i} \cdot \frac{a}{l_i} \right] + \ln \frac{\delta'}{\delta} \left(\frac{M}{m} \frac{T_e}{T_i} \right)^{1/2} \right\}$$

or from the electronic branch of the characteristics with the aid of potential V_2 , where the current is

$$j_e = \frac{j_e^{sat}}{1 + T_i/T_e}, \quad V_0 = \chi_3 + V_2 + \frac{\pi T_i}{q} \ln \frac{r'}{r} \frac{l_e}{l_i}.$$

Here χ_3 is the work function of the probe and the coefficients are $\gamma \approx 1$ [4] and $\gamma^1 = \frac{1}{4}$ [5]. The electron temperature was found from the slope of probe characteristics [3, 6], in the semilogarithmical scale as usually.

For the control of the errors of developed method special measurements of the quality of the probe insulation, the contribution value of thermionic current from probe were done.

We carried out firstly the investigation of the isothermperature plasma, which was created between two electrodes, heated to the same temperature, secondly the experiments with simultaneous measurements with two probes of different diameters, thirdly simultaneous probe and spectral measurements of the plasma parameters. All experiments proved, that the probe methode gives satisfactory results and may be used for the determination of parameters of a dense plasma in a wide range of pressure of cesium vapour. [6].

In fig.2 some results of these investigations are given. The experimental distribution of concentration in the interelectrode space of the thermionic converter in the regime of the thermodynamic equilibrium is represented here. In this regime the temperatures of cathode and anode are equal, and the current across the apparatus vanishes (fig.2a). The concentration distribution is represented in fig.2b when was possible to find the plasma parameters simultaneously from the electronic and ionic branches of the probe characteristics ($n \sim 10^{13} \text{ cm}^{-3}$). The distribution of the relative concentration between electrodes of the converter in the arc mode of operation is

represented in fig.2c from spectral and probe measurements, The ratio of absolute values of concentrations determined by various methods does not exceed 1,5 times. The temperatures of electrons which were determined by probes and from 6P - continuum coincide with the exactness of 200 - 300°K.

Plasma Investigation in the Diffusion Regime.

The investigation of the diffusion regime has been performed over a range of temperatures $T_k = 1400-1800^{\circ}\text{K}$ and vapour pressure of cesium $P = 0,5 - 4$ torr. The distribution of the plasma parameters obtained is in full agreement with the theory [7]. For example, in the fig.4 we have plotted the current - voltage characteristics, distribution of the potential and the electron concentration in the regimes of no load (*), and short circuit (o) and With voltage when glow is visible near the anode (x) [8]. The full curves give the results of the theoretical calculation according to [7]. for the regime of short circuit.

The Investigation of Discharge Plasma

The parameters of the discharge plasma were investigated in the range $T_F = 800-1900^{\circ}\text{K}$, $P_{Cs} = 0,5-4,0$ torr, $d = 0,6 - 2,5$ mm, The cathode vacuum work function was in the range 4,3 - 5 ev.

We have measured the distributions of the electron concentration, the electron temperature and the potential in the interelectrode space. The results obtained were used in calculation of the ionic current in plasma as well as the distributions of the separate components of the current. (fig.3). We have checked the obtained values of the plasma parameters by comparing the sum of the calculated components of the electron current with the experimental value of the converter current (fig.3b) at the di-

fferent cross - sections of the plasma. Another way of the control was the calculation of the anode barrier. (fig.3a).

Some results are plotted in the fig.5a, b, c. Different points on the current - voltage characteristics are shown. The distributions of the concentration n , of the potential V_0^* , of the electron temperature T_e and ionic current J_i in the gap were found for each point.

According to the experimental data the maximum of the electron concentration is located at 0.3-0.4 mm from the cathode and always exists in discharge plasma of the thermionic converter. Approximately linear decreasing of the concentration is observed behind the maximum in the anode direction. If the current increases the maximum of the concentration displaces towards the cathode.

The potential distribution has the following features. The main drop falls on the cathode barrier. Further the little potential drop is observed, behind this drop the potential increases a little to the anode, where the small anode barrier prevents the electrons to leave from plasma to anode. The fall of the potential near the cathode is in general less than the energy of the first excited level of the Cs atom.

Our measurements show that if $n > 10^{13} \text{ cm}^{-3}$ the probe characteristics in semilogarithmic scale are linear up to the electron energy of 2.5 ev. It means that the electron distribution is Maxwellian one. In such cases according to probe and spectroscopic measurements the variation of electronic temperature is rather small. The absolute values of T_e are in the interval 2400 - 2800°K.

When $n_e \leq 10^{13} \text{ cm}^{-3}$ in addition to plasma electrons the more ^{or} less pronounced beam is observed on the probe characteristics. The energy of beam electrons is approxi-

* The Fermi level of the cathode is taken as the potential zero.

mately equal to the cathode potential fall. The observed beam relaxation does not contradict to the point of view that pair electron - electron collisions are the main mechanism of Maxwellisation [5]. The experiments show, that the contributions to the total electron current are given by the field and diffusion components, (the thermodiffusion component is negligibly small). In the near - cathode region the field current prevails, while in near - anode one the total current is directed against the field and diffusion component is predominated (fig.3).

The ion current in plasma changes rather strongly. In the part of the gap adjacent to the cathode J_i is positive, i.e. j_i is directed to the cathode. At the distance

0.4-0.5 mm j_i changes the sign after passing through zero, in the anode part of the gap j_i is directed to the anode. Thus the conditions for the maximum draining of ions to the electrodes are created. The investigation show, that the thermionic converter plasma is weakly ionized and essentially nonequilibrium. The ionization prevails in the region near the cathode, recombination being predominate in the region near the anode in the case of sufficiently large gaps. Maxwellisation is often occurs in comparatively narrow layer near the cathode, more narrow than the region of the main generation [9]. At larger currents the plasma approaches the thermodynamic equilibrium.

The high efficiency of the thermionic converter in the arc mode is explained by comparatively low plasma temperature as well as relatively small radiation, ionization and deexcitation losses.

Literature cited.
(References).

1. Bullis R.H. Adv. Energy Conversion , v.2, p.525, Pergamon Press 1962.
2. V.B.Kaplan, B.Ya.Moizhes, G.E.Pikus, G.A.Shahnazarova, V.G.Yuriev. Zhur. Tekhn. Fiz., 36, 1901 (1966).
3. G.A.Djuzhev, A.M.Martsinovskii, B.Ya.Moizhes, G.E.Pikus, B.I.Tsirkel, V.G.Yuriev. Zhur. Tekhn. Fiz. 36, 679,692 (1966).
4. F.G.Bakst, B.Ya.Moizhes, V.A.Nemchinskiy. "Of the Plasma Sheath Theory". Report on this Conference.
5. F.G.Bakst, B.Ya.Moizhes, V.A.Nemchinskiy. "The Electron Energy Distribution Function in the Near Electrode Layer of Slightly Ionized Plasma and the Rate of Ionization in Thermionic Converter." Report on this Conference.
6. G.A.Djuzhev. Dissertation. Institute of Semiconductors, Leningrad.
7. B.Ya.Moizhes, G.E.Pikus. Fiz. Tv. Tela, 2, 756 (1960).
8. G.A.Djuzhev, A.M.Martsinovskii, G.E.Pikus, B.I.Tsirkel, V.G.Yuriev. Zhur. Tekhn. Fiz., 35, 2054 (1965).
9. F.G.Bakst, G.A.Djuzhev, I.L.Korobova, V.B.Kaplan, A.M.Martsinovskii, B.Ya.Moizhes, G.A.Shahnazarova, V.G.Yuriev. "Theoretical and Experimental Investigation of Low-Voltage Arc in Thermionic Converter". Report on this Conference.

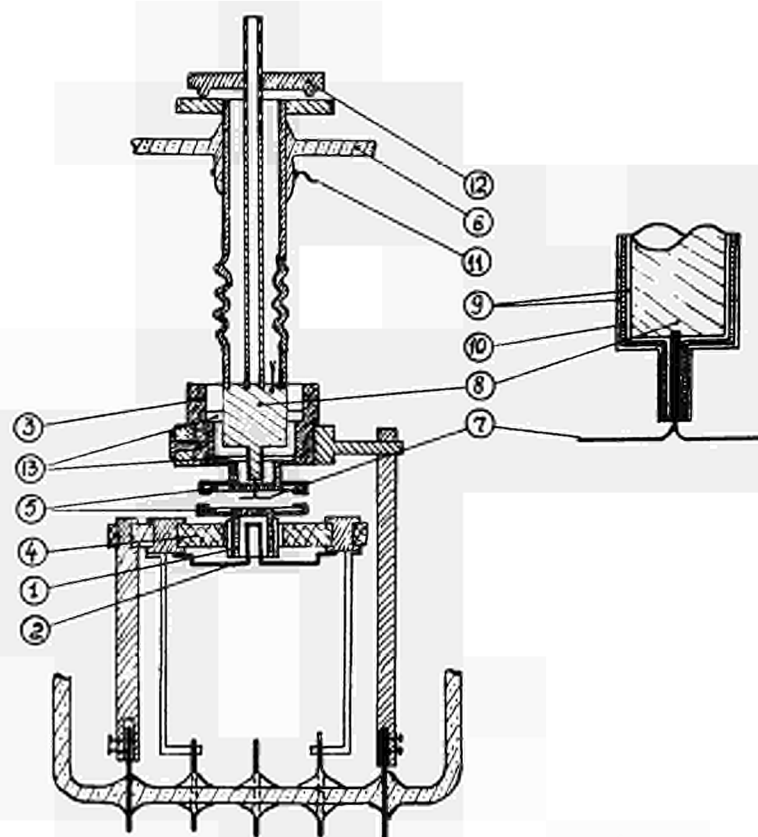


Fig.1
Experimental device.

1-Cathode with thermocouple, 2-high current heater, 3-copper collector, 4-ceramic, 5-sapphire screen, 6-envelope of the device, 7-molybdenum probe (diameter 0,1 mm), 8-copper probe support, 9-sapphire insulator, 10-metallic screen with lead, 11-equipotential screen, 12-nut for probe shift, 13-sapphire discs for probe shift.

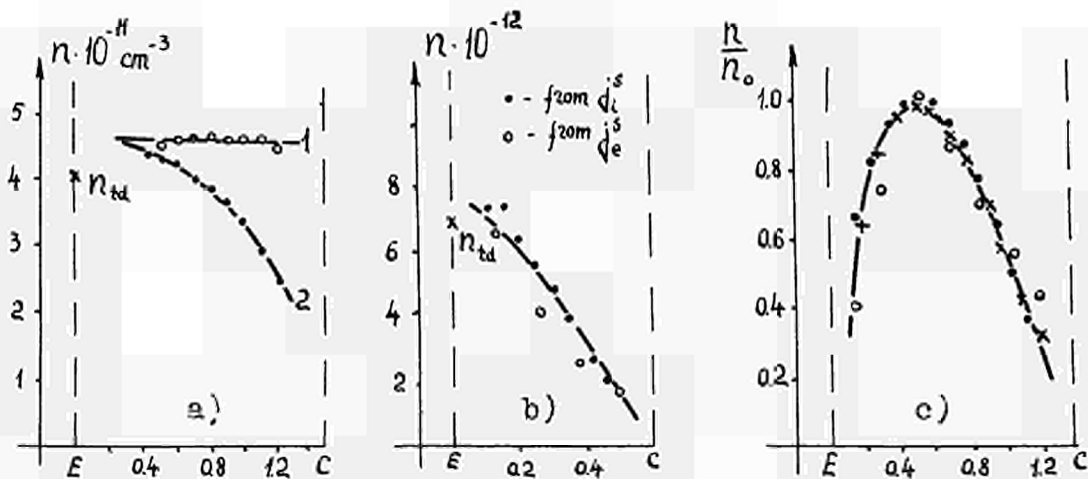


Fig.2

- a) Probe in the equilibrium plasma regime, $P_{cs}=2$ torr, $j=0$, $T_e=T_c=1480^\circ K$ (1), and no load work regime $T_c=750^\circ K$ (2).
 b) Comparison of the concentration, determined from the electron and ion saturation current of probe characteristics. $P_{cs}=2$ torr, $T_e=1880^\circ K$, no load work regime.
 c) The distribution of concentration, determined by various methods in the arc mode operation. $T_e=1065^\circ K$, $j=4,5$ A/cm²
 x - probe measurements, $n_0 = 9 \cdot 10^{13}$ cm⁻³
 • - intensity of 6P continuum, $n_0 = 12,8 \cdot 10^{13}$ cm⁻³
 o - spectral lines broadening, $n_0 = 7,8 \cdot 10^{13}$ cm⁻³

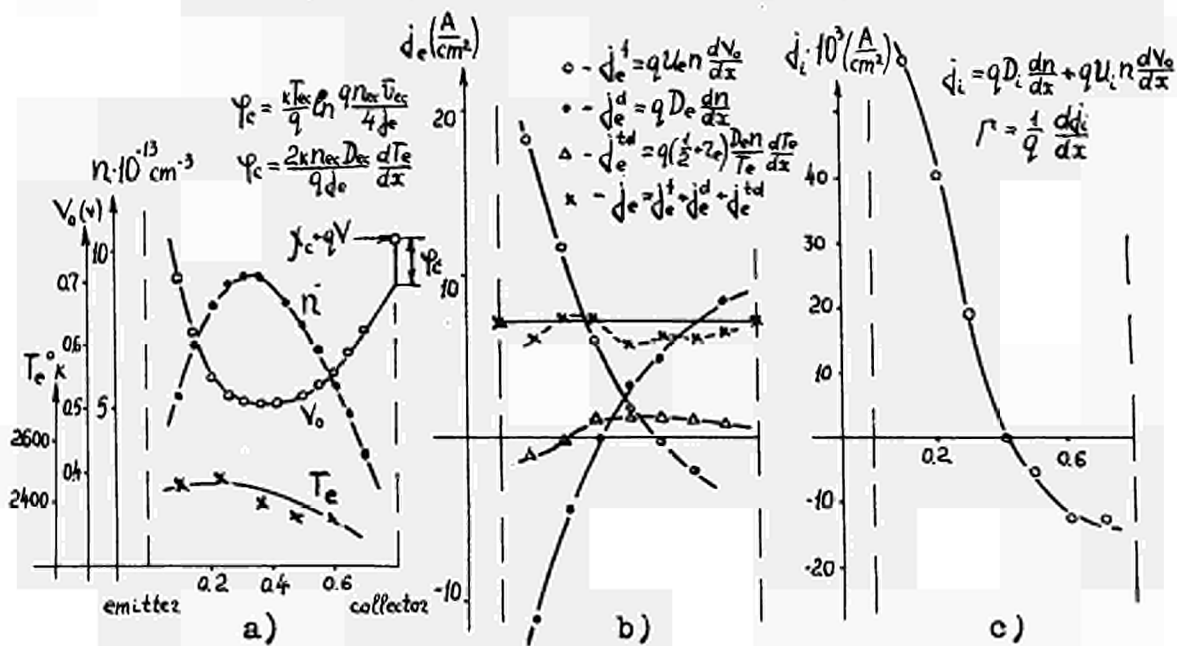


Fig.3

Measurements in the arc mode operation of thermionic converter.

- a) Concentration n , potential V_0 , electron temperature T_e distributions in the interelectrode gap. j_c -collector work function, qV - load voltage, ψ_c -collector barrier.
 b) Calculation of field (j_e^i), diffusion (j_e^d) and thermodiffusion (j_e^{td}) components of the electron current in the various points of the gap and comparison of the whole current with the experimental one.
 c) Calculation of the ion current (j_i) in the various points of the gap.

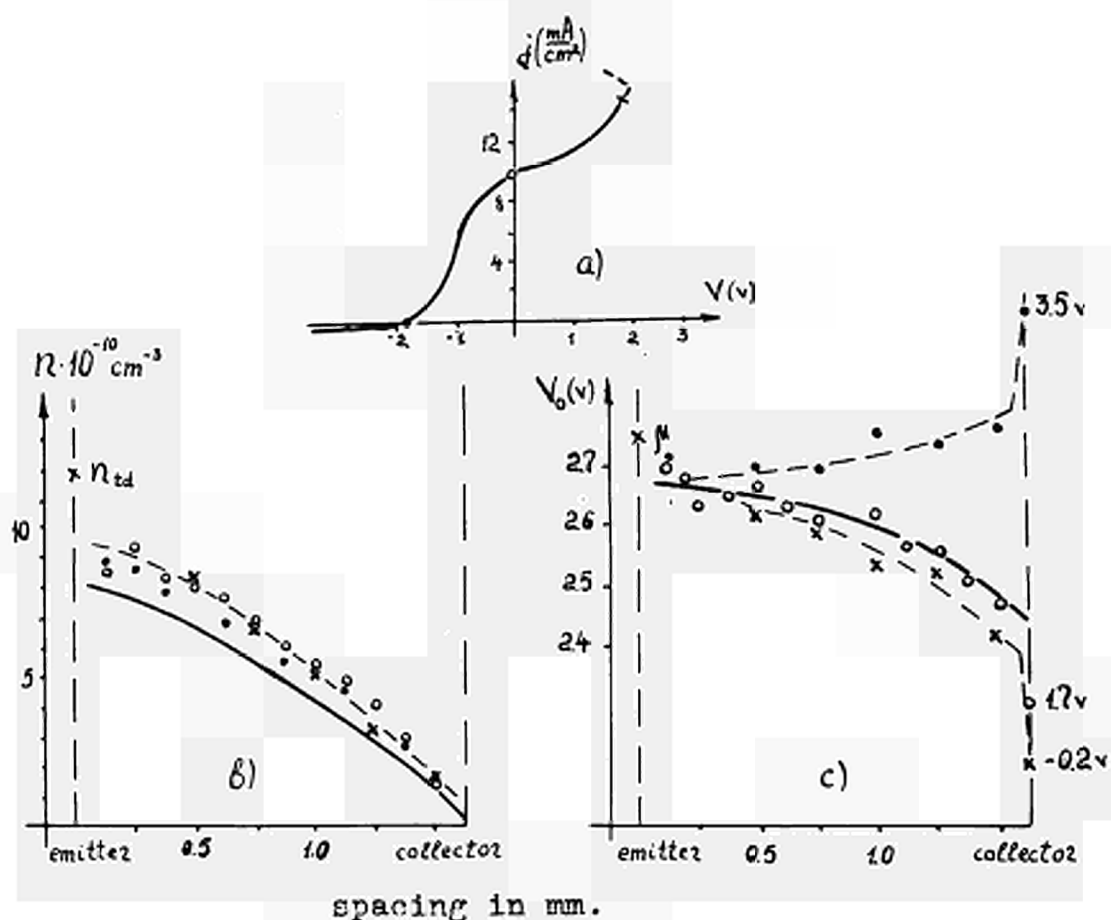


Fig.4

Investigation of the plasma parameters in the diffusion mode of operation.

Voltage-current characteristics (a), and the distributions of concentration (b) and potential (c) in the various points of voltage-current characteristics.

n_{td} - equilibrium concentration, μ - Fermi level of plasma. Continuous curve is the result of the diffusion theory calculation.

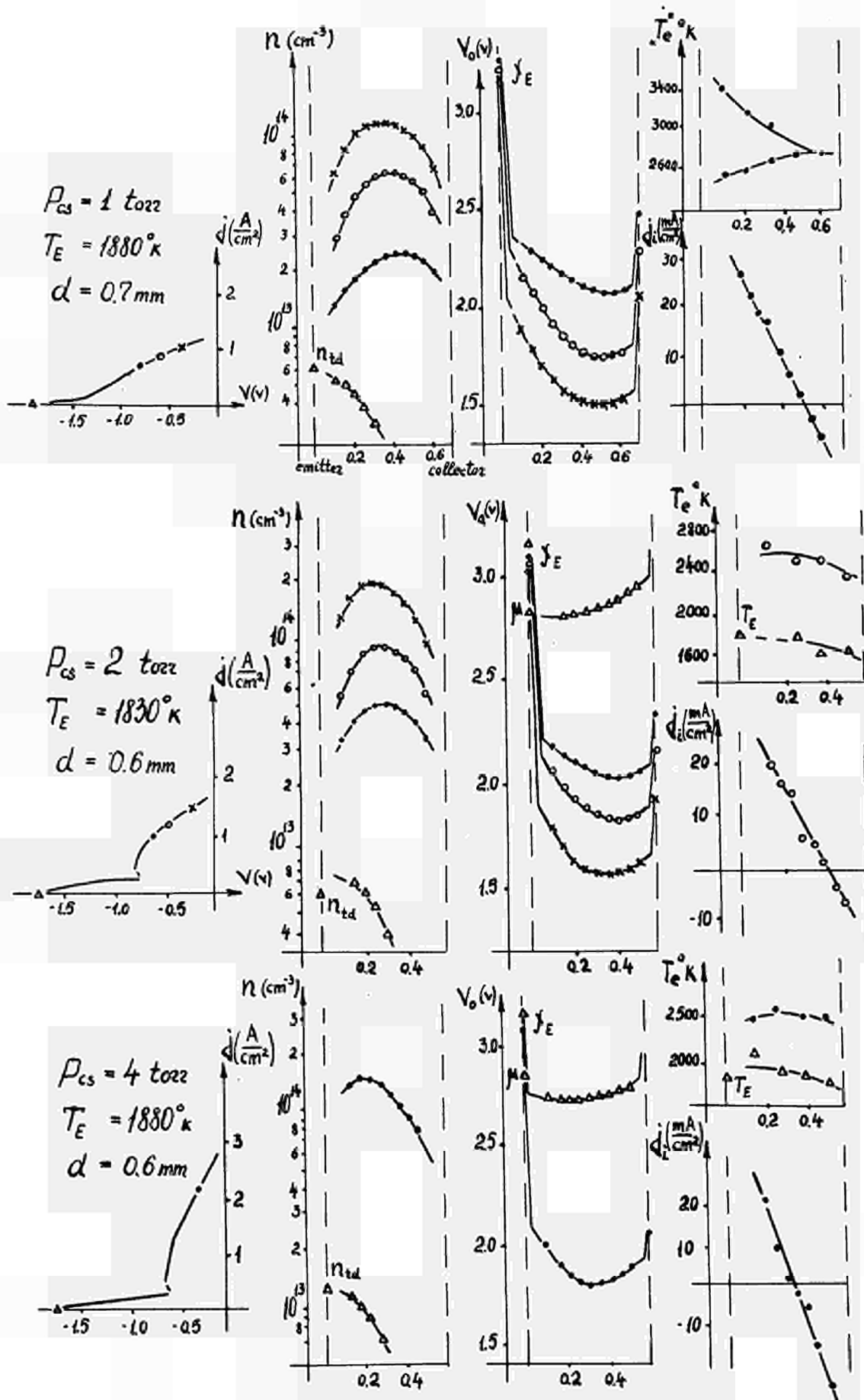


Fig.5

Investigation of plasma parameters in the arc mode of operation.

ON THE PLASMA SHEATH THEORY

F.G.Baksht, B.Ya.Moizhes, V.A.Nemchinskiy.

Semiconductor Institute of the Academy of Sciences of
USSR.
Leningrad.

Introduction

In the present paper the potential distribution and distribution of the concentration in the near - electrode layer are considered. Such a consideration is necessary for ionic current to the electrode, potential difference between plasma and electrode, electric field strength at the surface defining the Schottky effect calculations and for undisturb plasma parameters determination from the probe voltage-current characteristic.

One usually divides the near-electrode shell into two principal parts: I) the region afar off the electrode where plasma is quasi-neutral and the current can be determined by means of constant mobility and diffusion coefficient:

II) the narrow collisionless near-electrode layer of space-charge.

In the more correct stating of the problem it is necessary to introduce the intermediate region III in which plasma characteristics vary so rapid, that this region can

not be described by means of local diffusion coefficient and mobility and plasma parameters must be obtained from the solution of the integral equation. Besides, joining the solutions, describing the collisionness and the collisionless regions is concerned with certain difficulties, first pointed out by Bohm [1]. Incorrect joining can lead to nonmonotonous plasma parameters distributions and even to fiction potential barrier formations. Nonmonotonous plasma parameters distributions also can be obtained, joining the solutions, describing diffusive region and the region of rapid variation, being insufficient correct.

The contact of plasma and unemitting electrode is considered in that case, when potential barrier is much greater than electron thermal energy. Electron concentration dependence upon the potential is therefore of Boltzmann type in the whole near - electrode sheath

$$n_e = n_0 \exp \frac{q\varphi}{kT_e} \quad (1)$$

The near - electrode sheath description depends on the electron temperature T_e to atomic one T_a ratio. The latter determines the ion velocity just after collision - charge exchange. If $\frac{T_e}{T_a} \gg 1$, even when potential variation is slight, the field can be strong for ions, i.e. the velocity ion obtains under electrical field influence is much greater than it's initial velocity. If $\frac{T_e}{T_a} \gg 1$ the strong field extent is much greater than ion mean - free path $-l_i$ and the whole near - electrode sheath can be described under ion initial velocity neglectation. If $\frac{T_e}{T_a} \geq 1$ the strong field is realized only in the small part of the region I, yet region I can be described by diffusion equation, taking into account the dependence of the mobility and the diffusion coefficient upon the field

strength. Both the cases are considered in the present paper. The space charge region II and the joining of the solutions at it's border, we consider only when $\frac{T_e}{T_a} \gg 1$. Corresponding consideration in the case of $\frac{T_e}{T_a} \approx 1$ can be made by the same way and that is why it was not done.

Part 1. $\frac{T_e}{T_a} \gg 1$.

§1. Quasi - neutral Plasma.

Under ionization and recombination neglect in the near - electrode shell, the ion concentration n_i satisfy the following equation:

$$n_i(x) = \frac{j}{e_i} \int_x^\infty \frac{e^{-\frac{x'-x}{e_i}} dx'}{\sqrt{\frac{2q}{m_i} [\varphi(x') - \varphi(x)]}}$$

This equation was obtained in [2,3], but was solved only in the case of small variation on the ion mean-free path. Combining this equation with equation (1) leads to equation, describing the potential distribution in the quasi-neutral plasma

$$e^{\phi(z)} = \gamma_0 \int_z^\infty \frac{e^{-(z'-z)}}{\sqrt{\phi(z') - \phi(z)}} dz' \quad (2)$$

where

$$\phi = \frac{q\varphi}{kT_e} \quad z = \frac{x}{e_i} \quad \gamma_0 = \frac{j}{n_0 \sqrt{2kT_a/m_i}} \quad (3)$$

m_i is the ion mass. Equation (2) is unlocal equation, fair not only in the region I, but in the region III also.

γ_0 parameter defines direct ion current j to concentration n_0 ratio at that point, where the potential is equal to zero. Changing of the γ_0 physically means that another

point (of another concentration) is chosen as a point of zero potential. So, equation (2) does not depend on any parameter. It was solved numerically by means of electronic computer. The solution is represented on Fig.2 and Fig.3. Integration of this equation was made, the point of $\gamma_0 = 0,3$ being the initial, because far from electrode, the local mobility approximation operates, the latter can be obtained by setting in the equation (2) $\varphi(x') - \varphi(x) = \varphi'(x)(x' - x)$ The field strength increases rapidly with potential diminution and at the certain potential $\frac{d\phi}{dz}$ and higher derivatives increase infinitely. This means that potential drop in the quasi - neutral area is limited by potential about kT_e . The value of γ_0 , determining the drift velocity is limited also.

The quasi - neutrality maintaining demands the collisions, because in their absence ion and electron concentrations depend on potential by different ways i.e. electron concentration varies versus potential by exponential way, while ion concentration by square root one. That is why, with field strength increasing, when significant potential difference arises on the distances small compared with ion mean - free path, the quasi - neutrality must be broken.

Near the electrode the space - charge decompensation rapidly increases

$$\frac{\Delta n}{n} = \frac{n_i - n_e}{n_e} = \frac{r_0^2}{l_i^2} e^{-\phi(z)} \frac{d^2 \phi}{dz^2} \quad (4)$$

where $r_0 = \sqrt{\frac{kT_e}{4\pi n_p q^2}}$ - the Debye radius at that point where $\phi = 0$. The region of applicability of the equation (2) is restricted on the left by the condition $\frac{\Delta n}{n} \ll 1$. and on the right by the condition of the strong field, i.e. $\frac{T_e}{T_a} \frac{d\phi}{dz} \gg 1$. Evidently, that if $\frac{T_e}{T_a} \gg 1$ and $\frac{l_i^2}{r_0^2} \gg 1$, one could satisfy the both conditions.

§2. Space - charge region.

While approaching the electrode, the space - charge decompensation increases and it is necessary to solve the Poisson's equation instead of equation (2)

$$\frac{r_0^2}{l_i^2} \frac{d^2\phi}{dz^2} = e^{\phi(z)} - \gamma_0 \int_z^\infty \frac{e^{-(z'-z)} dz'}{\sqrt{\phi(z') - \phi(z)}} \quad (5)$$

If $\frac{r_0^2}{l_i^2} \ll 1$ and if the potential difference between the plasma and the electrode is not large, space - charge layer extent is small compared with mean - free path l_i . By this reason one usually neglects collisions everywhere in the space - charge region.

Equation (5) in this case takes the following form

$$\frac{r_0^2}{l_i^2} \frac{d^2\phi}{dz^2} = e^{\phi(z)} - \gamma_0 \int_\delta^\infty \frac{e^{-(z'-z)} dz'}{\sqrt{\phi(z') - \phi(z)}} \quad (6)$$

where point $z = \delta$ corresponds the border of collisionness and the collisionless regions. Although in view of narrowness of the space - charge layer, the neglected in (6) term is small compared with the net ion concentration, it is very important in solving of the Poisson's equation near the border. Incorrectness of such a neglect leads in particularly, to infinite derivative of the right part of the equation (6) when $z = \delta$. and to rapid increase of the ion concentration. If one does not consider the border space - charge decompensation at all, that leads to electron space - charge predominance and to altering the sign of $\phi''|_{z=\delta}$. Neglecting the border field strength $\phi'|_{z=\delta}$ leads in this case to nonmonotonous potential distribution. Appearance of such oscillations is a result of the incorrect model. Correct potential distribution

demands the consideration of the collisions near the border.

Equation (5) was solved numerically by means of electronic computer for a set values of $\frac{T_e}{T_a}$. At the border ϕ and ϕ' were joined. Extent of the space - charge layer depends on the potential difference between the plasma and the electrode. If the latter is large enough, the space - charge layer extent exceeds Debye radius and approaches the free path l_i , that also leads to necessity of the collisions in this region.

Fig.4 represents the results of the numerical integration of equation (5). Fig.5 represents the solution of the Poisson's equation while neglecting the collisions in the space - charge region taking into account the initial field strength and the initial space - charge decompensation (curve 2) and without it (curve 1). Exact solution is represented by curve 3.

Thus, solutions of the Poisson's equation, taking into account the collisions, occurring in the space - charge region, are such, that the distributions of the field strength, concentrations of the charged particles etc. are monotonous in the near - electrode shell.

$$\text{Part 2. } \frac{T_e}{T_a} \geq 1$$

§3. Region I.

If electron temperature exceeds the atomic one only in few times, the field can be treated as a weak almost in the whole region I. Although, in it's part, which borders with region III, the field is not weak and therefore while describing region I by means of diffusion equation, we take into account the dependence of the mobility U and the diffusion coefficient D upon the field strength. The dependence of the mobility was determined by Perel [4]. His calculations can be approximated by the following de-

pendence

$$U = \frac{1}{2,1 + \frac{1,25 B^{3/2}}{B+5}} \frac{q l_i}{\sqrt{2kT_a m_i}} \quad (7)$$

where $B = \frac{q\phi l_i}{2kT_a}$ - dimensionless field strength. By method, analogous to that of [4], we determined the dependence of diffusion coefficient D upon the B . With the same accuracy this dependence can be approximated by:

$$D = \left(0,24 + \frac{0,4 B^{3/2}}{B+2,9} \right) l_i \sqrt{2kT_a / m_i} \quad (8)$$

We are interested especially with the confirmation of our method of probe voltage - current characteristics consideration in the dense plasma [5] and that is why, for obtaining the finite potential drop in the plasma, we solve the diffusion equation in the region I in the case of spherical probe

$$D \left(\frac{d\phi}{dr} \right) \frac{dn}{dr} + \frac{d\phi}{dr} U \left(\frac{d\phi}{dr} \right) n = \frac{I}{4\pi r^2 a} \quad (9)$$

We introduced the following dimensionless parameters

$$\eta = - \frac{q\phi}{kT_e} \quad \rho = \frac{r}{l_i} \quad A = \frac{I}{4\pi l_i^2 n_0 a \sqrt{2kT_a / m_i}} \quad (10)$$

Equation (9) was solved at the set of the A and $\frac{T_e}{T_a}$ values. Fig.6 represents the solution of this equation in the case of $\frac{T_e}{T_a} = 2$ and $A=4$ (curve 1).

Validity of the diffusion approximation in the region of the large gradients is restricted by inequalities

$$l_i \frac{d \ln n/n_0}{dr} \ll 1 \quad l_i \frac{d \ln q\phi l_i / 2kT_a}{dr} \ll 1 \quad (11)$$

Supposing the justice of the equation (9) up to the point, where inequalities change to equalities, one can estimate the error which arises in region I when neglecting D and U dependence upon the field strength. Curve 2 Fig.6 represents the solution of the diffusion equation under cons-

tant D and U and with the same $\frac{T_e}{T_a}$ and A. It is seen, that the error in the potential difference in the region I determination is about $0,2 kT_e$ and in the border position determination is about $0,21_i$. Under another values of the parameters this error remanes small, increasing only when $\frac{T_e}{T_a} \sim 10$.

As before, one can introduce parameter γ , defining the direct ion current to chaotic one ratio

$$\gamma = \frac{A e^\eta}{\rho^2} = \frac{I}{4\pi r^2 e^{-\eta} q \sqrt{2kT_a/m_i}} \quad (12)$$

Within the rather wide interval of the parameters $\frac{T_e}{T_a}$ and A values, the border value of γ is within $0,6 \div 0,8$.

Thus, introduction of the constant mobility and the diffusion coefficient does not lead to any sufficient error and the border value of γ is about unity.

§4. Region III

The region III begins in that point, where inequalities (11) are broken and the diffusion approximation becomes incorrect. In this region the field is strong, but one cannot apply the consideration, analogous to that in §1, because this method demands the on the right, from the given region existence of the area of the strong field and the extent of this area must be at least about a free path. This demand fulfils only when $\frac{T_e}{T_a}$ is large.

Equation in the rregion III can be considerably simplified by neglecting the initial ion velocities just after collisions, occurring in the region III. In this case the equation takes the form

$$n_0 e^{\frac{q\varphi}{kT_e}} = \frac{j}{e_i} \int_{r_0}^{r} \frac{e^{-\frac{r'-r}{l_i}} dr'}{\sqrt{\frac{2q}{m_i} [\varphi(r') - \varphi(r)]}} + e^{-\frac{r_0-r}{l_i}} \int_0^\infty \frac{f(v_r) v_r dv_r}{\sqrt{v_r^2 + \frac{2q}{m} [\varphi(r_0) - \varphi(r)]}} \quad (13)$$

where the point $r=r_0$ corresponds to the I-III border. We do not know the distribution function $f(V_r)$ exactly, but it can be chosen in such a way that to obtain 1) the given values of ion current and concentration at the border and 2) the field strength without any irregularities, but the continuous field strength and its derivative. The distribution function was taken in the form, depending on five arbitrary parameters, which were chosen according to above mentioned conditions.

The Equation (13) does not take into account the ion current variation versus radius r because, as we shall see further, the region III is so narrow, that one can neglect this variation.

The region III, as in the case $\frac{T_e}{T_a} \gg 1$, is restricted on the left by condition $\frac{\Delta n}{n} \ll 1$. The solution of equation (13) shows that the field strength and therefore the space - charge decompensation increase very rapidly on approaching the electrode. By this reason the region III extent and the potential drop on it are small. For example, in the case of $A=4$ and $\frac{T_e}{T_a}=2$, the width of the region III is about $0,2l_i$ and the potential difference on it is about $0,3kT_e$.

Thus, in the case of $\frac{T_e}{T_a} \gg 1$, the quasi-neutral area of the near-electrode shell satisfactory describes by the constant mobility and diffusion coefficient up to the point where $\gamma=0,6 \div 0,8$ and one can reckon that the region I transits directly to the space-charge layer. Such an approximation does not lead to any sufficient error in the determination neither of near-electrode sheath extent nor of potential drop on it.

Conclusion

The present calculations show the justice of the boundary conditions, used in [5,6] for describing arc mode operation of the thermionic converter and for ion current

to the probe in the dense plasma determination. If $\frac{T_e}{T_a} \sim 1-2$ utilization of the constant mobility and diffusion coefficient up to that point where ion drift velocity is equal to the mean chaotic one ($\gamma=1$) is equivalent to the small (of order of $0,2l_i$) error in the electrode position (radius) determination and to the small (of order of $0,3 kT_e$) error in the potential drop on the quasi-neutral plasma determination.

References

1. Bohm D. Characteristics of Electrical Discharges in Magnetic Fields pp77-86 New York (1949)
2. К.М.Каран, В.И.Перель ДАН СССР 108 (1956) 222
3. G.Ciobanu, I.Popescu J.Electronics and Control 16 (1964) 59
4. В.И.Перель ЭТФ 32 (1957) 526
5. Djuzhev G.A. et al. "The Probe and Spectrum Investigation of Dense Plasma of Thermionic Converter" (report on the conference)
6. Baksht F.G., Moizhes B.Ya., Nemchinskiy V.A. "The Electron Energy Distribution Function and the Rate of Nonequilibrium Ionization in the Near-Electrode Layer of the Thermionic Converter" (report on the Conference).

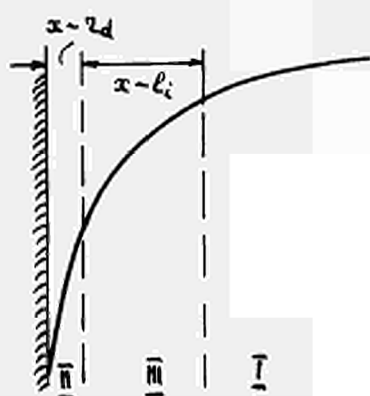


Fig. 1
Potential distribution near the negative electrode.

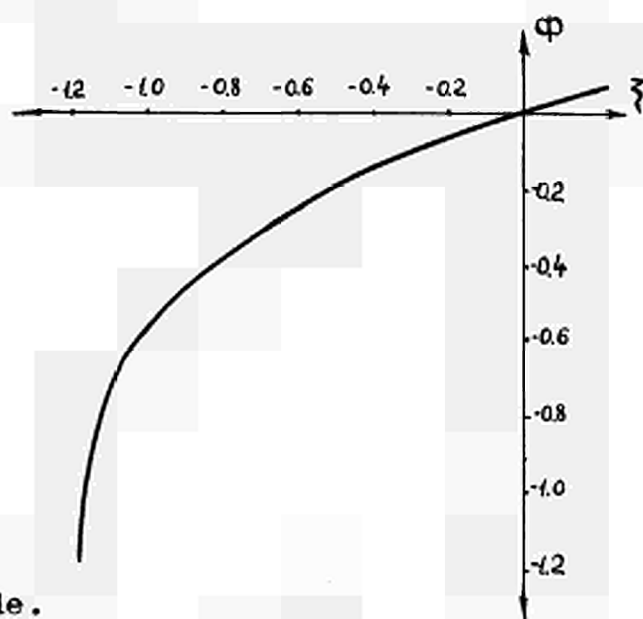


Fig. 2
Potential distribution in the quasi-neutral plasma, when $\frac{T_e}{T_a} \gg 1$.

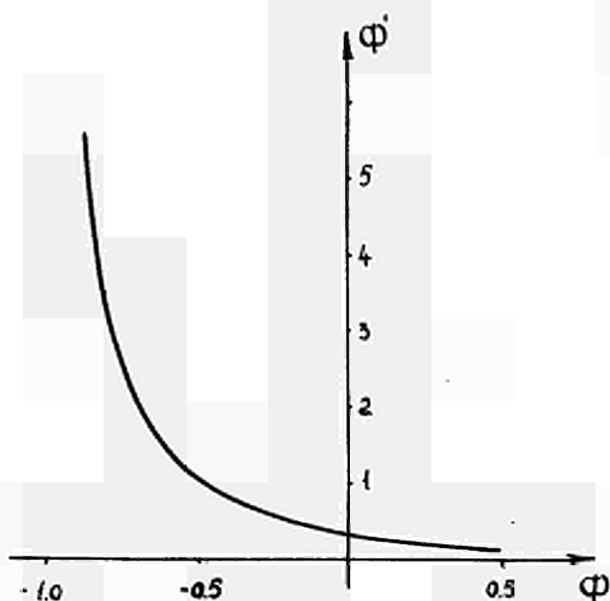


Fig. 3
The field strength ϕ' dependence upon potential in the quasi-neutral plasma, when $\frac{T_e}{T_a} \gg 1$.

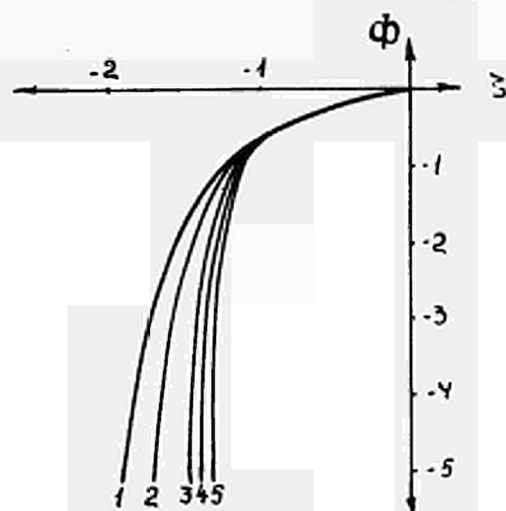


Fig. 4
Potential distribution in the near-electrode shell of various ion free path l_i to Debye radius r_D ratios.
 $\frac{r_D^2}{l_i^2} = 10^{-2}$ (1); $5 \cdot 10^{-3}$ (2); 10^{-3} (3); $5 \cdot 10^{-4}$ (4); 10^{-4} (5).

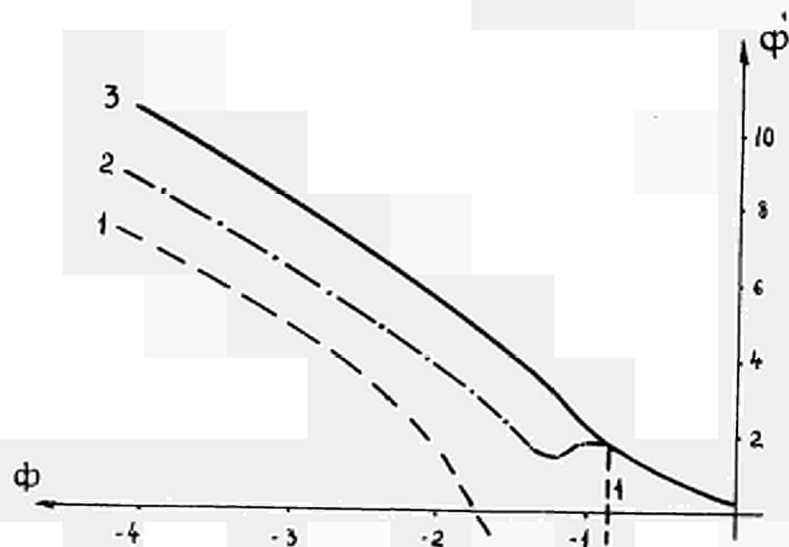


Fig.5

The field strength dependence upon potential in the space charge layer.

curve 1 - without taking into account a) the collisions in the region III; b) the initial field strength and the initial space charge decomposition.

curve 2 - with b) and without a).

curve 3 - exact solution.

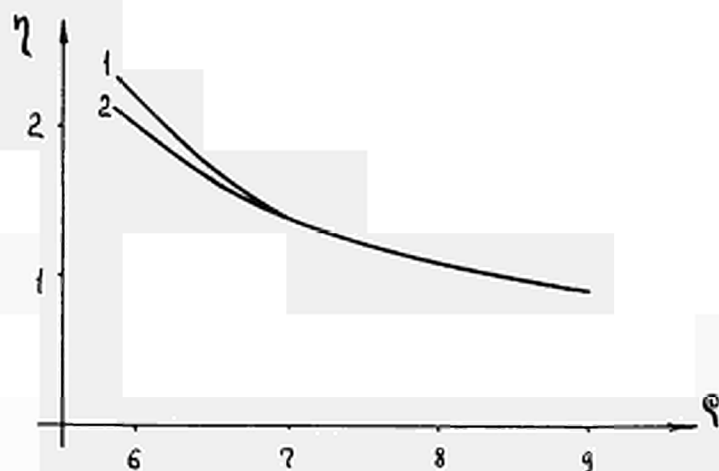


Fig.6

Potential distribution near the spherical probe,

when $\frac{T_e}{T_i} = 2$.

curve 1 - without taking into account D and U dependence upon the field strength.

curve 2 - with taking into account this dependence.

DISCUSSION

Speaker of papers J-1, J-2, J-3 and J-4: G. DJUZHEV.

RASOR (USA): I am troubled by the very good agreement that you get in the plasma diagnostics internally in the converter as compared with the rather obvious difficulty with the current-voltage output characteristics.

E. g., curve 2 in Fig. 2 of paper J-1 shows a very sharp negative resistance region. Yet, at this temperature and pressure-spacing product, this is not observed in converters with adequate guard rings. I wonder if you can in any way reconcile these two seemingly contradictory results?

DJUZHEV (USSR): In the negative resistance region you mention, we observe experimentally that the one-dimensional character of the discharge is lost, and that the discharge begins to contract. Since the theory is based on a one-dimensional discharge, it cannot be compared with experiment in this region. Therefore, the comparison between theoretical and experimental plasma parameters was made only in the upper or saturation region of the output characteristics. Does this answer your question?

RASOR: Yes, but only in part. The theory you have given yields a large negative resistance region even for a one-dimensional discharge, whereas this effect is not observed in experimental devices with electrodes carefully guarded to suppress edge (two-dimensional) effects. Since other theories exist which are consistent with this experimental behavior, I am curious as to the basic reason why your theory gives a different result.

DJUZHEV: The theory has not yet been compared in detail with experiment in the lower or negative resistance region.

WARNER (USA): We run into difficulties in our computer calculations at larger currents. Your calculations were made at approximately 1 to 2 Amps/cm². Do you run into difficulties at high currents?

DJUZHEV: I personally did not do the theoretical work, but as far as I know there were such difficulties, when we went to high currents. At the present time, attempts are being made to program the machine taking into account the high currents.

RASOR: Have you taken into account the conservation or loss of resonance radiation from the plasma in this particular theory?

DJUZHEV: Yes, we did. We did calculate the loss of resonance radiation.

AN INVESTIGATION OF THE IONIZATION MECHANISMS IN THE IGNITED MODE CESIUM THERMIONIC CONVERTER*

Edward L. Burgess+ and Denys O. Akhurst++

Abstract

The ionization mechanisms present in the ignited mode cesium thermionic converter have been studied in order to determine the dominant mechanism producing positive ions for electron space charge neutralization. The theoretical ion density, produced by each ionization mechanism, has been calculated for electron impact ionization from the cesium ground state and from cesium excited states, and for molecular ion formation through excited state impact. Calculations, based on rate balance considerations, assume a Maxwellian energy distribution and a uniform spatial temperature distribution of ions and electrons in the interelectrode region. The ion density is assumed to be limited by recombination processes. The calculations show that ion formation from electron impact of cesium 6p states is the dominant mechanism. The theoretical studies are supported by experimental results from current-voltage characteristic measurements and from investigations of plasma density and electron temperature.

Introduction

Under certain conditions, positive ions for space charge neutralization may be generated by inelastic electron-cesium atom collisions in the interelectrode region of a cesium thermionic converter^{1,2**}. A converter is said to be operating in the ignited mode under these conditions. This mode of operation has received considerable attention¹⁻⁶ and the following ionization mechanisms have been suggested: (1) electron impact ionization from the cesium ground state, (2) electron impact ionization from cesium excited states and (3) molecular ion formation through excited state impact. There is support in the literature for each of these mechanisms; however, recently, Witting⁷ and Reichelt and Agnew⁸ have presented experimental results which show that atomic ions are the dominant ionic species in the ignited mode. The present study considers the theoretical basis for ionization by electron impact and shows that electron impact of cesium 6p states is the most productive mechanism for the considered emitter temperatures and cesium pressures.

Theoretical Considerations

In this discussion the following assumptions are made: (1) electrons and ions in the interelectrode space have a Maxwellian energy distribution, (2) electron and ion temperatures are uniform across the interelectrode region and (3) ion density is limited by recombination processes only.

*This work was supported in part by the U. S. Atomic Energy Commission and in part by the Arkansas Power and Light Company

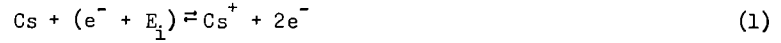
+Sandia Laboratory, Albuquerque, New Mexico, U.S.A.

++University of Arkansas, Fayetteville, Arkansas, U.S.A.

**Superscripts refer to references listed at the end of the paper.

I. Electron Impact Ionization from the Ground State

Cesium atoms in the ground state may be ionized by electron impact according to the equation,



where E_1 is the ionization potential of cesium (3.89 eV). The rate at which atomic ions are produced by this mechanism can be defined by

$$R_{ig} = N_0 n_e \int_{E_1}^{\infty} f_e(E) \sigma_{ig}(E) v_e(E) dE \quad (2)$$

and the recombination rate defined by

$$R_{rg} = n_{ig} n_e \int_0^{\infty} f_e(E) \sigma_{rg}(E) v_e(E) dE \quad (3)$$

where N_0 is the cesium atom density, n_e is the electron density, n_{ig} is the ion density, $f_e(E)$ is the electron energy distribution, $\sigma_{ig}(E)$ is the ionization cross section, $\sigma_{rg}(E)$ is the recombination cross section and $v_e(E)$ is the electron speed.

The recombination cross section can be related to the ionization cross section by the principle of detailed rate balance⁹ and is given by

$$\sigma_{rg}(E) = \frac{w_0}{w_i} \left[\frac{E+E_1}{E} \right] \sigma_{ig}(E+E_1) \quad (4)$$

where w_0 and w_i are the statistical weights of the ground state atom and ion, respectively. Combining equations (2) - (4), we have

$$\frac{R_{ig}}{R_{rg}} = \frac{N_0}{n_{ig}} \frac{w_0}{w_i} \exp(-eE_1/kT_e) \quad (5)$$

where T_e is the electron temperature. Since we are assuming $R_{ig} = R_{rg}$, equation (5) becomes

$$n_{ig} = \frac{w_0}{w_i} N_0 \exp(-eE_1/kT_e) \quad (6)$$

II. Electron Impact Ionization from Cesium Excited States

In general, atomic ions may be formed by electron impact ionization from all levels of excitation of the cesium atom; however, the 6p states should be more important since the population of these states is larger. We will consider only the 6p states and treat them as one excited state with an average excitation energy (E_x) of 1.4 eV. The equations are



where E_{xi} is the energy required to ionize the excited atom.

The rate at which ions are produced by this mechanism can be defined by

$$R_{ia} = N_x n_e \int_{E_{xi}}^{\infty} f_e(E) \sigma_{xi}(E) v_e(E) dE \quad (9)$$

and the rate of recombination defined by

$$R_{ra} = \alpha_{ra} n_{ia} n_e \quad (10)$$

where N_x is the excited state atom density, n_{ia} is the atomic ion density, $\sigma_{xi}(E)$ is the ionization cross section, and α_{ra} is the recombination coefficient.

Hinnov and Hirschberg¹¹ have derived an expression for the recombination coefficient for hydrogen. Bates, Kingston and McWhirter¹² have predicted that the recombination rate is not very sensitive to the species of singly charged ions. Wada and Knechtli¹³ have made measurements of the recombination coefficient in a cesium plasma and their results are in good quantitative agreement with both the theories of Hinnov and Hirschberg and Bates, Kingston and McWhirter. The expression obtained by Hinnov and Hirschberg for the recombination coefficient will be used here. Their expression is

$$\alpha_{ra} = 1.09 \times 10^{-14} T_e^{-9/2} n_e \quad (11)$$

Thus equation (10) becomes

$$R_{ra} = 1.09 \times 10^{-14} T_e^{-9/2} n_e^2 n_{ia} \quad (12)$$

From the classical Thomson theory¹⁴, the ionization cross section may be written as

$$\sigma_{xi}(E) = \pi \left(\frac{e}{4\pi\epsilon_0} \right)^2 \frac{1}{E} \left(\frac{1}{E_{xi}} - \frac{1}{E} \right) \quad (13)$$

Combining equations (9) - (13) and using the expression given by Witting and Gyftopoulos⁵ for the excited state density, i.e.,

$$N_x = \frac{\omega_0}{\omega_x} N_0 \exp(-eE_x/kT_e) \quad (14)$$

we obtain

$$n_{ia} n_e = 3.75 \times 10^{-18} N_0 T_e^3 \left[3.45 \times 10^{-5} T_e \exp(-eE_x/kT_e) - I \right] \quad (15)$$

where

$$I = \int_{E_{xi}}^{\infty} \frac{1}{E} \exp \left[-e(E+E_x)/kT_e \right] dE \quad (16)$$

III. Molecular Ion Formation

It was suggested by Freudenberg¹⁵ that the collision of two excited cesium atoms, each excited to the 6p state, could lead to the formation of the molecular cesium ion. The equations for this mechanism are



where E_x is the energy required to excite the cesium atom to the 6p state (1.4 eV). Witting and Gyftopoulos⁵ have treated this mechanism in detail; however, since their paper was published, improved data on the ionization cross section¹⁶ and recombination coefficient¹⁷ have been reported. Using the analysis of Witting and Gyftopoulos and more recent data^{16,17} we obtain

$$n_{im} n_e = 2.51 \times 10^{-10} N_0^2 T_a^{1/2} T_e^{3/2} \exp(-2eE_x/kT_e) \quad (19)$$

where n_{im} is the molecular ion density and T_a is the cesium atom temperature.

IV. Numerical Comparison of Ion Generation Mechanisms

It is apparent from equation (6) that the electron temperature would have to be of the order of 10,000°K before significant ionization would result. This is much higher than observed electron temperatures¹⁰; therefore, it is concluded that ionization by electron impact from the cesium ground state is not important in cesium thermionic converters operating in the ignited mode.

If we take the ratio of equations (19) and (15), we obtain

$$\frac{n_{im}}{n_{ia}} = 6.69 \times 10^{-29} N_o T_a^{1/2} T_e^{-3/2} \frac{\exp(-2eE_x/kT_e)}{[3.45 \times 10^{-5} T_e \exp(-eE_i/kT_e) - 1]} \quad (20)$$

This ratio is plotted as a function of reciprocal electron temperature in figure 1 for three different combinations of atom temperature, T_a , and cesium pressure, P_{Cs} . The atom density, N_o , is related to the cesium pressure by the ideal gas law. This graph indicates that $n_{im} \ll n_{ia}$ for a large range of atom temperatures and cesium pressures. This fact is in agreement with the experimental studies of Witting⁷ and Reichelt and Agnew⁸.

For a neutral plasma in the interelectrode region, the total ion density is equal to the electron density and hence

$$n_{ia} + n_{im} = n_e \quad (21)$$

Since $n_{im} \ll n_{ia}$, equation (21) becomes

$$n_e \approx n_{ia} = n_i \quad (22)$$

and the ion density, n_i , is determined from equation (15) as

$$n_i = 1.92 \times 10^9 N_o^{1/2} T_e^{3/2} \left[3.45 \times 10^{-5} T_e \exp(-eE_i/kT_e) - 1 \right]^{1/2} \quad (23)$$

Comparison of Theoretical and Experimental Results

Figure 2 shows a comparison of theoretical current-voltage characteristics with some experimental data by Paquin and Bornhorst¹⁸. The theoretical current-voltage characteristics were calculated using the model for the ignited mode given by Ingold⁶ and equation (23) for the ion density. The cesiated work functions used in the theoretical calculations are consistent with the adsorption theory of Rasor and Warner¹⁹.

The current-voltage characteristic for $T_{Cs} = 568^\circ\text{K}$ of figure 2 is reproduced in figure 3 and the electron temperatures which were used in the calculation of the theoretical curve are indicated on the curve. These values are in the range of experimental electron temperatures reported¹⁰.

Although successful correlation of current-voltage characteristics is necessary, it is not sufficient to verify the validity of a particular theoretical model for the ionization mechanisms in the ignited mode⁴. A more direct verification would be to compare the model with experimental data on plasma density and electron temperature. Figure 4 is such a comparison of the ion density as a function of electron temperature calculated by equation (23) and some recent experimental data^{8,10}.

The reported experimental data^{8,10} shows that electron temperature and, hence, plasma density decreases across the interelectrode space from emitter to collector. For purposes of presentation in figure 4, values near the midpoint of the interelectrode space were chosen; however, equation (23) also predicts satisfactorily the values at other points. This

indicates that assumption 2 is more restrictive than is necessary; however, it was convenient to make this assumption for purposes of calculating the current-voltage characteristics.

Conclusions

From the study, it is concluded that electron space charge neutralization in the ignited mode is provided primarily by atomic ions produced by electron impact of cesium 6p states. The conclusion is made on the basis of the theoretical analysis which is supported with good agreement by experimental results.

References

- (1) STEEL, H. L.; GILLETTE, R. B., "The transition to the arc mode and its influence on thermionic converter performance," *Adv. Energy Conv.* 2 (1962) 483.
- (2) HERNQVIST, K. G., "Analysis of the arc mode operation of the cesium vapor thermionic energy converter," *Proc. IEEE* 51 (1963) 748.
- (3) RIZZO, J.E.; BELL, D. W., "Spectrographic observations of an arc-mode cesium thermionic converter," *Proceedings of Symposium on High Temperature Conversion of Heat to Electricity*, Univ. of Arizona, Feb. 1964, p. 321.
- (4) WILKINS, D. R.; GYFTOPOULOS, E. P., "Thermionic Converters Operating in the ignited mode. Part I: Theoretical output-current characteristics," *J. Appl. Phys.* 37 (1966) 2888.
- (5) WITTING, H. L.; GYFTOPOULOS, E. P., "An Ionization process in a low-energy cesium plasma," *J. Appl. Phys.* 36 (1965) 1328.
- (6) INGOLD, J. H., "A theoretical model for the arc-mode cesium converter," *Proceedings of Twenty-Sixth Annual Conference on Physical Electronics*, Mass. Inst. of Tech., March 1966, p. 85.
- (7) WITTING, H. L., "Mass spectrometer analysis of cesium ions from a thermionic converter," *Proceedings of Thermionic Conversion Specialists Conference*, Houston, Texas, Nov. 1966, p. 75.
- (8) REICHELDT, W. H.; AGNEW, L., "Identification of the ionic species in a cesium plasma diode," *ibid*, p. 70.
- (9) FOWLER, R. H., "Statistical equilibrium with specific reference to the mechanism of ionization by electron impacts," *Phil. Mag.* 47 (1924) 257.
- (10) REICHELDT, W. H., "Spectrographic investigation of the ignited mode of thermionic converter operation," *Proceedings of International Conference on Thermionic Electrical Power Generation*, London, England, Sept. 1965.
- (11) HINNOV, E.; HIRSCHBERG, J. G., "Electron-ion recombination in dense plasmas," *Phys. Rev.* 125 (1962) 695.
- (12) BATES, D. R.; KINGSTON, A. E.; McWHIRTER, R. W.P., "Recombination between electrons and atomic ions. I. Optically thin plasmas," *Proc. Roy. Soc.* A267 (1962) 297.
- (13) WADA, J. Y.; KNECHTLI, R. C., "Measurements of electron-ion recombination in a thermal cesium plasma," *Phys. Rev. Letters* 10 (1963) 513.
- (14) THOMSON, J. J., "Recombination of gaseous ions, the chemical combination of gases and monomolecular reactions," *Phil. Mag.* 47 (1924) 337.
- (15) FREUDENBERG, K., "Über Photoionisation des Cäsiumdampfes durch Absorption von Linien der Hauptserie," *Z. Physik* 67 (1931) 417.
- (16) KNIAZZEH, A. G. F.; CARABATEAS, E. N., "Cesium molecular-ion formation by collision of two excited atoms," *Proceeding of Thermionic Conversion Specialist Conference*, San Diego, Calif., Oct. 1965, p. 109.
- (17) HARRIS, L. P., "Ionization and recombination in cesium-seeded plasmas near thermal equilibrium," *J. Appl. Phys.* 36 (1965) 1543.
- (18) PAQUIN, M. L.; BORNHORST, W. J., "Diode parametric performance calculations," Appendix D, AEC Research and Development Report GEMS 2055-1 prepared by General Electric Missile and Space Division under contract AT(29-2)-2055.
- (19) RASOR, N. S.; WARNER, C., "Correlation of emission processes for adsorbed alkali films on metal surfaces," *J. Appl. Phys.* 35 (1964) 2589.

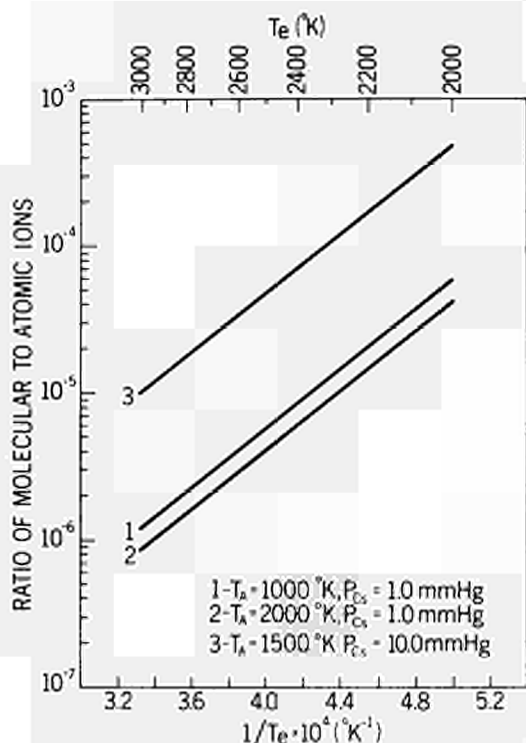


FIGURE 1 -- RATIO OF MOLECULAR TO ATOMIC IONS AS A FUNCTION OF RECIPROCAL ELECTRON TEMPERATURE.

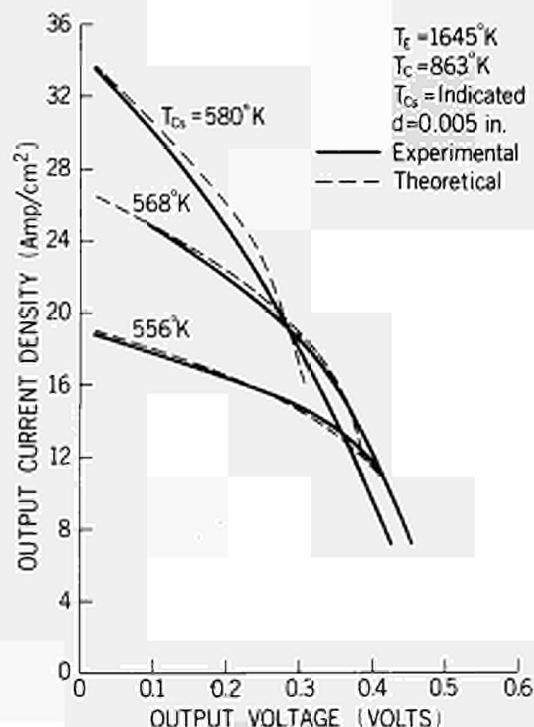


FIGURE 2 -- COMPARISON OF THEORETICAL CURRENT-VOLTAGE CHARACTERISTICS WITH EXPERIMENTAL DATA FROM PAQUIN & BORNHORST (REFERENCE 18)

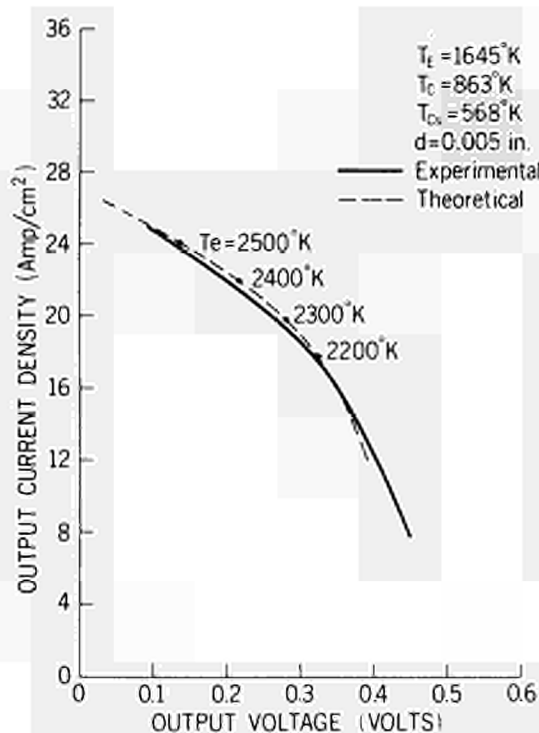


FIGURE 3 -- COMPARISON OF THEORETICAL AND EXPERIMENTAL (PAQUIN & BORNHORST, REFERENCE 18) CHARACTERISTIC SHOWING THEORETICAL ELECTRON TEMPERATURES.

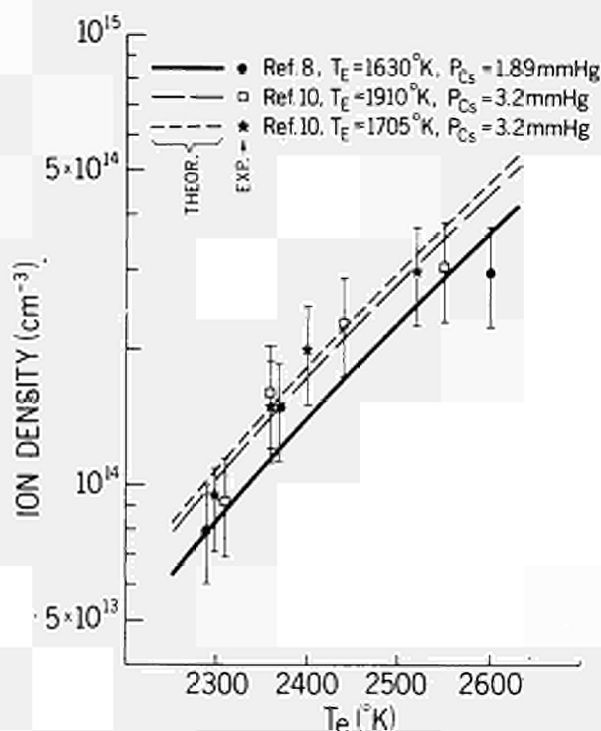


FIGURE 4 -- ION DENSITY AS A FUNCTION OF ELECTRON TEMPERATURE CALCULATED BY EQUATION 23 AND COMPARED TO SOME RECENT EXPERIMENTAL DATA.

Spectroscopic Investigations in a Thermionic Converter Plasma

C. G. Stojanoff⁺, W. Hoffmann, K. Sewing

Institut für Kernenergetik der Universität Stuttgart

Electron temperature T_e and density N_e distributions across the inter-electrode gap of a Cs-converter have been determined spectroscopically. The adjustable planar geometry of the converter and the precision of the optical system facilitated measurements with 50 microns spatial resolution at $d = 0.05$ cm and $pd = 40$ mil-torr. The emitter temperature T_E was varied between 1600 and 1800°K. The T_e and N_e distributions exhibit pronounced maxima, which move toward the emitter with increasing current density and emitter temperature.

Experimental Apparatus and Instrumentation

The thermionic converter cell consists of two adjustable Ta-electrodes in planar geometry (2 cm dia), enclosed by a stainless steel body with 4 mutually perpendicular, demountable, sapphire windows. Bakeable metal-to-metal seals, used throughout the UHV-system, ensure high vacuum operational conditions at temperatures as high as 800°K (background pressure better than 10^{-7} torr). The emitter is heated by means of an electron gun. Its temperature is measured pyrometrically and kept constant. The Cs-reservoir temperature is automatically regulated with accuracy better than 0.5%. The interelectrode gap is imaged in 1 : 1 ratio on the entrance slit of a 0.5 m Ebert scanning spectrometer. An adjustable mirror system is used simultaneously for alignment of the gap image parallel to the entrance slit and sweeping it across. The sensed radiation emerged in a 10^{-5} sr solid angle from a plasma volume of 40 microns width, 20 mm depth and 5 mm height. A good signal recovery was attained with an EMI 9558 AQ photomultiplier and a PAR HR-8 Lock-in amplifier. The BW was 0.3 Hz and 0.1 Hz for the line and continuum intensity measurements correspondingly (Fig. 1).

⁺Columbia University-ERL, New York. Fellow of the A. v. Humboldt-Foundation at Institut für Kernenergetik, Universität Stuttgart.

Work supported by the Bundesministerium f. wiss. Forschung, Bonn.

Spectroscopic Analysis

The analysis of the plasma-broadened lines of the fundamental series of Cs, reported elsewhere^{1, 2}, is used for the determination of the electron densities N_e from the measured profiles of the $5D_{3/2} - nF_{5/2}$, $n = 7, 9, 10$, transitions. The experimental profiles are shape corrected for apparatus imperfection, unfolded and evaluated via Voigt profiles³. The electron temperature is determined from the radiative recombination continuum of the 6P state :



The rate of electron transitions from the continuum into any atomic state is given by the expression⁴ :

$$\frac{dN_e}{dt} dv = N_+ N_e \sigma(v) v f(v) dv \quad (2), \text{ where:}$$

$f(v)$ = electron velocity distribution function
 $\sigma(v)$ = cross section for radiative recombination⁵
 N_+, N_e = ion and electron densities respectively

Suitable transformation of Eq. (2) yields for steady state :

$$\ln(S_\lambda \lambda^3) = K - \frac{hc}{\lambda k T_e} \quad (3), \text{ where:}$$

S_λ = intensity of radiation at wavelength λ
 K = constant

However, noting that one measures directly the amplitude of the photo-multiplier signal I_λ and not S_λ , a useful form of Eq. (3) is straightforwardly obtained :

$$\ln(I_\lambda \lambda^2 \eta^{-1}) = K^* - \frac{hc}{\lambda k T_e} \quad (4), \text{ where:}$$

I_λ = signal amplitude in volts
 η = quantum efficiency
 K^* = constant

The temperature T_e is determined from the slope $\frac{hc}{kT_e}$ of the plot of Eq. (4) vs. $1/\lambda$.

Experimental Results and Discussion

Figs. 2 and 3 represent typical line and continuum shapes. The axial distributions of the N_e and T_e ($z = 0$ at emitter) are shown in Figs. 4-9. Due to limited experimental data at this time, the curves are regarded as general trend, to be checked by farther measurements. The error limits strongly depend upon the signal-to-noise ratio and the small linewidths involved. The strong resonance transitions $7P_{3/2, 1/2} - 6S_{1/2}$ distort the shape of the continuum, thus enhancing the error in T_e . Typical error limits for N_e and T_e are presented in Fig. 6 a, b. Measurements in the proximity of the emitter are in addition impeded by the radiation of the latter and have to be corrected for. Moreover, a departure from linearity in Eqs. (3, 4) was observed for positions $z < 0.1$ mm, which suggest as an explanation the deviation, to some extent, of $f(v)$ from Maxwellian. Summarizing the results of this investigation, the following conclusions are pointed out :

1. Within the investigated range of emitter temperatures and current densities the N_e is in the order of magnitude of $10^{13} - 10^{14}/\text{cm}^3$. A comparison of $N_{e, \text{Saha}}$ to the $N_{e, \text{meas.}}$ indicates a departure from LTE. The measured densities are in most cases appreciably less than the computed N_e from Sahas equation.
2. The N_e distributions exhibit pronounced maxima in the vicinity of the emitter, which move toward the emitter with increasing T_E and current density.
3. The electron temperatures T_e increase toward the emitter and exhibit maxima in its vicinity. The electron energy distribution $f(v)$ in the very proximity of the emitter is most probably not Maxwellian.

References

1. Griem, H. R. , Plasma Spectroscopy, McGraw-Hill, New York, 1964, 1st ed. , pp. 63-104.
2. Stone, P. M. , Agnew, L. , Phys. Rev. 127 (1962), 1157.
3. Wiese, W. L. , Plasma Diag. Techniques, AP New York, 1965, p. 303.
4. Reichelt, H. H. , Thermionic Power El. Gen. , London, 1965.
5. Norcross, D. W. , Stone, P. M. , JQSRT 6 (1966), 277.

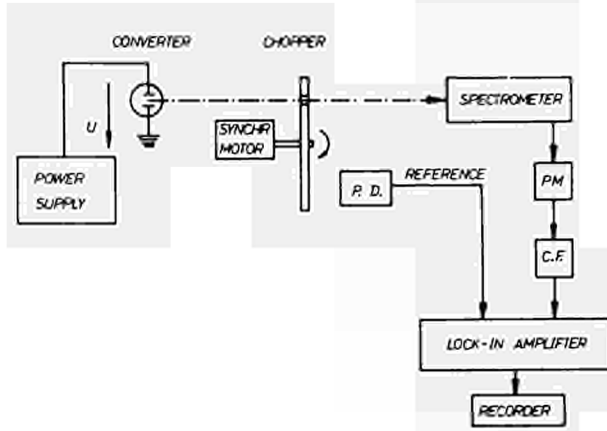


Fig. 1 Measuring Diagram

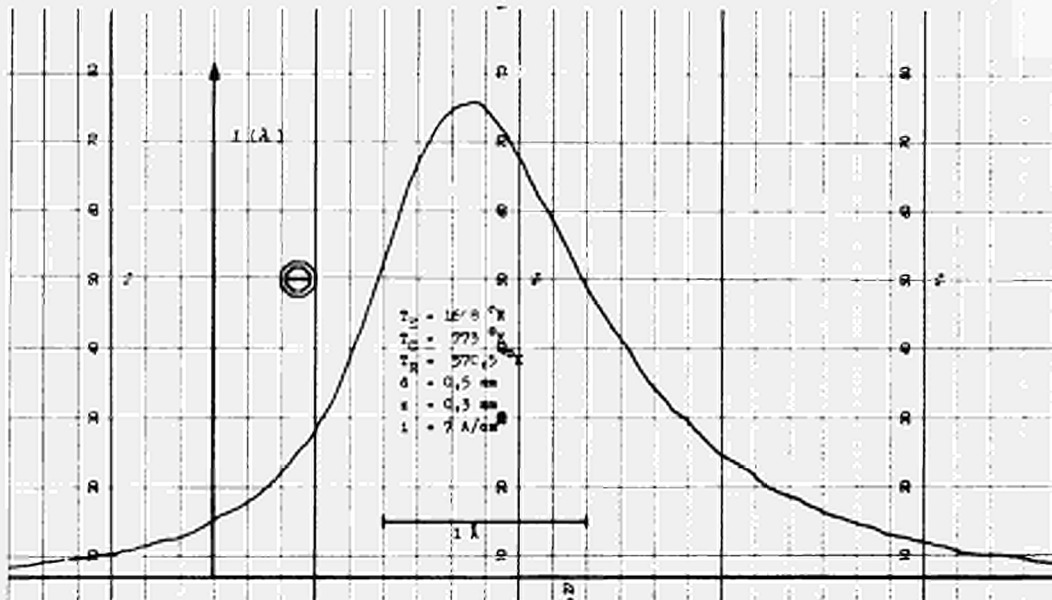


Fig. 2 Transition
7F - 5D ($I = 6825 \text{ A}$)

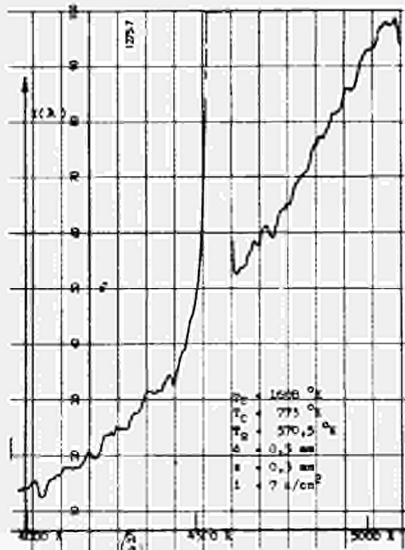


Fig. 3 Continuum Intensity

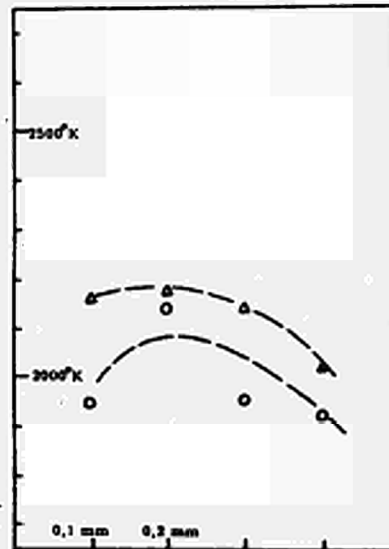
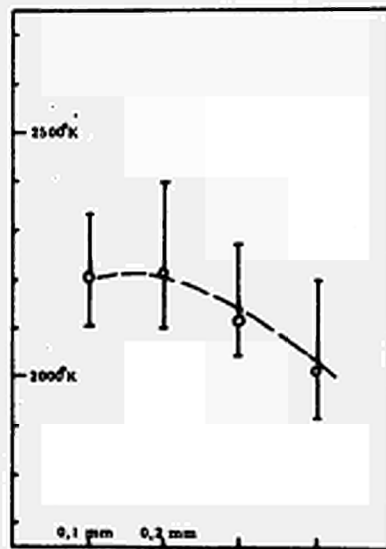
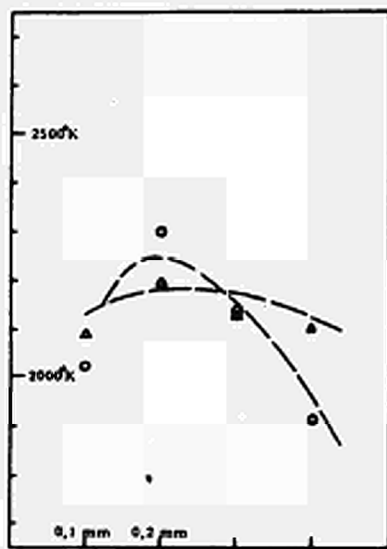
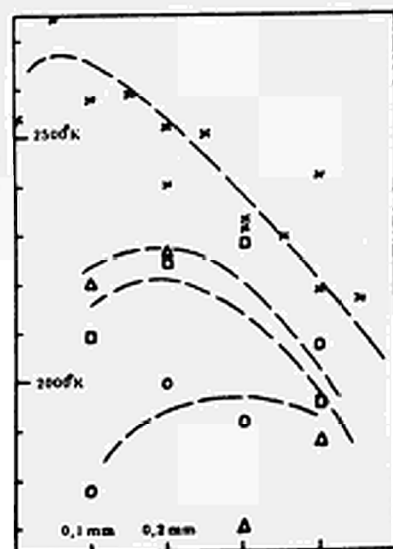
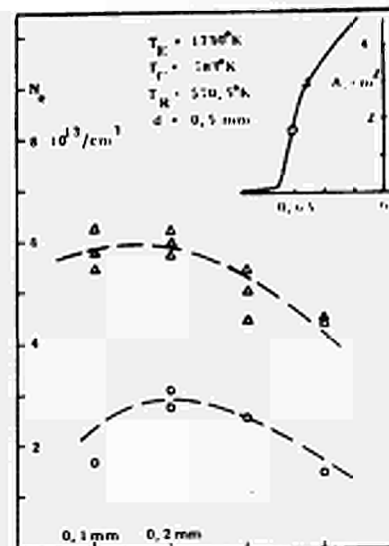
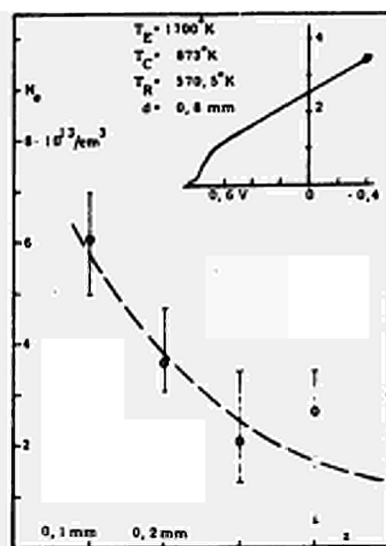
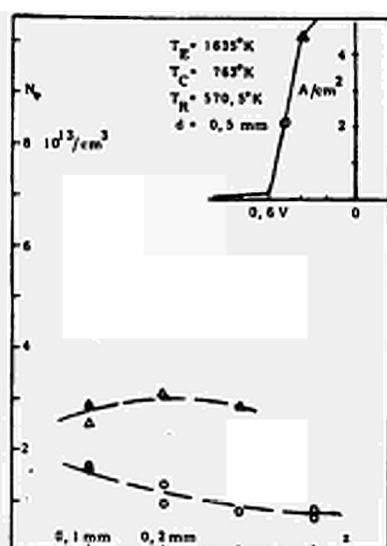
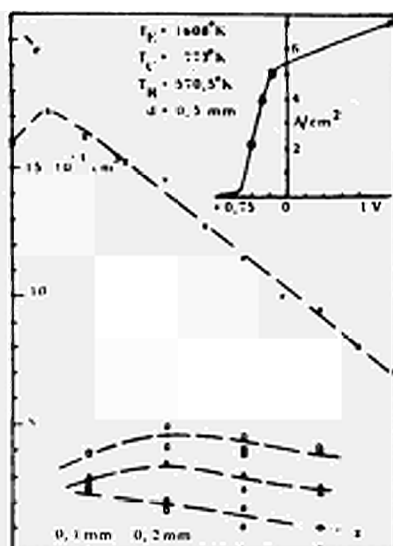


Fig. 4 a, b

Fig. 5 a, b

Fig. 6 a, b

Fig. 7 a, b

Electron Density and Temperature Profiles

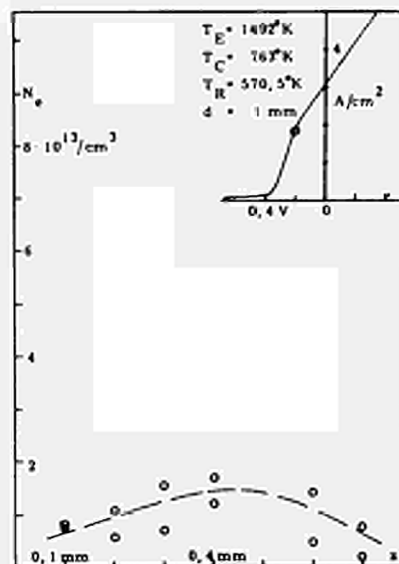
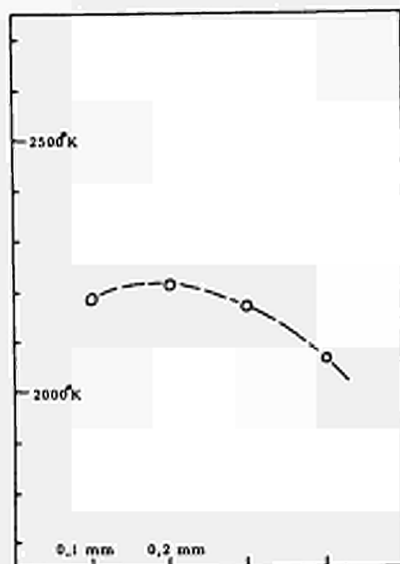
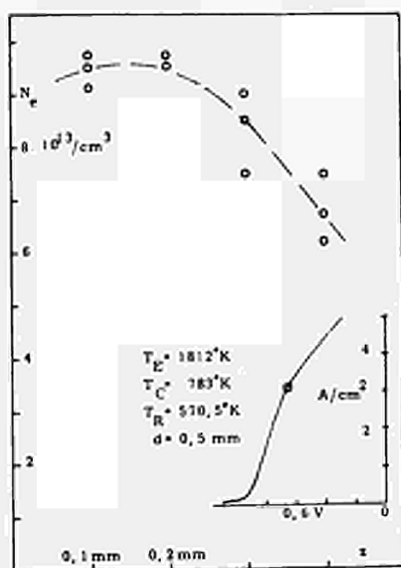


Fig. 8 a, b

Fig. 9 a

Electron Density and
Temperature Profiles

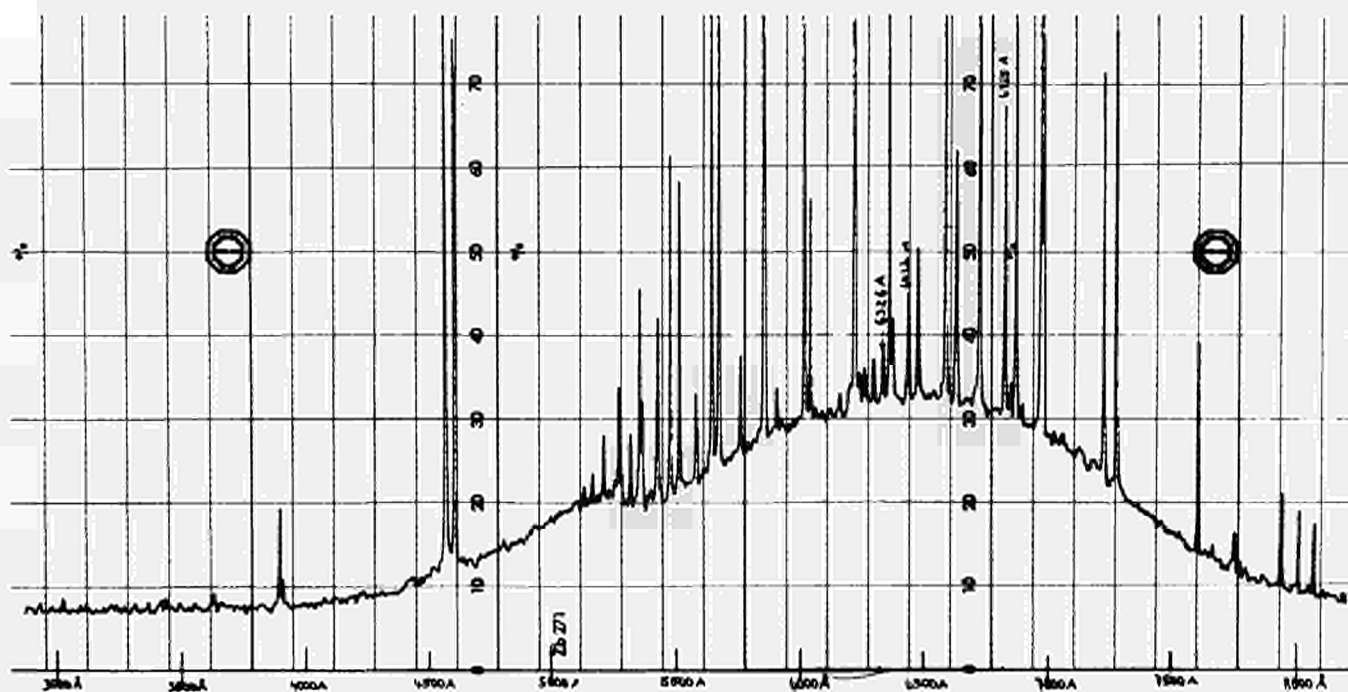


Fig. 10

Cs-Spectrum

DISCUSSION

Speaker of paper J-7: C. G. STOJANOFF.

RASOR (USA): At what point on the volt-ampere curve relative to the transition point did you take your data?

STOJANOFF (USSR): The experimental data was taken in three different points of the volt-ampere characteristic. We took one exactly in the transition region, one above and one below. That is how we obtained the result that the maximum moved towards the emitter with increasing current densities.

RASOR: What happens to the electron temperature near the emitter as you pass into the saturation region?

STOJANOFF: The electron temperature increased and the maximum moved towards the emitter.

RASOR: This change in electron temperature should correlate with changes in the dark region before the emitter. Have you compared the intensity of radiation with the existence of the maximum in electron temperature?

STOJANOFF: Actually we did not observe the dark region, in this particular set of data at least not visually. We did not do any scanning of the spectrum in that region. We just took the spectrum at the continuum.

RASOR: It does appear that the maximum is a characteristic of the obstructed mode, because it is tending to disappear in the saturation mode. Is that correct?

STOJANOFF: That depends on how you interpret this result. It is true that it tends to disappear; that is what the data says. But also the tendency is there that this maximum moves towards the emitter at increased current densities in the saturated mode. It could be first, that the maximum is not there any more or the maximum occurs very close to the emitter. We are going to perform more careful experimentation in order to confirm whether this is the case. We have been able to get as close as 50 microns to the emitter. That is presently the limit to experimental techniques.

AGNEW (IAEA): In your oral presentation you report discrepancies by factors of 3 to 5 between measured ion density and the Saha ion density.

STOJANOFF: For the calculations we used the electron temperature but I

would like to point out that the calculated densities are very sensitive to temperature variation in the Saha-equation. If you have noticed, in our experimental results we do have errors of about 200-300^o so I'm not very sure that the factor of 3 to 5 for the Saha-densities over the experimental densities is correct.

WARNER (USA): I believe that REICHELDT did observe a maximum in the electron temperature near the emitter. This was reported at the San Diego Specialist Conference.

STOJANOFF: Yes, I've heard of this but I do not have any information about it. The only information, or at least correlation with other experimental data that I am aware of, was given in the paper J-3 by Dr. DJUZHEV which was obtained by means of probes.

HANSEN (Euratom): If the electron distribution function is very non-Maxwellian in the region of the emitter, in what way would this affect the spectroscopic measurements?

STOJANOFF: The electron energy distribution, as a weight-function actually goes very strongly into the expression, so any deviation from the Maxwellian distribution would affect the spectroscopic measurements. It usually would tend to bend the shape of the continuum and we have observed some deviation from the linearity of the equation which we give in the paper, which relates the intensity of the continuum to the electron temperature near the emitter. We believe that in that region the distribution is not Maxwellian, but we do not have any further investigation in that matter.

RASOR: In paper H-7 by KUCHEROV there were some data shown in which the electron temperature measured by certain methods did show a maximum and by other methods showed quite the opposite behavior, an increase at the emitter. I wonder whether Dr. KARETNIKOV could comment on what was the difference in measurement techniques for those different electron temperatures and compare them to your measurements; i. e. which one of these acted in which way?

KARETNIKOV (USSR): In paper H-7, the electron temperatures determined from ionization level (Saha), and from line reversal, both showed the existence of a maximum near the emitter; i. e. the electron temperature drops near the emitter. However, the electron temperature determined from the recombination continuum showed an increase near the emitter, contrary to the result of STOJANOFF.

SPECTRUM OF THE LOW-VOLTAGE DISCHARGE IN A CAESIUM-FILLED DIODE

D. Glas, Eindhoven Technological University; The Netherlands

Measurements were carried out on a caesium-filled diode with a hot cathode. Its construction is shown in fig. 1. The current-voltage relation of this diode is shown for

$$P_{cs} = 0.2 \text{ mm Hg} \quad \text{and} \quad T_k = 1500^\circ\text{K} \quad (\text{fig. 2})$$

For these values of the Cs-pressure and the cathode temperature only a small part of the characteristic is found at negative anode voltages. In this part of the characteristic the diode acts as a thermionic converter.

At positive values of the anode voltage we distinguish the ignited mode and the extinguished mode. At higher cathode temperatures the characteristic shifts to the right and it is possible to find point A at negative values of the anode voltage.

The emitted spectral lines with wave lengths between 4555 \AA and 8943 \AA were studied in both modes of operation. We observed the following phenomena:

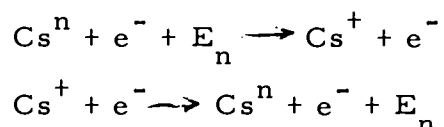
- I) In the extinguished mode only the 8943 \AA and 8521 \AA lines could be measured. So the other lines were not present or very weak.
- II) In the ignited mode also other spectral lines were present at any voltage at which that mode exists. So in the ignited mode the spectral lines can be emitted at voltages lower than their excitation voltage (except the two resonance lines mentioned above). When the anode voltage passed the excitation voltage of a specific line there was no marked change in the intensity of

of this line; also the current showed no marked change when the anode voltage passed the ionization voltage at Cs.

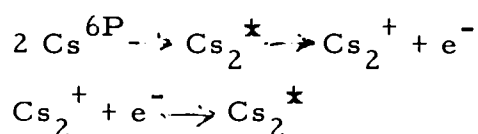
III) Transition of the ignited mode back to the extinguished mode occurs when the anode voltage \star) is decreased to 1.4 Volt i. e. the excitation potential of the 8943 Å line and at the same moment the spectrum disappears.

From III) one may conclude that the ignited mode and hence the volume ionization is coupled to the excitation voltage of the 6P state. From II) we conclude that (except for the resonance lines $6P_{1/2}$ and $6P_{3/2}$) the emission of the spectral lines is not coupled to the excitation voltage of the lines.

In recent publications (1-4) a theory is developed that in the ignited mode multi-stage ionization and recombination is the predominant process to establish the ion density



The results of the measurements III) and the above theory suggest, that the excitation of the 6P level by electrons is the first step of the multistage ionization process. Apparently photon-induced excitation ⁶⁾ is not significant at the cathode temperature and electrodes spacing used during our measurements. However also molecular ion formation takes place (through impact of two excited 6P atoms)



The dissociative recombination occurs at a high rate and Witting ⁵⁾ showed that there is a high probability of dissociation of the excited molecule Cs_2^\star in two neutral atoms, one or both of which may be in an excited state. This suggests, that the emission of the spectral lines is due also to the transition to lower states of the excited atoms formed after the dissociation of the Cs_2^\star molecule.

Acknowledgements

I would like to express my thanks to Prof. Groendijk and Mr. Kuis for the helpful discussions on the subject.

I gratefully acknowledge the assistance of Mr. Bogaerts for carrying out the measurements.

\star) corrected for the contact-potential difference

transition to lower states of the excited atoms formed after the dissociation of the Cs_2^* molecule.

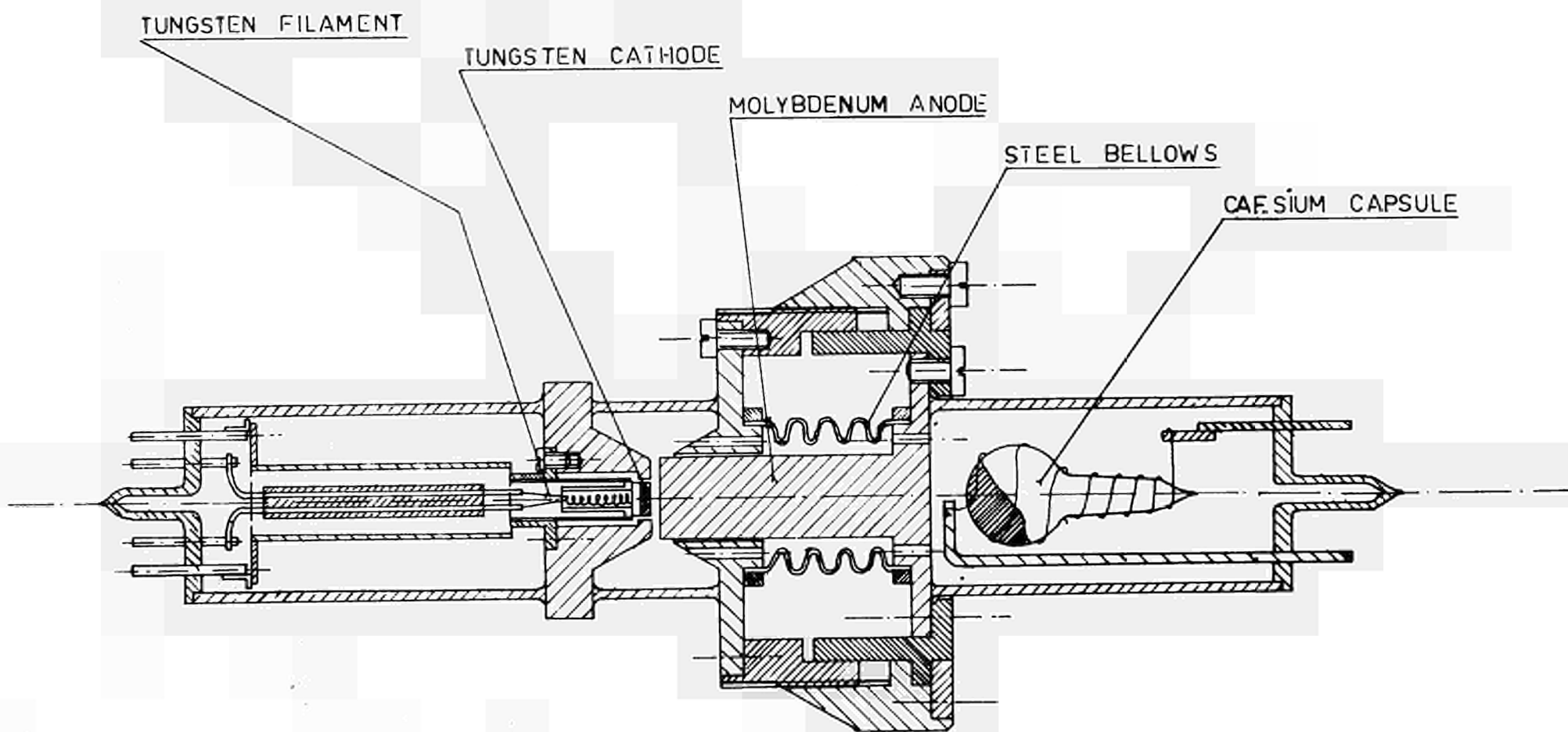
Acknowledgments

I would like to express my thanks to Prof. Groendijk and Mr. Kuis for the helpful discussions on the subject.

I gratefully acknowledge the assistance of Mr. Bogaerts for carrying out the measurements.

References

- (1) WILKINS, D.R.; GYFTOPOULOS, E.P.; "Journal of applied Physics" 37, 2888 and 2892 (1966).
- (2) HINNOV, E.; HIRSHBERG, J.G., "Electron-ion Recombination in Dense Plasmas" Phys. Rev. 125, 3, February 1962 (page 795).
- (3) KUCKES, A.F.; MOTLEY, R.W.; HINNOV, E.; and HIRSHBERG, J.G., "Recombination in a Helium Plasma", Phys. Rev. Letters 6, 7, page 337, April 1961.
- (4) BYRON, S.; STABLER, R.C.; and BORTZ, P.I., "Electron-Ion Recombination by Collisional and Radiative Processes" Phys. Rev. Letters 8, 9 May 1962 (page 376).
- (5) WITTING, H.L.; and GYFTOPOULOS, E.P., "Journal of applied Physics" 36, 1328 (1965).
- (6) POLLOCK, D.H.; and JENSEN, A.O., "Journal of applied Physics" 36, 3184 (1965).



EXPERIMENTAL DIODE

fig. 1

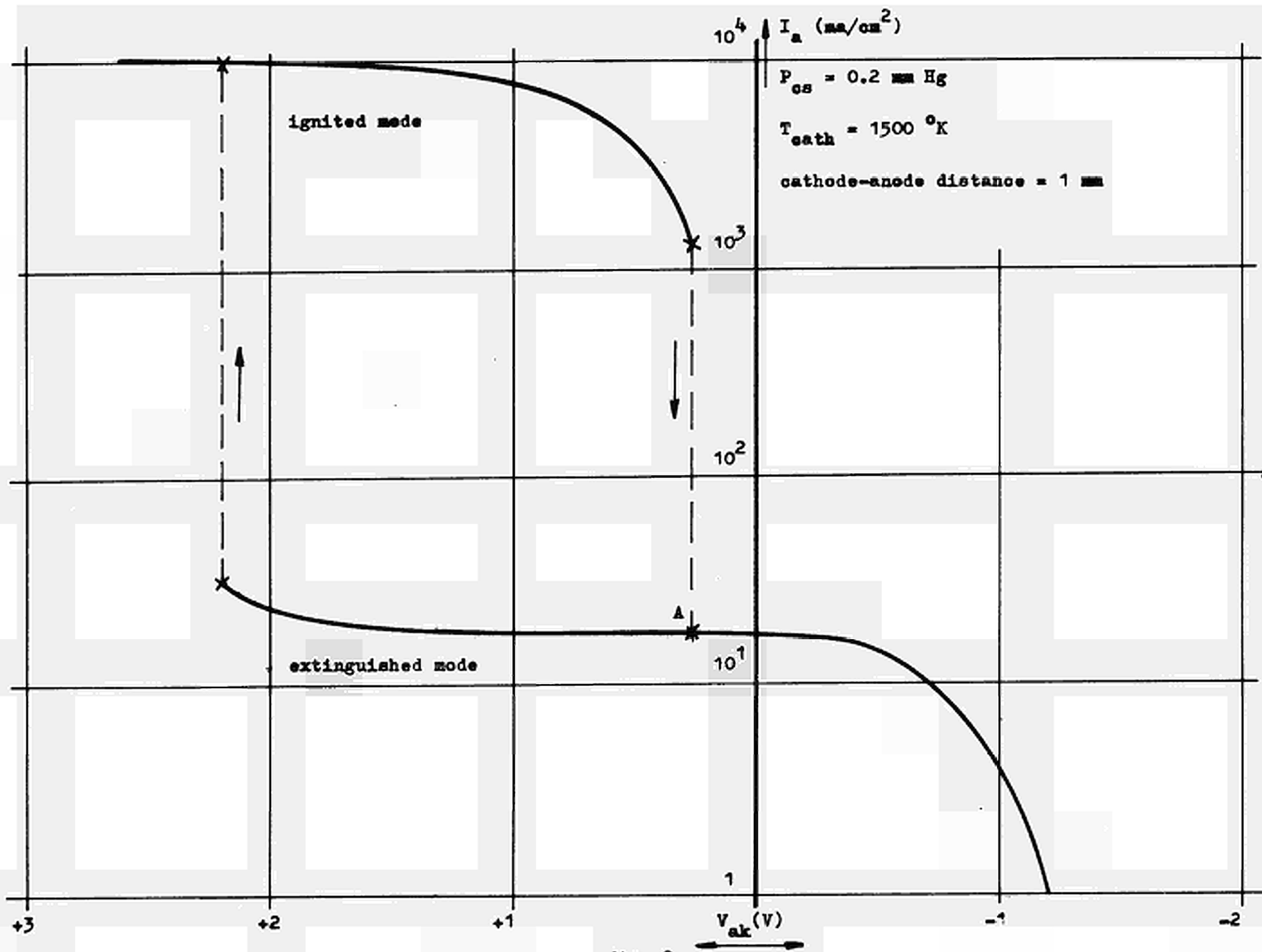


Fig. 2

DISCUSSION

Speaker of paper J-8: D. GLAS.

MOSHKVIN (USSR): Can you consider the results of this work as a proof that the main mechanism of ionization is the molecular mechanism?

GLAS (The Netherlands): The molecular ion formation is not the dominant process in establishing the ion-density because the dissociative recombination process is a very fast process and however molecular ion formation takes place, every ion formed is immediately removed by the fast dissociation process, so the main process in establishing the ion-density is the multi-stage process, giving atomic ions.

WILSON (USA): H. WITTING built a converter with a pin hole in the collector. Behind the pin hole he had a mass spectrograph. He observed that just as the arc initiated there were some Cs_2^+ ions. At greater current densities the ions were essentially all single atoms, not molecular ions.

ACTION DU RAYONNEMENT SUR LE FONCTIONNEMENT DE CONVERTISSEURS THERMOIONIQUES CONVERSION DU RAYONNEMENT SOLAIRE

J.P. DAVID et F. FLORET
Faculté des Sciences de Marseille

RESUME

On étudie la possibilité de déplacer le point de fonctionnement d'un convertisseur thermoionique à vapeur de césium en faisant interagir un rayonnement visible ou proche ultra-violet avec les atomes alcalins de manière à parfaire la neutralisation de la charge d'espace par création d'ions supplémentaires. Divers mécanismes sont examinés : photoionisation directe, photoionisation par étapes, ionisation par les électrons, action sur l'ionisation de surface. Expérimentalement, deux effets sont observés, en illuminant l'espace inter-électrode du convertisseur avec le rayonnement issu d'un flash au xénon : un effet réversible, pour les régimes à faible température d'émetteur, et un effet irréversible avec amorçage du régime d'arc, dans d'autres conditions de fonctionnement. Des applications solaires ont été envisagées et une première réalisation est décrite.

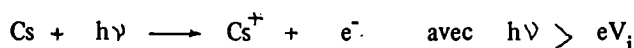
INTRODUCTION

On sait que, dans les convertisseurs thermoioniques à vapeur de césium, la plupart des ions nécessaires à la neutralisation de la charge d'espace sont produits par ionisation des atomes alcalins sur la surface chaude de l'émetteur. La condition de neutralisation totale n'est vérifiée que si la température de l'émetteur T_E dépasse une valeur minimale T_{Emin} , la température du bain de césium T_{Cs} étant fixée. Nous nous sommes donc intéressés dans le cas de convertisseurs dont $T_E < T_{Emin}$ à la possibilité d'améliorer cette neutralisation par l'action d'un rayonnement, lequel peut également servir pour le chauffage de l'émetteur. Sur le plan expérimental, cela entraîne quelques difficultés techniques, pour faire pénétrer le rayonnement dans l'espace inter-électrode; sur le plan fondamental, cela conduit à examiner les processus pouvant donner lieu, en volume ou à la surface de l'émetteur, à la création d'ions supplémentaires.

I - MECANISMES D'INTERACTION RAYONNEMENT - VAPEUR ALCALINE

Les processus envisagés, sont les suivants : photoionisation directe, photoionisation par étapes, ionisation par collisions électroniques, action sur l'ionisation de surface.

a - La photoionisation directe correspond à l'interaction



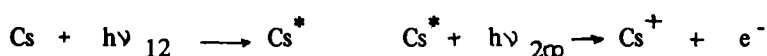
V_i étant le potentiel d'ionisation de l'alcalin. LUKE (1) a examiné cette influence du rayonnement en calculant la variation de l'intensité du courant débité par un convertisseur recevant, dans l'espace inter-électrode, un tel flux photonique.

En utilisant la distribution spectrale du rayonnement solaire, en empruntant la section efficace d'ionisation à BRADDICK et DITCHBURN (2) et le coefficient de recombinaison à MOHLER (3), il obtient une densité de courant électronique.

$$J = 1,63 \cdot 10^3 C^{1/2} T_E^{1/2} T_{Cs}^{-3/4} \exp\left(-\frac{4455}{T_{Cs}}\right) \text{ A. cm}^{-2}$$

C étant un facteur de concentration du rayonnement reçu. Pour $C = 1000$, $T_E = 1500^\circ \text{K}$, J prend des valeurs comprises entre 1 et 10 A. cm^{-2} lorsque T_{Cs} varie entre 450°K et 600°K . Mais, dans les convertisseurs que nous avons expérimentés, la proportion de rayonnement d'énergie $h\nu > eV_i$ (soit $3,89 \text{ eV}$ pour le césium, donc de longueur d'onde $\lambda < 3189 \text{ \AA}$) qui parvient dans l'espace inter-électrode reste faible et ce processus doit être limité.

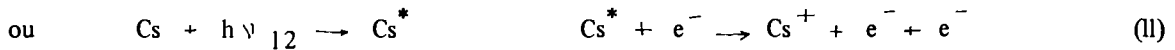
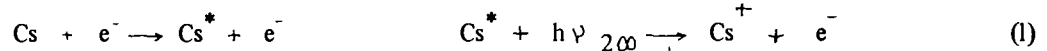
b - Photoionisation par étapes correspond au schéma réactionnel



L'ionisation se fait par absorption successive de deux photons. Le rendement ionique a été calculé par divers auteurs (4), (5) et peut s'écrire :

$$\left(\frac{N^+}{N_1}\right)^2 = \frac{1}{N_1} \frac{B_{12} C u(\nu_{12})}{(\alpha_T - \alpha_{\omega_2})C + \alpha_T A_{21}} \quad \text{avec} \quad C = \int_{\nu_{200}}^{\infty} \sigma(\nu) c \frac{u(\nu)}{h\nu} d\nu$$

où N^+ désigne la densité d'ions, N_1 la densité d'atomes dans l'état fondamental, $u(\nu)$ la densité spectrale monochromatique, $\sigma(\nu)$ la section efficace de photoionisation, α_T , α_{ω_2} les coefficients de recombinaisons total et sur le niveau 2, A et B les coefficients d'Einstein. Ce rendement reste faible pour les densités photoniques classiques. On peut envisager aussi l'ionisation par étapes, faisant intervenir des électrons pour l'une des étapes ou par les deux :



Les électrons libres qui interviennent sont ceux de la queue de la distribution ou ceux qui sont activés par interaction avec le rayonnement. Pour le processus II, BENSIMON (4) a donné le rendement ionique :

$$\frac{N^+}{N_1} = \frac{1}{\alpha_T} \int_{V_i - V^*}^{\infty} \left(\frac{2eV}{m}\right)^{1/2} f_e(V) Q \frac{c^3}{8\pi h \nu_{12}} u(\nu_{12}) dV$$

où V est le potentiel de l'électron
 Q la section efficace totale de collision
 $f_e(V)$ la fonction de distribution des électrons libres.

Cet auteur a calculé, en se fixant certaines données numériques, l'importance de ce rendement. Aux basses températures électroniques (inférieures à 2000 °K), ce rendement ne dépasse pas 10^{-4} , avec prédominance des transitions utilisant l'état excité 8P comme étape. Pour des températures électroniques supérieures à 3500 °K, les transitions par les états 6P deviennent prépondérantes et pour des températures électroniques de 8000 °K, le rendement ionique pourrait atteindre quelques pour cent.

c - Action sur l'ionisation de surface

Dans ce processus (6), les atomes de césium seraient excités par absorption d'un quantum lumineux avant d'être ionisés sur la surface chaude de l'émetteur, ce qui devrait se traduire par une amélioration du rendement ionique. Un calcul simple conduit à un rapport entre les flux d'ions provenant d'atomes excités, soit μ^{+*} et d'atomes non excités, soit μ^+ .

$$\frac{\mu^{+*}}{\mu^+} = \frac{\epsilon}{1-\epsilon} \frac{1 + 2 \exp\left\{e(V_i - \phi_E)/kT_E\right\}}{1 + 2 \exp\left\{e(V_i^* - \phi_E)/kT_E\right\}}$$

où ϵ donne la proportion d'atomes excités, V_i^* est le potentiel d'ionisation à partir de l'état excité considéré. Pour $V_i = 3,89$ V, $V_i^* = 2,44$ V, $T_E = 1500$ °K, $\epsilon = 10^{-2}$, pour un flux d'atomes neutres incidents de 10^{18} cm $^{-2}$ s $^{-1}$, ce rapport peut atteindre la valeur 10. Ce processus d'activation de l'effet Langmuir implique que le rayonnement excitateur puisse pénétrer suffisamment dans l'espace inter-électrode.

II - ETUDE EXPERIMENTALE

Pour montrer l'influence du rayonnement sur le fonctionnement d'un convertisseur, nous avons expérimenté sur des enceintes permettant de faire pénétrer le rayonnement dans l'espace inter-électrode, soit tangentiellement à l'émetteur (fig.1) soit perpendiculairement à l'émetteur, à travers un collecteur percé de trous (fig.2). Les fenêtres transparentes sont en saphir peu attaqué par le césium à chaud. L'émetteur en molybdène est chauffé par bombardement électronique. L'espace inter-électrode est, suivant le cas compris entre 0,5mm et 1mm. La figure 3 donne les caractéristiques I-V relevées dans le cas d'un convertisseur du premier type et fonctionnant dans les conditions suivantes : $T_{Cs} = 623^{\circ}K$ et $T_E = 1685^{\circ}K, 1730^{\circ}K, 1785^{\circ}K$. Les caractéristiques (1) et (2) correspondent au régime d'arc. La figure 4 montre la variation du courant débité dans la résistance de charge lorsqu'on illumine l'espace inter-électrode avec le rayonnement provenant d'une lampe flash au xénon, le convertisseur fonctionnant dans les conditions $T_{Cs} = 623^{\circ}K, T_E = 1685^{\circ}K, I = 0,2 A$. On note alors pour une impulsion lumineuse de quelques millisecondes, une variation d'intensité atteignant 100 %.

Une autre action du rayonnement peut être observée avec le convertisseur précédent, fonctionnant dans des conditions voisines de celles correspondant à l'apparition du régime d'arc : pour $T_{Cs} = 623^{\circ}K, 1685^{\circ}K < T_E < 1730 K, I_{cc} = 2A, V = 0,1 V$. L'illumination dans l'espace inter-électrode par le rayonnement issu du flash fait passer de façon irréversible le courant à une valeur d'environ 5 ampères. Si maintenant on fait varier la résistance de charge jusqu'à annuler pratiquement le courant, on décrit une caractéristique d'arc, puis en ramenant la charge à sa valeur initiale, on revient à $I_{cc} = 2A$. Le cycle peut être décrit plusieurs fois de suite, l'amorçage du régime d'arc étant obtenu par action de l'impulsion lumineuse. Ces résultats ont été retrouvés sur des convertisseurs du type représenté figure 2, en éclairant à travers le collecteur percé de trous. La figure 5 donne quelques caractéristiques I-V d'un tel convertisseur fonctionnant dans les conditions $T_E = 1430^{\circ}K$ et pour des températures du bain de césium s'échelonnant entre $498^{\circ}K$ et $598^{\circ}K$. Le dispositif expérimental permettant de relever les caractéristiques I-V a été modifié de façon à pouvoir balayer un domaine de tensions s'étendant entre $+3V$ et $-3V$ et permettant d'explorer la zone où l'enceinte ne fonctionne plus en convertisseur. :

La figure 6 donne, en trait fin, la caractéristique I-V pour le convertisseur fonctionnant à $T_{Cs} = 548^{\circ}K$ et $T_E = 1460^{\circ}K$. Le régime d'arc ne peut être amorcé que si V devient légèrement "négatif". Fixons la charge du convertisseur de façon à ce que le point de fonctionnement soit en A. Le rayonnement issu du flash le fait passer en B avec amorçage de l'arc. Ces quelques expériences montrent l'intérêt pratique que l'on peut avoir à introduire le rayonnement dans l'espace inter-électrode d'un convertisseur à césium et l'application éventuelle à la conversion solaire. Elles sont en accord, avec les résultats obtenus par J. BENSIMON (4) dans des conditions expérimentales différentes.

III - REALISATION ET ESSAIS DE CONVERTISSEURS SOLAIRES

Nous avons réalisé des convertisseurs solaires dans lesquels le rayonnement peut intervenir :

- comme moyen de chauffage de l'émetteur
- comme moyen de parfaire la neutralisation de la charge d'espace ou d'amorcer le régime d'arc suivant les conditions de fonctionnement.

A la suite de travaux réalisés à la C.S.F. sur des convertisseurs à émetteur multicapillaire, nous nous sommes proposés d'adapter cette structure d'émetteur à des convertisseurs solaires.

L'ensemble du convertisseur est en titane qui convient mieux au point de vue technologique pour les soudures et scellements utilisés. L'émetteur est constitué par un ruban de molybdène en le faisant passer entre deux molettes et en l'enroulant ensuite en spirale. Il a une hauteur $h = 6mm$, un diamètre $\Phi = 12mm$. Les fenêtres sont soit en saphir, soit en quartz, et ont pour diamètre 50 ou 60 mm. Mais les fenêtres en saphir résistent mal aux chocs thermiques que nous leur avons fait subir et pour le moment nos résultats correspondent à des convertisseurs à fenêtre de quartz.

Le convertisseur est placé au foyer d'un miroir parabolique recevant le rayonnement issu d'un arc au carbone. La puissance lumineuse disponible au foyer est de l'ordre du kilowatt. La tache focale a 14mm de diamètre. Les figures 8 et 9 donnent les caractéristiques courant-tension relevées pour $T_E = 1430^\circ\text{K}$ et $T_E = 1710^\circ\text{K}$ et pour des températures du césium variant entre 175°C et 350°C . Ces courbes montrent qu'il faut atteindre des températures d'émetteur de l'ordre de 1700°K pour commencer à avoir des courants et des puissances dignes d'intérêt. Il semble qu'il soit possible d'accroître les courants en agissant sur la résistance propre de l'émetteur multicapillaire.

CONCLUSION

D'autres résultats de conversion solaire nous paraissent nécessaires avant de pouvoir tirer des conclusions définitives. Mais de nombreux problèmes technologiques restent encore à résoudre.

Néanmoins, les expériences décrites mettent en évidence l'influence que peut avoir le rayonnement sur le fonctionnement d'un convertisseur thermoïonique.

BIBLIOGRAPHIE

- (1) LUKE, K.P.
" Photoionisation of Cesium Atoms by Solar Radiation : Application to a low temperature cesium thermoionic diode ", Solar Energy, Vol. IX (1965), 110
- (2) BRADDICK, H.J.J. et DITCHBURN, R.W.
" Continuous absorption of light in cesium vapour"
Proc. Roy. Soc. A, 143 (1935), 472
- (3) MOHLER, F.L.
" Recombination in the afterglow of a cesium discharge "
J: of Research of the National Bureau of Standards, 19, (1937), 447
- (4) BENSIMON, J.
" Le convertisseur thermoélectronique - Problèmes relatifs à la charge d'espace électronique et sa neutralisation "
Thèse de Doctorat - Paris 1966
- (5) MILLET, J.
" Etude des processus de photoionisation de la vapeur de césium "
Thèse de Doctorat de 3ème cycle - Marseille 1967 -
- (6) FLORET, F.
" Originalité des convertisseurs thermoïoniques solaires "
Thèse de Doctorat de 3ème cycle - Marseille 1967 -

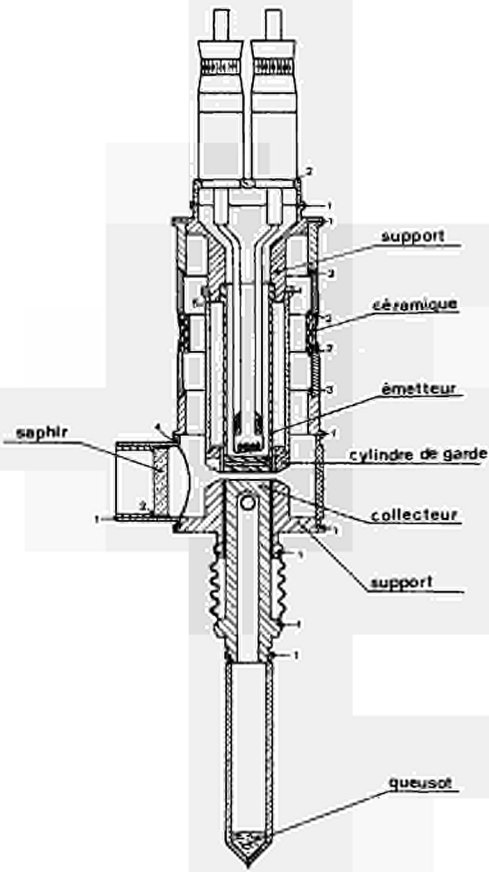


fig . 1

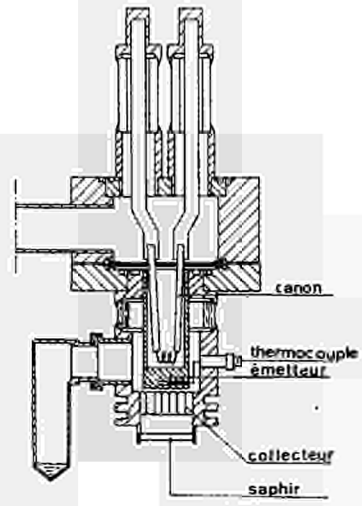


fig . 2

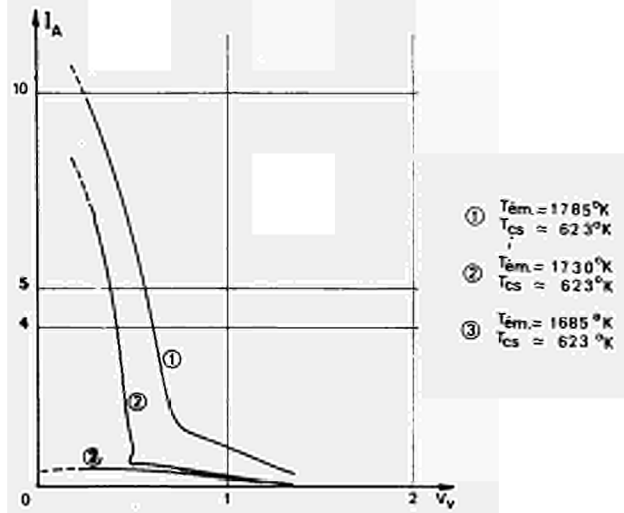


fig.3

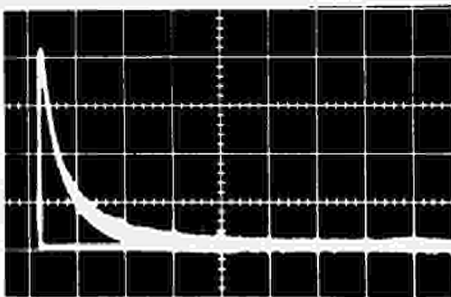


fig.4 : $I = f(t)$

dév. hor. : 1 car = 2 ms

dév. vert. : 1 car = 50 mA

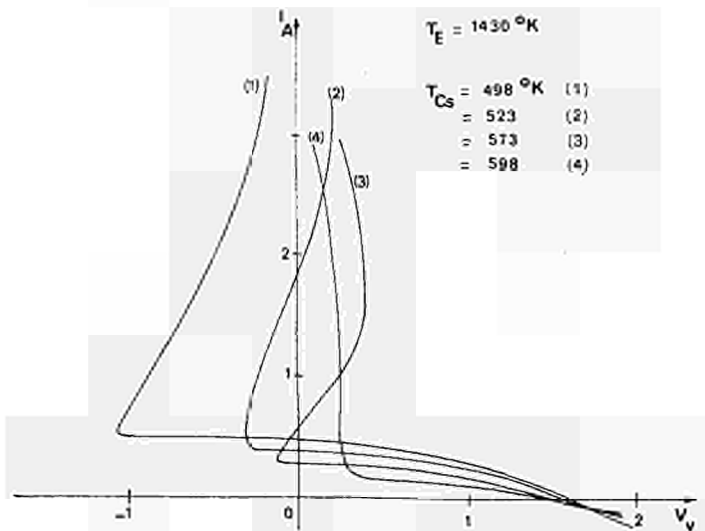


fig. 5

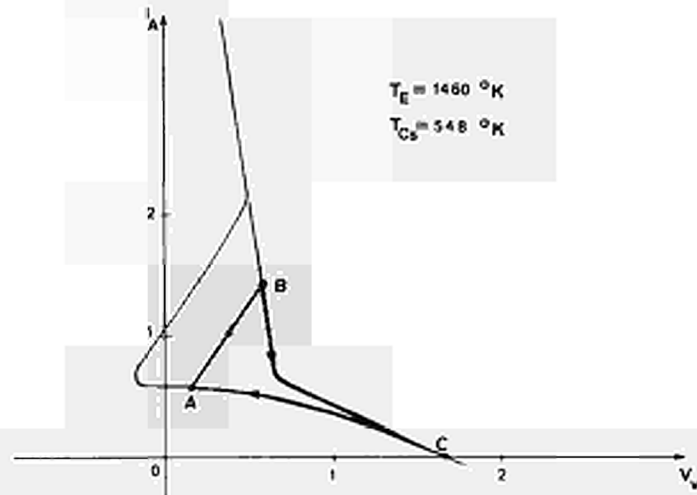


fig. 6

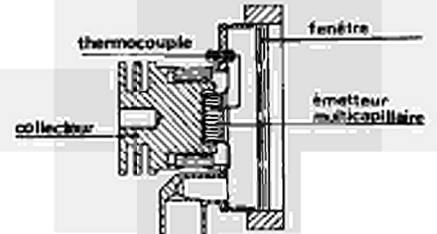


fig. 7

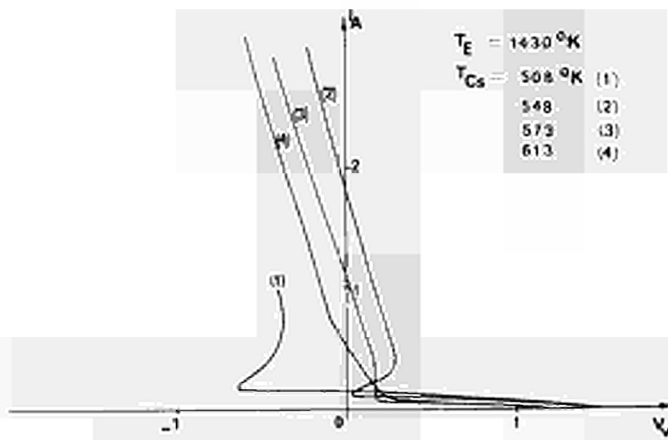


fig. 8

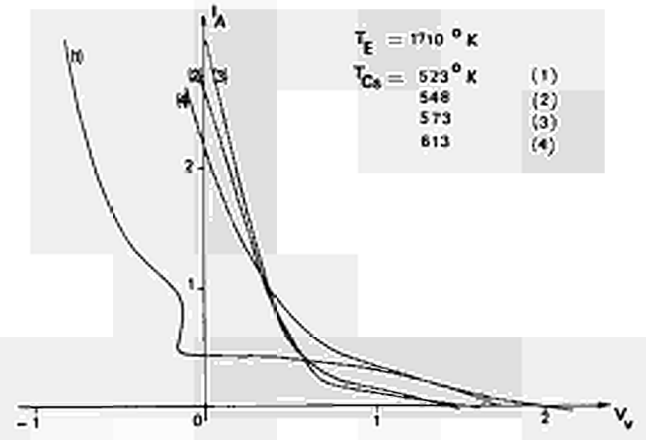


fig. 9

COMMENTS ON
WORK FUNCTION THEORIES*

by

Elias P. Gyftopoulos
Thermo Electron Corporation[‡]
Waltham, Massachusetts (USA)

INTRODUCTION

The emission properties of the surfaces of the electrodes of a thermionic converter play the most important role in the determination of the optimum performance characteristics of the converter. Future advances in converter performance may well be achieved by means of better electrode surfaces. This point is illustrated by the substantial experimental effort which presently is devoted to the study of surface properties. An example of such a property is the work function. The value of the work function depends on the material, the crystallographic orientation of the surface, the degree to which the surface is covered by adsorbates, and the temperature of the surface.

The theoretical understanding of surface properties is not as advanced as it might be. Although many practical results have been obtained, there is still a lot of work which needs to be done.

The purpose of this paper is to discuss briefly some of the theoretical work which has been done about surface properties, with emphasis on the work function of electrodes for thermionic converters only. The paper is not meant to be an exhaustive or even adequate review of the literature on the subject. It attempts to focus attention on a few points only.

* Invited paper.

[‡] On sabbatical leave from Massachusetts Institute of Technology, Cambridge, Massachusetts, U. S. A.

The paper is organized as follows. First, the definition of the work function ϕ is given. Although this definition is well known, it is repeated here in order to focus attention on the importance of the points just outside the surface and on the requirements for a rigorous calculation of the work function. Second, the information needed for the calculation of ϕ is discussed. This information is not available and very likely will not become available for many years to come. Third, theoretical analyses of bare work functions are briefly reviewed. From the review of the limited number of approximate calculations which have been performed it is concluded that the understanding of surface phenomena is neither complete nor accurate. From the review of the semi-empirical correlations it is concluded that only one of these correlations attempts to account for the dependence of ϕ on crystallographic orientation. Fourth, analyses of work functions of composite surfaces are briefly summarized. From the summary of some approximate calculations it is seen that work in this area is minimal and inconclusive. From the summary of the two semi-empirical correlations used in the field of thermionic conversion it is concluded that both correlations yield practical numerical results but that no particular fundamental significance can be assigned to the models used for their derivation.

DEFINITION OF WORK FUNCTION

Given a surface of a crystal lattice, the work function ϕ of the surface is defined as the reversible work per electron required to take an infinitesimal charge in equilibrium with the electrically neutral lattice to a state of zero entropy and zero energy at a point just outside the surface. This is also the definition of the negative of the value of

the chemical potential of the points just outside, or the negative of the value of the electrochemical potential with respect to the points just outside. Work function is, in general, a function of the temperature of the surface.

It must be noted that ϕ can be regarded as a meaningful property of a surface only with respect to the points just outside. These points are about 500 Å from the plane of the surface lattice-sites. Operationally, they are defined as the points at which the value of the image force experienced by an electron escaping from the surface (the value of the correlation force) equals that of the force due to the space charge, in an arrangement in which the crystal and the adjacent electron gas phase are in thermodynamic equilibrium. Such an arrangement may be a thermionic converter with identical electrode surfaces, kept at the same temperature. The equality of the two types of forces means the following. Beyond the points just outside, the change in the potential energy of the image force is negligibly small while that of the space charge may be appreciable. On the other hand, before the points just outside, the change in the potential energy of the image and other interfacial forces is abrupt while space charge effects are completely negligible.

Without the concept of the points just outside, all surfaces of a given material would have either the same value of work function, independent of crystallographic orientation, or values of work function which depend on the magnitude of the space charge effects.

Experimentally, an apparent or Richardson work function ϕ^* is deduced from Schottky plots at different temperatures, extrapolated to zero field conditions. Implicit in this measurement of ϕ^* is the

assumption that ϕ is approximately a linear function of temperature. It can be readily shown that this assumption is equivalent to saying that the value of the apparent work function equals that of ϕ at zero degrees Kelvin.

More often than not, it is difficult to associate an accurate experimental value with the work function of a surface. The reason is not only because of errors in the experimental procedure but primarily because it is difficult to establish the nature of the surface with regard to either crystallographic orientation, or degree of contamination, or both.

INFORMATION NEEDED FOR THE CALCULATION OF ϕ

The rigorous calculation of the work function ϕ of a surface of a metal would require knowledge of the energy eigenvalues of the crystal regarded as an open thermodynamic system, namely the eigenvalues for all possible degrees of charging. In other words, given a piece of metal, complete sets of energy eigenvalues must be found for the metal being electrically neutral, being charged by one, two, . . . positive units of charge, and being charged by one, two, . . . negative units of charge. These sets of eigenvalues can be used in a well specified formalism, namely the formalism of grand canonical ensembles, to compute the electrochemical potential of the neutral metal.¹ If the arbitrary zero energy reference level is taken at the points just outside the surface, the negative of this electrochemical potential will be equal to ϕ^\ddagger . For an example of such a calculation of the electrochemical potential of an atom with Z electrons see reference 2. The procedure for the calculation of ϕ would be the same as that in reference 2, except that the energy eigenvalues would be those of the metal.

[‡] Thermodynamically, the value of the work function at zero temperature can be defined only as a limit of the value of ϕ as the temperature T approaches zero from positive values of T.

It is clear that the above rigorous approach to the calculation of ϕ is presently impossible and, therefore, drastic approximations are necessary. Nevertheless, knowledge of the exact procedure provides a useful reference for the interpretation of the various approximations that might be used in practice.

BARE WORK FUNCTIONS

Approximate Calculations. For the calculation of the work function of a surface of a pure metal, of the so-called bare work function, the following approximate procedure has been used. First, the calculation is restricted to that of the value ϕ^* of ϕ at zero temperature. Attempts are subsequently made to estimate an approximate temperature coefficient of ϕ .³ Second, the motions of the ion cores of the crystal are neglected. In other words, the Born-Oppenheimer approximation is used for the quantum-mechanical operator of the crystal. This approximation results in a many-electron problem. Third, the many-electron problem is approximated by an one-electron problem. The one-electron eigenvalue problem is solved and the interfacial electron motive corresponding to the ground state of the electronic structure is computed. In the context of the one-electron approximation, the value of ϕ^* is given by the difference between the values ψ_1 of the motive of the points just outside the metal surface and μ_F of the Fermi energy. The Fermi energy is taken either as that of the free-electron model or as that of some band structure calculation.

The interfacial motive is found to be the sum of three terms. One term is purely electrostatic and is due to the asymmetric charge distribution at the surface. This term is called the dipole moment effect. Another term accounts for the fact that an electron does not

act on itself. It is called the exchange effect (or exchange correction). Finally, the third term accounts for the fact that the presence of one electron at a particular position alters the distribution of and, hence, the potential energy due to the other charges. The third term is called the correlation effect. The three effects are not independent of each other but very closely interrelated.

Approximate calculations of the type discussed above have been made by several authors.⁴⁻⁷ Because of numerical difficulties, only monovalent metals are treated, and the crystallographic orientation of the surface is not considered explicitly (i. e. , all interfacial phenomena are analyzed as one-dimensional). The results are qualitatively similar and suggest the following conclusions.⁴

(a) The interfacial motive is largely due to exchange and correlation effects rather than ordinary electrostatic effects. A similar conclusion applies to ϕ^* .

(b) There is no single interfacial motive which is satisfactory for electrons of all velocities. Each electron, so to speak, has its own motive.

(c) The dipole moment effect is relatively small for monovalent metals.

Although these conclusions are informative, their generality is questionable. For example, it is generally accepted that exchange and correlation effects are important in determining both the electronic structure and the interfacial electron motive of a metal. As discussed by Slater,⁸ however, the dependence of these effects on electron velocity (conclusion (b) above) is a consequence of the approximations

introduced in the calculations rather than a representation of a true physical phenomenon.

With regard to the dipole moment effect, the situation is even more ambiguous. For monovalent metals, conclusion (c) cannot be judged because the accuracy of the expressions used for exchange and correlation effects is not known. For multivalent elements, many authors believe that the dipole moment effect is larger than that for monovalent elements. In fact, it is often stated that differences in the values of work functions of surfaces of the same metal but of different crystallographic orientations are due only to differences in the magnitude of the dipole moment effect.⁹⁻¹⁰ This statement cannot be correct. Exchange and correlation effects may be substantially different for different surfaces of the same element and, hence, may be partly the cause of the differences in work functions. Moreover, it may be argued that since the dipole moment effect is closely inter-related to the other effects, if the dipole moment effect changes the other effects must also change. It appears that no general conclusions can be stated until surface exchange and correlation effects are analyzed more accurately and by means of three-dimensional models, namely models which account explicitly for the crystallographic orientation of the surface.

The thermodynamic proof that "the difference in work functions of two surfaces of the same metal is due to dipole moment effects"¹⁰ is not correct. The reason is as follows. Essential to the proof in reference 10 is the assumption that the average electrostatic potential ψ_0 in the metal is uniform. The value of the average potential, however, depends on the direction along which the averaging is performed and, therefore, this value is different for directions normal to surfaces of

different crystallographic orientation. The dependence of the average of the electrostatic potential on the direction along which the averaging is performed is related to the directional dependence of thermoelectric properties of crystals.¹¹

In summary, much work needs to be done on surfaces even for a satisfactory qualitative understanding of the factors which contribute to the value of the work function.

Semi-empirical Correlations. A number of semi-empirical correlations have been derived for ϕ^* . These correlations attempt to relate ϕ^* to known experimental quantities either of the metal itself or of the atoms of the metal. They are derived by means of a variety of arguments borrowed from quantum mechanics, electrostatics, chemistry, etc.¹²⁻¹⁷ With the exception of one correlation,¹⁷ all others do not account for the dependence of ϕ^* on crystallographic orientation. Because of its relative newness, the correlation of reference 17 is discussed in the Appendix.

It should be noted that an important consideration in any attempt to correlate values of work functions of polycrystalline surfaces is the distribution of patches on the surface. The important problem of patch effects is not discussed in this paper.

WORK FUNCTION OF COMPOSITE SURFACES

General Remarks. A composite surface is defined as the uniform or non-uniform surface of the solid of an element covered by a fractional or a full monolayer of one or more different elements. For example, a cesiated tungsten surface is defined as a composite surface.

The analysis of the work function of a composite surface is much more difficult than that of a pure metal surface. For this reason, quantum-mechanical treatments of this problem have been restricted to a partial understanding of the interaction of one adsorbate atom with a substrate metal surface by means of perturbation methods. These treatments are summarized and discussed in reference 18. The conclusions about the nature of the atom-metal interactions are not universal. At this time, it is not possible to state which results are conclusive because the accuracy of the perturbation schemes used in the analyses is not known. Much more work is needed in this area.

Semi-empirical Correlations. A number of correlations have been derived for the work function of composite surfaces. Common to all the correlations is the idea that the effect of the adsorbate particles can be considered as a perturbation on the work function of the substrate. The difference between correlations lies in the models used for the calculation of the perturbation and the type of information which is assumed as known, namely as input information for the correlation.

The following remarks are devoted to two of these correlations only. These two correlations have been proposed for metal surfaces coated by metallic films and have found several applications in the field of thermionic conversion. One has been developed by Rasor and Warner,¹⁹ and the other is the result of the works of Gyftopoulos, Levine and Steiner.^{20, 21}

For the derivation of their correlation, Rasor and Warner make the following major assumptions.

(a) The substrate material has a fixed electronic structure, namely a structure independent of the presence of adsorbate particles on the surface.

(b) For the substrate-adsorbate interactions, the surface of the substrate can be regarded as that of a perfect conductor.

(c) The adsorbate particles exist on the surface of the perfect conductor in two distinct energy eigenstates, one ionized and one neutral. The energy difference between these two states equals E . This energy can assume both positive and negative values.

(d) The relative degrees of coverage, Θ_i of the ionic state and Θ_a of the neutral state, are given by the Boltzmann relation

$$\Theta_a / \Theta_i = 2 \exp(-E/kT),$$

where T is the surface temperature. The degree of coverage Θ of the surface by the adsorbate particles equals the sum of Θ_i and Θ_a .

(e) The ion core is at a distance r_i from the surface, where r_i is the effective ionic radius of the adsorbate. This core is held on the surface by the image force.

(f) The ions and their image charges form a double layer on the surface, an array of dipoles on the surface. The potential drop across the double layer yields the change $\Delta\phi$ of the work function of the substrate.

By virtue of these assumptions plus considerations regarding depolarization effects and energy balances, Rasor and Warner obtain their correlation for $\Delta\phi$. This correlation may be expressed either as a function, $\Delta\phi(\Theta, T)$, of the coverage Θ and the temperature T , or,

under certain conditions, as a function, $\Delta\phi(T/T_R)$, of the ratio of T and the adsorbate reservoir temperature T_R .

For the correlation $\Delta\phi(\Theta, T)$, the following information is needed: the adsorbate surface density σ_f (#/cm²) at a coverage of one monolayer, the effective ionic radius r_i , the polarizability α_i of the ionic state, and the value E_o of the energy difference E at zero coverage. If the value of E_o is not known, the value of the bare work function ϕ_o and the values ϕ_{io} of the ion and ϕ_{ao} of the atom desorption energies at zero coverage are also required. A unique feature of this correlation, not included in any other correlation, is the dependence of $\Delta\phi(\Theta, T)$ on T. For certain degrees of coverage the dependence on T is appreciable.

For the correlation $\Delta\phi(T/T_R)$, the following information is needed: the value ϕ_o of the bare work function, the value ϕ_{io} of the ion desorption energy at zero coverage, the ionization energy I of the adsorbate, and the heat of vaporization h of the adsorbate from its reservoir. A unique feature of this correlation is that for a fixed adsorbate, say cesium, $\Delta\phi(T/T_R)$ depends only on the value ϕ_o of the bare work function, because ϕ_{io} is taken as the dipole energy at zero coverage.

The correlation derived by Gyftopoulos and Steiner (G-S)²⁰ is numerically similar to that obtained earlier by Gyftopoulos and Levine.²¹ However, because in the former ideas are more sharply defined than in the latter, the subsequent discussion is presented in connection with the G-S correlation. The major assumptions made are as follows:

(a) The electronic structure of a metallic system may be regarded as consisting of spin-orbitals localized around individual lattice sites.

In particular, valence electrons localized around surface lattice-sites are thought of as surface atoms.

(b) Thermionically emitted electrons originate from surface atoms. The charge condition of a surface atom is the same before and after emission, namely electrically neutral, since the charge of an emitter must be continuously replenished.

(c) Each surface atom (namely a valence spin-orbital localized around a surface lattice-site) can be assigned a neutral orbital electronegativity.

By virtue of the definitions of the work function ϕ and the neutral orbital electronegativity x , it is concluded that ϕ is identically equal to x .⁺

(d) The neutral orbital electronegativity of a composite surface is taken as the sum of the electronegativity of the substrate plus electronegativity perturbations introduced by the chemical interactions between substrate surface-atoms and adsorbate atoms. The procedure is similar as that used in molecular chemistry.

(e) For a valence orbital of an adsorbate atom, the chemical interactions result in an overlap charge Q with another adsorbate valence orbital, and in a charge transfer F and an overlap charge Q_1 with a substrate valence orbital localized at a surface lattice-site.

(f) The change in electronegativity and, hence, $\Delta\phi$ depends linearly on F and Q only.

(g) The charge transfer F is found by maximizing the partially ionic and partially covalent bond energy of the adsorbate atom with respect to F .

⁺ Assumptions (a) through (c) have been confirmed quantum-thermodynamically in references 2 and 25.

(h) The overlap charge is proportional to a Morse function for Θ greater than about 0.3, and a modified Morse function for Θ smaller than about 0.3. The modified Morse function versus Θ has a slope different than zero at Θ equals zero in contrast to the Morse function versus Θ which has a slope equal to zero at Θ equals zero.

(i) The neutral orbital electronegativity at a coverage of one monolayer equals that of a pure adsorbate surface with the same particle arrangement. This is equivalent to saying that the work function of the composite surface at a coverage of one monolayer equals that of the pure adsorbate surface with the same particle arrangement.

By virtue of these assumptions plus considerations of depolarization effects, Gyftopoulos and Steiner obtain a correlation for $\Delta\phi$ versus Θ only, as well as a correlation for the desorption energy of the adsorbate versus Θ only. These correlations are then combined with the statistical analyses of Levine and Gyftopoulos^{22, 23} to find that, under certain conditions, the change $\Delta\phi$ in work function depends on T/T_R only.

For the correlation $\Delta\phi(\Theta)$ the following information is needed: the surface densities σ_s for the substrate and σ_f for the adsorbate, the atomic radii of the substrate and the adsorbate, the crystallographic orientation of the substrate surface, the polarizabilities of the substrate and adsorbate atoms, the valence of the adsorbate, the work functions ϕ_s at zero coverage and ϕ_f at full coverage, the energy D_o of the purely covalent substrate-adsorbate bond, and the sum of the differences of the ionization energy and electron affinity of the substrate and the adsorbate. The energy D_o is related to the heats of sublimation

of the substrate and the adsorbate.²⁴ For the correlation $\Delta\phi(T/T_R)$ the information required is the same as that for $\Delta\phi(\Theta)$.

This completes the discussion of the major assumptions and input information required for the correlations by Rasor and Warner, and by Gyftopoulos and Steiner. The assumptions and information needed are illustrative of the differences and similarities between the two correlations. Numerically, both correlations yield reasonable practical results for a variety of bimetallic systems, and have been found useful tools for the representation of data obtained from thermionic converters.

It should be noted that in spite of the numerical success of the correlations, no fundamental significance can be assigned to the models used for the calculation of the perturbation. What is meant by this observation is that no experiment can be devised which would conclusively indicate that the adsorbate particles exist on the surface as suggested by the models of either of the correlations.

In attempting to evaluate the practicality of these two correlations or any other correlation, a fruitful approach might be to check experimentally their internal consistency. Some questions which might be asked along this approach are as follows:

- (a) For a given Θ , does $\Delta\phi$ depend on T ?
- (b) Is the work function at a coverage of one monolayer primarily controlled by the adsorbate?
- (c) In fitting experimental data, are the resulting values of the input information consistent with the values that are expected from the definitions of these quantities?

(d) For a given adsorbate, does $\Delta\phi(T/T_R)$ depend only on the bare work function? etc.

Presently, the available experimental information is neither sufficiently accurate nor does it cover a sufficiently large range of surface conditions to allow conclusive answers to some of these questions. It is hoped that such information will become available in the future.

There are other important aspects of composite surfaces, such as the problem of work function in the presence of two adsorbates (for example oxygen and cesium), which as already stated are not discussed here.

In closing these brief remarks, it is fair to state that the progress which has been made with regard to the theoretical understanding of surface properties has provided us with sufficient insight to recognize many new, exciting and challenging problems.

APPENDIX

A CORRELATION FOR THE PREDICTION OF BARE WORK FUNCTIONS

The purpose of this appendix is to discuss briefly the correlation for bare work functions proposed in reference 17.

From the arguments presented in references 2, 17, and 25, it is concluded that, at T equals zero, the work function ϕ^* of a pure uniform surface equals the neutral orbital electronegativity $x_s(0)$ of a valence spin-orbital localized around a surface lattice-site and, therefore, ϕ^* would be known if $x_s(0)$ were known. The electronegativity at zero temperature may be computed by a direct extension to surface orbitals

of a correlation which has been derived for orbitals of atoms in a molecule.

To this end, it is noted that according to the works of Gordy²⁶ and of Pritchard and Skinner,²⁷ the neutral orbital electronegativity $x(0)$ of an atom in a molecule can be approximated by the relation

$$x(0) = 0.98 \frac{v+1}{r} + 1.57 \text{ (ev)}, \quad (\text{A-1})$$

where v is the number of electrons per atom which participate in bonding, and r is the effective size in Å of the atom in the bonded state.

Now, it is assumed that relation A-1 is also applicable to surface orbitals and, consequently,

$$\phi^* = x_s(0) = 0.98 \frac{v_s + 1}{r_m} + 1.57 \text{ (ev)}, \quad (\text{A-2})$$

where v_s is the number of electrons per surface atom which participate in bonding, and r_m is the effective size of these atoms in Å. The quantity v_s will be referred to as the surface valence.

The effective size of atoms on the surface is assumed to be equal to the atomic radius given by Slater.⁸ The surface valence, v_s , is derived from the metallic valence v_m and fractional bond numbers of atoms in the bulk, as discussed below.

Surface Valence. The metallic valence, v_m , is defined as the number of electrons per atom which participate in bonding in the bulk of a metal. The fractional bond number, n , is defined²⁸ such that $2n$ equals the average number of bonding electrons shared by two interacting atoms at an interatomic separation R . According to Pauling²⁹,

the fractional bond numbers n_1 and n_2 associated with the interatomic separations R_1 and R_2 , respectively, satisfy the following empirical relation:

$$R_2 - R_1 = 0.26 \ln(n_1/n_2). \quad (\text{A-3})$$

For body centered cubic (BCC), and for closed packed hexagonal (CPH) crystal structures, fractional bond numbers between atoms further distant than next-nearest neighbors are negligible. For face centered cubic (FCC) crystal structures, fractional bond numbers between atoms further distant than nearest neighbors are negligible. Thus, for each crystal structure, metallic valence and fractional bond numbers are interrelated as follows:

$$\text{BCC:} \quad v_m = 8n_a + 6n_b ; \quad (\text{A-4a})$$

$$\text{CPH:} \quad v_m = 6n_a + 6n_b ; \quad (\text{A-4b})$$

$$\text{FCC:} \quad v_m = 12n_a , \quad (\text{A-4c})$$

where n_a and n_b are the fractional bond numbers for nearest and next-nearest neighbors, respectively. Tabulated values of metallic valences and interatomic distances can be used in Eqs. A-3 and A-4 to compute the fractional bond numbers n_a and n_b for different materials.

If it is assumed that the fractional bond numbers of atoms on the surface are identical to those of atoms in the bulk, then the surface valence, v_s , is given by a summation of the form:

$$\text{BCC:} \quad v_s = N_a n_a + N_b n_b ; \quad (\text{A-5a})$$

$$\text{CPH:} \quad v_s = N_a n_a + N_b n_b ; \quad (\text{A-5b})$$

$$\text{FCC:} \quad v_s = N_a n_a , \quad (\text{A-5c})$$

where N_a and N_b are the number of nearest and next-nearest neighbors of surface atoms, respectively. The numbers N_a and N_b are fixed by

the crystallographic orientation of the surface. Table A-I lists values of N_a and N_b for various crystallographic planes of the BCC, CPH and FCC structures.

In summary, v_s can be computed from known properties of metal through the procedure described above. Computed values of v_s and tabulated values of r_m can then be used in Eq. A-2 to calculate bare work functions.

Results. Equation A-2 has been used to compute bare work functions for a large number of metal surfaces. The values of metallic valences, atomic radii, and interatomic distances, used in the calculations, are given in Table A-2.

The results for tungsten, molybdenum, tantalum and rhenium are presented in Tables A-3 through A-6, respectively. These tables also contain experimental values derived from thermionic emission data. It is seen that the predicted work functions are in very good agreement with the experimental values.

Bare work functions of individual planes have not yet been measured for most metals. Predicted values for a number of metals of interest are presented in Table A-7.

A significant implication of Eq. A-2 is that the bare work function of a metal surface is determined by three factors: (a) the number of ligands possessed by an atom on the surface; (b) the interatomic distances between that atom and its ligands; and (c) the metallic valence. As indicated by the results, a surface exhibits a high bare work function when the number of ligands and the metallic valence are large, and the interatomic distances are small.

Table A-2
Properties of Atoms in the Bulk^{8, 29}

Table A-1 <u>Ligands of Surface Atoms</u>			Interatomic Distances to Neighbors (Å)				
Plane	Number of Neighbors		Element	Metallic Valence, v_m	Atomic Radius, r_m (Å)	Nearest, R_a	Next Nearest, R_b
	Nearest, N_a	Next-Nearest, N_b					
BCC							
110	6	4	W	6	1.35	2.74	3.16
112	5	3	Mo	6	1.45	2.72	3.15
100	4	5	Ta	5	1.45	2.86	3.31
111	4	3	V	5	1.35	2.62	3.02
116	4	3	Li	1	1.45	3.04	3.50
FCC							
111	9		Ir	6	1.35	2.71	3.83
100	8		Pt	6	1.35	2.78	3.93
110	7		Ni	6	1.35	2.49	3.52
CPH($c/a < 1.633$)							
0001	3	6	Au	5.56	1.35	2.88	4.07
10 $\bar{1}0$	4	4	Cu	5.56	1.35	2.56	3.62
			Th	4	1.80	3.60	5.10
CPH							
			Re	6	1.35	2.74	2.76
			Os	6	1.30	2.68	2.74
			Zr	4	1.55	3.18	3.23
			Ti	4	1.40	2.90	2.95

Table A-3

Bare Work Functions of Tungsten

Plane	Work Function, ϕ (ev)			
	Theory	Experiment		
110	5.50	5.29 ³⁰	5.35 ³¹	5.40 ³²
112	4.94	4.65	4.80	4.80
100	4.66	4.52	4.60	4.55
111	4.47	4.38	4.40	4.42
116	4.47	4.29	4.32	

Table A-4

Bare Work Functions of Molybdenum

Plane	Work Function, ϕ (ev)			
	Theory	Experiment		
110	5.23	5.00 ³¹	5.10 ³³	4.90 ³⁴
112	4.71	4.55		
100	4.44	4.40	4.40	4.35
111	4.27	4.10	4.15	4.18
116	4.27	4.00		

Table A-5

Bare Work Functions of Tantalum

Plane	Work Function, ϕ (ev)	
	Theory	Experiment
110	4.75	4.80 ³¹
112	4.31	4.3-4.4
100	4.08	4.15
111	3.94	4.00
116	3.94	3.90

Table A-6
Bare Work Functions of Rhenium

Plane	Work Function, ϕ (ev)	
	Theory	Experiment
0001	5.53	5.59 ³⁵
10 $\bar{1}0$	5.20	5.15

Table A-7
Predicted Bare Work Functions
for Various Metal Surfaces

Plane	110	112	100	111	0001	10 $\bar{1}0$
BCC						
Element						
V	4.97	4.50	4.28	4.11		
Li	2.78	2.66	2.61	2.58		
FCC						
Ir	4.84		5.20	5.56		
Pt	4.84		5.20	5.56		
Ni	4.84		5.20	5.56		
Au	4.65		4.99	5.32		
Cu	4.65		4.99	5.32		
Th	3.38		3.57	3.75		
CPH						
Os					5.59	5.34
Zr					4.04	3.89
Ti					4.29	4.13

REFERENCES

1. HATSOPOULOS, G. N.; KEENAN, J. H.; "Principles of General Thermodynamics." John Wiley, New York, (1965), Chapter 48.
2. GYFTOPOULOS, E. P.; HATSOPOULOS, G. N.; "Quantum-Thermodynamic Definition of Electronegativity," Proc. National Academy of Sciences, July (1968).
3. HERRING, C.; NICHOLS, M. H.; "Thermionic Emission." Rev. Modern Physics 21(1949), p. 239.
4. BARDEEN, J.; "Theory of the Work Function, II. The Surface Double Layer," Phys. Rev. 49 (1936) p. 653.
5. LOUCKS, T. L.; CUTLER, P. H.; "The Effect of Correlation on the Surface Potential of a Free Electron Metal," J. Phys. Chem. Solids, Pergamon Press, 25 (1964), p. 105.
6. JURETSCHKE, H. J.; "Exchange Potential in the Surface Region of a Free-Electron Metal," Phys. Rev. 92, (1953) p. 1140.
7. GADZUK, J., "Many-Body Theory of a Rapidly Varying Inhomogeneous Electron Gas," NASA-PM-67 (1967).
8. SLATER, J. C., "Quantum Theory of Molecules and Solids," Vol. 2, McGraw-Hill, New York, (1965).
9. SMOLUCHOWSKI, R., "Anisotropy of the Electronic Work Function of Metals," Phys. Rev. 60 (1941) p. 661.
10. KOSKINEN, M. F.; "A Comparison of Two Theories of Cesium Adsorption," Proc. First International Conference on Thermionic Electrical Power Generation, London (1965) Paper 6-7.
11. BRIDGMAN, P. W.; "The Thermodynamics of Electrical Phenomena in Metals and a Condensed Collection of Thermodynamic Formulas," Dover Publications, New York (1961).
12. WIGNER, E.; BARDEEN, J.; "Theory of the Work Functions of Monovalent Metals," Phys. Rev. 48 (1935) p. 84.
13. GORDY, W.; THOMAS, W. J. O.; "Electronegativities of the Elements," J. Chem. Phys. 24 (1955) p. 439.
14. SACHTLER, W. M. H.; "Halbempirische Methode für Berechnung des Elektronen Austrittspotentials von Metallen," Z. Electrochem. 59 (1959) p. 119.

15. DEMCHENKO, V. V.; KHOMOTOV, N. E.; Tr. Mosk, Khim. - Technol. Inst. No. 39 (1962) p. 115.
16. RASOR, N.; WARNER, C., III; "Correlation of Electron, Ion and Atom Emission Energies," Atomics International Report AI-6799 (1961) p. 46.
17. STEINER, D.; GYFTOPOULOS, E. P.; "An Equation for the Prediction of Bare Work Functions," Report 27th Annual Conference Physical Electronics, MIT, Cambridge (1967) p. 160.
18. GADZUK, J. W., "Theory of Atom-Metal Interactions," Surface Science 6 (1967) p. 133.
19. RASOR, N.; WARNER, C., III; "Correlation of Emission Processes for Adsorbed Alkali Films on Metal Surfaces," J. Appl. Phys. 35 (1964) p. 2589.
20. GYFTOPOULOS, E. P.; STEINER, D.; "Orbital Electronegativity and Physical Properties of Bimetallic Adsorption Systems," Report 27th Annual Conference Physical Electronics, MIT, Cambridge (1967) p. 169.
21. GYFTOPOULOS, E. P.; LEVINE, J. D.; "Work Function Variation of Metals Coated by Metallic Films," J. Appl. Phys. 33 (1962) p. 67.
22. LEVINE, J. D.; GYFTOPOULOS, E. P.; "Adsorption Physics of Metals Partially Covered by Metallic Particles, II: Desorption Rates of Atoms and Ions," Surface Science 1 (1964) p. 225.
23. LEVINE, J. D.; GYFTOPOULOS, E. P.; "Adsorption Physics of Metals Partially Covered by Metallic Particles, Part III: Equations of State and Electron Emission S-Curves," Surface Science 1 (1964) p. 349.
24. LEVINE, J. D.; GYFTOPOULOS, E. P.; "Adsorption Physics of Metallic Surfaces Partially Covered by Metallic Particles, I: Atom and Ion Desorption Energies," Surface Science 1 (1964) p. 171).
25. GYFTOPOULOS, E. P.; HATSOPOULOS, G. N. "Quantum - Thermodynamic Meaning of Electronegativity and Work Function, Proc. Second International Conference on Thermionic Electrical Power Generation, Stresa, Italy (1968) Paper K-2.

26. GORDY, W. E. ; "A New Method of Determining Electronegativity from Other Atomic Properties," Phys. Rev. 69 (1946) p. 604.
27. PRITCHARD, H. O. ; SKINNER, H. A. ; "The Concept of Electronegativity," Chem. Rev. 55 (1955) p. 757.
28. COULSON, C. A. ; "Valence," Oxford University Press, London, 2nd Edition, (1961) p. 336.
29. PAULING, L. ; "The Nature of the Chemical Bond," Cornell University Press, Ithaca, New York, 3rd Edition (1960) p. 393-448.
30. SMITH, G. F. ; "Thermionic and Surface Properties of Tungsten Crystals," Phys. Rev. 94 (1954) p. 295.
31. PROTOPOPOV, O. D. et al. ; "Emission Parameters of Tantalum and Molybdenum Single Crystals," Soviet Phys. -Solid State 8 (1966) p. 909.
32. AZIZOV, U. V. ; SHUPPE, G. N. ; "Emission and Adsorption Characteristics of Faces of a Tungsten Single Crystal," Soviet Phys. -Solid State 7 (1966) p. 1591.
33. AZIZOV, U. V. ; et al. ; "Emission Properties of a Molybdenum Single Crystal," Soviet Phys. -Solid State 7 (1966) p. 2232.
34. SAVITSKII, E. M. ; et al. ; "Anisotropic Work Function of Molybdenum Single Crystals," Soviet Phys. -Technical Phys. 11 (1967) p. 974.
35. WICHNER, R. ; PIGFORD, T. H. ; "Work Function of Monocrystalline and Polycrystalline Rhenium," Report Thermionic Convention Specialist Conference, Houston (1966) p. 405.

QUANTUM THERMODYNAMIC MEANING OF
ELECTRONEGATIVITY AND WORK FUNCTION[†]

by

Elias P. Gyftopoulos[†] and George N. Hatsopoulos
Thermo Electron Corporation
Waltham, Massachusetts (USA)

ABSTRACT

The purpose of this paper is to discuss the relation between surface orbital electronegativity and work function, both from the standpoint of thermodynamics and that of quantum mechanics.

First, it is shown that the electronic structure of crystals can be described by means of spin-orbitals which are localized around individual lattice sites. Second, electronegativity is related to the chemical potential of an electron in a spin-orbital. Third, it is shown that the work function of a uniform surface equals the neutral orbital electronegativity of a spin-orbital localized around a surface atom.

[†] This work was performed for the Jet Propulsion Laboratory, California Institute of Technology, sponsored by the National Aeronautics and Space Administration under Contract NAS7-100.

+ On sabbatical leave from the Massachusetts Institute of Technology

INTRODUCTION

In previous publications by Steiner and Gyftopoulos,¹⁻³ emission phenomena, occurring at metallic surfaces, are analyzed in terms of surface atoms and their orbital electronegativity. For example, in reference 1 the view is advanced that electrons, emitted thermionically from a pure uniform surface of a crystal, originate from a "valence orbital" of an "atom on the surface." It is assumed that the shape, the ionization energy, the electron affinity, and the excitation energies of this orbital are precisely defined, although not necessarily spectroscopically observable, and that they are determined by the many-body interactions of the crystal. On the basis of this picture, it is concluded that the work function of the surface must equal the neutral orbital electronegativity of the valence orbital of the surface atom.

This way of thinking about a crystal and its surface raises two questions. The first relates to the validity of viewing the electronic structure of a crystal in terms of orbitals which are associated with individual lattice sites, such as a valence orbital of a surface atom. It is customary to think of the electrons as belonging to the crystal as a whole and, therefore, it is not obvious that electrons can be assigned to, localized around, individual lattice sites.

The second is a relatively old question. It refers to the meaning of electronegativity. This quantity has been found useful in many chemical studies and yet it has not been given a rigorous definition.

The purpose of the present communication is to discuss the preceding two questions, in the context of the one-electron approximation for the electronic structure of many-electron systems. It is shown that the picture of localized orbitals is valid, and that electronegativity equals the negative of the chemical potential of an electron in an orbital.

The paper is organized as follows. First, the procedure for the derivation of the localized orbitals is discussed. These orbitals are shown to provide a description of the electronic structure of crystals which is entirely equivalent to the well known quantum-mechanical picture of electrons in metals. Second, the work of the authors on the identification of electronegativity⁴ with the chemical potential is summarized. Third, it is shown that the work function of a pure uniform surface equals the orbital electronegativity of a surface atom.

LOCALIZED SPIN-ORBITALS FOR CRYSTAL LATTICES

The equivalence between the descriptions of the electronic structure of crystals by means of either nonlocalized, band structure theory, or localized spin-orbitals is best understood through a brief review of procedures employed for the analysis of any N-electron system.

Quantum-mechanically, the analysis of the energy eigenstates of the electronic structure of N-electron systems is very difficult. To avoid the difficulty, the electrons are treated as an ideal substance. In other words, the N-electron Hamiltonian operator is reduced to a sum of N separable one-electron Hamiltonian operators. Various methods are used for the reduction. Differences between methods arise from the degree to which exchange and correlation effects are included in the one-electron potential energy. In this regard, all methods are approximate and not all methods are equally accurate.

A given one-electron Hamiltonian operator defines an energy eigenvalue problem. The eigenfunctions and eigenvalues of this operator can be more readily found than those of the complete N-electron operator. Each eigenfunction, one-electron orbital, of a system with more than one nucleus, is delocalized throughout the system and is given the same interpretation as, say, the eigenfunctions of the hydrogen atom. For example, the orbital can accommodate at most two electrons with opposite spins. The negative of the eigenvalue equals approximately the energy required to extract an electron from the orbital, and it represents an

ionization energy of the system. When the orbital is occupied by an electron with a given spin, it is called a spin-orbital. In many applications, a different orbital is used for each spin. In other words, each spin-orbital has its own spatial dependence.

By virtue of the ideal substance assumption, the eigenfunction ψ_N , for a given state of the system as a whole, should be given by the product of the occupied spin-orbitals. This, however, is not consistent with the symmetry rules of quantum mechanics.⁵ For this reason ψ_N is represented by an antisymmetric, determinantal function of spin-orbitals, a Slater determinant.⁶ The determinant is given by the relation

$$\psi_N = \frac{1}{(N!)^{1/2}} \begin{vmatrix} u_1(q_1) & u_2(q_1) & \dots & u_N(q_1) \\ u_1(q_2) & u_2(q_2) & \dots & u_N(q_2) \\ \cdot & \cdot & \dots & \cdot \\ \cdot & \cdot & \dots & \cdot \\ u_1(q_N) & u_2(q_N) & \dots & u_N(q_N) \end{vmatrix} \quad (1)$$

where q_j represents the coordinates and spin of the j -th electron, u_i is the i -th orbital, and $u_i(q_j)$ is the i -th spin-orbital occupied by the j -th electron.

In general, it is found that one-electron energies E_i , eigenvalues E_i , are in good agreement with experimentally observed ionization energies of the system (atom, molecule, or crystal). However, the sum of the E_i , the eigenvalue of ψ_N with respect to the sum of the N one-electron operators, is not in good agreement with the total energy of the system, namely the energy which would be derived from the exact ψ_N and the exact N -electron operator. Nevertheless, ψ_N in the form of Eq. 1 is often considered as an adequate approximation for the exact ψ_N .

For crystals, the one-electron results can also be described in terms of localized orbitals by means of the following procedure. Consider a crystal bounded by a uniform surface. Suppose that a relatively

accurate one-electron equation has been established, say, by the method suggested by Slater.⁷ The one-electron eigenvalue problem may be written in the form

$$(H_0 + H_1) u = E u, \quad (2)$$

where H_0 is the one-electron, spatially periodic, Hamiltonian operator that would be derived if the solid were imbedded in an infinite lattice, and H_1 is the one-electron operator which accounts for the perturbation introduced by the uniform surface. The spatial part of the eigenfunctions of Eq. 2 can be expanded into a series of Wannier functions⁸ $a_n(\underline{r} - \underline{R}_s)$ associated with the operator H_0 .[†] Thus the i -th eigenfunction is given by the relation⁹

$$u_i(\underline{r}) = \sum_s \sum_n U_{in}(\underline{R}_s) a_n(\underline{r} - \underline{R}_s), \quad (3)$$

where $U_{in}(\underline{R}_s)$ is a constant, and the sums are over all lattice sites \underline{R}_s and over all bands n . Mathematically, Eq. 3 is exact if an infinite number

[†] Recall that the Bloch functions $b_n(\underline{k}, \underline{r})$ of the n -th band of the infinite crystal are given by the relation¹⁰

$$H_0 b_n(\underline{k}, \underline{r}) = E_n(\underline{k}) b_n(\underline{k}, \underline{r}),$$

and that the Wannier functions $a_n(\underline{r} - \underline{R}_s)$ of the n -th band are determined by the expression

$$a_n(\underline{r} - \underline{R}_s) = N_L^{-1/2} \sum_{\underline{k}} b_n(\underline{k}, \underline{r}) \exp(-i\underline{k} \cdot \underline{R}_s),$$

where \underline{R}_s is the s -th site of the lattice, and N_L is the number of lattice sites. The Wannier functions form a complete, orthonormal set over all bands and over all lattice sites, namely

$$\int a_m^*(\underline{r} - \underline{R}_j) a_n(\underline{r} - \underline{R}_i) d\underline{r} = \delta_{mn} \delta_{ij}.$$

Moreover, each Wannier function $a_n(\underline{r} - \underline{R}_s)$ is localized around, associated with, the s -th site.

of bands is included in the expansion. As in all practical problems, however, through a judicious choice of localized, Wannier-like functions $w_n(\underline{r}, \underline{R}_s)$ (for example, a suitable linear combination of Wannier functions at the site \underline{R}_s), the summation over n may be reduced to a number equal to the number of valence electrons per atom, without great loss of accuracy. Thus, if different orbitals are used for different spins, a spin-orbital $u_i(q_j)$ may be adequately represented by the relation

$$u_i(q_j) = \sum_s \sum_n^v c_{in}(\underline{R}_s) w_n(q_j, \underline{R}_s), \quad (4)$$

where v is the number of valence electrons per atom, and $c_{in}(\underline{R}_s)$ is a constant.

Without loss of generality, suppose the crystal is that of a monovalent metal, v equals unity and the number N_L of lattice sites equals the number N of valence electrons. For this crystal, substitution of Eq. 4 into the determinantal relation, Eq. 1, for the overall eigenfunction ψ_N yields

$$\psi_N = \frac{1}{(N!)^{1/2}} \begin{vmatrix} \sum_s c_1(\underline{R}_s) w(q_1, \underline{R}_s) & \dots & \sum_s c_N(\underline{R}_s) w(q_1, \underline{R}_s) \\ \sum_s c_1(\underline{R}_s) w(q_2, \underline{R}_s) & \dots & \sum_s c_N(\underline{R}_s) w(q_2, \underline{R}_s) \\ \cdot & \dots & \cdot \\ \cdot & \dots & \cdot \\ \cdot & \dots & \cdot \\ \sum_s c_1(\underline{R}_s) w(q_N, \underline{R}_s) & \dots & \sum_s c_N(\underline{R}_s) w(q_N, \underline{R}_s) \end{vmatrix}, \quad (5)$$

where the subscript n equals unity has been omitted from the w 's and the c 's. Note that each column of the determinant in Eq. 5 is a linear combination of the N Wannier-like functions associated with the N sites of the crystal. It follows from the rules for the product of two determinants that Eq. 5 can be written in the form

$$\psi_N = \frac{1}{(N!)^{1/2}} \begin{vmatrix} w(q_1, \underline{R}_1) & \dots & w(q_1, \underline{R}_N) \\ w(q_2, \underline{R}_1) & \dots & w(q_2, \underline{R}_N) \\ \vdots & \ddots & \vdots \\ w(q_N, \underline{R}_1) & \dots & w(q_N, \underline{R}_N) \end{vmatrix} \times \begin{vmatrix} c_1(\underline{R}_1) & c_2(\underline{R}_2) & \dots & c_N(\underline{R}_1) \\ c_1(\underline{R}_2) & c_2(\underline{R}_2) & \dots & c_N(\underline{R}_2) \\ \vdots & \vdots & \ddots & \vdots \\ c_1(\underline{R}_N) & c_2(\underline{R}_N) & \dots & c_N(\underline{R}_N) \end{vmatrix} \quad (6)$$

In the form of Eq. 6, the eigenfunction ψ_N for the whole crystal admits the localized spin-orbital interpretation which is sought. Indeed, note that each Wannier-like function $w(q, \underline{R}_s)$ is a spin-orbital associated with, localized around, lattice site \underline{R}_s (the set of constants $C_i(\underline{R}_s)$, for $i = 1, 2, N$, is also associated with the same site \underline{R}_s). If the N electrons of the crystal are distributed among the N spin-orbitals $w(q, \underline{R}_s)$, an antisymmetric determinantal function, Eq. 6, can be formed. This function is completely equivalent to that obtained from the delocalized orbitals. In other words, the ψ_N 's constructed from either the localized or the delocalized spin-orbitals are identical.

It should be noted that the localized spin-orbitals $w(q, \underline{R}_s)$ are not energy eigenfunctions of the one-electron equations. Only ψ_N , Eq. 6, is an approximate eigenfunction of the Hamiltonian operator for the whole crystal. Nevertheless, each localized spin-orbital can be assigned precise values for the ionization energy, electron affinity, and excitation energies of the electron in the spin-orbital, in a manner which is consistent with the usual definitions of these quantities. The values of the ionization energy, electron affinity, etc., of a localized spin-orbital are not equal to the corresponding values of the delocalized spin-orbitals. This point can be seen from the definition of the ionization energy given below.

Suppose that ψ_N , Eq. 6, represents the ground state of the crystal. The ionization energy of a spin-orbital localized around lattice site \underline{R}_s is defined as the difference between the energy corresponding to an eigenfunction ψ_{N-1} and that of the ground state. The eigenfunction ψ_{N-1} is given by Eq. 6 except that the s -th column and the s -th row of the first and the

second determinants are replaced by zeros, respectively, and $(N!)^{1/2}$ is replaced by $[(N-1)!]^{1/2}$. The Hamiltonian operator for ψ_{N-1} is that corresponding to N lattice sites and $N-1$ valence electrons. This definition of the ionization energy assumes that removal of a localized spin-orbital from the system does not alter the functional dependence of the other $N-1$ localized spin-orbitals. Such an assumption is used in practically all approaches to the analysis of the electronic structure of solids (see, for example, Koopmans' theorem for the one-electron Hartree-Fock equations¹¹).

The other energies of a localized spin-orbital can be defined in a manner analogous to that used for the ionization energy.

ELECTRONEGATIVITY AND CHEMICAL POTENTIAL

In this section, the work of the authors⁴ on the identification of electronegativity with the negative of the chemical potential of an electron in an atom is summarized.[†]

In reference 4, an ensemble of identical, one-atom systems is considered. Each atom is thought of as consisting of two components, electrons and ions. The systems are in thermodynamic equilibrium with a reservoir of electrons and ions at a small temperature T (degrees Kelvin). The components can flow back and forth between the systems and the reservoir. The energy eigenstates of the atoms are assumed to be derivable from the one-electron Hartree-Fock equations.¹² In other words, the electrons are viewed in an ideal substance.

According to the theory of statistics of ensembles,¹³ the physical situation described above obeys the rules of grand canonical ensembles. Use of these rules yields the following important conclusions.

[†] Strictly speaking, the electronegativity has been identified with the electrochemical potential. For the reference level of energy selected in this paper, however, the values of the chemical and the electrochemical potential are identical.

(a) Statistically, the energy E of an one-atom system can be expressed as a continuous function $E(q)$ of a continuous variable q which represents a statistical measure of the charge in a valence spin-orbital. The range of the value of the charge q is from minus one electronic charge ($-e$), the orbital is doubly occupied, through zero, the orbital is occupied by one electron, to plus one electronic charge ($+e$), the orbital is ionized.

(b) The chemical potential μ_c of a valence electron is given by the relation

$$\mu_c = - (\partial E(q) / \partial q) \text{ at constant entropy.} \quad (7)$$

In the limit of very small temperatures, this potential is found to have the following exact values

$$\mu_c = -(I + A) / 2e \quad \text{for } q = 0 \quad (\text{neutral atom}),$$

$$\mu_c = \infty \quad \text{for } q = e \quad (\text{positive ion}),$$

and

$$\mu_c = -\infty \quad \text{for } q = -e \quad (\text{negative ion}),$$

where I and A are the first ionization energy and the electron affinity of the atom, respectively. The quantities I and A can also be referred to the valence electron spin-orbital.

(c) For fractional values q and for small T , μ_c is a function of both q and T .

(d) By virtue of (b) above, it is found that for small temperatures (in the limit of zero temperature) an excellent approximation for $E(q)$ is given by the relation

$$E(q) = \frac{I + A}{2e} q + \frac{I - A}{2} \left[1 - \left(1 - \frac{q^2}{e^2} \right)^{1/2} \right] \quad (8)$$

when the zero energy level is taken to be at the energy of the neutral atom (q equals zero). Note that this approximation yields exact values for $E(q)$ and μ_c for $q = -e, 0, e$.

(e) The orbital electronegativity $x(q)$ of a valence electron is defined as

$$\begin{aligned} x(q) &= (\partial E(q) / \partial q) \text{ at constant entropy} = \\ &= -\mu_c \end{aligned}$$

This is the first time that a rigorous definition of $x(q)$ is given.

(f) The value of the neutral orbital electronegativity $x(0)$ obtained from Eq. 8 is identical to the value of electronegativity suggested by Mulliken¹⁴. It should be noted however, that Mulliken's value is considered to be approximate. Here, the thermodynamic analysis yields that, in the limit of small temperatures, $x(0)$ has the exact value given by the relation

$$x(0) \equiv \frac{I + A}{2e} \quad (9)$$

(g) The definition of the orbital electronegativity given above can be easily extended to orbitals in systems other than atoms. Such an extension is discussed in the next section.

WORK FUNCTION AND ELECTRONEGATIVITY

Without loss of generality, consider a crystal of a monovalent metal, bounded by a uniform surface. Suppose the analysis of the electronic structure of this metal has been carried out with respect to a zero energy level taken at the points just outside the surface. Moreover, suppose that both the delocalized and the localized spin-orbitals have been established, in accordance with the procedure discussed in Section 2.

Thermodynamically, for a system of N -electrons, any set of N spin-orbitals which describes the system may be thought of as representing N degrees of freedom. When these N degrees of freedom are treated statistically, the following results can be obtained.

(a) Given the N delocalized spin-orbitals, one-electron spin-orbitals, the negative of the chemical potential of the surface, with respect to the points just outside the surface, equals the work function. This is the well-known thermodynamic definition of work function.^{15,16}

(b) Given the N localized spin-orbitals, Wannier-like functions, suppose that all degrees of freedom are frozen except that corresponding to the spin-orbital localized around the surface site \underline{R}_s . Under this condition, the surface spin-orbital can be treated statistically by the same procedure as that used for atoms in Section 3. In other words, this

orbital may be thought of as a surface atom. Thus, a chemical potential for the electron in the orbital can be defined. For example, in the limit of small temperatures, the value of the chemical potential of the localized spin-orbital equals

$$-(I_s + A_s)/2e,$$

where I_s and A_s are the ionization energy and the electron affinity of the orbital as defined in Section 2. This value equals the negative of the neutral orbital electronegativity of the spin-orbital, Eq. 9.

(c) From thermodynamic equilibrium considerations, it can be shown that the chemical potential of the localized spin-orbital as defined in (b) must be equal to the chemical potential of the surface, as defined in (a).[†]

(d) By virtue of (a), (b), and (c), it follows that the work function equals the neutral orbital electronegativity of a spin-orbital localized around a surface atom.

In conclusion: (a) the characterization of the electronic structure of metals by localized spin-orbitals is equivalent to the ordinary picture of electrons in metals; (b) electronegativity can be given a rigorous thermodynamic definition; and (c) the neutral orbital electronegativity of a surface spin-orbital, atom, equals the work function of the surface.

[†] The proof of this statement is analogous to that used in the study of chemical reactions with or without a catalyst.¹⁷

REFERENCES

- (1) STEINER, D.; GYFTOPOULOS, E. P., "An Equation for the Prediction of Bare Work Functions". Report 27th Annual Conf. Physical Electronics, MIT, Cambridge (1967) 160.
- (2) GYFTOPOULOS, E. P.; STEINER, D., "Orbital Electronegativity and Physical Properties of Bimetallic Adsorption Systems". Report 27th Annual Conf. Physical Electronics, MIT, Cambridge (1967) 169.
- (3) STEINER, D.; GYFTOPOULOS, E. P., "Orbital Electronegativity and Physical Properties of Metal-Gas Adsorption Systems". Report Thermionic Conversion Specialist Conf., San Francisco (1967) 145.
- (4) GYFTOPOULOS, E. P.; HATSOPOULOS, G. N., "Quantum Thermodynamic Definition of Electronegativity". To be published.
- (5) TOLMAN, R. C., "The Principles of Statistical Mechanics". Oxford University Press, New York (1938), pp. 312-324.
- (6) SLATER, J. C., "Quantum Theory of Molecules and Solids", Vol. 1, McGraw-Hill, New York (1963), p. 43.
- (7) SLATER, J. C., "Quantum Theory of Molecules and Solids", Vol. 3, McGraw-Hill, New York (1967), p. 265-271.
- (8) SLATER, J. C., "Quantum Theory of Molecules and Solids", Vol. 2, McGraw-Hill, New York (1965), p. 154-158.
- (9) KOSTER, G. F.; SLATER, J. C., "Wave Functions for Impurity Levels". Phys. Rev. 95 (1954) 1167.
- (10) Reference 6, Chapter 9.
- (11) Ibid., p. 96.
- (12) Ibid., Appendix 4.
- (13) HATSOPOULOS, G. N.; KEENAN, J. H., "Principles of General Thermodynamics". John Wiley, New York (1965), Chapter 48.
- (14) MULLIKEN, R. S., "A New Electroaffinity Scale". J. Chem. Phys. 2 (1934) 782.
- (15) Reference 13, pp. 557-558.
- (16) HERRING, C.; NICHOLS, M. H., "Thermionic Emission". Rev. Modern Phys. 21 (1949), p. 190.
- (17) Reference 13, pp. 329-330.

DISCUSSION

Speaker of the invited paper and paper K-1: E. P. GYFTOPOULOS.

RASOR (USA): I would like to comment on the invited paper, which is a survey of two alternate approaches, from the standpoint of someone prejudiced toward the other viewpoint. I think that Prof. GYFTOPOULOS' statements were enlightening, and I do not want to diminish what he has said. However, I would like to modify his unqualified statement that the RASOR-WARNER theory assumes two distinct states: an atom (a neutral particle) and an ion (a fully charged particle). An unqualified identification of these states as atoms and ions in the same sense as they exist in a gas is an oversimplification and misleading. In reality they should be considered as different charge states, conveniently identified by the names "atom" and "ion". Furthermore, it is misleading to imply that this approach is confined to only two such charge states. The effect of multiple states is considered in our original paper, but the detailed comparison with data is made on the basis of only two states since the computation is much simpler, and indeed is adequate to correlate the experimental results. The importance of recognizing such charge states is that it then is possible to compute the time-average charge of the layer of adsorbed particles by statistical mechanics, and to thereafter apply the familiar physical-electronic-thermodynamic formalism developed by LANGMUIR. A rigorous analytical description of the charge states by modern quantum-mechanical methods is possible in the same sense as is the solution of other problems in solid state physics, and steps in this direction have been taken by GADZUK and others.

Therefore, it is particularly misleading to imply that the GYFTOPOULOS-LEVINE-STEINER approach, based on the molecular-bond and electronegativity tradition of PAULING, is any more firmly based in thermodynamics or quantum theory than is the RASOR-WARNER approach, based on the physical-electronic tradition of LANGMUIR, SLATER and BARDEEN. In fact the opposite can be argued since the PAULING physical-chemistry tradition has been quite empirical in the past, whereas the LANGMUIR-SLATER-BARDEEN tradition has been based almost entirely on quantum-statistical-mechanics.

At their present primitive state of development, both the RASOR-WARNER and the GYFTOPOULOS approaches must rely heavily on approximations, since the exact solutions required are very complex and presently poorly

defined. As they are both refined, they probably will approach each other in formalism. However, I personally believe that the final description, say 20 years from now, will more closely resemble the physical-electronic tradition of LANGMUIR-BARDEEN than the physical-chemistry tradition of PAULING. In fact, in removing some of the empirical nature of the PAULING approach, Prof. GYFTOPOULOS has now re-defined electronegativity to be equivalent to work function. Certainly, I no longer can be critical of the empirical nature of electronegativity since it would be like impugning the ancestry of my own mother.

I have felt for some time now that the RASOR-WARNER approach should have its greatest use and validity in the region of 0 to $3/4$ surface coverage by cesium, and the GYFTOPOULOS-LEVINE approach should be valid only near full coverage, at least for clean surfaces. Unfortunately, the full coverage region is significant only for the collector of thermionic converters, and the collector is usually not clean, so that probably neither theory describes the situation on the collector.

WARNER (USA): I believe in the first part of your talk you stated that there was no fundamental way to distinguish between adatoms and adions on the surface. I would like to disagree with this and throw the question into a different light. I think that in a metal you have free electrons and you may also have, with cesium on the surface, electrons which are localized. I think with experiments, e. g. like MUZ is doing with the photo-electric effect, you could probe the surface to find what kinds of electrons exist there.

Therefore, I think this fundamental question can be answered. I also believe that if you took these WANNIER-functions, in a rigorous calculation they would lead to just those electrons which you could interpret under the high coverage conditions as adatoms on the surface. Would you comment on that?

GYFTOPOULOS (USA): Yes, I disagree with what you said. Let me review briefly the picture used by RASOR and WARNER. The adsorbate particles on the surface are viewed as ions of ionic radius r_i and as neutral atoms. These two types of particles are regarded as states.

Now, let me raise the question: "What do we mean when we say that we have an ionized state on the surface?"

What we really mean is that if we draw a sphere with a radius of about the ionic radius then we will find inside the sphere a net positive charge equal to one electronic charge. Now all of you realize that there is nothing definite

about the ionic radius of any element in a compound. So let us examine how we might check this picture experimentally. We might, for example, measure the charge density around the nucleus of the adsorbate. Then we might draw different spheres (spheres of different radii) around the nucleus. It is clear that depending on the size of the sphere that we draw, the net charge in the vicinity of a particular site on the surface may correspond to something which appears to be doubly charged, triply charged, neutral, negatively ionized, or whatever we please. It is that kind of conceptual difficulty, that forbids the establishment of certain postulates in either your model or mine. Now, let me review our model, lest you feel that I have these comments only for the positive ion. Our picture is that we put the cesium particles on the surface and then we examine the various interactions. The interactions that occur on the surface consist of an overlap charge between adsorbate particles, overlap charge between adsorbate and substrate particles, and a charge transfer between substrate and adsorbate particles. This picture leads to the concept of partially ionic, and partially covalent bonds. This is what you might call an anthropomorphic way of describing a very difficult situation. There is no definite fundamental way, by means of which one could de-couple the interactions and describe them by overlap charges and charge transfer. The two types of charges are very tightly knit together. This is not true only for surfaces. Any book on molecular chemistry, e. g. COULSON on VALENCE discusses this to a large extent. The crux of the matter lies in the fact that we cannot observe spectroscopically, or by some other means the assumptions inherent in the description of binding as partially ionic and partially covalent. Another way of describing the difficulty is in terms of quantum-mechanics. Let me use a simple molecular picture because then we have got fewer things to talk about. The simplest molecule I could think of is the hydrogen molecule. Now, in the hydrogen molecule, even in the context of the one electron approximation, we have molecular orbitals, namely the electrons belong to both ion cores of the molecule. On the other hand, no calculation is made directly in terms of molecular orbitals. These orbitals are always approximated by a linear combination of atomic orbitals. The concepts of overlap charge and charge transfer emerge only when the linear combination is in a special form.

MUZ (Germany): I would like to point out that the picture of an isolated ion core on the metal surface and the picture of overlap bonds are both simplified, because the electron atmosphere in front of the surface is neglected.

It seems to me, that the differences in the approach to adsorption by you and Dr. LEVINE and by Dr. RASOR and Dr. WARNER are not fundamental. In the first model a space average is used, in the second approach a statistical time average of charge distribution is used. The difference concerns the way of performing the averaging.

GYFTOPOULOS: I think that the discussion has got off a little bit on a tangent. My remarks were not concerned with the differences that you mentioned. I addressed myself to the following question: " Is it possible to perform an experiment which would lead to the conclusion that the adsorbate particles on the surface look like positive ions or to the conclusion that the adsorbate particles on the surface look like neutral atoms? " My answer to this question is no.

HATSOPOULOS (USA): I would like to make just a brief comment that may be helpful in clarifying some of the discussion. There is no doubt that work function and electro-chemical potential are thermodynamic averages over several states, and we all know that the number of states is very large. The difference between RASOR and the electronegativity approach is this. In the case of RASOR, in order to conduct the averaging, he had to assume, in order to simplify his averaging procedure, two states and then he averages over these two states. On the other hand the electronegativity approach, as you were shown thermodynamically, the electronegativity being associated with the electro-chemical potential, implies that electronegativity has built into it a thermodynamic average of all possible states; and there are two paths to follow from there on, once you have realized this. Either you conduct the averaging which is a numerically very difficult process to conduct over all possible allowed states on the surface or you take an empirical equation that relates the electronegativity, which is a statistical average as we showed, to some other quantities. This is exactly what GYFTOPOULOS and LEVINE have done. Therefore, I would like to say that drawing a picture for the electronegativity and implying that this is one state is incorrect. Electronegativity implies by definition a statistical average over all the possible states.

RASOR: I think that it would be a good idea to make reference to some work that dwells on these problems. One is some work that has been done by GADZUK in the USA. He made a detailed calculation at the surface. This addresses itself specifically to the problem whether or not you can describe

a particle on the surface in terms of distinct states. The second reference I would like to make is to a paper at the end of this session in which is shown some photo-electric evidence, emission evidence of the existence of such states. Now whether this particular data shows the existences or not, I don't think that is the important thing. The point is that it is conceptually possible to do so.

A NEW INTERPRETATION OF THE THERMIONIC EMISSION FROM BARE
AND COVERED METAL SURFACES

J. Bohdanský
Euratom CCR, Ispra (Varese), Italy

Abstract

Thermionic emission is described as an activation process of surface atoms. The interpretation is based on the model of localized electron orbitals at the surface, which has been introduced most recently by D. Steiner and E. P. Gyftopoulos [1]. Following their concept it is concluded that electrons can be emitted from atoms at and on the surface. A new formula for the emission current is indicated. Consequences for Cs-covered surfaces are discussed in detail and an estimation for the minimum work function of cesiated surfaces is given.

Introduction

Most recently D. Steiner and E. P. Gyftopoulos [1] calculated work function data of bare metal surfaces, based on the view "that each extracted electron originates from a valence orbital of a surface atom". Their results are in good agreement with measured work function data, although they used the concept of electronegativity [2] which has not been founded rigorously on basic principles of quantum physics. However, this concept proved very useful in chemistry, and therefore their statement about localized valence orbitals for surface atoms must be considered as a realistic alternative to the free electron concept discussed so far.

In this paper consequences are discussed for the emission process if the electrons originate from localized valence orbitals at the surface. In a first part the thermionic emission from bare surfaces is investigated and a special interpretation for the emission process is given.

In a second part thermionic emission from cesiated surfaces is considered in more detail. The existing interpretations of the emission data are compared regarding the new concept for electron emission.

A rather simple relation for the possible minimum work function of cesiated surfaces is derived in the third part of the paper as a result of this discussion.

Thermionic emission from bare surfaces

If the emitted electrons originate from a localized valence orbital, the common description of the emission process as an escape of free electrons across a potential barrier is not the only possible interpretation for the electron emission. However, we can interpret the emission as a transition process of a localized electron configuration in the solid structure. Such a transition process is normally described in solid state physics by the concept of activated states [3]. In this case the calculated electronegativity would appear as the activation energy for the emission process. Such an interpretation leads to a relation for the emission current density j which corresponds completely to the relation for the evaporation process of surface atoms. j is given by the expression

$$j = en_o \tau_o \cdot e^{-\phi'/T} \tag{1}$$

where the symbols have the following meaning:

- e : charge of electron
- n_o : number of surface particles per unit area
- τ_o : characteristic lattice frequency
- ϕ' : electronegativity, ref. [1]
- T : temperature (expressed in units of energy).

This formula has to be compared with the Richardson formula:

$$j = AT^2 \cdot e^{-\phi/T} \tag{2}$$

which is normally derived from principles of thermodynamics [4].

If the derivation of formula (2) is based only on thermodynamic principles, the temperature dependence of the "true work function" ϕ remains undefined. Therefore, j can have any dependence on T in formula (2). This is nicely characterized if we use a Carnot process to derive the Richardson equation [5]. We get from such a derivation for the heat of vaporization (per electron) the relation

$$l(T) = l_o - \int^T C(T') d T' + 5 k T \tag{3}$$

$C(T)$ is the temperature derivative of the average energy loss of the solid system per activation process [6]. One has to take for the integral in equation (3) the average energy equal to $2 kT$ to get an expression analogous

to equation (1)

$$j = B \cdot e^{-\phi_0/T} \quad (4)$$

To see whether the proposed process might be responsible for electron emission or not we have also to compare formula (1) with measured emission current data. From the report of Steiner-Gyftopoulos [1] we know that their electronegativity - which is the activation energy for the emission process in our concept - is practically equal to the measured work functions taken from a Richardson plot.

It need not be mentioned that measured thermionic emission data plotted in a logarithmic j or j/T^2 presentation form a straight line in both cases. In other words, it cannot be decided from measured data whether equation (1) or (2) is valid with a constant ϕ' respectively ϕ value. In addition both values inferred from the slope of the line should be practically equal due to the weak influence of the AT^2 term compared with the exponential function. Therefore the good agreement of measured work function and calculated electronegativity is one support for the given interpretation. Another may be found in the comparison of the expression $e n_0 \tau_0 / T^2$ with measured A values. In table 1 such a comparison for different metals is given. The calculation of $\tau_0 n_0$ is based on measured lattice distances and characteristic frequencies deduced from Debye temperatures [7] . T is taken as an average temperature in the investigated region. This comparison shows that the proposed emission mechanism is reasonable and measured emission current densities can be explained quantitatively by the discussed interpretation of the emission process. The large scatter of measured A values as well as the fact that these values should be inferred from a presentation in $\ln j$ and not in $\ln j/T^2$ does explain sufficiently well the difference between measured and calculated data.

Before we discuss the conditions for Cs covered surfaces we may consider what happens to a substrate atom at the surface. Substrate atoms are present also at bare surfaces especially at high temperature. Therefore such a discussion is by no means a hypothetical one. Also atoms at the surface have of course localized electron orbitals and therefore substrate (- and

other) atoms at the surface cannot be excluded from the electron emission process. A naive application of the concept of electronegativity would give different electronegativities for surface atoms and atoms at the surface [1]. However, from a simple cycle process (fig. 1) (including the emission from one species and the reverse process from the other) we have to conclude that the "emission electronegativity" for surface atoms and atoms at the surface must be equal due to thermodynamic principles. We have a similar situation for surfaces of different orientation and analog to that case the difficulty can be overcome if we assume that atoms at the surface and surface atoms are at different electrical potentials. This potential difference causes an additional change in "emission electronegativities".

A change in potential and therefore a change in electronegativity of surface atoms can equally be produced by an external influence as for instance by a dipole layer or by the electric field of an electron (just outside the surface). A detailed discussion of this influence shows that the classical calculations concerning the change in work function by a surface dipole layer or the creation of an image force by charged particles just outside the surface are valid also for the concept of localized electron orbitals. Such a discussion would exceed the limits of this paper and will be presented elsewhere [8] .

Thermionic emission from Cs covered surfaces

In recent times two different explanations for the thermionic emission from Cs covered surfaces have been given. Gyftopoulos and coworkers [9, 10] applied the concept of electronegativity to Cs-atoms adsorbed at the surface in order to calculate the change of the work function in dependence of Cs-coverage. Rasor and Warner [11] used a classical interpretation for this phenomena and explained the increase in thermionic emission by the formation of a dipole layer (created by Cs ions at the surface). We mentioned already that in principle the latter interpretation does not contradict the concept of the localized electron orbitals and therefore it seems reasonable to discuss both concepts in connection with the new interpretation of the emission process. In this case the electron emission from surface atoms and atoms at the surface must be considered. But as we pointed out in the first section we have to imply that the "emission electronegativity" is equal for all species involved in the emission process.

The dipole layer concept can be regarded as a calculation for the variation of the electronegativity of substrate surface atoms [11] whereas the calculations in refs. [9][10] are related in principle to the electronegativity of adsorbed Cs atoms. Therefore in both concepts the same quantity is investigated as long as substrate surface atoms take part on the emission process. The emission is suppressed if bonds between Cs atoms are formed. Of course this limited range of validity for the dipole layer concept has not been discussed in the paper of Rasor-Warner because a different emission process was considered.

Having this in mind there is only one difference in both descriptions.

Gyftopoulos and Levin assume only one state for the adsorbed Cs particle at the surface, whereas Rasor and Warner differ between an adsorbed Cs atom and Cs ion. Principally both assumptions are reasonable and in fact, if we include all excited electron orbitals, even more than two states should be included into the consideration. The question is whether two orbitals of such different dipole moments and electron structure can exist having nearly the same energy. The author believes that this can be the case for Cs atoms due to two reasons:

1. Cs has a low free atom ionization energy and therefore an "idealized ionization process at the surface" (this means the ion is only kept by its image force at the surface [11]) needs a small amount of (positive or negative) energy.
2. The Cs ions have a noble gas electron configuration, which does not form common orbitals with surface atoms as we know from the surface adsorption of noble gas. Therefore the idealized ion adsorption may be rather realistic. This interpretation is also supported by measured values of the ion adsorption energy (of 2.15 eV) [12] which corresponds nicely to the calculated data (of 2.04 eV) [11].

In the following discussion common features of the one and two surface states concept are considered. To get also a good comparison to experimental data the work function variation is calculated in dependence of the temperature ratio T/T_R . T_R means the Cs reservoir temperature characterizing a certain Cs pressure. Normally, the emission current is taken at conditions where only neutral atoms can escape from the emitter surface. Therefore we only have to obey the particle balance equation for neutrals, which is

given for both cases as

<p>R - W</p> $n \cdot \tau_0 \cdot e^{-V_a/T} = n_{Cs} \cdot \tau_{Cs} \cdot e^{-h/T} \quad (5R)$ <p>where V_a is equal to</p> $V_a = E + \phi + V_i - V_j \quad (6R)$		<p>G - L</p> $n^* \cdot \tau_0 \cdot e^{-V_a^*/T} = n_{Cs} \cdot \tau_{Cs} \cdot e^{-h/T} \quad (5G)$ <p>where V_a^* is equal to</p> $V_a^* = \phi + V_i^* - V_j \quad (6G)$
---	--	---

The symbols have the following meaning (all n values are related to unit surface area)

n number of adsorbed Cs atoms | n^* number of adsorbed Cs particles

τ_0 characteristic frequency of the substrate lattice

V_a evaporation energy of a Cs atom from the substrate | V_a^* evaporation energy of a particle as atom

n_{Cs} number of Cs atoms on the Cs surface (this number should also be equal to the number of sites available for Cs atoms at the substrate surface)

τ_{Cs} characteristic frequency of Cs

h evaporation energy of Cs from the Cs surface

T_R Cs reservoir temperature

E ionization energy for a Cs atom at the substrate surface |

ϕ substrate work function

V_i evaporation energy of a Cs ion from the surface | V_i^* evaporation energy of a Cs particle as an ion

V_j ionization energy of a free Cs atom

For the number of surface ions n^+ we get the relation |

$$\frac{n^+}{n} = g \cdot e^{-E/T} \quad (7R) |$$

where g is the ratio of weight factors for the Cs atoms and ion adsorption state.

If we combine equations (5R) (6R) and (7R) or (5G) and (6G) and form the logarithmic expression, we get

$$\ln\left(\frac{n^+}{n_{Cs}} \frac{\tau_0}{\tau_{Cs}} \cdot g\right) = -\frac{h}{T_R} + \frac{\phi + V_i - V_j}{T} \quad (8R) \quad \left| \quad \ln \frac{n^*}{n_{Cs}} \frac{\tau_0}{\tau_{Cs}} = -\frac{h}{T_R} + \frac{\phi + V_i^* - V_j}{T} \quad (8G)$$

The lefthand side of both equations is of the order of one for the region of medium coverage. In equation (8G) we have the product of surface coverage and ratio of characteristic frequencies or Debye temperatures in the logarithmic expression. Also in expression (8R) we can prove this statement if we multiply the ratio n^+/n_{Cs} by the dipole moment p_o of a surface ion plus its image charge and realize that $ep_o n^+ \approx \Delta \phi$ whereas $ep_o n_{Cs}$ is about 8 eV (fig. 2 in ref. [11]). The ratio of weight factors is of course of the order of one.

Therefore we can write for this interval of coverage

$$\phi + V_i \approx h \frac{T}{T_R} + V_j \quad (9R) \quad \left| \quad \phi + V_i^* \approx h \frac{T}{T_R} + V_j \quad (9G)$$

We know from experiments [11] that in this interval ϕ is already a linear function of T/T_R (fig. 2) and therefore V_i must also be a linear function of T/T_R . For both models the relation must hold

$$\Delta \phi = -f \Delta V_i \quad (10R) \quad \left| \quad \Delta \phi = -f \Delta V_i^* \quad (10G)$$

f , is a constant factor and Δ means the difference between work function or adsorption energy at bare and covered surface conditions. f can be concluded from the slope of the line (fig. 2) which is given by $\frac{1}{1-f} \cdot h$ (9G, R).

Rasor and Warner gave a simple explanation for the appearance of f . The ions have only to overcome a part of the dipole potential whereas the electron work function is reduced by the whole amount of this potential difference.

In the concept of Gyftopoulos Levin such a simple explanation of relation (10G) is not possible and therefore the assumption of two adsorbed states leads to a more convenient description for the range of medium coverage. In the following section another example is given which confirms that statement.

At high coverage however, the dipole layer concept can no more be applied to explain experimental data. A formation of bonds between adsorbed Cs atoms restrict the emission from the substrate surface*). In this region the only reasonable description, which exists up till now, is that of Gyftopoulos and coworkers [9, 10]. Calculations based on their concept agree very well with measured emission data at high coverage. This can be due to the fact that in this region the influence of the ions is of minor importance or even that an ion formation is practically suppressed by the Cs-Cs bonds at the surface.

Minimum work function calculation

In this section it is shown that reasonable minimum work function values for cesiated surfaces can be calculated based on the assumption that atoms and ions are present at the surface and formation of bonds can be neglected even for medium coverage. For the calculation the additional assumption is made that V_a is independent of coverage [11]. We use for V_a the empirical relation

$$V_a = \frac{1}{2} (h_s + h_g) \quad (11)$$

where h_g is the evaporation energy of a substrate atom. Relation (11) can also be justified by the concept of electronegativity [13]. Desorption experiments, although with other atoms, showed that V_a can be constant at least up to a coverage of 50% [14].

We will further neglect the polarizability of the Cs ion, which simplifies the calculation. In this case the change in work function is simply given by the relation

$$\Delta \phi = e n^+ p_0 \quad (12)$$

where p_0 is the dipole moment of a single ion plus image charge. If we ex-

*) The author believes that the formation of bonds between Cs atoms at the surface has been overestimated in ref. [9, 10] for the range of medium coverage.

press n^+ by equation (7R) and substituting (12) we get the relation

$$\frac{\Delta\phi}{e p_o n} = g \cdot e^{-E/T} \quad (13)$$

The logarithmic form of equation (13) can be written

$$\ln \frac{\Delta\phi}{e p_o n \cdot g} = \frac{\phi_o + V_{i0}}{T} - \frac{V_j - V_a}{T} - \frac{(1-f) \Delta\phi}{T} \quad (14)$$

if equations (6R) and (10R) are substituted. ϕ_o and V_{i0} are related to bare surface conditions.

We realize that even at full coverage ($n = n_{Cs}$) the value $e n_{Cs} p_o$ is about 8 V (ref. [11] fig. 2) whereas the measured $\Delta\phi$ values for refractory metals are in the order of 3 V. Therefore $\Delta\phi$ does not depend sensitively on n in the range where minimum work function occurs. This means equation (14) can be used to estimate minimum work function even if we do not know exactly the numerical value of n for the minimum conditions.

Of course this conclusion is only correct if we further suppose that the formation of bonds between Cs atoms at the surface increases the work function monotonously towards the value of Cesium (a similar assumption has been made in ref. [10]).

We substitute $\Delta\phi$ by $\phi_o - \phi_{min}$ in equation (14) and express V_a by equation (11) to derive

$$\phi_{min} = \left(1 - \frac{1}{1-f}\right) \phi_o + \frac{1}{2(1-f)} (h h_s) + \frac{V_j - V_{i0} + T \cdot b}{1-f} \quad (15)$$

The ratio $\frac{1}{1-f}$ can be concluded from work function data taken in the linear range of the Rasor plot (fig. 2).

The factor b means the expression $\ln \frac{\Delta\phi}{p_o n} \cdot \frac{1}{g}$ which should be in the order of -1.

If we take T equal 0.1 eV (characteristic for collector temperatures in thermionic converters) we get the best fit to experimental values taking $g = -1.5$. The quantities V_j (3.89 eV) and V_{i0} (2.05 eV) are known and therefore ϕ_{min} can be calculated for materials which have been investigated in the range of low Cs surface coverage.

In table 1 theoretical values of minimum work function for different materials are indicated. ($\frac{1}{1-f}$ concluded from ref. [11] and [12] ; h taken from ref.[11]

Although the calculation must be considered as a rough approximation, the agreement with experiments is surprisingly good. Due to this data Ir, Mo, Ni and Re have lower work functions than the other metals listed in table 2.

This theoretical result corresponds with the experience that Mo and Ni turned out as two of the best collector materials.

Due to the large scatter of reported minimum work function data, a detailed comparison with such values is not very instructive. However, the gained results confirm again that the assumption of Cs ions leads to reasonable conclusion.

Bibliography

- [1] D. STEINER, E. P. GYFTOPOULOS, 27th Annual Conf. Physical Electronics (1967) 160
- [2] H. O. PRITCHARD, H. A. SKINNER, Chem. Rev. 55 (1955) 745
- [3] J. FRENKEL, "Kinetic theory of liquids", Dover Publications, New York 1955
- [4] C. HERRING, M. H. NICHOLS, Rev. Mod. Phys. 21 (1949) 185
- [5] L. N. DOBREZOW, "Electronen und Ionenemission", VEB Verlag Technik Berlin (1954) 47
- [6] P. W. BRIDGMAN, Phys. Rev. 27 (1926) 173
- [7] F. SEITZ, "Modern theory of solids", McGraw-Hill Book Company Inc., 1940
- [8] J. BOHDANSKY, in preparation
- [9] E. P. GYFTOPOULOS, J. D. LEVIN, J. Appl. Phys. 33 (1962) 67
- [10] E. P. GYFTOPOULOS, D. STEINER, 27th Annual Conf. Physical Electronics (1967) 169
- [11] N. S. RASOR, C. WARNER, J. Appl. Phys. 35 (1964) 2589
- [12] R. G. WILSON, 26th Annual Conf. Physical Electronics (1966) 157
- [13] L. PAULING, "The nature of chemical bond", Cornell Univ. Press 1960, p 82
- [14] J. R. ARTHUR Jr., 27th Annual Conf. Physical Electronics (1967) 188

Material	$\frac{en_0 \bar{T}_0}{T_0^2}$	A Measured
W	260	30-200
Mo	310	20-300
Ta	210	10-100

Table 1: Comparison of the emission constants.
($T_0=1800$ °K)

Material	V_a (in eV)	$\frac{1}{1-T}$	ϕ_0 (in eV)	ϕ_{min} (in eV)
W	2,58	1,73	4,6	1,6
Ta	2,48	1,8	4,3	1,7
Nb	2,38	1,78	4,1	1,7
Mo	2,28	1,8	4,4	1,4
Re	2,5	1,8	4,9	1,4
Ir	2,24	1,55	5,4	1,5
Ni	1,82	~ 1,6	4,5	1,5 ?
Os	2,4	~ 1,6	5,1	1,5 ?

Table 2: Calculated minimum work function values.

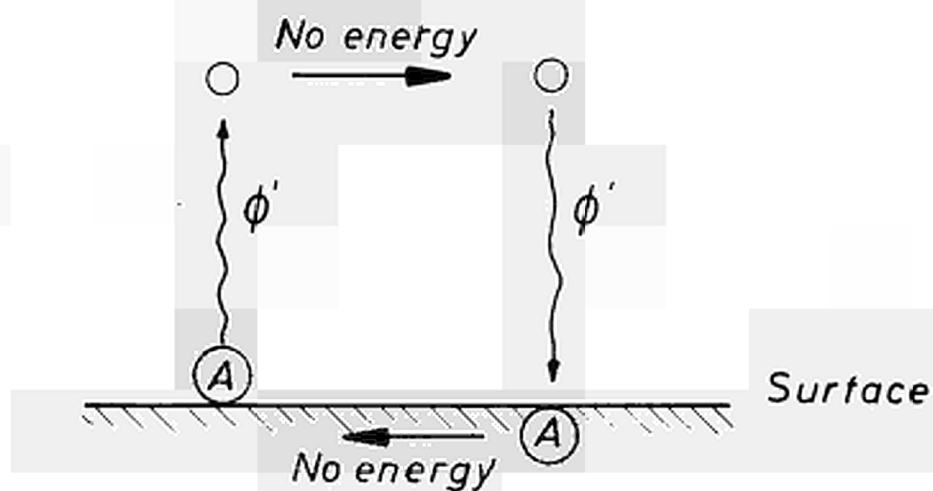


Fig.1: Emission from surface atoms and atoms at the surface.

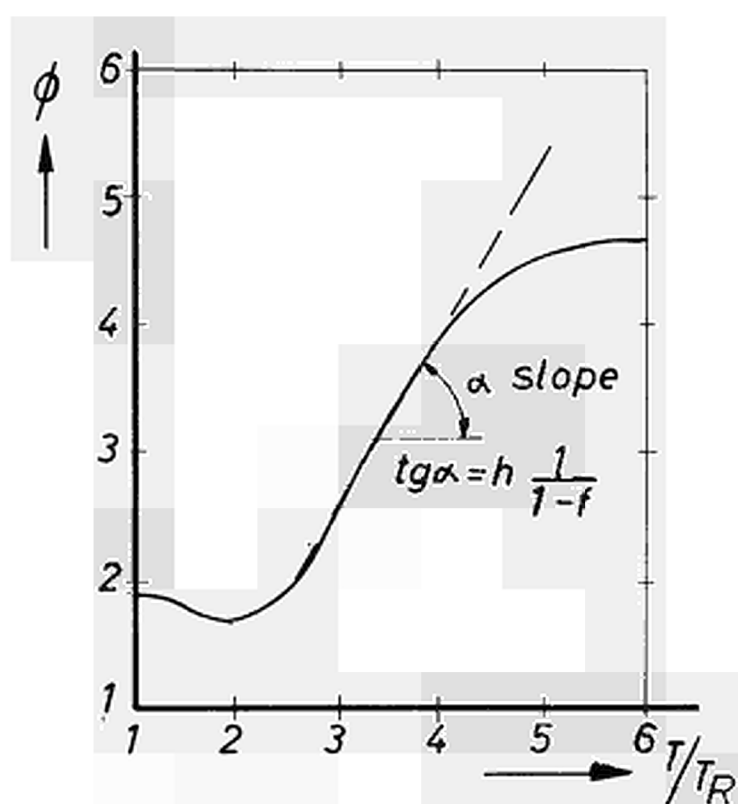


Fig.2: Typical result for workfunction decrease in dependence of Cs coverage (example W)

DISCUSSION

Speaker of paper K-2: J. BOHDANSKY.

MUZ (Germany): Dr. BOHDANSKY, the equation used to describe the work function decrease, that is $\Delta \phi = Kn \cdot \exp(-E/T)$ seems to be a very rough approximation. I wonder, how you can calculate a minimum in work function from this simple assumption, and if so, should there be not a very strong temperature dependence of this minimum?

BOHDANSKY (Euratom): We obtain a minimum in the work function by assuming that ions and atoms are at the surface according to the theory of RASOR and WARNER and that the surface has nearly full cesium coverage. For this condition the energy term in the exponential function becomes about zero. Therefore, the influence of temperature on this minimum value is very weak.

THE CATHODE MATERIALS OF THE THERMOEMISSION
CONVERTERS RESEARCH (TEC)

Belomytzev Yu.S., Babina F.L., Dmitrieva I.B., Kolobkov Yu.G.,
Malykh V.A., Moskalev Yu.I., Moskaleva A.N., Prilezhaeva I.N.,
Privalova M.M., Pumpurs V.M., Savitzkii E.M., Saratovskii
L.N., Smirnov A.A., Solomonov N.E., Spyvak G.V., Tilkina M.A.,
Shyshkin B.B.

INSTITUTE OF PHYSICS AND POWER ENGINEERING

OBNINSK

THE MOSCOW STATE UNIVERSITY
THE INSTITUTE OF METALLURGY

MOSCOW, USSR.

The cathode materials of TEC must possess the complex of the physical-mechanical and technological properties. They also satisfy a number of the specific requirements connected with their utilization as the thermoemitters in the alkali metal vapours. The pure refractory metals have not satisfactory mechanical and technological characteristics /1/. The mechanical and technological properties of

the refractory materials can be improved by making of the alloys /2/.

The possibility of utilization the alloys as the emitter covers of TEC are determined by their emission characteristics and their stability in the work conditions. For the investigation were choosed low and high alloys on the basis of molibdenum and tungsten (see Table 1), obtained by the electrical arc melting in vacuum with the expensing electrode.

It is known, that the more high specific parameters of TEC can be obtained either in the arc regime (pressure of the cesium vapours 3-20 mm Hg), or at low cesium pressures, when the value of cathode-anode gap is of the order of electron free path length /3/. At present, the practical importance has the first direction. In this case the high specific parameters are determined by the properties of effective metallic film emitter, forming on the cathode surface, and with the cathodic jump of potential, reducing the effective work function.

Materials having the near values of mean work function in vacuum, has the different effectiveness in the arc regime of TEC working /4/. The latter is explained with the different spotting of the cathodes and with the anomalous Schottky effect. In our opinion, the increasing of emission current in the arc regime can be explained also with the increasing of cesium heat desorption on arising at the cathode of the positive excessive charge. At little degrees of cover the desorption heat increases on the value $e I_{loc}$, where I_{loc} - local work function of the cathode in vacuum /5/. γ - potential of cesium ionisation.

In connection with that the cathodes of TEC must be characterized by not average, but the local values of work function. As the development of the specific electrical parameters is limited by the desorption process of cesium, at rising temperature the cathodes with large value I_{loc} are more effective.

The work at high level of the residual gases and also at the accumulation of fission products in the volume are the specific conditions for the reactor TEC. In the present work for this reason the measurements \mathcal{I}_{loc} were carried out at the residual pressure of the order $5 \cdot 10^{-5}$ mm Hg in the device. We originated from the fact, that the oxygen partial equilibrium pressure determined by the cesium film on the anode is of the order $5 - 10^{-5}$ mm Hg /6/.

The distribution function of the cathode surface S on the work function \mathcal{Y} is leaded into the consideration:

$$\beta(\mathcal{Y}) = \frac{1}{S} \frac{dS}{d\mathcal{Y}} \quad (1)$$

As the grains of different crystallites, forming the alloy, are distributed accidently, on his surface, the function $\beta(\mathcal{Y})$ can be approximated by Gaussian distribution

$$\beta(\mathcal{Y}) = \alpha \exp[-\gamma^2(\mathcal{Y} - \bar{\mathcal{Y}})^2] \quad (2)$$

where $\alpha, \gamma, \bar{\mathcal{Y}}$, - parameters, characterizing the each alloy and the definite medium of residual gases. The knowledge of function $\beta(\mathcal{Y})$ of the materials, using as the emitters of TEC, allows to value their effectiveness.

For the determination of function $\beta(\mathcal{Y})$ were used the two methods: the method of electron emission microscopy /7/ and the method based upon the calculation of necessary functions from the curves of thermocurrent delay /8/. For the first method the experiments was carried out in the device EEM-75/7/ at the pressure of residual gases $5 \cdot 10^{-6}$ mm Hg. The sample had the thickness $15-20 \mu$ and the length $15-22$ mm. The sample serves as cathode of the immersion objective. The heating of cathode was realized either by means of the electron bombardment or with the current putting through the sample. The cathode temperature was determined to the nearest $\pm 20^\circ\text{C}$. The part of electron beam, creating the image was collected in the Faraday cylinder through the hole $\phi 0,34$ mm in the screen and was measured by the electrometrical amplifier d.current. Knowing the linear increasing of

the device we can calculate the current emission density from measured area of sample (in the present case the value of this microarea was $\sim 5,2 \cdot 10^{-6} \text{ cm}^2$), and consequently, the effective local work function. For exception, of the influence the generalized field of "spots" on the emission current the latter was measured in the centre of crystallites (the dimensions of which on samples were 10μ and more) /7/. As the calculations shows, in the case, the field of "spots" can't to account. The work function was measured in 100-300 different points of surface by means transferring of the sample in plane of object.

If N -the total number of the measurements, N_1 -the number of the measurements of the work function, laying within the limits from \mathcal{Y} to $\mathcal{Y} \pm \Delta \mathcal{Y}$, ($\Delta \mathcal{Y} = \pm 0,05 - 0,07 \text{ V}$ - the error of determination of the local work function in our experiments) we have:

$$\beta(\mathcal{Y}) = \frac{1}{N} \frac{N_1}{2 \Delta \mathcal{Y}} \quad (3)$$

The functions $\beta(\mathcal{Y})$ were determined by this methodic for a number of alloys on the basis of the molybdenum.

In Fig.1 is given the emission photography of alloy N4 in which the grain boundaries are revealed. The contrast of image depends on the different emission ability of the grains.

The typical curves $\beta(\mathcal{Y})$ are given in fig.2. The displacement of the curve $\beta(\mathcal{Y})$ after heating is connected with degassing of the sample. The curve 1 - is reproduced after staying of the sample in the atmosphere. It is necessary to mark, that the data obtained are depended from time and temperature of heating of the sample. This accounts because in the choosing vacuum conditions the system of alloy-film the chemisorption oxygen is studied.

On the basis of the experimental results can be concluded as follows:

1. The functions $\beta(\mathcal{Y})$ of the studied alloys are Gaussian.
2. At pressure in the device $5 \cdot 10^{-6}$ top mm Hg the system of alloy-oxygen is studied. It is characterized with the

negligible half-width of the distribution work function on the surface ($\sim 0,15v.$)

At investigation by method of the delay curves the experiments have been carried out in the three-electrode system, mounted in the device in which vacuum $5 \cdot 10^{-9}$ tor can be ensured. The work have been carried out at pressure of the residual gases of the order $5 \cdot 10^{-6}$ tor for comparison of the methods of determination $\beta(\mathcal{Y})$.

The diagram of the experimental set up are given in the Fig.3. At fixed cathode temperature the grid bias is defined at which the current on the grid are reaching the saturation. By supplying on the anode of the delaying potential the curve of delay was measured. The grid was choosed with low transparency and the measurements was carried out in the anode current region 10^{-10} - 10^{-11} a. The electron temperature is determined by measuring curve of the delay /8/. The coincidence of the electron and lattice temperatures (the latter was determined with the optical pyrometer) was the criterium of accuracy of the delay curves. In accordance with /8/ the function $\beta(\mathcal{Y})$ have been determined by differentiation twice and normalization of the delay curves. The determination accuracy of the function $\beta(\mathcal{Y})$ in the point ~ 15 - 20% , the determination accuracy of $\mathcal{Y} \sim 0,05v.$ This method permits to establish reliably the initial area of the function $\beta(\mathcal{Y})$, suitable for our case to the large \mathcal{Y} . The errors are arising at differentiation of the curve in points, near to saturation. This errors were excluded as follows. Calculating the initial area of the curve $\beta(\mathcal{Y})$ we have approximate her by the formulas (2) and from coefficients α, γ, ζ , determined thus all the curve was recovered.

In the Fig.4 are given the results of the investigation of alloy N1 by this method. The curve 1 is described by function $\beta(\mathcal{Y}) = 1,71 \exp[-5,14(\mathcal{Y} - 4,24)^2]$

Thus, the method of delay curves can be used for the determination of the function $\beta(\mathcal{Y})$ in the conditions

of the superhigh vacuum and for the exclusion of the ion bombardment of the sample. The investigation of the distribution local work function $\beta(\varphi)$ was carried out in parallel with the measurements of output parameters of TEC with emitters from the series of alloys (see Table 1). The investigations were carried out on the sets with the TEC of flat configuration and with the electron heating of samples. The measurement of cathode temperature was conducted with accuracy about $\pm 30^{\circ}\text{C}$. The variation of distance between the cathode and anode was carried out within the limits 0,1-0,7 mm with accuracy about $\pm 0,005$ mm.

In Fig.5 are given the dependence curves of the specific power from the pressure of cesium vapour for three molybdenum alloys at the cathode temperature 1600°C . It is clear, that addition of the rhenium to molybdenum gives some increasing of parameters. The addition of rhenium leads to more influence in the case of testing in residual vacuum $2-4 \cdot 10^{-2}$ mm Hg and some other conditions of degassing.

In the Fig.6 are given the values of specific electrical power at temperatures 1600 and 1800°C for the alloy N4 at gap 0,5 mm. The dependence of specific power from the gap at temperature 1800°C is given in the Fig.7.

In the Fig.8 are given the optical values of specific power of alloy N5 for some interelectrode distances. In the Fig.9 are given the comparison of output parameters of alloys NN5 and 6 in the identical conditions at the gap 0,4 mm the pressure of cesium vapour 6,2 mm Hg. The testings shows, that the optimal specific parameters of TEC are provided in the identical conditions by alloys N5 and N6. The alloys on the basis of molybdenum show the essential dependence of the specific parameters from vacuum conditions of testing.

Methods of analysis of components of alloys and of impurity in cesium were developed.

The determination of alloy components Mo-Re and Mo-W-Re have been carried out by differential-spectropho-

ometric methods in presence of masking complexing agents or after separation of elements by extraction. The separation of rhenium from the molybdenum reached with extraction by cyclohexanone from the solutions of sulphuric acid. The extraction of rhenium from the solution of sulphuric and nitric acid was applicated also at concentrating of the impurities Nb, Zr, W, U, Ta, Fe, Mn, Mg, Pb, Cr, Sn, Ni, Bi, Cu, In, Co, Cd, Zn and other in 10-80 times before the spectral determination with the sensitivity 10^{-3} -n. 10^{-6} %.

The concentrating of the impurities Fe, Al, Ni, Pb, Bi, Ga, Co, Cd, Cu, In, Zn, Mo, Mn, Ti, Ag, Sr, V, Be, in 20-50 times for the spectral determination at analysis of Cs carried out with the extraction by means organic solvents with group reagents-oxyquinoline and dithizon. The impurities Ca, Mg, Ba, Cr, Sr, determined by spectral method without concentrating. The sensitivity of the method $1 \cdot 10^{-3}$ - $1 \cdot 10^{-6}$ %. The determination Na, K, Li, in the Cs were conducted by the method of flame photometry with the sensitivity $1 \cdot 10^{-3}$ %.

The concentrating of the oxygen impurity produced by distillation of the metallic Cs from the sample in vacuum. In the residue after distillation have been determined the concentration of oxygen by acid titration of aque solution of the residue. The sensitivity of method $1 \cdot 10^{-3}$ w/o of oxygen. The mechanical properties of research alloys on the plate samples in different conditions are given in Table 2.

The molybdenum alloys can be treated well by the method of hot and cold deformation. They had a low temperature of cold brittleness and the satisfactory technological plasticity allowing to recieve the rod, sheet, foil, tube and wire. The alloy can be welded by electron beam welding.

The tungsten alloy N5 possesses with insufficient technological properties. The optimal composition of alloys of the Mo and W with Re possessing a well technological properties, weldability and simultaneously the high mechanically properties at room and high temperatures lays near to the boundary of saturation of solid solutions (20-30%Re, in W and

40-50% in Mo). The W alloy N6 is one of the most plastic alloys at room temperature. On technological properties weldability, processing and temperature of recrystallization the alloy N4 of the triple system Mo-W-Re takes up the intermediate position between the alloys of molybdenum, Re and W-Re.

Conclusion

1. The method of determination of local work function by means the emission microscope, and also by the method of the delay curves were developed.
2. The investigation of output parameters of TEC with the emitters from the alloys on the basis of Mo and W at temperature about 1600-2000°C was carried out. It is shown, that TEC with the emitter from the alloys on the basis of W possesses the more high output parameters.

References

1. Savitzkii E.M., Burchanov G.S. The metallography of refractory metals. "Nauka", 1967.
2. Savitzkii E.M., Tilkina M.A., Povarova K.B. The alloys of rhenium. "Nauka", 1965.
3. Majev S.A., Gus'kov Yu.K., et al. Journ. Tekhn. Fiz., 37, 6, p. 1079-1090 (1967).
4. Wilson V.C., Lawrence J. Operating characteristics of two thermoionic converters having Cs-Ni and W-Ni electrodes. Adv. Energy Conversion, 4, p. 195-221, 1964.
5. Mackinson P. The cathode corrosion of TEC. The thermo-emission conversion of energy. The collection of simposium materials, v. 1, p. 112, Atomizdat, 1967.
6. Kaminskii M. The atomic and ion collision on the metallic surface. "Mir", 1967.
7. Spyyvak G.V., Shyshkin B.B. Radiotekhnika and Elektronika XI, 1826 (1966).
8. Buliginskii D.B., Dobretzov L.N. Journ. Tekhn. Fiz., 26, 977, (1967).

Table I

The composition of alloys and condition of testing

N alloy	Composi. of alloy %	The regime of emitter degassing			the parameters of testing
		time hour	temperatur. °C	vacuum mm Hg	
1	Mo+0,4	a)10	1800	$1 \cdot 10^{-6}$	Anode T= 580-630°C Res.vacuum $1 \cdot 10^{-6}$ mmHg Anode T= 600°C Res.vacuum $4 \cdot 10^{-5}$ mmHg
	Ti+0,2 Zr	b)10	1650	$4 \cdot 10^{-5}$	
2	Mo+8Re	a/10	1800	$1 \cdot 10^{-6}$	Anode T=580+ 630°C Res. vacuum $1 \cdot 10^{-6}$ mm Hg Anode T=600°C Res.vacuum $3 \cdot 10^{-5}$ mm Hg
		b/10	1650	$3 \cdot 10^{-5}$	
3	Mo+47Re	10	1800	$1 \cdot 10^{-6}$	Anode T =580- 630°C Res. vacuum $1 \cdot 10^{-6}$ mm Hg
4	Mo+27Re+ +39W	10	1900	$1 \cdot 10^{-6}$	Anode T= 600- 700°C Res. vacuum $1 \cdot 10^{-6}$ mm Hg
5	W+0,05Nb	14	1900	$1 \cdot 10^{-5}$ - $5 \cdot 10^{-6}$	Anode T = 690-730°C Res. vacuum $5 \cdot 10^{-6}$ mm Hg
6	W+27Re	14	1900	$1 \cdot 10^{-5}$ - $5 \cdot 10^{-6}$	Anode T = 690-740°C Res.vacuum $5 \cdot 10^{-6}$ mm Hg

Table II

The mechanical conditions of alloys

NN alloy	Condition	T or measure. °C	The mechanical properties		
			σ_v kg/mm ²	$\sigma_{0,2}$ kg/mm ²	δ %
1	Cold work-				
	ing	20	143,0	140	5,5
	- " -	1200	57,1	51	4,5
	1100 ^o hour	20	106,0	101	8,2
		1200	45,5	39	4,7
2	Cold work.	20	105,3	105	4,8
	1200 ^o 30min	20	56,4	40	17,8
	-"-	1200	16,5	15	14,3
3	Cold work.	20	178	-	2-4
	-"-	1500	15,2	-	9
	Recrystal.	20	110	-	15-25
	Recrystal.	1500	15	-	-
4	Cold work.	20	220	-	2-3
	-"-	1800	9,3	-	23,5
	Recrystal.	20	120	-	15-20
	Recrystal.	1500	25	-	-
5	Recrystal.	400	50,5	34	40,0
	Recrystal.	1200	24,0	8	33,5
6	Cold work.	20	250	-	2-3
	-"-	1500	30	-	6,7
	Recrystal.	20	150	-	15-20
	Recrystal.	1500	35	-	-



Fig.1 The emission electron-microscopical image of alloy #4.

The cathode temperature $\geq 2000^{\circ}\text{K}$. $\times 1000$.

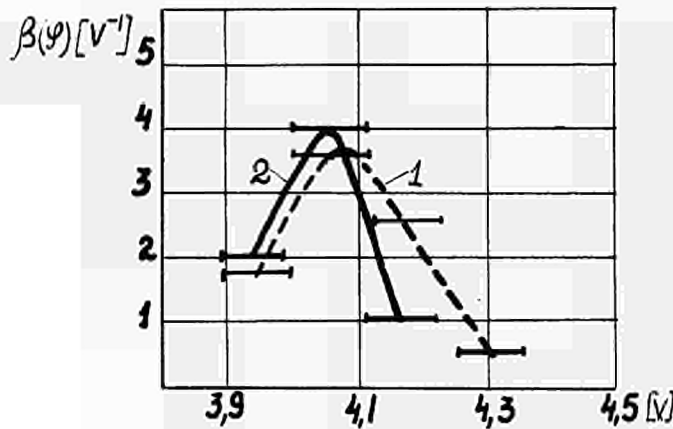


Fig.2 The distribution function of area of the sample on work functions $\beta(\varphi)$ for the alloy N1, by measuring at 1800°K :

1 - before degassing
2 - after degassing at temperature 1850°K for 5 hour.

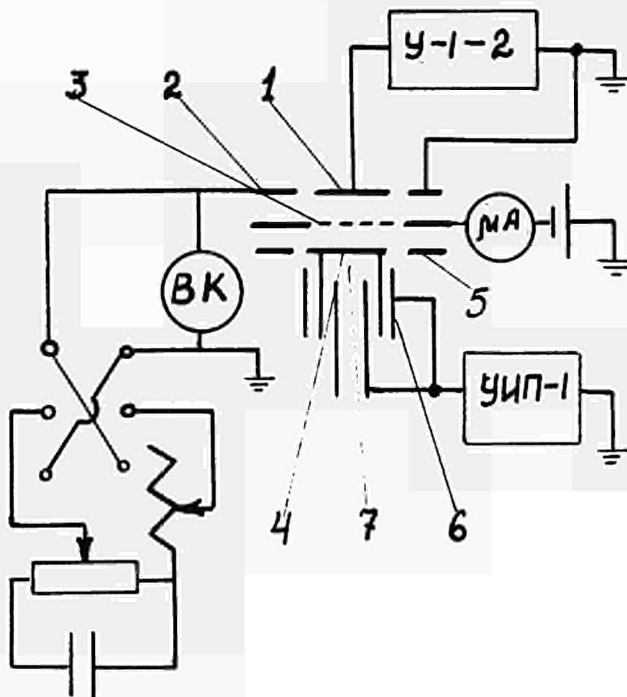


Fig.3 The diagram of the experimental set up for the measurements $\beta(\varphi)$ on the method of the delay curves.

1 - anode;
5, 2 - guarding rings;
3 - grid (platinum 120x120)
4 - object;
6 - cylinder, screening of the heater 7.
BK - the cathodic voltmeter
Y-1-2 - galvanometer
YUП-1 - rectifier

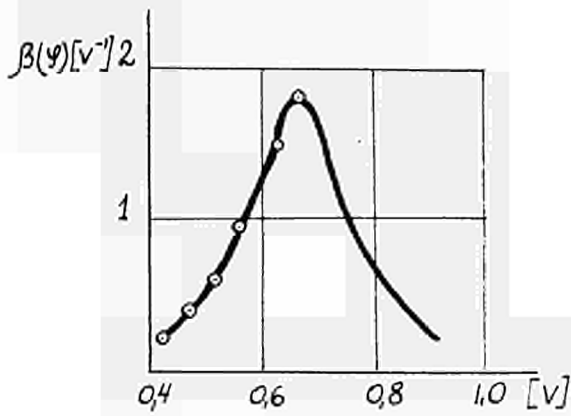


Fig.4 The distribution function $\beta(y)$ for the same sample from the alloys N1, on the method of the delay curves. At temperature 1600°K by degassing at 1850°K for 1,5 hour. Half-width of function equal fig.2.

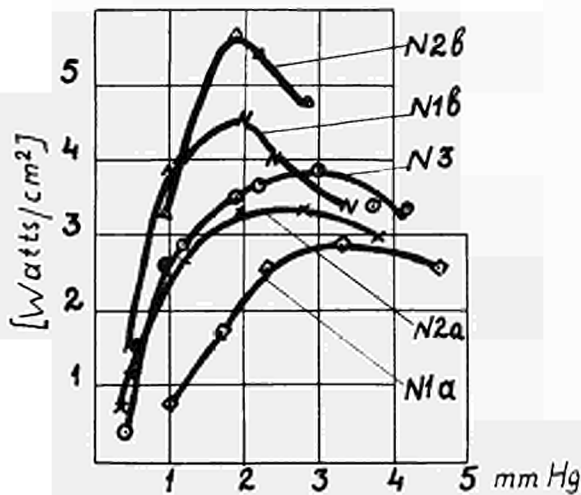


Fig.5 The dependence of specific power TEC from pressure Cs vapour for the alloys NN1,2,3: N1a,2a,3 - taking at residual vacuum $1 \cdot 10^{-6}$ mm Hg. N1b,2b - taking at residual vacuum $2 + 4 \cdot 10^{-5}$ mm Hg interelectrode gap 0,5 mm.

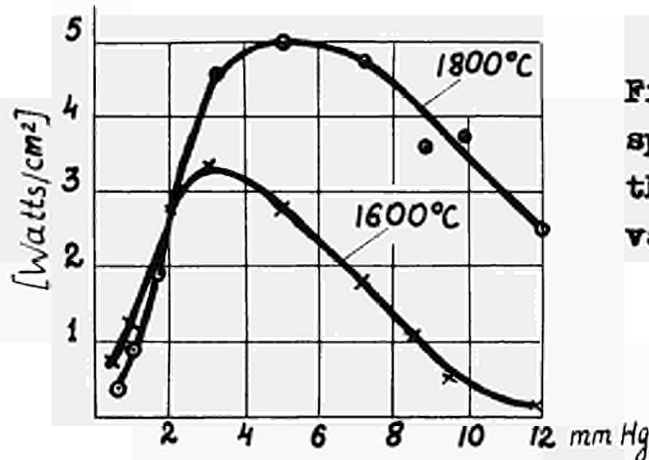


Fig.6 The dependence of the specific power TEC from the pressure of cesium vapour for the alloy N4.

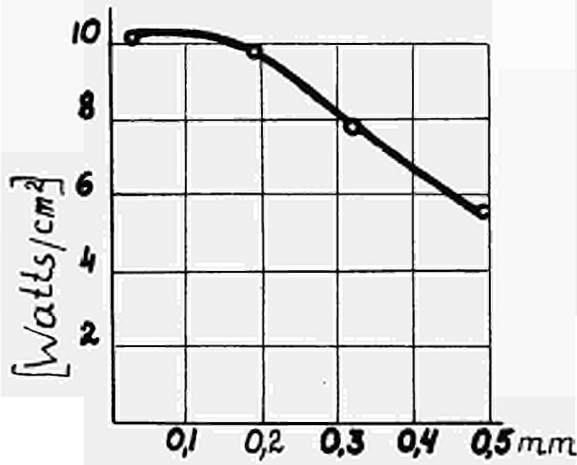


Fig.7 The dependence of the specific power TEC from the value of inter-electrode gap for the alloy N4. At the pressure of cesium 5 mm Hg.

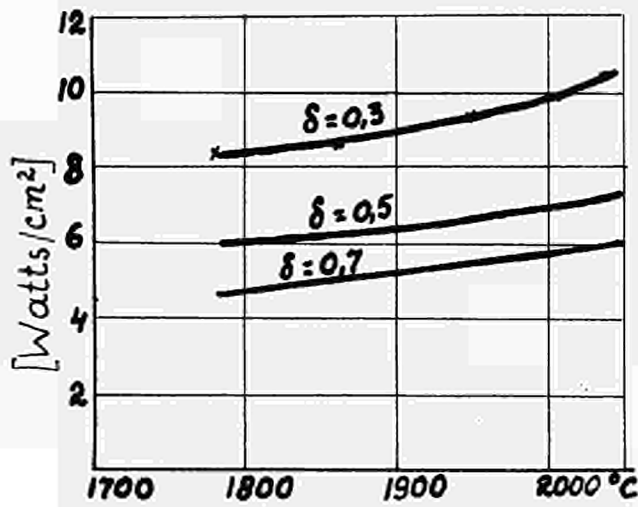


Fig.8 The dependence of the optical specific power TEC from temperature of emitter. The pressure of cesium vapour 6-17 mm Hg at gaps 0,3; 0,5; 0,7 mm. The alloy N5.

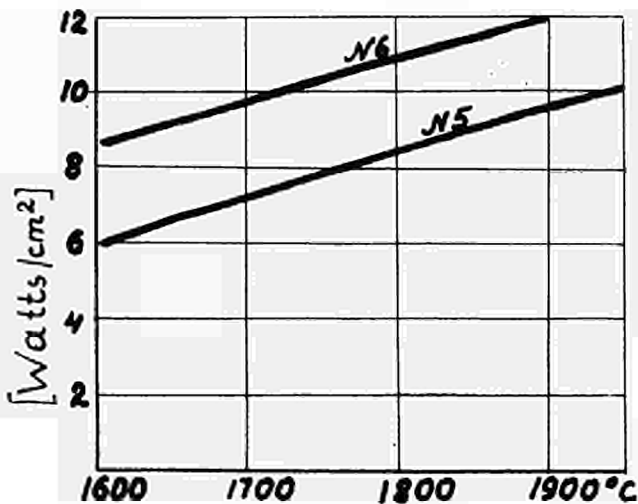


Fig.9 The dependence of specific power TEC from temperature of emitter for the alloy N6 and N5. At the pressure of cesium 6,5 mm Hg and at gaps 0,4 mm.

Work Function Measurements of Refractory Metals in a High Pressure Cesium Plasma for Low Probe Temperature Range

V. Bundschuh

Institut für Technische Physik der Kernforschungsanlage
Jülich GmbH, Germany

Summary

A special plasma anode technique was used for the analysis of the workfunction of polycrystalline tungsten, rhenium and nickel-disks in cesium vapour. These measurements were carried out at a cesium bath temperature between 470° and 540° K and at a probe temperature range from about 1300° K down to near the bath temperature. The results are represented in Raso-Warner diagramm ϕ versus T_{Pr}/T_{Cs} .

The smallest value of the workfunction of cesium covered probes, which is important for the collector of thermionic converters, depends on the "bare" workfunction. The higher the "bare" workfunction the lower is the minimum of the workfunction of covered probes. This result corresponds to the theory of Raso and Warner.

Introduction

During the last years many measurements of the workfunction in dependence of the cesium pressure and the probe temperature are reported. However, for high cesium pressure and low probe temperature there are known only few results. These temperature ranges are important for the practical application of the thermionic converter and the theory of adsorption. Further, the most used methods require wire shaped emitters. Because measurements of single crystal faces are necessary to prove the theory, it is desirable

to develop a method for disk shaped probes.

These conditions can be fulfilled approximately by a method similar to the plasma-anode method described first by P. M. Marchuk [1] and experimentally performed by J. M. Houston and P. K. Dedericks [2].

Description of the method

In the plasma anode method the probe is situated inside a cesium plasma between two auxiliary electrodes. The plasma surrounding the probe represents the anode. An electrical isolated probe takes a negative potential U_0 with regard to the surrounding plasma potential U_p . This floating potential is defined by the condition, that the total current vanishes. If the probe is "cold" (not heated) and does not emit electrons, then the total current consists of an ion current and an electron current both flowing from the plasma to the probe (fig. 1). In this case the floating potential is defined by the equation

$$i_i = \nu_e e^{-\frac{e(U_p - U_0)}{k T_e}} \quad (1)$$

i_i = ion current, ν_e = electron current
 T_e = plasma electron temperature

An electron current j_e emitted by the hot probe is imposed to the ion current. Then the equation for this floating potential U_0' is

$$i_i + j_e = \nu_e e^{-\frac{e(U_p - U_0')}{k T_e}} \quad (2)$$

The amount ΔU_2 of the shifting of the floating potential can be calculated by means of these two equations:

$$\Delta U_2 = (U_0' - U_0) = \frac{k T_e}{e} \ln \left(1 + \frac{j_e}{i_i} \right) \quad (3)$$

An additional shifting of the floating potential is caused by the change of the contact potential. The probe voltage is measured with respect to one of the discharge electrodes (this was always the anode). Assuming that the workfunction of this electrode is constant during the measurements, then the change of the contact potential is equal to the change of the workfunction of the probe only.

$$\Delta U_1 = (\phi_h - \phi_c) \quad (4)$$

ϕ_h, ϕ_c workfunction of the hot respectively the cold probe.

The total difference of the floating potential between a cold and hot probe is therefore (fig. 2).

$$\Delta U(T_{Pr}) = \Delta U_1 + \Delta U_2 = (\phi_h(T_{Pr}) - \phi_c) + \frac{kT}{e} \ln \left(1 + \frac{j_e(\phi_h, T_{Pr})}{i_i} \right) \quad (5)$$

T_{Pr} = probe temperature

Provided that the three values \bar{T}_e, ϕ_c, i_i are constant, then one can calculate the workfunction of the hot probe from a measurement of the floating potential in dependence of the probe temperature. While the ion current can be measured directly, the other two constants can be determined from a measurement of the Richardson current j_e for at least two different values of the probe temperature, according to equ. (5).

Experimental apparatus

The gas discharge tube was a pyrex glass vessel (fig. 3). The distance between cathode and anode was about 150 mm. The discharge current was varied between 2 A and 10 A and the corresponding voltages 10 V to 15 V.

The disk shaped probes were 0.5 cm in diameter and 0.15 cm in thickness. The leads of the probes were 0.5 cm thick tungsten wires and the 0.0125 cm thick W-Re thermo-

couples were welded to the border of the probes (fig. 4). All wires were fused in the pyrex glass vessels directly and isolated against the cesium plasma by aluminium oxyd tubes.

Before each measurement the probe was heated by plasma electron bombardement several minutes. During the cooling down the floating potential in dependence of the probe temperature was measured by a X-Y recorder.

For measurements of the Richardson current (necessary for the calculation of the constants) the probe was held a few volts negative with respect to the plasma. Under these experimental conditions the measurement of the Richardson current is difficult because the surrounding plasma is disturbed by this current [3]. However, it is possible to make corrections, if the current is very small. Each measurement of the voltage and current is reproducible very well.

Experimental results

The results for polycrystalline tungsten, rhenium and nickel are represented in a Rasor-Warner diagramm ϕ versus T_{Pr}/T_{Cs} in the figures 5-7. The deviations of the different curves are principally caused by an experimental error in the measurements of the voltages and the currents (ion current and Richardson current) by the resolution of the X-Y recorder. An essential improvement of the accuracy could be obtained by a digital electronic equipment for recording the voltage and the current, which is projected.

In table 1 the values of the minimum workfunction and the electron temperatures are listed.

Table 1

	ϕ_{min} eV	T_{Pr}/T_{Cs}	T_{Cs} °K	T_e °K	τ_D A
W	1,61	1,68	542	1963	4
				2114	6
	1,59	1,75	473	2486	6
Re	1,47	1,66	523	2143	5
	1,44	1,66	430	2320	5
Ni	1,57	1,65	523	1963	5
	1,57	1,63	503	2109	5

Conclusions

The described method is apt to measure the workfunction for high cesium pressure and low probe temperature. Another advantage is, that one can use disk shaped probes.

A detailed description of the method and a discussion of its limits relatively to cesium bath temperature, probe temperature size of the probes will be published later on.

Literature

- [1] Marchuk, P. M.; Trudy Inst. Fiz. Akad. Nauk. Ukr. 7 (1956) 17
- [2] Houston, J. M. ; Dederick, P. K. ; Therm. Conv. Spec. Conf. San Diego, Calif. 1965
- [3] Miyake, M ; Bundschuh, V. ; "Messung des Elektronenemissionsstromes von Wolfram in einem Caesium-Plasma", Jül-508-TP Dezember 1967

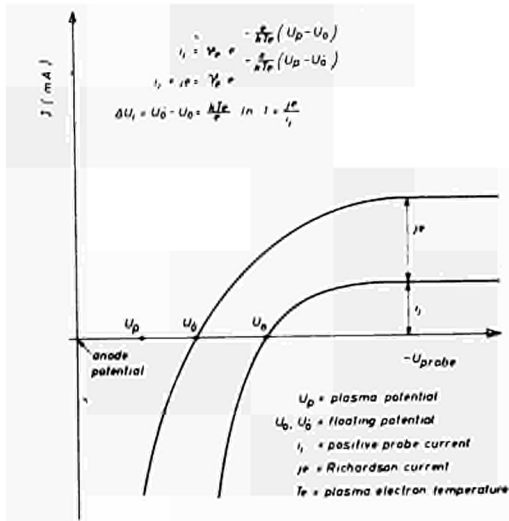


Fig. 1: I-U-Characteristic (schematically)

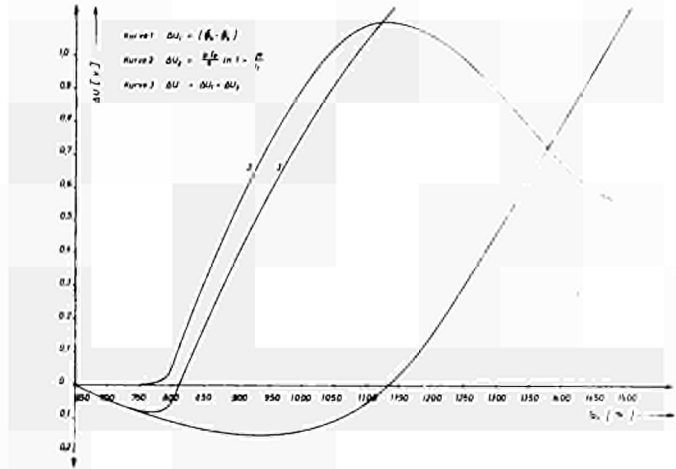


Fig. 2: Calculation of the floating potential ΔU (equ. 5) for tungsten by means of the theory of Raser-Warner

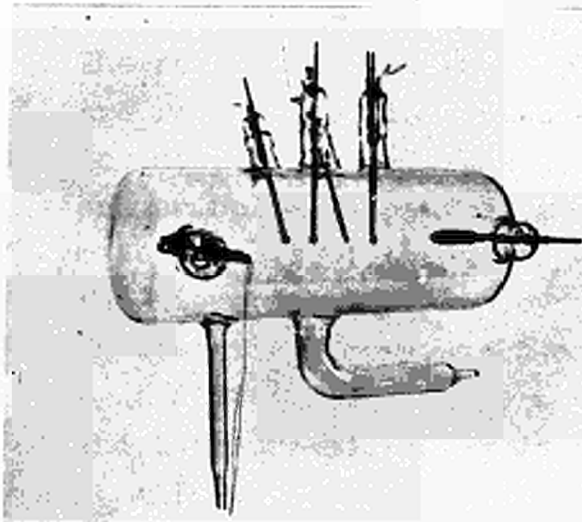


Fig.: 3 Gas discharge tube

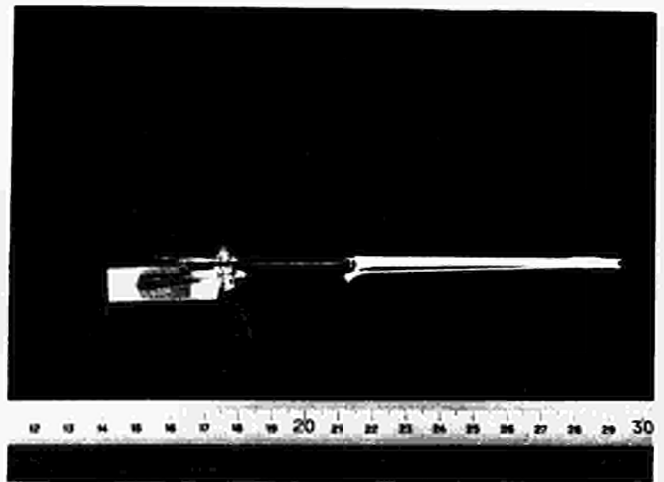


Fig. 4: Probe construction

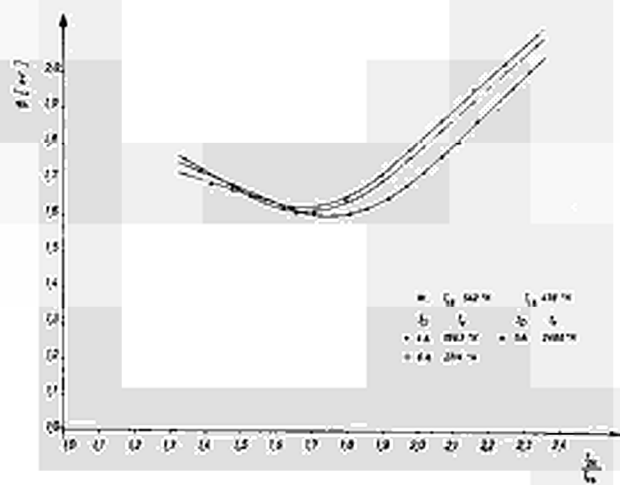


Fig. 5: Results for tungsten

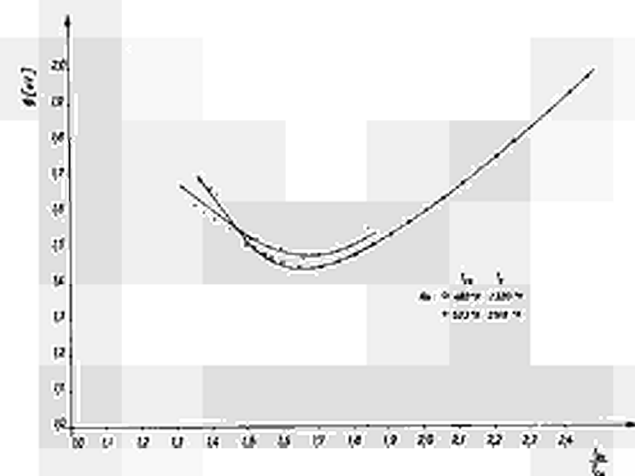


Fig. 6: Results for rhenium

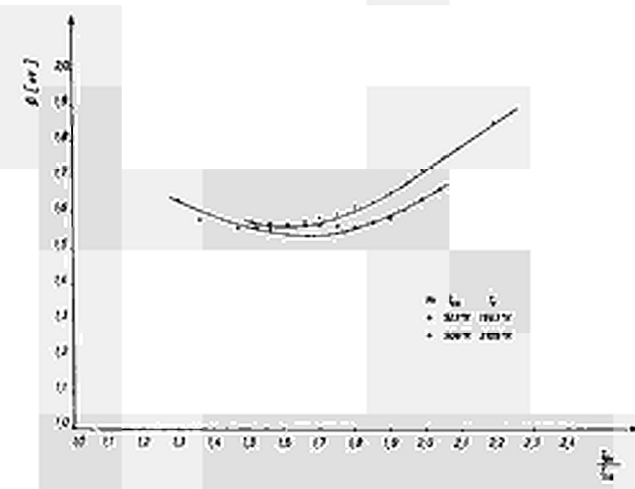


Fig. 7: Results for nickel

DISCUSSION

Speaker of paper K-4: V. BUNDSCHUH.

VON BRADKE (Germany): What do you estimate is the accuracy of this measuring method, and by which effects is it limited? What was the amount of the partial pressures during your experiments; i. e. was the measuring tube pumped during the measurements?

BUNDSCHUH (Germany): I have not made a theoretical calculation for the accuracy because the electronics equipment was not the best. A new electronic equipment is being designed and these are only the first results for this method.

VON BRADKE: Are you saying that for now the accuracy is determined by the electronic equipment?

And another question: What was your residual gas pressure; was the tube pumped during the measurement?

BUNDSCHUH: Yes, the accuracy is determined by the electronic equipment. In answer to your second question: The pump system was only a normal diffusion pump system. During the measurement I did not pump the test cell.

PREPARATION AND INVESTIGATION OF TUNGSTEN SURFACES
WITH PREFERRED ORIENTATIONS *

P. Batzies, J. Demny, H.-E. Schmid
Brown, Boveri & Cie, Mannheim, Deutschland
Zentrales Forschungslabor

Summary

High work function surfaces are generated on tungsten single crystals, polycrystals and vapor-deposited layers by electrochemical etching. The increased work functions are compared with those of the unetched surfaces. Different crystals give different amounts of work function increase. Tungsten {111} showed the greatest gain (0.4 eV) and greatest absolute value (4.85 eV).

When an etched crystal is heat-treated in ultrahigh vacuum, its surface is smoothed, and the work function decreases. A heat-treatment index, which was used to describe the combined effects of time and temperature [1] on the aging of rhenium is shown to rule the smoothing process of tungsten. Using this, a quantitative and graphic description of the work function dependence on heat-treatment becomes possible. It allows comparison of the different crystals studied and results from the literature [2]. Different crystals show different work function increase and surface stability. Different behaviour of similar crystals may presumably be due to different pre-etching heat-treatment.

The lifetime of an etched surface can hereby be calculated in advance, even at temperatures too low for reasonable life testing. The tungsten polycrystal is found to have the most stable etched surface, although the gain in work function is 0.2 eV only.

It is to note that the smoothing process was carried out in vacuum. Therefore the results cannot be directly used in the design of a cesium filled thermionic converter.

* This work was partially supported by the German "Bundesministerium für wissenschaftliche Forschung"

Introduction

One of the means for improving the efficiency of a thermionic converter is to increase its emitter bare work function. This can be done in different ways. One possibility, which has been applied [1], is the electrochemical etching. By this method {110}-faces are developed in the case of bodycentered cubic metals as tungsten. Therefore the work function will be increased. The gain, however, is lost partially or totally by necessary subsequent heat-treatment in vacuum. One purpose of this contribution is to find out the increase for different tungsten single crystals, polycrystalline and vapor-deposited material and to compare it to results obtained by others [2]. The other not less important point is the thermodynamic stability of these etched surfaces at elevated temperatures, which is necessary for use in a thermionic converter. It is known from the literature [2] that the etched surface is smoothed and the high work function lowered by annealing in vacuum. The emitters are therefore examined regarding their thermionic vacuum emission and their surface structure before and after the etching process and during the following heat-treatment.

Some restrictions concerning the possible results have to be made in advance:

1. The increase in work function is accompanied by an increase in surface area, which is not known exactly. Because the work function is calculated from the Richardson equation, which uses the emitting area, this uncertainty enters the work function. A rough estimate gives a maximum surface-factor of two and an apparent loss of work function in the order of a tenth of a volt, using the value of the unetched surface area, instead. This effect vanishes when the surface is smoothed.

2. No well founded forecast can be given on the influence of this increase in bare work function on the converter performance because of the difficult surface geometry and a lack of information on the numerical influence of the bare work function on the converter efficiency.
3. No theory is known to us, which relates the thermodynamic stability of the surface in vacuum to that in a cesium atmosphere.

Surface Preparation

The materials used are zone refined tungsten single crystal rods of ultra purity, polycrystal tungsten of 99.94 % purity, and vapor plated layers, formed by thermal decomposition of WF_6 on molybdenum substrates. For measurements the crystals were used in form of disks, 2 mm thick and 5 mm in diameter, with a black body hole for temperature measurements of 0.5 mm in diameter and of 1 mm in depth on the back side.

The orientations of the single crystals were determined by reflection electron diffraction. Small deviations were eliminated by definite grinding. The surfaces of the crystals were mechanically ground and polished with 15 μ diamond paste, and then heated half an hour at about 1500 $^{\circ}C$ to recrystallise the Beilbylayer. For elektropolishing a solution of 2 % NaOH in water at room temperature was used, the voltage being 15 - 17 V. Etching was carried out in 10 % NaOH, at a voltage of 1 V. Fig. 1 shows an electron-micrograph of a replica of an etched tungsten $\{111\}$ -surface. It reveals an interesting feature. There are many etch-pits with large planes of $\{110\}$ -orientation. Areas between these large pits show smaller, but similar etching structures. This will be of importance for the discussion of results, following later on.

Work Function Measurements, Experimental Apparatus and Performance

The work functions of the emitters are measured in a diode with a screened emitter surface of $0,16 \text{ cm}^2$, using the Richardson equation. The emitter is heated by electron bombardment, using a special electron gun of small size. The collector is a ring, in order to allow fast removal of gases adsorbed on the emitter, and to prevent contamination of the emitter by the collector. The latter was outgassed at $2200 \text{ }^\circ\text{K}$ in ultrahigh vacuum, before the measurements were performed.

The emission current is taken as a function of applied voltage, until the space charge is removed. The Schottky effect is taken into account. The emitter temperature is measured pyrometrically in the black body hole on the back side of the emitter. It is corrected for losses in the glass window, the prism and the ratio of depth to diameter. To eliminate the influence of oxygen on the work function, the measurements are performed in ultrahigh vacuum. How the pressure is calculated, which is necessary to avoid mistakes, will be published elsewhere [3,4] .

At the beginning of every measurement the crystal is outgassed at low temperatures in order to avoid destruction of the etched surface as far as possible, until a pressure of $2 \cdot 10^{-9}$ torr is obtained.

Afterwards the temperature is raised stepwise, and the work function measured (The temperatures and heating intervals can be extracted from Fig. 4).

Results

At first the work functions of the unetched, electropolished crystals were measured. The results were reasonable and in good agreement with the literature (Table 1).

The etched crystals, using the same materials and prepared as cited above, were investigated and their work function measured (Table 1). The difference "etched-polished" is called gain and also listed in Table 1. At temperatures below 1850 °K and pressures above $2 \cdot 10^{-9}$ torr no reliable results could be obtained [3,4]. Therefore the highest work functions measured may not be those of the undisturbed etched surfaces, but already be lowered by the beginning of the smoothing process. The annealing is finished, when the work function is no longer decreasing, i.e. an equilibrium is obtained. These values are given in Table 1, labeled "smoothed". With the exception of the vapor-deposited emitter all "smoothed" values are nearly as low as the "polished" ones, that means that the surface structure has been smoothed so far that the gain in work function has been lost completely.

Work Functions in eV

	polished	etched	smoothed	gain
W-{111}	4,48	4,85	4,50	0,37
W-{100}	4,54	4,80	4,52	0,26
W-Poly	4,57	4,75	4,59	0,18
W-Vap.	4,50	4,68	4,58	0,18

Table I Work functions of different tungsten-crystals after different treatments.

Fig. 2 shows an optical micrograph of an etched surface of a tungsten-{111}-single-crystal after a heat-treatment, as indicated in Fig. 4 by an arrow. It can be seen clearly that the microstructure has been smoothed completely. Only large etch-pits have remained. The edges of these large structures have been smoothed too. The electron micrograph (Fig. 3)

reveals only slight shadows, indicating that the smoothing process is more complete than one would guess from the optical micrograph (Fig. 2).

The speed of the smoothing process, which is assumed to be caused by surface diffusion, depends on temperature T and time t . Van Someren, Lieb, and Kitrilakis [1] have suggested a function of the form $t \cdot \exp - Q/RT$, where Q is an energy of about 100 kcal/mol and R is the gas constant. It is not known yet, whether this is correct or not and what the dependence of the work function on this argument is. Nevertheless the work functions, obtained after heat-treatments at various temperatures T and times t , were plotted as a function of $t \cdot \exp - Q/RT$ as shown in Fig. 4.

Discussion

In connection with Fig. 4, it is worth noting that points, measured at different temperatures, lie on one curve. That means that the function $\{t \cdot \exp - Q/RT\}$ seems to be the right one for describing the combined effects of time and temperature. The absolute value of Q is of no great influence on the form of the curves. Fig. 4 shows some interesting features. Principally three different kinds of curves can be distinguished. The two single crystals ($\{111\}$, $\{100\}$) start with a relatively high work function, but the decrease begins very soon. The dependence of work function decrease on $\log (t \cdot \exp - Q/RT)$ is a linear one in the greater part of the curve. The final value is nearly that of the polished surface (see also Table 1). That means that the smoothing process completely removed the etched structure as far as it was responsible for the gain in bare work function.

The etched vapor plated crystal shows a curve of different shape. Its work function is also decreasing from the very beginning, but becomes constant at a value, which is one tenth of a volt above that of the polished surface. It is possible that the work function can decrease once more, if the heat-treatment is continued, and also reach its original value.

The third type is the curve of the polycrystalline material. It shows a constant work function over a long period of time from the beginning, even at elevated temperatures, and then decreases very fast, until the value of the polished surface is reached. As an example, a similar curve (2B - 1d, Fig.4) was calculated, using results obtained by Yang and Hudson [2] with an etched vapor-deposited tungsten sample. In principle, it is in good agreement with our results, as far as the method of evaluation is concerned.

These different types of curves can be explained as follows: Due to different treatment of the crystals during fabrication and preparation, a different number of dislocations is present, when the crystal is etched. This leads to a different etch-structure, especially regarding the ratio of small and large structures, as discussed above. The small structures will be smoothed much faster than the large ones. This may already happen during the outgassing of a crystal before any work function can be measured.

If large areas were covered with the small structure, we will find a low and relatively stable work function, which will begin decreasing, when the large etch-pits are removed noticeable. The polycrystal and the vapor-deposited sample [2] belong to this category.

Another parameter, which influences the shape of the curve, is the orientation of the unetched surface and the shape of etch-pits, resulting from this orientation. This effect could

be responsible for the different starting points of the decrease after the premeasurement heat-treatment. In the case of polycrystalline and vapor-plated material the influence of grain boundaries may not be negligible.

Accepting this model one can use these measured curves for a practical purpose in thermionic converter technology. It enables us to predict the lifetime of an etched emitter at temperatures, where no measurements have been taken. Another advantage is that the time needed for investigating an etched emitter can be reduced by orders of magnitude. As an example, the lifetime calculated from the polycrystalline curve, using an emitter temperature of 1800°K , gave a lifetime at constant work function of about 1000 hours. As indicated by measurements of others [2], this can be improved, presumably by changed pre-etching heat-treatment.

Conclusions

A method has been developed and used, by which it is possible to judge the performance of an etched emitter more precisely than up to now. But it will be successfully used in thermionic converter technology only, if it is accomplished by measurements on crystals which have been aged in a cesium atmosphere.

Literature

- [1] VON SOMEREN, L.; LIEB, D.; KITRILAKIS, S.S.,
"Evaluation of thermionic emitter surfaces", Thermionic Conversion Specialist Conference, San Diego, California, Oct. 1965, 266-475
- [2] YANG, L.; HUDSON, R.G., "Effect of preferred crystal orientation and surface treatment on the work function of vapor-deposited tungsten", Thermionic Conversion Specialist Conference, Houston, Texas, Nov. 1966, 395-403
- [3] BATZIES, P.; DEMNY, J.; SCHMID, H.-E.; ZÖLLER, R.,
"Entwicklung von Emittlern für thermionische Reaktor-Brennstoffelemente", Forschungsbericht des Bundesministeriums für wissenschaftliche Forschung, Förderungsvorhaben St.N. 423-67, Jan. 1968
- [4] BATZIES, P., "The influence of oxygen on the work function of tungsten", Second International Conference on Thermionic Electrical Power Generation, Stresa 1968



Fig. 1
Electron micrograph of a replica of an etched tungsten-{111}-surface, 2500 x

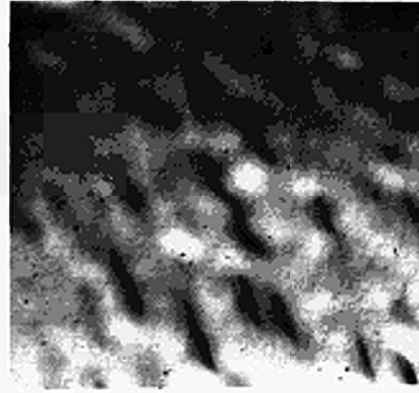


Fig. 3
Electron micrograph of a replica of an etched tungsten-{111}-surface after heat-treatment, 2500 x (arrow in Fig. 4)

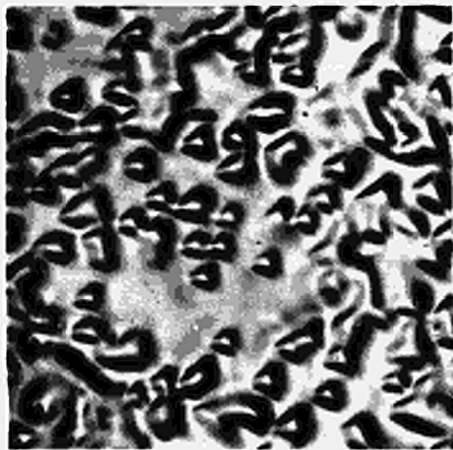


Fig. 2
Optical micrograph of an etched tungsten-{111}-surface after heat-treatment, 500 x (arrow in Fig. 4)

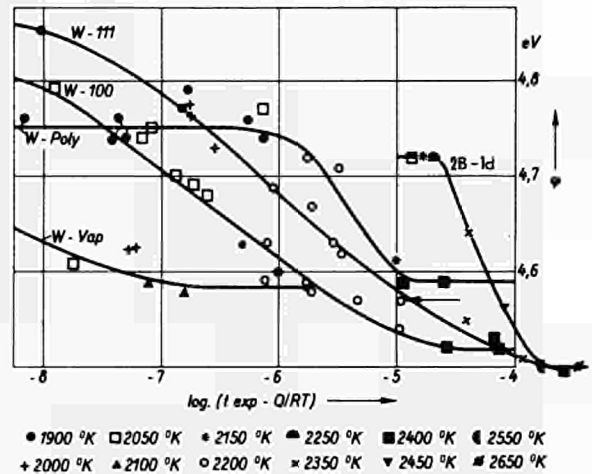


Fig. 4
Work function of different tungsten crystals as function of the smoothing parameter (t in sec., T in °K)

RECHERCHE DE SURFACES DE TUNGSTENE A TRAVAIL DE SORTIE ELEVE

D. THIVELLIER

DM/SER - Centre d'Etudes Nucléaires de Saclay
91 Gif-sur-Yvette (France)Résumé -

Le but de cette recherche est d'améliorer le travail de sortie ϕ_e des surfaces émettrices en tungstène, en y faisant apparaître des plans cristallins denses $\langle 110 \rangle$

On étudie les possibilités d'obtenir de telles surfaces, soit au cours de la croissance des dépôts pyrolytiques ou électrolytiques, soit par attaque chimique ou électrolytique d'une surface lisse. La stabilité de ces surfaces est étudiée à haute température, avec ou sans adsorption de gaz, en vue de leurs utilisations dans les convertisseurs thermoioniques.

1. Introduction.

L'obtention d'un émetteur à travail de sortie élevé, permet d'optimiser l'influence du césium dans les convertisseurs thermoioniques. Le tungstène a un travail de sortie effectif moyen de 4,52 eV [1] ; mais si, dans les émetteurs en tungstène déposé, on peut amener en surface des plans cristallins (110), ce travail de sortie atteint alors 5,3 eV [1]. D'après la théorie des surfaces en terrasses-marches-crans, (exposée par Y. ADDA et J. PHILIBERT [2]), appliquée au tungstène, le système cubique centré présente trois surfaces singulières, constituées d'un réseau dense d'atomes : (110), (112) et (100) ; la coordinance et le travail de sortie y sont élevés respectivement (5,3 eV, 4,75 eV, 4,62 eV). Les autres surfaces sont constituées d'éléments de surfaces singulières en terrasses, séparés par des marches et des crans monoatomiques ; la coordinance et le travail de sortie y sont plus faibles [$\phi(111) = 4,40$ eV, $\phi(116) = 4,32$ eV].

2. Faciès de croissance cristalline.

Le mécanisme de la croissance à partir d'une solution ou d'une vapeur saturée est le suivant : les atomes du métal sont adsorbés sur les terrasses ; ils diffusent jusqu'au moment où ils sont "piégés" par les crans et les marches, provoquant ainsi l'avancement des marches, et la croissance du cristal. La vitesse de croissance est donc, d'autant plus rapide que le nombre de marches est grand, et elle est minimale pour les surfaces singulières. Le faciès, qui est formé de surfaces à faible vitesse de croissance, ne devrait comprendre que des surfaces singulières. En réalité, ce n'est pas toujours le cas, car d'autres facteurs influencent la vitesse de croissance, tels que le gradient thermique, et la présence de substances étrangères adsorbées.

2.1. Influence du gradient thermique.

D'après les travaux de B. CHALMERS et F.C. FRANK [3], lorsque le flux de chaleur est dirigé de l'extérieur vers l'intérieur du cristal, on a la croissance cellulaire qui donne des petits cristaux d'orientation aléatoire. Lorsque le flux de chaleur est dirigé de l'intérieur du cristal vers l'extérieur, on a la croissance dendritique, qui donne, dans le cas d'un système cubique centré, des cristaux allongés suivant l'axe $\langle 100 \rangle$ (c'est l'axe de croissance maximale pour un

crystal isolé). Ces cristaux présentent en surface un faciès de plans (110) (c'est la surface d'énergie minimale pour un cristal isolé). Des dépôts dendritiques obtenus par réduction de WF_6 en présence d'hydrogène, sur un support chauffé par induction, ont un axe de croissance $< 100 \text{ \AA}$ en effet le flux de chaleur est dirigé de l'intérieur vers l'extérieur du cristal.

2.2. Influence des substances étrangères adsorbées.

Par leur présence, les substances étrangères adsorbées, gênent la progression des marches, et dans certains cas, entraînent un changement de faciès [4]. U. BERTOCCI [5] a développé des calculs sur la forme des marches et leur vitesse d'avancement en présence d'adsorbat, au cours des dépôts électrolytiques. Il montre qu'il existe deux régimes de croissance : L'un est obtenu aux tensions élevées, et donne un faciès lisse ; l'autre est obtenu aux tensions plus faibles, et donne un faciès constitué de surfaces singulières.

3. Faciès d'attaque électrochimique.

U. BERTOCCI [5] traite de même le cas de l'attaque électrolytique, et montre qu'il existe aussi deux régimes d'attaque : l'un est obtenu aux tensions élevées et donne un faciès lisse, c'est le polissage électrolytique, que nous avons observé entre 2 et 30 V avec des solutions de soude, de concentrations variables ; l'autre est obtenu aux tensions plus faibles, et donne un faciès de surfaces singulières ; nous l'avons observé pour les tensions inférieures à 2 V. L'étude de l'oxydation anodique du tungstène a été effectuée dans des solutions de soude (5 à 100 g/l). Les ions OH^- donnent au contact du tungstène des radicaux (OH) qui forment des acides tungstiques ionisés, et l'on obtient en solution des ions WO_4^{2-} , $W_2O_6^-$, WO_3^- , OH^- , Na^+ , H^+ , c'est-à-dire des tungstates de sodium. Les variations des paramètres tension, intensité et concentration s'expliquent très bien par la théorie de l'électrode réversible qui permet de calculer le saut de potentiel à la traversée de la surface des électrodes, et par la théorie de la double couche de diffusion qui permet de calculer l'intensité du courant en faisant intervenir la présence d'une double couche de charges électriques au voisinage des électrodes. En ajoutant du ferricyanure de potassium qui abaisse le potentiel d'oxydation, l'attaque se produit sans f. e. m. auxiliaire. Dans tous les cas d'attaques chimiques ou électrochimiques, on observe d'abord l'apparition de piqûres limitées par des facettes (110) avec tronçatures (100), et dont la forme dépend de l'orientation (fig. n° 1, 2 et 4). L'attaque prolongée produit des facettes (110) et (100) (fig. n° 3, 5 et 6).

4. Distribution du travail de sortie des surfaces brutes.

Le travail de sortie ϕ (h k l) est d'autant plus élevé que la coordinance est forte ; la théorie de D. STEINER et E. P. GYFTOPOULOS [6] permet de calculer la fonction ϕ (h k l) (fig. n° 7) d'après la relation :

$$\phi (h k l) = 0,98 \frac{v_s (h k l) + 1}{r_m} + 1,57 \quad (\text{eV})$$

v_s étant le nombre d'électrons par atome en surface qui participent aux liaisons, r_m étant le rayon de ces atomes en Å. En mesurant sur cette figure n° 7 les aires correspondant à chaque tranche de valeur de ϕ , on obtient la distribution de ϕ sur le triangle élémentaire de la projection stéréographique. C'est aussi la distribution de ϕ pour un échantillon polycristallin poli, où les orientations des grains sont équiprobables (fig. n° 8).

5. Stabilité des surfaces dans le vide.

La stabilité des surfaces dépend de leur énergie. L'énergie libre de surface est proportionnelle au nombre de liaisons libres des atomes de la surface. Elle est donc d'autant plus faible que la coordinance est grande, et elle est minimale pour les surfaces singulières, à l'inverse du travail de sortie. Les calculs de J. K. Mac KENZIE et al. [7] montrent que la fonction énergie libre de surface γ (h k l) présente deux minima pointus pour (110) et (100) (fig. n° 12), et une "vallée" de minimums relatifs entre (112) et (110), suivant un schéma analogue à la figure n° 7, mais avec un relief inversé.

En faisant apparaître une facette (110) sur une surface lisse quelconque (h k l), on augmente l'aire dans le rapport : $1 \cdot \cos \theta$ [θ étant l'angle ($< h k l >$, $< 110 >$)], et on

diminue l'énergie spécifique de surface de la valeur $\gamma(h k l)$ à la valeur $\gamma(110)$. La facette est stable si l'énergie de la surface facetée est inférieure à celle de la surface lisse, soit :

$$\frac{\gamma(110)}{\cos \theta} < \gamma(h k l)$$

Pour une distribution quelconque de facettes (110) faisant l'angle θ_i avec la surface (h k l), et d'aire respective f_i , la condition de stabilité s'écrit :

$$\frac{\sum f_i \gamma(110)}{\sum f_i \cos \theta_i} < \gamma(h k l)$$

La fonction $\gamma(h k l)$ présente, comme on l'a vu, un minimum pointu pour (110), alors que la fonction

$$\frac{\sum f_i \gamma(110)}{\sum f_i \cos \theta_i} \quad \text{présente un minimum plat (fig. n° 12).}$$

Il en résulte que la condition de stabilité est réalisée dans une plage d'orientations voisines de (110). Le même phénomène a lieu pour des facettes (100), autour de (100). Pour un échantillon polycristallin, la surface stable est formée de facettes (110) pour les grains ayant une orientation voisine de (110), de facettes (100) pour les grains ayant une orientation voisine de (100), et elle est lisse pour les grains ayant une autre orientation.

6. Stabilité des surfaces en présence d'un adsorbat.

La présence d'atomes adsorbés en surface entraîne une redistribution des liaisons interatomiques et abaisse l'énergie de surface. Dans le cas d'une adsorption sur les terrasses, à l'exclusion des marches et des crans, le taux d'adsorption est plus grand sur les surfaces singulières qui n'ont ni marches ni crans ; l'abaissement d'énergie de surface est alors plus marqué pour les surfaces singulières. Les minima pointus de la fonction $\gamma(h k l)$ sont accusés et, pour un taux d'adsorption convenable, la plage de stabilité des facettes (110) recouvre toutes les orientations (fig. n° 13). F. P. DUMONT [8] a étudié l'adsorption d'oxygène sur des faces monocristallines de tungstène pour diverses conditions de température et de pression. Ses résultats permettent de définir deux zones : une zone "polluée" où le taux de gaz adsorbés n'est pas nul, et une zone "propre" où ce taux est négligeable [$\theta < 10^{-3}$] (fig. n° 14).

7. Changement de faciès par diffusion de surface.

La surface stable tend naturellement à apparaître si on permet aux atomes de se déplacer par diffusion de surface. En chauffant une surface lisse dans des conditions de température et de pression correspondant à la zone "propre", on obtient le facetage partiel, conformément aux critères de stabilité définis au paragraphe 5 : il apparaît des surfaces singulières d'énergie minimale. Ce facetage modifie la distribution de θ (fig. n° 8) et ce phénomène a été observé expérimentalement par T. ALLEAU [9] (fig. n° 15 et 16). Un exemple est donné figure n° 9 : 5 h à 2 200 °K sous $2,5 \cdot 10^{-6}$ torr.

En chauffant une surface gravée par attaque électrochimique, toujours dans les conditions de la zone "propre", on obtient au contraire un lissage partiel : par exemple 5 h à 2 500 °K sous $6 \cdot 10^{-6}$ torr (fig. n° 11).

En chauffant une surface lisse dans les conditions de la zone "polluée", on obtient le facetage total de la surface : par exemple 1 h à 1 700 °K sous 10^{-4} torr (fig. n° 10).

8. Conclusion.

Si on peut réaliser au cours du dépôt, une croissance cristalline suivant l'axe $\langle 110 \rangle$, on obtient après polissage, une surface (110) parfaitement stable. Mais si la surface est un faciès de croissance, ou d'attaque, constitué de facettes (110), elle n'est stable à haute température, que dans les conditions de température et de pression correspondant à la zone "polluée". Dans les conditions de la zone "propre", elle tend à se lisser d'autant plus vite que la température est élevée, et que les facettes sont petites [9]. Aussi, l'amélioration du travail de sortie effectif ne dépasse pas 0,25 eV, dans le vide, par rapport au tungstène polycristallin : 4,55 à 4,80 eV. La présence de césium n'atténue pas le phénomène de lissage et un tel émetteur ne garde ses caractéristiques que quelques heures à haute température (2 000 °K) [10].

REFERENCES.

- [1] FOMENKO V. S.
"Handbook of thermionic properties", 1966. Plenum Press Data Division. N. Y.
- [2] ADDA Y., PHILIBERT J.
"La diffusion dans les solides", 1966, t. II, p. 751.
- [3] CHALMERS B., FRANCK F. C.
"Conf. int. sur la croissance cristalline", Coopertown, 1958.
- [4] HARTMAN P.
"Adsorption et croissance cristalline", Colloque int. du CNRS, Nancy 1965, pp. 477-513.
- [5] BERTOCCI U.
"A theoretical treatment of the influence of time dependent impurity adsorption on electrocrystallization", Surface Science 9, n° 1 (1966), pp. 18-30.
- [6] STEINER D., GYFTOPOULOS E. P.
"An equation for prediction of bare work function", Conf. int. MIT, Mass. USA, 1967
- [7] Mc KENZIE J. K.
J. Phys. Chem. Solids, 23, 185 (1962)
- [8] DUMONT F. P., MAURIES J.
"Adsorption de gaz sur des monocristaux de tungstène", Conf. int. sur la production thermoionique, Stresa, 1968.
- [9] ALLEAU T., SHROFF A. M.
"Work function distribution of thermoemissive refractory layers", Conf. int. MIT, Mass. USA, 1967.
- [10] WILSON V. C., LAWRENCE J.
"Characteristics of a thermoionic converter with a fluoride vapor deposited tungsten emitter etched to preferentially expose the (110) crystal planes", Thermionic specialist conf., Palo Alto, USA, 1967.

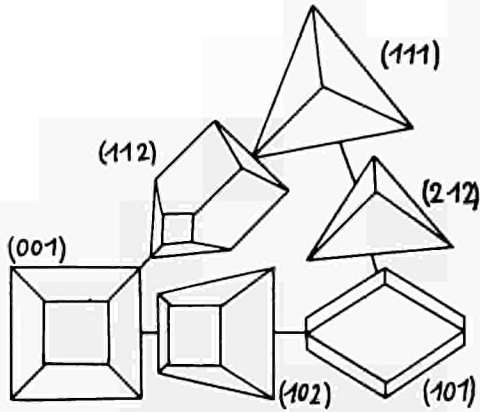


Fig.n°1 - Forme des piqures d'attaque

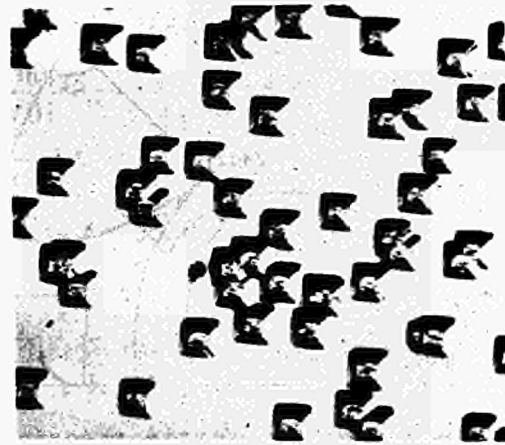


Fig.n°2 - Orientation (100) X1000

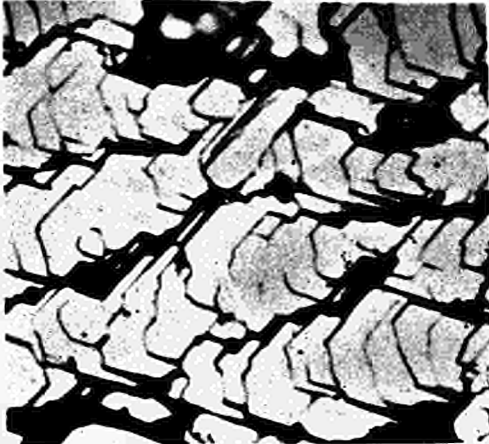


Fig.n°3 - Orientation (110) X1000

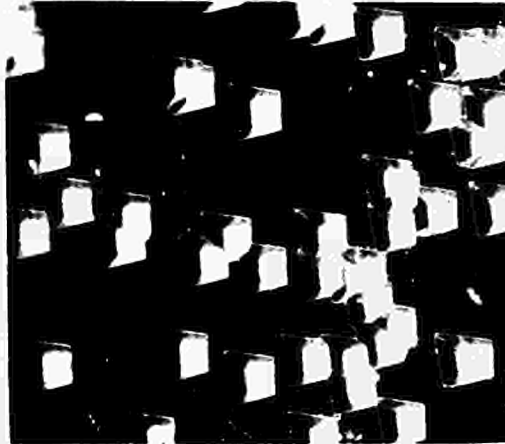


Fig.n°4 - Orientation (116) X150



Fig.n°5 - Orientation (111) X1500



Fig.n°6 - Orientation (221) X1500

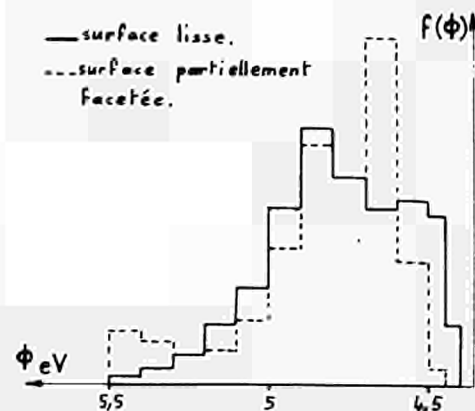
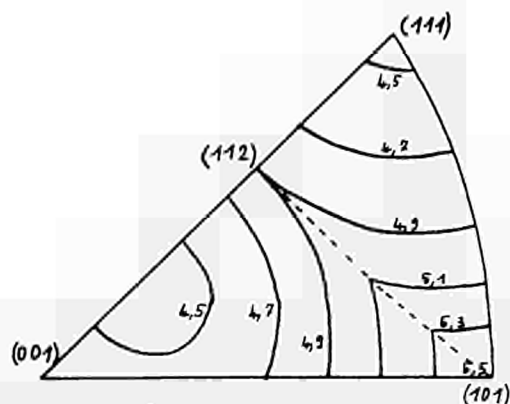


Fig.n°7 - Travail de sortie théorique. Fig.n°8 - Distribution théorique.

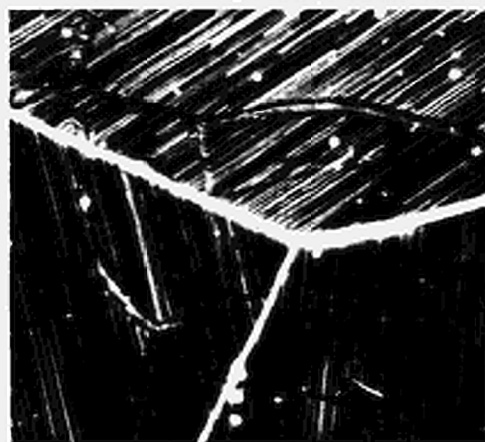
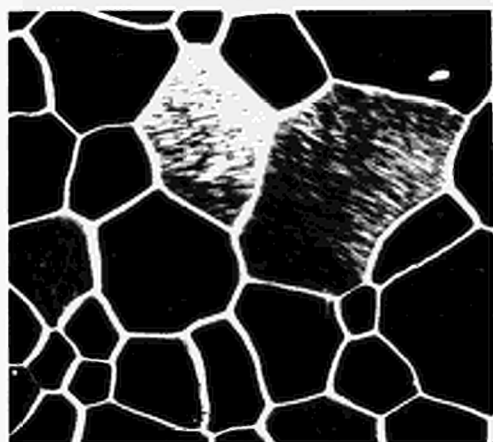


Fig.n°9 - Facetage partiel. X500

Fig.n°10 - Facetage total. X500

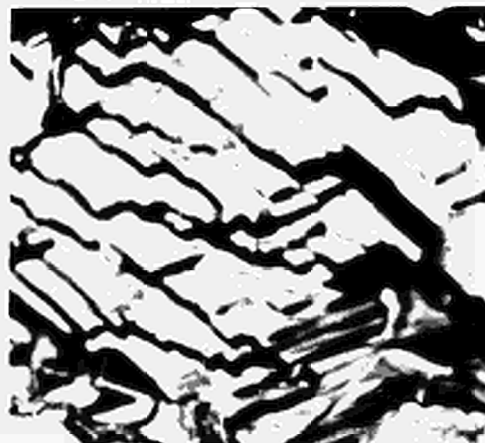
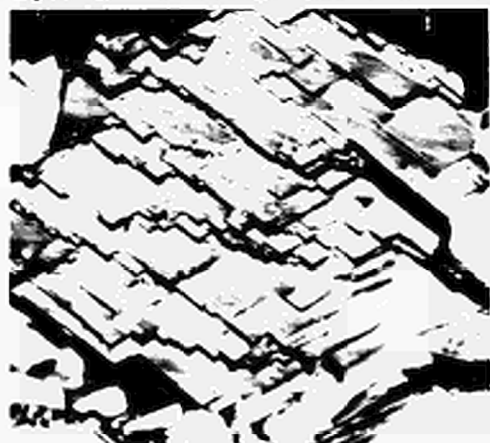


Fig.n°11 - Lissage partiel d'une surface gravée après 5h à 2500°K (X500)

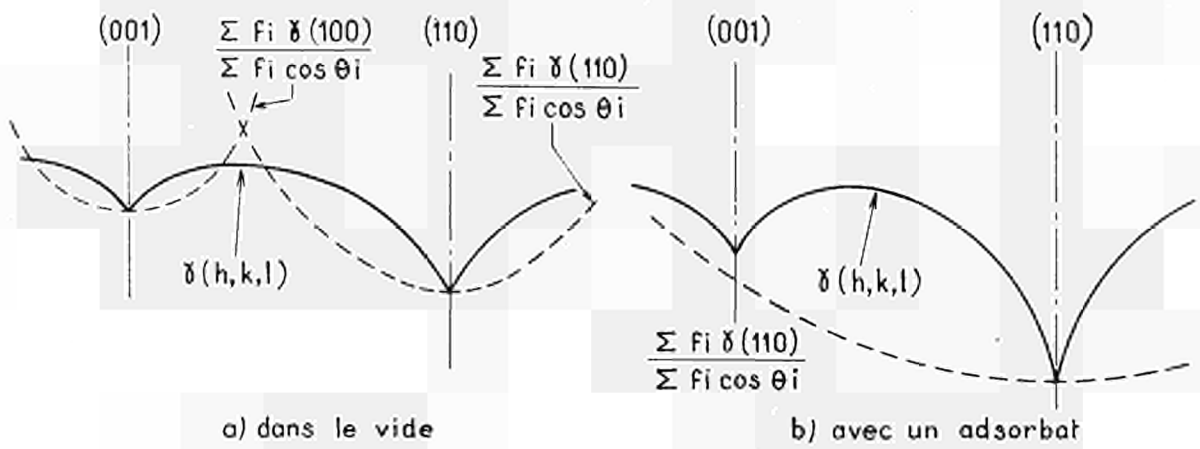


Fig.n°13-13 - Schéma des fonctions $\frac{\sum F_i \delta}{\sum F_i \cos \theta_i}$ et $\delta(h,k,l)$ pour les orientations dans le plan (010).

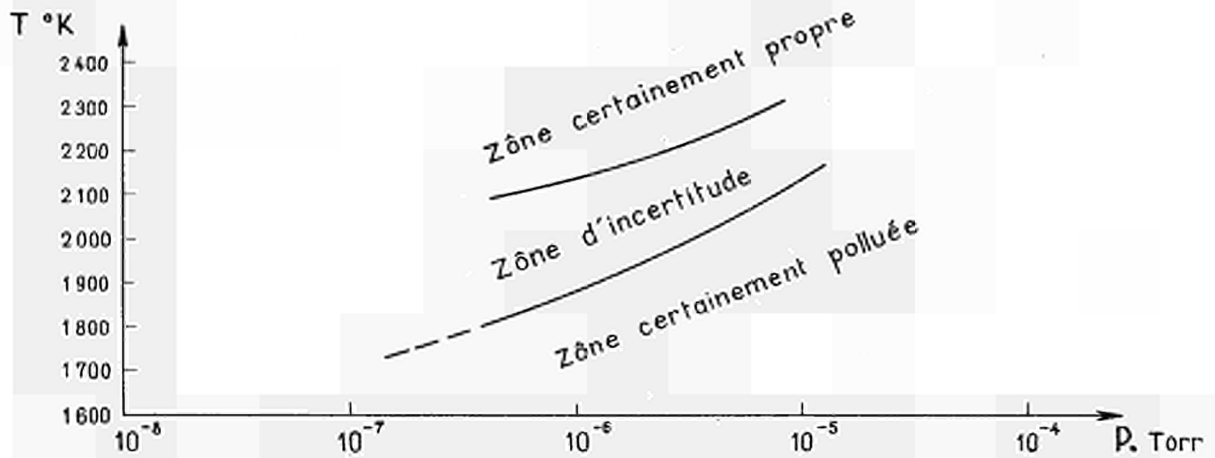


Fig.n°14 - Influence de la température et de la pression sur le taux d'adsorption d'Oxygène.

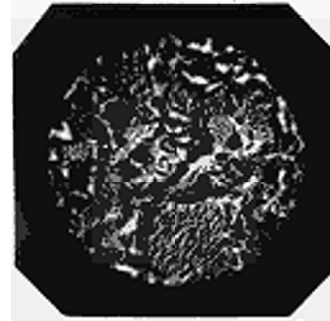
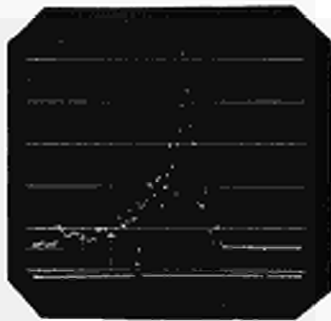


Fig.n°15 - $f(\phi)$ relevé au microscope électronique à émission.

Fig.n°16 - Emission d'une surface gravée au microscope électronique. $T=2000^\circ\text{K}$, $G=75$.

DISCUSSION

Speaker of paper K-6: Th. ALLEAU.

WILSON (USA): I would like to make the remark that the San Fernando Laboratory in California, USA, makes (100) oriented tungsten from WF_6 and (110) oriented tungsten from WCl_6 . H. F. WEBSTER has developed a NaOH solution for etching W to preferentially expose the (110) surfaces. His technique is described in a paper by V. C. WILSON in the proceedings of the 1967 Specialist Conference at Palo Alto.

ALLEAU (France): Yes, as regards the orientation (110), which we have obtained and the ones that you have mentioned obtained by various people, I thought one did not know how the (110) orientation was obtained. I think Mr. FEDERER is working on this in the US. Isn't it difficult to give a conclusive judgement on the subject? We personally bought samples with (110) orientation made by the San Fernando Laboratory, and indeed there was (110) orientation, more or less 100% of the surface as deposited. But after the thermo-treatment and the polishing we only had about 20-30% of the surface left. The rest of it was still (100). The literature on high work function on the basis of these samples, I think, is more due to impurities in the metal than to the (110) orientation. In the paper I was discussing, emission characteristics were obtained, which were equivalent to the (110), but which were only due to the presence either of impurities, perhaps oxygen. I don't know what we should conclude. Perhaps one can retain the (110) orientation as obtained by pyrolytic deposition.

EVALUATION OF SEMICONDUCTING COLLECTOR SURFACES
IN THERMIONIC CONVERTERS*)

R. Maly, H. Rapp, W. Kluge

(Institut für Gasentladungstechnik und
Photoelektronik, Universität Stuttgart,
Breitscheidstrasse 2 (Germany))

Abstract

Experimental results of measurements in cylindrical diodes with Molybdenum emitters and collectors of the type Al-Al₂O₃ and Cr-Ni-steel are presented.

It is shown that the work function of Al₂O₃ collectors, evaluated from experimental I-V-characteristics of thermionic converters, may be 0,1 to 0,2 eV lower compared with the work function of the Cr-Ni-steel collectors under optimum conditions. The experimental apparatus and the evaluation method are described. The range of application for the Al-Al₂O₃ collector type is deduced from the experimental data.

When the diodes operated in the ignited mode, overall efficiencies in the range of 8 to 9 per cent have been obtained at emitter temperatures below 1500°K.

Introduction

Previous investigations¹⁾²⁾³⁾ on low work function collectors seemed to indicate that collectors of the type Al-Al₂O₃ are suitable for obtaining high efficiency. The Al₂O₃-Cs as a representative of the class of semiconducting materials is an ideal semiconductor due to the compatibility with cesium and the ease of preparation.

The mentioned investigations have been carried out with homogeneous oxide layers in vacuum at low current densities. The electrical resistance and the behaviour of semiconducting layers at high current densities are difficult to measure and

can only be valuated under operation conditions in thermionic converters.

The present paper is an extension of earlier work on oxidized Aluminium collectors in Cesium vapor. The following sections describe a method for obtaining values of collector work functions from experimental I-V-characteristics of thermionic converters.

Experimental Apparatus

The experimental measurements were carried out with thermionic converters of the type shown in Fig. 1 with cylindrical Molybdenum emitters, interelectrode spacings of 1 mm and collectors of the type Al-Al₂O₃ or bare Cr-Ni-steel. All parts of the converters were cleaned carefully and outgassed just before the assembly. The emitter was heated by electron bombardment. The bombardment filament was designed to maintain an effective emitter surface area of about 10 cm².

To avoid impurities in the coating of the collectors the Aluminium films were formed by evaporation in high vacuum. The oxidation of these collectors was carried out by means of glow discharge in oxygen atmosphere in the assembled converter. However, the best results were obtained when the Aluminium was oxidized by atmospheric air during the assembly. In this case the thickness of the Aluminium oxide is appr. 30 Å.

In addition, the converters were outgassed under operating conditions. After having obtained a satisfying vacuum the highly pure Cesium was distilled into the Cesium reservoir. Then the converter was sealed.

Evaluation Method

For the evaluation of plasma and work function data a semilog plot of current versus voltage was drawn. A typical characteristic is shown in Fig. 2.

As long as electron cooling is negligible, T_E is constant.

To each point on the Boltzmann line, drawn as a tangent to the lower part of the experimental curve, an apparent work function ϕ'_E , including the negative emitter sheath, can be attributed. From the apparent contact potential for this point a first order approximation for the collector work function ϕ_C is obtained. By means of this value the back emission is calculated, which may cause a shift of the Boltzmann line and thus a correction of ϕ_C , which can be determined to ± 0.02 eV. In the range of high current densities the effective work function ϕ_E is calculated assuming that no negative space charge sheath is present in the arc mode. The difference of $\phi_E - U_a$ (output voltage) gives the sum of $\phi_C + U_B$ (voltage drop in the arc). Usually the emitter temperature was measured by a W-WRh-thermocouple. However, it is possible to obtain T_E very accurately from the power balance of input power and radiation and lead losses with and without electron cooling. Thus, changes in arc voltage and of the collector resistance can be evaluated.

Converter Performance

The performance of converters having Al_2O_3 collectors have been compared with diodes provided with Cr-Ni-steel collectors. Whilst from the beginning steel collectors need no activation time and work stable, the I-V-characteristic of diodes with Al_2O_3 collector layers indicates high inner resistance. After five to ten hours of converter operation Cs-vapor has obviously reacted with Al_2O_3 forming an Al- Al_2O_3 -Cs semiconductor with high conductivity. Hereafter the collector surface works stable.

In Fig. 3 the effective collector work function of converters with Al_2O_3 collector layers and without such layers are plotted for different reservoir temperatures versus T_C/T_{Cs} . In all cases the data were taken under optimum conditions. For comparison a curve for Ni by Lawrence and Perdew⁴⁾ is

also shown. If the values of Cr-Ni-steel are very low this indicates that the collector is not absolutely clean. Under optimum conditions Al_2O_3 -Cs collectors, however, show a work function which is 0.2 eV lower. The minimum work function for a given material is always obtained for a specific value of T_c/T_{Cs} .

(1.25 for steel, 1.4 for Al_2O_3 -Cs). The absolute value of work function, however, is a strong function of temperature.

The general behaviour of Al_2O_3 -Cs collectors is unchanged after a long period of operation. The minimum work function, however, is very sensitive to an increased residual gas pressure. A family of curves taken after 150 hours of operation is shown in Fig. 2.

Conclusions

Semiconducting layers of Al_2O_3 -Cs proved to be suitable for collector surfaces at temperatures up to 800°K. Such layers show a work function which is lower by 0.2 eV compared to Cr-Ni-steel. No effect of collector-resistance could be detected for current densities up to 10 A/cm². Minimum work functions as low as 1.25 eV could be obtained in converters. The absolute value of collector work function is very much affected by temperature and vacuum conditions.

*This work has been sponsored by EURATOM, Ispra (Varese)

References

- (1) CHAPMAN, R. A., J. Appl. Phys. 35, 2832, (1964).
- (2) MUZ, E.; ALBRECHT, H., Int. Conf. Therm. Power Gen., London 1965.
- (3) BLOSS, W.; MUZ, E., Therm. Conv. Spec. Conf., Houston 1966.
- (4) LAWRENCE, J.; PERDEW, J. P., Therm. Conv. Spec. Conf., San Diego 1965.



Fig. 1 Experimental converter

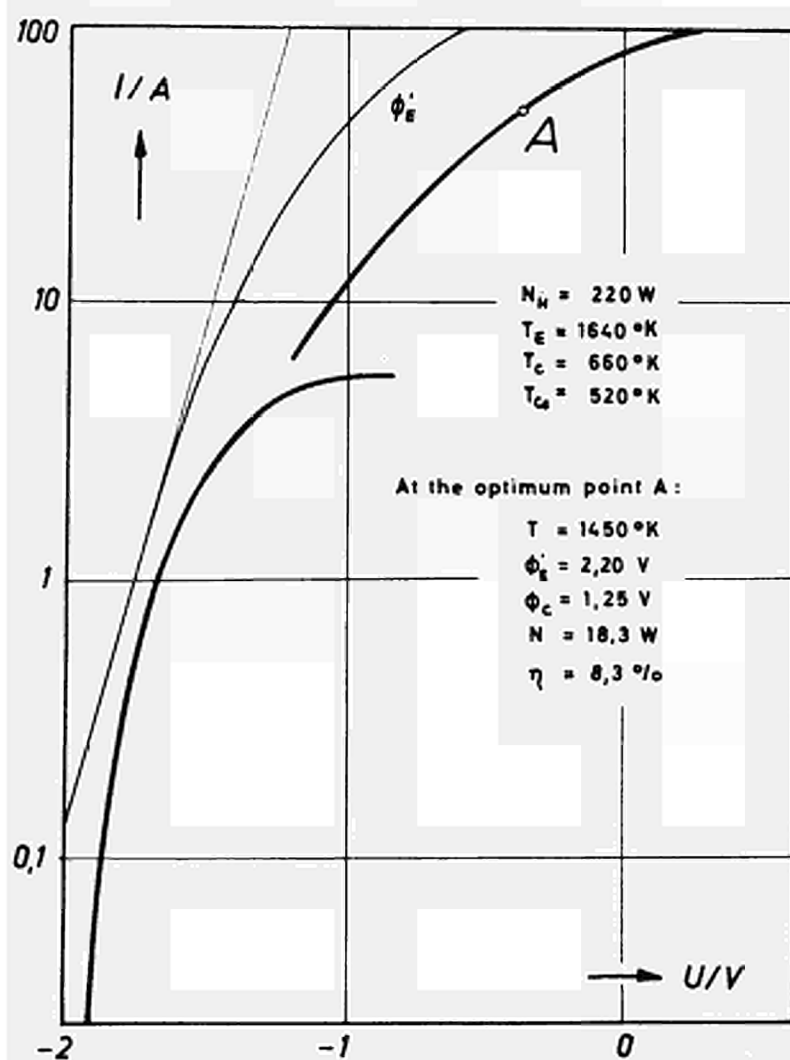


Fig. 2 I-V-characteristic for a diode with Mo-emitter and Al-Al₂O₃-collector at optimum conditions.

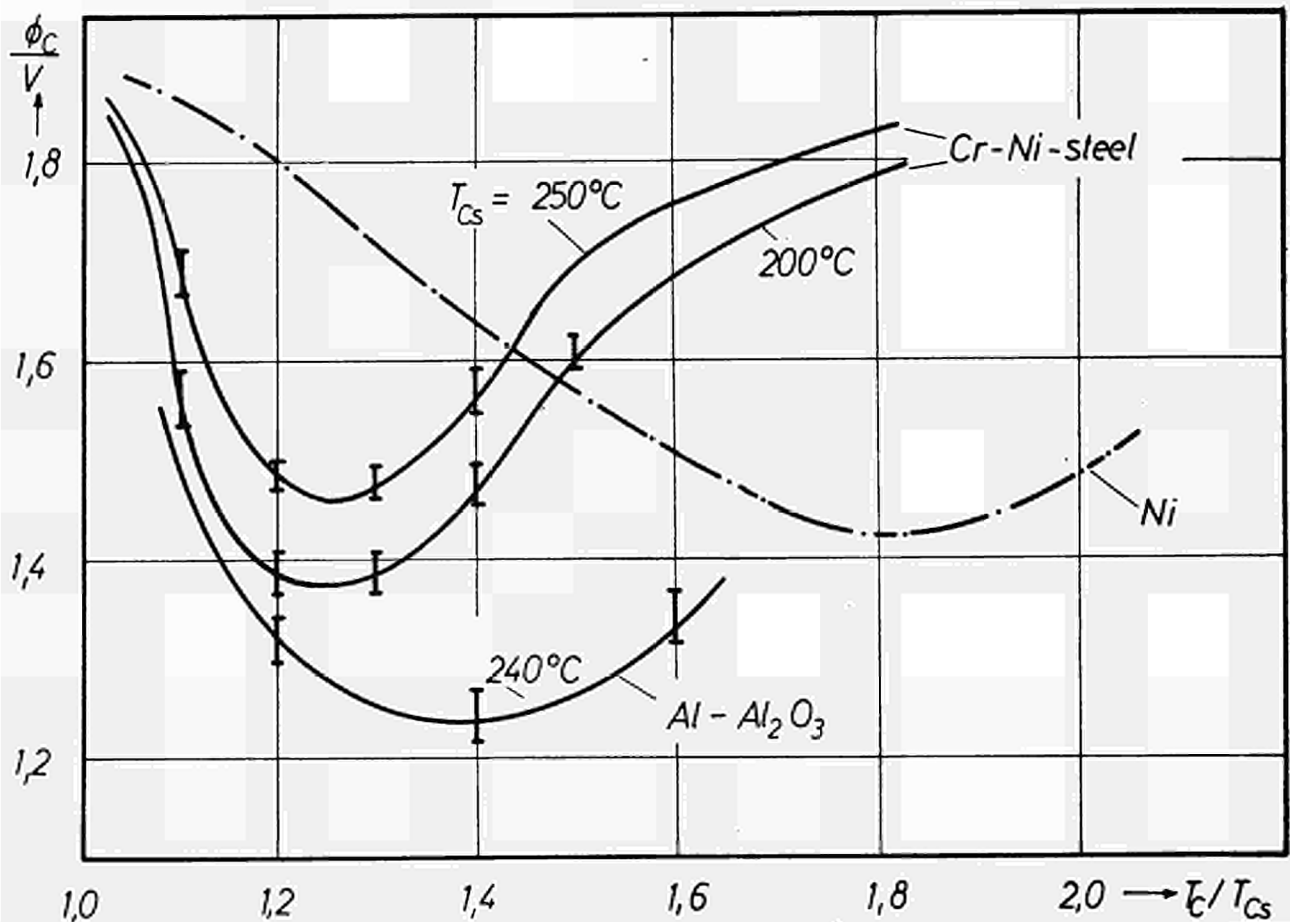


Fig. 3 Work function of a Cr-Ni-steel collector compared with an Al-Al₂O₃-collector at optimum conditions

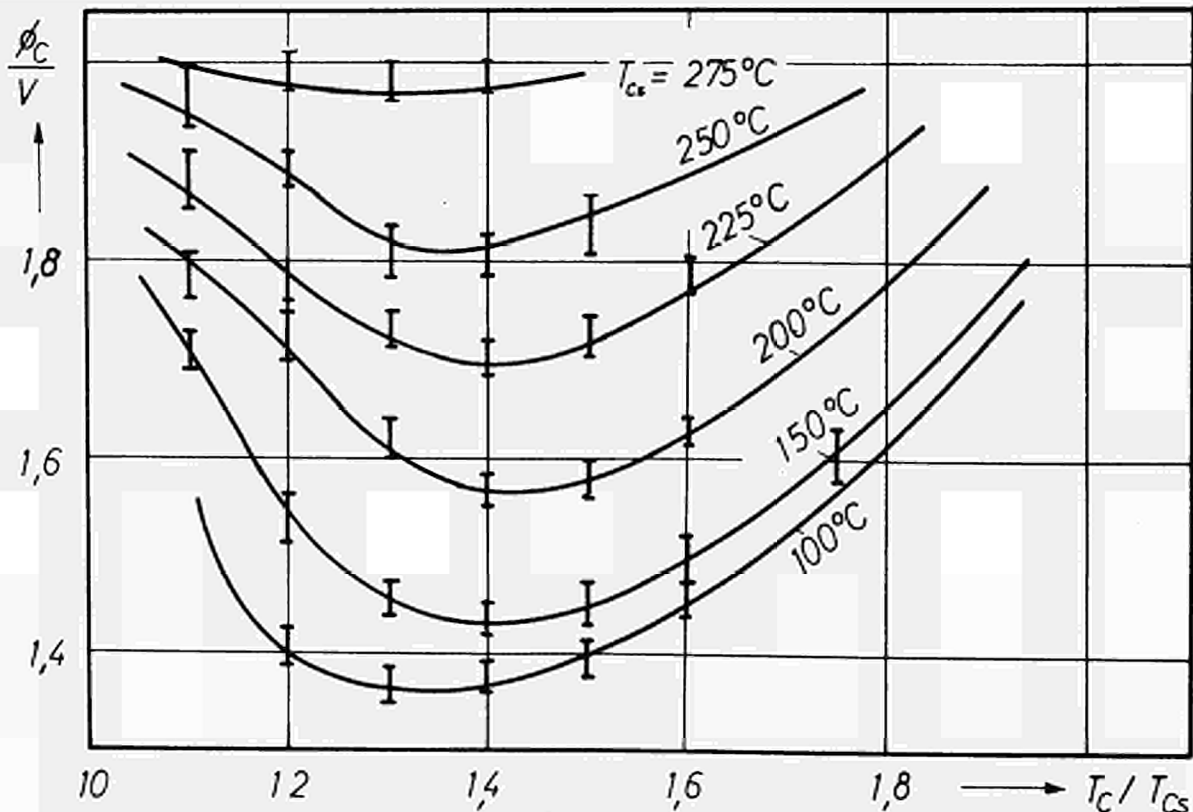


Fig. 4 Work function of an Al-Al₂O₃-collector as function of the quotient T_c/T_{Cs} after 150 operating hours

DISCUSSION

Speaker of paper K-7: R. MALY.

RASOR (USA): I understand that even though the minimum work function was something like 1.25 eV initially, after one hundred hours of operation it had gone up to something like 1.4 eV. Now my question is, do you expect this process of degradation to continue? At the end of 1,000 hours would it perhaps even be higher?

MALY (Germany): Yes, if your vacuum conditions are becoming worse.

RASOR: If this condition is assumed to be a monolayer of oxygen, the vacuum conditions would have to be very good to not put a monolayer of oxygen on the surface during 1,000 hours or 10,000 hours, would they not?

MALY: It seems possible to us to keep up a reasonable good vacuum in a real converter also under operation conditions. Thus life times of several thousand hours are not unrealistic.

DESTEESE (USA): At what collector temperature is the Al-Al₂O₃ surface thermally destroyed?

MALY: The maximum possible temperature is approx. 600°C. In practical application it proved to be about 450°C.

SCHOCK (USA): Is this work directed toward space applications or toward terrestrial applications?

MALY: The Al₂O₃ collectors are not intended to be used in converters for space application.

Wetting of Some Refractory Metals by Cesium, Potassium, and Sodium*

Harold F. Webster
General Electric Research and Development Center
Schenectady, New York

Abstract

Contact angles of sessile drops of three alkali liquid metals on rhenium, tungsten, molybdenum, tantalum, and niobium substrates have been measured and found to be related to the bare work function of the substrate surface. The contact angles vary from grain to grain of the substrates and are affected by monolayer amounts of impurities. The liquid drops used have been so small that all observations have been done with an optical microscope. An electron emission microscope has been used to compare the bare work functions of individual grains in the substrate samples. Lower work function surfaces show complete wetting.

Experimental Procedure

All of the substrates were thin ribbons mounted in ultra-high vacuum tubes near optical flat windows.

The tubes were sealed off in the 10^{-9} torr residual gas range and cesium, potassium, or sodium was introduced from breakable glass ampules. The substrates were cleaned by

*This work was supported in part by Air Force Cambridge Research Laboratories.

flashing them to high temperatures before deposition of the alkali metals.

Three different techniques were used to measure the contact angles of the alkali metal drops. The first of these makes use of a light beam which can be directed at the sample from different directions and is moved until the reflection from the drop meets the substrate surface.

The second method makes use of a tipping stage on the microscope which can be used to measure the angle between direct reflection from the drop edge and from the substrate.

The third method makes use of a Nomarski interference attachment to the microscope which permits a contour map of the alkali metal drop to be made from which the contact angle can be calculated.

Most measurements were made by the first method but all three methods yielded contact angles which agreed to about $\pm 1^\circ$.

Wetting of the Substrates by Cesium

The polycrystalline tungsten sample showed a variety of contact angles for the cesium drops ranging from 17° to 0° . There was only one grain in the sample which wet completely (i.e. had 0° contact angle).

The polycrystalline molybdenum sample with the liquid cesium deposit, appeared to be different than the tungsten sample because about half of its grains wet completely.

The other grains showed contact angles as high as 12° .

The polycrystalline tantalum sample had about 80% of its surface wet by cesium but the unwet grains showed a variety of contact angles with some as high as 11° .

The (110) tantalum sample consisted of two large grains both of which had surface orientations within a few degrees of the (110) plane. No parts of this sample were wet by cesium and the drops on both grains had contact angles within 1° of 11° .

The polycrystalline niobium sample had almost all of its surface wet by the cesium except for a few grains. None of the drops on the non-wetting grains had contact angles greater than 2° to 3° .

This qualitative dependence of wetting upon material suggests a correlation with work function. The high work function grains of the high work function materials show the highest contact angles. Detailed analysis of these results suggest that surfaces with work functions less than 4.3 wet by cesium while those with higher work functions hold drops.

To check this supposed relationship between contact angle and bare work function, some measured values of contact angle have been plotted vs the thermionic work function of the particular crystal face. The work function of the actual grain in the wetting tube was not measured but instead its

orientation determined and the work function of this crystal face determined in a previous measurement²⁻⁸ used as its value. The resulting plot is shown in Fig. 1. It will be seen that the graph is approximately a straight line which has an intercept at 0° contact angle which is near 4.3 e.v. in agreement with the previous deduction.

Wetting of the Rhenium Substrate by Cesium, Potassium, and Sodium

The same rhenium sample described in reference 1 was remounted and run in potassium vapor, sodium vapor, and in a vacuum emission microscope. Deposits of potassium on this surface are shown in Fig. 2. The same grains used as substrates for cesium in reference 1 are indicated and numbered in Fig. 2. All of the numbered grains except 1 are wet by potassium. The image of this area obtained in the vacuum emission microscope is shown in Fig. 3, and it will be seen that the brightest grains and thus those with the lowest bare work function are numbers 5 and 6 while, 2, 3, and 4 are of intermediate work function. The basal oriented grain number 1 appears almost black. The contact angles of drops of the three alkali metals on these six grains is summarized in Table I. It will be seen that the contact angles increase with increasing work function. Points for grains of known work function are shown in Fig. 1.

Table I
Contact Angle In

<u>Grain No.</u>	<u>Cesium</u>	<u>Potassium</u>	<u>Sodium</u>
1	25°	17.5°	14°
2	16°	0°	5°
3	13.5°	0°	0° to 2°
4	11°	0°	0°
5	0°	0°	0°
6	0°	0°	0°

It was previously thought that the linear dependence of contact angle on bare work function shown in Fig. 1 for the high work function grains would also apply to all grains. When this assumption was made, the data for sodium fell on a line parallel to that for cesium. The new data for potassium, however, fails to fall on a parallel line and more work using measured values for the bare work functions of the various grains is necessary to check this assumption.

References

1. Webster, H.F., "Liquid and solid cesium on a rhenium substrate", J. Appl. Phys. 38 (1967) 3700.
2. Wichner, R. and Pigford, T.H., "Work functions of monocrystalline and polycrystalline rhenium", 1966 IEEE Conf. Record of Thermionic Conversion Specialist Conference, p. 405.
3. Norris, W.T., "Work function of the (110) face of tantalum in a cesium vapor", J. Appl. Phys. 35 (1964) 467.
4. Webster, H.F., "Work function of the (110) plane of tantalum as a function of cesium coverage", 1963 Report Thermionic Conversion Specialist Conference, p. 187
5. Milton, O., Thesis, Brown University (1963).
6. Houston, J.M., Thesis, M.I.T.
7. Steele, H. and Shimada, K., "Evaluation of "Single" crystal molybdenum as an emitter material", 1963 Report Thermionic Conversion Specialist Conference, p. 240.
8. Webster, H.F., "Uniform work function surfaces", 1964 Report Thermionic Conversion Specialist Conference, p. 31.

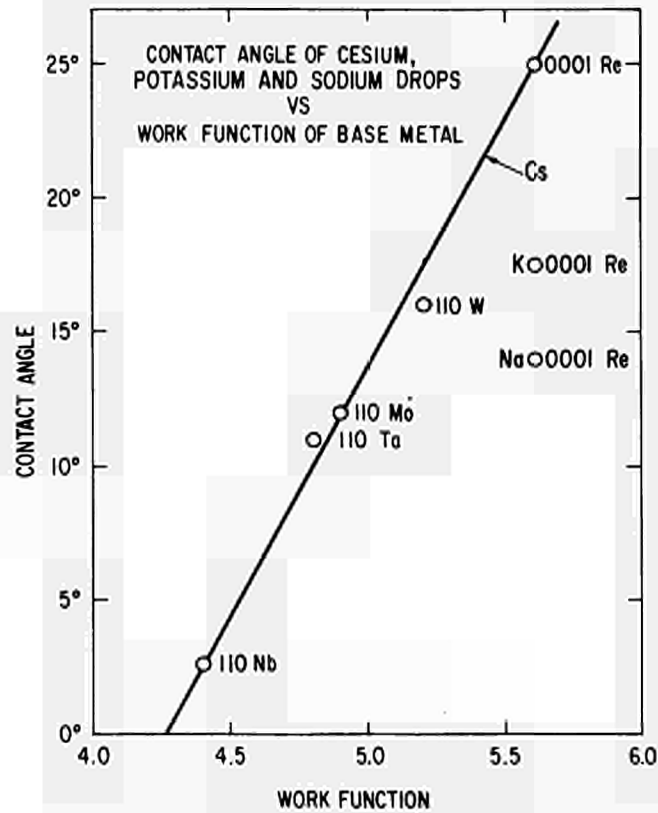


Fig. 1 - Contact angle of cesium, potassium, and sodium drops vs work function of the base metal.



Fig. 2 - Deposits of liquid potassium on the rhenium substrate.



Fig. 3 - Vacuum emission microscope image of the rhenium substrate.

DISCUSSION

Speaker of paper K-8: V. C. WILSON.

BOHDANSKY (Euratom): Was the wetting angle measured as a function of temperature? Did the author find any influence of contamination?

WEBSTER^{*} (USA): The measurements were done just at room temperature. Contaminants did change the contact angle (see Jour. Appl. Phys. 38, 3700 (1967)).

GYFTOPOULOS (USA): Was there a layer of liquid cesium between the droplets?

WEBSTER: There probably was cesium between the droplets because the arrival rate from the vapor would deposit a monolayer every 2 seconds.

DESTEESE (USA): 1. Was a getter used in this experiment? 2. Were the alkalis contaminated with material from the flashed ribbons? 3. Was it possible that each ribbon could contaminate the other ribbons when flashed?

WEBSTER: The getter was cesium. The ribbons were thoroughly outgassed while the tube was on the pump before the cesium was admitted and the flash before measurement should introduce relatively few parts per million of contaminants in the bulk cesium. The ribbons all were in a plane and deposition from one ribbon to the next should be reduced to a minimum.

MUZ (Germany): The contact angle is strongly influenced by films of a thickness smaller than a monolayer. If there is no adsorption between the droplets, I wonder if the system is stable?

WEBSTER: The results are difficult to understand unless there is a cesium film between the droplets. The system was stable over long periods of time.

VAN ANDEL (Euratom): Do you remember the colour of the cesium metal? Was it gold or white?

WEBSTER: The cesium metal appeared gold in color while both the potassium and sodium were like silver.

^{*}) H. F. WEBSTER was not present at the Conference. These are the author's answers to the questions.

ETUDE DE L'ADSORPTION DU CESIUM SUR DES MONOCRISTAUX DE TUNGSTENE.

T. ALLEAU, J. L. DESPLAT

Service d'Electronique Physique, Centre d'Etudes Nucléaires de Saclay.

91 Gif-sur-Yvette (France)

I - Résumé.

La mise en programme du calcul de GYFTOPOULOS, STEINER et LEVINE, permet de tracer les réseaux de courbes en "S" de LANGMUIR. Il a été appliqué aux cas de monocristaux de tungstène d'orientation (100), (112) et (110) en présence de césium. La comparaison avec les résultats expérimentaux est bonne.

Des courbes en "S" expérimentales, obtenues au microscope à émission thermo-ionique, sont présentées pour des orientations (100) et (110) du tungstène, en présence de césium, dans le domaine de 10^{15} à 10^{18} atomes/cm²/s.

II - Etude théorique.

Le concept d'électronégativité orbitale, étendu par E. P. GYFTOPOULOS et D. STEINER [1] aux surfaces bi-métalliques permet de relier plus rigoureusement le travail de sortie d'une surface, au taux de recouvrement d'un adsorbé quelconque. L'application de la deuxième partie de la théorie de J. D. LEVINE et E. P. GYFTOPOULOS [2], conduit au tracé direct des courbes en "S".

II.1 - Théorie de GYFTOPOULOS-STEINER-LEVINE.

Le travail de sortie dont il est question par la suite est le travail de sortie effectif qui est lié à la constante $A = 120$. En identifiant le travail de sortie d'une surface bi-métallique à l'électronégativité orbitale neutre des atomes du substrat, perturbée par les liaisons adsorbat-adsorbat et adsorbat-substrat, GYFTOPOULOS et STEINER ont complété et précisé la première théorie de GYFTOPOULOS et LEVINE. Nous avons pu ainsi tracer les courbes en "S" de tous les systèmes métaux de transition-alcalins (ou alcalino-terreux) [3].

Les principales relations utilisées sont les suivantes, les détails des calculs étant donnés dans les références [1] et [2] ; les notations étant identiques :

$$\phi = \phi_s + cQ + bF$$

ϕ_s est le travail de sortie du substrat, cQ et bF sont donnés par :

$$cQ = - (\phi_s - \phi_f) M$$

ϕ_f : travail de sortie de l'adsorbé,

M : fonction de MORSE.

$$bF = - 2 \pi \sigma_f \theta \mu$$

σ_f : densité d'atomes adsorbés à $\theta = 1$

μ : moment dipolaire effectif.

Pour calculer le réseau de courbes en "S", il faut relier cette fonction $\Phi(\theta)$ à la fonction $\theta(T, T')$, T et T' étant les températures d'émetteur et de réservoir. Il est nécessaire de connaître l'énergie de désorption des atomes et des ions sur la surface, soit $\psi_a(\theta)$ et $\psi_p(\theta)$. GYFTOPOULOS et STEINER donnent une relation $\psi_a(\theta)$ en affirmant que l'énergie de désorption d'un atome n'est que l'énergie d'une liaison adsorbat-surface. Mais si cette expression donne de très bons résultats pour $\psi_{a0}(\theta = 0)$, la courbe $\psi_a(\theta)$ s'éloigne beaucoup des courbes expérimentales relevées dans la littérature. En particulier, la relation de G.S. donne à l'origine ($\theta = 0$), une pente nulle, alors que tous les résultats expérimentaux semblent prouver une variation rapide de ψ_a avec θ , pour les taux de recouvrement faibles ; si bien que l'application de cette expression conduit à de très mauvais résultats sur les courbes en "S". On peut déduire de cela que l'adsorption étant très inhomogène (groupements des atomes autour des dislocations ou irrégularités du réseau: "active spots" de I. LANGMUIR), il faudrait tenir compte de l'interaction des orbitales des atomes adsorbés voisins. Nous avons préféré reprendre l'expression de $\psi_a(\theta)$ donnée par [2], qui associe ψ_a à la somme d'une liaison covalente et d'une liaison ionique. Seulement il est nécessaire de connaître le transfert de charge F entre l'adsorbat et le substrat, différent suivant les 2 théories [1] et [2]. Nous avons constaté qu'il existait un rapport constant, voisin de 3, entre les deux, ce qui nous a permis d'écrire :

$$\psi_a = \frac{F}{3e} \Phi(1 + \delta) + (\lambda_f \lambda_s)^{1/2} S_{fs} Q_{fs}$$

les différents termes étant explicités dans la réf. [2].

Les taux de désorption E_a et E_p sont calculés suivant [2], ainsi que les taux d'évaporation E' au-dessus du réservoir de césium. L'équation d'état de la surface s'écrit en supposant une gaine de potentiel Φ_x au voisinage de l'émetteur :

$$E' = E_a + E_p \exp(-\Phi_x/kT)$$

C'est la résolution de cette équation d'état qui permet de calculer $\theta(T, T')$, d'où on déduit le tracé des courbes en "S". Le programme complet a été mis sur ordinateur, et le tracé des courbes s'effectue automatiquement sur un traceur BENSON, en unité périphérique de l'ordinateur utilisé.

II. 2. - Cas étudiés.

a) W (100) - Cs (fig. 1).

- Principaux paramètres choisis :

$$\Phi_s = 4,52 \text{ eV}$$

$$D_1 = 1,07$$

$$\Phi_f = 1,63 \text{ eV}$$

$$\Phi_x = 0,5 \text{ eV}$$

$$r = 2,60 \text{ \AA}$$

$$\cos \beta = 0,91$$

$$\sigma_f = 2,5 \cdot 10^{14} \text{ at/cm}^2$$

- Chaleurs d'adsorption obtenues :

$$\psi_{a0}(\theta = 5 \cdot 10^{-3}) = 2,84 \text{ eV}$$

$$\psi_{p0}(\theta = 5 \cdot 10^{-3}) = 2,21 \text{ eV.}$$

- Références des résultats expérimentaux : R.G. WILSON [4], J.M. HOUSTON [5], H.F. WEBSTER [6], D. KOENIG [7], I. LANGMUIR [13].

Le travail de sortie du césium est souvent pris égal à 1,81 eV. Néanmoins il semble, d'après les nombreux résultats existant dans la littérature que la couche monoatomique de césium ait une configuration qui dépende de la nature du substrat et de la disposition du réseau cristallin qu'il présente à sa surface. V.M. GAVRILYUK [8] envisage même la possibilité d'une épitaxie des atomes de césium, ayant trouvé des travaux de sortie de couches de Cs variant dans le même sens que les travaux de sortie du substrat, cette étude ayant été faite sur des monocristaux de tungstène. La valeur 1,63 eV a été prise en fonction des résultats expérimentaux ci-dessus cités en référence. Une autre explication de cette faible valeur de ϕ_f pourrait être une contamination par des traces d'oxygène ou d'autres gaz, de l'enceinte dans laquelle ont été effectuées les mesures. En ce qui concerne l'expérience de notre laboratoire, où les études du système W-Cs sont actuellement menées au microscope électronique à émission, nous avons pu faire varier le travail de sortie d'une couche de tungstène (100) de 1,8 à 1,5 eV, par une dégradation volontaire du vide de l'enceinte du microscope (fig. n° 6). Nous pencherions donc vers cette deuxième hypothèse pour expliquer les valeurs de ϕ_f anormalement basses, généralement données dans la littérature.

b) W (112) - Cs (fig. n° 2)

- Principaux paramètres choisis :

$$\begin{array}{ll} \phi_s & = 4,80 \text{ eV} & \sigma_f & = 4,1 \cdot 10^{14} \text{ at/cm}^2 \\ \phi_f & = 1,81 \text{ eV} & D_1 & = 0,5 \text{ eV} \\ r & = 2,60 \text{ \AA} & \phi_x & = 1 \text{ eV} \\ \cos \beta & = 0,745 \end{array}$$

- Chaleurs d'adsorption obtenues :

$$\begin{array}{ll} \psi_{ao} (\theta = 5 \cdot 10^{-3}) & = 3,0 \text{ eV} \\ \psi_{po} (\theta = 5 \cdot 10^{-3}) & = 2,10 \text{ eV.} \end{array}$$

- Références des résultats expérimentaux : J.L. COGGINS et R.E. STICKNEY [9].

c) W (110) - Cs (fig. n° 3)

- Principaux paramètres choisis :

$$\begin{array}{ll} \phi_s & = 5,30 \text{ eV} & \sigma_f & = 7,07 \cdot 10^{14} \text{ at/cm}^2 \\ \phi_f & = 1,81 \text{ eV} & D_1 & = 0,8 \\ r & = 2,60 \text{ \AA} & \phi_x & = 2 \text{ eV} \\ \cos \beta & = 0,906 \end{array}$$

- Chaleurs d'adsorption obtenues :

$$\begin{array}{ll} \psi_{ao} (\theta = 5 \cdot 10^{-3}) & = 3,16 \text{ eV} \\ \psi_{po} (\theta = 5 \cdot 10^{-3}) & = 1,80 \text{ eV.} \end{array}$$

- Références des résultats expérimentaux : J.L. COGGINS et R.E. STICKNEY [9], H.F. WEBSTER [6], D.H. POLLOCK [10].

III - Etude expérimentale.

III.1. Appareillage de mesure.

Des monocristaux de tungstène (SEMI-ELEMENTS INC. 99,999 %) d'orientation (100) et (110) se présentant sous forme de disques de diamètre 6 mm, polis mécaniquement et électrolytiquement, sont chauffés par bombardement électronique. Les électrons émis sont focalisés par une optique électrostatique à immersion, type SEPTIER [11], et projetés sur un écran luminescent. Au centre de cet écran est percé un trou en face duquel une électrode entourée d'un anneau de garde collecte les électrons. La connaissance du diamètre de l'électrode et du grossissement du microscope permet de déduire la densité de courant émis. La température de l'échantillon est mesurée par un thermocouple W-Re 5-26 % préalablement étalonné, et logé dans un trou diamétral de la pastille. Le courant est mesuré par un pico-ampère-mètre logarithmique dont la sortie est branchée sur une voie d'un enregistreur XY, l'autre voie recevant la tension du thermocouple. Les courbes $J(T)$ sont directement relevées sur toute leur étendue. Cet ensemble de mesure est présenté plus en détail dans [11]. Le vide dans l'enceinte est assuré par une pompe à diffusion de mercure surmontée d'un piège à azote liquide ; un tamis moléculaire l'isole de la pompe primaire, et évite le transport de vapeur d'huile. Le vide est de l'ordre de $3 \cdot 10^{-7}$ mmHg au niveau de la jauge pendant les expériences. Le césium est injecté par un conduit logé dans le wehnelt (fig. n° 4). Le réservoir est constitué d'un bloc de graphite dans lequel sont insérés des atomes de césium. La pression de césium au-dessus de ce système est connue [12]. Le flux de césium au niveau de l'échantillon est donné par un calcul de conductance. Des vérifications expérimentales de ce calcul ont été faites, par mesure de courant ionique, en inversant les tensions de polarisation des électrodes. L'étude du champ électrique a été faite, et les mesures effectuées dans des conditions telles que le courant de saturation est tiré en évitant de créer des décharges. La tension de polarisation de l'anode est généralement voisine de 200 V.

III.2. Résultats expérimentaux.

a) W (100) - Cs (fig. n° 5).

Le flux de césium varie de $1,5 \cdot 10^{15}$ à $2,4 \cdot 10^{17}$ at/cm²/sec. Les courants mesurés varient de 10^{-11} à 10^{-8} A au niveau de l'électrode, c'est-à-dire 10^{-5} à 10^{-2} A/cm² au niveau de l'échantillon. La mesure du travail de sortie nu, en l'absence de césium, a donné :

$$\phi(100) = 4,60 \pm 0,04 \text{ eV}$$

Les résultats sont présentés en comparaison avec deux courbes du réseau de D. KOENIG [7]. On constate immédiatement que pour des flux équivalents, la partie intermédiaire est sensiblement identique, mais le maximum se situe pour des courants plus forts, le minimum de travail de sortie atteignant 1,5 eV : ce fait est très caractéristique d'une contamination, par des traces d'oxygène probablement, de l'enceinte dans laquelle D. KOENIG a effectué ses mesures.

Il est en effet bien connu que les systèmes W-O-Cs donnent des travaux de sortie très bas [14], il est donc naturel de trouver des courants plus forts. Nous avons pu confirmer ce fait expérimentalement en polluant volontairement l'enceinte du microscope par un dégazage excessif de certaines pièces, le vide au niveau de la jauge atteignant $3 \cdot 10^{-6}$ mmHg. On constate sur la figure n° 6, que pour un flux sensiblement équivalent, la pente de la partie intermédiaire est plus forte, le courant est augmenté d'un facteur 10 au voisinage du maximum, et le minimum de travail de sortie est inférieur à 1,5 eV. L'augmentation de la pente signifie que le minimum de courant se situe plus bas ; en ce point, le taux de recouvrement en césium est pratiquement nul, et seul le système W-O est présent. L'oxygène augmentant le travail de sortie de tungstène [15], il est naturel d'y trouver un courant plus faible.

b) W (110) - Cs (fig. n° 7).

La mesure du travail de sortie nu, en l'absence de césium, a donné :

$$\Phi (110) = 4,95 \pm 0,04 \text{ eV}$$

Cette valeur est inférieure à des mesures faites précédemment sur le même échantillon avec lequel une valeur de 5,3 eV a été trouvée. Un polissage mécanique ayant été effectué entre les deux séries de mesure, il est probable qu'une désorientation de quelques degrés se soit produite. Le cristal utilisé ne présente donc pas rigoureusement l'orientation (110). Les résultats sont présentés en comparaison avec une courbe donnée par STICKNEY [9] ; les courants mesurés sont inférieurs dans la région présentée, ce qui est naturel étant donné que ce dernier avait mesuré 5,3 eV sur son échantillon. On constate que la pente de la partie intermédiaire est plus forte que dans le cas du W (100), ce que le tracé théorique avait montré. On constate d'autre part un minimum de travail de sortie décroissant pour des pressions de césium croissantes : ceci est dû à une contamination progressive du césium provoquée par le dégazage des parois du réservoir.

IV - Conclusion.

Nous avons pu mettre au point un programme de calcul satisfaisant pour le tracé des courbes en "S" de LANGMUIR, malgré quelques difficultés dans la détermination des chaleurs de désorption. Parallèlement le microscope à émission thermo-ionique à injecteur de césium nous permet de vérifier que la théorie de GYFTOPOULOS, LEVINE et STEINER concorde bien avec l'expérience. Nous avons mis en évidence l'importance de la pression résiduelle de gaz, pour la formation de couches à bas travail de sortie : élément défavorable pour la vérification expérimentale d'une théorie, mais pouvant devenir favorable dans le cas d'un fonctionnement de convertisseur thermo-ionique.

REFERENCES.

- [1] E.P. GYFTOPOULOS, D. STEINER,
27th Annual Conf. Phys. Elec. M.I.T. (Mass). Mars 1967.
- [2] J.D. LEVINE, E.P. GYFTOPOULOS.
Surface Science 1 (1964), p. 171, 225 et 349.
- [3] T. ALLEAU, J.L. DESPLAT
Rapport C. E. A. (à parafire).
- [4] R.G. WILSON,
J.A.P. vol. 37, n° 11, oct. 1966, p. 4125-4130.
- [5] J.M. HOUSTON, P.K. DEDERICK.
Rep. General Electric. Res. Lab. n° 65-RL-3872 E. Fev. 1965.
- [6] H.F. WEBSTER, P.L. READ.
Surface Science (2), 1964, p. 200-209.
- [7] D.R. LOENIG, T.A. PIGFORD.
Univ. of Calif. UCRL-16805. Avril 1966.
- [8] V.M. GAVRILYUK et al.
Soviet Physics J.E.T.P. vol. 24, n° 5, mai 1967, p. 899-904.
- [9] J.L. COGGINS et R.E. STICKNEY
25th Annual Conf. Phys. Elec. M.I.T. (Mass). 1965.
- [10] D.H. POLLOCK.
Therm. Conv. Spec. Conf. Oct 1965, San Diego (Calif.).
- [11] A. SEPTIER
Thèse présentée à la Fac. des Sc. de Paris, n° 2583, série A (1954).
- [12] B. DEVIN, R. LESUEUR, R. SETTON.
1967. Therm. Conv. Spec. Conf. Palo-Alto, U.S.A.
- [13] I. LANGMUIR et J.B. TAYLOR.
Phys. Rev. 44, 423 (1933).
- [14] V.S. FOMENKO
Handbook of therm. Prop. Plenum Press Data. Div. 1966 (N.Y.).
- [15] F.P. DUMONT, J. MAURIES.
Therm. Elec. Power Gener. Stresa, 1968.

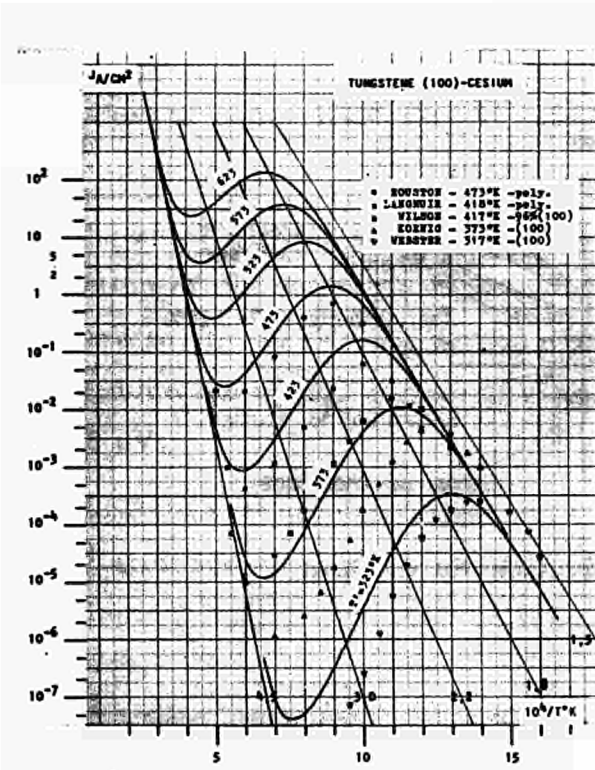


Fig. 1- Tungstène (100)-Césium

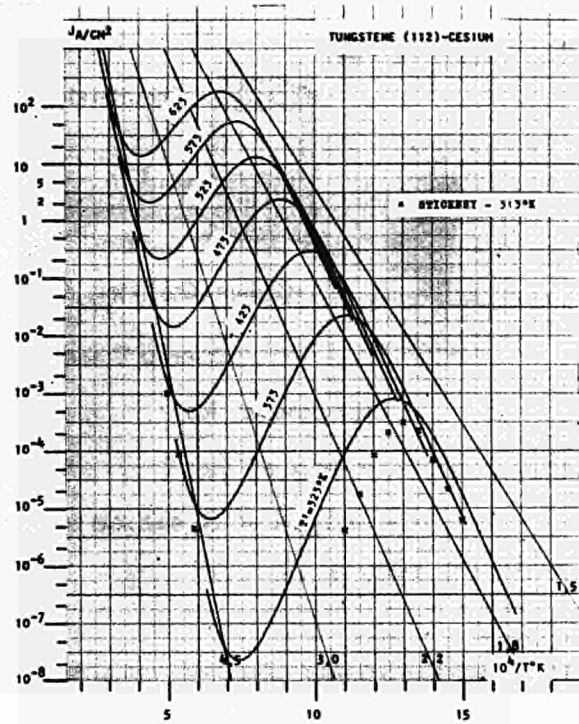


Fig. 2 - Tungstène (112)- Césium

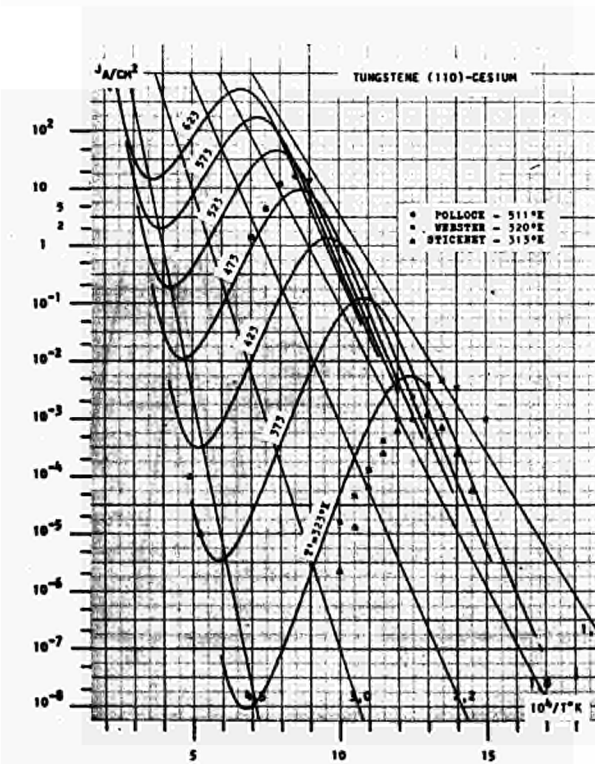


Fig. 3 - Tungstène(110)- Césium

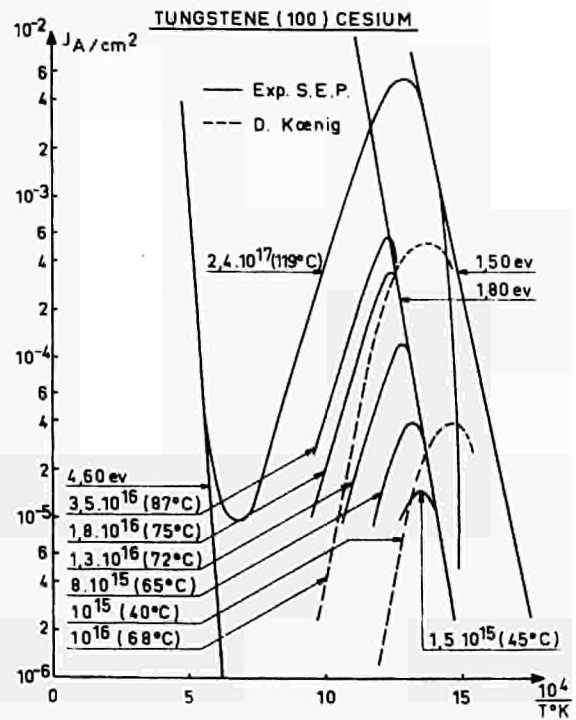


Fig. 5- W(100)-Cs expérimental

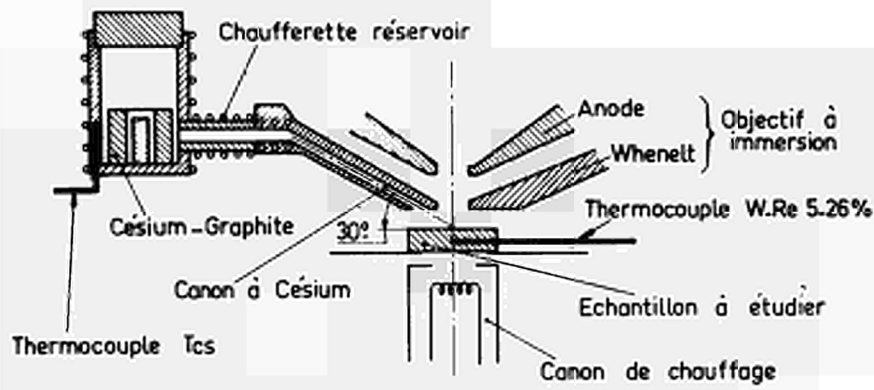


Fig.4 - Système d'introduction du césium

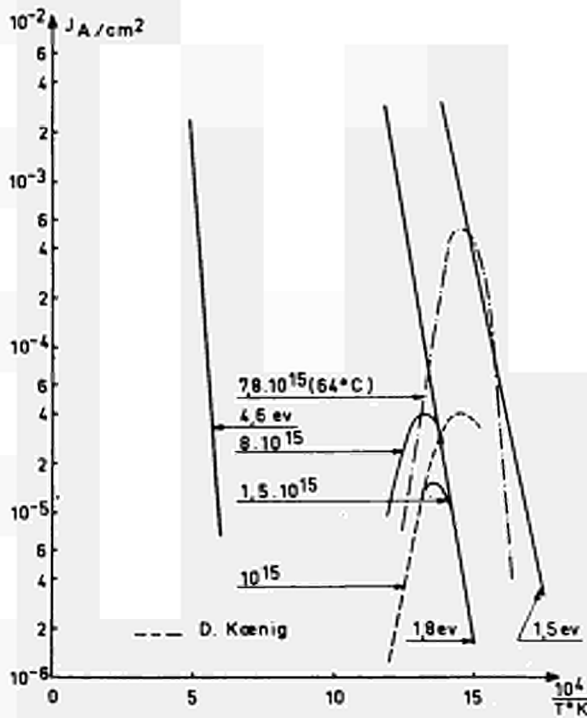


Fig.6- Influence des gaz résiduels

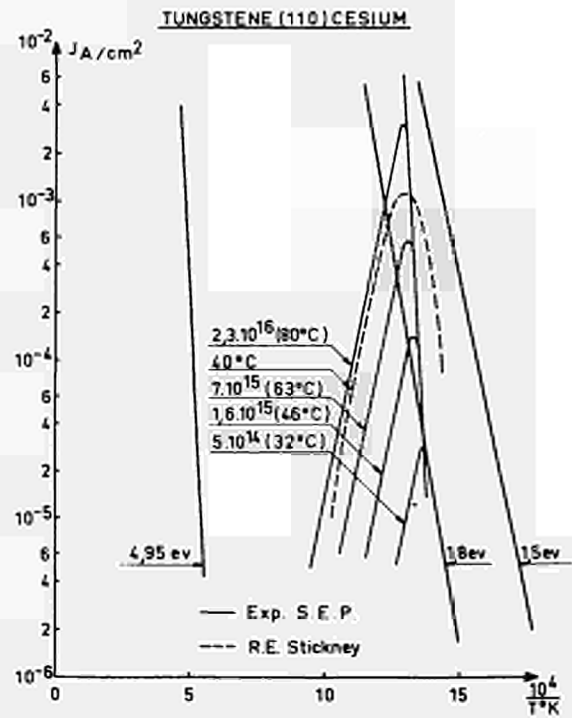


Fig.7- W(110)-Cs Expérimental

DISCUSSION

Speaker of paper K-9: Th. ALLEAU.

WILSON (USA): I would like to remark that I have observed almost exactly the same thing. In paper A-2 I mentioned two cases in which the work function of the collector changed while the converter was left at room temperature for three or four weeks. The contamination, presumably O₂, seems to reduce the work function of the cesium coated collector, by about 0.1 or 0.15 eV.

ALLEAU (France): Ceci confirme la contamination, je crois simplement, et l'influence des contaminants dans le convertisseur, vu qu'il marche probablement beaucoup mieux qu'il ne devrait marcher..... le vide était très propre.

ADSORPTION DE GAZ SUR DES MONOCRISTAUX DE TUNGSTENE

F. P. DUMONT et J. MAURIES
Service d'Electronique Physique
Centre d'Etudes Nucléaires de Saclay
91 Gif-sur-Yvette (France)

RESUME. -

On a mesuré au microscope électronique à émission et par la méthode de Kelvin, les variations du travail de sortie de divers échantillons monocristallins de tungstène en présence d'une atmosphère d'oxygène ou d'oxyde de carbone.

Avec le microscope à émission thermoionique, on a étudié les variations du travail de sortie en fonction de la pression d'oxygène entre 1900°K et 2300°K. Au cours d'une première série d'expériences on a constaté que l'adsorption d'oxygène provoquait d'abord une diminution du travail de sortie suivie d'une augmentation au delà de la valeur caractéristique du métal nu. On pense que la diminution observée doit être attribuée à une impureté dont la nature n'a pas encore été reconnue, car par la suite, ces phénomènes se sont avérés peu reproductibles : dans une deuxième série d'expériences on a constaté une augmentation continue du travail de sortie en fonction de la pression totale.

Par la méthode de Kelvin on a constaté une croissance du travail de sortie en fonction du recouvrement (jusqu'à un maximum de 6,4 eV pour une face (100) couverte d'oxygène). Mais les résultats obtenus concordent assez mal avec les prévisions théoriques de D. STEINER et E. P. GYFTOPOULOS.

INTRODUCTION. -

Le problème de l'adsorption de l'oxygène sur le tungstène a suscité ces dernières années d'abondantes études en raison de son intérêt dans le domaine de la conversion thermoionique. Divers auteurs⁽¹⁾ ⁽²⁾ ont constaté une amélioration des performances de convertisseurs thermoioniques en y introduisant de l'oxygène. Cependant cette méthode est un peu empirique et pour obtenir des résultats plus précis il est nécessaire d'opérer dans des conditions mieux définies. C'est ce que nous avons tenté de faire en étudiant l'adsorption d'oxygène sur des monocristaux de tungstène par deux méthodes différentes.

I-1. Microscope Electronique à Emission Thermoionique (T.E.E.M.)

L'intérêt du microscope provient de ce qu'il permet d'observer une image électronique des échantillons tout en mesurant le travail de sortie. En outre, on explore seulement une petite portion de la surface métallique étudiée (diamètre 33 μ), ce qui permet de mettre en évidence des variations locales du travail de sortie.

On peut étudier un échantillon de $\phi = 4,6\text{eV}$, à partir de 1500°K environ. Le chauffage par bombardement électronique nous permet d'atteindre 2300°K au cours des mesures et 2500°K pendant quelques minutes lors des dégazages.

II-2. Méthode de Kelvin (ou du condensateur vibrant)

Cette méthode permet de mesurer le travail de sortie en champ nul, mais ne donne que la différence des travaux de sortie de l'échantillon et d'une lame de référence polycristalline saturée de gaz adsorbé, dont le travail de sortie moyen est en fait assez mal connu. C'est une méthode relative dont la précision peut atteindre 10 mV.

Au contraire du microscope électronique, la méthode de Kelvin mesure le travail de sortie de l'échantillon entier. De plus, opérant à température ambiante, on peut obtenir un recouvrement total de l'échantillon par le gaz.

En contrepartie, il faut descendre à des pressions très basses pour être certain que les gaz résiduels ne faussent pas les mesures (100 s à 10^{-8} Torr pour obtenir une couche monoatomique).

Les monocristaux de tungstène utilisés ont une pureté de 99,999 % ; leur orientation a été vérifiée aux rayons X avec une précision de 2° . La pureté de l'oxygène est 99,998 %, celle de l'oxyde de carbone 99,995 %.

On a étudié les mêmes échantillons métalliques par chacune des deux méthodes, cependant il est très probable que l'arrangement des atomes de gaz diffère dans les deux cas, étant donné la différence des températures d'étude. Ceci limite les possibilités de comparaison entre les résultats des deux méthodes.

II. MICROSCOPE ELECTRONIQUE A EMISSION THERMOIONIQUE (TEEM) -Figure 1-

II.1 - Dispositif de mesure -

Le microscope dont nous disposons a été décrit par B.DEVIN et N.X.PHUC⁽³⁾. Il permet d'observer des échantillons métalliques avec un grandissement de l'ordre de 150. On forme une image électronique de l'objet sur un écran luminescent. Ce dernier est percé d'un trou derrière lequel une électrode, reliée à un picoampèremètre, collecte les électrons

La température de l'échantillon est mesurée par un pyromètre à disparition de filament visant une cavité percée dans l'échantillon. On déduit le travail de sortie effectif de la loi de Richardson-Dushman :

$$J = AT^2 \exp \frac{-\phi_R}{k T} \quad \text{avec } A = 120$$

Le vide est assuré par une pompe à diffusion d'huile surmontée d'un piège à azote liquide. La pression limite atteinte dans ces conditions est $4,10^{-7}$ torr au niveau de la jauge qui est placée aussi près que possible de l'échantillon. Mais la présence du piège à azote liquide ne suffit pas à garantir l'obtention d'un vide parfaitement "propre"

On a tracé sur la figure 2 les "zones de sécurité" obtenues de la manière suivante :

En diminuant progressivement la vitesse de pompage, on a fait croître la pression des gaz résiduels jusqu'à ce qu'ils s'adsorbent et provoquent une augmentation du travail de sortie de 50 mV au dessus de la valeur du matériau nu (50 mV est la précision de la méthode de mesure). Pour chaque valeur de la température on obtient ainsi une pression critique au delà de laquelle la mesure du travail de sortie est erronée. Naturellement la valeur de cette pression critique dépend de la nature des gaz résiduels et en particulier de leur teneur en oxygène : c'est pourquoi on a tracé deux courbes séparées par une "zone d'incertitude". On constate qu'au dessus de 2100°K on peut être certain d'obtenir un résultat correct.

L'oxygène est contenu dans une bouteille métallique ; il est introduit dans le microscope par un capillaire (figure 1).

On mesure les variations du travail de sortie en fonction de la température de l'échantillon, et de la pression d'oxygène donnée par la variation de lecture d'une jauge à ionisation.

II.2- Résultats Expérimentaux -

Au cours d'une première série d'expériences, nous avons constaté les phénomènes suivants :

Lorsqu'on ouvre le robinet d'admission de gaz, on constate que la pression augmente progressivement sans que le travail de sortie ne varie, puis après quelques minutes, on voit sur l'écran du microscope la surface de l'échantillon se recouvrir d'une sorte de "nuage" sombre bordé d'un liseré plus clair que le métal nu (figure 3). Cela signifie que l'adsorption provoque d'abord une diminution du travail de sortie, suivie rapidement d'une augmentation .

La figure 4 donne un exemple de ce comportement : à l'adsorption comme à la désorption on observe un "nuage" à travail de sortie élevé bordé d'une frange à faible travail de sortie.

Ces résultats paraissent étonnants car on attendrait plutôt une adsorption progressive de l'oxygène provoquant un assombrissement progressif de l'image électronique.

Pour expliquer la diminution du travail de sortie, on peut avancer plusieurs hypothèses.

a) L'oxygène s'enterre sous les premiers plans du réseau du tungstène, ainsi que l'ont suggéré ZINGERMAN et coll.⁽⁴⁾, ESTRUP et ANDERSON⁽⁵⁾ selon le mécanisme d'échange de place avancé par LANYON et TRAPNELL⁽⁶⁾. Un atome d'oxygène adsorbé et un atome de métal échangent leur place, éventuellement avec l'aide d'une lacune, puis les atomes métalliques ainsi exposés à l'oxygène adsorbent de nouveau un atome de gaz .

L'échange des places entre l'oxygène et le métal peut être énergétiquement favorable, car dans la situation initiale la surface se présente comme un réseau de dipôles électriques tous parallèles, et possède une énergie électrostatique élevée.

b) Il y a formation de microfacettes sur les plans autres que les plans denses (110)⁽⁷⁾ ⁽⁸⁾ ; la diminution du travail de sortie s'explique alors par un effet de champ sur les pointes des microfacettes.

c) La diminution du travail de sortie est due non à de l'oxygène, mais à une impureté de nature inconnue pour l'instant qui s'adsorbe avant l'oxygène en diminuant le travail de sortie, et qui est ensuite recouverte d'oxygène.

Il semble que la dernière explication proposée soit exacte, car au cours des expériences suivantes, les phénomènes précédemment décrits se sont montrés très peu reproductibles. En effet, on a pu constater par la suite une adsorption progressive sans "nuage" apparent, ni aucune diminution du travail de sortie ainsi qu'on le constate sur la figure 5 qui présente les résultats obtenus en opérant sur un monocristal d'orientation (100) à 2100°K.

Les figures 6 et 7 représentent le réseau des isothermes d'adsorption sur les cristaux d'orientation respective (110) et (100) ; elles donnent la variation du travail de sortie en fonction de la pression d'oxygène à diverses températures. Pour le tungstène nu, on a mesuré :

$$\begin{aligned}\phi(100) &= 4,60 \text{ eV} \\ \phi(110) &= 5,05 \text{ eV} : \text{ valeur un peu faible, ce cristal semble} \\ &\quad \text{légèrement désorienté.}\end{aligned}$$

Certaines courbes présentent, vers les basses pressions, une portion inaccessible à la mesure du fait de la pression résiduelle : W.ENGELMAIER et R.E.STICKNEY⁽⁹⁾ ont montré qu'il fallait atteindre des pressions aussi basses que 10^{-9} torr pour effectuer des mesures correctes à 1900°K.

II.3 - Interprétation des Résultats -

Les courbes que nous présentons sont comparées à celles publiées par W.ENGELMAIER et R.E. STICKNEY⁽⁹⁾. Les deux réseaux concordent assez bien dans le domaine des pressions suffisamment élevées. Au dessous de 10^{-6} torr environ, l'erreur commise est assez élevée car la pression partielle des gaz résiduels est du même ordre que celle de l'oxygène.

Pour comparer plus aisément nos résultats à ceux de W.ENGELMAIER et R.E.STICKNEY, nous avons tracé les variations du travail de sortie à partir de la valeur du métal nu puisque nous ne sommes pas en accord exact sur cette dernière valeur.

On constate qu'à température et pression égales, l'augmentation du travail de sortie est plus faible sur la face (110) que sur la face (100).

Enfin, on n'a pas mis en évidence, entre 1900°K et 2300°K, la possibilité que l'oxygène puisse s'enterrer sous les premiers plans du réseau cristallin, suivant l'hypothèse avancée dans (4) (5).

III . METHODE DE KELVIN -

III.1 - Appareillage de Mesure -

La figure 8 présente le schéma de principe de l'appareillage : l'échantillon étudié forme avec la lame de référence un condensateur vibrant. Si on ajuste V_a de façon à annuler le signal observé sur l'écran de l'oscilloscope, la différence des travaux de sortie $\phi - \phi_R$ est égale à $e V_a$. $\phi - \phi_R$ est mesuré avec une précision de l'ordre de 10 mV.

La lame utilisée comme référence est un polycristal de tungstène qui n'a pas subi auparavant de traitement spécial. Un examen au microscope à émission a montré une assez grande homogénéité de la surface composée de très petits cristaux (travail de sortie moyen 4,71 eV).

Le vide est assuré par un ensemble -pompe primaire à adsorption, pompe ionique, sublimateur à filaments de titane et panneau cryogénique-. La pression résiduelle se situe aux alentours de $3 \cdot 10^{-10}$ torr d'un gaz contenant 80 % d'hydrogène (mesure faite au spectromètre de masse).

Le gaz est introduit par une microfuite réglable RIBER dans l'enceinte préalablement vidée et dégazée. On commence alors la manipulation en recouvrant entièrement de gaz la surface des deux armatures (échantillon et lame vibrante). Ensuite on chauffe l'échantillon seul à 2500°K par bombardement électronique afin de désorber le gaz dont il est recouvert. Enfin, on admet progressivement le gaz en ouvrant la microfuite réglable ; on peut régler la valeur de la pression entre 10^{-9} et 10^{-6} torr. En opérant de cette manière, la lame de référence est constamment saturée de gaz adsorbés et son travail de sortie est supposé constant, au contraire l'échantillon se recouvre progressivement de gaz et on peut suivre l'évolution de son travail de sortie.

III.2 - Résultats des Mesures -

a) oxygène :

La figure 9 représente la variation du travail de sortie du tungstène (100) et (111) en fonction du taux de recouvrement en oxygène ; cette dernière grandeur a été reliée au flux d'atomes arrivant sur la surface, à partir des valeurs données par SINGLETON⁽¹⁰⁾ pour la probabilité d'adhésion de l'oxygène. L'exposition a été portée en Langmuir : unité proposée par GERMER et MAY⁽¹⁵⁾ qui équivaut à 10^{-6} torr-seconde.

Pour le (100), nous avons tenté une comparaison avec les résultats publiés par HOPKINS et PENDER⁽¹¹⁾ en utilisant encore les données de SINGLETON et avec les prévisions théoriques de D. STEINER et E.P. GYFTOPOULOS⁽¹²⁾. On constate que l'accord est loin d'être réalisé entre les trois courbes.

b) oxyde de carbone :

La figure 10 représente la variation du travail de sortie en fonction du recouvrement d'oxyde de carbone pour un échantillon de tungstène polycristallin et pour un échantillon (100) ayant subi une attaque électrolytique dans une solution de soude à 10 g/l sous une tension de 2 V.

Les valeurs du travail de sortie en présence d'une couche monoatomique adsorbée, sont :

polycristal	$\phi = 5,18$ eV
face (100) attaquée	$\phi = 5,10$ eV

Pour calculer le taux de recouvrement Θ , on a utilisé les valeurs de la probabilité d'adhésion données par GAVRILYUK⁽¹⁴⁾.

La figure 10 reproduit également les résultats de GAVRILYUK pour la face (113).

Dans tous les cas on observe une saturation du travail de sortie en présence d'un recouvrement de l'ordre de $\Theta = 0,9$.

IV - CONCLUSION -

En ce qui concerne l'oxygène, la comparaison entre les résultats des deux méthodes utilisées est difficile car elles n'opèrent pas dans le même domaine de température. Au dessus de 1900°K et dans le domaine des pressions explorées, le recouvrement est toujours nettement inférieur à 1, comme on peut s'en convaincre en comparant les travaux de sortie atteints par chacune des deux méthodes. Dans ces conditions, on mesure le travail de sortie lorsque l'oxygène gazeux est en équilibre avec l'oxygène adsorbé.

Au contraire, à température ambiante, le recouvrement est pratiquement total à l'équilibre et on étudie la phase transitoire qui précède l'établissement de cet équilibre.

En outre l'arrangement des atomes d'oxygène sur le tungstène n'est vraisemblablement pas le même dans les deux cas.

L'intérêt de cette étude est de permettre la connaissance des paramètres indispensables à la prédétermination de convertisseurs fonctionnant avec une pression partielle d'oxygène, pour obtenir d'une part des émetteurs à travail de sortie élevé, et d'autre part des collecteurs à bas travail de sortie (par formation de W-O-Cs par exemple)

REFERENCES -

- 1 F. RUFEB, D. LIEB et F. FRAIM, Thermionic Conversion Specialist Conference, Palo Alto (1967), 25.
- 2 D. LIEB, S. S. KITRILAKIS, Thermionic Conversion Specialist Conference, Houston (1966) 348
- 3 B. DEVIN, N. X. PHUC, Rapport C. E. A. R 2519 (1964) 28.
- 4 Ya. P. ZINGERMAN, V. A. ISHCHUK, T. A. KRUTILINA, Soviet Physics Solid State 7 (1966) 2078.
Ya. P. ZINGERMAN, V. A. ISHCHUK, Soviet Physics Solid State 8 (1967) 2394 et 9 (1967) 623.
- 5 P. J. ESTRUP, J. ANDERSON, 27^{ème} Conférence d'Electronique Physique MIT (1967) 47.
- 6 M. A. H. LANYON, B. M. W. TRAPNELL, Proc. Roy. Soc. (London) A 227 (1955) 387.
- 7 D. THIVELLIER, 2^o Conf. Intern. sur la Conversion Thermoionique, Stresa (1968)
- 8 J. BENARD éd., "l'Oxydation des Métaux" tome I, Gauthier-Villars, Paris
- 9 W. ENGELMAIER, R. E. STICKNEY, 26^o Conf. d'Electronique Physique, MIT (1966) 260.
- 10 J. H. SINGLETON, Westinghouse Research Laboratories, WERL 2823, 23 (1966)
- 11 B. J. HOPKINS, K. R. PENDER, Surface Science 5 (1966) 155.
- 12 D. STEINER, E. P. GYFTOPOULOS, Thermionic Conversion Specialist Conf. Palo Alto (1967)
- 13 Yu. G. PTUSHINSKII, CHUIKOV, Surface Science 6 (1967) 42.
- 14 V. M. GAVRILYUK, V. K. MEDVEDEV, Soviet Physics Solid State 4 (1963) 1737.
- 15 L. H. GERMER, J. W. MAY, Surface Science 4 (1966) 452-470.

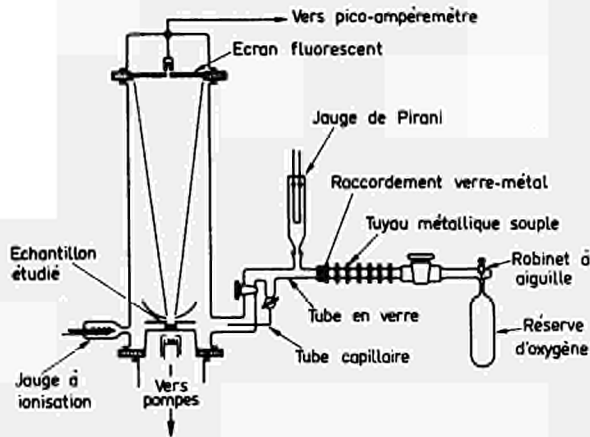


Fig.1-Schéma du microscope à émission



Fig.3- Effet de "nuage" avec minimum

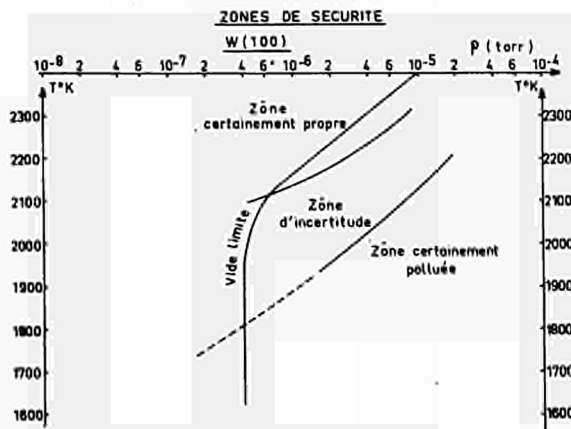


Fig.2 - Zones de sécurité

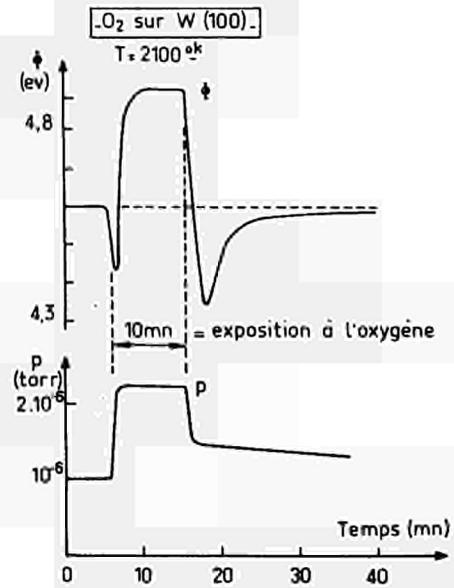


Fig.4- Variations du travail de sortie en présence d'oxygène, avec "nuage"

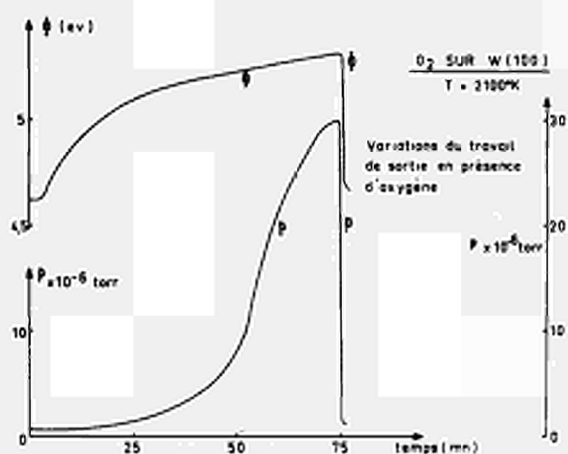


Fig. 5-Variations du travail de sortie en présence d'oxygène, sans nuage

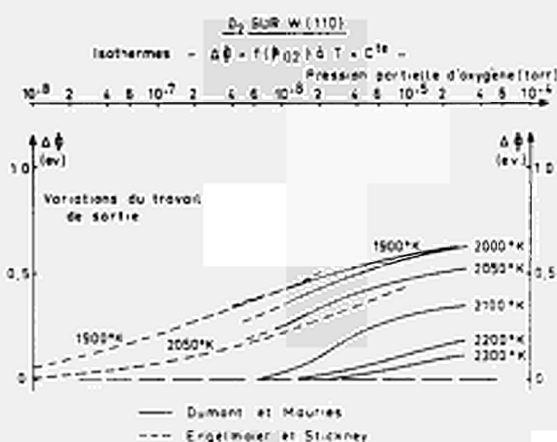


Fig. 6- Isothermes d'adsorption sur (110)

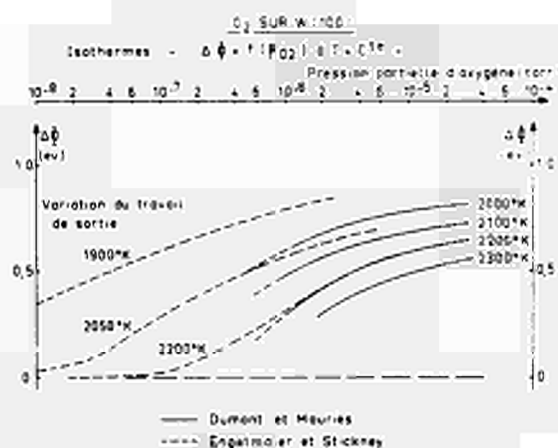


Fig. 7-Isothermes d'adsorption sur (100)

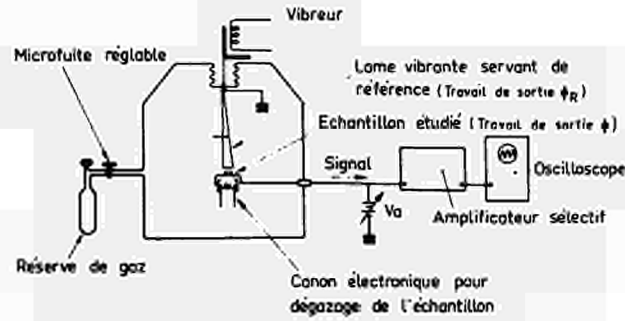


Fig.8- Schéma de l'appareillage
Méthode de Kelvin

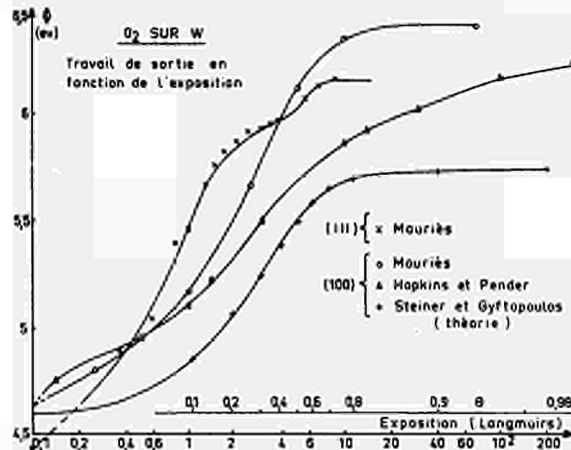


Fig.9- Variations du travail de sortie
en fonction de l'exposition à l'oxygène

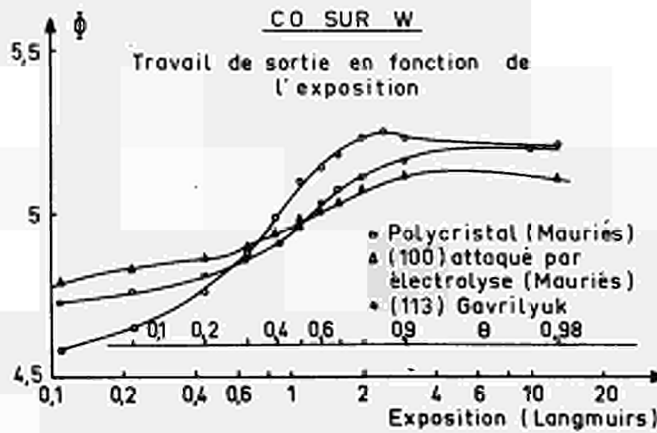


Fig.10-Variations du travail de sortie
en fonction de l'exposition à l'oxyde de
carbone

THE INFLUENCE OF OXYGEN ON THE WORK FUNCTION
OF TUNGSTEN*

P. Batzies

Brown, Boveri & Cie, Mannheim, Deutschland
Zentrales Forschungslabor

Summary

The work function increase of tungsten caused by oxygen is measured in a planar diode with screened emitter and ring shaped collector, using thermionic emission. Tungsten single crystals of {111}, {100} and {110} orientation, polycrystalline material and vapor deposited layers are investigated.

The background pressure with the diode in operation is in the 10^{-9} torr range. The oxygen is introduced by means of a bakable gas inlet valve. The gas composition is controlled by a mass filter. Work function measurements were taken with oxygen pressures from $2 \cdot 10^{-8}$ to $2 \cdot 10^{-5}$ torr and emitter temperatures T_E from 1800 °K to 2400 °K.

From the oxygen pressure a fictitious oxygen reservoir temperature T_R is calculated. It is found that the work function increase is only dependent on the ratio T_E/T_R . This makes it possible to estimate the oxygen pressure necessary to obtain a given work function as function of emitter temperature.

Introduction

Besides other ways one possibility to increase the efficiency of a thermionic converter is to choose high emitter bare work functions [1,2,3]. Since there are often difficulties in doing so it has been tried to achieve the same result by using electronegative additives [4], as for example oxygen [5] in the form of cesium-oxide. Although the application in the

* This work was partially supported by the German "Bundesministerium für wissenschaftliche Forschung"

thermionic converter necessarily includes the presence of cesium, it is reasonable to study the system emitter-oxygen without cesium in advance. But it is to be kept in mind that for example the Rasor-Warner theory [1] cannot be used in this case to predict the behavior in the presence of cesium. In order to get as close as possible to circumstances in a thermionic converter thermionic emission is used for studying the influence of oxygen on the work function of different oriented tungsten samples.

Experimental Apparatus

The apparatus used is same as already described in [6]. It consists of a planar diode which is operated in an ultrahigh vacuum system, to which a gas inlet valve and a mass-filter are attached. The work function is calculated from emitter temperature and saturation current, using the Richardson equation. The emitter has an effective surface of $0,16 \text{ cm}^2$ and is heated by electron bombardment. The emitter temperature is measured pyrometrically in a black body hole on the back side of the emitter. To allow an undisturbed interaction of the oxygen with the surface the collector is a ring with a central opening of emitter diameter. The all-metal vacuum system is bakable, ion getter and sorption pumps are used. The ultimate pressure is below $1 \cdot 10^{-9}$ torr. With the diode in operation the background pressure is in the 10^{-9} torr range. The oxygen is of ultrapure quality introduced by a bakable gas inlet valve. The oxygen pressure is measured by the ion getter pump and a Bayard-Alpert-ionisation gauge. Both gave compatible pressure readings. The mass-filter was used to make sure that the gas introduced did not contain any impurities in detectible quantities.

The saturation current is measured by means of a microammeter, a galvanometer or an electrometer amplifier.

Emitter Preparation and Measuring Performance

The tungsten emitters used are zone refined single crystals, polycrystalline material of ultra purity and vapor-deposited layers, produced by thermal decomposition of WF_6 on molybdenum.

The emitters are mechanically ground, heat-treated, electro-polished and then outgassed in the ultrahigh vacuum system up to 2500 °K. Simultaneously the collector is outgassed by electron bombardment. The work function in vacuum is measured, when the pressure has fallen to $5 \cdot 10^{-9}$ torr with the diode running. The temperature range is 1800 °K to 2400 °K.

Afterwards the oxygen is introduced. Since it is continually pumped by the getter ion pump a dynamic equilibrium is obtained. The emitter temperature is then varied at different constant oxygen pressures in the range from $2 \cdot 10^{-8}$ to $2 \cdot 10^{-5}$ torr and the work function measured.

Results

The bare work functions (without influence of oxygen) which were calculated from the measurements are given in table I.

	W-{100}	W-{111}	W-{110}	W-Vap.	W-Poly
φ_E [eV]	4,48	4,45	4,92	4,50	4,55

They are compatible with the values known from the literature [7], although the work function of the {110}-single crystal seems to be somewhat low. This may be due to some gross imperfections visible on the surface of the otherwise well prepared and oriented sample.

Since the measurements with oxygen admitted were performed at constant pressure by varying the emitter temperature the results are given in the same way.

Fig. 1 shows as an example the influence of oxygen on the work function of a tungsten- $\{100\}$ -single crystal. As one can see easily the emitter work function φ_E is increasing with decreasing emitter temperature T_E at constant oxygen pressure p_{O_2} and increasing with increasing oxygen pressure at fixed emitter temperature. It is also remarkable to note that even without oxygen admitted (p_{back}) an increase in work function is found at temperatures below 2000 °K.

Similar families of curves were obtained for tungsten $\{111\}$ -, $\{110\}$ -single crystals, a polycrystalline sample and a vapor deposited tungsten $\{100\}$ -layer. They are not given here explicitly, but can be recomputed from the following figure 3. For adsorption of electropositive atoms on a metal as cesium on tungsten it is known [1] that the change in work function in this case is only dependent on the ratio of T_E/T_R , T_R being the cesium reservoir temperature, but not on the absolute values of T_E and T_R .

The same principle has now been tried with oxygen on tungsten. The admitted oxygen pressure p_{O_2} was converted into a fictitious liquid-oxygen reservoir temperature T_R by means of the vapor pressure curve [8,9]. The result is shown in fig. 2. It reveals a good agreement between points measured at different pressures. All points, obtained in the range of four orders of magnitude in pressure, lie on one curve. As was pointed out to me by Dr. Rasor, a similar result had already been obtained by Engelmaier and Stickney [10]. Additional values were obtained by using the oxygen partial pressure of the background pressure (without any oxygen admitted) as indicated by the mass-filter measurements.

Fig. 3 displays the dependence of work function on T_E/T_R for

all samples measured. The polycrystalline curve is dotted because some irregularities as a small influence of the absolute values of temperature and pressure seemed to have occurred. The tungsten-{110}-curve could only be measured down to a T_E/T_R -ratio of 68 because a failure of the bombardment gun took place.

Discussion

From fig. 3 some general conclusions can be drawn. The first one is that all curves nearly start rising at the same T_E/T_R -value of 75. The same result had been qualitatively and quantitatively found by Engelmaier and Stickney [10]. From this ratio one can calculate the oxygen pressure p_{O_2} as a function of emitter temperature T_E , which must not be exceeded in bare work function measurements. The resulting curve (a) is shown in fig. 4. It shows that very low oxygen (or background) pressures must be obtained to get reliable work function values below 2000 °K. Thus all results of vacuum emission measurements published in the literature can be checked regarding this point and possibly corrected.

Another point is that no systematic connection can already be detected between the course of the different curves and their work functions. This could be cleared by more complete measurements with different oriented single crystals.

Furthermore, no saturation could be found in the range which was covered by these measurements. Therefore measurements below a T_E/T_R -ratio of 55 would be desirable. But further expansion in this direction will not be easy, because this would include high oxygen-pressures ($>10^{-5}$ torr), low temperatures (<1700 °K) and high work functions ($>5,5$ eV), the latter two resulting in very low current densities ($<10^{-9}$ A/cm²).

Since the aim of the application of oxygen in a thermionic converter is the increase of the emitter "bare" work function, one can ask for the oxygen pressures, which are necessary to obtain a certain work function, for example 5,0 eV.

These were calculated from fig. 3 for all samples as a function of emitter temperature and are also shown in fig. 4. Tungsten {111}, {100} and the polycrystalline material are summed up into one curve (b2). The two others are for the vapor-deposited tungsten {100}-sample (b1) and the {110}-single crystals (b3). Surprisingly very low oxygen pressures are needed at an emitter temperature of 1800 °K to obtain a work function value of 5,0 eV. Table II gives the oxygen pressures and the gain in work function under these conditions.

	p_{O_2} torr	gain eV
W-{111}	$4,8 \cdot 10^{-9}$	0,55
W-{100}	$4,8 \cdot 10^{-9}$	0,52
W-Poly	$4,8 \cdot 10^{-9}$	0,45
W-Vap.	$6,4 \cdot 10^{-8}$	0,50
W-{110}	$6,0 \cdot 10^{-10}$	0,08

Table II

Oxygen pressures and work function gain for different oriented tungsten samples at 1800 °K and 5,0 eV.

Conclusions

It has been shown and confirmed that the influence of oxygen on the work function of different oriented tungsten samples is only dependent on the ratio T_E/T_R . Surprisingly very low oxygen pressures are sufficient for work function increases of about 0,5 eV.

As a consequence, this point must be taken care of, if one is measuring thermionic emission constants in vacuum with an oxygen partial pressure.

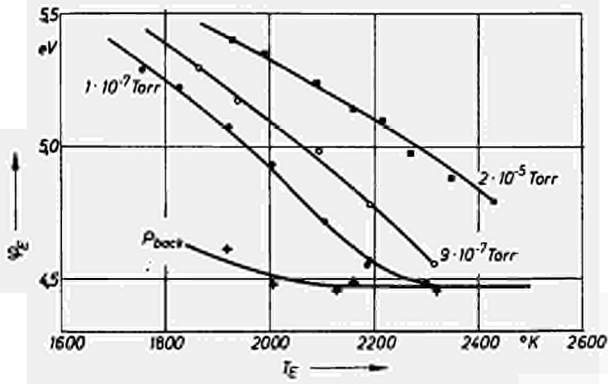


Fig. 1
Work function of a {100}-tungsten single crystal at various oxygen pressures as function of crystal temperature

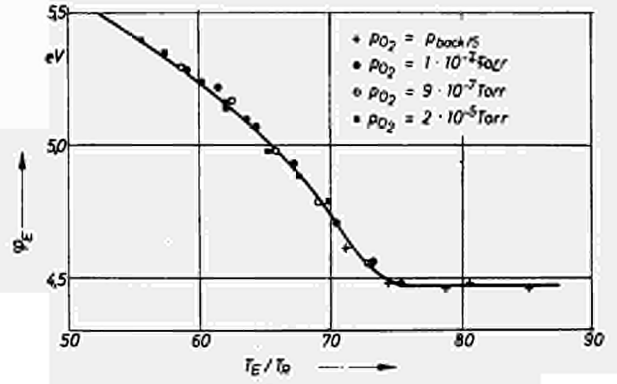


Fig. 2
Work function of a {100}-tungsten single crystal as function of T_E/T_R (T_R : oxygen reservoir temperature)

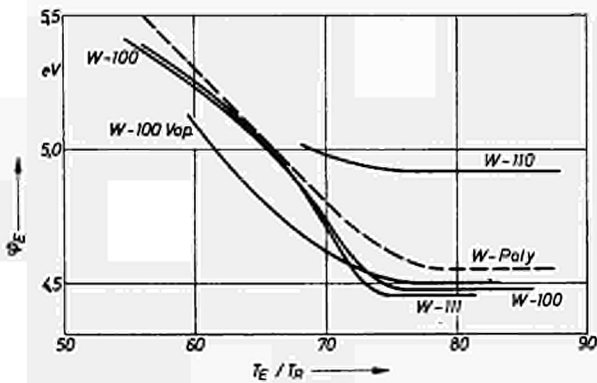


Fig. 3
Work function of tungsten {100}-, {111}-, {110}-single crystals, tungsten polycrystal and tungsten vapor deposited layer as function of T_E/T_R (T_R : oxygen reservoir temperature)

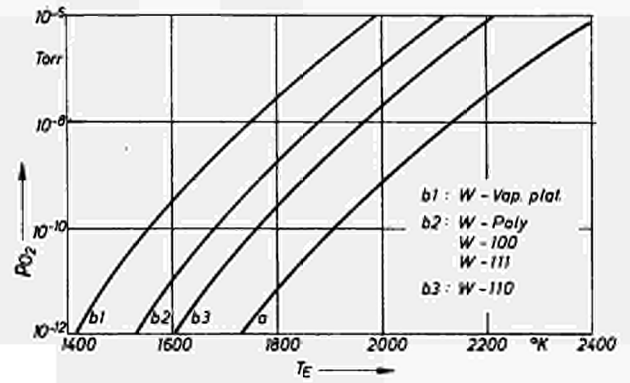


Fig. 4
Oxygen pressure as function of emitter temperature.
a) no oxygen adsorbed
b) work function increased to 5,0 eV

Literature

- [1] RASOR, N.S.; WARNER, C., "Correlation of emission processes for adsorbed alkali films on metal surfaces", J. Appl. Phys. 35 (1964) 1564-1600
- [2] BATZIES, P., "Die Grundaustrittsarbeit der Emitteroberfläche und ihr Einfluß auf Wirkungsgrad und optimalen Elektrodenabstand der Cäsium-Diode", BBC-Nachrichten 49 (1967), 10, 16-23
- [3] BATZIES, P.; DEMNY, J.; SCHMID, H.-E.; ZÖLLER, R., "Entwicklung von Emittern für thermionische Reaktor-brennstoffelemente", Forschungsbericht des Bundesministerium für wissenschaftliche Forschung, Förderungsvorhaben St.N. 423-67, Jan. 1968
- [4] LANGPAPE, R.; MINOR, A., "Influence of Cs and Cs + CsF on the work function of refractory metals", Thermionic Specialist Conference, Cleveland, Ohio (1964) 87-92
- [5] LANGPAPE, R.; MINOR, A., "Work function of polycrystalline W and Re in an atmosphere of cesium and oxygen", Second Internat. Conference on Electrical Power Generation, Stresa, May 1968
- [6] BATZIES, P.; DEMNY, J.; SCHMID, H.-E., "Preparation and investigation of tungsten surfaces with preferred orientations", Second International Conference on Electrical Power Generation, Stresa, May 1968
- [7] FOMENKO, F.S., Handbook of thermionic properties, Plenum Press Data Division, New York, 1966
- [8] D'ANS-LAX, Taschenbuch für Chemiker und Physiker, Springer-Verlag Berlin-Heidelberg-New York
- [9] HONIG, R.E.; HOOK, H.O., R.C.A. Review 21 (1960) 360
- [10] ENGELMAIER, W.; STICKNEY, R.E., "Thermionic and adsorption characteristic of a single crystal tungst.filam. exposed to oxygen", 26th Annual Conference Physical Electronics (1966), 260-277

DISCUSSION

Speaker of paper K-11: P. BATZIES.

BOHDANSKY (Euratom): Did you find a saturation effect, that is a constant work function above a certain oxygen pressure?

BATZIES (Germany): No, we didn't. This is only the beginning of our measurements and we had some difficulties, as I explained in the paper. We will go on to lower T_E/T_R -values and we do hope to find it there. But the difficulty is that the work function is increasing and the temperature decreasing. This gives a very low current. Moreover you need very high oxygen pressures and that is a difficulty in a vacuum system.

GYFTOPOULOS (USA): Did you observe any time requirement for the system to reach its thermodynamic equilibrium?

BATZIES: There was some time required to reach equilibrium but this time was very short. In the order of magnitude of seconds.

STRECKER (Germany): Can you give some remarks about the increase of work function even without oxygen admission (Fig. 1)?

BATZIES: We had a mass filter attached to our vacuum system to examine the residual gas. We found that we had about 20 or 25% oxygen. In the second slide if you look at the crosses, we found that the points measured at the background pressure fit very well into the curve obtained by pure oxygen and that means that it is the background oxygen that influences the increase of the work function.

STRECKER: You had in the first slide curves at different pressures of oxygen and here in the second slide you have the same differences in the pressure of oxygen but you received only one curve. How is this to be understood?

BATZIES: Only the ratio of T_E/T_R is important. You see if we had only a very low residual gas pressure, which contains about 20% oxygen you have in a sense a very low oxygen pressure. Here you can go towards lower temperatures before you get an influence of the oxygen, as shown in slide 4.

WORK FUNCTIONS OF POLYCRYSTALLINE W AND RE IN
AN ATMOSPHERE OF CESIUM AND OXYGEN *

R. Langpape and A. Minor

Brown, Boveri & Cie, Heidelberg, Germany

Summary

By means of the plasma anode technique the work functions of polycrystalline tungsten and rhenium wires were measured in cesium vapor and with cesium oxide as additive. Most of the measurements were performed at a cesium reservoir temperature of 120 °C and cesium oxide temperatures between 200 °C and 400 °C. The probe temperatures varied between 1150 °K and 2250 °K. The results are described in Rasor-Warner diagrams ϕ versus T_p/T_{Cs} .

In the region of high cesium coverage, which is of interest for emitters of thermionic converters the work function at a certain T_p/T_{Cs} decreases monotonically with increasing $T_{Cs-oxide}$ and reaches a saturation value, which depends on T_p/T_{Cs} . At low cesium coverage the work function decreases first with increasing $T_{Cs-oxide}$, takes a minimum value lower than the saturation work function, and increases then with further increasing $T_{Cs-oxide}$ until reaching the saturation value. The saturation values for different T_p/T_{Cs} form a Rasor curve corresponding to a "bare" work function which is about 0.5 eV higher than the clean surface work function.

Introduction

Several experiments performed during the last years have shown that the performance of cesium diodes can be considerably enhanced by the addition of electronegative gases. These gases

*This work was partially supported by the German Bundesministerium für wissenschaftliche Forschung

reduce the cesium pressure which is required for adjusting the emitter work function and so reduce the plasma losses. At first fluorine had been used as additive [1 - 3], but later investigations showed that the beneficial effect found with fluorine was most probably caused by oxygen impurities [4]. The influence of a controlled oxygen additive on both the work function of refractory metals and the performance of cesium diodes has also been investigated by several authors [5 - 7].

In this paper work function measurements on polycrystalline tungsten and rhenium wires in an atmosphere of cesium and oxygen are described. The oxygen was generated by thermal dissociation of cesium oxide. The measurements were performed at low pressures of cesium and oxygen, but comparison with measurements of other authors suggest that the results of our measurements should be transferable to the normal working conditions of emitters in thermionic converters.

Experimental Apparatus

The work functions were measured by the plasma anode technique, developed by Marchuk [8] and improved by Houston [9]. In this technique small loops of wire are immersed in the plasma of a conventional cesium vapor gas discharge tube. The work functions of the wire materials are calculated from the electron current densities emitted by the wire probes. An electron flow from the plasma to the probes is avoided by holding the probes a few volts negative with respect to the plasma. The electron space charge is compensated by cesium ions flowing from the plasma to the probes.

The data reported here were taken with several measuring tubes being different in some details, therefore only the main features which were common for all tubes shall be described. The tubes made of "Jenaer Geräteglas" had a tungsten coil as cathode, a

nickel disc as anode, and probes of 0.1 mm tungsten wire and 0.25 mm rhenium wire respectively (Fig. 1). The distance between cathode and anode was about 300 mm. The base of each probe was equipped with a guard ring in order to minimize leakage currents along the glass wall of the tube (Fig. 2). Cathode, anode, and probes were spot welded to vacon rods molten into the glass tube. With exception of the emitting loops the whole probe wires including the vacon rods were shielded by pure alumina tubes. In order to avoid discharges between guard rings and anode each guard ring was shielded by a glass tube surrounding it (Fig. 2). Between measuring tube and cesium reservoir there was an orifice of about 4 mm diameter in order to minimize oxygen losses.

The tube was outgassed up to 450 °C at about 10^{-7} torr while the cathode and the probes were flashed to at least 2200 °K. During outgassing two glass ampoules containing cesium and cesium oxide respectively were located in side arms of the measuring tube (Fig. 1). The cesium oxide had been prepared by oxidizing cesium in pure oxygen of some hundred torr pressure. In this way one gets a mixture of several cesium-oxygen compounds of different stoichiometric composition. The glass ampoules were crashed later by pieces of steel.

During all the measurements the measuring tube was continuously pumped out through the cesium reservoir by a Vac-ion getter pump. The cesium which diffused into the tube connecting the cesium reservoir with the getter pump condensed at the cold wall of the tube and dropped back into its reservoir. The residual gas pressure at the getter pump was always lower than 10^{-7} torr.

During the measurements the measuring tube was surrounded by an oven, therefore the probe temperatures had been measured before pyrometrically as a function of heating current. The electron emission of the probes was always so low that electron

cooling did not affect the probe temperature.

Experimental Results

At first the work functions were measured in cesium vapor only. The cesium temperature was held constant at 120 °C and 150 °C respectively and the probe temperature varied between 2150 °K and 1150 °K. Before taking a new data point the probe was always flashed to 2200 °K in order to eliminate an influence of the residual gases on the work functions. Such an influence had been found to be noticeable at low probe temperatures. Only measurements are reported here, which were reproducible within about 0.05 eV. The glass wall of the measuring tube was held at 200 °C during these measurements.

Some of the measurements were repeated then at 400 °C wall temperature. Within certain ranges of probe temperatures the electron emission at 400 °C wall temperature was somewhat higher than at 200 °C. This effect is not yet fully understood. It is unlikely that it was caused by impurities, because the residual gas pressure in the tube was not affected by the wall temperature. Possibly the effect was due to an additional electron emission of the alumina tubes shielding the nonemitting parts of the probe wires. These tubes could have been slightly metallized during outgassing and so be able to emit electrons. A rough estimation shows that their electron emission should be negligible at 200 °C wall temperature, but at 400 °C wall temperature and a correspondingly higher temperature of the alumina tubes their electron emission in cesium vapor could be in the order of magnitude to explain that effect. The influence of the wall temperature on the electron emission required small corrections of the work functions measured in cesium and oxygen as will be discussed later.

After finishing the measurements in cesium only the glass ampoule containing cesium oxide was opened, and the work functions were measured over the same ranges of temperatures as before. Again during each series of measurements the temperatures of both cesium and cesium oxide were held constant and only the probe temperature stepwise varied starting at the highest temperature. Because of the low oxygen pressures used it took some minutes after every change of probe temperature to reach the new equilibrium coverage of the probe surface. In order to keep this time small the probe was not flashed to a high temperature until a series of measurements at different probe temperatures was finished. The influence of the residual gases on the probe work functions had been found before to be always small compared with the influence of oxygen.

Figs. 3 and 4 show the work functions of the tungsten and rhenium probe respectively in Rasor-Warner diagrams. All data of Figs. 3 and 4 were taken at a constant $T_{Cs} = 120^{\circ}C$, parameter is the cesium oxide temperature $T_{Cs-oxide}$. For comparison some theoretical Rasor curves are shown, too. The glass wall of the measuring tube was always held at the temperature of the cesium oxide reservoir, therefore the data at higher $T_{Cs-oxide}$ had to be corrected for the additional electron emission at high wall temperatures as mentioned above. But that correction was only small (<0.02 eV) because the probe emission at higher $T_{Cs-oxide}$ was much larger than without cesium oxide so that the additional electron emission was only a small percentage of the probe emission at high cesium oxide temperatures.

Discussion

The work functions without cesium oxide follow quite well Rasor curves corresponding to the bare work functions of the probe materials. This agrees with the results of several other authors showing that there is no systematical error in our measurements.

In order to discuss the influence of oxygen one can roughly distinguish three ranges of T_P/T_{Cs} (note, that a variation of T_P/T_{Cs} means only a variation of T_P here, because T_{Cs} was held constant).

a) $T_P/T_{Cs} > 5.5$:

In this range the probe surfaces are not yet noticeably covered with oxygen and cesium, therefore the work functions are nearly independent of $T_{Cs-oxide}$ and T_P/T_{Cs} .

b) $4.0 < T_P/T_{Cs} < 5.5$:

In this range the probe surfaces are slightly covered with cesium. At a low oxygen coverage the work function at a certain T_P/T_{Cs} decreases with increasing $T_{Cs-oxide}$. That is the expected behaviour. But there is a minimum value, above a certain $T_{Cs-oxide}$ the work function becomes larger again (see Fig. 4, at $T_P/T_{Cs} > 4,5$ the work functions at $T_{Cs-oxide} = 400$ °C are higher than the values at $T_{Cs-oxide} = 300$ °C).

This behaviour can perhaps be explained in the following way: When the probe surface is only slightly covered with oxygen and cesium most of the adsorbed cesium particles are arranged around the oxygen particles. The adsorption energy of these cesium particles is enhanced by the oxygen particles and therefore the work function is the lower, the higher the oxygen coverage is. In this range of low oxygen coverage and low cesium coverage the ϕ versus T_P/T_{Cs} -curves deviate from Rasor curves, because the adsorption energy of the cesium particles is mainly determined by the oxygen particles and not so much by the bare work function of the surface.

When the oxygen coverage becomes too large the work function decrease, caused by the enhancement of the cesium adsorption energy, is overcompensated by the work function increase, caused by the oxygen particles. Therefore above a certain $T_{Cs-oxide}$ depending on T_P/T_{Cs} the work function becomes higher again with increasing $T_{Cs-oxide}$ and reaches at last a saturation value, which is discussed in the following section.

c) $T_p/T_{Cs} < 4.0$:

This is the range of interest for emitters of thermionic converters. The cesium coverage is rather high in this range, so that only some of the adsorbed cesium particles can be located in the neighbourhood of oxygen particles, while the adsorption energy of the remaining cesium particles is not enhanced by the adsorbed oxygen particles. Therefore in this range of high cesium coverage the work function is not so strongly influenced by oxygen as it is at a lower cesium coverage. At a certain T_p/T_{Cs} the work function decreases monotonically with increasing $T_{Cs-oxide}$, there is no minimum value.

The curves of different $T_{Cs-oxide}$ approach with decreasing probe temperature (i.e. increasing oxygen coverage) a common "saturation curve", which is reached probably at a monolayer oxygen coverage. A very interesting fact is that the saturation curve follows again quite well a Rasor curve corresponding to a "bare work function" of about 5 eV for tungsten and about 5.4 to 5.5 eV for rhenium respectively. That means, an emitter surface saturated with oxygen behaves with respect to cesium adsorption like a stable surface with a higher work function. But this new "bare work function" seems to be only a value determining the work function in cesium vapor and probably being different from the real work function of the same surface saturated with oxygen only, which Engelmaier and Stickney have found to be higher than 5.4 eV for several tungsten monocrystals [5].

The measurements reported here are limited to low pressures of cesium and oxygen, and therefore a high oxygen and cesium coverage could be realized only at probe temperatures much lower than the normal emitter temperatures in thermionic converters. There are other measurements, however, suggesting that the work function of a cesiated surface saturated with oxygen depends only on the T_p/T_{Cs} -ratio and not on the

absolute T_p and T_{Cs} . Fig. 5 shows again the work function of the tungsten probe as a function of T_p/T_{Cs} with $T_{Cs-oxide}$ as parameter. The data were taken in the same way as before, the only difference to Fig. 3 is that T_{Cs} was held at 150 °C instead of 120 °C, so that a certain T_p/T_{Cs} corresponds in Fig. 5 to a higher T_p than in Fig. 3. Consequently at a certain T_p/T_{Cs} a higher $T_{Cs-oxide}$ is required to get saturation, but the saturation curve is the same in both figures. Lieb and Kitrilakis [7] determined the work function of a rhenium emitter in cesium and cesium oxide at $T_p = 1650$ °K and $T_{Cs} = 513$ °K ($T_p/T_{Cs} = 3.22$). When $T_{Cs-oxide}$ was raised in steps of 50 °C the work function decreased monotonically but it seems to approach a saturation value. At $T_{Cs-oxide} = 500$ °C, the highest temperature used in that experiment, saturation was not yet reached, but by extrapolating the data to higher oxygen pressures, one can roughly estimate the saturation value to about 2.3 eV, which agrees well with the rhenium data in this paper (Fig. 4). So one can expect the saturation curves of Figs. 3 to 5 to be also valid for the normal T_p and T_{Cs} of emitters in thermionic converters.

Conclusions

From the foregoing discussion one can predict in general the largest possible effect of oxygen additives on the emitter work function in thermionic converters. Oxygen additives can at best (i.e. at a sufficiently high oxygen pressure) shift the ϕ versus T_E/T_{Cs} -curve from the clean surface curve to a new Rasor curve corresponding to a "bare work function" of about 5.0 eV for polycrystalline tungsten and about 5.4 to 5.5 eV for polycrystalline rhenium respectively. A higher oxygen pressure does not further lower the cesium pressure, which is required to reduce the emitter work function to a certain value.

One can expect, however, that high work function emitters as for example W-110 will also get a still higher "bare work function" by oxygen additives. So the lowest possible cesium pressure in a thermionic converter can probably be realized by using high work function emitters and additives.

Acknowledgements

The authors would like to thank Mr. G. Gammel, Dr. M.F. Koskinen, and Dr. N.S. Rasor for many valuable suggestions and discussions.

References

- [1] AAMODT, R.L.; BROWN, R.J.; NICHOLS, B.D., "Thermionic emission from molybdenum in vapors of cesium and cesium fluoride", J. Appl. Phys. 33 (1962) 2080-2085
- [2] LANGPAPE, R.; MINOR, A., "Influence of CsF and Cs + CsF on the work function of refractory metals", Thermionic Conv. Spec. Conf., Cleveland/Ohio (1964) 87-92
- [3] JESTER, A.A., "The influence of a cesium fluoride additive on the power output of cesium diodes with molybdenum and rhenium emitters", Thermionic Conv. Spec. Conf., Cleveland/Ohio (1964) 93-99
- [4] LIEB, D.; KITRILAKIS, S.S., "The influence of CsF on the work function of a tungsten surface", Thermionic Conv. Spec. Conf., Houston/Texas (1966) 340-347
- [5] ENGELMAIER, W.; STICKNEY, R.E., "Thermionic and adsorption characteristics of a single crystal tungsten filament exposed to oxygen", 26th Ann. Conf. Phys. Electronics, Cambridge/Mass. (1966) 260-276
- [6] LEVINE, J.D.; HARBAUGH, W.E.; SHOEMAKER, R.E., "Oxygen as a controllable, reversible, and beneficial additive in the cesium converter", Thermionic Conv. Spec. Conf., San Diego/Calif. (1965) 276-280
- [7] LIEB, D.; KITRILAKIS, S.S., "Oxygen as a steadystate electronegative additive in a cesium thermionic converter", Thermionic Conv. Spec. Conf., Houston/Texas (1966) 348-354
- [8] MARCHUK, P.M., Trudy Inst. Fiz. Ak. Nauk. Ukraine 7 (1956) 17
- [9] HOUSTON, J.M.; DEDERICK, P.K., "Thermionic emission of thermionic converter collector materials in Cs vapor", Air Force Camb. Res. Labs. Rep. AFCRL-64-409 (1964)

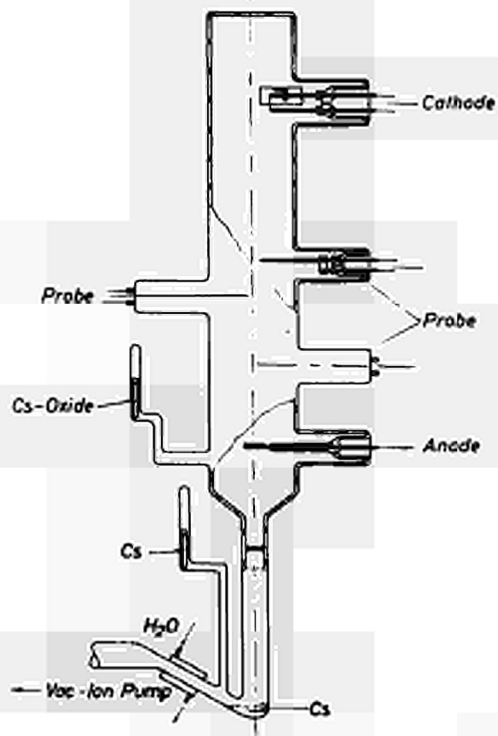


Fig. 1:
Measuring tube

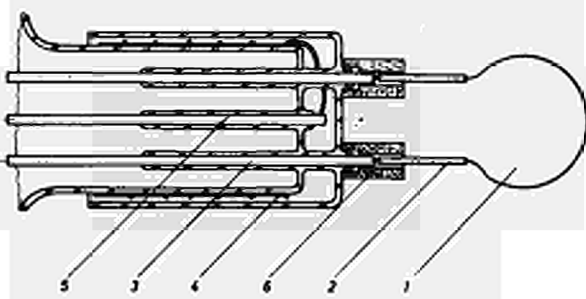


Fig. 2:
1 : Emitting wire loop
2;6 : Alumina tubes
3;5 : Vacon rods
4 : Guard ring

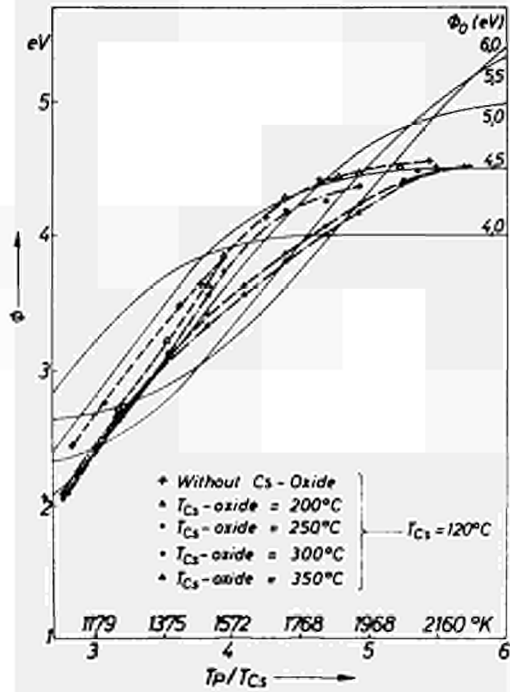


Fig. 3

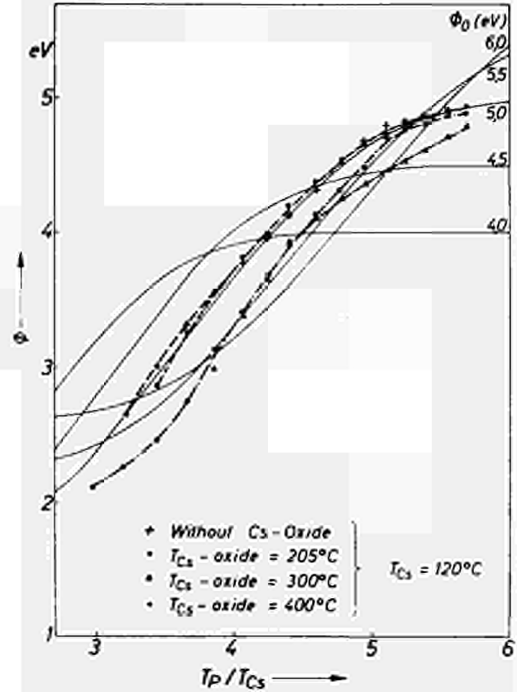


Fig. 4

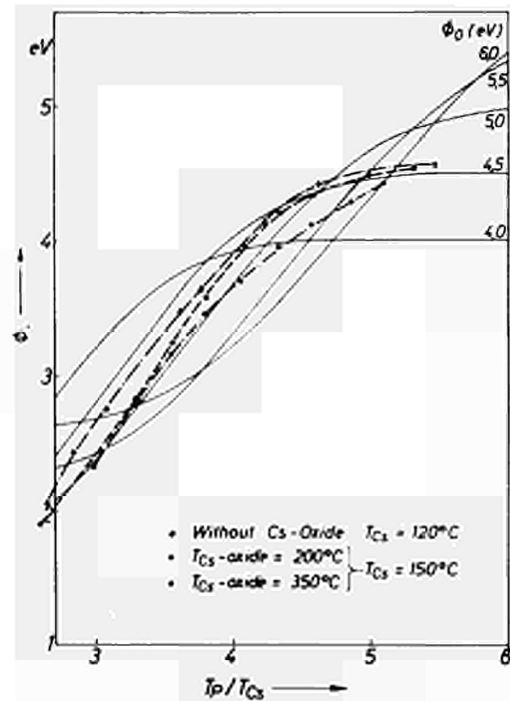


Fig. 5

Fig. 3:
Work function of the tungsten probe versus T_p/T_{Cs} .
 $T_{Cs} = 120^\circ C$;
Parameter: $T_{Cs-oxide}$

Fig. 4:
Work function of the rhenium probe versus T_p/T_{Cs} .
 $T_{Cs} = 120^\circ C$;
Parameter: $T_{Cs-oxide}$

Fig. 5:
Work function of the tungsten probe versus T_p/T_{Cs} .
 $T_{Cs} = 150^\circ C$
Parameter: $T_{Cs-oxide}$

DISCUSSION

Speaker of paper K-12: R. LANGPAPE.

GYFTOPOULOS (USA): There is not necessarily a unique correlation between the oxide temperature and the oxygen pressure, seen by your probe. Is that your explanation?

LANGPAPE (Germany): No, that is not our explanation. We oxidized cesium in a rather high oxygen pressure. In this way one gets several cesium oxide compounds, so we expected to have a mixture of all cesium oxygen compounds. If at higher cesium oxide temperatures some compounds change partly into other ones, only the enrichment of the different compounds changes. So I think in all the measurements we had quantities of each compound present.

GYFTOPOULOS: It is not a matter of changing your compound, but rather changing the relative partial pressure of each one of the specific compounds.

LANGPAPE: Yes, but the partial pressure depends on the compound and on the temperature. Of course, by changing the temperature we change the oxygen pressure but we think we changed it monotonically and there is not a step. The step would only arise if one compound would completely disappear or a new one would be generated.

MUZ (Germany): Did you find decomposition of cesium oxide and could the oxygen have affected your plasma and thus give rise to the limitations you report?

LANGPAPE: We did not investigate this point but we expect that we always had pure oxygen on the surface. That is, the oxygen is provided by decomposition of cesium oxide. But the oxygen pressure was low, below 10^{-8} Torr, therefore we don't think that the oxygen has any influence on the plasma.

RASOR (USA): At the 1966 Thermionic Conversion Specialist Conference, Mr. GAMMEL and I presented an analysis of the effect of electronegative additives on the work function of cesiated surfaces, based essentially on the two-dimensional Saha-equation. The analysis predicted a behavior which is very similar qualitatively to that which your data show. In particular, the departure from the Cs-only behavior at $T/T_R \simeq 3.5$ is consistent with the onset of dissociation of the adsorbed Cs_2O molecule, and the disappearance of this deviation at high oxygen coverage is consistent with

the equilibrium being driven back toward the associated state. Did you apply the results of this analysis to your data?

LANGPAPPE: We realized these facts and our intention was to apply your theory to our measurements. Unfortunately time was too short, these are very recent data, and therefore we could not do it before this conference. But of course we will try to apply this theory to our data.

A CRITICAL EXPERIMENT ON THE NATURE OF AD-
SORBED CESIUM FILMS

E. MUZ

(Institut für Gasentladungstechnik und
Photoelektronik, Universität Stuttgart,
Breitscheidstraße 2 (Germany))

Abstract

Adsorption of alkaline metals on high work function metals involves charge transfer from the adsorbate to the substrate.

In the model proposed by Levine and Gyftopoulos¹⁾ the space average of charge distribution is taken to account for the amount of charge transfer, assuming there is no difference in energy for an electron being inside or outside the surface of the substrate.

In Rasor's²⁾ model the charge distribution is assumed to be determined by a difference in energy for an electron being inside the metal substrate or at the ion core of an adsorbed species.

In order to check these assumptions, the photoelectric emission of polycrystalline Mo was measured as a function of coverage with Cesium.

Two selective photoelectric humps could be detected for $\theta > 0.5$ and were separated from the normal photoemission of the substrate by means of Fowler's theory. The energy of the electron emitting states, as deduced from the spectral distribution, varies as a function of coverage.

Though no precise determination of the energy levels involved is possible, as nothing is known about excitation probabilities, one of the selective humps shows a variation in energy in accord with the theories of Rasor²⁾ and the author.

Introduction

Adsorption of alkaline metals on high work function metals usually involves charge transfer from the adsorbate to the substrate. In order to calculate the work function change caused by adsorption it is necessary to make assumptions about the charge distribution in the surface layer. In the model proposed by Gyftopoulos¹⁾ and Levine the adsorbed particles are assumed to be partly ionized. Thus a space average of charge distribution is deduced from the time average.

In Rasor's²⁾ model the charge distribution is assumed to be governed by the difference in energy for an electron being inside or outside the metal surface. The question arises, whether this energy difference has a sound physical base and can be measured experimentally. It was attempted in this work to solve this problem by photoelectric measurements.

Theory

The relation between the adsorption energy for atoms q_a , for ions q_i , the work function of the substrate $e\phi$ and the ionization potential J_o of the adsorbate was first deduced by Schottky³⁾ and reads:

$$q_a = q_i + e\phi - J_o \quad (1)$$

Applying this equation to adsorption, one assumes, that there is no energy difference for an electron being inside the metal surface or in the potential well of an adsorbed ion. M. von Laue⁴⁾ showed that this is true for condensation of vapor on the bulk material. If there is a difference, the energy to move an electron from the metal to an adsorbed ion has to be added to (1):

$$q_a = q_i + e\phi - J_o - q_R \quad (2)$$

Now the following energy cycle can be considered:

Bring a neutral atom to the surface. The same state can be achieved by ionisation of an atom in the gas phase. Let the ion be adsorbed and let the electron recombine directly with the adsorbed ion core. The energy gained by this recombination process would correspond to the activation energy J_{ph} , necessary to bring an electron from a neutral atom in the adsorbed state into free space. If the energy relation

$$q_a = q_i - J_o + J_{ph} \quad (3)$$

is combined with (2) one yields

$$J_{ph} = e\phi - q_R \quad (4)$$

In the experiments described in the next sections it is tried to measure $e\phi$ and J_{ph} simultaneously and thus determine q_R .

Experimental Tube

In a tube made of pyrex glass a Tungsten wire of 0.2 mm diameter is mounted in the center of two concentric Ta cylinders (Fig. 1). Each of the cylinders has a horizontal slit. In front of the outer slit the target, a very thin rod of polycrystalline Mo is mounted, which is guarded by two concentric electrodes. Through a slit in one of the guard electrodes a well defined area of the target can be covered by Cs by means of a Cs-beam. This area can be viewed through a quartz window. The work function can be evaluated from retarding potential measurements with electrons emitted by the W-wire. The pressure in the tube was below $5 \cdot 10^{-9}$ Torr.

Experimental Procedure

The idea was to measure the spectral distribution of the photoelectric emission and the work function as a function of Cesium coverage. Probably because of surface migration and the influence of residual gases, reproducible results could not be obtained in steady state due to long time changes in work function and photoelectric emission⁵⁾. Therefore, the

Cesium arrival rate to the target was calibrated by surface ionisation and the work function decrease caused by adsorption was measured by a dc electron current of 10^{-10} A. The result is given in Fig. 3. For the measurement of the photoelectric effect, the electron current for a small interval of wavelength (ac-current in the range of 10^{-13} A) was plotted simultaneously together with the course of work function on a two channel plotter. Thus the long time drift of Cesium arrival rate could be eliminated. The photoelectric yield for 360, 370, ..., 800, 850 nm was obtained as a function of coverage.

Experimental Results

From the above described experiment, the spectral photoelectric yield can be computed for any degree of coverage. Applying Fowler's theory of the photoelectric emission from metals, that part of electrons coming from the base metal can be evaluated. Comparing this to the experimental curves, two selective photoelectric humps can be detected. This is shown in Fig. 2. These humps appear at $\theta = 0.4$, where they are very weak. They both are shifted to lower energies for increasing coverage. For $\theta \approx 1$ they start to go towards higher energies. At $\theta > 3$ only one selective hump is left, which corresponds to the well known selective hump for thin alkaline metal films. Although not much can be said about the activation probability for electrons from adsorbed atoms, the energy levels can be estimated. The energetic levels thus computed for the two selective humps (1 and 2) from the experiments are shown in Fig. 4 as a function of coverage. In addition, the work function as evaluated from retarding potential measurements (solid line) and the photoelectric work function (circles) are compared. Clearly the long wavelength peak can be energetically attributed to a process as described by Equation (4).

Summary

Photoelectric measurements have been performed at cesiated Mo. There can be no doubt that additional electron levels at the surface of the base metal are formed by Cs adsorption, which are at least partly filled with electrons for $\theta > 0.4$. No final decision can be deduced, however, as far as the energy difference between an electron inside or outside the substrate surface is concerned. The results seem to compare more favorably with Rasor's theory for $\theta < 0.7$, for $\theta > 0.7$ with the theory of Gyftopoulos. No theoretical model can be given at the time for the second selective emission peak.

References

- (1) GYFTOPOULOS, E. P.; LEVINE, J. D., J. Appl. Phys. 33, 67, (1961).
- (2) RASOR, N.; WARNER, C., J. Appl. Phys. 35, 2589, (1964).
- (3) SCHOTTKY, W., Ann. d. Phys. 62, 142 (1920).
- (4) LAUE, M. v., Sitzber. Preuss. Akad. Wiss. 32, 334, (1923).
- (5) MAYER, H., Ann. Phys. 33, 419, (1938).

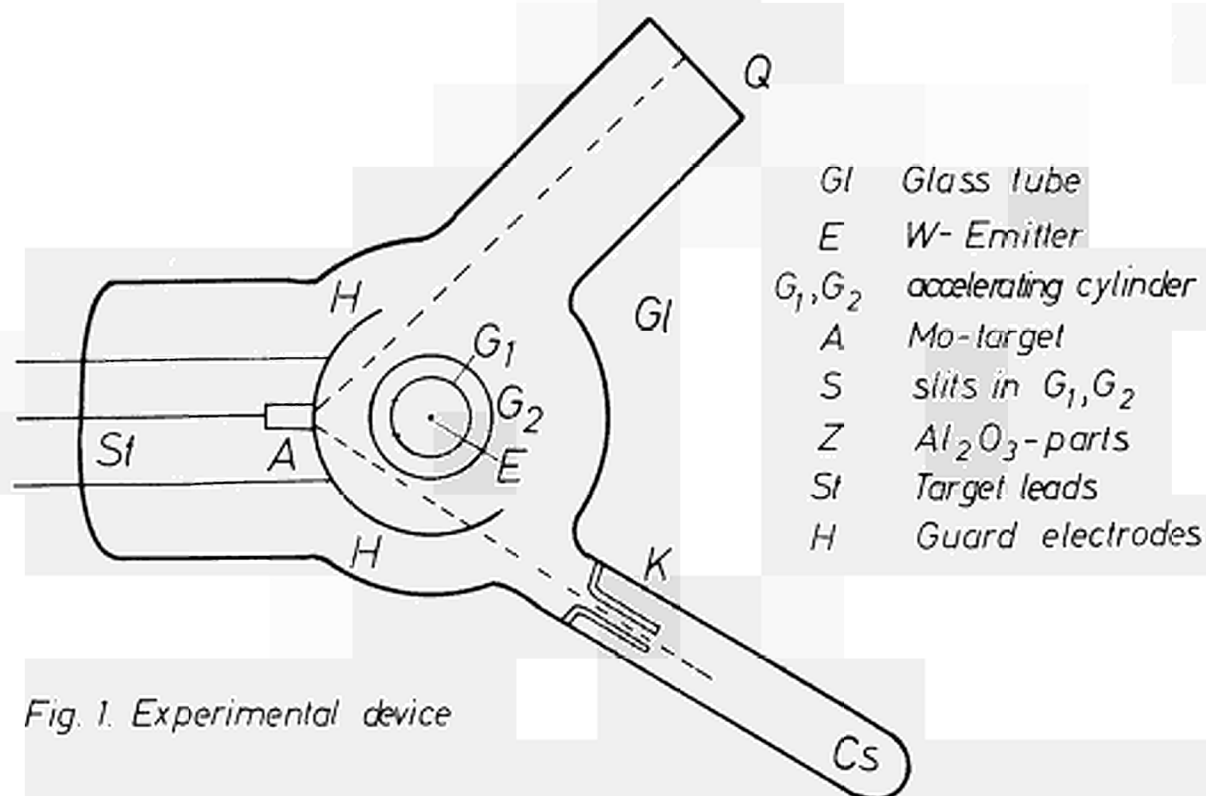


Fig. 1. Experimental device

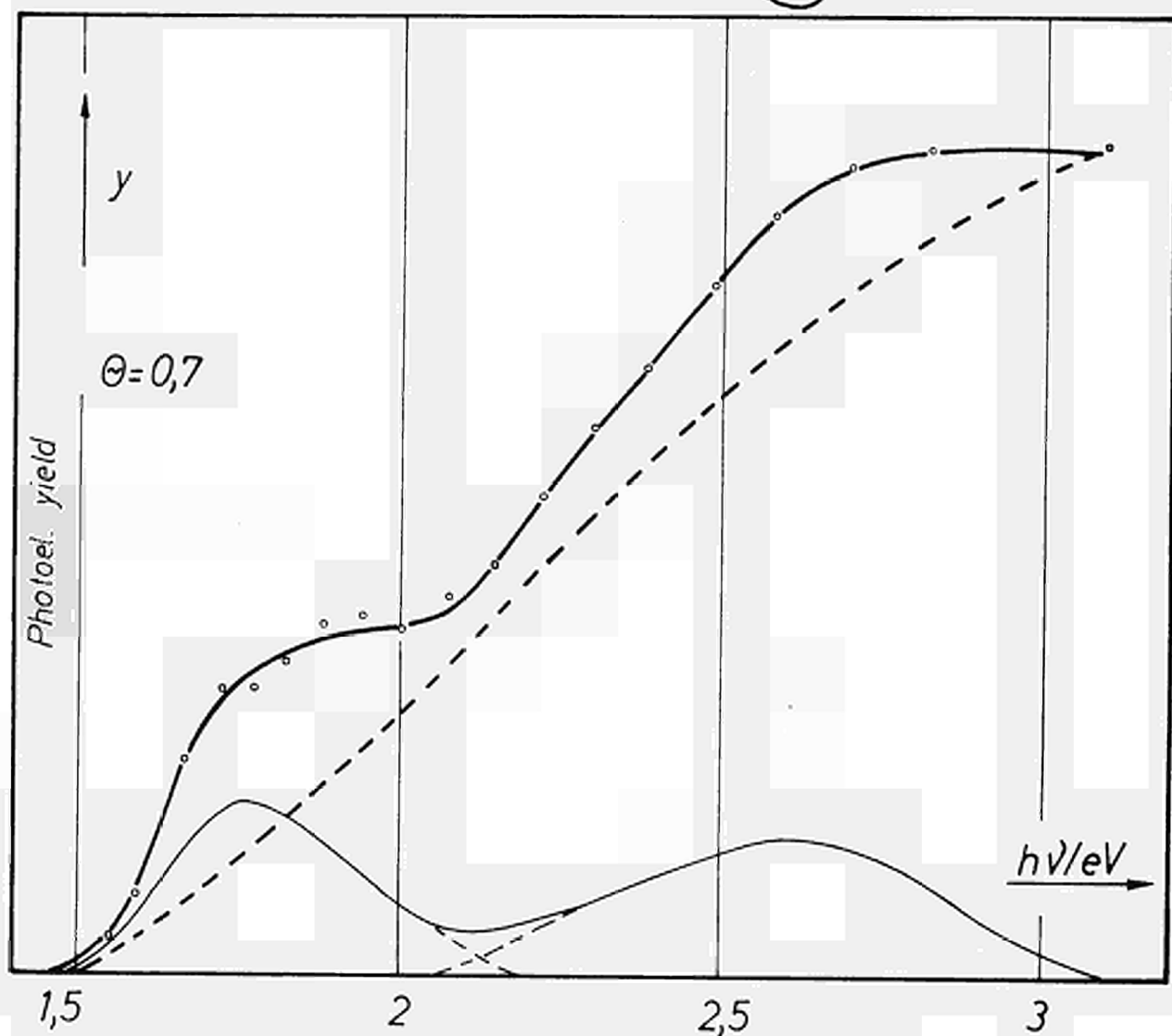


Fig. 2. Photoel. Yield from Cs covered Mo ($\theta = 0,7$)

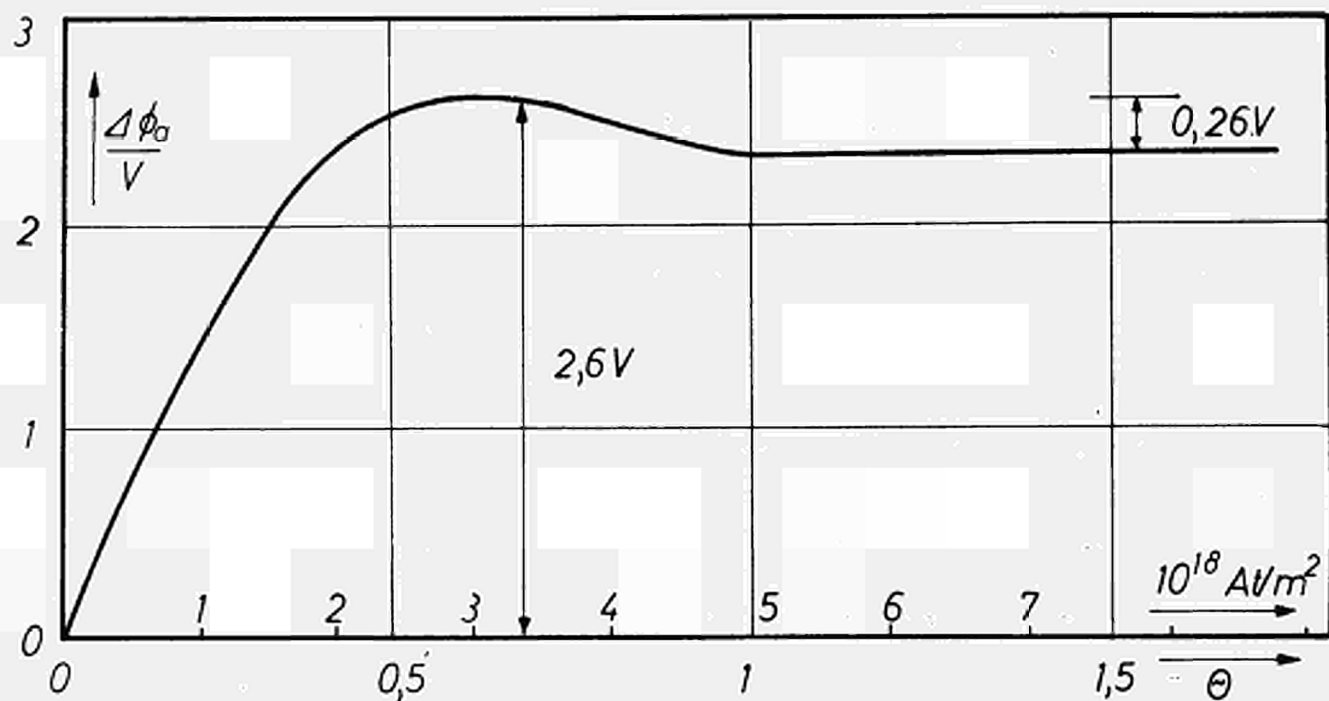


Fig. 3 Work function decrease of Mo covered by Cs

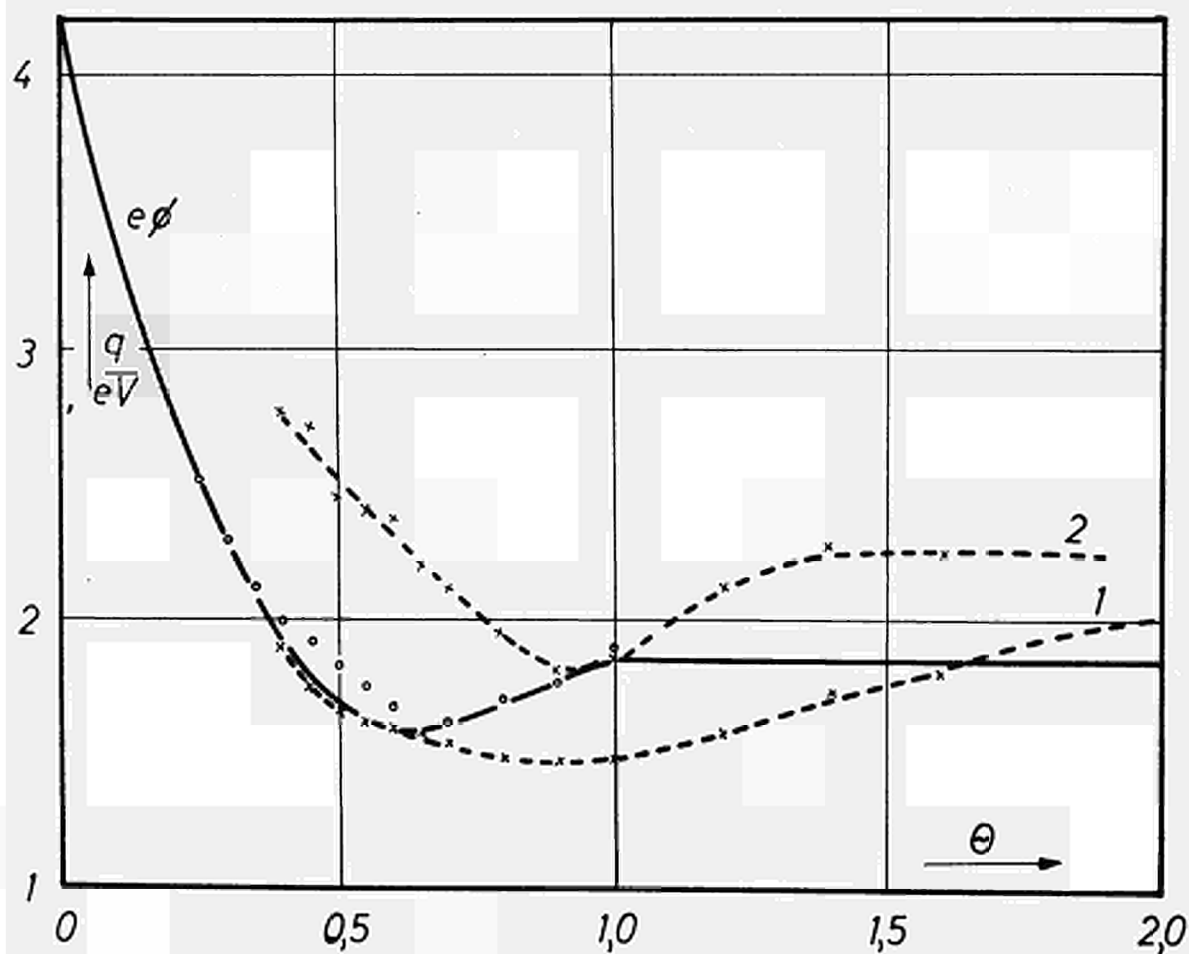


Fig. 4 Energetic correlation of work function and relative photoel. peaks

DISCUSSION

Speaker of paper K-13: E. MUZ.

RASOR (USA): This is addressed both to you and Dr. GYFTOPOULOS. This selective photo-electric effect which you observe is what you would expect from a two-state or multiple-state adsorption. Now, the question is, is there anything characteristic of the molecular-type adsorption theory that would give a similar behaviour? This would seem to be a sensitive critical test of the two theories.

MUZ (Germany): The experiments in fact indicate two states of an adsorbed Cs-particle, for $\theta < 0.7$. This can be deduced from the variation of the low energy selective peak, which is in accordance with your theory.

WARNER (USA): How do you measure your coverage?

MUZ: The procedure of measuring the degree of coverage was as follows: The arrival rate of Cs-atoms from a beam was measured by surface ionization. The photo-electric yield for a selected wavelength was plotted together with the course of work function versus increasing coverage.

MASKEVITCH (USSR): How did the polycrystalline character of the tungsten filament influence the results of the measurements?

MUZ: The filament to be measured was made of polycrystalline molybdenum. Before the experiments have been performed, the Mo-rod was thermally etched, so that the surface showed very large grains. A post mortem analysis showed, that probably only one grain was involved in the measurements.

ETUDE AU MICROSCOPE A EMISSION DE SURFACES REFRACTAIRES
EN PRESENCE DE VAPEUR DE CESIUM

J.L. DESPLAT et Ph. DEFRANOULD

Laboratoires de Recherches Générales
Compagnie Française THOMSON HOUSTON - HOTCHKISS BRANDT
92 - BAGNEUX

Résumé -

Pour étudier l'émission électronique ou ionique d'une surface métallique plongée dans une vapeur de césium, nous avons utilisé une optique électrostatique (objectif à immersion). Nous avons fait des mesures de courant électronique sur divers émetteurs (polycristal de molybdène, monocristal de tungstène) en présence ou non de vapeur de césium. En analysant à l'aide d'un photomultiplicateur l'image obtenue sur l'écran, nous avons déterminé le profil du potentiel de sortie présenté par une surface polycristalline.

Lors d'une étude qualitative de l'émission ionique, nous avons pu obtenir une image électronique et une image ionique de la même surface émissive pour des conditions expérimentales identiques.

1 - Optique électrostatique -

L'objectif à immersion est soit du type Septier /1/ à deux électrodes (grandissement fixe pour des distances interélectrodes données), soit du type Johanson à trois électrodes (grandissement variable de 40 à 120).

Pour l'observation des images ioniques, il suffit d'inverser la polarité des tensions appliquées aux électrodes ; toutefois, pour éviter la détérioration de l'écran, nous utilisons un convertisseur d'image : une grille en cuivre, à maille fine (30 μ) émet des électrons secondaires sous l'effet des impacts ioniques /2/.

2 - Injection de la vapeur de césium -

Une réserve de césium liquide est raccordée à une vanne métallique, l'ensemble est placé dans une enceinte thermostatée (stabilisation à ± 1 °C). La vapeur de césium est éjectée sur l'émetteur par un capillaire de diamètre 1 mm percé dans le corps du wehnelt et incliné à 60° par rapport à l'axe optique /3/. Le calcul des conductances (effectué en régime moléculaire) permet de relier le flux d'atomes neutres μ a tombant sur l'émetteur

au flux moyen dans le réservoir de césium, c'est-à-dire finalement à sa température T_R : il est alors possible d'introduire une température équivalente T_{CS} définie comme la température d'un réservoir de césium liquide en équilibre avec sa vapeur où le flux a la valeur μ . Elle s'écrit :

$$T_{CS} = T_R / (1 + 4.10^{-4} \cdot T_R)$$

3 - Mesure de la température d'émetteur T_E -

L'émetteur est chauffé par bombardement électronique. Il est nécessaire de connaître sa température avec une bonne précision pour l'évaluation du potentiel de sortie. Nous employons deux méthodes dont les résultats sont concordants : par un thermocouple platine-platine rhodié logé dans la masse de l'émetteur, par pyrométrie optique dans un trou (température du corps noir).

4 - Mesures d'émission électroniques -

La densité du courant émis J_e est évaluée en mesurant le courant tombant sur l'écran (gamme de mesure 2.10^{-12} A à 10^{-3} A).

Pour faire varier le taux de recouvrement en atomes de césium, nous opérons à température de réservoir de césium fixe et seule la température de l'émetteur est variable.

4.1. Molybdène polycristallin -

La figure 1 rassemble les résultats expérimentaux obtenus sur deux échantillons. La concordance avec les mesures de R.G. WILSON /4/ est bonne. Cependant, il faut remarquer que le potentiel de sortie moyen dans le vide est voisin de 4,55 V, alors que la valeur couramment admise est de 4,40 V : cette différence est sans doute due à une contamination de la surface par des traces d'oxygène (le vide dans l'enceinte est voisin de 5.10^{-7} Torr, mais la température T_E est insuffisante pour empêcher l'adsorption d'oxygène).

Cette contamination par l'oxygène est vraisemblablement responsable également des débordements vers les potentiels de sortie inférieurs à 1,6 V.

D'autre part, l'apparition de décharges dues à la présence de césium limite la densité de courant observable aux environs de 10^{-3} A/cm².

Nous avons évalué indirectement le courant émis par chaque cristal élémentaire en mesurant la luminosité de la portion d'écran correspondante avec un photomultiplicateur. Si on dispose derrière celui-ci un amplificateur logarithmique, on obtient un signal proportionnel au potentiel de

sortie. La correspondance courant-luminosité établie à l'aide d'un monocristal nous a permis de suivre l'évolution du potentiel de sortie de quelques grains en fonction du recouvrement en césium (figure 2).

4.2. Tungstène orienté 1.1.0. -

Nous avons étudié l'émission d'un monocristal 1.1.0. (désorientation inférieure à 4"). Les mesures du potentiel de sortie dans le vide ont fourni la valeur de 5,28 V en excellent accord avec la détermination de WEBSTER /5/.

La courbe de la figure 4 représente la variation du potentiel de sortie en fonction du rapport T_E/T_{CS}

Le minimum se situe à 1,60 V en bon accord avec les résultats de GAVRILYUK V.M. /6/.

5 - Emission ionique -

5.1. Observation d'images ioniques

L'observation d'une image ionique est difficile : le courant maximum admissible dans l'optique sans que le phénomène de charge d'espace ne devienne gênant est 500 fois plus faible avec des ions Cs^+ qu'avec un faisceau d'électrons. Il n'existe pas d'écran fluorescent compatible avec un faisceau électronique ou un faisceau ionique. L'utilisation d'un convertisseur ion-électron permet d'obtenir des images répliques de l'émission ionique, mais empêche toute mesure directe.

La figure 3 montre deux photographies de l'écran qui ont été obtenues en inversant la polarité des tensions : on y remarque une inversion complète du contraste, conformément aux résultats donnés par la loi de SAHA-LANGMUIR.

Les photographies de la figure 5 montrent l'aspect de l'émission ionique à flux de césium constant, quand la température d'émetteur décroît. On peut remarquer les points suivants :

- A température élevée (photo a), l'ionisation est pratiquement complète et indépendante du potentiel de sortie, ce qui rend l'émission uniforme.

- Il existe un domaine de températures extrêmement étroit (5°) où l'émission ionique présente une transition brutale (photo c).

- Le contraste n'apparaît entre les différents grains que lorsque le taux d'ionisation est inférieur à 10^{-2} environ (photos d et e).

5.2. Mesures d'émission ionique

En supprimant le convertisseur ions-électrons, nous pouvons mesurer le courant ionique (sans former d'image visible, l'écran fluorescent étant recouvert d'une couche conductrice opaque aux ions lourds).

Nous replaçant dans les mêmes conditions expérimentales, nous avons pu tracer la courbe de la figure 5 et y situer les différentes images ioniques.

On y remarque la transition correspondant à la photographie c. Son origine est sans doute l'hystérésis d'émission ionique déjà rencontré par différents expérimentateurs /4/, /7/.

6 - Conclusion -

Le microscope à émission nous a permis de faire des mesures d'émission électronique en présence de vapeur de césium et de retrouver des résultats obtenus par d'autres méthodes, tout en fournissant une image de l'émetteur, ce qui est particulièrement utile dans le cas d'un polycristal.

Nous pouvons également faire des mesures d'émission ionique dans les mêmes conditions, ce qui permet de vérifier la relation de SAHA-LANGMUIR.

REFERENCES -

- /1/ SEPTIER A., Thèse (Paris) 1953
- /2/ MARCHANT A.B. ; KUSKEVICS G., A.I.A.A. Electric Propulsion Conf. Colorado Springs (1963)
- /3/ CAHEN O. ; DIEULESAINT E. ; TORGUET R. ; Thermionic Electrical Power Generation, Londres (1965)
- /4/ WILSON R.G. ; J.A.P. 37 4125 (1966)
- /5/ WEBSTER H.F. ; Thermionic Conversion Specialist Conf., Cleveland (1964), p. 31
- /6/ GAVRILYUK V.M. and all. ; Soviet Physics Solid State 9, 4, p. 881 Oct. 1967
- /7/ JAMBA D.M. and O.K. HUSMANN ; J.A.P. 38 2630 (1967)

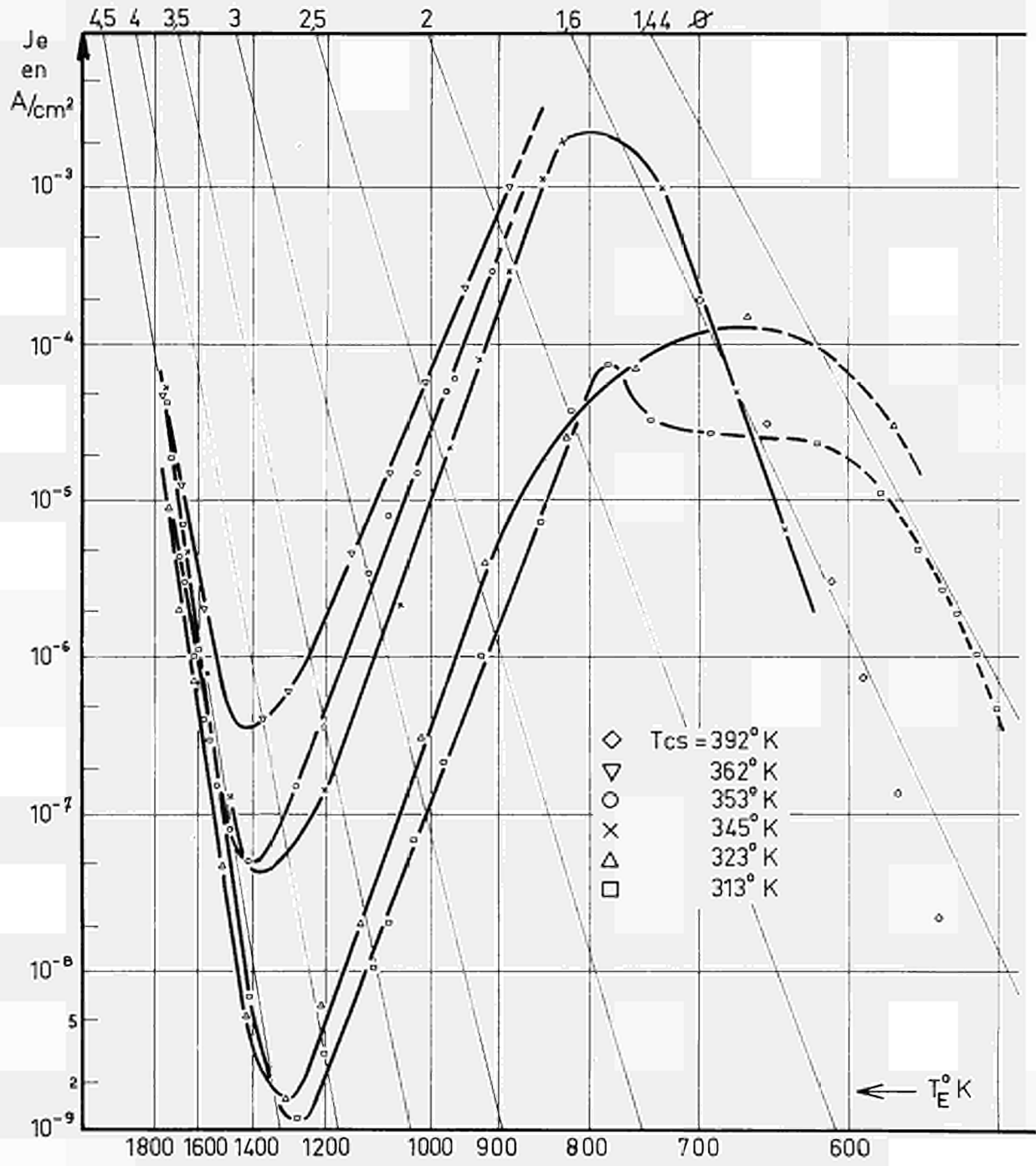


FIG.1 - EMISSION ELECTRONIQUE RELEVÉE AU MICROSCOPE
POUR UN POLYCRISTAL DE MOLYBDENE

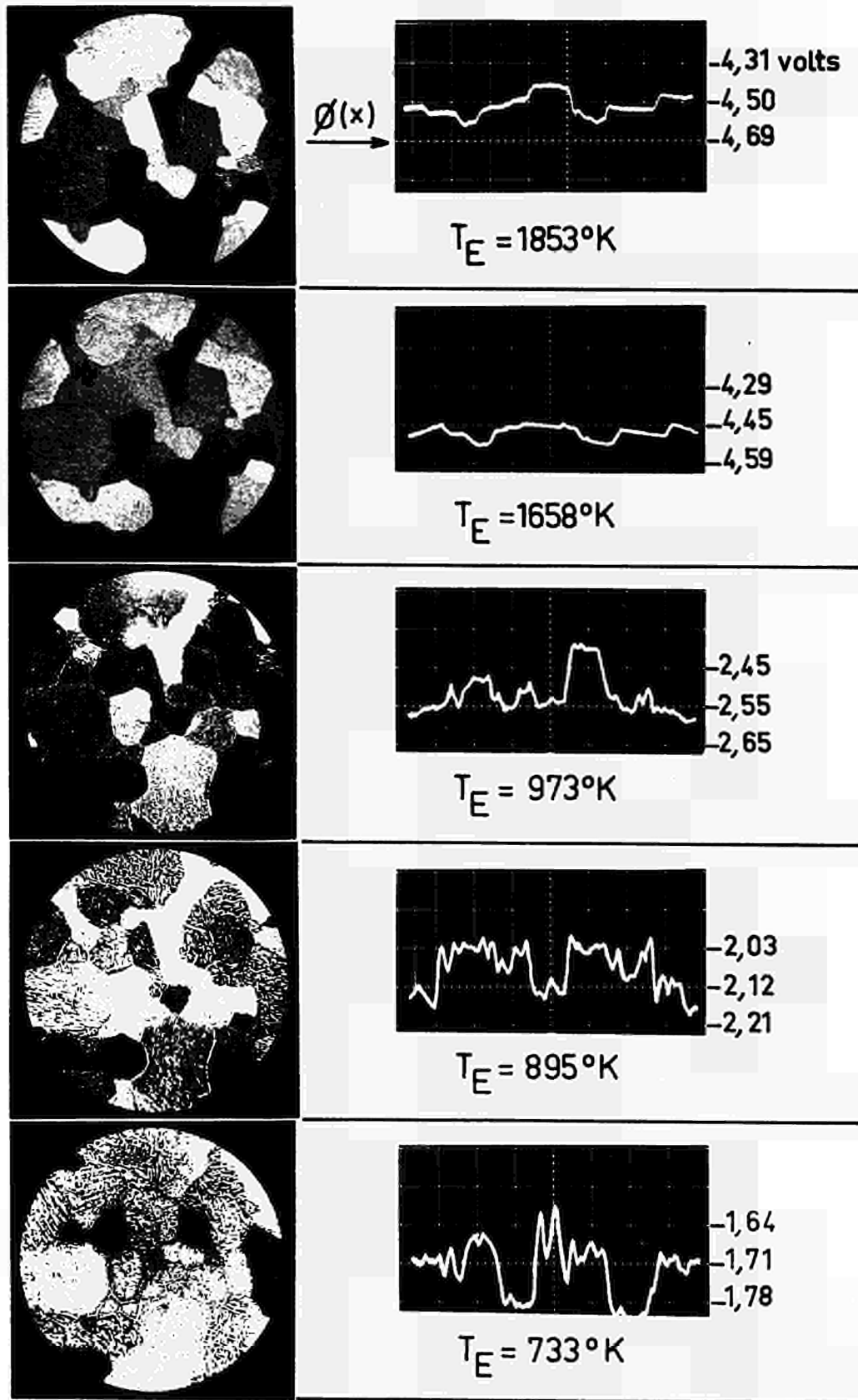


FIG.2 - POTENTIEL DE SORTIE D'UN POLYCRISTAL DE MOLYBDENE EN PRESENCE DE CESIUM ($T_{CS} = 345^{\circ}K$)

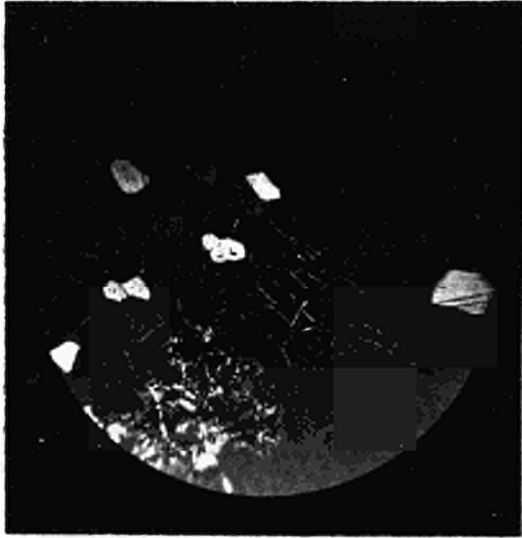


IMAGE ELECTRONIQUE

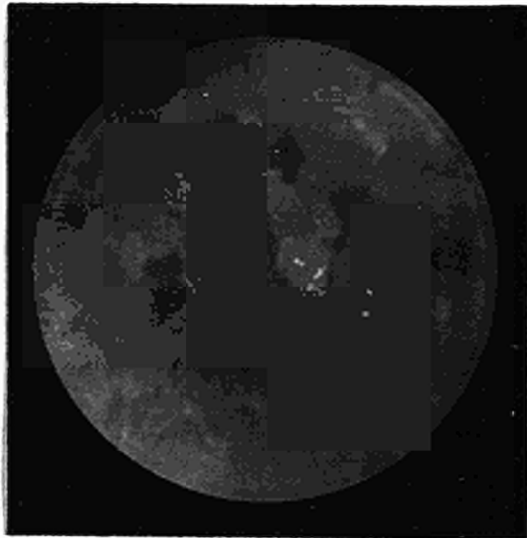


IMAGE IONIQUE

$T_E = 1033^\circ\text{K}$, $T_{CS} = 323^\circ\text{K}$

FIG.3

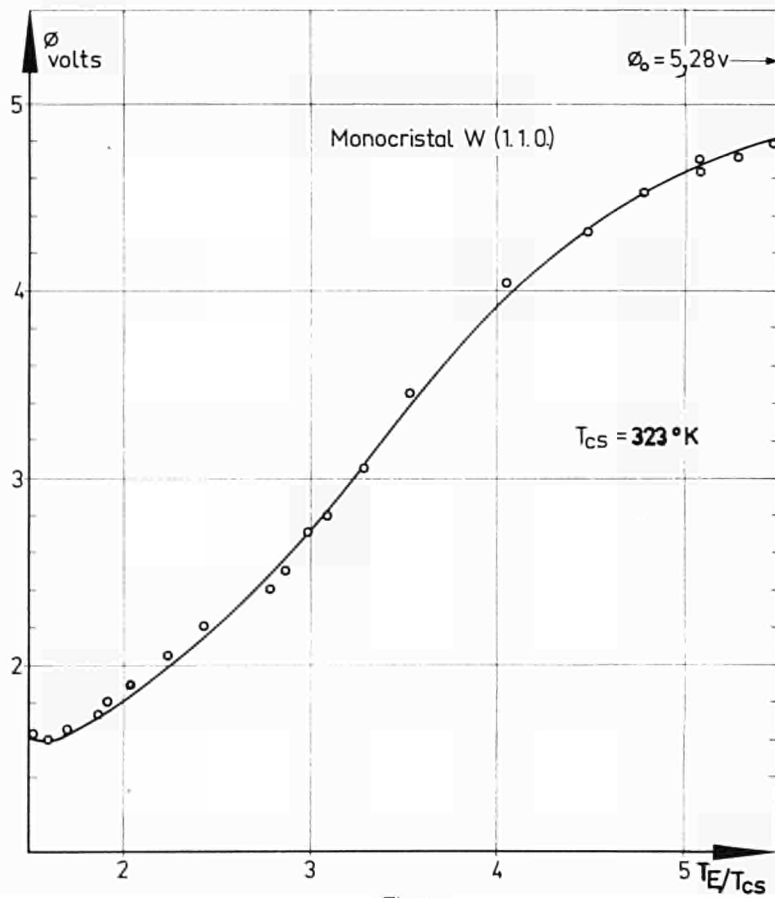


Fig.4

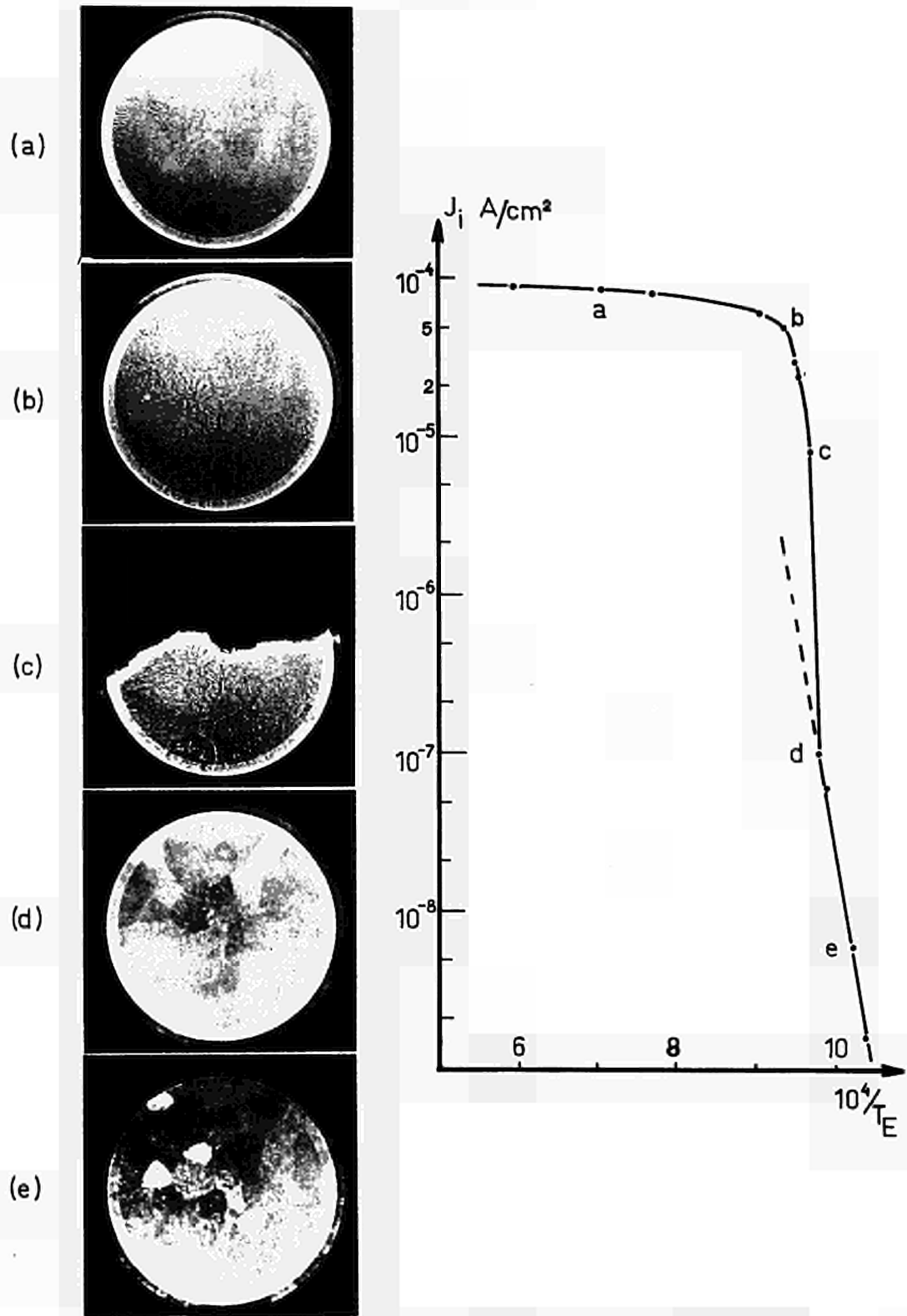


FIG. 5- EMISSION IONIQUE D'UN POLYCRISTAL DE MOLYBDENE EN PRESENCE DE CESIUM ($T_{CS} = 338^{\circ}K$)

SURVEY OF EXPERIMENTAL WORK IN THE USSR

by Yu. L. DANILOV

I have been asked, in addition to the program, to say a few words about some of the experimental work that has been done by Soviet scientists and engineers and about the work now being done. In the Soviet Union, we have the viewpoint that the possibility of setting up thermionic reactors of a small power output from 5 to 50 kW has been shown and we can already begin to develop such reactors. This development has already been started. For high power reactors there are many difficult problems to overcome, but we feel, that thermionic reactors are promising for the future for space power and for other purposes. For this reason we are carrying out work concerning these high power devices. Work is proceeding along these two lines. On the one hand, we already have some applied research that is directed toward setting up such small power reactors. In addition, we are also studying the scientific and technical problems connected with the high power reactors of a few megawatts of electrical power. These two trends are represented in the papers that have been submitted to the conference, but the high power reactors have not yet been discussed fully.

What particular questions are being studied and how is our work proceeding in the Soviet Union?

First, we are trying to optimize the design parameters of the reactors. We are varying the lattice parameter of the reactors, the diameters of the thermionic elements, the number of elements, the height and length of the core and we are also varying the system parameters. Second, we are studying the heat exchange processes in the reactor and are considering ways to decrease the useless parasitic heat losses. Third, we are trying to estimate the construction variations with respect to neutron physics, taking into account complications of the physical assemblies. Over the past few years we have investigated some 10 model assemblies of different design. Fourth, we are carrying out optimization studies and we are working on a large range of questions, for example, the physical characteristics, the question of compatibility in the reactors, and technological characteristics.

For the time being, we are not investigating very much the cost question.

We are also trying to decrease the fuel content in the reactors and are deter-

mining what the optimum figures will be, by decreasing the number of absorbing substances in the core and by introducing moderators in the core. In the small sized reactors we have not succeeded in getting the neutrons we wanted. But in getting the intermediate energy neutrons, we have had more success. We are furthermore studying the various non-stationary processes which can occur in the operation of the reactor. I'm thinking of the thermal processes, in connection with the heat inertia and also sudden changes of the electrical parameters, that is, the change of the I-V characteristics during operation. The latter is connected with the study of the effect on the device design and on possible failures in the overall system. In this respect we have been studying very carefully the question of reliability, so there will be no failure of the reactor. Our engineers and scientists have been working very carefully on optimizing the programs of ground tests not only with the various parts, but with the reactor as a whole, so with a small number of tests we can obtain reliable objective representative information.

Naturally, we have also been studying characteristics and design possibilities on thermionic reactor elements. Our scientists of the conference have on a number of occasions during the conference drawn attention to the questions why the Soviet Union have not shown the results of their in-pile tests. In this connection I would like to make a comment. We have been carrying out these in-pile tests for over seven years. At the London Conference a summary paper was read and we spoke about the tests in the reactor with the series connected three-element thermionic converter. By that time we had carried out some 10 in-pile tests. Over the past 3 years, we have made more than 15 in-pile experiments. At the present time these experiments are still continuing. It should be pointed out particularly that all these tests are not experiments that can be reported.

Very serious work is being done now according to a specific scientific program. This program is not yet completed, it is still underway. And when the organizing Committee of the Soviet Scientists, belonging to the Academy of Soviet Scientists, selected the papers for this conference, they did not think it was necessary to speak about work that is not yet completed.

Nevertheless, what can be said concerning the final results of these experiments? In our country, the problem was set at the first stage, which was confirming the efficiency, the working capacity of thermionic elements for a test period of 1,000 hours to 4,000 hours. We did not wish to go further

than this time period in the first stage. We think that going by the results of these tests we may consider it demonstrated that small power elements are workable. I'm thinking of electrical power density of 2 to 6 Watts/cm². This working ability has been shown in experiments, using 800 or 1,000 hours or 1,200 hours or 1,500 hours. As I said, there have been 15 of these experiments. Unfortunately, as in the case of the American scientists and among European scientists, many of the experiments in our country were interrupted not because of the thermionic converter, but because of the failures in the experimental set-up; the channels were no longer hermetic in some cases and in other cases there were other problems. However, an examination of the elements that were opened in the hot-laboratories have shown that the emitter and the collector, the connections and insulation elements are in a good condition, work well and could continue to operate. We have also carried out some tests of certain series connected converters in a reactor and we have every reason to believe that for small powers the series connection inside the reactor is fully realistic and workable.

The experimental work on the reactors is being carried out in the Physical and Energetic Institute in Obninsk and also in the Atomic Energy Institute named after I. V. Kurchatov, in Moscow. At the present time we have prepared a number of other in-pile experiments in reactors of the Academy of Sciences of the Constituent Republics of the USSR. As is known, these reactors are very similar in many ways to the Ispra-I reactor. This work is going to get underway very soon and as I already pointed out we have very detailed research plans in view; our scientists and engineers believe in the success of setting up a thermionic reactor of this type.

DISCUSSION

Speaker of invited contribution "Survey of Experimental Work in the USSR":
Yu. L. DANILOV.

HATSOPOULOS (USA): At the beginning of your talk Prof. DANILOV, you mentioned that you work in two areas. Small reactors and large reactors. May be I have misunderstood the translation, but I believe I heard that you said that the small reactors have already been built. Is that correct or did I misinterpret the translation?

DANILOV (USSR): If these reactors were built, then we would be able to tell you of our findings. At the present time we are working on the setting up and the engineering of these reactors and in a few years we shall have our findings to report on.

HOWARD (USA): Could you tell us the general type of design of reactor, both for the small power and for the large power model. In other words do you have one cell that goes the whole length of the reactor, do you have them broken up, do you have the moderator on the outside or the inside; is it a thermal reactor, or a fast reactor?

DANILOV: I could answer the question in this way. The opinion of our scientists is, that a high capacity reactor of a few megawatts could be built only for fast neutrons. In view of the very high temperature, the moderator requires care. At this temperature it is not possible to use a hydride moderator. But we have not yet made our final choice. We are working on several variations for our type of reactor and the neutron physics tests have shown us that a high capacity reactor could be built with a moderator with hydride of several metals, but how this is going to be in practice when you have your working temperature so high we do not yet know.

Now, for the smaller reactor we have not yet selected the type and we are working on several configurations. In this case it appeared that hydrides of different metals can be used as a moderator. We are looking at this case but in practice it has not yet been shown feasible.

HOWARD: The second half of the question was on the geometry of the reactor.

DANILOV: We had considered a reactor the geometry of which would be cylindrical, with the thermionic converters within the core. The cubic type

reported by Dr. NEU we had not thought of, perhaps a failure on our part.

SCHOCK (USA): In your talk you mentioned that during the past year you had carried out neutronic studies on ten model assemblies of different designs. The phrase used is somewhat ambiguous in English, since it could refer either to theoretical nuclear analysis, or to what we call zero-power critical assembly experiments. In which sense did you employ the phrase?

DANILOV: What I had in mind were neutron physical assemblies or mock-ups. And we are modelling with the relevant engineering materials: a critical mass of the fission materials, the structure materials, the moderator, etc. It is not a practical construction, but it has the physical and the dynamic properties of a real reactor. In certain cases we have determined the thermal capacity and the thermal reactivity.

SCHOCK: You mentioned that you had carried out experiments on three-element converter assemblies. Presumably, these used a ceramic insulating layer between the 3 collectors and the outer sheath. Was a voltage applied across this insulator during the tests, or was it merely subjected to the 1.5 to 2 volts generated by the diodes?

DANILOV: The test was performed in-pile, using only the electrical potential as provided by the converter itself. Tests with applied voltage were done out-of-pile. So far as I remember the applied voltage during the out-of-pile test across the insulator was about 50 to 100 Volts.

SCHOCK: Of the 15 experiments you reported in your talk, how many were in-pile, and what fuel compositions were used?

DANILOV: Actually there were more than 15, perhaps 16 or 17 experiments were carried out in the reactor. I do not have the statistical account here. I cannot speak in detail of the fuel composition in each test because, I do not have the relevant information with me. In many channels the fuel was uranium dioxide; but I can not go into further detail about that.

EINFELD (Germany): At the last Geneva Conference on Peaceful Uses of Atomic Energy, you have presented the "Romaska" reactor and I'm wondering whether this reactor is still in consideration for use together with thermionic converter elements.

DANILOV: It is one of the variants of reactors that we are working on, one of several. As I already reported to this distinguished assembly, we have

not yet made our final choice and I stress we have not yet completed the tests. But one of the variants, the one that you mentioned, is one that we have worked on.

VAN HOOMISSEN (USA): In the USA we either contain fission product gases in fuel, vent them into the interelectrode space, or vent them into a cavity. Which method of fission product accommodation is stressed in your work?

DANILOV: We tested and experimented with all the possible variants that you have mentioned. We did not succeed with high temperature to retain the fission products within the cathode. Our scientists think that the fission products should not be allowed to vent into the interelectrode space because even if you vent the cesium mixture into the outer space it does not entirely save the situation. There are always fragments, decay products, fission products that remain in the interelectrode space and change the converter characteristics. We think it is better to eliminate the fission products through the heat conduct elements or through special channels into outer space.

GYFTOPOULOS (USA): In your remarks you mentioned how you will use nuclear fission as a heat source for thermionics. I wonder whether you also are considering radio-isotopes and if so, what is your experience with them.

DANILOV: For a detailed research on this application for thermionic converters, we have had individual interesting tasks that perhaps we could discuss separately, but these results and findings that would be of interest is something we do not have for discussion to-day.

BUDNICK (Germany): For small power reactors you talked about moderated reactors. Was it correct that you are thinking of epithermal reactors, that is reactors which have an epithermal neutron spectrum because they are only low-moderated?

DANILOV: I have already explained that due to the limited dimensions and the high temperatures we were unable to completely moderate the reactor.

RASOR (USA): Are the experiments that you are conducting on the mock-ups as you call them directed towards the large reactor systems or the small reactor systems at present?

DANILOV: This physical experiment concerns a low power reactor.

DAVIS (USA): Have you conducted studies on turbine plants with reactors, RANKIN-cycles and BRAYTON-cycles compared to thermionic plants for

space application and have you reached any preferences at this time.

DANILOV: In the project stage we had considered this but we have no final conclusions. Like the United States of America, we have some who are in favour of turbine reactor generators and some who are in favour of the other type of generators and of the thermoelectric converter type.

PRUSCHEK (Germany): During Session B various thermionic reactor systems have been discussed. Did you take any design under consideration which differs basically from those of Session B? If so, would you please comment on it?

DANILOV: Perhaps we even had thought of a smaller variety than those discussed in Session B. We have concentrated our efforts on the cylindrical geometry reactor with the thermionic element inside the reactor core.

NEU (Euratom): You mentioned the difficulties for the moderator to operate at high temperature. Did you not consider to cool the moderator by a separate cooling system, that is operated at a sufficient low temperature?

DANILOV: Yes, of course we did think of that and many other variants of that too. But you must understand our position. It is necessary to make a first model of this type as simple as possible, and then we can have additional changes. If we want to add separate cooling systems, it is going to make the assembly more complicated and the earth-bound tests we want to carry out would be more complicated, to say nothing of what will happen if we get into space. And we do see very complicated things even with the beginning.

HATSOPOULOS: I would like to ask a clarification. You referred several times to a cylindrical type of reactor. Does it mean a fuel element where segments are stacked one on top of the other? This element we call the flash-light type of element. Is that what you mean by cylindrical?

DANILOV: Yes. Just that. I was thinking that the simplest of all in the first phase would be to have a reactor where the form of the reactor would be a cylinder, the can, and the thermionic elements should be placed axially and would also be cylindrical.

HARBOUGH (USA): Have heat pipes been employed in your experiments?

DANILOV: I would have to say that we thought a low power reactor could be made without using heat pipes. For this reason these heat pipes had not been considered. The work on them is being done separately, from the reactor work. The interesting things we have heard here in Dr. NEU's report, un-

fortunately we had not considered.

VAN HOOMISSEN: In some of your designs do you have single emitter and collector electrodes that run the full length of the reactor core?

DANILOV: Yes. It is one of our ideas, and one of the designs that we are studying. But it is not the only variant. We are very attracted by the one of a multi-converter element, but we are considering and studying that of one element for the whole length of the reactor core.

HANSEN (USA): I understand that 5,000 hours for a maximum lifetime of a converter was reported at London. Is this number bigger, now, three years later?

DANILOV: I had spoken and particularly stressed that our task in the first phase was to study a duration of 1,000 to 4,000 hours. We understand that the further space task will, I'm sure, require 8,000, 9,000, 10,000 and more hours, but our task to begin with was simply in testing 1,000, 1,200, 1,500 hours and then longer tests, but not up to 8,000; we have not had that yet.

UNGER (Germany): Are you using zirconium hydride or lithium hydride in your thermal reactor?

DANILOV: I reported various types of hydrides, hydrides of various metals, including zirconium and lithium.

UNGER: You said that you are studying the "Romashka" type also as a heat source for thermionic converters. Have you made critical tests or power tests together with thermionic converters?

DANILOV: I ought to explain to the meeting that the "Romashka" reactor, which works successfully, is a thermoelectric one, not thermionic. It might be interesting to talk about "Romashka" but it is not the subject of this conference.

SCHOCK: Have you carried out any experiments to determine the effect of irradiation on insulators, and if so what were the results?

DANILOV: Our detailed research concerns the low power reactor where the integral flux of neutrons is 10^{15} to 10^{19} nvt. The radiation effect on the insulator in these conditions is practically non-existent and should not exist, because the ceramics behave well under these flux. When we go up to the high power, 10^{21} and 10^{22} nvt, then of course radiation damage will become a problem.

PANEL DISCUSSION

"Present and Future of Thermionic Energy Conversion"

THE UNITED STATES' THERMIONIC PROGRAM

Remarks by Dr. Gerald F. TAPE, Commissioner US Atomic Energy Commission.

Mr. Chairman, Ladies and Gentlemen,

My one regret is that I was not able to join you at the first of this week. However, I did have a few minutes last night to try to get up to date with some of your discussions. I certainly have been assured, that it has been a most fruitful conference.

I think in the few minutes which I talk to you this afternoon, I would like to address some of the more general considerations, looking at how we in the US are trying to approach the program of the various systems of energy sources, and energy converters and to see where the thermionic system may fit in. To be sure this discussion emphasizes those aspects of the program that we know best and I am sure would be seen differently by other people. However, I would like to assure you as a member of our Atomic Energy Commission that the discussions and the work that will be touched upon here represents a more general position of the government including the AEC, NASA and the other elements of the government involved in these considerations.

The principal remarks will, as we all understand, address to thermionic systems and the coupling of these systems with nuclear energy sources. I'd like to start by noting that several factors can arise which make the use of nuclear power advantageous for a source of energy in space applications. Briefly these are: the lack of sunlight, high radiation fields, high atmospheric drag, high power level, long life and sometimes heat as required for the payload itself. All of these indicate that nuclear sources are indeed attractive and in fact quite necessary for the continuation of a vigorous program in space.

While these considerations present a very attractive potential for nuclear power sources, we must recognize the competition that these systems face. Solar cells, batteries and fuel cells have already gained acceptance in the space community. Therefore it is necessary for the nuclear sources to demonstrate that they are not only competitive but in many cases have a clear-

cut advantage over the systems that are already in being, if these new ones are to gain acceptance.

Most of the experience with the nuclear power systems in space to date have been with isotopic systems, rather than with reactor systems. Several isotopic systems have been flown and some of them are actually still operating. The major disadvantage of such systems tends to be the fuel cost and the development cost in making such systems safe during launch and during re-entry, after use in orbit. Since each of these particular factors becomes more of a problem as the thermal power increases, we presently feel that the isotope systems have an upper limit of around 10 kWe.

There are three reactor concepts that have received primary consideration in our US space electric power program. These are shown in Fig. 1. Across the top of the figure the reactor system are indicated and along the vertical direction, some of the conversion systems which may go with them, are listed. An explanation is needed for the meaning of the solid line box and the dashed line box: the solid lines enclose systems which have received considerable development effort, whereas the dashed boxes are indications of work that is going on, perhaps in other related systems which would have application to these particular systems or reactors. For example, consider the zirconium hydride reactor. As most of you know this is a liquid metal cooled thermal reactor, operating at roughly 1300°F. The conversion systems of immediate interest for this reactor are thermoelectrics, in the 5-30 kWe range, and the mercury RANKINE-cycle, in the 30-70 kWe range. However, as Fig. 1 indicates, this reactor can also be used with other conversion schemes such as the low temperature BRAYTON-cycle and organic RANKINE-cycle systems. For more advanced system concepts, the in-core thermionic system and the liquid metal cooled reactor, coupled to a potassium RANKINE-cycle are listed. These offer very high performance at high power levels and have always been considered as suitable candidates for electric propulsion.

The thermionic system of course offers static conversion with the possibility of series or parallel electric networks for very high reliability. However, as we know from your own work these systems do require very high fuel and emitter temperatures. The potassium RANKINE-cycle on the other hand seems to offer somewhat lower weights in certain classes and the development program utilizes to a greater extent previous engineering experience. However,

we also recognize, that this particular system requires boiling and condensing in zero-gravity conditions. Also, the utilization of the high speed turbo machinery has caused some mission-planners to exhibit concern with the question of reliability. When these two advanced system concepts are scaled down to power levels below 200-300 kWe, some disadvantages arise for thermionics. The fast in-core thermionic system does not retain the favourable specific weight advantage as well as the potassium RANKINE-cycle does. However, there are also problems with the scaling down of the potassium RANKINE-cycle.

I think it is interesting to note that a typical minimum sized thermionic reactor concept which is optimized for specific weight is probably going to be in the 200-300 kWe range. Obviously, we can drop this by reducing the emitter temperatures and by other ways. But this perhaps gets us below a power level where we would like to operate. However, I think that in the power range below this 200-300 kWe we are going to find some programs of prime interest and prime importance over the next several years. I'll try to mention later some of the ideas that we have and that we are looking at with respect to achieving these scaled down units.

Let us consider for a few minutes some of the possible space missions for thermionic power units. In Fig. 2 we list some of the classes of missions and some of the power level requirements. I think that you will agree with me that we are being a little bit speculative on the dates that are listed but in any planning of this kind one has to leave some attention paid to the dates in order to coordinate the progress of the program. I think that there is no question on our part that the power sources we have discussed will play a very significant role in many of the proposed systems, both manned and unmanned. It is not surprising that most of the near-term missions are going to involve the lower power requirement of say up to a several hundred Watts and undoubtedly the thermoelectric systems that use isotope fuels as they are being currently developed, will play a big role in this area. However, I think that in the next few years as the efficiency and the specific weight requirements become more stringent and higher power levels are needed the isotopic thermionic systems will break into the area that may have been dominated at that time by the other systems. The isotope systems, as I'm sure we all recognize, do have some rather difficult problems facing them as they go to higher power densities and higher temperature fuel forms and of course

one has the problem of allowing the helium-venting which is required for the alpha-emitters.

If we look now toward the missions in the mid-70's and later, the power levels get into the few or tens of kW and these tend to point toward the reactor systems as the prime contenders. The only reactor systems as I have indicated earlier, which is under active development in the US and which can supply power in this power range and which will be available at the time period of the mid-70's, is the zirconiumhydride reactor system used with the thermoelectric or the mercury RANKIN conversion systems. I think that you have also heard in this conference that it may be possible to marry the same reactor system to thermionics.

Let us now look at the primary applications for the thermionic systems. These appear to be the group which is in the lower half of Fig. 2, that is, advanced manned stations, TDE-communication satellites, and lunar bases. We expect these to appear in the late 70's and in the 1980's. These missions cover a wide range of power levels. Therefore, the systems chosen must be scalable, or at least the basic technology that would be required should be scalable so we can cover a rather large range of sizes. This we believe is one of the very attractive features of the thermionic system. The manned planetary and the manned electric propulsion missions require even higher power levels, ultimately in the megawatt range. These have been given considerable attention and thought but unfortunately at the present time the date must be shown as a question mark. We do not at this time have a good feeling as to when that date may occur.

I recognize that none of the missions that I have mentioned here have actually been approved or is actually on a firm schedule. On the other hand, we firmly believe that these will come about and that it is our responsibility, to provide the technology and the engineering necessary to meet these requirements in time. This conclusion is, I think, a good one. It says, that both nuclear energy and thermionics together, embodied in both reactor and isotopic systems will play a major role in future space programs.

I'd like to set forth a few of the specifics on the technical program. It should be clear from the presentations this week that the approach we have taken for the last several years in thermionic development has really been to develop the technology which will be required for these future systems. Since the key-part of any future thermionic system will be the fuel element itself,

the development work on such elements has been a main portion of the program. Although reactor analysis and development efforts which parallel the fuel element development have gone forward they have been primarily concerned with fast spectrum reactors, which have a power output equal to or greater than around 300 kW. As I mentioned earlier, however, we are looking for ways which might permit us to decrease this power level. "Derated" systems are being studied in which the minimum critical size fast assembly is operated at a lower emitter temperature or power density. We are also looking at externally fueled converter systems which offer much higher fuel volume fractions. In addition "fast driver" systems have been studied where part of the core is without converters and therefore has a higher fuel volume fraction. Moderated systems are attractive because of past experience in this area. A thermal "driver" concept has been considered in which thermionic fuel elements are interspersed in a fueled moderator. Though each of these is still a contender at this stage, I think the main point to emphasize here is that the basic requirements placed on the thermionic fuel element, namely operation in a completely fast system, are not exceeded and in most cases are relaxed in the various alternatives which have been mentioned for these lower power levels. For this reason our goals in the hardware development program are aimed toward an eventual fast reactor application of several hundred kW and are therefore more ambitious than they need to be to meet the lower power requirements.

We are currently testing diodes of two types, the experimental diodes and the prototype diodes. These are shown conceptually in Fig. 3. In this conference reference has been made to these diodes. Fig. 3 indicates the general progress that one would like to have. The experimental diode is on the far left. These progress to the so-called prototype device which has many of the features that would be found in an actual application. Finally one moves from experimental and prototype diodes into the reference fuel elements themselves and ultimately into some sort of reactor experiment which is undefined but might use any one of the arrangements that has been talked about during this session.

The experimental program has looked at realistic configurations. Detailed test results have been reported at this conference. The primary objectives of the experimental diode program of course have been to look at the fuel/emitter development, life test behaviour and thermionic performance and to consider the improvements that could be made. The prototype diodes on the

other hand have several purposes. They provide testing for more realistic geometrical configurations. They incorporate the components for actual reactor applications and are operated at design temperatures for long periods of time. Again, the progress which has been made has been reported by individual authors. However, in Fig. 4 we have assembled the results of our experience over the last 3 or 4 years. The white dots represent the experimental diodes which have had in-pile experience. We have plotted the operating time in hours as the ordinate. As can be seen there is considerable scatter in the lifetime. On the other hand, you will find that some of the diodes have performed exceptionally well, the two most recent ones in the 1968 period having run for over 5,000 hours and for over 8,000 hours. There are some 36 spots for the experimental diodes on the diagram. The prototype or multi-cell diodes are, on the other hand, indicated by dark spots. The testing is somewhat later in time and has reached, as you notice, something like 2,000 hours at the current reading. This, I think will give you a feeling for some of the experience of our research investigators in this area.

The development schedule for the whole program is shown in Fig. 5. First, let me call your attention to the fact that we have broken the schedule into three phases, the fuel element development, the reactor experiment itself and finally a flight system development which we ultimately would move into at the time of flight utilization of such a system. The primary emphasis at this time of course is on the first step. This involves the building and testing of the experimental diodes, the prototype diodes and the reference fuel elements. You will notice that the upper bar indicates the progress expected in this phase. The major goal of this phase is to achieve satisfactory performance over a 10,000 hour lifetime by the 1970-71 time frame. This should be followed soon by similar performance with the prototype diodes. This work of course leads into decisions which we would want to make with respect to the reactor experiment itself. You will notice that the reactor experiments involve only preliminary design work through the immediate future. This will be followed by the detailed design work after more experience has been obtained with the diode program. Hopefully, after going through construction, fabrication and installation phases, we will have a reactor experiment operating by 1974. Certainly, while this development is occurring, we will be continuing the technology development of the diodes and we would hope to extend lifetimes beyond the nominal 10,000 hours that we have indicated on the chart. Obviously, at this time it is impossible to write down a time scale

for the flight system development. In this case one needs to know more about the particular mission before proceeding with such a specific program.

I think it would be inappropriate to conclude my remarks at this time without discussing some of the factors that will undoubtedly affect the schedules that I have indicated on the chart. Obviously, we are operating in time frames where many changes take place from year to year. Technological developments are necessary but they are not always the entire story which controls a program of this kind. I'm sure I don't have to state to this audience that in any program involving space applications, there are certain aspects of the program that have to come before others. In particular there will have to be decisions as to what specific post-Apollo programs will be authorized and approved before some of the more advanced missions that we have talked about today will be forthcoming. Secondly, I think I should remark that thermionics is a popular subject in these days. There is tremendous interest, not only in this room but in general where there is interest in energy applications and especially energy applications in space.

I think this is due principally to the very excellent progress which has been made in thermionics over the past few years; I don't have to remind you here that there were many sceptics, who first believed that it would be almost impossible, to build one of these diodes, let alone to think about operating it for any useful period of time. But it is the solid progress that has been made so far which must be continued if the thermionic field is to retain the enthusiasm of its supporters.

In all of the space systems and nuclear power systems there is tremendous emphasis these days on reliability, long periods of continuous and uninterrupted operation. Here again the attractive features of thermionic devices are going to have to be demonstrated. We will have to produce high reliability, low weights, high performance, all of the features which will permit us to sell, if you will, the thermionic system most easily.

I think, therefore, that although there are many uncertainties, many questions to be answered, we have a challenging technological development program ahead of us. I am very optimistic that as the technology progresses, enthusiasm for the use of these systems will increase and we will all be seeing applications in space in the not too distant future. Thank you very much.

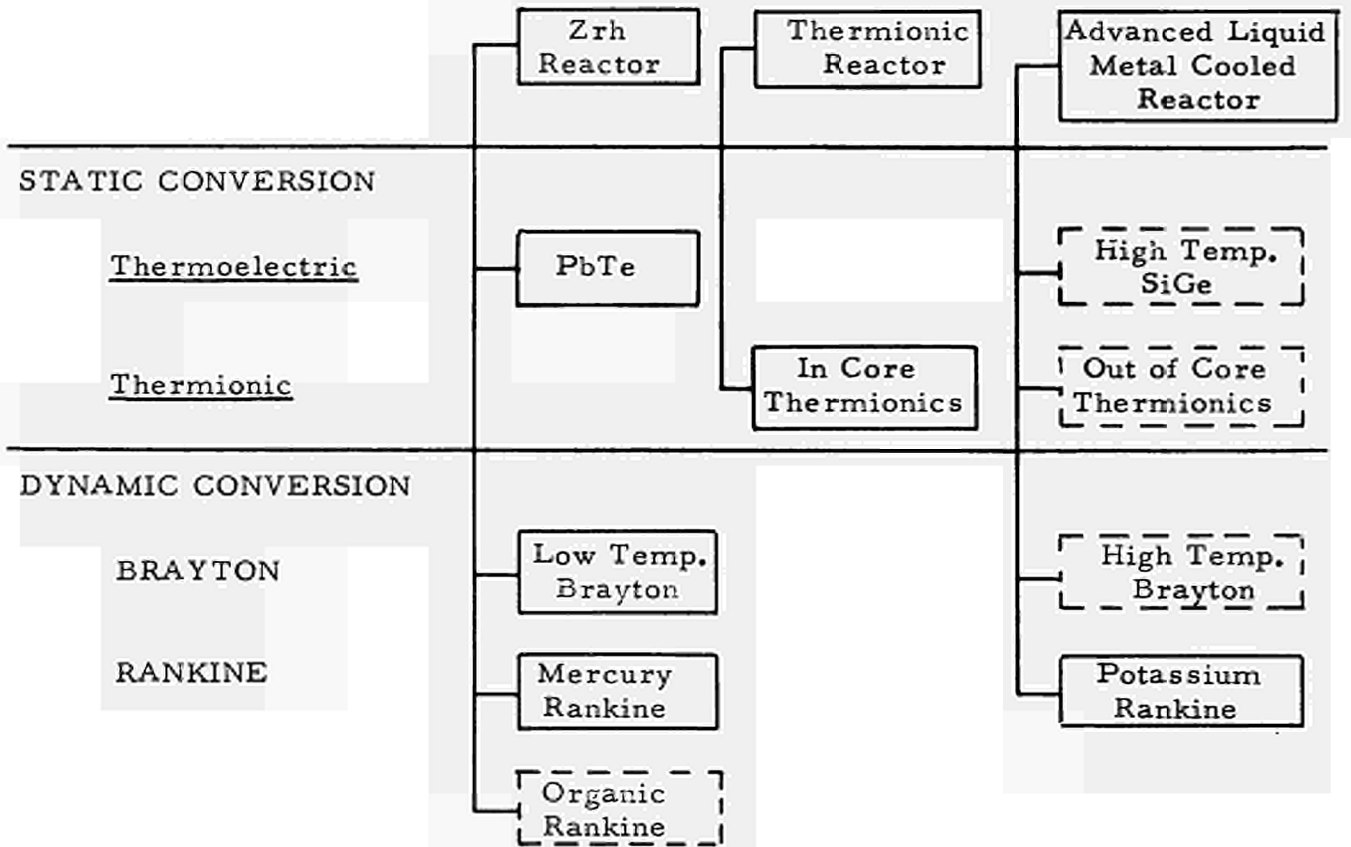


Fig. 1 - REACTOR SPACE POWER SYSTEMS

<u>CLASS OF MISSIONS</u>	<u>PERIOD</u>	<u>POWER LEVELS</u>
Unmanned Probes Experiment Packages Landers	Early-mid 1970's	50 - 150 W 25 - 50 W 100 - 500 W
Early Manned Stations	1970's	3 - 25 kW
Unmanned Elec. Propulsion Advanced Manned Stations TV and Comm. Satellites Lunar Base	late 1970's and 1980's	10 - 300 kW
Manned Planetary Manned Electric Propulsion	? ?	10 - 60 kW Megawatts

Fig. 2 - CLASS OF MISSIONS AND POWER LEVELS CONCERNED

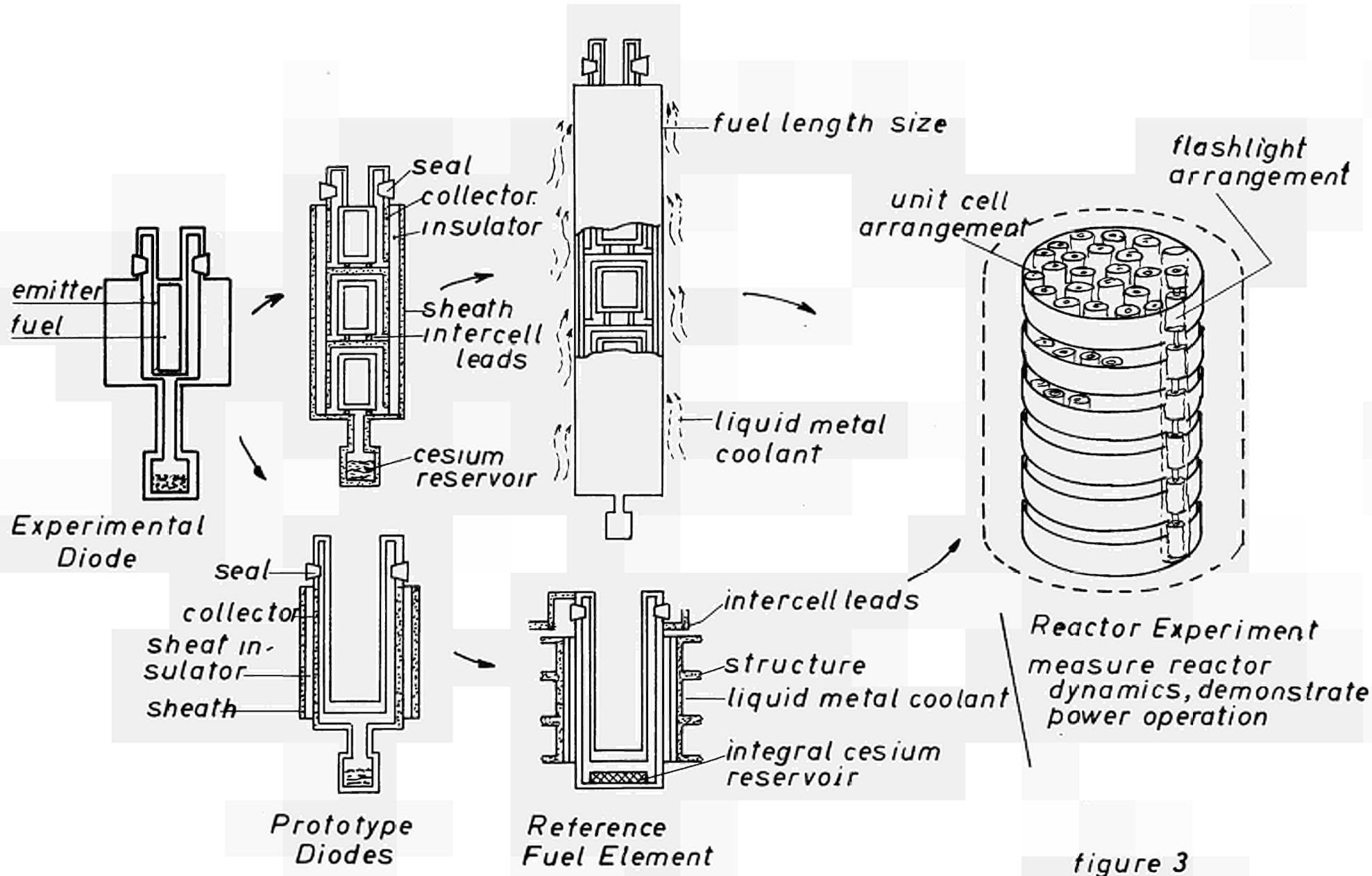


figure 3

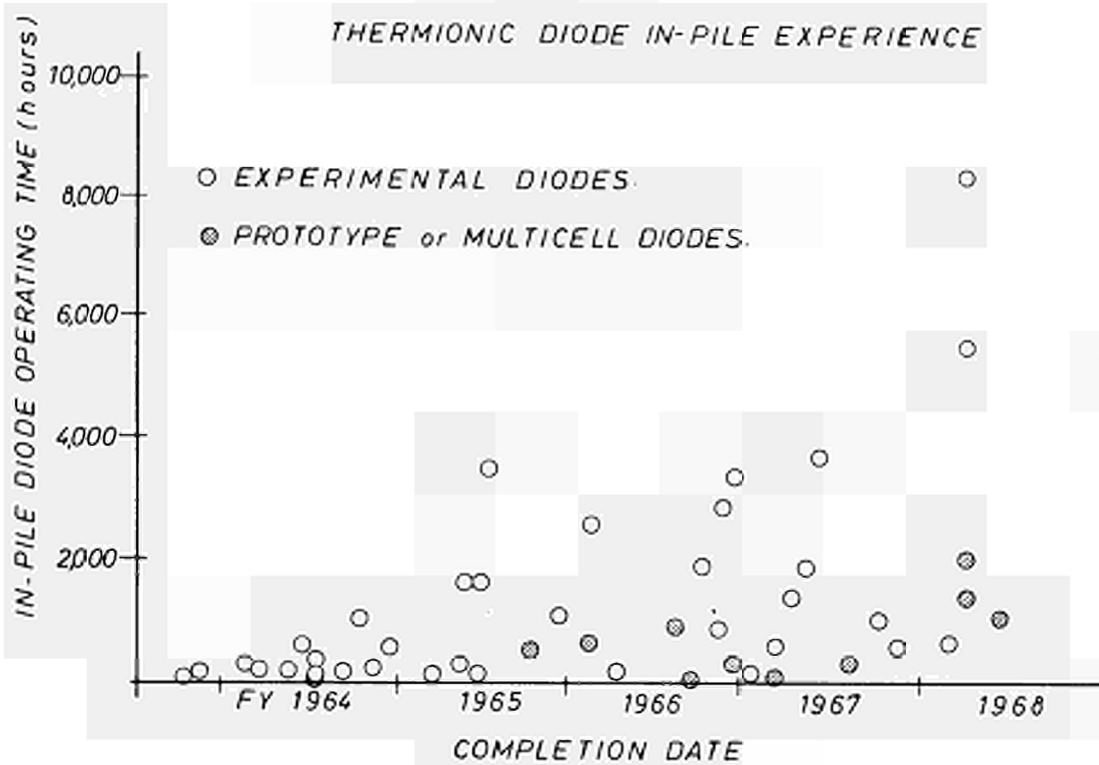


figure 4

THERMIONIC REACTOR PROGRAM

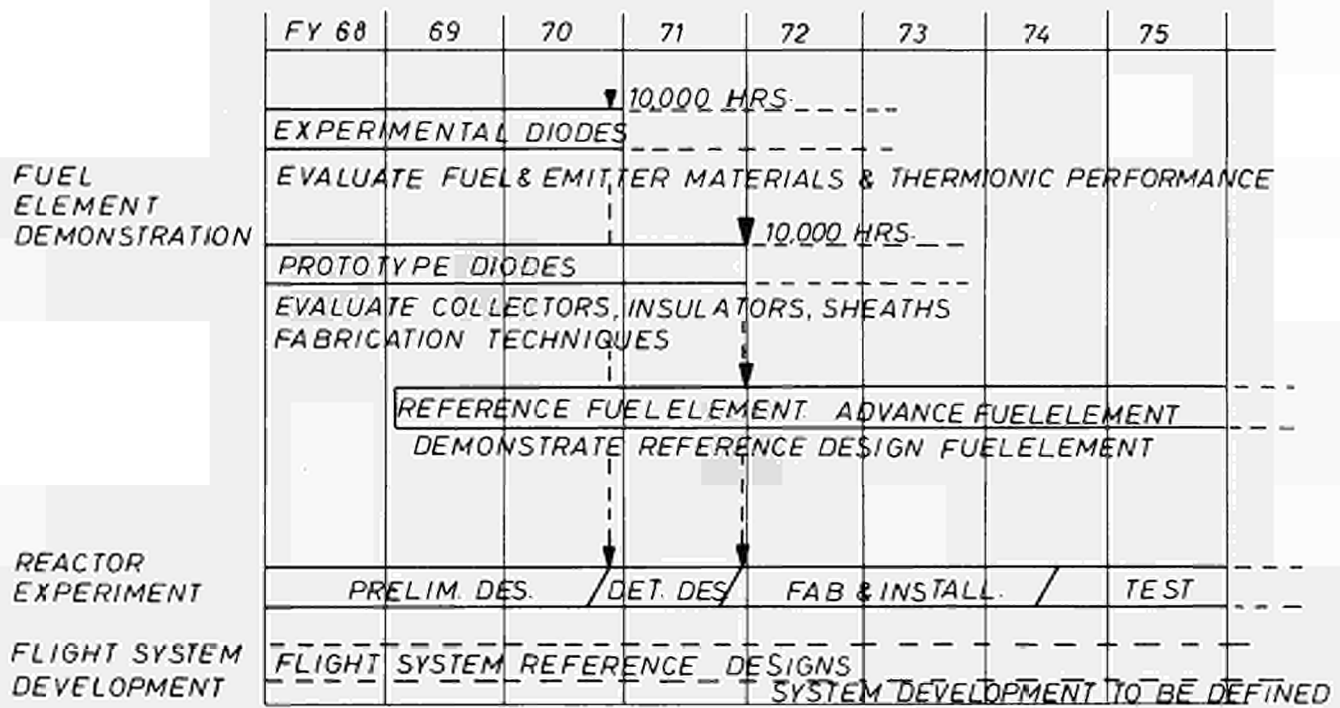


figure 5

APPLICATION OF THERMIONIC ENERGY CONVERSION IN THE USSR

Remarks by Dr. Yu. L. DANILOV, Consultant of the "State Committee for the Utilization of Atomic Energy", USSR.

Mr. Chairman, Colleagues,

I should like, in a short time, to take advantage of this occasion and say how grateful I am to the organizers of the Conference, to the Program Committee and to Dr. NEU in particular, for the enormous amount of work that they have been doing to give us this opportunity to meet and to exchange very valuable information. I would like to thank also all participants for their very active interest. We may hope that this interest will be of benefit to us all for the future. Thank you very much indeed.

After the very exhaustive account of Dr. TAPE it is very difficult for me to add anything. I should like to limit myself to just a few comments.

Some of the considerations concerning programs, do not exist with us. Now with respect to what is happening in the Soviet Union considerable work is being done in the field of thermionic generators. This we have told you about in the papers that have been read here. What are our hopes for the future and concerning the creation of these devices?

Well, I would like to apologize if I talk about things that you are already aware of, but since we are dealing with fundamentals here, I wanted to recall some of them.

First, we are attracted by the thermodynamic advantages of the thermionic converter systems. As you are aware the efficiency in any thermal device, η , is the product of Carnot efficiency η_c and the coefficient η_r , which indicates the deviation of the real situation from the theoretical one:

$$\eta = \eta_c \cdot \eta_r.$$

The Carnot efficiency is given by $\eta_c = 1 - T_f/T_i$, where T_i and T_f are, respectively, the initial and final temperatures of the system. Naturally, in this case, the temperature ratio is of great importance, the higher the maximum temperature in the cycle, the higher the efficiency, all other things being equal.

Of all those systems which are realistic today the thermionic power generating systems have the highest temperature levels. In engineering today (in aviation for example, which is a highly developed industry) the maximum temperatures are confined within a range up to 1500°K whereas in thermionic sys-

tems we can already talk about 1800 to 2200 and even 2500^oK. Of course this advantage is irrespective of other circumstances or variables.

The minimum temperatures are also of importance both for space devices and others. For space application it is very inconvenient to have low temperatures at the radiator. We know that the higher the radiator temperature, the smaller its dimensions and therefore the more convenient it will be. So, these two main advantages lie at the basis of our interest in the thermionic power system.

Another advantage that is no less important and is very promising for the future, of course, is the lack of mechanically moving or rotating working elements. This is very important from the point of view of reliability and rigidity. It is important from the astronautic point of view, since the guidance of space vehicles is thus much easier.

Now, if we look at the power dependence of the specific powers for thermodevices, we obtain a dependence like that shown in Fig. 1.

The comparison for the isotope and reactor systems can be seen in this figure. In our opinion, the region where the two types of systems must be compared is in the power region of 0.5 to 2.0 kWe. For higher power systems the isotopes maintain certain advantages with respect to specific weight but, as has been pointed out, their cost is very high.

This graph, in fact, includes all the existing systems and projects for the future. What is particularly attractive to us is that for both the isotope systems and the reactor systems (though this is still in the blue-print stage) the thermionic devices lie at the higher limit. In other words at the present time they are devices which are the most advantageous in this respect. This is an additional reason for our interest in thermionic systems.

Turning now to the isotope power generating systems, there is a remark that is called for which relates to a number of papers in this conference. We feel that the importance of long lived isotopes such as Plutonium 238 (half-life 86.4 yr) and Curium 244 (12.6 yr) has been overestimated. Why do we think that? At the present time existing systems have an active life from a few months to a year, sometimes a little more than a year. For these systems use of isotopes which are capable of working for tens to even more than a 100 years is not very advantageous, both from the view of economics and from the point of view of radiation safety. Certain unfavorable circum-

stances may arise in operation, in launching, or after re-entry. The consequences of damage can be very longlasting and can be a very serious health hazard. For this reason it would be better to use shorter lived elements which decompose very rapidly. But this is also true from the point of view of economies. As is well known the power of isotope devices can be described by the exponent

$$P \sim e^{-t/\tau}$$

where τ is the half-life. This dependence is shown in Fig. 2.

With longlife isotopes we are essentially working only at the beginning of this power curve. Thus the energy of the isotope actually utilized would correspond to a thin area under this curve such as the cross-hatched area A. Only a small fraction of the isotope energy is used.

In order to illustrate this point in a simple way we may consider that what we need for a particular mission is a constant power P_0 for the mission lifetime t_0 . Thus, in Fig. 2, to achieve maximum power utilization, it is of interest to maximize the square area B with respect to working time t_0 . We find that this occurs when $t_0 = \tau$. In this case the fraction of the energy utilized is thus e^{-1} or about 1/3. Thus we see that from the point of view of power utilization it would be more advantageous to use isotopes such as Polonium 210 (138.4 days) or Curium 242 (163 days). One could think of utilizing power from these isotopes for periods of 200 to 300 days. A problem arises about the regulation of the power at the early stages of work, but we must decide which is more advantageous, to regulate this power or to utilize less than 1/2% of the stored energy.

These are some short observations concerning isotope systems.

Now, I would like to make some comments about applications for thermionic converter reactors. Probably in the years to come these devices can be usefully applied for communication satellites, for television broadcasting covering the whole world, and we may expect that small 50-60 kW devices can be used for meteorological satellites which work at much lower heights than communication satellites. For this purpose it may be difficult to use solar energy. Perhaps a thermionic device or some other device will lead to an increase in weight, but it can be thought that in this region it should be possible to use a small power device of about 50-60 kWe.

We think that our hopes with respect to thermionic converters are justified

and that thermionic power supplies are warranted. I agree with the preceding speaker to the effect that thermionic converters are presently popular and that we shall derive benefit from this. Our present attention to this area of development should make it possible for us to have devices of this type.

Ladies and Gentlemen, these are in brief our views on this subject. Thank you very much for your attention.

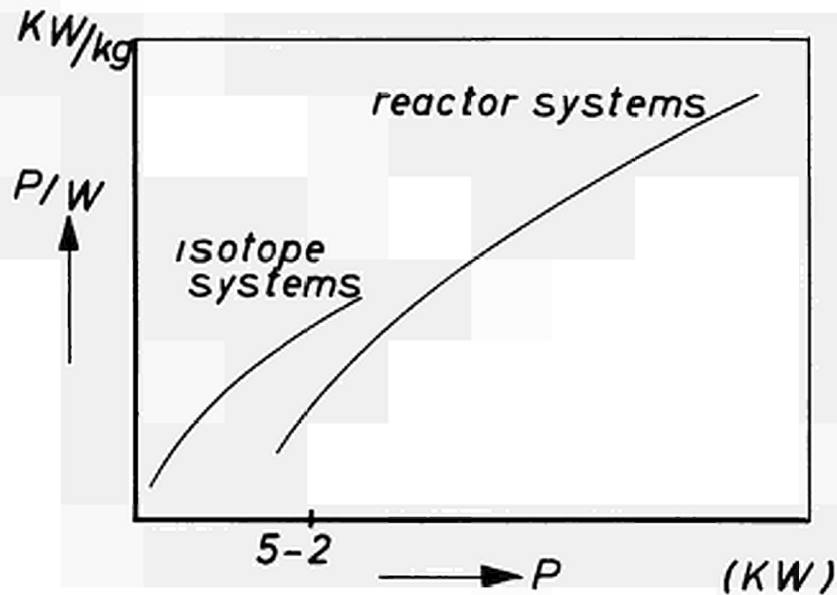


Fig. 1

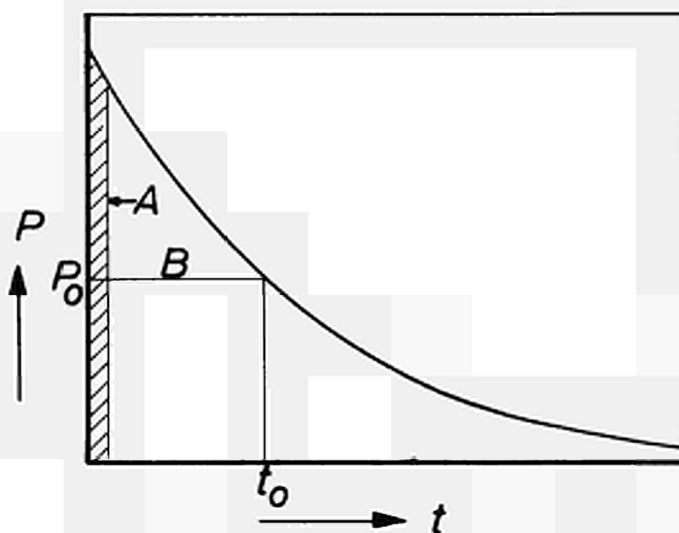


Fig. 2

DISCUSSION

Moderator: Prof. P.D. DUNN, University of Reading (United Kingdom)

Members of the Panel:

Mr. D.S. BEARD, Space Nuclear Systems Division, USAEC

Prof. Yu. L. DANILOV, USSR State Committee for the Utilization of Atomic Energy

Dr. F. GROSS, Head of the Central Research Laboratory, Brown Boveri u. Cie. (Germany)

Dr. G.N. HATSOPOULOS, President Thermo Electron Corporation (USA)

Dr. H. NEU, Head of the Direct Conversion Division, EURATOM, Joint Research Centre, Ispra (Italy)

Dr. G.F. TAPE, USAEC Commissioner

DUNN: Comparing this conference to the one 2 1/2 years ago in London, the first thing that strikes me is the great simplification in the possibilities; the increased confidence and understanding, the reporting of far more hardware and the emergence of specific applications. Taking some of these in turn, and perhaps being slightly mischievous in the sense of overstating, if one considers the heat sources, we seem to have confined ourselves exclusively to nuclear sources, with I think one exception. Do we now agree that solar and fossil heating are not really of prime importance in this subject? Again, the high pressure cesium diode has emerged as the only significant converter. We seem to have dismissed things which used to interest us: binary mixtures, inert gas additives, auxiliary discharges and three electrode devices. Perhaps the Panel would not agree with me, and I hope we will take this up with them. On the performance of the high pressure cesium generator, confidence seems to have increased enormously, the control is much better and one can predict performance and achieve long life. One would like to know what developments to expect, in efficiency, lifetime and power density.

On the physics and theoretical understanding, there still seem to be problems of detailed mechanisms as discussed in Prof. HATSOPOULOS' paper yesterday. On the other hand as Dr. RASOR pointed out, there is a broad understanding of the diodes behaviour now, though there still remains the need for important measurements and one thinks immediately of the papers e.g. of the KURCHATOV and the JOFFE Institutes on plasma properties and surface physics.

Turning to applications, have we dismissed all terrestrial possibilities? At one time we were interested in toppers for power stations. Are these now ruled out, and are there no other terrestrial applications? If this is so and we are restricted to space, then we have various arrangements incorporating thermionic generators which Dr. TAPE has raised and we also have the alternative systems. Since, I suppose, we can describe ourselves as lovers of diodes, we have to look at the latter as the enemy. In the case of unmanned space applications these alternatives are the BRAYTON and RANKINE-cycles, solar cells, and maybe fuel cells. In the case of the manned applications, I think it will be cost that will limit our work, particularly for European countries. It may well be that no single country can produce a manned system and a collaborative program will be necessary,

Turning now to systems we have had interesting discussions on low power systems, including the in-core proposals, by the German workers, the inside-out, or external fuel in-core device and the out-of-core heat pipe extraction system, described by ISPRA and also by LIVERMORE.

An important question is whether there is a cross-over between the in-core and out-of-core and if so where is it. Again one has the question of thermal versus fast reactor. It almost seems to me that one can eliminate the thermal reactor, or perhaps one should say the reactor with moderator since these are intermediate spectrum reactors; at power levels above about 25-50 kW, but I think this is a topic that would be of interest to discuss.

On in-pile testing a tremendous amount of new material has been presented from the USA, France, Germany, Euratom and the USSR. Lifetimes up to 8,000 hours have been mentioned. This clearly shows us what is possible. On the other hand, Dr. TAPE showed on his slide that this was the best of a large number of tests and all the other diodes failed at shorter lifetimes. One is conscious of the large number of elements in a reactor system. This does raise the question of reliability and whether it can be achieved to the degree required.

On materials further work has been reported on compatibility. I think perhaps most interesting is the development in fuels. We still have the contenders, UO_2 , UO_2 -cermet, UC-ZrC. It is not at all clear to me, which one is best and again one would appreciate views on this. On heat pipes we have had the exciting news of the first flight in space of the water heat pipe and I think all of us are very glad to know that it was put up by the father of the heat

pipe, Dr. GROVER, who also reported this interesting double wick development. The ISPRA workers have demonstrated quite extraordinary advances in axial heat flow of heat pipes and have raised the limits from a few hundreds of Watts/cm² to 15 kW/cm². Dr. GROVER remarked that perhaps hundreds of kW per sq. cm. are not impossible and one would like to ask, what is the likely progress in this field.

Those are the points that I noticed. There was one further thing that struck me as particularly interesting, I think because I have always mentally written off the thermionic diode as a low temperature device, and that is the mini-diode. It really is an extraordinary device, 4 milliwatts, 780°K, 0.3% efficiency with the possibility of 3% efficiency at a 100 milliwatts.

The question one asks here is, what is this going to do to the thermo-electric generator, is it really going to compete strongly?

This resumé has probably demonstrated an ability to select the unimportant and ignore the important, but I am sure if this is the case that my colleagues on this Panel will point this out, one hopes, kindly.

So, with your permission I would now start the discussion, by asking Dr. HATSOPOULOS, if he would perhaps care to comment on the point that I put forward, that the only device that is worth considering is the nuclear heated high pressure cesium diode. Does he agree with this, and if so, will he also comment on the likely development possibilities of the efficiency limit, 25%, 30%, 40% or what?

HATSOPOULOS: Thank you Prof. DUNN. I think your observation is very well taken in that, except for one paper or a couple of papers, all of the other papers had addressed themselves to nuclear heated devices and one can raise very seriously the question of whether we, as a group, have abandoned other heat sources.

I don't believe that we have, but there are good reasons why the interest in other heat sources at the present time is not as intense as it was in previous conferences.

Two other types of heat sources were considered in addition to nuclear heat sources; these were solar and fossil fuel heated sources. With respect to solar, considerable work has been conducted and has been reported in the US in previous conferences and the state of the art of such generators has progressed probably far beyond that for any other thermionic generator system.

Right now, however, it appears that solar thermionic devices, although they have some advantages over other solar conversion devices such as photovoltaic systems in terms of being lighter and cheaper to build, have a serious disadvantage of orientation. This disadvantage has been considered to outweigh any potential advantage that you may gain by having a lower cost system or a lighter system. So work in this area in the US, and I believe in other parts of the world, has been reduced considerably and very little is being carried on. So, in this particular case I think that the answer would be that for the time being solar thermionic systems would probably not receive great attention unless, in the future, certain missions, such as solar probes possibly with specific requirements, warrant their use. This could be feasible because of the rather large reservoir of technology that has been built up in this area in such systems. This technology could be picked up again.

As to the second type of heat source, the fossil fuel, it is my personal opinion that this type of electric generation system still has a very vast area of application. Studies that we have made show that such systems for small production of power in the range of 1-10 kW using gasoline or other liquid fuels or gaseous fuels have many advantages over any other type of conversion system, including the internal combustion engine. They are silent, they are much lighter in weight, they are much more efficient than some of the other systems, more efficient than thermo-electrics and almost equal in efficiency as internal combustion engines. Economic studies that we carried out have indicated that they are economical. I think that the reason that so little attention has been paid to such studies in this conference is that there is one big draw-back that has to be solved and this is a materials problem of having a converter be compatible with an oxidizing flame. This problem of course requires the development of a protective coating of a diode in order to enable operation in a flamed environment. Work is being conducted in the States in this direction. Presently, reliable life of only 200 to 300 hours has been achieved although some coatings have shown up to 1,000 hours life. But this is not the level which makes this device practical. We may never develop a coating which will last for a few thousand hours; but, if we do, I think that there would be numerous applications of flame as a heat source.

I'm not going to make any comments on reactors because Dr. TAPE and Prof. DANILOV have made a very good case for their advantages and their

uses. Isotope thermionic systems have considerable future, particularly in space. They have the draw-back of needing a high temperature fuel capsule. Once this problem has been solved, we will have, as was pointed out by previous speakers, a system which is two or three times more efficient than thermo-electric systems which is considerably lighter and has many other operational advantages.

I just wanted to say a few words about the question you raised concerning the present state of performance and what we may anticipate in the future. My estimation is that presently we are approaching the following limits. As far as power density and efficiency is concerned, we can divide converters into two classes: plane converters which allow much closer spacings and the cylindrical converters to be used in reactors that require larger spacing. In the former, some of the papers presented during this week have demonstrated, that 20 W per sq. cm. and efficiencies of over 15% can be attained or approached with great reliabilities. In cylindrical converters, and I am not counting now the fuel, we are approaching power densities of about 10 Watts per sq. cm. and efficiencies of about 15%. How would these numbers change with time is hard to predict. Slow but steady changes are being made by having better emitter surfaces, by crystallographic orientation or by etching and various techniques of this sort. A very steady improvement of both power density and efficiency or conversely in the reduction of the operating temperature at constant power density and efficiency has been achieved; and I expect these improvements to continue. However, I do not believe that with just these improvements we can approach the projected efficiencies such as 25 or 28%, that we had hoped for early in the history of thermionics. There is one hope to keep in mind however. Some of the spectacular performances that have been demonstrated, not reproducible nor longlived, but nevertheless demonstrated occasionally with both electronegative or electropositive additives, show promise that there might be a time in the future when there would be a large improvement in efficiency and power density. When that time will come is very hard to predict because of the great complications associated with the chemistry of all these additives.

GROSS: I would like to comment on your last sentence regarding the future hope for additives. I don't believe that by using polycrystalline emitters you can get better results in performance than you can do by etching techniques. For instance, I don't think that one can get more than 5 eV in work function

using polycrystalline tungsten.

DUNN: There is a question that we might get views on. I'm afraid it is a question of finance but it has to be faced. It is, what do people think about the economic feasibility of a manned propulsion system? What is the order of cost that one must envisage in starting such programs?

TAPE: High.

DUNN: Thank you Dr. TAPE. Perhaps then we could consider the systems. I think that a point that will be rather interesting to raise with Dr. NEU and Dr. GROSS, is what they feel about the relative advantages and disadvantages of in-core, versus out-core in the power range that they are currently considering.

NEU: The situation here in Europe is characterized by the fact that we have no program on manned missions and we will not have, as far as I know, such a program in the near future. Therefore, in Europe, we are not interested in developing space reactors in the megawatt electrical power range as in the USA. We are, however, interested in an electrical power range up to approximately 100 kW or maybe later on several 100 kW, and we have in mind applications like the telecommunication satellites in an advanced stage, television broadcasting and unmanned scientific missions.

What I have realized from this conference is that in the megawatt range, the fast in-core system or a slightly moderated system as reported by the Los Alamos Laboratories, is the most attractive system because it shows the lowest specific mass.

In the lower power range up to a few 100 kW we have a quite different situation. As we have already heard from Dr. TAPE there are inherent problems for scaling down the fast in-core reactor to this power range. Neither the moderated in-core reactor appears to be an ideal solution. In a paper of the Monday afternoon Session, German companies presented a concept of a hydride-moderated reactor, which shows that in the power range up to almost 100 kW electrical power one has to provide a booster zone around the active zone where the conversion system is located in order to reach criticality. In the booster zone heat is generated but no electricity is produced. Since this useless heat must be radiated into the space, the total mass is again increased. Further, we heard about a fast, in-core external-fuel approach and proposals for locating the ceramics outside of the main flux by

using long diodes.

Our studies in Ispra on an out-of-core reactor with heat pipes have shown that it involves no higher specific mass than the in-core system but profits from the fact that the technology of reliable out-of-core converters is already much better established than that of in-core converters. The out-of-core concept avoids many technical problems which occur necessarily in the in-core concept. Surely, it has other disadvantages.

What I would like to say in conclusion is that in the low power range there is apparently not yet a single solution accepted by all as being the best. There are various possible solutions. It is our opinion at EURATOM that it may be quite reasonable to start with the realization of one solution but it is necessary to study other solutions and to work on the development of the key-components of such other systems in order to be in a better position to decide in the future which is the most appropriate reactor in this power range.

GROSS: I agree with Dr. NEU that we should not study only one reactor for the lower power range. As far as Germany is concerned, we have studied several concepts and have found that within the lower power range the out-of-core thermionic reactor types have one big disadvantage. They have no growth potential. But that is only one reason why the German Ministry of Scientific Research now intends to develop and build an in-core thermionic test reactor. There is also the feeling that a decision has to be made to overcome the "requirements merry-go-round", in order to make progress. The second reason is the consideration that the exploration of space will lead to commercial applications. This is in Europe the most interesting field for thermionics. We do not see any commercial benefit in very high powered or manned space systems, which will be very expensive. The development of the reactor type which we propose is directed toward use in broadcasting and communication satellites. Studies have been made on this subject in Germany and they will be reported at the United Nations Conference to be held in Vienna this fall.

The choice of the in-core-thermionic reactor as a power source is based on the following consideration. First, such a system has, as I said before, a growth potential up to 100 or 200 kWe. Secondly, in Germany there is a technology at hand with regard to metal hydride moderated, sodium cooled reactors. I may mention to you that at the research centre near Karlsruhe a sodium cooled 20 MWe reactor will go into operation next year, built by German companies. Thirdly, in our country there exist several development

groups in Universities, in research centres and in industry which have worked for a long time in the thermionic field. Here also a development potential is available, which should be used.

Let me answer some of the remarks of Dr. NEU, concerning our reactor concept. He stated that we are wasting the heat generated in the booster zone, We choose the two-zone reactor deliberately because we want to use it as a testbed reactor. It will enable us to test a large number of thermionic fuel rods. Moreover it is, as close as we can conceive, a first step, toward a reactor which can be used later in space.

One big advantage of this concept is that it can be easily matched to changing power requirements, that is, it has "growth potential". Raising the power output can be accomplished by replacing booster elements by thermionic fuel elements. Therefore, Dr. NEU's remarks about wasting thermal energy naturally do not concern a later space power reactor based on the same concept.

LOEWE (USA): Concerning the question of power limitation on out-of-core systems, let me remark for the record, that the work done to date at the Lawrence Radiation Laboratories shows that for the systems we have considered, the out-of-core alternative in contrast to the in-pile systems, seems to become more attractive as the power level is increased into megawatts and more.

NEU: If I understood Dr. LOEWE correctly, his opinion is that the out-of-core concept is not limited to a certain power range. I have some doubt about this. I have doubts particularly about the realization of the concept proposed by the Lawrence Radiation Laboratory, because of the problem of high temperature electric insulation, that is electrical insulation at the emitter temperature. If one goes to a higher power (more than some 100 kWe) one can not avoid this problem. Therefore my opinion is that the out-of-core concept with heat pipes has a power limitation which is about the same as for the hydride moderated in-core concept, that is some 100 kWe.

LOEWE: That is an excellent point. We have used a beryllium oxide (completely out-of-core) insulator. On the other hand, some of our studies have indicated that if you choose specific mass, kg/kW, as a criterion and eliminate the insulator entirely, going simply to radiant heat transfer, there is only a cost of about 20% in the specific mass.

DUNN: Now, if we could move on to another question on applications, I think it would be most interesting to get the views of the Panel on the competition with solar cells and turbines at low power levels, less than say 10-20 kWe. Would Prof. DANILOV and Mr. BEARD care to say something on this?

DANILOV: In answer to your question, I have already tried to stress our general point of view on this matter. A detailed answer is something we do not have. We do not have the necessary data at this time to allow a comparison to solar or photovoltaic cells. We think that from the viewpoint of purely thermodynamics and efficiency these cells are not able to compete with the thermionic converter. On the other hand it is difficult to judge the complexity of the problem where one requires precise orientation of a mirror. Specialists tell us that adjustments to a second change in angle are required. We consider this to be an extraordinary, complicated task. For these reasons we feel that for these low power densities we should use the thermionic reactor system. And that is what we are working on.

BEARD: I don't think I can add very much to this. It seems that disagreement on which is the best system is a state of affairs which is spread internationally. As was pointed out earlier, the solar cells are already being used in a number of missions quite successfully. They will be good competition on certain missions for quite a few years. As Dr. TAPE also pointed out, these competitors will also not be standing still, waiting for thermionics. I don't think I can add much more to what Prof. DANILOV said. I think we view things pretty much the same way. He mentioned earlier this week that they have advocates of RANKINE versus BRAYTON in the USSR. We also have these two groups in the US.

I would like to go back for just a moment to Dr. HATSOPOULOS' comment on performance. We are entirely satisfied with 15% efficiency. If we can achieve that, systems will be very attractive. At this time if we could build a system utilizing the present state of technology it would be a very interesting system. The added performance is not needed; it would be sugar on the frosting so to speak.

DUNN: I am nevertheless rather uncertain about the solar cell. People have quoted figures like \$ 1,000 per Watt for current cells with predicted extrapolations to as little as \$ 20 per Watt using the cadmium sulphide type cell. Now, providing one is able to stick this enormous umbrella up into space, one is up against very serious competition when one has to justify the cost of de-

veloping a complete reactor system against this very cheap competitor. Would anyone care to make comments?

NEU: One of the questions that have been discussed in Europe is the power limit of such solar cell arrays. Some years ago one could hear limits of approximately 10 kW. Now we have heard that there are studies underway, e. g. in the Jet Propulsion Laboratory which go up to 50 kW. We know very well what the complications are in the performance of our thermionic converters and in making reactors, but we are not experts of the field of solar cells. I would ask if anybody could answer the question, where are the inherent difficulties of solar cell arrays in the power range up to 50 kW?

DUNN: Thank you Dr. NEU. As friends of thermionic converters, we are looking for something wrong with the solar cell. Perhaps either Dr. TAPE could say something about this, or possibly a member of the audience.

DAVIS (USA): There is an active program at the JPL on a 50 kW solar electric propulsion study. The specific weights of the system that people are talking about are remarkably low. Numbers for the solar arrays themselves are in the neighbourhood of 50 lbs per kW. For a total system including the thrusters and tankage, specific weights are about 75 to 100 lbs per kW, that is, per kW in earth orbit. There are certainly problems in deployment, guidance, navigation and control. None of these appear to be untenable at the present time. Interesting missions have been postulated for these systems as far out as Jupiter. So perhaps there really is some competition for thermionics at least for these types of missions. Now, there are certainly classes of missions where solar cells are totally inapplicable: Lander missions, orbiting missions, which require continuous power and classes of missions where orientation simply becomes an untenable situation. Perhaps in those categories there really is no competition from the solar cells in so far as thermionic reactor systems are concerned.

TAPE: I might add one or two remarks mostly in a philosophical vein. This is not the only area of research in which we find competition. Almost anyone who is working in a particular field dear to his heart finds that there are borderline areas that he must watch out for. Too many times in the development of nuclear energy we have looked for the application which is clearly nuclear only, in which we can freeze out all of the competition. There are not very many of these, let me assure you. Some of the early successes in nuclear sources made us so optimistic that we started thinking about certain

space applications as being just prime applications for nuclear sources. That was in the time when we thought of solar cells strictly in the watt-category, but as Mr. DAVIS, and Mr. BEARD have said, solar cells provide a moving target; they will get better. They may get better before thermionics can move down, so philosophically I would tend to worry less about the competition in these cross-over areas than I do in directing our attention to these areas where we have a much clearer mode of application.

I don't want to get into long discussions relating to how low can we go in parallels and compete. I would like to emphasize however, that these large solar arrays and assemblies probably have specific applications and therefore one can not generalize. I know in one of the earlier applications of the solar energy, in which it was necessary to do quite a bit of pannel orientating and we had some disappointments. The orienting mechanisms froze and we wished that we had had more nuclear power available at that time. But these are specific applications that one does not plan on. One does not plan to have the pannel mechanism freeze either. But again, in time one would hope that to be overcome. So I don't think this question does have a universal answer but I would hope that although we look at these cross-over areas we would not lament the fact that the competition is improving too.

RASOR (USA): There is one particular application where a thermionic reactor might be a unique power supply, i. e. having no real competitors. Although I cannot assess the importance of this mission, solar cells cannot provide high powers for long-duration missions in low earth-orbit. If you need say 10-50 kW of power in low earth-orbit, the drag on the solar cell array is so great that the weight of propellant required to keep it in orbit is prohibitive. Now the thermionic system has such a great advantage here over other energy converters because it has a very small radiator area and associated drag cross-section.

I would also like to comment on an entirely different subject. We heard some of the speakers say that we might be able to push efficiency up to may be 25% and other speakers say we don't need 25%. Perhaps this lack of enthusiasm for advances is based on the fact that we are not seeing rapid developments taking place any more in the basic technology such as they did early in the game. In the US I believe, using the dollar as an index, there is a demphasis on research in thermionic conversion. If this were only a change in the relative emphasis on research, with respect to hardware development,

I would not be concerned since that is appropriate in a maturing technology. However, it seems that the total amount of research is diminishing. Therefore, I don't think it should be surprising that the rate of new developments would also fall off in the same way. To say it in another way, if you want to have great improvements in thermionics, you must fund them.

Now in surface physics, the basic work has paid off, and we are actually seeing substantial improvements in converters resulting from that. I think I can say just as certainly that the work in plasma physics has not paid off. We have been spending all of this time in plasma physics trying to find out how the converter works and, as a matter of fact, trying to find out why it works so very well. However, I think we are just now beginning to find out how the spontaneous processes in this simple two-electrode device manage to proceed so efficiently without any basic innovations on our part. Therefore, now is the time to take advantage of this knowledge to improve this raw natural system which is about to be the basis of large expenditures for development of engineering prototypes. So I would like to put these questions before the Panel: Is the role of research diminishing? Should it diminish at this point? Should it be expanding or held constant?

GROSS: May I comment on this with regard to the situation in our country? We feel that we have to do more in the research area. We hope to persuade our government to fund university- and research institutes to do research work in this field.

TAPE: I would like to answer Dr. RASOR. Those of us who live in Washington or in a nation's capital whatever the nation, tend to look at these problems in a slightly different light than you who are in the laboratories. Sometimes, it is referred to as being in the real world and the unreal world, and apparently each of us has his own definition as to which is which.... If one looks at the total support for what is defined as thermionics e. g. in the US, one finds that it has been decreasing over the last few years. On the other hand if one looks at the elements of the program, as supported by different agencies of the government, some have been decreasing, some of them have been increasing. I know, that in our own agency, the Atomic Energy Commission, this subject has been getting increasing attention. As we have appeared before the Congress, to justify and to propose different programs in this area, the thermionics work in my opinion has received very favorable support from our "Joint Committee on Atomic Energy". This is an area in which they have

shown considerable interest. I think this is in no small measure because, as I said earlier, the progress has been good and the promise potential is high. I think that you will all find that the people in the government like to ride a winner. And they believe that in this particular case, that of the future space programs, thermionic programs will play a very definite role.

One other comment. Considering the support received by thermionics in contrast to other programs, one has to make a relative evaluation whereas there is a tendency to view this in absolute terms. Whether support goes up or whether it goes down, we should also observe it in terms of how it is doing in comparison with other systems. I think that those of you who are more intimately acquainted with our program will have to agree that in contrast with some of our other programs thermionics is doing quite well.

HEFFELS (ESRO): I would like to comment on Dr. RASOR's statement that low orbiting satellites are an application where thermionics have an advantage. In this application solar cells will represent a moving target difficult to catch up with by other power systems. Low orbit satellites with a high eclipse ratio are ideal for solar cell arrays with a variable operating voltage. This technique permits a maximum power transfer (e. g. to the batteries) at all temperatures, which is not possible with arrays operating at a fixed voltage calculated for worst operating conditions. The array power utilization can thus be improved by about 30%. Electronic hardware to accomplish this type of operation is being developed in the US.

RASOR: I was referring more to an order of magnitude improvement.

DESTEESE (USA): I would like to add to this discussion the considerations from the system integrator's point of view which apply to the selection of a flyable nuclear power system. Previous speakers have compared the virtues of, in some cases, quite complex concepts based on subtle differences in specific power and efficiency. Given several devices of the same general order of performance the space vehicle designer will not be impressed by small differences in output characteristics. For example, a slightly superior specific weight of a power system would be rendered insignificant by the weight of peripheral structures needed to integrate it into the vehicle. In the real world of system integration the most important criteria are reliability, ruggedness and system simplicity. I think this point has been missed in the previous discussion.

HEFFELS: I would just like to ask the previous speaker if he was speaking for or against thermionic reactors?

DESTEESE: I am for those thermionic reactor designs which meet the selection criteria of the system integrator.

WILSON (USA): I was surprised to hear Dr. HATSOPOULOS say that he thought the limit was 25% efficiency. Perhaps he was thinking in terms of an engineer device rather than in terms of a research device. I still think we will achieve 30% efficiency. In addition, my experience and observation has been that if you can achieve 30% in the laboratory, when you mass produce the device, you can usually do better. This results because in a well engineered device you can control purity things of this sort. So I think that the future is much more brighter than the Panel has indicated, at least in terms of efficiency and output power. When we do get to the higher efficiencies and the high power, I think we will begin to look at the possibility of using thermionic converters as topping devices to other power systems like steam turbines and central station power plants.

HATSOPOULOS: I would like to make a few remarks relating to several questions what were raised by Dr. WILSON and Dr. RASOR.

First of all, let me say that I agree with Mr. BEARD that 15% efficiency is adequate for the systems that we are considering now; and it is certainly adequate to warrant the development of a reactor. In fact, I will go further; even if our efficiency were only 10% it probably would be adequate as well, so that is not the point. I think, however, that the higher efficiency at which we are operating the systems, or the higher the power density that we are obtaining from the converters at a given temperature, or conversely the lower the temperature will get for a given performance, a great variety of applications will open up. For example, there is no question that the out-of-core becomes more attractive as you lower the emitter temperatures.

Many other systems that Dr. WILSON pointed out will come within the realm of application of thermionics if the efficiency were higher. Therefore, although we have something adequate for some application, there is a tremendous incentive to get better performance; and, in that light, I would like to support the point of Dr. RASOR by saying that more research and more understanding will lead to better performance. Not directly do I think that we will ever come to the point where one equation will show us how to make a converter more efficient or how to make a break-through in converter per-

formance. I don't think that this is going to happen. However, break-throughs of this type occur because of invention; and invention takes place when you start understanding things. Therefore, through the process of research and understanding, the converter will lead us into more intuition, not something that ties to any particular equation or any particular theory, but the totality of equations and theories and discussions will lead to a better understanding which will result in significant progress. I agree with Dr. WILSON that we are still quite far from exploiting the full potential of converters. I would still stick with my 25% simply because there is a difference in the definition of efficiency and because I am talking more of an efficiency relating to a system than is Dr. WILSON. But, essentially, I second the previous speakers on this subject.

DUNN: It was my intention to give a summary of the proceedings but I think instead I will merely say that clearly there is enough meat left in this subject to justify another international conference, and I will not attempt to give a survey at this time. I would like to thank on your behalf our distinguished contributors, Dr. TAPE and Prof. DANILOV and also the member of the Panel, Drs. NEU, GROSS, HATSOPOULOS and BEARD and also to thank Mr. ROUKLOVE for standing in to help us with the translations.

We will close the final session of the Panel Discussion. I would like to ask the Chairman of our Organizing Committee, Dr. NEU, to say a few words.

Dr. NEU thanked all contributors and participants of the Conference, interpreters and technicians and especially for the assistance of Mr. ROUKLOVE in English-Russian translating of special items.

Prof. DUNN, in turn, thanked Dr. NEU on behalf of the conference attenders for his efforts which have contributed to a successful, informative conference.

AUTHOR INDEX

A

Abbate, M.J., B-6, F-3
Akhurst, D.O., J-6
Albrecht, H., H-13
Alleau, T., K-9
Andrae, H., B-1
Arkin, E.S.A., E-15, F-7
Armand, M., D-7

B

Babina, F.L., K-3
Bacal, M., A-13
Bähr, A., D-6
Baksht, F.G., J-1, J-2, J-4
Barabash, M.B., H-15
Baranov, V.I., A-6
Barishnikov, G.A., A-12
Batzies, P., K-5, K-11
Beleytsev, A.T., A-12
Belomytzev, Yu. S., K-3
Belyanina, R.G., E-9
Blatoy, D.A., A-6
Blet, G., A-4
Blieaux, J., A-11, C-5
Bohdansky, J., H-2, K-2
Bondarenko, V.D., H-3
Bondarenko, V.L., E-9
Borisova, A.A., E-9
Borzenko, V.L., H-5
Brabers, M.J., B-13
Budnick, D., B-1
Bundschuh, V., K-4
Burck, E., D-6
Burgess, E.L., J-6
Busigin, E.P., H-15

Busse, C.A., D-2, E-5
Bykov, V.N., E-18

C

Cahen, O., A-4
Campbell, A.E., A-9
Cappelletti, C.M., E-5
Chaney, M.C., C-4
Chekhovich, V.S., E-15
Cherepanov, P.Z., E-15, F-7
Chernukhina, G.M., F-5
Clémot, M., A-11, C-5, E-12, E-17
Cristescu, M., A-13

D

Dagbjartsson, S., B-2
Danilov, Yu.I., E-11
David, J.P., J-9
Davis, J.P., B-7, B-10
Defranould, Ph., A-3, K-14
De Jonghe, P., B-13
Demny, J., K-5
Derbilov, V.I., H-8
Desplat, J.L., K-9, K-14
DeSteese, J.G., B-15
De Troyer, A., B-13
Devin, B., A-14, C-5
Diakov, B.B., F-10
Djuzev, G.A., J-1, J-3
Dmitrieva, I.B., K-3
Doncev, T., H-17
Dörre, E.A., E-5
Drobjazko, L.A., H-5
Drobjazko, S.V., H-5

Dumas, P., C-5
Dumont, F.P., K-10
Dunlay, J.B., B-12, C-2, E-7
Durand, J.P., A-11, C-5, E-12,
E-17

Dvinakikh, Yu.V., E-9

E

Eisen, C.L., B-6
Eliseyev, V.B., A-12
Emendörfer, D., B-2
Ender, A., G-9
Esnaud, S., E-6

F

Fiebelmann, P., B-8
Fitzpatrick, G.O., E-20
Floret, F., J-9
Frolov, A.V., E-18
Fustie, G., E-17

G

Gammel, G., B-13
Gasper, K.A., B-15
Gayte, B., A-11
Gebhardt, E., E-19
Geiger, F., D-2
Gietzen, A.J., B-5
Glas, D., J-8
Gorancev, B., H-17
Gorban, Yu.A., E-18
Gorelov, I.N., E-9
Grigoryjants, V.G., H-15
Groll, M., B-2
Gronroos, H.G., B-7, B-10
Gross, F., B-1, B-13, C-6, C-7
Grover, G.M., D-1
Guskov, Yu.K., H-3

Gutshin, G.I., F-5
Gverdtsiteli, I.G., H-10, H-11, H-12
Gyftopoulos, E.P., K-1

H

Hansen, L.K., G-1
Hasson, R., E-21
Hatsopoulos, G.N., K-1
Haug, W., B-2
Heath, C.A., B-5
Henne, R., E-10
Hill, P.R., B-3, F-1
Hoffmann, W., J-7
Holick, H., C-6
Holland, J.W., C-3
Homeyer, W.G., B-5
Hotslag, D.J., C-1
Howard, R.C., B-11, B-12, C-2
Hudson, R.G., E-1, E-2
Hübner, H., E-14
Huet, J.J., E-16
Hufschmidt, W., D-6

I

Ievleva, J.I., E-9

J

Jacquin, B., E-17
Jahns, W., B-1
Janner, K., B-1, E-14
Jensen, A.O., A-9
Jester, A., B-1, C-6
Josso, E.R., E-12

K

Kaplan, V.B., J-1, J-3
Karakhanov, V.Ja., H-10, H-12
Karetnikov, D.V., H-8

Kassikov, I.I., G-7
Kay, J., C-3
Keddy, E.S., D-1
Kemme, J.E., D-1
Kluge, W., K-7
Knizhnikov, V.N., H-5
Kolmakov, A.P., F-5
Kolobkov, Yu.G., K-3
Kondratiev, F.V., H-6
Korolev, A.A., E-18
Korolyov, A.A., E-9
Koshkin, V.K., E-11
Koskinen, M.F., B-13
Kosyrev, F.K., H-7
Kosyreva, N.P., H-7, H-8
Kraft, G., D-2
Krapf, R., C-6
Kucherov, R.Ja., H-9, H-10, H-11,
H-12
Kukushkin, S.F., E-15
Kunkina, A.D., E-9

L

Langpape, R., B-13, K-12
Latouche-Halle, A-8
Lebedev, V.F., A-12
Lidorenko, N.S., A-12
Lieb, D., A-1, H-16
Loewe, W.E., B-9
Loshkarev, A.I., A-12
Lunev, E.I., H-7
Luppov, A.N., F-7

M

Maly, R., K-7
Malykh, B.A., E-9
Malykh, V.A., E-18, K-3
Martzinovskiy, A.M., J-1, J-3

Mauries, J., K-10
Maximov, N.P., E-9
Mayer, R., H-4
Medunov, S.D., A-12
Mikhailova, T.V., E-11
Mikheev, Yu.S., E-11
Minor, A., K-12
Moizhes, B.Ya., J-1, J-2, J-3, J-4
Mosevitsky, I.S., F-4
Moskaleva, Yu.I., K-3
Muchnic, G.F., A-6
Mukhin, I.P., E-18
Murinson, H.A., E-15, F-7
Musa, G., H-17
Muz, E., K-13

N

Nakonechnikov, A.I., E-18
Nastojashchy, A.E., H-9
Nastojashchy, A.F., H-8
Nemchinskiy, Y.A., J-2, J-4
Neu, H., B-8
Neye de Mevergnies, E., B-13
Neveshin, O.E., A-6
Nevzorov, B.A., E-18

O

Oganezov, Z.A., H-10
Oglobin, B.G., E-15, F-7
Ondracek, G., E-19
Orlin, S.A., E-11
Orlinov, V., H-17
Ostapov, M.L., A-12

P

Patrick, A.J., C-4
Pavlinov, L.V., E-18
Peehs, M., E-4, E-8, E-14

Pereslavitsev, E. B., F-5
Pikus, G. E., J-3
Pöttschke, M., D-2
Prilezhaeva, I. N., K-3
Privalova, M. M., K-3
Protsenko, B. P., A-12
Pruschek, R., B-2
Pumpurs, V. M., K-3
Pupko, V. Ya., F-5

R

Raab, B., B-6
Ragot, P., A-14
Ranken, W. A., B-4, C-4
Rapp, H., K-7
Rasor, N. S., B-15, G-8
Reiss, F., D-3
Rinaldini, C., B-8
Röhrborn, B., B-2
Rouklove, P., A-5
Rubanovich, I. M., A-6
Rufeh, F., A-1, H-16
Ryabikov, C. V., A-6
Ryabikov, S. V., A-12

S

Saggau, B., G-4, H-13
Salmi, E. W., B-4
Saratov, I. M., E-9
Saratovskii, L. N., K-3
Savitzkii, E. M., K-3
Sawyer, C. D., B-3, F-1
Scherbinin, P. P., G-12
Schindler, M., H-4
Schmid, H. E., K-5
Schmidt, E., D-4, E-19
Schock, A., B-6, F-3, F-12, G-11

Schörner, H., E-8
Schretzmann, K., D-3
Schwarzer, D. E., C-3
Segurens, L., E-12
Semeria, R., D-4
Sewing, K., J-7
Shahnasarova, G. A., J-1, J-3
Sharov, V. P., E-9
Shatalin, A. S., E-18
Shimada, K., H-18
Shroff, A. M., A-10, D-7, E-3, E-6
Shyahkin, B. B., K-3
Silin, L. L., A-12
Sinyutin, G. V., H-6
Sluyter, M. M., B-16
Smirnov, A. A., K-3
Solomonov, N. E., K-3
Sonin, E. B., G-2
Spyvak, G. V., K-3
Stakhanov, I. P., G-7, G-12
Steehle, H., E-4, E-8, E-14
Stefanov, B., A-7
Stojanoff, C. G., J-7
Strecker, H., G-4, H-13
Strub, H., D-2
Subbotin, V. I., F-5

T

Tagami, T., E-1
Thivellier, D., K-6
Tilkina, M. A., K-3
Tkeshelashvili, G. I., H-11, H-12
Tourneyan, K. J., B-16
Truchevsky, S. N., A-6
Tsiberev, V. P., H-12
Tskhakaya, V. K., H-10, H-11, H-12
Turundajevsky, V. B., H-8

U

Unger, H., B-2

V

van Andel, E., D-5, H-2

van Geel, J., E-16

van Hoomissen, J.E., C-1

van Someren, L., A-1

Voci, C., A-13

W

Warner, C., G-5

Webster, H.F., K-8

Wilkins, D.R., B-3, F-1

Williams, E.W., B-11

Wilson, V.C., A-2

Wolf, E., H-4

Y

Yakovleva, D.D., E-9

Yang, L., E-1, E-2

Yates, M.K., C-3, E-20

Yavor, I.P., H-15

Yurev, Yu.S., F-5

Yuriev, V.G., J-1, J-3

Yurin, E.M., A-6

Z

Zakharova, M.I., E-18

Zarcova, L., A-7

Zasorin, I.P., E-9

Zöller, R., C-6, C-7

CDNA042102AC

